

Sunday Afternoon, October 27, 2013

Biomembranes and Emerging Tools in Bioscience

Plenary Session

Room: 201 B - Session BP+AS-SuA

Biomembranes and Emerging Tools in Bioscience

Plenary Session

Moderator: P. Kingshott, Swinburne University of Technology

3:00pm **BP+AS-SuA1 A "GoogleMAP"-type Molecular View of Microbes and Biofilms - From Culture to People, P.C. Dorrestein, University of California San Diego** **INVITED**

The world is covered in one large biofilm. The molecules the microbes produce affect all areas of biology—from crop growth to the balance of health and disease in humans. In this presentation we highlight the spatial analysis of molecules and mapping of structural space through molecular networking using a variety of mass spectrometry and informatics methodologies. We will show its applicability to understanding the molecular nature of interacting microbes grown in Petri-dishes all the way to interacting microbes on people. In effect we are beginning to lay the foundation to create a "GoogleMAP" for our molecular understanding of microbes.

4:20pm **BP+AS-SuA5 Tools for Organisation of Proteins on the Nanometer Scale, G.J. Leggett, University of Sheffield, UK** **INVITED**

The organisation of proteins on biologically relevant length-scales – tens of nm – remains challenging. Protein molecules present substantial problems because of their tendency to become rapidly and irreversibly adsorbed onto many surfaces, and their propensity for post-adsorption conformational change. On nanometre length-scales, where characterisation of structures remains difficult, any problems associated with non-specific adsorption, or with ineffectual control over protein binding and orientation, are exacerbated. Our goal has been to integrate top-down and bottom up fabrication methods to yield robust, repeatable routes to the fabrication of protein nanostructures. We have developed a suite of photochemical routes to molecular nanopatterning. Near-field techniques may be used for the fabrication of arbitrary patterns in regions tens of micrometres in size, and interferometric methods yield periodic structures over square cm areas in fast, simple, cost-effective processes. Oligo(ethylene glycol)-derivatised nitrophenyl protecting groups have proved to be highly effective at eliminating non-specific adsorption, and may be readily deprotected to yield amine groups that can be coupled to biotin or nitrilotriacetic acid for site-specific immobilisation of proteins. UV photodegradation may be accomplished in a variety of ways – by direct degradation of oligoethylene glycol functional groups to yield reactive aldehyde functional groups in a single step; by unzipping of methacrylate brushes; by dehalogenation of initiators for atom-transfer radical polymerisation; and by localised photocatalytic lithography to yield 50 – 70 nm protein structures that may be readily imaged by confocal microscopy. Finally, simple photochemical methods also provide routes to the fabrication of polymeric and metallic nanostructures (for plasmonic readout) for use in fundamental studies of membrane protein organisation and function.

5:00pm **BP+AS-SuA7 Surface-Specific Sum-Frequency Vibrational Spectroscopy, Y.R. Shen, University of California, Berkeley** **INVITED**

Infrared-visible sum-frequency generation has become a most powerful and versatile spectroscopic tool for surface and interface studies in recent years. It is based on the simple idea that surface and bulk of a material generally have different symmetries. The technique has many advantages over other probes: it is highly surface-specific, has high spatial, temporal and spectral resolution, is capable of remote sensing and probing surfaces in hostile environment, and most importantly, can be applied to any interfaces assessable by light. Consequently, it has opened many new opportunities for investigation of surface and interface properties and processes in various disciplines.

In this talk, we shall give a brief review on the recent development of sum-frequency vibrational spectroscopy. We shall describe how the technique can be used to probe surface and interface structures of neat materials from their surface vibrational spectra. Water interfaces will be presented as examples. Future prospects will be discussed.

Monday Morning, October 28, 2013

Actinides and Rare Earths Focus Topic

Room: 102 C - Session AC+MI+SA+TF-MoM

Actinides and Rare Earths: Experiment and Electron Correlation

Moderator: T. Durakiewicz, Los Alamos National Laboratory

8:20am AC+MI+SA+TF-MoM1 Our Understanding of the Condensed-Matter Physics of Actinides: What have we Learned in 50 Years?, G. Lander, ITU, Karlsruhe, Germany **INVITED**

By 1950 the Manhattan Project and the early nuclear industry had a large legacy of new materials that were poorly understood from a physics perspective. The physics of uranium and plutonium are good examples.

By the mid-1960s progress had been made in applying many physical techniques (many of which, such as sensitive transducers to measure elastic constants, had also been a development of WW II) on the actinide elements and many of their compounds, particularly the simple dioxides. Most theoretical treatments considered the elements and their metallic compounds within the framework of *d* transition-metals, as many properties seemed to follow these metals, rather than those of the *4f* lanthanide series.

By the mid-1970s the group at Argonne National Laboratory had shown, *inter alia*, that a large orbital moment existed in the actinides even if many properties followed itinerant-electron behavior, and the first band-structure calculations showed how difficult it was to resolve this dichotomy.

The discovery of so-called heavy-fermion superconductors, such as UBe₁₃, at Los Alamos National Laboratory in the early 1980s brought considerable prominence to the field and was a precursor, although not recognized at the time, to the discovery of high-T_c materials in 1986. The further discovery (in 2001) of superconductivity at 18 K in PuCoGa₅, also at Los Alamos, shows the key importance of the electronic ground state of the *5f* electrons and how this drastically affects the physical properties.

Theory has always been “behind” experiments in the actinides; however, the experimental results have proved a sensitive test to the most advanced electronic-structure calculations, such as dynamical mean-field theory (DMFT) within the local-density approximation, so that in some respects the actinides have become a “test bed” for the newest theoretical models.

60 years after some of the pioneering condensed-matter experiments on these materials, we have a far better picture of the actinides, the importance of the orbital moments, the relevance of intermediate coupling, and the criterion that determine whether the *5f* states behave as localized or itinerant. However, we do not have *predictive* theories – they are all *reactive*. This implies that we still need to maintain an experimental capability, as these materials will be with us a very long time, even if we abandon nuclear energy.

The challenge today is how to maintain and nurture that experimental capability in a climate where even depleted uranium is regarded with suspicion and its handling demands kilograms of paperwork? Without experiments will theory follow?

9:00am AC+MI+SA+TF-MoM3 5f Electron Localization, J.L. Smith, Los Alamos National Laboratory **INVITED**

The light actinide elements show a large number of crystal structures and low-melting points. At the element americium, this *5f*-electron series finally settles down and looks like the rare-earth series. This occurs because the *5f* electrons have ceased to form energy bands and have localized. The superconductivity of americium proved this. I will review how the tug of war between itinerant and localized behavior leads to all of the interesting properties and touch on such things as quantum critical points. This has impact on the understanding of the other long rows in the periodic table.

9:40am AC+MI+SA+TF-MoM5 Historical Aspects and Perspectives of X-Ray Spectroscopy in Lanthanide and Actinide Materials, G. Kaindl, Freie Universität Berlin, Germany **INVITED**

The talk addresses some aspects in the use of tunable x-rays in studies of electronic and magnetic properties of lanthanide and actinide materials by x-ray absorption fine-structure (XANES) and resonant elastic x-ray scattering (REXS), emphasizing related features of these *4f* and *5f* materials.

Based on early applications of L- and M-edge XANES to lanthanide valence studies, the method was applied to U and Th compounds, exploring XANES at various thresholds (L, M, N, O) [1], and then to the more

radioactive actinides Np, Pu, and Am as well as to high-pressure studies. Subsequently, the method has been improved both experimentally (e.g. high-resolution XANES [2]) and theoretically [3], and even compounds of Pa, Cm, and Cf in solid and aqueous environments have been investigated by now.

Resonant magnetic x-ray scattering was first applied to Ho metal, where the magnetic scattering cross-section is enhanced by a factor of 50, when the x-ray energy is tuned across the L_{III} absorption edge of Ho [4]. Subsequently, much larger enhancements up to 5 magnitudes were observed at the M_V edges of U in UAs [5] and of Eu in the antiferromagnetic (AFM) semiconductor EuTe [6]. In the latter, an epitaxial thin EuTe(111) film was studied, and virtually background-free magnetic Bragg-peaks with pronounced Laue oscillations were found. From these, the AFM order in the EuTe(111) film could be derived with atomic-layer resolution. The magnetization of the outermost layer was found to decrease significantly stronger with temperature than that of the bulk layer [6]. In a further pioneering experiment that employed a synchrotron slicing source for the production of tunable soft x-rays with pulse widths as short as 100 fs (probe pulses) and synchronized pump pulses of 400 nm wavelength, the dynamics of the AFM order could be studied by fs soft x-ray diffraction [7].

References

- [1] G. Kalkowski, G. Kaindl, W. D. Brewer, W. Krone, Phys. Rev. B **35**, 2667 (1987).
- [2] J.-P. Rueff, S. Raymond, A. Yaresko, D. Braithwaite, Ph. Leininger, G. Vanko, A. Huxley, J. Rebizant, N. Sato, Phys. Rev. B **76**, 085113 (2007).
- [3] J. G. Tobin, K. T. Moore, B. W. Chung, M. A. Wall, A. J. Schwartz, G. van der Laan, A. I. Kutepov, Phys. Rev. B **72**, 085109 (2005).
- [4] D. Gibbs, D. Mills, C. Vettier, Phys. Rev. Lett. **61**, 1241 (1988).
- [5] S. Langridge, W. G. Stirling, G. H. Lander, J. Rebizant, Phys. Rev. B **49**, 12010 (1994).
- [6] E. Schierle, E. Weschke, A. Gottberg, W. Söllinger, W. Heiss, G. Springholz, G. Kaindl, Phys. Rev. Lett. **101**, 267202 (2008).
- [7] K. Holdack, N. Pontius, E. Schierle, T. Kachel, V. Soltwisch, R. Mitzner, T. Quast, G. Springholz, E. Weschke, Appl. Phys. Lett. **97**, 062502 (2010).

11:00am AC+MI+SA+TF-MoM9 High Energy Resolution X-ray Spectroscopy of f-electron Systems, K.O. Kvashnina, European Synchrotron Radiation Facility (ESRF), France, J.G. Tobin, Lawrence Livermore National Laboratory

This contribution will provide an overview of the possible spectroscopic techniques and experiments that become available for f-electron systems using high energy resolution X-ray emission spectrometer^[1]. As an example we will show the studies of the electronic structure of cerium (Ce) and uranium (U) nanostructured materials by means of high energy resolution fluorescence detection (HERFD) and resonant inelastic X-ray scattering (RIXS) via transitions between core levels and between core and valence levels^[2-5]. The experimental spectral features will be characterized using a variety of theoretical codes including the LDA+*U* approximation within DFT^[6], atomic multiplet theory^[7] and full multiple scattering FEFF^[8].

References:

- [1] P. Glatzel, T.-C. Weng, K. Kvashnina, J. Swarbrick, M. Sikora, E. Gallo, N. Smolentsev, R. A. Mori, *Journal of Electron Spectroscopy and Related Phenomena* **2012**, 2-10.
- [2] K. O. Kvashnina, S. M. Butorin, P. Glatzel, *Journal of Analytical Atomic Spectrometry* **2011**, 26, 1265.
- [3] A. Kotani, K. Kvashnina, P. Glatzel, J. Parlebas, G. Schmerber, *Physical Review Letters* **2012**, 108, DOI 10.1103/PhysRevLett.108.036403.
- [4] A. Kotani, K. O. Kvashnina, S. M. Butorin, P. Glatzel, *The European Physical Journal B* **2012**, 85, DOI 10.1140/epjb/e2012-30079-1.
- [5] T. Vitova, K. Kvashnina, G. Nocton, G. Sukharina, M. Denecke, S. Butorin, M. Mazzanti, R. Caciuffo, A. Soldatov, T. Behrends, et al., *Physical Review B* **2010**, 82, 2-7.
- [6] V. I. Anisimov, J. Zaanen, O. K. Andersen, *Physical Review B* **1991**, 44, 943-954.
- [7] Cowan R.D., University of California Press, Berkeley, **1981**.
- [8] A. L. Ankudinov, J. J. Rehr, S. D. Conradson, *Physical Review B* **1998**, 58, 7565-7576.

11:20am **AC+MI+SA+TF-MoM10 Signatures of the γ - α Volume Collapse in Cerium, M.J. Lipp**, Lawrence Livermore National Laboratory
INVITED

High-pressure x-ray emission measurements of the $L\gamma_1$ (L_2N_4) emission line were used to decide the longstanding debate over the nature of the famous iso-structural (γ - α) volume collapse at 0.75 GPa in elemental cerium that ends in a critical point at 1.5 GPa and 480 K. The satellite structure of this line offers direct access to the total angular momentum observable $\langle J^2 \rangle$ as shown by extended local atomic model calculations and experiences a 30% step-like decrease across the volume collapse. This validates the Kondo model in conjunction with previous measurements of the equation of state at high temperature that were also well fit by the Kondo volume collapse model plus a quasiharmonic representation of the phonons - but could also be reproduced within the Hubbard-Mott framework. The remaining satellite in the α -phase after the volume collapse does not change significantly over the pressure range studied. Direct comparison is made with previous predictions by dynamical mean field theory.

This work was performed under the auspices of the US Department of Energy by Lawrence Livermore National Laboratory under Contract No. DE-AC52-07NA27344 and funded by the Laboratory Directed Research and Development Program at LLNL under project tracking code 12-LW-014. Portions of this work were performed at HPCAT (Sector 16), Advanced Photon Source (APS), Argonne National Laboratory. HPCAT operations are supported by DOE-NNSA under Award No. DE-NA0001974 and DOE-BES under Award No. DE-FG02-99ER45775, with partial instrumentation funding by NSF. APS is supported by DOE-BES, under Contract No. DE-AC02-06CH11357.

Applied Surface Science

Room: 204 - Session AS+BI-MoM

Organic Depth Profiling

Moderator: K.G. Lloyd, DuPont, D. Moon, DGIST

8:20am **AS+BI-MoM1 Combining Gas Cluster Ion Beam (GCIB) and Angle-Resolved XPS (ARXPS) Depth-Profiling, P. Cumpson, A. Barlow, N. Sano, J. Portoles**, Newcastle University, UK

Over the last decade there have been progressive developments in analytical sputter sources within the surface analysis community[1]. These sources (moving from monoatomic ions, to polyatomic ions, to large gas cluster ions) have progressively reduced damage, but importantly gradually reduced the thickness of the damaged layer. With argon GCIB sources at low-to-medium energy-per-atom this depth *should now be smaller than the inelastic mean free path (IMFP)* for analysis by XPS for normal monochromated lab x-ray sources. This offers the prospect of *seeing through the damage* to produce XPS depth-profiles of polymer and other organic materials that are damage-free for the first time. Angle-Resolved XPS[2] has the potential to give information at each step in the sputter-depth profile so that the undamaged profile can be faithfully reconstructed.

We have a new XPS instrument that combines an argon GCIB source with a parallel-acquisition Angle-Resolved XPS analyser, meaning that we can acquire Angle-Resolved XPS spectra simultaneously from analytical points without tilting the specimen. This combination of GCIB and parallel-acquisition ARXPS is unique as yet, so far as we know. This instrument allows us to take angle-resolved spectra at each step of a GCIB sputter-depth profile, and reconstruct the surface concentration as a function of depth. Instrument performance has been reliable and very effective since the instrument was installed in January 2013.

We have developed numerical algorithms to “unfold” damage from GCIB/ARXPS depth-profiles. These are stable and virtually automatic. X-ray damage can be an important limiting factor[3] in the case of some specific polymer types, but we present some strategies to overcome this. Otherwise the almost automatic nature of GCIB/ARXPS depth-profiling (i.e. involving no time from an expert in interpretation of damage artefacts) suggests this combination of GCIB and ARXPS is a powerful technique for the surface analysis community, especially where (such as in organic electronics) electronic information is sought as function of depth, or cases where we start with very little *a priori* certainty about the structure of samples (as is often the case in analysing biological materials).

[1] S. Rabbani, A. M. Barber, J. S. Fletcher, N. P. Lockyer, and J. C. Vickerman, *Anal. Chem.* 83, 3793 (2011).

[2] P.J. Cumpson, *J. Elec spectrosc* 73 (1), 25-52 (1995)

[3] X-ray enhanced sputter rates in argon cluster ion sputter-depth profiling of polymers. P. J. Cumpson, J. F. Portoles, N. Sano and A. J. Barlow, *J. Vac. Sci. Technol. B* 31, 021208 (2013)

8:40am **AS+BI-MoM2 XPS Analysis of Oxygen Plasma Modified Polyethylene Surfaces, S.S. Alnabulsi**, Physical Electronics Inc., N. De Geyer, R. Morent, Ghent University, Belgium, J.F. Moulder, Physical Electronics Inc.

Plasma modification of polymers is of great interest for surface preparation to enhance the covalent binding of functional groups and the surface adhesion in biomedical applications. The depth of the plasma treatment is expected to be limited to the top few nanometers, and in this study, we are investigating the extent of oxygen incorporation through plasma surface modification of a polyethylene surface while varying treatment parameters, and examining the effects of aging on the stability of the modified layer.

Obtaining quantitative chemical state information of the extent of the plasma modification as a function of depth and determining the extent of the depletion region is accomplished through the application of XPS depth profiling utilizing two complimentary methods; the first is with the application of an angle dependent profile to probe the outer most layers of the modified surface, and the second is a sputter depth profile with C_{60} cluster ion beam.

We will present complimentary XPS results of angle dependent profiles and C_{60} sputter depth profile analyses of plasma modified polyethylene to reveal changes in the composition of the modified surface layers, which may explain the effects of varying the plasma treatment parameters, and the effects of sample aging on the shelf life of these modified polymers.

9:00am **AS+BI-MoM3 XPS Valence Band Profiling of Polymer Mixtures with Argon Cluster Ions, P. Mack, A.E. Wright**, Thermo Fisher Scientific, UK

Modern food packaging materials can be complex mixtures of polymers, with a wide range of surface properties, compositions and structures. X-ray Photoelectron Spectroscopy (XPS) is typically the technique of choice for analyzing polymeric surfaces, combining chemical selectivity and surface specificity. Core level XPS spectroscopy, however, is not always sensitive to compositional changes in complex mixtures of polymers. A commonly cited example of this would be in the analysis of blends of polypropylene and polyethylene. Each of the individual polymers in this case has an almost identical $C1s$ spectrum, meaning the polymeric mixtures cannot be quantified using the core level data.

The valence region of the XPS spectrum, however, has been shown to be sensitive to compositional changes in polymeric mixtures even when the core level spectra are not. The XPS valence band of polyethylene and polypropylene, for example, are significantly different and using reference data for each of the individual polymers, it is possible to quantify mixtures of the two.

There has also been an increasing requirement for compositional profiling of these complex materials. Profiling with monoatomic argon can result in a high degree of chemical modification during the acquisition of depth profiles for organic materials, but it has been shown recently that the use of argon cluster beams for depth profiling can preserve chemical information during analysis of organic materials. This talk will present data from cluster profiling studies of polymer blends, using XPS valence band analysis to quantify the polymeric mixtures during the profile.

9:20am **AS+BI-MoM4 Successful XPS Sputter Depth Profiling of Organic Materials Using Massive Argon Cluster Ions, S.J. Hutton**, Kratos Analytical Limited, UK, J. Walton, The University of Manchester, UK, W. Boxford, C.J. Blomfield, J.D.P. Counsell, S.C. Page, Kratos Analytical Limited, UK

Several XPS vendors currently offer massive Argon gas cluster ion sources as accessories for sputter depth profiling of organic materials. These sources utilise Argon cluster ions formed via adiabatic isentropic expansion of Argon gas into a vacuum followed by subsequent electron impact ionisation and cluster size selection. In ideal cases the aforementioned massive cluster ions efficiently sputter the surface of organic materials revealing undamaged subsurface structure for analysis.

Advanced software controlled ion sources and flexible sample handling equipment allow a wide range of experimental conditions to be routinely employed during sputter depth profiling with these massive Argon clusters. In this study we investigate these parameters including: incident ion energy; cluster size distribution; ion angle of incidence; and sample condition (temperature, rotation). A range of organic materials are analysed and optimum sputter depth profiling conditions determined.

9:40am **AS+BI-MoM5 3D Characterization of Multi-Layer Polymer Films by XPS and TOF-SIMS, S. Iida, T. Miyayama**, ULVAC-PHI, Inc., Japan, G.L. Fisher, J.S. Hammond, S.R. Bryan, Physical Electronics Inc.

The recent introduction of Gas Cluster Ion Beams (GCIB) and FIB-TOF has provided new possibilities for 3D characterization of organic materials. The use of GCIB as a sputter beam for both XPS and TOF-SIMS has made it

possible to acquire molecular depth profiles on a wide variety of polymers. The purpose of this study was to compare XPS and TOF-SIMS depth profiling to FIB-TOF analysis of a model Polystyrene (PS)/PS+Nylon/Nylon/PS+Nylon/PS multi-layer structure. Total thickness of the multi-layer stack is 10 μm . XPS depth profiling provided quantitative analysis that could be used to calibrate the TOF-SIMS data. Both TOF-SIMS depth profiling and FIB-TOF can provide 3D characterization of the polymer stack. The TOF-SIMS data provided imaging of the heterogeneous distributions found in each of the PS+Nylon layers as well as trace molecular components found throughout the multi-layer stack. Advantages and disadvantages of both approaches to 3D analysis will be discussed using data from this polymer multi-layer model system.

10:00am **AS+BI-MoM6 In Situ TOF-SIMS and SFM Measurements Providing Real 3D Chemical Information**, E. Niehuis, S. Kayser, R. Möllers, ION-TOF GmbH, Germany, L. Bernard, H.-J. Hug, EMPA, Switzerland, N. Havercroft, ION-TOF USA, Inc., R. Dianoux, A. Scheidemann, NanoScan AG, Switzerland

Advances in analytical instrumentation and nanometrology have been the key to the remarkable progress in nanoscience and nanotechnology research over the last two decades. Detailed knowledge of the chemical composition, physical properties and the three dimensional structure of materials and devices at the nanometer scale is required in all phases of the development from exploratory research to concept and prototyping and finally manufacturing.

Time-of-flight secondary ion mass spectrometry (TOF-SIMS) is a very sensitive surface analytical technique. It provides detailed elemental and molecular information about surfaces, thin layers, interfaces, and full three-dimensional analysis of the sample.

In recent years bismuth clusters have become the standard analysis species for all imaging applications providing a lateral resolution of down to 80 nm. 3D chemical information can be derived by a well-controlled removal of surface layers with an additional sputter beam in a so-called dual beam experiment. Inherent to all 3D TOF-SIMS data is a z-axis with a native time scale instead of a length scale. A starting topography of the initial sample surface as well as an evolving topography due to different erosion rates of the compounds cannot be identified by the technique and yields to relevant distortions.

Scanning force microscopy (SFM), has become the most versatile scanning probe microscopy (SPM) technique since its first application in 1986. In a scanning force microscope, a microscopic tip is scanned over the surface of interest and probes the local properties at each pixel of the scan region. A SFM cannot only map topography up to atomic resolution; it can also map other sample properties with nanometer scale resolution such as local mechanical properties, materials contrast, or electric and magnetic stray fields emanating from the surface.

We have developed a TOF-SIMS / SFM instrument which combines both complementary techniques in a single UHV chamber. The core piece of the new instrument is a high precision, five axes piezo stage which allows fast and accurate navigation between the TOF-SIMS and the SFM analysis position. The combination makes it possible to acquire SFM data before, after and in between TOF-SIMS acquisitions at exactly the same sample position.

In this paper we will present first measurements illustrating the strength of this novel instrument and its potential for a wide range of applications including sputter induced effects on the surface morphology of organic surfaces.

10:40am **AS+BI-MoM8 Time of Flight Secondary Ion Mass Spectroscopy (ToF SIMS) Analysis of Stress Tolerant Polymer (STP) in GenGard Corrosion Inhibitors**, G. Zorn, M. Karadge, M.M. Morra, GE Global Research, J. Davis, C.C. Pierce, J.I. Melzer, GE Power & Water
GE Power & Water GenGard technology is GE's most advanced and effective water treatment technology for open recirculating cooling systems. It can be applied across a broad pH spectrum and provide superior results, even under the most stressed system conditions. The patented GenGard technology includes a new Stress Tolerant Polymer (STP) in combination with phosphate-based steel corrosion inhibitors. The GenGard technology, when used, develops complex multilayered structures that incorporate metal, ceramic and polymer, where the STP is designed to maintain phosphate-based corrosion inhibitors' solubility. For optimal performance it is important to understand the structure, morphology and composition of different layers. However, characterizing these nano scale films is very challenging, as they can be sensitive to preparation technique and damage. Moreover, surface roughness and homogeneity of the layers should be considered.

This work is focused on the ToF SIMS study of the multilayered structures formed by the GenGard technology, with an emphasis on the STP analysis

and its distribution within the inhibition layers. ToF-SIMS is capable of high detection sensitivity (ppb), very high surface specificity (analysis of the top 1-3 surface layers during data acquisition, high mass resolution ($\Delta m/m$ greater than 8000), and is able to detect high mass molecular fragments associated with the STP. ToF SIMS allows rapid data collection while analyzing through multilayers, and provides high interfacial resolution during a depth profile measurement.

ToF SIMS depth profiling of the structures formed by the GenGard technology showed a calcium phosphate / iron oxide two layer structures on the base metal. This structure was further confirmed by Transmission Electron Microscopy (TEM) equipped with Energy Dispersive X-Ray Spectrometer (EDS). The STP that is added in ppm levels was identified in the ToF-SIMS by three high mass $\text{Na}_x\text{S}_y\text{O}_z$ fragments at $m/z=229,245$ and 261 amu. In order to eliminate the possibility that these fragments are associated with surface contamination, Ion Chromatography (IC) was performed. After identifying the STP characteristic tags, ToF SIMS depth profiling of the inhibition layers allows showing that the STP is incorporated within the entire inhibition layers at the initial steps (after 7 days) but later it starts to migrate to the surfaces of these films as they grow with time. This ToF SIMS study combined with TEM and IC provides a detailed picture of the complex structures and compositions as well as the kinetic behavior of the inhibition films formed by the GenGard technology.

11:00am **AS+BI-MoM9 Argon Gas Cluster Beam Etching of Organic Contaminants on Graphene and HOPG**, B.J. Tyler, A.J. Pollard, I.S. Gilmore, National Physical Laboratory, UK

Under ambient conditions, the surface of graphene is contaminated with a range of organic compounds. These compounds include both those that derive from the production of the graphene, such as photo-resists and transfer agents, and adventitious organic compounds that adsorb rapidly to the high energy graphene surface. The ability to remove and control this contamination layer without damaging the graphene is crucial to reproducible production of graphene devices as well as in fundamental studies of graphene properties. In this study, we have investigated cleaning of HOPG and graphene surfaces via heating in vacuum and sputtering with Argon Gas Clusters. Common adventitious organic contaminants have been identified via temperature programmed SIMS experiments and include fatty acids and their fatty acid amides, as well as PAHs and siloxanes. While contamination with siloxanes can be avoided with careful handling, adsorption of fatty acids and amides is virtually instantaneous upon exposure to the ambient environment. Damage to the graphene layer via the sputtering process has been assessed via micro-Raman analysis. Formation of defects due to sputtering with Argon Gas Clusters is dependent on the cluster size, impact energy and ion fluence. An impact energy of less than 1eV per atom in the cluster is needed to minimize defect formation. Optimized conditions for sputter profiling these organic overlayers without damaging the underlying graphene will be presented.

11:20am **AS+BI-MoM10 Why is Low Energy Cesium so Efficient for Depth-profiling Organics?**, L. Houssiau, University of Namur, Belgium
INVITED

Organic materials are known to be very sensitive to ion bombardment, mostly owing to free radical creation upon etching, leading to many chemical reactions like hydrogen abstraction, double bond creation and crosslinking. Most organics eventually degrade into a graphitized material, with no memory left of the initial material's chemistry. However, this picture has dramatically evolved over the last decade thanks to breakthrough developments in the field of molecular depth profiling. It started with the use of polyatomic ion sources (SF_5^+ , C_{60}^+), followed by massive Ar_n^+ clusters which are now considered as standards for molecular depth profiling. Those cluster sources exhibit a sputtering yield high enough to sputter molecular damages away. Our group has followed a thoroughly different approach since 2007, when we showed that, surprisingly, low energy (~250 eV) Cs^+ ions could also be used to depth profile polymers. We have extended the study to many different organic materials, including amino acid thin films, analyzed in the energy range 150-1000 eV. So far, it appears that most organics are amenable to depth-profiling with this method, making it a complementary approach to cluster ion beams. We will review our understanding on how low energy Cs^+ ions prevent material degradation. Cs^+ ions are neutralized as soon as they hit the surface, for electrostatic reasons, leaving implanted Cs atoms in the subsurface region. Cs being an extremely reactive element quickly reacts with free radicals generated by ion impact, preventing cross-linking reactions, thus allowing molecular depth profiling. This reaction goes along with a strong negative ionization, as an electron is transferred from the alkali to the molecule. Indeed, negative molecular ion detection in ToF-SIMS experiments is much increased with respect to inert ions. Our model is supported by XPS data, showing changes in the charge state of various molecules (amino acids, polymers) irradiated with Cs^+ ions. Moreover, the existence of neutral cesium at the surface was detected by optical emission spectroscopy

measurements. We will present our most recent data on Phenylalanine delta layers embedded in a Tyrosine matrix, on which a depth resolution below 5 nm was observed. We will also discuss the decisive influence of the analysis beam (i.e. Ga⁺ or Bi₃⁺) in a ToF-SIMS dual beam experiment. Besides its fundamental interest, low energy Cs⁺ sputtering appears to be an efficient tool to depth profile both organics and inorganics. Its major assets are a high negative ion signal combined with an excellent depth resolution.

Biomolecules at Aqueous Interfaces Focus Topic

Room: 203 A - Session BA+AI+AS+BI+IS+NL-MoM

Biomolecules at Aqueous Interfaces

Moderator: P. Koelsch, University of Washington

8:20am **BA+AI+AS+BI+IS+NL-MoM1 Selected Studies of Biomolecular Interactions**, *K.B. Eisenthal, B. Doughy, Y. Rao, S.M. Kazer, S.J.J. Kwok, N.T. Turro*, Columbia University **INVITED**

The work reported here utilizes a sensitive method for the investigation of biomolecular interactions that has the important characteristic of not requiring chemical labels, e.g. fluorophores, nor invasive detection methods. The surface selective second order spectroscopies, second harmonic, SHG, and sum frequency generation, SFG, allow one to probe equilibrium properties and time dependent changes in the electronic and vibrational structure of molecules located at interfaces. In addition they have the special feature of being able to monitor changes in the electrical charge of the interacting molecules. 1) A new way is presented to measure the binding constants of molecules, e.g. drugs and proteins, with DNA tethered to colloidal microparticles suspended in aqueous solution. 2) Time resolved second harmonic generation was used to observe the binding of an enzyme to its recognition site on DNA, followed by the cleaving of DNA into a small and a large fragment, and the subsequent DNA rehybridization dynamics. 3) The relative orientation of two molecules bound to DNA is manipulated by changing the number of nucleotide base pairs separating them. The interference between the SH electric fields generated by the pair of molecules is modulated because their relative orientation changes as the number of nucleotide base pairs separating them is changed. With this method we have a new way to probe structural changes in DNA due to the binding of biomolecules to it.

9:00am **BA+AI+AS+BI+IS+NL-MoM3 Probing Nanoparticle-lipid Bilayer Interactions with Nonlinear Optics**, *F. Geiger*, Northwestern University **INVITED**

The interaction of engineered nanoparticles with biological membranes is an important and necessary first step for cellular uptake. Here, we probe this interaction by applying second harmonic and vibrational sum frequency generation as well as the Eisenthal chi(3) method to supported bilayer-based model systems as well as shewanella and daphnia magna, chosen as important biological endpoints, exposed to 4 nm sized noble metal nanoparticles surrounded by negatively and positively charged ligands. Our studies are complemented by a plethora of supporting experiments based on quartz crystal microbalance, zeta potential, and related experiments. We find that Coulomb's law dictates much of the interactions in the particular systems studied here.

9:40am **BA+AI+AS+BI+IS+NL-MoM5 Characterizing the Protein-Surface Interactions that Control Diatom Biomineralization**, *J.E. Baio*, Oregon State University, *M. Bonn, T. Weidner*, Max Planck Institute for Polymer Research, Germany

The assembly of mineralized tissues can be initiated and controlled by proteins. One such system, is the formation of silica-based cell walls in marine, single celled organisms, where biomineralization is regulated by protein-mineral interactions. The diatom species *Cylindrotheca fusiformis* assembles supramolecular silica structures via proteins called sillafins. In a silicic acid solution, specific repeat units within this protein, SSKKSGSYSGSKGSKRRIL (R5), induce the formation of silica-protein composite nanoparticles. The protein-surface interaction that drives self-assembly is likely controlled by both the secondary structural motifs of the protein and specific contacts between the surface atoms and key protein side chains. In this study, we characterized the R5-SiO₂ interactions that drive this self-assembly process by both near edge x-ray absorption fine structure (NEXAFS) spectroscopy and *in situ* sum frequency generation (SFG) spectroscopy. Two peaks within the amide I vibrational band of the SFG spectra, 1640 and 1670 cm⁻¹, indicate that the R5 peptide retains a beta sheet conformation when interacting with SiO₂. Expanding upon this characterization of secondary structure, the introduction of isotopic labeled amino acids within the peptide allowed us to probe the orientations of individual side chains by SFG. This SFG characterization was

complemented by the observed polarization dependence of the NEXAFS C1s to π* transition which provided details of the binding geometry of the single tyrosine within R5.

10:00am **BA+AI+AS+BI+IS+NL-MoM6 Probing the Effects of Different Ions on the Formation of Microstructure Within Collagen Hydrogels by Second Harmonic Generation (SHG) Microscopy**, *X. Lang, J.G. Lyubovitsky*, University of California, Riverside

In this study we aimed to explore the nucleation, assembly and the 3-D microstructure of collagen hydrogels *in situ* with second harmonic generation (SHG) microscopy. Transmission electron microscopy (TEM) and optical density (OD) were carried out as well in order to complement the SHG measurements. The goal was to generate the knowledge to accelerate rational design of collagen-based biomedical products. In this work, we employed 0, 150, 300, 600, 900 mM NaCl concentrations and in a separate experiment 0, 5, 10, 20, 50, 75, 100, 150, 300 mM Na₂SO₄ concentrations of salts needed for the assembly of collagen hydrogels. Specifically, we characterized collagen hydrogels prepared from 2 g/l and 4 g/l initial collagen concentrations as well as several incubation temperatures. For samples incubated with NaCl, incubation under the room temperature (RT) and 27°C gave similar OD values. These OD values were higher than the OD values for 37°C incubated samples. Delay time became shorter upon elevating the polymerization temperature. For samples incubated with Na₂SO₄, there were two regimes for collagen polymerization, Na₂SO₄ concentration 5 mM – 50 mM and 100 mM -300 mM. Fibers were longer when NaCl concentration was 150-600 mM compared to 0 and 900 mM NaCl for both collagen concentrations under RT, 27°C and 37°C. In general, fibers were small when incubated at 37°C compared to fibers formed under RT and 27°C. TEM measurement showed that there were collagen fibers with a characteristic striation structure in all collagen and NaCl concentrations. The fibrils exhibited a twisted morphology in 2 g/l collagen hydrogels.

10:40am **BA+AI+AS+BI+IS+NL-MoM8 Sum Frequency Generation (SFG) Vibrational Spectroscopy Studies of Molecules at Solid-Liquid and Solid-Gas Interfaces**, *G.A. Somorjai*, University of California, Berkeley and Lawrence Berkeley National Laboratory, *X. Cai*, Lawrence Berkeley National Laboratory **INVITED**

Construction of a femtosecond broad-band laser enables us to simultaneously monitor the CH and CO vibrational SFG spectra, thus allowing more actual characterization of reaction intermediates at solid-liquid and solid-gas interfaces. Using a picosecond laser we compare the spectroscopy using these two different laser systems and they will be discussed in some detail. In addition, sum frequency generation vibrational spectroscopy, high-pressure scanning tunneling microscopy and ambient-pressure X-ray photoelectron spectroscopy as well as other synchrotron-based techniques (X-ray adsorption) that enable the investigation of surfaces under reaction conditions on the atomic and molecular level will be reviewed.

We investigate solid-liquid and solid-solid interfaces (buried interfaces) as they adsorb and react with diatomic and organic molecules in dynamic state at various pressures and temperatures.

11:20am **BA+AI+AS+BI+IS+NL-MoM10 A Molecular View of Water Interacting with Climate-active Ice Nucleating Proteins**, *R. Pandey*, Max Planck Institute for Polymer Research, Germany, *J. Fröhlich, U. Pöschl*, Max Planck Institute for Chemistry, Germany, *M. Bonn, T. Weidner*, Max Planck Institute for Polymer Research, Germany

Specific bacteria, such as *Pseudomonas syringae*, effectively attack plants by using ice-nucleating proteins anchored to their outer cell surfaces. Ice nucleating proteins promote the local crystallization of ice at temperatures that would otherwise not allow ice formation. The frost damage caused by ice crystals then facilitates bacterial invasion of the affected plants. Ice nucleating proteins not only play an important role for agriculture, but are also very important for atmospheric processes: airborne ice-nucleating proteins have been shown to be among the most effective promoters of ice particle formation in the atmosphere. A recent survey of microorganisms in the troposphere biome by NASA has discovered massive emissions of biogenic ice nucleators from large forest areas like the amazon, which likely change precipitation patterns and may affect the global climate. To understand biogenic ice formation, a detailed molecular level picture of the mechanism by which ice-nucleating proteins interact with water molecules is important. Sum frequency generation (SFG) spectroscopy – owing to its inherent interface sensitivity – is ideally suited to determine the structure and dynamics of water molecules at interfaces. We have investigated the interaction a monolayer of the ice-nucleating protein inaZ with water using static and time-resolved SFG spectroscopy. When cooling the sample from room temperature to near-freezing temperatures (~5°C for D₂O), inaZ significantly increases the structural order of water molecules in contact

with inAz proteins. This effect was not observed for liquid water surfaces without the protein or for protein monolayers which are not ice nucleators. SFG spectra in the CH and the amide I region also indicated a change of protein structure near the nucleation temperature. Femtosecond, time-resolved 2-dimensional SFG spectroscopy is used to quantify the heterogeneity of protein-bound water molecules and their structural dynamics.

Biomaterial Interfaces

Room: 201 B - Session BI+AS+IS+NL-MoM

Surfaces to Control Cell Response

Moderator: H.E. Canavan, University of New Mexico

8:20am **BI+AS+IS+NL-MoM1 Modulation of Cell Behaviour using Self-assembled Binary Colloidal Crystals**, P.Y. Wang, P. Kingshott, Swinburne University of Technology, Australia

The control of cell behaviour on surfaces is the key to a broad range of biomedical applications. Biomaterial surfaces with tuneable surface topographies and chemistries can profoundly influence the development of advanced biomaterials used in applications including tissue engineering and regenerative medicine. Recently, we developed an elaborate and feasible method to display an ordered surface topography with tuneable surface chemistry using binary colloidal crystal particles. Using this binary colloidal system, various combinations of particle size and surface chemistry can be readily employed. In this study, two combinations of binary colloidal crystals, i.e. PS-COOH (2 μm)/PMMA (0.4 μm) and SiO₂ (2 μm)/PMMA (0.4 μm) were assembled on ozone-treated silicon wafers. The preliminary results of cell attachment and morphology of L929 fibroblasts and MG63 osteoblasts were studied after 24h.

In general, cells had a small projection area rather than fully spread morphology on the crystal surfaces compared with the flat control. Fibroblasts have abundance of cell protrusions called filopodia which can be observed using scanning electron microscopy (SEM), whilst osteoblasts don't have. Fibroblasts had long and thin extended filopodia on the PS/PMMA crystal surfaces, whilst they had short and thick filopodia on the SiO₂/PMMA crystal surfaces. Regarding the surface chemistry, both SiO₂ and PMMA particles were not as favourable as the PS-COOH particles for fibroblasts attachment, and resulted in the cell projection area on the PS/PMMA being larger compared to the SiO₂/PMMA crystal surfaces. On the contrary, the cell projection area of osteoblasts didn't have significant differences between these two crystal surfaces. After fibronectin coating, cell projection area of osteoblasts on SiO₂/PMMA crystal surfaces increased significantly, whilst fibroblasts didn't, suggesting that different cell types respond to surfaces differently.

These results show for the first time that cell-substrate interactions can be easily controlled by precise positioning of different particles with various sizes and chemistries. The present results will help gain a more thorough understanding of cell-material interactions benefiting the development of advanced biomaterials and materials for tissue engineering.

8:40am **BI+AS+IS+NL-MoM2 Achieving Differential Cell Adhesion with Novel Polymer Surfaces Identified using Microarrays**, F.A. Simoes, C. Alexander, G. Mantovani, L. Buttery, M.R. Alexander, University of Nottingham, UK

Stem cells have the ability to repair, replace or regenerate tissues. As a result their potential for regenerative medicine is vast. The processing of cells for therapeutic use and clinical diagnostics will rely on cell sorting steps to ensure a homogeneous population is obtained.¹

Several techniques exist to achieve this, which rely on the physical properties of cells but tend to provide poor specificity.²⁻⁴ Fluorescence Activated Cell Sorting (FACS) and Magnetic-Activated Cell Sorting (MACS) rely on specific biomarkers. However cells require labelling and label removal steps, which can affect the phenotype.⁵

There is a need for a fully synthetic, inexpensive, label-free separation system, capable of sorting cells with minimum manipulation. In order to generate robust surfaces for such a system, we have developed a method to immobilize thiol-functionalised materials to a polymer substrate using thiol-ene "click" chemistry in a high throughput format. Microarrays of these functionalised polymers comprising of 6 replicates, are fabricated using pin printing to generate a combinatorial library of materials. A mixture of differentiated cells derived from mouse embryoid bodies are then seeded onto the arrays.

Immunohistochemistry techniques are employed to track the differentiation of cells into different lineages, thus enabling the visualisation of multiple cell lines. These techniques also allow for the high throughput

quantification of attachment by the means of automatic fluorescence microscopy.

Surface characterisation of the "click" immobilization procedure is performed by X-Ray Photoelectron Spectroscopy. In contrast the characterisation of microarrayed materials is performed using Time of Flight - Secondary ion Mass Spectrometry, which is followed by the ranking of materials using Partial Least Square (PLS) regression analysis. This process allows for the correlation of cell attachment with key molecular ions generated from each material by mass spectrometry.

Successful materials that selectively induce cell attachment are identified and investigated further. This is the first step in the generation of new surface-based devices that have the capacity to be fully synthetic, selective, inexpensive and disposable.⁶

1. McIntyre C. *et al.*, *Bioprocess International*, 2010, 44-53.

2. Chabert M. and Viovy J., *PNAS*, 2008, **105**, 3191-3196.

3. Shim S. *et al.*, *Integrative Biology*, 2011, **3**, 850-862.

4. Kose A. R. *et al.*, *PNAS*, 2009, **106**, 21478-21483.

5. Bulte J. W. M. *et al.*, *Blood*, 2004, **104**, 3410-3413.

6. Singh A. *et al.*, *Nature Methods*, 2013, **10**, 438-444

9:00am **BI+AS+IS+NL-MoM3 Interaction of Hematopoietic and Leukemic Cells with their Microenvironment**, A. Rosenhahn, Ruhr-University Bochum, Germany, M. Hanke, C. Christophis, Karlsruhe Institute of Technology, Germany, I. Taubert, N. Baran, P. Wuchter, A.D. Ho, University of Heidelberg, Germany

Especially for leukemic and haematopoietic cells, the interaction with their microenvironment is of utmost importance for extravasation and homing. One key mechanism is the interaction of the CD44 receptor with extracellular hyaluronan (HA) binding motifs. To quantitatively assess the interaction, a microfluidic experiment has been developed that allows studying the interaction of cells with interfaces under well-defined flow conditions [1]. Shear flow activated catch bond interaction is well characterized for selectin mediated extravasation of leukocytes [2]. We recently found that also the CD44 interaction with HA requires a minimum shear stress to become activated and enable cells to roll on HA surfaces [3]. Similar critical shear values were found for rolling on mesenchymal stroma cells, which are present in the bone marrow niche creating the microenvironment required for haematopoietic stem cell renewal. Interestingly not only hematopoietic stem cells but also acute leukemic blasts show a shear flow induced rolling. The proportion of rolling cells will be discussed on the basis of the pathogenesis of the disease.

[1] C. Christophis, M. Grunze, A. Rosenhahn, *PCCP* 2010, 12, 4498.

[2] E.B. Finger, K.D. Puri, R. Alon, M.B. Lawrence, U.H. von Andrian, T.A. Springer, *Nature* 1996, 379, 266

[3] C. Christophis, I. Taubert, G. Meseck, M. Schubert, M. Grunze, A. D. Ho, A. Rosenhahn, *Biophys. J.* 2011, 101, 585.

9:20am **BI+AS+IS+NL-MoM4 The Creation of Polymeric Biointerfaces using Non-Contact Dispensing Technology**, C. Dufresne, Scienion

Polymeric surfaces of varied composition have been created in high density microarray formats. These patterned surfaces have been used to study a number of biointerface processes such as stem cell differentiation, and bacterial adhesion. Scienion offers non-contact picoliter dispensing technology that enables the creation of such surfaces. The inert glass capillaries allow for the use of a wide range of chemical reagents. Precision positioning enables drop-on-drop dispensing and mixing. Image analysis of the substrates in turns makes it possible to accurately dispense the materials onto almost any surface. This presentation will cover how Scienion technology is implemented for the production of polymeric surfaces.

9:40am **BI+AS+IS+NL-MoM5 The Role of Cell-Substrate Interactions on Cell Stiffness and Cell Volume**, D.A. Weitz, Harvard University
INVITED

Cell stiffness is often observed correlate with the stiffness of the substrate on which the cells are grown. This talk will present data which suggest that cell-substrate interactions are more diverse, and depend as well on the adhesion area. It will discuss the impact of the substrate on cell volume and the consequences of this on cell stiffness. The data presented will suggest that cell volume is a control for cell stiffness.

10:40am **BI+AS+IS+NL-MoM8 Quantitative, Predictive Models of Adhesion of Cells to Polymers**, V.C. *Epa*, D.A. *Winkler*, CSIRO Materials Science & Engineering, Australia, A.L. *Hook*, C. *Chang*, J. *Yang*, University of Nottingham, UK, R. *Langer*, D.G. *Anderson*, MIT, P. *Williams*, M.C. *Davies*, M.R. *Alexander*, University of Nottingham, UK

Designing materials to control biology is an intense focus of biomaterials and regenerative medicine research. Discovering and designing materials with appropriate biological compatibility or active control of cells, tissues, or pathogens is being increasingly undertaken using high throughput synthesis and assessment methods.

In particular, culture of multipotent cells such as stem cells is a major research focus in regenerative medicine. Much research effort is focused on designing chemically defined, serum-free, feeder-free synthetic substrates and media to support robust self-renewal of pluripotent cells. Changes in cellular properties such as adhesion, morphology, motility, gene expression and differentiation are influenced by surface properties of the materials on which cells have been cultured. Similarly, designing new materials to control the growth of pathogens on implantable and indwelling devices such as pacemakers, and catheters, is critical given the high level of device-centred infections.

We report a relatively simple but powerful machine-learning method of generating models that link microscopic or molecular properties of polymers or other materials to their biological effects. We illustrate the potential of these platform modelling methods by developing the first robust, predictive, quantitative, and purely computational models of adhesion of human embryonic stem cell embryoid bodies, and three clinically important pathogens, *Staphylococcus aureus*, *Pseudomonas aeruginosa*, and uropathogenic *Escherichia coli*, to the surfaces of 496 polymers.

11:00am **BI+AS+IS+NL-MoM9 Smart Surfaces for Studies of Real-Time Dynamic Cell Behavior**, M.N. *Yousaf*, York University, Canada

Active migration, local tissue invasion and seeding of distant metastases are all characteristics of malignant cells. These complex cellular events require the integration of information derived from soluble growth factors with positional information gained from interactions with the extracellular matrix and with other cells. The biochemical events of the signaling cascades occur in a spatially and temporally coordinated manner that then dynamically shape the cytoskeleton in specific sub-cellular regions. Therefore cell migration and invasion involve a precise but constantly changing subcellular nano-architecture. To fully understand the complex signaling and cytoskeletal aspects of the cellular nano-architecture during migration requires a multidisciplinary coordinated effort. The long-term goal of this research program is to develop new surface chemistry and cell biological tools to generate a class of tailored dynamic nanopatterned substrates for a variety of cell adhesion and migration experiments. The combined application of dynamic smart substrates, molecular surface gradients and in vivo biosensors will potentially allow for the analysis and quantitation of the events of cell migration at each step from initial engagement with extracellular matrix ligands, to localized activation of signaling proteins, to organization and activation of the cytoskeleton, to overall movement of the cell.

11:20am **BI+AS+IS+NL-MoM10 What Makes the Heart Grow Fonder? Chemically Diverse Polyacrylate and Polyacrylamide Surfaces for Human Cardiomyocyte Culture and Their Effect on Phenotype**, A.K. *Patel*, University of Nottingham, UK, D.G. *Anderson*, R. *Langer*, Massachusetts Institute of Technology, M.C. *Davies*, M.R. *Alexander*, C. *Denning*, University of Nottingham, UK

Human pluripotent stem cell (hPSC) derived cardiomyocytes hold the potential to strengthen pharmaceutical toxicity testing and to provide disease models for development of treatment targets¹. The maturation and maintenance of the cardiomyocyte phenotype may be controlled by the manipulation of the substrate supporting the cells². However, the surfaces currently in use still fall short of producing cardiomyocytes of adult maturity. Standard culture-ware requires coating with biological substrates such as fibronectin which can be expensive and subject to poor reproducibility due to batch variation. We are exploring an alternative, combinatorial materials high throughput screening approach³ to identify novel materials that can improve cardiomyocyte culture. Polymer microarrays comprising of 6 replicates of 116 acrylates and acrylamides are fabricated using contact printing. Cardiomyocytes derived from the HUES7 human stem cell line are seeded onto the arrays. Immunostaining of nuclei (DAPI) and the cardiomyocyte specific motor protein, sarcomeric alpha actinin is performed to visually estimate cell function and maturity and enable quantification of cell attachment in a high throughput manner using automated fluorescence microscopy and image analysis software. Surface characterisation of the arrays is performed using time of flight secondary ion mass spectrometry. Partial least squares (PLS) regression analysis

allows for correlation of cell attachment with key molecular ions identified from mass spectrometry⁴.

Successful monomers that permit cardiomyocyte attachment, spreading and contraction are identified from the first generation homopolymer microarray and are mixed pair-wise to form second generation microarrays. This diverse library of copolymers enables unique combinations of chemical moieties to be investigated. Hit monomers and combinations identified to be synergistic can be analysed for their effect on cardiomyocyte function including electrophysiology measured by patch clamping, myofibril alignment and gene expression.

The lead materials generated by this approach are the first step in a discovery process for novel synthetic biomaterials capable of enhancing the culture of cardiomyocytes to move towards more reproducible, economical and defined conditions.

References:

1. Matsa E. et al. *European Heart Journal*. 2011;32(8):952-62
2. Engler A. et al. *The Journal of Cell Biology*. 2004;166(6):877-887
3. Hook A. et al. *Biomaterials*. 2010;31(2):187-198
4. Yang J. et al. *Biomaterials*. 2010;31(34): 8827-8838

11:40am **BI+AS+IS+NL-MoM11 Selectivity in Platelet Activation by the Titania Surface: A Model System for In Vitro Modulation of Platelet Activity**, S. *Gupta*, CIC biomaGUNE, Spain, I. *Reviakine*, Karlsruhe Institute of Technology, Germany

Platelet are anuclear cell fragments circulating in blood. Their major function is haemostasis: they catalyze the formation of the fibrin clot that stops the bleeding. Recently it was shown that they have a multitude of other functions in processes such as the immune response, inflammation, angiogenesis, implant rejection or integration.

Platelets circulate in the blood in a quiescent form. They become activated at wound sites, implant surfaces, or through the action of soluble agonists secreted by activated platelets or produced in the blood as a result of the clotting process. Activated platelets express on their surface a variety of protein and lipid receptors that catalyze the clotting process, interact with other platelets, leukocytes, and endothelial cells, and adhere to the extracellular matrix exposed at the wound sites. They also secrete a variety of active substances, including growth factors, that are stored inside special granules within the platelets.

Recently discovered diversity of platelet functions implies a tight regulation of the activation processes. Indeed, there is evidence to suggest that platelet activation is a selective process with a spectrum of activated states, rather than a two-state process involving quiescent vs. pro-coagulant platelets. In this context, we have previously shown that platelet activation profile on TiO₂ depends on the surface-bound Ca. Here, we measure intracellular calcium currents in surface-adsorbed platelets in order to understand how this manifestation of platelet activation selectivity is related to the internal signaling pathways. Such an understanding is a prerequisite for designing new, platelet-based approaches to the treatment of haemostatic and inflammation-based disorders, to enhancing implant integration and wound repair, and to tissue engineering applications.

Electronic Materials and Processing Room: 101 B - Session EM+TF-MoM

High-k Gate Oxides for High Mobility Semiconductors I Moderator: C.L. Hinkle, University of Texas at Dallas

8:20am **EM+TF-MoM1 Ultrathin Titanyl Phthalocyanine Active Layer on Graphene for Atomic Layer Deposition**, A.C. *Kummel*, H.H. *Park*, University of California, San Diego, S.W. *Park*, University of California at San Diego

Several novel designs for beyond CMOS devices have emerged using two-dimensional semiconductors. These devices require deposition of thin insulator on the 2D semiconductor or between two sheets of 2D semiconductors. However, 2D semiconductors are nearly inert surface thereby making uniform nucleation of oxide growth challenging thereby preventing scaling of the insulator thickness. A new technique has been developed to employ a monolayer of ordered metal phthalocyanines (MPc) on graphene directly as a monolayer low-k dielectric or as a nucleation layer for growth of high-k insulator. MPc molecules act as electron donors during reaction with oxidative species; therefore, they are expected to react with high-k gate oxide metal precursors. This study demonstrates the molecular scale observation of formation of O-TiPc mono and bilayers on graphene UHV scanning tunneling microscopy. O-TiPc monolayers were deposited

on HOPG surfaces by organic molecular beam epitaxy. After deposition, O-TiPc forms a monolayer with only few defects, and the crystal structure of monolayer has four-fold symmetry. In the monolayer, a bright spot at the center of each O-TiPc molecules is assigned to O. Observation of bright protrusion indicates that O-TiPc of monolayer is directed outward to vacuum consistent with previous photoelectron studies. After further deposition of O-TiPc on the monolayer, growth of second layer is observed. O-TiPc of second layer covers the first layer, and both the first and second layers are highly ordered with four fold crystal structure. However, in second layer, central ion appears as a dark hole, unlike with in the monolayer. This implies O species of O-TiPc is directed downwards. For bilayer 2D semiconductors devices, when using O-Ti-Pc as a low-k insulator, the stacking of the 1st and 2nd layers of Ti-OPc is critical since the monolayer might provide differential doping of the top and bottom layer while the bilayer would provide a non-polar low K insulating layer. Scanning tunneling spectroscopy showed that the Fermi level of O-TiPc is slightly shifted to the lowest unoccupied molecular orbital, although EF is still in the midgap. O-TiPc is $\alpha\text{-CN-type}^{\ominus}$ in vacuum, while it becomes to $\beta\text{-CN P-type}^{\ominus}$ in air due to reaction with oxygen species. In the air, oxidative molecules take electrons from O-TiPc during chemisorption via central ion of O-TiPc. At same time, holes are injected into the O-TiPc layer. Due to this property, O-TiPc molecules are expected to have strong reactivity with ALD precursors. Consequently, O-TiPc can not only act as a low-K dielectric but also induce nucleation of ALD source on central ion of O-TiPc for high-k dielectric growth.

8:40am **EM+TF-MoM2 Correlation between Current-Voltage Measurements and the Barrier Height Determined by XPS in Ge p-MOS Capacitors**, S. Fadida, F. Palumbo, Technion Israel Institute of Technology, Israel, L. Nyns, H.C. Lin, S. Van Elshocht, M. Caymax, IMEC, Belgium, M. Eizenberg, Technion Israel Institute of Technology, Israel

One of the solutions to the constantly growing demands of the microelectronic industry is to replace Si, the channel material in metal oxide field effect transistors (MOSFETs), with a higher mobility semiconductor. Being a leading candidate, Ge has recently been the center of numerous research works. Ge surface passivation was a major challenge which was almost exclusively addressed in Ge related research. Once a few options for good passivation of Ge were found, the current challenge in Ge MOSFET research is to find a gate dielectric with the desired properties. This dielectric should have a large band gap, large band offsets with respect to Ge, chemical and thermal stability on top of Ge or on top of the passivation layer, and a high dielectric constant (high-k).

In this work the dielectric stack $\text{HfMOx}/\text{Al}_2\text{O}_3/\text{GeO}_2$ with the nominal thicknesses 4/2/0.7 nm was studied on top of p-Ge. GeO_2 served as the passivation layer, while Al_2O_3 was chosen for its wide band gap and band offsets with respect to Ge, and its excellent chemical stability on GeO_2 . Since the dielectric constant of Al_2O_3 , is not sufficiently high, an additional top high-k dielectric is needed. We have studied Hf-based oxides (HfO_2 , HfAlOx , HfGdOx , and HfZrOx) as the top high-k dielectric.

In order to examine the suitability of the dielectric materials, current-voltage (I-V) measurements were conducted. The results show a significant difference between HfAlOx and the other high-k studied. While HfO_2 , HfGdOx and HfZrOx display similar I-V curves, with the same trend and the same level of leakage current, the leakage current of the HfAlOx containing sample is one order of magnitude lower.

In order to understand the root cause of this phenomenon, the band alignments of the samples were studied using X-Ray Photoemission Spectroscopy (XPS). Here, again, the HfAlOx sample stands out: only in this high-k dielectric the valence band offset (VBO) with respect to Ge is larger than the VBO of Al_2O_3 (3.6 and 3.1 eV respectively), while for the other dielectrics it is equal to the VBO of Al_2O_3 (3.0-3.1 eV). Examination of the conduction band offsets (CBO) shows no difference between the samples. The CBO of the Hf-based high-k dielectrics with respect to Ge are in the range of 1.5-1.7 eV, while the CBO of Al_2O_3 with respect to Ge is 3.1eV.

These results can be correlated with our I-V results leading to the conclusion that the dominant mechanism of current in these samples is hole tunneling in the Fowler-Nordheim mechanism. In order to establish this conclusion, we have also measured the leakage current of a reference sample with the structure: $\text{Al}_2\text{O}_3/\text{GeO}_2/\text{Ge}$. The results confirm the model suggested.

9:00am **EM+TF-MoM3 Gate Dielectrics on Graphene**, J. Kim, The University of Texas at Dallas **INVITED**

2-D nano-materials, like graphene and Van Der Waals layered materials, have attracted lots of attentions as new generation electronic materials for device applications because of their prominent properties such as high-mobility, flexibility and optical transparency compared to conventional semiconductor materials like silicon. Therefore, it is desperately required to

develop techniques to integrate robust gate dielectrics with high-quality interfaces for these materials in order to attain maximum performance. To date, a variety of methods including physical vapor deposition, atomic layer deposition, physical assembly among others have been employed in order to integrate dielectrics for graphene based field-effect transistors. Owing to the difficulty in wetting pristine surfaces of graphene, most of the atomic layer deposition methods require a seeding technique involving non-covalent functionalization of their surfaces in order to nucleate dielectric growth while maintaining their intrinsic properties. A review regarding the various dielectric integration schemes will be provided. Effects of ALD process on transport characteristics of 2D channel layers including graphene and TMD (transition metal dichalcogenide) will be also discussed.

This work was financially supported by the SWAN program funded through NRI-SRC.

9:40am **EM+TF-MoM5 Impact of N_2 and Forming Gas Plasma Exposure on the Growth and Interfacial Characteristics of Al_2O_3 on $\text{Al}_{0.25}\text{Ga}_{0.75}\text{N}$** , X. Qin, B. Brennan, H. Dong, A. Azcatl, R.M. Wallace, University of Texas at Dallas

$\text{AlGaIn}/\text{GaIn}$ high electron mobility transistors (HEMTs) are of significant interest for high power, high frequency and high temperature devices due to their large band gaps, high mobility and chemical stability compared to Si and other high mobility III-V materials. However, a large leakage current and frequency dependent current collapse degrades the performance of $\text{AlGaIn}/\text{GaIn}$ HEMTs. The surface passivation process consisting of a suitable surface treatment and growth of a high-k oxide layer between the semiconductor and the gate metal is one of the proposed methods to address these issues.

In this study, we investigate atomic layer deposition (ALD) of Al_2O_3 on the native oxide, N_2 plasma and forming gas plasma exposed AlGaIn surface, respectively. X-ray photoelectron spectroscopy (XPS), low energy electron diffraction (LEED) is used to determine the interface after N_2 or forming gas plasma exposure. Initial results indicate that N_2 or forming gas plasma is able to remove carbon and decrease the concentration of oxygen. And the contamination level is lower than various alternative wet chemical treatments. The interaction between the Al_2O_3 and the AlGaIn surfaces during deposition is also studied by XPS. The XPS and LEED are carried out *in-situ* by transferring the samples between the plasma chamber, the ALD reactor and the analysis chamber under UHV conditions ($< 2 \times 10^{-10}$ mbar) to prevent contamination due to atmospheric exposure.

The work is supported by the AOARD under AFOSR Grant No. FA2386-11-14077

10:00am **EM+TF-MoM6 Monitoring the HfO_2 -InAs Interface during the ALD Process using Ambient Pressure X-ray Photoemission Spectroscopy**, R. Timm, S. Yngman, A. Head, J. Knutsson, M. Hjort, J. Knudsen, J. Schmadt, L.-E. Wernersson, A. Mikkelsen, Lund University, Sweden

MOS structures based on III-V semiconductors with high-k oxide layers formed by atomic layer deposition (ALD) are highly promising. In order to achieve superior device performance, a precise control and profound knowledge of the semiconductor-oxide interface is crucial, but not fully reached yet. One of the great challenges is to characterize the chemical reactions taking place at the interface between the III-V semiconductor, its native oxide, and the high-k dielectric material during the ALD process. X-ray photoemission spectroscopy (XPS) has successfully been used to investigate this interface before and after individual steps of the ALD reaction [1,2], but was until now limited to ultrahigh vacuum conditions.

Here we present ambient pressure XPS studies of the atomic layer deposition of HfO_2 on InAs: By performing subsequent half-cycle steps of the ALD process within the reaction cell of an ambient pressure XPS system, we were able to monitor the slowed down ALD reaction by XPS and thus obtain fully *in-situ* and real-time XPS measurements of the high-k deposition on III-V semiconductors for the first time. The experiments were performed at the HP-XPS endstation of synchrotron beamline I511 at the MAX IV Laboratory [3]. Tetrakis(dimethylamino)hafnium (TDMA-Hf) and water were used as precursors, deposited at pressures between 10^{-3} and 10^{-2} mbar.

After an activation time of up to several minutes, a complete reduction of the As-oxides within about 20 s could be seen in the real-time As 3d spectra during exposure to TDMA-Hf. Hf 4f spectra show a significant amount of hafnium to be present on the surface only when the As-oxide reduction sets in, indicating that the reaction occurs immediately as soon as hafnium precursors are adsorbed on the surface. During the second half-cycle, surface hydroxylation occurs within about a minute as seen in O 1s spectra during water exposure. N 1s and C 1s spectra taken under vacuum conditions between subsequent ALD half-cycles change reversibly between different N- and C-based components. If the substrate temperature is reduced from 220°C to 160°C, an incomplete As-oxide reduction together

with significant adsorption of non-reacting hafnium precursor material on the surface is observed. We will discuss the dependence of the chemical reactions on further ALD conditions and the relevance of such ambient pressure XPS studies for an improved understanding and control of the semiconductor-oxide interface.

[1] Hinkle *et al.*, *Curr. Opin. Solid St. M.* **15**, 188 (2011)

[2] Timm *et al.*, *Appl. Phys. Lett.* **97**, 132904 (2010)

[3] Schnadt *et al.*, *J. Synchrotron Radiat.* **19**, 701 (2012)

10:40am **EM+TF-MoM8 Challenges and Progress in Complementary Tunnel FETs**, M. Wistey, G. Zhou, Y. Lu, R. Li, Q. Zhang, W.S. Hwang, Q. Liu, T. Vasen, C. Chen, M. Qi, H. Zhu, J.-M. Kuo, S. Chae, Y. Lu, H. Zhu, J.-M. Kuo, T. Kosel, S. Koswatta, P.J. Fay, A. Seabaugh, H. Xing, University of Notre Dame

INVITED

Tunneling field effect transistors (TFETs) may offer logic performance comparable with low-power CMOS while consuming far less power. This talk summarizes recent work on TFETs based on III-V and 2D materials. In this talk, we discuss recent results in modeling and fabrication of TFETs with high on current, low off current, and low subthreshold swing (SS). Self-aligned, planar III-V TFETs are shown with high on-current of $I_{ON}=0.18\text{mA}/\mu\text{m}$ at $V_{GS}=0.5\text{V}$. An analytic and simulation model was developed to compare between in-line (vertical) and transverse tunneling geometries, as well as to compare the supply voltage, bandgap, SS and Ion for single-gate, double-gate, and gate-all-around (nanowire) geometries. The optimal bandgap was found to depend on device geometry and size, leading to possible variability between devices. Also, for gate lengths below 10 nm, the minimum VDD for planar TFETs increases to 4.8 V, reducing the advantage over MOSFETs. But GAA and 2D materials still offer VDD as low as 0.22 V with $I_{ON}/I_{OFF}=10^5$. As with MOSFETs, gate dielectrics play a predominant role in performance. High Dit easily hinders device performance and requires SS above 60 mV/decade. Test dielectric interfaces with strained InP and InAs/ZnTe interfaces were studied for low-voltage applications. Models and experiments both showed that TFETs are sensitive to fabrication misalignment in the gate overlap regions. Self-aligned devices show the best performance and highest yield. Finally, to replace CMOS, we need an inverter with low static power dissipation. This requires complementary devices analogous to NMOS and PMOS. The talk discusses some of the lessons from the previous work for moving forward with pTFETs.

11:20am **EM+TF-MoM10 In Situ Infrared Study on the Interfacial Layer Formation during the Atomic Layer Deposition of Aluminum Silicate on Chemically-treated InP(100)**, W. Cabrera, K. Bernal-Ramos, A. Vega, The University of Texas at Dallas, I.M. Povey, Tyndall National Institute, Ireland, H. Dong, B. Brennan, R.M. Wallace, Y.J. Chabal, The University of Texas at Dallas

Growing suitable high-k dielectrics for high-performance III-V metal-oxide semiconductor field effect transistor (MOSFET) devices remains a challenge because native oxides on III-V semiconductors contain a high number of interfacial defects. In particular, atomic layer deposition (ALD) of Al_2O_3 has been thoroughly studied, featuring a “self-cleaning” phenomenon or reduction process of the initial native oxide by trimethyl aluminum. Despite notable progress in improving the interface quality, the number of interfacial defects still prevents the manufacturing of quality MOSFET devices. A fundamental understanding of the chemical composition of the interface and its evolution during processing is important to make further progress. In this study, *in-situ* infrared (IR) spectroscopy is used to examine the growth at 300°C of aluminum silicate (AlSiO_x) using trimethylaluminum (TMA), silicon tetrachloride (SiCl_4) and heavy water (D_2O) on degreased native oxides and chemically-treated (5% vol. HF and 10% vol. $(\text{NH}_4)_2\text{S}$) InP(100) surfaces. After an initial TMA exposure, the formation of Al-O-P species is observed, with a loss of $\text{In}(\text{PO}_3)_3$ and gain of $x\text{-(PO}_4\text{)}$ ($x = \text{In and Al}$) (at 1007 and 1145 cm^{-1} , respectively) along with the formation of Al-O-Al bonds (absorption band at 800 cm^{-1}). This observation is consistent with the “self-cleaning” effect whereby the native oxides are reduced by formation of aluminum oxide and different chemical species. Upon the subsequent D_2O exposure, the loss of the 1217 cm^{-1} and 2942 cm^{-1} bands indicates the removal of the aluminum-bound methyl groups through ligand exchange. Interestingly, a subsequent pulse of SiCl_4 gives rise to a vibrational mode at 1060 cm^{-1} , assigned to Si-O-P. This indicates that SiCl_4 molecules primarily react surface P-O(D) groups to form a silicon phosphate structure on the native oxides. After the subsequent D_2O exposure, further growth of the mode at 1060 cm^{-1} suggests the continued formation of surface Si-O-P. The presence of AlSiO_x is observed on the degreased native oxide InP(100) substrates after eight supercycles. In conclusion, a complex consisting of primarily of Al-O-P develops initially, associated with a self-cleaning mechanism. As further growth develops, a complex of Al-O-Si becomes apparent, as indicated by the appearance and growth of the mode at 1151 cm^{-1} . The information

derived from this study makes it possible to optimize the growth conditions for tailored aluminum silicate layers on InP surfaces. This work is made possible by National Science Foundation as a part of the U.S.–Ireland R&D Partnership (Grant no. NSF-ECCS-0925844) and Science Foundation Ireland [Grant No.09/IN.1/I2633.]

11:40am **EM+TF-MoM11 Density Function Theory Simulations of a- $\text{Al}_2\text{O}_3/\text{GaN}(0001)$ Interfaces Resulting from Ex Situ and In Situ Surface Preparation**, A.C. Kummel, E. Chagarov, S. Gu, P. Asbeck, University of California San Diego, S. Madisetti, S. Oktyabrsky, University at Albany-SUNY, T. Kaufman-Osborn, A.J. Kerr, University of California San Diego

The structural and electronic properties of amorphous a- $\text{Al}_2\text{O}_3/\text{GaN}(0001)$ interfaces were investigated by density-functional theory (DFT) molecular dynamics (MD) simulations. Realistic amorphous a- Al_2O_3 samples were generated using a hybrid classical-DFT MD “melt-and-quench” approach and tested against experimental properties. Every stack was annealed at 800K, cooled to 0K and relaxed to the ground state giving the system enough freedom to form realistic interface. The simulated stacks were recalculated with HSE 06 hybrid-functional to provide accurate electronic structure analysis and bandgap representation. Subsequently, a series of a- $\text{Al}_2\text{O}_3/\text{GaN}(0001)$ interfaces were investigated by bonding the oxide to various GaN(0001) surfaces and annealing the stacks at 800K for 2000 time steps, cooling to 0K and relaxing to form the final structures. GaN(0001) (Ga-polar) models were chosen to simulate the surfaces obtained with different ex-situ wet cleaning and in-situ dry cleaning including $\text{NH}_4\text{OH}(\text{aq})$, $\text{O}_2(\text{g})$ oxidation, $(\text{NH}_4)_2\text{S}$, $\text{NH}_3(\text{plasma})$, and TMA /H(plasma treatments). Nearly all MBE GaN(0001) surfaces are prepared with a Ga adlayer. The inclusion of Ga-adlayer resulted in an a- $\text{Al}_2\text{O}_3/\text{GaN}(0001)$ bonding with multiple midgap states mainly from metal-metal (Al-Ga) bonds. In-situ O_2 reaction at 500°C has been previous shown to eliminate metal-metal bonding within the Ga-adlayer/GaN(0001); DFT-MD simulations show that the resultant O-Ga-O layer provides an excellent passivation layer between a- Al_2O_3 and GaN. The DFT-MD simulations of direct bonding between a- Al_2O_3 and GaN(0001) revealed predominantly Ga-O bonding with no intermixing; the simulations show the key to forming a passive interface is nucleating the ALD in each unit cells to remove all Ga dangling bond states. A 5-step combined ex-situ wet cleaning and in-situ cyclic TMA /H treatment resulted in an extremely high nucleation density and concurrent lower dispersion in both threshold and accumulation capacitance consistent with lower interfacial defect density and lower border trap density. XPS experiments showed the bonding at the interface was covalent consistent with the DFT calculations.

Energy Frontiers Focus Topic

Room: 101 A - Session EN+PS+TF-MoM

Thin Film, Organic, and Chalcogenide Solar Cells

Moderator: Y. Xu, Oak Ridge National Laboratory

8:20am **EN+PS+TF-MoM1 Understanding (?) Solar Devices through Soft X-Ray and Electron Spectroscopy**, C. Heske, UNLV and KIT

INVITED

The purpose of this talk is to demonstrate how a tool chest of soft x-ray and electron spectroscopies (in particular using high-brilliance synchrotron radiation) is uniquely suited to unravel the electronic and chemical properties of surfaces and interfaces in thin film solar cells. We will show how photoelectron spectroscopy (PES), Auger electron spectroscopy (AES), inverse photoemission (IPES), x-ray emission spectroscopy (XES), and x-ray absorption spectroscopy (XAS) can be suitably combined to derive band gaps, study local chemical bonding and electronic level alignment, and derive insights into chemical stability at surfaces and interfaces. As examples, $\text{Cu}(\text{In,Ga})(\text{S,Se})_2$ and CdTe thin films and devices will be discussed.

9:20am **EN+PS+TF-MoM4 Continuous-Flow Chemical Bath Deposition of $\text{Zn}_x\text{Cd}_{1-x}\text{S}$ Thin Films For Chalcopyrite Solar Cells**, B.S. Tosun, J.T. Abrahamson, A.A. Gunawan, K.A. Mkhoyan, S.A. Campbell, E.S. Aydil, University of Minnesota

Kesterite and chalcopyrite thin film solar cells have an n-type metal sulfide (e.g., CdS, ZnS or $\text{Zn}_x\text{Cd}_{1-x}\text{S}$) buffer layer deposited on the p-type absorber. This buffer layer is typically grown using chemical bath deposition (CBD) from metal salts and thiourea in basic aqueous solutions. In a typical CBD system, the entire solution, including the substrate, is heated. This leads to homogeneous nucleation of the metal sulfide particles in addition to the heterogeneous reaction that deposits the desired buffer layer on the substrate. This homogeneous nucleation and growth of particles wastes chemicals and causes problems with solar cells when the particles stick on

the absorber surface. To solve these problems we have developed a continuous chemical bath deposition (CF-CBD) system that allows the deposition of $Zn_xCd_{1-x}S$ films on 4-inch diameter substrates at temperatures ranging from 50 to 85 °C without significant solution temperature rise and without homogeneous nucleation and growth. Only the substrate is heated to the deposition temperature while the CBD solution is rapidly circulated between the bath and a chilled reservoir. The key features of the design are easily scalable and adaptable to roll-to-roll deposition. We have demonstrated that the CF-CBD system can be used to deposit uniform thickness and composition $Zn_xCd_{1-x}S$ films across 4-inch diameter substrates for a variety of x values by changing the concentrations of the Zn and Cd salts in the bath. Addition of ethylenediaminetetraacetic acid disodium to the chemical bath deposition is the key to preventing deposition on surfaces other than the heated substrate surface and key to obtaining films with uniform composition and structure across the film's thickness. Films were characterized using x-ray diffraction, Auger depth profiling, spectroscopic ellipsometry, transmission electron microscopy and Kelvin probe force microscopy. The effect of deposition parameters such as temperature, bath stirring rate and bath composition on the structure and composition of the films will be discussed.

9:40am **EN+PS+TF-MoM5 Development of Plasma-Enhanced Vapor Transport Deposition of CdTe Absorbers**, *J. Beach, C.A. Wolden, J.J. Li*, Colorado School of Mines

Development of plasma-enhanced vapor transport deposition of CdTe absorbers

Jiaojiao Li, Joseph Beach, and Colin A Wolden

Colorado School of Mines, Golden, CO 80401

Cadmium telluride is a leading absorber material for thin-film solar cells. However, state-of-the art open circuit voltages (V_{oc}) of CdTe thin film solar cells fall ~350 mV below the value expected based on the band gap of CdTe. V_{oc} is mainly compromised by the structural defects, low carrier density and low recombination lifetime. Conventional methods to eliminate defects require the use of high temperature deposition or annealing processes which are incompatible with low cost soda-lime glass. The low hole density is because CdTe is difficult to dope due to numerous self-compensation mechanisms. $CdCl_2$ treatment is always used to passivate the grain boundaries and increase carrier lifetime, but additional Cd may induce Te vacancies. In this work we introduce plasma-enhanced vapor transport deposition (PEVTD) as an alternative technique for thin film CdTe synthesis. The viability of vapor transport deposition (VTD) is demonstrated by First Solar's use of this approach to produce both the lowest cost modules. Plasma deposition techniques are able to introduce energy to films at low thermal budget. PEVTD is a hybrid of these two technologies, and we expect it to also be amenable to scale-up. In this method, high energy electrons dissociate Te_2 dimers into reactive Te species, so a high quality Te rich film may be achieved at low temperature. Moreover, plasma enhancement may activate group V dopants to dope CdTe at a higher concentration. Finally, active gases such as H_2S or SO_2 are added to the carrier gas stream to passivate interface defects and increase minority carrier lifetime. In this talk we discuss the design, construction, and operation of this reactor. We describe the dependence of the CdTe film quality on the kind of gases we use, plasma power, and substrate temperature. Films are characterized using XRD, SEM, UV-Vis-NIR spectrophotometry, Hall and light and dark current-voltage measurements.

10:00am **EN+PS+TF-MoM6 Self-Limiting Growth of Pyrite Solar Absorbers using Pulsed PECVD**, *C. Sentman*, Colorado School of Mines, *M. O'Brien*, Trinity College Dublin, Ireland, *C.A. Wolden*, Colorado School of Mines

Pyrite, FeS_2 , is a non-toxic, earth abundant semiconductor that offers several potential advantages as a photovoltaic material, including low cost, large absorption coefficients and a band gap that is suitable for the harnessing of solar energy. Conventional thin film deposition techniques typically require the use of a post-deposition annealing step in elemental sulfur in order to achieve stoichiometric material. This cumbersome step is usually conducted in sealed quartz ampoule, requiring precise control over sulfur mass, time, and temperature. In this talk we introduce pulsed plasma-enhanced chemical vapor deposition (PECVD) as an alternative technique for thin film pyrite synthesis. In pulsed PECVD a mixture of iron pentacarbonyl (IPC, $Fe(CO)_5$) diluted in H_2S is delivered continuously to the reactor while the plasma is pulsed using square wave modulation at low frequency (~1 Hz). The concept is that IPC absorbs during the plasma off step, and that it is fully sulfurized *in situ* during the plasma on step. The process offers digital control over thickness with control on the order of ~1 Å/pulse. In this work we demonstrate the conditions required to achieve self-limiting growth of pyrite thin films. The dependence of pyrite deposition rate and material quality as a function of relevant variables such as H_2S :IPC ratio, plasma duty cycle, plasma power, pressure and substrate

temperature is described. Films are characterized using a suite of analytical techniques including Raman, XRD, FESEM, and UV-Vis-NIR spectrophotometry. Through appropriate control of deposition parameters stoichiometric FeS_2 could be deposited at controllable rates between 0.1 – 1 Å/pulse without the need for post-deposition annealing. The onset of thermal CVD between these precursors was found to be ~300 °C, and it is shown that this process leads to the formation of undesirable sulfur-deficient phases. Processing could also be used to tune the pyrite to marcasite ratio. Films display expected absorption coefficient (~ 10^5 cm⁻¹) and optical band gap (~1 eV). We are currently analyzing their optoelectronic properties and will report on the process-structure-property relationships in this system.

10:40am **EN+PS+TF-MoM8 Surface Energetics of AgInSe₂ Thin Films**, *P. Peña Martín, A. Rockett*, University of Illinois at Urbana Champaign

The chalcopyrite system has contributed the top performing absorber layer for thin film photovoltaic devices, $Cu(In,Ga)Se_2$, but the surface properties of these compounds are not well understood. While $CuInSe_2$ (CIS) has proven difficult to obtain atomically resolved surface images, the $AgInSe_2$ (AIS) surface has been recently observed. Study of the surface structure, growth mechanics and defects of AIS can provide important details of its behavior, as well as yielding insight into other chalcopyrites, like CIS, by comparison of the results. This work presents the results of growing epitaxial AIS films and studying their surface morphology to help understand its growth behavior and to transfer this knowledge to help understand the growth of chalcopyrites in general.

Thin films of AIS were grown by hybrid sputtering and evaporation technique on (110), (110), (111), and (-1-1-1) GaAs substrates. Film thicknesses were around 500 nm, and the substrate temperature was varied from 500-700°C. Their microstructures were characterized by a variety of techniques including scanning electron (SEM), scanning tunneling (STM), and atomic force (AFM) microscopies, as well as x-ray diffraction (XRD). SEM shows that the films all exhibit facets or features that are aligned across the sample, indicating that the films are epitaxial, confirmed by x-ray diffraction.

AIS was found to show a similar preference as does CIS for polar facets. The films grown on GaAs (111) and (-1-1-1) are very smooth with individual atomic steps resolvable, while growth on GaAs (110) results in films that spontaneously facet to two polar faces with roughness that differ dramatically. AFM line profiles indicate an angle of ~68° between the faces, as expected for the angle between polar (112) planes. One side of the facets is stepped, with triangular features pointed toward the “peak” of the facet. The other side shows fewer features, with occasional triangular terraces pointed toward the “valley” instead. This is consistent with a chemical difference between these two surfaces. The films grown on (100) GaAs are highly featured, with rectangular pits that are likely (111) terminated. The features on films grown on both (100) and (110) substrates both show smaller size than films grown on CIS, even with a higher homologous temperature for AIS.

11:00am **EN+PS+TF-MoM9 Microstructure Evolution During Annealing of Copper Zinc Tin Sulfide Colloidal Nanocrystal Coatings to form Large-Grain Polycrystalline Thin Films**, *B.D. Chernomordik, A.E. Beland, D.D. Deng, A.A. Gunawan*, University of Minnesota, *D.J. Norris*, ETH Zürich, Switzerland, *E.S. Aydil*, University of Minnesota

Copper zinc tin sulfide (Cu_2ZnSnS_4 , or CZTS), copper zinc tin selenide ($Cu_2ZnSnSe_4$, or CZTSe), or their alloys are candidates for environmentally sustainable light absorbing materials for thin film solar cells because they are composed of abundant elements. In one potentially low-cost approach to making solar cells, coatings drop-cast from colloidal dispersions of CZTS nanocrystals (NCs) (inks) are annealed to form 1-3 micron thick polycrystalline films with 1-3 micron grains. We synthesize CZTS NC inks using rapid thermal decomposition of copper, zinc, and tin diethyldithiocarbamate precursors in presence of hot (150-300 °C) oleylamine. The synthesis temperature determines the NC size, which can be tuned from 2 to 25 nm. The formation of CZTS is confirmed using X-ray diffraction (XRD), Raman spectroscopy, and energy dispersive X-ray spectroscopy (EDS). Following synthesis, the NCs are dispersed in toluene and NC films are cast on various substrates including quartz and soda lime glass. One micron or thicker films cast from <10 nm NCs crack due to capillary forces during drying. Cracks are reduced significantly when films are cast from 25 nm nanoparticles. The NC films are then placed in quartz tubes with pure S, Se, or a mixture of the two, evacuated to 10^{-6} Torr, sealed, and then heated for the desired times (1-8 hours) at the desired temperatures (500-800 °C). This annealing approach provides excellent and very reproducible control of the annealing temperature and S and/or Se pressure over the film. The resulting films are characterized using a suite of techniques, including XRD, electron microscopy, EDS, and Raman scattering. We have explored the extent to which vapor species, vapor

pressure, substrate choice, carbon content in the NC film, annealing time, and annealing temperature affect the mechanisms by which the polycrystalline films form and how their microstructure evolves. Depending on the annealing conditions, the CZTS NCs sinter and grow to sizes ranging from a hundred nanometers to a few microns. In addition to sintering, we observe abnormal grain growth, which, if encouraged, can lead to formation of single-crystal CZTS grains up to 10 microns in size. Raman scattering spectra collected from these large CZTS crystals show that the crystals have texture, preferring two orientations. The surface energy difference between the NCs and the large grains is the driving force for abnormal grain growth, which appears to be enhanced at high temperatures but reduced significantly on SLG and at high S pressures. The abnormal grain growth can be turned on or off via control of these variables.

11:20am **EN+PS+TF-MoM10 Enhanced Grain Growth in Cu₂ZnSnS₄ Thin Films via Vapor Transport of Alkali Metal Impurities**, M. Johnson*, University of Minnesota, S. Baryshev, Argonne National Laboratory, E. Thimsen, M. Manno, X. Zhang, C. Leighton, E.S. Aydil, University of Minnesota

While power conversion efficiencies of Cu₂ZnSnS₄ (CZTS) based solar cells have increased relatively rapidly, very little research has been focused on the effects of the substrate on CZTS films. To date, the best performing CZTS solar cells have been deposited on Mo-coated soda lime glass (SLG), a carryover from Cu(In_xGa_{1-x})Se₂ (CIGS) solar cells where Na diffusion from the SLG into the CIGS layer enhances the power conversion efficiency. Impurity diffusion is also expected when CZTS is deposited on Mo-coated SLG, but SLG hosts many other impurities including K, Ca, Mg, and Al and a systematic investigation of whether these impurities diffuse into CZTS and what effect they may have on the film properties has not been conducted. To this end, we have investigated the effects of these impurities on the microstructure of CZTS films. Thin CZTS films were synthesized via *ex situ* sulfidation of Cu-Zn-Sn films co-sputtered on a variety of substrates, including, SLG, quartz, and Pyrex. The metallic precursor films were loaded into a quartz ampoule with 1 mg of S, evacuated to 10⁻⁶ Torr, sealed and sulfidized at 600 °C for 8 hours. The sulfidized films were then characterized using X-ray diffraction, Raman spectroscopy and scanning electron microscopy. Concentration depth profiles were examined using time-of-flight secondary ion mass spectrometry (TOF-SIMS). CZTS films synthesized on SLG have significantly larger grains than films grown on other substrates. We have conducted experiments where identical Cu-Zn-Sn precursor films on quartz were sulfidized both in the absence and in the presence of a bare additional piece of SLG in the sulfidation tube. Remarkably, the grain sizes (>1 μm) in CZTS films sulfidized with SLG present are dramatically larger than the grain sizes (100's of nm) in CZTS films sulfidized without SLG. This demonstrates conclusively that impurities in SLG volatilize in a S atmosphere and incorporate into nearby CZTS films synthesized on a quartz substrate. Of all the impurities present in SLG, the TOF-SIMS experiments implicated Na, K and Ca as possible elements responsible for enhanced grain growth. To investigate the effects of these impurities individually, we then introduced very small and controllable amounts of Na, K, or Ca into the ampoule during sulfidation of the CZTS. Impurity amounts as low as 10⁻⁶ moles of Na or 10⁻⁷ moles of K loaded into the sulfidation tube resulted in a dramatic increase in grain size for films deposited on quartz, while Ca loading had little effect on the final microstructure. The results presented will demonstrate that subtle changes in impurity types and compositions lead to drastic changes in CZTS films.

Graphene and Other 2D Materials Focus Topic

Room: 104 B - Session GR+EM+NS+PS+SS+TF-MoM

Growth of 2D Materials

Moderator: T. Ohta, Sandia National Laboratories, B. Ozyilmaz, National University of Singapore

8:20am **GR+EM+NS+PS+SS+TF-MoM1 Using Nitrogenated SiC to Produce Wide-gap Semiconducting Graphene**, P.I. Cohen, S. Rothwell, University of Minnesota, L.C. Feldman, G. Liu, Rutgers University, E.H. Conrad, F. Wang, Georgia Institute of Technology

All carbon electronics based on graphene has been an elusive goal. For more than a decade, the inability to produce significant band gaps in this material has prevented the development of semiconducting graphene. While chemical functionalization was thought to be a route to semiconducting graphene, disorder in the chemical adsorbates leads to low mobilities that

have proved to be a hurdle in its production. In this work we demonstrate a new approach to produce semiconducting graphene that uses a small concentration of covalently bonded nitrogen, not as a means to functionalize graphene, but instead as a way to constrain and bend graphene. First, about half a monolayer of nitrogen was adsorbed onto a carbon-polar SiC(000-1) surface by annealing in NO. X-ray photoelectron spectroscopy (XPS) indicates that the layer of N that is introduced forms both C=N and C-N bonds that are stable up to 1550C. Then graphene is grown using a controlled silicon sublimation technique, producing, in this case, 3 or 8 layers of graphene. The N coverage and bonding during this process is determined from the XPS signal. After graphene growth the N coverage is about 7 at. % with its bonding unchanged. Examination of the peak intensity in variable energy XPS suggests that the N remains at the interface and there are no other peaks normally associated with either intercalated or substitutional N in graphene. Scanning tunneling microscopy (STM) confirmed that for the case of either 3 layer or 8 layer graphene, N was not present in the top layer. STM, however, showed that the graphene sheet is buckled with 2-4 nm wide folds. The folds can meander and are 5-25 nm long. In addition, atomic resolution images show that the folds are part of a continuous graphene sheet. The implication is that sp³ bonded N at the interface produces this buckling. Finally, angle resolved photoelectron spectroscopy from the buckled, 3-layer graphene is dramatically different than that from pristine 3-layer graphene. With N at the interface, a bandgap of at least 0.7 eV is resolved, presumably due to a finite size effect. For both 3-layer and 8-layer graphene the Fermi velocity is 0.8 x 10⁶ m/s.

9:00am **GR+EM+NS+PS+SS+TF-MoM3 Graphene Growth on C-face SiC in Argon**, Z. Robinson, G.G. Jernigan, K. Bussmann, R.L. Myers-Ward, V.D. Wheeler, L.O. Nyakiti, U.S. Naval Research Laboratory, S. Oida, J. Hannon, IBM T.J. Watson Research Center, M. Currie, C. Eddy, D.K. Gaskill, U.S. Naval Research Laboratory

Graphene growth on Si-face SiC has been shown to have improved uniformity when synthesized in an argon environment instead of in UHV. For C-face growth, which is expected to yield graphene with superior electronic properties due to the absence of the interfacial layer, similar progress has not yet been achieved. It has been shown that growth by confinement controlled sublimation, where the C-face SiC is put in a graphite pillbox during growth, can result in improved quality graphene films. However, it remains unclear whether growth by low pressure sublimation (LPS) in a conventional furnace with an argon overpressure can achieve uniformity and thickness control similar to the Si-face. Therefore, a systematic study of SiC surface preparation by hydrogen etching and subsequent graphene growth in argon has been carried out for C-face SiC substrates in a commercially available Aixtron CVD reactor that has been modified for LPS. This reactor exhibits laminar Ar flow and a uniform temperature profile. In this system, which has the advantage of being able to subject different substrates to identical growth conditions simultaneously, it has been found that relatively small differences in the substrate, such as polytype, can have a drastic effect on the resulting graphene film. In fact, growth conditions that result in complete coverage of at least a single layer of graphene on a nominally on-axis 4H substrate have been shown to result in 60% coverage for a nominally on-axis 6H substrate. Therefore, it has been found that optimizing the growth conditions for a particular substrate is crucial if graphene thickness and uniformity are to be controlled. Additionally, it has been suggested that unintentional oxidation of the SiC substrate during growth in high pressures of argon is a potential cause for the non-uniform growth that is observed on the C-face [1]. Several experiments in which LPS grown C-face graphene was transferred to a UHV system equipped with *in situ* XPS have been conducted, and it has been found that UHV anneals of up to 1200 °C were necessary in order to desorb the oxygen. Following the anneal, exposure to atmospheric conditions resulted in the return of only ~20% of the original oxygen concentration. This suggests that a robust oxide which is stable at high temperature may be influencing the graphene growth process. A detailed LEED, LEEM and STM study has been initiated to determine the effect that this oxygen has on the graphene film's properties and new results will be presented.

References:

[1] L. Srivastava, G. He et al., Phys. Rev. B 82, 235406 (2010)

9:20am **GR+EM+NS+PS+SS+TF-MoM4 Microscopic Control of Epitaxial Graphene on SiC(111) and SiC(100) Thin Films on a Microfabricated Si(100) Substrate**, H. Fukidome, T. Ide, M. Suemitsu, Y. Kawai, Tohoku University, Japan, T. Ohkouchi, M. Kotsugi, T. Kinoshita, JASRI/SPring-8, Japan, T. Shinohara, N. Nagamura, S. Toyoda, K. Horiba, M. Oshima, University of Tokyo, Japan

Graphene is the promising material for the next-generation devices due to its excellent electronic properties. We have developed epitaxy of graphene on SiC thin films on Si substrates (GOS) toward fusion of graphene with Si-based electronics. We have found that structural and electronic properties of

* TFD James Harper Award Finalist

graphene are tuned by crystallographic orientation of the Si substrates [1,2]. This result indicates that, in combination with Si microfabrication technologies, the electronic properties of GOS may be tuned by microfaceting Si surface [3].

A Si(100) substrate was fabricated by combining electron-beam lithography [3] and alkaline etching which produces (111) and (100) microfacet on the Si(100) substrate. On the microfabricated Si(100) substrate, SiC thin films were grown by using gas-source MBE, followed by graphitization in vacuum at 1500 K. Microscopic characterization of graphene was performed by using 3D NanoESCA for microscopic XPS (micro-XPS) and low-energy electron microscope for microscopic low-energy electron diffraction (micro-LEED). Vibrational and bandstructure characterization was done by Raman microspectroscopy.

The micro-LEED observation reveals that graphene is Bernal stacked on the SiC(111)/Si(111) facet, while it is non-Bernal stacked on the SiC(100)/Si(100) microfacet. The observation is in consistent with the previous result on the epitaxy of graphene on non-fabricated SiC(111)/Si(111) and SiC(100)/Si(100) [1, 2]. The variation of the stacking is explained by the micro-XPS observation. The buffer layer which works as a template for the epitaxy of graphene exists only in between graphene and the SiC(111)/Si(111) microfacet. The existence of the buffer layer is also confirmed by cross-sectional transmission electron microscopy observations. Furthermore, Raman microscopy reveals that the band dispersion (splitting) microscopically changes depending on the variation of the stacking with the microfacet.

Our work can open a new way to microscopically tune control of electronic properties of graphene, semiconductive or metallic, which can make graphene devices multi-functionalized on Si substrates.

One of the authors (H. F.) acknowledges a financial support by KAKENHI (23560003).

References: [1] H. Fukidome et al., *J. Mater. Chem.* 21 (2011) 17242. [2] H. Fukidome et al., *Appl. Phys. Exp.* 4 (2011) 115104. [3] H. Fukidome et al., *Jpn. J. Appl. Phys.* 51 (2012) 06FD02.

9:40am **GR+EM+NS+PS+SS+TF-MoM5 STM Studies on Direction-Selective Epitaxial Graphene: Growth Mechanism and Moiré Superstructures**, *H. Lim, Y. Kim*, RIKEN, Japan

Chemical vapor deposition on a Cu surface is one of the feasible methods for industrial applications, because large-area monolayer graphene film can be achieved.¹ However, grain boundaries and wrinkle formation in the graphene film are known to reduce the electrical performance of graphene. An atomic scale understanding of the growth mechanism on a Cu substrate is therefore of great importance for the synthesis of higher-quality graphene films.

Herein, we present the direction-selective growth of epitaxial graphene (EG) on a Cu(111) surface. All EGs had an identical $R0^\circ$ rotational angle with respect to the lattice direction of Cu(111), although it is distinguished from the general understanding that graphene grown on weakly-interacting metal surfaces generally shows various rotation angles.² The EG growth mechanism was also elucidated with microscopic evidence of characteristic step edge formation of the Cu layers underneath individual EGs. We also observed various kinds of Moiré patterns in EGs with an identical rotational angle. The variety of Moiré patterns, even with an identical rotational angle, cannot be explained by conventional analysis showing that different rotational angles induce the different types of Moiré patterns. We suggest a “compressive strain” effect to explain the various Moiré superstructures observed in the atomically-resolved STM images.

1. Li, X.; Cai, W.; An, J.; Kim, S.; Nah, J.; Yang, D.; Piner, R.; Velamakanni, A.; Jung, I.; Tutuc, E.; Banerjee, S. K.; Colombo, L.; Ruoff, R. S. *Science* **2009**, 324, (5932), 1312-1314.

2. Batzill, M. *Surf. Sci. Rep.* **2012**, 67, (3-4), 83-115.

10:00am **GR+EM+NS+PS+SS+TF-MoM6 Epitaxial Graphene on Ag(111)**, *B.T. Kiraly*, Northwestern University, *E. Iski*, Argonne National Laboratory, *A.J. Mannix*, Northwestern University, *B. Fisher*, Argonne National Laboratory, *M.C. Hersam*, Northwestern University, *N.P. Guisinger*, Argonne National Laboratory

Graphene plasmonics has recently combined near field optics with the exotic properties of graphene to demonstrate remarkable optical, biochemical, and optoelectronic architectures capable of extreme light concentration and manipulation, highly efficient photoconversion, and single molecule detection. Graphene's unique electronic structure and chemical stability make it an optimal platform to interface with both light and matter; however, current devices are limited by the low-throughput or non-pristine processing steps to produce either the exfoliated or CVD transferred graphene, respectively. In this regard, it would be highly useful to grow a layer of graphene directly on top of a plasmonic metal substrate.

In this work, we report the novel growth of graphene on a bare Ag(111) single crystal. Growth was accomplished by evaporating atomic carbon onto a Ag(111) surface at elevated temperatures under ultra-high vacuum (UHV) conditions. The growth was verified and examined in-situ via scanning tunneling microscopy (STM)/scanning tunneling spectroscopy (STS) and further qualified via ex-situ Raman spectroscopy, scanning electron microscopy (SEM), and x-ray photoelectron spectroscopy (XPS). While the minimal C solubility in Ag suggests similar growth behavior to other noble metals (Cu, Au), this growth mode demonstrates markedly different signatures: nanoscale dendritic features, both terrace and step nucleation, strong electronic scattering at the graphene boundaries, and highly mobile Ag adatoms interacting with the graphene growth front. Furthermore, the growth was carried out at temperatures (600°C-700°C) much lower than the temperatures commonly used for conventional chemical vapor deposition (CVD) techniques (>1000°C) and it could be extended to a variety of weakly interacting substrates, including non-metals. All the observed growth was electronically characterized as single-layer graphene, and was further supported by the narrow full-width half-maximum (FWHM) of the 2D Raman band. All the observed growth was electronically characterized as single-layer graphene, and was further supported by the narrow full-width half-maximum (FWHM) of the 2D Raman band. A 65% decrease in the Ag-O peak in the O1s spectrum reveals that the graphene layer protects the underlying silver from environmental degradation. Two predominant Moiré patterns were observed in the graphene; their periodicity was ~1.55nm and ~0.95 nm corresponding to lattice offsets of ~4.5° and ~13°, respectively. Finally, the graphene grown on Ag is weakly bound to the surface indicated by the stark contrast between the dI/dV spectra of the graphene and bare silver surface. The graphene-Ag system demonstrated in this study could immediately be applied to tip-based molecular spectroscopies and will lead to the development of more advanced hybrid graphene plasmonics.

10:40am **GR+EM+NS+PS+SS+TF-MoM8 A Universal Scheme to Convert Aromatic Monolayers Into Functional Carbon Nanomembranes**, *A. Angelova, H. Vieker, N.J. Weber, D. Matei*, University of Bielefeld, Germany, *S. Kurasch, U. Kaiser*, University of Ulm, Germany, *K. Müllen, Max Planck Institute for Polymer Research*, Germany, *A. Götzhäuser, A. Turchanin*, University of Bielefeld, Germany

The engineering of free-standing nanomembranes with molecular or atomic thickness and with well-defined structural and functional properties is a challenge for materials research. Here we present a broadly applicable scheme to create mechanically stable carbon nanomembranes (CNMs) with a thickness of ~0.5 to ~3 nm. Monolayers of polyaromatic molecules (oligophenyls, hexaphenylbenzene and polycyclic aromatic hydrocarbons) were assembled and exposed to electrons that crosslink them into CNMs; subsequent pyrolysis converts the CNMs into graphene sheets. In this transformation thickness, porosity and surface functionality of the nanomembranes are determined by the monolayers, and structural and functional features are passed on from the molecules through their monolayers to the CNMs and finally on to the graphene. Our procedure is scalable to large areas and allows the engineering of ultrathin nanomembranes by controlling the composition and structure of precursor molecules and their monolayers.

11:00am **GR+EM+NS+PS+SS+TF-MoM9 Hydrogenation of Monolayer and Bilayer Graphene and Nanodiamond Growth on Ni(111) Substrate**, *I.I. Oleynik, L. Adamska, M. Batzill*, University of South Florida

Hydrogenation of a few layer graphene is known to result in the change of sp^2 to sp^3 hybridization, which can be exploited to grow nanodiamond thin films. First-principles studies of hydrogenated monolayer, bilayer, and trilayer graphene, supported on Ni(111) substrate are performed using first-principles density functional theory. The monolayer graphene and AB-stacked bilayer graphene are shown to rehybridize to form sp^3 bonds, thus promoting the formation of nanodiamond thin films. Structural, electronic and magnetic properties of the hydrogenated monolayer, bilayer, and trilayer graphene are discussed.

11:20am **GR+EM+NS+PS+SS+TF-MoM10 Graphene-based, Graphene-derived, and New Carbon Materials**, *R.S. Ruoff*, The University of Texas at Austin

INVITED

Graphene-based materials are of interest because of their electronic and thermal transport, mechanical properties, high specific surface area, and that they can act as an atom thick layer, barrier, or membrane, among other reasons. Our micromechanical exfoliation approaches [1,2] conceived of in 1998 yielded multilayer graphene and one paper described in detail how monolayer graphene could be obtained [1]. Three main research areas of our group are: (i) Growth of large area graphene on metal substrates, characterization and physical properties, and studies of devices having such CVD-grown graphene as a central component; (ii) Generation, study, and

use of chemically modified graphene 'platelets' (typically derived from graphite oxide) including as dispersed in liquids forming colloids, and powders derived from such colloids or separately generated by microwave or thermal treatment of graphite oxide; (iii) Generation and study of new types of carbon derived from graphene-based precursors, such as *activated microwave expanded graphite oxide* ('aMEGO')[3].

Here, I will focus on growth of graphene and h-BN from research projects underway in my group and also *briefly* describe what I think are some important new directions in carbon and *first row element* research, for the next 10-20 years, that will introduce new issues involving interfaces for these new material classes that have not yet been made experimentally [4].

Current or prior support of our work by the W. M. Keck Foundation, NSF, DARPA 'iMINT', DARPA 'CERA', ONR, SWAN NRI, ARO, AEC, DOE, and the SRC, is appreciated.

1. Lu XK, Yu MF, Huang H, and Ruoff RS, *Tailoring graphite with the goal of achieving single sheets*, *Nanotechnology*, **10**, 269-272 (1999).

2. Lu XK, Huang H, Nemchuk N, and Ruoff RS, *Patterning of highly oriented pyrolytic graphite by oxygen plasma etching*, *Applied Physics Letters*, **75**, 193-195 (1999).

3. Zhu, Yanwu; Murali, Shanthi; Stoller, Meryl D.; Ganesh, K. J.; Cai, Weiwei; Ferreira, Paulo J.; Pirkle, Adam; Wallace, Robert M.; Cychosz, Katie A.; Thommes, Matthias; Su, Dong; Stach, Eric A.; Ruoff, Rodney S. *Carbon-Based Supercapacitors Produced by Activation of Graphene*. *Science* **332**, 1537-1541 (2011).

4. Ruoff, Rodney S. *Personal perspectives on graphene: New graphene-related materials on the horizon*. *MRS Bulletin* **37**, 1314-1318 (2012).

Magnetic Interfaces and Nanostructures

Room: 202 A - Session MI-MoM

Topological Materials, Rashba Systems, and Heusler Alloys

Moderator: V. Lauter, Oak Ridge National Laboratory

8:20am **MI-MoM1 Rotating Spin and Giant Splitting: Unoccupied Surface State at TI/Si(111)**, M. Donath, S.D. Stolwijk, A.B. Schmidt, Muenster University, Germany, K. Sakamoto, Chiba University, Japan, P. Krueger, Muenster University, Germany

Tl/Si(111)-(1x1) is an outstanding example for a system with peculiar spin-orbit-induced spin effects in the surface electronic structure. An occupied surface state with classical in-plane Rashba-type spin topology around the center of the surface Brillouin zone was found to exhibit an out-of-plane spin rotation upon approaching the K point [1].

We used spin- and angle-resolved inverse photoemission with sensitivity to the in-plane and the out-of-plane spin-polarization directions to explore the unoccupied states. A recently developed rotatable source for spin-polarized electrons provided access to two spin-polarization directions. We identified an unoccupied surface state with the same spin topology as the occupied state, yet with a much larger spin-dependent splitting in energy of 0.6 eV. Theoretical calculations provide an explanation for this giant splitting. It is attributed to the strong localization of the unoccupied surface state close to the heavy TI atom in contrast to the occupied state, which is located at the outermost Si atoms.

Since the lower-lying spin component approaches the Fermi level, this leads to almost completely out-of-plane polarized valleys in the vicinity of the Fermi level. As the valley polarization is oppositely oriented at the K and K' points, backscattering should be strongly suppressed in this system.

[1] K. Sakamoto *et al.*, *Phys. Rev. Lett.* **102**, 096805 (2009).

8:40am **MI-MoM2 Searching Majorana Fermion in Topological Insulator/Superconductor Heterojunction**, J. Jia, Shanghai Jiao Tong University, China

Topological superconductors (TSCs) have attracted a great deal of attention recently because of the Majorana modes they host, which can be used in fault-tolerant quantum computation relying on their non-Abelian braiding statistics. While TSCs are very rare in nature, it has been proposed that an alternative way to realize them is by inducing superconductivity in the surface states of a topological insulator (TI) through the proximity effect (PE). Here we report the first experimental evidence for PE induced TSC in Bi₂Te₃/NbSe₂ heterojunction and the observation of Abrikosov vortices and core states. In particular, we found unusual splitting behavior in the zero-bias peak of the core states that may be attributed to the formation of Majorana fermions. Our work demonstrates the promise of using proximity

effect induced TSC for realizing Majorana fermions and topological quantum computing.

9:00am **MI-MoM3 Visualizing Topological States of Matter**, A. Yazdani, Princeton University **INVITED**

Soon after the discovery of quantum mechanics it was realized why some solids are insulating (like diamond) and others are highly conducting (like graphite), even though they could be comprised of the same element. Now, 80 years later, the concept of insulators and metals is again being fundamentally revised. During the last few years, it has become apparent that there can be a distinct type of insulator, which can occur because of the topology of electronic wavefunctions in materials comprised of heavier elements. Strong interaction between the spin and the orbital angular momentum of electrons in these compounds alters the sequence in energy of their electronic states. The key consequence of this topological characteristic (and the way to distinguish a topological insulator from an ordinary one) is the presence of metallic electrons with helical spin texture at their surfaces. I will describe experiments that directly visualize these novel quantum states of matter and demonstrate their unusual properties through spectroscopic mapping with the scanning tunneling microscope (STM). These experiments show that the spin texture of these states protects them against backscattering and localization. These states appear to penetrate through barriers that stop other electronic states. I will describe these experiments and our most recent attempts to create and visualize other topological states such as creation of Majorana fermions, which are another instance of boundary state associated with topological order.

[1] P. Roushan *et al.* *Nature* **460** 1106 (2009).

[2] J. Seo *et al.* *Nature*, **466** 434 (2010).

[3] H. Beidenkopf *et al.* *Nature Physics*, (2011).

9:40am **MI-MoM5 Probing Spin Textures of Topological Surface States in Ternary Chalcogenides**, A. Kimura, Hiroshima University, Japan **INVITED**

Three-dimensional topological insulators (3D TIs) with a gapless topological surface state (TSS) in a bulk energy gap induced by a strong spin-orbit coupling have attracted much attention as key materials to revolutionize current electronic devices. A spin helical texture of a TSS, where the electron spin is locked to its momentum, is a manifestation of a 3D TI.

A number of well-known thermoelectric and phase-change materials have so far been predicted to be 3D TIs. In order to experimentally confirm their topological natures, spin- and angle- resolved photoemission spectroscopy (ARPES) is one of the most powerful tools and it has actually been playing major roles in finding some real 3D TIs [1, 2]. Among the established 3D TIs, Bi₂Se₃ has been most extensively studied because of its relatively large energy gap and the simplest TSS. However, the topological surface state is energetically obscured by bulk continuum near and below the Dirac point, which is disadvantageous for spintronic applications.

ARPES experiments were performed at the ESPRESSO end station attached to the APPLE-II type variable polarization undulator beam line (BL-9B) at Hiroshima Synchrotron Radiation Center (HSRC) [3]. The VLEED-type spin detector utilized in the ESPRESSO machine achieves a 100 times higher efficiency compared to that of conventional Mott-type spin detectors [2]. Photoelectron spin polarizations are measured by switching the direction of in-plane target magnetizations, thereby simultaneously eliminating the instrumental asymmetry, which is a great advantage for a quantitative spin analysis of nonmagnetic systems such as 3D TIs.

In this talk, some of the ternary 3D TIs such as TlBiSe₂ [4], GeBi₂Te₄ [5], Bi₂Te₂Se, and Bi₂Se₂Te [6] are shown to possess TSSs with marked spin polarizations. It has been revealed for GeBi₂Te₄ that a disorder in the crystal has a minor effect on the surface-state spin polarization, which is ~70% near the Dirac point in the bulk energy gap region (~180 meV). Highly spin-polarized features are also found for Bi₂Te₂Se and Bi₂Se₂Te, which are persistent across the Dirac point. The availability of both upper and lower TSSs promises to extend the variety of spintronic application, for instance, to dual gate TI devices and topological p-n junctions.

[1] M. Z. Hasan *et al.*, *Rev. Mod. Phys.* **82**, 3045 (2010).

[2] T. Okuda and A. Kimura, *J. Phys. Soc. Jpn.* **82**, 021002 (2013).

[3] T. Okuda *et al.*, *Rev. Sci. Instrum.* **82**, 103302 (2011).

[4] K. Kuroda *et al.*, submitted.

[5] K. Okamoto *et al.*, *Phys. Rev. B* **86**, 195304 (2012).

[6] K. Miyamoto *et al.*, *Phys. Rev. Lett.* **109**, 166802 (2012).

10:40am **MI-MoM8 (Un)expected Spin Topology in Unoccupied Bands of Bi/Ag(111)**, *S.N.P. Wissing, A.B. Schmidt*, Westfälische Wilhelms-Universität Münster, Germany, *Chr.R. Ast*, Max-Planck-Institut für Festkörperforschung Stuttgart, Germany, *H. Mirhosseini*, Max-Planck-Institut für Mikrostrukturphysik Halle, Germany, *J. Henk*, Martin-Luther-Universität Halle-Wittenberg, Germany, *M. Donath*, Westfälische Wilhelms-Universität Münster, Germany

The spin topology of electronic bands, caused by spin-orbit interaction in Rashba systems and topological insulators, is subject of current debate. In some cases, the experiments findings are in conflict with theoretical predictions. In this contribution, we will discuss this issue with respect to the spin-resolved unoccupied electronic structure of the surface alloy Bi/Ag(111) ($\sqrt{3}\times\sqrt{3}$)R30°.

Surface alloys of heavy elements on noble metal fcc(111) surfaces exhibit surface states with giant Rashba-type spin splittings. Therefore, they have been investigated thoroughly in recent years, in particular their occupied band structure by spin- and angle-resolved photoemission. Above the Fermi level, however, there is basically a blank area on the $E(k_{\parallel})$ map.

We present a study on the unoccupied electronic structure of Bi/Ag(111) with spin- and angle-resolved inverse photoemission. Above the Fermi level, we identified several states with distinct spin dependence. We determined their nature concerning symmetry, bulk vs. surface character, energy vs. momentum dispersion, and spin dependence. In particular, we focused our attention to the spin character of the $m_{\parallel}=1/2$ surface state. While theoretical calculations [1] predict a complex spin topology, where the spin polarization changes sign at the band maximum, our experimental findings indicate a spin splitting compatible with the classical Rashba model. To shed more light on this issue, we investigated the spin topology with the help of first-principles electronic-structure calculations. We will discuss the difficulty of assigning a pure spin character to a particular Rashba band, especially in view of the experimental geometry, which itself influences the measured spin character.

[1] G. Bihlmayer *et al.*, Phys. Rev. B **75**, 195414 (2007)

11:00am **MI-MoM9 Growth and Properties of Skymionic MnSi Thin Film**, *J.Y. Yi, S.W. Tang*, University of Tennessee, *G.X. Cao*, Oak Ridge National Laboratory, *D.G. Mandrus*, University of Tennessee, *Z. Gai*, Oak Ridge National Laboratory

MnSi is well-known for its magnetic chiral structure due to lack of inversion symmetry of B20 crystal structure at 29.5K to 43K. The helical magnetic structure results from Dzyaloshinsky-Moriya (DM) spin-orbit interactions. Inspired by its magnetic structure, which is left-handed spiral oriented along $\langle 111 \rangle$ axes, and low mismatch between Si(111) and MnSi(111) as well, we successfully grew the MnSi(111) thin film by co-evaporating Mn and Si on Si(111) in UHV. The structural, electric properties and magnetic properties of MnSi(111) thin film are examined using in-situ low temperature STM, STS and ex-situ SQUID magnetometer.

11:20am **MI-MoM10 Skymionic MnSi Nanowires on Si: SiO₂ Layer as a Catalyst Assistant for the CVD Growth**, *S.W. Tang*, University of Tennessee, *I. Kravchenko*, Oak Ridge National Laboratory, *J.Y. Yi, G.X. Cao*, University of Tennessee, *J. Howe*, Oak Ridge National Laboratory, *D.G. Mandrus*, University of Tennessee, *Z. Gai*, Oak Ridge National Laboratory

Magnetic skymion, a vortex-like spin-swirling object recently observed in chiral-lattice magnets, are of great interest to future spin-electronic related data storage and other information technology applications. We report that single crystal helimagnetic MnSi nanowires could be synthesized in large amounts via SiO₂ thin film assisted chemical vapor deposition comparing to previous reports, SiO₂ plays an important role in controlling amount of diffusing Si to achieve relative low supersaturation ratio. Growth process is controlled so as to find the optimized parameters. Based on that, a temperature-time-distance growth phase diagram is plotted. The ac and DC magnetic properties of MnSi nanowires reveal the persistent of the helimagnetic and skymion magnetic ordering in the one-dimensional wires. Devices are fabricated via photolithography and e-beam lithography. Transport properties of this single wire device are measured.

11:40am **MI-MoM11 Epitaxial Growth, Transport, and Electronic Structure of Half Heusler Compounds: CoTiSb, NiTiSn, and Ni_{1-x}TiSn/NiTiSn Nanocomposite Films**, *J.K. Kawasaki*, UCSB, *L.M. Johansson*, Lund University, Sweden, *J. Shabani*, A. Rice, UCSB, *M. Hjort*, R. Timm, Lund University, Sweden, *B.D. Schultz*, UCSB, *T. Balasubramanian*, A. Mikkelsen, Lund University, Sweden, *C.J. Palmstrom*, UCSB

The Half Heuslers are an attractive family of compounds for high temperature thermoelectrics, and recently there has been renewed interest in these compounds since some are proposed to be topological insulators. We report the epitaxial growth, transport, and angle resolved photoemission

spectroscopy (ARPES) measurements of epitaxial films of the Half Heusler compounds CoTiSb and NiTiSn. Both belong to the subset of Half Heuslers with 18 valence electrons per formula unit that are predicted to be trivial insulators despite being composed entirely of metallic components. Here the CoTiSb and NiTiSn films were grown by molecular beam epitaxy on lattice matched InAlAs/InP (001) and (111), or on MgO (001), respectively. The films are epitaxial and single crystalline, as measured by reflection high-energy electron diffraction, low energy electron diffraction, and X-ray diffraction. Both CoTiSb and NiTiSn films also show surface reconstructions that vary with anneal temperature.

For the CoTiSb, scanning tunnelling spectroscopy and temperature-dependent transport measurements reveal that the films are insulating, with unintentionally doped carrier concentrations and mobilities comparable to that of highly doped conventional compound semiconductors ($n = 10^{18} \text{ cm}^{-3}$ and $\mu = 500 \text{ cm}^2/\text{Vs}$ at 300 K). The CoTiSb films also show a peak in the low temperature (1.8-10 K) magnetoresistance that may result from localization or some other mechanism. ARPES measurements reveal that CoTiSb is a bulk insulator but has surface states within the band gap.

Stoichiometric NiTiSn films also show semiconducting-like transport. Additionally, composites of Full Heusler Ni₂TiSn inclusions within a Half Heusler NiTiSn matrix have been grown by codeposition with excess Ni. Despite the large lattice mismatch (2.9%) between the Ni₂TiSn and NiTiSn, the Ni_{1-x}TiSn films remain epitaxial for compositions in excess of $\delta > 50\%$. These Half Heusler / Full Heusler nanocomposites show promise for phonon scattering in thermoelectric applications.

This work was supported by the ARO, ONR, and NSF.

MEMS and NEMS

Room: 102 A - Session MN+AS+SS-MoM

Fabrication and Multi-scale Interactions of Materials, Surfaces, and Interfaces at the Micro- and Nano-scale
Moderator: A.V. Sumant, Argonne National Laboratory

8:20am **MN+AS+SS-MoM1 Enhancing Selectivity and Sensitivity of Microfabricated Sensors using Multi-Scale Interactions**, *T.G. Thundat*, University of Alberta, Canada **INVITED**

Achieving selectivity and sensitivity simultaneously in microfabricated chemical sensors has been a longstanding challenge. Chemical selectivity based on immobilized chemoselective receptors on sensor surfaces fails to achieve speciation in complex environments due to the generality of molecular interactions. However, by incorporating functions which can provide orthogonal signals, it is possible to achieve selectivity, sensitivity, and fast regeneration in miniature sensors. Modulating the physical properties of the surface adsorbed target molecules provides multi-scale information which can be analyzed for molecular recognition. The physical patterning of the sensor surface increases the number of target molecules adsorbed on the surface which results in higher sensitivity. I will discuss recent advances in the integration of multimodal signal generation onto a single platform in microfabricated sensors in order to achieve selectivity, sensitivity, and fast regeneration.

9:00am **MN+AS+SS-MoM3 Meso Scale MEMS Inertial Switch Fabricated using Electroplated Metal on Insulator (MOI) Technique**, *Y. Gerson, D. Schreiber*, Tel Aviv University, Israel, *H. Gerou*, Microsystems Design Center, RAFAEL LTD, *S. Krylov*, Tel Aviv University, Israel

Micro switches triggered by inertia are widely used as safety and protection devices in airbags, arming and firing systems. These devices are typically fabricated of silicon and incorporate a movable proof mass suspended on flexure-type springs. When a sufficient acceleration is applied, the mass moves towards the fixed electrode resulting in an electrical path that triggers an electric circuit. Electrodeposited metallic devices offer an attractive alternative to silicon in the fabrication of high aspect ratio devices. Nickel is one of the most common materials used for this purpose. The Young's modulus of nickel is close to that of silicon though its density is nearly four times higher and the electric conductivity is five orders of magnitude higher than of highly doped silicon. Nickel is also exceptionally resistant to wet and dry chemical etching, aggressive chemicals and corrosion.

In this work, we report on a novel approach for the fabrication of high aspect ratio electrodeposited nickel MEMS devices. The two mask process is distinguished by its simplicity and does not require formation of anchors/vias for the attachment of the device to the substrate. In this context, similarity between this process and common silicon on insulator (SOI) fabrication paradigm can be mentioned. KMPR negative photoresist is used as a mold due to its ability to yield high aspect ratio structures (>5:1)

with vertical sidewalls as well as the relative ease of removal. The devices are fabricated on a 2" single side polished wafers with 4 μm of thermally grown silicon dioxide (TOX). First, a lift-off metallization is performed to define a patterned Cr/Cu seed layer. At the second stage, a 40 μm thick KMPR 1050 negative photoresist is spun on top of the seed layer followed by electrodeposition of a 35 μm thick nickel layer. Next, the stripping of the KMPR mold is performed by ultrasonication bath of remover PG followed by etching with O_2 plasma to remove the resist leftovers. Finally, the wafer is diced into $3\text{mm} \times 3\text{mm}$ chips and the devices are released first by dipping in a HF to etch the sacrificial oxide and then by etching the copper and chrome. The HF etch time is tailored in such a way that the anchors remain unreleased whereas the free standing elements are released by undercut. The fabricated devices were mounted in a ceramic enclosure and characterized using a drop tester. The triggering event was captured by registered the steep decrease of the resistance down to less than 10 Ω value and functionality of the device was demonstrated in the experiment. Good agreement between the designed values of the triggering time and the experimental data was observed.

9:20am **MN+AS+SS-MoM4 Fabrication and Characterization of Porous Carbon Nanotube Composite Resonators**, *S. Noyce, R.C. Davis, R.R. Vanfleet, D.D. Allred, B.D. Jensen*, Brigham Young University

Porous resonators have the potential to overcome limitations in the micro-resonator field. For example, such structures with high surface area are potentially capable of higher detection limits than solid resonators when used as sensors, due to a higher mass change in a gas or liquid sensing environment. An important consideration for such resonators is the effect of thermo-elastic dampening. We present a versatile micro-resonator fabrication process in which carbon nanotubes are grown from a patterned catalyst, after which the space between the tubes is filled to various degrees of porosity with carbon through Chemical Vapor Deposition. Structural and mechanical characterization data regarding resonators fabricated with this process are presented.

9:40am **MN+AS+SS-MoM5 Fabrication of 3D Nickel Microstructures by Pulsed Electrodeposition on Carbon Coated Carbon Nanotubes**, *L. Barrett, D. Barton, R.C. Davis, R.R. Vanfleet, D.D. Allred*, Brigham Young University

High aspect ratio metallic microstructures have a variety of potential applications in sensing and actuation. However, fabrication remains a challenge. We have fabricated Ni microstructures with aspect ratios greater than 20:1 by electroplating a pattern of carbon coated carbon nanotubes (CNTs). Patterned CNT forests were grown from ethylene by an atmospheric chemical vapor deposition (CVD) at 750°C followed by a second ethylene CVD step at 900°C. The second step coats the CNTs and the substrate with a 10nm carbon layer. This coating locks the CNTs together at the points where they touch each other and adheres the CNT forest to the substrate which prevents the forest from deforming or delaminating in the electroplating bath. This carbon coated CNT structure is approximately 95% void space. The void space was then filled with Ni by pulsed electroplating the carbon coated CNTs in a low stress nickel sulfamate bath with a 3ms on time and a 15ms off time. The off time allows the Ni ions to diffuse into the structure to improve uniformity. We will present on the development of the fabrication process and characterization of the resulting C-Ni composite 3D microstructure.

10:00am **MN+AS+SS-MoM6 Dielectric Properties of Electroactive Polymer P(VDF-TrFE-CFE) for Sensor and Actuator Applications**, *L. Engel, S. Kruk, J. Shklovsky, Y. Shacham-Diamand, S. Krylov*, Tel Aviv University, Israel

The rapidly developing field of polymeric electronic and microelectromechanical (MEMS) devices has attracted much attention in recent years. Applications of polymeric MEMS devices include thin film transistors, waveguides for optical sensors, stretchable electronics as well as electroactive polymers (EAP) and dielectric elastomers actuators (DEAs). Polymeric actuators are distinguished by their very low fabrication cost, are often biocompatible, demonstrate large strain under small forces, and exhibit fast response times with relatively large actuation forces and high efficiency. The present work focuses on the integration of the recently developed relaxor ferroelectric polymer poly(vinylidene fluoride-trifluoroethylene-chlorofluoroethylene)(P(VDF-TrFE-CFE)) with MEMS/NEMS. The high electrostrictive strains, low hysteresis, and high dielectric constant exhibited by this polymer make it particularly attractive for device fabrication, however, these properties depend strongly on the dielectric nature of the polymer. Because of the coupling between P(VDF-TrFE-CFE)'s mechanical behavior and electrical properties, it is critical to device design that we fully understand its dielectric behavior in a MEMS capacity.

We report on the patterning and electrical characterization of a terpolymer of composition $\text{VF}_2 : 61.3\% / \text{VF}_3 : 29.7\% / \text{CFE} : 9\%$ at the micron scale. Through the use of micro-capacitor test structures, we explored the dielectric constant of the P(VDF-TrFE-CFE) as a function of temperature, frequency, and different processing conditions. The morphology of the semi-crystalline polymer under different microprocessing techniques was examined using AFM and XRD, providing a correlation between the material properties and electrical behavior of the polymer. At ~ 57 , dielectric constant at room temperature of this terpolymer is an order of magnitude higher than is typical for polymers, making P(VDF-TrFE-CFE) attractive for MEMS and in particular, organic electronic type sensors.

Acknowledgements

This project was supported by Arkema/Piezotech. P(VDF-TrFE-CFE) materials were supplied by Piezotech S.A.S

10:40am **MN+AS+SS-MoM8 Silicon Carbide Micro-/Nanosystems for Sensing and Energy Applications**, *R. Maboudian, C. Carraro*, UC Berkeley

INVITED

Silicon has been the dominant semiconducting material in micro-/nanosystems technologies. However, the material and surface properties of silicon impose limitations on its use in applications involving harsh environment (such as high temperature, high radiation and corrosive conditions). Silicon carbide (SiC), a wide bandgap semiconductor, is emerging as a material to address the limitations of Si as it is temperature tolerant, radiation resistant, and chemically inert. In this talk, I will present recent advances, by our group and others, in the materials science and manufacturing technology of SiC thin film and low dimensional structures. This includes deposition, metallization, and fabrication of semiconductor microdevices, with particular emphasis on sensor and energy technologies.

11:20am **MN+AS+SS-MoM10 Development of Through-Silicon via Contacts for Front Side Electrodes in ISFET Sensors**, *A. Erten, S. Park, E. Briggs, D. Martin, Y. Takeshita, T. Martz, A.C. Kummel*, University of California San Diego

Ion-Sensitive Field Effective Transistors (ISFETs) are used for measuring the activity and concentration of ions in solutions. ISFETs are modified Metal-Oxide-Semiconductor FET (MOSFET), which utilize changes in the floating potential on the gate insulator to modulate the current between source and drain. When employed as a pH sensor, ISFETs are operated at constant source-drain current by modulating the potential of the solution via a reference electrode of ISFET. The overall potential change at gate is a direct measurement of the solution pH. Adding an additional gold electrode near the gate region of the ISFET allows the total alkalinity to be determined, which has critical applications in oceanography to study ocean acidification as well as temporary variability in the marine CO_2 system. The gold electrode is used to generate protons (H^+) which react with the OH^- (aq) thereby neutralizing the pH, which is being monitored by the ISFET gate. This has been successfully demonstrated by using a front side contact to the gold electrode. In a simple 0.5 M NaCl solution, the differences in total alkalinity with 1 millimolar precision were measured within 15 second as predicted by simple device models. However, for practical applications, a backside contact to the front side gold electrode is needed so that all the circuitry and wire bonds can be protected from the solution. In this study, a method for fabrication of through-silicon via contacts for front side electrodes in ISFET dies is discussed. To form backside contacts for front side gold electrodes, it requires patterning and deep etching of a chip with an extremely corrugated topology. The ISFET dies already have two backside quasi-through chip vias for backside contact to the source and drain regions, and this non-planar surface obviates the ability of conventional photoresist coating methods to form a uniform film. A new patterning technique was developed for through-chip etching on highly non-planar surfaces using a roll-on photoresist film to overcome the challenges presented by non-planar surfaces. An oxygen plasma was employed to clean the surface and enhance the adhesion between substrate and photoresist film. In comparison with spray coating and spin coating techniques, roll-on photoresist film method showed significantly improved uniformity and adhesion. This method was also employed to protect the substrate from etch plasma. Reactive ion etching was used to etch away oxide layer before gold deposition and Bosch process. Using through-silicon Bosch etching, a via could be made and gold coating could be employed to contact the front side electrode of ISFET.

11:40am **MN+AS+SS-MoM11 A New MEMS-Based Voltage Controlled Variable Capacitor for Gamma Ray Detection**, *M. Serry, A. Sharaf*, The American University in Cairo, Egypt

This paper reports on a new MEMS-based technique for the rapid and highly sensitive detection of gamma irradiation. The proposed sensor detects small doses of gamma photons through changes in the mechanical and electrical properties of the MEMS structure, which consists of a voltage

controlled variable capacitor coated with a gamma photons sensitive polymer. Upon exposure to photons, the polymer crystallizes, triggering a coupled effect: increased stiffness in the folded beam suspensions and altered permittivity, which result in measurable shifts in resonance frequency and capacitance. Based on these mutually reinforcing effects, the proposed design is an unprecedented method for multiplying a sensor's sensitivities for more accurate detection of gamma photons. Two preliminary devices have been fabricated and exposed to gamma radiation doses (5-35 kG) using a Co60 source; the results indicate the sensor's elevated sensitivity (1.1 pF/G), which is higher than current state-of-the-art devices. MEMS integrated devices could replace most current conventional radiation sensors, the majority of which rely mainly on one mode of detection alone—lattice defects in single crystal silicon structures that are induced by irradiation. These defects are detected through resistance or capacitance changes. The current techniques, however, have substantial drawbacks: 1) limited sensitivity; 2) high probability of error; and 3) limited efficacy (i.e., one-time usage). To overcome these drawbacks, we introduce selective electro-deposition of gamma photon sensitive polymers on the combs and folded beam suspensions of the sensors. The mechanical design of the structure yields a more responsive sensor with a stronger output signal by coupling changes in mechanical resonance due to increased stiffness with changes in capacitance as a result of alterations in the dielectric constant of the media. Both effects work together to enhance sensitivity as well as increase the accuracy of the measurements. An SOI wafer is etched on to the front and back sides of the sensor to release the shuttle mass and expose the areas that need to be selectively coated by the gamma-sensitive polymer. Preliminary structures have been employed to test the device's response under different gamma-ray dosages using a Co60 source ranging from 5-35 kG. Capacitance voltage characteristics and the loss factor through the dielectric layer versus the applied voltage across the dielectric media have been characterized. A sensitivity of up to 1.1 pF/G can be achieved.

Manufacturing Science and Technology

Room: 202 B - Session MS+AS+EM+EN+NS+TF-MoM

IPF 2013-Manufacturing Challenges: R&D Perspective (8:20-9:40 am) / Energy Storage (9:40 am-12:00 pm)

Moderator: K. Amm, GE Global Research, B.R. Rogers, Vanderbilt University

8:20am **MS+AS+EM+EN+NS+TF-MoM1 From Quanta to the Continuum: Opportunities for Mesoscale Science, G. Crabtree**, Argonne National Laboratory **INVITED**

Mesoscale science embraces the regime where atomic granularity and quantization of energy yield to continuous matter and energy, where high levels of complexity and functionality emerge from simple components, and where disparate degrees of freedom interact to produce entirely new behavior. Mesoscale science builds on the ever-growing foundation of nanoscale tools and insights that the community has developed over the last decade and continues to develop. Control of mesoscale complexity offers new scientific and technological opportunities: applying our mastery of nanoscale interactions to discover and design new architectures from the “bottom up” that display innovative macroscopic behavior and functionality. This constructionist approach to designing and building new functional architectures creates new horizons for mesoscale manufacturing, where principles of design and implementation differ fundamentally from conventional “top down” macroscopic approaches. Examples of mesoscale successes, challenges and opportunities will be described.

A more complete discussion of mesoscale science can be found in the BESAC report, *From Quanta to the Continuum: Opportunities for Mesoscale Science*, <http://science.energy.gov/bes/news-and-resources/reports/basic-research-needs/>

Innovative community input on opportunities for mesoscale science can be found on the *Mesosopic Materials and Chemistry* website, <http://www.meso2012.com/>

9:00am **MS+AS+EM+EN+NS+TF-MoM3 The National Network for Manufacturing Innovation – Towards a New Innovation Ecosystem for Advanced Manufacturing, M. Molnar**, National Institute of Standards and Technology **INVITED**

A key challenge to restoring U.S. leadership in advanced manufacturing is addressing the so-called “missing middle” – the technical and business barriers of scaling-up an innovative new material, process, or technology for robust production use. This plenary talk explores the National Network for Manufacturing Innovation as a means to accelerate U.S. innovation. As

proposed by President Obama NNMI is a network of manufacturing institutes where Industry and Academia partner on industry-relevant challenges. Each institute would be chartered in a competitively selected topic and focus on nationally important, precompetitive technologies to create “innovation hubs” for transformational impact.

This plenary will review the NNMI progress to date, including the current design of the institute and supporting network and core functions. The emerging design builds on the extensive public input and the progress of the pilot institute on Additive Manufacturing, explored in detail in the following plenary. The discussion concludes with a review of the three manufacturing institutes topics being established this year.

9:40am **MS+AS+EM+EN+NS+TF-MoM5 Conformal Thin Films- The Use of Atomic Layer Deposition in Energy Related Applications, G.M. Sundaram**, Ultratech/Cambridge NanoTech **INVITED**

Atomic Layer Deposition (ALD) is a unique thin film deposition technique based on sequential precursor usage with self-limiting reactions, which yields films with excellent uniformity, density, conformality, and interface quality. This is turn has set the stage for its use in a wide array of technology areas. In this work, the principles of ALD will be covered, along with an examination of the intersection points between ALD and a number energy related structures - including storage devices.

10:40am **MS+AS+EM+EN+NS+TF-MoM8 Manufacturing a Three-dimensional, Solid-state Rechargeable Battery, A. Prieto**, Colorado State University, D. Johnson, Prieto Battery, Inc. **INVITED**

There are two main limitations to the rate of charging for Li-ion batteries: slow diffusion of Li^+ into the electrodes and slow diffusion *between* them. The synthesis of high surface area electrodes has been shown to dramatically enhance performance because reducing the particle size of the electrode material reduces the distance the Li^+ ions have to diffuse. *The problem of decreasing the Li^+ diffusion length between electrodes has not yet been solved.* We are working to incorporate high surface area foams of a novel anode material into a new battery architecture wherein the foam is conformally coated with an electrolyte made by electrochemical deposition, then surrounded by the cathode electrode. The significant advantage to this geometry is that the diffusion length for Li^+ between the cathode and anode will be dramatically reduced, which should lead to much faster charging rates. However, if this battery is going to be useful and commercializable, it must be manufactured using low cost, reliable, scalable methods. I will present preliminary results on the initial stages of the battery architecture, including the fabrication of anode foams conformally coated with a polymer electrolyte. The reversibility of the intercalation into the anode and the ionic conductivity of the polymer electrolyte will be discussed.

11:20am **MS+AS+EM+EN+NS+TF-MoM10 Defects, Nonuniformities, and Degradation Mechanisms in Batteries, S. Harris**, Lawrence Berkeley National Laboratory **INVITED**

We review work from our laboratory that suggests to us that most Li-ion battery failure can be ascribed to the presence of nano- and microscale inhomogeneities that interact at the mesoscale, as is the case with almost every material; and that these inhomogeneities act by hindering Li transport. (Li does not get to the right place at the right time.) For this purpose, we define inhomogeneities as regions with sharply varying properties—which includes interfaces—whether present by “accident” or design. We have used digital image correlation, X-Ray tomography, FIB-SEM serial sectioning, and isotope tracer techniques with TOF-SIMS to observe and quantify these inhomogeneities. We propose new research approaches to make more durable, high energy density lithium ion batteries.

Nanometer-scale Science and Technology

Room: 203 B - Session NS+BI+EM-MoM

Nanophotonics and Plasmonics

Moderator: D. Wei, University of Florida

9:00am **NS+BI+EM-MoM3 Predetermining Paths of Nanoscale Crack by Local Thermally Induced Strain Fields, M.R. Cho, P.K. Kim, Y.D. Park**, Seoul National University, Republic of Korea

We demonstrate well-defined path control of nanoscale cracks in SiO_2 thin-films on Si substrate. When cracks are initiated their paths are confined in a predetermined track of arbitrary shape. The confinement of the crack paths is attributed to local thermally induced strain fields. We define the strain fields by utilizing the large differences between coefficients of linear thermal expansion between metallic thin-films and SiO_2 . On top of the substrate, a metallic strip of arbitrary shape is first predefined. Next, a layer

of SiO₂ is e-beam evaporated, followed by a thermal cycling. We then initiate the cracks by either a predetermined notch or by, more simply, a macro scratch far from the predefined track. Once the leading edge of the crack enters the predefined track, the crack, with width at the surface of SiO₂ of ~50-200 nm, is laterally confined within a width > 2 μm, predefined path length in the millimeter range (or higher), and a minimal turn radius of curvature > 20 μm, and its path shape within the confined track is of nontrivial oscillatory. We present finite element analysis simulations as well as a model that explains and fits well the crack path shape within the track. We also discuss utilizing our results to realize bulk fabrication of nano-gap plasmonic device, nano-gap electrode and nano fluidic channel devices.

9:40am NS+BI+EM-MoM5 Single-Molecule Surface Enhanced Raman Scattering using Silver Coated Nickel Nanorod Arrays, A. Nash, D. Ye, Virginia Commonwealth University

Nickel nanorods arrays were prepared on silicon (100) substrates using the glancing angle deposition (GLAD) technique. Subsequently, the nanorods were coated with 30 nm thick silver on the tip of the nanorods without breaking vacuum. The surface enhanced Raman scattering (SERS) at near single molecule levels was verified in a Horiba confocal Raman microscope using low concentration Rhodamine 6G. At the concentration 3×10^{-14} M, blinking of the Raman peaks were observed. We found that the Raman signal intensities can be related to the concentration of the analytes by the Langmuir-Freundlich adsorption isotherm.

10:00am NS+BI+EM-MoM6 Merged Photonic Crystal Slot Waveguide - ALD Coated Silicon Nanophotonics, P. Stenberg, M. Roussey, S. Honkanen, M. Kuitinen, University of Eastern Finland

Research related to Silicon photonics is a topic of high interest in the photonics community. Demands in the field of all optical signal processing are driving research and industry towards faster and more efficient devices and processes. The interest against Silicon is not merely because of the optical characteristics of the material but also because the fabrication of Silicon photonic devices can be adapted to the existing production lines enabling cost efficient mass fabrication.

Our study is focused on a Silicon photonic nanodevice called Merged Photonic Crystal Slot Waveguide (MPCSW), in which features of photonic crystals (PhC) and slot waveguides are compiling, by taking advantage of the slow light effect in the PhC [1] and the field confinement in the slot region [2]. We propose to create the PhC by directly patterning the rails of the slot waveguide. The device is designed on a Silicon on insulator (SOI) substrate and it is coated with amorphous TiO₂ by Atomic Layer Deposition (ALD) technique to fill the structure with optically interesting nonlinear material.

We have studied the possibility to use the device as a band pass filter in near infrared region. The MPCSW structure is designed by using three dimensional Finite Difference Time Domain (3D-FDTD) method to create a photonic band gap (PBG) and a transmission peak appearing in the center of it.

For easier coupling, the input and output waveguides are 3 μm wide and are tapered to nano-waveguides. Coupling from a nano-waveguide to a slot waveguide is made by using an adiabatic coupler to reduce the conversion loss. The adiabatic couplers and nano-to-micro tapers are at both ends of the fabricated waveguide structure. The MPCSW is placed in the middle of the waveguide structure and it contains 10 periods of photonic crystal on both sides of the cavity. The whole device is embedded in conformally coated amorphous TiO₂.

In our presentation we show results concerning simulation and characterization. In simulation we introduce normalized transmission spectra as a function of the fill factor, the cavity length and the period. Also the group index corresponding to the transmission spectra for the same parameters is presented. The fabrication of the structure is discussed where electron beam lithography, plasma etching and ALD techniques are used. Finally we propose possibilities to use the device in nonlinear guided-wave optics by taking advantages of the slow light effect in the PhC and the field confinement in the slot region when the structure is filled with a nonlinear material.

[1] M. Roussey, J. Opt. Soc. Am. B, **24**, 1416-1422, (2007)

[2] A. Säynätjoki, Optics Express, **17**, 21066-21075, (2009)

10:40am NS+BI+EM-MoM8 Engineering Multimodal Localized Surface Plasmon Resonances in Silicon Nanowires, L.-W. Chou, M.A. Filler, Georgia Institute of Technology

Semiconductors, as a result of their widely tunable carrier density (10^{19} - 10^{21} cm⁻³), are emerging as promising plasmonic materials for applications in the infrared and near-infrared. Silicon, in particular, is inexpensive relative to the noble metals and benefits from a robust suite of processing tools due to its extensive use in the semiconductor industry. To this end, we

recently reported that phosphorus-doped Si nanowires can support mid-infrared localized surface plasmon resonances (LSPRs) with quality factors comparable to those of the noble metals [1]. Herein, we demonstrate that axial control of dopant profile in individual nanowires permits complex, user-programmable, multimodal spectral responses. Highly aligned Si nanowire arrays are synthesized via the vapor-liquid-solid (VLS) technique with a combination of Si- and P-containing precursors. *In-situ* infrared absorption spectroscopy measurements reveal intense absorption bands (5 - 10 μm) with dopant concentration and shape-dependent spectral shifts consistent with longitudinal LSPRs. Discrete dipole approximation (DDA) calculations confirm that the observed spectral response results from resonant absorption and free carrier concentrations on the order of 10^{20} cm⁻³. We also observe near-field coupling between neighboring plasmonic domains, which varies as a function of intrinsic spacer length and can be described with hybridization theory. Our results highlight the utility of VLS synthesis for surface plasmon engineering in semiconductors, create new opportunities to study basic surface plasmon physics, and pave the way for applications including ultra-sensitive molecular detection and thermal energy harvesting.

[1] Chou, L.-W.; Shin, N.; Sivaram, S. V.; Filler, M. A. *J. Am. Chem. Soc.* **2012**, *134*, 16155.

11:00am NS+BI+EM-MoM9 Exploiting Plasmon Induced Hot Electrons in Molecular Electronic Devices, D. Conklin, S. nanayakkara, T.-H. Park, University of Pennsylvania, M. Lagadec, ETH Zürich, Switzerland, J. Stecher, Duke University, X. Chen, University of Pennsylvania, M. Therien, Duke University, D.A. Bonnell, University of Pennsylvania

Plasmonic nanostructures can induce a number of interesting responses in devices. Here we show that hot electrons can be extracted from plasmonic particles and directed into a molecular electronic device, which represents a new mechanism of transfer from light to electronic transport. To isolate this phenomenon from alternative and sometimes simultaneous mechanisms of plasmon-exciton interactions we designed a family of hybrid nanostructure devices consisting of Au nanoparticles and optoelectronically functional porphyrin molecules that enable precise control of electronic and optical properties. Temperature and wavelength dependent transport measurements are analyzed in the context of optical absorption spectra of the molecules, the Au particle arrays and the devices. Enhanced photocurrent associated with exciton generation in the molecule is distinguished from enhancements due to plasmon interactions. Mechanisms of plasmon induced current are examined and it is found that hot electron generation can be distinguished from other possibilities.

11:20am NS+BI+EM-MoM10 Coherent Imaging of Surface Plasmon Dynamics by Time-resolved Photoelectron Emission Microscopy, H. Petek, University of Pittsburgh

INVITED

We study surface plasmon polariton (SPP) generation, propagation, diffraction, interference, focusing, and decay by femtosecond time-resolved photoemission electron microscopy (PEEM) and electromagnetic simulations. Equal-pulse pump-probe pulses with interferometrically defined delay excite two-photon photoemission from Ag surfaces. The imaging of the spatial distribution of photoemitted electrons by PEEM reveals a nonlinear map of the total surface electromagnetic fields impressed on the sample. On a nanostructured surface the images reveal coherent polarization gratings consisting of superposition of the incoming excitation pulses and propagating SPP wave packets that are generated at nanofabricated coupling structures. By changing the delay between the pump and probe pulses in steps of ~330 as we record movies of the evolving coherent polarization at the Ag/interface, which reflects the evolution of the surface electromagnetic fields. Through the combination of femtosecond laser excited photoemission and imaging of photoelectrons we can record <10 fs time scale coherent polarization dynamics with ~50 nm spatial resolution. [1]

The SPP fields are generated by specifically designed coupling structures formed by lithographic techniques in Ag films. The physical properties of the coupling structures and the geometry of the excitation define the subsequent SPP dynamics. To obtain a quantitative understanding of the SPP generation and PEEM imaging we perform FDTD calculations on the coupling of the external field into the SPP mode and compare them to experiments for slit coupling structures with different geometries. [4] Using more complicated coupling structures, we demonstrate SPP interference and focusing. [5] Through time-resolved PEEM measurements on nanostructured metal films we will explore the techniques for the coherent control of electromagnetic fields in nanostructured electronic materials on the femtosecond temporal and nanometer spatial scales.

References

[1] A. Kubo, K. Onda, H. Petek, Z. Sun, Y. S. Jung, and H. K. Kim, *Nano Lett.*, **5**, 1123 (2005).

- [2] A. Kubo, N. Pontius, and H. Petek, *Nano Lett.*, 470 (2007).
- [3] A. Kubo, Y. S. Jung, H. K. Kim, and H. Petek, *J. Phys. B*, S259 (2007).
- [4] L. Zhang, A. Kubo, L. Wang, H. Petek, and T. Seideman, *Phys. Rev. B*, 245442 (2011).
- [5] H. Petek and A. Kubo, in *Handbook of Instrumentation and Techniques for Semiconductor Nanostructure Characterization*, Haight, R.; Ross, F.; Hannon, J., Eds. World Scientific Publishing/Imperial College Press: 2011.

Plasma Science and Technology

Room: 102 B - Session PS+AS+BI+SE-MoM

Atmospheric Plasma Processing: Fundamental and Applications

Moderator: M.A. Lieberman, University of California, Berkeley

8:20am **PS+AS+BI+SE-MoM1 Field Emission in Microscale Dimensions: A New Approach to Atmospheric Pressure Gas Discharges**, *Y. Li, P. Rumbach, D.B. Go*, University of Notre Dame
INVITED

Electron field emission is traditionally considered a low-pressure phenomenon and most field emission-based technologies, such as scanning electron microscopes, generate field emission under high vacuum conditions. However, over the course of past decade, advances in microscale devices have led to the field emission devices that operate at high pressures, including at and near to atmospheric pressure. At these pressures, the field-emitted electrons can ionize the interstitial gas between the electrodes, leading to the formation of gas discharges. With emerging applications in gas sensing and gas reforming, this new approach to gas discharges not only introduces new, interesting physics but also offers many new technological opportunities. This work will focus on the theory and generation of stable, field emission-driven Townsend discharges. The physical concepts underpinning these discharges will be discussed as theoretical and modeling efforts have highlighted many significant features of this discharge mode – including very high electron densities ($\sim 10^{14}$ cm⁻³) and highly non-Maxwellian electron densities. Experimental studies and the role of the cathode material will also be discussed as evidence of pressure scaling for field emission will be presented. Finally, new applications and future opportunities for discovery will be covered.

9:00am **PS+AS+BI+SE-MoM3 Simulation of Microplasma Based Pressure Sensors**, *J.-C. Wang, Z. Xiong, C. Eun, X. Luo, Y. Gianchandani, M.J. Kushner*, University of Michigan

Pressure monitors in hostile environments often use piezoresistive and capacitive based sensors. The smallest dimension of this class of sensors is about 1 mm. Recently, a microplasma-based pressure sensor has been developed which is capable of dimensions at least an order of magnitude smaller. In these sensors, a plasma is initiated between an anode and two competing cathodes in a sealed chamber having a diaphragm as one surface. External pressure deflects the diaphragm which changes the inter-electrode spacing for one of the anode-cathode pairs, thereby redistributing the current collected by the two competing cathodes. Pressure is then proportional to the relative difference in current collected by the two cathodes.

In this presentation, we will discuss the properties of microplasma-based pressure sensors using results from a two-dimensional simulation. The model, *nonPDPSIM*, solves Poisson's equation, transport equations for charged and neutral species, and the electron energy conservation equation for electron temperature. Radiation transport is addressed using a Green's function approach, and sheath accelerated electrons are addressed using Monte Carlo methods. The microplasma is sustained between an anode (A) biased with hundreds of volts and two grounded cathodes (K₁, K₂) in a sealed chamber filled with 1 atm of Ar or rare gas mixtures. The reference cathode (K₁) is located adjacent to the anode while the sensing cathode (K₂) is mounted on the diaphragm separated by a gap of 10 to 100 μm. We find that following a small amount of electric field emission of electrons from the edges of K₁ and K₂, the electrons rapidly avalanche in the geometrically enhanced electric field at the edge of the anode and creates a conductive plasma within tens of ns. The current distribution on K₁ and K₂ varies with inter-electrode spacing (AK₂) which is changed by deflection of the diaphragm due to the external pressure. The current distribution can also be optimized by adjusting the impedance connected to electrodes.

*Work was supported by the Advanced Energy Consortium.

9:20am **PS+AS+BI+SE-MoM4 A Flexible Paper-based Microdischarge Array Device for Maskless Patterning on Nonflat Surfaces**, *Y.J. Yang*, M.Y. Tsai, W.C. Liang, H.Y. Chen, C.C. Hsu*, National Taiwan University, Taiwan, Republic of China

This study presents a simple and economical paper-based microdischarge array for maskless surface patterning under atmospheric pressure condition. This paper-based system is a dielectric-barrier-discharge (DBD)-type device and stable plasmas can be sustained in an array of cavities. Due to its flexible feature, this paper-based device allows for performing non-flat surface patterning processes with a feature size down to 500 μm. When a flat or a curved glass surface with 6 mm in its curvature is directly treated by the Ar plasma generated by this device, hydrophilic spots can be generated on the flat or curved surface, respectively. While using tetraglyme as the precursor in Ar atmosphere, this paper-based device is able to perform plasma polymerization and to pattern polyethylene oxide (PEO)-like array of patterns on glass surfaces. Under this arrangement, the optical emission spectrum emanating from the plasma show CO emissions at 561 nm during the deposition process, suggesting that the participation of precursor molecules in the process. The FTIR spectra of deposited films show absorption of C-O-C bonding at 1100 cm⁻¹, indicating retaining of ether groups. To test the anti-fouling property of this film, Alexa Fluor 546-conjugated fibrinogen was utilized as a model reporter molecule for protein absorption test. The fluorescence image shows clear contrast between the coated and non-coated area. The PEO-patterned regions appear to be dark since no protein absorption occurs. This work demonstrates a flexible and cost-effective approach to pattern flat and non-flat surfaces with a maskless process. This work was supported by National Science Council of Taiwan, the Republic of China (101-2221-E-002-163-MY2)

9:40am **PS+AS+BI+SE-MoM5 Hydrophobic Fluorocarbon Films Synthesized from Liquid Monomers by Atmospheric Pressure Plasma**, *J. Hubert, N. Vandencastele, T. Dufour*, Univ. Libre de Bruxelles, Belgium, *C. Poleunis*, Univ. catholique de Louvain, Belgium, *P. Laha*, Vrije Univ. Brussel, Belgium, *P. Viville*, Materia Nova, Belgium, *A. Delcorte, P. Bertrand*, Univ. catholique de Louvain, Belgium, *H.A. Terryn*, Vrije Univ. Brussel, Belgium, *R. Lazzaroni*, Materia Nova, Belgium, *F.A.B. Reniers*, Univ. Libre de Bruxelles, Belgium

The exceptionally low surface energy of polytetrafluoroethylene (PTFE), due to the CF₂ functional groups present on its surface gives the polymer advantageous properties such as hydrophobicity. In order to create PTFE-like films, low pressure plasma deposition of fluorocarbon films has been extensively studied in the last decade. These works focus however on the use of gaseous precursors such as CF₄, C₂F₆ or C₄F₈.

In the present study, hydrophobic fluorocarbon coatings have been synthesized from two different precursors, which are liquid at room temperature. Perfluorohexane (C₆F₁₄), a fully saturated monomer and perfluoro(2-methylpent-2-ene) (C₆F₁₂) containing one unsaturated bond are injected in a dielectric barrier discharge (DBD) by a continuous argon or helium flow. In order to characterize the plasma polymer films and the texturization process, both, analysis of the surface and the gas phase have been performed.

Secondary ion mass spectrometry (SIMS) and X-ray photoelectron spectroscopy (XPS) measurements have been performed to highlight the structure and composition of the C_xF_y films depending on the Yasuda factor (W/FM), throughout the influence of the power and the monomer flow rate. Water contact angle (WCA) measurements have shown that the hydrophobicity properties of the fluorocarbon films were similar to that of PTFE as WCA of 110° have been obtained. However, the structure also depends on the nature of the carrier gas (argon or helium) and in some cases, WCA as high as 140° were achieved. Atomic force microscopy AFM measurements are used to correlate the increase in hydrophobicity with the increase in roughness, which could be linked to the film thickness.

In order to complete the analysis of the polymerization process, mass spectrometry (MS) and optical emission spectroscopy (OES) have been performed. Fluorocarbon compounds such as CF, CF₂, CF₃, or higher mass fragments such as C₃F₃ or C₂F₄ have clearly been identified. Their detection combined to the SIMS analysis could help us to understand the polymerization mechanism/reaction of the two precursors.

10:00am **PS+AS+BI+SE-MoM6 Deciphering Gas-Phase and Solution-Phase Reactions Initiated by Plasmas at the Surface of Aqueous Solutions**, *P. Rumbach*, University of Notre Dame, *R.M. Sankaran*, Case Western Reserve University, *D.B. Go*, University of Notre Dame
Recent advancements in atmospheric-pressure plasma technology have enabled applications in polymer processing, plasma medicine, and water treatment. Many of these applications rely heavily on physical and chemical

* Coburn & Winters Student Award Finalist

interactions between plasmas and aqueous solutions. We have recently shown that plasma electrons are involved in electrolytic reactions such as the reduction of aqueous hydrogen ions (H⁺) to hydrogen gas[1]. In this work, we show that the reactions are more complex and involve a competition between plasma chemistry and solution chemistry.

To study interactions between a plasma and liquid, saline solutions were exposed to an argon (Ar) DC microplasma jet, and the effects of various reactions occurring in the plasma and solution phase were characterized. When the plasma jet was run in a background of argon or oxygen gas, traditional electrolytic reactions yielding sodium hydroxide (NaOH) were found to be dominant, making the solution more basic (pH ~ 8). Running the plasma jet in a background of atmospheric air produced significant amounts of nitric acid (HNO₃) and hydrogen peroxide (H₂O₂) in solution. Production of HNO₃ in air typically occurs at a rate two orders of magnitude higher than NaOH, making the solution more acidic (pH ~ 3). In a background of nitrogen gas, HNO₃ was also produced, but at a rate that is limited by oxygen gas evolution from water electrolysis. Overall, the chemical composition of the solution is affected by both electrolytic reactions at the plasma-liquid interface as well as reactions occurring in the bulk plasma.

[1] M. Witzke, P. Rumbach, D. B. Go, and R. M. Sankaran, *J. Phys. D: Appl. Phys.* **45**, 442001 (2012).

10:40am **PS+AS+BI+SE-MoM8 Prostate Cancer Treatment using Low-Temperature Atmospheric Pressure Plasmas: Advanced Optical Diagnostics and Multi-scale Numerical Simulations**, *D. O'Connell*, University of York, UK

INVITED

Non-equilibrium plasmas, operated at ambient atmospheric pressure and temperature, are very efficient sources for highly reactive neutral particles e.g. reactive oxygen and nitrogen species (RONS) (such as atomic oxygen, atomic nitrogen, nitrogen oxides), charged particles, UV-radiation, and electro-magnetic fields. Individually many of these components have been implicated in therapeutics. Plasmas have the advantage of delivering these components simultaneously providing potentially superior processes through synergies. This has led to the establishment of low-temperature plasmas with potential in disease therapeutics and plasma pharmacology. The challenges lie in understanding the mechanism of interaction, quantifying and accurately tailoring the plasma and its power dissipation. Suitable optimized plasma sources are currently lacking, and improbable through empirical investigations. Therefore, quantifying the power dissipation and energy transport mechanisms through the different interfaces from the plasma regime to ambient air, towards the liquid interface and associated impact on the biological system through a new regime of liquid chemistry initiated by the synergy of delivering multiple energy carrying species, is crucial.

This presentation will include examining our interaction studies of atmospheric pressure plasma jets with prostate cancer cells and our results of employing advanced diagnostic techniques for direct measurements of reactive plasma species and comparison to chemical kinetics simulations. These include absolute densities of atomic oxygen and atomic nitrogen using non-linear laser spectroscopy and vacuum ultra-violet (VUV) absorption spectroscopy, where the VUV radiation was produced using a synchrotron and detected with a high-resolution Fourier-transform spectrometer.

11:20am **PS+AS+BI+SE-MoM10 Conformal Encapsulation of Three-Dimensional, Bioresorbable Polymeric Scaffolds Using Plasma Enhanced Chemical Vapor Deposition**, *M. Hawker, A. Pegalajar-Jurado, E.R. Fisher*, Colorado State University

Bioresorbable polymers such as poly(ϵ -caprolactone) (PCL) have a multitude of potential biomaterial applications such as controlled-release drug delivery and regenerative tissue engineering. Fabricating these polymers into porous, three-dimensional (3D) materials is critical for such biological applications to maximize their surface-to-volume ratio, mimic the extracellular matrix, and increase drug-loading capacity. Three-dimensional porous PCL scaffold materials have been fabricated via the porogen leaching method. These scaffolds can be plasma-treated to improve or modify their surface properties while maintaining the desirable bulk polymer characteristics. For example, plasma polymerization can be used to encapsulate the polymer scaffold, thereby potentially providing a mechanism for controlled release drug delivery. Here, two different fluorocarbon (FC) precursors, octafluoropropane (C₃F₈) and hexafluoropropylene oxide (HFPO), were used to deposit FC films on PCL scaffolds using plasma enhanced chemical vapor deposition. X-ray photoelectron spectroscopy (XPS) analysis showed that high-CF₂ content films were deposited on the PCL scaffolds, similar to those previously deposited in our labs on one-dimensional and two-dimensional materials. Cross-sectional XPS data demonstrated that FC film deposition occurred both on the outer scaffold surface and throughout the 3D structure.

Scanning electron microscopy data confirmed that FC film deposition yielded conformal rather than blanket coatings as the porous scaffold structure was maintained after plasma treatment. Additional parameter studies suggest that treatment time, substrate location, and precursor gas have significant impact on the nature of the deposited films. This work demonstrates that conformal FC coatings can be deposited on 3D polymeric scaffolds using plasma processing. Results from cell adhesion studies as well as other film deposition systems and alternate bioresorbable scaffold materials will also be presented.

11:40am **PS+AS+BI+SE-MoM11 Deactivation of Lipopolysaccharide by an Atmospheric Pressure Plasma Jet**, *E.J. Bartis, C. Hart, Q. Yang*, University of Maryland, College Park, *T.-Y. Chung, D.B. Graves*, University of California, Berkeley, *J. Seog, G.S. Oehrlein*, University of Maryland, College Park

Low temperature plasma treatment of surfaces has been shown to degrade and sterilize bacteria as well as deactivate harmful biomolecules. However, a major knowledge gap exists regarding which plasma species are responsible for the modifications required for deactivation. Lipopolysaccharide (LPS) and lipid A, the toxic element of LPS, are the main components of the outer membrane of Gram-negative bacteria and induce a strong immune response in animals. In this study, LPS-coated silicon substrates were exposed to the effluent of an atmospheric pressure plasma jet (APPJ) under a controlled environment to examine the effect of plasma-generated reactive species on the surface chemistry and biological activity. Additionally, spatially-resolved optical emission spectroscopy, UV absorption spectroscopy, and electrical characterization were performed on the jet to identify and characterize plasma-generated species. Biological activity of LPS was measured using an enzyme-linked immunosorbent assay (ELISA) and correlated with changes in surface chemistry measured by vacuum transfer to x-ray photoelectron spectroscopy (XPS). The kHz-driven atmospheric pressure plasma jet consists of two tubular electrodes surrounding an alumina tube. By flowing Ar with small admixtures of O₂/N₂ through the tube and applying a high voltage across the electrodes, the plasma ignites to form a stable jet. The species that arrive at the sample can be regulated by adjusting the distance from the source to the sample. At longer source-to-sample distances, species with short lifetimes will not reach the sample. Adding oxygen to the gas flow causes the most significant changes. For source-to-sample distances > 10 cm, where radical species dominate, higher levels of deactivation were observed for O₂/Ar plasma than for Ar and N₂/Ar plasmas. O₂/N₂/Ar plasma showed decreased deactivation compared to O₂/Ar plasma with the same O₂ admixture due to creation of NO_x, whose formation consumes reactive oxygen species. With XPS, we observed that O₂-containing discharges remove C-C bonding from the surface while N₂-containing discharges cause minimal changes. XPS studies of APPJ-treated films showed that deactivation depends on C-C bonding measured in the C 1s, which depends on the admixture of O₂ into the APPJ. The decrease in C-C bonding correlates with the loss of lipid A's aliphatic chains, which are partially responsible for its toxicity. The authors gratefully acknowledge financial support from US Department of Energy (DE-SC0005105 and DE-SC0001939) and National Science Foundation (PHY-1004256).

Plasma Science and Technology

Room: 104 C - Session PS-MoM

Innovative Chemistries for Advanced Etch Processes

Moderator: J.P. Chang, University of California at Los Angeles

8:20am **PS-MoM1 Effects of Plasma-Induced Si Damage Structures on Annealing Process Design—Gas Chemistry Impact**, *A. Matsuda, Y. Nakakubo*, Kyoto University, Japan, *M. Fukasawa*, Sony Corporation, Japan, *Y. Takao, K. Eriguchi*, Kyoto University, Japan, *T. Tatsumi*, Sony Corporation, Japan, *K. Ono*, Kyoto University, Japan

Plasma-induced Si substrate damage during shallow trench isolation, 3D-fin, and gate electrode formation processes have been believed to lead to "Si recess" (Si loss) [1] and latent defect generation resulting in performance degradation of metal-oxide-semiconductor field-effect transistor (MOSFET)—an off-state leakage (power consumption) increase [2] and the drain current (chip clock-frequency) decrease [3], respectively. Various plasma gas chemistries are employed for these Si etching processes. Regarding annealing process parameters, it was reported [4] that conventional thermal budgets could no longer be applied—the annealing temperature might be primal—in particular, in the case of hydrogen-containing plasmas (HBr/O₂- and H₂-processes). Based on this finding, two questions may be pointed out; (1) does this temperature-dependent feature

hold for other plasmas? and (2) what is the principal mechanism? To answer these questions, Si-damage formation and the following annealing mechanisms were comprehensively investigated for various plasma processes (HBr/O₂, H₂, Ar, and He) and annealing conditions (750–1050C) in this study. An electrical capacitance–voltage (C–V) technique was employed to quantitatively evaluate the plasma-induced defect density, and a molecular dynamics simulation was carried out to study in detail the localized defect structures.

Silicon wafers covered with thermal oxide layer (2 nm) were damaged by various plasma processes and annealed in N₂ ambient with various conditions. Defect densities before and after annealing were quantified by 1/C²-based analysis. It was found that the temperature-dependent damage-recovery dynamics holds for overall plasma processes, although H₂- and He-plasma damage exhibit complicated features. We speculate that both the localized defect structure with its low density (10¹⁸-10¹⁹ cm⁻³) and the profile in the damaged region play major role in this mechanism—being confirmed also from molecular dynamics simulations. The present findings imply that not only the defect structure but also the profile in the damaged region should be identified in advance for designing the annealing conditions in future advanced MOSFET process technologies.

- [1] M. Fukasawa *et al.*: J. Vac. Sci. Technol. **A 29**, 041301 (2011).
- [2] K. Eriguchi *et al.*: J. Vac. Sci. Technol. **A 29**, 041303 (2011).
- [3] K. Eriguchi *et al.*: IEEE Electron Device Lett. **EDL-30**, 1275 (2009).
- [4] Y. Nakakubo *et al.*: AVS 59th Annual International Symposium and Exhibition, PS-MoM10 (2012).

8:40am **PS-MoM2 Advancing Patterning Processes Further by Employing a New Gas**, S.U. Engelmann, E.A. Joseph, R.L. Bruce, H. Miyazoe, W.S. Graham, E.M. Sikorski, IBM T.J. Watson Research Center, M. Nakamura, T. Suzuki, Zeon Chemicals LP, H. Matsumoto, A. Itou, T. Suzuki, Zeon Corporation

Improving patterning processes is a very crucial element of advancing microelectronics manufacturing processes. Deformation of organic soft masks is a very commonly observed phenomenon. Other issues include extensive plasma damage or mask retention for post-lithography solutions. [1]

Our team has recently introduced a new etch gas which is able to etch by selective deposition of a fluorocarbon layer, [2] analogue to the well established oxide etch mechanism commonly used in manufacturing. [3] Selective deposition was achieved by redesigning the FC etch gas, where reaction with a nitride substrate layer reduces the FC film thickness compared to silicon or oxide substrates. This mechanism was most prominently applied to the spacer module, where high selectivities to oxide and silicon substrates is required. In contrast to conventional spacer processes, an excellent resistance to PR materials opened the processing capabilities for this new gas tremendously.

We will demonstrate how this new gas can be used in patterning solutions, where a high degree of accuracy is needed. The wiggling performance of the new gas will be discussed, as well as direct patterning and/or trilayer patterning using the new gas. Lastly, we also evaluated the new gas for applications beyond optical lithography.

- [1] S. Engelmann *et al.*, Proc. SPIE 8328-9
- [2] S. Engelmann *et al.*, AVS 58th Int. Symp. & Exhibit. (2011)
- [3] M. Schaepekens *et al.*, J. Vac. Sci. Technol. A 17, 26 (1999)

9:00am **PS-MoM3 Advanced Etching Gas Development for High Aspect Ratio Structures**, R. Gupta, C. Anderson, V. Surla, B. Lefevre, V. Pallem, N. Stafford, Air Liquide

In order to enable high aspect ratio etching capabilities in materials such as SiO and SiN, it is highly desirable to determine what role the plasma etch chemistry can play. Both saturated and unsaturated fluorocarbons have been introduced over the years, as well as simple hydrofluorocarbon molecules. Mixtures of the above are often employed to allow control of etching species in the plasma recipe. In this work we systematically study the role of the gas molecule structure on the etching behavior that can be achieved. The ultimate goal is to identify ideal candidate molecules that will allow achieving the future process requirements.

This study will provide a comparative study of fluorocarbon-based etch chemistries, wherein a 200mm dual-CCP tool has been employed to produce high aspect ratio structures. By studying the specific effects of H, C=C double bonds, F:C ratio, and molecule structure, we can identify relationships to the etching performance. The model chemistries for this work include both cyclic- and linear-type structures. The performance of each molecule is initially studied on blanket wafers, measuring etch rates of silicon oxide, silicon nitride, amorphous carbon, and undoped poly-Si. For selected conditions of optimized etch rate and mask selectivity, 100nm trench width patterns are also etched and examined in cross-section SEM.

In order to develop a strong correlation between etch performance and the molecule structure, we perform mass spec measurements of the gases by direct injection of the fluorocarbon gas, measuring the electron-impact fragmentation of each gas. Electron energies from 10-100 eV are recorded, and the relative abundance of each fragment species is plotted against the electron energy. By studying the dominant fragments, we observe that oxide etch rate and mask selectivity can be predicted based on the C:F ratio of majority species.

9:20am **PS-MoM4 Highly Selective Etch of PMMA to PS for DSA Lithography by Using Carbon Containing Gas 100 MHz CCP RIE System**, T. Imamura, H. Yamamoto, M. Omura, I. Sakai, H. Hayashi, Toshiba Corporation Semiconductor Company, Japan

As critical dimension (CD) continue to shrink, optical lithography has become increasingly difficult. Directed-self assembly (DSA) of block copolymer (BCP) is a promising candidate for a low cost 1X patterning process. CD of DSA lithography is determined by composition of the BCP. 12.5 nm hp patterns is formed using polystyrene-block-poly methyl methacrylate (PS-b-PMMA) [1]. DSA lithography process using PS-b-PMMA needs selective removal of PMMA to PS, which is called “development process”. Wet development process has enough selectivity, but there is a possibility of collapse of the remaining PS pattern. Because this problem arises due to surface tension of liquid, it is difficult to solve in principle. Dry development process has an advantage in that point. Generally, O₂-based plasma is used for the PMMA removal and selectivity is around 2. Some have reported that the selectivity exceeds 4 by keeping the ion bombardment energy low in O₂/Ar plasma. Also, because we use the remaining PS pattern as a mask of underlayer etch, high selectivity is needed to keep the PS pattern thick.

In this study, we focused on differences of material components of PS and PMMA. Based on that the PMMA has more oxygen in the film than in PS, we designed a new gas chemistry using carbon containing gas to realize high selective PMMA to PS etching.

Single layer film of PS and PMMA were spin-coated on a silicon wafer, and then baked. The thicknesses were 240 nm and 340 nm, respectively. We used 100 / 13.56 MHz dual frequency superimposed (DFS) capacitive coupled plasma (CCP) system. Plasma etching conditions were as follows. The pressure was 10 mTorr, 100MHz RF power 700W, 13.56 MHz RF power 70W, substrate temperature 40°C, and the total flow rate of the gas mixture of carbon containing gas and Ar was 300sccm. We changed the flow rate ratio of carbon containing gas and measured the film thickness by ellipsometry measurement.

When the carbon-containing gas ratio was increased from 7% to 10 % and 13 %, both the PMMA and PS etch rates decreased. The etch rate of PMMA decreased slightly, from 42.4 to 39.6 and 38.2 nm/min, while the rate of PS decreased drastically, from 5.4 nm/min to 1.8 and 0.3 nm/min. As a result, very high selectivity could be obtained at 13 %. We assumed that carbon atom from carbon containing gas was absorbed on PS and PMMA films. The carbon atoms on PMMA film reacted with oxygen in the film and volatilized as CO or CO₂. On the other hand, the carbon remained on PS film and protected etching. As a result, carbon containing gas plasma achieved highly selective PMMA etching.

Reference

- [1] C. Bencher *et al.*, Proc. SPIE 7970, 79700F (2011)

9:40am **PS-MoM5 New Fluorocarbon Free Chemistry Proposed As Solution to Limit Porous SiOCH Film Modification during Etching**, N. Posseme, CEA-LETI, France, L. Vallier, CNRS-LTM, France, C.-L. Kao, AMAT, C. Licitra, CEA-LETI, France, C. Mannequin, CNRS-LTM, France, J. Pender, S. Nemani, AMAT

Today etching processes involved during the porous SiOCH (p-SiOCH) integration combined with a metallic hard mask (MHM) generate serious issues such as film damage, residue growth, bottom line roughness. The last critical issue we are facing today is that the wet cleaning (HF based chemistry) is not efficient enough to remove all the fluorocarbon layer formed on sidewall during etching. Fluorine is remaining on sidewall after wet cleaning. This Fluorine is encapsulated during the metal barrier deposition (prior to copper deposition) and can lead to reliability degradation of the p-SiOCH film. Today there is no solution to this problem except the use of aggressive wet cleaning, inducing in this case important CD loss. In this context we developed a new fluorocarbon (FC) free chemistry solving these issues.

In this work, p-SiOCH (deposited by PECVD, composition: Si 28%, O 29%, C 43%, k= 2.5, porosity <30 %) film modification has been studied using patterned and floating coupons (deposit/film modification formed on the floating sample gives a rough estimation of passivation layer formed on the sidewalls) and characterized by ellipsometry porosimetry (EP), infrared spectroscopy in attenuated total reflection configuration (ATR), X-ray

photoelectron spectroscopy (XPS) and dielectric constant measurement comparing the new FC free chemistry to conventional FC (CF₄/C₄F₈/N₂/Ar) chemistry.

It will be demonstrated that the FC free etch chemistry presents a wide process window to adjust the taper profile by playing on plasma parameters with a hardly impact on p-SiOCH film modification (+4% k value increase compared to +16% with conventional FC chemistry, correlated with ATR analyses). The efficiency of wet cleaning to fully remove the passivation layer formed on sidewalls without degrading the profile will also be presented.

10:00am PS-MoM6 Characterization of the Effects of Mildly Oxidizing Chemistries on Silicon Oxidation for Advanced Photoresist-Strip Applications. *B. Thedjoisworo, B. Jacobs, I. Berry, D. Cheung, J. Park, Lam Research*

For the advanced technology nodes, there is a need to strip photoresist quickly while meeting the stringent requirement of ultra-low oxidation and loss of the semiconductor substrate, silicon (Si). Two chemistries, NH₃/O₂ and H₂/N₂, have garnered attention for their ability to strip photoresist reasonably quickly while incurring low material loss. In this work, Si surfaces were exposed to either downstream NH₃/O₂ or H₂/N₂ plasmas, and the effects of these chemistries on Si oxidation were characterized and compared. For the NH₃/O₂ chemistry, Si oxidation was found to occur during the plasma-exposure step, while the extent of post-plasma oxidation was determined to be relatively minor. Accordingly, we evaluated the behaviors of Si oxidation as a function of plasma process parameters, and substrate temperature and NH₃ concentration in the gas feed were determined to exert strong effects on Si oxidation. Specifically, oxidation decreases with increasing temperature and with increasing NH₃ concentration. These process trends provide insight into the mechanism of the Si oxidation as well as to the nature of the radicals that induce the oxidation. Furthermore, the above finding demonstrated that Si oxidation can be controlled through judicious choice of the process parameters. When compared to the NH₃/O₂ (90% NH₃) chemistry, the H₂/N₂ chemistry generally led to lower Si oxide growth. Although the H₂/N₂ chemistry gives rise to lower Si oxidation, the NH₃/O₂ could offer other advantages, such as higher ash rate and better photoresist-residue performance. Therefore, the desired trade-offs among ash rate, residue performance, and level of substrate oxidation will ultimately govern the choice between the two chemistries.

10:40am PS-MoM8 Challenges in Etching of Multicomponent Oxides and Other Difficult-To-Etch Materials. *J. Margot, Université de Montréal, Canada, M. Chaker, INRS, Canada*

INVITED

Despite its successful implementation in industry, etching was mainly evolved empirically. Very often recipes are developed by users for specific materials. However the absence of actual scientific investigation considerably limits technology transfer. Therefore, except for a few classical materials like Si et SiO₂, only a limited amount of publications is available for unconventional materials used for example in microelectronics, photonics and telecommunications. Among these more or less exotic materials let us mention ferroelectric materials (PLZT, BST, SBT), electro-optic materials (SrTiO₃, LiNbO₃, CaBaNb₂O₆), metal-insulator transition materials (VO₂), and unconventional conductors (Pt, IrO₂, ITO, LaNiO₃). Optimizing etching processes for such materials is difficult as most of them present a low reactivity with usual etching gases such as fluorinated and chlorinated gases. Their etching is mainly governed by ion sputtering and the reactive gases forming the plasma sometimes interact with materials surface to form compounds that inhibit etching.

In this presentation, we will review the work performed by our group over the last decade on the etching of multicomponent oxides, with a particular focus on the etching of SrTiO₃ and CaBaNb₂O₆. We will also show how simulation can provide information on the redeposition of sputtered species on patterned surfaces, taking as an example the case of an unconventional conductor.

11:20am PS-MoM10 Thermodynamic Approach to Select Viable Etch Chemistry for Magnetic Metals. *T. Kim, K. Chen, J.P. Chang, University of California at Los Angeles*

Magnetic tunnel junctions (MTJ) which are based on magnetic hysteresis for data storage are an important part of spin-electronics. An MTJ-based magnetoresistive random-access memory (MRAM) has several advantages, such as nonvolatility, fast writing speeds (2-4 ns). Thus MRAM has the potential to be a universal memory solution. In past few years, some important progress has been reported to fabricate durable, high-yield MTJ arrays, using the advances in materials.

Among the challenges of fabrication, MTJ etching processes is one of the most critical. Ion beam etching was a general etching technique at the beginning of MTJ fabrication, however the etched material tends to re-

deposit on the sidewalls and form fences. The approach using a reactive ion etch (RIE) has been recognized as an important strategy for integrating MRAM because it can potentially generate volatile etch products to avoid sidewall re-deposition. Halogen-gas-based RIE processes have been used to etch ferromagnetic layers. Some chemical enhancement induced by RIE has been reported for NiFe and NiFeCo using Cl₂ gases,^[1] however the low etch rate requires high-density plasma conditions.

In this work, a thermodynamic approach is used to assess the feasibility of various etch chemistries, beginning with the consideration of reactions between the dominant vapor phase/condensed species and the surface at various temperatures and reactant partial pressures. The volatility of etch product was determined to aid the selection of viable etch chemistry leading to improved etch rate of RIE process.^[2] In this report, a few magnetic metals are considered (Co, Fe, and Ni) along with various halogen and organometallic based chemistries. The thermodynamically favorable reaction has been investigated and the vapor pressure of its product has been calculated. In addition, the vapor pressure enhancement induced by adding secondary gas such as hydrogen has also been studied. Experimental validation is an important part to prove the prediction.

[1] K.B. Jung et al., J. Electron. Mat., 27, 972 (1998)

[2] N.S. Kulkarni et al., J. Electro. Soc., 149, G620 (2002)

11:40am PS-MoM11 Studies on Highly Selective Si₃N₄ Spacer Etching over Si/SiO₂ using CH₃F/O₂ Plasmas. *B. Parkinson, A. Raley, A. Ranjan, K. Kumar, P. Biolsi, TEL Technology Center, America, LLC*

Recent advancements in device scaling have led to the widespread introduction of 3-D gate structures (i.e. FINFET, tri-gate). Introduction of 3D structures has increased the challenges of spacer etching. Planner gate structures typically require shorter over-etches (10-30%) and thus requirement of selectivity of spacer film over underlying films (Si and SiO₂) is not as stringent as for 3-D structures. In the case of 3D gate structures, the spacer film will also surround the Si-fins. Surface of Si-fins must be pristine (residue-free and without surface modification) in order for epitaxial silicon growth. Complete removal of SiN around Si-fins typically requires over-etches ranging from 150 to 300%. This dramatic increase in OE time requires an increase in spacer film selectivity to Silicon (fins) and Silicon Oxide (gate-mask and isolation Oxide). CH₃F/O₂ based etching chemistries are typically used to achieve high Nitride-to-Oxide and Nitride-to-Silicon selectivity. This paper explores a CH₃F/O₂ chemistry created in a RLSATM plasma reactor. The impact of block photoresist masking on oxidation etching mechanisms is presented. An analysis of plasma characteristics using Optical Emission Spectroscopy (OES) is also provided. Experimental results indicate a correlation between ion energy (derived from peak-to-peak voltage, V_{pp}), passivation over SiN/Si/SiO₂ (derived from gas-phase radical concentration) and selectivity. Microwave power and pressure provides control of relative concentrations of etchants/passivants (via control of electron energy distribution) and ion energies can be tuned by bias power. High Nitride-to-Oxide selectivity and minimal Si- and SiO₂-loss can be effectively achieved by balancing passivation layer on SiN/Si/SiO₂ and tuning Microwave Power and pressure to provide optimal V_{pp}.

Surface Science

Room: 201 A - Session SS+AS+NS-MoM

Nanostructures: Growth & Characterization

Moderator: F.P. Netzer, Karl-Franzens University, Austria

8:20am SS+AS+NS-MoM1 Measuring Homogeneity of Nanocluster Size Distributions using Charge Resolved Low Energy Alkali Ion Scattering. *A.B. Arjad, J.A. Yarmoff, University of California, Riverside*

Gold nanoclusters on silicon dioxide are interrogated by charge-state resolved Low Energy Ion Scattering (LEIS). The LEIS data are analyzed in a novel way that quantitatively reveals information about the homogeneity of the clusters' size distribution. The method utilizes the fact that the neutralization probability and the probability of multiple scattering (MS) both depend on the cluster size, but in different ways. Smaller nanoclusters are more likely to neutralize scattered alkali ions [1], while larger nanoclusters lead to more MS. Thus, in a system with a bimodal distribution of cluster sizes, multiply scattered ions are less likely to be neutralized. This leads to a difference in the spectral shapes of the scattered ions and neutrals. In contrast, a system with a homogeneous cluster size distribution yields identical spectral shapes. LEIS has advantages over the use of STM for measuring cluster size distributions, as it is easier to deploy over a wide range of preparation conditions and STM cannot probe disordered materials.

We collected time-of-flight LEIS spectra for 2 keV Na⁺ ions scattered from Au nanoclusters formed by deposition onto SiO₂ at room temperature and after annealing to increasing temperatures. The inhomogeneity in the cluster size distribution is quantified with a metric obtained by analyzing spectra collected for different charge states of the scattered projectiles. It is found that the cluster sizes are fairly uniform after the initial deposition, but a heterogeneous distribution, presumably due to Ostwald ripening, develops after annealing above 700 K.

[1] G. F. Liu, Z. Sroubek, and J. A. Yarmoff, Phys. Rev. Lett. **92**, 216801 (2004).

8:40am **SS+AS+NS-MoM2 Surface Hydrogen Stabilized Semiconductor Nanowire Growth**, S. Sivaram, N. Shin, L.-W. Chou, M.A. Filler, Georgia Institute of Technology

Semiconductor nanowires exhibit tunable optoelectronic properties that are attractive for applications in energy conversion, electronics, and photonics. A fundamental knowledge of the chemical bonding that governs nanowire synthesis is essential for the *a priori* manufacture of nanowires with enhanced complexity and functionality. To that end, we studied the role of sidewall hydrogen during germanium nanowire synthesis with real-time *in situ* infrared spectroscopy. We show that covalently bonded hydrogen atoms are essential for stable <111> oriented growth and strongly influence sidewall morphology. Nanowire arrays with fixed diameter distributions and areal densities were synthesized via the vapor-liquid-solid (VLS) technique at a range of process conditions (210 – 280 °C, 5.0×10^{-5} – 1.5×10^{-4} Torr). Our spectra exhibit two intense absorption bands, at 1980 cm⁻¹ and 1965 cm⁻¹, whose intensities are a function of substrate temperature, precursor pressure, and nanowire elongation time. Planar adsorption studies suggest that these bands result from hydrogen bonded at Ge(100)-like and Ge(111)-like surface sites, respectively. We also demonstrate that the *in situ* delivery of atomic hydrogen modifies the nanowire sidewall taper, which unambiguously confirms the importance of surface chemistry on nanowire growth.

9:00am **SS+AS+NS-MoM3 Analyzing Capture Zone Distributions (CZD) in Growth: Theory and Applications**, T.L. Einstein, University of Maryland, A. Pimpinelli, UMD and Rice Univ., D.L. Gonzalez, UMD and Univ. del Valle, Colombia, R. Sathiyarayanan, IBM Semiconductor R&D, India

In submonolayer epitaxial island growth, it is fruitful to consider the distribution of the area of capture zones, i.e. Voronoi (proximity) cells constructed from the island centers. For random nucleation centers (Poisson Voronoi diagrams) the CZD is expected to follow a Gamma distribution, but more generally we have argued [1], drawing from experiences analyzing the terrace-width distributions of vicinal surfaces, that the CZD is better described by the single-parameter generalized Wigner distribution (GWD). Painstaking simulations by Amar's and Evans's groups showed inadequacies in our mean field Fokker-Planck argument relating the characteristic GWD exponent β to the critical nucleus size (conventionally called $i+1$), i.e. the size of the smallest cluster assumed not to decay. We refine our derivation to retrieve their finding that β is nearly $i + 2$ [2]. While the GWD describes the CZD in the regime in which there is significant data in experiments (i.e. between half and twice the mean), it has shortcomings in the tails at both high and low areas. For large areas, the distribution may decay exponentially rather than in gaussian fashion. We discuss several treatments of this issue, emphasizing the fragmentation model we developed [3], which depends on two physically motivated scaling exponents.

We discuss applications of this formula and methodology to experiments involving Ge/Si(001), various organics on SiO₂, and para-hexaphenyl (6P) films on amorphous mica. We report a series of studies by Fanfoni et al. of InAs quantum dots on GaAs and very recent applications to metallic droplets by Millunchick's group, also on GaAs. (The former also shows that the more-often-probed island-size distribution is comparable the CZD at lower temperatures but not at higher temperatures when detachment--and consequent coarsening--becomes important.)

We have also used the GWD framework to elucidate kinetic Monte Carlo studies of homoepitaxial growth on Cu(100) with codeposited impurities of different sorts. Finally, we have applied this approach to the distribution of metro stations in Paris [3] and to the distribution of the areas of French districts (arrondissements) [3,4], counties in southeastern US states [4], and other such secondary administrative units.

*Supported by NSF-MRSEC at UMD, Grant DMR 05-20471 and NSF-CHE Grant 07-50334.

[1] Alberto Pimpinelli and TLE, Phys. Rev. Lett. **99**, 226102 (2007)

[2] Alberto Pimpinelli and TLE, Phys. Rev. Lett. **104**, 149602 (2010)

[3] Diego Luis González and TLE, Phys. Rev. E **84**, 051135 (2011)

[4] Rajesh Sathiyarayanan, Ph.D. thesis, U. Maryland, 2009; RS et al., preprint.

9:20am **SS+AS+NS-MoM4 Novel Behavior in Droplet-Mediated Growth of III-V Nanostructures**, J. Tersoff, IBM Watson Center INVITED

A variety of self-assembled nanostructures can be grown from either group IV or III-V semiconductors, including nanowires, quantum dots, and more complex structures. In many ways, the behavior of different semiconductors is surprisingly similar. However, the growth of III-V nanostructures has an additional degree of freedom, the III/V ratio; and in important respects III-V growth can be very different than group IV. This talk will present recent results for two widely-studied III-V systems: nanowire growth, and droplet epitaxy. In each case, theoretical modeling explains some surprising results of recent experiments. Using in-situ microscopy to study growth of GaP nanowires, Chou, Ross et al. have found remarkable differences in kinetics depending on III/V ratio. In particular, the presence of crystal defects causes dramatic fluctuations in growth rate in one regime, but not the other. For droplet epitaxy, Zhou, Jesson et al. used in-situ microscopy of GaAs to observe how different structures form. In particular, for the exotic double-ring structures, they found that the outer ring grows in an extended zone outside the droplet. For both nanowire growth and droplet epitaxy, the surprising experimental behavior is reproduced and explained theoretically, as arising from the competition between evaporation and diffusion on the surface, with very different kinetics for the group V vs group III species.

10:00am **SS+AS+NS-MoM6 Size-effects in Photoemission and Optical Second Harmonic Generation Spectroscopy of Ge Nano-dots on Si(111)**, K. Pedersen, J. Rafaelsen, Aalborg University, Denmark

Silicon and germanium nano-dots self-organized on silicon surfaces are interesting from the point of view of silicon-based optoelectronic devices. In the size range from a few nm to a few tens of nanometers such structures show size-dependent electronic and optical properties [1].

Ge nano-dots have been grown on Si(111) covered by a thin oxide layer (~0.8 nm) using a wedge shaped deposition profile, resulting in varying nano-dot size along the sample profile. The presence of the thin oxide triggers growth of nano-dots rather than flat Ge domains.

Samples were investigated by optical second harmonic generation (SHG) and photoemission spectroscopy (PES). Characterization of the growth of nano-dots with core level PES showed the decaying Si2p signal from the substrate and the increasing Ge3d signal from the growing amount of deposited Ge along the sample. The core level spectra confirm the growth mode discussed in the literature where it is suggested that contact is created between the Ge nano-dots and the Si substrate through the tin oxide [1]. Scanning electron microscopy on focused ion beam cut cross sections of the sample show that the nano-dots are largely spherical. Valence band PES shows that the position of the valence band maximum depends on nano-dot size in agreement with previous results in the literature [1].

Investigations of this system with SHG show that this technique provides a coherent surface sensitive optical probe of Ge nano-crystals on a Si surface. The signal from the nano-crystals is clearly separated from that of the substrate. It is found that the Si substrate resonance grows with Ge deposition, probably due to charges causing field induced SHG. The resonance in the Ge SHG signal can be ascribed to interband transitions at the L-point of the Ge band structure, usually referred to as the E1 critical point. With increasing particle size the Ge SHG resonance shifts towards lower energy and approaches the position expected for a plane surface. It should thus be noted that while size effects in valence band PES originate from states close to the Fermi level at the Γ - point the initial states for the SHG resonance are ~1.8 eV further down in energy at the L- point.

[1] A. A. Shklyaev and M. Ichikawa, Surface Science **514**, 19 (2002).

10:40am **SS+AS+NS-MoM8 Study of the Coupling of Ultra-thin CdSe Double Quantum Wells**, J.A. Lorenzo-Andrade, F. Sutar, I. Hernández-Calderón, Cinvestav, Mexico

The degree of coupling between adjacent quantum wells (QW) will depend on the sample structure and electronic properties of the QW and barrier materials. The design of heterostructures containing multiple QWs requires the precise knowledge of the minimum barrier thickness to couple/uncouple the neighboring QWs. In this work we present the results obtained from calculations employing the matrix transfer method (MTM) and the analysis of the excitonic spectra of heterostructures containing two CdSe ultra-thin quantum wells (UTQWs). The thickness of each quantum well, in the range from 1 to 3 monolayers (ML), was identical (symmetrical structure) or different (asymmetrical structure). The UTQWs were grown by atomic layer epitaxy (ALE) within ZnSe barriers onto GaAs(001) substrates. Due to the finite confinement the wave function of electron and holes will penetrate the ZnSe barriers, the degree of coupling of the CdSe QUTWs will depend on the thickness of the separating barrier. Then, a practical approach to determine the thickness to uncouple the pair of symmetrical QWs is the analysis of the evolution of the energy levels of the QWs as a function of the separating barrier thickness: as soon as the energy levels

present a negligible change (and then identical values), we have uncoupled the QWs. We observed that, the thinnest the quantum well the largest the penetration of the electron and hole wave functions into the ZnSe barrier. From the MTM calculations barriers in the range from 12 to 26 ML are necessary to uncouple symmetrical UTQWs with thickness in the range from 5 to 1 ML. These results are also useful to explain the behavior of the FWHM of the UTQWs as a function of their thickness. A similar approach was employed for the case of asymmetrical UTQWs. The coupling/uncoupling of asymmetrical structures was experimentally verified by the analysis of the excitonic spectra at low and room temperature: in the case of coupling only the lowest energy transition is observed; for the case of uncoupled UTQWs the photoluminescence spectrum presents two peaks, one for each independent UTQW.

*Partially supported by Conacyt-Mexico.

11:00am **SS+AS+NS-MoM9 Fine Tuning of the Self-Ordered Nanostructured O/Cu(110) Surface**, *F. Wiame, C. Poulain, Z. Budinska, V. Maurice, P. Marcus*, Chimie ParisTech, France

Self-organized nanostructured surfaces have been the object of much interest in recent years due to their potential applications as possible alternative to standard lithography techniques. Kern *et al.* [1] demonstrate that a submonolayer coverage of oxygen deposited on Cu(110) may form periodic stripes aligned along the [001] direction and that the periodicity of the system depends on the coverage. However, although this method appears very promising for the growth of nanostructured materials, the practical applications are limited due to the relatively small domains of periodicity and size as defined by the Marchenko-Vanderbilt (MV) model [2]. For oxygen coverage θ_o ranging from $0.1 < \theta_o < 0.4$ (the full coverage corresponds to $\theta_o = 0.5$), the periodicity only varies from 6.5 nm to 11 nm and the oxide band width from 2 nm to 9 nm. We will show that these ranges can be significantly increased by the co-adsorption of small amounts of sulphur at the surface.

The new preparation method presented here, which consists in the partial coverage of the surface by sulphur before annealing of the oxidized surface, enables us to significantly enlarge the domain of accessible periodic structures. Periodicity up to 200 nm and oxide band width up to 30 nm can be reached in a straightforward, reproducible and controlled way. The band width and periodicity dispersions are not modified by the sulphur adsorption. Moreover, while the structure of the O/Cu(110)-(2x1) is fully determined by the surface coverage, our method allows us to define the periodicity independently of the oxygen coverage by adjusting the sulphur amount at the surface. A new model has been proposed in order to take into account the effect of the sulphur on the elastic constant of the system. This model allows a reinterpretation of results from the literature [3].

This new system may be used as a template for the growth of nanostructures as well as more fundamental purposes. Indeed, the use of such a versatile structure should enable to gain information e.g. on the elastic and electrostatic properties that are responsible for the nanostructuring of the surface or on the effect of quantum confinement by quasi-one-dimensional structure and how it is influenced by structural modification at the nanometer scale. Moreover, it may be seen as an ideal playground to test the change in the reactivity of a surface as a function of its structure.

[1] K. Kern, H. Niehus, A. Schatz, P. Zeppenfeld, J. Goerge, G. Comsa, *Phys. Rev. Lett.* 67, 855 (1991).

[2] V. I. Marchenko, *JETP Lett* 55, 73 (1992) ; D. Vanderbilt, *Surf. Sci.* 268, L300 (1992).

[3] K Bobrov, L. Guillemot, *Surf. Sci.* 604, 1894 (2010).

11:20am **SS+AS+NS-MoM10 DFT Studies on the Adsorption and Diffusion of Small Rh and Au Clusters on Graphene/Ru(0001)**, *D. Teng, D. Sholl*, Georgia Institute of Technology, *B. Habenicht, L. Semidey-Flecha, Y. Xu*, Oak Ridge National Laboratory

Stable metal nanoparticles grown on metal-supported graphene can in some circumstances form a periodic array and have potential applications in fields such as catalysis and nano-electronics. To understand their formation mechanism, we studied the adsorption and diffusion of monomers, dimers, and trimers of Rh and Au on graphene/Ru(0001) using Density Functional Theory (DFT). These two metal species exhibit distinct behaviors in cluster formation on graphene/Ru(0001). We determined the global minimum structure of Au₈ cluster on graphene/Ru(0001) using genetic algorithm. Our results on adsorption and diffusion of small metal clusters M_n (n=1, 2, 3) and Au₈ have given us insights into the nucleation process of metal clusters on graphene moiré and aid us on building a general model to describe the cluster growth mechanism on graphene moiré, which will provide guidance on designing supported sintering-resistant nanoclusters.

11:40am **SS+AS+NS-MoM11 Nucleation of Copper Islands on Graphite**, *D. Appy, H. Lei, C.Z. Wang, D. Shao, E. Kwolek, P.A. Thiel*, Ames Laboratory, Iowa State University

Graphite, and surface processes on graphite, serves as a valuable benchmark for carbon-based materials such as graphene. We have studied copper on graphite, using STM in UHV, to determine the characteristic features of nucleation and growth of metal islands in this system. We have varied the parameters of deposition temperature, Cu coverage, and Cu flux. In the pre-coalescence regime of coverage, we find that Cu decorates step edges and also forms three-dimensional islands on the terraces. The areal density of the islands is 10^{-4} to 10^{-3} nm⁻², after growth at temperatures of 180 to 300 K, over a range of Cu flux and Cu coverage. This relatively-invariant density indicates that nucleation is heterogeneous. After annealing above room temperature (but well below the onset of desorption at about 900 K), both the density of Cu islands and the total volume of Cu are much lower. DFT is used to understand the processes and energetics in this system.

Thin Film

Room: 104 A - Session TF+EN-MoM

ALD for Energy

Moderator: W.M.M. Kessels, Eindhoven University of Technology, Netherlands

8:20am **TF+EN-MoM1 Thin Film Electrolyte via Atomic Layer Deposition for Low Temperature Solid Oxide Fuel Cells**, *G. Cho, S. Cha, J. Paek, J. Park, I. Change*, Seoul National University, Republic of Korea

Solid Oxide Fuel Cells (SOFCs) were considered most promising solutions for the next generation power generator. SOFCs usually operate at high temperature due to poor ionic conductivity of their oxide electrolyte. This high operation temperature caused many drawbacks like requirement of high cost thermal-resistive materials, thermal degradation and long start-up time.

There were many investigations to lower the operation temperature of SOFCs to solve aforementioned drawbacks. Among many researches to lower operation temperature, thin film SOFCs showed most impressive outcomes. The thickness reduction of oxide electrolyte by thin film technique led to the ohmic resistance reduction and low operation temperature of SOFCs. Due to thin electrolyte, thin film SOFCs showed high performance at low temperature. Thin film SOFCs were fabricated by thin film technique, i.e. sputter, pulsed laser deposition (PLD), chemical vapor deposition (CVD), atomic layer deposition (ALD) and etc.

The ALD was an advanced thin film technique for various applications. The unique characteristic of ALD, self-limiting growth, led to many advantages, i.e. precise thickness control, excellent step coverage, film uniformity and large area capability. In thin film SOFCs, very uniform and conformal thin film electrolyte was prepared by ALD to remove pin-holes and defects in electrolyte. Most well known materials of electrolyte for SOFCs, Ytria-Stabilized Zirconia (YSZ) was successfully fabricated by combination of deposition processes for Y₂O₃ and ZrO₂ of ALD.

In this research, we prepared thin film YSZ electrolyte for LT-SOFCs via ALD and applied to LT-SOFCs. First, chemical and physical characteristics of thin film YSZ related with different deposition conditions were investigated to confirm the most appropriate YSZ electrolyte for LT-SOFCs. After investigations of thin film YSZ electrolyte, LT-SOFCs with ALD-fabricated YSZ electrolyte were prepared. Nano-porous Anodizing Alumina Oxide (AAO) template was used as the supported structure. Platinum was used for both anode and cathode catalyst to suppress activation loss and current collection resistance. Then, effects of different ALD-fabricated thin film YSZ electrolyte to LT-SOFCs, i.e. open circuit voltage, power density, and electrochemical impedance spectroscopy were investigated.

9:00am **TF+EN-MoM3 Coaxial ALD Nanotube Structures for Functional Nanopore Battery**, *C. Liu, X. Chen, M. Schroeder, K. Gregorczyk*, University of Maryland, College Park, *S.B. Lee*, University of Maryland, College Park and Korea Advanced Institute of Science and Technology, *G.W. Rubloff*, University of Maryland, College Park

Nanowire arrays improve ion access and transport to utilize electrode materials, but the potential power-energy advantage of nanostructuring also requires fast electron transport to the ion storage material throughout high-aspect ratio nanowire geometries. To realize this for high performance nanostructured energy storage, we fabricated uniformly aligned arrays of core-shell nanotube devices (half-cells) by atomic laser deposition (ALD) into anodic aluminum oxide (AAO) templates, using ruthenium (Ru) metal

as current collecting layer and then crystalline V_2O_5 as active battery material to form composite nanoelectrodes penetrating part way into the AAO nanopores. The extraordinary conformality of ALD enables controlled formation of the coaxial electrode, with highly conductive Ru metal providing fast electron transport to overlying V_2O_5 storage material.

The 3-D V_2O_5 -Ru coaxial nanocathode array was configured as a half-cell, with $LiPF_6$ based organic electrolyte in the nanopores and a separator and Li anode incorporated into a coin cell. A high specific capacity of 172 mAh/g was measured at 1C rate over the voltage range 4.0-2.6 V corresponding to 1 Li per V_2O_5 . The areal capacity of 59 $\mu\text{Ah}/\text{cm}^2$ was 46X that of a planar V_2O_5 thin film cathode. Excellent cycling performance was demonstrated by capacity retention of 79% after 1000 cycles. Energy density was maintained well at high power – 129mAh/g at 50C rate and 82mAh/g at 200C rate, corresponding to 21 and 52 kW/kg power respectively. Cyclic voltammetry indicates that the capacity at high rate is dominated by double-layer capacitance rather than intercalation processes. The crucial role of electron transport was illustrated by the 4X reduction in capacity - even at 1C rate - when the 15 μm deep Ru current collector was replaced by a 0.6 μm TiN. Part of this difference may be the absence of the TiN current collector adjacent to most of the V_2O_5 storage layer.

9:20am **TF+EN-MoM4 Engineering Lithium-Containing Ionic Conductive Thin Films by Atomic Layer Deposition for Lithium-ion Battery Applications**, *J. Cho, Y. Perng, D. Membreno, N. Cirigliano, B. Dunn, J.P. Chang, UCLA*

Lithium (Li)-ion batteries have drawn much attention for their outstanding performance in portable electronic applications with the potentials to function as a power source for further miniaturized devices including micro-systems through the utilization of 3-dimensional electrodes based on high aspect ratio pillars. To fully utilize such potential, however, an ultra-thin and highly conformal electrolyte layer is required to coat the 3D electrode array. The solid oxide Li-ion conductors lithium aluminosilicate (LASO) synthesized by atomic layer deposition (ALD) are promising electrolyte materials for 3D battery applications not only due to their adequate ionic conductivities for electrolyte applications in Li-ion microbatteries and improve the cell cycling stability upon coating these ultra-thin metal-oxide films synthesized via ALD directly on electrodes.

The self-limiting characteristic of ALD allows for precise control of thickness and composition of complex oxides and results in a highly conformal and pinhole-free coating suitable in 3D micro-battery applications or electrolyte surface coatings. The metal precursors used in this work are tetraethyl orthosilicate (TEOS), trimethylaluminum (TMA) and lithium t-butoxide (LTB). These precursors, along with water vapor as the oxidant, were used to deposit Li_2O , Al_2O_3 , and SiO_2 with the deposition rates in the range of 0.8–2Å/cycles. The deposition rate of stoichiometric $LiAlSiO_4$ was ~20Å/cycle at a temperature of 290°C. The concentration of each metal element in $Li_xAl_ySi_zO$ (LASO) was found to correlate closely to ALD cycles of the constituent oxides. Based on this class of material and the change in the Li to Al(Si), thin films of LAO, LSO and LASO are synthesized to assess the effect of materials' composition and structure. The as-deposited materials were amorphous and the crystallinity of the LASO/LAO/LSO films after post-deposition rapid thermal annealing (RTA) was found to be a function of cation atomic percentage. Li-ionic conductivities and the activation energy of as-deposited LASO/LAO/LSO films with respect to lithium contents and the film thickness were studied.

The detection and characterization of pinholes on the deposited LASO/LAO/LSO films were investigated by cyclic voltammetry. Lithiation cycling tests of thin LASO/LAO/LSO films were found to be both functions of composition and thickness. The reversibility and kinetics of insertion as well as cycling stability enhancement effects from the direct deposition of LASO/LAO/LSO on 2D and 3D electrode materials such as carbon and porous silicon anodes were investigated as a half-cell.

9:40am **TF+EN-MoM5 Manganese Oxide Pseudocapacitive Supercapacitors from Electrochemical Oxidation of MnO ALD Films**, *M.J. Young, C.B. Musgrave, S.M. George, University of Colorado, Boulder*
Pseudocapacitive supercapacitors are a class of electrochemical storage device based on Faradaic charge transfer at the electrode/electrolyte interface. These supercapacitors exhibit higher energy density than electric double-layer capacitors and higher power density than Li ion batteries. Manganese oxide is a well-known pseudocapacitance material. In this work, MnO atomic layer deposition (ALD) was used to study manganese oxide as a pseudocapacitive supercapacitor. MnO ALD films were grown using sequential exposures of $Mn(EtCp)_2$ and H_2O on conducting stainless steel substrates. The MnO ALD films were then oxidized electrochemically to produce oxidized MnO_{1+x} films. The electrochemical capacities of these films were measured using cyclic voltammetry. Capacities were found to increase from capacities of ~80 F/g for the as-deposited MnO ALD films to capacities of ~200 F/g after oxidation. These capacities after oxidation are

comparable with the reported capacities of 150-250 F/g for α - MnO_2 which is the crystalline phase of manganese oxide with the highest reported pseudocapacitance. The electrochemical capacity of manganese oxide is not purely a surface effect in contradiction with previous reports in the literature. The results suggest an optimal manganese oxide thickness for the highest specific capacity.

10:00am **TF+EN-MoM6 Low Temperature Atomic Layer Deposition Processes for Flexible Dye-Sensitized Solar Cells**, *M. Creator, D. Garcia-Alonso, A.J.M. Mackus, Eindhoven University of Technology, Netherlands, V. Zardetto, T.M. Brown, University of Rome "Tor Vergata", Italy, W.M.M. Kessels, Eindhoven University of Technology, Netherlands*

Atomic Layer Deposition (ALD) has been applied to different photovoltaic technologies, including Dye-Sensitized Solar Cells (DSCs), due to its exceptional control of film thickness and composition, high conformality on high aspect ratio structures and uniformity. Thermal ALD for DSCs has been employed to deposit metal oxides for passivation layers on mesoporous TiO_2 photoelectrodes and recombination blocking layers (TiO_2 and HfO_2) on TCOs. In this work, we investigate other potential benefits of ALD not yet applied to DSCs. Low temperature processing by plasma-assisted ALD (PA-ALD) has been successfully applied in flexible DSCs to deliver the synthesis of nano-particles (NPs) for the Pt counter-electrode, and the deposition of compact layers. We demonstrate the potential of low temperature PA-ALD processes to deposit metallic Pt NPs on PEN/ITO substrates with the control in particle size. The counter-electrode (CE) layer (for back-side illumination) requires high transparency and small, evenly distributed particles to enhance its catalytic activity. Two newly developed PA-ALD processes were applied for the deposition of Pt CE layers at 150 °C. The Pt CE electrocatalytic activity towards the iodine-based electrolyte was analysed by electrochemical impedance spectroscopy (EIS). Pt CE layers deposited by both processes exhibit similar transmittance for less than 100 ALD cycles while the charge transfer resistance (R_{CT}) values show a significant difference for a number of ALD cycles lower than 50. Pt layers deposited using between 50 and 150 cycles yielded the best compromise between R_{CT} and transparency, and fulfil the requirements for back-side illuminated DSCs, allowing for an efficiency of 3.5%. When compared to sputtered or electro-deposited Pt layers, the PA-ALD Pt NPs lead to higher solar cell efficiency due to the enhancement in J_{SC} and V_{OC} because of the increased number of photons reaching the active material due to the higher Pt ALD layer transmittance. We also used PA-ALD to successfully deposit TiO_2 compact layers and ultra-thin dielectric Al_2O_3 . The aim of these layers is to decrease the recombination processes at the interface between the PEN/ITO substrate and the mediator (liquid electrolyte or organic material), especially at low light intensity, and thus to increase the performance of flexible DSCs for indoor applications. Both compact layers reduce the recombination path at the TCO/electrolyte interface without any effect on the electron collection (EIS analysis). The compact layers improve the generated power as compared to a compact layer-free DSC (Al_2O_3 : +26% and TiO_2 : +40 %) under low level illumination (300 lux, CFL lamp).

11:00am **TF+EN-MoM9 Performance of ALD Oxide Films in Polarized Infrared Power Generation**, *G.S. Scarel, Y. Schwab, H.S. Mann, B.N. Lang, James Madison University, J.L. Lancaster, University of North Carolina at Greensboro, R.J. Parise, Parise Research Technologies*

Currently there is a large demand for alternative sources of clean, inexpensive, renewable energy. Solar radiation is very promising in this context. While the visible and near infrared (NIR) portions of the solar radiation spectrum are receiving much attention, thus far little work has been devoted to harvesting and transforming the middle and far (MIR and FIR) regions of the infrared (IR) portion of the spectrum. Here we describe the principle of IR power generation, which transforms IR radiation into electricity using a power generator (PG). While the physical mechanism of IR power generation is not yet fully understood, there is a clear indication that the termination of the external surface of the hot junction of the PG can be used to tune the electricity that is produced. The hot junction of the PG is usually made of a thin copper substrate with about a 1 mm thick alumina ceramic material on the external surface exposed to the IR radiation which absorbs on average about 60 % of the incident IR energy [1]. By terminating the hot junction with a spectrally black surface (emissivity approaching 1.0), this percentage can be greatly enhanced. Also, radiative polaritons [2] in thin alumina films on metallic, semiconducting, and insulating coatings further contribute to absorbing the IR radiation [1]. Thus, a 250 nm thick Al_2O_3 film deposited using atomic layer deposition (ALD) on Al foil placed on the hot junction of the PG can tune the response of IR power generation [3]. The behavior of voltage difference as a function of time measured with non-polarized IR radiation at variable incidence angle θ_0 to the normal of the hot junction of the PG was recently published [3]. The presentation here will summarize the first results of the polarized IR power generation obtained from the 250 nm thick ALD Al_2O_3 films on Al foil. Finally, the future technological and scientific challenges for IR

power generation using PGs, such as the development of Nighttime Solar Cells® [4] and the discovery of the physical mechanism, will be briefly summarized.

- [1] A.J. Vincent-Johnson, K.A. Vasquez, G. Scarel, J.S. Hammonds, and M. Francoeur, *Appl. Spectrosc.* **66**, 188-197 (2012).
- [2] A.J. Vincent-Johnson, Y. Schwab, H.S. Mann, M. Francoeur, J.S. Hammonds, and G. Scarel, *J. Phys.: Condens. Matter* **25**, 035901 (2013).
- [3] A.J. Vincent-Johnson, K.A. Vasquez, J.E. Bridstrup, A.E. Masters, X. Hu, and G. Scarel, *Appl. Phys. Lett.* **99**, 131901 1-3 (2011).
- [4] R. J. Parise and G. F. Jones, Collection of Technical papers – 2nd International Energy Conversion Engineering Conference, 1172–1181 (2004).

11:20am **TF+EN-MoM10 Synthesis of Pd and Pt Nanoparticles by Atomic Layer Deposition for Catalysis Applications**, *M. Weber, M.A. Verheijen, A.A. Bol, W.M.M. Kessels*, Eindhoven University of Technology, Netherlands

Noble metal nanoparticles (NPs) are known to be very efficient catalysts and are of crucial importance to pharmaceutical, (petro)chemical and environmental industries. Although ALD was primarily developed to deposit conformal thin films, metals have the tendency to form nanoclusters on the substrate during the initial cycles of the process. Using this Volmer-Weber growth mode, Pd and Pt NPs supported on Al₂O₃ were synthesized with the aim to design efficient model catalysts systems. The Pd process was based on Pd(hfac)₂ (hfac= hexafluoroacetylacetonate) as the precursor, and H₂ plasma as co-reactant, whereas the Pt process was carried out with the use of MeCpPtMe₃ and O₂ plasma. The deposition temperature was 100°C. The Pd and Pt NPs resulting from the ALD nucleation stage have been characterized by High Angle Annular Dark Field Transmission Electron Microscopy (HAADF-TEM). High density values of 10^{12} NPs/cm² and narrow size distribution (in particular for Pd) of 2-3 nm NPs have been obtained on alumina substrates, and depositions carried out with one year time interval have shown excellent reproducibility. The tailoring of such NPs by changing the ALD process parameters in order to obtain different particle sizes and composition is also demonstrated. Furthermore, preliminary experiments have shown that these noble metal NPs are efficient as photocatalysts and towards the CO-oxidation. These results open up prospects in the engineering of metallic nanoparticles for fuel cells and micro-reactors applications, for which ALD can be feasible.

11:40am **TF+EN-MoM11 In Situ Characterization of Plasma-Assisted Pt ALD on W ALD Adhesion Layers with Spectroscopic Ellipsometry**, *A.S. Cavanagh, L. Baker, J. Clancey, J. Yin*, University of Colorado at Boulder, *A. Kongkanand, F.T. Wagner*, General Motors Research and Development, *S.M. George*, University of Colorado at Boulder

Platinum is an excellent catalyst for many applications. The high cost of Pt requires that Pt be used as efficiently as possible. For the oxygen reduction reaction in H₂ fuel cells, experiments show that a continuous Pt film is 5-10 times more active per Pt surface atom than a 3 nm Pt nanoparticle. Consequently, understanding the process conditions under which thin continuous films of Pt can be deposited is critical.

Pt has a high surface energy of ~2.5 J/m and does not readily wet most substrates which typically have much lower surface energies. Pt nanoparticles are generally formed during Pt atomic layer deposition (ALD) on oxide substrates. A continuous Pt film is possible only after the coalescence of the Pt nanoparticles. The result is a thick Pt film and the inefficient use of Pt resulting from the thickness.

One possible route to obtain a continuous and ultrathin Pt film is to deposit on an adhesion layer that has a higher surface energy than Pt. In this case, the Pt should wet the adhesion layer because the deposited Pt film will lower the surface energy. One material that has a higher surface energy than nearly all other metals, including Pt, is W. The surface energy of W is ~3.5 J/m.

In situ spectroscopic ellipsometry (SE) allowed for the characterization of Pt ALD nucleation on W ALD adhesion layers. *In situ* measurements of nucleation during plasma-assisted ALD provided rapid feedback on the process variables including plasma power, plasma exposure time and the process gas mixture. *Ex situ* characterization with X-ray photoelectron spectroscopy and X-ray reflectivity was used to verify the SE models employed during *in situ* monitoring of the nucleation of plasma-assisted Pt ALD.

Tribology Focus Topic

Room: 203 C - Session TR+AS-MoM

Bridging Scales and Characterization

Moderator: R.W. Carpick, University of Pennsylvania, L. Marks, Northwestern University

9:00am **TR+AS-MoM3 Friction in Full View**, *L. Marks*, Northwestern University **INVITED**

Friction is a pervasive problem, by some estimates consuming about 5% of the GDP of the economies of the developed world, and a recent analysis has indicated that about one third of the fuel energy in automobiles goes to overcoming frictional losses. While the importance of minimizing friction can be traced back at least as far as the tomb of Tehuti-Hetep, circa 1880 B.C. where a man can be seen pouring a lubricant to assist moving a statue, there are still many unknowns in the field of tribology which encompasses friction as well as other critical processes such as wear and lubrication. For many of the phenomena in tribology there are still numerous unknowns, due in large part to what has been called the buried interface problem. The triboactive layer, is almost always hidden by the materials on both sides of it so the exact details of what is occurring are often hidden, only accessible by post-facto analyses and sometimes a matter for debate. While there have been several attempts to image the triboactive layer directly at the atomic scale dating from the original work by Gane and Bowden, progress has been slow. Over the last few years we have been developing both models from a materials science viewpoint via dislocations as well as in-situ techniques for imaging the buried interface. Related to this (perhaps not obviously) we have recently become involved in understanding the nanoscale tribology of hip replacements, including the perhaps surprising observation of a graphitic layer *in-vivo* that appears to play a major role in reducing implant failures. This talk will focus upon some of the recent results, ranging from more basic observation such as connecting wear fragment size and a new layer-by-layer wear mechanism to the standoff distance of interfacial dislocations through the formation of graphitic materials *in-vivo* as well as some direct observations of wear and sliding at the atomic scale.

9:40am **TR+AS-MoM5 Combining In Situ Nanotribology and Atomistic Simulations to Reveal the Strong Effect of Atomic-Scale Roughness on Nanoscale Adhesion**, *T.D.B. Jacobs*, University of Pennsylvania, *K.E. Ryan, P.L. Keating*, United States Naval Academy, *D.S. Grierson*, systemECH, LLC, *J.A. Lefever, K.T. Turner*, University of Pennsylvania, *J.A. Harrison*, United States Naval Academy, *R.W. Carpick*, University of Pennsylvania

As components in devices and microscopy applications shrink to nanometer length scales, adhesion forces play an increasingly dominant role in the physics of contact. In particular, tip-based approaches for data storage, nanomanufacturing, and nanoelectromechanical systems rely on accurate knowledge and control of adhesion between a sharp asperity and a surface. It is well known that surface roughness affects adhesion at macro- and microscopic scales. However, the atomic-scale roughness of nanoscale tips is rarely measured or accounted for. Here, we characterized the atomic-scale roughness of carbon-based probes, and measured the corresponding effect on adhesion using simulations and experimental techniques.

We have conducted contact and sliding experiments inside of a transmission electron microscope (TEM), using a modified *in situ* nanoindentation apparatus. Similar experiments were used recently to study wear of nanoscale silicon probes¹. In the present work, nanoscale asperities composed of either diamond-like carbon (DLC) or ultrananocrystalline diamond (UNCD) were brought into contact and separated from a flat diamond substrate. The *in situ* nature of the testing allowed characterization of surface roughness with sub-nanometer resolution immediately before and after contact. Additionally, complementary adhesion simulations were conducted using molecular dynamics (MD) with conditions matched as closely as possible with the experiments (e.g., materials, asperity shape, environment). The RMS roughness for the experimental tips spanned 0.18 - 1.6 nm; for the simulated tips, the range was 0.03 nm (atomic corrugation) to 0.12 nm. Over the tested range of roughness, the measured work of adhesion was found to decrease by more than an order of magnitude as roughness increased, with a consistent trend observed between experimental and simulation results². The dependence of adhesion upon roughness was accurately described by a simple analytical model.

This combination of simulation and novel *in situ* experimental methodologies allowed for an exploration of an unprecedented range of tip sizes and length scales for roughness, while also intrinsically verifying consistent behavior between the two approaches. These results demonstrate a high sensitivity of adhesion to interfacial roughness down to the atomic limit. Furthermore, they indicate that present approaches for extracting work of adhesion values from experimental measurements of adhesion

forces contain significant uncertainty due to an unmeasured variable – atomic-scale roughness.

¹ T. D. B. Jacobs, R. W. Carpick, *Nature Nanotech.*, **8**, 108-112 (2013)

² T. D. B. Jacobs, *et al.*, *Tribol. Lett.*, **50**, 81-93 (2013)

10:00am **TR+AS-MoM6 Nanotribological Properties of Positively and Negatively Charged Nanodiamonds as Additives to Solutions**, *Z. Liu, S.D. Corely*, North Carolina State University, *O.A. Shenderova*, International Technology Center, *D. Brenner, J. Krim*, North Carolina State University

Nano-diamond (ND) particles are known to be beneficial for wear and friction reduction when used as additives in liquids,^[1] but the fundamental origins of the improvement in tribological properties has not been established. In order to explore this issue, we have investigated the nanotribological properties of ND coated with self-assembled monolayers (SAM) as additives to solutions, employing gold/chrome coated quartz crystal microbalances (QCM). Measurements were performed with the QCM initially immersed in deionized water. ND particles with positively and negatively charged SAM end groups were then added to the water, while the frequency and amplitude of the QCM were monitored. Negative shifts in both the QCM frequency and amplitude were observed when ND with positively charged SAM end groups were added, while positive shifts in both the QCM frequency and amplitude were observed when ND with negatively charged ND end groups were added. The results are consistent with a lubricating effect for the negatively charged ND, but were only observed for sufficiently small negative ND particle size. Experiments on QCM surfaces with differing textures and roughness are in progress, to determine the separate contributing effects of surface roughness charge-water interactions.

Funding provided by NSF DMR.

1. Vadym N. Mochalin, Olga Shenderova, Dean Ho & Yury Gogotsi, *Nature Nanotechnology* **7**, 11–23 (2012) doi:10.1038/nnano.2011.209

10:40am **TR+AS-MoM8 Atomic-scale Processes in Single Asperity Friction and Wear**, *R.W. Carpick*, University of Pennsylvania **INVITED**

I will discuss recent atomic force microscopy studies of nanoscale single asperity contacts that reveal surprising new behavior and insights. First, the behavior of nanoscale contacts with truly 2-dimensional materials will be discussed. For nanoscale contacts to graphene, we find that the friction force exhibits a significant dependence on the number of 2-D layers¹. Surprisingly, adhesion (the pull-off force) does not. However, studies as a function of scanning history reveal further complexities that arise from the combined effects of high flexibility and variable substrate interactions that occur at the limit of atomically-thin sheets. An even stronger effect occurs when graphene is fluorinated, where experiments and simulations both show that friction between nanoscale tips and fluorinated graphene (FGr) monolayers exceeds that for pristine graphene by an order of magnitude. The results can be interpreted in the context of the Prandtl-Tomlinson model of stick-slip friction.

I will then discuss new insights into the physics of nanoscale wear. A better understanding of wear would allow the development of rational strategies for controlling it at all length scales, and would help enable applications for which wear is a primary limitation such as micro-/nano-electromechanical systems (MEMS/NEMS). We have demonstrated the ability to characterize single-asperity wear with a high degree of precision by performing *in-situ* wear tests inside of a transmission electron microscope. For silicon probes slid against a flat diamond substrate, the shape evolution and volume loss due to wear are well described by kinetic model based on stress-assisted bond breaking mechanisms². This allows new insights to be gained about the kinetics of atomic-scale wear³.

[1] Lee, C., Li, Q., Kalb, W., Liu, X.-Z., Berger, H., Carpick, R.W. and Hone, J. "Frictional Characteristics of Atomically-Thin Sheets," *Science*, **328**, 2010, 76-80.

[2] Jacobs, T.D. and Carpick, R.W. "Nanoscale Wear as a Stress-Assisted Chemical Reaction," *Nature Nanotech.*, **8**, 2013, 108-112.

[3] Jacobs, T.D., Gotsmann, B., Lantz, M.A. and Carpick, R.W. "On the Application of Transition State Theory to Atomic-Scale Wear," *Tribol. Lett.*, **39**, 2010, 257-271.

11:20am **TR+AS-MoM10 Examination of Adhesion and Friction of Hydrocarbon-based Materials: Elucidating Atomic-scale Wear Processes via Molecular Dynamics**, *J.A. Harrison, K.E. Ryan, P.L. Keating*, United States Naval Academy, *J.D. Schall*, Oakland University, *K.T. Turner*, University of Pennsylvania, *D.S. Grierson*, systeMECH, LLC, *R.W. Carpick, V. Vahdat, T.D.B. Jacobs*, University of Pennsylvania
Molecular dynamics (MD) simulations are unique in their ability to elucidate atomic-scale phenomena because the positions, velocities, and

forces of all atoms in the system are known as a function of time. We have performed complementary atomic force microscope (AFM) experiments and MD simulations aimed at examining adhesion, friction, and wear in diamond, ultrananocrystalline diamond (UNCD), and amorphous carbon (a-C:H) materials. Atomic-scale wear in nanoscale contacts is of particular importance for tip-based nanomanufacturing applications. In this paper, we examine the normal contact of a-C:H and UNCD axisymmetric tips with diamond, UNCD and a-C:H substrates. Adhesion and wear as a function of material, surface termination, impact point, and roughness were all examined. Results from the MD simulations were compared, and lend insight into, complementary AFM experiments. In addition, separate sets of MD simulations were performed using two different potential energy functions. The AIREBO potential is a bond-order potential that contains intermolecular interactions that was developed to model bond-breaking and bond-making processes. Results obtained using the AIREBO potential will be compared results obtained using the recently developed REBO+S potential. The REBO+S potential differs from the AIREBO potential in that alterations were made to the REBO potential cutoff distances, which alters the forces required to make and break bonds. Differences in adhesion and wear events obtained using the two different potentials with identical material pairs will be quantified. Supported by the National Science Foundation

11:40am **TR+AS-MoM11 Speed-Dependence of Atomic-Scale Friction**,

A. Martini, Z. Ye, University of California Merced, *Y. Dong*, Purdue University, *P. Egberts, XZ. Liu, R.W. Carpick*, University of Pennsylvania

Atomistic simulations and experimental atomic force microscopy measurements on a variety of different materials have shown that atomic-scale single asperity friction can be significantly affected by sliding speed. However, physical insights into how and why sliding speed affects friction are limited because the speeds accessible to most simulations are several orders of magnitude faster than those in the corresponding experiments. Typical simulations must be run at fast sliding speeds due to their necessarily short time scale, and accurate experimental nanoscale asperity friction measurements are limited to slow speeds because of difficulties in measuring high-speed forces with picoNewton resolution. Here we present friction results from molecular dynamics simulations where the sliding speeds are greatly reduced by using parallel replica dynamics. Parallel replica dynamics is an accelerated simulation technique that distributes simulation time across multiple processors and therefore adequately samples the various possible state-to-state pathways accessible to the system, as would a standard, single-processor simulation run for a very long time. This technique, accompanied by experiments where data is obtained using a novel high-speed data acquisition method, enables measurements and simulations to be quantitatively compared within the same physical regime; specifically, at the same sliding speed. Furthermore, the materials, load, contact size and orientation, system compliance, and temperature are identical within experimental uncertainty so as to minimize differences between experiments and simulations, allowing robust comparisons and interpretations. These coordinated studies enable us to understand the dependence of atomic-scale friction on sliding speed, and to determine the limits of validity of the Tomlinson-Prandtl model, a reduced-order model widely-used to describe atomic-scale sliding.

Vacuum Technology

Room: 202 C - Session VT-MoM

Vacuum Measurement and Metrology

Moderator: R. Versluis, TNO Technical Sciences, Netherlands

8:20am **VT-MoM1 The Important Role of Vacuum Technology in the Redefinition of the Kilogram**, *P.J. Abbott*, NIST **INVITED**

The kilogram is the sole remaining unit in the International System of Units (SI) that is still defined by a physical artifact, namely, the International Prototype Kilogram (IPK). There are two motivations for redefinition: To comply with a "New SI" that realizes units from invariant natural constants, and to address the discovery of a divergence in the mass values between the IPK and its official copies that was discovered during the third periodic verification of national prototypes of the kilogram (1988-1992). Because mass is such an important area of metrology for commerce, any redefinition of the kilogram must not hinder the metrological community in terms of unacceptably large uncertainties compared to what is currently available through traceability to the IPK. After careful consideration, in October of 2011 the General Conference on Weights and Measures (CGPM) adopted a resolution to redefine the kilogram in terms of the Planck constant, h . The Consultative Committee for Mass and Related Quantities (CCM) has

recommended that the Planck constant be known to within a standard relative uncertainty of 2 parts in 10^8 before redefinition occurs in order to address the metrological concerns mentioned above. World-wide, several efforts that measure the Planck constant are in progress, and more are expected to begin in the next few years. The two major apparatus used to measure the Planck constant are the Watt balance and the X-ray crystal diffraction (XRCD) experiments. Though these methods use very different physical principals, they have in common the necessity to operate in medium to high vacuum conditions in order to mitigate contamination and reduce uncertainties. Therefore, the new kilogram will be realized in a vacuum environment, which obviates the need for transferring this realization to air where it can easily be disseminated via conventional mass metrology. This transference from vacuum to air requires precision mass metrology under vacuum, an understanding of adsorption and desorption phenomena related to mass artifacts, transportation of mass artifacts under vacuum between experiments for inter-comparisons, and an understanding of the effects of long-term storage of mass artifacts in air, inert gases, and under vacuum. In short, application of many of the fundamentals of vacuum technology is absolutely essential in the realization and dissemination of a kilogram that is defined in terms of the Planck constant. This talk will provide details of the many experiments that are underway to address the vacuum technology challenges presented in the redefinition of the kilogram.

9:00am VT-MoM3 Reinventing Pressure and Vacuum Metrology: Development of an Optical Pressure Standard, J.H. Hendricks, J.A. Stone, G.F. Strouse, D.A. Olson, J.E. Ricker, P. Egan, G. Scace, NIST, D. Gerty, Sandia National Laboratories

We have now concluded the first year of a five year program that aims to fundamentally change the method for realizing and disseminating the SI unit for pressure. The innovative technique represents a paradigm shift in the way the unit for pressure and vacuum is realized, creates new measurement infrastructure for NIST, and has the potential to create exciting spin-off technology that will have large impacts for US manufacturing and world metrology. We will move from primary standards based on artifacts for pressure and temperature and move to standards based on quantum-chemistry calculations of helium's refractive index. The underlying metrology behind this advance is the ultra-accurate determination of the refractive index of gases by picometer optical interferometry. The optical-based primary pressure standard will improve accuracy and allow the complete replacement of all mercury-based pressure standards which are expensive to operate and have environmental and health hazards. We describe our progress in designing and building our fixed length and variable length optical cavities and will discuss the uncertainty budget and technical challenges associated with this project to build an optical primary pressure standard.

9:20am VT-MoM4 Uncertainty of a NIST Transfer Standard for Inter-Laboratory Comparison of National Metrology Institutes, J.E. Ricker, J.H. Hendricks, NIST

For over a decade, NIST has been developing portable Transfer Standards Packages (TSP) which can disseminate pressure at significantly lower uncertainties than commercially available transfer standards. Because of this experience, NIST was tasked with piloting an International Inter-laboratory Comparison of seven countries. From April 2012 to June 2013, a NIST designed TSP circled the globe visiting each National Metrology Institute as a reference to provide an International Inter-laboratory comparison from 1 Pa to 10 kPa. The most important aspect of the TSP was to have an uncertainty value ranging from 0.5 % at 1 Pa to 0.01 % at 10 kPa.

Key to reaching the uncertainty goal was using special techniques to improve the uncertainty of commercial gauges. These techniques include temperature stabilization, maintaining level, and improving the calibration stability of the gauges. The crucial advantage of the NIST TSP is the ability to exploit the advantage of the Capacitance Diaphragm Gauge's (CDG) unbeatable resolution at lower pressures (typically 1 part in 10^6 of full scale range) and the Resonance Silicon Gauge's (RSG) drift uncertainties of 0.01% ($k=2$). Each gauge type individually cannot achieve the necessary uncertainty, with the CDGs subject to up to 0.5% uncertainty ($k=2$) due to long term stability (drift uncertainty) and RSGs low resolution/inability to measure low pressures. However, the short term stability (< 8 hours) of a CDG is excellent (less than 0.01%) and has been found to drift in a correctable manner. Because of these characteristics, it is possible to calibrate the CDGs using the RSG just before use and wind up with a very low uncertainty measurement. The talk will cover primary gauge stability data on two transfer standard packages and will discuss some of the technical challenges in running an international key comparison.

9:40am VT-MoM5 Fully Automated Flowmeter for Low Gas-Flows Based on Pinhole Apertures, J.A. Fedchak, National Institute of Standards and Technology (NIST)

We report results from a new flowmeter built at NIST that based upon gas flow through a laser-drilled pin-hole orifice. Dubbed the orifice flowmeter (OFM), it is based on a relatively simple principle: A pinhole orifice with a known conductance can be used as a secondary flow standard; the gas flow is determined from the known conductance and the upstream pressure and temperature. A flowmeter based upon an appropriate set of orifices is easy to operate and automate. We are primarily interested in using the OFM as a standard to produce nitrogen gas flows into vacuum in the range of 10^{-11} mol/s to 10^{-6} mol/s (10^{-7} to 10^{-2} cm³/s; STP) for vacuum gauge calibrations. Commercially available laser-drilled pinhole orifices with diameters from 1 μ m to 50 μ m can have molecular-flow conductances ranging from about 0.1 μ L/s to 230 μ L/s for N₂ at 23 °C, and can be used to produce gas flows in the range of interest by applying an upstream pressure in the range of 10 Pa to 100 kPa (0.1 to 760 torr). Accurate measurements of the orifice conductance, or gas flow, as a function of pressure are required to use the pinhole orifice as a basis of a flowmeter. This was performed using the NIST bellows flowmeter, a primary gas flow standard, to directly measure the conductance of a pinhole orifice over the entire pressure range of interest. We have constructed a fully automated flowmeter based upon conductance measurements of two pin-hole orifices that can be used for nitrogen and other gas flows. In this presentation, the construction and characterization of the OFM will be described and recent results will be presented.

10:40am VT-MoM8 Evaluation and Discussion of Performance Characteristics of Modern-Day Cold Cathode Ionization Gauges, P.C. Arnold, T.C. Swinney, B.J. Kelly, Brooks Automation, Inc., Granville-Phillips Products

Cold Cathode Ionization Gauges (CCIGs), as in all high and ultrahigh vacuum gauges, possess a myriad of idiosyncrasies which will be discussed. The basic physical electronics of the CCIG will be the basis for discussion of gauge characteristics. The physical electronics source of these characteristics will be pursued in terms of geometry, electric fields, magnetic fields, and common methods of use. The CCIG is found to solve many user environment operation issues and has many good points. The discussion of causes and possible theoretical remedies will address various issues at many regions of the common pressure-use regimes, including both the high and low ends of use. The role of magnet design and its contribution to magnetic fields internal to the gauge will be evaluated in interaction with the applied electric field. Computer simulation of these interactions will be displayed to aid in the understanding of the CCIG operation.

11:00am VT-MoM9 An Inverted Magnetron Pirani Combination Gauge with Low Magnetic Stray Fields, M. Wüest, B. Andreaus, J. Marki, R. Enderes, D. Oertel, INFICON Ltd, Liechtenstein

Electromagnetic interference from low-intensity static magnetic fields has been observed to affect the operation of pacemakers and other medical electronic devices. The ICNIRP Guidelines [1] recommend that those devices are not adversely affected by static magnetic fields below 0.5 mT. This recommendation has been incorporated into the Semiconductor Manufacturing Standard SEMI S2-0302 [2] and requires that the magnetic field at exterior surfaces of the equipment (2 to 3 cm from the surface) has to be smaller than 0.5 mT or a pacemaker warning needs to be posted. For these reasons, presently available cold cathode gauges should (but most do not) carry a pacemaker warning label, because they do not fulfill the SEMI S2 standard. We have developed an inverted magnetron that has a novel magnetic field design with exterior magnetic stray fields below the threshold set by the SEMI norm. Therefore, this device does not need to carry a warning label. A low external magnetic field is also of benefit to analytical instrumentation, where the external magnetic field might influence the trajectories of ions. We will present the magnetic design and other pertinent features of this inverted magnetron gauge. [1] Guidelines on Limits of Exposure to Static Magnetic Fields, International Commission on Non-Ionizing Radiation Protection, 2009. [2] Environmental, Health, and Safety Guideline for Semiconductor Manufacturing Equipment, Semi S2-0302, Appendix 5, 2002.

Monday Afternoon, October 28, 2013

Actinides and Rare Earths Focus Topic

Room: 102 C - Session AC+MI+SA+TF-MoA

Actinides and Rare Earths: Theory and Electron Correlation

Moderator: L. Havela, Charles University, Czech Republic

2:00pm AC+MI+SA+TF-MoA1 **Structural and Electronic Relationships Between the Lanthanide and Actinide Elements, B. Johansson**, Uppsala University, Sweden **INVITED**

The similarity and difference between the solid state properties of the 4f and 5f transition

metals are pointed out. The heavier 5f elements show properties which have direct

correspondence to the early 4f transition metals, suggesting a localized behaviour of the

5f electrons for those metals. On the other hand, the fact that Pu metal has a 30% lower

volume than its neighbour heavier element, Am, suggests a tremendous difference in the

properties of the 5f electrons for this element relative to the heavier actinides. This change

in behaviour between Pu and Am can be viewed as a Mott transition within the 5f shell

as a function of the atomic number Z. On the metallic 5f side of the Mott transition (i.e.,

early actinides), the elements show most unusual crystal structures, the common feature

being their low symmetry. An analogous behaviour for the lanthanides is found in cerium

metal under compression, where structures typical for the light actinides have been observed

experimentally. A generalized phase diagram for the actinides is shown to contain features

comparable to the individual phase diagram of Ce metal. The crystal structure behaviour of

the lanthanides and heavier actinides is determined by the number of 5d (or 6d) electrons

in the metallic state, since for these elements the f electrons are localized and nonbonding.

For the earlier actinide metals electronic structure calculations – where the 5f orbitals

are treated as part of the valence bands – account very well for the observed ground state

crystal structures. The distorted structures can be understood as Peierls distortions away

from the symmetric bcc structure and originate from strongly bonding 5f electrons occupying

relatively narrow 5f states.

2:40pm AC+MI+SA+TF-MoA3 **Signature of Strong Correlations in Actinides and its Compounds: A Dynamical Mean Field Theory Perspective, G. Kotliar**, Rutgers University **INVITED**

Plutonium is a unique element, poised at the edge of a localization delocalization transition. Its compounds exhibit

remarkable phenomena, ranging from insulating behavior with a topologically non trivial band structure in PuB₆ [1]

to high temperature superconductivity PuCoGa₅ [2].

In the last decade a new paradigm for understanding, modeling and predicting physical properties of these materials

has emerged based on realistic implementations of dynamical mean field theory (DMFT) concepts [3][8] [9]. This theory

treats the wave (band-like) and the (particle-like) multiconfigurational multiplet aspects of the f-electrons on the same

footing. This theory accounts for the volume of δ Pu in a paramagnetic configuration [6] and predicted its phonon

spectra [7].

In DMFT, an underlying self consistent impurity model can be used to reconstruct local observables of a material.

An illustrative example is the valence histogram, describing the weight of each atomic configuration in the ground

state of the solid. This important concept, and the resulting prediction for Pu can now be probed experimentally

using resonant XES [5] and neutron form factor measurements [11].

There are now many applications by many groups which have extended the reach of this approach to many actinide

based compounds. We will review the basis of the DMFT approach and compare some results with selected experiments

on 5f electron system. We will conclude with some new directions to face the challenge for material design in this

field [10].

[1] XY Deng, K. Haule and G. Kotliar preprint(2013).

[2] J. L. Sarrao et al., Nature 420, 297 (2002)

[3] A. Georges, G. Kotliar, W. Krauth, and M. Rozenberg, Rev. of Mod. Phys. 68, 13-125 (1996).

[4] Per Soderlind, G. Kotliar, K. Haule, P. Oppeneer and D. Guillaumont, MRS Bulletin vol 35, 883, (2010).

[5] C.H. Booth, Y. Jiang, D.L.Wang, J.N. Mitchell, P.H. Tobash, E.D. Bauer, M.A.Wall, P.G. Allen, D. Sokaras, D. Nordlund,

T.-C. Weng, M.A. Torrez, and J.L. Sarrao PNAS 109, 10205-10209 (2012)

[6] J. H. Shim, K. Haule, and G. Kotliar, Science 318, 1615- 1617 (2007).

[7] X. Dai, S. Y. Savrasov, G. Kotliar, A. Migliori, H. Ledbetter, and E. Abrahams, Science Mag. 300, 953-955 (2003).

[8] (2007) Advances in Physics, 56:6, 829 - 926 (2007)

[9] G. Kotliar, S. Savrasov, K. Haule, V. Oudovenko, O. Parcollet, and C. Marianetti, Rev. of Mod. Phys. 78, 000865 (2006).

[10] Z. P. Yin, Xiaoyu Deng, K. Basu, Q. Yin, G. Kotliar, arXiv:1303.3322 (2013).

[11] M. E. Pezzoli, K. Haule, and G. Kotliar, Phys. Rev. Lett. 106, 016403 (2011).

3:40pm AC+MI+SA+TF-MoA6 **Towards a Better Understanding of Low-Energy Excitations in Heavy-Fermion Systems, G. Zwicknagl**, Technische Universität Braunschweig, Germany **INVITED**

Metals containing lanthanide or actinide ions have been at the focus of interest in condensed matter physics during the past decades. The presence of the partially filled f-shells leads to unexpected "anomalous" behavior such as heavy fermions, unconventional superconductivity, unusual magnetism as well as their co-existence.

The f-electron systems lie at the intersection of a large number of long-standing problems in the physics of metals. In metals containing ions with partially filled inner shells, we immediately face the fundamental question which picture provides the better starting point for theoretical models, a delocalized description in terms of energy bands or a localized representation which accounts for the atomic properties. The answer to the question which of the above-mentioned pictures is the appropriate starting point seems to depend on the physical quantities under consideration. This fact is a consequence of electronic correlations which prevent to describe the influence of the f-states over the entire temperature and energy range in terms of a unique simple model. While the high-temperature (high-energy) properties of lanthanide compounds can be understood in terms of localized f-moments it is generally accepted by now that the f-electrons should also be described in within a band picture as delocalized states as far as the low-energy excitations are concerned.

Concerning the underlying microscopic picture, it is generally accepted that the formation of strongly renormalized 4f-bands in lanthanides is a consequence of the Kondo effect where the degrees of freedom of the 4f-shell form a collective singlet ground state with the conduction electrons. The Kondo model, however, does not apply to actinide compounds where the situation is more complex. In some compounds, experiments suggest the co-existence of both localized atomic-like 5f-degrees of freedom with itinerant 5f-band states at low temperatures/ low energies. Microscopic model calculations suggest that partial localization of 5f-electrons may result from the intra-atomic Hund's rule-type correlations.

In the present talk, I shall give an overview over our present understanding of the "Dual Nature" of f-electrons. I present recent results on the suppression of the Kondo state in YbRh₂Si₂ [1]. I discuss microscopic

calculations for electron spectroscopies in actinide compounds emphasizing the consequences of strong intra-atomic correlations of the 5f-shell [2,3].

[1] H. Pfau et. al., arXiv:1302.6867

[2] Gertrud Zwicknagl, MRS Online Proceedings Library, Volume 1444, (2012)

[3] Gertrud Zwicknagl, Phys. Stat. Sol. B 250, 634 (2013)

4:20pm AC+MI+SA+TF-MoA8 Electronic Structure of EuO under Pressure, L. Petit, D. Szotek, M. Lueders, W.M. Temmerman, Daresbury Laboratory, UK, A. Svane, Aarhus University, Denmark

We present results of an ab-initio study of EuO under pressure. The calculations are based on a first-principles methodology that adequately describes the dual character of electrons, itinerant versus localized by correcting for the unphysical self-interaction that underpins the local spin density approximation. We find that EuO, which at ambient conditions crystallizes in the NaCl structure, undergoes an isostructural insulator to metal transition around 35 GPa. The transition is associated with a change in the ground state valency configuration from $\text{Eu}^{2+}(f^7)$ to $\text{Eu}^{3+}(f^6)$. At even higher pressure we observe a transition to the CsCl structure. The ground state valency configuration remains Eu^{3+} , i.e. this latter transition is isovalent. We compare our results to a recent experimental investigation that postulates a reentrant valence transition to a nearly divalent Eu^{2+} configuration at high pressures.

Applied Surface Science

Room: 204 - Session AS-MoA

Analyses Using Novel Ion Beams

Moderator: X. Dong, Eli Lilly and Company, W.F. Stickle, Hewlett Packard

2:00pm AS-MoA1 Status and Prospects for ICP Focused Ion Beams, N. Smith, P. Tesch, N. Martin, Oregon Physics LLC, R. Boswell, Oregon Physics LLC and Australian National University **INVITED**

Milling speeds with a gallium focused ion beam (FIB) are often much too slow for many sample preparation and surface engineering applications. For example, cross-sectioning stacked-die semiconductor devices, prototyping micro-mechanical structures and delayering IC's for circuit mapping are growing applications that require a milling rate that far exceeds that provided by the gallium FIB.

In the more general area of direct-write surface engineering, milling with nanometer precision is limited to volumes of $<10^4 \mu\text{m}^3$ when using gallium FIB systems. Also, engineered devices must generally be tolerant of high gallium concentrations being implanted in the near-surface region. These are major restrictions when fabricating micromechanical devices.

Furthermore, elemental secondary ion mass spectrometric imaging (SIMS-Imaging) has been limited to a lateral resolution of 200nm when using an oxygen focused ion beam for high sensitivity surface analysis. Many areas of material science could benefit from an ability to image trace level surface chemistry with $<20\text{nm}$ resolution. Example applications include, sub-cellular imaging of trace metals in the brain for neurodegenerative disease studies, analysis of trace element segregation in metal alloys and studying isotope distributions in meteorites.

Here, we review inductively coupled plasma ion source technology that can provide a focused ion beam capable of milling silicon at a rate of $>5000 \mu\text{m}^3/\text{s}$ with $<4\mu\text{m}$ milling resolution and $<25\text{nm}$ imaging resolution with 30keV xenon ions. The latest generation ICP-FIB, readily operates as a high brightness source of not only any inert ion, but also positively and negatively ionized oxygen for trace element SIMS imaging.

By transferring energy to plasma electrons via a radio frequency induction field, it is possible to create a plasma state without a cathodic electrode. This method of plasma creation can create energy normalized beam brightness values that now exceed $1 \times 10^4 \text{ Am}^{-2} \text{ sr}^{-1} \text{ V}^{-1}$. This high brightness can be attained with long lifetimes ($>>2000$ hours), stable beam current ($\leq \pm 0.5\%$ drift per 30 minutes) and an axial energy spread for the extracted ion beam of 5-6eV and for a broad array of ion species.

At Oregon Physics, we have developed the HyperionTM inductively coupled plasma ion source that is already capable of generating smaller probe diameters (Xe^+) than the liquid metal ion source (LMIS, Ga^+) FIB at beam currents in excess of 20nA. When operated with oxygen, imaging resolution, source lifetime and current stability are significantly higher than provided by a duoplasmatron.

This paper presents FIB and SIMS data from this new ion source technology, to exemplify the impact on surface science. The operating

principles of the inductively coupled plasma source, the properties of the ion beam(s) being created and the projected future for this technology are also described.

2:40pm AS-MoA3 Detection of Small Molecules on Intact Biofilms using Femtosecond Laser Desorption Postionization Mass Spectrometry, Y. Cui, C. Bhardwaj, S. Milasinovic, R. Gordon, L. Hanley, University of Illinois at Chicago

Matrix assisted laser desorption ionization and secondary ion mass spectrometry are the two dominant mass spectrometric imaging methods, but signal stability in the former degrades when spatial resolution increases, while the latter can suffer from extensive fragmentation that complicates peak identification. Laser desorption with ultrashort pulses can remove material from a solid with minimal damage to the remaining sample [Milasinovic, *et al.*, Anal. Chem. 84 (2012) 3945]. Furthermore, laser desorbed neutrals can undergo soft postionization by vacuum ultraviolet (VUV) radiation for subsequent detection by MS. Here, we demonstrate the small molecule imaging capability of this method on intact microbial biofilms. Baker's yeast and *E. coli* biofilms grown on polycarbonate membranes were studied using a previously reported instrument [Cui, *et al.*, Rev. Sci. Instrum. 83 (2012) 093702] equipped with a long Rayleigh range focusing lens and a VUV postionization source [Bhardwaj, *et al.*, Anal. Bioanal. Chem. (2012) <http://dx.doi.org/10.1007/s00216-012-6454-0>]. Comparisons were made between laser desorption using direct ionization and VUV postionization. The effects of nanosecond vs. femtosecond desorption pulse lengths were also compared. The results from fs and ns pulses were similar, differing mostly in their relative peak intensities, presumably because of the dependence of the desorption mechanism on laser pulse length. Different delays between the desorption and VUV lasers were also investigated. The imaging capability was demonstrated using baker's yeast and *E. coli* cocultured biofilms. Results showed significant differences between films containing yeast, *E. coli*, and a mixture. Although these capabilities were applied here to intact biological samples, they can be extended to a wide variety of materials including polymers, metals, semiconductors, and insulators.

3:00pm AS-MoA4 TOF-MEIS Analysis of Nanostructured Materials, K. Jung, DGIST, Republic of Korea, W. Min, KMAC, Republic of Korea, H. Yu, KRIS, Republic of Korea, K. Yu, KMAC, Republic of Korea, M. Sirtica, P.L. Grande, UFRGS, Brazil, D. Moon, DGIST, Republic of Korea
We report the quantitative compositional profiling with single atomic layer resolution for 0.5~3 nm CdSe/ZnS QDs with a conjugated layer and ultra shallow junctions of As and B implanted Si using a newly developed time-of-flight medium energy ion scattering (MEIS)/Direct Recoil (DR) spectroscopy, which utilizes a pulsed 70~100 keV He⁺ and Ne⁺ ion beam of ~10 μm diameter for energy resolution of ~5x10⁻³.

The composition and core shell structure of CdSe cores and ZnS shells were determined with ~1% uncertainty and ~0.1 nm resolution, respectively. The number of conjugated molecules per QD can be also determined quantitatively. The composition and size of QDs estimated with TOF-MEIS were compared with XPS and HRTEM, respectively.

As depth profiles in As/Si ultra shallow junctions (USJs) were measured by TOF-MEIS for 2 keV As implantation ion energy with the nominal ion dose of 2x10¹⁵/cm² before and after annealing. Before annealing, the As profile shows a Gaussian shaped distribution with the ion range at 4~5 nm. After annealing, the As atoms diffused out to 3~4 nm with a skewed Gaussian distribution with an extended tail to 11 nm. The dependence of the As profiles on annealing conditions were also observed. The As depth profiles measured by dynamic SIMS were compared with those from TOF-MEIS, which clearly shows the surface transient effect and ion beam mixing effect. Quantitative As depth profiles from TOF-MEIS were compared with SIMS profiles for the calibration of SIMS artifacts in USJ depth profiling. Light elements in heavy substrates can be hardly measured by ion scattering spectroscopy in general. We demonstrated that the TOF-MEIS can be used in the direct recoil mode for the depth profiling analysis of B in B/Si USJ before and after annealing.

With this new TOF-MEIS nano analysis technique, the core-shell structure with conjugated layer structure of QDs, activated As depth profiles in As/Si USJ, B depth profiles in B/Si USJ could be measured quantitatively. Progresses in TOF-MEIS analysis of other nano-structured materials and devices in various nano & bio technology will be discussed.

3:40pm AS-MoA6 Effect of Ion Bombardment of Novel Electronic Materials, J.D.P. Counsell, S.J. Coultas, C.J. Blomfield, S.J. Hutton, A.J. Roberts, Kratos Analytical Limited, UK

Lead zirconate titanate (PZT) is a ceramic perovskite material which exhibits piezoelectric properties. PZT is currently used in numerous applications including sensors and actuators and is currently being developed for use in memory devices. Thin-films of PZT were grown on

Pt/TiO₂/SiO₂/Si substrates using CVD. Chemical analysis and stoichiometry of the surface was performed using XPS.

This paper will discuss the changes in stoichiometry and chemical states under ion bombardment. A variety of different ions (Ar⁺, C₂₄H₁₂⁺, Ar₍₅₀₀₋₂₀₀₀₎⁺) and beam energies were used to gain information regarding the internal structure of this material. Depth profiling showed good compositional homogeneity through each film thickness, with some lead segregation at the film surface. Optimised conditions for depth profiling inorganic materials are proposed. Processes such as preferential sputtering, sample damage and surface charging are discussed. Previous studies have concentrated on the use of Ar⁺ as the bombardment ion however we show that by using gentler ions it is possible to reduced bulk damage and preferential sputtering of the complex surface.

[1] Aleksey Etin, Gennady E. Shter, Reuven Brenner, Sioma Baltianski, and Gideon S. Grader., J. Am. Ceram. Soc., 90 [12], 2007, 3800–3803.

[2] Jae-Nam Kim, Kwang-Soo Shin, Dae-Hwan Kim, Byung-Ok Park, Nam-Kyoung Kim, Sang-Hee Cho., Appl. Surf. Sci., 206, [1–4], 2003, 119–128.

4:00pm AS-MoA7 Adventures in Mass Spectrometry Imaging - From Pictures to Words, I.S. Gilmore, National Physical Laboratory, UK INVITED

The three principal mass spectrometry imaging techniques are secondary ion mass spectrometry (SIMS), matrix assisted laser desorption ionisation mass spectrometry (MALDI MS) and the growing family of ambient mass spectrometries. These powerful techniques allow molecular imaging in 2 and 3 dimensions, from macroscale to the nanoscale and in ambient conditions in real-time. The adage says that “a picture is worth a thousand words”. However, images can be seductive⁽¹⁾ but the interpretation of the picture to words of understanding requires a robust metrology framework.

In SIMS, one of the most important advances has been the use of large cluster ions, most notably, argon clusters to allow 3D imaging with a depth resolution approaching 5 nm. The metrology will be reviewed and recommendations for optimum analysis conditions provided. Important artefacts including the effect of primary and secondary ion on the relative depth position and effects of electron beam damage will be identified. The lateral resolution of SIMS for organics is two orders of magnitude worse, which is insufficient for many important applications such as measuring intracellular drug concentration. Future prospects to meet these challenges will be discussed.

Ambient mass spectrometries, such as desorption electrospray ionisation (DESI) and plasma assisted desorption ionisation (PADI) are relatively new but are growing strongly owing to their ability to analyse *in situ*. We have recently conducted a VAMAS interlaboratory study on the repeatability and constancy of the relative intensity and preliminary results will be presented. PADI has great promise for the analysis of polymers including depth profiling, however, present PADI sources are limited to the mm range. NPL and the University of Liverpool are developing novel sources with an aim to achieve 10 micrometre spatial resolution. Recent developments in PADI metrology will also be highlighted.

MALDI is a popular technique for tissue imaging since large peptides and proteins may be detected. However, the sample preparation results in a complex of the matrix, tissue and analyte. NPL has recently started a new metrology programme to support MALDI MS imaging and progress will be presented.

NPL has recently established a National Centre of Excellence in Mass Spectrometry Imaging (NiCE-MSI) including all the above techniques. An important objective of the centre is to provide the metrology and standardisation that ensures that pictures do translate to meaningful knowledge.

References:

1. J C Vickerman, Analyst 136, (2011) 2199

4:40pm AS-MoA9 Argon Gas Cluster Ion Beam (GCIB) Sputter Yields: Measurements for 22 Biological and Organic Electronic Materials, Metals and Oxides, P. Cumpson, J. Portoles, A. Barlow, N. Sano, Newcastle University, UK

Argon Gas Cluster-Ion Beam (GCIB) sources[1,2] are likely to become widely-available on XPS and SIMS instruments in the next few years. Much attention has been devoted to their ability to depth-profile organic materials with minimum damage. What has not been the focus of attention (possibly because it has been very difficult to measure) is the large ratio of sputter rate for organic materials compared to inorganic materials using these sources, and the special opportunities this presents for studies of organic/inorganic interfaces. This large ratio offers a special opportunity to characterise practical organic/inorganic interfaces with near atomic resolution and high sensitivity.

Recently we published argon GCIB sputter yield measurements for 19 polymers[3], using a combination of white-light interferometry and contact masking to provide accurate measurements of sputter crater depth. This technique overcomes the need to form a thin, uniform film of the material of interest, which can be problematic in some cases. These data showed an unexpectedly wide range, the sputter yield of PMMA being more than ten times that of PEEK when using argon ion clusters of around 4 eV/atom, with other polymers being widely distributed between these extremes.

We have extended these measurements to a further 22 materials of wide technological interest, including metals (gold, stainless steel), oxides (Si, Al, Ti oxides), biological materials (collagen, bovine serum albumen, fibronectin etc), and organic materials commonly used in organic electronics and organic photovoltaics, plus a few more polymers. Clearly there is a wide range of sputter yield across this large dataset, with inorganic materials having very low, but measurable, sputter yields. We discuss some systematic trends in these data, and the prospect of developing semi-empirical equations for estimating sputter yield in metals, oxides and molecular solids as well as polymers.

[1] S Rabbani, A M Barber, J S Fletcher, N P Lockyer, and J C Vickerman, Anal. Chem. 83 (2011) 3793.

[2] I Yamada, J Matsuo, N Toyoda, and A Kirkpatrick, Mater. Sci. Eng. R. 34 (2001) 231.

[3] Peter J. Cumpson, Jose F. Portoles and Naoko Sano, J. Vac. Sci. Technol. (2013) A 31, 020605

5:00pm AS-MoA10 Mass Imaging of Biological Samples with Focused Massive Ar Cluster Ion Beams, J. Matsuo, QSEC, Kyoto University, CREST, Japan, S. Nakagawa, Kyoto University, CREST, Japan, M. Fujii, QSEC, Kyoto University, CREST, Japan, T. Aoki, T. Seki, Kyoto University, CREST, Japan

Following the development of novel primary ion beams, such as SF₅, C₆₀, Bi₃, and Ar_n, material analysis with secondary ion mass spectrometry (SIMS) has been widely used for organic and biological materials. In particular, with such ion beams the time-of-flight (TOF) SIMS system can provide whole mass spectra for the determining molecular structures on surfaces, and very recently these beams have been used in molecular depth profiling to investigate multilayer structures consisting of various organic materials. Thus, TOF-SIMS is considered to be an important surface analysis technique for organic and biological materials. Furthermore, mass spectrometric imaging with high lateral resolution can be achieved with the TOF-SIMS technique, because ion beams are easily focused down to submicrometer dimension.

However, there are still numerous challenges in applying TOF-SIMS to real biological samples. For instance, to compete with other mass spectrometry techniques, such as MALDI, DESI, DART, PADI, etc., mass resolution and sensitivity are expected to be improved. We have demonstrated that massive Ar cluster beams are quite useful as a primary beam in SIMS. Because of the high-density energy deposition and multiple collisions with low energy atoms on the surface, there are much less fragmented ions in the SIMS spectra of large organic materials. This is one of the advantages of massive Ar cluster beams, because many biological samples are crude and contain many similar but different molecules. For instance, when di-stearoyl-phosphatidyl-choline (DSPC), which is generally the most abundant lipid in animal cell membranes, is measured with SIMS, fragmented ions (184 Da) as well as protonated secondary molecular ions (791 Da) are detected. The ratio of fragmented ions to molecular ions measured with massive Ar cluster beams is around 10, which is two orders lower than the ratio measured with Bi₃ ion beam. One of the technical problems of massive Ar cluster beams was the difficulty of obtaining a short-pulsed beam, because of the large mass distribution. We have developed a TOF-SIMS mass spectro meter system with ortho gonal acceleration (oa-TOF), which allows use of a continuous beam. The mass resolution of this system is better than 16,000, which is comparable to the conventional SIMS with pulsed ion beams.

The latest results of massive Ar cluster SIMS will be presented and discussed in comparison with other techniques.

Acknowledgements

This work is supported by the Core Research of Evolutional Science and Technology (CREST) of JST.

J. Matsuo, S. Ninomiya, H. Yamada, K. Ichiki, Y. Wakamatsu, M. Hada, T. Seki and T. Aoki, Surf. Interface Anal. (2011) 42, 1612

5:20pm AS-MoA11 Dissociation of Argon Cluster Ions by Impact on Metal Surfaces, K. Mochiji, N. Inui, K. Moritani, University of Hyogo, Japan

Argon cluster ions, typically consisting of hundreds to thousands of argon atoms, have been used in nanometer-scale fabrications such as thin film

deposition or primary ion source for SIMS. The average kinetic energy per atom in the cluster ion is equal to the energy used to accelerate the cluster ion divided by the number of atoms in the cluster ion (called the cluster size). For example, when a cluster of 1000 atoms is accelerated to 5 kV, the average kinetic energy per atom of the cluster ions is only as low as 5 eV. Furthermore, when a cluster ion collides with a surface, chemical reactions such as sputtering or etching of target materials can be occurred within a very thin layer by multiple collisions among the numerous atoms constituting the cluster ion. Such the characteristics of the argon cluster ion are strongly effective to low damage and high throughput processing.

In this study, we have investigated the dissociation of an argon cluster ion by the impact on material surfaces. The ion emission from the target material by the bombardment of the argon cluster ions (cluster size: 1000-5000 atoms) was analyzed by a time of flight mass analyzer. Smaller sizes of argon cluster ions were observed in the mass spectra by lowering the kinetic energy per atom of the incident cluster ion below 10 eV/atom. The prominent ions were dimer (Ar_2^+) and trimer ions (Ar_3^+), but monomer ions (Ar^+) were not observed. This can be explained as follows. It was reported that the charge of an argon cluster ion is localized on the central three atoms, which forms trimeric ion core and the ion core is much more stable as compared with the shell of neutral argon atoms surrounding the ion core. Consequently, an argon cluster ion dissociates into many neutral argon atoms and a small argon cluster ion whose size could depend on the impulsive force at the impact. We measured the mass spectra of the dissociated cluster ions by the impact on several kinds of metals. As a result, the mass spectra changed by the metal even at the same bombardment condition. As a degree of dissociation, the ion-yield ratio of $\text{Ar}_2^+ / (\text{Ar}_2^+ + \text{Ar}_3^+)$ was plotted as a function of the stress acting on the contact area between the incident cluster ion and the metal surface, which can be calculated by using the values of elastic coefficient and density of the argon cluster and the metals. The result clearly showed that the ion-yield ratio is linearly increased with the stress. Such the correlation could be used as a new method for measuring the mechanical strength such as elastic coefficient or hardness of metals.

Biomaterial Interfaces

Room: 201 B - Session BI+AI+BA+IS-MoA

Biofouling

Moderator: D.E. Barlow, Naval Research Laboratory

2:00pm **BI+AI+BA+IS-MoA1 Biofouling of Carbon Steel: Effects of Microstructure and Test Media on Initial Bacterial Attachment and Subsequent Corrosion**, M.A. Javed, P.R. Stoddart, S.M. McArthur, S.A. Wade, Swinburne University of Technology, Australia

Biofouling of surfaces causes numerous problems in a wide range of industries such as shipping, health care, oil and gas production and food production. Of specific interest to the current work is the accelerated corrosion of metals that can arise as a consequence of bacterial biofilm formation, which is commonly known as microbiologically influenced corrosion (MIC).

The initial attachment of bacteria to a surface is one of the first steps in the process of biofouling. The attachment is dependent upon a large number of factors, which are broadly related to the properties of the bacteria, substrate/surface and environment. Changes in these properties can not only influence the initial attachment step, but also the interrelated production of extracellular polymeric substances (EPS) by the bacteria and the subsequent corrosion.

A large amount of the work performed to date on bacterial attachment in relation to MIC has focused on stainless steels, possibly due to reports of rapid failures of these materials such as through thickness pitting of piping welds. These studies have highlighted how a range of material properties (e.g. chemical composition, surface roughness, grain size and boundaries) can influence attachment and biofilm formation on steel surfaces. This range of influences means that a high level of care must be taken when designing and carrying out bacterial attachment tests in order to avoid the situation where a number of material variables affect the outcome of a single test. For example one of the criticisms of some of the previous work in this area is the lack of control of surface roughness of the substrates used in the studies.

In this work we will report results of studies of the initial attachment and EPS production of *E. coli* bacteria on highly polished carbon steel samples, with a number of different microstructures, for a number of different test media. We have found that the microstructure and test medium can have a significant effect on the rate of bacterial attachment, the distribution of

attached bacteria, the onset of EPS production and the corrosion of samples immersed in *E. coli* inoculated test media.

2:20pm **BI+AI+BA+IS-MoA2 Charged SAMs as Model Surfaces to Understand Anti-fouling Properties of Zwitterionic Coatings**, S. Bauer, University of Heidelberg, Germany, J. Finlay, M.E. Callow, J.A. Callow, University of Birmingham, UK, A. Rosenhahn, Ruhr-University Bochum, Germany

Zwitterionic surfaces are a class of coatings that receive increasing attention due to their good antifouling performance.¹ Since early work on protein resistance of mixed, charged self-assembled monolayers (SAMs), charge neutrality seems to be a prerequisite for their inert properties.^{2,3} Similar to established non-fouling ethylene glycol chemistries, zwitterionic systems rely on a strong hydration of the coating. In this study we attempt a systematic analysis to which extend charge neutrality and the chemical nature of the charged groups affect their antifouling performance. Positively charged trimethylammonium terminated thiols were therefore mixed with sulfonate-, carboxylate- and phosphonate-terminated undecanethiols in varying ratios. Optimized preparation conditions and surface analysis will be presented that demonstrates successful assembly of the coatings and characterizes their physicochemical properties. The antifouling properties were tested against a range of laboratory organisms such as diatoms and spores of algae and compared to protein resistance. The obtained trends will be discussed and correlated with field experiments in the real marine environment.

(1) Chen, S.; Jiang, S. **2008** A new avenue to nonfouling materials. *Advanced Materials*, 20, 335-338.

(2) Holmlin, R. E.; Chen, X. X.; Chapman, R. G.; Takayama, S.; Whitesides, G. M. **2001** Zwitterionic SAMs that resist nonspecific adsorption of protein from aqueous buffer. *Langmuir*, 17, 2841-2850.

(3) Chen, S. F.; Yu, F. C.; Yu, Q. M.; He, Y.; Jiang, S. Y. **2006** Strong resistance of a thin crystalline layer of balanced charged groups to protein adsorption. *Langmuir*, 22, 8186-8191.

2:40pm **BI+AI+BA+IS-MoA3 The Role of Bacterial Physiology in Biodeterioration of Polyurethane Coatings**, S. Zingarelli, Air Force Research Laboratory, D.E. Barlow, J.C. Biffinger, Naval Research Laboratory, L.J. Nadeau, Air Force Research Laboratory, D. Babson, Naval Research Laboratory, B.W. Stamps, University of Oklahoma, R.K. Pirlo, Naval Research Laboratory, C.N. Drake, Air Force Research Laboratory, B.S. Stevenson, University of Oklahoma, J.N. Russell, Jr., Naval Research Laboratory, W.J. Crookes-Goodson, Air Force Research Laboratory
INVITED

Microbial biofilms frequently contaminate surfaces and can cause degradation of polyurethane coatings that are intended to protect against environmental degradation. Historically, investigations of polyurethane biodeterioration have focused on identification and characterization of the organisms and 'polyurethanase' enzymes involved in the degradation process. However, many questions remain unanswered. For example, microbes capable of polymer degradation are ubiquitous in the environment, yet only affect polymers under some circumstances. What controls the production of polyurethanases? What is the role of planktonic vs. biofilm populations in the biodeterioration process? The goal of our research is to define the parameters and regulatory mechanisms that result in polyurethane biodeterioration by *Pseudomonas protegens* Pf-5, with a focus on environmental conditions (nutrients, pH, oxygen) and microbial 'lifestyles' (planktonic vs. biofilm populations). First, we screened a variety of carbon sources with a polyurethane agar plate-clearing assay using the polyester polyurethane Impranil DLN. Results showed that strain Pf-5 could grow on a variety of carbon sources but that degradation of polyurethane varied depending on the carbon source. We observed strong polyurethane degradation in the presence of M9-citrate medium but severely reduced clearing of polyurethane when glucose was provided as a carbon source. Subsequent studies with planktonic cultures of *P. protegens* Pf-5 verified the inhibitory effect of glucose on polyurethanase activity. Using proteomic tools, activity in citrate-grown planktonic culture supernatants was ascribed to two esterases, polyurethane esterases A and B. Currently the regulation of these enzymes is being investigated through a combination of genetic and transcriptomic approaches. Biofilms were grown on Impranil DLN in M9-citrate or -glucose to determine if these nutrients also regulated polyurethanase secretion in biofilms. Micro ATR-FTIR surface chemical analysis of the coatings after biofilm removal showed that degradation proceeds through preferential loss of the ester component. However, optical microscopy and profilometry clearly show that subsequent bulk coating loss can occur under certain conditions, resulting in complete loss of the original coating surface, and eventually complete loss of the coating. Transmission FTIR microscopy was also used to detect bulk coating degradation in a biofilm culture plate assay we developed to complement the Impranil clearing assay. This assay demonstrated significant Impranil coating

degradation from citrate-grown biofilms versus minor degradation for glucose-grown biofilms.

3:40pm **BI+AI+BA+IS-MoA6 Multifunctional Active Nano and Microstructured Surfaces for Biofouling Management, G.P. López, Duke University** **INVITED**

This talk will present (i) recent developments of stimuli responsive surfaces that exhibit dynamic structure on lateral length scales of the order of 10 microns and below, (ii) a prospectus for the formation of multifunctional bioactive surfaces based on such dynamic micro- and nanostructured materials, and (iii) results from study of bioadhesion and biorecognition on these surfaces. Stimuli responsive polymer surfaces include patterned polymer brushes and elastomers; biological systems of interest include protein solutions, adherent mammalian cell lines, as well as marine and infectious bacteria. Our previous studies have demonstrated that stimuli responsive polymers can be used to control the adhesion of such systems and, in this presentation, we will provide our latest advancements in this line of study, as regards to both molecular and cellular biointerfacial phenomena. Methods for preparing dynamic micro- and nanopatterns of stimuli responsive polymers will be presented, along with characterization of their structure, dynamic behavior and bioadhesion resistant character.

4:40pm **BI+AI+BA+IS-MoA9 Roles of Extracellular DNA in the Development and Expansion of Bacterial Biofilms, C.B. Whitchurch, University of Technology, Sydney, Australia** **INVITED**

Biofilms are multicellular communities of bacteria that are often found attached to surfaces and cause significant problems in medical, industrial, and marine settings. Cells within biofilms are enmeshed in an extracellular polymeric matrix comprised of polysaccharides, proteins, lipids, and nucleic acids. Over the past decade, extracellular DNA (eDNA) has been found to be essential for biofilm formation by many species of bacteria where it is thought to function as an intercellular "glue" that binds cells together. Interestingly, whilst it has been known for over a decade that eDNA is essential during the early stages of biofilm development by the opportunistic pathogen *Pseudomonas aeruginosa*, the precise roles of eDNA in this process have yet to be elucidated. We have used advanced techniques in microscopy, computer vision and image informatics to explore the roles of eDNA during early biofilm development and during active expansion of biofilms formed by *P.aeruginosa*. Many species of bacteria, including *P. aeruginosa* utilize type IV pili mediated twitching motility to actively translocate across solid and semi-solid surfaces. Twitching motility can manifest as a complex, multicellular behavior that enables the active expansion of bacterial biofilms. Under appropriate conditions, such as those encountered at the interface of a glass coverslip and semi-solid nutrient media, the expanding biofilm can develop dramatic networks of intersecting trails. Our analyses reveal that at the leading edge of the interstitial biofilm, highly coherent groups of bacteria migrate across the surface of the semi-solid media, and in doing so, create furrows along which following cells preferentially migrate. This leads to the emergence of a network of trails that guide mass transit toward the leading edges of the biofilm. We have determined that eDNA facilitates efficient traffic flow throughout the expanding biofilm by maintaining coherent cell alignments, thereby avoiding traffic jams and ensuring an efficient supply of cells to the migrating front. Our analyses reveal that eDNA also co-ordinates the movements of cells in the leading edge rafts and is required for the assembly of cells into aggregates that forge the interconnecting furrows. Our observations have revealed that large-scale self-organization of cells in actively expanding biofilms of *P. aeruginosa* occurs through construction of an intricate network of furrows that is facilitated by eDNA.

5:20pm **BI+AI+BA+IS-MoA11 Sample Preparation and Optimization for Bacterial Identification by Raman Spectroscopy, M.M. Hlaing, M. Dunn, S.M. McArthur, P.R. Stoddart, Swinburne University of Technology, Australia**

The characterisation and identification of individual bacteria using Raman spectroscopy can aid in rapid, in situ microbiological diagnosis and hence timely, appropriate treatment and control measures [1, 2]. Appropriate sample preparation methods and experimental conditions are crucial to avoid some potential difficulties in analysing the information-rich Raman spectra from bacterial cells. In this study, the Raman spectra of fresh and stored samples of bacterial isolates (*Escherichia coli*) were analysed to determine any variations caused by sample processing. Analysis based on principal components suggests that different methods of sample preparation and storage affect the spectral components associated with different biochemical compounds in bacterial cells. The effect of long term storage in glycerol stock at freezing temperatures on the Raman spectrum of cells from the early exponential phase was observed in this study and found to modify the bacteria cells. Furthermore, the presence of extracellular polymeric substance (EPS) matrix around bacterial cells at later stages of the growth cycle provide higher resistance to environmental stress

compared with other phases. Based on these results, a specific experimental protocol has been developed in order to obtain interpretable, comparable and reliable Raman data from bacterial samples.

Keywords: Raman spectroscopy; Bacterial identification; Sample preparation.

References

- [1] W. E. Huang, R. I. Griffiths. *Anal. Chem.* 2004, **76**(15): 4452-4458.
- [2] T. J. Moritz, S. T. Douglas. *J. Clin. Microbiol.* 2010, **48**(11): 4287-4290.

Electronic Materials and Processing

Room: 101 B - Session EM-MoA

High-k Gate Oxides for High Mobility Semiconductors II

Moderator: A.C. Kummel, University of California San Diego

2:00pm **EM-MoA1 Silicene, an Option for Future Electronics, A. Molle, D. Chiappe, E. Cinquanta, CNR-IMM, Italy, C. Grazianetti, M. Fanciulli, Università degli Studi di Milano Bicocca, Italy** **INVITED**

The silicon counterpart of graphene, the so called "silicene" [1,2], has been so far a theoretical option but its synthesis constituted a formidable challenge. Nonetheless, recent efforts have moved up this fascinating hypothesis to a concrete evidence [3][4] thus triggering a tremendous interest in silicene for electronic applications and fundamental investigations.

Non-trivial atomic arrangements of the silicene are expected to occur which are dictated by a delicate balance between planar and buckled bonding. Indeed, due to the large ionic radius of silicon, silicene is naturally prone to occur with a variety of slightly-buckled configurations which can be driven by the silicene/substrate local interactions [1]. This structural complexity discriminates the experimentally observed silicene from graphene, and it is expected to bring basically new physical properties such as topological phase transitions, quantum spin Hall effect, or band gap opening [5]. Here we report on recent experimental results showing the formation of 2D epitaxial silicene on Ag(111) substrates [4] based on *in situ* scanning tunnelling microscopy-spectroscopy investigations.

Despite its structural flexibility, silicene is technologically limited by its chemical instability. Indeed, silicene undergoes oxidation when exposed to dry air. Then, interfacing silicene with a gate dielectric is essential for any feasible voltage bias application but also to barely save it from possibly destructive reactivity in ambient conditions.

While disentangling silicene from metallic templates is still an open challenge, on-top interface engineering of silicene is here addressed with the goal to develop a non-reactive encapsulation process. This effort enabled us to fabricate a chemically stable Al₂O₃/silicene/Ag heterostructure through a carefully tailored co-deposition of Al and O₂ [6]. Raman spectroscopy was then used to demonstrate the structural stability of the encapsulated silicene. Finally, new hints at Si nanosheets grown on *ad hoc* 2D material templates are also discussed aiming at the silicene "portability" for device-oriented exploitation.

These outcomes disclose exceptionally novel issues in the physics of the emerging silicene and promote a renewed interest in nanoscaled silicon as active material for electronic devices.

References

1. S. Cahangirov, et al, *Phys. Rev. Lett.* 102, 236804 (2009).
2. M. Houssa, et al., *Appl. Phys. Lett.*, 97, 112106 (2010).
3. P. Vogt, et al., *Phys. Rev. Lett.* 108, 155501 (2012).
4. D. Chiappe, et al., *Adv. Mater.* 24, 37, 5088 (2012).
5. M. Ezawa, *Phys. Rev. Lett.* 109, 055502 (2012).
6. A. Molle, et al., *Adv. Func. Mat.* 2013, 10.1002/adfm.201300354 (just accepted).

2:40pm **EM-MoA3 Fabrication and Electrical Characterization of High-k/Germanium Tri Gate MOSFETs Grown by MBE on Bulk Silicon, S. Anwar, C. Buie, C.L. Hinkle, University of Texas at Dallas**

Germanium has long been considered as a replacement channel material due to its higher intrinsic hole mobility compared to silicon and its relative compatibility with current CMOS processing. Growth of Ge channel materials on bulk Si would be ideal for minimizing cost and allow for the continued use of current manufacturing tools. Ge grown on Si, however, results in a significant defect density due to the 4.2% lattice mismatch, reducing device performance.

In this work, we study the fabrication of tri-gate Ge MOSFETs, grown by MBE, on Si using Aspect Ratio Trapping (ART)^{1,2} to reduce the Ge defect density. ART is a growth technique that allows for the reduction of defects for lattice mismatched materials by trapping the threading dislocations into the sidewalls of patterned nanoscale trenches in which the epitaxial growth takes place. This technique has the added benefit of producing the necessary geometric structure required for highly scaled tri-gate devices, alleviating short channel effects, while simultaneously reducing defect density. The fabrication of high aspect ratio (>2) trenches in SiO₂ for epitaxial growth of Ge will be discussed as well as the issues and solutions associated with the inherent non-selectivity of solid-source MBE growth. TEM, SEM, and AFM are employed to characterize the growth quality and assess the various device fabrication steps.

Tri-gate MBE-grown Ge MOSFETs on Si are fabricated using a gate first process. A high-quality Ge interfacial region is obtained by a surface functionalization technique using 50 pre-pulses of DI-H₂O in an ALD chamber at 250°C, followed by a 2 nm thick interfacial Al₂O₃ deposition at 250 °C followed by a forming gas anneal (FGA) at 350 °C.³ The FGA step converts the functionalized surface to a thin layer of GeO₂, improving the electrical characteristics of the devices. 2.5 nm of HfO₂ is then deposited by ALD followed by a 500 °C post-deposition anneal in N₂. 150 nm of reactively sputtered TiN is deposited as the gate metal. Schottky junction source and drain regions are formed by sputtering 20 nm of Pt, capped with TiN, and annealed at 400 °C to form PtGe₂.⁴ A final 350 °C FGA completes the device processing. Detailed electrical characterization, using a suite of techniques, was performed and correlated with the MBE growth and gate stack formation.

This work is sponsored in part by the SRC Global Research Corporation.

1 T. A. Langdo, *et al.*, Appl. Phys. Lett. **76**, 3700 (2000).

2 J. Bai, *et al.*, Appl. Phys. Lett. **90**, 101902 (2007).

3 S. Swaminathan, *et al.*, J. Appl. Phys. **110**, 094105 (2011).

4 R. Li, *et al.*, IEEE EDL, **27**, 476 (2006).

3:00pm **EM-MoA4 Sub 1-nm Ge-MOSFET with TiO₂/Al₂O₃ Gate Stacks and Interface Trap Passivation by Forming Gas Anneal, L. Zhang, P.C. McIntyre, Stanford University**

Equivalent oxide thickness (EOT) scaling is one of the most critical challenges for future Ge-MOSFET technology. It is difficult to achieve sub-1 nm EOT with a single dielectric material, due to the intrinsic trade-off between dielectric constants and band gaps. Recently, bilayer high-k materials, such as TiO₂/Al₂O₃, HfO₂/Al₂O₃, have been paid increasing attention. However, there are several challenges remaining for bilayer high-k stacks on Ge substrate: 1) an ultra-thin high-quality GeO₂/GeO_x layer is generally reported to be necessary for effective Ge surface passivation, but this is difficult to obtain by routine thermal oxidation. It has been reported that processes such as post-dielectric deposition plasma oxidation are beneficial for preparing such interface layers. 2) The interface between the two high-k materials in the bilayer must be abrupt and their thicknesses well-controlled, to reduce gate leakage as the EOT is scaled. In this paper, we address these challenges by a simple, low-temperature process flow using thermal annealing. Using carefully-controlled atomic layer deposition (ALD) of the dielectric layers and a forming gas anneal (FGA), a TiO₂/Al₂O₃/Ge gate stack is demonstrated with EOT = 0.63 nm that achieves low D_{it} and gate leakage current density in MOS capacitors. Pt gated Ge-pMOSFETs with TiO₂/Al₂O₃ gate stacks are fabricated, and have a sub-1nm EOT, 75 mV/dec subthreshold swing, 10m A/m m on state current and avoid gate metal/TiO₂ reaction or interdiffusion.

In our process, a high quality Al₂O₃ layer on the Ge substrate is grown by atomic layer deposition with the help of efficient sites for Al(CH₃)₃ precursor adsorption produced by oxidant pre-dosing the Ge(100) surface prior to ALD. Forming gas anneal (FGA) is found to be a critical step to realize low interface trap densities in low EOT Ge transistors. We observed great improvement of device performance after FGA on both MOSCAPs and MOSFETs, the effectiveness of FGA determined by Al₂O₃ thickness, FGA conditions, and the identity of the overlying gate metal.

We have used both hard and soft x-ray synchrotron photoemission electron spectroscopy (PES) to investigate the Al₂O₃/Ge interface and the TiO₂ layer in various Al₂O₃/Ge and Pt/TiO₂/Al₂O₃/Ge structures before and after FGA. An increase in intensity of the Ge+4 feature is observed after FGA of Al₂O₃/Ge samples, and emergence of a detectable Ti +3 peak, consistent with loss of oxygen during FGA, is also identified in Pt/TiO₂/Al₂O₃/Ge samples. Effects of these local chemical changes on the MOS performance of the resulting gate stacks will be discussed.

3:40pm **EM-MoA6 Surface Passivation of III-V Antimonides and Ge Based MOSFETs, K.C. Saraswat, S. Gupta, A. Nainani, Stanford University, B. Yang, GLOBALFOUNDRIES U.S. Inc., Z. Yuan, Stanford University**

INVITED

Si CMOS scaling is reaching practical and fundamental limits. Currently, use of strain engineering to boost mobility is the dominant technology for high performance Si MOSFETs. However, mobility boosting by straining Si will also saturate with future scaling. Therefore, looking into future it becomes important to look at higher mobility materials like Ge and III-Vs to continue scaling of MOSFETs. For these materials to become mainstream several problems need to be solved, including surface passivation. In this talk we will present our recent results on passivation of Ge, GeSn and III-V antimonides.

Ge and GeSn have recently emerged as promising candidates not only for high performance CMOS but also for optoelectronics. Ge PMOS with several different high-k dielectrics have been demonstrated with excellent performance. Ge surface passivation with GeO₂ shows low D_{it} near valence band (E_v). However, Ge NMOS have so far exhibited poor drive current. This is partially attributed to high D_{it} near the conduction band (E_c). In recent work we have achieved low and symmetric D_{it} through sulfur passivation followed by ALD of Al₂O₃ and then annealing in ozone. With these two treatments, a record-low D_{it} (<1E11/cm²eV) at both band edges is achieved

In GeSn with increasing Sn content G valley comes down with respect to the indirect valleys, increasing population of electrons in this low electron mass valley which boosts mobility. A novel surface passivation scheme using ozone oxidation of thin Ge cap has been demonstrated with record low D_{it} of 3E10¹¹/cm²eV at high-κ/GeSn interface.

While there have been many demonstrations on n-channel MOS in III-V semiconductors showing excellent electron mobility and high drive currents, hole mobility in III-V p-channel MOS has traditionally lagged in comparison to Si. GaSb is an attractive candidate for high-performance III-V pMOS due to its high hole mobility. Performance degradation due to interfacial traps is generally considered one of the main challenges for III-V MOSFETs. We have demonstrated passivation of GaSb with an ALD Al₂O₃ gate dielectric with a midband-gap D_{it} of 3E10¹¹/cm²eV and demonstrated excellent pMOSFETs.

We have further investigated the suppression of interface state response using band engineering in III-V quantum well MOSFETs and experimentally verified the concept in antimonide compounds system using a gate-stack consisting of Al₂O₃/GaSb/InAlSb. It is shown that if the thickness of the interfacial layer of GaSb is scaled down to a few monolayers, the effective bandgap of the interfacial layer increases dramatically due to quantum confinement, which leads to the suppression of interface-trap response.

4:20pm **EM-MoA8 High-Carrier-Mobility p- and n-Type Field Effect Transistors Fabricated on Large-Area Wafer-Scale Ge Film Epitaxially Grown on Si, S. Ghosh, S.M. Han, University of New Mexico**

Implementing a unique two-step simple molecular beam epitaxy (MBE) growth technique in our laboratory, we have successfully demonstrated heteroepitaxial growth of high-quality Ge on Si (GoS) that opens up a possibility for many applications, including high-mobility transistors integrated on Si substrates and high-speed, read-only memory using Ge as the channel material. We note that our Ge film covers the entire underlying Si substrate at the wafer scale without mesas or limited-area growth. However, the ultimate test of materials quality is device demonstration on engineered GoS substrates. Herein, we have investigated the characteristics of two such devices: p-MESFETs as well as p- and n-MOSFETs fabricated on GoS substrates. For p-MESFETs, we have measured a low-field peak effective hole mobility of 310 cm²/V-sec and a cut-off frequency of 10 GHz at 200K. In this presentation, we will provide additional details of the device characterization. In addition to MESFETs, we have investigated electrical characteristics of planar p-MOSFETs fabricated on n-type GoS substrates. The defect density in n-type GoS obtained from etch pit density measurements is consistently below 1x10⁶ cm⁻². p-MOS capacitors are first fabricated, using Ti/HfO₂/GeO_xN_y/n-Ge gate-stack structure. Angle-resolved X-ray photoelectron spectroscopy is employed to quantify nitrogen content within the GeO_xN_y layer. The corresponding gate leakage current density is below 10⁻³ A/cm² and D_{it} of 6x10¹² cm⁻² eV⁻¹ at 300K. After characterizing p-MOSCAPs, we have fabricated p-MOSFETs from n-GoS substrates. In this work, a two-step thermally activated method, instead of ion-implantation, is used to define p+ doped source and drain. The sheet resistivity from Hall measurements supports the presence of p+ regions. Forward and transfer current-voltage characteristics are measured, and the p-MOSFETs built on GoS substrates show a subthreshold slope (SS) of ~100 mV/decade, compared to ~80 mV/decade for the identical p-MOSFETs built on Ge substrates. The effective peak mobility obtained from our optimized p-MOSFETs is 401 cm²/V-sec. This is an 82% increase

in the effective carrier mobility in the inversion channel in GoS, compared to the universal effective hole mobility in Si. In summary, a wafer-scale, epitaxial Ge layer on Si is used to fabricate high-hole-mobility p-MESFETs and p-MOSFETs. In this talk, we will further discuss n-MOSFETs fabricated on p-type GoS substrates, exploring the possibility of fabricating high-carrier-mobility CMOS devices from GoS substrates.

4:40pm **EM-MoA9 Passivation, Functionalization, and Atomic Layer Deposition Nucleation of SiGe(100) via H₂O and H₂O₂.** *T. Kaufman-Osborn, A.J. Kerr, A.C. Kummel*, University of California, San Diego

Silicon-germanium is a promising candidate for potential channel or contact materials due to its higher hole and electron mobility. To minimize the oxide-semiconductor interfacial defect density, a chemical and electronic passivation layer must be formed before the oxide layer is deposited. In this study, a monolayer of H₂O or H₂O₂ chemisorbates is shown to activate Trimethylaluminum (TMA) chemisorption due to the Si/Ge-OH bonds catalyzing the formation of an ultrathin passivation layer which can serve as an ideal ALD nucleation template on SiGe. However, since H₂O chemisorption results in equal density of Si/Ge-H and Si/Ge-OH sites on the SiGe(100), H₂O can only provide a maximum of 0.5 monolayer of Si/Ge-OH sites, limiting the TMA nucleation density. By using H₂O₂ dosing, the density of Ge-OH sites can be doubled thereby increasing the potential TMA nucleation density. This study compares the passivation of the SiGe(100) surface via H₂O and H₂O₂, for the application of nucleating ALD growth on the surface, using scanning tunneling microscopy (STM), scanning tunneling spectroscopy (STS), and x-ray photoelectron spectroscopy (XPS).

Using a differentially pumped dosing system, a clean SiGe(100) sample was dosed at room temperature with a saturation dose of either H₂O or H₂O₂. STM and XPS measurements indicate that H₂O₂ dosing leaves the SiGe(100) surface, which is mostly Ge atoms due to surface segregation, terminated with an ordered monolayer Ge-OH sites. A very small density of unreacted atoms are left unpassivated on the surface and have half filled dangling bond states causing a large local amount of conduction band edge states in the bandgap. STS measurements of the Ge-OH sites show the conduction band edge dangling bond states are eliminated due to the passivating Ge-OH bonds, but the Fermi level is pinned near the valence band edge due to the large surface dipole. When the surface is annealed to 310°C, XPS measurements indicate that the -OH species on the surface break bonds with the Ge atom and bond instead to the Si atoms, raising Si atoms towards the surface. XPS also verifies that no oxygen leaves the surface due to the 310°C anneal. Instead, the oxygen remains on the surface in the form on Si-OH or SiO_x species. It is hypothesized that a lower temperature anneal would prevent SiO_x species from forming, leaving a surface which is only terminated by Si-OH bonds which would serve as an ideal template for ALD nucleation of TMA for Al₂O₃ growth. STS measurements show that TMA nucleation on the H₂O₂ functionalized SiGe(100) surface unpins the Fermi level and has a wide bandgap with no band edge states demonstrating very good interface quality.

5:00pm **EM-MoA10 III-V on Insulator (XOI): Processes, Materials, and Devices.** *A. Javey*, University of California at Berkeley **INVITED**

Two-dimensional (2-D) semiconductors exhibit excellent device characteristics, as well as novel optical, electrical, and optoelectronic properties due to quantum size-effects. In this talk, I will discuss layer transfer of single crystalline III-V semiconductors with nanoscale thicknesses on Si/SiO₂ substrates. The resulting III-V-on-insulator (XOI) substrates enable the exploration of a wide-range of device applications, while allowing for fundamental science exploration of the carrier properties as a function of thickness, without the constraints of the original growth substrates. Specifically, the quantized sub-bands of ultrathin III-V membranes (3-20 nm in thickness) are directly visualized by optical absorption studies. The measured effective bandgap is shown to increase by ~3x for InAs XOI as the layer thickness is reduced to ~3nm. Through experiments and modeling, we demonstrate the drastic role of carrier quantum confinement on the contact resistance and carrier transport properties of field-effect transistors (FETs). These results provide an important advance towards establishing the fundamental device physics of 2-D semiconductors. Additionally, high performance InAs and InGaSb complementary XOI-FETs are fabricated on Si substrates with electron and hole mobilities of ~4000 and 800 cm²/Vs, respectively. This presents the first III-V CMOS demonstration. Overall, the results shed light on the performance limits of III-V ultrathin body FETs.

Energy Frontiers Focus Topic

Room: 101 A - Session EN+AS+NS+SS-MoA

Interfacial Challenges in Nanostructured Solar Cells

Moderator: M.A. Filler, Georgia Institute of Technology

2:00pm **EN+AS+NS+SS-MoA1 Solar Energy Conversion Beyond the Limit.** *X.Y. Zhu*, Columbia University **INVITED**

This lecture aims to explore key mechanistic issues in an emerging photovoltaic technology based on organic and polymeric molecules, i.e., plastic solar cells. I will present two examples from recent research in my laboratory. The first example is within the realm of conventional theories and we aim to understand a critical step in charge separation at donor/acceptor interfaces in organic photovoltaics, namely the formation and dissociation of interfacial charge transfer excitons [1]. In particular, we show the critical role of hot charge transfer excitons in setting the fundamental time limit for charge separation in organic photovoltaics [2]. The second example shows how an intriguing physical phenomenon, exciton fission in which a singlet exciton breaks up into two triplet excitons in organic semiconductor materials, may be used to build solar cells with power conversion efficiency exceeding the fundamental limit (the so-called Shockley-Queisser limit) of conventional solar cells. We show how singlet exciton fission can occur in organic semiconductors due to a many electron quantum coherent process [3-4], and how we can efficiently extract two electrons from the quantum superposition [5].

[1] M. Muntwiler, Q. Yang, W. A. Tisdale, X.-Y. Zhu, "Coulomb barrier for charge separation at an organic semiconductor interface," *Phys. Rev. Lett.* 101 (2008) 196403.

[2] A. Jailaubekov, et al., "Hot charge transfer excitons set the time limit for charge separation at donor/acceptor interfaces in organic photovoltaics," *Nature Mater.* 12 (2013) 66-73.

[3] W.-L. Chan, M. Ligges, A. Jailaubekov, L. Kaake, L. Miaja-Avila, X.-Y. Zhu, "Observing the Multi-Exciton State in Singlet Fission and Ensuing Ultrafast Multi-Electron Transfer," *Science* 334 (2011) 1541-1545.

[4] W.-L. Chan, M. Ligges, X.-Y. Zhu, "The energy barrier in singlet fission can be overcome through coherent coupling and entropic gain," *Nature Chem.* 4 (2012) 840-845.

[5] W.-L. Chan, J. R. Tritsch, X.-Y. Zhu, "Harvesting singlet fission for solar energy conversion: one versus two electron transfer from the quantum mechanical superposition," *J. Am. Chem. Soc.* 134 (2012) 18295-18302.

2:40pm **EN+AS+NS+SS-MoA3 Photocurrent Generation Characteristics of Ge Quantum-Dot Solar Cells.** *G. Uchida, D. Ichida, H. Seo, K. Kamataki, N. Itagaki, K. Koga, M. Shiratani*, Kyushu University, Japan

The pressing need for massively scalable carbon-free energy sources has focused attention on both increasing the efficiency and decreasing the cost of solar cells. Quantum-dot (QD) solar cells employing multiple exciton generation (MEG) have attracted much attention as a candidate for the third generation solar cells, because MEG represents a promising route to increase solar conversion efficiencies up to about 44 % in single junction. Our interest has been concerned with QD solar cells using group IV semiconductor nanoparticles [1-4]. The main purpose of this study is to discuss characteristics of quantum efficiency of Ge QD solar cells in view of the MEG effect.

QD thin films containing Ge nanoparticles were deposited using 13.56 MHz radio-frequency (rf) magnetron sputtering process in Ar and H₂ gas mixture under a high pressure condition of 1.5 Torr. The sputtering target was a poly-crystal Ge disk (1 inch) with a purity of 99.99%. The rf power was 50 W.

X-ray diffraction spectra of Ge nanoparticle films show transition from amorphous to crystalline structure by adding H₂ gas, where the diffraction peaks appear at $2\theta = 27^\circ$, 45° , and 53° corresponding to the (111), (220), and (311) crystal planes of Ge, respectively. Then, optical property of the films was investigated to reveal effects of crystalline Ge nanoparticles on the light absorption properties. For amorphous Ge films, absorption coefficient was $1.5 \times 10^5 \text{ cm}^{-1}$ at 840 nm, while for crystalline Ge films absorption coefficient drastically increased from $0.6 \times 10^5 \text{ cm}^{-1}$ at 840 nm to $4.9 \times 10^5 \text{ cm}^{-1}$ at 450 nm, which is close to $5\text{-}6 \times 10^5 \text{ cm}^{-1}$ at 450 nm in single crystal Ge. Finally, we fabricated Ge QD sensitized solar cells with rectification in the TiO₂/Ge/polysulfide electrolyte system. The incident photo-to-current conversion efficiency increases with decreasing the wavelength, and it is 10 % at 400 nm. The result indicates that excitons generated in Ge nanoparticles were separated into electrons and holes, and such carriers successfully extracted to the outer circuit.

[1] G. Uchida, et al., *Phys. Stat. Sol. (c)* 8 (2011) 3021.

[2] G. Uchida, *et al.*, Jpn. J. Appl. Phys. 51 (2011) 01AD01.

[3] H. Seo, *et al.*, Electrochim. Acta 87 (2013) 213.

[4] H. Seo, *et al.*, Electrochim. Acta 95 (2013) 43.

3:00pm **EN+AS+NS+SS-MoA4 Interfacial Charge Transfer in Extremely Thin Absorber Solar Cells**, *M.E. Edley, H. Majidi, G.W. Guglietta II, L. Spangler, J.B. Baxter*, Drexel University

Solar cells can provide an abundant, clean, and sustainable source of electricity, but high costs have limited their implementation. The use of sensitized nanostructured architectures may enable both low-cost processing and high efficiency by decoupling the functions of light harvesting and charge transport into different materials. We report on extremely thin absorber (ETA) solar cells that use ZnO nanowire arrays coated with a thin CdSe layer and filled with a liquid electrolyte. CdSe absorbs visible light, and photoexcited electrons are injected into the ZnO while photoexcited holes oxidize the redox species. Nanowire arrays provide direct pathways for electron transport as well as sufficient surface area for sensitization. The CdSe coatings should be crystalline and conformal with well-controlled thickness. With this ETA architecture, interfacial recombination is the dominant loss process, so controlling the interfacial chemistry, morphology, and microstructure of the materials during processing is critical.

Our approach utilizes a combination of solar cell measurements and ultrafast transient absorption spectroscopy to understand the effects of CdSe thickness, annealing conditions, and interfacial treatments on the dynamics and efficiency of charge carrier separation, and ultimately on the solar-to-electric energy conversion efficiency. These studies provide guidelines for architecture design and materials selection for ETA solar cells. For example, we have found that an optimum thickness exists for planar cells that balances light absorption with photoexcited carrier collection, and that this optimum thickness depends on annealing conditions of the CdSe. Coatings on nanowires should be designed to use the largest thickness that gives the maximum internal quantum efficiency in planar cells, which is ~30 nm when annealing at 400 C. The nanowire geometry is then designed to achieve efficient light harvesting with a coating thickness of 30 nm. Such thin electrodeposited coatings are subject to pinholes and shunt pathways. However, these were overcome through the deposition of an ultrathin (<5 nm) CdS interfacial layer using successive ionic layer adsorption and reaction (SILAR), improving efficiency to above 2%. Ultrafast transient absorption spectroscopy shows that the lifetime of photoexcited carriers depends strongly on defect density, with lifetimes increasing from ~50 ps to ~500 ps upon annealing. Importantly, this lifetime is much longer than the characteristic time for electron transfer into ZnO (~2 ps) and hole transfer into the electrolyte (~100 ps), indicating that charge separation is very efficient.

3:40pm **EN+AS+NS+SS-MoA6 Solar Photochemical Fuel Generation using Semiconductor Nanocrystals**, *G. Dukovic*, University of Colorado, Boulder **INVITED**

Semiconductor nanocrystals are remarkable light harvesters with readily tunable absorption spectra and surface chemistry. They have recently been coupled with redox catalysts to drive photochemical multi-electron transfer reactions such as generation of H₂. We use ultrafast laser spectroscopy to characterize the excited state dynamics of nanocrystal-catalyst hybrids and measure the rates and efficiencies of charge transfer processes necessary for photochemical fuel generation. This presentation will focus on the relationships between charge transfer dynamics and overall photochemical reactivity. The design principles derived from the insights provided by these experiments will be described.

4:40pm **EN+AS+NS+SS-MoA9 Graphene as a Transparent Front Contact for Heterojunction Silicon Solar Cells**, *K. Sharma*, Eindhoven University of Technology, Netherlands, *D. Deligiannis*, Delft University of Technology, Netherlands, *J. Willem Weber, S. Smit, A.A. Bol*, Eindhoven University of Technology, Netherlands, *M.C.M. van de Sanden*, Dutch Institute for Fundamental Energy Research (DIFFER), Netherlands, *M. Creatore*, Eindhoven University of Technology, Netherlands, *R.A.C.M.M. van Swaaij*, Delft University of Technology, Netherlands, *W.M.M. Kessels*, Eindhoven University of Technology, Netherlands

Silicon heterojunction solar cells (SHJ) have achieved excellent conversion efficiencies both at lab (~25%) and industrial scale (>20%).¹ Further enhancement towards theoretical efficiencies (~28%) is expected to occur when novel concepts and/or new functional materials are implemented to address the present optical and resistive losses in ITO and doped layers utilized in SHJ solar cells. Recently, graphene on silicon has been successfully tested as a Schottky barrier junction.² Innovative solar cell structures are required to realize the true potential of graphene. To this end, we are reporting a novel device structure where undoped graphene was tested as a transparent conductive layer. Conversion efficiencies of about 10% have been achieved, which is an order of magnitude higher than

reported so far in the literature for undoped graphene. CVD grown graphene was transferred onto SHJ device structures in an advanced multi-step procedure and the following solar cell layouts were used: stack A-graphene/(i)a-Si:H/(n)c-Si/(i)a-Si:H/(n)a-Si:H; and stack B-graphene/(p)a-Si:H/(i)a-Si:H/(n)c-Si/(i)a-Si:H/(n)a-Si:H. The amorphous silicon layers were deposited by means of RF-PECVD in a cluster tool. Current-voltage (J-V) and external quantum efficiency (EQE) measurements were carried out to characterize the devices. A minority carrier lifetime as high as 2 ns was achieved for the investigated stacks, largely due to the excellent surface passivation induced by (i)a-Si:H layers. Open-circuit voltage, short-circuit current density, fill-factor, and conversion efficiency values of 384 mV, 25 mA/cm², 60%, and 5.8%, respectively, were achieved for stack A. Simulations of the band structure have shown that graphene, due to its self-adaptive nature² acts as an energy barrier for charge transport, which could be further enhanced if the graphene is doped. For stack B, with the graphene applied onto a p-type a-Si:H layer, the open-circuit voltage was significantly enhanced up to 569 mV, while the fill-factor increased to 74%. However, in this case the short-circuit current density dropped to 24 mA/cm² due to enhanced absorption losses in the (p)a-Si:H. The conversion efficiency of 10.1% was achieved. These initial results suggest that graphene can potentially be used to decouple electrical and optical properties of the front contact in SHJ solar cells to achieve higher conversion efficiencies.

¹ A. Descoeudres, Z.C. Holman, L. Barraud, S. Morel, S. De Wolf, and C. Ballif, IEEE Journal of Photovoltaics 3, 83 (2013).

² H. Zhong, Z. Liu, G. Xu, Y. Fan, J. Wang, X. Zhang, L. Liu, K. Xu, and H. Yang, Applied Physics Letters 100, 122108 (2012). (ref. 7-9 therein)

5:00pm **EN+AS+NS+SS-MoA10 Tuning Energy Level Alignment at Organic/Semiconductor Interfaces using a Built-in Dipole in Chromophore-Bridge-Anchors**, *S. Rangan, A. Batarseh, K.P. Chitre, A. Kopecky, E. Galoppini, R.A. Bartynski*, Rutgers University

The problem of energy level alignment at heterointerfaces is central to the issues of charge transport and charge separation in solid state or hybrid photovoltaic devices, as well as in organic electronic and water splitting applications. In most cases, the energy alignment at interfaces is an ad-hoc property of two materials brought into contact, with the relative ionization or affinity energies possibly altered by charge reorganization at the interface, often called the interface dipole. Attempts to alter this ad-hoc energy alignment have employed strategies ranging from modifying bulk properties to intentionally altering charge redistribution at the interface by local doping. Such approaches, however, offer a very limited level of control.

In this work, we demonstrate that it is possible to separate the contributions of ad-hoc interfacial dipoles from a designed oriented dipole in order to finely tune energy alignment at the interface between a chromophore and a wide band gap oxide. The approach employs a chromophore-bridge-anchor molecular architecture where the three components are electronically decoupled. By introducing electron donor (D) and acceptor (A) groups to the bridge, an intramolecular dipole is introduced between the chromophore and the anchor. When a monolayer of such molecules is bonded to a metal oxide surface, the resulting dipole layer establishes a potential difference that shifts the chromophore levels with respect to those of the substrate.

This concept is demonstrated using a chromophore (ZnTPP)-bridge (substituted with an electron donating (NMe₂) and electron withdrawing (NO₂) groups) to create a built-in dipole-anchor (Isophthalic acid) architecture. Shifts of the chromophore's HOMOs on the order of plus or minus 0.1 eV with respect to the ZnO valence band edge have been observed, without altering the photoabsorption properties of the chromophore or the HOMO-LUMO gap. An important strength of this concept is that it provides a general design applicable to a large number of anchoring functional groups, built-in dipole bridges, and redox-active centers.

5:20pm **EN+AS+NS+SS-MoA11 Plasmonic Sensing of Impregnation Kinetics of Dye Sensitized Solar Cells (DSSC)**, *V. Gusak*, Chalmers University of Technology, Sweden, *LP. Heiniger*, Ecole Polytechnique Fédérale de Lausanne, Switzerland, *V. Zhdanov*, Borek Institute of Catalysis, Russian Federation, *M. Graetzel*, Ecole Polytechnique Fédérale de Lausanne, Switzerland, *B.H. Kasemo*, *C. Langhammer*, Chalmers University of Technology, Sweden

Dye sensitized solar cells (DSSCs) represent a low cost and environmentally friendly alternative to conventional Si solar cells. Recent advances (electrolyte and sensitizer) have resulted in a boost of their efficiency up to 13%. In DSSCs, interaction between dye molecules and the TiO₂ electrode influences the device performance. The kinetics of impregnation of mesoporous TiO₂ films with dye molecules is an important step in fabrication and key for potential mass production. Employing localized surface plasmon resonance (LSPR) sensing we explored the dye adsorption and impregnation process for flat TiO₂ films and mesoporous

TiO₂ electrodes (1 - 10 μm thick) of the kind used as photoelectrodes in DSSCs. The flat films provide detailed monolayer adsorption - desorption kinetics that assist interpretation of the data from the complex mesoporous samples. For the latter the dye impregnation kinetics were followed, in real time, by a special version of LSPR sensing, Hidden Interface-Indirect Nanoplasmonic Sensing (HI-INPS) combined with optical absorption spectroscopy. The LSPR/HI-INPS technique employs plasmonic sensor nanoparticles embedded under the flat films or under the mesoporous TiO₂ sample. In the former case this yields submonolayer sensitivity to dye molecule adsorption/desorption. For the mesoporous samples HI-INPS detects when dye molecules reach the "bottom" of the sample. The typical sensing range in this work was < 70 nm, a few percent or less of the mesoporous sample thicknesses. The measurements revealed an initial fast (minutes) and a later slow (>> 1hour) impregnation process (responsible for ca. 70 and 30 %, respectively, of the total uptake). The dye percolation time to the bottom of the 2 - 10 μm thick TiO₂ photoelectrode films, was measured by HI-INPS for the dye Z907 in a mixture of acetonitrile and *tert*-butanol for *different dye concentrations* and for *different thicknesses* of the TiO₂ sample. The total amount of adsorbed dye was simultaneously measured by optical absorption spectroscopy. The experimental data for the fast impregnation process were analyzed, with excellent agreement, by employing a diffusion-front model, combining diffusion and first order Langmuir type adsorption, which allows extracting the effective diffusion coefficient for the system. The latter value is about 15 μm²/s, an order of magnitude or more smaller than that for "free" diffusion of dye molecules in bulk solvents. The data from flat films, in addition to providing adsorption kinetics, also reveals that dye desorption and time dependent re-organization of dye molecules in the dye adlayer are significant processes.

Graphene and Other 2D Materials Focus Topic Room: 104 B - Session GR+EM+NS+SP+TF-MoA

Electronic Properties and Charge Transport in 2D Materials

Moderator: K.I. Bolotin, Vanderbilt University, R.S. Ruoff, The University of Texas at Austin

2:00pm **GR+EM+NS+SP+TF-MoA1 Broken Symmetry Quantum Hall States in Dual Gated ABA and ABC Trilayer Graphene.** *Y.J. Lee, J. Velasco Jr, D. Tran, University of California, Riverside, F. Zhang, University of Pennsylvania, W. Bao, L. Jing, K. Myhro, University of California, Riverside, D. Smirnov, National High Magnetic Field Laboratory, C.N. Lau, University of California, Riverside*

We perform low temperature transport measurements on dual-gated suspended Bernal-stacked(ABA) and Rhombohedral-stacked(ABC) trilayer graphene in the quantum Hall (QH) regime. In ABA Bernal stacking order trilayer, we observe QH plateaus at filling factors $\nu=-8, -2, 2, 6, \text{ and } 10$, in agreement with the full-parameter tight binding calculations. In high magnetic fields, odd integer plateaus are also resolved, indicating almost complete lifting of the 12-fold degeneracy of the lowest Landau levels (LL). Under an out-of-plane electric field E_{\perp} , we observe degeneracy breaking and transitions between QH plateaus. Interestingly, depending on its direction, E_{\perp} selectively breaks the LL degeneracies in the electron-doped or hole-doped regimes. In ABC Rhombohedral stacking order trilayer, we observe QH plateaus at filling factors $\nu=0, 1, 2 \text{ and } 3$ in a high magnetic field.

2:20pm **GR+EM+NS+SP+TF-MoA2 Electrical Properties of Graphene on Non-Conventional Substrates.** *R. Rojas Delgado, F. Cavallo, University of Wisconsin, H. Xing, University of Notre Dame, M.G. Lagally, University of Wisconsin*

The excellent electrical-transport properties of graphene make it an outstanding candidate for electronic-device applications. Therefore continued improvements in these properties are being sought, especially as graphene contacts other materials. Theories have shown that charge carrier mobilities of the order of $10^4 - 10^9 \text{ cm}^2\text{V}^{-1}\text{s}^{-1}$ for carrier densities of $10^{13}\text{-}10^9 \text{ cm}^{-2}$ should be possible on a free-standing sheet. Experiments have demonstrated values $10^5 - 10^7 \text{ cm}^2\text{V}^{-1}\text{s}^{-1}$ at low temperatures (5-50K). Mobilities measured for graphene supported by dielectrics have been much lower ($10^3 - 10^5 \text{ cm}^2\text{V}^{-1}\text{s}^{-1}$), but the range of substrates explored has been quite limited. Here we suggest that semiconductor substrates may make good candidates for substrate-supported graphene-based devices. In particular, Ge appears to maintain a high mobility in graphene transferred and bonded to it. For graphene grown by CVD on Cu transferred to an almost intrinsic Ge(001) substrate with carrier density of $2 \times 10^{13} \text{ cm}^{-2}$ and resistivity of $55\Omega\text{-cm}$, we measure a mobility of $2 \times 10^6 \text{ cm}^2 \text{V}^{-1}\text{s}^{-1}$ at 20K and $2 \times 10^5 \text{ cm}^2 \text{V}^{-1}\text{s}^{-1}$ at 80K which is 1000 times higher than what we expect

from bulk Ge(001). We discuss these results in terms of possible charge transfer at the graphene/Ge(001) interface. Research supported by DOE.

2:40pm **GR+EM+NS+SP+TF-MoA3 Electronic Dispersion in Two Overlapping Graphene Sheets: Impacts of Long-Range Atomic Ordering, Periodic Potentials, and Disorder.** *T. Ohta, Sandia National Laboratories*

INVITED

A worldwide effort is underway to build devices that take advantage of the remarkable electronic properties of graphene and other two-dimensional crystals. An outstanding question is how stacking two or a few such crystals affects their joint electronic behavior. This talk concerns "twisted bilayer graphene (TBG)," that is, two graphene layers azimuthally misoriented. Applying angle-resolved photoemission spectroscopy and density functional theory, we have found van Hove singularities (vHs) and associated mini-gaps in the TBG electronic spectrum, which represent unambiguous proof that the layers interact. Of particular interest is that the measured and calculated electronic dispersions reflect the periodicity of the moiré superlattice formed by the twist. Thus, there are vHs not just where the Dirac cones of the two layers overlap, but also at the boundaries of the moiré superlattice Brillouin zone. Such changes in the electronic dispersion also manifest themselves in TBG's optical properties. The result is that the material's color varies depending on the twist angle, and can be seen under optical microscope. Moirés, ubiquitous in hybrid solids based on two-dimensional crystals, accordingly present themselves as tools for manipulating the electronic behavior.

This work is carried out in collaboration with J. T. Robinson, S. W. Schmucker, J. P. Long, J. C. Culbertson, A. L. Friedman at Naval Research Laboratory, P. J. Feibelman, T. E. Beechem, B. Diaconescu, G. L. Kellogg at Sandia National Laboratories, and A. Bostwick, E. Rotenberg at Lawrence Berkeley National Laboratory. Sandia National Laboratories is a multi-program laboratory managed and operated by Sandia Corporation, a wholly owned subsidiary of Lockheed Martin Corporation, for the U.S. Department of Energy's National Nuclear Security Administration under contract DE-AC04-94AL85000.

3:40pm **GR+EM+NS+SP+TF-MoA6 Modification of Density of States in Fluorinated Epitaxial Graphene with Electric Bias.** *K. McAllister, H.B.M. Shashikala, Clark Atlanta University, S.D. Sherpa, Georgia Institute of Technology, M.D. Williams, Clark Atlanta University*

Ultraviolet photoemission spectroscopy measurements of fluorinated epitaxial graphene on the carbon face of silicon carbide show that there are changes in the electron density of states in the valence band near the Fermi level with applied electrical bias. The strong modification of density of states may be due to doping or piezoelectric effects. The experimentally observed changes in the electronic structure are compared to analysis using first principles density-functional theory including interlayer Van der Waals interactions. The results indicate that the p-doping inherent with the fluorination strongly effects the changes in the electronic band structure near the valence band maximum of the joint density of states region.

4:00pm **GR+EM+NS+SP+TF-MoA7 Low-Frequency Current Fluctuations in Graphene and 2D Van-der-Waals Materials.** *A.A. Balandin, University of California, Riverside, S. Rumyantsev, Ioffe Institute, Russian Academy of Sciences, M. Shur, Rensselaer Polytechnic Institute*

Low-frequency current fluctuations with the spectral density $S(f) \sim 1/f$ (f is the frequency) is a ubiquitous phenomenon observed in a wide variety of electronic materials and devices. Low-frequency $1/f$ noise limits the sensitivity of sensors and makes the main contribution to the phase-noise of communication systems via its up-conversion. For this reason, practical applications of every new material system require a thorough investigation of specific features of the low-frequency noise in this material and developing methods for its reduction. It has already been demonstrated that the low-frequency current fluctuations in graphene [1-3] and thin films of van der Waals materials [4] reveal unusual gate bias dependence, which cannot be described with conventional Hooge parameter or McWhorter model. In this talk, I will review state-of-the-art in the $1/f$ noise field in graphene and van der Waals materials, and describe possibilities for deeper understanding of $1/f$ noise offered by availability of continuous atomically thin films. A long-standing question of importance for electronics is whether $1/f$ noise is generated on the surface of conductors or inside their volumes. Using graphene multilayers we were able to directly address this fundamental problem of the noise origin. Unlike the thickness of metal or semiconductor films, the thickness of graphene multilayers can be continuously and uniformly varied all the way down to a single atomic layer of graphene – the actual surface. We found that $1/f$ noise becomes dominated by the volume noise when the thickness exceeds ~ 7 atomic layers ($\sim 2.5 \text{ nm}$). The $1/f$ noise is the surface phenomenon below this thickness [5]. We investigated experimentally the effect of the electron-

beam irradiation on the level of the low-frequency $1/f$ noise in graphene devices. It was found unexpectedly that $1/f$ noise in graphene reduces with increasing concentration of defects induced by irradiation [6]. The bombardment of graphene devices with 20-keV electrons reduced the noise spectral density by an order-of magnitude at the radiation dose of 10^4 mC/cm². The noise reduction can be explained within the mobility fluctuation mechanism. The obtained results are important for the proposed applications of graphene and van der Waals materials in sensors and communications.

[1] G. Liu, et al., Appl. Phys. Lett., 95, 033103 (2009); [2] S. Rumyantsev, et al., J. Phys.: Cond. Matter, 22, 395302 (2010); [3] G. Liu, et al., Appl. Phys. Lett., 100, 033103 (2012); [4] M.Z. Hossain, et al., ACS Nano, 5, 2657 (2011); [5] G. Liu, et al., Appl. Phys. Lett., 102, 093111 (2013); [6] M. Z. Hossain, et al. Appl. Phys. Lett., 102, 153512 (2013).

4:20pm **GR+EM+NS+SP+TF-MoA8 Peter Mark Memorial Award Lecture - Opportunities Offered by a Graphene Line Defect, D. Gunlycke***, Naval Research Laboratory **INVITED**

The symmetry of the extended 5-5-8 line defect discovered in graphene in 2010 provides many interesting properties that could potentially be exploited in graphene-based electronic applications. Intrinsically, this line defect is approximately semitransparent, meaning that about 50% of carriers transmit through the line defect with the remaining 50% being subject to specular reflection. Another feature is that the transmission probability depends strongly on the valley of the incident carriers, making the line defect a valley filter, an essential component for valley-based electronics. Numerical simulations suggest that the line defect might offer ferromagnetically aligned local moments, which could also have implications for spin-based devices.

The properties of the line defect could be dramatically altered through chemical decoration. By turning sp² bonds into sp³ bonds, the transmission probability is significantly reduced. Structures with two such line defects in a parallel configuration therefore exhibit confined graphene states, closely related to the states in zigzag nanoribbons. Unlike the nanoribbons, the railroad track structure formed by two parallel line defects allows carrier transport not only along the structure but also across it. The latter transverse transport occurs within resonance bands that closely trace the dispersion of the bands within the confinement. Owing to a dimensional crossover, the resonance bands must terminate, which leaves behind a transport gap. This transport gap could be used in lateral graphene-based resonant tunneling transistors.

This work was supported by the Office of Naval Research, directly and through the Naval Research Laboratory.

5:00pm **GR+EM+NS+SP+TF-MoA10 Electronic and Optical Excitations in Graphene and Related 2D Systems: Symmetry and Many-body Effects, S.G. Louie**, University of California, Berkeley and Lawrence Berkeley National Laboratory **INVITED**

In this talk, we discuss results from some recent theoretical studies on the electronic and optical properties of graphene, monolayer MoS₂, and surface states of topological insulators. Owing to their reduced dimensionality and unique electronic structure, these systems present opportunities for study of unusual manifestation of concepts/phenomena that may not be so prominent or have not been seen in bulk materials. Many-body effects and symmetry play a critical role in shaping both qualitatively and quantitatively their spectroscopic properties. Several phenomena will be discussed: 1) Excitonic effects in the optical spectra of graphene, in the form of a strong resonant (hyperbolic) exciton, and how they are altered by carrier doping and quasiparticle lifetime are predicted. 2) The physical origin of the intriguing satellite structures seen in angle-resolved photoemission spectra of graphene is explained. 3) The optical response of monolayer MoS₂ is shown to be very rich in features and is dictated by excitonic states with huge binding energies of ~1 eV. 4) For topological insulators, we show that the spin orientation of photoelectrons from the topologically protected surface states in general can be very different from that of the initial states and is controlled by the photon polarization.

This work is supported in part by the National Science Foundation, U.S. Department of Energy, and the Office of Naval Research.

Ions at Aqueous Interfaces Focus Topic **Room: 203 A - Session IA+AI+BI+IS+NL+SS-MoA**

Ions at Aqueous Interfaces

Moderator: M.H. Grunze, University of Heidelberg, Germany

2:00pm **IA+AI+BI+IS+NL+SS-MoA1 Sum-frequency Vibrational Spectroscopy for Studies of Ions Emerging at Water Interfaces, Y.R. Shen**, University of California, Berkeley **INVITED**

Ions at water interfaces can significantly change the chemical and physical properties, and hence the functionality, of the interfaces. They play a key role in many important processes in many disciplines. In recent years, sum-frequency vibrational spectroscopy (SFVS) has been demonstrated to be a unique, effective tool to study such interfaces. We discuss here SFVS investigations of ions at various water interfaces: soluble ions at air/water interfaces, ions attached to Langmuir monolayers on water, and hydrophilic and hydrophobic water interfaces. Formation of an electric double charge layer by ions near an interface usually occurs. It induces significant polar reorientation of interfacial water molecules and alters their vibrational spectra that can be detected by SFVS. Useful structural information can be deduced from the results, but work is still needed for complete understanding of the results.

2:40pm **IA+AI+BI+IS+NL+SS-MoA3 Experimental Quantification of Surface Propensity of Halide Ions by Femtosecond Surface Vibrational Spectroscopy, M. Bonn**, Max Planck Institute for Polymer Research, Germany, *H.J. Bakker*, FOM Institute AMOLF, Netherlands, *Z. Zhang, E.H.G. Backus*, Max Planck Institute for Polymer Research, Germany, *L. Piatkowski*, FOM Institute AMOLF, Netherlands **INVITED**

We investigate the vibrational dynamics and energy transfer between interfacial water molecules, in the presence of sodium chloride and sodium iodide salts, using 2-dimensional, femtosecond surface-specific vibrational spectroscopy. We find that both the vibrational lifetime and the intramolecular energy transfer for anion associated interfacial water molecules is slower than for non ion-bound interfacial water molecules. The analysis of the time-dependent slope of the 2-dimensional sum frequency response reveals that the intermolecular resonant energy transfer between the interfacial water molecules is significantly slowed down by the presence of ions. Accordingly, the decay of the frequency-frequency correlation function is slower for NaI than for NaCl solution. This finding provides direct evidence of the higher surface propensity for iodide than for chloride ion, and allows for the quantification of interfacial density of halide ions for both systems.

3:40pm **IA+AI+BI+IS+NL+SS-MoA6 Specific Ion Effects on Acid-Base Equilibria at the Planar Silica/Water Interface, J.M. Gibbs-Davis**, University of Alberta, Canada

The interaction of ions with biological and environmental interfaces depends not only on their valency but also their identity. These specific ion interactions can influence other processes like deprotonation at mineral oxide interfaces. To monitor such interactions we utilized surface specific second harmonic generation (SHG) to report on changes in the surface charge density of silica in real time. We observe that the intrinsic equilibrium constant of the silanol groups is sensitive to the identity of the alkali ion. In contrast, varying the identity of the anion does not affect the intrinsic acidity of the sites but rather their mechanism of deprotonation. Specifically, positive cooperativity is observed in the deprotonation of silanol groups with increasing anion size and polarizability. These results and complementary measurements of the water structure using sum frequency generation spectroscopy will be discussed.

4:00pm **IA+AI+BI+IS+NL+SS-MoA7 Molecular Insight Into the Preferential Adsorption of Monovalent Ions to Selected Polar Surfaces: A Vibrational Sum Frequency Study, E.C. Tyrode, R. Corkery**, KTH Royal Institute of Technology, Sweden

Vibrational Sum Frequency Spectroscopy (VSFS) has been used to systematically study the preferential adsorption of a series of monovalent ions to charged and uncharged fatty acid monolayers. Ion enrichment is mainly determined indirectly by targeting surface water vibrational modes. In selected cases however, the ion presence is also directly determined by targeting the fatty acid carboxylate headgroups. A major effort is made to understand the effect of co-ions in the molecular properties of these biophysically relevant interfaces.

* Peter Mark Memorial Award Winner

4:20pm **IA+AI+BI+IS+NL+SS-MoA8 Dielectric Interfacial Effects, R. Netz**, FU Berlin, Germany **INVITED**

The molecular layer of water molecules on surfaces, the so-called hydration layer, is important for a whole number of properties of biological as well as technological surfaces. Insight can be gained from all-atomistic simulations in conjunction with appropriate continuum modeling.

- Dielectric properties of interfacial water layers are important for the design of high-power capacitors, and can be resolved using simulations.

- At the same time, ions accumulate into a highly condensed interfacial layer, leading to the well-known saturation of the electro-osmotic mobility at large surface charge density regardless of the hydrodynamic boundary conditions. The experimentally well-established apparent excess surface conductivity follows for all hydrodynamic boundary conditions without additional assumptions.

- Hydration water at biological membranes absorbs electromagnetic radiation specifically in the 0.1-10 GHz range that is used for radio communication. Possible health issues are discussed.

5:00pm **IA+AI+BI+IS+NL+SS-MoA10 Liquid Jet -XPS Studies of Ions and Nitriles at the Aqueous Interface, K.A. Perrine, M.H.C. Van Spyk, A.M. Margarella**, University of California, Irvine, *H. Bluhm*, Lawrence Berkeley National Laboratory, *B. Winter*, Helmholtz-Zentrum Berlin für Materialien und Energie/Elektronenspeicherung BESSY II, Germany, *M. Faubel*, Max Planck Institute for Dynamik und Selbstorganisation, Germany, *J.C. Hemminger*, University of California, Irvine

Acetonitrile in water is known to exhibit non-ideal behavior. At low concentrations, acetonitrile molecules migrate towards the solution interface leaving water mostly in the bulk. At 0.2 mole fraction, the surface saturates with a full monolayer. Above 0.2 mf, the acetonitrile signal at the surface is enhanced relative to that of the bulk with increasing solution concentration. In the bulk, acetonitrile and water form clusters between 0.2 and 0.7 mole fraction and interact with each other through dipole interactions. Propionitrile, another nitrile with a lower solubility, is also shown have a propensity for the surface of aqueous solutions.

Ions have been shown to impact the properties and solvation structure of aqueous solutions, both at the surface and in the bulk of solution. Potassium iodide (KI) was added to acetonitrile and propionitrile aqueous solutions to observe the effects of ions on nitrile distributions. Liquid jet-X-ray photoelectron spectroscopy (LJ-XPS) was used to characterize the elemental compositions of ions and nitrile species. By tuning the incident photon energy, different depths of the solutions is observed; at low kinetic energies the solution surface is probed and the high kinetic energies the bulk of solution is probed. After adding KI, the interfacial photoelectron spectroscopy signal reveals a reduction in nitrogen and carbon signals in acetonitrile, demonstrating the salting-in effect. With addition of ions to aqueous propionitrile solutions, nitrogen and carbon signals are increased, suggesting a salting-out effect. Sodium chloride ions are also added to aqueous propionitrile studies to determine differences between ions effects from the KI and NaCl salts on propionitrile solutions. These studies help elucidate the role ions play at the interface of aqueous organic solutions.

5:20pm **IA+AI+BI+IS+NL+SS-MoA11 Study of the Structural and Adhesion Forces in Highly Concentrated Electrolytes using Atomic Force Microscopy (AFM), T. Baimpos, M. Valtiner**, Max Planck Institut für Eisenforschung GmbH, Germany

The understanding of the surface interaction in electrolyte solutions is of paramount importance in many fields such as biology, electrochemistry and surface chemistry. Aqueous solutions of high concentrations are mainly interesting from practical point of view (batteries). In principle, AFM through the Force versus Distance curves (F-D) can be successfully used to probe the electrolyte layering at solid-liquid interfaces and investigate the nature of hydration forces in the presence of various electrolytes of different ion valency, ion concentration or pH [1].

In the current work AFM has been used to measure hydration forces between a non-coated Silicon colloid probe and atomically smooth, flat freshly cleaved Mica surfaces, in highly concentrated monovalent electrolytes (LiCl, NaCl, CsCl). The effect of i) the cation hydration diameter ($\text{Li}^+ > \text{Na}^+ > \text{Cs}^+$) and ii) the electrolyte's concentration (0.05-3.0 M), on both the structural (F_{STR}) and adhesion (F_{ADH}) forces are studied. In all environments, F_{ADH} values pass through a minimum as a function of electrolyte's concentration, while for each salt solution, the frequency of structural events is calculated as a function of its concentration. The number of the F-D curves, were classified in appropriate tables according to the number of the structural hydration layers observed. Furthermore, depending on the concentration, 1, 2 or even up to 5 consecutive hydration layers can be clearly distinguished in the same F-D curve from which both the force and the range of each layer can be measured. These results are compared

with the hydrated radii of the above ions enabling the extrusion of useful statements concerning the re-arrangement of the structured cation/water layer at the liquid/solid interface.

Magnetic Interfaces and Nanostructures Room: 202 A - Session MI+EM+MG-MoA

Frontiers of Complex Oxides

Moderator: G.J. Szulczewski, The University of Alabama,
Z. Gai, Oak Ridge National Laboratory

2:00pm **MI+EM+MG-MoA1 Deposition of AgFeO₂ Thin Films with the Delafossite Structure by Combinatorial Sputtering, F. Mao, T. Nyberg, T. Thersleff, U. Jansson**, Uppsala University, Sweden

Delafossites AMO_2 (A= Cu, Ag, Pd, Pt; M=Fe, Co, Ni, Cr, Al, Mn, etc) have received considerable attention due to their potential applications as transparent conducting oxides, photocatalysts, luminescent materials, batteries and thermoelectric materials. Recently, high temperature superconductivity was also suggested for doped members of this type of oxide compounds. Many of the interesting properties of delafossites are related to the crystal structure where linear O-A-O bonds connect layers of slightly distorted edge-sharing MO_6 octahedra. Consequently, the delafossites can be described as natural nanolaminates of MO_2 layers separated by A atoms.

Copper-based delafossite materials have been studied intensely through synthesis of solid-state reaction, hydrothermal synthesis method, sol-gel methods and, in a few cases, reactive sputtering with high temperature post-annealing ($\geq 700^\circ\text{C}$). To our knowledge, however, no studies have previously been published on silver-based delafossite films deposited directly by sputtering. The main challenge is that the silver based delafossites tend to decompose at high temperature ($>400^\circ\text{C}$). Furthermore, the synthesis of Ag-based delafossites by reactive sputtering is usually restricted to small window of stoichiometric composition and also the sputtering condition.

The combinatorial materials science enables rapid discovery and optimization of new or known materials for creating "library" of composition-structure-property relationship. Compared with the "one-at-a-time" sputtering, the combinatorial sputtering with large composition gradient is powerful tool for time-saving and economical development of silver-based delafossite films.

In this work, we demonstrate the combinatorial deposition of delafossite AgFeO_2 thin films using co-sputtering of silver and iron targets in a reactive Ar-O₂ mixture atmosphere. Rapid screenings of XRD, XPS, XRF were employed to determine the chemical composition and phase structure. The most interesting parts of the materials were studied by TEM. Optical and electrical properties have also been investigated. Our results show that the AgFeO_2 films have been successfully deposited by the combinatorial reactive sputtering without post-annealing but the process window is very narrow and strongly dependent on deposition temperature, sputtering power ratio, pulse frequency, O₂ flow rate, working pressure, etc. The XRD and TEM showed that the AgFeO_2 films grew epitaxially with the direction of (001) in the optimal sputtering condition.

2:20pm **MI+EM+MG-MoA2 MBE Growth and Properties of SrCrO₃ Thin Films, Y. Du, H. Zhang, R.J. Colby, V. Shutthanandan, S.A. Chambers**, Pacific Northwest National Laboratory

Complex oxides with the perovskite structure exhibit a range of interesting electronic, magnetic, and optical properties. Material synthesis of those structures in thin-film form is of fundamental importance to realize their full potential. SrCrO_3 was first reported to be a paramagnetic metallic oxide with a cubic structure, but the property measurements thereafter have been controversial. Almost all SrCrO_3 structures have been synthesized through higher pressure and high temperature conditions and no epitaxial thin-film form has been reported to our knowledge. In this talk, we will present on the growth of epitaxial, near-stoichiometric SrCrO_3 films on $\text{LaAlO}_3(001)$ substrates by molecular beam epitaxy using O₂ as the oxidant. Coherently strained films are shown to grow in a layer-by-layer fashion. The cation stoichiometry was determined by XPS and RBS. *In-situ* XPS Cr 2p core-level spectra show that majority of the Cr cations in SrCrO_3 films are in the 4+ oxidation state, although there is a small amount of Cr^{3+} and higher oxidation states, which could be a result of charge disproportionation. The films are appreciable oxygen deficient, as judged by XPS, RBS, and STEM. The structure and properties of SrCrO_3 films will be compared to that of LaCrO_3 films grown with similar conditions in the same chamber.

2:40pm **MI+EM+MG-MoA3 Oxygen Stoichiometry and Topotactic Phase Reversal in SrCoO_x Epitaxial Films**, *H.N. Lee*, Oak Ridge National Laboratory **INVITED**

Strontium cobaltites (SrCoO_x) exhibit a wide spectrum of magnetic and electronic phases, ranging from antiferromagnetic insulator to ferromagnetic metal, depending on the oxygen stoichiometry (*x*). The Co valence state change due to the modification of *x* in SCO mainly governs the physical properties. In particular, the redox reactions and subsequent changes in the physical properties are essential ingredient in applications such as solid oxide fuel cells, gas sensors, and many other devices that exploit the redox reactions. In this work, we examined the topotactic transformation between two structurally distinct perovskite (SrCoO_{3-δ}) and brownmillerite (SrCoO_{2.5}) phases. Temperature dependent, ambient controlled real-time x-ray diffraction and ellipsometry conspicuously showed that the topotactic phase transitions accompany a rapid, drastic change in the crystallographic and electronic structures. Interestingly, the topotactic phases were found to be reversible through oxygen (de)intercalation at greatly reduced temperatures. Therefore, we envision that the phase stability of strontium cobaltites may lead to discovery of new oxygen membranes and cathode materials for high performance energy storage.

*The work was supported by the U.S. Department of Energy, Basic Energy Sciences, Materials Sciences and Engineering Division.

3:40pm **MI+EM+MG-MoA6 Medard W. Welch Award Lecture - Complex Oxide Interfaces: Conquering the (Polar) Catastrophe**, *C.G. Van de Walle**, University of California, Santa Barbara **INVITED**

The formation of a two-dimensional electron gas (2DEG) at the interface between two insulators, SrTiO₃ (STO) and LaAlO₃ (LAO), has sparked huge interest in oxide electronics. In spite of almost a decade of research, the mechanisms that determine the density of this 2DEG have remained controversial. The electronic behavior of these polar/nonpolar interfaces is often modeled using electrostatics based on an ionic representation of the solids. This leads to a “polar catastrophe” in which the potential in the overlayer diverges—similar to the case of (001) interfaces between heterovalent semiconductors (e.g., Ge/GaAs) that were studied 35 years ago [1].

In fact, if the electrons resulting from the polar discontinuity can be confined at the interface, the “catastrophe” can be entirely avoided, and a 2DEG with an electron density of $3.3 \times 10^{14} \text{ cm}^{-2}$ (0.5 electrons per unit cell) can be generated. However, experimentally observed densities at the STO/LAO interface are more than an order of magnitude lower.

We have used a combination of first-principles calculations and Schrödinger-Poisson simulations to investigate this problem [2]. The termination of the wider-band-gap overlayer is key: surface states that act as a sink for electrons limit the 2DEG density. I will discuss the effects of LAO surface reconstructions, including hydrogenation. These results apply to oxide interfaces in general, and explain why the SrTiO₃/GdTiO₃(GTO) interface has been found to exhibit the full density of 0.5 electrons per unit cell [3].

An interesting question can be raised now: why is it that oxide interface can sustain this huge 2DEG density, while semiconductor interfaces are commonly accepted to undergo atomic reconstructions to eliminate the polar catastrophe? I will suggest that the insights gained from oxide interfaces may be used to design semiconductor interfaces that could sustain similar 2DEGs.

Work performed in collaboration with L. Bjaalie, L. Gordon, K. Krishnaswamy, and A. Janotti, and supported by the ARO, ONR, and NSF.

[1] W. A. Harrison, E. A. Kraut, J. R. Waldrop, and R. W. Grant, *Phys. Rev. B* **18**, 4402 (1978).

[2] A. Janotti, L. Bjaalie, L. Gordon, and C. G. Van de Walle, *Phys. Rev. B* **86**, 241108(R) (2012).

[3] P. Moetakef, T. A. Cain, D. G. Ouellette, J. Y. Zhang, D. O. Klenov, A. Janotti, C. G. Van de Walle, S. Rajan, S. J. Allen, and S. Stemmer, *Appl. Phys. Lett.* **99**, 232116 (2011).

4:20pm **MI+EM+MG-MoA8 Magnetic Reconstructions in Ultrathin Oxide Heterostructures**, *H. Hwang*, Stanford University **INVITED**

Complex oxides are fascinating systems which host a vast array of unique phenomena, such as high temperature (and unconventional) superconductivity, ‘colossal’ magnetoresistance, all forms of magnetism and ferroelectricity, as well as (quantum) phase transitions and couplings between these states. In recent years, there has been a mini-revolution in the ability to grow thin film heterostructures of these materials with atomic precision. With this level of control, the boundary conditions at oxide surfaces and interfaces have been used to form new electronic phases. Here

we focus on the magnetic reconstructions found in perovskites heterostructures, particularly for manganite thin films and rectifying junctions. In the later case, a direct correlation is found between the junction properties and the reconstructions at the interface.

5:00pm **MI+EM+MG-MoA10 A New Tool to Manipulate the Transition Metal Crystal Field: Creating Local Dipoles via Cation Ordering**, *B. Nelson-Cheeseman*, University of St. Thomas, *H. Zhou, J. Hoffman*, Argonne National Laboratory, *P. Balchandran, A. Cammarata, J.M. Rondinelli*, Drexel University, *A. Bhattacharya*, Argonne National Laboratory

In complex oxides, the intriguing electronic, magnetic and orbital properties often result from how the oxygen anions surround the transition metal cation. Altering this bonding geometry, and thus the transition metal crystal field, can stabilize new and exciting ground states. Here, we present a novel method to tune the positions of the oxygen anions—and, thus, the crystal field—by creating polar interfaces *within* a single thin film material. By using the atomic monolayer control of molecular beam epitaxy (MBE), we are able to introduce “artificial” interfaces into a thin film of LaSrNiO₄—a material in which the La and Sr dopant cations are usually randomly arranged over the A-sites. Using MBE, we interleave full layers of SrO (+0) and LaO(+1) in a series of chemically equivalent LaSrNiO₄ films, varying the pattern of SrO and LaO layers relative to the NiO₂ layers. This technique allows us, in one material, to capitalize on the polar interface phenomena found in more traditional multi-component systems (e.g. LAO/STO). Through synchrotron surface x-ray diffraction and Coherent Bragg Rod Analysis (COBRA) performed at the Advanced Photon Source, we directly investigate the La and Sr cation order and the resulting atomic displacements throughout the film thickness for each ordering pattern. We correlate these results with theoretical calculations and transport measurements of the layered nickelate films. For a particular interface pattern, we find that the nickel-oxygen bond lengths change by as much as 10% compared to the random alloy control films. The ability to modify the bond lengths by such a significant amount, while still maintaining the overall chemical equivalency of the material, could have broad implications for re-envisioning the electronic, magnetic and orbital properties of well-known oxide materials.

5:20pm **MI+EM+MG-MoA11 Hybridized L1' Ordered Phase Induced by Strain in Epitaxial Fe_{38.5}Pd_{61.5} Thin Films**, *M.A. Steiner, R.B. Comes, J.A. Floro, W.A. Soffa, J.M. Fitz-Gerald*, University of Virginia

Thin films of 3d-4d/5d magnetic alloys such as Fe-Pt, Co-Pt, and Fe-Pd are of technological interest due to their ordered L1₀ tetragonal intermetallic phase which exhibits a high magnetocrystalline anisotropy of $K \sim 10^7$ to 10^8 ergs/cm³, comparable to that of 3d-4f rare earth magnets. Strong hard-magnet properties, combined with the ductility and chemical inertness from their ennobled metallic nature, make these alloys ideal for applications in ultra-high-density magnetic storage or micro-electro-mechanical systems where the thermally induced KV/k_BT superparamagnetic limit is an important constraint. The Co-Pt system has been shown to decompose under bulk conditions into a novel, strain-induced chessboard microstructure at the eutectoid composition between its ordered L1₀ and L1₂ intermetallic phases, and related 3d-4d/5d material systems may also be expected to produce strain-induced microstructural behavior. Within this class of materials, Fe-Pd alloys possess comparatively moderate magnetocrystalline anisotropies relative to Co-Pt and Fe-Pt. The Fe-Pd phase diagram, however, exhibits a considerably lower order-disorder transition temperature range that renders the material well-suited for nanostructured magnetic applications by enabling lower processing temperatures.

Epitaxial films of Fe_{38.5}Pd_{61.5} at the L1₀-L1₂ eutectoid composition have been grown on MgO (001) oriented substrates by pulsed laser deposition. It is found that ordered thin films of Fe_{38.5}Pd_{61.5} are deposited as a single phase, initially surmised to be L1₂ due magnetic data and the location and orientation of the X-Ray Diffraction (XRD) peaks. Careful analysis of peak intensities, however, results in an anomalously large long-range ordering parameter. Quantitative XRD analysis of the films shows that this is due to a perturbation in the Pd-site occupancy of the non-stoichiometric Fe atoms in the films; resulting in a hybridization of the L1₀ and L1₂ ordered structures. This L1' hybridized ordered structure, first postulated by thermodynamic principles to exist for the Au-Cu system[†], is believed to be induced by the accommodation of epitaxial strain from the substrate. In addition to its verification, the thermodynamic behavior of this new strain-induced phase is addressed in relation to the equilibrium phase diagram.

[†] W. Shockley, *J. Chem. Phys.* **6**, 130 (1938)

* **Medard W. Welch Award Winner**

Optomechanics, Photonics, and Quantum Nanosystems

Moderator: S.L. Burkett, The University of Alabama

2:00pm MN+NS-MoA1 **Silicon Integrated Optoelectronics**, *M. Hochberg, W. Baehr-Jones*, University of Delaware **INVITED**

CMOS-compatible silicon is not an obvious material system for building high-performance optical devices. But, over the last ten years, it has become possible to build fairly complex integrated optical systems at telecommunications wavelengths on electronics-compatible silicon substrates. In fact the complexity of these systems has been approximately doubling every year, and this trend is projected to continue for at least the next several years. With a combination of CMOS electronics and photonics, we can gain control of both photons and electrons, while preserving the powerful economics of the VLSI revolution. The focus of this talk will be on the OPSIS project, which is a new initiative led out of UW aimed at creating an open infrastructure for building fully integrated optoelectronic devices in silicon, and on some of the new science and engineering that are enabled by these devices.

2:40pm MN+NS-MoA3 **Multiplexed Nanomechanical Devices with Single Wavelength Nanophotonic Actuation and Detection**, *V.T.K. Sauer, Z. Diao, M.R. Freeman, W.K. Hiebert*, University of Alberta and The National Institute for Nanotechnology, Canada

Nano-optomechanical system (NOMS) devices offer great opportunity for use in on-chip inertial based mass sensing. They have demonstrated large displacement sensitivity, and their large operational bandwidth allows for very high frequency measurements. These properties are conducive to the transduction of very small nanomechanical resonator motion, and smaller nanomechanical resonators allow for smaller detectable masses. The ultimate goal is to create on-chip sensors that are as sensitive as time-of-flight mass spectrometers. Integrated NOMS systems see a nanomechanical structure modulate the optical properties of a nanophotonic device. This is detected with very high sensitivity by a single probe beam travelling along an integrated nanophotonic waveguide. Optical systems are advantageous in detecting multiplexed arrays of devices due to the reduced complexity of integration. Unlike electrical devices, multiple devices can be probed using a single input and output. This is done by designing the devices to respond to different wavelengths through isolated optical cavities. As a result, multiple signals can be sent along the same waveguide at different wavelength channels to reduce the overall complexity of the design. Here, a multiplexed system is investigated where cantilever and doubly clamped beam nanomechanical resonators are detected using racetrack resonator optical cavities. These devices can also be optically pumped using a modulated laser power in the waveguide which modulates the optical gradient force present on the nanomechanical beam. This is usually done at a wavelength different to the probe laser so the pump signal can be filtered prior to the photo detector. This dual laser pump/probe system can be simplified further using a single beam to act simultaneously as both the pump and probe. Here, the probe laser itself is modulated in power to pump the mechanical motion of the beam. This acts as a homodyne system where the modulated probe power is mixed with the signal created by the nanomechanical beam's motion. This would further simplify implementation of a multiplexed nanomechanical resonator system due to reducing the number of input signals. This homodyne signal is implemented in a phase locked loop using a lock-in amplifier, and the frequency stability is tracked to estimate the mass sensitivity of a single beam driven and detected device.

3:00pm MN+NS-MoA4 **Photonic Readout of Higher Flexural Modes of Nanomechanical Doubly Clamped Beams**, *Z. Diao, V.T.K. Sauer, J.E. Losby*, National Institute for Nanotechnology and University of Alberta, Canada, *M.R. Freeman*, University of Alberta and The National Institute for Nanotechnology, Canada, *W.K. Hiebert*, National Institute for Nanotechnology and University of Alberta, Canada

In the past few years nanophotonic transduction, in which a nanomechanical resonator is coupled to a high finesse optical cavity and its displacement is monitored through the cavity near-field has been demonstrated as a highly flexible, ultra-sensitive, wide bandwidth scheme for nanomechanical resonator displacement readout. A common design of the so-called nano-optomechanical devices (NOMS) involves either releasing a part of a nanophotonic waveguide in a race-track optical cavity, so the evanescent field of the guided mode is coupling to the remaining substrate [1], or laterally coupling a doubly clamped mechanical beam to an optical cavity [2]. In both cases, only the fundamental flexural mode is usually investigated [3].

The quest for large bandwidth mass sensors draws attention to higher flexural modes of nanomechanical resonators. Compared to the fundamental flexural mode, higher modes of a mechanical beam offer much higher operating bandwidth while incurring only a modest (or no) increase in its effective mass, depending on the boundary conditions. Higher modes of nanomechanical devices are also of interest for realizing cavity-optomechanics in the resolved-sideband limit [4], and nonlinear modal coupling among different mechanical modes has recently attracted renewed attention [5]. Hence, there is a demand to fully understand the behaviour of higher flexural modes in NOMS devices.

In this work, we fabricate NOMS devices by releasing parts of a nanophotonic waveguide in a race-track optical cavity. Sensitive photonic transduction allows thermomechanical noise of odd flexural modes (up to 50 MHz limited by our measurement electronics) to be observed. However, the transduction responsivity diminishes for even modes, due to the geometrical symmetry of the device design. We show that breaking this symmetry can increase the transduction responsivity for even flexural modes. The nanophotonically transduced displacement responsivity for different modes is also compared to that measured using a free-space interferometry setup. We further discuss the internal stress of the devices and its influence on the mode frequency, shape and transduction responsivity.

[1] W. H. P. Pernice *et al.*, *Opt. Express* **17**, 12424 (2009).[2] O. Basarir *et al.*, *Opt. Express* **20**, 4272 (2012).[3] M. Li *et al.*, *Appl. Phys. Lett.* **97**, 183110 (2010).[4] G. Anetsberger *et al.*, *Nature Physics* **5**, 909 (2009).[5] M. H. Matheny *et al.*, *Nano Lett.* **13**, 1622 (2013).3:40pm MN+NS-MoA6 **Progress in Coupling a Superconducting Qubit to Light**, *A.N. Cleland, J. Bochmann*, University of California, Santa Barbara **INVITED**

My group at UC Santa Barbara has been developing a chip-based, fully integrated microwave-to-optical frequency up-converter based on a piezoelectrically-actuated optomechanical crystal. The device is designed to use the 1550 nm telecommunications wavelength band, trapping photons of that wavelength in an optomechanics crystal, then modulating the frequency of these photons through interactions with GHz-frequency phonons, the latter generated using the piezoelectric response of the crystal. We hope to use this device to create optical frequency entangled photons, produced using entangled microwave-frequency phonon states, generated by a superconducting qubit. This will enable the transfer of quantum information from a millikelvin cryostat to a fiber optic transmission line, with the potential of coupling hybrid quantum systems. I will report on our progress in developing this novel device.

4:20pm MN+NS-MoA8 **Silicon Carbide (SiC) Optical Interferometry for Ultrasensitive Motion Transduction of High Frequency Mechanical Resonators**, *Z. Wang, J. Lee, T. He, P. X.-L. Feng*, Case Western Reserve University

We report on the first experimental demonstration of an ultrasensitive laser optical interferometric technology based on thin-film silicon carbide (SiC) micromechanical and nanomechanical resonant systems, which offer motion transduction with displacement sensitivities down to the sub-10fm/rtHz level, at room temperature.

Position and motion detection with advanced optical techniques have been widely used for studying the static and dynamic motions of various systems, ranging from the classical scanning probe microscopes to the emerging resonant nano/micromechanical systems (NEMS/MEMS). In particular, in recent years significant efforts and advances [1,2] have been made in developing laser optical interferometric systems based on various NEMS/MEMS resonators, with constituting materials in Si, SiN, GaAs, AlN, and more recently two-dimensional (2D) crystals such as graphene and MoS₂. These advances have kept enabling very sensitive detection of motions in various NEMS/MEMS resonators, with ever improving displacement sensitivities, from ~nm/rtHz to ~pm/rtHz levels. In many of these systems, there are limitations intrinsic to the device structures and constituting materials. For instance, light absorption and parasitic heating effects can compromise these interferometric systems from achieving better sensitivities.

In this work, we explore new optical interferometric techniques by exploiting some unique properties of SiC thin films, particularly the high transparency and ultralow photon absorption (60 times lower than Si) in the wide visible range, as well as the excellent thermal conductivity. The SiC thin films are prepared by low-pressure chemical vapor deposition (LPCVD) on various substrates, which enables us to develop a novel SiC-on-SiO₂ material platform. The suspended MEMS/NEMS devices fabricated in this thin-film platform all share important features such as smooth surfaces and a uniform interferometric gap. These structural

features, combined with SiC's outstanding physical properties, have permitted us to demonstrate unprecedented displacement sensitivities at ~5-10fm/rtHz levels, better than other MEMS/NEMS-based optical interferometric techniques reported to date. We demonstrate such ultrasensitive techniques for motion detections in high frequency SiC microdisk resonators and nanocantilever resonators. In both systems, we have measured the undriven, intrinsic thermomechanical resonances up to high-order modes.

- [1] W. K. Hiebert, et al., *J. Micromech. Microeng.* **20**, 115038 (2010).
[2] J. Lee, et al., *Proc. IEEE Inter. Freq. Contr. Symp. (IFCS2012)*, DOI: 10.1109/IFCS.2012.6243742.

Manufacturing Science and Technology Room: 202 B - Session MS+AS+EM+NS+PS+TF-MoA

IPF 2013-Manufacturing Challenges for Emerging Technologies: III. Manufacturing Challenges: Electronics

Moderator: D. Seiler, National Institute of Standards and Technology (NIST), J. Hollenhorst, Agilent Technologies

2:00pm MS+AS+EM+NS+PS+TF-MoA1 Graphene Materials and Devices Roadmap, L. Colombo, Texas Instruments INVITED

The advancement of graphene and graphene based products will require a research and development progression similar to materials and development programs are now in full production, e.g. Si industry. The graphene research community has made significant progress over the past nearly a decade now in the physics and chemistry of graphene. We are now full engaged in the materials and device development and in some cases initial product stages. The introduction of any graphene based product will require the identification of materials, device and product metrics in order to properly keep track of the progress toward the product goals. In this presentation I will review and discuss the roadmap for various graphene based applications and present the status of materials and devices for nanoelectronic applications.

2:40pm MS+AS+EM+NS+PS+TF-MoA3 Devices and Materials for the Post CMOS Area - What Are We Looking For?, W. Haensch, IBM T.J. Watson Research Center INVITED

The long predicted end of scaling is coming. Many times it was predicted that the IC industry will hit a brick wall. Beginning in the early 1980's when patterning solutions were doomed to fail, then through the late 1990's when gate oxide scaling was thought to be at its end, and now in the recent years when device performance is thought to hit its physical limits. The truth is however that none of these posed an obstacle that could not be addressed. The reason while the progress of the industry enjoyed in the last several decades is slowing down is related to the ever increased power consumed to achieve ever higher performance. Seeing the end approaching, the quest for what is coming next is on! In this presentation I will give short review how we got where we are and what are the wonderful properties of MOSFET devices that allowed this extraordinary development. I will then look at the possibilities of a possible extension of the existing core logic technology. Finally I will discuss some alternate device options and provide a critical evaluation how they might fit into the IT landscape.

3:40pm MS+AS+EM+NS+PS+TF-MoA6 Manufacturing Challenges of Directed Self-Assembly, R. Gronheid, IMEC, Belgium, P.A. Rincon Delgado, University of Chicago, T.R. Younkin, Intel Corporation, B.T. Chan, L. Van Look, I. Pollentier, IMEC, Belgium, P.F. Nealey, University of Chicago INVITED

Directed Self-Assembly (DSA) of block copolymers (BCP) is based on nano-scale phase separation. Depending on the relative volume fraction of the blocks, different morphological structures may form in the bulk of these materials. In the case of di-block copolymers, specifically the lamellar and cylindrical phase provide structures that may be used to form line/space and hole-type patterns, respectively. When thin films of BCPs are applied on substrates that provide a pre-pattern to guide the assembly process, the orientation and direction of the resulting structures can be controlled. DSA has gained significant attention as a next method for mainstream nanofabrication in a time span of just a few years. The primary interest in the DSA technology includes the inherent variability control (since dimension is controlled through the polymer molecular weight) and the high pattern densities (typical length scales are on the order of 3-50nm) that are accessible. The outstanding questions that need to be answered in order to

prove readiness of DSA for semiconductor manufacturing include defectivity, pattern transfer capabilities, pattern placement accuracy, design rule restrictions that are imposed by DSA and demonstration in an electrically functional device.

At imec, DSA based patterning has been implemented on 300mm wafers in various process flows that are compatible with semi-conductor manufacturing. These flows have been used as test vehicles to study the above-mentioned issues. In this paper, an overview will be given of the main recent accomplishments from the imec DSA program.

4:20pm MS+AS+EM+NS+PS+TF-MoA8 Phase Change Memory, R. Bez, Micron, Italy INVITED

Phase Change Memory (PCM) is a Non-Volatile Memory (NVM) technology that provides a set of features interesting for new applications, combining features of NVM and DRAM. PCM is at the same time a sustaining and a disruptive technology. From application point of view, PCM can be exploited by all the memory systems, especially the ones resulting from the convergence of consumer, computer and communication electronics. PCM technology relies on the ability of chalcogenide alloys, typically Ge₂Sb₂Te₅ (GST), to reversibly switch from amorphous state to poly-crystalline state. The two stable states differs for electrical resistivity, thus the information is stored in the resistance of the bit.

The alteration of the bit is possible thanks to melt-quench of the active material achieved by fast (10-100ns) electrical pulses. The energy delivered to program a bit is in the order of 10pJ, with a state of the art access time of 85ns, read throughput 266MB/s and write throughput 9MB/s. These peculiar features combined with data retention, single bit alterability, execution in place and good cycling performance enables traditional NVM utilizations but also already opened applications in LPDDR filed. Moreover PCM is considered the essential ingredient to push to the market the so called Storage-Class Memory (SCM), a non-volatile solid-state memory technology that is capable of fill the gap between CPU and disks.

In this perspective PCM technology can be effectively exploited in wireless systems, in solid state storage subsystem, in PCIe-attached storage arrays and in computing platform, exploiting the non-volatility to reduce the power consumption.

In order to be able to enter into a well established memory market there are key factors that must be fulfilled: i) match the cost of the existing technology in terms of cell size and process complexity, ii) find application opportunities optimizing the overall "memory system" and iii) provide a good perspective in terms of scalability. Phase Change Memory has been able so far to progress in line with all these requirements. Aim of this presentation is to review the PCM technology status and to discuss specific opportunities for PCM to enter in the broad memory market.

5:00pm MS+AS+EM+NS+PS+TF-MoA10 450 mm Project, P. Farrar, University at Albany-SUNY INVITED

The talk will focus on the leadership role the G450C consortium in driving the industry transition from 300mm to 450mm wafers. The current Status of the work at CNSE will be explored as well as the key role this public private partnership play is developing the process capability Required for High Volume Manufacturing. In addition critical success factors, and the ability to manage in a collaborative manner will be focused on.

Nanometer-scale Science and Technology Room: 203 B - Session NS+AS+EM-MoA

Nanowires and Nanotubes Moderator: C. Mattevi, Imperial College, London

2:00pm NS+AS+EM-MoA1 Fe-doped Titania Nanotubes: Iron Role in Structural Modification, P.M. Hosseinpour, Northeastern University, J. Liu, Northeastern University and Brookhaven National Laboratory, I. McDonald, Northeastern University, D. Arena, Brookhaven National Laboratory, D. Heiman, L. Menon, L.H. Lewis, Northeastern University

Ordered arrays of Fe-doped TiO₂ nanotubes are semiconductors with potential enhanced catalytic properties and have prospective applications in photocatalytic devices, sensors and dye-sensitized solar cells. Unified understanding of the interrelations between the band structure, crystal structure and response in presence of dopants is fundamental for tailoring functionality. In this study, Fe (1.8 at%)-doped TiO₂ nanotubes are synthesized via electrochemical anodization followed by annealing in an oxygen-rich environment at 450 °C to induce crystallization. The morphology, crystal structure and electronic structure of nominally-pure and Fe-doped titania nanotubes are investigated in the as-anodized and annealed states. Regardless of precise composition, scanning electron

micrographs show that the nanotubes are 50 microns in length with 100-nm pore size, arranged in a closed-packed architecture. In the as-anodized state the nanostructures are amorphous; upon annealing in oxygen the anatase structure forms, with a slight expansion (~0.3% increase) in the unit cell volume and larger calculated crystallite size in presence of iron. Near-edge x-ray absorption fine structure spectroscopy (NEXAFS) carried out at the U7A beamline of the National Synchrotron Light Source at Brookhaven National Laboratory clarifies the electronic structure and chemical environment in pure and Fe-doped titania nanotubes. Preliminary results obtained from the oxygen K-edge and the Ti and Fe L-edge data of the nanotube surface confirm formation of the anatase structure upon annealing, with a lower oxidation state of titanium (lower than Ti^{4+}) noted in presence of iron. Furthermore, the surface anatase formation was more significant (higher surface crystallinity) in the pure nanotubes versus the iron-doped nanotubes. Annealing the nanotubes in an oxygen-rich environment changes the oxidation state of iron. Correlations between the surface and bulk characteristics of the pure and Fe-doped titania nanotubes confirm incorporation of the iron into the lattice structure which modifies the electronic structure by changing the bonding and oxidation state of titanium. These results highlight potential pathways towards further optimization of these nanostructures in order to enhance catalytic functionality.

Funding: National Science Foundation (Grants No. DMR-0906608 and DMR-0908767), U.S. Department of Energy, Division of Materials Science, Office of Basic Energy Sciences (Contract No. DE-SC0005250). Use of the National Synchrotron Light Source, Brookhaven National Laboratory, was supported by the U.S. Department of Energy, Office of Basic Energy Sciences (Contract No. DE-AC02-98CH10886).

2:20pm **NS+AS+EM-MoA2 Impact of Crystallinity, Chemical Environment and Electronic Structure of TiO_2 Nanotube Arrays for Photocatalysis**, J. Liu, P.M. Hossainpour, Northeastern University, S. Luo, Brookhaven National Laboratory and SUNY Stony Brook, D. Arena, Brookhaven National Laboratory, L.H. Lewis, Northeastern University

The photocatalytic ability of TiO_2 nanostructures to remove organic pollutants in wastewater has attracted considerable attention [1]. Understanding the influence of crystallinity, chemical environment and electronic structure of TiO_2 nanotubes on the photocatalytic activity is very important in optimizing this functionality. In this work, TiO_2 nanotube arrays with an average tube length of 25 μm were prepared by the electrochemical anodization of Ti foil, followed by thermal treatment in O_2 (oxidizing), Ar (inert), and H_2 (reducing) environments at 350 $^\circ C$ to induce crystallization. The nanotube structure-property correlations were examined with x-ray diffraction (XRD), scanning electron microscopy (SEM) and x-ray absorption spectroscopy (XAS). The photocatalytic properties of the TiO_2 nanotubes (as-anodized and annealed) were evaluated using degradation of methyl orange (a model dye compound of water pollution) in an aqueous solution under UV-visible light irradiation. The Ti $L_{3,2}$ -edge and O K-edge x-ray absorption spectra provide the information concerning the near-surface (~5 nm) local bonding environment and electronic structure of the nanotubes. The XAS results show that while the as-anodized amorphous TiO_2 nanotubes were partially transformed to anatase phase via thermal treatment, variations in crystallinity and surface defects were observed to depend on the type of annealing atmospheres. Characteristics of anatase were more evident in both the Ti $L_{3,2}$ -edge and the O K-edge XAS spectra of TiO_2 nanotubes annealed in O_2 than in those annealed in H_2 and Ar, which indicate relatively higher local order and less local defects in O_2 annealed nanotubes. Nanotubes annealed in H_2 exhibited a higher photodegradation rate of methyl orange than those annealed in Ar and O_2 . These results can be correlated with the different electronic structures that reflect the different degrees of crystallinity and the varied nature of the surface defects (i.e., oxygen vacancies) of TiO_2 nanotubes that result from different processing conditions.

[1] Paramasivam, H. Jha, N. Liu and P. Schmuki, Small (2012), 8, 3073-3013.

Research supported by the National Science Foundation under Grants No. DMR-0906608 and DMR-0908767, and by the U.S. Department of Energy, Division of Materials Science, Office of Basic Energy Sciences under Contract No. DE-SC0005250. Use of the National Synchrotron Light Source, Brookhaven National Laboratory, was supported by the U.S. Department of Energy, Office of Basic Energy Sciences, under Contract No. DE-AC02-98CH10886. This work was also financed by the U.S. Department of Energy, Office of Basic Energy Sciences under Contract DE-AC02-98CH10886.

2:40pm **NS+AS+EM-MoA3 Enhanced Field Emission from Oxygen-deficient TiO_2 Nanotube Arrays**, C.W. Wang, J.-B. Chen, W.-D. Zhu, Northwest Normal University, China

Due to their high aspect ratio, low work function, and excellent controllability of morphology, TiO_2 nanotube arrays (TNAs) are found to be

promising candidate for field emitters. Further improvement on the field emission (FE) properties of TNAs requires more precise control of both the morphology and the electronic structure. Reduction treatment including hydrogenation, nitriding and carbonization to obtain oxygen-deficient TNAs, is known as a facile strategy to modify the morphology and electronic structure of TNAs [1-3]. In this study, TNAs obtained by anodization are treated by various reduction treatments. It is found that the morphology shows no significant change after hydrogenation at the temperature below 550 $^\circ C$. But the electronic structure exhibits large variation, which is critically depended on the treatment temperature. When the temperatures of hydrogenation are 400, 450, 500, and 550 $^\circ C$, the work functions are 3.68, 3.48, 3.03 and 2.20 eV. However, after the treatments of nitriding and carbonization, both the morphology and the electronic structure of TNAs are substantially modified. The nitriding treatment can reconstruct the amorphous TNAs to be nanoworm/nanotube hierarchical structures and implant nitrogen into them, which show lower work function, higher electrical conductivity, and larger field enhancement factor. Correspondingly, after the carbonization treatment, the as-anodized TNAs are successfully transformed to be simetal and a retained tubular morphology with rough surface can be obtained. With respect to FE, compared to as-anodized TNAs, oxygen-deficient TNAs prepared by hydrogenation, nitriding and carbonization show dramatically enhanced FE properties including a lower turn-on field of 1.75 V/ μm , a higher FE current density of 4.0 mA/cm² at 4.50 V/ μm , and a remarkable FE stability. These results indicated that oxygen-deficient TNAs can be promising candidates for FE.

Acknowledgements

This work was supported by the National Natural Science Foundation of China (Grant Nos. 10974155 and 10774121), the Natural Science Foundation of Gansu Province of China (Grant No. 1208RJZA197).

References

- [1] X. B. Chen, L. Liu, P. Y. Yu and S. S. Mao, Science 2011, 331, 746.
- [2] Y. M. Kang, C.W. Wang*, J. B. Chen, L. Q. Wang, D. S. Li, W. D. Zhu and F. Zhou, J. Vac. Sci. Technol. B 2012, 30, 041801.
- [3] W. D. Zhu, C. W. Wang*, J. B. Chen, D. S. Li, F. Zhou and H. L. Zhang, Nanotechnology, 2012, 23, 455204.

3:00pm **NS+AS+EM-MoA4 Fabrication and Controlled *In Situ* Morphological Transformation of Highly Ordered Hollow Oxide Nanostructures based on Nanoscale Kirkendall Effect**, A. El Mel, Univ. of Mons, Belgium, M. Buffière, IMEC, KU Leuven, Belgium, P.-Y. Tessier, Inst. des Matériaux Jean Rouxel – Univ. de Nantes, Belgium, K. Du, C.H. Choi, Stevens Inst. of Technology, L. Molina-Luna, S. Schildt, H.J. Kleebe, Technische Univ. Darmstadt, Germany, S. Konstantinidis, C. Bitencourt, R. Snyders, Univ. of Mons, Belgium

Huge efforts are nowadays dedicated to the development of relevant methods to fabricate hollow nanostructures of a wide variety of materials. Among hollow nanostructures, oxide nanotubes appear to be an interesting building block for nanoelectronics. Until today, the oxide nanotubes suffer of their short length and poor organization. In this contribution, we report on highly organized ultra-long metal oxide nanotube arrays (length-up to several centimeters) fabricated by thermal oxidation of metal nanowire arrays. The metal nanowires were grown on nano-grated surface by the plasma-assisted inverse-template method that we have developed recently. Based on the extensive structural study, performed by transmission electron microscopy, the fundamental mechanisms occurring during the formation of such oxide nanotubes will be discussed and explained according to the nanoscale Kirkendall effect. We further show that such method can be extended to the fabrication of periodic zero-dimensional hollow nano-objects.

In addition, we present an extensively structural study of the morphological transformation of oxide nanotubes upon *in situ* annealing in a transmission electron microscope. Based on this, the role of oxygen on the fundamental mechanisms occurring during the formation of such oxide nanotubes will be discussed. These results show the structural transformation and copper ions diffusion inside an oxide nanotube due to the effect of heating.

3:40pm **NS+AS+EM-MoA6 Carbon Nanotube Macroelectronics and Nanoelectronics**, C. Zhou, University of Southern California **INVITED**

Carbon nanotubes and graphene offer great promise but also face significant challenges for future beyond-silicon nanoelectronics. This talk will focus on our recent work on nanoelectronics based on aligned nanotubes, macroelectronics based on separated nanotubes, and wafer-scale CVD graphene. We have developed the synthesis of massively aligned single-walled carbon nanotubes atop sapphire and quartz substrates, and we will also present our recent progress toward type-controlled and chirality-controlled carbon nanotube synthesis. In addition, we will report macroelectronics based on separated nanotube thin film transistors,

including key technology components such as assembly of separated nanotube networks, high-yield fabrication of devices, and applications for AMOLED displays and printed electronics. Furthermore, we will present scalable fabrication of self-aligned T-gate graphene transistors for RF applications.

4:20pm **NS+AS+EM-MoA8 Geometry-Dependent Formation of Multiple Twins in Si Nanowires**, *N. Shin*, Georgia Institute of Technology, *M. Chi*, Oak Ridge National Laboratory, *M.A. Filler*, Georgia Institute of Technology

Precise control of twin boundaries and stacking faults in semiconductor nanowires provides a number of exciting opportunities to fundamentally manipulate their optical, electrical, and thermal properties. Group IV nanowires, as opposed to their III-V counterparts, rarely exhibit planar defects perpendicular to the {111} orientation and rationally engineering their insertion remains challenging. Here we extend our recent demonstration of defect introduction in vapor-liquid-solid (VLS) synthesized, {111} oriented Si nanowires¹ and report on the appearance of consecutive, geometry-dependent twin boundaries for the first time. Si nanowires with double twins were grown with a Au catalyst by initiating growth at $T = 490\text{ }^\circ\text{C}$ and $P = 2 \times 10^{-4}$ Torr for 10 min before changing to $T = 410\text{ }^\circ\text{C}$ and $P = 5 \times 10^{-4}$ Torr for another 10 min. While the position of the first twin boundary (TB₁) corresponds to the point where growth conditions were changed, and was the same for all nanowires, the second twin boundary (TB₂) exhibits a diameter-dependent axial position. Detailed electron microscopy analysis shows that thin {111} sidewall facets, which elongate following TB₁ and deform the triple-phase line, are responsible for the formation of TB₂. We hypothesize that an increased amount of surface hydrogen, present as a result of the condition change, favors the thin {111} facets. Our findings help to elucidate the mechanisms that underlie defect introduction in semiconductor nanowires and represent an important step toward the creation of complex defect superstructures in Si.

(1) Shin, N.; Chi, M.; Howe, J. Y.; Filler, M. A. *Nano Lett.*, **2013**, *in press*

5:00pm **NS+AS+EM-MoA10 Plasma Modification of Chemically Vapor Deposited SnO₂ Nanowires and SnO₂ Nanoparticles for Enhanced Gas Sensing**, *E. Stuckert*, *E.R. Fisher*, Colorado State University

As toxic gases like NO_x, benzene, and formaldehyde continue to be emitted globally, their negative impacts on people's health persist. With gases capable of causing harm on the part per billion level, it is critical to accurately sense toxic gases in real time. This requires creating sensors that operate at lower temperatures, are more sensitive, and are more selective for sensing a desired gas than what is commercially available. SnO₂ is commonly used to create sensing materials because it has enhanced gas-surface interactions as a result of its variable oxidation states, namely Sn²⁺ and Sn⁴⁺. Plasma modification is one method of altering the SnO₂ surface to enhance sensitivity and selectivity. The plasma treatments create more surface oxygen vacancies in the SnO₂, which allows for increased sites for atmospheric oxygen to adsorb. The sorption of gases is highly dependent on the predominant oxygen species on the sensor surface at a given plasma treatment and temperature. Our results demonstrate that SnO₂ nanowires grown by chemical vapor deposition (CVD) and commercial SnO₂ nanoparticles treated in Ar/O₂ plasmas have lattice oxygen removed from the surface. Removal of surface oxygen is corroborated through X-ray photoelectron spectroscopy (XPS), Fourier-transform infrared spectroscopy (FTIR), and X-ray diffraction (XRD). XPS data show that low plasma power treatments (10-60 W) alter the surface oxygen composition of SnO₂ nanowires and nanoparticles, with the maximum change in composition peaking at 30 W. More importantly, the oxygen vacancies in the treated nanowires are significantly higher than those observed for treated nanoparticles. In addition to surface analysis results, resistance of SnO₂ nanowire and nanoparticle sensors when exposed to a range of gases (i.e., methanol, ethanol, propanol, benzene, and formaldehyde) is used to explore specific gas-surface interactions. By relating plasma treatment conditions to the resulting surface composition and the sensor's response upon exposure to gases, insight into how surface modification affects gas-surface interactions in sensors will be presented.

Keywords:

Plasma modification, Gas sensor, Tin oxide, Nanowire, Nanoparticle

5:20pm **NS+AS+EM-MoA11 Vapor Transport Growth and Thermal Conductivity Measurement of Chalcogenide Nanowires with Axial Heterojunctions**, *C.J. Hawley*, *J.E. Spanier*, Drexel University

We report on the controlled vapor transport growth of bismuth chalcogenide nanowires by the vapor-liquid-solid (VLS) mechanism, both in the form of ternary alloys as well as axial variation of the binary compounds bismuth telluride and bismuth selenide. The nanowires exhibiting axial heterojunctions are of specific interest as they promise to reduce a device's

effective thermal conductivity through the incorporation of boundary impedances at each junction. These nanowires are measured by suspending a single nanowire between contacts and joule heating the nanowires in a four-probe configuration. The change in resistivity due to the joule heating, in combination with numerical modeling of the axially varying nanowire system, allows for the calculation of the effective thermal conductivity of the nanowires, useful for their exploration as a more efficient low temperature thermoelectric nanostructured material.

Work was supported by the U.S. Army Research Office (W911NF-08-1-0067) and C.J.H. was supported by the GAANN-RETAIN program supported by the U. S. Dept. of Education (P200A100117).

Plasma Science and Technology Room: 102 B - Session PS+TF-MoA

Plasma Deposition

Moderator: S. Agarwal, Colorado School of Mines

2:00pm **PS+TF-MoA1 Practical Aspects of using Tailored Voltage Waveforms for Thin Film Processing of Photovoltaic Devices**, *E.V. Johnson*, *B. Bruneau*, LPICM-CNRS, Ecole Polytechnique, France, *P.A. Delattre*, *T. Lafleur*, *J.-P. Booth*, LPP-CNRS, Ecole Polytechnique, France

The use of Tailored Voltage Waveforms (TVWs) to manipulate the Electrical Asymmetry Effect in a capacitively coupled plasma-enhanced chemical vapour deposition (CCPECVD) chamber has been shown to be an effective technique for device quality thin-film deposition [1,2], and a useful tool to study the interaction of the bulk and sheath properties of processing plasmas [3] and their impact on growth surfaces [4].

We have used this technique to directly study the influence of mean ion-bombardment energy (IBE) on the growth of hydrogenated microcrystalline silicon ($\mu\text{-Si:H}$) in a CCP chamber, with otherwise unchanged plasma conditions. In this work, we discuss recent results on a specific aspect of $\mu\text{-Si:H}$ growth for photovoltaic applications, the amorphous to μc phase transition. The dependence of this transition on many other parameters (power, pressure, dilution) makes the direct observation of the effect of IBE very difficult, as recently demonstrated by the efforts of other authors [5]. We instead use TVWs to vary the IBE, and in-situ ellipsometry to observe the transition in real time for a number of deposition chemistries, such as H₂/SiH₄ and Ar/H₂/SiF₄. Furthermore, in addition to maximizing or minimizing the IBE by changing the waveform shape, the sheath expansion/contraction rates at the powered electrode can equally be controlled. The unexpected impact of these conditions for the $\mu\text{-Si:H}$ nucleation rate are presented, underlining the importance of "Tailoring" the waveform to the specific plasma processing goal.

Finally, we address an outstanding issue that has challenged the use of TVW's in an industrial setting – the difficulty of matching a TVW source to a CCP chamber. This has previously limited their use to only two harmonics for exciting a large area reactor at high power. We present experimental results for a prototype, high-power multifrequency matchbox that allows the effective coupling of the full output power of the amplifier to the PECVD chamber, enabling high deposition rate $\mu\text{-Si:H}$. These increased deposition rates, along with in-situ observation of the film evolution during growth, will be shown.

[1] E.V. Johnson, P-A. Delattre, and J.P. Booth, *Appl. Phys. Lett.* **100** (2012) 133504.

[2] D. Hrunski, *et al*, *Vacuum* **87** (2013) 114.

[3] T. Lafleur, P.A. Delattre, E.V. Johnson, and J.P. Booth, *Appl. Phys. Lett.* **101**, (2012)124104.

[4] E.V. Johnson, S. Pouliquen, P-A. Delattre, and J.P. Booth, *J. Non-Cryst. Solids* **358**. (2012), 1974.

[5] A. C. Bronneberg, N. Cankoy, M. C. M. van de Sanden, and M. Creatore, *J. Vac. Sci. Technol.* **A30**, 061512 (2012).

2:20pm **PS+TF-MoA2 Characteristics of Plasma Generated by ICP-CVD with Various H₂/SiH₄ Ratios and the Resultant Properties of nc-Si:H Thin Films**, *J.H. Hsieh*, *Y.L. Lie*, *S.C. Lin*, Ming Chi University of Technology, Taiwan, Republic of China

Nc-SiH thin films were deposited with an ICP-CVD system attached with four internal antennas, under the variation of H₂/SiH₄ ratios (R). During deposition, the generated plasma was characterized using a Langmuir probe and an optical emission spectrometer (OES). The films' properties were characterized using Raman spectrometry and FTIR. The results were correlated with those obtained from probe and OES studies. It was found that the crystallinity of nc-Si:H film was significantly affected by plasma density which was increased with the increase of R, but only to a certain

extent. Both the plasma density and Xc reached the maximum at R=10, then leveled off. The deposition rate decreased with the increase of IHa* which is obtained from the OES results. Also, it was also found that the crystallinity could be proportionally related to the increase of I*(SiH2+SiH3)/I(SiH+SiH2+SiH3) in FTIR spectra. This is could be due to that di-/poly- hydride bonding could serve to passivate the grain boundaries of Si nano-crystalline clusters.

2:40pm **PS+TF-MoA3 Medium Range Order (MRO) in "Amorphous (a)-Si(H)" Alloys in PV and TFT Devices with Intrinsic, B and P Doped a-Si(H) and a-Si,Ge(H) Layers: Reduction of Photo- and Stress-induced Defects by O-bonding.** G. Lucovsky, D. Zeller, C. Cheng, Y. Zhang, North Carolina State University

INVITED

Intrinsic photo-absorbing regions, and B and P doped contacts comprised of hydrogenated amorphous silicon, a-Si_{1-x}H_x, with ~10 at.% or x ~0.1±0.02, are used in photovoltaic devices (PV), and thin film transistors (TFT's). A-Si thin films, assumed to be free of H, are used as precursors for polycrystalline gate electrodes in microelectronics. Intrinsic, and p-type and n-type layers in multi-layer stacks that include "a-Si,Ge(H)" have been assumed to be "amorphous continuous random networks (CRN)", with limited short range order (SRO) extending to 1st nearest neighbor (NN) bond lengths, and 2nd N-N bond-angles. A-Si(H) films are not CRNs. They have medium range order (MRO) extending to self-organized and symmetry determined dihedral angles. MRO and formation of non-periodic organized nm-scale *ordered* regions with crystalline-Si symmetries is responsible for enabling properties in a-Si(H) devices. Intrinsic a-Si(H) thin films have been deposited by glow discharge (GD), remote plasma-enhanced chemical vapor deposition (RPECVD), and reactive magnetron sputtering (RMS). The concentrations of bonded-H are determined by deposition precursors and substrate temperatures. Two conditions are necessary for low Si dangling bond densities to ~0.5 to 1x10¹⁶ cm⁻³: (i) a bonded mono-hydride, Si-H, concentration of ~10 at.% H, and (ii) a deposition, and/or a post-deposition anneal at ~240°C to 300°C [1]. These combine to reduce strain-induced defects by introducing MRO as 1 nm-ordered clusters. Si L_{2,3} X-ray absorption spectroscopy (XAS) confirms MRO by yielding non-vanishing ligand-field splittings (DLF) of e_g and t_{2g} atomic d-states. The MRO basis states are symmetry-adapted linear combinations (SALC) of atomic states and form molecular orbital valence bands. MRO symmetry promotes a H-atom transfer reaction from a the Si-H bond at the apex of the MRO cluster into a Si-H-Si bonds at NN sites. This reaction establishes the low level of dangling bond defect sites. The same H-atom transfer is induced by sunlight absorption in PV devices. This increase dangling bond concentrations is the Staebler-Wronski effect (SWE). The local bonding arrangements of P and B dopant atoms are qualitatively different. If the bonding sites were the same as substitutional sites in c-Si, each of these dopants would be 4-fold coordinated. The incorporation of P is the same as in crystalline Si, 4-fold coordinated, and the ionization energy of the P⁺ site is small giving rise to a high doping efficiency, i.e., in electrons/P atom [2]. B is 3-fold coordinated, and p-orbitals perpendicular to the 3-fold coordinated bonding plane act as an electron acceptor creating hole transport.

Each of the preferred bonding arrangements for P- and B-atoms includes remote induction stabilized Si-H reducing Si-atom dangling bond densities. This accounts for a reduction of the E' center signal strength in electron spin resonance (ESR) measurements. Finally, the local bonding of 2-fold coordinated O-atoms, and 3-fold coordinated N-atoms have similar effects as 1-fold coordinated H-atoms, introducing new MRO local bonding arrangements. When combined with 1-fold coordinated NN Si-H bonds, the 2- and 3-fold local symmetries introduce coupled mode motions that stabilize unique MRO clusters by increasing their total binding energy. This stabilization provides a reduction in the Staebler-Wronski Effect photo-degradation in PV devices by process-controlled low densities (<10¹⁸ cm⁻³) of plasma processing incorporation of O- and N-atoms and coupled O-H/H-H bonds.

Similar reductions reduce electron trapping in TFTs.

1. G. Lucovsky and F.L. Galeener, J. of Non-Cryst. Solids 35 & 36 (1980) 1209.
2. G.N. Parsons, C. Wang and M.J. Williams, Appl. Phys. Lett. 56, 1985 (1990).
3. D.E. Steabler and C.R. Wronski, J. Appl. Phys. 51 (6), (1980) 3262.

3:40pm **PS+TF-MoA6 Plasma Prize Talk - Plasma Processing Advances at Illinois, D.N. Ruzic**, University of Illinois at Urbana Champaign

INVITED

Recent advances in plasma processing at Illinois will be discussed. The first is the investigation of high-powered pulsed magnetron sputtering (HiPIMS) by creating a hole in the target racetrack and placing a gridded energy analyzer and quartz-crystal monitor (QCM) behind it. In this way the metal ion and Ar ion flux can be measured, as well as the neutral metal atom flux. These measurements show the true mechanism behind the high surge in

current during a HiPIMS pulse. The next subject is creating PVD-like coatings at atmospheric pressure. This is done by introducing atoms of the coating material directly into the plasma plume of an atmospheric-pressure torch either through laser ablation or by evaporation. These coatings have many industrial applications and since they can be made in the field instead of inside a vacuum chamber, their utility is increased and their cost reduced. Lastly, the use of a metal-surface-wave plasma source will be described. Low-damage crystalline and amorphous silicon can be produced with it leading to higher-efficiency solar cells and other applications.

4:20pm **PS+TF-MoA8 PECVD, Rf vs Dual Frequency : Investigation of Plasma Influence on Metalorganic Precursors Decomposition and Material Characteristics.** F. Pierrat, STMicroelectronics, France, C. Vallee, Ltm - Minatec - Cea/leti, France, R. Gassilloud, P. Michallon, CEA-LETI, France, B. Pelissier, Ltm - Minatec - Cea/leti, France, P. Caubet, STMicroelectronics, France

In the last decade, Dual Frequency (DF) reactors have been considerably developed as fine etching tool for microelectronic manufacturing. In this case, the CCP source is driven by a high frequency (HF) and a LF sources attached on either one electrode or two electrodes separately. Usually one frequency is chosen to be much higher than the other in order to achieve an independent control of ion bombardment and electron density (i.e. ion flux). In the case of deposition process, it has been observed for Silicon Nitride deposition that the HF to LF ratio in the plasma modify the ion flux and energy and so the mechanical properties of the material [3]. Moreover, addition of LF to HF can modify the sheath thickness of the plasma and so increase the electron temperature of the gas [4]. In this way, the precursor fragmentation can be tuned by tuning the LF power what will impact the deposition rate and thin film properties.

In this study we compare RF and Dual frequency deposition of materials for metal gate applications such as TiCN and TaCN. The reactor used is a 300 mm Metal Organic PECVD industrial tool in which the plasma is sustained capacitively by a RF power supply (13.56 MHz) and a LF (350 kHz) source. Impact of LF addition on the metal composition and its physical properties is analyzed and correlated to plasma modification observed by OES (Optical Emission Spectroscopy). For both metalorganic precursors we observe a strong modification of the metal properties and deposition rate when adding 25 to 100 W LF to a 200 W RF plasma. As an example, in case of TiN, with 50 W LF added to a 200 W RF, the deposition rate increased more than twice, the film appears to be less resistive (50%) and denser. These modifications highlight the change of deposition mechanisms/reactions. The beneficial effect of adding a weak LF power to the RF power can be correlated to a modification of the precursor fragmentation as observed by OES. These results are less pronounced and not obtained when only RF plasma is used, whatever the increasing power (from 200 to 300 W). Finally, with LF addition, we also hope, to reduce the RF plasma impact on the dielectric leading to a regrowth of Equivalent Oxide Thickness (EOT) observed previously in our p-like metal MOS capacitors [5].

- [1] H. N. Alshareef *et al*, Electrochemical and Solid-State Letters **11** (2008) H18
- [2] H. Zhu *et al*, Phys. Review B **80** (2009) 201406
- [3] W.S. Tan *et al*, Journal of Electronic Materials **33** (2004) 400-407
- [4] W-J Huang *et al*, Phys. Plasmas **16** (2009) 043509
- [5] F. Pierrat *et al*, AVS 59th Tampa (Florida, USA)

4:40pm **PS+TF-MoA9 Reactive High Power Impulse Magnetron Sputtering (HiPIMS), J.T. Gudmundsson**, University of Iceland, F. Magnus, Uppsala University, Sweden, T.K. Tryggvason, S. Shayestehaminzadeh, S. Olafsson, University of Iceland

Reactive high power impulse magnetron sputtering (HiPIMS) [1] provides both a high ionization fraction of a high dissociation fraction of the molecular gas. Here we discuss reactive high power impulse magnetron sputtering (HiPIMS) of Ti target in Ar/N₂ and Ar/O₂ atmosphere. The discharge current waveform is highly dependent on the reactive gas flowrate, pulse repetition frequency and discharge voltage. The discharge current increases with decreasing repetition frequency. This we attribute to an increase in the secondary electron emission yield during the self-sputtering phase of the pulse, as nitride [2] or oxide [3] forms on the target. We also discuss the growth of TiN films on SiO₂ at temperatures of 22-600 °C. The HiPIMS process produces denser films at lower growth temperature and the surface is much smoother and have a significantly lower resistivity than dc magnetron sputtered films on SiO₂ at all growth temperatures due to reduced grain boundary scattering [4,5].

- [1] J. T. Gudmundsson, N. Brenning, D. Lundin and U. Helmersson, J. Vac. Sci. Technol. A, **30** 030801 (2012)
- [2] F. Magnus, O. B. Sveinsson, S. Olafsson and J. T. Gudmundsson, J. Appl. Phys., **110** 083306 (2011)

[3] F. Magnus, T. K. Tryggvason, S. Olafsson and J. T. Gudmundsson, *J. Vac. Sci. Technol.*, **30** (2012) 050601

[4] F. Magnus, A. S. Ingason, S. Olafsson and J. T. Gudmundsson, *IEEE Elec. Dev. Lett.*, **33** (2012) 1045 - 1047

[5] S. Shayestehaminzadeh, T. K. Tryggvason, L. Karlsson, S. Olafsson and J. T. Gudmundsson, *Thin Solid Films*, submitted 2012

5:00pm **PS+TF-MoA10 Sputtering Yields and Selectivity of Magnetic Materials by Chemically Reactive Plasmas**, *H. Li, Y. Muraki, K. Karahashi, S. Hamaguchi*, Osaka University, Japan

Based on highly developed reactive ion etching (RIE) technologies, micro-fabrication of Si-based semiconductor devices has been considerably developed for the last few decades. However, as non-conventional micro devices, such as magnetic random access memory (MRAM) devices, have been developed recently, there has been a considerable demand for RIE processes of non-conventional materials such as magnetic materials with nonconventional gases such as CO/NH₃ and methanol. In this study, we examine sputtering yields and surface reaction characteristics for MRAM etching by CO/NH₃ or methanol plasmas. Especially we focus on effects of oxygen and nitrogen in incident ions that are likely to induce selectivity of magnetic materials over Ta, i.e., a widely used mask material in such processes. In this study, we use a multi-beam system (i.e., mass-selected ion beam system), which allows only selected ions with specified energy to be injected into a sample substrate set in an ultra-high-vacuum (UHV) chamber. Using the beam system, rather than an actual plasma etching system, we can examine specific surface reactions caused by a specific combination of a sample material and incident ions (and/or radicals). In the beam system, chemical surface compositions are analyzed by *in-situ* XPS. In this study, the incident ion energy and angle of incidence were varied from 300eV to 1000eV and from 0° to 75°. The sputtering yields were measured as functions of energy and/or angle of incidence for various materials including Ni, Fe, Co, Ta, and TaO_x. It has been found that, in most cases, etching processes for these materials are nearly of physical sputtering. For simple physical sputtering (by, e.g., Ar⁺ ions), the sputtering yield of Ta is much lower than the magnetic materials (Ni, Co, Fe), which justifies the use of Ta as a mask material. Furthermore, from XPS spectrum observation, it has been found that, when N or O are in the incident ionic species, Ta form a nitride or an oxide and its sputtering yield becomes even lower. These results have confirmed that, in CO/NH₃ or methanol plasma etching processes of magnetic materials with Ta masks, the observed selectivity is essentially caused by the formation of hard-to-etch oxides and/or nitrides of masks, rather than enhanced etching yields of magnetic materials by these plasmas.

5:20pm **PS+TF-MoA11 Two-dimensional Growth of Novel ZnO based Semiconductor ZnInON with Tunable Bandgap by Magnetron Sputtering**, *K. Matsushima, R. Shimizu, D. Yamashita, G. Uchida, H. Seo, K. Kamataki, K. Koga, M. Shiratani, N. Itagaki*, Kyushu University, Japan
Materials with tunable bandgap are required for optoelectronics applications such as photo detectors, solar cells, light emitting diodes, and so on. Recently we have developed a novel ZnO based semiconductor, ZnInON (ZION), with tunable bandgap from 1.6 eV to 3.3 eV, being fabricated by sputtering method [1]. ZION has wurtzite crystal structure and high absorption coefficient of 10⁵ cm⁻¹. Here we have studied effects of Ar partial pressure during the sputtering deposition on the crystal growth of ZION films by means of plasma parameter measurements and evaluation of film properties such as crystallinity and electrical properties. Furthermore, we have demonstrated two-dimensional growth of single crystalline ZION films.

First, 10-nm-thick ZnO buffer layers were fabricated on c-Al₂O₃ substrates via nitrogen mediated crystallization (NMC) in N₂-Ar atmosphere at 700°C [2]. Then, 1-μm-thick ZnO templates were fabricated on the ZnO buffer layers by RF magnetron sputtering at 700°C in Ar-O₂ atmosphere. Finally, epitaxial ZION films were fabricated on the ZnO templates by RF magnetron sputtering. For fabrication of ZION films, N₂, O₂ and Ar gasses were used. The total pressure was 0.28 Pa and the partial pressure of Ar was 0.04-0.17 Pa. The supplied RF power was 0.49-3.95 W/cm² and the deposition temperature was 360°C. The ZION film thickness was 30-50 nm.

X-ray diffraction measurements show that the full width at half maximum (FWHM) of rocking curves from (002) plane for the ZION films are noticeably small of 0.09°, being independent of the partial pressure of Ar in the sputtering atmosphere. Hall-effect measurements using the Van Der Pauw configuration reveal that the carrier density of ZION films decreases from 1.1×10²⁰ cm⁻³ to 3.7×10¹⁹ cm⁻³ and the electron mobility increases from 66 cm²/Vsec to 87 cm²/Vsec with decreasing the partial pressure of Ar from 0.17 Pa to 0.04 Pa. This is because electron temperature in the plasma increases with decreasing the partial pressure of Ar, and thus the dissociation of oxygen and nitrogen molecules is enhanced, which can suppress the lattice defects related to nitrogen and/or oxygen deficiencies.

Moreover, two-dimensional crystal growth of ZION films was observed at a low Ar partial pressure of 0.04 Pa. These results show that Ar partial pressure in sputtering atmosphere is an important parameter to control the growth mode and to improve electrical properties of ZION films.

This work was partially supported by JSPS and PRESTO.

[1] N. Itagaki, et al., "Metal oxynitride semiconductor containing zinc", U.S. Patent No. 8274078 (2008-04-23).

[2] N. Itagaki, et al., *Appl. Phys. Express* **4** (2011) 011101.

Plasma Science and Technology Room: 104 C - Session PS-MoA

Advanced BEOL/Interconnect Etching

Moderator: S. Hamaguchi, Osaka University, Japan

2:00pm **PS-MoA1 Etching Challenges in the BEOL for sub 20nm Technology Nodes**, *K. Kumar, Y.P. Feurprier, L. Wang, J. Stillahn, Y. Chiba, A. Ranjan, A. Metz, A. Ko, D.M. Morvay, A. Selino, P. Biolsi*, TEL Technology Center, America, LLC **INVITED**

In the sub-32nm technology node, Trench First Metal Hard Mask (TFMHM) integration scheme has gained traction and become the preferred integration of low-k materials for BEOL. This integration scheme also enables Self-Aligned Via (SAV) patterning which prevents via CD growth and confines via by line trenches to better control via to line spacing. In addition to this, lack of scaling of 193nm Lithography and non-availability of EUV based lithography beyond concept, has placed focus on novel multiple patterning schemes. This added complexity has resulted in multiple etch schemes to enable technology scaling below 80nm Pitches, as shown by the memory manufacturers. Double-Patterning and Quad-Patterning have become increasingly used techniques to achieve 64nm, 56nm and 45nm Pitch technologies in Back-end-of-the-line. Challenges associated in the plasma etching of these integration schemes, along with the challenges posed with etching EUV resists, in concert with shape formation of the dual-damascene will be discussed in the presentation.

2:40pm **PS-MoA3 Plasma Etch Challenges at 10nm and beyond Technology Nodes using Multi Patterning Techniques in the BEOL to Produce Metallization-Friendly Profiles**, *Y. Mignot, STMICROELECTRONICS, M. Beard, B.G. Morris, B. Peethala, IBM, Y. Loquet, STMICROELECTRONICS, J.H. Chen, IBM, S. Nam, GLOBALFOUNDRIES U.S. Inc., B. Nagabhirava, P. Fridde*, Lam Research Corp

As feature critical dimension (CD) shrinks towards and beyond the 48nm pitch, new patterning techniques within the context of a trench-first-metal-hard-mask (TFMHM) patterning scheme have been developed to generate trenches and vias below 48nm pitch. One of the main challenges at advanced nodes is to create structures (i.e., trenches & vias) that can be robustly metalized. This requires several elements of focus for the etches: first, there must be zero dielectric etch damage that results in undercut of any hard masks in the film stack; second, the aspect ratio of the final etch structure must be minimized; and third, the shape of the trench or via profile must be tailored to be metallization-friendly (i.e., slight angle better than vertical) and finally a good selectivity on lower metallization in case of wet HMO faceting. These requirements often conflict with each other, especially within a patterning scheme that requires self-aligned vias, where the desired high selectivity to the hard mask conflicts with the need to minimize the amount of hard mask left in order to decrease aspect ratio. In this paper, we will discuss some of the approaches that we have investigated to achieve the best profile for metallization. This includes plasma etch all-in-one (AIO) dielectric etch optimization as well as multi-step solutions that potentially can use techniques including wet chemistries plus dry faceting and dry metal HMO removal. In addition, data will present an overview of the multi-patterning techniques such as multiple Litho-Etch (LE3), Sidewall Image transfer (SIT) and double patterning for self aligned via (DPSAV) to expose and understand the multiple underlying interactions at Dielectric RIE such as the SIT Block Mask with the DPSAV features.

This work was performed by the Research Alliance Teams at various IBM Research and Development Facilities

3:40pm **PS-MoA6 Fine Patterning of Copper by Plasma Etch Process for Advanced BEOL Interconnects**, *H. Miyazoe, IBM T.J. Watson Research Center, M. Hoinkis, Applied Materials Inc., B.N. To, G. Fritz, A. Pyszyna, M. Brink, C. Cabral, IBM T.J. Watson Research Center, C. Yan, I. Ne'eman, Applied Materials Inc., E.A. Joseph, IBM T.J. Watson Research Center*

As device scaling continues beyond the 10 nm node, challenges in back end of line (BEOL) interconnect technology continue to multiply. Expanding

beyond the known issues of patterning and integration of porous ultra low-k (ULK) materials, new issues such as line edge roughness and line width roughness (LER/LWR) as well as increased resistivity (emanating from grain boundary scattering) are only compounding the difficulties at hand and may require significant modifications to the typical damascene integration flow. Subtractive etching of Cu has a potential to overcome current difficulties in interconnects integration such as the increase of resistivity caused by electron scattering at grain boundary, poor coverage of liner/seed materials, and a time dependent dielectric breakthrough (TDDB) issue of ULK material by starting from blanket Cu film with large crystal ($>1 \mu\text{m}$), by depositing it directly on Cu patterns, and by minimizing plasma damage during ULK etch, respectively. In this work, we examine one such alternative approach to conventional dual damascene copper integration, in which subtractive patterning of copper is employed. Successful patterning of copper at smaller than 50 nm critical dimension (CD) with smaller than 100nm in pitch is demonstrated using a novel high density plasma based dry etch process. Consisting of a reactive sputter based etch chemistry, appreciable etch rates on the order of $\sim 15\text{Å/s}$ are achieved, with high selectivity ($>6:1$) to masking layers. The angle of sidewall of approximately 85° was achieved at an optimized condition while we obtained $\sim 45^\circ$ in case of physical sputtering using pure Ar plasma. We confirmed that the resistivity of fabricate Cu line increases with the decrease of line CD. The resistivity of isolated Cu line at CD of $\sim 30\text{ nm}$ is ranging from 10 to 20 $\mu\text{ohm cm}$. A full review of the etch process, its mechanism and the positive implications on ULK materials, LER and LWR, metal resistivity and overall reliability will be discussed in detail.

4:00pm PS-MoA7 Virtual Fabrication for BEOL Module Optimization Beyond the 22nm Technology Node, R. Patz, D. Fried, K. Greiner, M. Stock, D. Faken, J. Lehto, A. Pap, B. van Dyk, M. Kamon, S. Breit, Coventor, Inc.

Virtual fabrication provides a powerful platform for exploring process interactions in 3D, reducing time-consuming and costly trial-and-error silicon experimentation. A Trench First Metal Hard Mask BEOL integration scheme including Self-Aligned Vias (TFMHM-SAV) has been characterized using a M1-V1-M2 example. Experiments focused on the patterning operations involved, and were based on 64nm Mx pitch designs. Variation studies were used to determine the key drivers of V1-M1 contact area, liner coverage and via spacing. A full-wafer study showed the impact of patterning and deposition non-uniformity. This full-wafer virtual fabrication data can focus attention on the most critical unit processes and enable Automated Process Control (APC).

V1-M1 contact area, a critical electrical and reliability criterion, was primarily determined in this integration scheme by M1 lithography bias. Through a $\pm 3\text{nm}$ range of M1 exposure, the contact area varied more than 3x, from 322nm^2 to 1091nm^2 . Chamfer profile, critical for electromigration reliability, was dictated by the Mx Overetch (OE) depth and sputter ratio (ion energy). Cross-sectional analysis was used to characterize the final metallization, enabling conclusions regarding resistance and yield. TiN selectivity during the M2 etch dominated the profile, leading to metallization differences. Surprisingly, the cross-sectional area of Mx copper decreased slightly ($\sim 3\%$) with reduced TiN selectivity (from 40:1 to 10:1), a change that opened the top profile and was expected to lead to improved copper fill. 3D model inspection revealed that this effect was driven by a "shoulder" in the cap layer, resulting in a metallization profile degrade.

Geometries beyond the 22nm technology node and resulting unit process requirements push the limits of process tool capability and cross-wafer uniformity. A module-level approach must be considered to compensate for uniformity limitations of any single process by adjusting specifications elsewhere in the process flow. A full-wafer virtual fabrication experiment explored cross-wafer deposition and patterning variation in the M1-V1-M2 module to quantify the aggregate effect of many realistic unit process steps on the fully-integrated structure. While these cross-wafer variations yielded a 1σ uniformity of 12% in Mx copper cross-sectional area, the sensitivities lay the foundation for APC-based yield improvement.

4:20pm PS-MoA8 Improvements in Low-k Damage and Hard Mask Selectivity in BEOL Dielectric Etch Using C5HF7, R.L. Bruce, IBM T.J. Watson Research Center, T. Suzuki, M. Nakamura, Zeon Chemicals LP, S.U. Engelmann, E.A. Joseph, N. Fuller, E.M. Sikorski, IBM T.J. Watson Research Center, A. Itou, Zeon Corporation

As feature sizes continue to decrease, significant issues are found using highly selective fluorocarbon gases to etch interconnect low-k dielectrics. Three examples of these challenges include; line wiggling, low-k damage, and low selectivity (e.g. to organic masks). To address these challenging issues, we have evaluated C5HF7 and other novel etch gases for 14nm and 22nm devices to determine if they enable the optimized fabrication of BEOL interconnects. Etch performance is assessed for both trench and via patterns and also when incorporated into full dual-damascene structures.

Compared to conventional fluorocarbon etch gases such as C4F6 and CF4/CHF3 mixtures, experiments with C5HF7 have shown a substantial increase in low-k dielectric to metal hard mask and capping layer selectivity for trench and self-aligned via etching. Low-k damage is also investigated by post-etch HF treatment to measure critical dimension loss from dissolution of plasma-damaged dielectric. A significant reduction in damage is observed with C5HF7 in low-k films of two different dielectric constants. Finally, we propose a mechanism for high selectivity, low damage dielectric etch at sub-80nm pitch structures using rationally-designed novel etch gases.

4:40pm PS-MoA9 Mitigation of Plasma-induced Damage of Advanced 2.0 Porous Dielectrics by the Pore Stuffing Approach, M.H. Heyne, L. Zhang, KU Leuven, Belgium, J.-F. De Marneffe, R. Gronheid, C.J. Wilson, M. Baklanov, IMEC, Belgium

Plasma-induced damage is a major hurdle for the integration of 2.0 dielectrics in advanced interconnects targeting sub-10 nm nodes. State-of-the-art low-k dielectrics are porous organo-silicate glass (p-OSG) films, with high carbon content and interconnected porosities up to 50 %, making the material sensitive to modifications by plasma reactive radicals and VUV photons. A possible solution is the so-called pore stuffing approach: after porogen burnout, a sacrificial polymer is introduced into the porous matrix, hampering diffusion of radicals in the bulk material and attenuating VUV light propagation.

PECVD ultra-low-k dielectric films with $k = 2.0$ and porosity of 40 – 50 % were stuffed with PMMA. The protection efficiency was evaluated against fluorocarbon-based, oxygen-based plasmas and 147 nm VUV light generated in industrially relevant 300 mm CCP chambers. The material damage was determined by FTIR, spectroscopic ellipsometry, ellipsometric porosimetry, TOF-SIMS, water contact angle measurements, and capacitance measurements. Plasma damage was significantly reduced in PMMA protected samples, resulting in lower hydrophilicity, smaller carbon loss, smaller fluorine penetration, and lower dielectric constants in comparison to unprotected material. PMMAs of molecular weights between 2000 and 7000 g/mol influenced the filling conditions and filling process window, but gave similar level of plasma protection. Plasma-induced VUV light led to significant PMMA degradation, through carbonyl bonds depletion and formation of other polymer by-products, resulting in only a short-term protection of the dielectric against 147 nm radiation. Pattern transfer for 40 nm lines required small changes in discharge parameters, and resulted in lowered sidewall damage when compared to non-stuffed samples.

After the etching, the polymer is usually removed from the pores by a thermal burn-out above 400°C , which is not compatible with BEOL processing. An alternative approach is proposed, using a non-damaging He/H₂ downstream plasma at 280°C , allowing a full CMOS process compatibility.

Pore stuffing is a promising approach to mitigate the plasma damage in porous ultra-low-k material by using a temporary hybrid material approach. In contrast to former hybrid solutions, this one is not suffering from shrinkage or material interaction and therefore, might allow one further step to $k_{\text{eff}} \leq 2.0$ interconnect systems.

5:00pm PS-MoA10 EPR Studies of SiOC:H BEOL (Low-k) Dielectrics, T.A. Pomorski, P.M. Lenahan, M. Mutch, Penn State University, S.W. King, Intel Corporation

Low-k interlayer dielectrics with dielectric constants significantly less than those of SiO₂ and are utilized to reduce capacitance induced RC delays in ULSI circuits. [1,2] At the present time, very little is known about the underlying physical mechanisms involved in electronic transport within these films. Recent electron paramagnetic resonance (EPR) studies have reported on defect centers in some of these films [3,4]. In one study, comparisons were made between EPR defect densities and leakage currents before and after exposure to UV light under conditions generally similar to those during industrial UV curing. That study noted that large UV induced changes in spin density were accompanied by large changes in dielectric leakage, suggesting a link between the defects and leakage.[3] In this study we have conducted a considerable more extensive survey specifically focused upon low-k SiOC:H films. We find that a large variety of paramagnetic centers are present in the dielectrics and that both the types of defects present and the defect densities are quite strong functions of processing parameters. Defects include silicon dangling bond centers in which the silicon is back bonded to three oxygens (E² centers), silicon dangling bond centers complexed to a single hydrogen atom, a dangling bond center complexed to three equivalent hydrogens, and very likely carbon dangling bond centers. In, limited cross section of samples, all with the EPR dominated by a center with a zero crossing $g=2.0026 \pm 0.0003$ and all similarly processed, we observe strong correlation between defect density and dielectric leakage currents. It should be noted that quite recent

SiOC:H studies which have utilized another analytical approach has also identified the presence of E' centers in similar films. King et. al. recently reported on reflection electron energy loss spectrometry (REELS) on similar dielectric films and noted the presence of REELS spectra consistent with E' centers a result which our EPR data supports.[5]

[1] K. Maex, D. Shamiryan, F. Iacopi, S.H. Brongersma, and Z.S. Yanovitskaya, *J. Appl. Phys.*, **93**, 11 (2003).

[2] W. Volksen, R.D. Miller, and G. Dubois, *Chem Rev.* **110**, 56 (2010).

[3] B. Bittel, P. Lenahan, S. King, *Appl. Phys. Lett.* **97**, 6 (2010)

[4] H. Ren, et. al. *Appl. Phys. Lett.* **98**, 10 (2011)

[5] S.W. King, B. French, E. Mays, *J. Appl. Phys.*, **113**, 044109 (2013)

5:20pm PS-MoA11 Effect of NH₃/N₂ Ratio in Plasma Treatment on Porous Low Dielectric Constant SiCOH Dielectric, Y.L. Cheng, J.F. Huang, T.C. Bo, National Chi-Nan University, Taiwan, Republic of China

The influence of N₂/NH₃ ratio in the plasma treatment on physical, electrical properties and reliability characteristics is investigated in this study. It is found that all the plasma treatments resulted in the formation of a thin and modified layer on the surface of the porous low-*k* films, and the properties of this modified layer is affected by N₂/NH₃ ratio in the plasma. Results indicate that pure N₂ plasma treatment forms an amide-like layer on the surface, which apparently leads to a higher increase in the dielectric constant. A mixture of N₂/NH₃ gas plasma treatment induces more moisture uptake on the low-*k* dielectric's surface, which degrade the electrical performance and reliability. Among N₂/NH₃ gas plasma treatment, plasma-treated low-*k* dielectric has better electrical and reliability characteristics as N₂/NH₃ gas ratio equals to 1.

Surface Science

Room: 201 A - Session SS-MoA

Metal Oxides: Reactivity and Catalysis

2:00pm SS-MoA1 Controlling Surface Reactivity of an Ultrathin MgO Film by Interface Tuning, Y. Kim, J. Jung, RIKEN, Japan, H.-J. Shin, UNIST, Republic of Korea, M. Kawai, University of Tokyo, Japan

Ultrathin oxide films grown on metal substrates have been a subject of great interest not only as a supporting material for chemically active nanoparticles but also as a catalyst in the field of heterogeneous catalysis. We have demonstrated that the chemical reactivity for water dissociation on an ultrathin MgO film supported by the Ag(100) substrate depends greatly on film thickness and be enhanced compared to that achieved with their bulk counterpart using scanning tunneling microscopy (STM) and density functional theory (DFT) calculations [1]. The change of chemical reactivity of ultrathin MgO film depending on the film thickness can be explained by the strengthening of the interaction between the oxide and metal interface layers [2]. This result implies that the artificial manipulation of the local structure at the oxide-metal interface is expected to play a pivotal role in controlling the catalytic activity of oxide film. We have also examined and compared the water dissociation on various model systems with defects at the oxide-metal interface of the 2-ML MgO/Ag(100) using periodic DFT calculations [2]. Our results clearly show that such structural imperfections at the interface can improve the chemical reactivity of the MgO film supported by an Ag substrate. This is closely correlated with the accompanied change of charge distribution of the oxide surface due to the accumulation of transferred charge density at the interface. In addition, the chemical reactions on the ultrathin oxide film surface can be tuned by interface defects regardless of the charging of adsorbates. A recent result of coupling between molecular vibration and surface phonon in the CO hopping process on MgO/Ag(100) with tunneling electrons will also be introduced [3].

[1] H.-J. Shin, J. Jung, K. Motobayashi, S. Yanagisawa, Y. Morikawa, Y. Kim, and M. Kawai, *Nat. Mater.* **9**, 442 (2010).

[2] J. Jung, H.-J. Shin, Y. Kim, and M. Kawai, *Phys. Rev. B* **82**, 085413 (2010); *J. Am. Chem. Soc.* **133**, 6142 (2011); *J. Am. Chem. Soc.* **134**, 10554 (2012).

[3] H.-J. Shin, J. Jung, M. Kawai, and Y. Kim, submitted.

2:20pm SS-MoA2 Energetics of Adsorption of D₂O on Fe₃O₄ (111) Studied by Microcalorimetry, C.A. Wolcott, I.X. Green, C.T. Campbell, University of Washington

Metal oxides represent an important class of materials whose interfacial properties play an important role in chemical sensors, catalysis, environmental science, biology, and many other fields [1]. This poster presents for the first time the direct measurement of the heat of adsorption

and reaction of a molecular species on an oxide surface. The energetics of the adsorption and reaction of D₂O with a Fe₃O₄ (111) surface were studied using single crystal adsorption calorimetry (SCAC). SCAC allows for the direct measurements of surface reaction heats by using a pulsed molecular beam, a thin sample, and a temperature transducer. A 4nm thick film of Fe₃O₄(111) was grown on a 1μm thick Pt(111) crystal using the method of Weiss and Ranke[1]. Following the work of Weiss et al. [2], water is expected to form three species on an Fe₃O₄ (111) surface. Initially water reacts and dissociates on the surface producing surface hydroxyls bound to iron sites and hydrogen bound to oxygen sites. Upon continued dosing some water is seen to adsorb molecularly on the surface before eventually forming multilayers. In the present work we explored the heat of adsorption of D₂O as a function of both surface temperature and surface coverage using a pulsed molecular beam and a liquid nitrogen cryostat. By analyzing how the heat of adsorption changes as a function of temperature and coverage and correlating with the surface species observed by Weiss and others, heats of reaction for the formation of surface hydroxyls and molecular water on Fe₃O₄(111) are calculated. These results are compared with the heats measured indirectly by Weiss et al using TPD and UPS [2] and with DFT results [3].

[1] Weiss W., Ranke W., *Progress in Surface Science*, **70**, 2002, 1.

[2] Joseph Y., Kuhrs C., Ranke W., Weiss W., *Surface Science*, **433**, 1999, 114.

[3] Yang T., Wen X.D., Cao D.B, Li Y.W, Wang J.G., Huo C.F., *J Fuel Chem Technol*, **37** (4), 2009, 506.

2:40pm SS-MoA3 Surface Chemistry of PdO(101), J.F. Weaver, University of Florida, A. Asthagiri, The Ohio State University, C. Hakanoglu, A. Antony, F. Zhang, University of Florida INVITED

The formation of palladium oxide (PdO) is thought to be responsible for the exceptional activity of supported Pd catalysts toward the complete oxidation of alkanes under oxygen-rich conditions. In this talk, I will discuss our investigations of the surface chemical properties of a PdO(101) thin film, focusing particularly on the adsorption and selective activation of alkanes. We find that *n*-alkanes adsorb relatively strongly on the PdO(101) surface by forming σ-complexes along rows of coordinatively-unsaturated Pd atoms, and that this adsorbed state acts as the precursor for initial C-H bond cleavage. I will discuss characteristics of the binding and activation of alkane σ-complexes on PdO(101) as determined from both experiment and density functional theory calculations. I will also discuss elementary processes involved in adsorbate oxidation and surface reduction of PdO(101), and make comparisons with the chemical reactivity of other late transition metal oxides.

3:40pm SS-MoA6 Elemental Steps in Dehydration of Diols on TiO₂(110), D. Acharya, Y. Yoon, Pacific Northwest National Laboratory, Z. Zhang, Baylor University, Z. Li, X. Lin, L. Chen, R. Mu, B.D. Kay, R. Rousseau, Z. Dohnalek, Pacific Northwest National Laboratory

Simple diols (ethylene and propylene glycols) are employed as models for deoxygenation reactions of biomass. TiO₂(110) is selected as a prototypical oxide catalyst to attain detailed mechanistic understanding of such reactions. In these studies atomically resolved imaging by scanning tunneling microscopy (STM) is combined with ensemble-averaging spectroscopic techniques such as temperature programmed desorption (TPD) and theoretical investigations via density functional theory (DFT). STM studies reveal that at low temperatures (140 K), diols adsorb on five-fold coordinated Ti⁴⁺ sites. The molecules readily dissociate via O-H bond scission forming Ti-bound hydroxyalkoxy and bridging hydroxy (HO_b) species. The reverse reaction leading to molecularly bound diols is also observed indicating the attainment of a dynamic equilibrium between these conjugate acid/base pairs. Above 250 K, diols readily diffuse to oxygen vacancies and irreversibly dissociate via O-H bond scission of one of the OH groups forming geminate pairs of hydroxyalkoxy and hydroxyl species, both anchored on bridging oxygen (O_b) rows. The hydroxyalkoxy species rotate around their O_b anchor, switching the position of their OH between the two adjacent Ti rows. The rotating species are also found to assist cross-O_b row HO_b hydrogen transfer. The OH group of the hydroxyalkoxy species is further observed to dissociate forming a dioxy species and an additional HO_b. Annealing to ~450 K results in the formation of new dioxy intermediates that are centered on top of the O_b rows. Alkenes as final products are observed to desorb between 600 and 700 K. For ethylene glycol, our coverage dependent TPD studies further show acetaldehyde as a second carbon containing product at high coverages. Detailed theoretical calculations yield a deep insight into the mechanism and energetics of the observed reaction steps.

4:00pm **SS-MoA7 Site-specific Chemistry in Aqueous Solutions Produces Atomically Flat Rutile (110)**, *D. Jing, A. Song, M.A. Hines*, Cornell University

The high photocatalytic reactivity of nanocrystalline TiO₂ has attracted widespread interest for applications ranging from next-generation solar cells to self-cleaning surfaces; however, surface science investigations of these materials under technically relevant conditions have been hindered by a number of experimental difficulties. Moreover, the correlation between the chemical properties of clean TiO₂ surfaces produced in vacuum by repeated sputter-and-anneal cycles, the standard surface science technique, to those present in solution or in humid environments is unclear. We have used STM to investigate the atomic-scale reactivity of the most commonly studied TiO₂ polymorph, rutile, in pH-controlled aqueous solutions. Clean, atomically flat rutile (110) surfaces with well controlled step structures can be prepared using a simple aqueous solution. After mild heating (~150°C) to remove adsorbed water, STM reveals atomically flat surfaces of comparable quality to those produced using standard sputter-and-high-temperature-anneal cycles. The nature of the highly site-specific chemical reactions that produce these surfaces is revealed by kinetic simulations of pH-dependent changes in the etch morphology. A chemical mechanism for the production of atomically flat surfaces that is consistent with the inorganic chemistry of Ti(IV) compounds and the observed anisotropic reactivity is proposed.

4:20pm **SS-MoA8 Coverage Dependence of Photocatalysis of Trimethyl Acetate on TiO₂(110)**, *Z.T. Wang, I. Lyubinetsky*, Pacific Northwest National Laboratory

Photocatalysis on titania (TiO₂) has attracted much attention due to the potential applications on water splitting and pollutant destructions. Various photocatalytic applications of TiO₂ often involve interfaces with carboxylate-anchored organic molecules. From the fundamental point of view, one of the most interesting carboxylate-anchored molecules in probing photochemistry on TiO₂ is trimethyl acetate (TMA). We employed the high-resolution scanning tunneling microscopy (STM) to investigate the coverage influence for the TMA photocatalysis on rutile TiO₂(110) at 300 K. TMA species were deposited through deprotonative dissociation of trimethylacetic acid (TMAA) on TiO₂(110). In the deprotonative process, the dissociated TMAA's generate an equal amount of TMA's and hydroxyl groups (OH_b) on TiO₂(110). We found that TMA's adsorbed at Ti sites exhibit the same photoreaction (complete hole-induced decomposition) at all coverages but coverage-dependent reaction dynamics, where the reaction rates decrease with increasing TMA coverages. Furthermore, our results reveal that pre-adsorbing hydroxyl groups on TiO₂(110) also suppress the TMA photodecomposition. We demonstrate that the coverage-dependence of TMA reaction rates should be attributed to the variation of hydroxyl group concentration on TiO₂(110). It appears that OH_b species likely being the surface electron-traps decrease TiO₂ reactivity toward hole-mediated reactions, which results in the decreasing of TMA photoreaction rates with increasing its coverages.

4:40pm **SS-MoA9 TiO_x Thin Films on Au(111): Water Dissociation Properties**, *M.H. Farstad*, Norwegian University of Science and Technology, Norway, *D. Ragazzon*, Uppsala University, Sweden, *A. Schaefer*, University of Bremen, Germany, *L.E. Walle, A. Borg*, Norwegian University of Science and Technology, Norway, *A. Sandell*, Uppsala University, Sweden

When TiO_x (x ≤ 2) thin films are deposited onto various metal substrates different structures with unique properties may form. This method therefore offers the possibility for guided design of TiO₂ structures, which can lead to new kinds of TiO₂-based materials for heterogeneous catalysis, photocatalysis and solar cells [1]. Since water is an integral part of these applications a solid understanding of the interaction between water and novel, supported titania structures is essential.

In the present work, we present results on water adsorption on ordered TiO_x structures on Au(111) grown in situ by chemical vapor deposition (CVD). Depending on the conditions during deposition four different ordered phases can be produced. These phases have previously been studied and characterized with high-resolution photoelectron spectroscopy (HR-PES), scanning tunneling microscopy (STM) and low energy electron diffraction (LEED). Two phases, denoted honeycomb (HC) and wagon wheel (WW), are monolayer thick, reduced and wet the surface. The other two phases, denoted Star and Ring, are different forms of stoichiometric TiO₂. The Star phase is the thermodynamically stable form of titania on Au(111) and it grows in the form of islands that partially covers the surface. The Ring phase is a multi-domain structure that covers basically the whole surface. The analysis of the LEED pattern gives an oblique unit cell, strongly indicating the formation of TiO₂-B [2], a phase which surface properties are largely unknown.

Upon water adsorption all four TiO_x phases show evidence of dissociation. The maximum hydroxyl coverage for the 2x2 and Star phases is close to that formed on the rutile (110) surface [3], while the hydroxyl coverage on the Ring phase is significantly lower. On the defect free rutile (110) surface, nearly all hydroxyl groups are gone at 300 K. In contrast, the hydroxyls on the 2x2 and Star phases persists up to 500-600 K, that is, a temperature regime typically associated with recombination at defect sites. The Ring phase interacts weakly with water with little dissociation. The amount of dissociated water corresponds to an active site density of about 7%. The correlation between the water adsorption and dissociation behavior and the structural properties of the TiO_x phases will be discussed.

[1] U. Diebold, Surf. Sci. Reports 48, 53 (2003).

[2] A. Vittadini, M. Casarin, A. Selloni, The Journal of Physical Chemistry C 113 (44), 18973-18977 (2009).

[3] L. E. Walle, A. Borg, P. Uvdal, A. Sandell, Phys. Rev. B 80, 235436 (2009).

5:00pm **SS-MoA10 Probing Charge Transfer Following Molecular Adsorption on CeO₂(100) using Resonant Photoemission**, *D.R. Mullins, P.M. Albrecht*, Oak Ridge National Laboratory

Resonant photoemission excited at the Ce N_{IV,V}-edge was used to study electron transfer from molecular adsorbates to the Ce cation on fully oxidized CeO₂(100). Two features near the top of the valence band in CeO₂ are extremely sensitive to the oxidation state of the Ce cation. The O 2p feature at a binding energy of 4 eV is proportional to the Ce⁴⁺ content in the surface. The Ce 4f peak at a binding energy of 1.5 eV is proportional to the Ce³⁺ content. The ratio of these two peaks at their respective resonance maxima provides a measure of the Ce³⁺/Ce⁴⁺ content. This ratio is extremely sensitive because the Ce 4f feature rises from a flat, low count background in fully oxidized CeO₂ to a peak with thousands of counts at even modest levels of Ce reduction. The kinetic energy of the valence electrons at resonance is ca. 120 eV which places them near the minimum for the electron mean free path and therefore provides excellent surface sensitivity.

A variety of molecules were adsorbed on CeO₂(100) at 190 K. CeO₂ is a reducible oxide and removal of O from the surface will result in a reduction of Ce⁴⁺ to Ce³⁺. At 190 K none of the molecules studied resulted in desorption from the surface and therefore reduction did not result from the removal of O but from charge transfer from the adsorbate to the Ce. At elevated temperatures products such as water and CO₂ were observed that clearly resulted in reduction of the Ce due to O removal.

Methanol and water undergo similar adsorption processes by breaking an O-H bond, depositing H on a surface O anion and adsorbing R-O- on the Ce cations. For methanol the methoxy adsorbate produced ca. 10% Ce³⁺ following adsorption whereas the hydroxyl adsorbate resulting from water exposure produced a negligible change in the Ce³⁺ content. This suggests that the C in the alcohol is partially oxidized following adsorption whereas there is no net transfer of charge from the H and O in the water to the Ce.

Acetaldehyde does act as a Bronsted acid by breaking an O-H bond yet it also produces a 10% reduction of the Ce. This may result from a partial oxidation of the C in the dioxy / η₂ adsorption state and also from an oxidation of a small amount of the acetaldehyde to acetate. Pyridine, a classic probe of acid sites through the lone-pair electrons on the N, results in no change in the Ce³⁺ content. N 1s XPS and C k-edge NEXAFS suggest that the pyridine may not bond to the surface through the N atom.

Research sponsored by the Division of Chemical Sciences, Geosciences, and Biosciences, Office of Basic Energy Sciences, U.S. Department of Energy.

5:20pm **SS-MoA11 Reactivity of Acetaldehyde on CeO₂(111) Surfaces and the Roles of Oxygen Vacancies**, *Y. Xu*, Louisiana State University, *F. Calaza, D.R. Mullins, S.H. Overbury*, Oak Ridge National Laboratory

Ceria is a widely used catalytic and functional catalyst support material, well known for its ability to store oxygen and change oxidation state. There is a growing body of evidence that the surface reactivity of ceria can vary significantly with the extent of reduction. We use acetaldehyde as a probe molecule to explore this phenomenon and to elucidate the roles of oxygen vacancies in redox reactions on ceria surfaces. Multiple surface characterization techniques and theoretical density functional theory (DFT) calculations have been applied in combination to elucidate the mechanism of the temperature-program desorption (TPD) of acetaldehyde on CeO₂(111) thin-film surfaces. In TPD, acetaldehyde desorbs without reaction from the stoichiometric CeO₂(111) surface at 210 K. When the surface is partially reduced, acetaldehyde loses its carbonyl bond character at low temperatures. Annealing to 400 K leads to the desorption of some of this strongly adsorbed species as acetaldehyde and the appearance of another species, conclusively identified by RAIRS and DFT to be the enolate form of acetaldehyde (CH₂CHO), which has not been captured previously on ceria surfaces. A microkinetic model based on the identified

surface intermediates on CeO₂(111) and DFT energetics has been constructed to simulate the TPD, and finds close agreement with the experimental results. Our findings demonstrate that surface oxygen vacancies are key to activating acetaldehyde and stabilizing it for further reactions, and that the dominant surface reaction pathway changes as a function of vacancy concentration. This work has relevance to the conversion of biomass-derived oxygenates because enolate species are key intermediates in C-C coupling reactions including aldol condensation.

Thin Film

Room: 104 A - Session TF+AS+SE+SS-MoA

ALD/MLD Surface Reactions, Precursors, and Properties

Moderator: R.K. Grubbs, Sandia National Laboratories,
J.S. Jur, North Carolina State University

2:00pm TF+AS+SE+SS-MoA1 Growth of Metallic First Row Transition Metal Films by Atomic Layer Deposition from New Precursors, C.H. Winter, L.C. Kalutarage, Wayne State University
INVITED

Our laboratory seeks to develop the growth of metallic first row transition metal thin films using atomic layer deposition (ALD). The microelectronics industry is calling for the growth of metallic first row transition metal films by the ALD method for a variety of applications, including copper metallization, seed layers for copper metallization, copper/manganese alloys for self-forming copper diffusion barriers, and magnetic alloys. The ALD growth of noble metal thin films has been explored extensively in the past ten years, due to the positive electrochemical potentials of these metal ions and relative ease of reduction to the metallic state.¹ The low temperature ALD of high purity, low resistivity Cu films has been described,² but ALD routes to the other metallic first row transition metal films remain poorly developed, largely because of the negative electrochemical potentials of most of the ions and a corresponding lack of powerful reducing co-reagents that can convert precursors in positive oxidation states to the metals. We will describe the synthesis, structure, and properties of a large series of new first row transition metal ALD precursors containing alkoxide ligands that combine high volatilities, high thermal stabilities, and high reactivities toward reducing agents. We will also report borane reducing agents that can react with the metal precursors to afford metallic films. Additionally, we will overview the thermal growth of metallic copper, nickel, cobalt, iron, manganese, and chromium thin films from these new precursors. Key advances include development of optimized ALD precursors with very similar ligands and chemistry, and identification of new reducing co-reagents that can rapidly reduce the positive oxidation state precursors to the metals.

1. M. Leskelä, M. Ritala, O. Nilsen, *MRS Bull.* **2011**, 36, 877-884.
2. B.H. Lee, J.K. Hwang, J.W. Nam, S.U. Lee, J.T. Kim, S.-M. Koo, A. Baunemann, R.A. Fischer, M.M. Sung, *Angew. Chem. Int. Ed.* **2009**, 48, 4536-4539. T.J. Knisley, T.C. Ariyasena, T. Sajavaara, M.J. Saly, C. H. Winter, *Chem. Mater.* **2011**, 23, 4417-4419.

2:40pm TF+AS+SE+SS-MoA3 O₂ based Ru ALD using CpRu(CO)₂Et: First-principles, Experiments and Micro-kinetic Modeling, C.K. Ande, N. Leick, Eindhoven University of Technology, Netherlands, S.D. Elliott, Tyndall National Institute, Ireland, W.M.M. Kessels, Eindhoven University of Technology, Netherlands

In the present work, we use a combination of first-principles calculations, QMS experiments and micro-kinetic modeling to reveal the reactive pathways in operation during an O₂ based Ru ALD using CpRu(CO)₂Et as the metal precursor. Analysis of the gas phase species in our QMS experiments showed that the surface chemisorption of CpRu(CO)₂Et resulted in the formation of dehydrogenation and combustion products such as H₂, CO₂, CO and H₂O. H₂ was detected as a major surface reaction product during the metal precursor pulse. Strikingly, during the O₂ pulse virtually no H₂, H₂O or other H-containing reaction products were measured. These results suggest that a number of surfaces might be involved: bare, O-covered Ru and RuO₂ surfaces (Leick et al. *Chem. Mat.*, 24, 3696, (2012)).

While it is still experimentally difficult to accurately identify the surface and reactions happening at the surface, Density Functional Theory (DFT) provides an elegant way to study the same. Therefore, we used DFT calculations to study the role of bare and O-covered surfaces on dehydrogenation reactions during the ALD process. Since most of the dehydrogenation occurs from the Et and Cp ligands, as a first step, we studied dehydrogenation of ethane. In order to probe the role of O-covered

surfaces in the dehydrogenation reactions, we studied the reactions on both bare (Ru(0001)) and O-covered (0.25 ML and 0.5 ML) Ru surfaces. It is clear from the calculations that the dehydrogenation on the bare Ru(0001) is the most energetically favorable process. Interestingly, they also show that the presence of O on the Ru(0001) surface inhibits the dehydrogenation reactions from taking place. Thus, dehydrogenation reactions happening on O-rich patches of the growing Ru surface can be excluded.

Although DFT calculations provide accurate energy changes and activation energies of each of the possible elementary reactions, they still do not predict the collective behavior when all the processes are possibly happening simultaneously. To resolve this problem we use micro-kinetic modeling and go up to the next higher length and time scales in an ALD process. In micro-kinetic modeling, information about elementary reactions that happen at the gas surface interface is used to describe the overall time evolution of the system which includes species in the gas phase and on the surface. We use accurate activation energies obtained from our DFT calculations in the micro-kinetic model. Preliminary results clearly show the evolution of H₂ from the decomposition of ethane. We hope to extend the method and present results about the decomposition of the complete precursor on the bare Ru(0001) surface.

3:00pm TF+AS+SE+SS-MoA4 The Chemistry of the Cu(I) s-Butyl Amidinate Atomic Layer Deposition (ALD) Precursor on Ni and Cu Surfaces, Y. Yao, T. Kim, J. Coyle, S.T. Barry, F. Zaera, University of California, Riverside

Thanks to the self-limiting and complementary nature of the reactions involved, atomic layer deposition (ALD) has become a promising method for making uniform and conformal thin films. Cu(I) amidinates have been introduced in recent years as promising precursors for the ALD of copper interconnects. An understanding of the surface chemistry of these copper(I) amidinates is essential to the design of the corresponding ALD processes. Here we report the results from our studies on the surface chemistry of Cu(I) s-butyl amidinate on Ni and Cu surfaces using X-ray photoelectron spectroscopy (XPS) and temperature programmed desorption (TPD).

It was determined that, on Ni surfaces, the reduction of Cu(I) to metallic Cu happens already at room temperature. The Cu(I) s-butyl amidinate adsorbs dissociatively on those Ni surfaces, and decompose thermally to produce H₂, HCN and N₂, at about 500 K, 570 K and 830 K, respectively. After annealing to temperatures above 800 K, all N-containing species desorb as HCN or N₂, but some carbon left on the surface. It was found that Cu (I) s-butyl amidinate adsorption on Ni between 300 K and 400 K is self-limited, with an estimated Cu saturation coverage of 0.15 ML, but switches above 500 K to a behavior where continuous copper deposition occurs, as typically seen in chemical vapor deposition (CVD) processes. It was also found that surface oxygen on Ni substrates exerts a great effect on the surface chemistry of the Cu precursor. On oxygen covered Ni surface, the Cu(I) reduction to metallic Cu only happens above 500 K, at which point the Ni surface oxide is reduced by the organic surface species that result from Cu(I) s-butyl amidinate adsorption to form H₂O and CO₂. The presence of surface oxygen greatly reduces the carbon deposition in the annealing process.

On Cu surfaces, which form after several ALD cycles on any substrate, the Cu(I) s-butyl amidinate precursor shows less activity than on Ni surfaces. The molecule adsorbs molecularly on Cu at 300 K, and the Cu(I) center is reduced to metallic Cu only after annealing above 500 K. Chemisorbed Cu (I) s-butyl amidinate starts to dissociate at about 460 K, via the breaking of a C-N bond and the formation of pyrrolaminium (C₄H₇N₂) and butene. H₂ desorption is detected at about 510 K, and HCN and N₂ desorption above 800 K. As on Ni surfaces, self-limited copper uptake on Cu substrates takes place between 300 K and 400 K, with an estimated Cu saturation coverage of 0.06 ML, and changes to CVD above 500 K. On O/Cu(110), H₂O desorption peaks at 470 K and a broad CO₂ desorption feature is seen between 450 K and 600 K. H₂ desorption was detected at 595 K.

3:40pm TF+AS+SE+SS-MoA6 Quantitative In Situ Infrared Analysis of Reactions between Trimethylaluminum and Polymers during Al₂O₃ Atomic Layer Deposition, G.N. Parsons, B. Gong, P.S. Williams, North Carolina State University

The reactions of trimethylaluminum (TMA) toward substrates during the Al₂O₃ atomic layer deposition (ALD) on a variety of polymers were studied by in-situ Fourier transform infrared spectroscopy (FTIR). The experiments demonstrate that TMA reacts with certain nucleophilic functional groups on the polymer surface during the first several ALD cycles. For some polymer substrates, TMA vapor penetrates into the polymer and reacts in the polymer bulk. In both cases, the initial reaction plays an important role in the nucleation and growth of Al₂O₃. For chemically inert polymers nucleation of Al₂O₃ ALD is relative slow at the initial stage due to the lack of reactive groups on the substrate. However, polyester, polyamide and polyether are more reactive, and in-situ FTIR spectra showed a larger extent

of reaction with TMA, facilitating the nucleation of ALD film on these polymers. By comparing FTIR spectra, we quantitatively estimate the extent of TMA reaction towards different polymers, and confirmed the results using X-ray photoelectron spectroscopy and scanning electron microscopy. Results give insight into the importance of polymer structure in determining the nature and extent of reaction during ALD film processing on polymer substrates.

4:00pm TF+AS+SE+SS-MoA7 Surface Reactions during the ALD of TiO₂ on Si and GaAs Surfaces Studied by *In Situ* ATR-FTIR, L. Ye, T. Gougousi, University of Maryland, Baltimore County

The atomic level mechanisms during the deposition of TiO₂ on etched and chemical oxide Si (100) and GaAs (100) surfaces from tetrakis dimethyl amino titanium (TDMAT) and H₂O at 100 and 200C have been studied using *in situ* attenuated total reflection Fourier transform infrared spectroscopy (ATR-FTIR). The adsorption of TDMAT on Si and GaAs surfaces is confirmed by the observation of CH and NC vibration modes. Exposure to H₂O removes most of the CH bonds, but species associated with reaction by-products remain on the surface and increase in intensity as the deposition progresses. For the deposition on both chemical oxide and hydrogen terminated Si surfaces at 100 and 200C, the amount of TDMAT adsorbed on the surfaces generally decreases with increasing number of cycles and reaches similar steady state coverage at about the 20th cycle of deposition. For depositions on hydrogen terminated Si surfaces, about 50% of the initial Si-H bonds remain unreacted after 20 process cycles. For deposition on both Si and GaAs surfaces, C=O bonds at 1595 cm⁻¹ associated with formate species accumulate during the deposition. The use of GaAs internal reflection elements allows extension of the useful range just around 700 cm⁻¹ permitting possible observation of the precursor reaction with the surface As and Ga oxides.

4:20pm TF+AS+SE+SS-MoA8 Metal Oxide/Carbon Composite Films by Pyrolysis of Hybrid Organic-Inorganic MLD Films, J. Travis, S.M. George, University of Colorado at Boulder

Many metal oxides with desirable electrochemical properties have limited use in electrochemical devices due to their low electrical conductivities. One way to improve the electrical conductivity is to integrate carbon domains as a conductive additive in the metal oxide. We have developed a method to produce metal oxide/carbon composite thin films via pyrolysis of hybrid organic-inorganic molecular layer deposition (MLD) films under inert atmosphere. This method is general and has been applied to form TiO₂/C, Al₂O₃/C, ZnO/C, ZrO₂/C and HfO₂/C composite films from titanocene, alucone, zincone, zircone and hafnicone MLD films, respectively. Most of the work has focused on TiO₂/C and Al₂O₃/C composite films. Raman measurements have observed the growth of the signature D and G peaks of graphitic carbon after pyrolysis under argon at ≥600°C. The sheet resistance of the pyrolyzed MLD films also decreased by orders of magnitude with increasing pyrolysis temperature. Minimum sheet resistances were obtained for titanocene and alucone MLD films after pyrolysis at 800 and 850°C, respectively. The ability to coat conformally high aspect ratio electrodes with hybrid organic-inorganic MLD films and then pyrolyze these MLD films to obtain conducting metal oxide/carbon composite films will have many important applications in electrochemistry. Possible areas include Li ion batteries and pseudocapacitance supercapacitors.

4:40pm TF+AS+SE+SS-MoA9 Molecular Layer Deposition of Organic-Inorganic Hybrid Materials for Implant BARC Applications, L.N.J. Rodriguez, C. Adelman, B. Sutens, G. Winroth, A. Delabie, R. Gronheid, S. Van Elshocht, IMEC, Belgium

Molecular Layer Deposition (MLD), a variant of Atomic Layer Deposition (ALD) whereby organic groups are used to link the metal atoms within the growing film can create films with optical properties which are unreachable by ALD alone. The ability to make highly conformal films of specified thickness and optical properties should be of use in supplying Bottom Anti-Reflective Coatings (BARC) for lithography processes. The advantage lies in finely tuned patterning control, minimizing etch damage to the underlying topography in applications such as ion implantation masking. Optical simulations were performed for a 110nm trench using 193nm exposure at 0.85NA with conventional illumination and with the MLD thickness of 5nm and having n=1.4 and k=0.8, in order to validate this approach. The growth rate of alucones by MLD was highly dependent on the temperature but did show self-limiting growth. While the refractive index of the alucones is lowered towards the target region, the absorption constant was too low. Therefore the ethylene glycol in the MLD was replaced with aromatic precursors so as to increase the optical absorption of the films. The conformality of the films was tested with fin structures and the process developed for transfer from coupons to full wafers.

5:00pm TF+AS+SE+SS-MoA10 Mechanical Property Modification of Fiber Forming Polymers by Sequential Organometallic Exposures, R.P. Padbury, J.S. Jur, North Carolina State University

Hybrid organic-inorganic materials are of increasing interest in the development of novel materials that unite characteristic properties of both organic and inorganic constituents. This work explores the infiltration of ALD precursors into fiber forming polymers and the subsequent formation of a hybrid material interface. The hybrid functionalization is formed as a result of precursor diffusion through the porous sub-surface of the organic material which is followed by chemical reaction and nucleation. Previous research exploring the infiltration of organometallic precursors into polyamide-6 (PA-6) films via in-situ quartz crystal microgravimetry (QCM) indicates a strong dependence on the glass transition temperature of the polymer film. To explore this in more detail, in-situ QCM is employed to investigate the infiltration behavior of a series of polyesters and polymethacrylates that possess variations in functional group concentration and glass transition temperatures. The effect of this processing on the mechanical behavior of fibrous materials is also investigated. In particular this report highlights the structure-process-property relationships between modified and unmodified polyester fibers that have been infiltrated with trimethylaluminum (TMA). The results indicate that as the number of TMA cycles increases the peak load and elongation of the single fiber also increases. Mechanical testing is complemented by ex-situ characterization methods such as TEM to examine the interaction between the precursor and polymer and the composition of the hybrid layer. This work has important implications on sustainable textiles processes as well as the introduction of hybrid material properties to polymer systems.

5:20pm TF+AS+SE+SS-MoA11 Vapor-Phase Modification of Simple Sugars Towards New Hybrid Organic-Inorganic Materials, K. Gregorczyk, L. Zhang, M. Knez, CIC nanoGUNE, Spain

The incorporation of transition metals into organic materials has lead to a variety of unusual or improved physical and chemical properties. Of particular interest is the use of inexpensive biological materials as substrates or scaffolds due to their naturally occurring, and often complex, morphologies. For simple coatings atomic layer deposition (ALD) has been proven to be the technique of choice due to its low reaction temperatures, monolayer thickness control, and extreme conformality. Furthermore, recent modifications to this technique have allowed infiltration of the metal-organic precursors into a variety of organic materials including spider silk[1], porphyrins [2], and polytetrafluoroethylene (PTFE)[3], leading to a more detailed understanding of the reaction between these organic substrates and the metal-organic precursors. Using this technique, we present work studying the interaction of trimethyl aluminum and diethyl zinc with simple sugar molecules (monomers, dimers, and polymers). We report chemical and mechanical modifications to the simple monosaccharide glucose, the polysaccharide sucrose, and the polymer cellulose. Reaction detail differences between the simple monomer molecules (glucose) and their corresponding polymers (cellulose) will be discussed though mass spectrometry, Raman spectroscopy, and UV-vis. Mechanical and chemical changes to these materials will also be presented.

1. Lee, SM *et al.* Science, **324**, 488 (2009)
2. Zhang, L, *et al.* Angew. Chem. Int. Ed., **48** (2009)
3. Lee, SM, *et al.* Adv. Funct. Mater, **21** (2011)

Tribology Focus Topic

Room: 203 C - Session TR+AS+NS+SS-MoA

Molecular Origins of Friction

Moderator: I. Szlufarska, University of Wisconsin-Madison, M. Müser, Saarland University, Germany

2:00pm TR+AS+NS+SS-MoA1 Unraveling and Eliminating Dissipation Mechanisms in Polymer Brush Interfaces, M.H. Müser, FZ Jülich, Germany
INVITED

Surfaces covered with end-anchored polymers under good solvent conditions have excellent tribological properties. Friction between such surfaces is commonly attributed to the interdigitation of opposing polymer brushes. However, this conclusion tends to be based on idealized geometries neglecting capillaries or surface roughness. Using molecular dynamics simulations, we find that, depending on the direction of motion, dissipation due to capillary and shape hysteresis can contribute in a similar fashion as interdigitation. The two alternative mechanisms are even likely to become dominant at small sliding velocity. We also analyze how friction can be tuned through the solvent quality, thereby providing guidelines for the optimization of the investigated systems.

2:40pm **TR+AS+NS+SS-MoA3 Molecular Dynamics Simulations of Adhesion & Friction between Carbon-based Materials, Silicon, and Silicon Carbide, K.E. Ryan, United States Naval Academy, K. Vummaneni, J.D. Schall, Oakland University, J.A. Harrison, United States Naval Academy**

The nanoscale properties of two bodies in contact cannot be fully analyzed on an atomistic level using experimental methods or understood solely using continuum mechanics. Molecular dynamics (MD) simulations allow nanoscale behavior to be modeled by resolving the positions, velocities, and forces of discrete atoms in the system. Diamond has been of interest as both an object of scientific study and as an ideal material for applications such as, cutting tool coatings, waste water purifiers, chemical sensors, electronic devices, and micro- and nanoelectromechanical systems (M/NEMS) because of its unique electrical, mechanical, and tribological properties. Due to its high fracture strength and chemical robustness, it can withstand exposure to harsh environments and resist mechanical wear. It can be grown in nanocrystalline form with nearly equivalent mechanical performance to the crystalline form. Silicon, due to the ability to create atomically sharp tips, is frequently used in scanning probe microscopy. Recently, carbon implantation of preformed Si-tips has been used to improve wear properties. In this work, MD was used to simulate the nanoscale adhesion and tribological behavior between diamond, diamond-like carbon (DLC) surfaces and silicon, and silicon carbide tips. Work of adhesion values from the MD simulations with axisymmetric tips are compared to, and discussed within the context of, complementary AFM experiments where available, finite element simulations, and continuum mechanics-based analytical models. MD simulations show that the work of adhesion is sensitive to the identity of the contacting materials because they have inherent roughness differences. In addition, work of adhesion values obtained from continuum mechanics-based analytical models are consistently higher than values obtained using the atomic-force microscope, which are higher than the simulated values. A recently developed bond-order potential for C-, H-, and Si-containing systems was used to carry out these simulations. The novel aspects of this model will be discussed.

3:00pm **TR+AS+NS+SS-MoA4 Electronic Friction at the Atomic Scale: Conduction, Electrostatic and Magnetic Effects, Z. Fredricks, K.M. Stevens, J. Krim, North Carolina State University**

In the study of friction at the nanoscale, phononic, electrostatic, conduction electron and magnetic effects all contribute to the dissipation mechanisms [1,2]. Magnetic contributions are increasingly alluded to in current studies, but remain poorly characterized. We report here our observations magnetic friction for sliding adsorbed films on various magnetic films substrates in the presence and absence of an external field. Using a quartz crystal microbalance (QCM), we record the sliding friction of liquid monolayers of nitrogen, a diamagnetic material, as well as liquid oxygen, a paramagnetic material, on nickel alloy and graphene/nickel surfaces. In the prior literature, these systems have been reported to exhibit sensitivity to external fields. The work presented here compares and contrasts fundamental dissipation mechanisms in sliding adsorbed films [3] to studies performed by means of magnetic tip microscopy [1]. [1] I. Altfeder and J. Krim, J. Appl. Phys. (2012), [2] Highland et al., PRL (2006) [3] J. Krim, Advances in Physics, Vol. 61, Iss. 3, 155-323 (2012); Work supported by NSF DMR

3:40pm **TR+AS+NS+SS-MoA6 Chemical Origins of Interfacial Friction: Insights from Atomistic Simulations, I. Szlufarska, K. Huang, University of Wisconsin-Madison, Y. Liu, Massachusetts Institute of Technology** **INVITED**

While interfacial chemistry plays a critical role in frictional response of materials, understanding chemical changes that occur in sliding mechanical contacts has been challenging. Experimentally, the difficulty lies in the limited ability to characterize contacts *in situ* and typically chemical characterization of interfaces is carried out before or after sliding. Modeling and simulations can provide powerful insights into the chemistry of frictional contacts, however models that possess a high level of chemical fidelity are often limited to small system sizes and short simulation time scales. Here, we overcome this limitation by bringing together complementary simulations methods that range from *ab initio* calculations based on the density functional theory (DFT), large scale molecular dynamics (MD) simulations with reactive empirical potentials, and the kinetic Monte Carlo (kMC) technique. In this talk we will discuss examples of how these methodologies have been used to identify chemical origins of friction. One example is the discovery of mechanisms that underlie aging of silica in aqueous environments, which is of interest for multiple phenomena ranging from wafer bonding to shallow tectonic earthquakes. We have demonstrated that in the absence of deformation creep, aging of silica takes place by formation of interfacial siloxane bridges. We have discovered a new mechanism for interaction between these bridges and have shown that this interaction is critical to explain experimentally observed logarithmic dependence of aging on time. In addition, we will discuss our newly

develop theory that enables efficient and accurate calculations of friction at solid/liquid interfaces directly from MD simulations and that overcomes the typical time scale limitations of standard MD simulations. This theory has been validated for multiple types of surfaces and liquids and it can be used for design of chemical interfaces for applications in aqueous environments, such as nano- and micro-fluidics.

4:20pm **TR+AS+NS+SS-MoA8 The Relationship Between Molecular Contact Thermodynamics and Surface Contact Mechanics, N. Nikoogorgos, C.A. Hunter, G.J. Leggett, University of Sheffield, UK**

The atomic force microscope (AFM) has been used widely to study nanoscale tribological phenomena, but a unified model for the mechanics of the tip-sample interaction is lacking. Experimental data show that nanoscale friction depends strongly on interfacial chemistry, but these correlations are not explained adequately by existing models. Here we report measurements of interactions between hydrogen bond-forming molecules adsorbed onto solid surfaces and AFM tips. By making measurements in liquid mixtures, we demonstrate a quantitative correlation between the surface shear strength in a nanoscale contact and the free energy of solution-phase hydrogen bonding interactions, uniting classical contact mechanics with equilibrium thermodynamics. We demonstrate that the thermodynamics of intermolecular interactions may be determined quantitatively from nanoscale friction measurements. It has been found that the contact mechanics are best modeled by treating the friction force as the sum of a load-dependent term (attributed to "molecular plowing") and an area-dependent term attributed to shearing (adhesion). The relative contributions of plowing and shearing are determined by the coefficient of friction, μ , and the surface shear strength τ . The transition from adhesion- to load-determined friction is controlled by the solvation state of the surface: solvated surfaces represent a limiting case in which the shear term approaches zero, and the friction-load relationship is linear, while in other circumstances, the friction-load relationship is non-linear and consistent with Derjaguin-Muller-Toporov (DMT) mechanics. A striking correlation has been observed between the concentration-dependence of the association constant (K_a) for the formation of 1:1 hydrogen-bonded complexes and the pull-off force F_a and surface shear strength τ for the same molecules when one partner is immobilized by attachment to an AFM probe and the other is adsorbed to a surface. Analysis of the concentration-dependence of F_a and τ enables the prediction of K_a with remarkably high precision, indicating that for these hydrogen bonding systems, the tip-sample adhesion is dominated by the H-bond thermodynamics. For hydrocarbon surfaces, we have found that friction-load relationships are also fitted by DMT mechanics, and experimentally determined works of adhesion correlate closely with predictions from Lifshitz theory. For polymer brushes, a broader range of behavior is observed, but this may also be understood if the contact mechanics are modeled by treating the friction force as the sum of a load-dependent term and an area-dependent term attributed to shearing.

4:40pm **TR+AS+NS+SS-MoA9 Friction of a Thermally Activated Ensemble of Nanocontacts, P.V. Antonov, J.W.M. Frenken, Leiden University, Netherlands**

We report the first stages of an experiment to lower dry, unlubricated friction by use of a tailor-made nanostructure. In previous studies, we have demonstrated that random thermal fluctuations change the familiar, atomic stick-slip motion of the tip of a friction force microscope (FFM) into a thermal drifting motion, when these fluctuations are strong enough with respect to the barriers in the energy landscape. Based on a two-mass-two-spring model of an FFM [1], we know that these excitations are concentrated in the last nanometers of the tip, because of its extremely small mass and its flexibility. To achieve similar behavior in a macroscopic contact with an area well beyond that of the very specific tip-surface geometry of an FFM, we have shaped one of the two, macroscopic contacting surfaces in the form of a micro-fabricated array of Si nanopillars, each with a well-defined spring coefficient, equal to that of a standard FFM tip. This pattern can be regarded as a large multitude of FFM-like tips, each one exhibiting the thermal fluctuation motion that we identified as a lubricating effect in an FFM. Since the density of these asperities is high, the forces on each individual asperity are always low enough to keep its deformations completely elastic. We expect that each of the tip-like pillars will fluctuate independently under the load of a ball-shaped AFM tip and as a result of this, it should be possible to translate the entire, multi-asperity contact by an extremely low lateral force. This approach should lead not only to low friction, but also to a characteristic, strong dependence of the sliding motion and the friction force on temperature and on sliding velocity. We will also explore how the thermal fluctuation behavior changes as a function of the dynamic properties of the individual nanopillars and how it evolves when we scale up the total number of asperities that are simultaneously in contact.

[1] S.Yu. Krylov, J.W.M. Frenken, *Phys. Rev. B* **80**, 235435 (2009).

5:00pm **TR+AS+NS+SS-MoA10 Nanoprobing of Friction and Charge Transport Properties of Vanadium Dioxide under the Metal-Insulator Transition**, *J.H. Kim*, KAIST, Republic of Korea, *D. Fu, K. Wang, J. Wu*, University of California, Berkeley, *J.Y. Park*, KAIST, Republic of Korea

The nanomechanical and electrical properties of vanadium dioxide (VO₂) thin films across thermal-driven phase transitions were investigated using ultra-high vacuum atomic force microscopy. VO₂ thin films were deposited on an n-type, heavily-doped silicon wafer by pulsed laser deposition. X-ray diffraction revealed textured polycrystalline structures in the monoclinic phase with preferential orientations in the (100) and (120) planes. Friction and conductance mapping were obtained as a function of temperature across the metal-insulator transition. When below the transition temperature, the friction decreased, whereas the friction increased markedly when above the transition temperature. This peculiar result can be attributed to the combined effects of thermally-activated tip sliding, associated with phonon at the insulating phase, and electronic contributions in the metallic phase.

5:20pm **TR+AS+NS+SS-MoA11 Non-Uniform Friction-Area Dependency for Antimony Oxide Surfaces Sliding on Graphite**, *M.Z. Baykara*, Bilkent University, Turkey, *C. Ritter*, Humboldt Universität zu Berlin, Germany, *B. Stegemann*, HTW Berlin – University of Applied Sciences, Germany, *M. Heyde*, Fritz-Haber-Institut der Max-Planck-Gesellschaft, Germany, *K. Rademann*, Humboldt Universität zu Berlin, Germany, *J. Schroers, U.D. Schwarz*, Yale University

We present frictional measurements involving controlled lateral manipulation of antimony nanoparticles on graphite featuring atomically smooth particle-substrate interfaces via tapping- and contact-mode atomic force microscopy. As expected from earlier studies, the power required for lateral manipulation as well as the frictional forces recorded during the manipulation events exhibit a linear dependence on contact area over a wide size range from 2000 nm² to 120,000 nm². However, we observe a significant and abrupt increase in frictional force and dissipated power per contact area at a value of about 20,000 nm², coinciding with a phase transition from amorphous to crystalline within the antimony particles. Our results suggest that variations in the structural arrangement and stoichiometry of antimony oxide at the interface between the particles and the substrate may be responsible for the observed effect.

Vacuum Technology

Room: 202 C - Session VT-MoA

Dynamic Vacuum Processes and Outgassing

Moderator: J.A. Fedchak, National Institute of Standards and Technology (NIST)

2:40pm **VT-MoA3 Modeling and Simulation of Fast Flows in the Vacuum Regime**, *S. Pantazis*, Physikalisch-Technische Bundesanstalt (PTB), Germany **INVITED**

It is well known that the Navier-Stokes-Fourier formulation may provide inaccurate solutions for low pressure gas flows. On the other hand, the numerical solution of the Boltzmann equation poses up to date great challenges in problems of engineering interest. Several modeling techniques have been developed to provide results in corresponding ranges of the vacuum regime. Among them is the Direct Simulation Monte Carlo (DSMC) method, which is usually the method of choice for the simulation of fast flows due to its simplicity and the fact that it can accurately reproduce solutions of the Boltzmann equation in the whole range of the Knudsen number. Problems arise when the density levels increase, as the computational effort may reach prohibitively high levels. For the simulation of such flows, a method able to deal with locally rarefied flows may be required if the problem is not susceptible to modeling simplifications without significant sacrifices in accuracy. Hybrid particle-continuum algorithms are often used as viable alternatives for this purpose. The flow domain is decomposed in different regions based on appropriate criteria, such as the local Knudsen number, and treated either by a continuum or a particle method. However, such methods are less frequently encountered in problems of unsteady nature due to modeling difficulties.

An efficient implementation of a hybrid simulation algorithm is presented. The characteristics of such algorithms, such as the coupling at the interface between the two methods, as well as computational features, such as parallel computing capabilities and arbitrary geometry handling, are explained. The main differences with other works in the literature are highlighted. The validation is performed through comparison with simplified but relevant cases of fast flows in the vacuum regime, such as shock tube and orifice flow, and the benefits of the approach as opposed to pure DSMC are commented. Furthermore, a challenging application of the code on a practical problem is discussed. A dynamic vacuum expansion

calibration facility is studied, constructed in PTB to study the response time of vacuum gauges to rapid pressure changes, such as in the control of load locks in industrial applications. The pressure may change from 100 kPa to 100 Pa in less than 1 s by expansion to a vessel with a larger volume through a fast opening gate DN40 valve. Experiments have been performed with capacitance diaphragm gauges with improved electronics, leading to an update time of 0.7 ms. The modeling approximations are explained and measurements are compared with simulation results.

3:40pm **VT-MoA6 Capacitance Diaphragm Gauges with Sub-Millisecond Measuring Rate**, *Ch. Berg, M. Wuest, F. Mullis, H. Hanselmann*, INFICON Ltd, Liechtenstein

Capacitance Diaphragm Gauges (CDG) are used in many pressure control applications in industry. In a typical application the CDG pressure signal is used in the butterfly valve controller to regulate the pressure in a vacuum chamber. The control loop performance is often limited by the measuring rate of the vacuum gauge. Currently the fastest commercially available CDG has a time constant of about 8 ms, while most CDGs have rates between 20 and 30 ms. In this talk we will present a CDG that can deliver a new pressure value in less than 1 ms.

4:00pm **VT-MoA7 Measuring Static Outgassing Pressures at Elevated Temperatures**, *L. Wang*, Los Alamos National Laboratory

In our material thermal aging studies, we need to accurately measure pressure of gas evolved from the material at elevated temperatures to reliably measure the quantity of total gas released. MKS 121A absolute capacitance manometer was selected for this in-situ pressure measurement because its electronic components are contained in a separated housing that can be located outside of the heating chamber. In this configuration, the sensor and the connecting cable can operate at an elevated temperature up to 150°C. To determine the performance of this type of gauges, pressure measurements were conducted with seven MKS 121A sensors of three different ranges (10, 100, and 1000 torr) in an oven at 25, 55, 80, and 145°C, and the measurements were compared with two reference pressure gauges (MKS 690A) located outside of the oven. The performance test results, the temperature effects on zero drift and pressure error, and the pressure measurement results of a static outgassing run with three materials at 145°C will be presented and discussed.

4:20pm **VT-MoA8 Gas Permeation Measurements on Low Temperature Cofired Ceramics**, *R.S. Goeke, S.X. Dai, R.K. Grubbs*, Sandia National Laboratories

Commercial low temperature cofired ceramic (LTCC) technology is established in microelectronics and microsystems packaging, multichip and radio frequency (RF) modules, and sensors. The ability to combine structural considerations with embedded traces and components using laminated glass-ceramic tapes has created solutions to unconventional packaging requirements of micro-electro-mechanical systems (MEMS) devices. Many MEMS devices such as resonators are very sensitive to pressure and require packaging in a vacuum environment. Attaining and maintaining desirable pressure levels in sealed vacuum packages requires knowledge of the permeation characteristics of the vacuum envelope and the sealing materials.

An experimental system to measure the time dependent gas permeation through LTCC at temperatures from room temperature to 500°C has been developed. This system utilizes a membrane technique in which a gas is allowed to permeate through a test sample, held at a constant temperature, into a high vacuum chamber where it is detected using a mass spectrometer. The gas permeation value is determined from the steady state gas flux through the sample. The gas diffusivity and solubility in the material were calculated using data from the time dependent approach to the steady state condition. The gas-solid permeation data for helium and hydrogen through DuPont 951 and 9K7 LTCC will be presented and compared to the permeation through other common vacuum envelope materials such as glasses and high-purity alumina ceramics. Application of the permeation data to the prediction of vacuum levels inside hermetic LTCC packaged devices will be discussed. This data can further be utilized in designs to create LTCC packages that meet specific pressure/time operating requirements.

Sandia National Laboratories is a multi-program laboratory managed and operated by Sandia Corporation, a wholly owned subsidiary of Lockheed Martin Corporation, for the U.S. Department of Energy's National Nuclear Security Administration under contract DE-AC04-94AL85000

Tuesday Morning, October 29, 2013

Actinides and Rare Earths Focus Topic
Room: 102 C - Session AC+AS+SS-TuM

The Surface Science of Actinides and Rare Earths
Moderator: D. Shuh, Lawrence Berkeley National
Laboratory

8:00am **AC+AS+SS-TuM1 From Berkeley to Bristol: Defect Structures in Actinide Oxides, G.C. Allen, University of Bristol, UK**
INVITED

The first generation of British gas-cooled reactors used natural uranium metal as fuel but UO₂ is far and away the most important fuel in use today. It is in fact the first in a complex family of oxides, initially based on the fluorite UO₂ unit cell (U₄O₉ and U₃O₇) but giving way to layered-type oxides as the O/U ratio increases (U₃O₈ and UO₃). Oxidation in UO₂ is known to occur via accumulation of point oxygen interstitials and defect aggregates such as Willis, cuboctahedral and split-interstitial clusters. Spectroscopic evidence is used to demonstrate that the link between defect clusters and the U₄O₉ and U₃O₇ structures can be rationalised in terms of multiple Willis, cuboctahedral and split-interstitial clusters. DFT models have been used to examine the stability of different defect clusters in UO₂ supercells. The formation energy of each cluster is calculated along with the variation of their concentrations with increasing the temperature. All interstitial clusters are found to be charge compensated by U⁵⁺ ions, suggesting this is the highest uranium oxidation state reached amongst the fluorite based structure.

8:40am **AC+AS+SS-TuM3 Covalent Interactions in Metal Oxides, P.S. Bagus, University of North Texas, E.S. Ilton, Pacific Northwest National Laboratory, C.J. Nelin, Consultant**

The covalent character of ionic metal compounds, in particular oxides, may lead to substantial departures from nominal oxidation states. [1, 2] Since this covalent character changes the effective charge of the cation, it contributes to the chemical and physical properties of these compounds. We present a new and novel method of determining the degree of the covalent mixing by projection of cation and ligand orbitals [2, 3] on the total wavefunctions for clusters used to model the electronic structure of these compounds. An important advantage of this method is that it provides estimates of the uncertainties of the assignments of effective charges to the cations and anions. Such estimates of the uncertainty directly reflect the overlap of cation and anion orbitals and, hence, their potential for chemical bonding; estimates of the uncertainty of charge assignments are not generally available. There is evidence that the properties of the spectra from X-Ray photoemission spectroscopy, XPS, [2] and X-Ray Adsorption spectroscopy, XAS, [4] reflect the extent of the covalent mixing of the cation and anion orbitals. We will consider how the covalent character changes between the initial and final state configurations in these spectroscopies, which arise from the screening of the core-hole, affect the interpretation of the core-level spectroscopies.

1. P. S. Bagus and E. S. Ilton, Phys. Rev. B **73**, 155110 (2006).
2. P. S. Bagus, E. S. Ilton, and C. J. Nelin, Surf. Sci. Rep. (in press).
3. C. J. Nelin, P. S. Bagus, and M. R. Philpott, J. Chem. Phys. **87**, 2170 (1987).
4. S. G. Minasian, J. M. Keith, E. R. Batista, K. S. Boland, D. L. Clark, S. D. Conradson, S. A. Kozimor, R. L. Martin, D. E. Schwarz, D. K. Shuh, G. L. Wagner, M. P. Wilkerson, L. E. Wolfsberg, and P. Yang, J. Am. Chem. Soc. **134**, 5586 (2012).

9:00am **AC+AS+SS-TuM4 Historical Perspective on Studies of the Surface Reactivity of Actinides at the AWE, UK, D.A. Geeson, AWE, UK**
INVITED

Actinides play an important role in the business of the AWE.

The corrosion behaviour of uranium- and plutonium-based systems is of particular interest with a view to considering material stability during long-term storage as well as aspects of surface segregation and fundamental electronic structure.

The historical use of modern surface science techniques to investigate many aspects of the actinide gas-solid interface is reviewed with emphasis on the development of in-house capabilities and their adaptation for use in a nuclear environment studying highly hazardous materials. Key conclusions from several aspects of corrosion phenomena are presented together with strategies for continuing studies. Examples are drawn from: the corrosion of uranium in dry and moist atmospheres, the mechanism of initiation of

hydriding on uranium surfaces, the oxidation of plutonium alloys, americium segregation in plutonium and inverse photoemission studies of actinide surfaces.

AWE's engagement with the wider UK and international community, as part of a broad strategy to collaboratively support our work in areas of more novel aspects of actinide surface phenomena, is described.

The discussion concludes with consideration of the future direction of studies at AWE supported by the provision of enhanced capabilities to explore surface and bulk phenomena.

© British Crown Owned Copyright 2013/AWE

11:00am **AC+AS+SS-TuM10 Exploring Plutonium Electronic Structure Using a Unique Photoemission Capability, J.J. Joyce, Los Alamos National Laboratory**
INVITED

The understanding of complex materials has made remarkable advances in recent years. Much of this understanding has been realized through new spectroscopy capabilities at synchrotron facilities. While the vast majority of materials can take advantage of public synchrotrons, transuranic materials are excluded when multiple containment barriers are incompatible with the chosen spectroscopy. Photoemission requires no physical barrier between photons, sample surface and the electron analyzer, thus photoemission on Pu materials is generally not allowed at public synchrotrons.

The Laser Plasma Light Source has been developed at Los Alamos for transuranic photoemission. Using several different variants of photoemission we have explored a range of Pu materials which has led to a significant improvement in our understanding of transuranic electronic structure. Examples of these successes will be given along with details of the unique facility. Using the capabilities of our transuranic photoemission system we exploit opportunities in angle-resolved photoemission (ARPES) providing insight into the details of both the energy and crystal momentum for a material. Additional information is obtained using tunable photons used to isolate the 5f electron contribution to the valence electronic structure. Between ARPES and tunable photoemission, we construct a fairly detailed picture of the bonding and hybridization for transuranic materials. By adding temperature-dependent photoemission to the experimental tools, we cross over phase transition boundaries as well as quantify electron-phonon coupling. We also have the capability for 1.5 and 3 keV core-level spectroscopy using a monochromatized x-ray source.

By combining the above photoemission tools with a variety of surface preparation capabilities including cleaving, laser ablation, and thermal desorption, we have a flexible photoemission facility that provides unique insight into the electronic structure of transuranic materials. We will show photoemission results for PuCoGa₅, PuCoIn₅, PuO₂, PuTe and Pu metal that span the range of materials from Mott insulators to heavy fermion superconductors. The latest developments in Pu electronic structure combine a multivalent configuration for Pu with ongoing efforts to quantify the localized/delocalized 5f electron boundary. We will discuss details of Pu electronic structure in light of both valence configurations and localization.

Work supported by the U.S. DOE Basic Energy Science, Materials Sciences and Engineering; LANL LDRD program, and Science Campaign 2.

Applied Surface Science
Room: 204 - Session AS-TuM

Developments in Electron Spectroscopies for Non-Ideal Samples

Moderator: J.C. Woicik, National Institute of Standards and Technology (NIST), D.R. Baer, Pacific Northwest National Laboratory

8:00am **AS-TuM1 Chemical Analysis of Surfaces and Ultra-thin Films: At the Forefront of XPS Analytical Methods, A. Rossi, Università degli Studi di Cagliari and ETH Zurich, Italy**
INVITED

For decades it has been well known that the presence of layers of nanometer thickness can dramatically change the functional properties of a material, i.e. the corrosion resistance in aggressive environments, the wear and friction properties and more recently the leaching of minerals, the protein resistance and the biocompatibility of an implant.

Recent advances in x-ray photoelectron spectroscopy (XPS) enable examination of surface-chemical properties with far greater spatial

resolution and accuracy than ever before, allowing the development of analytical strategies for understanding the mechanisms of surface-chemical reactions. These results offer unique possibilities for tailoring the surface properties of materials and for designing more sustainable and environmentally benign chemicals.

This presentation will focus on the most recent results: some of them are unpublished and others are already published within the framework of collaborations with other groups.

From XPS-spectra to thickness and composition of nanostructured materials and of solutions

One of the unique characteristics of XPS is its capability of providing information on the thickness and composition of materials with layers of nanometer thickness in a non-destructive way. In this presentation, I will discuss the results of the research performed with the aim of understanding films only a few nanometers thick. Topics are the chemical-state identification of different elements and the ordering of molecules within the films. Examples from our research on multi-component alloys, including 'real systems' such as steels, self-assembled monolayers (SAM) and organically functionalized bio-surfaces will be presented. The mathematical algorithms will be critically evaluated for practical applications.

Very recent angular-resolved XPS results of tetraethyl-ammonium bromide (TEABr) in polyethylene glycol (PEG) 200 are shown to demonstrate the spatial distribution at the vacuum-solution interface.

Imaging XPS: the importance of visualization of chemical information

Imaging XPS is one of the most powerful tools that are available nowadays for investigating the surface of heterogeneous samples. Chemical maps recorded on steel samples after tribological testing at pressures of some GPa and up to 150°C are processed with principal component analysis, allowing the identification of polyphosphates with different chain lengths and the reconstruction of compositional and thickness maps. The relevance of these results for the development of new, more environmentally compatible and sustainable anti-wear and friction modifier additives will be discussed.

8:40am **AS-TuM3 Sample-Morphology Effects on XPS Peak Intensities: Estimation of Detection Limits**, C.J. Powell, National Institute of Standards and Technology (NIST), W.S.M. Werner, W. Smekal, Technical University of Vienna, Austria

It has long been known that variations in sample morphology can have drastic effects on photoelectron intensities in XPS and thus on the results of quantitative analyses [1]. While detection limits for minor species in homogeneous samples have often been estimated to be between 0.1 and 1 atomic percent, no estimates are generally available for inhomogeneous samples. In general, detection limits depend on the detectability of a particular peak (which depends on the peak-detection method, the measurement statistics, peak identification, and interpretation in relation to the known or assumed sample morphology).

We have used the NIST Database for the Simulation of Electron Spectra for Surface Analysis (SESSA) [2,3] to estimate detection limits for buried thin films. Test simulations have been performed for thin W films of varying thicknesses buried at varying depths in a Ru matrix. For these simulations, the X-rays were incident normally on the sample and the photoelectrons were detected at an emission angle of 55° with respect to the sample normal. We initially established that the W 4d_{5/2} peak intensity would likely be detectable in a RuW_{0.001} alloy (for which the ratio of the W 4d_{5/2} peak intensity to the Ru 3d_{5/2} peak intensity was 1.25×10^{-3}). Simulations were then performed with a thin W film on a Ru substrate and for thin W films at selected depths in the Ru matrix. In each case, we varied the W film thickness to obtain the same W 4d_{5/2} peak intensity (within 1%) as for the RuW_{0.001} alloy. We find that the defined detection limit in this example varies by over three orders of magnitude for a thin W surface film to a W film buried to depths up to six times the inelastic mean free path.

[1] S. Tougaard, J. Vac. Sci. Technol. A 14, 1415 (1996).

[2] NIST SRD 100, Version 1.3 (2011); <http://www.nist.gov/srd/nist100.cfm>.

[3] W. Smekal, W. S. M. Werner, and C. J. Powell, Surf. Interface Anal. 37, 1059 (2005).

9:00am **AS-TuM4 The Active-Background Method in XPS Data Peak-fitting**, A. Herrera-Gomez, CINVESTAV-Queretaro, Mexico

Quantifying the intensity of peaks in x-ray photoelectron spectroscopy (XPS) data requires the proper modeling of the background signal. This is traditionally accomplished by first assessing the background intensity and then peak-fitting the backgroundless spectrum. One of the main disadvantages of the traditional or static method is that it usually requires forcing the background to pass through two user-defined points, one at each side of the spectrum. In contrast, with the active-background method the

intensity and shape of the background are defined during the peak-fitting process. Other advantages of the active method are the following:

- The area of the peaks is frequently underestimated when the static method is employed. This is because the operator typically cannot guarantee that there is no appreciable contribution to the signal at the two chosen points; instead, the operator has to assume it.[1].
- The relative contributions of the Gaussian and Lorentzian widths to the FWHM of the peaks are dependent on the fitting energy range when the static method is employed.
- The traditional (static) iterative Shirley-Sherwood background algorithm might fail for some types of spectra. This is not the case for the Shirley Sherwood background when the active method is employed. Another issue is that it takes longer to converge, that is, more iterations are required with the static than with the active method.
- The active treatment allows for simultaneously applying a combination of background types.
- When the background is subtracted before peak-fitting, the Poisson-character of the data is no longer applicable, so the uncertainty of the peak parameters cannot be calculated employing the covariant matrix method.
- The operator might stop thinking about about the background once it has been subtracted, which can lead to errors in the static method. In the active method, the changing role of the background is accounted for as the operator considers other options during peak-fitting.
- Last, but not least, the active method always provides better fits than the static method.

The importance of implementing the active background had been discussed in other reports.[2,3] In this talk some practical examples of the application of the active-background method are fully discussed.

[1] J. Muñoz-Flores, A. Herrera-Gomez. "Underestimation of the peak areas for the static and active background methods in XPS data peak-fitting." To be submitted.

[2] A.M. Salvi and J.E. Castle. J. Elec. Spec. Rel. Phen. 95 (1988) 45.

[3] J. Vegh. J. Elec. Spec. Rel. Phen. 46 (1988) 411.

9:20am **AS-TuM5 Angle-Resolved XPS of Compound Semiconductors: A Straightforward Route beyond the "Relative Depth" Plot**, A. Barlow, P. Cumpson, NEXUS, Newcastle University, UK

There is an ever-present need to characterise surfaces and interfaces with increasing sensitivity and precision. One frequently-used tool to do this is the "Relative Depth Plot" (RDP) that can be derived very easily from Angle-Resolved XPS spectra. Despite the name, this does *not* plot relative depth, but relative *attenuation* of the signal electrons. For peaks widely-separated in energy this will lead to errors, so that even the order of layers, not just their depth, is incorrect. This may be obvious to XPS practitioners, but to those collaborating with them, or those new to XPS such as many of our clients, the name "Relative Depth Plot" plot can be extremely misleading.

Compound semiconductors are a class of specimen that is ideal for illustrating these issues. Available in good quality they have known compositions, low roughness and have a high degree of homogeneity, so that the composition as a function of depth is well-known. We have analysed a wide range of compound semiconductors including ZnSe, InAs, InSb, GaAs, GaP and CdTe using our parallel acquisition Angle-Resolved XPS instrument, using an argon gas cluster ion beam (GCIB) to clean these surfaces without damage. We present the results of applying RDP, Stratification[1], and some variants of these methods.

We develop a very simple correction factor that greatly improves (but does not completely eliminate) the RDP problem and which can be applied automatically. This is particularly valuable for many semiconductor materials that are of industrial significance. Understanding the nature of the surface of an active material, or the interface between two active materials, such as in a junction or at the surface of a photo-active sensor, is crucial for novel device development and advancement. It is even more important to interpret Angle-Resolved XPS spectra correctly in cases where layer order is genuinely unknown, as is often the case in biological problems, for example.

Finally, some investigations of sputter depth profiling of these materials using novel ion beam technology, argon gas clusters, will be discussed.

[1] M P Seah et al, Surf and Interface Anal. 21 (1994) 336–341

9:40am **AS-TuM6 The Effect of Electronic Relaxation on the First-Principles Prediction of XPS Spectra**, K. Artyushkova, S. Akbir, University of New Mexico, B. Kiefer, New Mexico State University
Catalysts find use in many scientific and engineering applications. One of the recurring themes in this context is the quest for the design of suitable

catalysts with improved performance. A prerequisite for the rational design is the identification of the nature of the catalytic site(s). XPS is a widely used experimental technique for this purpose. However, the unique identification of structural motifs from XPS observations remains challenging. First-principles computations can provide the missing link by predicting core-level shifts for candidate structural motifs of the catalytic sites. Here we focus on carbon supported TM-Nx (TM=Fe, Co) electrocatalysts, a class of ORR electrocatalysts that continues to attract significant attention for applications in fuel cells. Using density-functional-theory (DFT) we predict the Fe2p and N1s core level shifts for carbon embedded candidate TM-Nx (TM=Fe, Co; x=1-4) motifs. In particular we will discuss single versus multi-electron excitations, the effect of electronic relaxation in the final state approximation and provide a comparison our experimental observations.

10:40am **AS-TuM9 XPS for Characterisation of Optical and Electronic Devices under Operation**, *S. Suzer*, Bilkent University, Turkey
A noncontact chemical and electrical measurement technique of XPS is performed to investigate a number of optical and electronic devices under operation. The main objective of the technique is to trace chemical and location specified surface potential variations as shifts of the XPS peak positions under operating conditions. Devices consisting of single and multi p-n junctions made out of Si, GaN and Graphene have been investigated under light illumination and/or under forward as well as reverse bias. The main advantage of the technique is its ability to assess element-specific surface electrical potentials of devices under operation based on the energy deviation of core level peaks in surface domains/structures. Detection of the variations in electrical potentials and especially their responses to the energy of the illuminating source under operation is also shown to be capable of detecting, locating, and identifying the chemical nature of structural and other types of defects.

11:00am **AS-TuM10 Practical Auger Spectroscopy**, *M.D. Johnson*, Hewlett Packard, *D.F. Paul*, Physical Electronics Inc., *W.F. Stickle*, Hewlett Packard, *J.F. Moulder*, Physical Electronics Inc.

Auger spectroscopy is a mainstay in many analytical laboratories where high spatial resolution and compositional analysis are necessary for problem solving. Two related questions often come up during an analysis. The first question has to do with quantification and is there a way to sort out the different chemistries observed on a sample, either spatially in x or y or as a function of depth. The second analytical question has to do with detection of trace amounts of a material especially in the presence of peak overlap. Various approaches to these practical questions can be used such refining relative sensitivity factors and the application of numerical methods. Further, the use of high spectral resolution data may increase the ability to detect trace amounts of a material in a complex matrix as well as to increase the detection limits of the analysis. These questions are explored using practical systems of silicon, silicon dioxide, silicon nitride and silicon carbide where the Si KLL peaks shift and change lines shape. Practical aspects of detection limits are illustrated in the examination of trace amounts of silicon and/or hafnium in a tantalum oxide matrix where there is overlap between the Si KLL, Ta MNN series and the Hf MNN series Auger transitions.

11:20am **AS-TuM11 Angle-resolved Photoemission from Curved Surfaces**, *J.E. Ortega*, Universidad del País Vasco, Spain, *F.M. Schiller*, *J. Lobo-Checa*, CSIC, Spain, *A. Mugarza*, Institut Catala de Nanotecnologia, Spain

Surfaces that are vicinal to high symmetry directions have frequently demonstrated their enormous potential for surface science research and applications. Vicinal surfaces characterized by arrays of atomic steps exhibit distinct chemical and physical properties, but they are also useful as templates for nanostructure growth, and, more generally, to transmit uniaxial and/or chiral symmetry to epitaxial layers. In this context, curved surfaces with a smooth variation of the vicinal angle, i.e., a tunable step lattice constant, allow a straightforward and rational investigation of all physical-chemical phenomena related to the presence of atomic steps. In particular, we have used curved noble metal surfaces to investigate the electron scattering problem at atomic steps on bare surfaces, monolayers and thin films, using Angle-resolved photoemission and micron-size light spots that are scanned over the surface. I will discuss through a number of cases the limits and advantages of using such curved surface approach for ARPES studies.

11:40am **AS-TuM12 Uncovering the Mechanism of Bioleaching of Enargite by XPS**, *M. Fantauzzi*, *B. Elsener*, *G. Rossi*, *A. Rossi*, Università degli Studi di Cagliari, Italy

Sulfide minerals biooxidation processes (oxidation mediated by microorganisms) are particularly suitable for gold recovery from low-grade

ores and are more environmentally friendly compared to conventional physicochemical mineral beneficiation processes. Oxidative dissolution mediated by microorganisms besides being of economic interest is environmentally significant since the latter usually occur in AMD (Acid Mine Drainage) and play a decisive role in the release of toxic elements such as Arsenic into the environment. According to the integral model for bioleaching [1], Fe (III) and H⁺ ions control sulfides dissolution and the role of bacteria is to catalyze Fe (III) and H⁺ regeneration and to concentrate those oxidants at the mineral surfaces by extra-cellular polymeric substances (EPS). EPS is produced by the living bacteria and forms kind of a bridge between the cell and the mineral surface. As the EPS layer is able to complex iron (III) ions into glucuronic acid-iron complexes, the actual concentration of iron (III) ions on the mineral surface may be higher than their concentration in the surrounding solution. This work aims to provide surface analytical and electrochemical evidences of the dissolution mechanism of enargite (Cu₃AsS₄). All experiments were carried out in presence of a strain of *Acidithiobacillus ferrooxidans* adapted to arsenic and of iron ranging from 10⁻⁵ M to 10⁻³ M at pH 2. The electrochemical potential was found to increase explaining the higher dissolution rate observed in the presence of bacteria. The enargite solubility was strongly enhanced by *A. ferrooxidans*: solution analyses showed that Cu and As dissolved stoichiometrically with a dissolution rate of about 3 - 5 times higher compared to the abiotic control.

The XPS C1s, O1s, N1s and P2p regions acquired on bacterial cells and on bioleached mineral grains were processed so that the surface composition of the EPS layer was obtained. The fraction of proteins, hydrocarbon and polysaccharides of the EPS was estimated and monitored for a period of time up to 157 days. Also the iron signal initially absent was observed after bioleaching.

The average thickness of the EPS layer at the mineral surfaces, as well as the protein content, increases with bioleaching time from 1 nm (after 44 days) to 2.5 nm (after 157 days) whereas the hydrocarbons and polysaccharides amount decrease with leaching time. These results are thus demonstrating the role of EPS in the sulphide dissolution and substantiate the model for bioleaching.

1. W. Sand, T. Gehrke, P. Josza, A. Schipper, Hydrometallurgy 59 (2001) 159 - 175

Biomaterial Interfaces

Room: 201 B - Session BI+AS+BA+NL-TuM

Biointerface, Energy and Environmental Applications of QCM

Moderator: L. Hanley, University of Illinois at Chicago

8:00am **BI+AS+BA+NL-TuM1 QCM-D for Energy and Environmental Applications**, *B.H. Kasemo*, Chalmers University of Technology, Sweden **INVITED**

QCM-D has over the past ca. 15 years matured to a measurement technique with a manifold of applications for liquid or gas phase applications. "D" stands for *dissipation* or damping of the sensor oscillation. It yields new information about sample visco-elastic properties, in addition to the mass changes at the ng/cm² level obtained from the QCM frequency shift. New information is obtained when the overlayer or film that is studied, causes significant energy dissipation. This is e.g. the case with viscous or visco-elastic films and molecular adlayers. In such cases the two independent quantities, the frequency shift Δf and the dissipation change ΔD , via modeling, allow unique new information to be extracted from the measurements, compared to conventional QCM. In addition, the magnitude of ΔD provides an immediate hint if the Sauerbrey relation, converting Δf to a proportional change in mass, is applicable or not. Major application areas of QCM-D in the past and currently are biomolecule adsorption on surfaces, e.g. on medical implant materials, supported lipid bilayers mimicking cell membranes, polyelectrolytes e.g. layer-by-layer growth, polymer coatings and their curing and phase changes, and more recently cell and bacterial studies. Well over 1200 QCM-D publications have been produced in these areas, cited over 15 000 times. More recently studies related to applications in the energy and environmental areas have rapidly increased. Energy technology examples include solar cells (dye impregnation of DSSC), fuel cell electrode corrosion, studies related to fossil fuel properties and processes, hydrogen storage and CO₂ capture/sorption. In the environmental area many applications relate to nanoparticle safety and toxicity, e.g. measuring (surface) affinities between NPs and other materials or agglomeration between NPs. Yet another growing area is to use supported lipid membranes as up-stream model and screening systems, mimicking cell membranes, for testing of NP affinity to such membranes.

The method is also used for other aspects of waste water cleaning, such as measuring affinities to filtering materials and membranes of heavy metal ions and other impurities.

9:00am **BI+AS+BA+NL-TuM4 Accounting for Unintended Binding Events in the Analysis of Quartz Crystal Microbalance Kinetic Data**, G. Heller, T. Zwang, M. Sazinsky, A. Radunskaya, M.S. Johal, Pomona College

Previous methods for analyzing protein-ligand binding events using the Quartz Crystal Microbalance with Dissipation Monitoring (QCM-D) fail to account for unintended binding that inevitably occurs during surface measurements and obscure kinetic information. In this talk, I present a system of differential equations that accounts for both reversible and irreversible unintended interactions. This model is tested on three well-characterized protein-ligand systems, each of which has different features, to establish the feasibility of using the QCM-D for protein binding analysis. The first system presented is the binding of hemin to human serum albumin. The second is the binding of Fe (III) 2,5-dihydroxybenzoic acid complex to neutrophil gelatinase-associated lipocalin tagged with glutathione S-transferase. The third system presented is the interaction of caffeine and bovine serum albumin. Characteristics of the QCM-D binding data for these three systems that are inconsistent with previous QCM-D kinetic models are 1) a non-constant deposition rate in the association phase, 2) a non-zero mass near the steady state of the rinse phase, 3) a non-linear dependence on ligand concentration, and 4) a non-constant ligand concentration for runs lasting short periods of time. Our model accounts for these factors and demonstrates the feasibility of using QCM-D to extract kinetic information and accurately determine affinity constants (K_d) for protein-ligand complexes.

9:20am **BI+AS+BA+NL-TuM5 Silica Nanoparticle – Lipid Membrane Interaction Studies Towards Nano(Q)SAR?**, L. De Battice, R. Frost, Chalmers University of Technology, Sweden, A. Sundblom, M. Persson, AkzoNobel PPC, Sweden, M. Wallin, J. Sturve, University of Gothenburg, Sweden, S. Svedhem, Chalmers University of Technology, Sweden

To improve on the performance of silica-based nanomaterials, and to reduce environmental and health risks related to this development, it is important to learn about how engineered nanomaterials interact with e.g. biomolecules and biological barriers. We are also interested in the development of a generic screening methodology for nanoparticles, and to identify nanoparticle features which are likely to lead to effects in cells. The present results have been obtained with a set of five silica nanoparticles, four of which were spherical (about 20 nm in diameter) and one of which had an elongated shape (roughly 4 x 20 nm). Size and zeta potential measurements were performed, and the adsorption profiles for the nanoparticles when interacting with each of four model lipid membranes of different composition and net charge were monitored in real time using the quartz crystal microbalance with dissipation monitoring (QCM-D). We found clear differences in adsorption profiles on the model membranes with respect to surface coating, and particle shape. These results were compared to the results obtained when exposing frog cells to the same particles, using a conventional assay detecting cellular damage and cytotoxicity (through cell lactate dehydrogenase (LDH) release) and as well in experiments where the function of frog cells cultured on QCM-D sensors was studied by QCM-D (the method is published in Frost et al., Analytical Biochemistry, in press). In general, there were small effects on the cells.

The results will be discussed in the perspective of establishing (Q)SAR for nanoparticles.

9:40am **BI+AS+BA+NL-TuM6 Using Real-Time Acoustical Sensing by QCM-D to follow Dynamic Processes in Live Cell Morphology and Cell-Surface Interactions**, E. Nilebäck, Biolin Scientific, Sweden, N. Tymchenko, A. Kunze, Chalmers University of Technology, Sweden, L. Enochson, University of Gothenburg, Sweden, P. Wallin, J. Gold, S. Svedhem, Chalmers University of Technology, Sweden, A. Lindahl, University of Gothenburg, Sweden

The mechanical properties and morphology of living cells are dynamic and regulated by cell signaling pathways that can be triggered by both external and internal stimuli. The dynamic nature of these cellular shape changes leaves a great potential for real-time techniques to reveal new time-resolved information in addition to microscopy methods based on fluorescence that are typically end-point measurements. By using quartz crystal microbalance with dissipation monitoring (QCM-D), the nano-mechanical properties at the cell-surface interface can be studied. How the cells interact with the surface greatly influences the QCM-D response, particularly at cell adhesion and when the cells undergo morphological changes due to internal or external stimuli.

To explore the potential of acoustically sensing the cell-surface interface in real-time, we have used QCM-D as the main technique in several cell studies:

i) Changes in cell morphology were studied simultaneously by QCM-D and light microscopy as 3T3 and human derived fibroblasts were subjected to the actin disrupting agent cytochalasin D that depolymerizes actin in the cytoskeleton. This resulted in a dramatic change in cell morphology that was reversible upon rinsing and could repeatedly be detected as significant changes in the energy dissipation. [1]

ii) Cell adhesion and cell-surface interactions were studied for human derived chondrocytes as they were subjected to well-defined layers of the glycosaminoglycan (GAG) hyaluronan (HA). HA is present in e.g. extra cellular matrix of cartilage and the chondrocytes could be seen in the QCM-D signal to degrade the GAG layer in 2 hours.

iii) Cell adhesion and fixation studies of 3T3 fibroblasts were performed on silicon dioxide coated surfaces with and without a coating of serum proteins. This revealed that the protein layer greatly affected the QCM-D response from the cells. The later fixation by formaldehyde was performed *in situ* and from the QCM-D data it was shown that the viscoelastic behavior of the cells was to a large extent retained after fixation.

1. Tymchenko, N., Nilebäck, E. et al., *Reversible Changes in Cell Morphology due to Cytoskeletal Rearrangements Measured in Real-time by QCM-D*, Biointerphases, 2012. (1): p. 1-9.

11:00am **BI+AS+BA+NL-TuM10 QCM-D as a Novel Technique to Investigate Nuclear Pore Transport**, M. Sorci, Rensselaer Polytechnic Institute, R. Hayama, B.T. Chait, M.P. Rout, Rockefeller University, G. Belfort, Rensselaer Polytechnic Institute

A quartz crystal microbalance (QCM-D) is a simple and highly sensitive mass and dissipation sensor which has been used to study interfacial adsorption reactions and conformational changes on a variety of supports in real time. In this paper we aim to apply this technique to gain a better understanding of nuclear transport. In particular, we are investigating the transport of proteins through the Nuclear Pore Complex (NPC), which is the sole mediator of exchange between the nucleus and the cytoplasm in all eukaryotic cells¹. Recent publications have further improved our understanding of the architecture and evolutionary origins of this macromolecular gate,^{2,3} yet the molecular transport mechanism remains unclear. Transport across the NPC is fast, energy-dependent (to give directionality) and often receptor-mediated. While small molecules pass through the NPCs unchallenged, large macromolecules (>40 kDa) are excluded unless chaperoned across by transport factors collectively termed Karyopherins (Kaps). The translocation of the complexes of Kaps and their cargo proteins/RNAs occurs through the specific affinity and binding between Kaps and particular nuclear pore complex proteins (nucleoporins) called FG-Nups, which share a degenerate multiple-repeated “Phe-Gly” motif. In an attempt to better understand the transport and the selective process under crowding conditions, we immobilized Nsp1 and truncated variations of it onto QCM-D sensors. The binding and unbinding of Kap95, other binding proteins, as well as control proteins (e.g. BSA), was studied in order to investigate specificity, kinetics rate constants, effect of competitive binding. Ultimately we aim to gain sufficient understanding of the molecular scale engineering principles behind nuclear transport to allow us to design the next generation of synthetic selective nanosorters capable of purifying any protein that we desire.

1. Grünwald, Singer and Rout, Nature 2011, 475, 333

2. Alber et al., Nature 2007, 450, 683

3. Alber et al., Nature 2007, 450, 695

11:20am **BI+AS+BA+NL-TuM11 Using QCM-D and Ellipsometry to Determine the Orientation and State of Hydration of Antibodies Adsorbed on a Hydrophobic Surface**, C.W. Frank, Stanford University, M.E. Wiseman, DSM Research

INVITED

Adsorbed antibodies can take several orientations: end-on/fab-up, end-on/fab-down, side-on, and flat-on. Since the accessibility of antigens will depend on the antibody orientation, we have used QCM-D to monitor transient adsorption and have determined the orientation as a function of coverage. In addition, we have used simultaneous QCM-D and ellipsometry to distinguish between the “wet” mass consisting of protein plus coupled water and the “dry” mass consisting only of the protein. Finally, we have applied an alternative protocol for determining the state of hydration using only QCM-D. This involves a D₂O exchange that allows determination of the dry mass. We conclude that the QCM-D signal of proteins in liquids contains a major component from coupled water.

High-k Oxides for MOSFETs and Memory Devices I
Moderator: A.C. Kummel, University of California San Diego

8:00am **EM+PS-TuM1 Calibration of Capacitance Force Microscopy using Micro-scale Gold Dots**, *K. Sardashti, A.C. Kummel*, University of California San Diego

Capacitance force microscopy (CFM) is a variant of atomic force microscopy (AFM) and a powerful tool in characterization of metal-oxide-semiconductor capacitors (MOSCAPs). A high accuracy CFM system can be built by modifying a commercially available AFM, connecting the tip and sample to capacitance bridge of tunable frequency. The electric field distribution and, as a result, minority carriers' response to the applied bias strongly depend on the contact area between the gate and oxide. Furthermore, the frequency dependence of the capacitance-voltage measurement (C-V) is a function of the electrode size due to the radial diffusion of minority carriers near the periphery of the electrode as the dimension shrinks to the size of AFM tips. Therefore, contact area between the tip and sample is a crucial factor in CFM measurements. An experimental method is required to determine the effect of contact area on the shape and frequency-dependence of C-V curves measured by CFM. Scanning capacitance calibration samples are being fabricated with gold dots of diameters ranging from 2 to 600 μm on heavily doped silicon with 100 nm thick SiO_2 grown on top. The capacitance of resulting $\text{Au/SiO}_2/\text{Si}^+$ stacks with a 90000x range of area will be measured both by a conventional probe station (Agilent B-1500) and a CFM system (Veeco Multimode[®] connected to an AH 2700A capacitance bridge). After calibration, second set of samples including gold dots of similar size on Al_2O_3 layers, grown by atomic layer deposition (ALD), on GaN substrates will be characterized by both the probe station and CFM systems.

8:20am **EM+PS-TuM2 RF-PVD Si Capping for CET Decrease in High-k/Metal Gate 14nm FDSOI**, *C. Suarez Segovia, P. Caubet, STMicroelectronics, France, C. Leroux, CEA-LETI, France, M. Juhel, S. Zoll, O. Weber, STMicroelectronics, France, G. Ghibaudo, IMEP-LAHC, France*

Further miniaturization of CMOS technologies will require low values for Capacitance Equivalent Thickness (CET) of gate dielectrics. Below 28nm node, it becomes more difficult for high-k/metal gate (HKMG) MOSFET to reach low CET without degrading gate leakage. One technique for CET scaling already reported [1-4] is based on oxygen scavenging from the HKMG stack after thermal treatment (drive-in anneal). Unlike other reported CET scaling solutions, oxygen scavenging is a promising approach to extend HF-based HK dielectrics to future nodes [2].

Scavenging techniques incorporating the scavenging elements such as Hf, La, Ti, Al, and Ta directly within the high-k layers have been proposed by many researchers [2-3]. However, this approach can present several drawbacks such as excessive carrier mobility degradation, leakage current increase and effective work function change by formation of fixed charges and/or interface dipoles [3].

In this study, in-situ RF-PVD Si-cap was deposited on top of metal gate in an Applied Materials Endura chamber. HfO_2 and TiN metal gate were used on 300mm FDSOI wafers, using a gate-first integration scheme in a 14nm process flow. The use of an in-situ Si-cap for achieving CET reduction has already been reported in the literature [4]; but, for the first time in this article, we have evaluated a new RF mode PVD Si-cap process, designed to avoid device degradation due to charging.

Firstly, SIMS and XRD measurements were carried out on blanket wafers containing either 20Å or 100Å thick RF-PVD Si-cap deposited in-situ on sacrificial 35Å TiN layer followed or not by drive-in anneal. SIMS results show that amorphous silicon is oxidized at TiN/Si-cap interface during drive-in anneal by pumping oxygen from TiN and high-k, which reduces CET. We demonstrate that Si-cap deposited by RF-PVD remains amorphous for both studied thicknesses whereas sacrificial 35Å TiN layer crystallizes after drive-in anneal, as indicated by XRD. We believe that oxygen diffusion through TiN is possible by means of the grain boundaries formed in TiN during annealing. Secondly, electrical measurements were obtained on 14nm FDSOI devices. As expected, with TiN capping by RF-PVD Si, we succeed to reduce CET by 1Å (6.25%) in PMOS and 0.5Å (4%) in NMOS with no significant degradation of the gate current leakage, no measurable impact on VT, and no device degradation due to charging.

[1] T. Ando et al., Proceedings of IEEE IEDM, Washington, DC, USA 2009; pp. 423-426

[2] Takashi Ando, Materials 2012, 5, 478-500

[3] C. Choi et al J. Appl. Phys. 2010, 108, 064107:1-064107:4

[4] L.-Å. Ragnarsson et al, Proceedings of IEEE IEDM, Baltimore, MA, USA 2009; pp. 663-666

8:40am **EM+PS-TuM3 Growth of Oxides for Negative Capacitance Gate Dielectrics**, *R. Droopad*, Texas State University **INVITED**

The need to reduce power in CMOS devices is critical to the evolution of the next generation devices as scaling continues. The use of new materials for the gate dielectric, and with the possibility of using III-V semiconductors in the channel, there is additional new challenges to maintaining high on-off ratios. One way to reducing the subthreshold slope in low power MOSFET application is through the use of the negative capacitance of ferroelectric layers as part of the gate dielectric proposed by Salahuddin and Datta [1]. This concept has been demonstrated in a polymer ferroelectric MOSFET device exhibiting a sub-60 mV/decade switching behavior [2]. Capacitance enhancement in crystalline ferroelectric-dielectric bilayer has also been demonstrated using a PZT-STO bilayer [3]. Unlike the present amorphous gate stack, ferroelectric gate materials need to be crystalline for the realization of polarization that is oriented along the growth direction. This presentation will detail the growth of ferroelectric complex oxide gate stacks epitaxially on both Si and III-V heterostructures. Deposition is carried out using MBE with careful control of the interfacial nucleation ensuring that the ferroelectric polarization is in the growth direction.

[1] S. Salahuddin, S. Datta, Nanolett. 8 (2008) 405.

[2] A. Rusu, G.A. Salvatore, D. Jiménez, A.M. Ionescu, IEDM 2010

[3] A.I. Khan, D. Bhowmik, P. Yu, S. J. Kim, X. Q. Pan, R. Ramesh, S. Salahuddin, Appl. Phys. Letts., 99 (2011) 113501

9:20am **EM+PS-TuM5 Switching Aspects of RRAM – First Principles and Model Simulations Insight**, *S. Clima, R. Degraeve, K. Sankaran, Y.Y. Chen, A. Fantini, A. Belmonte, L. Zhang, N. Raghavan, L. Goux, B. Govoreanu, D.J. Wouters, M. Jurczak, G. Pourtois*, IMEC, Belgium **INVITED**

The Resistive Random Access Memory with its great potential for scalability to the nanoscale dimensions, high speed, low energy switching and CMOS compatibility, is emerging as a promising candidate for non-volatile memories.¹⁻⁴ Having a good understanding of the mechanisms at the origin of the switching at the atomic level is important for designing high performance resistive memory stack. For instance, the thermodynamic driving forces that help shaping a suitable oxygen profile for low forming voltages might prove to be disadvantageous for a good endurance. Another trade-off that needs further considerations is the compromise between the retention and the switching dynamics, determined by the kinetic energy barriers of the conducting defect. With the help of classical DFT and bond-boosted Accelerated Ab Initio Molecular Dynamics (AIMD) technique,⁵ we evaluated the thermodynamics of the defects formation and the diffusion kinetics of the conducting species in RRAM materials.^{6,7} The experimental and first-principles outputs were used to develop a stochastic model simulator, which we use to interpret the experimental set/reset dynamics, endurance and retention measurements.⁸ Modeling and simulations play an important role in understanding the atomistic mechanisms that take place during the manufacture, operation or storage of the resistive memory element. Through this talk we present our most recent advancements for oxide and Cu-based RRAM.

1. Z. Wei, et al., in *Electron Devices Meeting (IEDM)*, (2011), p. 31.4.1.

2. S. Shyh-Shyuan, et al., in *Symposium on VLSI Circuits (2009)*, p. 82.

3. L. Seung Ryoul, et al., 2012 IEEE Symposium on VLSI Technology, 71 (2012).

4. B. Govoreanu, et al., Ext. Abstr. SSDM Conf., Nagoya, Japan, pp.1005 (2011).

5. R. A. Miron and K. A. Fichthorn, *Journal of Chemical Physics* **119**, 6210 (2003).

6. S. Clima, et al., *Applied Physics Letters* **100**, 133102 (2012).

7. L. Goux, et al., in *Symposium on VLSI Technology (VLSIT)*, (2012), p. 69.

8. R. Degraeve, et al., 2012 IEEE Symposium on VLSI Technology (2012).

10:40am **EM+PS-TuM9 Comparison of Surface Defects on Cleaved GaAs(110) and MBE Grown InGaAs(110)**, *M. Edmonds, T. Kent*, University of California San Diego, *R. Droopad*, Texas State University, A.C. Kummel, University of California San Diego

The dominant crystallographic face of InGaAs(001) based FinFETs is the (110) surface. These sidewall surfaces do not have metallic group III bonds and therefore with proper passivation might provide ideal interfaces to the gate oxide. It has been shown that with trimethyl aluminum (TMA)

passivation of GaAs(110), monolayer nucleation density with zero lattice disruption can be achieved which is ideal for sub 0.5nm EOT scaling. Furthermore, dual passivation with an oxidant such as $H_2O(g)$ has been shown to remove conduction band edge states associated with Al-Ga bonds results from TMA bonding. DFT studies confirm that TMA bridge bonds between the Ga and As atoms on the GaAs(110) surface while-OH from $H_2O(g)$ dual passivation can readily insert into the Al-Ga bond thereby unpinning the surface. This study focuses on examining and characterizing surface defects and features of cleaved GaAs(110) in comparison with molecular beam epitaxy (MBE) grown InGaAs/InP(110) samples via scanning tunneling microscopy/spectroscopy (STM/STS) studies. Models of the various surface defects are proposed.

The MBE grown InGaAs/InP(110) samples are grown with an As_2 cap in order to protect the surface from oxidation. The samples are decapped at 350°C in an ultra-high vacuum chamber system prior to STM imaging. The initial STM image results show the surface contains a much higher step density compared to cleaved GaAs(110). The STM images of MBE grown InGaAs(110) also shows bright site features which have an average height of $\sim 2.5 \text{ \AA}$ and a site width variation from 1.8 nm to 3.6nm. These bright site features are consistent with excess As on the surface from an incomplete decapping procedure, or from surface undercoordinated atoms. A commercially available thermal gas cracker will be used to expose the surface to atomic hydrogen. It is believed this will remove any excess As on the surface and potentially passivating intrinsic surface defects. The dry in-situ atomic hydrogen cleaning of the MBE InGaAs(110) decapped samples will be compared with the cleaved GaAs(110) samples in aim to remove excess As_2 from the surface and make the InGaAs(110) surface comparable in low surface defect sites with cleaved GaAs(110).

11:00am **EM+PS-TuM10 Scalability of Doped Cubic HfO_2 Films, C. Adelman, K. Opsomer, Imec, Belgium, S. Brizzi, M. Tallarida, D. Schmeisser, BTU Cottbus, Germany, T. Schram, S.A. Chew, N. Horiguchi, S. Van Elshocht, L.-A. Ragnarsson, Imec, Belgium**

HfO_2 has been the standard gate dielectric for MOSFETs for several technology nodes because of its large dielectric constant (~ 18 for amorphous or monoclinic HfO_2). To continue MOSFET scaling, replacement dielectrics for HfO_2 are of interest with an even larger dielectric constant. The polymorphism of HfO_2 offers the possibility to increase the dielectric constant by stabilizing the cubic phase of HfO_2 with a dielectric constant of ~ 30 . The stabilization of the cubic phase has been demonstrated by introducing dopants (typically about 10%) such as Al, Si, or rare earths.

Numerous studies have demonstrated the advantage of doped cubic HfO_2 over undoped HfO_2 in terms of leakage vs. equivalent oxide thickness (EOT) for films with thicknesses of ~ 5 -10 nm. These stacks lead to EOT values $\gg 1$ nm and are thus not relevant for future CMOS technology nodes. However, no clear advantage has been shown for scaled films with EOT values < 1 nm.

In this paper, we study the behavior of Gd- and Al-doped HfO_2 in capacitors with EOT values below 1 nm (physical thicknesses of 2-3 nm). While Gd- and Al-doped HfO_2 show similar leakage for 10 nm thick films, capacitors with 2.5 nm Gd-doped HfO_2 show several orders of magnitude higher leakage than their Al-doped counterparts, indicating that the behavior for thick and thin films is not correlated. However, EOT vs. HfO_2 thickness measurements show that dielectric constants of the order of 30 can be maintained even for 2.5 nm thick films.

The ultimate scaling limits were explored for Al-doped HfO_2 . It was found that the scaling of Al-doped HfO_2 is limited by the crystallization temperature of the films, which becomes too large for acceptable temperature budgets for (gate-last) MOSFET processing for thicknesses approaching 2 nm. This was confirmed by x-ray absorption spectroscopy at the O K-edge. Thinner doped HfO_2 films remain amorphous and exhibit a lower dielectric constant. In-situ XRD showed that the crystallization temperature of thick films (10 nm) was increased significantly by Al-doping. However, for 2 nm films, the comparison with undoped HfO_2 led to similar crystallization behavior indicating that the effects of thin films and doping do not necessarily add up. The lowest EOT values that could be achieved for gate-last MOSFET compatible processing were of the order of 8 \AA including an interfacial SiO_2 contribution of about 4 \AA . However, for such stacks, leakage current densities could be achieved which were about 2 orders of magnitude lower than HfO_2 capacitors with identical EOT values. This indicates that doped HfO_2 films offer solutions for very low gate leakage at scaled EOT values down to values as low as 8 \AA .

11:20am **EM+PS-TuM11 Advance of 3D-stackable Binary-oxide ReRAM for Storage-class Memory Applications, T.H. Hou, C.W. Hsu, I.T. Wang, National Chiao Tung University, Taiwan, Republic of China**
INVITED

Crossbar resistive-switching random access memory (RRAM) with a minimum cell size of $4F^2$ has attracted much attention recently because of its superior memory performance, ultrahigh density, and ultimate scaling potential. The most anticipating emerging application of RRAM in future high-speed information systems is the storage-class memory (SCM) aiming to revolutionize inefficient data-storage hierarchy based on hard disks and present memory technologies. The requirements of the SCM technology include high data bandwidth, large storage capability, and low bit cost.

Replacing the current 2D memory with 3D memory architecture is one of the most feasible options to further increase storage capability per unit area. The types of 3D memory architectures can be divided into the 3D stacking of horizontal memory arrays and the bit-cost scalable (BiCS) 3D vertical memory. In the first part of this paper, two crossbar RRAM architectures, namely one diode-one resistor (1D1R) and one selector-one resistor (1S1R) fabricated using low process temperature applicable to the 3D stacking of horizontal memory arrays, are discussed. Their high-bandwidth parallel read/write capabilities are also investigated.

Despite the increase of bit density, the formation of multiple horizontal memory arrays requires a larger number of photolithography steps, and thus is unable to reduce bit cost. By contrast, multiple layers of thin film deposition and a small number of photolithography steps are used to produce high-density 3D vertical RRAM arrays potentially at extremely low cost. Stacking two individual selection and memory devices as a 1D1R or 1S1R cell is extremely challenging in 3D vertical RRAM arrays because the metal electrodes between two devices cannot be easily patterned at the vertical sidewall. Therefore, it is of great interest to develop a nonlinear RRAM device requiring no external selection device. In the second part of this paper, the latest advance of self-rectifying devices compatible to 3D vertical RRAM arrays are reviewed.

Energy Frontiers Focus Topic
Room: 101 A - Session EN-TuM

Energy Past, Present, and Future

Moderator: M.A. Filler, Georgia Institute of Technology

8:00am **EN-TuM1 Chasing the Photovoltaic Race with Quantum Dot Solar Cells, P. Kamat, University of Notre Dame**
INVITED

Assembling semiconductor nanostructures on electrode surfaces in a controlled fashion is an attractive approach for designing next generation solar cells. Quantum dot solar cells (QDSC) have emerged as the potential contender for making transformative changes. The size dependent electronic structure of quantum dots enables the design of photovoltaic devices with tailored electronic properties. We have now exploited this aspect in solar cells by assembling different size CdSe quantum dots on mesoscopic TiO_2 films either by direct adsorption or with the aid of molecular linkers. Upon bandgap excitation, CdSe quantum dots inject electrons into TiO_2 thus enabling the generation of photocurrent in a photoelectrochemical solar cell. Crystalline ternary metal chalcogenides ($CuInS_2$ and $CdSeS$) have been deposited within the mesoscopic TiO_2 film by electrophoretic deposition with a sequentially layered architecture. This approach has enabled us to design tandem layers of CdSeS QDs of varying bandgap within the photoactive anode of Quantum Dot Solar Cell (QDSC). Recent advances in the development of high efficiency QDSC will be described.

8:40am **EN-TuM3 Extremes of Heat Conduction in Molecular Materials, D.G. Cahill, University of Illinois at Urbana Champaign**
INVITED

Thermal conductivity is a basic and familiar property of materials that plays a pivotal role in a broad range of topics in energy science and engineering systems. In this talk I will emphasize recent examples of extreme behavior—and behavior under extreme conditions—in polymers and molecular solids. Our measurements of heat conduction in novel materials are enabled by variety of ultrafast optical pump-probe metrology tools developed over the past decade. At the low end of the thermal conductivity spectrum, fullerene derivatives display the lowest thermal conductivity ever observed in a fully dense solid, comparable to the conductivity of disordered layered WSe_2 and only twice that of air. Extremes of high pressures (up to 60 GPa) allow us to continuously change the strength of molecular interactions in glassy polymers and test theoretical descriptions of the mechanisms for heat conduction. The thermal conductivity of aligned, crystalline and liquid crystalline polymer fibers can be surprisingly high, comparable to that of stainless-steel. The dominant carriers of heat

appear to be longitudinal acoustic modes with lifetimes dictated by anharmonic processes.

9:20am **EN-TuM5 The Role of Catalysis in Developing Energy Resources for the Future**, *A. Bell*, University of California, Berkeley
INVITED

The continuing economic success of developed nations and the growth in the economies of developing nations is intimately connected to the availability inexpensive sources of energy. For the past century, the primary energy resources have been coal, petroleum, and natural gas. Coal and natural gas have been used primarily for the generation of electricity, and petroleum as the primary source of transportation fuels. While these traditional resources are projected to last to the end of this century, it is recognized that they are finite and that their consumption contributes to the growing levels of atmospheric carbon dioxide and consequently to detrimental changes in the global climate. For these reasons, there has been a growing interest in finding more efficient means for utilizing traditional energy resources and developing sustainable energy resources such as biomass and solar radiation as alternatives. This talk will focus on the role of catalysis in enabling the efficient conversion of biomass and solar radiation to transportation fuels. It will be shown that the conversion of biomass to diesel and gasoline can be accomplished in a sequence of steps that involve dehydration, aldol condensation, hydrodeoxygenation, and hydrogenation, each of which requires a catalyst in order to achieve reaction rates that are commercially viable. The photoelectrochemical splitting of water and the photoelectrochemical reduction of carbon dioxide offer longer range means for producing fuels from sustainable resources. Here too, catalysts are required to achieve the formation of products at acceptable rates. This presentation will end with a set of illustrations showing how advances in methods of catalyst synthesis, screening, and characterization can be used to accelerate the discovery and evaluation of catalysts for the conversion of sustainable energy resources to fuels.

10:40am **EN-TuM9 A Direct Thin-Film Path towards Low-Cost Large-Area III-V Photovoltaics**, *R. Kapadia, Z. Yu, A. Javey*, University of California, Berkeley

III-V photovoltaics (PVs) have demonstrated the highest power conversion efficiencies for both single- and multi-junction cells. However, expensive epitaxial growth substrates, low precursor utilization rates, long growth times, and large equipment investments restrict applications to concentrated and space photovoltaics (PVs). Here, we demonstrate the first vapor-liquid-solid (VLS) growth of *high-quality* III-V *thin-films* on metal foils as a promising platform for large-area terrestrial PVs overcoming the above obstacles. We demonstrate 1-3 mm thick InP thin-films on Mo foils with *ultra-large* grain size up to 100 μm , which is ~ 100 times larger than those obtained by conventional growth processes. The films exhibit electron mobilities as high as 500 $\text{cm}^2/\text{V}\cdot\text{s}$ and minority carrier lifetimes as long as 2.5 ns. Furthermore, under 1-sun equivalent illumination, photoluminescence efficiency measurements indicate that an open circuit voltage of up to 930 mV can be achieved with our films, only 40 mV lower than what we measure on a single crystal reference wafer.

11:20am **EN-TuM11 III-nitride Nanowires: Novel Materials for Light Emission**, *G.T. Wang*, Sandia National Laboratories
INVITED

Nanowires based on the III nitride (AlGaInN) materials system have attracted attention as potential nanoscale building blocks in LEDs, lasers, sensors, photovoltaics, and high speed electronics. Compared to conventional LEDs based on planar architectures, future LEDs based on III-nitride nanowires have several potential advantages which could enable cheaper and more efficient lighting. Nanolasers based on III-nitride nanowires also offer the potential for ultracompact, low-power, and coherent light sources in the UV-visible wavelengths for a number of applications. However, before the promise of nanowire-based optoelectronics can be fully realized, a greater understanding of and control over their synthesis, properties, and device integration needs to be achieved. I will discuss research involving the aligned, bottom-up growth of Ni-catalyzed GaN and III-nitride core-shell nanowires, along with results providing insights into the nanowire properties obtained using cutting-edge structural, electrical, and optical nanocharacterization techniques. I will also describe a more recent "top-down" approach for fabricating ordered arrays of high quality GaN-based nanowires with controllable height, pitch and diameter. Using this top-down approach, both axial and radial nanowire device heterostructures can be realized. The fabrication, structure, optical properties, lasing characteristics, and performance of top-down-fabricated nanowires and nanowire LEDs and lasers will be discussed. Sandia National Laboratories is a multi-program laboratory managed and operated by Sandia Corporation, a wholly owned subsidiary of Lockheed Martin Corporation, for the U.S. Department of Energy's National Nuclear Security Administration under contract DE-AC04-94AL85000.

Exhibitor Technology Spotlight
Room: Hall A - Session EW-TuM

Exhibitor Technology Spotlight I
Moderator: C. Moffitt, Kratos Analytical Limited, UK

10:00am **EW-TuM7 Nothing to Fret about Fretting**, *S. Shaffer*, Bruker
Fretting occurs when two materials come in contact with each other under load and are subject to a very low amplitude relative motion, often due to vibration. Usually, the amplitude of the vibration is 50 microns or less. This phenomenon occurs across a wide range of industries, and understanding this wear process, as well as the effectiveness of palliatives is important. In electronic packaging fretting can occur where two contacts mate. In aerospace applications, this process occurs where the turbine vanes dovetail to the rotor disk. In the automotive industry, this can occur in under-the-hood applications like engine mounts. A new UMT drive with a fully programmable stroke length and frequency will be used to demonstrate how materials can be tested to make sure that materials and coatings selected for these types of applications are suitable. The new drive is designed to work in a variety of application-specific environments.

10:20am **EW-TuM8 A New Truly Easy-to-Use Dedicated Infrared Microscope**, *T. Tague, S. Wang*, Bruker

A new stand-alone infrared microscope (LumosTM) has been developed for the rapid analysis of small samples. The new microscope was developed with the intent of providing state-of-the-art microanalysis capabilities with a truly easy-to-use user interface. The visual image quality of the Lumos is excellent so the important first step in the analysis, visualization, is easily accomplished. The Lumos utilizes a unique objective design, where the numerical is low for sample viewing and high for the infrared data collection. This makes it very easy to locate and view the sample without sacrificing infrared performance.

The novel Wizard user interface controls all aspects of the microscope and guides the user through the analysis process. The sample stage, sample focus assembly, condenser, aperture, polarizers, and ATR mode are controlled in the software providing true "point and shoot operation". ATR microanalysis is accomplished by simply clicking on the area of interest in the software to center it and selecting ATR. Area reflection, transmission, and ATR images are collected by simply drawing the desired analysis and starting the desired acquisition. The image processing software interface provides research quality analysis tools with an intuitive interface.

The Lumos also has a unique ability to readily analyze samples with traditional sampling accessories. A port is provided to attach accessory modules from Bruker's Alpha FTIR Series. Standard ATR, transmission, reflection, and even gas cell analysis can be readily conducted with the Lumos. Lastly, the Lumos comes with a comprehensive validation package to support any range of validation requirements.

Graphene and Other 2D Materials Focus Topic
Room: 104 B - Session GR+AS+EM+MI+MN-TuM

Optical, Magnetic, Mechanical and Thermal Properties of 2D Materials

Moderator: A.A. Balandin, University of California, Riverside, D. Gunlycke, Naval Research Laboratory

8:00am **GR+AS+EM+MI+MN-TuM1 Long-range Magnetic Order in a Purely Organic 2D Layer Adsorbed on Epitaxial Graphene**, *M. Garnica, D. Stradi, S. Barja, F. Calleja, C. Diaz, M. Alcami, N. Martin, A.L. Vazquez-de-Parga, F. Martin, R. Miranda*, Universidad Autónoma de Madrid, Spain

Collective magnetic properties are usually associated to d or f electrons which carry the individual magnetic moments. Band magnetism in organic materials based on π electrons has remained an experimental challenge, in spite of rigorous predictions of a fully spin polarized ground state in half-filled flat band organic systems. Cryogenic Scanning Tunneling Microscopy (STM) and Spectroscopy in UHV and accurate Density Functional Theory (DFT) simulations show that isolated TCNQ molecules deposited on a monolayer of graphene epitaxially grown on Ru(0001) acquire charge from the substrate and develop a sizeable magnetic moment, which is revealed by a prominent Kondo resonance. The magnetic moment is preserved upon dimer and monolayer formation. The self-assembled 2D monolayer of magnetic molecules develops spatially extended spin-split electronic bands visualized in the real space by STM, where only the majority band is filled,

thus becoming a 2D, purely-organic magnet whose predicted spin alignment in the ground state is visualized by spin-polarized STM at 4.6 K [1]. Since the added charge occupies spatially extended intermolecular bands with well-defined spin character, one might speculate that the TCNQ monolayer could act as a spin filter or 2D spin polarizer, adding magnetic functionalities to graphene by altering the spin polarization of a current flowing in graphene.

[1] M. Garnica et al, Nature Physics <http://dx.doi.org/10.1038/NPHYS2610> (2013)

8:20am **GR+AS+EM+MI+MN-TuM2 Graphene Thermal Properties and Applications for Thermal Management of Li-Ion Batteries**, *P. Goli, S. Legedza, A.A. Balandin*, University of California, Riverside

Graphene's superior intrinsic thermal conductivity, flat geometry, flexibility and demonstrated capability for integration with other materials make graphene very promising for thermal management applications [1-2]. The thermal conductivity of graphene flakes incorporated within different materials can degrade due to coupling to the adjacent layers and phonon scattering on defects and edges [2]. At the same time, the thermal conductivity of graphene and FLG in different composite materials can remain relatively high compared to conventional thin films [3]. A possibility of using a mixture of graphene and FLG as fillers in thermal interface materials (TIM) has also been demonstrated [4-5]. In this talk we report on a possibility of using graphene as a filler material in phase-change materials (PCMs) for thermal management of Lithium-ion batteries. Lithium-ion batteries are superior to other types of batteries owing to their high-energy storage density. However, their applications are limited due to strong self-heating effects coupled with the adverse effect of temperature on the battery life-time. Prior work on thermal issues in Li-ion battery packs has demonstrated that a passive thermal management system based on PCMs is a promising approach. The PCM thermal management uses the latent heat stored in the material as its phase changes over a small temperature range. However, PCMs typically have low thermal conductivity (below 1 W/mK at room temperature). They store heat from the batteries rather than transfer it outside. For this reason, the usefulness of PCM passive thermal management for the high-power Li-ion batteries is limited. We found that incorporation of graphene to the hydrocarbon-based PCM allows one to increase its thermal conductivity by more than two orders of magnitude while preserving its latent heat storage ability. A combination of the sensible and latent heat storage together with the improved heat conduction outside of the battery pack leads to a significant decrease in the temperature rise inside a typical Li-ion battery pack. The described combined heat storage – heat conduction approach can lead to a transformative change in thermal management of Li-ion and other types of batteries [6].

[1] A.A. Balandin, et al., Nano Lett., 8, 902 (2008); [2] A.A. Balandin, Nature Mat., 10, 569 (2011); [3] Z. Yan, G. Liu, J.M. Khan and A.A. Balandin, Nature Comm., 3, 827 (2012); [4] K.M.F. Shahil and A.A. Balandin, Nano Lett., 12, 861 (2012); [5] V. Goyal and A.A. Balandin, Appl. Phys. Lett., 100, 073113 (2012); [6] For details, see at <http://ndl.ee.ucr.edu> [<http://ndl.ee.ucr.edu>]

8:40am **GR+AS+EM+MI+MN-TuM3 Graphene Nano-Photonics and Carrier Dynamics**, *F. Koppens, P.A. Gonzalez*, ICFO - The Institute of Photonic Sciences, Spain **INVITED**

In this talk I will review the new and strongly emerging field of graphene nano-photonics. In particular, I will show how to exploit graphene as a host for guiding, switching and manipulating light and electrons at the nanoscale [1,2]. This is achieved by exploiting surface plasmons: surface waves coupled to the charge carrier excitations of the conducting sheet. Due to the unique characteristics of graphene, light can be squeezed into extremely small volumes and thus facilitate strongly enhanced light-matter interactions.

One particular example of these enhanced light-matter interactions is the non-radiative energy transfer from light emitters to graphene. We experimentally and theoretically quantified this energy transfer process and find that the emitter decay rate follows a universal distance-scaling relation and is enhanced by a factor 90 [3]. Additionally, I will discuss novel types of hybrid graphene photodetectors [4] and new exciting results on carrier dynamics and carrier multiplication in graphene. By studying the ultrafast energy relaxation of photo-excited carriers after excitation with light of varying photon energy, we find that electron-electron scattering (and thus carrier multiplication) dominates the energy relaxation cascade rather than electron-phonon interaction [5]. This singles out graphene as a promising material for highly efficient broadband extraction of light energy into electronic degrees of freedom, enabling a new class of high-efficiency optoelectronic and photovoltaic applications.

References

[1] J. Chen, M. Badioli, P. Alonso-González, S. Thongrattanasiri, F. Huth, J. Osmond, M. Spasenović, A. Centeno, A. Pesquera, P. Godignon, A. Zurutuza, N. Camara, J. Garcia de Abajo, R. Hillenbrand, F. Koppens, “Optical nano- imaging of gate-tuneable graphene plasmons”, Nature (2012)

[2] F. Koppens, D. Chang, J. García de Abajo, “Graphene Plasmonics: A Platform for Strong Light–Matter Interactions”, Nano Letters 11, 3370–3377 (2011).

[3] L. Gaudreau, K. J. Tielrooij, G. E. D. K. Prawiroatmodjo, J. Osmond, F. J. García de Abajo, and F. H. L. Koppens, “Universal Distance-Scaling of Non-radiative Energy Transfer to Graphene”, Nano Letters 2012

[4] G. Konstantatos, M. Badioli, L. Gaudreau, J. Osmond, M. Bernechea, P. Garcia de Arquer, F. Gatti, F. Koppens, “Hybrid graphene-quantum dot phototransistors with ultrahigh gain”, Nature Nanotechnology (2012)

[5] K.J. Tielrooij, J.C.W. Song, S.A. Jensen, A. Centeno, A. Pesquera, A. Zurutuza Elorza, M. Bonn, L.S. Levitov, and F.H.L. Koppens. Nature Physics (2012)

9:20am **GR+AS+EM+MI+MN-TuM5 Graphene Mechanics and NEMS Applications**, *J.C. Hone*, Columbia University **INVITED**

This talk will review collaborative efforts in characterizing the mechanical properties of graphene, and its application to nano-electromechanical devices (NEMS). We use nano-indentation of freely suspended membranes to measure mechanical properties. These measurements, when combined with nonlinear anisotropic continuum modeling, reveal that graphene is both ultrastiff (in-plane Young's modulus equivalent to 1 TPa) and the strongest known material (in-plane breaking strength equivalent to 100 GPa). Our recent work demonstrates that CVD-grown graphene, even in the presence of grain boundaries, can retain almost all of this intrinsic strength, opening the door to large-area high-strength films. For NEMS applications, we have developed techniques that allow fast, highly sensitive electronic readout. We are applying graphene NEMS to studies of fundamental physics in the quantum Hall regime and applications in electro-mechanical signal processing. In particular, I will discuss our recent work on graphene voltage controlled oscillators for generation of frequency modulated signals.

10:40am **GR+AS+EM+MI+MN-TuM9 Nano-plasmonic Phenomena in Graphene**, *D.N. Basov*, University of California San Diego **INVITED**

Infrared nano-spectroscopy and nano-imaging experiments have uncovered rich optical effects associated with the Dirac plasmons of graphene [*Nano Lett.* 11, 4701 (2011)]. We were able to directly image Dirac plasmons propagating over sub-micron distances [*Nature* 487, 82 (2012)]. We have succeeded in altering both the amplitude and wavelength of these plasmons by gate voltage in common graphene/SiO₂/Si back-gated structures. Scanning plasmon interferometry has allowed us to visualize grain boundaries in CVD graphene. These experiments revealed that grain boundaries tend to form electronic barriers that impede both electrical transport and plasmon propagation. Our results attest to the feasibility of using electronic barriers to realize tunable plasmon reflectors: a precondition for implementation of various metamaterials concepts. Finally, we have carried out pump-probe experiments probing ultra-fast dynamics of plasmons in exfoliated graphene with the nano-scale spatial resolution.

11:20am **GR+AS+EM+MI+MN-TuM11 Controlled Growth of Large-Area Mono-, Bi-, and Few-Layer Graphene by Chemical Vapor Deposition on Copper Substrate**, *C.-Y. Park, Y. Kim*, Sungkyunkwan University, Republic of Korea

Direct synthesis of graphene using a chemical vapor deposition (CVD) has been considered a facile way to produce large-area and uniform graphene film, which is an accessible method from an application standpoint. Hence, their fundamental understanding is highly required. Unfortunately, the CVD growth mechanism of graphene on Cu remains elusive and controversial.

Here, we present the effect of graphene growth parameters on the number of graphene layers were systematically studied and growth mechanism on copper substrate was proposed. Parameters that could affect the thickness of graphene growth include the pressure in the system, gas flow rate, growth pressure, growth temperature, and cooling rate. We hypothesize that the partial pressure of both the carbon sources and hydrogen gas in the growth process, which is set by the total pressure and the mole fraction of the feedstock, could be the factor that controls the thickness of the graphene. The graphene on Cu was grown by the diffusion and precipitation mode not by the surface adsorption mode, because similar results were observed in graphene/Ni system. The carbon-diffused Cu layer was also observed after graphene growth under high CH₄ pressure. Our findings may facilitate both the large-area synthesis of well-controlled graphene features and wide range of applications of graphene.

11:40am **GR+AS+EM+MI+MN-TuM12 Charged Vacancy Defects in Graphene: Stability and Charge States**, *Y. Liu, M. Weinert, L. Li*, University of Wisconsin Milwaukee

We perform atomic resolution imaging of vacancy defects in graphene using non-contact atomic force microscopy, and directly determine their charges by local contact potential difference measurement. We observe reconstruction, healing, and merging of vacancy defects. Combined with first-principles calculations, we further show that vacancy defects are typically positively charged, while H adsorbates at these sites can produce negatively charged structures, and their charge states are not necessarily integer-valued. These results provide new insights into the stability of charged vacancy defects in graphene, as well as the functionalization of graphene for chemical sensing and catalysis, and underline the tunability of these functions by controlling the size and doping of vacancy defects.

Magnetic Interfaces and Nanostructures

Room: 202 A - Session MI+EM-TuM

Spintronics and Magnetolectrics

Moderator: P. Fischer, Lawrence Berkeley National Laboratory, M. Donath, Muenster University, Germany

8:00am **MI+EM-TuM1 Molecular Beam Epitaxy and Spintronics**, *S. Andrieu, F. Bonell, T. Hauet*, Institut Jean Lamour, CNRS-Université de Lorraine, France, *F. Bertran*, Synchrotron SOLEIL, France **INVITED**

The growth and control of thin magnetic films has enabled the emergence of new branches of physics like nanomagnetism and spintronics, which stimulate an intense and successful research activity both in fundamental and applied directions. The reduced size of films and devices yields to the occurrence of new magnetic behaviors not present in bulk materials. Similarly, a new electronics based on the use of the spin of the electron was born in the 80's. The role of the Molecular Beam Epitaxy (MBE) was of prime importance in the development of these activities. The discovery of new phenomena was often highlighted from the synthesis of perfectly controlled systems by MBE (GMR in Fe/Cr(001), Half-metal magnetic effect in LaSrMnO₃, electric-field effect on magnetic anisotropy in FePt,...). Since the knowledge on the electronic properties of such thin films is crucial to understand the magnetic and electronic transport properties in these MBE-grown model systems, synchrotron radiation facilities were also used (XMCD, spin- and symmetry-resolved photoemission, diffraction,...). The strong impact of MBE growth and SR characterization in the understanding of fundamental issues in nanomagnetism and spintronics is then illustrated through the example of fully epitaxial MgO-based Magnetic Tunnel Junctions (MTJs). The physics of coherent tunneling will be first introduced using the example of Fe/MgO/Fe(001) MTJs [1]. The effect of dislocations in the MgO barrier on transport properties will be illustrated using the example of FeV_x/MgO MTJs [2]. Unexpected transport properties in FeCo_x/MgO will be presented and explained with the help of spin and symmetry resolved photoemission [3]. Finally, very recent results will be presented, like manipulation of the magnetic anisotropy at the Fe/MgO interface using an electric field [4], or insertion of the Half-metallic ferromagnetic (CoFe)₂Ge in MgO-based MTJs.

[1] - C. Tiusan et al, *J. Phys. Cond. Mat.* 19, 165201, (2007)

[2] - F. Bonell et al, *Phys. Rev. B*, 82, 092405 (2010)

[3] - F. Bonell et al, *Phys. Rev. Lett.*, 108, 176602 (2012)

[4] - C-H. Lambert et al, *Appl. Phys. Lett.* 102, 122410 (2013) and A. Rajanikanth et al, (2013), submitted

8:40am **MI+EM-TuM3 Engineering Single Spins in Semiconductors for Sensing and Computation**, *D. Awschalom*, University of California, Santa Barbara, *W.F. Koehl, A.L. Falk*, University of Chicago, *G. Calusine*, University of California, Santa Barbara, *F.J. Heremans*, University of Chicago, *V.V. Dobrovitski*, Ames Laboratory, Iowa State University, *A. Politi*, University of California, Santa Barbara **INVITED**

Semiconductor defects, while generally considered undesirable in traditional electronic devices, can confine isolated electronic spins and are promising candidates for solid-state quantum bits (qubits) [1]. Alongside research efforts focusing on nitrogen vacancy (NV) centers in diamond, an alternative approach seeks to identify and control new spin systems with an expanded set of technological capabilities, a strategy that could ultimately lead to "designer" spins with tailored properties for future quantum information processing. We discuss recent experimental results identifying such spin systems in the 4H, 6H, and 3C crystal polymorphs of silicon carbide (SiC) [2,3]. Using infrared light at near-telecom wavelengths and gigahertz microwaves, we show that these spin states can be coherently

addressed at temperatures ranging from 20 K to room temperature. Long spin coherence times allow us to use double electron-electron resonance to measure magnetic dipole interactions between spin ensembles in inequivalent lattice sites of the same crystal. Since the inequivalent spin states have distinct optical and spin transition energies, these interactions could lead to engineered dipole-coupled networks of separately addressable qubits. Together with the availability of industrial scale crystal growth and advanced microfabrication techniques for SiC, these results make this system a promising platform for photonic, spintronic, and quantum information applications that merge quantum degrees of freedom with classical electronic and optical technologies.

This work is funded by the AFOSR and DARPA.

[1] J. R. Weber, W. F. Koehl, J. B. Varley, A. Janotti, B. B. Buckley, C. G. Van de Walle, and D. D. Awschalom, *Proc. Natl Acad. Sci. USA* **107**, 8513 (2010).

[2] W. F. Koehl, B. B. Buckley, F. J. Heremans, G. Calusine, and D. D. Awschalom, *Nature* **479**, 84 (2011); A. Dzurak, *Nature* **479**, 47 (2011).

[3] A. L. Falk, B. B. Buckley, G. Calusine, W. F. Koehl, V. V. Dobrovitski, A. Politi, C. A. Zorman, P. X.-L. Feng, and D. D. Awschalom, *Nature Comm.* **4**, 1819 (2013).

9:20am **MI+EM-TuM5 Semiconductor Spintronics -- New Avenues and Perspectives: Graphene as a Spin Tunnel Barrier in MTJs and Silicon**, *B.T. Jonker, E. Cobas, O.M.J. van 't Erve, C.H. Li, A.L. Friedman, J.T. Robinson*, Naval Research Laboratory **INVITED**

Graphene has been widely studied for its high in-plane charge carrier mobility and long spin diffusion lengths. In contrast, the out-of-plane charge and spin transport behavior of this atomically thin material have not been well addressed. Tunnel barriers are the basis for many spintronic devices, and to date have relied upon oxides which often exhibit defects, trap states and interdiffusion which compromise performance and reliability. We show here that while graphene exhibits metallic conductivity in-plane, it serves effectively as an insulator for transport perpendicular to the plane. We fabricate magnetic tunnel junctions, and demonstrate electrical spin injection/detection in silicon using graphene as a tunnel barrier.

The graphene was grown by chemical vapor deposition on copper foil and incorporated as the tunnel barrier by physical transfer and standard lithographic processes to form Co / graphene / NiFe magnetic tunnel junctions (MTJs) 20-40 um in diameter [1]. Non-linear *I-V* curves and weak temperature dependence of the zero-bias resistance provide clear evidence for tunneling. The magnetic field dependence exhibits the classic signature of MTJ behavior, and the structures exhibit tunneling magnetoresistance (TMR) to 425 K, in good agreement with theory [2]. The TMR decreases monotonically with both bias and temperature, typical of MTJ behavior.

Single-layer graphene also successfully circumvents the classic issue of conductivity mismatch between a metal and a semiconductor for electrical spin injection and detection, providing a highly uniform, chemically inert and thermally robust tunnel barrier. Hanle spin precession measurements demonstrate spin injection and provide quantitative values for spin lifetimes. Devices with NiFe / single layer graphene / Si contacts exhibit the classic Lorentzian lineshape due to spin injection and dephasing. We demonstrate electrical generation and detection of spin accumulation in silicon above room temperature, and show that (a) the corresponding spin lifetimes correlate with the silicon carrier concentration, and (b) the contact resistance-area products are two to three orders of magnitude lower than those achieved with oxide tunnel barriers on silicon substrates with identical doping levels [3]. This reduction of contact resistance enables spin injection and quantitative measurements of spin lifetimes in silicon nanowires, as well.

[1] Cobas, Friedman, van't Erve, Robinson, Jonker, *Nano Letters* **12**, 3000 (2012).

[2] Karpan et al, *Phys. Rev. Lett.* **99**, 176602 (2007); *Phys. Rev. B* **78**, 195419 (2008).

[3] van't Erve, Friedman, Cobas, Li, Robinson, Jonker, *Nature Nanotechnology* **7**, 737(2012).

10:40am **MI+EM-TuM9 Graphene Direct Growth on Magnetic Oxides on Co(0001): Graphene Effects on Oxide Magnetic Behavior**, *F. Paquale, Y. Cao, H. Kasi, S. Gaddam*, University of North Texas, *L. Kong, Y. Wang, C. Binek, P.A. Dowben*, University of Nebraska-Lincoln, *J. Kelber*, University of North Texas

The direct growth of graphene on thin (< 50 Å) magnetic oxides on cobalt or other ferromagnetic substrates (Gr/oxide/Co) presents interesting opportunities for development of practical magnetic and magnetoelectric graphene devices. We have grown single and few layer graphene (Gr) directly on Co₃O₄(111)/Co(0001) by MBE, and have very recently grown

graphene by e-beam-assisted deposition on Cr₂O₃(0001)/Co(0001). XPS data demonstrate the presence of a sp²-indicative $\pi \rightarrow \pi^*$ shakeup feature but with C(1s) peak binding energies of 284.9 (± 0.2) eV for Gr/Co₃O₄(0001) -- significantly larger than the 284.5 eV value common for graphitic systems. This indicates significant graphene-to-oxide charge transfer. LEED images yield the expected C_{6v} symmetry and 2.5(± 0.1) Å lattice spacing for graphene, with a 2.8(± 0.1) Å O-O distance at the oxide surface. All are consistent with the literature and indicate incommensurate graphene/oxide interfaces. Domain sizes of ~ 1800 Å are estimated from the LEED data for Gr/Co₃O₄(111), comparable to HOPG. 3 monolayer (ML) Gr/Co₃O₄(111)/Co(0001) exhibits room temperature resistivity 10²⁻³ times smaller than for graphene transferred to other substrates, and consistent with strong p-type doping, as indicated by XPS. Magneto-optic Kerr effect (MOKE) results demonstrate the presence of antiferromagnetic (AF) ordering for the Gr/Co₃O₄(111)/Co(0001) heterostructures up to at least 420 K, with evidence of exchange interaction effects as well. No antiferromagnetic polarization is observed for Co₃O₄/Co films in the absence of graphene, indicating a role played by graphene in the magnetic ordering of the oxide. These results indicate the potential suitability of such films for non-local spin valves and similar devices operating at realistic device temperatures. This talk will also present results for on-going MOKE and transport measurements on graphene/Cr₂O₃/Co(0001) samples. The ability to apply both magnetic and electric fields to such stacks provides the potential for magnetoelectric spin-transistors and tunneling devices.

Acknowledgement: This work was supported by the Semiconductor Research Corporation under Task ID 2123.001 and by C-SPIN, a STARnet center, a Semiconductor Research Corporation program sponsored by MARCO and DARPA.

11:00am **MI+EM-TuM10 Nanocluster Size Effects in Au-Co Nanocomposite Thin Films: Correlated Non-linear Magneto-Optics and Magneto-Transport Studies.** *K. Yang*, The College of William and Mary, *V. Kryutyanskiy*, *I. Kolmychek*, *T. Murzina*, Moscow State University, Russian Federation, *R.A. Lukaszew*, The College of William and Mary

Magnetic materials in nanometer scale typically exhibit significant different magnetic and magnetic-optical properties compared to bulk materials. Composite thin films with magnetic metal clusters embedded in a non-magnetic metal matrix offer a tailored self-assembled nanoscale platform to investigate magneto-optical and magneto-transport properties and possible correlations between them in constrained geometries. The magnetic clusters size as well as the overall composite thin film thickness can be tailored via adequate deposition conditions to achieve a viable nanocluster binary system. We have previously shown that Au/Co/Au trilayers as well as Au-Co nanocomposite thin films exhibit strong enhancement of the linear magneto-optical properties under surface plasmon polariton excitation. [1] Based on these previous results on linear optics measurements, we investigate now the non-linear optical properties such as second harmonic generation (SHG) as well as the magneto-transport properties in Au-Co nanocomposite thin films. Optical SHG is a sensitive probe of surface and buried interfaces due to inversion symmetry breaking at the interfaces of center-symmetric materials which allows probing structural and morphological properties near interfaces. Here we observe a non-monotonous dependence of the SHG magnetic contrast on the cobalt content in Au-Co films, which reveals a sharp increase close to the transition from a granular-like type structure with Co clusters embedded in gold, to an interconnected composite structure when percolation of the cobalt clusters sets in. We also find a SHG enhancement for Co fractional content of 0.35, within the granular structure regime, that can be associated with localized surface plasmon resonance as well as with local field enhancement in an inhomogeneous composite. Furthermore, the magneto-transport measurement (i.e. the magneto-resistance, MR) properties of the Au-Co composite thin films follow similar trend as a function of Co content as the non-linear SHG magnetic contrast before percolation and dramatically deviate once percolation sets in. Thus, our correlated SHG-MR results in Au-Co nanocomposite thin films with varying Co content will be presented and discussed.

[1]. K. Yang et al. Journal of Applied Physics **107**, 103924 (2010); C. Clavero, K. Yang, J. R. Skuza, and R. A. Lukaszew, Optics Express **18**, 7743 (2010).

11:20am **MI+EM-TuM11 Spin and Heat Transport through Interfaces between Metals and Magnetic Insulators.** *G.E.W. Bauer*, Tohoku University, Japan **INVITED**

Spin caloritronics is the science and technology of the physical phenomena (and their control) associated with the coupling of charge, spin, and heat currents in nanoscale structures and devices [1]. Bilayers of magnetic insulators and normal metals have attracted interest in this field because they display the spin Seebeck effect, i.e. the generation of a spin motive force by an applied temperature difference over the interface. In this talk I

will address the theory and applications of power and voltage generation by thermally excited magnetization dynamics at the interface of a magnetic insulator such as yttrium iron garnet (YIG) and normal metals such as platinum.

[1] G.E.W. Bauer, E. Saitoh & B. J. van Wees, Nature Materials **11**, 391–399 (2012)

MEMS and NEMS

Room: 102 A - Session MN+NS-TuM

Micro and Nano Systems based on Carbon and Piezoelectric Materials

Moderator: P. X.-L. Feng, Case Western Reserve University

8:00am **MN+NS-TuM1 Science and Technology of Integrated Piezoelectric and Ultrananocrystalline Diamond Films for a New Generation of High Performance MEMS and NEMS Devices.** *O. Auciello*, University of Texas at Dallas **INVITED**

This review will focus on a discussion of the science and technology for a novel integration of ultrananocrystalline diamond (UNCD) and piezoelectric thin films to enable a new generation of hybrid piezo/diamond heterostructures for low voltage piezoactuated high-performance diamond-based MEMS/NEMS devices. A main component of the new MEMS/NEMS systems is the new UNCD film discovered, developed and patented by our group. UNCD exhibits multifunctionalities applicable to a broad range of multifunctional devices from the macro to the nanoscale. UNCD films are grown using plasma enhanced chemical vapor deposition (PECVD) with a new patented Ar-rich/CH₄ chemistry, which yields insulating films with 2-5 nm grains and 0.4 nm wide grain boundaries or electrically conductive films (NUNCD), with 10 nm grains and 1-2 nm grain boundaries, via nitrogen incorporation into grain boundaries when growing the film with an Ar/CH₄/N₂ gas mixture.

Concurrently with the development of the UNCD film technology, our group has been developing a ferroelectric/piezoelectric thin film technology, based on three main piezo materials (PbZr_xTi_{1-x}O₃, AlN, and the newest BiFeO₃), and the UNCD/piezoelectric thin films integration, which are being used to develop new low voltage/high performance piezoactuated MEMS/NEMS devices for several applications, namely: energy harvesting devices, piezoactuated NEMS switches for a new NEMS logic, biosensors, implantable MEMS/NEMS drug deliver devices, and biologically enabled piezo-MEMS micro-power generators.

In addition to the application to piezo-actuated MEMS, UNCD has been demonstrated as a unique dielectric with fast charging-discharging (in the microsecond range) layer that eliminates RF MEMS switch charging-induced failure, due to fast charge motion in and out of the film through the nano-grain boundaries, enabling a new technology based on reliable RF-MEMS switches integrated with driving CMOS devices for a new generation of phase array antennas for radars and mobile communication devices.

8:40am **MN+NS-TuM3 Utilizing Piezoelectric MEMS Across Length Scales.** *S. Trolrier-McKinstry*, Penn State University **INVITED**

Piezoelectric microelectromechanical systems offer an interesting way of achieving sensing and actuating capabilities on-chip, at voltage levels that are compatible with many CMOS devices. As a result, there is a burgeoning interest in exploiting films that can produce large strains over a wide range in length scales. This talk will address the use of perovskite thin films (especially PbZr_{0.52}Ti_{0.48})O₃, PZT, and 70PbMg_{1/3}Nb_{2/3}O₃ – 30PbTiO₃, PMN-PT) in applications where the critical dimensions range from tens of nm to meters. Particular attention will be placed on 1) use of actuators to correct figure errors in next-generation X-ray space telescopes and 2) a potential CMOS – replacement technology for computation which hinges on use of a piezoelectric thin film to drive a resistance change in a piezoresistor.

On the extreme upper end are large area devices for applications such as adaptive optics. In this case, the piezoelectric film can be used to produce local deformation of a mirror surface, in order to correct figure errors associated with fabrication of the component or to correct for atmospheric distortion. For example, should a mission such as Gen-X be flown, it would require up to 10,000 m² of actuatable optics in order to correct the figures of the nested hyperboloid reflecting segments. The piezoelectric layers were deposited by sputtering; the best insulation properties were obtained in films that avoided lead excess phases at the grain boundaries. Measurements of the influence function resulting from actuation of one or

more of the piezoelectric cells (to change the local curvature of the substrate) demonstrate that such adjustable optics should be able to increase the resolution of X-ray telescopes by an order of magnitude.

A fast, low power, transistor-type switching device has been proposed in which piezoelectric and piezoresistive materials are employed in a stacked sandwich structure of nanometer dimension. Of particular interest to this program is the functionality of the high aspect ratio piezoelectric $70\text{Pb}(\text{Mg}_{1/3}\text{Nb}_{2/3})\text{O}_3\text{-}30\text{PbTiO}_3$ (PMN-PT) component. PMN-PT films of 0.3 – 1.1 microns in thickness were made by a 2MOE solvent sol-gel route. These films were phase pure by XRD with dielectric constants exceeding 1500 and loss tangents of approximately 0.05. The films showed slim hysteresis loops with remanent polarizations of about $8 \mu\text{C}/\text{cm}^2$ and breakdown field $> 1.5 \text{ MV}/\text{cm}$. The films exhibited large signal strain $> 1\%$ with $d_{33,f}$ of approximately $80 \text{ pm}/\text{V}$. It has been found that laterally patterning the piezoelectric layer in this case produces an increased dielectric response indicative of a reduction in substrate-induced clamping.

9:40am MN+NS-TuM6 Two-Dimensional (2D) MoS₂ Semiconducting Crystal Nanomechanical Resonators with Frequency Scaling. J. Lee, Z. Wang, K. He, J. Shan, P. X.-L. Feng, Case Western Reserve University

We report the first demonstration of resonant nanoelectromechanical systems (NEMS) based on ultrathin molybdenum disulfide (MoS_2) crystals down to only a few atomic layers, with measurements of resonances in the high frequency and very high frequency (HF/VHF) bands, and studies of frequency scaling pathways toward the ultrahigh frequency (UHF) and microwave regimes. Atomically-thin two-dimensional (2D) crystals have recently shown interesting promises for enabling new nanoelectronic and optoelectronic devices [1]. The unique mechanical properties of these 2D crystals, including excellent elastic modulus ($\sim 0.2\text{-}1\text{TPa}$) and extremely high strain limits ($\sim 10^2\text{-}10^3$ times higher than in 3D crystals), also make them attractive for 2D NEMS [2,3]. To date, most 2D NEMS have been based upon graphene, the hallmark of 2D crystals. 2D MoS_2 , an ultrathin crystal of transition metal dichalcogenides (TMDCs), has emerged as a new class of 2D layered materials beyond graphene. Unlike graphene being a semimetal, 2D MoS_2 is a semiconducting crystal with a sizeable bandgap and hence opens up new device opportunities. In this work, we describe experiments on realizing drumhead-structured MoS_2 NEMS resonators based upon suspended MoS_2 diaphragms as thin as 6nm (9 layers of the crystal unit cell). We demonstrate resonators operating at up to $\sim 60\text{MHz}$ in the VHF band at room temperature, with measurements of Brownian-motion thermomechanical noise spectra. We also measure quality (Q) factors of these MoS_2 resonators and explore the dominating energy dissipation mechanisms in these 2D structures. The extensive measurements and analysis in this work with many devices establish MoS_2 as a new material for frequency-scalable 2D NEMS resonators and transducers. Our study opens up possibilities for new types of NEMS, where the mechanical properties of 2D MoS_2 can be coupled to its semiconducting attributes.

[1] Q. H. Wang, *et al.*, *Nature Nanotechnology* **7**, 699-712 (2012).

[2] R. A. Barton, *et al.*, *J. Vac. Sci. Technol. B* **29**, 050801 (2011).

[3] J. Lee, P. X.-L. Feng, *Proc. IEEE Inter. Freq. Contr. Symp. (IFCS2012)*, DOI: 10.1109/IFCS.2012.6243742

Manufacturing Science and Technology

Room: 202 B - Session MS+AS+BA+BI+PS+TF-TuM

IPF 2013-Manufacturing Challenges for Emerging Technologies: IV. Manufacturing Challenges: The Life Sciences

Moderator: D.G. Castner, University of Washington, L.J. Gamble, University of Washington

8:00am MS+AS+BA+BI+PS+TF-TuM1 Microfluidics for Chemical Analysis. L. Carr, Q. Bai, R. Brennen, S. Post, G. Staples, K. Seaward, H. Yin, L. Martinez, D. Ritchey, K. Killeen, Agilent Technologies **INVITED**

Chemical analysis is an essential tool for pharmaceuticals, environmental testing, food safety, forensics, energy and many other industries. The need for faster, more accurate and more sensitive measurements continuously pushes the limits of measurement technology and creates opportunities for advances in chemical analysis instruments and applications. One way in which this need can be addressed is by incorporating microfluidic devices in High Pressure Liquid Chromatography (HPLC). Pressure-based microfluidic chips have enabled a new class of reproducible integrated workflow devices that combine sample preparation, enrichment, and HPLC separation *with an integrated ESI/MS (Electrospray Ionization/Mass*

Spectrometry) interface for high sensitivity nanoflow Liquid Chromatography-Mass Spectrometry (LC-MS). These devices have most commonly been fabricated using polymer, ceramic, and glass materials but the next generation of higher capacity and throughput microfluidic chips for LC-MS requires materials and structures capable of ultra high pressure operation. In this work, we describe the fabrication and performance of diffusion-bonded metal chips for high performance nano- and microflow LC-MS operation. The microfabrication technology required to make these devices includes semiconductor fabrication standards such as photolithography and thin film deposition, as well as laser ablation, electrochemical etching, and diffusion bonding. These novel metal devices exhibit state of the art performance in resolution and throughput for microfluidic LC-MS chips. These chips are an example of improvements in measurement sensitivity, resolution, speed, and ease of use that have been made possible by utilizing microfluidic devices for chemical analysis.

8:40am MS+AS+BA+BI+PS+TF-TuM3 Challenges in the Fabrication of Nanoscale Devices for DNA Base Sensing. S. Papa Rao, J. Bai, E.A. Joseph, R.L. Bruce, M. Lofaro, M. Krishnan, M. Brink, M. Guillorn, S.M. Rosnagel, Q. Lin, J. Cotte, C. Jahnke, Smith, Gignac, Reuter, Nam, Astier, Wang, Stolovitsky, Goldblatt, IBM Research Division, T.J. Watson Research Center **INVITED**

The fabrication of integrated circuits with increasingly fine geometries has required the development of advanced process technologies, which can be further refined for the purpose of building devices for biological applications. Applications such as sensing nucleotides in DNA require structures that are of the order of a few nanometers. This talk will focus on the specific challenges encountered in the fabrication of such nano-scale devices – broadly classified into materials-related challenges, unit-process challenges and process integration-related challenges. Issues such as dielectric integrity, metal recrystallization, and materials compatibility with chemistries used down-stream will be discussed. Dimension control during fabrication of $\sim 10 \text{ nm}$ sized structures was achieved through intense process development efforts of reactive ion etch and chemical mechanical planarization (both manufacturing-friendly techniques). Device layout issues that affect manufacturability will be presented. Finally, some of the important lessons learned in achieving a high yield of reliable devices through process-integration changes will also be discussed.

9:20am MS+AS+BA+BI+PS+TF-TuM5 Nucleic Acid Synthesis and Applications. S. Laderman, Agilent Technologies **INVITED**

The pursuit of perfect and practical *de novo* chemical syntheses of nucleic acids has been the foundation of a broad range of life science accomplishments over many decades in the past. Its further pursuit is enabling a broad range of opportunities many decades into the future. These themes will be elucidated by examining the precedents and improvements enabling high throughput genomics for research and diagnostics through the manufacturing of high quality DNA microarrays and complex pools of long oligonucleotides. Looking forward, new ways to synthesize RNA will enable deeper understanding and improved manipulations of cells, tissues and organisms. At the same time, multiple applications of synthetic biology are motivating additional focus on further advances in flexibly and cost-effectively constructing perfect DNA.

10:40am MS+AS+BA+BI+PS+TF-TuM9 Single Molecule, Real-Time DNA Sequencing. S. Turner, Pacific Biosciences **INVITED**

In this talk, I'll convey the story of the development and commercialization of Pacific Biosciences' Single Molecule, Real-Time DNA Sequencing technology. I will start with an overview of the method, how it works, and how it differs from sequencing methods that came before it. I will continue with a discussion of some key technology milestones, with an emphasis on the technological advances in materials engineering and nanofabrication. I'll finish by showing some examples of how this technology has transformed the field of DNA sequencing and genome analysis.

11:20am MS+AS+BA+BI+PS+TF-TuM11 Opportunities and Challenges in the Biobased Products Manufacturing. J. Flatt, S. Bailey, S. Bower, D. Gibson, S. Farah, J. Butler, J. Hannon, Synthetic Genomics **INVITED**

Biobased production of life's necessities, including food, fuels, chemicals and medicines provides a foundation for sustainable and geographically distributed manufacturing processes. Biobased manufacturing utilizes photosynthetic processes directly through conversion of carbon dioxide and light energy or indirectly through conversion of renewable biomass feedstocks to products. Biological cells (biocatalysts) are the operating systems for these biobased manufacturing processes. Rapid advances in synthetic biology enable the engineering of biocatalysts which can produce a broader range of products than previously possible, at high yields and productivities necessary for achievement of desired economics.

Improvements in biocatalysts are achieved through modifications of DNA, which is the software of living systems. Significant advances in the costs, fidelity and speed of DNA synthesis, along with improving understanding of gene function and regulation is enabling the more rapid development of biocatalysts which achieve required performance for commercially viable manufacturing processes. The current state of the art of synthetic biology and technology trends which will impact future development of biobased processes will be discussed. Additional market-specific and process-specific challenges exist, and will be discussed in context of the specific examples taken from manufacture of synthetic vaccines, biobased chemicals and fuels. Recently, Novartis and Synthetic Genomics demonstrated the ability to successfully produce vaccines for prevention of seasonal influenza using synthetic DNA constructs, which significantly reduces the time from influenza strain identification to production of the vaccine seed. Development of this revolutionary process required significant improvement of the fidelity of DNA synthesis and assembly, which provides insight into the challenge of engineering more complex biocatalysts. On the other end of the spectrum, phototrophic microalgae have great long-term potential to provide a sustainable and alternative source of food and liquid transportation fuels. Phototrophic microalgae can be cultivated using non-potable water on non-arable land. Techno-economic analysis (TEA) and life cycle assessment (LCA) both suggest that significant improvements in biocatalyst productivity and capital cost reduction will be required to achieve competitive economics. Maximum observed algal biomass productivities in the range of 20 to 25 g/m²/day are far lower than generally-agreed upon theoretically-achievable productivities based upon the actual solar energy available. Improvement of photosynthetic efficiency in mass culture is required for economical algal-based processes. Limited availability of light in mass culture also limits the maximum achievable cell density, which results in increased downstream processing costs. The challenges of "dilute solution economics" associated with commercial algae production and potential biological and engineering solutions will be discussed.

Nanometer-scale Science and Technology Room: 203 B - Session NS+EM+EN-TuM

Nanoscale Transport and Devices

Moderator: V.P. LaBella, University at Albany-SUNY

8:00am **NS+EM+EN-TuM1 Electrical Transport in 2-dimensional van der Waals Material Heterostacks**, *P. Kim*, Columbia University, *C. Dean*, CCNY

INVITED

The recent advent of atomically thin 2-dimensional materials such as graphene, hexa boronitride, layered transition metal chalcogenide and many strongly correlated materials, has provide a new opportunity of studying novel quantum phenomena in low dimensional systems and their heterostructures utilizing them for novel electronic devices. With a strong built-in anisotropy in their components, vdW materials often show a quasi-low dimensionality leading to strongly correlated electron behaviors. Moreover, combination of different layered constituents may produce heterogeneous and functional materials. In this lecture, we will discuss to develop the method of transferring two-dimensional atomic layers of van der Waals solids to build functional heterostacks. We will discuss novel electron transport phenomena can occur across the heterointerfaces of designed quantum stacks to realize exotic charge transport phenomena in atomically controlled quantum heterostructures.

8:40am **NS+EM+EN-TuM3 Transition in Mechanisms of Size Dependent Properties at Nanoscale Interfaces**, *J. Hou*, *S.S. Nonnenmann*, *W. Qin*, *D.A. Bonnell*, University of Pennsylvania

As electronic and optoelectronic devices scale down to nanometer lengths, the properties of interfaces dictate performance. An important class of interfaces, metal-semiconductor and/or oxide contacts, have been shown to exhibit size dependent electronic properties. In this work, the mechanisms of size dependent properties at interfaces of noble metal nanoparticles and substrates is examined. Electron transport and interfacial atomic structure of a model system -- Au/SrTiO₃ (STO) junctions, is systematically investigated with conductive Atomic Force Microscopy (AFM) and Transmission Electron Microscopy (TEM). In the range of 200 nm to 20 nm interface transport properties are size dependent, with ideality factor and Schottky barrier height derived from I-V curves. The relative amounts of tunneling and thermionic emission transport are quantified. A transition between two mechanisms of size dependence is identified. Implications to resistive switching are discussed.

9:00am **NS+EM+EN-TuM4 Quantum Correction to the Transition Localization in La_{2/3}Sr_{1/3}MnO₃ Thin Films at Low Temperatures**, *Y. Gao*, Max Planck Institute for Solid State Research, Germany, *W. Sigle*, Max Planck Institute for Intelligent Systems, Germany, *J. Zhang*, Shanghai University, Republic of China, *D. Zhou*, Max Planck Institute for Intelligent Systems, Germany, *G.X. Cao*, Oak Ridge National Laboratory, *H.U. Habermeier*, Max Planck Institute for Solid State Research, Germany

The low-temperature magnetotransport properties of manganite thin films are characterized by the occurrence of resistivity minima, ρ_{min} , below 60 K whose origin and especially role of disorder has not yet been explored in detail. In order to contribute to the clarification of the physical mechanism giving rise to the resistivity minimum in these systems, an appropriate concentration (20% and 30%) of nanoscaled nonmagnetic ZrO₂ particles are introduced as a secondary phase into La_{2/3}Sr_{1/3}MnO₃ thin films. We present the quantum corrections to conductivity in La_{2/3}Sr_{1/3}MnO₃ thin films with ZrO₂ nano-particles. As impurities increases, the upturn of resistivity enhances. The interesting results were analyzed by perturbation/quantum correction theory and a model which deviates from the traditional concept of localization was established, where the conductivity originates from the "impurity band". Using the tight-binding scaling theory of localization model, we change the density of impurities and tune the degree (intensity) of disorder, making the state of disorder change from weak localization to strong localization in 2 dimensional (2D) and 3 dimensional (3D) cases. The HR-TEM/ABF/HAADF images also confirm our conclusion that indicates the coexistence of 2D and 3D behavior in one system.

9:20am **NS+EM+EN-TuM5 Nano-enabled Chemical, Bio and Radiation Sensors**, *M. Meyyappan*, NASA Ames Research Center

INVITED

We have been pursuing development of chemical and biosensors using CNTs for the last several years and this talk will present our progress to date. In the case of chemical sensors, we use an interdigitated electrode as a chemiresistor, where purified SWCNTs serve as the conducting medium. When the chemiresistor is exposed to a gas or vapor, the change in resistance is recorded; if SWCNTs do not respond to a particular gas or vapor, then doping or functionalization strategies are used. A sensor array is constructed with 32-96 sensor elements with chemical variations across the sensor array. In the sensor training mode, a pattern of resistance changes is generated from the sensor array for a particular analyte at a given concentration and humidity level; this needs to be repeated for various concentrations and humidities and the generated information is stored for later use. In the identification mode, a pattern recognition algorithm is used to identify that analyte from the background using the information stored during training. This talk will present examples from our work to demonstrate the functioning of the sensor in security and biomedical applications. This sensor has also been integrated in an iPhone. We have recently made these sensors on cellulose paper substrates as well. In the case of the biosensor, a "lock and key" approach is used wherein a preselected probe for a given target is attached to the tip of a carbon nanofiber (CNF). CNFs in a patterned array are grown using PECVD on a silicon wafer which serve as individual, freestanding, vertical electrodes. This nanoelectrode array (NEA) can use DNA, aptamer and antibody probes, and electrochemical impedance spectroscopy is used upon probe-target binding for signal analysis. Results will be presented for identification of e-coli and ricin using this NEA and applications for security and biomedical sectors will be illustrated. For radiation sensing, we have developed a nanogap FINFET-like device wherein the nanogap can be filled with a radiation-responsive gel or liquid and demonstrated detection of gamma radiation. An array of devices with different liquids can be used in a multiplexed mode as a radiation nose. The author thanks Jing Li, Yijiang Lu, Jessica Koehne and Jinwoo Han.

10:40am **NS+EM+EN-TuM9 Ultraflexible and Stretchable Organic Devices for Biomedical Applications**, *T. Someya*, *M. Kaltenbrunner*, The University of Tokyo, Japan, *S. Bauer*, Johannes Kepler University, Austria, *T. Sekitani*, The University of Tokyo, Japan

INVITED

We have successfully manufactured ultraflexible organic thin-film transistors and photovoltaic cells on ultrathin plastic film with the thickness as small as 1.2 μ m. These novel organic devices are much lighter than bird's feathers. First, we have demonstrated polymer based photovoltaic devices on plastic foil substrates of 1.2 μ m thick, with equal power conversion efficiency to their glass-based counterparts. They can reversibly withstand extreme mechanical deformation and have unprecedented solar cell specific weight. Instead of a single bend, we were able to form a random network of folds within the device area. We have also manufactured organic transistors on ultrathin plastic films in order to achieve sharp bending radius less than 50 μ m. Bending cycle experiments will be presented to show the mechanical durability. Moreover, the issues and the future prospect of flexible organic devices such as thin-film transistors, photovoltaic cells, and memories will be addressed. Furthermore, ultraflexible and stretchable

electronic systems have been exploited for biomedical applications such as medical catheters and implantable devices.

11:20am **NS+EM+EN-TuM11 Ultrahigh Thermal Conductivity Gold Nanowire-Filled Polymer Composites and Interfaces, I. Seshadri, N. Balachander, R.J. Mehta, L. Schadler, T. Borca-Tasciuc, P. Koblinski, G. Ramanath**, Rensselaer Polytechnic Institute

Realizing high thermal conductivity nanocomposites is a major challenge because of difficulties in incorporating high fractions of uniformly dispersed nanofillers and countering low filler-matrix interfacial conductance. Here, we obviate these issues by using < 3 volume% ultrathin sub-10-nm gold nanowire fillers to obtain an unprecedented 30-fold increase in polydimethylsiloxane [1] thermal conductivity to $\sim 5 \text{ Wm}^{-1}\text{K}^{-1}$ that is 6-fold higher than any previously reported nanocomposite filler including graphene, carbon nanotubes and silver nanowires, at lower filler loadings, and exceeds theoretical predictions. The nanowire diameter and aspect ratio are key to obtaining cold-welded networks that enhance thermal conductivity, while fostering low modulus and electrical conductivity. The nanocomposites exhibit high compliance with a low elastic modulus of $\sim 5 \text{ MPa}$ conducive for conformal formation of interface contacts. However, the interfacial thermal contact conductance of the nanocomposites interfaced with copper is low, e.g., $\sim 1.5 \text{ kWm}^{-2}\text{K}^{-1}$. Rheology measurements reveal that the low conductance is due to a liquid-solid transition that is sensitive to the nanowire loading fraction. In particular, the filler loading corresponding to the formation of a percolation network and maximizing the nanocomposite thermal conductivity also corresponds to a large increase in the polymer pre-cure viscosity. These results provide insights on designing processes to increase the thermal contact conductance at interfaces where efficient heat transport is of importance, e.g., in device packaging applications.

I. N. Balachander, I. Seshadri, R.J. Mehta, L.S. Schadler, T. Borca-Tasciuc, P. Koblinski, and G. Ramanath, "Nanowire-filled polymer composites with ultrahigh thermal conductivity," *Applied Physics Letters*, vol. 102, 2013, pp 093117 – 093117-3.

11:40am **NS+EM+EN-TuM12 Microscopy and Spectroscopy Study of Immobilization of Molecularly Imprinted Nanoparticles on (3-glycidioxypropyl)trimethoxysilane Modified Silica, T. Kamra, L. Ye**, Lund University, Sweden

Molecularly imprinted nanoparticles (MIPs) are polymeric structures which are prepared to the attachment of specific molecules in bio-sensing applications. Ideally, MIPs should be covalently immobilized on solid supports to allow efficient and easy use. Here we have studied a particular two-step method of immobilization, which makes use of an epoxide binding layer. For characterization we have used an array of different methods: scanning electron microscopy (SEM), atomic force microscopy (AFM), fluorescence microscopy, water contact angle measurements, and x-ray photoelectron spectroscopy (XPS).

The first step of the method is the modification of a silica support by an epoxide binding layer. This is achieved by treating the surface with 3-glycidioxypropyltrimethoxysilane (GPTMS) [1]. We find that we can achieve uniform, stable, and dense GPTMS layers with the desired epoxide termination. In the second step the amine-functionalized core-shell MIPs (300nm) specific to the sensing of propranolol are bonded to the surface via the terminal epoxy groups of the GPTMS layer. Covalent bonding is achieved via a ring opening reaction. Our microscopy experiments and water contact angle measurement show that the procedure results in a MIP layer with good surface homogeneity and coverage, although XPS shows that the layer is not completely dense. Nonetheless, we can conclude that GPTMS is highly effective for holding large polymeric core-shell MIPs for robust sensor applications.

[1] Vladimir V. Tsukruk, Igor Luzinov, and Daungrut Julthongpipit, *Langmuir* **1999**, 15, 3029-3032.

Plasma Science and Technology
Room: 102 B - Session PS1-TuM

Plasma Sources

Moderator: S. Shannon, North Carolina State University

8:00am **PS1-TuM1 Non-ambipolar Electron Plasma and its Physical Properties, L. Chen, Z.Y. Chen, M. Funk**, Tokyo Electron America, Inc.

This report discloses a new type of plasma source: the Non-ambipolar Electron Plasma (NEP). Although, it is basically heated by electron beam, its power coupling and plasma physical property differentiate itself from the generic e^- -beam plasmas. Such differences open up potential applications

that could have been difficult with the generic plasmas. The NEP system consists of two plasmas separated by a dielectric charged-species injector. Plasma-1 is the ground-referenced electron-source plasma (e.g., Ar) and it is an inductively coupled source (ICP) in this study for convenience reason. Plasma-2 is the NEP itself whose majority plasma-boundary is the DC-conductive accelerator with the remaining minority plasma-boundary being dielectric. NEP is typically molecular (e.g., N_2) in the pressure range of 1-3 mtorr and its accelerator voltage varied from $V_A=+80$ to $V_A=+600\text{V}$. The NEP plasma potential (V_p) is boundary-driven. Therefore, NEP V_p tracks the accelerator voltage with its value just very slightly above V_A . The current across the dielectric charged-species injector is non-ambipolar: only electrons are transported from ICP to NEP and only positive-ions are transported from NEP to ICP. The non-ambipolar electron-current injected into NEP is in the range of $10s \text{ Acm}^{-2}$ with beam-energy $\sim eV_A$ and it heats NEP through beam-plasma instabilities. Its EEDf has a Maxwellian bulk followed by a broad energy-continuum connecting to the most energetic group with energies above the beam-energy. The remnant of the injected electron-beam power terminates at the NEP end-boundary floating-surface setting up sheath potentials from $V_S=80$ to $V_S=580\text{V}$ in response to the applied values of V_A . The floating-surface is bombarded by a space-charge neutral plasma-beam whose IEDf is near mono-energetic. When the injected electron-beam power is adequately damped by NEP, its end-boundary floating-surface V_S can be linearly controlled at almost 1:1 ratio by V_A . NEP does not have an electron-free sheath; its "sheath" is a wide presheath that consists of a thermal presheath followed by an "anisotropic" presheath, leading up to the end-boundary floating-surface. Its ion-current of the plasma-beam is much higher than what a conventional thermal presheath can supply. If the NEP parameters cannot damp the electron beam power sufficiently, V_S will collapse and becomes unresponsive to V_A .

8:20am **PS1-TuM2 Ion Energy-Angular Distributions in Dual Frequency Capacitively Coupled Plasmas Using Phase Control, Y. Zhang, M.J. Kushner**, University of Michigan

Dual frequency capacitively coupled plasmas (CCPs) provide the microelectronics fabrication industry with flexible control for high selectivity and uniformity. For a given low frequency (LF) bias, the magnitude and wavelength of the high frequency (HF) bias will affect the electron density, electron temperature, sheath thickness and so ion transit time through the sheath. These variations ultimately affect the ion energy and angular distributions (IEADs) to the substrate. For example, with higher HF power, the electron density and ion fluxes will increase, which will increase the etch rate. However, the higher HF power will also reduce the sheath thickness and reduce the ion transit time. This will produce more structure in the IEADs. One potential control mechanism for the IEADs is the relative phase of the LF and HF biases. In this paper, results from a two-dimensional computational investigation of Ar and Ar/ $\text{C}_4\text{F}_8/\text{O}_2$ plasma properties in an industrial CCP reactor are discussed. The resulting IEADs are used as inputs to a feature profile model to assess etch profiles. In this reactor, both the LF (2 MHz) and HF (up to 60 MHz) are applied to the lower electrode. The phase between the LF and HF is controlled.

To separately control rates of ionization and the shape of IEADs, the HF should be significantly higher than the LF. Under these conditions, there are many HF cycles per LF cycle. Although there are clear changes in the IEADs when varying the phase between the HF and LF, these changes are modulations to the IEADs whose shape is dominated by the LF. By sweeping the phase difference between the LF and HF, these modulations can be used to smooth and sculpt the IEADs. As the difference between the HF and LF becomes smaller, the IEADs become more sensitive to the phase differences between the HF and LF. These phase differences also affect the dc bias, an affect often call the electrical-asymmetry-effect when the frequencies are equal. Profile simulations are used to demonstrate possible control schemes for over-etch through phase control.

*Work supported by the Semiconductor Research Corp., DOE Office of Fusion Energy Science and the National Science Foundation.

8:40am **PS1-TuM3 Investigation of Photo-Assisted Etching in Different Halogen-Containing Plasmas and Synergetic Effects of a Tandem Plasma System, W. Zhu*, L. Liu, S. Sridhar, V.M. Donnelly, D.J. Economou**, University of Houston

Photo-assisted etching (PAE) of p-type Si in halogen-containing plasmas was discovered at sub-threshold ion energy in a Faraday-shielded, inductively coupled plasma (ICP). Halogen-containing feed gases (Br_2 , HBr , Br_2/Cl_2 and HBr/Cl_2) were explored and the strong dependence of PAE on different etchant gases was investigated. Sub-threshold etching rates in 50% halogen /50% Ar cw ICPs were ordered as 25% $\text{HBr}/25\% \text{Cl}_2 > 25\% \text{Br}_2/25\% \text{Cl}_2 > 50\% \text{Cl}_2 > 50\% \text{HBr} > 50\% \text{Br}_2$. H-atoms also caused isotropic etching in HBr plasmas; sub-threshold etching of patterned p-Si in

* **Coburn & Winters Student Award Finalist**

other gases was anisotropic. PAE was much less important for Br₂, with an etching rate 4 times slower than that for Cl₂, under similar conditions. The dependence of PAE on incident photon energy was characterized by filtering incident photons with different wavelength to the sample surface. Vacuum UV was much more important than UV or visible light in inducing PAE. PAE is expected to cause substantial complications for processes that require low ion energies to achieve high selectivity and low damage, such as atomic layer etching. To address this issue, a tandem plasma system was developed to inject one plasma (upper plasma) into another plasma (lower plasma) separated by a grid. A “boundary electrode” (BE) in contact with the upper plasma could be biased to influence the plasma potential. The goal was to manipulate the electron energy distribution functions (EEDF), and possibly enhance ion-assisted etching compared to PAE. Plasma parameters and EEDFs were measured with a Langmuir probe over a wide range of power, pressure and position in cw Ar plasmas. With both plasmas powered (100 W lower plasma/ 500W upper plasma) at 10 mTorr, low energy electrons were depleted in the lower plasma when the BE was grounded. However, with 60 V bias on the BE, low energy electron depletion did not occur, and the high energy tail was enhanced. The reverse behavior was found in the upper plasma under the same conditions. Pulsed lower plasma with cw upper plasma injection was also explored. High plasma density of $2 \times 10^{11} \text{ cm}^{-3}$ with selectable, nearly-constant T_e (e.g. 0.8 eV) was achieved in the afterglow of the lower plasma at 10 mTorr.

9:00am **PS1-TuM4 Control of Energy Distributions in Inductively Coupled Plasmas using Tandem Power Sources**, *M.D. Logue*, University of Michigan, *W. Zhu, H. Shin, L. Liu, S. Sridhar, V.M. Donnelly, D.J. Economou*, University of Houston, *M.J. Kushner*, University of Michigan

In plasma materials processing, finer control of the electron energy distribution, $f(\epsilon)$, enables better selectivity of generating reactants produced by electron impact excitation and dissociation. This is particularly important in low pressure, inductively coupled plasmas (ICPs) where dissociation products often react with surfaces before interacting with other gas phase species. Under these conditions, fluxes to surfaces are more directly a function of electron impact rate coefficients than gas phase chemistry. Externally sustained discharges are able to control $f(\epsilon)$ by, for example, augmenting ionization independent of the $f(\epsilon)$ of the bulk plasma so that $f(\epsilon)$ can be better matched to lower threshold processes. In this case, the tail the $f(\epsilon)$ is lowered. Following the same logic, introducing additional losses by external means will produce an increase in the tail of $f(\epsilon)$. To achieve this control, a tandem (dual) ICP source has been developed. In this device, the primary (lower) source is coupled to the secondary (upper) source through a biasable grid to control the transfer of species between the two sources with the intent of controlling $f(\epsilon)$ in the primary source. A boundary electrode (BE) at the top of the system, along with the grid, can be dc biased to shift the plasma potential. This controls the energy of charged species passing into the primary source as well as ion energy distributions (IEDs) to surfaces.

Results will be discussed from a computational investigation of the control of and IEDs, in a tandem source ICP system at pressures of tens of mTorr. The model used in this study is the Hybrid Plasma Equipment Model (HPeM) with which $f(\epsilon)$ and IEDs as a function of position and time are obtained using a Monte Carlo simulation. $f(\epsilon)$ and IEDs will be discussed while varying the relative power in the primary and secondary sources, and dc biases (BE and grids) in continuous and pulsed formats. Results from the model will be compared to experimental data of $f(\epsilon)$ and IED obtained using a Langmuir probe and a gridded retarding field ion energy analyzer.

* Work supported by the DOE Office of Fusion Energy Science, Semiconductor Research Corp. and the National Science Foundation.

9:20am **PS1-TuM5 Si-Gate Etching in Radial Line Slot Antenna Plasmas: Control of Selectivity, Anisotropy and Loading**, *S. Voronin, A. Ranjan, H. Kintaka, K. Kumar, P. Biolsi*, TEL Technology Center, America, LLC

Shrinkage of transistors as dictated by Moore’s law is required to make smaller, faster and less power-consuming devices at lower cost. 3-D gate transistors at 22nm technology node and beyond are needed to continue Moore’s law. To obtain all these advantages of 3-D transistors, their fabrication has stringent requirements to the etch process such as high anisotropy, high selectivity to Fin and Gate mask films and minimum loading between isolated and nested lines. In addition, precise control over the gate profile from a vertical to a slightly negative angle is important for integration purposes. In this work we present highly selective 3D gate etching in halogen-based Radial Line Slot Antenna plasma. Having spatially separated plasma generation and plasma processing regions, RLSA™ etchers benefit of a very low electron temperature ($T_e \sim 1\text{eV}$) processing plasma discharge compared to conventional sources. Low electron temperature in the process plasma provides low dissociation rates of by-product and precursor gas, and ion bombardment of the structure at very low energies resulting in small iso-nested loading and very high

process selectivity respectively. The ability of RLSA™ plasma sources to operate in a very wide range of the pressures allows the etch process well above 100mT. This leads to further decrease of the electron temperature in the bulk and the ion energy, providing notch-free etching of the structure. Changing by-product re-deposition rate by O₂ flow, etching times and bias power modulation regimes we can effectively control the gate profile from slightly tapered to slightly inverted tapered. Iso-nested delta can be minimized (and even reversed) by adjusting the process chemistry, bias power and pressure. Being very selective, RLSA™ plasma process allows very long over-etching times without damaging the mask. This makes the process universal, minimizes wafer-to-wafer profile variation and effective for etching the structures where Si layer thickness varies across the wafer. It is shown that artificial increase of the plasma electron temperature in the chamber to $\sim 2\text{eV}$ (an analog of a conventional plasma etcher) results in dramatic decrease of process selectivity to the oxide.

9:40am **PS1-TuM6 Vacuum-Ultraviolet Emission Spectra of Plasma-Processing Reactors**, *K. Mavrikakis, M. Nichols, W. Li, K. Katz*, University of Wisconsin-Madison, *J. McVittie, A. Hazeghi*, Stanford University, *S. Banna*, Applied Materials Inc., *Y. Nishi*, Stanford University, *J.L. Shohet*, University of Wisconsin-Madison

Plasma processing is an essential part of modern integrated circuit fabrication. The unique ability of plasmas to etch various materials in an anisotropic way and also to deposit thin films (PE-CVD) has made plasma processing the dominant method of processing modern IC circuits. One of the key problems with plasma exposure of low-k dielectric materials is that processing damage from vacuum ultraviolet emission (VUV) can take place. In order to further investigate the radiation-induced damage to dielectric films, it is important to determine whether different plasma reactors produce significant variations in their generated VUV spectra. In this work, we examine the VUV spectra generated by four unique plasma reactors using argon as the fill gas. They are: electron cyclotron resonance, capacitively coupled, neutral loop/ICP and microwave slot-plane antenna reactors. A McPherson Model 234 VUV monochromator was used for all measurements. The monochromator was fit to each reactor through a sequence of port aligners and collimation systems so that plasma light was well focused on the input slits. The output of the monochromator was focused on a sodium salicylate coating that scintillates in the visible portion of the spectrum and that light was detected by a photomultiplier. It was expected that the emission intensity varied with pressure and microwave power. However, depending on the reactor involved, this is not always the case. The resulting data shows that the emission intensity increases with the decrease of pressure and the increase of microwave power. The interesting result that we obtain is that argon does not always follow that trend over the same pressure and power ranges. As a result, it is important to optimize the processing conditions to minimize the VUV output whenever possible.

This work has been supported by the Semiconductor Research Corporation under Contract No. 2012-KJ-2359 and by the National Science Foundation under Grant CBET-1066231.

10:40am **PS1-TuM9 Counteractions to Plasma Chamber Corrosions by Earthquake**, *T. Moriya*, Tokyo Electron, Japan **INVITED**

At the Japan’s big earthquake in 2011, the plasma etching tools have received the big damages from the earthquake. Most of the etching tools were not able to be used normally. Many particles were contaminated to the wafers during etching process because the chambers were corroded by the outgassed acids during shutdown for several days. Just when the big earthquake attacked to the plant, some etching tools were on maintenance (doing wet cleaning). Because the technicians had to escape out of the clean room with leaving the tools as it is, some halogen gasses (fluorine, chlorine, bromine and so on) were outgassed from the process chambers. These gasses were combined with humidity in the room and became kinds of acids. In the process modules, the metal components were mostly corroded by the halogen-outgas related acids. Especially, as the gas feeding lines were contaminated, a lot of defects were created by the particles. In fact, a lot of particles were counted on wafers because of the corrosion related particle contaminations. By wet wiping of the process chambers, there were some good effects to the particle reduction but it was NOT completed. So, we checked and replaced many parts such as gas feeding line with using some special techniques. After that, the particle level was recovered to normal. The surface particle monitor was used to check the *in situ* particle level and worked effective. For checking the particles in the gas line, we suggest new method to observe the particles by using a wafer and creating a shockwave in the gas line. Since we already had the reference data which was obtained before the earthquake, we could compare between the normal condition and the current condition from the viewpoint of chamber contamination. There is another serious problem such as RF reflection alarms. This alarm means that the RF power cannot be supplied to the tool appropriately. As we changed some chamber parts, polished contacting areas and also changed the software parameters, and then, the RF reflection

alarms were eliminated completely. The static chamber impedance measurement was also done to check the electric property. We also recorded the normal condition of the plasma chamber before the earthquake. So, we could compare between the normal condition and the current condition from the viewpoint of chamber electricity. If we want to manage the risks of corrosion by the earthquake, not only the surface particle count but also the static chamber impedance and the conditions of metal parts should be recorded periodically during the normal situation.

11:20am **PS1-TuM11 An Improved Cathodic Arc Plasma Source for Large Area Coatings**, *J. Kolbeck, A. Anders*, Lawrence Berkeley National Laboratory

Cathodic arc plasmas are widely used in the hard coatings industry to produce binary and ternary metal nitrides and oxynitrides, some of them exhibiting superhardness (> 40 GPa) and high oxidation resistance at elevated temperature. High deposition rates (10-100 nm/min) and self-ion-assistance to film growth are attractive features of the arc deposition process. However, microscopic droplets or "macroparticles" produced at cathode spots have prevented broader application of this technology, for example to optical coatings or to thin films used in the electronics industry. Here we report on the development of a linear cathodic arc plasma source that can be coupled to a linear macroparticle filter. We aim to develop a plasma source suitable for high-rate, large-area coatings, where films are essentially free of macroparticles. Operation and performance of the improved source will be demonstrated with metal and metal oxide films.

Specifically, we deposited aluminum-doped zinc oxide (AZO), a transparent conducting oxide which is non-toxic and made from abundant materials, a prime candidate for replacing the more expensive indium tin oxide (ITO) in some applications. AZO deposited on glass by filtered cathodic arc plasma exhibit very high electron mobility (some samples exceeding $50 \text{ cm}^2/\text{Vs}$) for moderately high carrier concentrations ($\sim 10^{20} \text{ cm}^{-3}$), high transmittance in the visible and solar infrared (80-85%), with sheet resistance as low as 10 Ohms per square for relatively thick ($\sim 1 \mu\text{m}$) films. AZO was also deposited on polycarbonate plastic at room temperature, with properties of interest to flexible electronics.

11:40am **PS1-TuM12 High Density Narrow Tube Ozonizer by Increased Barrier Discharge Frequency**, *J. Tsujino, T. Kitajima, T. Nakano*, National Defense Academy of Japan

Atmospheric plasmas are being general tool for various surface treatment applications, such as cleaning, sterilization, hydrophilic property control, etc. Among these applications, oxygen related radicals are the key species to influence the surface chemistry of the target. For the transport of the radical, spraying plasma processed gases to the object is commonly applied among these uses. There are certain reasons to develop high density atmospheric plasma source which is compact and able to be introduced or "retrofit" to the current chemical processing systems. In the current study, we are developing the high frequency atmospheric ozonizer plasma source in general 1/4 inch O.D. tube which gives high density ozone.

High frequency barrier discharge at 280 kHz consists of the alumina tube, the copper grounded electrode, and the aluminum drive electrode. (shown in fig . 1) The aim of MF range of frequency is to shift power deposition target to electrons from ions, and to increase the barrier discharge frequency. High voltage for the barrier discharge (0.5 mm gap) is produced by the LC resonance circuit (fig . 2).

Comparison of ozone density between 50 Hz ($0.8 \text{ g}/\text{Nm}^3$, 40 kVpp) and 280 kHz ($30 \text{ g}/\text{Nm}^3$, 6.5 kVpp) shows the production rate is increased 40 times for realistic voltage range (fig . 3).

V-I characteristic of 280 kHz (fig . 4) shows the discharge current and power is increased steeply around 6 kVpp that corresponds to the rapid increase of ozone production rate.

The increase of power with voltage is explained by the change of waveform (fig . 5). Small change of the voltage leads to the forwarding of the current phase and increase of barrier discharge frequency.

The power efficiency of the ozonizer is $19 \text{ g}/\text{kWh}$ which is comparable to the commercial small scale unit.

Plasma Science and Technology Room: 104 C - Session PS2-TuM

Advanced FEOL/Gate Etching

Moderator: G.Y. Yeom, Sungkyunkwan University, Republic of Korea

8:00am **PS2-TuM1 Evaluation of Highly Selective ZrO₂ and HfO₂ based Hard Mask Stacks for sub 30 nm Node Dry Etch Pattern Transfer**, *J. Paul, X. Thrun, S. Riedel, M. Rudolph*, Fraunhofer Institute for Photonic Microsystems (IPMS-CNT), Germany, *S. Wege*, Plasway, Germany, *C. Hohle*, Fraunhofer Institute for Photonic Microsystems (IPMS-CNT), Germany

The main challenge for future leading edge patterning results from an aggressive trend in reduction of resist thickness for high resolution lithography. For instance, at the 25 nm DRAM technology node, a maximum resist thickness of 30 to 60 nm is predicted by the ITRS for 2014. Moreover, the hard mask thickness will be limited by the thickness of the photoresist. Different approaches such as multi-layer resists were discussed to enable pattern transfer with reduced resist thicknesses. These approaches are focusing more and more on innovative underlayer materials and anti-reflective coatings providing a higher etch selectivity. Novel hard mask concepts with reduced layer thickness and improved etch selectivity can be seen as an alternative strategy.

The present work reveals a new hard mask concept based on ZrO₂ and HfO₂ materials in combination with a SiO₂ capping layer to provide the high resolution pattern transfer into the substrate. An excellent silicon and carbon etch selectivity is focused for semiconductor manufacturing. Besides the scaling capability, the hard mask concept was evaluated in terms of etch selectivity, hard mask roughness, removal of remaining hard mask after etch and cost-saving deposition method. Therefore atomic layer and spin-on depositions of HfO₂ and ZrO₂-based hard masks were investigated. Additionally the influence of dopants on the etch properties and patterning results was evaluated.

The dual hard mask concept was demonstrated using 35 nm thin layers of ZrO₂ and HfO₂ based material and 45 nm SiO₂ deposited on 300 mm wafers. The resist (50 nm) was directly applied on the hard mask and arrays of holes and trenches (CD 30 nm to 500 nm) were printed by electron beam direct writing. The hard mask open was performed in a two-step process by CCP and ICP type etch chambers. The hole and trench pattern were transferred into silicon and carbon by dual-frequency MERIE CCP and triple-frequency CCP type etch system, respectively. Finally the remaining mask was removed by wet etching without deterioration of the etched profiles. This sequence allowed the preparation of structures with aspect ratios up to 20:1 (CD 30 to 60 nm) and revealed a high overall hard mask selectivity to silicon e.g. $\sim 35:1$.

This new dual-layer concept enables a significant reduction of overall hard mask thickness and the patterning of 30 nm structures and a potential technology approach for more critical structures in the sub 20 nm range.

8:20am **PS2-TuM2 Approach to LER/LWR Improvement with Combination of DCS Technology and Newly Developed Resist Material**, *M. Honda, K. Kobayashi*, Tokyo Electron Miyagi Limited, Japan, *M. Yamato, K. Oyama, H. Yaegashi, H. Mochiki*, Tokyo Electron Limited, Japan

Due to the continued scaling in semiconductor industry, reducing line edge roughness (LER) and line width roughness (LWR) during photoresist mask pattern transfer by etch becomes increasingly important at 10nm and beyond.

Our previous studies showed that successful LER/LWR reduction was achieved by optimizing plasma treatment conditions and DC superposition (DCS) technology which is resist hardening by highly energetic electrons incident onto wafer in DC+RF hybrid capacitively-coupled reactor [1,2]. On the other hand, newly developed PMMA-based 193nm resist material with low etching durability has been proposed for the further reduction of LER/LWR [3,4].

In this paper, we investigated the effect and mechanism of DCS technology on newly developed 193nm resist material. As a result, we achieved LER=1.2nm with new 193nm resist material by etching durability enhancement of DCS technology. We also found that DCS technology is very effective for CD shrink control especially required for future BEOL patterning. This integrated solution of resist material modification and DCS technology will allow us for expanded process window for LER/LWR control at 10nm and beyond critical patterning etch.

Reference

[1] M. Honda et al., Proc. of SPIE 8328-09 (2012)

- [2] M. Honda et al., AVS 59th Int. Symp. & Exhibit. (2012)
 [3] H. Yaegashi et al., Proc. of SPIE 8325-11 (2012)
 [4] K. Ohmori et al., Proc. of SPIE 8325-12 (2012)

8:40am **PS2-TuM3 Metrology and Linewidth Roughness Issues during Complex High-k/Metal Gate Stack Patterning for sub-20nm Technological Nodes**, E. Pargon, M. Fouchier, CNRS-LTM, France, O. Ros Bengochea, STMicroelectronics, J. Jussot, UJF, France, E. Dupuy, M. Brihoum, CNRS-LTM, France

INVITED

Gate Line Width Roughness (LWR) or Line Edge Roughness (LER) is considered today as a factor limiting CMOS downscaling. No technological solution is currently known to reach the 1.7nm gate LWR required for the sub-20nm technological node. The origin of the LWR/LER of the final transistor gate is mainly attributed to the significant roughness of the photoresist (PR) pattern printed by the lithography step, which is partially transferred into the gate stack during the subsequent plasma etching steps. Thus, those passed few years, many efforts have been focused on the development of post-lithography resist treatments in order to minimize the LWR of resist patterns prior to plasma transfer. Another issue related to LWR/LER is the availability of accurate and convenient metrology tools for their evaluation. The status on LER/LWR metrology is that there is today no reliable and efficient metrology equipment to determine LWR at the very bottom of structures, where the key LWR information lies, as well as to estimate sidewall roughness of complex high-k/metal gate stacks composed of a multitude of very thin layers of dielectrics, metals and semiconductors.

We first propose a method based on AFM to measure LER accurately down to feature bottom for any types of pattern profiles (anisotropic, tapered or re-entrant). We will show that it presents a great potential for better understanding the mechanism of LER transfer during complex high-k/metal gate stack patterning.

Various post-lithography processes based on thermal or plasma treatments are also evaluated to decrease resist pattern LWR. A particular attention is paid to characterize the roughness by its frequency spectrum since for gate applications low frequency roughness components remain the key issue. We will show that optimized plasma treatment for LWR reduction may use plasma conditions leading to intense optical emission in the vacuum ultra violet (VUV) range (<200nm), and limiting the deposition of carbon outgassed resist byproducts on the pattern sidewalls. Moreover, we show that thermal process applied after plasma treatment can improve further the resist LWR, provided that no carbon deposition be previously formed on the resist sidewalls during the plasma treatment. The best available post-lithography treatment allows a 50% LWR reduction, while maintaining the critical dimension control. Finally, the developed AFM technique is used in comparison with CD-SEM to study the transfer of the reduced resist LWR into the gate stack during the patterning.

9:20am **PS2-TuM5 Possible Si Damage Formation and Redeposition in Vertical Gate Etching Processes by HBr Plasmas**, Y. Muraki, H. Li, T. Ito, K. Karahashi, Osaka University, Japan, M. Matsukuma, Tokyo Electron Ltd., Japan, S. Hamaguchi, Osaka University, Japan

Reactive ion etching (RIE) by halogen-based plasmas such HBr plasmas are widely used for Si etching in semiconductor manufacturing processes. It has been known that, for a Si surface, Br ions have high etching yields, high selectivity over SiO₂ and SiN, and high etching anisotropy. However, in recent years, as non-classical CMOS structures such as vertical multi gates have been introduced for near-future devices, there has been a concern on possible damages caused by highly energetic hydrogen ions (H⁺) that hit a Si surface even at grazing angles. For vertical multi gates, the Si surfaces subject to direct ion bombardment function as gate channels, ion bombardment damage to the surface must be minimized. In this study, we have evaluated sputtering yields of Si by Br⁺, H⁺ and SiBr⁺, as functions of incident energy in the range from 300 eV to 1000eV as well as functions of the incident angle. We have also examined Si substrate damages caused by ion bombardment by transmission electron microscopy (TEM) and High-resolution Rutherford Backscattering Spectrometry (HRBS). It has been found that there is strong angle dependence of the Si etching yield by Br⁺ ion irradiation, which indicates that Br⁺ ion etching has also an aspect of physical sputtering despite its high chemical reactivity with Si. Although, in actual HBr plasma processing, simultaneous surface passivation by Br radicals makes its Si etching more chemical, the nature of physical sputtering by energetic Br⁺ ion bombardment ensures anisotropic etching. The depth of damages in a Si substrate caused by Br⁺ ion bombardment, on the other hand, decreases with its angle of incidence as Br⁺ ions cannot penetrate deeply into the substrate at higher incident angles. However, it has been also found that energetic H⁺ ions can be damaging to the Si surface even at large incident angles since, due to their small mass, incident H⁺ ions are scattered nearly isotropically when they hit the substrate surface. In addition, due to their small atomic size, H⁺ ions penetrate far more deeply than Br⁺ ions do. Furthermore it has been found that SiBr_x⁺ ions can be

deposited at low energy. Since, at relatively high-pressure, SiBr_x⁺ ions can be rather abundant in HBr plasmas for Si etching. Therefore care must be taken in developing HBr etching processes for vertical multi gates to avoid surface damages by H⁺ ions and to control the profiles despite incident and/or re-sputtered species with higher sticking probabilities.

9:40am **PS2-TuM6 Impact of Etch Processes Over Dimensional Control and LWR for 14nm FDSOI Transistor Gate Patterning**, O. Ros, ST Microelectronics, France

Microelectronic evolution still relies on higher transistor gate integration and transistor size reduction. The major issue related to transistor downscaling is the control at the nanometer range of two main variability sources: Critical Dimension uniformity (CDU) and the Line Width Roughness (LWR). Nowadays, the best lithography conditions allow the definition of photo-resist patterns with a minimum roughness of 4-5nm and a CDU at 3σ < 2.5nm (for 28nm technologies), which will be then transferred into the underlying layers by etch processes. To improve lithography performances, post-lithography treatments such as plasma treatments have so far been introduced to increase photo-resist stability and to improve LWR and CDU during pattern transfer. If such a strategy allows to meet the CDU and LWR requirements of the 32 nm technological node, we will show that the unique use of conventional post-lithography treatments is not anymore efficient to address the specifications of the latest CMOS and beyond CMOS technologies. They indeed introduce several pattern deformations such as resist flowing and gate shifting, that inevitably cause process variability. Thus, new patterning strategies have to be implemented to ensure CMOS downscaling.

In this study, we compare different etch chemistry combinations in order to define the best etch process condition to pattern a 14 nm Fully Depleted Silicon On Insulator (FDSOI) gate stack guaranteeing control over the main variability sources, CD uniformity and LWR. We show that a combination of photo-resist pre-treatments and an optimization of each material's etch process are required to ensure process control during typical FDSOI gate stack patterning (consisting in Photoresist/Silicium Anti Reflective Coating (SiARC)/Carbon layer (SoC)/Oxide Hard Mask (HM)/Polysilicium/High-K Metal Gate (HKMG)). As an example, promising results over SiARC opening step show that the introduction of a new etch chemistry followed by an optimized trim step leads to better defined patterns and a 25% improvement over LWR compared to the values obtained after standard SiARC opening.

10:40am **PS2-TuM9 FinFET Patterning: Promises and Challenges of SIT² for Fin Formation for sub-40 nm Pitch Features**, S. Mignot, GLOBALFOUNDRIES U.S. Inc., I.C. Estrada-Raygoza, H. He, IBM, K. Akarvardar, J. Cantone, GLOBALFOUNDRIES U.S. Inc., B. Doris, IBM, A. Jacob, GLOBALFOUNDRIES U.S. Inc., S. Schmitz, J. Lee, P. Fridde, M. Goss, Lam Research Corp

FinFET device enables scaling of CMOS technology due to its reduced short-channel effects. Realization of this potential is highly dependent on achieving ideal fin structure shape and reducing variability at the front-end of the process. In particular, fin width and high uniformity are critical. The width of the fin structure is typically required to be at a critical dimension that is below resolution limit of single exposure conventional 193nm immersion lithography (i.e., <40nm half pitch). Over the last couple of technology nodes one common technique for fin formation at tight pitch is to use patterning process flow of Sidewall Image Transfer (SIT).

In this publication, a Double Sidewall Image Transfer (SIT²) etch patterning process has been demonstrated for sub 40nm pitch at fin step. The SIT² process scheme that has been explored includes silicon mandrel etch followed by Nitride Spacer deposition and etch. Process integration at this level requires a process free of collapsing features and with minimum pitch variations. SIT² main etch challenges will be reviewed. Etch process mechanisms both physical and chemical have been investigated to achieve silicon etch fin pattern and selectivity to the hard mask and spacer materials as well as uniformity for both macro-to-macro and across wafer.

This work was performed by the Research Alliance Teams at various IBM Research and Development Facilities.

11:20am **PS2-TuM11 Stack Patterning Challenges for the FinFET Architecture**, A. Banik, S. Kanakasabapathy, S. Burns, A. Aiyar, M.J. Brodsky, IBM Corporation

The FinFET device architecture, presents certain new gate patterning challenges. The gate stack aspect ratio is higher, compared to previous planar generations. We will illustrate how this aspect ratio is due to the presence of fins and the need for higher overetch in the offset spacer patterning. Controlling the gate profile to be vertical in both isolated and dense lines is challenging as the gate height increases. Further, Double expose Double etch (DE²) has been the process of record since the 45nm node. This is driven by the need for better tip-to-tip control while

maintaining across chip line width control (ACLV). It has typically relied on pattern assembly through DE², in the gate hardmask layers, followed by a transfer etch into the underlying gate polysilicon. In such a scheme, the dense-iso gate critical dimension (CD) variation is exacerbated by the tall gates needed for the FinFET architecture. Legacy techniques, such as higher ion energy in the polysilicon etch, are limited by the large overetch needed past the fin tops, and selectivity needed in that step.

We present in this paper, patterning sequencing options that reduce the dense-iso challenges for the unique FinFET geometry. We will present data that shows how Lithography and etch process modifications are needed to enable such modified patterning sequences.

This work has been performed by the independent SOI technology development projects at the IBM Microelectronics Division Semiconductor Research & Development Center, Hopewell Junction, NY 12533

11:40am **PS2-TuM12 Mechanisms of Etching and Selectivity for FINFET Gate Low-k Spacer using RLSA™ Microwave Plasma Reactor with Radial Line Slot Antenna**, A. Raley, B. Parkinson, A. Ranjan, S. Keisuke, K. Kumar, P. Biolsi, TEL Technology Center, America, LLC

Spacer design and materials for planar and FINFET transistors has become increasingly critical as gate length is shrinking. For technology node of 22nm and beyond, fringe capacitance between gate and contact/epi-facet are becoming significant component of device degradation.¹ Spacer films with low dielectric constant (Low-k spacer) minimize parasitic capacitances because low permittivity can reduce gate-fringing field effects. Several materials and methods for low-k spacers have been reported showing improved device performance^{2,3}. Incorporation of oxygen, boron, and carbon into SiN spacer film to form SiOCN or SiBCN low-k films with oxygen, boron and carbon contents tuned to minimize k value and provide good leakage performance are two of the low-k avenues being explored. Etching of these materials versus conventional SiN spacer has been characterized in simulated wafer product environment and demonstrated on FINFET structure using RLSA™ microwave plasma reactor with radial line slot antenna. RLSA™ microwave plasma source yields high ion flux with tunable ion energies to control polymer passivation. This is key to achieve the high SiN/Si and SiN/SiO₂ selectivities mandated by long over etch requirement in the FINFET spacer scheme. The etching mechanisms of low-k films have been compared to that of SiN and SiO₂ and it has been shown to strongly depend on the oxygen content of the film. A systematic study on process parameters impact on low-k film etching rate versus SiN and SiO₂ will be presented. Optical emission spectra analysis of relative intensities of the following species F, B, H, CF₂, and O will be analyzed. Impact of electron energy distribution (tuned by source power and pressure) and ion angular energy distribution (tuned by bias power and pressure) on the species considered will be shown to explain selectivity mechanisms and etch rate trends.

1. Kuhn, K, "22 nm Device Architecture and Performance Elements", IEDM, 2008
2. Ko, C.H, "A novel CVD-SiBCN Low-k spacer technology for high-speed applications", VLSI Technology Symposium, 2008, p108-109
3. Huang, E., "Low-k spacers for advanced low power CMOS devices with reduced parasitic capacitances", SOI Conference, 2008. SOI. IEEE International, p10-20

Surface Science

Room: 201 A - Session SS+AS-TuM

Synthesis, Structure and Characterization of Oxides

Moderator: Z. Dohnalek, Pacific Northwest National Laboratory

8:00am **SS+AS-TuM1 Low-Energy Electron Microscopy (LEEM) Studies of Langmuir-Blodgett (LB) Deposited Titania Films for Electrochemical Energy Storage**, C.K. Chan, L.B. Biedermann, Sandia National Laboratories, A.G. Dylla, The University of Texas at Austin, G.L. Kellogg, Sandia National Laboratories, K.J. Stevenson, The University of Texas at Austin

Nanostructured titania is a promising anode in Li-ion batteries because of its higher operating potential and minimal solid-electrolyte interphase formation. The TiO₂(B) polymorph has an open crystal structure, and TiO₂(B) nanosheets (NS) have higher surface areas to facilitate faster lithiation kinetics. Structure-dependent lithiation energetics and dynamics have been inferred from rate-dependent cyclic voltammetry, but the underlying mechanisms for this dependence have not been directly

measured. We aim to apply low-energy electron microscopy (LEEM) to directly image real-time lithium nucleation and migration on the surfaces of TiO₂(B)-NS, and to correlate these behaviors with fundamental chemical and electronic structure properties of the Li/TiO₂(B)-NS system. These studies require well-ordered "molecularly flat" TiO₂(B)-NS layers, but obtaining these ideal NS assemblies is challenging due to the tendency of nanomaterials to reduce free energy by minimizing surfaces. TiO₂(B)-NS generally accomplish this by folding to form nanoclusters. We solved this problem by suspending TiO₂(B)-NS in a spreading solvent, depositing the TiO₂(B)-NS across a liquid subphase, and transferring them onto substrates by Langmuir-Blodgett (LB) technique. After investigating various spreading solvents and subphases, the best conformal films were obtained using TiO₂(B)-NS suspended in TBAOH/water or TBAOH/methanol, and deposited on a water subphase. TiO₂(B)-NS were capped by residual ethylene glycol (EG) from their synthesis procedure, and a surfactant like TBAOH was likely required to displace the EG and stabilize the unfolded TiO₂(B) sheets. TiO₂(B)-NS were deposited by LB technique onto multicrystalline Au substrates. Imaging of these thin conformal films were difficult with standard SEM and AFM techniques, but LEEM showed large areas of densely packed nanosheets with discrete intensity steps. Electron reflectivity spectra was used to identify distinct TiO₂(B)-NS regions, where the discrete intensity steps corresponded to discrete increases in the TiO₂(B)-NS layer thickness. Low-energy electron diffraction (LEED) patterns of TiO₂(B)-NS deposited by TBAOH/water on water indicated rotational disorder in TiO₂(B) sheets, with a 1.65 Å⁻¹ diffraction ring consistent only with the (01) spacing of anatase. We believe that TBAOH acts as a surfactant to displace the protective EG capping ligand surrounding the TiO₂(B)-NS clusters, allowing the nanosheets to unfold. The resulting water ingress facilitates transformation of the metastable TiO₂(B) phase to the thermodynamically stable anatase phase. Preliminary results of *in situ* surface lithiation of TiO₂-NS will also be discussed.

8:40am **SS+AS-TuM3 Reactions on the Rutile TiO₂(110) Surface Studied by High-resolution STM and TPD**, S. Wendt, Aarhus University, Denmark **INVITED**

In this talk, I will summarize surface science studies conducted at the iNANO center addressing a prototypical model oxide system – the rutile TiO₂(110)-(1 × 1) surface. The identification of point defects on the terraces such as oxygen vacancies, hydroxyl groups, and near surface defect such as Ti interstitials will be discussed. Using high-resolution scanning tunnelling microscopy (STM) several examples for reaction of molecules with oxygen vacancies will be presented [1]. These reactions were directly imaged in so-called STM movies. Whereas the reactions on the terraces can be imaged directly, a combination of static STM results with temperature-programmed desorption (TPD) measurements was used to study the reactions at step edges, with the focus particularly on the <1-11> step edges [2,3]. Both, for the reaction on the terraces and at the step edges, water and ethanol were used as probe molecules [1-3]. Accompanying density functional theory (DFT) calculations support the assignments made in the STM studies. In addition, I will address the complex oxygen-TiO₂(110) interaction [4]. Specifically, the role of bulk defects in the oxygen chemistry on reduced rutile TiO₂(110) is highlighted. Finally, I will show that these surface science studies help to improve our understanding of TiO₂ as photocatalysts. Specifically, the photo-reaction of ethanol on differently prepared TiO₂(110) surfaces will be compared.

- [1] J. Ø. Hansen, P. Huo, U. Martinez, E. Lira, Y.Y. Wei, R. Streber, E. Lægsgaard, B. Hammer, S. Wendt, F. Besenbacher, Phys. Rev. Lett. **107**, 136102 (2011).
- [2] U. Martinez, J. Ø. Hansen, E. Lira, H. H. Kristoffersen, P. Huo, R. Bechstein, E. Lægsgaard, F. Besenbacher, B. Hammer, S. Wendt, Phys. Rev. Lett. **109**, 155501 (2012).
- [3] H. H. Kristoffersen, J. Ø. Hansen, U. Martinez, Y.Y. Wei, J. Mathiesen, R. Streber, R. Bechstein, E. Lægsgaard, F. Besenbacher, B. Hammer, S. Wendt, Phys. Rev. Lett. **101**, 146101 (2013).
- [4] S. Wendt, P. T. Sprunger, E. Lira, G. K. H. Madsen, Z. Li, J. Ø. Hansen, J. Mathiesen, A. Blekinge-Rasmussen, E. Lægsgaard, B. Hammer, F. Besenbacher, Science **320**, 1755 (2008).

9:20am **SS+AS-TuM5 Atomic Structures on BaTiO₃ (001): Reconstructions, Step Edges and Domain Boundaries**, E.H. Morales, D.A. Bonnell, J.M. Martinez, University of Pennsylvania, W.A. Al-Saidi, University of Pittsburgh, A.M. Rappe, University of Pennsylvania
BaTiO₃ is a ferroelectric material that finds applications in a range of traditional and emerging devices. Understanding the surface is prerequisite to controlling interactions during device processing, potential for surface mediated device properties and surface chemical reactions.

Here we present scanning tunneling microscopy (STM) and scanning tunneling spectroscopy (STS) of atomically resolved reconstructions on BaTiO₃ (001) surfaces, $\sqrt{5} \times \sqrt{5}$ R26.6° (circ), $\sqrt{2} \times \sqrt{2}$, $\sqrt{4} \times \sqrt{4}$, and

$\sqrt{13} \times \sqrt{13}$ R33.7 $^\circ$. We experimentally show the coexistence of two reconstructions $\sqrt{2} \times \sqrt{2}$ and $\sqrt{4} \times \sqrt{4}$ while DFT calculations indicate that $\sqrt{4} \times \sqrt{4}$ is a thermodynamically favorable phase, the $\sqrt{2} \times \sqrt{2}$ persists due to a more kinetically favorable path of formation. The structures of the boundaries between the two reconstructions is determined. In the case of the $\sqrt{5} \times \sqrt{5}$ R26.6 $^\circ$ surface a comparison of electronic structure determined by STS with theoretical calculations shows that the surface is Ti terminated. In this and other reconstructions Ti-ad atoms create filled and empty states that are imaged in STM. We will briefly discuss a complete BaTiO₃ (001) phase diagram and the influence to Ti adatoms in the choice of step edge direction in the case of the various surface reconstructions mentioned above.

9:40am **SS+AS-TuM6 Growth and Optical Properties of Cr- and V-Doped α -Fe₂O₃ Epitaxial Thin Films**, S.E. Chamberlin, Y. Wang, T.C. Kaspar, M.E. Bowden, Pacific Northwest National Laboratory, A.W. Cohn, D.R. Gamelin, University of Washington, P.V. Sushko, University College London, S.A. Chambers, Pacific Northwest National Laboratory

There is widespread interest in discovering materials that can effectively harvest sunlight in the visible region of the solar spectrum in order to drive chemical processes on surfaces. Hematite (α -Fe₂O₃) has received renewed interest recently as the active photoanode in photoelectrochemical water splitting to store solar energy as H₂ [1]. Hematite is very abundant, has a narrow bandgap of 2.1 eV, and is stable in aqueous and oxidizing environments. However, it has extremely poor electron and hole mobilities, which results in short hole diffusion lengths and ultrafast recombination of photogenerated e⁻ - h⁺ pairs. Additionally, it does not efficiently absorb photons in the 500-600 nm range where the solar spectrum is most intense. The utility of hematite could therefore be significantly increased by red shifting its band gap to harvest more of the solar spectrum.

Eskolaite (α -Cr₂O₃) has a band gap of 3.3 eV, but alloying Cr and Fe to make α -(Fe_{1-x}Cr_x)₂O₃ solid solutions as epitaxial films has been found to result in a reduction in gap down to as low as ~1.7 eV at $x = \sim 0.5$ [2,3]. We examine the optical absorption in α -(Fe_{1-x}Cr_x)₂O₃ thin films grown by oxygen-plasma-assisted molecular beam epitaxy (OPA-MBE) on α -Al₂O₃(0001) substrates and explain the observed excitations, and the nature of the band gap dependence on x , through first principles calculations. Photoconductivity (PC) measurements show that the onset of photocurrent decreases by nearly 0.5 eV when x is increased from 0 to ~0.4. However, for $x > \sim 0.6$, the films are not sufficiently conductive for PC to be measured.

Karelianite (α -V₂O₃) is weakly metallic at room temperature, so α -(Fe_{1-x}V_x)₂O₃ films may overcome the conductivity challenges of the α -(Fe_{1-x}Cr_x)₂O₃ system. Substitutional V impurities have also recently been predicted to lower the band gap of α -Fe₂O₃ further than that of Cr-doped α -Fe₂O₃ [4]. Heteroepitaxial thin films of α -(Fe_{1-x}V_x)₂O₃ were deposited on α -Al₂O₃(0001) substrates by OPA-MBE. Film quality was monitored *in situ* by reflection high energy electron diffraction (RHEED). *In situ* x-ray photoemission spectroscopy (XPS) was utilized to characterize the charge states of the cations. Film crystallinity and lattice parameters were determined *ex situ* by high resolution x-ray diffraction (HRXRD). The effects of the doping concentration on the conductivity and optical properties will be discussed.

[1] K. Sivula *et al.*, *Chemsuschem* **4**, 432 (2011).

[2] H. Mashiko, *et al.*, *Appl. Phys. Lett.* **99**, 241904 (2011).

[3] S.E. Chamberlin *et al.*, *J. Phys. Chem. Lett.*, submitted (2013).

[4] Z.D. Pozun and G. Henkelman, *J. Chem. Phys.* **134**, 224706 (2011).

10:40am **SS+AS-TuM9 Growth of Oxide Nanowires on Vicinal Metal Surfaces: Atom Exchange Processes at Step Edges**, L. Ma, A. Picone, M. Wagner, S. Sunnev, Karl-Franzens University, Austria, G. Barcaro, A. Fortunelli, CNR-IPCF, Italy, F.P. Netzer, Karl-Franzens University, Austria

Low-dimensional model systems are of fundamental importance to elucidate emergent phenomena in condensed matter physics and chemistry. Here we present 1-dimensional oxide-metal hybrid model systems, Co-oxide and Mn-oxide nanowires coupled to a Pd surface, which have been fabricated by the decoration of steps of a vicinal Pd(100) surface. We have studied the growth of Co-oxide and Mn-oxide nanostructures on a Pd(1 1 23) surface using LEED and STM, and have probed their electronic properties by STS in a low-T (5K) STM. At low oxide coverages and suitable kinetic conditions, the Pd step edges are decorated by oxide nanostripes, while the Pd(100)-like terraces are covered by a (2x2) layer of chemisorbed oxygen (as a result of the reactive metal oxide deposition procedure). However, there are significant structural differences between Co- and Mn-oxide nanowires: whereas Mn-oxide decorates the Pd steps by monoatomic MnO_x lines in a pseudomorphic (1x1) arrangement, Co-oxide

grows in form of 2-4 atom-wide CoO_x nanostripes, with a strained hexagonal structure partially embedded into the outer terrace areas. In addition, rod-like structures attached to the CoO_x step edges are periodically observed, which have been identified by STS as rows consisting of 4±1 Pd atoms that have been ejected from the Pd steps. This indicates that Co-Pd atom exchange at the step edges is a dominant feature during oxide step decoration and growth. The absence of such structures on the MnO_x covered Pd(1 1 23) surface demonstrates that Mn-Pd atom exchange is much less pronounced, thus revealing a significant difference in growth behavior between MnO_x and CoO_x nanostructures and in their interactions with Pd surfaces.

Work supported by the ERC Advanced Grant SEPON.

11:00am **SS+AS-TuM10 Surface Structure of α -Cr₂O₃(0001) by X-ray Photoelectron Diffraction after Activated Oxygen Exposure**, T.C. Kaspar, S.E. Chamberlin, S.A. Chambers, Pacific Northwest National Laboratory

The detailed structure and electronic properties of the surfaces of the corundum-type oxides α -Al₂O₃, α -V₂O₃, α -Cr₂O₃, and α -Fe₂O₃ continue to be of significant interest due to their importance in catalysis, photocatalysis, and environmental chemistry. The surface structure, and thus the properties of the surface, can be dramatically altered with different processing or treatment conditions. Recently, Henderson¹ has shown that the Cr-terminated α -Cr₂O₃(0001) surface can be fully passivated by exposure to activated oxygen from an electron cyclotron resonance (ECR) plasma source, blocking both the dissociative and the molecular H₂O adsorption channels. We use x-ray photoelectron spectroscopy (XPS) and x-ray photoelectron diffraction (XPD) to investigate the surface structure of α -Cr₂O₃(0001) epitaxial thin films before and after exposure to activated oxygen from an ECR plasma source. The films are deposited on α -Al₂O₃(0001) substrates by oxygen-plasma-assisted molecular beam epitaxy. When cooled or annealed in vacuum, strong evidence for a Cr-Cr-O₃ termination is obtained by comparing the Cr 3⁺ XPD angular scan to single scattering simulations. However, after plasma exposure, a high binding energy feature is observed in the Cr 2p XPS spectrum that possesses an ordered structure distinct from the underlying Cr³⁺ of Cr₂O₃, which remains Cr-Cr-O₃-like. Investigation of this new surface structure with simulations of various candidate structures tentatively rules out CrO₂-like configurations. The high binding energy feature likely arises from a higher oxidation state of Cr, although a quantitative charge state assignment is not straightforward. One possibility is the oxidation of the surface layer of Cr to Cr⁶⁺ with a double chromyl structure (O=Cr=O).

1. M. A. Henderson, *Surf. Sci.* **604**, 1502 (2010).

11:20am **SS+AS-TuM11 Preparation and Characterization of Rare Earth Oxide Thin Films on Metal and Silicon Substrates**, A. Schaefer, J.-H. Jhang, University of Bremen, Germany, W. Cartas, S.R. Eperi, University of Florida, M.H. Zöllner, IHP, Germany, H. Wilkens, University of Osnabrück, Germany, T. Schroeder, IHP, Germany, J.F. Weaver, University of Florida, M. Bäumer, University of Bremen, Germany

The rare earth oxides (REOs) have potentially versatile applications in heterogeneous catalysis. Catalysis of reactions like dehydrogenation and selective oxidation of organic compounds, methane conversion to syntheses gas or applications in three way catalysis may be mentioned as examples. The versatility of the REOs is based on the ease of valency changes of rare earth metals (change of f-electron configuration) as compared to, e.g., that of d-block elements. In particular, the possible dioxides in the REO series (ceria, praseodymia and terbia) are highly interesting materials for oxidation catalysis due to their ability to easily give off oxygen and switch to different oxidation states. As lattice oxygen participates directly in the molecule-surface reactions (cf. the Mars-van Krevelen mechanism), the selectivity of REO catalysts in oxidation chemistry depends strongly on their oxygen storage/release capabilities. The oxide of samarium for instance, which only forms the sesquioxide Sm₂O₃, seems to be the most effective REO catalyst for partial (selective) oxidation of methane.

In the recent years considerable progress has been made in the study of ceria thin films and oxide structures on a variety of transition metal substrates. Surface Science studies of REO films other than ceria are however fairly limited. In this context we will present two approaches to study other complex REOs like samaria, praseodymia and also terbia in ultra high vacuum (UHV). The presentation concerns a more classical approach for the preparation of samaria and terbia on a Pt(111) single crystal by reactive physical vapor deposition. Praseodymia thin films on the other hand were prepared on a Si(111) substrate by molecular beam epitaxy and new routes for adjusting the oxidation state of those films will be presented. By means of plasma treatment, e.g., we achieved to prepare even the dioxide of praseodymium (PrO₂), a complex oxide which has not been available for UHV studies up to now. In combination with temperature-programmed desorption of oxygen a range of different oxidation states from

PrO₂ to Pr₂O₃ can be adjusted and made accessible for model studies. This concept has been expanded to ceria on Si(111) as well, making it possible to even stabilize the surface of the iota-phase (Ce₇O₁₂), which contains ordered oxygen vacancies, for UHV model studies.

While it is a common concept in microelectronics and adjacent fields to dope and mix

oxides to tune their properties this concept has not yet entered the world of surface

catalytic studies of thin films to a large extent. The talk will close with an outlook and first results on the mixture of REOs for UHV model studies.

11:40am **SS+AS-TuM12 Surface Core Level BE Shifts for MgO, C.J. Nelin**, Consultant, *F. Uhl, V. Staemmler*, Ruhr-Universität Bochum, Germany, *P.S. Bagus*, University of North Texas, *H. Kühlenbeck, M. Stierer, H.-J. Freund*, Fritz-Haber-Institut der Max-Planck-Gesellschaft, Germany

We present theoretical and experimental results for the surface core-level shifts, SCLS, of MgO(100). Since MgO is an ideal ionic insulator, [1] one would expect shifts to higher binding energy, BE, for a surface Mg²⁺ cation and shifts to lower BE for a surface anion; furthermore, the magnitudes of the shifts of opposite sign should be comparable. This expectation follows from the electrostatics of the different coordination of the bulk and surface atoms. However, we have found that while the Mg(2p) core-level shift is ~+1 eV, as expected, the O(1s) SCLS is almost zero. This unexpected difference between the cation and anion SCLS has been found for a large range of theoretical models for MgO, which include extended embedded cluster models and periodic calculations. The experiments, which also show the different SCLS, were carried out for MgO films on Mo supports. While the electron density of the bulk Mg and O ions and the surface Mg ions have the dominantly spherical shape expected for closed shell species, the distortion of the surface O anions from spherical symmetry is the effect that leads to the different chemical shifts. Thus the SCLS provide another manifestation of the polarizability of the O anions that is associated with the catalytic activity of thin oxide films; see, for example, Ref. [2]. However, in this case the polarization is of the electronic charge density rather than of the geometric structure of the oxide. We analyze the nature of the polarization of the surface O anions and show how this leads to the anomalously small SCLS for these anions. We also consider the broadening of the XPS lines and we relate the Full Width at Half Maximum of the core-levels to the final state geometric modification of bond distances between Mg and O. [3]

1. C. Sousa, T. Minerva, G. Pacchioni, P. S. Bagus, and F. Parmigiani, *J. Electron Spectrosc. Relat. Phenom.* **63**, 189 (1993).
2. H. J. Freund, *Chem. Eur. J.* **16**, 9384 (2010).
3. C. J. Nelin, P. S. Bagus, M. A. Brown, M. Stierer, and H.-J. Freund, *Angew. Chem. Int. Ed.* **50**, 10174 (2011).

Thin Film

Room: 104 A - Session TF-TuM

ALD for Emerging Applications

Moderator: G.S. Scarel, James Madison University

8:00am **TF-TuM1 Fabrication of Top Gate Graphene Transistor using Physically Transferrable High-k Nanosheet using Atomic Layer Deposition, H. Jung, J. Lee, K. Ko, J. Park, H. Kim**, Yonsei University, Republic of Korea

Graphene, a single layer of hexagonal carbon atom structure with very high mobility (more than 200,000 cm²/Vs at 4.2 K for suspended) draws great attention as a promising material for future nanoelectronics and finally a substitution of silicon. To fabricate devices, especially transistors, gate dielectric is an essential component, which can significantly impact the device performance. Exploring graphene for future devices requires deposition of dielectric materials on graphene. However, deposition of high-κ dielectrics directly onto graphene is difficult task due to the nucleation problem preventing the formation of high quality oxide on graphene because of chemical inertness of graphene surface. Previous reports to deposit high-κ dielectrics on graphene have resulted in significant degradation in electrical properties of graphene. Here, we describe a new strategy to integrate graphene with high quality high-κ dielectrics by transferring high-κ dielectric nanosheet onto graphene. To fabricate a high-κ dielectric nanosheet, we firstly prepared spin-coated water-soluble poly(acrylic acid) (PAA) on Si substrate as a sacrificial layer and high-κ dielectric thin film was deposited on the sacrificial layer using atomic layer deposition (ALD) process. The high-κ dielectric nanosheet was fabricated

by soaking the sample in water and removing the sacrificial layer. Dielectric properties of high-κ nanosheet show similar dielectric constant with ALD thin film and lower hysteresis (~ 0 mV) and interface state density (1.7 x 10¹¹ cm⁻²eV⁻¹) than thin film (~ 200 mV, 7.6 x 10¹¹ cm⁻²eV⁻¹). We fabricated and characterized top gate graphene transistors using both directly deposited high-κ thin film on graphene using ALD and high-κ dielectric nanosheet as gate dielectrics. Fabricated graphene device using ALD on graphene did not operate properly. Using high-κ nanosheet as the gate dielectrics, we have demonstrated top gate graphene transistors with field-effect mobility up to 2,000 cm²/Vs and ~ 0 V of Dirac voltage. This method opens a new way to high-performance graphene devices to impact broadly from high frequency high speed circuits to flexible electronics.

8:20am **TF-TuM2 Resistive Switching Devices Based on Ozone assisted ZnO Films by Atomic Layer Deposition, R.M. Mundle, A.K. Pradhan**, Norfolk State University

Atomic layer deposition (ALD) is an ideal technique to deposit ultrathin films with high conformality and precise thickness control using water as one its precursors. We demonstrate the growth temperature dependence of film thickness and surface roughness of ZnO films grown by the atomic layer deposition using ozone as oxidizer. The significantly low growth rate of film using O₃ precursor is attributed to the recombinative surface loss of O₃. The variation of the spatial uniformity inferred from the surface roughness of ZnO films and O₃ concentration were explained by a transition from reaction to recombination limited growth. We have fabricated a MOS device consisting of insulating ZnO layer using O₃ source between metallic and semiconducting Al:ZnO layers. The device demonstrated a remarkable resistive switching behavior, indicating the insulating behavior of the ZnO layer due to the electrochemical migration of oxygen vacancies at the interfaces.

8:40am **TF-TuM3 Process Design and Development of ALD for Co(W) Alloy Films as Single Layered Barrier and Liner Material in Future Cu ULSI Interconnects, Y. Shimogaki**, The University of Tokyo, Japan
INVITED

The aggressive scaling of ULSI devices requires ultra-narrow Cu interconnect features which have width of 20nm or less and aspect ratio of over 5. Cu diffusion barrier metal (DBM) and adhesion promoting liner layer (APL) should be made on the side wall of these features to protect Low-κ layers from Cu diffusion and enhance the electro-migration life time of Cu lines. As the feature dimension is decreasing, the APL/DBM layers should be less than 3 nm in thickness which may result in poor diffusion barrier performance. We have proposed that Co(W) alloy may be a good alternative to the conventional Ta/TaN as APL/DBM. Co(W) alloy can have a lower resistivity and better barrier property compared to TaN. It can also enhance the adhesion of Cu, better than Ta. Thus Co(W) alloy can work as a single-layered APL/DBM for the future ULSIs.

We have developed novel ALD process using hot-wire assisted technique. Metalocene precursors were effectively reduced by using NH₂ radical generated by hot-wire from NH₃. Conventional ALD process using amidinate precursors was also developed to form Co(W) alloy thin film. The microstructure of the deposited Co(W) alloy films were intensively examined using TEM and the Cu diffusion barrier properties were correlated with the structure. As a summary, the developed ALD process could successfully deposit Co(W) alloy thin film with low resistivity and good barrier properties. The adhesion strength of Cu onto Co(W) alloy will be also discussed.

9:20am **TF-TuM5 Control of Oxygen Vacancies by Plasma Enhanced Atomic Layer Deposition (PEALD) of TiO₂ for Memristors, S.-J. Park, J.-P. Lee, J.S. Jang, H. Rhu, H. Yu, B.Y. You, C.S. Kim, K.J. Kim, Y.-J. Cho**, Korea Research Institute of Standards and Science (KRISS), Republic of Korea, *S. Baik*, POSTECH, Republic of Korea, *W. Lee*, Korea Research Institute of Standards and Science (KRISS), Republic of Korea

TiO_x is one of the promising candidates for resistive switching (RS) devices. It has been generally accepted that formation of oxygen deficient Magnéli phase resulting from field-induced migration and ordering of oxygen vacancies (V_O) is mainly responsible for the resistive switching (RS) in TiO_x-based RS devices [1,2]. In this regard, it is worth studying the effect of oxygen vacancy concentration on the RS behaviors of the memristors adopting TiO_x as a switching layer. To this end, Pt/TiO_x/Pt capacitors with different values of x were prepared in this study. It has been well established that stoichiometry of TiO_x was closely related to the oxygen vacancy concentration [3]. TiO_x films were grown by plasma enhanced atomic layer deposition (PEALD) at the substrate temperature of 150 °C. Titanium (IV) tetraisopropoxide (TTIP; Ti[OCH(CH₃)₂]₄) was used as a Ti precursor. High purity oxygen or mixture gas of pure oxygen and nitrogen was adopted as a reactant during the plasma exposure step. By taking advantage of versatile controlling capability of ALD over the film

properties, we were able to deliberately control the stoichiometry of TiO_x films by adjusting the flow rate ratio (R_F) of O_2 gas to $\text{N}_2 + \text{O}_2$ mixture gas from 0.25 to 1.00.

Microstructure and properties of the resulting films were characterized by Rutherford backscattering spectrometry (RBS), transmission electron microscopy (TEM), X-ray diffraction (XRD), confocal Raman spectroscopy, X-ray photoelectron spectroscopy (XPS), and spectroscopic ellipsometry (SE). According to RBS result, x in TiO_x was found to be varied from 1.62 to 1.70 when R_F was altered from 0.25 to 1.00. Phases of PEALD TiO_x films were observed to be amorphous at $R_F = 0.25$, whereas nanocrystalline anatase at $R_F = 1.00$. Raman spectroscopic analysis provided an additional evidence for R_F dependence of the film crystallinity. It turned out from the deconvolution of the O1s XPS peaks that non-lattice oxygen content increases from 15.3 to 20.7% with decreasing the R_F from 1.00 to 0.25, which manifests increases of oxygen vacancies in PEALD TiO_2 film with R_F . It was found from SE analyses that the absorption originated from defect states below bandgap, monotonously increases with decrease of x , i.e., increase of oxygen vacancy. Based on these results, the effect of oxygen vacancy concentration on RS behaviors of TiO_x -based memristors will be discussed in detail in this presentation.

References

- (1) R. Waser, *et al.*, *Adv. Mater.* **21**, 2632 (2009)
- (2) D. H. Kwon, *et al.*, *Nat. Nanotechnol.* **5**, 148 (2010)
- (3) H. Seo, *et al.*, *Nano Lett.* **11**, 751 (2010)

9:40am TF-TuM6 Area Selective Atomic Layer Deposition of Dielectric Films on Metal/Dielectric Patterns, F. Minaye Hashemi, S.F. Bent, Stanford University

Electronic devices consisting of a variety of different materials continue to undergo rigorous scaling to achieve higher switching speeds. Planar and 3-D structures such as those found in FinFETs and in the transistor backend contain metal/dielectric patterns, for which selective deposition processes may facilitate the fabrication of devices with feature sizes on the order of nanometers. Selective deposition approaches are required that can provide deposition of different materials with a variety of thicknesses while maintaining the selectivity up to higher thickness limits.

Atomic layer deposition (ALD) is a good choice for selective deposition because it is based on self-limiting reactions between gas phase precursors and specific functional groups at the growth surface. This chemical specificity provides a means to achieve selectivity in ALD on a spatially patterned substrate. In previous studies on area selective ALD of dielectrics on a dielectric pattern, deposited thicknesses were on the order of nanometers. The selectivity was generally obtained by passivation of the surface using self-assembled monolayers (SAM) in the regions where ALD was not desired. However, existing methods for selective ALD likely do not have the robustness needed for deposition of thicker films. Hence, there is a need for new approaches to achieve selective dielectric-on-dielectric growth for film thicknesses of 10 nm or more.

In this work, we probe the thickness limits of area selective deposition of dielectric-on-dielectric by selectively depositing an organic SAM as the blocking layer on metal parts of a metal/dielectric (Cu/SiO₂) pattern. Both alkanethiols and alkylphosphonic acids have been reported to form well packed SAMs on metal surfaces. Here, we apply them to area selective ALD, and examine the blocking properties of octadecylphosphonic acid (ODPA) and octadecanethiol (ODT) SAMs on Cu. We show that both of these SAMs can prevent subsequent deposition of metal oxide dielectric films via ALD. X-ray photoelectron spectroscopy (XPS) and Auger electron spectroscopy (AES) confirm no growth of the metal oxide on the ODPA-protected Cu for up to 36 nm of metal oxide deposition, while ellipsometry and XPS results show metal oxide growth on the dielectric regions of the samples, i.e. SiO₂. We also report results on regenerating the ODT SAM protecting layer between ALD cycles and show that this approach is effective in improving the blocking properties of the SAM on Cu. This strategy provides the ability to carry out selective deposition for film thicknesses greater than 30nm, opening up the possibility for new applications in next generation electronic devices.

10:40am TF-TuM9 Development of an Open-Ended Rotary Reactor for Plasma-Assisted ALD on Particles, J. Clancey, J. Yin, L. Baker, A.S. Cavanagh, S.M. George, University of Colorado, Boulder

The use of atomic layer deposition (ALD) to coat large quantities of particles with conformal thin films is important for many applications. One area that has received recent attention is the efficient deposition of precious catalytic metals such as Pt. The ALD of catalytic metals is particularly challenging because of nucleation difficulties. However, recent studies have shown that plasma-assisted ALD can improve the nucleation and leads to much more conformal metal films after fewer ALD cycles. In this work, a new open-ended rotary ALD reactor design is presented that combines

particle agitation in a rotary reactor with a remote inductively coupled plasma (ICP) plasma source. The plasma enters the open end of the rotary reactor with line-of-sight to the particles tumbling in the rotary reactor. A gate valve can separate the ICP plasma source from the open-ended rotary reactor during the metal precursor exposures. This design allows metals to be deposited on the particles without affecting the ICP plasma source. Results will be presented for Al₂O₃ ALD and W ALD on TiO₂ particles. Pt ALD on the TiO₂ particles will also be demonstrated using the W ALD adhesion layer to promote rapid Pt ALD nucleation and conformal film growth. This procedure was described earlier in L. Baker *et al.*, *Appl. Phys. Lett.* **101**, 111601 (2012).

11:00am TF-TuM10 Metal Ion Photoreduction on ALD Thin Films, J.C. Halbur, A. Madan, J.S. Jur, North Carolina State University

Photoreduction of metal ions onto atomic layer deposited semiconducting surfaces are examined as a means for water reclamation/filtration and development of conductive patterns on polymeric substrates. Specifically, ZnO (via diethyl zinc/H₂O) and TiO₂ (titanium tetrachloride/H₂O) thin films are deposited on polymer film and fabric substrates and evaluated for reducing Ag⁺, Cr⁶⁺, As³⁺, and Au³⁺ from solution into metallic and oxidized coatings. The effect of ALD film thickness and process temperature on the efficiency of UV-light enabled reduction of the metal ions is evaluated. The effect of nucleation behavior of the metal ion reduction is explored and shows dependence on the surface structure and the impurity content in the ALD thin films. For example, reduction on ZnO with a characteristic nanoscale surface roughness shows a distinct nanoflake-like nucleation. On TiO₂, with a much lower surface roughness, island-like nucleation is exhibited. Both nano- and micro-scale islands are shown, likely due to corresponding reduction of Cl impurities from the TiO₂ film as observed by X-ray diffraction. Hard contact masks are applied onto the ALD thin films to explore the efficacy of producing conductive patterned structures directly on the ALD thin films. For applications in water filtration, ZnO ALD functionalization of high surface area fabrics have shown the ability to reduce up to 35% of Cr⁶⁺ and a dependence on the number of ALD cycles is observed. Results for As³⁺ and mixed metal ion solutions are also presented.

11:20am TF-TuM11 Highly Conductive and Flexible Nylon-6 Nonwoven Fiber Mats Formed using Tungsten Atomic Layer Deposition, B. Kalanyan, C.J. Oldham, W.J. Sweet III, G.N. Parsons, North Carolina State University

Low temperature tungsten atomic layer deposition (ALD) using WF₆ and dilute silane (SiH₄, 2% in Ar) can yield highly conductive coatings on nylon-6 microfiber mats. Coated nonwoven mats are flexible and supple with conductivity of ~1,000 S/cm. We find that an alumina nucleation layer, reactant exposure, and deposition temperature all influence the rate of W mass uptake on 3D fibers. Transmission electron microscopy (TEM) reveals highly conformal tungsten coatings on nylon fibers with complex 'winged' cross-section. We calibrate tungsten growth rate on nylon-6 by imaging film thickness on high surface area anodic aluminum oxide. Using reactant gas 'hold' sequences during the ALD process, we conclude that reactant species can transport readily to reactive sites throughout the fiber mat, consistent with conformal uniform coverage observed by TEM. The conductivity of 1,000 S/cm for the W-coated nylon is much larger than found in other conductive nonwovens. W-coated nylon mats maintain 90% of their conductivity after being flexed around cylinders with radii as small as 0.3 cm. Metal ALD coatings on nonwovens make possible the solvent-free functionalization of textiles for electronic applications.

11:40am TF-TuM12 Room-Temperature Atomic Layer Deposition of Platinum, A.J.M. Mackus, D. Garcia-Alonso, H.C.M. Knoops, A.A. Bol, W.M.M. Kessels, Eindhoven University of Technology, Netherlands

The material Pt has many applications because of its catalytic activity, chemical stability, and high work function. Several Pt ALD processes have been reported for substrate temperatures in the range 100-300 °C. For certain applications involving temperature-sensitive materials such as polymers, fibers, and biological samples, it is valuable to have processes available for Pt ALD at lower substrate temperatures.

In this work, the temperature window for ALD of low-resistivity Pt has been extended to room temperature by the development of new plasma-assisted ALD processes. During thermal ALD of Pt from MeCpPtMe₃ and O₂ gas, the ligands of the precursor undergo dehydrogenation reactions on the catalytic Pt surface, which leads to a carbonaceous layer that poisons the surface inhibiting further surface reactions.¹ Combustion of this carbonaceous layer during the ALD cycle requires a substrate temperature above 200 °C, or alternatively, the use of strong oxidizing agents such as ozone or oxygen plasma. However, these strong oxidizing agents oxidize the deposited Pt to PtO₂ when the deposition is carried out at low substrate temperatures. The deposition of Pt at low temperatures can be achieved by

adding a H₂ gas or H₂ plasma exposure step to the ALD cycle in which the PtO₂ at the surface is reduced to metallic Pt in every cycle.^{2,3}

High-quality, virtually pure films with a resistivity of 18–24 μΩcm were obtained for the three-step ALD processes consisting of MeCpPtMe₃ dosing, O₂ plasma exposure, and H₂ gas or H₂ plasma exposure.³ The reaction mechanism of these processes was investigated by gas-phase Fourier transform infrared spectroscopy (FT-IR). It will be shown that the newly developed processes enable the deposition of Pt on polymer, textile, and paper surfaces. The ability to coat temperature-sensitive substrates significantly broadens the application range of Pt ALD.

1. Mackus *et al.*, *Chem. Mater.* **24**, 1752 (2012)
2. Hämäläinen *et al.*, *Thin Solid Films* **513**, 243 (2013)
3. Mackus *et al.*, *Chem. Mater.*, online early access; DOI: 10.1021/cm400274n

Tribology Focus Topic

Room: 203 C - Session TR+SE-TuM

Low Friction Materials

Moderator: R. Bennewitz, INM - Leibniz-Institute for New Materials, D. Irving, North Carolina State University

8:20am **TR+SE-TuM2 Ultra Low Friction Surface Designed by Biomimetic Approach.** A. Takahara, Y. Higaki, M. Minn, M. Kobayashi, JST ERATO Takahara Soft Interfaces Project, Japan

The environmentally friendly biomimetic lubrication system was designed by tethering polyelectrolytes on the substrates with sufficiently high grafting density, so-called 'polymer brushes'. The hydrated brushes in aqueous media formed water lubrication layer to reduce friction coefficient, which is useful not only for artificial joints and bio-devices but also for various mechanical devices. Macroscopic tribological properties of polyelectrolyte brushes bearing ammonium salt, sulfonic acid, or phosphorylcholine unit were characterized by ball-on-plate type tribotester in the air, water, and salt solution through sliding a glass ball on the surface under a normal pressure of ca. 130MPa. The low friction coefficient below 0.02 was observed in polyelectrolyte brushes in water.

8:40am **TR+SE-TuM3 Thin Organic Monolayers on Inorganic Substrate: Ultra-Low Adhesion Friction and Wear Resistance Properties.** S.P. Pujari, H. Zuilhof, Wageningen University, Netherlands

Micro and Nano Electro Mechanical Systems (MEMS/NEMS) are considered to be an important technology for the development of several products in daily life such as electronics, medical devices, and packaging. Despite the tremendous progress in micro-fabrication, the development of highly robust surfaces, having ultra-low adhesion as well as friction and resistance against wear, is still a challenging subject of accomplishment. To this aim, new fluorine-containing terminal alkynes and alkenes were synthesized and self-assembled onto inorganic substrates (Si(111), SiC, and CrN) to obtain fluorine containing organic monolayers. The resultant covalently bound organic monolayers have similar surface properties as polytetrafluoroethylene (PTFE), but they are more stable than traditionally coated PTFE.

A combination of spectroscopic (XPS, IR), nanoscopic (AFM), and contact angle measurements shows that these monolayers were ordered and highly hydrophobic. Increasing the amount of fluorine on the alkyne precursor resulted in monolayers with a greatly reduced adhesion to silica probes, as well as an almost 5-fold decrease in the coefficient of friction on the surface. Overall, this yields a friction coefficient that is – to the best of our knowledge – lower than reported for any other thin organic monolayer. In addition, these monolayer-coated Si(111), SiC, and CrN surfaces perform superiorly over uncoated.^{1,2,3} For instance, at a normal force of ~7 μN, the monolayer-coated samples are still nearly undamaged, while an uncoated Si surface displays already wear marks of 8 nm deep. The remarkable tribological properties make these fluorinated monolayers promising candidates for the development of robust, high-performance MEMS/NEMS systems.

1. Ultralow Adhesion and Friction of Fluoro-Hydro Alkyne-Derived Self-Assembled Monolayers on H-Terminated Si(111) Sidharam P. Pujari, Evan Spruijt, Martien A. Cohen Stuart, Cees J. M. van Rijn, Jos M. J. Paulusse, and Han Zuilhof Langmuir 2012 28 (51), 17690-17700.
2. Covalently Attached Organic Monolayers onto Silicon Carbide from 1-Alkynes: Molecular Structure and Tribological Properties Sidharam P. Pujari, Luc Scheres, Tobias Weidner, Joe E. Baio, Martien A. Cohen Stuart, Cees J. M. van Rijn, and Han Zuilhof Langmuir 2013 29 (12), 4019-4031.

3. Tribology and Stability of Organic Monolayers on CrN: A Comparison between Silane, Phosphonate, Alkene, and Alkyne Chemistries Sidharam P. Pujari, Li Yan, Regeling Remco, and Han Zuilhof Langmuir 2013 Submitted.

9:00am **TR+SE-TuM4 Mechanical and Tribological Behavior of Carbon-Based Coatings Sliding against PEEK Polymer Counterfaces.** E. Broitman, Linköping University, Sweden, S. Laino, University of Mar del Plata, Argentina, S. Schmidt, Linköping University, Sweden, P.M. Frontini, University of Mar del Plata, Argentina, L. Hultman, Linköping University, Sweden

Carbon-based coatings are known for their good mechanical and tribological properties. By tuning the C sp³-to-sp² bonding ratio and by alloying the carbon with other elements, it is possible to tailor hardness, elasticity, friction and wear resistance. Also, polyether-ether-ketone (PEEK) polymers are increasingly used by the industry because of their corrosion resistance, mechanical stability, and self-lubricating ability. Huge amount of data regarding their individual interaction with steel counterfaces is available; however, very little information is found regarding the interaction of both materials.

In this work, we studied mechanical and tribological properties of carbon nitride (CN_x) and carbon fluoride (CF_x) coatings sliding against PEEK. The coatings were deposited on SKF3-steel balls by high power impulse magnetron sputtering (HiPIMS) using an industrial deposition system CemeCon CC800/9ML. CN_x was prepared at room temperature (RT) and 180 °C (HT) by reactive sputtering from C target in a N₂/Ar discharge at 400 mPa. CF_x was prepared at RT by reactive sputtering from a C target in a CF₄/Ar mixture at 400 mPa. PEEK 6 mm-thick unfilled plates were produced via injection molding (GATONE™ 5600). The friction and wear properties were measured by a pin-on-disk device using 6.35 mm-dia coated and uncoated balls against PEEK in dry slide at pressure contacts from 860 to 1240 GPa. Optical and scanning electron microscopy, and EDX spectroscopy were used to observe the wear tracks and analyze the presence and composition of transfer films. A triboindenter TI-950 (Hysitron) was used to measure hardness, elastic modulus, and roughness of the materials.

For uncoated steel counterfaces, the running-in friction (μ) takes place during the first 300 s, and shows peak values in the range 0.40-0.47. In the steady state, μ decreases to 0.30-0.35. The contact area shows big and deep scratches, oxidation, and no film transfer.

RT-CF_x and HT-CN_x coatings have similar behavior. Both have running-in periods of 1000 s, μ in the range 0.25-0.45, which increases in the steady state to 0.45-0.50. The microscopy reveals that the coatings have failed; big wear scars and the presence of film transfer are easily observed.

RT-CN_x coatings show the best performance. At the end of 1000 s running-in period μ is in the range 0.25-0.33, and increases slightly to 0.35-0.38 after 6000 s. The coatings show a very small wear scar and the presence of film transfer.

Our results demonstrate that a RT-CN_x coating on a steel counterface sliding against a PEEK polymer improves the tribological behavior of the sliding couple, and also is advantageous due to the coating chemical inertness.

9:20am **TR+SE-TuM5 Microstructure, Mechanical and Friction Behavior of Magnetron-sputtered V-C Coatings.** M. Stüber, P. Stoyanov, Karlsruhe Institute of Technology, Germany, E. Nold, Fraunhofer-Institute for Mechanics of Materials IWM, Germany, J. Schneider, H.J. Seifert, S. Ulrich, Karlsruhe Institute of Technology, Germany

Transition metal carbides exhibit superior mechanical and tribological properties at a wide range of environmental conditions and contact pressures. More recently, vanadium carbide coatings have been considered for a number of industrial applications (e.g. automotive components, cutting tools, ball bearings) due to their high corrosion resistance and mechanical stability at elevated temperatures. While some studies have provided significant new insights on deposition methods of vanadium carbides, the friction and wear mechanisms of these coatings have received little attention. The goal of this study is to link micro- to macroscale tribology in order to provide an excessive understanding of the sliding mechanisms of various vanadium carbide-based (VC_{1-x}) coatings. More generally, we are studying the influence of V:C ratio over a wide range of normal loads and contact areas. The coatings are prepared using non-reactive d.c. magnetron sputtering with a segmented VC/graphite target (i.e. target diameter of 75 mm, 500 W target power, substrate temperature < 150°C, and Ar gas pressure of 0.6 Pa). The resulting V:C ratios vary between 1:1 and 1:3. The microstructures of the as deposited coatings are characterized using X-ray diffraction and cross-sectional focused ion beam imaging, while elemental analysis is performed by means of X-ray photoelectron spectroscopy, electron probe microanalysis, and micro-Raman spectroscopy. Mechanical properties measurements show that the hardness (H) and the reduced modulus (E_r) of the coatings decrease with increasing the carbon

concentration (i.e. H ranges between 15 and 33 GPa and Er ranges between 239 and 391 GPa for the low and high vanadium concentration respectively), which correlates well with the adhesion results obtained from scratch tests. However, reciprocating micro- and macroscale tribological tests reveal higher friction values and increased wear with the high vanadium content coatings. This sliding behavior is attributed to differences in the third body formation and velocity accommodation modes, which are analyzed *ex situ* by means of XPS, micro-Raman spectroscopy and atomic force microscopy. The results obtained on the V:C coatings are compared to friction and sliding mechanisms in W:C systems.

9:40am **TR+SE-TuM6 Interaction of Stearic Acid with Iron-based Surfaces Coupling Experimental and Numerical Approaches for a Better Understanding of its Friction Behavior.** C. Minfray, C. Matta, S. Loehle, T. Le Mogne, J.M. Martin, Ecole Centrale de Lyon - LTDS, France, R. Iovine, Total, Solaize Research Center, France, Y. Obara, R. Miura, A. Miyamoto, Tohoku University, Japan

Organic friction modifiers (OFMs) have been used for many years in metallic contacts to reduce friction under mild conditions. The interest for such friction modifiers is still very strong because environmental regulations ask for slightly hazardous lubricant additives. It is proposed here to revisit adsorption and friction behavior of fatty acids by coupling experimental and computational chemistry approaches.

The OFM studied is stearic acid, used as pure additive or blended at 1%w in PAO4 synthetic base oil. The surfaces of interest are iron-based materials (including pure iron and iron oxides) as they can be encountered in a steel/steel contact under mild or severe friction conditions. Adsorption and friction properties of such systems were studied experimentally (friction, XPS and PM-IRRAS surface analyses) and adsorption kinetics was also studied by computational chemistry (UA-QCMD).

Adsorption experiments of stearic acid (gas form) on the different surfaces (gold, pure iron, iron oxides) were carried out in an environmentally controlled chamber for different adsorption time (10 min to 2 hours). This was followed by *in-situ* XPS analyses of the surfaces. XPS analyses results, especially the position of the C1s peak contribution from the carboxylic group, show differences depending on the nature of surfaces.

Computational chemistry study was also performed to investigate the *in vacuo* interaction of stearic acid molecules with the different model surfaces (pure iron, Fe₂O₃, and FeOOH). An ultra-accelerated quantum chemical MD (UA-QCMD) simulator has been used in order to deal with chemical reaction dynamics for large complex systems. Different models have been built starting with one single molecule up to self-assembled monolayer (SAM) on iron based surfaces at 50 °C. We found differences in adsorption energy (physisorption or chemisorption) depending on the kind of surface and regarding the presence of one single molecule or a SAM.

Eventually, friction experiments were carried out on a cylinder-on-flat reciprocating tribometer using samples in AISI52100 steel. The lubricant was stearic acid blended at 1%w in PAO4 and temperature was set to 50°C, 100°C and 150°C with an applied load of 50 N (corresponding to a maximum contact pressure of 320 MPa). After the tribological tests, PM-IRRAS analyses were conducted on the tribofilms. Results show the presence of stearic acid in the wear track as well as carboxylate forms.

All experimental and simulation results of both adsorption and friction experiments are discussed for a better understanding of complex interactions between stearic acid and iron-based surfaces.

10:40am **TR+SE-TuM9 Low Friction on Metals – Glide Planes and Molecular Lubricants.** R. Bennewitz, INM - Leibniz-Institute for New Materials, Germany **INVITED**

Nanotribological investigations of flat crystalline metal surfaces by means of friction force microscopy often result in extremely low friction coefficients. Experimental results indicate that the actual glide occurs between the low-indexed crystalline surface and a metallic neck, which forms by transfer of metal to the tip of the force microscope [1]. In the case of Au(111) surfaces, the apparently simple gliding process requires surface diffusion to operate, as evident from a failure of atomic friction mechanisms at lower temperatures [2]. Friction coefficients measured by friction force microscopy approach values known from macroscopic experiments when the tip plastically deforms the surface by scratching [3].

Electrochemical methods allow for an in-situ modification of surfaces by electrochemical oxidation, reduction, ion adsorption, or change in surface reconstruction. All of these influence nanometer-scale friction. For example, variation of the surface reconstruction reveals that friction increases with atomic-scale roughness [4]. Friction experiments in ionic liquids demonstrate that the preferential adsorption of anions or cations opens an opportunity for reversible switching of lubrication [5].

[1] N.N. Gosvami et al., Microscopic Friction Studies on Metal Surfaces, Tribol Lett 39 (2010) 19

[2] N.N. Gosvami et al., Ageing of a Microscopic Sliding Gold Contact at Low Temperatures, Phys. Rev. Lett. 107 (2011) 144303

[3] M. Mishra et al., Friction model for single-asperity elastic-plastic contacts, Phys. Rev. B 86 (2012) 045452

[4] F. Hausen et al., Surface structures and frictional properties of Au(100) in an electrochemical environment, Surf. Sci., 607 (2013) 20

[5] J. Sweeney et al., Control of Nanoscale Friction on Gold in an Ionic Liquid by a Potential-Dependent Ionic Lubricant Layer, Phys. Rev. Lett., 109 (2012) 155502

11:20am **TR+SE-TuM11 Few Layer Graphene as a Potential Solid Lubricant.** D. Berman, A. Erdemir, A.V. Sumant, Argonne National Laboratory

In recent years, reducing friction and wear-related mechanical failures in moving mechanical systems has gained increased attention due to their adverse impacts on efficiency, durability and environmental compatibility of such systems. Accordingly, search continues for novel materials, coatings, and lubricants (both liquid and solid) that can potentially reduce friction and wear. The majority of the existing solid lubricants (MoS₂ graphite, hexagonal boron nitride, etc.) requires full coverage, strong bonding, and relatively thick layers to provide lubricity to sliding interfaces. Moreover, their lifetimes and lubricating properties vary a great deal when operated under different environmental and tribological conditions. In this study, we demonstrate that a few layers of graphene are able to drastically reduce friction and wear of sliding steel surfaces under both inert and humid environments. The reduction in wear is as much as 4 orders of magnitude while friction is cut down by factors of 4 to 5. We believe that the anti-corrosion property of graphene coupled with its self-lubricating nature is mainly responsible for such remarkable friction and wear properties and the surface microscopic and spectroscopic studies confirm our hypothesis by confirming the presence of very thin and continuous graphene layers on both the ball and disk surfaces which were slid against one another under 1 N load in both humid air and dry nitrogen environments. In addition, we show that graphene application as well as re-application does not require any additional processing steps other than just applying a small amount of ethanol solution containing graphene on the surface of interest making this process simple, cost effective, and environmental friendly. Most of all, we found that unlike conventional solid lubricants which are all sensitive to environmental conditions, graphene provides low friction and wear regardless of the operating environment.

[1] D. Berman, A. Erdemir, A.V. Sumant: "Few layer graphene to reduce wear and friction on sliding steel surfaces". Carbon, 54, 454-459 (2013)

[2] D. Berman, A. Erdemir, A.V. Sumant: "Reduced Wear and Friction Enabled by Graphene Layers on Sliding Steel Surfaces in Dry Nitrogen", Carbon, in press. <http://dx.doi.org/10.1016/j.carbon.2013.03.006>

ACKNOWLEDGMENTS

Use of the Center for Nanoscale Materials was supported by the U. S. Department of Energy, Office of Science, Office of Basic Energy Sciences, under Contract No. DE-AC02-06CH11357.

11:40am **TR+SE-TuM12 Scaling of Structural Lubricity.** D. Dietzel, M. Feldmann, University of Giessen, Germany, U.D. Schwarz, Yale University, H. Fuchs, University of Muenster, Germany, A. Schirmeisen, University of Giessen, Germany

In an effort to reduce the friction between sliding components scientists and engineers have developed a multitude of lubrication schemes. One of the most intriguing concepts is referred to as 'structural lubricity', where at surfaces are thought to slide past each other virtually frictionless if their atomic structures are incommensurate, i.e. they do not match. Corresponding theories are based on sub-linear power laws for the area-dependence of friction in the structural lubricity regime, but this unusual scaling has never been observed so far. Here, we present experiments that quantify nanoparticle sliding resistance of amorphous antimony particles on crystalline graphite [1,2]. Our results confirm the predicted sub-linear scaling behavior for incommensurate, disordered interfaces, and allow a direct link between mesoscopic friction and atomic principles. Additionally, the case of crystalline incommensurate interfaces is investigated for gold crystals on graphite, pointing towards a more complex scaling behavior that accounts for particle shape and orientation. Our findings point towards a new route to engineer surfaces with unprecedented low friction on the basis of well-defined nanocontacts.

[1] A. Schirmeisen and U. D. Schwarz, ChemPhysChem 10 (2009) 2358

[2] D. Dietzel et al., Physical Review Letters 101 (2008) 125505

Vacuum Technology

Room: 202 C - Session VT-TuM

History of Vacuum Technology

Moderator: J. Hochrein, Sandia National Laboratories

8:40am **VT-TuM3 60 Years of Vacuum Gate Valve Developments, J.F. Hartnett**, Vacuum Research Corporation **INVITED**

In the early 1950's the vacuum industry was just beginning and there were few commercially available components, such as gate valves, for those working in the field. In 1953 three people in northern California formed Vacuum Research Corporation and began a collaboration to develop low cost gate valves for use in high vacuum.

Andrew Guthrie (1915 – 1977) worked at what was then known as the 'Rad Lab' and in 1963 published *Vacuum Technology* (ISBN 63-20631).

Ernest Martinelli (1919 – 2010) also worked at 'Rad Lab'. He spent many years as deputy chief of the physics department at RAND Corporation.

Hugh Perazone (1900 – 1974) owned and operated a permanent mold aluminum foundry.

Between 1954 and 1963 VRC was issued four patents. Although these patents are long expired the VRC claims are still used today by almost every manufacturer of vacuum gate valves.

Rotary actuator shaft seals as still used today in the VAT Series 14, GNB C-Style, and VRC LPWA Bonnet and OP One Piece styles.

High conductance oversize bores using flanges with the standard ANSI (ASA) bolt circle and outside diameter but with larger inside diameters for higher conductance still used today by almost all vacuum valve makers including VAT, GNB, VRC, HVA, etc.

Remote actuation automatic electro-pneumatic actuators that allowed easy operation of gate valves, even when located in difficult to reach or hazardous locations.

Bonnet style body construction that allows all moving parts to be removed for cleaning or replacement in less than five minutes and without disruption to the pump stack or piping.

Throttle valves with powerful servo motors that also provide leak tight shut off and an unobstructed high conductance port eliminating the need for separate throttle and pump isolation valves.

Protective ring gate valves for dirty applications such as investment casting furnaces.

Water cooled gate valves with both water cooled gates and port flanges.

Rectangular port valves with ports up to 3 meters wide.

Fast closing valves that can close in milliseconds.

Many manufacturers have continued to work on gate valve developments and some of the more interesting developments are:

Pendulum plate valves

Port sizes up to 52" (1320 mm) and beyond

Aluminum valves with aluminum Conflat® flanges

9:20am **VT-TuM5 A History of Vacuum from My Perspective!, K.J. Lesker III, K.J. Lesker IV**, Kurt J. Lesker Company **INVITED**

Having grown up working for my Dad (beginning wage \$0.25 per hour) in our business which started in 1954, I have met a lot of people who started companies, where instrumental in vacuum companies, created new technologies, and competed or collaborated with many companies and people in the vacuum industry. Our industry starts to move forward in the late 1800s, but it is not till WWII and afterwards that it really get moving forward and Vacuum gets used to make many products and used in research to advance technology and the quality of life. I want to go back to before vacuum existed (or was thought not to exist) briefly and explain why there was no such thing as vacuum. How vacuum gets discovered, how it starts to flourish and then grows. There are interesting scientists, vacuum figures and industrialists that drive things ahead. Then I want to bring in the companies of today which form and thrive or merge and get acquired. Hopefully, there will be a few or several moments of "I didn't know that?" or "So, that is the guy or reason these things or companies happened?!" I hope it will be interesting and fun!

10:40am **VT-TuM9 How We've Learned More & More About Less and Less So That Now We Know a Whole Lot About Nearly Nothing - Vacuum Measurement Over the Years, S.R. Goldfarb**, Consultant **INVITED**

Not only have the instruments used to monitor, measure and analyze vacuum evolved over the years, but the terminology has also undergone change. So herein I attempt to create a perspective of where we were in ancient times before I came on the vacuum scene, and continue through the subsequent half century to the present. I start with a requisite but brief description of a "vacuum", then compare the various units of measure, their utility, and the wide variety of tools we once employed and currently employ to characterize the vacuum environment. In addition, I relate how the requirements of various vacuum processes have driven instrumentation design.

11:20am **VT-TuM11 The Quest for Extreme High Vacuum, H.F. Dylla**, American Institute of Physics **INVITED**

The quest for obtaining and controlling an extremely low gas density environment, typically classified by the vacuum science community as extreme high vacuum ($< 10^{-10}$ Pa), has been a journey spanning more than a half century. Unlike other quests for pushing a parameter on the scientific frontier, the push for the extreme high vacuum environment has not been driven simply by the desire to claim a new record breaking parameter. Rather, the need for an extreme high vacuum environment has come primarily from scientific and a technical applications which have driven the march to higher vacuum environments. This paper will review the interplay of applications that have required extreme high vacuum and the technology needed to produce, sustain and characterize the environment.

Tuesday Lunch, October 29, 2013

Exhibitor Technology Spotlight

Room: Hall A - Session EW-TuL

Exhibitor Technology Spotlight II

Moderator: C. Moffitt, Kratos Analytical Limited, UK

12:20pm **EW-TuL2 What's New from Physical Electronics, J.F. Moulder**, Physical Electronics Inc.

The latest innovations in our XPS, AES, and TOF-SIMS products will be presented and we will introduce an exciting new instrument at AVS.

12:40pm **EW-TuL3 Next Generation Data System for XPS, C.J. Blomfield**, Kratos Analytical Limited, UK

Analytical instrumentation often has a large number of users with various operational and data processing skill levels. Modern software should allow both the novice and expert user to acquire the data they need while following the appropriate protocols. Although the concept of an expert system for x-ray photoelectron spectroscopy was suggested over a decade ago (Castle and Powell¹) the implementation of such expert systems is only just being realized.

In this presentation we will introduce a new generation data system which provides data dependent acquisition capability independent of the Users experience. Based on an initial survey spectrum the software is used to define the hardware acquisition parameters appropriate to the results required. Thus the software will provide the User with element identification and acquisition parameters appropriate to the requirements of either trace element detection or elemental/chemical state identification.

By allowing the software to determine the appropriate acquisition parameters for specific applications based on easy to define parameters such as signal to noise ratio the precision and accuracy of quantification from photoelectron spectra can be increased. This also ensures that the data acquired in a multiuser, non-expert environment is valid. Furthermore in line with protocols required for regulatory environments full traceability from raw data to quantified spectra is incorporated into the new data acquisition and processing software.

Reference

1. JE Castle, CJ Powell, SIA, Vol 35, Issue 3 p25-237

1:00pm **EW-TuL4 New Developments in Materials Characterization from Thermo Fisher Scientific, A.E. Wright, T.S. Nunney, P. Mack**, Thermo Fisher Scientific, UK, *B. Strohmeier*, Thermo Fisher Scientific

Surface and subsurface structure and chemistry are crucial to the successful production and operation of innumerable devices, materials and coatings. Thermo Scientific offers a broad range of analytical techniques for the materials characterisation, including XPS, Raman, FTIR, EDS and EBSD. In this presentation we will discuss our latest developments in software and instrumentation.

1:20pm **EW-TuL5 Recent Instrument Development for State-of-the-Art Photoelectron Spectroscopy, H. Bergersen**, VG Scienta AB, Sweden

For several decades, VG Scienta has been the leading developer of instrumentation for Photoelectron Spectroscopy, with emphasis on ARPES, HAXPES and APPES. In our presentation we will describe the latest developments within each field along with recent scientific results.

1:40pm **EW-TuL6 Innovative Thin Film Deposition Tools for R&D from Blue Wave Semiconductors, R.D. Vispute**, Blue Wave Semiconductors

Unique properties of new materials are exploited in emerging applications including electronics, optical, biological nanoelectronics, and advanced electromechanical systems. Despite the extraordinary efforts in developing these materials, an efficient and compact single chamber vacuum deposition system capable of addressing needs of all thin films and nanomaterials is not available at a commercial level. For this reason, Blue Wave Semiconductors has developed an integrated physical and chemical vapor deposition tool for synthesizing all carbon based thin films and nanostructures including diamond, nanodiamond, CNTs and graphene, metals, oxides, nitride, carbide thin films and their nanostructures. We have successfully designed and developed chemical and physical vapor deposition processes in a single processing chamber to efficiently deposit a variety of advanced thin film materials and nanostructures. We will present our systematic study on identification of various processing parameters on growth of nanostructures of carbon materials. Some examples of

nanodiamond and graphene films synthesized using exploratory tool developed for carbon materials for electronics will be highlighted. Blue Wave Semiconductors, Inc. is a global supplier of advanced thin film and nanomaterial deposition systems and tools. The company manufactures reliable physical vapor deposition, chemical vapor deposition and integrated custom deposition systems involving laser, DC, rf plasma, sputtering, hot filament, and electron beam. Its thin film deposition systems combine multidisciplinary designs and processes involving filament generated atomic hydrogen, laser induced plasma, with chemical processes. Blue Wave's deposition tools are excellent for synthesis of novel coating materials of composite nanostructural carbides, oxides, nitrides, and carbon materials such as diamond, graphene, and CNTs. Its deposition equipment products are designed primarily for universities, research centers and leading national laboratories around the world. It also provides prototype runs of a variety of thin film coatings and device fabrication to its electronic thin film R&D customers.

Tuesday Afternoon, October 29, 2013

Actinides and Rare Earths Focus Topic
Room: 102 C - Session AC+AS+EN-TuA

Actinides and Rare Earths: The Nuclear Fuel Cycle and Critical Materials

Moderator: L. Petit, Daresbury Laboratory, UK

2:00pm **AC+AS+EN-TuA1 Prospects for Accident Tolerant Fuels in Light Water Reactors**, S.J. Zinkle, K.A. Terrani, L.L. Snead, Oak Ridge National Laboratory **INVITED**

Further enhancement of safety margins in current and next generation commercial fission reactors in general requires an integrated engineering systems design approach. However, tangible gains in safety margin (and performance) may be achievable by utilizing one or more materials science modifications to the fuel system. In this paper the specific attributes of what would constitute *accident tolerant (or enhanced safety margin)* fuels will be presented. There are four key metrics to be considered for such a fuel under transient accident conditions: reduced enthalpy production, reduced hydrogen production, improved resistance to clad ballooning and rupture (maintaining coolability of the core), and suppressed fission product release. There are a variety of materials science approaches that can be considered to address one or more of these four metrics for accident tolerant fuels, ranging from relatively incremental modifications to the cladding material to dramatic alternatives to the historical monolithic UO₂ ceramic fuel pellets surrounded by seamless Zr alloy tubing. For example, solute modifications and/or highly adherent coatings that improve the high temperature steam oxidation resistance of Zr alloy cladding would directly lead to reduced enthalpy and hydrogen production. For extended high temperature transient conditions, deployment of high thermal-creep strength, oxidation-resistant cladding (e.g. advanced steels, coated molybdenum, or SiC/SiC) would maintain the coolant channel geometry and significantly suppress the rate of enthalpy and hydrogen production in the core compared to current Zr alloy cladding. This will effectively delay the threshold for fission product release from the fuel while providing longer time periods for emergency core cooling systems to become activated to halt core degradation processes. In addition, the critical heat removal limit in the core to prevent severe degradation would be lowered. Utilization of microencapsulated fuel forms (i.e., triple-encapsulated fuel kernels) within a high thermal conductivity matrix (i.e. SiC) would reduce the stored energy under normal operating conditions compared to standard fuels, resulting in suppressed fuel temperature increase under loss of coolant accident conditions that could limit fuel cladding ballooning and burst. Improved fission product retention within the fuel during high temperature accidents would also be anticipated. This presentation will review several potential fuel system options and outline key feasibility challenges that need to be resolved, along with briefly discussing potential impact on reactor neutronics and overall electricity production costs.

2:40pm **AC+AS+EN-TuA3 Photoelectron Spectroscopy Study of Uranium Materials**, S. Fujimori, Japan Atomic Energy Agency, Japan **INVITED**

Electronic structure of uranium materials have been studied by means of photoelectron spectroscopy (PES) as well as angle-resolved PES (ARPES) using synchrotron radiations. The results on the nuclear fuel material UN as well as uranium heavy Fermion superconductors UPd₂Al₃ will be presented.

Uranium monoxide (UN) is a promising fuel material for the generation-IV advanced nuclear reactors since it has high melting point, a very good thermal conductivity at high temperatures as well as a high fuel density. We have revealed its electronic structure by ARPES, and found that they are well explained by the band structure calculation based on local density approximation (LDA) [1].

UPd₂Al₃ is a heavy Fermion superconductor. It shows transitions into the antiferromagnetic phase at T_N=14 K and into the superconducting phase at T_{SC}=2 K. Since U 5f electrons in these compounds show both pronounced localized and delocalized characters, the nature of U 5f electrons have been not well understood. Their detailed electronic structure was derived by ARPES by synchrotron radiation as well as very high resolution PES by laser. It was found that quasi-particle bands with strong U 5f character form Fermi surface at low temperatures, suggesting that U 5f electrons have itinerant nature in this compound. Furthermore, we have succeeded to observe the superconducting gap of this compound by PES [2]. This is the first observation of the superconducting states of actinide materials by PES.

[1] Shin-ichi Fujimori *et al.*, Phys. Rev. B **86**, 235108 (2012).

[2] Y. Ohta *et al.*, in preparation.

4:00pm **AC+AS+EN-TuA7 Interaction of γ -U alloys with Hydrogen**, L. Havela, I. Tkach, S. Maskova, Z. Matej, Charles University, Czech Republic, N.-T.H. Kim-Ngan, Pedagogical University Cracow, Poland, A.V. Andreev, Academy of Science of the Czech Republic

Uranium metal absorbs H readily at low pressures, forming a fine highly pyrophoric powder of β -UH₃, which is ferromagnetic with T_C ≈ 175 K. More technologically important than the orthorhombic α -U is the bcc γ -U, known as existing at high temperatures or stabilized by doping to low temperatures.

In the course of the study of fundamental properties of Mo-stabilized bcc U alloys [1] we have been testing their resistance to H. There was no interaction with H₂ at ambient pressure and room temperature. However, increasing pressure over approx. 4 bar a slow hydrogenation was observed after several days if incubation. Increasing the H₂ pressure makes the hydrogenation faster. The product, in which the H concentration corresponds to the 1U-3H ratio, does not turn into powder, but consist of large brittle fragments with metallic luster. X-ray diffraction indicates that the hydride is amorphous, with a basic structure pattern corresponding to β -UH₃, while the grain size is ≈ 1 nm only.

The hydrides obtained were subjected to studies of magnetic properties, electrical resistivity, and specific heat. The most striking fact is that the Curie temperature can be higher than in β -UH₃. It reaches T_C = 200 K for UH₃Mo_{0.18}, for both lower and higher Mo concentrations it weakly decreases. Also the magnetization values increase from 0.93 μ_B /f.u. to 1.2 μ_B /f.u. (both in $\mu_0 H$ = 14 T). At low temperatures a striking high coercivity, reaching 4 T, is seen from magnetization loops. It can be understood as due to a high anisotropy randomly distributed over spatial directions.

The Sommerfeld coefficient of electronic specific heat γ = 29.2 mJ/mol K² is similar to β -UH₃ values (29-33.2 mJ/mol K² by various authors) and higher than pure UMo_{0.18} (18.8 mJ/mol K²). Electrical resistivity exhibits the weakly negative slope known from the bcc U-Mo alloys [2] and other strongly disordered systems with a cusp-like anomaly at 200 K superimposed. The absolute values about 1 m Ω cm are about an order of magnitude higher than for UMo_{0.18}, and even higher than that of UH₃, which exceeds 600 $\mu\Omega$ cm at room T [3]. The most surprising fact is that the 5f magnetism, which is normally suppressed by disorder, is supported in the case of UH₃Mo_x, probably due to enhanced U-U spacing due to Mo included in the lattice.

This work was supported the Czech Science Foundation under the grant No. P204/12/0285.

[1] I. Tkach, N.-T.H. Kim-Ngan, S. Mašková, M. Dzevenko, L. Havela, J. Alloys Comp. 534 (2012) 101.

[2] B.S. Chandrasekhar, J.K. Hulm, J. Phys. Chem. Solids 7 (1958) 259.

[3] J.W. Ward, L.E. Cox, J.L. Smith, G.R. Stewart, J.H. Hood, J. Phys. 40 (1979) C4-15.

4:20pm **AC+AS+EN-TuA8 The Effect of U and Fe Cations on the Reduction of CeO₂ for Thermal Water Splitting to Hydrogen**, Y. Al Salik, SABIC, Saudi Arabia, I. Al Shankiti, SABIC and University of Colorado, H. Idriss, SABIC, Saudi Arabia **INVITED**

Thermal water splitting to hydrogen on reducible materials is one of the promising methods to secure renewable energy vectors for the future. The process relies on a redox cycle whereby steam is introduced to a prior reduced CeO₂ to generate hydrogen which is consequently oxidized. However to achieve this cycle CeO₂ needs be reduced at elevated temperatures (> 1500°C) [1, 2]. Mixing CeO₂ with metal cations can lower the energy needed for the reduction process. Among the methods of changing CeO₂ are the incorporation of metal cations smaller in size than Ce⁴⁺ cations such as Zr⁴⁺ [3] or the addition of a metal cation that can transfer electrons to Ce⁴⁺ [4, 5]. In this work we present a core and valence level study of the extent of reduction of Ce⁴⁺ cations by the addition of Fe and U cations. We compare XPS Ce3d, Ce4d of stoichiometric CeO₂ to those of Ce_xFe_{1-x}O₂ and Ce_xU_{1-x}O₂ (x<1). We also investigate the reduction of these materials upon Ar ions sputtering. We find that the addition of Fe or U cations in any proportions increases the reduction of Ce⁴⁺ cations. In particular considerable enhancement of the reduction of CeO₂ with Ar ions was noticed (compared to CeO₂ alone) when x>0.5 in both Ce_xFe_{1-x}O₂ and Ce_xU_{1-x}O₂ series of the oxide materials. The reasons for the enhancement of CeO₂ reduction by Fe cations can be linked to both size and electron transfer effect while in the case of U cations it is mainly due to electron transfer from the U5f to Ce4f levels. Tests for hydrogen production by thermal water splitting for both series were conducted and indicated the enhancement of the activity of the mixed oxide when compared to CeO₂ alone.

- [1] W.C. Chueh, C. Falter, M. Abbott, D. Scipio, P. Furler, S. M. Haile, A. Steinfeld, *Science* (2010) **330**: 1797-1801.
- [2] K-S Kang, C-H Kim, C-S Park, J-W Kim, *J. Ind. Eng. Chem.* (2007) **13**: 657-663.
- [3] S. Abanades, A. Legal, A. Cordier, G. Peraudeau, G. Flamant, A. Julbe, *J Mater Sci* (2010) **45**:4163-4173.
- [4] I. Al-Shankiti, F. Al-Otaibi, Y. Al-Salik, H. Idriss, *Topics in Catalysis* (2013) *in press*.
- [5] B.E. Hanken, C.R. Stanek, N. Grønbech-Jensen, M. Asta, *Phys. Rev. B* (2011) **84**: 085131-1 to 085131-9.

5:00pm **AC+AS+EN-TuA10 Soft X-ray Investigations of Covalent Orbital Mixing in Metal Oxides**, S. *Minasian*, Lawrence Berkeley National Lab (LBNL), J. *Keith*, E. *Batista*, K. *Boland*, Los Alamos National Lab (LANL), J. *Bradley*, Lawrence Livermore National Laboratory (LLNL), S. *Daly*, George Washington Univ., S. *Kozimor*, LANL, W. *Lukens*, LBNL, R.L. *Martin*, LANL, D. *Nordlund*, SLAC National Accelerator Lab, G. *Seidler*, Univ. of Washington, D. *Shuh*, LBNL, D. *Sokaras*, SLAC National Accelerator Lab, T. *Tyliszczak*, LBNL, G. *Wagner*, LANL, T.-C. *Weng*, SLAC National Accelerator Lab, P. *Yang*, Pacific Northwest National Lab

Developing a clear understanding of how metal oxide electronic structure changes for a range of compounds and materials will greatly benefit a variety of existing and emerging energy technologies. Many of the technologically desirable chemical, magnetic, electronic, and thermal properties of metal oxides are derived from strongly covalent metal-oxygen multiple bonds (metal oxos). Among approaches explored previously, ligand K-edge X-ray absorption spectroscopy (XAS) has emerged as an effective method for quantitatively probing electronic structure and orbital mixing. The presence of covalent mixing is observed as a pre-edge feature in the ligand K-edge XAS, which only has transition intensity if the final state metal orbital contains a component of ligand p orbital character. Recent advances have shown that insights regarding the nature of orbital mixing in metal oxides can be obtained at the K-edge for oxygen through a combination of XAS with a scanning transmission X-ray microscope (STXM), non-resonant inelastic X-ray scattering (NIXS), and hybrid density functional theory calculations (DFT). The spectroscopic work in this study was performed at the ALS Molecular Environmental Sciences beamline 11.0.2 (STXM), beamline 6.2 at SSRL (NIXS), and the LERIX facility at the APS (NIXS).

Herein, a new effort is discussed that employs these techniques to understand bonding interactions in d- and f-block oxides. Oxygen K-edge XAS measurements and DFT studies began with a series of six tetrahedral oxyanions, MO_4^{2-} and MO_4^{1-} (M = Cr, Mo W and Mn, Tc, Re). Despite the similarities of the isoelectronic $\text{d}^0 \text{MO}_4^{2-}$ and MO_4^{1-} anions, unexpected differences in metal oxo orbital mixing were observed for adjacent metals in the periodic table. The lanthanide dioxides and sesquioxides, LnO_2 and Ln_2O_3 (Ln = Ce, Pr, Tb), were chosen for subsequent work because their electronic structures are well-established from hard X-ray spectroscopies. Features in the O K-edge XAS follow anticipated trends based on 4f and 5d orbital energies and occupancies. Taken together with L_3 -edge intensities determined previously, a detailed picture of the electronic structure in lanthanide oxides emerges. Overall, the research shows that orbital composition is influenced by a complex interplay between periodic changes in both orbital energy and radial extension.

This work was funded by the U.S. Department of Energy, Office of Basic Energy Sciences, Division of Chemical Sciences, Geosciences, and Biosciences, under contracts DE-AC02-05CH11231 at LBNL and DE-AC52-06NA25396 at LANL. Operation of the ALS, SSRL, and the APS is supported by the U.S. Department of Energy, Office of Science.

5:20pm **AC+AS+EN-TuA11 The Microstructure of Cerium Hydride Growth Centres**, M. *Brierley*, J. *Knowles*, N. *Montgomery*, AWE, UK, M. *Preuss*, A. *Sherry*, University of Manchester, UK

Considerable work has been undertaken into the hydriding of rare earth metals and actinides [1]; specifically into the reaction rate of various hydrides on the surface of these materials [2]. Cerium is a reactive rare-earth metal and quickly forms a semi-protective oxide layer in air. Upon exposure of an oxide-covered sample to hydrogen, hydride is formed as discrete sites on the surface, often termed 'Growth Centres', which then grow radially across the surface [3]. In the present study, the emphasis was to investigate the microstructure of the cerium growth centres with the intention of understanding any hydriding nucleation and growth mechanisms which may occur. The samples were prepared to 1 μm finish before being exposed to ultra-pure hydrogen at pressures between 10 mbar and 300 mbar, for sufficient time to have nucleated a number of hydride Growth Centres. Post-test analysis was performed using Secondary Ionisation Mass Spectrometry (SIMS), Scanning Electron Microscopy (SEM) and Optical Microscopy (OM) to determine the microstructure of the

hydride growth centres. SIMS confirmed that the Growth Centres were comprised of cerium hydride, and that the hydrogen exists specifically within the features. The morphology of individual hydride Growth Centres was examined using OM and SEM and the data reported demonstrates that the hydride-metal interface has a discrete boundary between two distinct phases; a region of deformed metal surrounds the Growth Centres; the microstructure within the Growth Centres indicates that the microstructure of the parent metal was retained by the hydride product.

References

- [1] M. H. Mintz, J. Bloch, *Prog. Solid St. Chem.* Vol. 16, (1985) 163-194.
- [2] K. H. Gayer, W. G. Bos, *J. Phys. Chem.* Vol. 68, No. 9, (1964) 2569-2574.
- [3] G. W. McGillivray, J. P. Knowles, I. M. Findlay, M. J. Dawes, *J. Nucl. Mater.* 385 (2009) 212-215.

Atom Probe Tomography Focus Topic Room: 203 A - Session AP+AS+SS-TuA

Microstructural and Interface Analysis of Metals Subjected to Various Conditions

Moderator: A. Devaraj, Pacific Northwest National Laboratory

2:00pm **AP+AS+SS-TuA1 Multivariate Analysis of Atom Probe Tomography Data: Methods to Simplify Factor Interpretation**, M.R. *Keenan*, Consultant, V. *Smentkowski*, General Electric Global Research Center

Multivariate statistical analysis has been used successfully for several years to analyze spectral images acquired in three spatial dimensions. Examples include energy dispersive x-ray images obtained from serially sectioned samples, and depth profiles in ToF-SIMS. More recently, multivariate methods have begun to be applied to atom probe tomography (APT) data. The analysis of APT data, however, poses some unique challenges, and it is important for the APT community to understand the principles that underpin the multivariate approach in order to maximize its effectiveness. The basic assumption made during multivariate analysis is that the composition of a sample at a particular location can be described as a linear combination of a limited number of "pure components", with each component having a characteristic spectral signature. The job of multivariate analysis, then, is to discover the number of components, extract spectral information suitable for identifying them, and determine the spatial distributions of their abundances. The primary tool of multivariate analysis is the Singular Value Decomposition (SVD), or the closely related Principal Component Analysis (PCA). These techniques distill the chemically relevant information in high-dimensional raw data sets into a small number of factors or components. These components, however, are abstract and not easily interpreted. For instance, typical components may contain negative spectral features and abundances, which are not physically plausible. In order to find a more straightforward representation of the components, they can be post-processed to impose certain constraints or preferences on the factor model. In this talk, a chemically simple sample will be used to illustrate some of these multivariate concepts in geometric terms. In particular, factor rotation procedures, such as the Varimax rotation, will be shown suitable for obtaining factor models that are in some sense simple, either spectrally or spatially, and the natural duality of the spectral and spatial domains will be highlighted. Multivariate Curve Resolution (MCR) will also be considered. MCR imposes constraints, often non-negativity, on the model components. MCR is problematic, however, in the presence of high noise levels typical of APT data, and some approaches for improving the fidelity of MCR models will be presented. APT is capable of producing quantitative results. As will be shown, achieving them with multivariate analysis requires tailoring the methods to the specifics of APT and paying careful attention to the details.

2:40pm **AP+AS+SS-TuA3 The Renaissance in Metallurgical Design and the Role of Atom Probe Microscopy**, S.P. *Ringer*, The University of Sydney, Australia

INVITED

The design of materials that demonstrate properties that are ordinarily in conflict with each other is a tantalising frontier of materials science and engineering. The design of metallic (not glassy!) aluminium alloys and new 3rd generation steels with remarkable combinations of high strength and ductility¹, magnetic carbon with a tuneable bandgap², and materials that exhibit magnetism and superconductivity in the same phase³ represent examples of new metals and materials that exhibit highly sought after properties that are usually in conflict with each other. In these cases, our

approach to overcoming these property conflicts is via atomic clustering within the solid solution, and that is the topic of this presentation.

In fact, short-range ordering, atomic clustering, segregation and site-occupancy exert a major influence on the phase transformation pathways, and transformation kinetics in many technologically important supersaturated solid solutions. So, how can these non-periodic structures be described, measured and, ultimately, 'designed'.

I will discuss a new theory for short-range order^{4,5} that provides a framework for describing the atomistic configurations in *n*-component solid solutions. The characterisation of such materials will then be discussed, in detail. The challenging issues associated with scattering based approaches using X-rays, neutrons or electrons, will be set out and it will be shown that there exist complex convolutions in the diffracted intensity that make the measurement of this 3D atomic architecture extremely challenging.

Finally, I will discuss our approach to addressing these issues using atom probe microscopy. We have recently modelled the origins of resolution in the atom probe, computed advanced spatial distribution maps, which are analogous to Patterson functions in scattering experiments, and used these new tools to devise an approach for 'lattice rectification', analogous to aberration correction in TEM. These techniques⁶ are revealing a rich and complex hierarchical architecture of atomic structures within solid solutions, and at microstructural interfaces and these are all discussed in terms of the renaissance in metallurgical design that we in the midst of.

¹ Liddicoat, Liao, Zhao, Zhu, Murashkin, Lavernia, Valiev and Ringer, "Nanostructural hierarchy increases strength of aluminium alloys", *Nature Communications*, Vol. 1, Article 63 (2010).

² Cui, Zheng, Liu, Li, Delley, Stampfl and Ringer, "Magic numbers of nanoholes in graphene: tunable magnetism and semiconductivity," *Physical Review B*, Vol. 84, Article 125410 (2011).

³ Yeoh, Gault, Cui, Zhu, Moody, Li, Zheng, Li, Wang, Dou, Sun, Lin and Ringer, "Direct observation of local potassium variation and its correlation to electronic inhomogeneity in (Ba_{1-x}K_x)Fe₂As₂ pnictide", *Physical Review Letters*, Vol. 106, Article 247002 (2011).

⁴ Ceguerra, Powles, Petersen, Marceau, Moody and Ringer, Short-range ordering in multicomponent materials, *Acta Crystallographica A*, (2012, in press)

⁵ Ceguerra, Powles, Moody and Ringer, "Quantitative description of atomic architecture in solid solutions: a generalized theory for multicomponent short-range order", *Physical Review B*, Vol. 82, Article 132201 (2010).

⁶ Gault, Moody, Cairney and Ringer, "Atom probe microscopy", Springer – monograph series in materials science , (2012).

4:40pm AP+AS+SS-TuA9 Atom Probe Tomography Investigations of Surface and Grain Boundary Oxidation in Ni-Cr Alloys Exposed to High-Temperature Water, D.K. Schreiber, M.J. Olszta, S.M. Bruemmer, Pacific Northwest National Laboratory

Ni-base, Cr-containing alloys have been selected for use as structural components in many aggressive environments because of their well-known corrosion resistance. In most oxidizing environments, the high Cr content of these alloys results in the formation of a protective Cr-rich oxide film. However, Ni-Cr alloys have been shown to be susceptible to localized corrosion in high-temperature hydrogenated water environments as found in the primary system of pressurized water reactors. Mechanisms controlling this degradation are being investigated using high-resolution analytical electron microscopy and atom probe tomography. Examples will be presented from Ni-Cr model binary alloys (5-30Cr), commercial alloy 600 (Ni-17Cr-9Fe) and alloy 690 (Ni-30Cr-9Fe) samples. In all cases, grain boundaries are found to play a significant but varied role in the observed corrosion behavior. In lower Cr alloys (5-20%), the grain boundaries are preferentially attacked and exhibit extensive oxidation to a much greater depth than the surrounding matrix. In sharp contrast, alloys with 30% Cr form a continuous layer of Cr₂O₃ directly above grain boundaries that protects the grain boundary from oxidation. Localized filamentary oxidation is observed into the metal matrix away from the intersection of the grain boundary with the surface where a continuous layer of Cr₂O₃ does not form.

5:00pm AP+AS+SS-TuA10 Space Charge Effects in Atom Probe Tomography, I. Blum, F. Vurpillot, L. Rigutti, A. Gaillard, D. Shinde, J. Houard, A. Vella, B. Deconihout, Groupe de Physique des Matériaux, France

Because of the relatively low ion currents observed during an APT analysis (0.1 to 0.0001 atom/pulse), it is generally assumed that the evaporated ions do not interact with each other during the field evaporation of the sample. It was shown recently, however, that ion-ion interactions do occur after dissociation of molecular ions [1], which can be observed during the analysis of compound semiconductors [1-2]. Indeed, coulomb repulsion

between the dissociation products modifies their trajectory in a manner similar to space charge effects in high intensity beams of charged particles.

In this work, we combine the information on the time-of-flight and impact positions on the detector of multiple events to study this phenomenon. Experimental results on GaN and ZnO samples are explained by taking into account the orientation of the molecule during dissociation, the shape of the electric field around the tip and the dissociation potential. We show that the coulomb repulsion between the dissociation products occurs in a direction of space that depends on the orientation of the molecule during dissociation. Therefore, the coulomb interactions can have a significant effect on their impact positions on the detector but can also have an effect on the time-of-flight of the particles. The times-of-flight and impact positions of the dissociation products are correlated and contain potential information about the physics of the dissociation of the original molecule in high electric field. These results are compared to simple simulations of the ions trajectories in the electric field. We also discuss the potential effect of this phenomenon on the quality of APT data and provide simple methods for its identification.

[1] M. Müller, B. Gault, G. D. W. Smith, and C. R. M. Grovenor, "Accuracy of pulsed laser atom probe tomography for compound semiconductor analysis," *Journal of Physics: Conference Series*, vol. 326, p. 012031, Nov. 2011.

[2] D. W. Saxe, "Correlated ion analysis and the interpretation of atom probe mass spectra.," *Ultramicroscopy*, vol. 111, no. 6, pp. 473–479, May 2011.

5:20pm AP+AS+SS-TuA11 Atom Probe Analysis and Challenges to Study a High-k Dielectric Grown on GaN, B. Mazumder, X. Liu, F. Wu, U.K. Mishra, J.S. Speck, University of California, Santa Barbara

Al₂O₃ has emerged as an appropriate gate dielectric for III-nitride based electronic devices. Major growth challenges for such high-k/GaN interfaces include unwanted GaN oxidation, impurity etc during deposition may result in the formation of electrically active defects. In addition to prior structural investigations of such systems, the relation between atomic structure, chemistry and electrical properties of these interfaces is poorly understood. Atom probe tomography (APT) was used to determine structural information related to interface abruptness, layer composition including impurity content. It is quite challenging to analyze dielectric/insulating oxides multilayers using atom probe. Micro fractures, irregular evaporation etc due to the evaporation field difference between the layers can make the analysis challenging. Additionally, experimental parameters including tip temperatures, laser energy, and detection rate all strongly impact the field evaporation and subsequent data analysis. In this study we have reported reliable and reproducible data with high measurement yield by optimizing experimental parameters and using a suitable capping layer.

Ga-face ((0001) c-plane) GaN samples were grown by metal organic chemical vapor deposition (MOCVD). Al₂O₃ layers were grown on GaN, both by MOCVD and atomic layer deposition (ALD) system for a comparative study. These samples were then analyzed in Local Electrode Atom Probe 3000X HR. The experimental parameters were optimized for the oxide/semiconductor system. Initially the measurement yield was very low with a metal cap layer (Ni, Cr). Replacing it by a low temperature GaN cap layer the measurement yield was increased substantially. Thorough compositional analysis and roughness measurements were done and it was found that the interface is relatively rough and not atomically abrupt. However no presence of Ga_xO_y was found in both the cases. Qualitative estimation of carbon impurities within dielectric was done for both the samples and was found to be in the order of 10¹⁹/cm³, however the MOCVD sample shows higher carbon concentration than those grown by ALD. From the C-V measurements the volume trap charge density was estimated to be around 2 x10¹⁹ cm⁻³ and 3.9 x10¹⁹ cm⁻³ for ALD and MOCVD samples respectively, those are of the same order as the carbon concentration determined from the atom probe measurements. By varying the growth temperature the amount of C impurity was controlled. In conclusion, atom probe was successfully used to investigate the dielectric/III-V system in depth, which provides valuable feedback for growth optimization required for better device fabrication.

5:40pm AP+AS+SS-TuA12 A Correlated Micro-Photoluminescence, Scanning Transmission Electron Microscopy and Atom Probe Tomography Experiment on the Same Nano-Object Containing a Set of InGaN/GaN Multi-Quantum Wells, L. Rigutti, I. Blum, D. Shinde, D. Hernandez Maldonado, W. Lefebvre, J. Houard, A. Vella, F. Vurpillot, Groupe de Physique des Matériaux, France, M. Tchernycheva, Institut d'Electronique Fondamentale, France, C. Durand, J. Eymer, CEA/CNRS/Université Joseph Fourier, France, B. Deconihout, Groupe de Physique des Matériaux, France

In this contribution, we present a correlated experiment on a single nanoscale object containing a set of InGaN/GaN non-polar multiple-quantum wells. The nano-object has been analyzed by micro-

photoluminescence spectroscopy (μ PL), high-resolution scanning transmission electron microscopy (HR-STEM) and atom probe tomography (APT). The observed μ PL narrow emission lines, polarized perpendicularly to the crystal *c*-axis and with energy in the interval 2.9 eV – 3.3 eV. The STEM data allow concluding that the optical polarization is related to the crystallography through the selection rules for the lowest-energy excitonic transition in the wurtzite structure. STEM also constitutes an important reference for the 3D atom probe reconstruction of this large (16 QWs) multi-quantum well system. Atom probe data evidence that the In distribution in the wells is not regular, and that In-rich regions, with InN fraction up to 20%, form patterns propagating from one well to the other. All these observations coherently support the interpretation that the optical emission lines observed in μ PL are related to exciton states localized in potential minima induced by the irregular 3D In distribution within the QW planes. This novel correlative technique can be in principle applied to a wide class of quantum confining emitters and nano-objects, and is susceptible to be implemented as a coupled *in situ* technique within the atom probe itself.

Applied Surface Science

Room: 204 - Session AS+BI-TuA

Forensic Science, Art and Archaeology (2:00-3:20 pm)/Quasicrystals and Complex Metal Alloys (4:00-6:00 pm)

Moderator: J.A. Ohlhausen, Sandia National Laboratories, R. Opila, University of Delaware, S.J. Pachuta, 3M Company

2:00pm AS+BI-TuA1 Validation of Ultra-Trace Biological Agent Sample Matching Using NanoSIMS, P.K. Weber, M.L. Davissson, C.E. Ramon, S.P. Velsko, Lawrence Livermore National Laboratory INVITED

The threat associated with the potential use of radiological, nuclear, chemical and biological materials in terrorist acts has resulted in new fields of forensic science using state-of-the-science analytical techniques. One such method is high spatial resolution secondary ion mass spectrometry (SIMS) performed with a Cameca NanoSIMS 50. This instrument allows us to extract quantitative trace element and isotopic information for forensic purposes at a resolution of \sim 100 nanometers. With this capability, target particles with contaminated or ultra-trace samples can be analyzed. Here we present a general validation scheme and extend it to the analysis of small numbers (3-10) of anthrax spores. The scheme tests the hypothesis that two samples were produced in the same laboratory by the same process. This test is generally known as “sample matching”, though the term “match” is not used. Instead, the test uses receiver-operating characteristics (ROC) curves derived from test samples to generate a likelihood ratio that is combined with other data relating to the hypothesis. For our work, we are using the elemental composition of single anthrax spores as evidence.

To evaluate the sample matching test we used a well-defined statistical design to generate *B. anthracis* samples that are representative of agents made by benchtop scale processes that might be encountered in terrorism events. We used the NanoSIMS to profile the elemental composition of individual bacterial spores. Between 8 and 20 elements were monitored. The dynamic range of the analyses was on the order of one million. An objective metric for the “closeness” of two samples was defined in terms of the differences between elemental concentrations. A ROC curve for the same lab-same process and same batch hypothesis tests were calculated based on the difference metric. The ROC curves for averages of small numbers of spores (3-10) were determined, and were compared to bulk elemental analysis.

Our results support the following conclusions: The average elemental composition of two samples containing a small number of spores (3 - 10) can have reasonable inferential power for determining if the samples were made in the same laboratory using the same process. The ROC curve for determining if two samples originate from the same batch offer less inferential power than those for the same lab - same process test. ROC curves for NanoSIMS-based comparisons are optimized by using a particular set of elements, but the dependence on element set is relatively weak.

2:40pm AS+BI-TuA3 Characterization of Foreign Material from Buried Interfaces in the Medical Device Industry, W. Theilacker, A. Belu, A. Burand, Medtronic, Inc.

This presentation will highlight the use of surface analysis methods for the characterization of buried interfaces on medical devices. Manufacturing of

medical devices requires the highest level of quality to ensure optimal device performance and patient safety. Pacemakers, leads, and cardiovascular products often contain components and sub-systems that are potted in an overlay of semi-transparent material including silicones, urethanes, cyanoacrylates, and epoxies. This process serves to isolate electrical feedthroughs and contacts, fill gaps and voids, and to create water tight seals. Occasionally surface residues from raw materials, manufacturing processes, cleaning, and handling become trapped at this interface and are often not detected until later in the build process. Their presence could degrade performance, prevent adhesion, generate corrosion, or simply result in a cosmetic blemish. Identifying the elemental and chemical composition of foreign material from buried interfaces is a very difficult task and often requires a multi-technique approach. In this study, titanium, polycarbonate, and silicon-based substrates were coated with a thin layer of commonly observed inorganic and organic manufacturing residues and buried under overlayers (<100 nm) of various organic materials. Both non-destructive (e.g., confocal Raman spectroscopy) and destructive analysis (e.g., ion beam sputtering along with XPS and TOF-SIMS) were applied to gain insight into the chemical composition of the interfacial regions.

3:00pm AS+BI-TuA4 Forensic XPS Characterization of Surface-Modified Textile Fibers, B. Strohmeier, Thermo Fisher Scientific, C. Deeks, Thermo Fisher Scientific, UK, R. Blackledge, Forensic Chemist Consultant

Despite its many advantages and unique capabilities as a surface analytical technique, X-ray photoelectron spectroscopy (XPS) has not been widely used in forensic science for the examination of specimens gathered at the scene of a crime. Reasons for the lack of forensic XPS studies in the past include: 1) the absence of standard forensic XPS methods and standard reference materials for comparison to real world samples; and 2) the historical long analysis times (e.g., hours per sample), relatively large analysis areas (e.g., several square millimeters), and the relative high cost of XPS instrumentation compared to more common forensic analytical tools such as scanning electron microscopy combined with energy dispersive X-ray spectroscopy (SEM/EDS), Fourier transform infrared (FT-IR) microscopy, and Raman microscopy. Advances in XPS instrumentation over the last few decades, however, have improved typical analysis times to minutes per sample and analysis areas down to the range of tens to hundreds of micrometers. In addition, recently developed argon cluster ion sources now allow depth profiling of organic species with minimal ion beam damage, thus preserving the chemical information available from XPS. Therefore, XPS has increased potential for new applications in forensic science. One such area is the forensic surface characterization of textile fibers. White cotton fibers are so common and have so few visual distinguishing features that they are largely ignored by forensic scientists at crime scenes. However, most fabrics today have received one or more types of organic-based surface-modification treatments to provide stain resistance, permanent press characteristics, and/or waterproof properties. This presentation will discuss a proof of concept study on the use of XPS to differentiate individual textile fibers based on their surface chemistry. Materials examined in this study included swatches, threads, and individual fibers from a variety of different cotton and polyester/rayon fabrics before and after receiving one of several different commercial textile surface-treatments. Results indicated that small spot XPS combined with argon cluster ion depth profiling can: 1) distinguish among various untreated textile materials based on differences in surface chemistry resulting from their specific manufacturing process; and 2) distinguish between otherwise identical appearing fibers by differences in the textile surface treatment applied. These results demonstrate that XPS has the potential for identifying and distinguishing textile fibers found at crime scenes.

4:00pm AS+BI-TuA7 Surface Properties and Complexity of Al-based Intermetallics, J.-M. Dubois, CNRS, France INVITED

Quasicrystals represent the ultimate state of lattice complexity in a crystal. Shechtman, who discovered quasicrystals,¹ was awarded a Nobel Prize in Chemistry in 2011 for having led to a revolution in the way ordered solids are now understood in materials science. The talk will focus on a specific series of compounds, namely Al-based complex metallic alloys (CMAs) which comprise a significant number of crystalline compounds of changing lattice complexity, according to composition, and yield few icosahedral compounds that are thermodynamically stable and may be prepared into various sample shapes that allow for the measurement of surface physical properties.

Surface energy (γ_s) is one of the few fundamental properties of condensed matter: it defines the equilibrium shape of a crystal, it determines the interfacial behavior of any piece of liquid or solid against another body, etc. The talk will summarize a number of attempts to estimate the surface energy of a large variety of CMAs, including the stable, icosahedral Al-Cu-Fe and Al-Pd-Mn quasicrystals.

Pin-on-disk experiments, after appropriate calibration, lead to reliable data that fall in the range $0.5 < \gamma_s < 0.8 \text{ Jm}^{-2}$ for these compounds.² The average value of γ_s is about one half that of pure aluminum ($\gamma_s = 1.15\text{-}1.2 \text{ Jm}^{-2}$), and less than a quarter that of iron ($\gamma_s = 2.2\text{-}2.4 \text{ Jm}^{-2}$). It is consistent with the low wetting behavior and reduced adhesion force against hard steel observed in high vacuum for these quasicrystals. Correlation to specific features of the electronic density of states will be emphasized, in line with the varying complexity of the studied CMA compounds. Potential applications in high vacuum technology will be addressed.

References:

- 1- D. Shechtman, I. Blech, D. Gratias and J.W. Cahn, Phys. Rev. Lett., 1984, **53-20**, 1951.
- 2- E. Belin-Ferré and J.M. Dubois, Int. J. Mat. Res., **97** (2006) 7.

4:40pm **AS+BI-TuA9 Structural Investigation of the (001) Surface of Al_5Co_2** , M. Meier, J. Ledieu, M.-C. de Weerd, E. Gaudry, V. Fournée, CNRS-Université de Lorraine, France

Complex metallic alloys (CMAs) like quasicrystals and approximants are being considered as low-cost alternative materials for heterogeneous catalysis [1,2]. It relies on the so-called site-isolation concept in which the catalytic performance of a material is ascribed to small and well-separated atomic ensembles containing an active transition metal (TM) element at the crystal surface. Such atomic ensembles must be stable under reaction conditions, which in turn depend on the chemical bonding and the crystal structure of the intermetallic compound. Al_5TM_4 compounds have been identified as promising candidates for the heterogeneous hydrogenation catalysis [2, 3]. Here we focus on a related CMA system, the Al_5Co_2 crystal, which is also considered as a quasicrystalline approximant.

As a first step towards the understanding of the catalytic properties of this new phase, an atomic scale description of its surface is mandatory. First, a single crystal has been grown using the Czochralski method and oriented perpendicular to its [001] axis. The surface structure investigated under ultrahigh vacuum conditions by low energy electron diffraction and scanning tunnelling microscopy (STM) exhibits a $\sqrt{3}\times\sqrt{3}R30^\circ$ reconstruction. According to the bulk model, two types of atomic layers are stacked along the [001] direction: either pure Al puckered (P) layers or flat (F) layers containing both Al and Co atoms. The step height measured by STM indicates that only one type of plane appears as surface termination. Atomically resolved STM images show small triangular atomic ensembles separated by 13 Å from each other and consisting of 3 bright protrusions. Such local configurations can only be interpreted as a reconstructed P layer where a fraction of Al atoms are missing. First-principles calculations using density functional theory (DFT) confirm that P layers are preferred terminations compared to F layers. Calculated surface energies for various surface models, along with the corresponding simulated STM images, show that the $\sqrt{3}\times\sqrt{3}R30^\circ$ reconstruction is due to a specific set of missing Al surface atoms. Finally, a very nice agreement is obtained between simulated and experimental STM images, thus confirming the surface model. Other surfaces of interest for catalysis are currently being studied, namely the (100) and the (2-10) surfaces, together with their chemical reactivity towards small molecules of interest (O_2 , CO, acetylene,...).

- [1] T. Tanabe, S. Kameoka, A. P. Tsai, Appl. Catal., A 384, 241 (2010).
- [2] M. Armbrüster, K. Kovnir, M. Friedrich, *et al.* Nat. Mater. 11, 690 (2012).
- [3] J. Ledieu, É. Gaudry, L. N. Serkovic Loli, *et al.* Phys. Rev. Lett. 110, 076102 (2013).

5:00pm **AS+BI-TuA10 Temperature-Dependence of Ag Film Roughness and Interlayer Spacings During Deposition on Complex Al-Pd-Mn Surfaces: Comparison with Periodic Substrates**, B. Ůnal, Massachusetts Institute of Technology, J.W. Evans, P.A. Thiel, Ames Laboratory and Iowa State University

The morphology of thin metal films deposited on metal substrates is often dominated by kinetic rather than thermodynamic factors. These factors can be assessed by studying film characteristics as a function of deposition temperature. In this study, we report a comparison of the roughness of thin Ag films deposited on surfaces of a quasicrystal (five-fold icosahedral Al-Pd-Mn), an approximant of this quasicrystal, and low-index Ag surfaces, at temperatures below and up to ambient. Kinetic effects lead to an increase in roughness with increasing temperature for the Al-Pd-Mn substrates, but a decrease in roughness over the same range on Ag(111) and Ag(100). The nature of these effects is discussed. In addition, we observe that interlayer spacings in the film depend upon layer height, for the Al-Pd-Mn substrates. A useful refined definition of roughness for a system with variable interlayer spacing is addressed.

5:20pm **AS+BI-TuA11 Study of Quasicrystal / α - Mg Eutectic Structure in the Mg-Cd-Yb System by EBSD**, A.P. Tsai, Tohoku University, Japan

A pseudo-binary phase diagram composed of iQC (icosahedral quasicrystal) and α -Mg in Mg-Cd-Yb system reveals a eutectic reaction at $\text{Mg}_{68}\text{Cd}_{24}\text{Yb}_8$. The alloy with eutectic composition prepared by slow cooling shows irregular eutectic structure of QC and α phases. In terms of interface stability, the iQC / α interfaces are realized to be most stable since eutectic structure contains largest area of interface. This study is aiming at understanding an essential question; "how does a quasiperiodic lattice match a periodic lattice?" The other challenging topic is the application of EBSD (Electron Back Scattering Diffraction) for the first time to study microstructure of a quasicrystalline material.

In X-ray diffraction patterns, a number of main peaks of iQC coincide with those of α phase, indicating good lattice matches between two phases. For examples, basal plane and prismatic plane of α phase have the similar lattice spacing to 2-fold symmetry plane and 5-fold symmetry plane, respectively. EBSD analysis revealed that the growth direction of iQC- α eutectic is $\langle 2f \cdot iQC \parallel \langle 10 \cdot 10 \cdot \text{Mg} \rangle$, and a number of orientation relationships between QC and α phase have been verified. Furthermore, a number of directions normal to the planes of iQC coincide to those normal to the planes having similar lattice spacing of iQC in the α phase. The interface stability is likely due to good lattice matches between iQC and α phase.

5:40pm **AS+BI-TuA12 Plasmonic Quasicrystal Lattices**, T.W. Odom, Northwestern University

Quasicrystals are ordered materials that do not have translational symmetry but form stable structures with rotational symmetries higher than periodic materials. Artificially structured high-symmetry lattices based on quasicrystalline structures have recently been generated using nanoparticle building blocks and nanoholes. The design of quasicrystal arrays with subwavelength spacings is especially important in photonics since such symmetries can result in full band gaps in photonic crystals and omnidirectionally trap light in patterned photovoltaic devices. This talk will describe a novel nanofabrication method—moiré nanolithography—that can fabricate subwavelength lattices with high rotational symmetries over wafer-scale areas. By exposing elastomeric photomasks sequentially at multiple offset angles, we could create nanoscale arrays with rotational symmetries as high as 36-fold, which is three times higher than quasiperiodic lattices (≤ 12 -fold) and six times higher than two-dimensional periodic lattices (≤ 6 -fold). We transferred these patterns into noble metal films to generate plasmonic quasicrystal lattices, which show unique optical properties. A new scheme required for indexing these new plasmonic modes will be discussed.

Electronic Materials and Processing

Room: 101 B - Session EM+MI+NS+SS+TF-TuA

High-k Oxides for MOSFETs and Memory Devices II/Oxides and Dielectrics for Novel Devices and Ultra-dense Memory I

Moderator: J. Kim, University of Texas at Dallas, C.L. Hinkle, University of Texas at Dallas

2:00pm **EM+MI+NS+SS+TF-TuA1 Metal-Atom Dimer Model of Oxygen Vacancy Behaviour in Oxide RRAM**, J. Robertson, Cambridge University, UK

Resistive random access memories (RRAM) have great potential as future non-volatile memories with a faster read and write time than Flash memory. RRAM works by the forming of a conductive filament across a resistive film between the electrodes, which is then SET and RESET between its conductive and resistive states [1-2]. Typical films are oxides such as TiO_2 , Ta_2O_5 and HfO_2 , and the conductive filament is believed to consist of a percolation path of oxygen vacancies. Recently there have been various models of this oxygen vacancy path, in terms of molecular dynamics [3], or ordered vacancy structures [4]. Here we use an ordered model of vacancies in HfO_2 or TiO_2 , as in a local M_2O_3 structure in the MO_2 matrix. In Ti_2O_3 , the Ti atoms form an ordered line of Ti-Ti dimers along the c axis, and the bonding state stabilises the Ti^{3+} state along the path. The transition between the ordered and disordered phase of dimers describes the low to high resistivity state of RRAM, as in the metal-insulator transition in Ti_2O_3 .

1 R Waser *et al.*, Adv Mater 21 2632 (2009)

2 G Bersuker, SISC (2012)

3 S Clima *et al.*, App Phys Lett 100 133102 (2012)

2:20pm **EM+MI+NS+SS+TF-TuA2 Investigation of Sub-Gap Defect States in High-k Dielectric Materials Using Reflection Electron Energy Loss Spectroscopy**, *B. French, S.W. King*, Intel Corporation

The electrical reliability of high-k metal gate transistors is a growing concern as the nano-electronics industry moves to sub-12 nm dimensions and new 3D multi gate transistor technologies. In order to understand the various possible reliability failure mechanisms in high-k dielectric devices, knowledge of the band gap and defect states in high-k dielectrics is needed, but experimental identification of both the chemical identity and energy level of the defects contributing to reliability issues in high-k materials has gone largely unreported in many cases. In this regard, we have utilized Reflection Electron Energy Loss Spectroscopy (REELS) to determine the band gap of numerous single crystalline and amorphous high-k dielectric materials. We demonstrate that for standard single crystalline materials such as Quartz, Al₂O₃, and TiO₂ REELS band gap measurements agree with known values. For amorphous high-k thin film materials, we further demonstrate that REELS band gap measurements in most cases agree with optical measurements of the same materials. However, in some cases, we have observed that REELS analysis is complicated by the existence of defect states within the band gap of these materials. While troublesome for band gap measurements, we demonstrate that this sensitivity can be utilized to determine the energy level of various defects in pristine and sputter damaged high-k dielectrics and in some cases the chemical identity of the defect can be determined.

2:40pm **EM+MI+NS+SS+TF-TuA3 Atomistic Mechanism of RRAM Operations**, *G. Bersuker*, SEMATECH **INVITED**

Non-volatile resistive switching memory (RRAM) technology shows a promise to overcome the scaling limit approached by the conventional electron storage memories. Among a variety of RRAM systems, the HfO₂-based technology is especially attractive due to its fab-friendly fabrication process, high endurance and retention, and sub-nanosecond switching-speed assuming that low-current, low-variability operations can be achieved. This study aims to identify critical features of the material structure and operation conditions controlling the inherently stochastic switching process. The forming of the initial conductive filament in hafnia and its subsequent disruption/restoration responsible for the switching between high and low resistive states are modeled considering oxygen vacancies/ions generation and recombination and oxygen ion diffusion in the surrounding oxide driven by the local temperature and electric field. The simulations reveal the main structural characteristics of the dielectric stack affecting variability and allow assessing the effect of different forming conditions on the overall filament geometry/composition, thus, providing general guidelines for optimizing device operations.

4:00pm **EM+MI+NS+SS+TF-TuA7 Bipolar Selector Devices for Cross-point ReRAM**, *H.S. Hwang*, POSTECH, Republic of Korea **INVITED**

ReRAM has been considered as a promising candidate to overcome scaling limits of the conventional FLASH memory due to its superior performance. To realize the high density memory, 3D cross-point array or Vertical ReRAM are necessary [1]. To integrate cross-point (4F²) ReRAM device array, we need to develop bi-directional selector device to suppress the sneak current path through the unselected devices. Although various candidates with selector properties were recently reported, several problems such as insufficient current density at set/reset operations for nano-scale devices, low selectivity, and poor endurance have been raised. In this talk, two different types of selector device for cross-point ReRAM are introduced.

A. Threshold switching device

Various reports on threshold switching device with oxides of V, Nb, and Ti have been reported. This threshold switching is attributed to formation of a metallic phase as a result of local Joule heating induced metal-insulator transition (MIT) of the corresponding suboxides such as VO₂, NbO₂, and Ti₂O₃. Among them, we investigated threshold switching characteristics of NbO₂ [2]. Ultrathin NbO₂ layer (< 10nm) exhibits excellent threshold switching characteristics. Especially, thermal stability of threshold switching was obtained at a high temperature. Threshold switching property remains stable up to 433K, which is much higher than VO₂ material (only a 340K). Furthermore, we demonstrate hybrid memory characteristic, which exhibits both threshold and memory switching, by controlling the oxygen concentration of NbO_x layer.

B. Multi-layered oxide based device

Highly non-linear property of Ta₂O₅/TaO_x/TiO₂ structure was reported [3]. By using multi-layered oxide stack, a high current density of 10⁷A/cm² and

a high selectivity (~10⁴) were achieved. To maximize the selector performance, we have performed extensive tunnel barrier engineering such as the adoption of various materials and control of oxidation conditions to optimize the oxide stoichiometry, film thickness, and electrode material. Furthermore, in order to confirm the feasibility for cross-point array application, selector device was vertically-integrated with ReRAM.

We have demonstrated excellent selector characteristics of threshold switching device and multi-layered tunneling oxide based device. Superior performances of selector devices show good promise for future high density ReRAM applications.

REFERENCES

1. D. Kau et al., *IEDM*, 27.1, pp. 617-620, 2009.
2. S. Kim et al., *VLSI*, T18-3, pp. 155-156, 2012.
3. W. Lee et al., *VLSI*, T5-2, pp. 37-38, 2012.

4:40pm **EM+MI+NS+SS+TF-TuA9 Crystallization study of SrTiO₃ Thin Films Prepared on Si₃N₄, Al₂O₃ and Pt surfaces by Plasma-Assisted ALD**, *V. Longo, M.A. Verheijen, F. Roozeboom, W.M.M. Kessels*, Eindhoven University of Technology, Netherlands

SrTiO₃ (STO) has received much attention due to its favorable properties as ferro-electric, para-electric and *high-k* dielectric material, related to its crystalline perovskite structure. Thin STO films are to be employed as the dielectric layer in metal-insulator-metal (MIM) structures, for example for DRAM and/or RRAM applications. When deposited by Atomic Layer Deposition (ALD), STO films are amorphous and require an annealing step to crystallize. Recent reports have shown that Sr-rich films yield a finer crystalline structure than stoichiometric films upon crystallization by rapid thermal annealing (RTA). The finer grain structure results in reduced nanocrack formation, thus less leakage and improved dielectric properties. A deeper understanding of the crystallization behavior of STO is therefore of crucial importance to further optimize the film properties.

In this work SrTiO₃ thin films with different compositions ([Sr]/[Sr]+[Ti] from 0.50 to 0.65) were deposited by plasma-assisted ALD employing cyclopentadienyl-based precursors and an O₂ plasma. The crystallization of the as-deposited amorphous films was obtained by RTA in N₂ at temperatures ranging from 550 °C to 650 °C. Different annealing times (60 to 600 s) were employed to characterize the crystallization process at different stages. An in-depth analysis of the microstructure of the crystallized STO was carried out by transmission electron microscopy (TEM). As a first step, the analysis was performed on STO films deposited on Si₃N₄ TEM membranes, either bare or coated by ALD-grown Al₂O₃, due to the transparency of these materials to the electron beam. It was shown that the STO crystallites had grown in a *transrotational* manner and that an increased Sr-content resulted in films with reduced grain size and a more compact microstructure. Furthermore, two crystallization regimes were identified: 1) growth-dominated, where the crystallization process is dominated by growth of a low density of crystals, and 2) nucleation-dominated, where a high density of crystals is limited in lateral growth by their proximity. Finally, the STO films were also deposited on Pt-coated TEM windows (Pt prepared by plasma-assisted ALD) to compare the crystallization kinetics on a representative functional bottom electrode material as used in MIM structures. The TEM analysis and the X-ray diffraction patterns evidenced that these films show quite similar crystallization behavior as on Si₃N₄ and Al₂O₃ surfaces.

5:00pm **EM+MI+NS+SS+TF-TuA10 Superconformal Coating and Filling by Two-molecule CVD**, *W. Wang, N. Chang, T. Hitt, G.S. Girolami, J.R. Abelson*, University of Illinois at Urbana Champaign

An important fabrication challenge is to fill deep trenches or gaps with a dielectric material, such as shallow trench isolation or inter-metal dielectric in microelectronics. This is typically accomplished using chemical vapor deposition, which affords nearly conformal film growth, interspersed with one or more etching steps to prevent pinch-off of the feature opening. A superior alternative would be superconformal growth, in which the film thickness is inherently thicker towards the bottom of a deep feature than at the top, to afford complete filling in a single process.

We report a method, applicable to CVD processes that use two reactive molecules, to afford superconformal growth. It takes advantage of two insights. First, growth involves competitive adsorption on the film surface, such that the growth rate is maximum for a particular ratio of reactant fluxes (pressures) and falls on either side of this peak. Thus, there exists a regime in which *decreasing the pressure of one reactant will increase the film growth rate*. Second, the molecular (Knudsen) diffusion coefficient controls the rate of pressure drop down the axis of the feature. The reactant with the smaller diffusion coefficient (generally, the heavier molecule) will decrease in pressure faster than the other component. Combining these insights, we identify regimes of reactant pressure that afford superconformal growth in deep features.

We demonstrate superconformal growth, to a maximum depth beyond which the reactants are depleted, for two CVD systems. MgO is deposited at 220°C using the precursor Mg(DMADB)₂ with H₂O as the co-reactant; the growth rate increases from 1.0 nm/min at the trench opening to 1.8 nm/min at a depth/width ratio of 18. TiO₂ is deposited at 300°C using TiCl₄ and H₂O; the growth rate increases from 1.5 to 4.0 nm/min at depth/width ratio of 5. The TiO₂ coating inside trench is found to be stoichiometric and 88% of bulk density.

Finally, we describe a general model for the superconformal growth phenomenon. It uses as input the adsorption and reaction rate coefficients derived from growth on planar substrates, and suitable values for the molecular diffusivities. A first-order solution of the diffusion-reaction equation affords an analytic relationship that predicts the degree of superconformality in terms of the aspect ratio of the feature and the starting pressures of the reactants. It can be used to identify the regimes of useful operation and the necessary growth conditions. Given input data on reaction rates, this model can be used to predict which other two-molecule CVD systems would afford superconformal growth.

5:20pm **EM+MI+NS+SS+TF-TuA11 Resistive Switching Random Access Memory (RRAM) - Materials, Device, Scaling, and Array Design**, *Y. Wu, S. Yu, H.-Y. Chen, J. Liang, Z. Jiang, H.-S.P. Wong*, Stanford University **INVITED**

In this paper, we review our recent progress on resistive switching metal oxide memory (RRAM). We continue to explore the stochastic nature of resistive switching in metal oxide RRAM using the Kinetic Monte Carlo method. By including multiple conduction mechanisms, local field and local temperature profile, we substantially improved our stochastic model and studied the RRAM characteristics such as set/forming current overshoot, endurance and retention [1-3]. From an experimental perspective, we have demonstrated that HfOx-based RRAM devices can scale down to less than 10 nm diameter using electron beam lithography (e-beam) and atomic layered deposition (ALD) methods. The devices can switch more 10⁸ cycles with fast speed (~10 ns), large resistance window (~100X), multi-level storage capabilities, and good retention. We also characterized the scaling behavior of the HfOx-based devices such as forming, set/reset voltages [4]. Two-layer stacked HfOx vertical RRAM was fabricated for 3D cross-point architecture. The vertical RRAM devices show excellent performance such as low reset current (<50 uA), fast switching (~50 ns), good endurance (~10⁸ cycles), half-selected immunity (~10⁸ cycles), retention (>10⁵ s @125°C) [5]. Looking into the future, we investigated the impact of wordline/bitline metal wire scaling on the read/write performance, energy consumption, speed and reliability in the cross-point memory array architecture. Possible solutions were suggested to incorporate and mitigate the scaling effects of metal wire interconnect for the next-generation non-volatile memory (NVM) [6-7].

- [1] X. Guan, S. Yu, H. -S. P. Wong, IEEE Trans. Electron Devices, vol. 59, no. 4, pp. 1172-1182, 2012
- [2] S. Yu, X. Guan, H. -S. P. Wong, IEEE Trans. Electron Devices, vol. 59 no. 4, pp. 1183-1189, 2012
- [3] S. Yu, X. Guan, and H. -S. P. Wong, International Electron Devices Meeting (IEDM), pp. 585-588, 2012
- [4] Z. Zhang, Y. Wu, H.-S.P. Wong, and S. Wong, IEEE Electron Devices Letters, submitted
- [5] H.-Y. Chen, S. Yu, B. Gao, P. Huang, J. F. Kang, and H.-S. P. Wong, International Electron Devices Meeting (IEDM), pp. 497-500, 2012
- [6] J. Liang, S. Yeh, S.S. Wong, H. -S. P. Wong, ACM Journal on Emerging Technologies in Computing Systems (JETC), Vol. 9, No. 1, Article 9, pp. 9:1 – 9:14, 2013

Electronic Materials and Processing

Room: 102 A - Session EM-TuA

Evolution of Electronic Materials and the AVS

Moderator: S.M. Han, University of New Mexico, A.J. Muscat, University of Arizona

2:00pm **EM-TuA1 Division Chairs, Executive Committees and Perspectives on the Evolution of EMPD**, *A. Rockett*, University of Illinois at Urbana Champaign **INVITED**

The Electronic Materials and Processing Division (EMPD) has been through a long evolution from a division driven heavily by the electronic device fabrication community to a division with less of a clear home. The plasma processing that is the core of the Plasma Science and Technology Division and nanotechnology that is central to the Nanoscience and

Technology Division that now represent large fractions of the AVS program evolved from strong areas in the EMPD. The division now looks to organic and inorganic devices, oxides, metals, and many other less closely linked areas. As with several other divisions, the EMPD has had a strong intellectual connection to its topical conferences. However, unlike the other divisions, EMPD does not directly organize the three beams, molecular beam epitaxy workshop, physics and chemistry of surfaces and interfaces, and other topical conferences important to its core area. Although the senior members of the EMPD executive committee often have been senior organizers of these workshops, they run much more independently than do, for example, the ICMCTF and the Vacuum Technology Division or the ALD Workshop and the Thin Film Division. The leaders of the division over the years have struggled with the changes in the field and have worked hard to maintain the division as a vibrant part of the AVS. The EMPD looks forward to nucleating additional core areas of the AVS program in the future. It is truly the nursery for new AVS divisions and remains near the center of the AVS fields of interest.

2:40pm **EM-TuA3 Detonation Nanodiamond Particles for Electronic and Optical Applications**, *G.E. McGuire*, International Technology Center, *O.A. Shenderova*, Adamas Nanotechnologies **INVITED**

Recent achievement of the production of colloidal suspensions of individual nanodiamond particles only 4-5nm in size (so called single-digit nanodiamond) and the controlled production of nitrogen-vacancy (NV) centers in nanoscale diamond has opened up unprecedented perspectives in electronic and optical applications of nanodiamonds (ND). Production of nanodiamond particles containing specific impurity defects seems poised to revolutionize biological imaging and quantum optics applications, while nanometer-sized diamond particles are indispensable for seeding of substrates for growth of diamond films by chemical vapor deposition (CVD). The range of applications of NDs in electronics can be very broad if electrically conductive ND particles can be synthesized. Production of conductive doped ND particles can be very beneficial in high surface area carbon electrodes for electroanalysis, electrochemical double-layer capacitors, storage materials for batteries and other applications. Nanodiamond-derived conductive onion-like carbon nanoparticles are already being explored in carbon electrodes applications.

The two major breakthroughs, the production of ND particles 4-5nm in size and ND particles containing impurity defects exhibiting stable luminescence and unique spin properties, are related to nanodiamond particles synthesized by two different techniques, detonation of explosives and breakdown of diamond produced through the use of high pressure-high temperature techniques, correspondingly. Owing to the lack of optically active particles containing NV centers in useful amounts, ND synthesized from explosives has not historically been amongst the preferred candidates for imaging applications. In this presentation the nitrogen content of NDs produced by several representative classes of synthesis including detonation shock wave conversion of different carbon precursor materials, detonation of a graphite/hexogen mixture, as well as different combinations of explosives using different cooling methods (wet or dry cooling) will be discussed. Perspectives for the production of photoluminescent NDs as a result of the generation of NV centers will be summarized. Photoluminescent carbon dot decorated ND, produced from a mixture of graphitic carbon and ND demonstrating surprisingly strong photoluminescence of different colors, will be described. Recent advances of ND applications, particularly in seeding of substrates for chemical vapor deposition diamond growth, will be surveyed and areas of future scientific research highlighted.

4:00pm **EM-TuA7 High Efficiency, Durable Quantum-Dot Hybrid Light-Emitting Diodes**, *P. Holloway*, University of Florida, *Y. Zheng, L. Qian, Y. Yang, A. Titov, J. Hyvonen*, NanoPhotonics, *W. Cao, J. Xue*, University of Florida **INVITED**

Colloidal quantum-dot based hybrid light-emitting diodes (QD-LEDs) that exhibit record high efficiencies, long lifetimes, solution processability, color tunability and narrow emission bandwidths are reported. The devices exhibit world record quantum dot current and power efficiency of 3.2 cd/A and 2.1 lm/W for blue (B), 60 cd/A and 54 lm/W for green (G), and 15 cd/A and 18 lm/W for red (R) emission. With exceptional good lifetimes, these QD-LEDs are extremely promising for flat panel display applications. The record efficiencies result from the use of a polymer hole transport layer (HTL) and a zinc oxide nanoparticles electron transport layer (ETL) sandwiching the quantum dot emitting layer (EML). The size and composition of the QDs were controlled during the synthesis process to emit at B, G or R wavelengths. We report all-inorganic QD-LEDs by using either vacuum deposited or solution processed MoO₃ as the HTL. Improved device performance can be achieved by engineering the interface between the hole injection and QD layers, as will be described.

4:40pm **EM-TuA9 Semiconductor Heterojunctions: The Revolutionary Breakthrough that Enabled the Photonic and High-speed Device Industry, J. Woodall**, University of California, Davis
INVITED

Most people on the planet have some form of a personal electronic device. Most professional scientists and engineers know that all of these devices were enabled by integrated circuit (IC) based “chips” that employ silicon (Si) field effect transistor (FET) technology. Currently the worldwide Si chip market is well in excess of \$300 billion. One would not get an argument from someone who might claim that other than the airplane, Si chips were probably the single most revolutionary life-style changing breakthrough of the 20th century.

Important as this breakthrough was, it was limited to cost effective electronic devices and photo-detector ICs. However, only 7 years after the invention of the IC, another revolution was in the making: the invention of the lattice matched compound semiconductor heterojunction in 1967. This invention eventually morphed into, for example, injection lasers that enabled optical fiber communication, CD and DVD technology; high brightness and high efficiency visible (including white) LEDs that have enabled a photonic device industry that supplements the Si electronics industry. Furthermore, the heterojunction is employed in high speed, high power microwave devices that enabled cell phones and other remote wireless communication devices, e.g. i-phones, etc.

In this presentation the author will present a medium altitude review of how heterojunctions came about and why they do what they do.

Energy Frontiers Focus Topic

Room: 101 A - Session EN+AS+PS-TuA

Water Splitting and Carbon Dioxide Conversion

Moderator: D. Lutterman, Oak Ridge National Laboratory

2:00pm **EN+AS+PS-TuA1 Turning CO₂ into Liquid Fuel, M. Kanan**, Stanford University
INVITED

The longstanding reliance on fossil fuels as the principal energy source for society has boosted the atmospheric CO₂ concentration to a level that is unprecedented in modern geological history. Since the use of carbon-containing fuels is entrenched in society, controlling the atmospheric CO₂ concentration may ultimately require recycling CO₂ into liquid fuels and commodity chemicals using renewable energy inputs. Arguably the greatest challenge for this vision is to develop efficient CO₂ reduction catalysts. This talk will describe our development of “oxide-derived” metal nanoparticles as electroreduction catalysts. Oxide-derived metal nanoparticles are prepared by electrochemically reducing metal oxide precursors. This procedure results in highly strained metal nanocrystals, as determined by grazing incidence synchrotron x-ray diffraction. I will describe examples of these catalysts that electrochemically reduce CO₂ to CO with exceptional energetic efficiency as well as a catalyst that selectively reduces CO to two-carbon oxygenates. The catalysts operate in water at ambient temperature and pressure and are remarkably robust. The reduction mechanisms will be discussed based on electrokinetic measurements. Metal oxide reduction represents a “top-down” approach to metal nanoparticle synthesis that can result in unique surface structures for catalysis.

2:40pm **EN+AS+PS-TuA3 Efficient Conversion of CO₂ to Fuels using Inexpensive Cathode Materials, J. Rosenthal, J. DiMeglio, J. Medina-Ramos**, University of Delaware

The wide-scale implementation of solar and other renewable sources of electricity requires improved means for energy storage. An intriguing strategy in this regard is the reduction of CO₂ to CO, which generates an energy rich commodity chemical that can be coupled to liquid fuel production using Fischer-Tropsch methods. To this end, we have developed an inexpensive Bismuth Carbon Monoxide Evolving Catalyst (Bi-CMEC) that can be formed upon cathodic polarization of an inexpensive carbon or metallic electrode in acidic solutions containing Bi³⁺ ions. This catalyst can be used in conjunction with ionic liquids and other weak organic acids to effect the electrocatalytic conversion of CO₂ to CO with appreciable current density at low overpotential. The systems to be described are selective for production of CO, operating with very high Faradaic efficiency for conversion of CO₂ to this valuable product. As such the ability of this electrocatalyst system to drive production of CO from carbon dioxide is on par with that which has historically only been observed using expensive silver and gold cathodes.

4:00pm **EN+AS+PS-TuA7 Power Curves of the Artificial Leaf, D. Nocera**, Massachusetts Institute of Technology
INVITED

An artificial leaf can perform direct solar-to-fuels conversion via water splitting. The artificial leaf is a buried junction, in which the rectifying junctions are protected from solution or “buried”. Whereas water splitting catalysis is combined with charge separation, current rectification, and photovoltage generation in a solution junction PEC device, in a buried junction device, catalysis is separated from the current rectification, charge separation, and photovoltage generation, which occur at the internal junction. The buried junction photoelectrochemical (BJ-PEC) cell is free from many of the design limitations of a traditional solution junction photoelectrochemical (SJ-PEC) cell. First and foremost, in a SJ-PEC, water splitting catalysis is combined with charge separation, current rectification, and photovoltage generation. Accordingly, most candidate materials are based on metal-oxides. Decades of research have shown that it is extremely difficult to produce a competent photovoltaic (PV) material that at the same time is capable of facilitating the demanding four-electron, four-proton chemistry of water splitting. Second, in a SJ-PEC, the band edges of the flatband potentials of the semiconductor must straddle the thermodynamic potentials of OER and HER under the conditions of operation. These foregoing limitations are circumvented in a buried junction device. In a BJ-PEC, water-splitting catalysis is separated from the internal junction where current rectification, charge separation, and photovoltage generation occur. Accordingly, the OER and HER catalysts may be optimized independently from the PV device such that the maximum power characteristics of the PV and catalyst may be matched independently. Of equal significance, in a BJ-PEC, the potential drop across the outer Helmholtz layer will adjust automatically to move the Fermi levels to energetic positions that allow the water splitting reaction to proceed. For this reason, the photovoltages produced at buried junctions need not be fixed relative to a specific material flatband potential and consequently there is no requirement for the flatband potentials of the semiconductors to straddle the thermodynamic potentials of the OER and HER. There simply has to be sufficient potential generated by the PV device to enable water splitting. This talk will focus on the analysis of Tafel and photovoltaic power curves. The presented analysis highlights the importance of matching the electrochemical load of the water splitting catalyst to the onset of maximum current of the PV component, drawing a clear link between the kinetic profile of the water splitting catalyst and the SFE of devices such as the artificial leaf.

4:40pm **EN+AS+PS-TuA9 Transient Plasma for Green Technologies: Reduced Emissions, Greenhouse Gas Reduction, and Improved Combustion Efficiencies, M. Gundersen**, University of Southern California
INVITED

Transient plasma, that is, plasma during a formative, short time period prior to equilibration of a plasma electron energy distribution, is studied for applications to the fundamental improvement of fuel-burning engine efficiency in fuel-air mixtures, and in exhaust streams. This transient plasma requires operation with short (<100ns) pulsed high voltage, and typically requires only small pulse energy (10mJ to <1J). Transient plasma has been demonstrated shows promise for improving engine efficiency through improved combustion efficiency, and has been demonstrated to be efficient for NO_x conversion. Results for studies of engine types including internal combustion engines, pulse detonation engines, will be discussed, and ideas for future directions will be presented. This work has been supported by the AFOSR, ARO, and the TCC Corp.

5:20pm **EN+AS+PS-TuA11 Activation of CO₂ using Non-equilibrium Plasma: Mechanisms and Power Efficiency, M.C.M. van de Sanden, A.P.H. Goede, M. Graswinkel, W. Bongers**, Dutch Institute for Fundamental Energy Research (DIFFER), Netherlands, **F. Brehmer, S. Welzel, R. Engeln**, Eindhoven University of Technology, Netherlands
INVITED

Sustainable energy generation by means of, either photovoltaic conversion, concentrated solar power or wind, will certainly form a significant part of the energy mix in 2025. The intermittency as well as the temporal variation and the regional spread of this energy source, however, requires a means to store and transport energy on a large scale. In this presentation the means of storage will be addressed of sustainable energy transformed into fuels and the prominent role plasma science and technology can play in this great challenge.

The storage of sustainable energy in these so called solar fuels, e.g. hydrocarbons and alcohols, by means of *artificial photosynthesis* from the feedstock CO₂ and H₂O, will enable a CO₂ neutral power generation infrastructure, which is close to the present infrastructure based on fossil fuels. The challenge will be to achieve *power efficient* dissociation of CO₂ or H₂O or both, after which traditional chemical conversion (Fisher-Tropsch, Sabatier, etc.) towards fuels can take place.

Most of the research efforts are directed at the splitting of water in hydrogen and oxygen. However, no efficient catalytic or traditional chemical

alternative is yet available. A promising route is the dissociation or activation of CO₂ by means of plasma, possible combined with catalysis. Taking advantage of non-equilibrium plasma conditions to reach optimal energy efficiency the FOM institute DIFFER has started its solar fuels program at the beginning of 2012 focusing on CO₂ plasma dissociation into CO and O₂. The plasma is generated in a low loss microwave cavity with microwave powers up to 10 kW using a supersonic expansion to quench the plasma and prevent vibrational-translational relaxation losses. New ideas on the design of the facility and results on power efficient conversion (more than 50%) of large CO₂ flows (up to 75 standard liter per minute with 11% conversion) as determined from calibrated mass spectrometry measurements at low gas temperatures will be presented.

Exhibitor Technology Spotlight

Room: Hall A - Session EW-TuA

Exhibitor Technology Spotlight III

Moderator: C. Moffitt, Kratos Analytical Limited, UK

3:20pm **EW-TuA5 New Developments in Thin Film Technology, D. Bingaman**, Kurt J. Lesker Company

In this spotlight the Kurt J. Lesker Company® will update the industry on some of its new thin film deposition solutions from our Process Equipment Division.

3:40pm **EW-TuA6 Picolitre Dosing of Proteins onto Biomaterials Microarrays to Monitor Cell Response in a Combinatorial Assay, C. Dufresne**, Scienion US, Inc., *M. Hammad, M.R. Alexander*, University of Nottingham, UK

A high throughput model of protein pre-adsorption on biomaterials for control of cell adhesion and proliferation is being investigated using Scienion's non-contact low volume dispensing technology. Valuable proteins combinations (31 in triplicate) were piezo-dispensed and pre-adsorbed onto microarray spots representing seven biomaterials. Cell density correlates with the surface chemistry of the protein pre-adsorbed polymer spots as acquired by ToF-SIMS. It is only possible to rapidly produce and assess this many protein adsorption combinations with a high throughput platform combined with high throughput surface characterization. Details of this technology will be presented.

Graphene and Other 2D Materials Focus Topic

Room: 104 B - Session GR+AS+NS+SP+SS-TuA

Characterization including Microscopy and Spectroscopy of 2D Materials

Moderator: P.W. Sutter, Brookhaven National Laboratory

2:00pm **GR+AS+NS+SP+SS-TuA1 Intercalation of SiC(0001) with Silicon, S. Oida, J. Hannon, R.M. Tromp**, IBM T.J. Watson Research Center

Graphene growth on SiC is of interest, in part, because the synthesis takes place directly on an insulating substrate. Because of strong electronic coupling to the substrate, the first graphene layer (called the "buffer layer") does not have the unique electronic properties of graphene. The second layer has much weaker coupling to the substrate and exhibits the high carrier mobility associated with monolayer graphene. However, the synthesis of exactly two monolayers of graphene is difficult, and is usually accompanied by increased surface roughness. Therefore, it would be advantageous to electronically "decouple" the buffer layer and avoid the need to synthesize thicker layers. Here we show that by exposing a buffer layer surface to disilane in ultra-high vacuum it is possible to form Si-rich structures underneath the buffer layer domains. We do this by imaging the surface during disilane exposure using low-energy electron microscopy (LEEM). Furthermore, spatially-resolved electron-energy loss spectroscopy (EELS) shows that the intercalated Si strongly modifies the electronic coupling to the SiC substrate, effectively decoupling the graphene. Finally, we show that the intercalation is fully reversible. That is, with annealing in ultra-high vacuum, the intercalated silicon will desorb from the surface.

2:40pm **GR+AS+NS+SP+SS-TuA3 Imaging the Local Electronic Properties of Graphene, B.J. LeRoy**, University of Arizona **INVITED**
Scanning probe microscopy is a powerful tool to probe low-dimensional systems. The local information provided by scanning probe microscopy is

invaluable for studying effects such as interactions and scattering. Using this approach, we have probed the local electronic properties of graphene. The honeycomb lattice in graphene creates a unique linear dispersion relation and the charge carriers behave as massless fermions near the Dirac point. We have studied the effect of charged impurities and the underlying substrate on the local density of states. We find that long-range scattering from charged impurities locally shifts the charge neutrality point leading to electron and hole doped regions. By using boron nitride as a substrate, we observe an improvement in the electronic properties of the graphene as well as a moire pattern due to the misalignment of the graphene and boron nitride lattices [1]. We find that the periodic potential due to the boron nitride substrate creates a set of 6 new superlattice Dirac points in graphene [2]. The ultraflat and clean nature of graphene on boron nitride devices allows for the observation of scattering from buried step edges, which is used to map the dispersion relation [3]. More complicated graphene heterostructures can be created by adding additional layers or other two-dimensional materials. Our latest results with trilayer graphene and rotated bilayers will also be discussed.

[1] J. Xue et al., *Nature Materials* **10**, 282 (2011).

[2] M. Yankowitz et al., *Nature Physics* **8**, 382 (2012).

[3] J. Xue et al., *Phys. Rev. Lett.* **108**, 016801 (2012).

4:00pm **GR+AS+NS+SP+SS-TuA7 Tunable Optical Properties of Graphene, F. Wang**, University of California at Berkeley **INVITED**

Graphene, a single layer of carbon atoms, exhibits novel tunable optical properties. In this talk, I will describe electrical control of interband and intraband optical transitions in graphene and modification of graphene optical transition in a graphene-boron nitride heterostructure. I will also discuss how we can realize other tunable nanophotonics by combining graphene with plasmonic structures and photonic crystals.

4:40pm **GR+AS+NS+SP+SS-TuA9 Purity, Structure and Electronic Properties of Graphene Studied by Low Energy Ion Scattering, S. Prusa, P. Prochazka, P. Babor**, Brno University of Technology, Czech Republic, *P. Bruener, T. Grehl*, ION-TOF GmbH, Germany, *R. ter Veen*, Tascon GmbH, Germany, *H. Brongersma*, ION-TOF GmbH, Tascon GmbH, Germany

Based on the unique electronic properties and high chemical stability of graphene, a number of exciting applications are generated. However, since graphene films are only one or a few atomic layers thick, chemical analysis is hampered by the much larger information depth of most techniques. This leaves a gap which can be filled by Low Energy Ion Scattering (LEIS). LEIS is known for its extreme surface sensitivity. It gives a quantitative analysis of the outer atomic layer of a surface as well as in-depth information [1]. It can thus be used to selectively analyze a graphene layer. In general [2], the atomic sensitivities are independent of the neighboring atoms (no matrix effects), so a quantitative elemental characterization is feasible. Since carbon is a common contamination in surface analysis, it is crucial to distinguish such contamination from the carbon in graphene.

In an earlier LEIS study [3] of carbon segregation in C-doped rhenium it was shown that by varying the temperature the carbon species can be altered reversibly into a carbidic or graphitic state. The graphitic layer was one or a few atoms thick (depending on the temperature). A strong matrix effect was observed in LEIS, which is believed to be typical for graphene. The sp-band of graphitic carbon is so wide that it extends to the He 1s level. This gives a strong quasi-resonance neutralization of the scattered He⁺ ions.

In the present study graphene layers were grown on copper foils and then transferred to an oxidized Si wafer [4]. The samples were analyzed with a dedicated high-sensitivity LEIS instrument. As reference for a carbon containing material without a wide conduction band, silicon rubber was chosen.

It was found that the neutralization of He⁺ by graphene is much stronger than by the rubber. For example, the neutralization of 1.5 keV He⁺ ions is almost 100x more effective for graphene.

It will be shown how it is possible to quantify the amount of carbon contamination (hydrocarbons, alcohols, etc.) on graphene using the differences in neutralization. Thus LEIS cannot only be used to verify the closure of the graphene layer, its thickness and purity, but also to check its (wide band) electronic structure.

[1] H.H. Brongersma, *Low-Energy Ion Scattering*, in: Characterization of Materials, J. Wiley & Sons (2012). DOI: 10.1002/0471266965.com144

[2] H.H. Brongersma, M. Draxler, M. de Ridder, P. Bauer, *Surf. Sci. Repts* **62** (2007) 63-109.

[3] L.C.A. van den Oetelaar, S.N. Mikhailov, H.H. Brongersma, *Nucl. Instrum. Meth. B* **85** (1994) 420.

[4] Xuesong Li et al., *Science* **324**, 1312 (2009). DOI: 10.1126/science.1171245

5:00pm **GR+AS+NS+SP+SS-TuA10 Nanoscale Tribological Characteristics of Epitaxial Graphene on SiC: The Effect of Hydrogen Intercalation.** *S. Kwon, J. Ko*, KAIST, Republic of Korea, *G.E. Yang, W. Kim, KRIS, Republic of Korea, Y. Kim, J.Y. Park*, KAIST, Republic of Korea

Atomically-thin graphene is the ideal model system for studying nanoscale friction due to its intrinsic two-dimensional anisotropy. Here, we report the reduced nanoscale friction of epitaxial graphene on SiC, investigated with conductive-probe atomic force microscopy/friction force microscopy in ultra-high vacuum. The measured friction on a buffer layer was found to be 1/8 of that on a monolayer of epitaxial graphene. Conductive probe atomic force microscopy revealed a lower conductance on the buffer layer, compared to monolayer graphene. We associate this difference in friction with the difference in total lateral stiffness. Because bending stiffness is associated with flexural phonons in two-dimensional systems, nanoscale frictional energy should primarily dissipate through damping with the softest phonons. We investigated the influence of hydrogen intercalation on the nanoscale friction. We found that the friction decreased significantly after hydrogen intercalation, which is related to loose contact between the graphene and the substrate that results in a lower bending stiffness.

Ions at Aqueous Interfaces Focus Topic

Room: 201 B - Session IA+BA-TuA

Ions and Biomolecules at Aqueous Interfaces

Moderator: J.M. Gibbs-Davis, University of Alberta, Canada

2:00pm **IA+BA-TuA1 Selective Adsorption of Ions to Aqueous Interfaces and its Effects on Evaporation Rates.** *R.J. Saykally*, University of California, Berkeley **INVITED**

By exploiting the strong charge-transfer-to-solvent (CTTS) resonances of selected anions in aqueous electrolytes, their interfacial adsorption properties are measured by UV-SHG spectroscopy. Temperature and concentration dependences are determined, with the goal of establishing a complete molecular description of selective ion adsorption. A study of thiocyanate reveals that its strong adsorption is driven by hydration forces and impeded by a novel entropy effect. A study of nitrite indicates adsorption as an ion pair with sodium. Evaporation rates are measured by combining liquid microjet technology and Raman thermometry. The relationship between surface propensities of ions and evaporation rates is investigated. A detailed molecular mechanism for both selective ion adsorption and aqueous evaporation is explored.

2:40pm **IA+BA-TuA3 Exploring Ion Interactions at Aqueous Interfaces.** *P.S. Cremer*, Penn State University **INVITED**

We have employed a combination of surface specific techniques to interrogate the interactions of ions with self-assembled monolayers and proteins at aqueous interfaces. The results provide direct insight into ion pairing interactions. In particular, I will discuss the behavior of cations and anions as they relate to the Hofmeister series, which is a rank ordering of the efficacy of these species to influence the physical behavior of colloidal and interfacial systems in solution. The TiO₂/water, quartz/water, alkyl chain/water, and air/water interfaces were each explored.

Experiments consisted of a combination of sum frequency generation and thermodynamic measurements. Ion specific effects at these interfaces were found to be determined by several factors. These include the sign and magnitude of the surface potential, ion pairing effects, as well as the presence of polar and nonpolar interfacial moieties. At negatively charged, hydrophilic surfaces, we found that Na⁺ adsorption and double layer formation was modulated by the nature of the counterion in solution. For the anions, it was found that SCN⁻ was less depleted at the interface compared with better hydrated anions such as Cl⁻. The same ordering was observed for the anions whether this interface was relatively hydrophobic or hydrophilic. Changing the sign of the charge at the interface also led to a similar Hofmeister ordering. Curiously, the ordering for cations at these aqueous interfaces was found to be more sensitive to the specific surface chemistry. Moreover, at negatively charged hydrophilic surfaces, the smallest and best hydrated cations were mostly favored over more poorly hydrated cations. By contrast, well hydrated cations were repelled from more apolar surfaces. Li⁺ displayed somewhat anomalous behavior. All of these results will be discussed with an eye toward a broader model for interfacial partitioning of ions in aqueous solutions.

4:00pm **IA+BA-TuA7 Revealing the Dynamics of Lipid Composition in Phospholipid Bilayers by Sum-Frequency Vibrational Spectroscopy.** *J. Conboy*, University of Utah **INVITED**

A membrane, only two molecules thick, surrounds all cells and is responsible for controlling the passage of materials in and out of the cell in a selective manner. Our current understanding of the structure and dynamics of cellular membranes emerged in the early 1970's. However, there is still much we do not know about this seemingly simple "shell" which makes life as we know it possible. For example, the location of the negatively charged phosphatidylserine (PS) headgroup lipids has drastic effects on cell function, ranging from coagulation to apoptosis. The localization of PS in one leaflet of the membrane is governed by a complex interplay between kinetic and thermodynamic factors. However, the kinetics of PS exchange has not been studied in detail. Using methods of classical surface chemistry coupled with nonlinear optical methods, we have developed a novel analytical approach, using sum-frequency vibrational spectroscopy (SFVS), to selectively probe lipid compositional asymmetry in a planar supported lipid bilayer. SFVS has been used to measure both the compositional asymmetry and kinetics of PS and phosphatidylcholine (PC) lipid flip-flop in planar supported lipid bilayers composed of 1,2-distearoyl-sn-glycero-3-phosphocholine (DSPC) and 1,2-dihexadecanoyl-sn-glycero-3-phospho-L-serine (DPPS). The transition state thermodynamics of DSPC and DPPS were measured at biologically relevant compositions ranging from 10 to 35 % DPPS. The activation thermodynamics of DSPC and DPPS and their impact on compositional asymmetry will be discussed in detail.

4:40pm **IA+BA-TuA9 Characterization of Protein Secondary Structures at Interfaces Using Chiral Sum Frequency Generation.** *C.Y. Yan*, Yale University **INVITED**

Characterization of protein secondary structures using vibrational spectroscopy is challenging because of strong vibrational background from water and spectral overlapping of vibrational signatures for various secondary structures. Here, we present chiral vibrational spectra of amide I and N-H stretch of protein backbone in various secondary structures at interfaces obtained by chiral sum frequency generation (SFG) spectroscopy. These spectra show unique signatures for parallel beta-sheets, anti-parallel beta-sheets, alpha-helices, 3-10 helices, and random-coils. Because the chiral SFG spectra are muted to achiral solvent, the N-H stretch can be detected at zero water background. Thus, the N-H stretch frequency can probe local H-bond environments, providing an additional signature to distinguish secondary structures. This allows chiral SFG to resolve secondary structures at interfaces, such as alpha-helices versus 3-10 helices, which elude conventional vibrational methods and circular dichroism spectroscopy. Hence, chiral SFG holds promises to address fundamental and engineering problems in biomedical and material sciences.

5:20pm **IA+BA-TuA11 Order Matters – Detecting Non-Isotropic Structures in Complex Biological Samples.** *P. Koelsch*, University of Washington

Order is omnipresent in biological systems in various forms and on almost all length-scales. Here we discuss how to use order as a (label-free) contrast mechanism in microscopy or selectivity criteria in surface spectroscopy to detect and analyze non-isotropic arrangements in complex *in vitro* scenarios. Examples are fibrillar structures that can be visualized within tissue via second-harmonic-generation (SHG) microscopy or detected on surfaces via vibrational sum-frequency-generation (SFG) spectroscopy. The contrast mechanism in SHG microscopy is order and similarly is order (and chirality) the selectivity criteria when it comes to SFG spectroscopic measurements on surfaces. Examples to be discussed are fibrillar arrangements within the extracellular matrix of adherent cells on substrates or within cancerous tissue samples.

5:40pm **IA+BA-TuA12 Aqueous Solution Chemistry Studied by Soft X-ray Absorption Spectroscopy.** *T.Z. Regier*, Canadian Light Source, Canada, *C. Phillips, D. Peak, R. Green, A. Moewes, J. Tse*, University of Saskatchewan, Canada, *A. Achkar, D. Hawthorn*, University of Waterloo, Canada

X-ray absorption spectroscopy is a sensitive probe of transition metal coordination and bonding environment. Excitation of 2p electrons into unoccupied 3d orbitals allows for determination of crystal field parameters and ligand field strength. Measurement of the x-ray absorption spectra of Cu and Fe ions in solutions was performed using a continuous flow cell on the SGM beamline at the Canadian Light Source. Fluorescence yields and inverse partial fluorescence yields were measured using a multielement silicon drift detector. The interaction between Cu ions and various organic ligands was studied and the difference between the absorption and fluorescence intensities was examined for aqueous ferrous and ferric solutions.

Magnetic Interfaces and Nanostructures

Room: 202 A - Session MI+AS+NS+SP-TuA

Advanced Probes in Magnetic Imaging and Characterization

Moderator: H. Ohldag, SLAC National Accelerator Laboratory

2:00pm MI+AS+NS+SP-TuA1 Electron Correlation Spectroscopy on Magnetic Surfaces, F.O. Schumann, Max-Planck Institut für Mikrostrukturphysik, Germany **INVITED**

The emergence of long range magnetic order is a consequence of the mutual interaction between electrons. A key postulate of quantum mechanics is the requirement of the wave function to be antisymmetric upon exchange. This inclusion leads to a modification of the Coulomb interaction which is termed exchange interaction. For ferromagnets this leads to parallel spins while for antiferromagnets an antiparallel alignment is preferred.

Electron pair emission from surfaces is an advanced tool to study the relation between electrons which goes beyond the capabilities of single electron spectroscopy e.g. photoemission. The power of this approach will be demonstrated by two case studies on Fe and NiO films. The angular distributions of emitted electron pairs reveal a region of reduced intensity which can be traced back to the exchange-correlation hole.[1] This concept was introduced by Wigner, Seitz and Slater more than 75 years ago. It plays an important role in modern solid state theory. We performed experiments on Fe films to unravel the spin-dependence of the exchange-correlation hole. We find that the contribution of exchange is more extended than the Coulomb contribution as suggested by Slater.[2]

The investigation of correlation effects in solids is an active field of research. In this context metal oxides like NiO are usually termed "highly correlated", because the material properties are decisively determined by the electron-electron interaction. The very existence of a finite electron pair emission requires a finite electron-electron interaction. This immediately leads to the question whether the intensity level provides insight into the correlation strength. A theoretical study of pair emission from a strongly correlated system modeled by the Hubbard Hamiltonian gives an affirmative answer.[3] We tested this conjecture and find that the coincidence intensity for NiO is roughly an order of magnitude larger compared to the Ag(100) substrate.[4] This also holds for the comparison of other transition metals and their oxide phases. This result suggests that the electron correlation strength is accessible via the pair emission intensity.

Our results demonstrate that electron pair emission is a unique tool to unravel the nature of the electron correlation in solids.

[1] F.O. Schumann, C. Winkler, and J. Kirschner, Phys. Rev. Lett. **98**, 257604 (2007).

[2] F.O. Schumann, C. Winkler, J. Kirschner, F. Giebels, H. Gollisch, and R. Feder, Phys. Rev. Lett. **104**, 087602 (2010).

[3] B.D. Napitu and J. Berakdar, Phys. Rev. B **81**, 195108 (2010).

[4] F.O. Schumann, L. Behnke, C.H. Li, J. Kirschner, Y. Pavlyukh, and J. Berakdar, Phys. Rev. B **86**, 035131 (2012)

4:00pm MI+AS+NS+SP-TuA7 Probing Magnetic Interfaces and Nanostructures with Hard X-ray and Standing-Wave Excited Photoemission Spectroscopy, A.X. Gray, SLAC National Accelerator Laboratory, J. Minar, Ludwig Maximilian University, Germany, S. Ueda, National Institute for Materials Science, Japan, L. Plucinski, Forschungszentrum Jülich GmbH, Germany, A. Bostwick, E. Rotenberg, Advanced Light Source, C.M. Schneider, Forschungszentrum Jülich GmbH, Germany, H. Ebert, Ludwig Maximilian University, Germany, K. Kobayashi, National Institute for Materials Science, Japan, C.S. Fadley, University of California, Davis **INVITED**

The ever-growing demand for miniaturization and increased speeds of next-generation electronic devices has taken science to the quantum frontier in which emergent phenomena at the nanoscale require a clear differentiation between surface, bulk and interface properties. Thus, for many technologically-promising novel materials electronic structure varies dramatically as a function of depth and proximity to other materials. Therefore, novel depth-resolved characterization techniques are required to disentangle these rich electronic behaviors, including magnetism and spin. In this talk I will describe several new directions in the field of x-ray photoelectron spectroscopy, made possible with the advent of third-generation synchrotron light sources and recent advances in the fields of x-ray optics and photoelectron detection. I will present several case-studies wherein hard x-ray photoelectron spectroscopy (HAXPES) in the multi-keV regime is used to probe the bulk properties of complex thin-film materials and heterojunctions, which would be otherwise impossible to investigate

using conventional soft x-ray XPS. I will present the first results of hard x-ray angle-resolved photoemission measurements (HARPES), at excitation energies of 3 and 6 keV. Compared to the traditional ARPES, carried out in the UPS regime (20-100 eV), this new technique enables one to probe on average 10-40 times deeper into the bulk. Finally, I will introduce a new photoemission technique (SWARPES) which combines soft x-ray ARPES with standing-wave (SW) excited photoelectron spectroscopy, wherein the intensity profile of the exciting x-ray radiation is tailored within the sample in order to provide a depth-selective probe of the electronic structure of buried layers and interfaces.

4:40pm MI+AS+NS+SP-TuA9 Imaging Magnetization Dynamics on its Genuine Time Scale, G. Meier, University of Hamburg, Germany **INVITED**

A variety of excellent microscopies that provide magnetic contrast on the nanoscale matured to powerful tools. Today's scanning-probe techniques feature ultimate spin resolution, namely imaging of the magnetization of single atoms [1]. The temporal resolution of optical and x-ray methods reaches down to femtoseconds. It is intriguing to have spatial and time resolution simultaneously. The relevant frequency scale for ferromagnets is given by the ferromagnetic resonance which lies in the GHz range. Thus the required time resolution is in the sub-nanosecond regime. Magnetic microscopies available at synchrotron sources enable real-time imaging and provide lateral resolution down to the nanometer scale [2,3].

We investigate the switching criteria of nanometer-scaled magnetic vortices in micron-sized Permalloy squares. The vortices are excited by high frequency magnetic fields. Continuous core reversal is demonstrated for a wide range of frequencies and amplitudes of excitation by ferromagnetic absorption spectroscopy and for selected frequencies and amplitudes with time-resolved scanning x-ray microscopy. The boundary of this switching regime is derived from the Thiele equation when a critical velocity of $v_{crit} \approx 250$ m/s is considered [4].

Complexity created by periodic arrangement of well-understood building blocks plays an important role in biochemistry, photonics, and nanoelectronics. The periodic arrangement of atoms or molecules as basis determines the physical and even the chemical properties of crystals. With the flexibility of nanometer-precise electron-beam lithography we engineer magnetic interactions yielding two-dimensional magnonic crystals that benefit from the magnetic vortex core as crystal basis. Using scanning transmission x-ray microscopy at the MAXYMUS beamline at BESSY II in Berlin, Germany we image the magnonic crystal dynamics. We observe self-organized vortex core state formation by adiabatic reduction of high frequency magnetic field excitation [5]. The experimental results are described analytically by coupled Thiele equations of motion and are compared to micromagnetic simulations.

Financial support of the Deutsche Forschungsgemeinschaft via Sonderforschungsbereich 668 and Graduiertenkolleg 1286 is gratefully acknowledged. This work has been supported by the excellence cluster "The Hamburg Centre for Ultrafast Imaging" of the Deutsche Forschungsgemeinschaft.

References

- [1] A. Khajetoorians et al., Science **332**, 1062 (2011)
- [2] P. Fischer and C. Fadley, Nanotechnol. Rev. **1**, 5 (2012)
- [3] A. Vogel et al., Phys. Rev. Lett. **106**, 137201 (2011)
- [4] M. Martens et al., Phys. Rev. B **87**, 054426 (2013)
- [5] C. Adolff et al., submitted

5:20pm MI+AS+NS+SP-TuA11 Towards Magnetic 3dim X-ray Imaging, P. Fischer, M.-Y. Im, W. Chao, E.H. Anderson, Lawrence Berkeley National Laboratory

Nanomagnetism research focused on a fundamental understanding and controlling spins on a nanoscale. As the next step beyond the nanoscale, mesoscale phenomena have been recognized[1], since those add essential parameters to meet future challenges in terms of speed, size and energy efficiency of spin driven devices. The development and application of multidimensional visualization techniques, such as tomographic magnetic imaging will be crucial to achieve mesoscale goals.

Magnetic soft X-ray microscopy is a unique analytical technique combining X-ray magnetic circular dichroism (X-MCD) as element specific magnetic contrast mechanism with high spatial and temporal resolution [2]. Three-dimensional (3D) soft X-ray tomography using Fresnel zone plate based full field and scanning transmission soft x-ray microscopies have been developed and are routinely used at various synchrotron sources but mostly for biological imaging [3]. However, magnetic X-ray tomography is of large interest to understand e.g. interfaces in magnetic multilayers, the inner structure of magnetic nanocrystals, nanowires or the functionality of artificial 3D magnetic nanostructures.

There are several approaches for 3D X-ray imaging, such as utilizing standing waves in Bragg conditions [3], X-ray imaging in reflection geometry [4], X-ray ptychography [5] or computational reconstruction of projection X-ray images [6]. We have developed and implemented at the full-field soft X-ray microscopy beamline 6.1.2 at the ALS in Berkeley CA a new stage for tomography, which allows recording an angular series (up to 360 deg) of high precision 2D projection images. Applying state-of-the-art reconstruction algorithms it is possible to retrieve the full 3D structure. We will present recent results on prototype systems, such as glass capillaries coated with magnetic films. We will also discuss the complementarity of magnetic X-ray tomography to other 3D imaging approaches such as electron microscopy [7].

This work was supported by the Director, Office of Science, Office of Basic Energy Sciences, Materials Sciences and Engineering Division, of the U.S. Dept. of Energy under Contract No. DE-AC02-05-CH11231.

- [1] BESAC report: From Quanta to the Continuum: Opportunities for Mesoscale Science (2012), http://science.energy.gov/~media/bes/pdf/reports/files/OFMS_rpt.pdf
- [2] P. Fischer, Materials Science & Engineering R72 81 (2011)
- [3] A.X. Gray, et al. Appl Phys Lett 97, 062503 (2010)
- [4] G. Denbeaux, et al. IPAP Conf. Series 7 pp.375-386 (2006)
- [5] D.Y. Parkinson et al, J. Struct. Biology 177 259 (2012)
- [6] M. Dierolf et al. Nature 467, 436 (2010)
- [7] C. Phatak et al, Ultramicroscopy 109 264 (2009)

5:40pm **MI+AS+NS+SP-TuA12 Direct Visualization of Magnetoelectric Domains**, W. Wu, Y. Geng, X. Wang, S-W. Cheong, Rutgers University, C.J. Fennie, Cornell University, M. Mostovoy, University of Groningen, Netherlands

The coupling between the magnetic and electric dipoles in multiferroic and magnetoelectric materials holds promise of conceptually new electronic devices¹⁻⁴. The device miniaturization calls for development of local probes of the magnetoelectric response, in particular because such response is strongly affected by defects in magnetic and ferroelectric orders. For example, multiferroic hexagonal rare earth manganites exhibit a dense network of boundaries between six degenerate states of their crystal lattice, which are locked to both ferroelectric and magnetic domain walls. Here we present the first application of a newly-developed Magnetoelectric Force Microscopy (MeFM), which combines Magnetic Force Microscopy (MFM) with *in-situ* modulating high electric fields. This technique allowed us to directly image the magnetoelectric response of the domain patterns in hexagonal manganites. We found that this response changes sign at each structural domain wall. This MeFM result is corroborated by a symmetry analysis and a phenomenological model derived from microscopies and first-principles calculations⁵, providing compelling evidence for a lattice-mediated magnetoelectric coupling. Furthermore, our measurements reveal a diverging magnetoelectric response near a critical point below 2 K originating from enhanced critical fluctuations and the high sensitivity of spin ordering to applied electric and magnetic fields. The direct visualization of magnetoelectric domains at mesoscopic scales opens up explorations of emergent phenomena in multifunctional materials with multiple coupled orders.

1. Eerenstein, W., Mathur, N. D., and Scott, J. F., *Nature* **442** (7104), 759 (2006).
2. Ramesh, R. and Spaldin, N. A., *Nature Materials* **6** (1), 21 (2007).
3. Cheong, S. W. and Mostovoy, M., *Nat. Mater.* **6** (1), 13 (2007).
4. Spaldin, N. A., Cheong, S.-W., and Ramesh, R., *Physics Today* (2010).
5. Das, H., Wysocki, A. L., and Fennie, C. J., *arXiv:1302.1099* (2013).

Manufacturing Science and Technology

Room: 202 B - Session MS+AS+EL+EM+PS+TF-TuA

Manufacturing Challenges of Nanoscale Patterning

Moderator: E.B. Svedberg, The National Academies

2:00pm **MS+AS+EL+EM+PS+TF-TuA1 Alphabet-Based Template Design Rules - A Key Enabler for a Manufacturable DSA Technology**, H. Yi, H.-S.P. Wong, Stanford University **INVITED**

Block copolymer DSA is a result of spontaneous microphase separation of block copolymer films, forming periodic microdomains including cylinders, spheres, and lamellae. Among all the various self-assembled structures, cylinder patterns have attracted specific interest due to their great potential in patterning electrical contacts in Integrated Circuits (ICs). Due to the

random distribution of electrical contacts in layouts as well as the continuous scaling of IC circuits, patterning contacts has become increasingly challenging for traditional optical lithography. Due to the advantage of low cost and sub-20 nm feature sizes, block copolymer directed self-assembly (DSA) is a promising candidate for next generation device fabrication.

Traditionally, the study of DSA has been focused on achieving long range order and a periodic pattern in large area. Chemoepitaxy approaches including using chemical patterns of preferential affinity on the substrate surface or controlling pattern formations by tuning annealing conditions have been investigated and developed. They can improve the long range order self-assembly quality and lower the defect density over large areas. In order to use DSA to pattern the randomly distributed contacts in IC layouts, we adopt physical (topographical) templates to form irregularly distributed cylindrical patterns. Topographical templates use strong physical confinements in lateral directions to alter the natural symmetry of block copolymer and guide the formation of DSA patterns. Previously we have demonstrated that for the first time the self-assembled features can be almost arbitrarily placed as required by circuit fabrication and not limited to regular patterns, by combining templates of different types on one wafer. These various templates are akin to the letters of an alphabet and these letters can be composed to form the desired contact hole patterns for circuit layouts. The capability of arbitrary placement is demonstrated in industry-relevant circuits such as static-random-access-memory (SRAM) cells and standard logic gate libraries at a dimension that is the state-of-the-art semiconductor technology today [1]. To enable introduction of DSA into manufacturing we developed a general template design strategy that relates the DSA material properties to the target technology node requirements. This design strategy is experimentally demonstrated for DSA contact hole patterning for half adders at the 14 nm and 10 nm nodes [2].

Reference:

- [1] H. Yi et al. Adv. Mater, 2012.
- [2] H. Yi et al. SPIE, 2013.

2:40pm **MS+AS+EL+EM+PS+TF-TuA3 Characterizing the Sensitivity of Block Copolymer Directed Self-Assembly Processes to Material and Process Variations**, C. Henderson, A. Peters, R. Lawson, P. Ludovice, Georgia Institute of Technology

Future scaling of integrated circuits (IC) is in jeopardy due to a number of challenges related to both future material and process requirements that are needed to allow for fabrication of sub-20 nm IC devices. One of the most critical challenges is that of developing patterning technologies that can allow for formation of sub-20 nm patterned structures in a fast and economically viable manner. Due to difficulties with alternative technologies, techniques that can extend the use of current 193 nm optical lithography in a cost effective manner would be very attractive. Directed Self-Assembly (DSA) using block copolymers to perform pitch subdivision of lithographically generated primary patterns is one such promising technology. In this technique, a lithographic method is first used to define a topographic or chemical template pattern on a surface. This surface is then coated with a block copolymer that is further processed to induce microphase separation. The presence of the topographic or chemical patterns on the surface aligns, registers, and provides long range order to the formed block copolymer patterns. This microphase separation-based patterning process utilizes the propensity of the block copolymer to naturally form nanometer scale patterns whose size are dictated by the polymer block molecular weight.

The overarching goal of our work has been to develop both new block copolymers that can enable sub-20nm DSA patterning and to develop the experimental and modeling tools needed to understand the limits of such processes. In this paper, we will review our recent systematic studies of block copolymer DSA processes using state-of-the-art molecular dynamics simulations. The aim of these studies has been to identify the important material and process factors that affect the DSA process and to quantify the sensitivity of the DSA process to these factors. For example, the influence of polymer block molecular weight control and polydispersity on patterning have been rigorously quantified. Furthermore, processing factors such as guiding pattern mis-sizing and low level surface topography in the guiding pattern and their effect on DSA patterning have been studied in detail. Studies have also been performed via simulation using thermodynamic integration methods to calculate the free energy of defects in such DSA systems and the sensitivity of such defect free energies to important material and process parameters. We will review the outcomes of these studies to illustrate what the important material and process challenges will be in adapting block copolymer DSA methods into a manufacturable technology.

3:00pm **MS+AS+EL+EM+PS+TF-TuA4 DSA Patterning for sub-40 nm Pitch Features**, *I.C. Estrada-Raygoza, C. Liu, Y. Yin, J. Abdullah*, IBM Albany Nanotech Center, *S. Mignot*, GLOBALFOUNDRIES U.S. Inc., *B.G. Morris, M.E. Colburn*, IBM Albany Nanotech Center, *V. Rastogi, N. Mohanti, A. Raley, A. Ko*, TEL Technology Center, America, LLC

As the semiconductor industry targets sub-40 nm pitch features, there will be a necessity for new patterning techniques which allow for the extension beyond single ArF-immersion patterning capability of 38 half pitch features. To meet today's aggressive design requirements, double patterning techniques, such as Pitch Splitting (PS) Lithography and Sidewall Image Transfer (SIT), have been widely used. Below 38 nm pitch design the industry has looked toward Extreme Ultraviolet (EUV), Double Sidewall Image Transfer (SIT2) and Directed Self-Assembly (DSA) as strong emerging candidates. A major component to the success of the DSA technique is the development of effective etch processes. This talk targets to discuss the challenges and innovations of the plasma etch process on sub-40 nm pitch features produced by DSA chemo and grapho-epitaxy guiding patterns. Each DSA scheme presents different challenges, depending of the aspect ratio, density of the patterns and etch stack materials, but in general, the parameters that have been studied are selectivity to both masking and etched materials, across wafer profile uniformity, critical dimension (CD) uniformity and line-edge/line-width roughness (LER/LWR). This work was performed by the Research Alliance Teams at Albany IBM Research and Development Facilities.

4:40pm **MS+AS+EL+EM+PS+TF-TuA9 Advanced Gate Patterning Techniques for 14nm Node and Beyond**, *F.L. Lie, R. Jung, Y. Yin, A. Banik, S. Kanakasabapathy, J.C. Arnold, S. Seo, B. Haran*, IBM Corporation, *Y. Moon, L. Jang, S. Bentley*, GLOBALFOUNDRIES U.S. Inc., *H. Kang, D. Bae*, Samsung Electronics Co., *A. Metz, C. Cole, K. Ito, S. Voronin, A. Ko, A. Ranjan, K. Kumar*, TEL Technology Center, America, LLC

For advanced CMOS nodes, traditional patterning processes are challenged to meet the technology needs of certain key levels. For example, conventional 193nm immersion lithography is not able to resolve features below 40nm half pitch with a single exposure without severe design rule restrictions. Until further wavelength scaling through Extreme Ultraviolet (EUV) has matured, the industry's attention is focused on advanced patterning schemes such as Pitch Splitting (PS) Lithography and Sidewall Image Transfer (SIT). In PS, a pattern is defined by two lithography exposure with a certain coordinate shift between the two exposures. PS can be achieved through either litho-etch-litho-etch or litho-litho-etch. In SIT, a pattern is defined by creating a mandrel in one lithography exposure, depositing a conformal spacer film on the mandrel, and pulling out the mandrel, resulting in two standing spacer for the pattern frequency doubling. This work evaluated the advantages and technical challenges of PS and SIT patterning schemes for line-space application. We will focus on CD uniformity improvement, line edge/line width roughness control, pitch walk control, and the extendability of each technique. RIE challenges common to double patterning such as through pitch etch bias will also be discussed.

This work was performed by the Research Alliance Teams at various IBM Research and Development Facilities and in joint development with TEL Technology Center, America, LLC

5:00pm **MS+AS+EL+EM+PS+TF-TuA10 High Throughput Electrospinning of Ceramic Nanofibers**, *S. Sood, P. Gouma*, State University of New York at Stony Brook (Stony Brook University)

High yield nanomanufacturing has been the focus of greater attention due to the emerging importance of functional nanomaterials. Electrospinning is a nanomanufacturing process that faces challenges as far as its scalability is concerned. Even the existing high-throughput electrospinning systems are limited to processing thin layers of polymer nanofibrous mats. Nanofibrous ceramics have rarely been studied with respect to their electrospinning processing. On the other hand, electrospun nanowires of ceramics are key to nanotechnology and nanomedicine applications (e.g. electrospun MoO₃ nanowires have been used as ammonia sensors for application in non-invasive diagnostics [1]). In this study, the scalable synthesis of ceramic oxide nanomats by the multi-jet design that we developed and built and which enables very high yield of ceramic nanofibers is discussed. As a scaled up approach to traditional needle electrospinning [2], up to 24 jets are spun simultaneously using similar processing parameters as a traditional needle set up. Due to a thin metallic disc design, with tiny holes drilled at the disc, the electric field is evenly distributed to all jets. Continuous replenishment of the source disk at higher flow rates allows for high yields of nanofibers.

P. Gouma, K. Kalyanasundaram, and A. Bishop, "Electrospun Single Crystal MoO₃ Nanowires for Bio-Chem sensing probes", Journal of

Materials Research, Nanowires and Nanotubes special issue, 21(11), pp. 2904-2910, 2006.

S. Sood, S. Divya, P. Gouma, "High throughput electrospinning of 3D nano fibrous mats". Journal of Nanoengineering and Nanomanufacturing. Accepted Publication. In Print, 2013.

5:20pm **MS+AS+EL+EM+PS+TF-TuA11 Manufacture and Characterization of Silver and Copper Nanorods Produced via Forcespun Nylon 6 Nanofibers Templates**, *D.M. Mihut, K. Lozano, W. Zhao*, The University of Texas Pan American

The Nylon 6 nanofibers are produced using the forcespinning method and further on coated with metallic thin films using the thermal evaporation equipment. The Nylon 6 nanofibers are used as templates in order to obtain silver and copper nanorods where the polymer is removed after high temperature calcination from the metallic coated structures. The metallic nanorods morphology and electrical behavior are characterized using the scanning electron microscopy, scanning transmission electron microscopy (SEM, STEM), energy dispersive X-ray spectroscopy (EDX) and electrical measurements. This method of fabrication offers the ability to obtain controlled ultrafine size metallic nanorods.

Nanometer-scale Science and Technology Room: 203 B - Session NS+AS+EN+SS-TuA

Nanoscale Catalysis and Surface Chemistry

Moderator: J. Nogami, University of Toronto, Canada

2:00pm **NS+AS+EN+SS-TuA1 Scanning Tunneling Microscopy Analysis of Molybdenum Sulfide Structures**, *C.S. Wang, W. Lu*, University of California, Riverside

Already commonly used industrially in the hydrodesulfurization process, MoS₂ is a promising catalyst that can exist as a stable monolayer film, much like graphene. This poster describes a method for growing MoS₂ monolayers on a copper substrate at a relatively low temperature and under mild sulfurization conditions through the use of thiophenol. Additionally, this procedure yields other molybdenum sulfide structures, including Mo₂S₃ films and Mo₆S₆ nanowires. To analyze the catalytic activity of these structures, we titrate using anthraquinone and formic acid as test molecules, thus determining the relative affinities for adsorbate interactions.

2:20pm **NS+AS+EN+SS-TuA2 Nanostructures of Au on Pd₃Fe(111) and Their Role in Electrochemical Oxygen Reduction**, *X. Yang*, Princeton University, *J. Hu, R.Q. Wu*, University of California, Irvine, *B. Koel*, Princeton University

Sluggish kinetics of the electrochemical reduction of molecular oxygen (ORR) in polymer electrolyte membrane fuel cells (PEM-FCs) requires a continued search for advanced catalysts. Our work combines synthesis and characterization of well-defined, multimetallic model catalysts in UHV and direct evaluation of their catalytic performance in an electrochemical cell accessible by a multifunctional ambient-pressure antechamber and sample transfer system. Surface structures and electronic properties [#] [#] of these electrocatalysts were characterized by LEED, AES, LEIS, XPS, and STM. We found previously that Pd₃Fe(111) annealed at high temperature is highly active for ORR, but may lose activity due to slow dissolution of Fe. To address this issue, we developed a method to improve the stability while maintaining high activity of the catalyst involving a submonolayer amount of Au at the surface. While bulk gold is catalytically inactive, the surface prepared by submonolayer amounts of Au deposited on a Pd/Pd₃Fe(111) substrate was discovered to be highly active for the ORR, more active than Pt(111). The activity was strongly dependent on the Au coverage, with the highest activity found near 0.5-monolayer Au. The high activity and durability of this Au-modified Pd₃Fe(111) surface is associated with formation of 2D nanostructures at the step edges at the surface, small nano-islands, which were revealed by STM. DFT calculations of O₂ adsorption on these 2D Au islands and of Au diffusion barriers to the top of Au terraces with and without O and O₂ were used to provide a more thorough understanding of the origin of the high catalytic activity of this system. We found that adsorbed oxygen atoms can enhance diffusion in Au protrusions, resulting in a 3D Au nanostructure that can lead to O₂ dissociation. In this work, we not only discovered a potential candidate for non-Pt catalysts to replace Pt cathode catalysts for the ORR, but also identified conditions for activating gold for use in practical electrocatalysts.

B.E.K. acknowledges support by NSF Grant No. CHE-1129417. R.W. acknowledges support by NSF Grant No. CHE-0802913 and computing time at XSEDE.

2:40pm **NS+AS+EN+SS-TuA3 Oxygen Adsorption and Dissociation on Ag(110) and Au-Ag(110) Surfaces**, *M. Schmid, J. Klobas, R.J. Madix, C.M. Friend*, Harvard University

We have investigated the adsorption and dissociation of molecular oxygen on thin film Au-Ag alloys because of their potential for selective oxidation catalysis. Our work is motivated by an interest in fundamental understanding of nanoporous gold catalysts, which are a dilute Au-Ag alloy, typically containing 3-10% Ag; nevertheless, this dilute alloy is active for O₂ dissociation and for selective oxidation of CO and primary alcohols. We selected pure Ag(110) as a starting material because it strongly binds O₂ by donation of substantial charge density into the O=O bond. This species undergoes competing desorption of O₂ and dissociation to O atoms on the surface at ~170 K. We have investigated the effects of alloying with gold on the bonding and activity of O₂ using a combination of Scanning Tunneling Microscopy (STM), Temperature Programmed Reaction Spectroscopy (TPRS), and X-ray Photoelectron Spectroscopy (XPS). There is a rich morphology that develops on the surface depending on the Au content, and a substantially different reactivity towards oxygen as compared to pure Ag and Au substrates. Further investigations of selective oxidation processes on this surface are also planned.

3:00pm **NS+AS+EN+SS-TuA4 Trends in Reactivity of Organic Compounds on a Model Gold Catalyst**, *J.C. Rodriguez-Reyes*, Universidad de Ingeniería y Tecnología, UTEC, Peru, *C.M. Friend, R.J. Madix*, Harvard University

The perception that gold is chemically inert has faded in the light of the unique properties of this metal as an environmentally friendly catalyst. To date, the contrast between the large number of gold-based catalysts reported and the very limited number of probe molecules employed to test their efficiency has hindered the possibility of using gold beyond the laboratory scale and into an industrial scale as a practical catalyst. In this presentation, our efforts towards the elucidation of a reactivity scale for various organic molecules (including alcohols, amines, hydrocarbons, carboxylic acids and thiols) are discussed. The use of controlled (ultra-high vacuum) conditions allows for an assessment of the intrinsic behavior of gold as catalyst, with the mass spectrometric detection of desorbing products allowing both the identification of reactive species and the extraction of thermodynamics and kinetics parameters of importance for future studies. The results confirm that the first steps in gold-mediated reactions involve the dehydrogenation of a probe molecule and, therefore, there is a relationship between the gas-phase acidity of a molecule and its reactivity on gold. However, this relationship is modified by several factors including 1) the strength of the interaction of a functional group with the gold surface, 2) the presence of aromatic groups and long alkyl chains within a molecule, and 3) the presence of substituents able to modify the first two factors. The elucidation of a reactivity scale is anticipated to expand and direct the range of gold-mediated catalytic conversions.

4:40pm **NS+AS+EN+SS-TuA9 Single Atom Alloys as a Strategy for Selective Heterogeneous Hydrogenations**, *E.C.H. Sykes*, Tufts University

Hydrogenation reactions are central to the petrochemical, fine chemical, pharmaceutical, and food industries and are of increasing interest in energy production and storage technologies. Typical heterogeneous catalysts often involve noble metals and alloys based on platinum, palladium, rhodium and ruthenium. While these metals are active at modest temperature and pressure, they are not always completely selective and are expensive. We have demonstrated that single palladium atoms can convert the otherwise catalytically inert surface of an inexpensive metal into an ultrasensitive catalyst. We used high resolution imaging to characterize the active sites and temperature programmed reaction spectroscopy to probe the chemistry. The mechanism involves facile dissociation of molecular hydrogen at individual palladium atoms followed by spillover onto the copper surface, where ultrasensitive catalysis occurs by virtue of weak binding. The reaction selectivity is in fact much higher than that measured on palladium alone, illustrating the unique synergy of the system.

5:00pm **NS+AS+EN+SS-TuA10 Thin Film Synthesis and Oxidation: From C₆₀ and W Precursors to Intercalation, Nanospheres and Carbides**, *J. McClimon, P. Reinke*, University of Virginia

Tungsten carbide has garnered considerable interest for its catalytic activity and it is uniquely suited as an electrode/catalyst in microbial fuel cells. One of the bottlenecks in the use of W-carbide materials is their susceptibility to oxidation and concomitant loss in activity, albeit some surface processes benefit from the presence of surface oxide. The challenge is to establish the optimum oxide-carbide composition for a specific reaction and to stabilize this surface.

The W-carbide layers are synthesized from C₆₀ and W, which are deposited MgO(001) by electron and beam and thermal evaporation. This affords control of film composition, and lead us to an in-depth study of W-C₆₀

interaction, and discovery of a unique carbide nanosphere phase. The experiments are performed in UHV, and film growth and reactivity are studied with Scanning Tunneling Microscopy (STM) and Spectroscopy (STS), which delivers conductivity maps illustrating the progression of oxidation and variation in surface electronic structure.

Our work includes study of C₆₀-W interaction and carbide thin film growth using deposition of C₆₀ on W and vice versa, and co-deposition between 300-1000 K, and the study of oxidation of carbide films with a C/W ratio between 50/50 and 75/50, spanning the range from the line compound WC to carbon enriched films. The W/C 75/50 films have distinct graphite layers at the surface, while the W/C 60/40 surface presents mostly graphene patches. We will discuss the formation of carbide films, which retain some granularity defined by the C₆₀ molecule, in terms of thermodynamic and kinetic limitations. The progression of oxidation on the bare carbide surface, and competition with graphite/graphene etching define the overall reactivity. Conductivity maps yield a nano-scale view of the oxidation reaction as a function of temperature and p(O₂), which will be presented in the framework of a preliminary model.

We focus the discussion of W-C₆₀ interaction on the two major discoveries: (1) the intercalation of W into the C₆₀ matrix, and (2) the formation of carbide nanospheres.

The deposition of W on C₆₀ leads to the intercalation of W, and the cessation of molecule rotation due to the formation of W-C₆₀ complexes. The formation of exohedrally W-doped C₆₀ is described by a competition between complex formation and W-cluster growth. The inverted experiment, where C₆₀ is deposited on a W-surface and annealed at 600 (700)K leads to formation of carbide nanospheres, which are highly ordered with a narrow size distribution centered at 1.3 nm diameter. These nanospheres are metallic, and presumably form through the reaction between W and C₆₀, which acts as scaffold.

5:20pm **NS+AS+EN+SS-TuA11 Selective Growth of TiO₂ Nanotubes on Titanium Foil by Two Step Anodization Method**, *Z. Razavi Hesabi, N. Semenikhin, A. Bonecutter, F. Alamgir, E.M. Vogel*, Georgia Institute of Technology, *N.K. Allam*, The American University in Cairo, Egypt

One dimensional nanostructures such as nanotubes exhibit unique properties because of their special geometry, high surface area and high aspect ratio paving the way for transferring ions, electrons, photons, gases, and fluids. The photoactivity of TiO₂ nanotubes (TNTs) makes them promising candidates for use in solar cells, water splitting, sensors, tissue engineering, and drug delivery. Among different synthesis methods, particular interest has been given to the anodic growth of TiO₂ nanotubes on Ti foil as it leads to the formation of an array of closely packed vertically aligned tubes. However, in many applications such as MEMS and NEMS, it is desired to have TiO₂ nanotubes with a desired pattern on substrate of interest. Pittrof et al. [1] patterned grown TiO₂ nanotubes after the nanotube layer has been created. Recently, Chappanda et al. [2] deposited Ti on silicon substrate and grew patterned TiO₂ nanotubes. Selective growth of TiO₂ nanotubes on titanium foil has not ever been reported. In the present study, TiO₂ nanotubes were grown selectively on patterned titanium foil by anodization at room temperature. Conventional photolithography as well as laser patterning of scotch tape were used to copy desirable pattern on titanium foil. Anodization was done in an organic electrolyte containing ammonium fluoride for 5 to 60 minutes. SEM images show successful growth of TiO₂ nanotubes in open areas.

1. A. Pittrof et al., *Acta Biomaterialia* **7** (2011)

2. K. N. Chappanda et al., *Nanotechnology* **23** (2012)

5:40pm **NS+AS+EN+SS-TuA12 Process to Functionalize Polyaniline for Avidin-Biotin Biosensing Applications**, *T. Shaw*, Clark Atlanta University, *M.D. Williams*, Clark Atlanta University, *J. Reed*, Clark Atlanta University

Biotin-avidin technology is a widely explored interaction in bioscience. Biotin's affinity for the protein avidin, makes it ideal for protein and nucleic acid detection or purification methods. This strong interaction if often used in pretargeting strategies for cancer treatment. In most cases a probe molecule (antibody) is connected to a marker molecule (fluorophore or nanoparticle) through the biotin-avidin bridge. Biotinylated nanoparticles can play a role in improving this interaction and creating an electronic or optical detection method. Polyaniline is a polymer which can be easily functionalized to be specific for various biomolecules and has ideal sensor characteristics. In this study we will design a process to functionalize polyaniline with biotin to create a biotin-avidin biosensor. We began with a 2-aminophenol which is a hydroxyl substituted aniline monomer. This monomer undergoes polymerization to yield 2-hydroxy polyaniline. The polymer's hydroxyl group was functionalized by Steglich esterification which refluxes a carboxylic acid with an alcohol. This esterification drives the reaction and dehydrates the products shifting the equilibrium towards the product. In this reaction DCC (dicyclohexylcarbodiimide) activates the

carboxylic acid of biotin to further reaction and DMAP (4-dimethylaminopyridine) acts as the acyl transfer catalyst. The biotinylated polyaniline derivative was characterized using FT-IR spectroscopy, ¹H NMR spectroscopy, UV-VIS spectroscopy, and Scanning Electron Microscopy.

Plasma Science and Technology Room: 102 B - Session PS1-TuA

Plasma Diagnostics, Sensors and Control

Moderator: N.St.J. Braithwaite, The Open University, UK

2:00pm **PS1-TuA1 Real Time Feedback Control of Photoresist ashing in an Electron Cyclotron Resonance Plasma Chamber**, *B.J. Keville, C. Gaman, Y. Zhang, A.M. Holohan, S. Daniels, M.M. Turner*, Dublin City University, Ireland

Present practice in plasma-assisted semiconductor manufacturing specifies recipes in terms of inputs such as gas flow rates, power and pressure. However, ostensibly identical chambers running identical recipes may produce very different results. Extensive ‘chamber matching’, i.e. initial iterative, empirical tuning of the process recipe, which entails time-consuming, ex situ statistical analysis of process metrics, is required to ensure acceptable results. Once matched, chambers are run ‘open loop’ and are thus sensitive to disturbances such as actuator drift, wall seasoning and substrate loading, which may have deleterious effects on process metrics such as etch depth, uniformity, anisotropy and selectivity. An alternative approach, which may reduce sensitivity to disturbances of the plasma, would be to specify a recipe in terms of quantities such as active species densities, and to regulate these in real time by adjusting the inputs with a suitable multivariable control algorithm. Multivariable closed loop control of an SF₆/O₂/Ar plasma in an Electron Cyclotron Resonance (ECR) etcher is the focus of a major research program in the National Centre for Plasma Science and Technology (NCPST) in Dublin City University (DCU). As an intermediate step, real time control of an O₂/Ar plasma used for photoresist ashing has been implemented. More specifically, the oxygen 844 and argon 750 line intensities measured by optical emission spectrometry have been regulated by adjusting microwave power and oxygen flow rate in real time by means of a control algorithm. In order to test the efficacy of the control algorithm in reducing the sensitivity of the ashing rate to wall conditions, a wall disturbance was simulated by fluorinating the chamber walls using an SF₆ plasma prior to O₂/Ar ashing. In the open loop case, wall fluorination results in a large increase in the 844 line intensity, which is indicative of an increase in the density of atomic oxygen, and a concomitant increase in the ash rate is observed. However, under closed loop control, the average ash rate is unaffected by wall fluorination, thus demonstrating effective attenuation of the disturbance. Although this may not necessarily be of intrinsic interest – one generally ashes to end point without being overly concerned about tight control of the ash rate – it indicates that real time control of a plasma application – ashing, in this case – may be achieved indirectly by control of active species in the plasma. This has important implications for applications where tight control of dimensions is critical – etch profile, for example.

2:20pm **PS1-TuA2 Diagnostics of Inductively-Coupled Plasmas in Hydrogen Bromide : Bromine Atom and Electron Densities**, *J.-P. Booth, N. Sirse, P. Chabert, M. Foucher*, LPP-CNRS, Ecole Polytechnique, France

Inductively-coupled plasmas (ICP) containing hydrogen bromide are widely used for conductor-etch applications, often using mixtures with Cl₂ and O₂. However, very few scientific studies (whether theoretical, simulation or experimental) have been made of HBr plasmas [1, 2] . We have studied pure HBr plasmas in an industrial-scale ICP (diameter 550mm, height 100mm, excited at 13.56MHz by a 4-turn planar coil) adapted for advanced diagnostic techniques.

We have demonstrated the first detection of Br atoms by two-photon laser-induced fluorescence (TALIF). The relative variation of Br atoms was determined as a function of HBr pressure (5-90 mTorr) and RF power (20-500W). The Br density increases with pressure over this range, although the dissociation fraction (Br density divided by the total gas pressure) decreases with pressure. The Br density also increases with RF power up to about 100W, but then progressively saturates. This saturation could be attributed to complete dissociation of the HBr, or to the onset of gas heating leading to gas density reduction. Measurements of the Br decay rate in the afterglow of a pulsed plasma allow the surface reaction coefficient of Br to be estimated.

The electron density was determined using a microwave hairpin resonator [3] . With HBr pressure the electron density peaks at 10 mTorr, and it

increases with RF power. This behaviour is very similar to that observed in pure Cl₂, although the densities are about a factor 2 lower in HBr. The radial profiles of electron density are centre-peaked at low pressure, but at pressures above 50 mTorr the maximum is off-axis, peaking under the RF antenna coils.

This work was supported by Agence Nationale de la Recherche project INCLINE (ANR-09 BLAN 0019) and by the Applied Materials University Research Partnership Program. NS acknowledges the Ecole Polytechnique for a post-doctoral grant.

[1] Cunge G., Fouchier M., Brihoum M., et al., *J Phys D Appl Phys*, 2011, **44**,

[2] Sasic O., Dujko S., Makabe T., et al., *Chemical Physics*, 2012, **398**, 154-159

[3] Piejak R., Al-Khuzee J. and Braithwaite N. S., *Plasma Sources Sci. Technol.*, 2005, **14**, 734

2:40pm **PS1-TuA3 Ion Energy Distribution Measurements at the Substrate Location in Continuous-wave and Pulse Modulated Plasmas**, *D. Gahan, P. Scullin, D. O'Sullivan, M.B. Hopkins*, Impedans Ltd., Ireland
INVITED

Low pressure plasmas are used extensively in modern industry to process substrates. Both etching and deposition processes are controlled by energetic ion bombardment of the substrate. As substrates become larger, feature sizes smaller and film properties more complex there is an increasing demand for accurate monitoring and control of the ion energy distribution. Ion energy measurements have been reported in the literature for many decades. The two most common instruments that have been used are the quadrupole mass spectrometer and the retarding field energy analyzer (RFEA). The simplicity of the RFEA has led to its widespread use in various applications. The focus of this talk will be on the recent advances in RFEA technology for ion energy measurements in different types of plasma processes. In most cases the substrate is processed using an electrical bias. The substrate holder may be powered with radio-frequency (RF), pulsed-RF, direct current (DC) or pulsed-DC electrical signals. This complicates the use of RFEAs for ion energy measurement at the substrate location. The presence of the RFEA must not disturb the electrical bias and the electrical bias must not impair the RFEA data acquisition. Here we present an electrically filtered RFEA technology that allows for deployment at the biased substrate location. The filtering allows the RFEA sensor to float at the electrical bias voltage. We will discuss a number of filter configurations that cover the many frequencies, waveform shapes and bias levels that can be encountered. We also discuss a special configuration that permits time resolved measurements of the ion energy at the biased substrates under certain conditions. A number of novel extensions to the standard technology will also be presented. Spatially resolved measurements of the ion energy at multiple locations (simultaneously) across 300mm and 450mm substrate holders, used for plasma etching, will be presented. This RFEA design gives important information about the spatial uniformity of the plasma process under various plasma conditions. An embodiment of the RFEA design which can be used to determine the ion angular distribution is presented. This technique uses an additional orifice with variable aspect ratio to scan the angular distribution of the incoming ions across the energy range. Measurement of the ion angular distribution is particularly important near the edge of substrates, where yield is often poor due to sheath curvature in this region. Finally, the first results of a novel RFEA configuration that enables discrimination of the different ion species in the bombarding energy distribution will be presented and discussed.

4:00pm **PS1-TuA7 Time-resolved Optical and Electrical Diagnostics of Pulsed Plasmas Etching Processes**, *G. Cunge, M. Brihoum, M. Darnon, E. Despiau-Pujo, A. Davydova, M. Haass, R. Blanc*, Cnrs/ujf/ Cea - Ltm, France, *N.St.J. Braithwaite*, The Open University, UK, *D. Gahan*, Impedans Ltd, Ireland, *S. Banna, AMAT, O. Joubert, N. Sadeghi*, Cnrs/ujf/ Cea - Ltm, France
INVITED

Pulsed ICP plasmas are a promising solution to several issues related to IC fabrication. Recent results are indicating that pulsing the ICP power and/or the RF biasing power allows to increase the etch selectivity, to reduce plasma induced damages and to minimize ARDE. However, the reasons for these improvements remain unclear. In particular, the impact of plasma pulsing on the radicals flux, on the ion flux and on the ion energy in electronegative plasmas has not been studied in details. We have used a capacitively-coupled planar ion flux probe to monitor the time variations of the ions flux in an industrial ICP etch reactor from AMAT. At the same time, the time-averaged IEDF are measured by an RFA analyzer. Finally the radicals' densities are measured with a 10 μs time resolution by combining several diagnostic techniques: small polyatomic molecules are detected by broad band absorption spectroscopy (BBAS) in UV with highly stable LEDs as a light source, large closed shell molecules are detected by BBAS in the VUV and atomic species are monitored by threshold ionization

modulated beam mass spectrometry. We discuss in detail the experimental set-up that we have designed to carry out such time resolved measurements. Results are presented for various electronegative (Cl₂, BCl₃, SiCl₄, SF₆, CF₄) plasmas, that are synchronously pulsed (ICP and rf bias pulsed in phase) or in which only the rf bias power is pulsed. We will show that the duty cycle is the predominant parameter to control the ion flux, the ion energy and the plasma chemistry. These results are in good agreement with global models of electronegative Cl₂ plasmas. In particular, we show that in chlorine based plasmas, both the radical densities and the ion flux drops dramatically when the duty cycle is reduced. As a result for the same rf biasing power, the ion energy is much higher in pulsed plasma than in a CW plasma. By contrast, in a pulsed ICP without bias power the time averaged ion energy is bimodal, with the predominance of a very low energy peak (1-5 eV). Therefore, plasma pulsing allows to reach new domains of ion energy and radical fluxes, thereby extending the operating range of ICP reactor to that of CCP plasmas and downstream plasmas. This has interesting applications for ultrathin layer etching, ranging from graphene cleaning to metal gate and nitride spacer etching processes. Finally, both radical and ions flux oscillations in the kHz range are observed by time resolved diagnostics in pulsed plasmas. We will show that they are due to the propagation of acoustic waves in the reactor, with potentially interesting effect on the process uniformity.

4:40pm PS1-TuA9 Optical Emission and Langmuir Probe Diagnostics of CH₃F-O₂ Inductively Coupled Plasmas. E. Karakas, V.M. Donnelly, D.J. Economou, University of Houston

CH₃F plasmas, mostly with added O₂, are used in selective Si₃N₄ etching over Si or SiO₂. Despite their use, fundamental plasma studies in these gas mixtures are very scarce. In this work, optical and Langmuir probe diagnostics were employed to study inductively couple plasmas in CH₃F/O₂ gas mixtures. In 50% CH₃F/50% O₂ plasmas, the electron density increased linearly ($0.7 \times 10^{11} \rightarrow 2.7 \times 10^{11} \text{ cm}^{-3}$) as power was increased 150-400W at 10 mTorr, but only weakly ($1.7 \times 10^{11} \rightarrow 2.7 \times 10^{11} \text{ cm}^{-3}$) within the pressure range of 10-40 mTorr at 300W. The effective electron temperature representing the high energy tail of bi-Maxwellian EEPFs was nearly independent of power and pressure. The gas temperature increased from 400-900 K as a function of inductive mode power between 75 and 400 W at 10 mTorr. For a constant feed gas flow rate and composition, the absolute H, F and O atom densities, estimated by optical emission rare gas actinometry, increased linearly with power. The feedstock gas was highly dissociated and most of the fluorine and oxygen was contained in reaction products HF, CO, CO₂, H₂O and OH. Reaction mechanisms were proposed to explain the observed behavior of the relative density of F and HF vs. power and pressure. Measured relative densities as a function of O₂ addition to CH₃F/O₂ changed abruptly for H, O, and particularly F atoms (factor of 4) at 48% O₂. A corresponding transition was also observed in electron density, effective electron temperature and gas temperature, as well as in C, CF and CH optical emission. These abrupt transitions were attributed to the reactor wall reactivity, changing from a polymer-coated surface to a polymer-free surface, and vice-versa, as the O₂ content in the feed gas crossed 48%.

*Work supported by Lam Research Corp.

5:00pm PS1-TuA10 Non-contact Measurements of Substrate-Temperature by Frequency-Domain Low-Coherence Interferometry. T. Tsutsumi, Nagoya University, Japan, T. Ohta, Meijo University, Japan, K. Ishikawa, K. Takada, H. Kondo, M. Sekine, M. Hori, Nagoya University, Japan, M. Ito, Meijo University, Japan

High-precision, rapid temperature measurements on wafers such as silicon, sapphire, etc. are required for plasma processing. A method is demonstrated here that uses a frequency-domain low-coherence interferometer (FD-LCI).

In order to realize the plasma processing with high precision, the temperature control of wafer or chamber-wall is one of important factors. Especially the wafer temperature influences on etched profile and etching rates. Moreover, a spatial distribution of radicals in gas phase or plasma-surface interactions on the surface are affected by temperatures of the chamber-wall. Therefore, the precisely non-contact temperature-measurement technology is needed for the fabrication of electric devices.

In this study, we have developed a highly precise and non-contact temperature monitor using a Fourier domain low-coherence interferometer (FD-LCI) and a super luminescent diode (SLD: center wavelength: 1330 nm, spectral width: 37.6 nm) as a low coherence light source. The FD-LCI can measure an optical path length of wafer on the basis of auto-correlation signals, which are generated by interferences between the light reflected from the front and back surfaces, and analyzed by the inverse Fourier transform of spectral interferogram. Since the optical path is changed by thermal expansion and refractive-index, the wafer-temperatures can be analyzed. By this method, we have successfully achieved to estimate a temperature of various commercial wafers such as silicon, sapphire during plasma processes.

5:20pm PS1-TuA11 Detection of Vacuum Ultraviolet in Argon-containing Inductively Coupled Plasmas. S.B. Radovanov, Varian Semiconductor Equipment, Silicon Systems Group, Applied Materials Inc., H.M. Persing, Applied Materials Inc. Varian Semiconductor Equipment, Silicon Systems Group, Applied Materials Inc., J.B. Boffard, C.L. Culver, S. Wang, C.C. Lin, A.E. Wendt, University of Wisconsin-Madison

The spectrum of light emitted by plasmas used in materials processing applications includes vacuum ultraviolet (VUV) photons, which are known to play a significant role in critical surface reactions under certain process conditions. Monitoring of the surface flux of VUV photons emitted from the inductively coupled plasma (ICP) and its dependence on discharge parameters is thus highly desirable. However, non-invasive direct detection of VUV photons is generally difficult, as few window materials transmit in the VUV. We thus examine the argon resonance level atom concentration as a prospective proxy for VUV emission, as 106.7 and 104.8 nm VUV photons are produced in the spontaneous radiative decay from Ar resonance levels to the ground state. Argon resonance level concentrations have been measured in the center of an ICP with a planar spiral induction antenna through "branching fraction" analysis of the visible optical emission (OES) spectrum.* Measured concentrations are subsequently used as inputs to a VUV radiation transport model developed to determine the corresponding axial VUV photon flux. Reabsorption of VUV photons by ground state atoms is significant even at pressures as low as 1 mTorr, and a proper accounting in the model thus requires accurate representation of the gas temperature. Model results based on the resonance level concentrations over a range of pressures (1-25 mTorr) and RF (13.56 MHz) power (up to 1000 W) compare favorably with the axial VUV photon flux sampled directly through a small hole at the center of an electrode located opposite the ICP antenna. Absolute VUV fluxes were measured with a windowless aluminum oxide photodiode sensitive to wavelengths below ~110 nm. Additionally, relative VUV fluxes were also obtained using a sodium salicylate coating on the inside of a side port vacuum window. The sodium salicylate converts VUV into a detectable visible light signal through fluorescence, and, unlike the photodiode, is sensitive in the wavelength range of H atom VUV emissions (122 nm). Preliminary results suggest that a combination of photodiode and sodium salicylate signals thus allows discrimination between hydrogen and argon contributions to the VUV flux in Ar/H₂ gas mixtures.

Support from NSF grant PHY-1068670 and the Applied Materials Corporation is gratefully acknowledged.

*Plasma Sources Sci. Technol. **18** (2009) 035017.

5:40pm PS1-TuA12 Time-resolved In Situ Quantum Cascade Laser Diagnostics Applied to Transient Molecular Plasmas. S. Welzel, Eindhoven University of Technology, Netherlands, F. Brehmer, Eindhoven University of Technology, Netherlands; AFS GmbH, Germany, M.C.M. van de Sanden, Eindhoven University of Technology; DIFFER, Netherlands, R. Engeln, Eindhoven University of Technology, Netherlands

The detection of stable and transient species along with gas temperature measurements remains a challenge for the majority of molecular (complex) plasmas. Considering particularly plasmas at atmospheric pressure with inherently small discharge volumes, (optical) access to the active plasma is often hampered. On the other hand, phase- and time-resolved *in-situ* measurements are a valuable tool (i) to establish heavy particle temperatures, (ii) to identify excitation mechanisms in the plasma, (iii) to discriminate gas phase and surface reactions as they occur on significantly different time scales, and (iv) to unravel particularly temperature-dependent reaction mechanisms. Modern mid-infrared laser sources, known as quantum cascade lasers (QCLs), provide a means for highly time-resolved absorption spectroscopy in the molecular "fingerprint" region. The time-resolution can be thereby as good as a few tens of nanoseconds. Although continuous-wave QCLs are increasingly being applied for conventional monitoring purposes, pulsed distributed feedback QCLs are perfectly suited for diagnostic studies on transient plasmas.

CO₂ containing dielectric barrier discharges (DBDs) operated in the mid-frequency (kHz) range were studied by means of *in-situ* time-resolved QCL absorption spectroscopy. Special beam shaping optics was used to accommodate the laser beam diameter to typical gap widths of ~1 mm in single and multiple-pass configuration. Different synchronization schemes were applied to achieve phase-resolved measurements during individual AC cycles as well as to monitor molecular absorption signals during pulsed discharge operation. Mixing ratios of CO in its electronic and vibrational ground state were of the order of a few percent and thus confirmed earlier *ex-situ* studies of the effluent. More importantly, the concentrations levels were changing only slowly in time, i.e. of the order of the residence time. A direct CO₂-to-CO dissociation through electron impact appears very unlikely under these conditions. The kinetics of low-lying ro-vibrational states of CO₂ along with the evolution of the CO concentration were studied on a sub-millisecond time-scale to (i) establish (rotational) gas

temperatures, and (ii) to estimate the influence of vibrational-vibrational and vibrational-translational energy transfer processes.

Plasma Science and Technology Room: 104 C - Session PS2-TuA

Deep Etch Processes for Vias, Trenches and MEMS

Moderator: A. Agarwal, Applied Materials Inc.

2:00pm **PS2-TuA1 Plasma Deep Etching of Silicon, Titanium and Gallium Nitride for Microtechnology.** *R. Dussart*, GREMI CNRS/Université d'Orléans, France **INVITED**

Plasma deep etching is a necessary process step for the fabrication of most of microelectronic components, especially in power microelectronics and in MEMS technology. Although several etching processes were developed for silicon, deep etching of other materials such as titanium and gallium nitride is also of interest for innovative microdevices.

In this paper, deep etching of silicon using the so-called cryogenic process will be presented and compared with other processes. We will show and explain our characterization experiments by mass spectrometry, ellipsometry and in-situ XPS, which were carried out to investigate physical and chemical mechanisms involved in the silicon cryoetching process. These results were also used to develop the so-called STiGer cryoetching process, which will be also introduced. This particular process offers some advantages of the standard cryogenic process and is more robust.

Titanium deep etching using both fluorine and chlorine based chemistries was investigated by our group. Titanium is particularly interesting for bio MEMS applications. We developed the so-called APETi process to avoid roughness and increase the etch rate. With this process, we were able to etch up to 300 μm deep ring structures.

Finally, we will also show our process capabilities for deep GaN etching. For this material, a chlorine based chemistry is necessary to form volatile species. Measurements by Langmuir probe, by optical emission spectroscopy and by mass spectrometry were carried out to characterize the plasma in the different tested conditions. We will show that the material of the coverplate can play an important role in the etching mechanisms. Three types of defect were observed: « cavity » defects, « columnar » defects and the « white GaN ». The appearance mechanisms of these defects were studied and will be explained. Although we showed, by Transmission Electron Microscopy analysis, that the two first types of defect are clearly linked to intrinsic defects of the material itself, it is still possible to avoid their appearance during the etching.

2:40pm **PS2-TuA3 Simulation of Bosch Process Deep Silicon Etching - A Multi-scale Approach.** *A. Pateau, A. Rhallabi, M.C. Fernandez*, Université de Nantes, France, *M. Boufnichel, F. Roqueta*, STMicroelectronics Tours SAS

Deep etching of silicon is a very used process in the semi-conductor industry. Such high aspect ratio etchings can be obtained using Bosch process. This plasma process consists in alternating many etching and deposition steps at high etch rate (few seconds each). Two gases are mainly used: SF_6 for the etching step and C_4F_8 for the passivation.

To predict the silicon etch profile through the mask, we have developed an etching Bosch simulator. It permits to investigate plasma/surface interactions for both the deposition and the etching step. Based on a multi-scale approach the silicon etching simulator is composed of three modules: plasma, sheath and surface models. This allows to predict the etch profile as a function of the operating conditions (pressure, power, gas flow rates, time steps for deposition and etching cycles).

The plasma module is based on a global kinetic model which allows the calculation of the neutral and ion densities and fluxes as well as the electronic temperature and density using the machine parameter of the ICP reactor as input parameters.

The sheath module is based on the Monte-Carlo technique to calculate the Ion Angular and Energetic Distribution Functions (IAEDFs). Positive ion fluxes and electronic temperature and density calculated from de plasma module are used as input parameters in the evaluation of average sheath thickness and proportion of each considered positive ion.

The fluxes of neutral and ion species calculated from the plasma module and the IAEDF calculated from the sheath model are introduced as input parameters in the surface model. This model is based on the cellular Monte-Carlo method to describe the 2D etch profile through the mask and evaluate the etch rate evolution with time. Both the silicon substrate and the mask are discretized in uniform cells named super-sites. Each super-site contains a number of real atomic silicon sites which depends on the cell size. In our

etching simulations, 1nm by 1nm cells are considered. This allows a good compromise between computing time and spatial resolution. The particles used are atomic fluorine for the reactive etching, atomic carbon, CF and CF_2 for the passivation polymer growth, and positive ions for the sputtering.

The simulation results show the influence of the input Bosch process parameters (RF powers, pressure, gas flow rates, time steps for deposition and etching cycles and bias voltage) on the etching processes like the etch rate and the deep etch profile evolution with etch time. Such an etching simulation tool can contribute to improve the deep silicon etching processes in terms of anisotropy and scalloping reduction.

3:00pm **PS2-TuA4 Titanium Deep Etching for Medical Applications.** *T. Tillocher, P. Lefaucheur*, GREMI CNRS/Université d'Orléans, France, *B. Boutaud*, Sorin Crm, France, *R. Dussart*, GREMI CNRS/Université d'Orléans, France

Titanium is a biocompatible material which is of great interest in the biomedical field and more especially for bio-MEMS, which have emerged recently. The fabrication of Ti platform based devices is adapted from micromachining techniques derived from microelectronics technologies. Most of the research work reported in the literature relies on a Cl_2/Ar chemistry to deep etch titanium, using masks like TiO_2 , Ni or even SU8. Processes are performed at room temperature of the substrate with typical etch rates close to 1 $\mu\text{m}/\text{min}$. They provide rather smooth surfaces.

We report here the performances of deep titanium etching with SF_6 and Cl_2 based chemistries in an ICP etching tool. Samples are pieces of a patterned titanium wafer glued on a silicon carrier wafer. Mask is a 5 μm thick nickel layer.

Our preliminary results have shown that either a SF_6 plasma or a Cl_2/Ar plasma can be used separately to etch titanium. A SF_6 plasma helps to reach etch rates as high as 4 $\mu\text{m}/\text{min}$ at higher pressures (a few Pa) but profiles are isotropic. A Cl_2/Ar chemistry at low pressure (almost 1 Pa) is preferred to get vertical sidewalls but the etch rate is reduced. This is why we proposed to mix these two chemistries to increase the etch rate while keeping vertical sidewalls. However, this process is not reproducible in our conditions since, in most cases, it leads to a very high roughness and a drop in the etch rate.

This non-reproducibility may be due to the use of a silicon carrier wafer: SiCl_x species, coming from the etch by-products of the silicon wafer, may participate to one passivation layer growth on the Ti surface as well as the chamber walls. This induces a micro-masking effect which subsequently leads to the formation of an unwanted roughness.

A SF_6 plasma appears to be a good way to remove (at least partially) the layer inducing roughness, which hence leads to a better reproducibility. As the process presented previously already contains SF_6 , but is not reproducible, this means that the balance between etching and deposition becomes favorable to deposition from one process to another. This is why both the SF_6 injection and the whole process have been optimized to overcome this issue. It was then possible to etch 300 μm of Ti within nearly 3h30. Consequently, 300 μm have been etched with an average etch rate of 1.4 $\mu\text{m}/\text{min}$. The slope is slightly negative on the first half of the ring and tends to be more isotropic on the second half. A significant undercut can also be observed (a few 10s of μm). The estimated selectivity to the nickel mask is 35. The process has been repeated many times and the profiles were always reproducible, which is a significant improvement.

4:00pm **PS2-TuA7 Selection of non-PFC Chemistries for Through-Silicon via Etch.** *K. Chen, T. Kim, J.P. Chang*, University of California at Los Angeles

The continued extension of Moore's Law, which dictates that the density of integrated circuit (IC) devices doubles every two years, presents formidable challenges in realizing complex and three-dimensional interconnect structures. Through-silicon-via etch (TSV) is at the core of 3-D integration, which yields higher performance than conventional 2-D wiring systems, and has been demonstrated with Bosch deep reactive ion etching (DRIE), cryogenic DRIE, laser drilling, and wet etching. In order to achieve the desired and continuously increasing aspect ratio (AR) of the features required for the device integration, DRIE is the preferred method for TSV for the attainable vertical sidewalls and high AR. Unfortunately, the primary gases used in DRIE for TSV are SF_6 and perfluorocarbon (PFC) gases, which are high global warming potential (GWP) greenhouse gases, making their increased usage undesirable.

In this work, a thermodynamics approach is used to assess and select other viable etch chemistries for TSV that are non-PFC, in an effort to reduce the usage of PFC gases and minimize their environmental impact. A systematic study is based on the assessment of various halogen-based gases, utilizing a volatility diagram where the partial pressure of the etch products are determined as a function of the etchant pressure at various temperatures. This functional relation can be determined from the thermodynamic equilibrium between the surface and gas-phase species, by considering the

standard Gibbs free energy and the equilibrium constant. A careful control of the etchant partial pressure near the isomolar point, where the partial pressure of the volatile species would reach that of the equilibrium value, has been shown to be necessary to control the formation of volatile species. Amongst various candidates, NF_3 , a non-PFC gas with greenhouse rating only 1ppt in atmosphere, appears promising. From the thermodynamics analysis, the generation of fluorine atom from SF_6 and NF_3 is comparable, however, NF_3 is much more able to form more SiF_4 , the volatile etch product, than SF_6 . While this is promising, another significant reaction product from NF_3 is Si_3N_4 , which is non-volatile. The addition of a second chemical such as O_2 can necessitate its subsequent removal, through the formation of volatile products such as nitrogen oxides (N_xO_y). In addition, NF_3 is also capable of removing SiO_2 which is unintentionally formed during reaction with O_2 . This work will highlight the analysis to design a NF_3/O_2 process (sequential exposure versus mixture) that yields comparable etch results compared to that achieved by SF_6 , thereby offering a viable alternate for TSV etch.

4:20pm PS2-TuA8 Sub-22nm Node Mask Patterning for Deep Silicon Trench Etch. *B. Avasarala, S. Lefevre, V. Chakrapani, H. Haga, H. Matsumoto, Q. Yang, Y. Chiba, A. Ko, A. Selino Jr., K. Kumar, P. Biolsi,* TEL Technology Center, America, LLC, *F.L. Lie, I. Saraf, S. Kanakasabapathy,* IBM

The fabrication of ever smaller feature sizes at increasing density has driven more stringent requirements on photolithographic processes and patterning schemes. In the sub-22nm DRAM technology, the fabrication of deep silicon memory cells at aspect ratios greater than 30 ratio (depth > 3 μm : critical dimension < 0.1 μm) is enabled by a complex mask assembly. In this paper, we will discuss RIE process development for patterning the mask assembly as well as the high aspect ratio Si trenches. The mask assembly comprises of a photo resist layer, silicon anti-reflective coating, organic planarizing layer, oxide layer, and nitride layer deposited on top of a Silicon-on-Insulator (SOI) substrate. Achieving a vertical profile along the trench and across different material types of the mask, while still maintaining the required critical dimension, are major challenges in patterning the mask assembly. The verticality of the different layers in the mask assembly is key because it subsequently affects the deep Si etch process. We will discuss the challenges in achieving high aspect ratio Si trench and key process parameters that influence its dimensions. The paper also describes the capabilities of a commercially available Capacitively Coupled Plasma reactor to meet the requirements of these advanced complex film stacks.

This work was performed by the Research and Development team at TEL Technology Center America in joint development with IBM Semiconductor Research and Development teams in Albany & Hopewell Junction, NY

4:40pm PS2-TuA9 Reduction of Aspect Ratio Dependency in Silicon Trench Etch. *R.L. Bates,* University of Texas at Dallas

The etch rate of deep features in silicon, such as trenches and vias, can vary significantly with the changing aspect ratio of the feature. Developing a better understanding of the complex volumetric and surface chemistry as well as the etching mechanisms controlling the Aspect Ratio Dependent Etch-rate (ARDE) continues to present research opportunities. Recall that ARDE is generally characterized by small AR features etching at faster rates than large AR features. The main causes of ARDE include Knudsen transport of neutrals into and out of the features as well as ion loss to the walls due to angular spread in the velocity distribution function and differential charging of insulating microstructures [1]. This work focuses on using a continuous plasma process utilizing a gas mixture of $\text{SF}_6/\text{C}_4\text{F}_8/\text{Ar}$ to produce trenches of varying widths and depths. The experimental results were obtained using a Plasma-Therm Versaline processing system. Experiments were performed to show that the etch rate of low AR features can be reduced through the deposition of a passivation layer and thereby allow larger AR features to catch up. It is also possible to invert the ARDE in certain circumstances. We will present the insights we have gained into the ARDE process and the solution we have tested. [1] R. Gottschö & C. Jurgensen, *J. Vac. Sci. Tech. B*, **10**, 2133, (1992). This research was supported through SRC Award: 2012-VJ-2261. The authors thank the staff of the UTD clean room (G. Pollack, S. Riekens, B. Albert) for their gracious assistance in processing and measuring these samples.

5:20pm PS2-TuA11 Reaction Mechanism at the Sidewall of Through Si via (TSV) Etching by $\text{SF}_6/\text{O}_2/\text{SiF}_4$ Plasma. *I. Sakai,* Toshiba Corporation, Japan, *S. Amasaki, T. Takeuchi, K. Takeda, K. Ishikawa, H. Kondo, M. Sekine,* Nagoya University, Japan, *N. Sakurai, H. Hayashi, T. Ohiwa,* Toshiba Corporation, Japan, *M. Hori,* Nagoya University, Japan
One of the key processes for 3D-LSI is through Si via (TSV) formation. To form large and deep via holes through a wafer, a high etch rate deep etching technology using SF_6/O_2 plasma has been developed [1]. It is reported that

high etch rate is obtained by supplying a large amount of F radicals and the etch profile is controlled by forming an oxidized layer as an etch inhibitor on the TSV sidewall. In the previous study [2] we showed that, as a result of competitive reaction of etching and oxidation by F and O radicals, even at the 75% O_2 addition condition Si etching by F radicals is confirmed. In this study, we aimed to suppress sidewall etching further by addition of SiF_4 gas to SF_6/O_2 plasma, and examined its effect by analysis of the Si surface.

Si wafer was placed on a grounded electrode at the remote plasma region of a 500 MHz ultra high frequency plasma reactor. We assumed that the influence of ions was small and radical reaction dominant, so we could simulate the reactions at the sidewall of TSV RIE. The process gas chemistries used were SF_6/O_2 and $\text{SF}_6/\text{O}_2/\text{SiF}_4$.

The Si etch depth dependence of $\text{SF}_6/\text{O}_2/\text{SiF}_4$ plasma etching on O_2 gas addition was examined. The etch depth of Si after 3 min plasma exposure was measured from SEM images of 8 μm square hole patterned Si wafers with 2 μm thick SiO_2 as mask. Etch depth decreased with SiF_4 addition. For example, at 75% O_2 addition, the etch depth was about 0.25 μm , 1/4 of that without SiF_4 addition. Etch depth dependence on O_2 flow rate ratio showed a decreasing trend, same as that without SiF_4 addition. At 90% O_2 gas flow rate ratio, etching stopped and thickness increased, indicating that film was deposited on the Si surface. The thickness of the etch-inhibiting reaction layer including Si, F, O (SiOF film) was calculated from the Si2p spectra of XPS after 1 min plasma exposure. Thickness increased with O_2 addition, and especially when the O_2 flow rate ratio was more than 75% in the case of $\text{SF}_6/\text{O}_2/\text{SiF}_4$, it became profoundly thicker, more than 8.7nm. It is speculated that reaction of O radicals and SiF_4 occurred on the Si surface and etching was suppressed by Si atoms supplied from the plasma in addition to the inhibiting effect of the SiOF formation. Finally, the F/O ratio of the SiOF layer at the Si surface was calculated from the peaks of F1s and O1s. Under this experimental condition, it was found that the ratio was constant, about 2, regardless of O_2 gas flow rate ratio, which is similar to the previous result without SiF_4 addition.

[1] I. Sakai, et al: *J. Vac. Sci. Technol. A* 29, 021009 (2011).

[2] S. Amasaki, et al: *Proc. 32nd International Symp. on Dry Process* (2010) 97.

Synchrotron Analysis Focus Topic

Room: 203 C - Session SA+AS+MG+SS-TuA

HAXPES Studies on Interfaces and Buried Layers

Moderator: A. Rossi, University of Cagliari

2:00pm SA+AS+MG+SS-TuA1 Past and Present of Synchrotron Radiation, from Hard X-ray Photoemission to Soft X-ray and Back. *P. Pianetta,* Stanford University

INVITED

Synchrotron radiation has proven to be a very important tool for the study of materials in applications including earth sciences, energy and semiconductors. Most of the early applications focused on the study of surface phenomena using valence and core level spectroscopies using soft x-rays. Although one of the first studies at a multi-GeV synchrotron used hard x-rays, its practical use was limited by low counting rates. With the advent of high brightness synchrotron sources along with highly efficient electron energy analyzers, x-ray photoelectron spectroscopy using multi-keV x-rays has seen a rebirth for the study of buried interfaces and bulk materials properties. This talk will discuss the evolution of synchrotron radiation photoelectron spectroscopy from the early experiments to the present day.

2:40pm SA+AS+MG+SS-TuA3 Practical use of Photoemission with Synchrotron Radiation in Nanotechnology: From Soft to Hard X-rays. *O.J. Renault, E. Martinez,* CEA-LETI, France, *N. Barrett,* Cea Dsm Iramis Spcsi, France

Over the past 15 years, due to intrinsic limitations of laboratory X-ray sources, photoemission using synchrotron radiation has played an increasing role in solving issues of technologically-relevant materials and systems. With narrow spectral widths, synchrotron sources enable photoemission at uncomparable effective energy resolutions for refined assessment of chemical states at interfaces [1]. The broad energy range offers ultimate surface sensitivities with soft x-rays [2], and also much deeper photoelectron escape depths in the hard x-ray range which is crucial to investigate buried interfaces intrinsically found in devices. This contribution will highlight the advantages and achievements of hard x-ray photoemission (HAXPES) compared to soft x-ray photoemission, through a selection of recent studies performed on nanotechnological materials and devices (CMOS high-k/metal gate stacks, memory devices) [3]. Finally, we will briefly mention new developments: first, the extension of photoelectron

spectromicroscopy (XPEEM) from chemical state and band structure imaging, to hard x-rays excitation (HAXPEEM) [4]. Second, the application of inelastic background analysis of HAXPES spectra.

[1] O. Renault *et al.*, Appl. Phys. Lett. 81 (2002), 3627; 90 (2007), 052112; J. Appl. Phys. 96 (2004) 6362; E. Martinez *et al.*, Appl. Surf. Sci. 285 (2012), 2107.

[2] K. Huang, P. Reiss, O. Renault *et al.*, ACS Nano 4 (2010), 4799; O. Renault *et al.*, Appl. Phys. Lett. 87 (2005), 163119.

[3] R. Boujama *et al.*, J. Appl. Phys. 111 (2012), 054110; P. Calka *et al.*, J. Appl. Phys. 109 (2011) 124507.

[4] C. Wiemann *et al.*, Appl. Phys. Lett. 100 (2012), 223106.

3:00pm SA+AS+MG+SS-TuA4 Effective Attenuation Length for Titanium Nitride, Hafnium Oxide, Silicon, Silicon Dioxide, Lanthanum Lutetium Oxide, Lanthanum Calcium Manganite, and Gold from 1 keV up to 15 keV, J. Rubio-Zuazo, G.R. Castro, SpLine Spanish CRG beamline at the European Synchrotron Radiation Facility, France

Material composites, which combine different materials mostly multilayer hetero-structure, with specific and defined properties, are a promising way to create products with specific properties. In these materials the interfaces define many of their properties. The surfaces and interfaces play a fundamental role, and are the source of a great variety of new, and even unexpected, physical phenomena due to the existence of step changes in the structure and the electronic coordination. Third generation synchrotron radiation sources enables the extension of photoemission spectroscopy to higher electron kinetic energies (HAXPES, Hard X-ray Photoelectron Spectroscopy) compensating the decrease of the photoionization cross-section for excitation energies in the hard X-ray region. HAXPES allows the accessibility to buried interfaces and bulk materials due to the dramatic increase of the effective attenuation length (EAL). Electronic, compositional and chemical depth profiles can be then performed in a non-destructive way over the tens-of-nanometers scale with nanometer depth resolution. Such an important application of HAXPES is crucial for many condensed matter experiments and requires reliable EALs for high kinetic energy. EALs are well established for electrons with kinetic energies up to 2 keV. Even if EALs can be obtained by extrapolating well-known formulae, there is a lack of experimental data in the energy range between 1 and 15 keV. In the present study we have determined the EAL dependency on kinetic energy for titanium nitride (TiN), hafnium oxide (HfO₂), silicon (Si), silicon dioxide (SiO₂), lanthanum lutetium oxide (LaLuO₃), lanthanum calcium manganite (La_{0.66}Ca_{0.33}MnO₃), and gold (Au) from 1 keV up to 15 keV. A correlation between the EAL energy dependence and the material density is established. The EALs have been obtained by following either core level peak intensity dependence for a fixed kinetic energy as a function of the overlayer thickness or the core level peak intensity dependence with the photoelectron kinetic energy (i.e. photon energy) for a fixed overlayer thickness. The experimental set-up used is devoted to the combination of X-ray Diffraction (XRD) and HAXPES. Hence, we are able to determine the exact thickness and roughness of the layer from a fit of the X-ray reflectivity (Kiessig fringes) and simultaneously to obtain the EALs from the HAXPES signal evolution. It is important to stress that due to the simultaneous detection of the diffracted and photoemitted signal, the EALs, thickness and roughness determination correspond exactly to the same sample region.

4:00pm SA+AS+MG+SS-TuA7 Hard X-ray Photoelectron Spectroscopy (HAXPES) Investigations of Electronic Materials and Interfaces, J.C. Woicik, National Institute of Standards and Technology (NIST) **INVITED**

Photoelectron spectroscopy is a widely used technique that can uniquely measure the chemical and electronic structure of solids. Owing, however, to the historical use of low-energy photons and the resulting limited photoelectron inelastic mean-free path, the technique has found only general application to surfaces and shallow interfaces. With advances in both photon-source and electron-spectrometer instrumentation, hard x-ray photoelectron spectroscopy (HAXPES), where the photon energy is typically in the 2.1 – 10 keV range, has consequently emerged as a powerful tool for studying the bulk and interfacial properties of complex materials systems.

In this talk, we will discuss developments of the HAXPES technique at the NIST beamline X24A at the National Synchrotron Light Source for the study of electronic materials. Examples will include nitrogen treatment of HfO₂ gate stacks on Si, depth profiling of the HfO₂/SiO₂ interfaces, Ga and As “out-diffusion” at semiconductor/oxide interfaces, band offsets and Schottky barrier heights at semiconductor/oxide and diamond/metal interfaces, and oxygen vacancies in N doped TiO₂ and solid-oxide fuel cells. In all cases, the increased probing depth of HAXPES over traditional lab based XPS is crucial to study the electronic structure of entire

overlayers and/or buried interfaces with thicknesses of industrial significance.

4:40pm SA+AS+MG+SS-TuA9 HAXPES Study of Full High-κ/Metal Gate Stacks Deposited on Ge Substrates, C. Fleischmann, I. Kalpyris, T. Conard, C. Adelmann, S. Sioncke, IMEC, Belgium, J.P. Rueff, J. Ablett, Synchrotron SOLEIL, France, W. Vandervorst, IMEC, KU Leuven, Belgium

The introduction of Ge in CMOS devices beyond the 14 nm technology node requires effective passivation of the Ge gate stack. Besides the interface passivation, a highly scaled gate stack is needed for the next generation of CMOS devices. Scaling of the gate stack can be achieved by several means, for instance by changing process conditions. In this work, we investigate the influence of both the high-κ stack and the metal gate on the properties of a GeO_xS_y interfacial passivation layer by Hard X-ray Photoelectron Spectroscopy (HAXPES). Using high energy x-rays (4 to 8 keV), we are able to probe the buried interface between the high-κ layer and the Ge substrate, and hence to reveal direct information on the chemistry and the thickness of the GeO_xS_y passivation layer. Note that such a buried interface is not accessible using a “standard” XPS tool relying on Al K_α x-ray radiation.

In this study, we considered three high-κ materials (Al₂O₃, HfO₂ and an Al₂O₃/HfO₂ bi-layer) and three metal gates (TiN, TiW and Pt). Samples have been measured both directly after atomic layer deposition and after forming gas anneal, to investigate the effect of a thermal treatment on the interfacial properties. To disentangle the impact of the particular metal gate, comparison is made to a high-κ stack sample without metal gate.

We first demonstrate the importance of analyzing full stacks, as no effect of annealing was observed on the stacks without metal gates, while clear modification of the Ge/high-κ interfacial layer thickness is observed when a gate is present. We then show that this effect on interfacial layer thickness depends on both the high-κ and the metal gate material used. This can lead for example to an increase (i.e. HfO₂/TiN) or to a decrease (i.e. Al₂O₃/TiN) of the interfacial layer thickness after annealing. As a global trend, the thinnest interfacial layers are obtained for pure Al₂O₃. However, the interfacial layer thickness appears to be more sensitive to variations in the metal gate rather than the high-κ material. We also show that the introduction of a very thin Al₂O₃ layer (~2 Å) between the Ge substrate and the HfO₂ layer strongly influences this observed sensitivity of the interfacial layer properties to the metal gate and forming gas anneal. Aside from quantifying the interfacial layer thickness, we will also analyze changes in the interfacial layer from a chemical point of view. As a conclusion, the final layer structure (hence, the Equivalent Oxide Thickness of the gate stack) is thus a complex interplay between the initial GeO_xS_y thickness before forming gas anneal and the chemistry of the high-κ and metal gate materials.

5:00pm SA+AS+MG+SS-TuA10 X-ray Absorption Spectroscopy of Magnetic/Ferroelectric Complex Oxide Interfaces, M.B. Holcomb, J. Zhou, D. Chen, West Virginia University, C. Jenkins, M.A. Marcus, Lawrence Berkeley National Laboratory, Y.-H. Chu, National Chiao Tung University, Taiwan, Republic of China

Magnetolectric coupling (the electrical control of magnetic properties or vice versa) has promising applications in computer memory and logic, magnetic sensing and energy scavenging. Magnetolectric interfaces are a potential new method to improving magnetolectric coupling strength and controllability. We utilize x-ray absorption spectroscopy, photoemission electron microscopy, and second harmonic generation to understand both the order parameters of the individual layers and the resulting interface. This talk will focus on bilayers composed of ferromagnetic La_{0.7}St_{0.3}MnO₃ (LSMO) and ferroelectric PbZr_{0.2}Ti_{0.8}O₃ (PZT). Through photoemission electron microscopy imaging, ME coupling was confirmed at the interface. X-ray absorption spectroscopy of Mn was taken across wedged samples of varying ferroelectric and ferromagnetic thicknesses. The change of Mn valences at different thicknesses of LSMO and PZT helps to understand ME coupling and impact of thickness on the ME properties. This work suggests a strategy for improving not only magnetolectric devices, but also magnetic systems. This work is supported by West Virginia's Higher Education Policy Commission.

5:20pm SA+AS+MG+SS-TuA11 Local-Structure Determination Using Combined Fitting of EXAFS and Neutron Total Scattering Data, I. Levin, National Institute of Standards and Technology **INVITED**

The functional responses of many industrially-relevant materials are controlled by their *local structure* – a term that refers to the atomic arrangements on a scale ranging from atomic (sub-nanometer) to several nanometers. Today, multiple experimental techniques exist for probing the local atomic order. Nonetheless, finding accurate comprehensive structural solutions still remains a challenge, because any one of the existing methods

yields only a partial view of the structure. In this talk, we will discuss recent advances in local-structure determination using simultaneous fitting of EXAFS, X-ray/neutron total scattering, and electron diffuse scattering data. Examples will include several representative perovskite systems that find use as dielectrics and ferroelectrics.

Surface Science

Room: 201 A - Session SS-TuA

Metals and Alloys: Structure, Reactivity & Catalysis

Moderator: M. Trenary, University of Illinois at Chicago

2:00pm **SS-TuA1 A Density Functional Theory Study of Stability and Reactivity of H-C=O and C-OH Surface Reaction Intermediates on Pt(111) and Effects of Water on the Intermediates**, *L. Arnadottir*, Oregon State University

Two forms of the reaction intermediate with H:C:O stoichiometry were studied on Pt(111) using density functional theory. Three cases were studied: the intermediate on a clean surface, the intermediate and one water molecule on the surface and the intermediate with a water bilayer. Both the H-C=O (formyl) and C-OH configurations were found to be stable on clean Pt(111) and when coadsorbed with a single water molecule. On the clean surface interconversion between the two forms goes through stable a CO_{ads} and H_{ads} intermediates so although both HCO and COH are stable on the clean surface they will not interconvert without coadsorbed water. In the presence of coadsorbed water molecule the activation barrier for the interconversion from HCO to COH was found to be much lower or 0.62 eV. The HCO configuration is stable in the presence of a water bilayer with slight preference for bridge over atop adsorption site. The COH configuration is unstable under the water bilayer and dissociates into CO_{ads} and H that structurally diffuses into the water bilayer. That suggest that, in the presence of water, the HCO form will be the only stable form of the reaction intermediate of H:C:O stoichiometry. Various reactions paths for both of the reaction intermediates with OH and H_2O eventually leading to CO or CO_2 formation are also investigated.

2:40pm **SS-TuA3 Energetics of Elementary Reaction Steps of Importance in Clean Fuels Production and Utilization on Pt(111) by Microcalorimetry**, *C.T. Campbell*, University of Washington **INVITED**

Until recently, the heats of formation of some of the simplest adsorbed molecular fragments such as $-\text{CH}$, $-\text{CH}_2$, $-\text{CH}_3$, $-\text{OH}$, $-\text{OCH}_3$, $-\text{OOCH}$ and $-\text{C}(\text{CH}_3)_3$ were not known on any metal surface. However, these simple adsorbates are ubiquitous catalytic reaction intermediates involved in many industrially important reactions that are catalyzed by platinum-group metals, including water-gas shift, steam reforming of hydrocarbons and oxygenates, combustion and selective oxidation reactions of all sorts, methanation and Fischer-Tropsch, methanol synthesis and decomposition, several fuel cell reactions and photocatalytic water splitting. Here we summarize the first measurements of the heats of formation of these adsorbed intermediates on Pt(111) using single crystal adsorption calorimetry. We also use these heats of formation to predict reaction energies for important elementary steps in catalysis on Pt, which give insights into catalytic reaction pathways. The results will also be compared to Density Functional Theory (DFT) calculations, to assess which DFT methods are most accurate. These experimental benchmark energies are aiding in the ongoing development of more accurate computational methods, like DFT with van der Waals corrections.

4:00pm **SS-TuA7 RAIRS Study on the Kinetics of NH Formation and Dissociation on Ru(0001)**, *I. Waluyo, Y. Ren, M. Trenary*, University of Illinois at Chicago

We used reflection absorption infrared spectroscopy (RAIRS) to experimentally study the kinetics of the NH formation and dissociation reactions on Ru(0001). These reactions are important in ammonia synthesis, for which ruthenium is one of the most effective catalysts. While theoretical values for the heats of adsorption of each species and the activation barriers for each step in the ammonia synthesis reaction have been extensively reported, there are few, if any, direct experimentally measured values for the activation barriers of the elementary steps in the reaction on Ru(0001). In our study, the evolution of the NH stretch peak at 3318 cm^{-1} was monitored as a function of time during the course of the NH formation reaction between 320 and 370 K and NH dissociation between 370 and 400 K. An atomic N layer was prepared through the thermal decomposition of NH_3 . During the NH formation reaction, the sample was continuously exposed to a constant background pressure of H_2 to compensate for the loss of surface H due to the associative desorption of H_2 , which occurs in the same temperature range as NH formation. Both NH formation and

dissociation were found to follow first-order kinetics, and the experimental rate constants show good agreement with the theoretical values. The experimentally determined activation energies of 69.6 and 104.9 kJ/mol for NH formation and dissociation, respectively, are comparable to the theoretical values of 103.3 and 133.5 kJ/mol.

4:20pm **SS-TuA8 Calorimetric Measurement of Adsorption and Adhesion Energies of Cu on Pt(111)**, *S.L. Hemmingson, T.E. James, J.R.V. Sellers, C.T. Campbell*, University of Washington

Bimetallic catalysts are an important category of industrial catalysts that exhibit unique electronic and chemical properties from their parent metals. Pt-based bimetallic catalysts are the most commonly studied and well-characterized bimetallic systems, with many providing enhanced selectivity, activity, and stability for industrially significant reactions such as hydrogenation/dehydrogenation, CO oxidation, and the water-gas shift reaction. The modifications in the catalytic properties of Pt bimetallics are most significant when the admetal coverage is less than a single monolayer. Yet little is known about the strength of metal-metal bonds in some bimetallic catalysts because indirect energy measurement techniques such as temperature programmed desorption cannot be employed. This study employs a novel ultrahigh vacuum Single Crystal Adsorption Calorimeter (SCAC) to directly measure the adsorption energy of Cu overlayers on Pt(111) at 300 K. A pulsed and collimated Cu atomic beam is generated using an electron beam-heated source and deposited onto a Pt(111) single crystal surface. The measured heats of adsorption as a function of total Cu coverage were interpreted with respect to the known layer-by-layer growth mechanism of Cu overlayers on Pt(111). Two distinct Cu coverage regimes of heat of adsorption have been observed. From 0 to just above one monolayer (ML), the heat decreases from 357.4 kJ/mol to 334.5 kJ/mol where Cu grows pseudomorphically on Pt(111). The high initial heat of adsorption indicates a strong Cu-Pt interaction for isolated Cu atoms which are stronger than the Cu-Cu metallic bond. As Cu coverage increases the heats decrease due to repulsive interactions between neighboring Cu atoms or lattice strain buildup. From 1.3 and 3 ML, where Cu grows layer-by-layer with the Cu(111) lattice spacing, the heats of adsorption increases slowly to the bulk heat of sublimation of Cu, 337.4 kJ/mol, due to lattice mismatch between the first Cu monolayer and the subsequent monolayers. By 3 ML no further lattice strain is felt by additional Cu. This represents the first ever direct measurements of late transition metal bimetallic adsorption energies.

4:40pm **SS-TuA9 History of Surface Science at AVS**, *R.M. Tromp*, IBM T.J. Watson Research Center **INVITED**

Surface science has a long and illustrious history. The development of surface science and of the AVS have often intersected, and even coincided. In this talk I hope to discuss some of these intersections and coincidences.

5:20pm **SS-TuA11 Growth and Activity of Pt-Based Bimetallic Clusters on Titania**, *D.A. Chen, R.P. Galhenage, H. Yan, K. Xie, A.S. Duke*, University of South Carolina

The nucleation, growth and surface composition of Pt-Co and Pt-Re bimetallic clusters on $\text{TiO}_2(110)$ have been investigated as model systems for understanding how surface chemistry can be controlled by bimetallic composition and interactions between the clusters and the oxide support. Scanning tunneling microscopy studies demonstrate that bimetallic clusters can be formed from sequential deposition of the metals when the metal with the lower mobility on titania (Co or Re) is deposited first to serve as nucleation sites for Pt. For the Co-Pt clusters, the surface composition is slightly Pt-rich compared to the bulk, despite the lower surface free energy for Co compared to Pt. While Co-Pt clusters have similar surface compositions regardless of the order of deposition, the inter-diffusion of metals in Re-Pt clusters is inhibited when Pt is deposited on top of Re; for the reverse order of deposition, XPS data indicate that a Re-Pt alloy is formed. Temperature programmed desorption experiments with CO show that CO adsorbs at both Co and Pt sites on the bimetallic clusters. Methanol decomposition chemistry has also been studied as a function of changing bimetallic cluster composition. Methanol decomposition produces CO and hydrogen as the main products on both pure Pt and pure Co clusters. On the bimetallic Co-Pt clusters, the selectivity for methane production increases, and the desorption of H_2 at higher temperatures suggests that the intermediates have greater thermal stability.

5:40pm **SS-TuA12 An Atomic-Scale View of Carbon-Carbon Bond Formation on Cobalt Nanoparticles**, *E.A. Lewis, E.C.H. Sykes*, Tufts University

Fischer-Tropsch synthesis (FTS) has recently gained increased attention as it involves the formation of hydrocarbons (fuels) via the catalytic conversion of syngas (CO and H_2), which can be derived from renewable sources. FTS is often performed using cobalt-based catalysts, and although

the exact mechanism of the reaction is not known, it has been shown that the reactivity is affected by the adsorption state of reactants, as well as nanoparticle shape and size. Here we have used low-temperature scanning tunneling microscopy to study carbon-carbon bond formation during FTS. By using aryl-halides to form phenyl radicals on the cobalt surfaces, we can examine the preferred site for carbon-carbon bond formation. Initially at 5 K, the intact molecules form loosely-ordered arrays on the cobalt surfaces, but at 80 K, we find that phenyl radicals are stabilized in a series of highly ordered geometries on the cobalt terraces. Upon heating, a carbon-carbon bond is formed that results in surface-bound biphenyl. These results provide insight into the active site for carbon coupling during FTS, and we propose a mechanism that may explain the well-known phenomenon of surface roughening that occurs on cobalt surfaces under real FTS conditions.

Thin Film

Room: 104 A - Session TF-TuA

High Throughput ALD

Moderator: G.N. Parsons, North Carolina State University

2:00pm **TF-TuA1 A Comparison between Conventional- and Spatial ALD; The Effect of Pressure and Exposure Time on Film Properties.** *P. Poodt*, Holst Centre / TNO, Netherlands **INVITED**

The last few years have seen important developments in spatial Atomic Layer Deposition (ALD), enabling ALD with high deposition rates. Whereas in conventional ALD, precursors are dosed in a time-separated mode using a purge or pump step, in spatial ALD, precursors are dosed simultaneously and continuously at different physical locations. As a result, deposition rates exceeding 1 nm/s have been reported for spatial atmospheric ALD of Al₂O₃. This has led to the development of high-throughput, industrial scale spatial ALD tools for surface passivation of crystalline silicon wafers for solar cells as well as roll-to-roll spatial ALD concepts for flexible electronics.

From the point of view of chemistry, there is no difference between spatial and conventional ALD, as similar precursors and substrates are used to make similar materials. Important differences between spatial and conventional ALD, though, are the time-scales and pressure regime at which spatial ALD is performed. Whereas in conventional ALD, precursor exposure times typically range from a few tenths of seconds to a few seconds, in spatial ALD precursor exposure times can be as short as several milliseconds, during which the physical and chemical processes (e.g. diffusion, adsorption, reaction, crystallization, etc.) responsible for the film growth have to take place. Furthermore, spatial ALD is often performed at atmospheric pressure, where conventional ALD is usually done at low pressure. This especially impacts plasma-enhanced ALD, as the physics and chemistry of atmospheric pressure plasma's can be quite different from the low pressure plasma's typically used in conventional plasma enhanced ALD.

With this in mind, spatial ALD of several different material classes will be discussed, and a comparison with similar, conventional ALD processes, will be made. Similarities, as well as differences, in deposition processes, film properties and their performance in devices will be discussed for

1. Alumina (amorphous dielectric)
2. Zinc oxide (crystalline transparent conductor)
3. Alucone (hybrid material, deposited by spatial Molecular Layer Deposition (MLD))
4. Silver (metal, deposited by plasma enhanced spatial ALD).

Furthermore, possible consequences and opportunities for up-scaling these processes to industrial scales will be discussed.

2:40pm **TF-TuA3 Thin-film Electronics by Spatial ALD.** *S.F. Nelson, C.R. Ellinger, L.W. Tutt*, Eastman Kodak Company **INVITED**

In this talk we describe our approach to thin-film electronics using spatial atomic layer deposition (SALD). ALD has long been known for producing dense conformal films of conductors, insulators, and semiconducting layers from a limited set of precursors. However, in the more common vacuum- and chamber-based ALD processes, the deposition speed has generally been limited. In contrast, the SALD deposition process can be relatively fast. The coating takes place at atmospheric pressure in a localized region of a coating head, with no enclosure except that produced by gas isolation curtains, and thus without any pumping cycles.

Focusing on the field of metal oxide semiconductor thin-film transistors (TFTs), we have demonstrated that SALD produces high quality planar thin film transistors. TFTs with aluminum oxide for the insulator and zinc oxide (ZnO) for the semiconductor have high on/off ratios, and good uniformity

of the deposited layers for deposition temperatures at and below 200°C. We show that the regime of fast ALD cycles accessible by SALD produces particularly good performance.

Patterning and alignment of transistors on flexible substrates can present a challenge, especially for short channel lengths. We have investigated novel vertical device architectures enabled by the conformal nature of SALD deposition that unite high performance with generous alignment and resolution requirements. With self-aligned sub-micron channel lengths, these devices demonstrate remarkable current-carrying capability at low voltage.

Finally, we will present a "patterned-by-printing" technique for SALD-grown transistors. By printing an inhibitor ink on the surface, the growth of aluminum-doped ZnO (conductor), aluminum oxide (insulator), and ZnO (semiconductor) can be limited to selected areas of the substrate. The process produces TFTs with the same excellent performance as lithographically patterned TFTs, with high yield, and rapid throughput.

In summary, we will present a range of opportunities in the area of thin-film and "printed" electronics that are enabled by spatial ALD.

4:00pm **TF-TuA7 Roll to Roll PEALD of Mixed Oxide Films for High Barrier Applications.** *E.R. Dickey*, Lotus Applied Technology **INVITED**

Atomic Layer Deposition (ALD) via substrate motion, rather than pulse-purge cycling on a fixed substrate, is emerging as a promising path to high speed low cost roll to roll deposition of high quality ALD gas diffusion barriers. To date the majority of research in ALD barrier films has been conducted using Al₂O₃ in the thickness range of 20-100nm, with multiple groups reporting Water Vapor Transmission Rates (WVTR) below the detection limits of commonly used testing methods. A smaller body of research has examined TiO₂ films, which in some cases show comparable barrier performance over a similar thickness range. Here we report a Plasma Enabled ALD process incorporating mixtures of Al₂O₃ and TiO₂ from TMA, TiCl₄, and oxygen-containing plasma, formed by alternating single ALD cycles of each material in a spatial ALD reactor. RBS data indicates the resulting film has a volumetric ratio of Al₂O₃ to TiO₂ of approximately 1.5:1, reflecting the growth rates of each individual material. Use of the mixed material substantially reduces the required film thickness for a given WVTR performance compared to either pure Al₂O₃ or TiO₂. The relationship between barrier performance and ALD film thickness is examined over the range of 2nm to 25nm, with WVTR rates in the range of 10⁻⁴ g/m²/day for coatings of 5nm to 10nm thickness, and the mid 10⁻⁶ range, near the limit of the calcium test employed, for the thickest films. The process has been ramped from the spatial ALD reactor to a Pilot scale roll to roll reactor configured to deposit the mixed film on rolls of polymer 300mm wide by up to 500m long.

4:40pm **TF-TuA9 Spatial Atomic Layer Deposition for New Generation Solar Cells.** *D. Muñoz-Rojas, G. Ercolano, A.T. Marin, C.T. Armstrong, R.L.Z. Hoyer, K.P. Musselman, J.L. MacManus-Driscoll*, University of Cambridge, UK

A key factor for the success of new generation PV technologies is the ability to design low-cost, low-temperature, scalable and roll-to-roll compatible fabrication methods. In recent years progressive development of batch type vacuum-free ALD technologies has taken place with novel systems capable of working in the open atmosphere being presented. The key to atmospheric/spatial ALD (AALD/SALD) is that precursors are separated in space rather than in time (as opposed to conventional ALD, which has a sequence of pulse-purge steps), thus allowing orders of magnitude faster deposition rates and low precursor wastage, while keeping the advantages of conventional ALD. We have developed and optimised an AALD system for the deposition of solar cell components and which is compatible with roll-to-roll processing. We will illustrate its potential with several examples, namely, ultrafast deposition of high quality amorphous TiO₂ and ZnO blocking layers for inverted bulk heterojunction solar cells; low temperature deposition of high conductivity Cu₂O films and its use in back-surface-field (BSF) designs for low-cost inorganic solar cells; deposition of doped TiO₂ and ZnO films for application in hybrid solar cells.

5:00pm **TF-TuA10 Spatial Molecular Layer Deposition of Metalcones.** *M. Smets, F. van den Bruele, P. Poodt*, Holst Centre / TNO, Netherlands

Spatial-ALD is emerging as an industrially scalable deposition technology at atmospheric pressure which combines the advantages of temporal ALD, i.e. excellent control of film composition and uniformity on large area substrates, with high growth rates (~ nm/s). Whereas in conventional ALD, precursors are dosed in a time-separated mode using a purge or pump step, in spatial ALD, precursors are dosed simultaneously and continuously at different physical locations. As a result, deposition rates exceeding 1 nm/s have been reported for spatial atmospheric ALD of Al₂O₃. This has led to the development of high-throughput, industrial scale ALD tools for surface

passivation of crystalline silicon solar cells as well as roll-to-roll spatial ALD concepts for applications in flexible electronics.

Atomic layer deposition is mostly used to deposit conformal inorganic films. Organic- and hybrid organic-inorganic films can be also be deposited by ALD, which is then referred to as Molecular Layer Deposition (MLD). For example, by combining metal precursors and various organic alcohols, metal alkoxide films or “metalcones” can be obtained. By varying both the metal precursor and organic precursor, the optical, mechanical, electrical and chemical properties of the film can be tuned.

This presents opportunities for applications such as catalysis, light management, and many others.

We have combined both techniques to do Spatial MLD to deposit several metalcones by combining various metal- and organic precursors. E.g. alucone layers have been deposited using TMA with ethylene glycol, with a growth per cycle (GPC) of about 0.5 nm/cycle and a refractive index of 1.50 at 630 nm. The GPC decreases with increasing deposition temperature and there appears to be an optimum for the ethylene glycol concentration. The optical, chemical and mechanical properties of the films have been investigated by means of e.g. ellipsometry, ATR-FTIR and nano-indentation.

These results show that Spatial MLD is a promising technique to deposit a wide range of new, functional materials at high deposition rates.

Vacuum Technology

Room: 202 C - Session VT+EN+TF-TuA

Vacuum for Industrial Processing

Moderator: M. Wuest, INFICON Ltd., Liechtenstein

2:00pm **VT+EN+TF-TuA1 The Relationship Between Moisture Ingress, Hermeticity Testing, and Internal Gas Analysis (IGA) of Hermetic Structures**, *J.C. Pernicka*, Pernicka Corporation **INVITED**

For countless decades we have relied on Mil-Std 883 Method 1014 to insure not only military, but medical, telecommunication, aerospace, aviation, automotive, and hi-rel commercial devices were hermetic. The Howl-Mann equation, based on the ideal gas law, provided the fundamental theory necessary to relate air-equivalent leak rate measurements to tracer gas bombing pressures, times, and Pass/Fail points. Over the past three decades we have tried to find a relationship between moisture ingress and measured leak rate, and only in the last decade have we made fundamental progress toward that goal by using a highly sensitive leak detector and a specially designed mass spectrometer. Moisture ingress departs from ideal gas behavior because of its polar nature and the “three monolayer theory” proposed by Aaron DerMarderosian suggests that there is a surface migration component which is often overlooked. This paper will review leak test and IGA data taken over the past 40 years on commercially manufactured hermetic devices with the hope of identifying both dependent and independent variables which will help us predict moisture ingress, and as a result, reliability.

2:40pm **VT+EN+TF-TuA3 Applications and Limitations of Wear-Resistant PVD Coatings**, *A. Mueller*, OC Oerlikon Balzers AG, Liechtenstein **INVITED**

Nowadays a broad range of applications exists using PVD hard coatings produced under vacuum condition. For instance thin diamond-like carbon films and other carbon containing coatings are widely used in car engines and are mandatory for modern fuel saving high pressure Diesel injection systems. Coated cutting tools allow for more severe cutting conditions and/or increased life time which results in lower costs per work piece for the component manufacturer. In applications like steel sheet forming and blanking or plastic injection moulding the coated tools show less adhesive and abrasive wear so that cleaning cycles of the tool can be extended and life time is increased. In some applications the tribological advantages of hard coatings are combined with a desired decorative appearance.

This presentation will give an overview of typical applications of PVD coatings as well as the vacuum coating systems and processes used to manufacture those coatings. Typical failure mechanisms and approaches to overcome limitations and strategies to increase the performance of the coatings and to cope with new requirements in future applications will be presented. Coating performance and failure mechanisms will be reported using techniques like Rockwell indentation, calo test, pin-on-disc test, scanning electron microscopy, energy dispersive x-ray spectroscopy, micro indentation or x-ray diffraction.

4:00pm **VT+EN+TF-TuA7 Optics Contamination in EUV Lithography: Measurement, Modeling and Mitigation**, *S.B. Hill, N.S. Faradzhev, T.B. Lucatorto*, National Institute of Standards and Technology (NIST), *B.V. Yakshinskiy, R.A. Bartynski*, Rutgers University **INVITED**

Over the past decade the semiconductor industry has relied upon increasingly complex optical and processing techniques to reduce the feature size of microelectronic devices from 100 nm to 22 nm without reducing the wavelength of the lithographic light (193 nm). Since the cost to continue this trend is rapidly becoming prohibitive, the industry is poised to undergo a dramatic shift to Extreme-Ultraviolet Lithography (EUVL) using 13.5 nm (92 eV) radiation. One of the many technical challenges to this transition has been the degradation of throughput and optical resolution caused by the buildup of carbonaceous deposits on optic surfaces resulting from EUV-induced decomposition of organic species which are continuously outgassed during EUV irradiation of the chemically complex photoresists. The National Institute of Standards and Technology (NIST) is uniquely positioned to address this problem using our Synchrotron Ultraviolet Radiation Facility (SURF III) which has a peak output near 13.5 nm. We have directly measured EUV-induced contamination rates of various species over a wide range of partial pressures as a function of EUV intensity, dose and wavelength. Among other findings, these investigations revealed two regimes of contamination. For intensities high enough that the EUV-induced reaction rate far exceeds the thermal desorption rate, the contamination rate is independent of intensity and scales linearly with partial pressure since every adsorbed molecule photoreacts. In the opposite limit, the surface coverage of adsorbed precursor molecules in thermal equilibrium with the gas phase is only slightly perturbed by EUV irradiation. The contamination rate in this case scales linearly with intensity, as expected, but also displays a quasi-logarithmic dependence on partial pressure over many decades. Although initially surprising, this sub-linear pressure scaling was found to be consistent with temperature-programmed desorption measurements (in collaboration with Rutgers University) and with models of desorption kinetics on non-ideal surfaces. I will summarize these results and discuss how fundamental investigations such as these enabled the development of practical methods to systematically measure the contamination produced by outgassing of EUV resists. Together with additional measurements and models, this allowed the makers of EUVL tools to define the maximum allowable level of resist outgas contamination that could be managed by in situ mitigation and cleaning techniques. I will outline the resulting outgas testing protocols first fully implemented at NIST in 2011 to which all resists must be subjected before use in EUVL tools.

4:40pm **VT+EN+TF-TuA9 Extremely Clean Handling of EUV Reticles**, *R. Versluis, E.C. Fritz, W.E. Crowcombe*, TNO Technical Sciences, Netherlands

In lithography processes handling of reticles and reticle blanks is a very critical step. Defects (particles, scratches, pits and bumps) in a reticle will lead to printed defects on the wafer which is a very important cost and throughput driver. Particles on reticle blanks that are processed in a deposition are also critical. With decreasing node values particle size requirements are going down to values less than 50 nm and the requirements on allowed added particles per reticle pass (PRP) are going down to PRP<0.1 for reticle handlers. These values must be met for both atmospheric handlers and vacuum handlers. Currently there are no qualified atmospheric or vacuum robots and handlers that can meet this requirement.

Therefore TNO is initiating a Shared Research Development program on contamination control of ultra-clean electronics manufacturing to increase productivity, performance and lifetime of manufacturing equipment for the high tech electronics industry. One of the ongoing projects is the development of an ultraclean modular EUV reticle handling system consisting of a robot with a dual end effector, a DualPod opener and a reticle flip unit that will meet the industry requirements with respect to particle free handling.

In this talk we will show the design of the reticle handler, the design rules for meeting the PRP requirements both for an atmospheric handler and a vacuum handler and the issues involved with the qualification of such a machine. Given the total time needed for performing a full reticle pass (opening of DualPod, atmospheric transport of InnerPod, Evacuating LoadLock, Opening InnerPod inside vacuum, Transport of reticle in vacuum, flipping the reticle etc.) , the low number of particles that is allowed to be added per pass and the qualification time needed to measure the added particles, system qualification is a complicated process. The system is currently being built and qualified at TNO with our own in-house built particle scanner. After qualification the system can be added to any reticle processing system that meets SEMI standards and can also be used to qualify sub-modules, such as load locks, robots, flipping unit, etc.

5:00pm **VT+EN+TF-TuA10 Vacuum Environment Processing Studies for the Production of Commercial Thin Film Hydride Targets**, *J.L. Provo*, J. L. Provo, Consulting

An important aspect of understanding industrial processing is to know the characteristics of the materials used in such processes. A study was performed to study the effects of hydriding chamber material on the degree of hydriding for the commercial production of thin film hydride targets for various research universities, used in their accelerators for cancer research, and material studies, for the oil industry for oil well logging, for industrial nuclear waste assay, and for the Federal Aviation Administration (FAA) for contraband studies at ports and airports. It was desired to increase the degree of hydriding of various thin film hydrides and to study the vacuum environment during air- exposure hydriding. For this purpose dynamic residual gas analysis during deuterium gas hydride processing was utilized, employing a special set-up for direct dynamic hydride gas sampling for a process at elevated temperature and full gas pressure. Complete process data for a stainless-steel air fired passivated externally heated pipe type hydriding chamber is given and dynamic residual gas analysis comparisons during hydriding are presented for similar chambers constructed of alumina(99.8%), copper with an interior coating of aluminum, and for a wet hydrogen fired passivated copper-beryllium(1.83%) chamber. Dynamic data with gas in chamber at hydriding temperature showed the presence and growth of water vapor(D_2O) and related ion species(H_2O^+ , HDO^+ , D_2O^+ , and OD^+) during a one hour process time. Extensive hydrogen isotope exchange reactions were seen to be taking place. Mass peaks 12(C^+), 16(CD_2^+), 17(CHD_2^+), and 18(CD_3^+ , OD^+) grow for approximately the first half hour of a one hour hydriding process and then come to an equilibrium. Mass peaks 19(HDO^+) and 20(D_2O^+) continue to grow throughout the process cycle. Copper-beryllium(1.83%) passivated hydriding chambers were seen to be the best hydriding chamber material studied to date.

5:20pm **VT+EN+TF-TuA11 HBr Gas Mixture Analysis by FTIR for Non-Destructive Quality Control of Automotive Halogen Capsule Manufacturing**, *J.N. Greene, P.F. Somssich*, Osram Sylvania

Controlling the halogen content of an automotive capsule presents many challenges for quality control. It is not enough to identify a problem with a finished product, if the gas mixing at the front end is not properly controlled. With this in mind, the analysis of gas mixtures for the quantitative determination of $HBr(g)$ by Fourier Transform Infrared Spectroscopy (FTIR) was studied. Automotive halogen capsules had been non-destructively analyzed by FTIR and destructively analyzed by wet chemistry for HBr content at our production plant and analysis laboratory for many years. However, the identification of out of specification end product capsules with respect to halogen content, while useful, does not specifically identify the problem. Analysis of the gas mixtures for HBr content was needed at the front end of the production process. Therefore, the feasibility of using an FTIR equipped with a gas cell for quantitative determination of HBr was investigated with respect to HBr reactivity and handling, instrument calibration via gas mixing manifold and wet chemistry, and quantitative limits. The use of vacuum technology in the transport of corrosive HBr and the evacuation of the systems developed in this study are also discussed. Examples of problems detected and corrected in the manufacturing process will be discussed.

Tuesday Afternoon Poster Sessions

Atom Probe Tomography Focus Topic

Room: Hall B - Session AP-TuP

Atom Probe Tomography Poster Session

AP-TuP1 Atom Probe Tomography of Energy and Environmental Materials, D.E. Perea, A. Devaraj, R.J. Colby, J. Liu, D.K. Schreiber, J.E. Evans, S.A. Thevuthasan, Pacific Northwest National Laboratory

Buried interfaces and surfaces play an essential role in the function of many materials for energy, environmental, and biological applications. An understanding of the physics and ultimate the ability to engineer materials with specific properties is aided by an atomic level understanding of the composition and morphology of interfaces. Atom probe tomography (APT) is a 3-dimensional compositional mapping technique based on the field evaporation of individual atoms from the tip of a needle-shaped specimen. At the Environmental Molecular Sciences Laboratory (EMSL), we are pushing the limits of APT analysis to study a wide variety of energy and environmental materials. We will present several examples that exemplify the breadth of materials which include semiconductor nanowires for high performance solar cell and transistors, geologic minerals used for atmospheric carbon sequestration, and glass materials for the vitrification of controlled waste.

AP-TuP2 Advantage of NbTiN over NbN in Superconducting Properties of Ultra-thin Films, M. Guziewicz, A. Laszcz, J.Z. Domagala, K. Golaszewska, A. Czerwinski, W. Slysz, Institute of Electron Technology, Poland

Progress in quality of ultra-thin superconducting niobium nitride films for fabrication technology of Superconducting Single Photon Detectors is still observed. Photon detection bases on a recording of current collapse pulse caused by a photon absorbed in the nanostructure film. Materials proved to be effective are Nb-nitride layers and the layers containing Ti. The latter applied in the detector structure have the advantage in the quantum efficiency and reduced noise by one decade compared to the NbN film. So far, there are no known causes of advantages of this material, but can be traced to them in a better quality of structure and uniformity of composition, which reduces the probability of scattering electron pairs on superconductors current defects. The confirmation of these assumptions may be the observation that better parameters are characterized by the detectors made with layers of amorphous than polycrystalline NbN and compete well with epitaxial NbN layers of single crystal characteristics. It can be find some papers where influence of substrate, sputtering deposition parameters and film thickness of NbN or NbTiN on critical temperature were studied. Our niobium nitrides films deposited on (0001)Al₂O₃ reveal excellent both superconducting and structure properties. Extensive characterization of the films using XRD, high resolution TEM and AFM were performed. High epitaxial quality of NbN and NbTiN films grown on the Al₂O₃ substrates is proved by HRXRD and HRTEM studies. The results of the studies on both NbN and NbTiN films reveal one cubic phase with NaCl-type structure. The critical temperatures of NbN and NbTiN films with thickness of few nm grown on the Al₂O₃ substrates are in range 4K ÷ 7K, but post-grown annealing of the films at 1000°C in Ar increases temperature up to 12K or above. Moreover, the 5 nm thick NbTiN film deposited on sapphire at optimized conditions and annealed discloses the best superconducting properties - critical temperature of 14 K as well as extremely high critical current density of 12-MA/cm², while the critical current density of 3 MA/cm² was attained for the NbN film. This is the highest value measured on so thin Nb-nitrides films. The improvement in superconductor parameters can be explained due to reduced strain and defects by high temperature annealing of the film. Rocking Curve of the 111 Bragg reflection on the NbTiN is extremely narrow, ≈10 arcsec, characterising the best single crystals. Higher critical current density is almost certainly attained due to lower atomic concentration of oxygen contamination in the NbTiN films than in the NbN films.

Biomaterial Interfaces

Room: Hall B - Session BI-TuP

Biomaterials Interfaces Poster Session

BI-TuP2 Monocyte Adhesion to Protein Functionalized Nanopatterns, A.S. Andersen, D.S. Sutherland, Aarhus University, Denmark

Through a biofunctionalized nanopattern proteins are presented in circular nanopatches, which can range from 66nm-3µm in size. These protein nanopatches are used to study cell binding, specifically in regards to ligand clustering. Monocytes are the precursors for our body's macrophages, the scavenger cells, which for example help during inflammation and to remove apoptotic cells. Monocytes are found in the blood and needs to be recruited to sites of inflammation. This happens in four stages, rolling, binding, diapedesis and migration. The focus of this research is in the first two stages. During binding an integrin, LFA1, on the monocyte binds to its ligand, ICAM1, on the epithelial cells and it is known that these form focal adhesions (FA). The size of the FA, needed to get a strong binding, is not known. This research uses a nanopattern (1), biofunctionalized through a serial protein deposition (2) mimicking FA ICAM1 patches. The binding of THP1 cells to 100-800nm sized ICAM1 nanopatterns will be shown. It illustrates a cut off in size where the cell binding disappears indicating that there is a crucial size of FA for monocytes to adhere.

Further, results showing a protein nanopattern made inside a microfluidic channel are presented. The nanopattern consists of circular gold covered holes 800nm in diameter, in a PLL-g-PEG covered SiO₂ surface. The gold holes have been biofunctionalized through a serial protein deposition which gives an oriented antibody pattern, with the possibility to change to any protein with a FC domain attached. The microfluidic setup will allow for cell studies under flow and opens up the opportunity to mimic the flow conditions found in the blood stream during cellular adhesion, which have been shown to be an important factor in monocyte adhesion.

1: Jenny Malmström, Brian Christensen, Hans P. Jakobsen, Jette Lovmand, Rasmus Foldbjerg, Esben S. Sørensen, and Duncan S. Sutherland. Large Area Protein Patterning Reveals Nanoscale Control of Focal Adhesion Development. *Nano letters*, Vol 10, 686-694, 2010.

2: Stine H. Kristensen, Gitte A. Pedersen, Lene N. Nejsum and Duncan S. Sutherland. Nanoscale E-Cadherin Ligand Patterns Show Threshold Size for Cellular Adhesion and Adherence Junction Formation. *Nano Letters*, 12(4), 2129-2133 2012.

BI-TuP3 Ultrasound Imaging, Gamma Scintigraphy and HIFU Therapy with Perfluorocarbon Loaded Iron-Silica Nanoshells, A. Liberman, Z. Wu, C. Barback, R. Viveros, S.L. Blair, D. Vera, L.G. Ellies, R.F. Mattrey, W.C. Trogler, A.C. Kummel, University of California San Diego

The reported positive margin rate from wire localized excisions of breast cancers is approximately 20-50%; however, by preoperatively injecting a radioactive seed into the tumor under CT guidance, the excision rate is halved because the surgeon can constantly reorient the dissection to place the seed in the center of the specimen. Unfortunately, radioactive seed localization has several safety challenges, only single focus can be localized, and incisions are required to implant the seeds, so it is rarely employed. As an alternative, gas-filled hollow Fe-doped silica particles have been developed, which can be used for ultrasound-guided surgery even for multiple foci. The function of the Fe doping is to render the silica shells biodegradable. The particles are synthesized through a sol-gel method on a polystyrene template, and calcined to create hollow, rigid nanoshells. The Fe-doped silica shell is derived from tetramethyl orthosilicate and iron ethoxide, which forms a rigid, nanoporous shell upon calcination. The nanoshells are filled with perfluoropentane vapor or liquid. The flouorous phase is contained within the shell due to its extremely low solubility in water. *In vivo* particle longevity studies have been performed in tumor bearing mouse models show signal presence up to 10 days post injection. To study biodistribution, nanoshells were functionalized with DTPA and radiolabeled with ¹¹¹In and then imaged by γ-scintigraphy. Scintigraphic imaging and γ-counting confirm that particles undergoing IV delivery to tumor bearing mice will passively accumulate in the tumors which may allow for tumor detection and therapeutic applications. The nanoshells break under acoustic excitation to release gas pockets which increase acoustic energy absorption and reduce acoustic cavitation threshold. Therefore they may also be employed as a sensitizing agent in high intensity focused ultrasound (HIFU) therapy. Traditional ultrasound agents

which can be used as a HIFU sensitizing agent pose several potential drawbacks such as poor *in vivo* persistence (mins) and high risk during continuous perfusion. Preliminary *in vivo* HIFU ablation studies show that few particles are needed in order to develop a sensitizing effect to HIFU thereby substantially reduce the amount of HIFU exposure necessary to achieve an ablative effect. It was found that nanoshells systemically administered to breast tumor bearing mice could be cavitated by HIFU 24 hrs after administration. This cavitation caused liquification within the focal volume of the HIFU which contained the nanoshells within seconds. This may potentially allow for a larger area to be ablated in less time with less power.

BI-TuP4 Development of Nanofibrous Meshes as Smart Dressings for the Healing of Chronic Wounds, M. Abrigo, S.M. McArthur, P. Kingshott, Swinburne University of Technology, Australia

Diabetic, pressure, venous and arterial ulcers are a large social, economic and healthcare burden. These chronic non-healing wounds show delayed and incomplete healing processes exposing patients to high risk of infection. Chronic wound care currently focuses on dressings capable of preventing microbial infiltration and keeping a balanced moisture and gas exchange environment. The design of dressings that combine the necessary morphological and physical requirements for wound healing with the value-added capability to address optimal cell responses and impair bacterial proliferation represents a major challenge in wound care.

Polymeric nanofibrous meshes are good candidates as wound dressings and cell scaffolds due to their high surface area, micro-porosity and non-woven structure. Electrospinning is used for the fabrication of these structures because it is a simple, cost-effective and reproducible process. Moreover, electrospinning enables fibres of synthetic and natural polymers to be combined as multifunctional dressings capable of addressing a range of wound challenges.

In this study, a range of different synthetic polymers (Poly-lactic acid, Poly-glycolic acid and Polycaprolactone) have been blended and the parameters of the electrospinning process (such as spinning rate and electric field intensity) optimized to achieve a nanofibrous membrane. The morphological properties of the electrospun meshes have been analysed by three-dimensional optical profiler, Scanning Electron Microscopy (SEM) and Atomic Force Microscopy (AFM). As the first step to understand microbial infiltration and control in wound dressings, a number of studies have been completed using *E. Coli*, *P. Aeruginosa*, *S. Aureus* in an effort to understand how the morphological and structural properties of the electrospun meshes influence bacterial attachment, proliferation and growth.

BI-TuP5 Lipid Interactions with Plasma Polymers, H.J. Askew, S.M. McArthur, Swinburne University of Technology, Australia

The cell membrane encases and protects cellular components and plays an important role in transport, signalling and disease. Studying membrane behaviour is a challenging task due to the complexity and scale on which these processes occur. Supported lipid bilayers (SLBs) have provided researchers with stable and reproducible platforms to recreate cell membrane environments. The planar structure of the model means a variety of patterning techniques can be employed to recreate membrane architecture on both a micro and nanoscale. In particular pre-patterned substrates are of great interest as they eliminate complications associated with preserving membrane integrity during patterning. Plasma polymers provide a versatile method of creating thin films with a variety of different surface chemistries. In this work we explore the behaviour of plasma coatings in aqueous conditions and the use of plasma films for creating patterned SLBs using vesicle collapse. A variety of micropatterned surface chemistries were formed using commonly used plasma polymers such as allylamine and acrylic acid combined with standard UV photolithography techniques. Characterisation of film behaviour and bilayer formation was conducted using a variety of techniques including ellipsometry, quartz crystal microbalance with dissipation (QCM-D), confocal microscopy and atomic force microscopy (AFM). This study adds to the currently limited literature considering plasma film behaviour in aqueous conditions. Plasma coatings provide a versatile technique for micropatterning SLBs and have advantages over other commonly used techniques such as microcontact printing which suffers from PDMS contamination. Further optimisation of the plasma patterning process may yield increased resolution and chemistries to aid the development of increasingly complex SLB systems.

BI-TuP6 Pseudomonas Aeruginosa Biofilm Formation Mechanisms on Highly Ordered Micro and Nano-sized Colloidal-based Patterns, H. Pingle, P.Y. Wang, Swinburne University of Technology, Australia, C.B. Whitchurch, University of Technology Sydney, Australia, P. Koegler, S.M. McArthur, P. Kingshott, Swinburne University of Technology, Australia

Pseudomonas aeruginosa is an opportunistic pathogen with life threatening complications for hospitalised patients needing catheters or other medical devices when it forms biofilms on the surface of that device. Each year almost 16,000 catheters related blood stream infection cases are found in USA only, with estimated mortality rates ranging from 12% to 25% even with use of uncompromising antibiotics. Some research has shown that extra-cellular DNA is involved in *Pseudomonas aeruginosa* biofilm formation but the actual part it plays in initiating attachment and how it helps bacteria to form multicellular biofilms is unknown. New surfaces are therefore seriously needed to understand the exact mechanisms and prevent biofilm formation. We use a novel approach for making chemical micro and nano patterns on material surfaces with the help of self-assembled colloidal particles used as masks for creating advanced material surfaces. Recently we have prepared binary colloidal assembly of different crystal structure over a wide range of size ratios ($Y = \text{small}/\text{large}$) from 0.01 to 0.2 by tuning Y during assembly and characterised the surface using Scanning Electron Microscope (SEM). We found that zeta potential and size ratio are critical for self-assembly crystal formation. When zeta potential over -30 mV resulted in crystal structure formation. Beyond this range, disordered structure or particle-particle adsorption was found. The crystals are used as masks against gold and plasma polymer deposition to create chemical patterns on the surface that are used for immobilising of eDNA to study how *Pseudomonas aeruginosa* attaches to surfaces and form biofilms.

BI-TuP7 Quantification of the Adhesion Strength of the Diatom Navicula perminuta in a Microfluidic Assay, M. Alles, C. Christophis, University of Heidelberg, Germany, M.E. Callow, University of Birmingham, UK, M.H. Grunze, University of Heidelberg, Germany, A. Rosenhahn, Ruhr-University Bochum, Germany

In recent years Fouling-Release (FR) technologies have been significantly improved and can be considered as an environmental benign approach against marine biofouling [1]. FR coatings refer to those coatings on which microorganisms adhere only weakly allowing their release by low shear stresses present e.g. at the hull of a cruising ship. To study cell adhesion strength on different substrates quantitatively, a microfluidic shear force assay was developed [2-3]. After an attachment phase, the adhesion strength of cells can be measured by detaching them from substrates using a stepwise increased flow across 6 orders of magnitude starting with very low shear forces of $0.01 \text{ dyn}\cdot\text{cm}^{-2}$. With this device we can determine both, the fraction of adherent cells and the critical shear stress which is necessary to remove 50% of the adherent cells. Diatoms are frequently observed biofoulers and prevalent on fouling-release coatings commercially used [4]. In the presented work we tested the effect of different incubation conditions and attachment geometries on the attachment strength of the marine diatom *Navicula perminuta*. Furthermore we used chemically different substrates to determine if adhesion strength of *Navicula* is changed on potential foul-release chemistries. By this microfluidic approach, inert chemistries can readily be discriminated from surfaces with low foul release properties and the high sensitivity allows revealing even subtle differences in adhesion caused by a change in surface properties.

1. Callow, J.A. and M.E. Callow, *Trends in the development of environmentally friendly fouling-resistant marine coatings*. Nat Commun, 2011. 2: p. 244.
2. Christophis, C., M. Grunze, and A. Rosenhahn, *Quantification of the adhesion strength of fibroblast cells on ethylene glycol terminated self-assembled monolayers by a microfluidic shear force assay*. Physical Chemistry Chemical Physics, 2010. 12(17): p. 4498-4504.
3. Christophis, C., et al., *Shear Stress Regulates Adhesion and Rolling of CD44+ Leukemic and Hematopoietic Progenitor Cells on Hyaluronan*. Biophysical Journal, 2011. 101(3): p. 585-593.
4. Zargiel, K.A., J.S. Coogan, and G.W. Swain, *Diatom community structure on commercially available ship hull coatings*. Biofouling, 2011. 27(9): p. 955-965.

BI-TuP9 Bacterial Deposition of Patterned Cadmium Sulfide Thin Films, K.E. Marusak, S. Payne, Y. Cao, L. You, S. Zauscher, Duke University

The need for new energy harvesting techniques increases, and research in photovoltaics is becoming more and more essential. In particular, there has been a growing research effort focused on "green" manufacturing techniques, including the use of bacteria to precipitate semiconducting nanoparticles. We argue that *E. coli* has tremendous potential in the fabrication of patterned cadmium sulfide thin films for solar cell applications. Here we capitalize on the ability of genetically engineered *E.*

coli to precipitate cadmium sulfide nanoparticles, through the expression of the *Treponema denticola* cysteine desulfhydrase gene,¹ and we show that these genetically engineered *E. coli* have the ability to form patterns and monolayers on silica, glass, and indium tin oxide. Furthermore, we discuss the properties of the deposited cadmium sulfide nanoparticles and films, where we have used X-ray photoelectron spectroscopy, FTIR spectroscopy, X-ray diffraction, and scanning electron microscopy.

1. Wang, C.L., et al., *Applied Microbiology and Biotechnology*, 2001. (3): p. 425-430.

BI-TuP10 Lipid Membranes as Dynamic Templates for the Assembly of Inorganic Nanoparticles, P. Bao, G.R. Heath, J. Roth, B. Johnson, M. Cheetham, R.J. Bushby, S.D. Evans, University of Leeds, UK

Supported lipid bilayers have found widespread use as a model system for the investigation of basic properties of cell membranes, as well as for the development of diagnostic assays and in biosensing [1-3]. The potential of supported lipid bilayers however is still not fully realised considering the possibility of fine tuning the surface charge, fluidity, and organisation at the molecular level. In this work we have been interested in using the dynamic nature of the planar membrane as a substrate to support the crystallisation of monolayers gold nanoparticles. Two different methods of crystal formation have been investigated. In the first negatively charged gold nanoparticles were attached to a neutral lipid bilayer via cholesterol anchors and concentrated via the application of an electric field within the plane of the membrane [4-8]. This resulted regions of high nanoparticle density. We describe results of electric field annealing and the role of nanoparticle concentration on the structures formed. In the second approach we first created a bilayer displaying a phase-separation, into liquid ordered and disordered regimes and containing a small fraction of positively charged lipid. Interestingly the gold nanoparticles spontaneously assembled on the liquid ordered regimes to form quasi-crystals of nanoparticles.

The presentation will describe our combined fluorescence microscope and atom force microscope (AFM) studies on these systems and the role of temperature on assembly formation as well as the mechanism related to the crystallisation. Our results may inspire a wider application lipid bilayers as dynamic structures for the directed assembly of inorganic materials.

References

1. P. S. Cremer, T. L. Yang, *J. Am. Chem. Soc.*, 1999, 121, 8130
2. T. J. Groves, L. K. Mahai, and C. R. Bertozzi, *Langmuir*, 2001, 17, 5129
3. E. T. Castellana, and P. S. Cremer, *Surf. Sci. Rep.*, 2006, 61, 429
4. M. Stelzle, R. Miehlich and E. Sackmann, *Biophys. J.*, 1992, 63, 1346
5. J. T. Groves and S. G. Boxer, *Biophys. J.*, 1995, 69, 1972
6. C. Liu, C. F. Monson, T. Yang, H. Pace and P. S. Cremer, *Anal. Chem.*, 2011, 83, 7876
7. M. R. Cheetham, J. P. Bramble, D. G. G. McMillan, L. Krzeminski, X. Han, B. R. G. Johnson, R. J. Bushby, P. D. Olmsted, L. J. C. Jeuken, S. J. Marritt, J. N. Butt and S. D. Evans, *J. Am. Chem. Soc.*, 2011, 133, 6521
8. P. Bao, M. R. Cheetham, J. S. Roth, A. C. Blakeston, R. J. Bushby, S. D. Evans, *Anal. Chem.*, 2012, 84, 10702

BI-TuP14 Biocompatible Hydrogel Materials - Surface Properties and Deposition Comparison of Commercially Available Contact Lenses, K.A. Wygladacz, D.J. Hook, S.E. Norton, Bausch and Lomb

Hydrogel contact lenses are ophthalmic devices designed to correct refractive errors. Wettability, modulus, friction, oxygen permeability, and topography are some of the factors that influence lens comfort and performance. In addition, elimination of deposition of proteins and lipids on the lens surface from the tear fluid is of particular interest as it may influence contact lens surface wettability and impact comfort negatively. Thus, the surface chemistry and morphology of a durable and biocompatible hydrogel material should be carefully fashioned.

The objective of this research was to understand the properties of modern daily disposable contact lens materials. The surface composition, morphology, wettability and protein/lipid uptake of worn and unworn nesofilcon A and delefilcon A hydrogels were examined by X-ray Photoelectron Spectroscopy (XPS), Atomic Force Microscopy (AFM), and Captive Bubble (CBCA). Lenses from 5 healthy adults were examined after 4 hours of continuous wearing. A Dimension ICON AFM was used to characterize the unworn and worn hydrogels. Topography, peak to valley, and roughness (RMS) were recorded. AFM phase lag was used to evaluate lipid/protein deposition. Multipoint XPS spectral analysis was performed to establish the spatial distribution of elements over a large area of the hydrogel. CBCA was done to compare the wettability of unworn lenses.

AFM and XPS characterization revealed significant surface chemistry and morphology differences between worn and unworn lens materials. XPS mapping showed a uniform distribution of the identified elements on the

surface of unworn nesofilcon A and also detected the presence of a coating on delefilcon A. Unworn nesofilcon A exhibited a smooth featureless surface morphology with RMS of 1.9 ± 0.2 nm while unworn delefilcon A showed clear presence of a branched surface coating (RMS = 14.2 ± 5.5 nm) with peak to valley as deep as 61.4 ± 18.8 nm. It was established that the wear process changes the contact lens material morphology. The changes observed in the case of worn nesofilcon A were minor, while those observed for worn delefilcon A were quite pronounced. Both daily disposable materials attracted lipid/protein deposits. The topography of worn nesofilcon A was uniform and it was not altered by wear. The branched surface coating of delefilcon A collapsed during 4 hours of wear on eye and was no longer detected by AFM. In addition, delefilcon A attracted more deposits than the nesofilcon A. Topography and phase lag AFM imaging of worn delefilcon A did not detect any areas that would be lipid/protein deposit free. In terms of stability and lipid/protein deposition nesofilcon A was superior.

BI-TuP15 Nanoscale Topographical Control of Graphene Architecture by Replication of DNA Nanostructures, Y.K. Moon, Sungkyunkwan University, Republic of Korea

Graphene is a very fascinating material because of its unique mechanical and electronic properties. One of the major challenges for graphene is to control its electronic structure in a designed manner for various device applications. To control the electronic structure and unit size of graphene nanostructures, various approaches have been reported, including fabrication of graphene nanoribbons, chemical functionalization of graphene, control of strain applied to graphene by stretching or bending and nanoscale control of three-dimensional (3D) topography of graphene. Among these, the 3D topographical control of graphene showed interesting phenomena such as a pseudo-magnetic field, which was observed in 3D strained graphene on Pt nanobubbles by scanning tunneling microscopy. The 3D topographical control of graphene at the nanoscale level is quite difficult because graphene intrinsically prefers a two-dimensional (2D) structure. Although graphene with local 3D topography was reported to exist in the form of nanobubbles on a Pt (111) surface, ripples on CVD graphene, and corrugated structures on double strand deoxyribonucleic acids (ds-DNAs), there are limits to the geometrical shapes that can be constructed.

It is not possible for graphene itself to produce the designed 3D structures except by creating artificial defects in graphene. Designed templates with nanometer-scale precision are thus required to make various 3D graphene structures in a controlled manner. DNA nanotechnology has provided a platform to construct artificially designed nanostructures which were self-assembled with precisely controllable and programmable nanoscale features with the aid of oligonucleotide recognition. Here, we demonstrate that the nanoscale 3D topography of graphene can be controlled in a designed manner by using artificially designed DNA nanostructures with a high degree of geometrical freedom. Two DNA nanostructures, a one-dimensional (1D), five-helix ribbon (5HR) structure and a 2D double-crossover (DX) lattice, were self-assembled in a solution during annealing. After formation of DNA nanostructures, the samples were deposited on a mica surface. CVD graphene, which was grown on a Cu foil, was transferred onto the DNA nanostructures on the mica surface; during this process, graphene nanostructures were successfully replicated from DNA nanostructures. After the successful production of the designed 3D topography of graphene replicated from DNA nanostructures, we further studied its thermal stability. The influence of temperature on its topography and electrical properties was verified by atomic force microscopy (AFM) and a four point probe, respectively.

BI-TuP16 The Effects of Glycation on Serum Proteins' Affinities for Hemin, A.R. Mercer-Smith, M.S. Johal, Pomona College

Non-enzymatic glycosylation is the process by which sugars covalently bond to proteins, potentially altering their structure and function. We investigated the change in affinity of physiologically-relevant proteins for hemin, a small iron containing molecule when it was incubated for two weeks with three sugars: glucose, fructose, and glyoxal. The formation of protein-heme complexes was measured using a Quartz Crystal Microbalance (QCM). We hypothesize that as the protein's exposure time to sugar increases, less hemin will bind to the protein. A decrease in the protein's binding affinity for hemin can negatively impact the protein's ability to transport hemin, which can even lead to free hemin in the blood. Free hemin may lead to higher rates of bacterial infection as some bacteria may use it as a micronutrient.

Energy Frontiers Poster Session

EN-TuP1 CO₂ Conversion by RF Plasma – Mass Spectrometer Quantification, L. Nittler, M. Mugumaoderha Cubaka, J.-J. Pireaux, University of Namur, Belgium

One of the actual major societal challenges is the reduction of the CO₂ emission. This can be achieved either by controlling the production of this greenhouse gas, or by converting the ejected CO₂ into other molecule(s) which then can be used in other industrial processes, or by the sequestration of the gas.

In this fundamental study, pure CO₂ is transformed in an Inductively Coupled RF plasma at low pressure, under different experimental conditions (pressure, flow, power, pulsing...), in order to optimize its conversion into CO. The challenge of this approach consists in quantifying *in situ* the reaction yield. We show that by calibrating a quadrupole mass spectrometer with reference gases, it is possible to reach this goal. We present CO₂ → CO conversion rate reaching up to 70%, for different plasma and pressure conditions, with a reactor energy efficiency up to 2%.

The measurements were compared with the results from a 2D plasma simulation based on the drift and diffusion approximation.

Funded through the Greenwin Gazton project (Région wallonne, Belgium)

EN-TuP2 Deposition of Size-controlled Ge Nanoparticle Film by High-pressure rf Magnetron Sputtering for Quantum Dot Solar Cells, D. Ichida, G. Uchida, H. Seo, K. Kamataki, N. Itagaki, K. Koga, M. Shiratani, Kyushu University, Japan

We here present deposition of Ge nanoparticle films for quantum dot solar cell applications. Semiconductor nanoparticle films have attracted much attention because of the unique characteristics such as tunable band gap and multiple exciton generation effects of quantum dots [1]. Ge nanoparticles have more outstanding quantum confinement effects than Si nanoparticles due to the larger excitonic Bohr radius of 24.3 nm for bulk Ge than 4.9 nm for bulk Si. In this study, we deposited Ge nanoparticle films by radio frequency (rf) magnetron sputtering in argon and hydrogen gas mixture at 20 % H₂ dilution ratio under a high pressure condition of 1.5 Torr. At such high pressure, Ge nanoparticle formation in gas phase is possible, because the mean free path of Ge atoms is as short as an order of micrometer.

We measured Raman spectra of Ge thin films and bulk Ge crystal. We obtained the full width at half maximum (FWHM) and peak frequency of each peak of Raman spectra, as a function of gas flow rate (R_{gas flow}). The film deposited at R_{gas flow} = 80 sccm shows a peak at 298 cm⁻¹, and this peak is assigned to Ge crystal. As R_{gas flow} increases, the peak slightly shifts to higher frequency, and FWHM increases from 7.2 cm⁻¹ at R_{gas flow} = 80 sccm to 11.7 cm⁻¹ at R_{gas flow} = 250 sccm. FWHM and peak frequency strongly depend on the particle size [2]. From the dependence, the Ge particle size at R_{gas flow} = 250 sccm is deduced to be 6-7 nm. We also fabricated in Ge quantum-dot sensitized solar cells, and succeeded in carrier generation in Ge nanoparticles.

[1] G. Uchida, *et al.*, "Effect of nitridation of Si nano-particles on the performance of quantum-dot sensitized solar cells", *Jpn. J. Appl. Phys.*, Vol. 51, pp. 01AD01-1 – 01AD01-5, 2011.

[2] M. Fujii, *et al.*, "Raman scattering from quantum dots of Ge embedded in SiO₂ thin films", *Appl. Phys. Lett.* Vol. 57, pp. 2692 – 2694, 1990.

EN-TuP3 Fabrication and Characteristics of ZnO Nanowire-based DSSCs with Core-Shell Layers, E.C. Choi, B. Hong, Y. Seo, Sungkyunkwan University, Republic of Korea

Dye-sensitized solar cells (DSSCs) have been widely investigated as a next-generation solar cell because of their simple structure and low manufacturing cost. The TiO₂ film, which consists of nano-particles, acts as both a scaffold with a high surface-to-volume ratio for the dye loading and a pathway to remove the electrons. However, charge carriers have to move across many particle boundaries by a hopping mechanism. So, one-dimensional nano-structures such as nanotubes, nanorods and nanowires should improve charge carrier transportation by providing a facile direct electron pathway and lowering the diffusion resistance. Recently, ZnO nanowire-based DSSCs have great attractions due to higher electron mobility than TiO₂, potentially allowing for faster kinetics and fewer recombinations. However, the highest efficiencies of ZnO nanowire-based DSSCs are less than 2 %. It has been known that ZnO nanowire-based DSSCs have suffered from low efficiencies through a combination of low level of dye adsorption (due to the thinness of the active layer), defect states

and the formation of excessive Zn²⁺/dye agglomerates. According to the previous researches, it is considered that the ZnO nanowire-based DSSC performance could be improved through longer and well aligned nanowire arrays on the substrate and electrodes with core-shell structures. In this work, ZnO nanowire arrays were synthesized by hydrothermal method in aqueous solution of zinc nitrate (Zn(NO₃)₂·6H₂O) and hexamethylenetetramine (C₆H₁₂N₄). Properties of core-shell structures were investigated by various analysis methods such as X-ray diffraction, field emission scanning electron microscopy (FESEM), and UV-visible spectrophotometer. It was confirmed that the conversion efficiency of ZnO nanowire-based DSSCs depended on the nanowire properties.

EN-TuP4 A Study on High Efficiency Large Scale Dye-sensitized Solar Cell (DSSCs) Fabrication by the Reduction of Adsorption Time through the Varied Dye-Coating Condition, Y. Seo, B. Hong, E.C. Choi, Sungkyunkwan University, Republic of Korea

Dye-sensitized solar cell (DSSC) has been expected to be an alternative to the conventional silicon solar cell due to simple manufacturing process and low fabrication cost [1]. The condition of dye-coating process is one of the important factors in the fabrication process. In order to enhance dye adsorption on the TiO₂ layer of large scale DSSC, the condition was optimized for the dye-coating process such as temperature, time and concentration of base on reference paper [2].

In this work, we report dye-coating conditions to enhance the efficiency of which was made in the area of 0.25, 6 and 15 cm². The experiment shows the optimal coating condition with the coating temperature of 70 °C, the dye concentration of 10 mM and the coating time of 3 min. We confirmed that the energy conversion efficiencies of DSSCs with area 6cm² (3X2) and 15cm² (3X5) were about 5% and 4.5%, respectively.

REFERENCES

[1] B. O'Regan, M. Gratzel, *Nature*, 353, 737, 1991

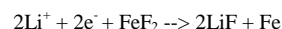
[2] *Electrochimica Acta* 66(2012)121-125

EN-TuP7 Angle-Resolved X-Ray Photoelectron Spectroscopy of Iron (II) Fluoride upon Lithiation as a Conversion Reaction Battery Material, R. Whitcomb, Rutgers Department of Physics and Astronomy Summer REU Program, R. Thorpe, S. Rangan, R.A. Bartynski, Rutgers, The State University of New Jersey

For the use of promising new technologies such as electric cars and smart power grids to become more widespread, batteries must be developed with the ability to store larger amounts of energy. Increases in energy density are often accomplished by substituting different compounds into already successful commercial battery architectures. As one of the most common types of portable power cells, conventional lithium ion batteries rely upon intercalation to store charge in the cathode:



This process can be improved by replacing lithium cobalt oxide with a conversion reaction material, whose structure and composition are instead chemically altered by lithiation. In particular, a cathode composed of FeF₂ can react with lithium ions to produce metallic iron, storing an additional electron per formula unit:¹



However, the mechanism by which this reaction progresses is not well understood, so it is important to investigate the chemical phase and morphological changes caused by the lithiation process in a model system. This has been accomplished by working with well-characterized samples outside of the electrolytic environment of a typical battery, thereby isolating the fundamental properties of the reacting materials. My poster describes the spectroscopic analysis of epitaxial iron (II) fluoride (110) thin films in ultrahigh vacuum, before and after a series of lithium exposures. Angle-Resolved X-Ray Photoelectron Spectroscopy (ARXPS) was used to determine the chemical concentrations of the material as a function of depth in the film. Evidence supports a uniform reaction front progression downwards from the surface of the film, but with the presence of a barrier to full conversion of the fluoride. Funding for this project was provided by the National Science Foundation grant PHY-1263280.

¹ Rangan, S.; Thorpe, R.; Bartynski, R. A.; Sina, M.; Cosandey, F.; Celik, O.; Mastrogiovanni, D. D. T. *J. Phys. Chem. C* **2012**, *116*, 10498-10503.

EN-TuP8 Growth and Characterization of Cu₂ZnSnSe₄ Thin Films for Photovoltaic Applications Obtained from Sputtered Precursors, K. Monfil-Leyva, BUAP, Mexico, P.J. Pathiyamattom, UNAM, Mexico, A.L. Muñoz Zurita, FIME-UAC, Mexico, F.J. Flores Gracia, BUAP, Mexico

The research on quaternary compound semiconductors has been increased in particular due to their photovoltaic applications and the increasing price and scarcity of many elements (Cd, Te). Currently, the semiconducting kesterite-type Cu₂ZnSnSe₄ (CZTSe) arises as an important and interesting

alternative to play an important role in the energy conversion domain in the future. This work shows the development of CZTSe thin films obtained by a dc sputtering equipment. First, multiple thin layers were deposited on glass substrates by alternate sputtering of single metallic sources: (Cu/Zn/ Sn). Samples had a selenization process at different temperature and time in order to study the effect on the optical, structural and electrical properties. The transmittance and reflection properties were determined using a UV-Vis Spectrophotometer. The absorption coefficient of the films was estimated to be around 10^5 cm^{-1} and the band gap energy was in the range between 1.35 and 1.65 eV. The $\text{Cu}_2\text{ZnSnSe}_4$ films were characterized using X-Ray Diffraction (XRD) and Scanning Electron Microscopy (SEM). The XRD data showed clear peaks corresponding to $\text{Cu}_2\text{ZnSnSe}_4$, the main growth orientations were [112], [213] and [312]. Grain size and lattice parameters were calculated and related with the selenization temperature. The SEM images indicated that selenization temperature controls the nanocluster size and density on surface. Photoconductivity measurements of the CZTSe samples showed an increase on photogeneration of charge carriers. Band gap energies, stoichiometry and photocurrent of CZTSe films obtained by sputtering of single metallic sources are suitable for photovoltaic applications.

Magnetic Interfaces and Nanostructures

Room: Hall B - Session MI-TuP

Magnetic Interfaces and Nanostructures Poster Session

MI-TuP1 Synthesis and Characterization of $\text{Zn}_{1-x}\text{Co}_x\text{O}/\text{ZnO}$ Hollow Nanosphere Structures. *D.R. Liu, W.-H. Cho, C.J. Weng*, ITRC, NARL, Taiwan, Republic of China

Diluted magnetic semiconductors (DMS) have recently attracted considerable attention due to their potential applications for spintronic devices, such as spin-valve transistors, nonvolatile memory, and magneto-optical switches. ZnCoO is one of the most promising diluted magnetic semiconductors materials due to its high temperature ferromagnetism. In this study, ZnO layer was conformally deposited on the surface of polystyrene (PS) nanosphere with different diameter (100nm~800nm) by atomic layer deposition (ALD). After removal of PS nanosphere by heating, ZnO hollow nanospheres were formed. Then the $\text{Zn}_{1-x}\text{Co}_x\text{O}$ ($x=0-0.1$) coatings were grown on ZnO hollow nanospheres by pulsed laser deposition (PLD). According to the results of high-resolution x-ray diffraction, the $\text{Zn}_{1-x}\text{Co}_x\text{O}/\text{ZnO}$ hollow nanospheres are polycrystalline with a preferential growth direction of (002). The surface and cross-section morphologies of the hollow nanospheres were analyzed using a field-emission scanning electron microscope (FE-SEM). The magnetic properties of the nanospheres were measured by a vibrating sample magnetometer (VSM) and x-ray magnetic circular dichroism (XMCD) spectroscopy. The results show the magnetic properties of $\text{Zn}_{1-x}\text{Co}_x\text{O}/\text{ZnO}$ hollow nanospheres strongly depend on the Co composition fraction and the size of nanospheres.

MI-TuP2 Exchange Bias Tuning with Temperature and Pt Ratios in $\text{Pt}_x\text{Co}_{1-x}/\text{CoO}$ Bilayer. *M. Erkovan, M. Ozturk, E. Demirci, N. Akdogan, O. Erdemir, O. Ozturk*, Gebze Institute of Technology, Turkey

In this study, we report EB effect observed in $\text{Pt}_x\text{Co}_{1-x}$ (x changes from 10 to 90 by 10 step)/ CoO bilayer thin films. PtCo alloys have very large magnetocrystalline anisotropy so they will be very good candidate for next generation data storage media. Besides EB effect is used in the read head sensors, so PtCo may find usage area in both the read head sensor and data storage media. Our goal was to determine how EB depends on Pt concentration in ferromagnetic PtCo layer and temperature.

All films were prepared at UHV conditions by magnetron sputtering deposition technique. The chemical ratios of PtCo layers and CoO layers for all composite films were characterized by Photoelectron Spectroscopy (XPS) technique. Quantum Design PPMS 9T vibrating sample magnetometer (VSM) was used to investigate EB properties of the films. Since the Néel temperature is about 290 K for antiferromagnetic CoO layer, $\text{Pt}_x\text{Co}_{1-x}/\text{CoO}$ films were heated up to 320K before cooling down to the measurement temperature to observe Exchange bias effect. An in-plane magnetic field of 2 kOe was applied while cooling the samples to the measurement temperatures.

Temperature-dependent magnetization measurements show that strength and onset temperature of exchange bias are enhanced by increasing Pt concentration. We observed also two different results from magnetization measurement. One of them is that the blocking temperature (T_B) of both samples is lower than the expected bulk value. The other one is that decreasing Pt concentration within the FM PtCo layer reduces T_B to lower values. In order to determine the effect of Pt concentration on magnetic

anisotropies, the samples have been investigated by using ferromagnetic resonance (FMR) technique at room temperature (RT). FMR experiments show uniaxial in-plane magnetic anisotropy at room temperature. This behavior becomes stronger when the Pt concentration is increased. According to these results, the manipulation of common interface between ferromagnetic and antiferromagnetic layers gives the possibility to tune the exchange bias with Pt concentration and temperature.

MI-TuP4 Internal Magnetic Friction of Gold-Nickel Alloy Substrates on a Quartz Crystal Microbalance. *K.M. Stevens, L. Pan, J. Krim*, North Carolina State University

The study of magnetic friction provides an opportunity to access bulk properties of the material and internal dissipation pathways. This gives benefits beyond that of surface studies, which assume a uniform substrate response and typically access phononic, conduction and charging pathways. This technique has been used successfully to study superconductivity-dependent friction [1,2] and nonhomogeneous magnetic microstructures[3-5].

We study gold-nickel alloys, as these provide an interesting spectrum of bulk magnetic properties. Samples with 5-20% nickel alloyed with gold were deposited as a homogenous solid-solution or as a two-phase FCC solid through the modification of annealing procedures. The solid solution is known to be paramagnetic for concentrations below 35% Ni [6], while the two phase solid maintains domains of ferromagnetism within bulk gold. These materials have been deposited onto a quartz crystal microbalance to allow properties to be monitored continuously by measuring the frequency and amplitude of the oscillator [7].

The two-phase Ni/Au material has demonstrated unique properties. Prior work has shown this to be an exceptional candidate for MEMS electrodes [8]. This work explores the impact of the bulk inhomogeneity. We have observed a “flexing” effect due to the application of an external magnetic field on two-phase alloy samples, which is measured as a discrete decrease of oscillator amplitude synchronized with the applied field; the effect is not seen on the solid solution samples of the same nickel-gold composition. The results are consistent with the formation of internal shear waves around the domains of nickel within bulk gold. An internal degree of freedom at the grain boundaries may decrease friction even in the absence of an external magnetic field.

Funding provided by NSF DMR.

- [1] I. Altfeder and J. Krim, *J. Appl. Phys.* **11** (2012)
- [2] M. Highland and J. Krim, *Phys. Rev. Lett.* **96** (2006)
- [3] M. Wünsche et al., *Z. Phys. Chem.*, **208**, 225-238 (1999)
- [4] G. Yu et al., *Rev. Sci. Inst.* **78**, 065111 (2007)
- [5] G. Yu et al., *J. App. Phys.* **104**, 043908 (2008)
- [6] A.R. Kaufmann et al., *Rev. Mod. Phys.* **17**, 1 (1945)
- [7] J. Krim, *Advances in Physics*, **61**, 3, 155-323 (2012)
- [8] L. Pan, Ph.D. Thesis, North Carolina State University (2011)

MEMS and NEMS

Room: Hall B - Session MN-TuP

MEMS and NEMS Poster Session

MN-TuP1 Analysis of Convective Performance in Confined Droplets with Various Working Fluids and Substrates for Polymerase Chain Reaction Applications. *P.L. Chen, C.S. Yu, C.C. Yang, Y.H. Lin, Y.H. Tang, M.H. Shiao, C.-N. Hsiao*, National Applied Research Laboratories, Taiwan, Republic of China

Polymerase chain reaction (PCR) is a procedure which repeating thermal cycles with three discrete temperature steps, including denaturation (95°C), annealing (60°C), and extension (72°C) for deoxyribonucleic acid (DNA) amplification. It usually takes 1 or 2 hour to complete the PCR process in commercial equipment. In order to reduce reagent solution and increase heat transfer rate, micro-electro-mechanical-systems (MEMS) and microfluidic technologies are utilized to miniaturize the PCR system. Furthermore, a new concept for the development of microchips that uses Rayleigh-Bénard (RB) convection to perform PCR amplification of DNA is rapidly increased in the past few years. However, the challenges for RB-PCR devices involve the control of flowing performance and chemical pollution. The aim of present work is to investigate the convective performance in a 2 μl droplet for the application of real-time PCR with computational fluid dynamics (CFD) techniques. The influence of several major parameters, such as the viscosity and density of working fluid, and the type of substrate on the overall temperature distribution, pressure drop

and velocity distribution were all analyzed and discussed. The simulated results show that the steady state was reached in 3 seconds and 30 cycles were completed in 10 minutes inside the droplet by controllable flowing conditions. The droplet based RB-PCR device offers a miniaturized thermal circulation system by natural convection without tedious three steps temperature control or flow control and potentially applicable for real-time DNA microarray analysis.

MN-TuP2 The Study of Convex Corner Compensation for Dry Anisotropic Etching of Single Crystal Silicon in ICP-RIE, Y.H. Lin, Y.H. Tang, ITRC, NARL, Taiwan, Republic of China, W. Hsu, NCTU, Taiwan, Republic of China, P.-L. Chen, C.C. Yang, M.-H. Shiao, C.-N. Hsiao, ITRC, NARL, Taiwan, Republic of China

In this paper, the compensation structure assisted the convex corner structures etch in inductively coupled plasma reactive ion etch (ICP-RIE) have been studied. The convex corner structures are widely used in many applications like micro optical devices or micro sensors. There are many researches to discuss the convex corner structure under wet etch, but rare researches for dry ICP-RIE etching. In anisotropic silicon etching, under the Bosch patent, sequentially alternating etch and passivation cycles can easily achieve high aspect ratio silicon structures. The feature size of the convex corner structures is difficult to maintain as original design at the bottom position in deep etch, due to some non-vertical movement plasma. The non-vertical movement plasma caused by collision between plasma ions, pollutants or rebounded from the etching mask. The compensation structure is design in front of the convex corner structure. The compensation structures can obstruct the non-vertical plasma to etch the convex corner structure and reduce the etch lag effect during the etch process leading to better profile at deep etch. The current study systematically investigates plasma condition to verify feasibility of the proposed method, and discusses effect of the gap between compensation structure and convex corner structure at three different gaps of 15, 10, 5 μ m. It demonstrate the convex corner structure have better profile with compensation structure at 5 μ m gap than other at deep ICP-RIE etching.

Keywords: Convex corner compensation, Inductively-Coupled-Plasma Reactive-Ion-Etch (ICP-RIE), High-aspect-ratio structure

MN-TuP3 Micro Fabrication on Quartz Glass by Inductively Coupled Plasma-reactive Ion Etching and its Optical Application, Y.H. Tang, Y.H. Lin, P.-L. Chen, M.-H. Shiao, C.-N. Hsiao, ITRC, NARL, Taiwan, Republic of China

The etching characteristics of inductively coupled plasma-reactive ion etching (ICP-IRE) on the micro structure of quartz glass were investigated with a negative photoresist (KMPR 1050) etching mask material. We found that a nearly vertical side wall of the fabricated quartz glass profile with KMPR 1050 mask (negative photoresist). Detailed process characterization was performed by varying the process parameters which include ICP power, bias power and chamber pressure. In the case of KMPR mask, which has excellent material strength and good verticality, the etched micro structure exhibited a depth of 44.6 μ m and vertical sidewall angle of 89 $^\circ$ by means of ICP power 1500 W, bias power 120 W, and chamber pressure at 10 mTorr under a mixture gas of C₄F₈ and He at 12 and 84 sccm of flow rates, respectively. Moreover, the etching rate was controlled approximately at 0.249 μ m per minute, the etching selectivity was more than a ratio of 1:2, and the roughness of etched surface was around 12.9 nm. Furthermore, the advantage of pattern transfer with high resolution and high accuracy has been demonstrated by fabricating subwavelength structure (SWS), achieving broadband antireflection (AR) and increasing the transmittance of incident light across the quartz glass. Consequently, smoothly tapered SWS surfaces with a width of 105 nm and a height of 190 nm could be produced on quartz wafer. This fabricated SWS decreased the surface reflectance to less than 6.75 % in the visible light spectrum.

MN-TuP4 Finite Element Model Verification of High Frequency Piezoelectric Contour-Mode MEMS Resonators Using Laser Vibrometry, K.R. Qalandar, B.A. Gibson, L.A. Shaw, S.Y. Chiu, University of California, Santa Barbara, A. Tazzoli, J. Segovia, Carnegie Mellon University, M. Rinaldi, Northeastern University, G. Piazza, Carnegie Mellon University, K.L. Turner, University of California, Santa Barbara

This paper reports the first FEA model verification of AlN contour-mode resonators (CMRs) using laser Doppler vibrometry (LDV) at frequencies above 1GHz. Full 3D models of UHF resonators are able to determine electrical and mechanical responses, including AF response, admittance curves, and full 3D mode shapes. The modal analysis here differs from previous works [1-3] by making direct quantitative comparisons between measured and simulated responses.

The 1GHz lateral-field CMRs consist of a thin film of AlN patterned with interdigitated metal electrodes on top and a floating electrode on bottom. An AC signal to the electrodes excites the contour-extensional mode

through the equivalent d₃₁ piezoelectric coefficient of the AlN [4,5]. The devices are characterized by mechanical and electrical measurements. A Polytec UHF120 LDV captures phase and out-of-plane displacement data, with $\pm 1.4\mu$ m resolution down to a noise floor of 4 μ m (Fig. 1). Spatial scans across the surface generate 3D mode shapes (Fig. 2). By performing frequency sweeps and fitting data to the equations of motion, we extract mechanical parameters such as the linear and nonlinear stiffness and damping coefficients. Electrical measurements further validate simulation results; through the electromechanical coupling coefficient the mechanical measurements can also be confirmed.

The 3D FEA models are developed in COMSOL and used to determine both mechanical and electrical responses. We compare simulated frequency response, out-of-plane displacement, and Q with experimental data to verify the models (Table 1). Fig. 2 shows the 3D mode shape, and the out-of-plane displacement profile of individual fingers is shown in Fig. 3. The maximum seen in experiments is 119.5 μ m, which agrees well with the simulated value of 117 μ m. To compare mechanical response, the wavelength λ in the lateral direction is studied. Simulations show a 3.2 μ m and 7.9 μ m wavelength at resonance. Experimentally, a 4 μ m and an 8 μ m wavelength appear. The multiple wavelengths at resonance are the result of a mismatch in acoustic velocity between AlN and Al and their existence in the simulation serves as further validation. Simplified five-finger device simulations show good fit with experimental admittance (Fig. 4). Full 33-finger device simulations, currently in progress, will improve this fit.

The experimental data gives further insight into the operation of the devices and is essential to the verification the 3D FEA models. With confirmed accuracy, these models can be used for predictive modeling of GHz-range CMRs. This allows optimization of geometric parameters such as electrode spacing and anchor performance.

MN-TuP5 Phase Noise-Based Bifurcation Sensing of Nonlinear MEMS Cantilevers, L. Li, L.A. Shaw, K.L. Turner, University of California, Santa Barbara

The objective of this work is to develop a high frequency MEMS-based mass sensor capable of pushing the limits of sensitivity for the detection of explosive materials. The specific objective is to utilize a nonlinear microcantilever mass sensor functionalized with xerogel-based molecularly imprinted polymers (MIPs) for the selective detection of DNT. This paper reports the implementation of a novel control method for sensing which is based on the phase squeezing phenomenon present in the nonlinear dynamics of a parametrically driven microcantilever. It is expected to significantly improve the mass detection limits compared to bifurcation tracking [1], as well as reduce measurement time by over three orders of magnitude. Sensor speed, sensitivity, and selectivity are all important for ppt level DNT/TNT detection.

Previous work focuses on tracking the resonance frequency shift of the microcantilever due to DNT absorption using bifurcation tracking [1]. Bifurcation sensing is achieved by sweeping the frequency or voltage until a jump event occurs, and tracking is done by repeating the process to detect the frequency shift. However, bifurcation tracking is a time-consuming process which requires time to reset the system back to an appropriate initial condition after each jump event to avoid hysteresis before the next bifurcation occurs. This work reports a new method of sensing which concentrates on monitoring changes in the phase response as the device approaches the bifurcation point. Just prior to bifurcation, noise squeezing occurs due to a slowing down of the response component associated with the bifurcation eigenvalue near the bifurcation point. The statistical variance of the phase response serves as a precursor to activate the feedback control scheme, which employs frequency modulation to stabilize a parametrically-excited sensor at the edge of instability. By maintaining close proximity to the bifurcation, but not allowing the large amplitude growth necessary for existing bifurcation tracking methods, over three orders of magnitude measurement time improvements in the acquisition rate near the location of the bifurcation point can be made [2]. Initial results show that the controller is capable of tracking the resonance frequency based on the phase variance of the microcantilever with close proximity to the edge of instability and control parameters can be tuned to optimize the sensitivity of the sensor. DNT gas sensing using the controller is yet to be experimented and the sensitivity of noised squeezing bifurcation sensing of nonlinear MEMS microcantilever is expected to be presented at the conference.

MN-TuP6 Simulation Study of Processing Parameters for Solder Filled Self Assembled 3D Micro-scale Structures, N. Oraon, International Institute of Information Technology, India, J.C. Luthi, S.L. Burkett, The University of Alabama, M. Rao, International Institute of Information Technology, India

Solder based self assembled (SBSA) structures are formed by transforming 2D patterns to 3D structures. SBSA processing involves conventional lithography, metal deposition, and etching methods in addition to dip

soldering and solder reflow. The processing involves free metals around a fixed metal, when reflowed; the free metal pattern is rotated towards the fixed metal pattern till the solder reaches minimum surface energy. In previous work, we investigated two types of soldering: face and edge-soldered SBSA structures. The 3D structure produces an excess solder when the amount of the solder deposited is more than the 3D volume. The excess solder which is measured from the top of the metal structure to the top of the solder in face-soldered SBSA structures is known as solder standoff height (SSH). SSH is envisioned as being useful as a solder bump that could be used to stack hybrid layers in 3D integration schemes. Experimentally, SSH was found to be heat resistant. The simulation study we performed reflects the effect of processing parameters such as gap-size between metal patterns, solder thickness, and solder coverage on the formation of 3D structures. Formation of 3D structures is influenced by the tilt of free metal towards the fixed metal. Hence tilt angle is considered as one of the output parameters. The processing parameters are analyzed for truncated square pyramid (TSP) and open cube (OC) structures using an open source simulation tool, Surface Evolver.

Surface Evolver is an interactive program for the study of surfaces shaped by surface tension. Simulation results show that as the gap size decreases, the minimum solder energy is attained at lower tilt angles for face-soldered TSP and OC structures. Edge-soldered OC structures follow a similar trend. The tilt angle remains constant for a range of gap sizes for edge-soldered TSP structures. Varying solder thickness varies the minimum energy tilt angle for face-soldered structures. For edge-soldered structures, tilt angle remains constant irrespective of solder thickness. Optimum tilt angle remains constant for solder coverage of 70 % and higher in both TSP and OC structures.

Manufacturing Science and Technology

Room: Hall B - Session MS-TuP

Aspects of Manufacturing Science and Technology

Poster Session

MS-TuP2 Investigation on Environment Concerns of Scanning Electron Microscopy (SEM) for Nanomanufacturing Application. *F.C. Hsieh, P.H. Lin, C.Y. Huang, N. Chu, J.S. Kao*, National Applied Research Laboratories, Taiwan, Republic of China

Scanning electron microscopy (SEM) is used for surface morphology measurement of thin films in nanomanufacturing such as: atomic layer deposition (ALD), nanosphere lithography, and nanoimprint et al. For those nanomanufacturing applications, the surface morphology of thin films could affect the desired properties. As a result, the quality of the image of surface morphology must be evaluated. In this study, the effects of microwave intensity and vibration frequency are investigated. For accelerating voltage of 15kV at magnification of 150,000, the microwave intensity of alternative current (ac) of electric equipment must be below 90nT. However, at 15kV accelerating voltage and 50,000 magnifications, the microwave intensity of ac must be below 70nT. Besides, the allowable amplitude increases with vibration frequency between 2Hz and 5Hz. The maximum amplitude was 6.0 μ m (peak to peak) at 5Hz of vibration frequency. The proposed investigation can provide a suggestion to ensure the accuracy and stability of measurement for SEM.

Nanometer-scale Science and Technology

Room: Hall B - Session NS-TuP

Nanometer-scale Science and Technology Poster Session

NS-TuP1 Photoluminescence Characterization of Crater-Typed Nanostructured Al Surfaces. *I. Atsuro, R. Hoshiya, H. Kato, S. Takemura, T. Hiramatsu*, Kanto Gakuin University, Japan

Fabrication of templates for creating nanoscale structures becomes an important subject for innovation of nanoscale devices. The authors proposed new types of nanoscale structures such as a linked-crater structure and highly-oriented line structure on Al surface by unique combination of chemical and electrochemical processes. In this study, the authors investigate the optical functionality of nanostructures by photoluminescence (PL) measurements. The nanoscale linked-crater structure was fabricated on an Al surface by treatment with Semi Clean, alkali surfactant, and successive electrochemical anodization in 0.37 N H₂SO₄ solution creating a nanoscale finer linked-crater structure on the Al surface. The PL spectra of non-ripple and ripple patterns were observed by using Horiba Jobin-Yvon

Spex Fluorolog-3 fluorimeter. In the case of non-ripple pattern, the PL spectrum showed that the main peak appeared around 400 nm with a long tail slope linearly downwards that stretched up to 550 nm regions. In the case of the ripple pattern, the PL spectrum exhibited a pattern composed of several ripple peaks in 350-550 nm range. The samples that exhibited rippled PL pattern were prepared under the optimized fabrication conditions : anodization current 7-9 mA for 40 min for the sample size of 10 mm \times 20 mm. The peak positions were invariant with the change of excitation wavelength through 300-420nm. Thus, the ripple pattern was originated from the nanostructure origin. The absorbance measurement was also conducted. The ripple absorbance peaks were observed and overlapped partially the rippled emission peaks. The absorbance peak positions were invariant with the change of excitation wavelength.

Non ripple-shaped emission peaks were observed in the case of the samples prepared under deviated conditions. The fabricated nanostructured surfaces were identified as alumina by Fourier transforms infrared spectroscopy (FT-IR). The FT-IR measurement showed that the difference between the ripple and non-ripple PL patterns might be attributed to the peak profiles and the intensity of Al-O mode. In the ripple emission and non ripple pattern, the intensity of Al-O mode at 1170 cm⁻¹ was different between two patterns. The lifetimes and the corresponding relative amplitudes were obtained by time-correlated single photon counting (TCSPC). In the case of ripple pattern, lifetimes and the relative amplitudes were definite values. On the other hand, in the non-ripple pattern, lifetimes and relative amplitudes were deviated from those values.

This work was aided by MEXT-supported Program for the Strategic Research Foundation at Private Universities.

NS-TuP2 Gallium Oxide and Gallium Nitride Nanoparticle Synthesis using Non-Thermal Plasma with O₂ and N₂ Gases. *J.H. Kim*, Korea Research Institute of Standards and Science, Republic of Korea, *K.H. You*, Korea Advanced Institute of Science and Technology, Republic of Korea, *S.J. You, J.I. Lee, D.J. Seong, Y.H. Shin*, Korea Research Institute of Standards and Science, Republic of Korea

Compounds of Ga, such as gallium oxide(Ga₂O₃) and gallium nitride(GaN), are of interest due to its various properties in semiconductor application. In particular, GaN has the potentially application for optoelectronic device such as light-emitting diodes(LEDs) and laser diodes(LDs). The Ga₂O₃ is a promising material for high temperature stable gas sensing, catalytic and optoelectronic device applications[1,2]. Nanoparticle is an interesting material due to its unique properties compared to the bulk equivalents.

In this report, we develop a synthesizing method for the gallium oxide and gallium nitride nanoparticle using non-thermal plasma. For gallium source, the gallium is evaporated by induction heating Nitrogen and oxygen source for nanoparticle synthesis are supplied from inductively coupled plasma with N₂ and O₂ gas. The synthesized nanoparticles are analyzed using field-emission scanning microscope(FESEM), transmission electron microscope(TEM) and x-ray photoelectron spectroscopy(XPS). The synthesized particles are investigated and discussed in wide range of experiment conditions such as flow rate, pressure and RF power.

References

1. L. Li, E. Auer, M. Liao, X. Fang, T. Zhai, U. K. Gautam, A. Lugstein, Y. Koide, Y. Bando and D. Golberg, *Nanoscale*, 3, 1120, 2011.
2. H. Yang, R. Shi, J. Yu, R. Liu, R. Zhang, H. Zhao, L. Zhang and H. Zheng, *J. Phys. Chem. C* 113 (52), 21548, 2009 .

NS-TuP3 Embedded SiGe Alloy Nanoparticles formed by Co-sputtering of Si, Ge. *A. Hernández-Hernández*, CINVESTAV-IPN, Mexico, *L.A. Hernández-Hernández*, ESFM-IPN, Mexico, *F. De Moure-Flores*, UAQ, Mexico, *J.G. Quiñones-Galván*, ININ, Mexico, *M. Meléndez-Lira*, CINVESTAV-IPN, Mexico

Using magnetron co-sputtering of Ge and Si targets, Si:Ge films were fabricated for exploring the influence of SiO₂ roughness on formation, structure, and phonon properties of nanocrystalline Si_{1-x}Ge_x (nc-Si_{1-x}Ge_x). Structural characterization was carried out by grazing angle X-ray diffraction and atomic force microscopy. The electronic properties were studied by room temperature photoluminescence and Raman spectroscopies. Surface roughness was quantified by atomic force microscopy. X-ray diffraction show diffraction peaks due to SiGe alloy nanoparticles and no peaks due to elemental Si or Ge. The nanoparticle size estimated from XRD is around 7.5-12 nm. Raman spectroscopy was revealed that each optical vibration mode (Ge-Ge, Ge-Si, or Si-Si mode) is of evident phonon confinement effect. Photoluminescence emission in visible range it is associated to the quantum confinement. The roughness of the as-deposited amorphous SiO₂ films is an essential factor in determining the crystallization behavior and in controlling NCs size.

*: partially funded by CONACyT-Mexico

NS-TuP4 Post-Annealing Effects on Germanium Nanocrystals Properties. A. Hernández-Hernández, CINVESTAV-IPN, Mexico, L.A. Hernández-Hernández, ESFM-IPN, Mexico, F. De Moure-Flores, UAQ, Mexico, J.G. Quiñones-Galván, ININ, Mexico, M. Meléndez-Lira, CINVESTAV-IPN, Mexico

As-grown light emitting self-assembled Ge nanocrystals (Ge-NCs) embedded in a SiO₂ matrix were produced by a sequential deposition process of SiO₂/Ge/SiO₂ layers employing reactive radio frequency sputtering technique. Obtained Ge-NCs shown a crystallographic phase whose proportion, size, quality and specific orientation are determined by the oxygen partial pressure. Photoluminescence (PL) spectra indicate that the size distribution of Ge-NCs is reduced and centered at around 8 nm when higher oxygen partial pressure is employed, their sizes are consistent with estimates from PL measurements. After vacuum annealing it is observed the elimination of an instable high pressure tetragonal phase of germanium present in as-grown samples. In addition, the PL peaks shifted to higher energies indicating the formation of Ge-NCs probably from Ge dispersed within SiO₂ matrix. It was also found that the PL intensity increases drastically after annealing process. The strong size dependence of the PL spectra indicates that the observed PL originates from the recombination of electron-hole pairs confined in Ge-NCs. This samples exhibit photoresponse in near infrared range.

† : partially funded by CONACyT-Mexico.

NS-TuP5 Photoresponse and Electrical Characterization of Silicon Nanocrystals Embedded within a SiO₂ Matrix. M.A. Melendez-Lira, Cinvestav-IPN, Mexico, E. Mota-Pineda, ESIME-IPN, Mexico

Silicon nanocrystals (Si-NC) embedded within a SiO₂ matrix deposited on p type Si(111) substrates have been successfully produced through a reactive RF sputtering technique employing the ratio of oxygen to argon as parameter to modulate the Si-NC size distribution [1]. The Si-NC shown photoluminescence emission with characteristics dependent on its size. Characterization of the transversal I vs V response present a rectifying-like behavior. The spectral photoresponse curves shown a maximum around 1100 nm with a FWHM dependent on the Si-NC size distribution. The intensity of the spectral photoresponse shown a dependence on the electrical polarization applied on the contacts. The zero of the I vs V curves does not change with the illumination of the sample indicating the absence of a photovoltaic driving force. Results are analyzed taking in account the size and distribution of Si-NC in the SiO₂ matrix.

[1]. E. Mota-Pineda et al. *Journal of Applied Physics* **108**, 094323(2010)

*: The partial financial support of ICyT-DF and CONACyT-Mex is acknowledged

NS-TuP6 Nanoscopic I-V, Photoluminescence and Lifetime Characterization of Polyaniline Dot and Line Patterns. S. Takemura, Y. Watanabe, T. Tomoya, H. Kato, T. Hiramatsu, Kanto Gakuin University, Japan

Fabrication of templates for creating nanoscale structures becomes an important subject for innovation of nanoscale devices. Authors have succeeded in fabricating unique nanostructures such as a line and crater structures on Al substrate surfaces using chemical treatments combining anodization. Polyaniline(PA) line pattern was fabricated on Si surface using these nanostructures as a template. The purpose of this study was to fabricate PA patterns on the Al template and investigate the possibility of optical devices. Nanoscopic polymerization of PA was performed nanoscopically in confined nanoscale structures fabricated on an aluminum surfaces by a chemical polymerization method. Polymerization of PA was carried out using as an oxidizing agent, ammonium peroxodisulfate (APS). Solution from 1 to 2 μ l contains aniline monomer, APS and HCl dropped on the nanostructures as a droplet utilizing micropipette and extended on the surface. PA patterns were successfully fabricated by this technique. The authors also conducted transfer of PA patterns formed on the nanostructured alumina to a Si wafer by a nano-contact method. A Si substrate was attached to the PA patterned Al substrate and was pressed for several ten seconds to transfer the PA pattern to the Si substrate. Then the Al template was removed and the Si substrate was dried naturally.

Photoluminescence (PL) spectra of the line-typed nanostructured Al surface and PA patterned Al surfaces were investigated by using Horiba Jobin-Yvon Spex Fluorolog-3 fluorimeter. Ripple-patterned PL peaks were observed for the line-typed nanostructured Al surface. PA line pattern was fabricated by dropping 1 μ l of PA on the line-patterned Al surface. The PL peak at 480 nm originated from the PA line overlapped the ripple pattern. For the densely deposited sample prepared by 10 μ l PA solution, a PL peak at 480 nm due to PA was clearly observed. PL lifetimes were measured by time-correlated single photon counting (TCSPC). Average PL lifetimes of PA deposited line-patterned Al surface were shorter than the original Al line-pattern. I-V characteristics of PA on the nanostructured Al surface and PA pattern-transferred Si wafer were obtained. Step-like curves were

obtained in the PA pattern that the dots were linearly oriented. Negative resistance was observed in the PA pattern-transferred Si wafer.

This work was aided by MEXT-supported Program for the Strategic Research Foundation at Private Universities.

NS-TuP7 Graphene Patterns on Line-Typed Nanostructured Al Surfaces by Carbon Drawing Techniques. K. Doi, T. Sugii, Y. Takarai, H. Kato, Y. Watanabe, S. Takemura, T. Hiramatsu, Kanto Gakuin University, Japan

Recently, carbon materials are attracting researcher's attention for the development of next-generation devices. In the present study, the authors focused on grapheme film fabrication on non-flat surfaces. In the present work, the authors selected carbon drawing rather than the other methods such as taping method because carbon drawing is applicable to fabricate grapheme film on the non-flat surface. The aim of present study is to fabricate grapheme films on chemically and electrochemically processed nanostructured Al surface by carbon drawing.

Carbon drawing is a nanofabrication method by gently pushing bulk graphite on the surface and drawing it. In the present study, the authors used HOPG for carbon drawing which was performed on a line-typed nanostructured Al substrate. The line-typed nanostructured Al template was fabricated by chemically and electrochemically processes. In the present study, carbon drawing was performed in the vertical direction to the paralleled lines on the line-typed Al template. Fabricated structures after carbon drawing were analyzed and characterized by atomic force microscopy/current imaging tunneling spectroscopy (AFM/CITS), dynamic force microscopy (DFM), optical microscopy with differential interference contrast (DIC) and laser Raman spectroscopy. The DFM image demonstrated that triangular structures of 1 μ m were created along the line structure and the triangular structures with a different thickness overlapped each other. The image in the large area of this sample obtained by optical microscopy with differential interference contrast (DIC) also showed that films with a different thickness overlapped each other. In the DFM image, terrace-like structures also appeared on the aluminum surface. Some characteristics peaks in the Raman spectrum were observed for this sample. A peak at 1600cm⁻¹ can be assigned to G band due to carbon. A peak at 1360cm⁻¹ can be assigned to D band. A peak at 2700cm⁻¹ can be assigned to G' band. The current image in the AFM/CITS measurements showed that the current flows on the overall area. In point-contact measurements, current flows differently at the different points. Quantum conductivity such as step-type was observed. At the different area, wrinkles of thick films were formed on the surface in the AFM image. High conductivity was observed in the hill area whereas the valley area shows low conductivity. In the point-contact measurements, current flows on the overall area. Step-like conductivity was obtained in the I-V characteristics by point contact measurements.

This work was aided by MEXT-supported Program for the Strategic Research Foundation at Private Universities.

NS-TuP8 Nanopatterning of Cup-stack Carbon Nanotubes using Nanostructured Al Templates. Y. Watanabe, R. Takeuchi, H. Kato, S. Takemura, k. Shimada, T. Hiramatsu, Kanto Gakuin University, Japan

The authors intend to develop a patterning method of cup-stack carbon nanotubes (CSCNTs) on a nanostructured Al surface and characterize the patterns by scanning probe microscopy (SPM), scanning electron microscopy (SEM), laser Raman spectroscopy and x-ray photoelectron spectroscopy (XPS). A nanostructured line-typed Al template for patterning was fabricated by combined process of chemical treatments and anodization. CSCNTs dissolved in distilled water under the ultra sonic wave to separate the bundles of carbon nanotubes. Then droplets of this solution were dropped on the Al template or a single crystal Si wafer utilizing micropipette. Dynamic force microscopy (DFM) and SEM images of dispersed CSCNT densely deposited on a line-typed Al template and a Si wafer surface show net-work patterns on the nanostructured Al surface and the Si wafer. Highly oriented CSCNT pattern was also obtained on the line-typed Al template. CSCNT molecules were highly oriented along the line of the template. In the measurement of I-V characteristics for this sample by point contact measurements, quantum conductivities such as step-type and negative resistance were observed. The proposed method can be applied to the CNT arrangements on different surfaces such as Si and glass substrates by a nanoscale imprinting method. The nano-contact transcription was performed according to the following steps: The CSCNT patterned Al template was attached on a silicon substrate and was pressed for 30 sec. Then the Al template was removed. Using a 50 ml solution that contained CSCNT 0.02g, a networking-pattern of CSCNTs was demonstrated to be transferred to a Si wafer. In the case of 50 ml solution that contained CSCNT 0.01g, a single isolated CSCNT that was bending and twisting was obtained by DFM. In the measurement of laser Raman spectroscopy, carbon nanotube's specific peak such as G band was observed. Radial breathing

mode (RBM) was not observed because of large diameters of cup structures. In the case of SWCNT, several RBM peaks were observed between 400-100 cm^{-1} . Furthermore, the intensity of D band was higher than that of the G-band because boundaries of cup structures. Binding energy components due to CSCNT were appeared in the C 1s core level spectra for CSCNTs dropped Si wafer by XPS. A lower binding energy component at 281.5eV and higher binding energy components at 283-290eV appeared in the C 1s core level spectra of CSCNTs assigned to CSCNTs. Furthermore, the authors performed a composite patterning of dye molecules and CSCNT as the next research step. This work was aided by MEXT-supported Program for the Strategic Research Foundation at Private Universities.

NS-TuP9 Optical Properties of Carbon Nanotube Forests with Various Growth Structures, K. Sekiya, H. Koji, H. Furuta, A. Hatta, Kochi University of Technology, Japan

Carbon Nanotubes (CNTs) have attracted particular attention because of their unique properties in various application fields. Especially, CNTs are strong candidate for the anisotropic opt-material in the future optical devices. Some unique optical properties of CNTs have been reported, such as polarization dependent absorption of vertically aligned (VA) short length SWNTs[1], and black body behavior of VA long length SWNTs[2].

There are few reports for the optical properties of CNT forests with controlled structures. We focused on the early growth stage of the CNT forests whose heights are near the light wavelength. In this paper, we investigated optical properties of CNTs having various lengths with controlled structure parameters, such as vertical alignment.

Fe/Al or Fe/AIO multi-layered catalyst films were prepared on Si substrates by magnetron sputtering method. CNT forests were grown on the substrates with the catalyst films by thermal CVD method from C_2H_2 source gas at 730 °C. The CNT growth height was controlled precisely at the order of micro meter by adjusting synthesis period using electronic valves with electric circuits. Optical properties of CNTs were observed by a reflectance spectroscopy (HITACHI U-3900).

Two different CNT forest samples were prepared by controlling CVD condition, one is highly oriented VA CNTs (Sample high-VA) with the average diameter of about 15 nm and the other is relatively low-oriented CNT forest (Sample low-VA) with the average diameter of about 13 nm. The average growth height of Sample high-VA and low-VA were controlled at about 1, 2, and 3 μm . Their growth densities of sample high-VA and low-VA were almost same at $10^{11}/\text{cm}^2$, which were estimated from the cross-sectional SEM images. From the diffuse reflectance spectra, it was found that the CNT forests had low reflectivity with the diffusion reflectance below 5%. From specular reflectance, it was found that the specular reflectance was reduced with increase of forest height for both of sample high-VA and low-VA. It is noted that specular reflectance of sample high-VA was lower than sample low-VA at the same growth height. Absorption coefficients per $1\mu\text{m}$ calculated from the specular reflectance of sample low-VA were lower than that of sample high-VA.

In conclusion, those anisotropic optical properties of CNT forests were considered caused by their unique anisotropic structural parameters of vertical orientation and diameters.

This work was supported by Japan Society for the Science (JSPS) KAKENHI (No. 24560050, Grant-in-Aid for Scientific Research (C)).

[1] Y. Murakami *et al.*, Carbon. 43(13) (2005) 2664–2676.

[2] K. Mizuno *et al.*, PNAS 106 (2009) 6044–6047.

NS-TuP10 Silicone Nanotube Coating, S. Oliveira, S. Seeger, University of Zurich, Switzerland

Artificial superhydrophobic surfaces have generated considerable attention in the last two decades due to their significant potential for industrial and scientific applications. We introduced silicone nanofilaments (SNF) which grow on a variety of technologically important substrates via a convenient gas or solvent phase process. Coated substrates exhibited superhydrophobic behavior with contact angles higher than 160°. The simple one step production process includes only low cost starting materials and is ecologically friendly because it does not contain any fluorine compounds. Therefore it is of high interest for industrial applications. Until recently a drawback of the process was the release of hydrochloric acid which restricts the coating to acid-resistant substrates. Therefore we developed a similar solvent phase coating procedure using different starting materials to reduce the acid formation tremendously. Acid sensitive substrates were coated with SNF and also Silicone Nanotubes (SNT) without any damages to the material. In particular modified surfaces covered with homogenous SNT showed extreme water repellent properties with contact angles over 175° and sliding angles below 4°. The nanotubes were up to several micrometers long with diameters between 80 - 100 nm and channel diameters between 10-20 nm (Fig.1). This new acid-reduced process extends the number of materials suitable for superhydrophobic coating. Furthermore a convenient

gas phase process for the fabrication of SNT-modified surfaces was developed. The process includes chemical vapor deposition at room temperature. The structure of the tubes can be easily controlled by adjusting the relative humidity in the reaction chamber. Such surfaces showed also superhydrophobic properties with contact angle higher than 179° and sliding angles below 1°. To the best of our knowledge the production of silicone nanotubes is reported for the first time. This new structures opens the opportunities in the field of silicone chemistry and might be of interest for potential applications.

NS-TuP11 Towards the Heat Dissipation in Suspended Self-heated Nanowire Sensors, J. Zhang, Southern Illinois University Carbondale, E. Strelcov, Oak Ridge National Laboratory, A. Kolmakov, Southern Illinois University Carbondale

Self-heating is a prospective power-efficient energy delivery channel to the conductometric chemical sensors that require elevated temperatures for their operation. Strong temperature dependence of the electrical conductivity in semiconductors was employed with a self-heated n-doped silicon nanowire resistor whose surfaces were passivated with native oxide layer. The conductivity in such a device depends on heat dissipation and partitioning inside the device what was studied comparatively for both suspended and supported device architectures. The onset of the exhaustion region in the temperature-dependent resistivity of a Joule-heated nanowire was used as a temperature marker for implementation of the quasi-constant temperature operation mode. As the thermal conductivity of the environment around the nanowire changing upon analyte admission into the chamber, the semiconductor nanowire temperature changes and as a result, an electrical conductivity alters as well. In such a case a nanowire is inert toward the used analytes, the sensing action due to analyte-induced heat dissipation variations can be extracted. Our approach is close to the effort to create membrane-based ultra-sensitive Pirani type thermal pressure sensor with significantly enlarged pressure range and very recent nanowire Pirani gauge. At low pressures, the sensor is idle due to dominating heat dissipation from the nanowire to the substrate and/or electrodes. Above ca 10 Torr the sensitivity to gases has strong dependence on pressure as well as type of the gas and is determined by heat exchange between nanowire surface and ambient. Unlike classical Pirani sensors, we found that the sensitivity of this nanowire pressure sensor does not exhibit the saturation behavior at subatmospheric pressure thanks to nanoscopic size of the nanowire and microchannel architecture of the device. Additionally, the sensitivity of the sensor to reactive gases depends on the effectiveness of the particular endothermic/exothermic reaction at the surface of the nanowires and was explored for the case of acetone-air mixture with Pt decorated silicon nanowire devices suspended across ca 20 μm wide trench of Si/SiO₂ substrate. Strong coupling of the electrical and thermal properties in the individual Joule heated semiconducting nanowire allows fabrication of power-efficient multi-parametric nanoscopic gas/pressure sensors that are analog of Pirani and pellistor type detectors.

NS-TuP12 Thermal Stability and Optical Properties of Vertically Aligned Ag, Au, and Ag/Au Alloy Nanorods Synthesized by the Electrodeposition, M.I. Nandasiri, S. Vilayrganapathy, G. Coffey, A. Joly, P. El-Khoury, T. Varga, A. Devaraj, S.A. Thevuthasan, W.P. Hess, Pacific Northwest National Laboratory

One dimensional metal nanostructures such as nanorods and nanowires have a wide range of applications in electronic, photonic and sensing devices due to their interesting linear and non-linear optical properties. The optical properties of these nanostructures are dominated by localized surface plasmon resonance (LSPR), which results from the oscillations of conduction electrons in response to an external field. The LSPR frequency of the electrons depends strongly on the size, shape, and distribution of the particles and the surrounding dielectric medium. Hence the electronic and optical properties of these nanostructures can be tuned by controlling the physical and chemical properties. In this study, Ag, Au and Ag/Au alloy nanorods with well controlled aspect ratios were grown on anodized aluminum oxide (AAO) templates by the electrodeposition method. One side of the AAO templates was coated with an Ag or Au layer to obtain a good electrical conductivity. The electrodeposition was carried out in the galvanostatic mode by varying the current and deposition time to optimize the properties of nanorods. Following the electrodeposition, the AAO template was etched away using 1M NaOH solution leaving behind free standing and vertically aligned nanorods. These nanorods were imaged using scanning electron microscopy (SEM) to study the size, shape, and distribution as a function of the deposition time. The length of the nanorods varied as a function of deposition time allowing an excellent control over the aspect ratio. The nanorods were further characterized using x-ray diffraction and transmission electron microscopy. The as-grown nanorods were also annealed at high temperatures in vacuum and characterized by x-ray photoelectron spectroscopy and SEM to study their thermal stability. The optical measurements of Ag, Au, and Ag/Au alloy nanorods carried out

using surface enhanced Raman scattering and photoemission electron microscopy will also be discussed. This work was supported by the Laboratory Directed Research and Development (LDRD) program of Pacific Northwest National Laboratory. The work was conducted in the William R. Wiley Environmental Molecular Sciences Laboratory (EMSL), a national scientific user facility sponsored by DOE's Office of Biological and Environmental Research and located at PNNL. PNNL is operated by Battelle for the DOE under Contract DE-AC05-76RLO1830.

NS-TuP13 Optical Properties of InN/InGaN/GaN Dot-in-a-Nanowire Heterostructure, M.D. Kim, Chungnam National University, Republic of Korea

During the last few years, light sources have been investigated with application potential for the implementation of quantum information technologies. In this research field, quantum dots (QDs) have attracted considerable interest both as single photon light sources and high efficiency light sources. Single photon emission from semiconductor QDs has been reported for many different material systems covering different wavelengths and maximum operation temperatures. Group-III-nitrides have the prospect that the emission energy can be engineered over a wider spectral range by varying their alloy contents. In this study, we report a near infrared (IR) emission of InN/InGaN(In~11%)/GaN dot-in-a nanorods (NRs) grown by plasma-assisted molecular beam epitaxy (PAMBE) on Si(111) substrate. Catalyst-free InN/InGaN/GaN dot-in-a NRs were grown in holes of a patterned Si(111) substrate. Arrays of nano-holes with diameter of 80 nm on the Si substrate were obtained by reactive ion etching of polystyrene beads as a nano-hole mask. Scanning electron microscopy, X-ray diffraction, micro-photoluminescence (PL), and high-resolution transmission electron microscopy (HRTEM) were performed to investigate the NRs shape, micro-structural and optical characterizations. Fig. 1(a) show the TEM images of the InN/InGaN/GaN dot-in-a-NRs heterostructure. It is seen that the InN dot height is about 10 nm, which is much smaller than the wire diameter with around 30 nm. It is also show that the InN/InGaN dots aligned along growth direction of the GaN NRs. Fig. 1(b) and (c) show sharp and isolated single exciton emission line in the near IR spectral range (1131 nm) was observed. Radiative and nonradiative lifetimes are also measured in the NRs by time resolved PL measurements. The experimental results are comparable with the data obtained by numerical simulation (by APSYS (CROSS-LIGHT)) of near IR emission. Based on the experimental data, we will present a schematic model of the InN/InGaN NRs formation and the probability of application of light emitting diode and single photon light source for the optical communication.

Fig. 1. (a) TEM images of the active region of an InN/InGaN/GaN dot-in-a-nanorods heterostructures. The (b) and (c) show the micro-photoluminescence on the InN/InGaN/GaN dot-in-a-nanorods heterostructures.

NS-TuP15 Refreshable Pt-TiO₂ Nano-Composite for Direct Methanol Oxidation, C.-T. Lin, Y.-C. Yeh, M.H. Shiao, C.-N. Hsiao, National Applied Research Laboratories, Taiwan, Republic of China

Direct Methanol Fuel Cell (DMFC) has been deemed as one of the many feasible candidates for the portable power supply of the next generation. However, the slow process of methanol oxidation has been the root problem in the development of DMFC. Platinum based alloys have been widely developed and commonly utilized as the catalyst in methanol oxidation. In another field of technology, metal-titanium oxide composite has been adopted in distillation for decades due to the improved photo-catalytic capability resulting from the prolongation of recombination time between electrons and holes thereof. In this paper, Pt-TiO₂ composite nanostructure was deposited on carbon cloth by a one-step photo-deposition process in the atmospheric condition. Various surface compositions of Pt-TiO₂ nano composites were prepared. Also, a comparative study was conducted aiming at assessing the enhancement on the oxidation current of methanol, the suppression of CO poison, and the durability in acidic surrounding among the aforesaid Pt-TiO₂ nano composites. Furthermore, the electrochemical characteristics of photo enhanced methanol oxidation were studied via cyclic voltammetry and chronoamperometry under various illumination conditions. More than 40% of enhancement on the oxidation current density was found on the Pt-TiO₂ modified carbon cloth under UV illumination. The photo induced hydrophilicity also contributed to the local mass transfer on the surface of the aforesaid composite catalyst during the durability test. Moreover, the durability test also suggests the dispersion of TiO₂ NPs and the adhesion between TiO₂ NPs and carbon fibers play crucial roles in the performance of DMFC. In summary, the preliminary results suggest, with proper design on the surface composition, the Pt-TiO₂ nano-composite exists a great potential to serve as the anodic catalyst in DMFC.

NS-TuP16 Redox Signal Enhancement using Nanogap Electrodes via Control of Gap Distance, D.K. Park, J. Park, S. Kim, W.S. Yun, Sungkyunkwan University, Republic of Korea

We report on a redox signal enhancement using nanogap electrodes (NGEs). The distance between NGEs was controlled from 1 μm to a few tens of nanometer where NGEs was narrowed by chemical deposition of reduced Au ion on the pre-defined electrodes. Enhanced redox current of ferri/ferrocyanide was obtained by redox cycling between the two working electrodes. The faradaic current is amplified about a thousand times in this redox system by narrowing the gap distance about 200 nm to 30 nm. The experimental results were discussed on the basis of the cyclic voltammetry (CV), atomic force microscope (AFM) and scanning electron microscope (SEM) measurements.

NS-TuP17 Construction of a Spin Lab Measurement System to Enable Measurement of Spin Carrier Transport in Materials, W. Nolting, A. Jayanthinarasimham, A. Matsubayashi, V.P. LaBella, College of Nanoscale Science and Engineering

Measuring electron spin transport metrics of materials and devices is becoming increasingly important as there is a great desire to fabricate devices that utilize the spin of the electron as well as its charge. This creates a need to measure ultra-low current without creating an increase in the signal-to-noise ratio with variable temperature and magnetic fields. In this poster we will present our custom built spin transport measurement system called the "Spin Lab Measurement System" (SLMS). This system can perform spin relaxation time measurements using non-local spin detection with spin precession (i.e. Hanle technique), along with other standard measurements such as Hall Effect, spin Hall Effect, Kondo Effect and other transport measurements. We will also describe how to measure spin Hall effect (SHE) using the SLMS. Two Primary measurements are able to be carried out, the spin Hall effect and non-local spin detection with spin precession.

**Plasma Science and Technology
Room: Hall B - Session PS-TuP**

Plasma Science and Technology Poster Session

PS-TuP1 Dry Deep Etching of GaN Wide Band-gap Semiconductor, N. Gosset, GREMI CNRS/Université d'Orléans, France, **J. Ladroue,** STMicroelectronics Tours SAS, France, **T. Tillocher, P. Lefauchaux,** GREMI CNRS/Université d'Orléans, France, **M. Boufnichel,** STMicroelectronics Tours SAS, France, **R. Dussart,** GREMI CNRS/Université d'Orléans, France

Gallium nitride (GaN) is a III-V semiconductor with a large and direct band-gap (3.4 eV). Furthermore, GaN has a high electron mobility and strong chemical bonds. These physical properties make GaN very interesting and open new prospects for microelectronics power devices. Indeed, GaN-based devices, compared to silicon devices, can operate under high temperature, high power and high frequency. For GaN-based power devices, an etched depth as high as 6 to 10 μm is typically required. This is considered as deep etching compared to the etch depth necessary for light emitter devices (a few hundred nanometers). It was shown that wet etching of GaN c-plan (plan where etching is generally needed) is limited due to its chemical inertness. Therefore GaN deep etching is achieved by plasma etching. Chlorine-based chemistries are commonly used because GaCl₃ is the most volatile Ga etching product. We studied GaN etching (7 μm thick epilayer grown on Si) in Cl₂/Ar plasma using two industrial Inductively Coupled Plasma (ICP) reactors (Corial 200IL and Alcatel 601 E) and by Ion Beam Etching (IBE) (Plassys MU450). After etching, three regimes of defects were observed: columns, pits and "White GaN". It was shown that both columns and pits are linked to nanopipes and dislocations created during epitaxial growth of GaN. In addition, oxygen based species, coming from either the SiO₂ coverplate or the alumina/quartz tube, play an important role in the columnar regime. They preferentially oxidize dislocations, leading to the observed columns. "White GaN" is a very high roughness coming from surface over-oxidation. For industrial applications, all these defects and roughness must be limited. Plasma investigations, using Langmuir probe, mass spectrometry and optical emission spectroscopy, revealed that SiCl₄ can scavenge oxygen. This subsequently results in elimination of defects. Consequently, using Si coverplate or injection of SiCl₄ leads to defect free surfaces. An optimized IBE process appears to be also a way to reduce defects. The addition of other gases (like BCl₃, CHF₃ and SF₆) will be also investigated to evaluate the impact on both GaN etch rate and selectivity in Cl₂/Ar chemistry. XPS and AFM surface analysis will be performed to better understand the formation mechanism of defects. Finally, regardless of defects, etch rate as high as 1 μm.min⁻¹ and a selectivity of 6 can be obtained.

PS-TuP8 Fluorocarbon Films Deposited by c-C₄F₈/N₂/Ar Plasmas: The Effect of N₂-addition on Gas Phase Kinetics and Surface Chemistry, P.K. Kao, National Taiwan University, Taiwan, Republic of China, P.J. Kuo, P.W. Chiou, C.C. Chou, Tokyo Electron Taiwan Limited, Taiwan, Republic of China, C.C. Hsu, National Taiwan University, Taiwan, Republic of China

Fluorocarbon films deposited using c-C₄F₈/N₂/Ar capacitively coupled plasmas are studied with the goal of understanding the effects of N₂-addition on surface chemistry. The plasma system used is a parallel-plate discharge sustained by a 13.56 MHz power source with the electrode diameter 25.4 cm and a gap distance 6 cm. Quartz crystal microbalance (QCM), Fourier transform infrared spectroscopy (FTIR), x-ray photoelectron spectroscopy (XPS), and contact angle measurement are used to characterize the film properties. QCM measurements show a monotonically increase in the deposition rate with N₂ addition, suggesting that CN_xF_y deposition rate surpassed the rate of forming volatile species. FTIR spectra show an additional adsorption near 1350 cm⁻¹ for conditions with N₂ addition. This can be caused by either the incorporation of nitrogen into the polymer chain or by creation of additional disordered sp² carbon in the film. The XPS C_{1s} spectrum of the film shows four major peaks, assigned to CF_x (x= 1, 2, 3) and C-CF_nbonds. With N₂ admixture, CF_n bonds appear in the C_{1s} spectrum, while the amount of CF₃ and CF₂ bonds only decrease slightly. In support of the XPS data, the water contact angle on FC films remains 100~110° and does not change noticeably with N₂-addition. At the end of the presentation, the process significance in N₂ addition into c-C₄F₈/Ar/N₂ plasmas will be discussed.

PS-TuP11 Etching Characteristics of AlGa_nN and GaN in Inductively Coupled Cl₂ Plasma, J. Cao, Y. Lu, R. Kometani, J. Park, K. Ishikawa, K. Takeda, H. Kondo, M. Sekine, M. Hori, Nagoya University, Japan

Gallium nitride and related alloys have been expanding their applications for next-generation optoelectronics such as HEMTs or white LEDs. Plasma etching processes are necessary especially for ternary compounds such as AlGa_nN and InGa_nN. To control precisely profiles at nano-scale and to reduce plasma-induced damages, which influencing the device performance,¹⁻³ the mechanism of reaction of ions and radicals in plasma with surfaces should be clarified. In this research, we investigated the etching mechanism of AlGa_nN in chlorine plasma with focusing on surface stoichiometric composition.

Samples were Al_{0.32}GaN, Al_{0.47}GaN and GaN epitaxial films grown on Si substrate. Photolithographic patterning of UV photoresist was conducted. After chemical cleaning, an inductive coupled plasma etcher was used; the typical condition is antenna power of 200 W, bias RF power of 0 - 120 W, Cl₂/Ar mixture gas flow rate of 30 sccm at 1 Pa. The samples were chucked electrostatically on the stage kept at room temperature. X-ray photoelectron spectroscopy (XPS) was used for stoichiometric composition analysis.

When changing the ratio of Cl₂/(Cl₂+Ar) from 0 to 100%, the etch rate of GaN and AlGa_nN was increasing with the Cl₂ ratio. The etch rate in all cases saturated as increased the Cl₂ flow ratio above 40%. Order of the etch rate among the films were Al_{0.47}GaN < Al_{0.32}GaN < GaN, which could be explained by their sputtering threshold energies for Al-N of 11.52 eV and Ga-N of 8.92 eV.⁴ Since the etching products such as AlCl_x have high volatility compared with GaCl_x, a layer consisting of low Al-to-Ga ratio was possibly formed on the AlGa_nN surface. We will discuss the effects of plasma parameters on both etching profiles and surface stoichiometry in order to elucidate comprehensively understanding of the etching mechanism.

This work was supported by the Knowledge Cluster Initiative (Second Stage), MEXT, Japan. We would like to thank Taiyo Nippon Sanso Corp. for sample preparations.

1. S. Chen, *et al.*, AIP adv. 2, 022149 (2012).
2. S. Chen, *et al.*, J. Appl. Phys. 112, 053513 (2012).
3. S. Chen, *et al.*, Jpn. J. Appl. Phys. 51, 111002 (2012).
4. J. Ladroue, *et al.*, J. Vac. Sci. Technol. A 28, 5 (2010).

PS-TuP12 Selection of Materials and Surface Finishes for Reduced Particle Formation Upon Ion Beam Bombardment in EUV Mask Blank Production Devices, A.M. Lietz, D. Curreli, University of Illinois at Urbana Champaign, A.V. Hayes, A. Devashayam, Veeco, D.N. Ruzic, University of Illinois at Urbana Champaign

Extreme UltraViolet Lithography (EUVL) requires reflective mask blanks, manufactured by ion beam sputtering a multilayer stack of thin films, primarily Mo and Si, onto a mask substrate. At least 40 bilayers of Mo and Si are necessary to produce a surface which has sufficient EUV light reflectivity for use in high volume manufacturing exposure tools. When contaminant particles deposit between these layers, the EUV light is absorbed or scatters irregularly, rendering the mask blank unusable. One possible source of such particles is bombardment of shields in the

deposition chamber by energetic particles scattered from the ion beam and target and “overspill” of the tails of the ion beam off the edge of the target under oblique target angle of incidence. Shields are used to cover targets that are not in use and prevent deposition or sputtering nearby surfaces and equipment. These shields must be able to accept many successive layers of deposition without flaking and forming particles of deposited material. They must also be able to withstand ion beam overspill bombardment, while forming a minimal amount of particles.

In order to evaluate improved shield materials and surface finishes, shield samples were placed under a broad angle ion beam and particles were collected on a witness plate. Shields of various materials and surface finishes were compared to determine the lowest level of particle formation. The total number of particles on the witness plates was quantified using laser scattering particle detection. Particle sizes and shapes were quantified with high resolution SEM imaging of the witness plate, and their composition was determined using backscattered electron imaging. The shield samples themselves were also analyzed using SEM to check for qualitative features, such as plateau formation, that may indicate the mechanism of particle formation.

PS-TuP13 The Influence of Plasma and Vacuum Ultraviolet Radiation on the Time-Dependent Dielectric Breakdown of Porous Low-k Dielectric Films, D. Pei, M. Nichols, H. Sinha, University of Wisconsin-Madison, S. Banna, Applied Materials Inc., Y. Nishi, Stanford University, J.L. Shohet, University of Wisconsin-Madison

Time-dependent dielectric breakdown (TDDB) is a major concern for low-k dielectrics. The TDDB properties of porous organosilicate glass (OSG) and photopatternable low-k dielectric (PPLK) films after plasma and/or VUV exposure are evaluated using constant voltage time-to-breakdown measurements. To examine the effect of plasma exposure on TDDB degradation, dielectric films were exposed to Ar plasma in an ECR reactor. To separate the effect of vacuum ultraviolet (VUV) radiation on TDDB from charged particle bombardment, synchrotron radiation was used. This also has the advantage of being able to vary the wavelength of the radiation continuously. Dielectric films were exposed under different photon energies with the same fluence. After plasma or VUV exposures constant-voltage time-to-breakdown measurements were made for each sample. Weibull statistics were used. Both the results from PPLK and OSG showed that when the samples were exposed to plasma, significant degradation in breakdown time was observed. The VUV radiation under different photon energies shows less effect on the TDDB of both PPLK and OSG for the same fluence as the plasma. Charge-to-breakdown measurements also show similar results.

This work has been supported by the Semiconductor Research Corporation under Contract No. 2012-KJ-2359 and by the National Science Foundation under Grant CBET-1066231.

PS-TuP14 Noninvasive, Real-Time Measurements of Plasma Parameters via Optical Emission Spectroscopy, S. Wang, J.B. Boffard, C.C. Lin, A.E. Wendt, University of Wisconsin-Madison, S.B. Radovanov, H.M. Persing, Varian Semiconductor Equipment, Silicon Systems Group, Applied Materials Inc.

Plasma process control applications require acquisition of diagnostic data at a rate faster than the characteristic time scale of perturbations to the plasma. Diagnostics based on optical emission spectroscopy (OES) of intense emission lines permit rapid noninvasive measurements with low-resolution (~1nm), fiber-coupled spectrographs, which are included on many plasma process tools for semiconductor processing. The use of OES is an established practice to determine when a process is completed, i.e., the process “endpoint,” by detecting changes in intensity in optical emissions of key gas-phase chemical species, and OES can also be used to detect the presence of impurities and monitor changing reactor wall conditions. More detailed real-time information about the plasma state is increasingly desirable for process monitoring, however, due to progression in the semiconductor industry toward plasma processes with both tighter tolerances and multiple steps, i.e., where operating parameters are varied over the course of the process. In this work,* we examine the utility of plasma optical emissions from argon measured with a low-resolution spectrograph (Verity 1024 SH) as a real-time monitor of plasma parameters during the course of a plasma process, based on a rapid method to monitor and analyze the intensities of a select group of Ar emission lines to dynamically determine the following plasma parameters. Electron temperature and density are relevant parameters for characterization of the dynamic behavior of processing plasmas, because gas phase reactions are driven by collisions involving energetic plasma electrons. Metastable and resonance level concentrations are also relevant as these species play significant roles in plasma processing, through energy released when they de-excite upon reaching substrate surfaces, and through the emission of VUV photons which enhance surface reactions. These parameters are unambiguous indicators of the instantaneous plasma state and as such may

play a valuable role as monitors for closed-loop process control. Results will be presented for argon and argon/mixed-gas (Ar/N₂, Ar/O₂, Ar/H₂) inductively coupled plasmas. Accuracy of the results (which are compared to measurements under static conditions made by Langmuir probe and white-light absorption spectroscopy) are typically better than ±15%. The system time resolution is ~0.1 s, which is more than sufficient to capture the transient behavior of many processes, limited only by the time response of the spectrograph used.

Support by NSF grant PHY-1068670 and Applied Materials Inc. is gratefully acknowledged.

* J. Vac. Sci. Technol. A 31(2), 021303 (2013).

PS-TuP16 80 MHz Capacitively Coupled SiH₄/H₂ Discharge for m-Si Thin Film Deposition - 2 Dimensional Fluid Model Simulation. *H.B. Lin, S.E. Lien, C.H. Hsieh, K.C. Leou*, National Tsing Hua University, Taiwan, Republic of China, *C.C. Hsieh, C.F. Ai*, Institute of Nuclear Energy Research, Taiwan, Republic of China

Capacitively coupled SiH₄/H₂ plasmas (CCP) have been widely employed for deposition of Si film for applications such as thin film transistors and thin film solar cells. For Si thin film solar cells, requirements for yielding higher conversion efficiency at a lower cost calls for a high rate and high uniformity plasma process for deposition of microcrystalline silicon (m-Si) film. A better understanding of the plasma discharge is needed. In this study, a 80 MHz SiH₄/H₂ CCP discharge has been investigated by numerical simulation based on fluid model, with 27 species and 47 reactions. Simulation results show that plasma density, as well as the number densities and fluxes of H, SiH₂, and SiH₃, important reactive species for the growth of m-Si film, as well as the ratio of H/SiH₃ flux, a key indicator for crystal fraction of m-Si film, increase with rf power, as expected. Compared with the case in 27.12 MHz, the results also show that plasma density for the 80 MHz discharge are higher, due to frequency effect in the dominate electron heating mechanism, and, consequently, the densities of the key radical species also drop. More importantly, the ratio of H/SiH₃ flux is also higher for the 80 MHz cases. Further more, the plasma potential, which determines the energy of ions incident on the grounded substrate electrode, decreases as operation frequency decreases. Consequently, a higher crystal fraction can be obtained by increasing the frequency of the rf power of plasma reactors, due to less damage on films causes energy ions bombardment. Simulations have also been carried out for different gap spacing between two electrodes and calculation results show that plasma density increases as the gap spacing decreases, as a result of lower electric field strength.

*Work supported by the National Science Council of ROC.

PS-TuP17 Numerical Investigation of Electron Heating in a Neutral-Loop Discharge Plasma. *S. Kim*, University of Wisconsin-Madison, *S. Banna*, Applied Materials Inc., *Y. Nishi*, Stanford University, *J.L. Shohet*, University of Wisconsin-Madison

Neutral Loop Discharge (NLD) plasmas are being investigated as a new plasma source to produce good directionality and high fluxes of ion bombardment at substrate surface¹ for semiconductor device fabrication. In an NLD plasma reactor, a Neutral Loop (NL) can be produced (zero-field path) that is generated by cusp-shaped magnetic field from direct current magnets. It has been shown theoretically that magnetic reconnection occurs in the neutral loop region when radio-frequency fields are applied². During the reconnection process, the DC magnetic field and the r.f. magnetic field cause disconnection and reconnection of the magnetic-field lines over an r.f. period. The reconnection results in the potential to heat electrons stochastically on the NL. Changing the position and the diameter of the NL can modify processing uniformity over a large area and thus improves plasma processing without need to move or rotate the workpiece. However, to confirm this, the details of plasma parameters as a function of position of the NL are produced by numerical simulations of electron motions near the NL in the presence of an r.f. The relationship between the r.f. magnetic field and its corresponding electric field and the average electron energy is also investigated.

This Work was supported by the Semiconductor Research Corporation under Contact No. 2012-KJ-2359 and the National Science Foundation under Grant CBET-1066231.

[1] T. Uchida and S. Hamaguchi., J. Phys. D: Appl. Phys. **41** (2008) 083001

[2] Z. Yoshida et al., Phys. Rev. Lett. **81** (1998) 2458.

PS-TuP18 Hydrocarbon Conversion by Non-Equilibrium, Atmospheric-Pressure Microplasma. *J. Cole, R.M. Sankaran*, Case Western Reserve University

Hydrocarbon conversion plays an important role in our energy economy. For example, the conversion of natural resources such as methane into hydrogen, carbon monoxide, ethanol, and other chemical fuels is essential

to current and future energy needs. Typically, hydrocarbon conversion (specifically, methane reforming) is carried out by high-temperature (>500 °C), catalytic processes. To lower the temperature requirements and improve the conversion and selectivity, non-equilibrium plasmas have been explored for the conversion of hydrocarbon feedstocks¹. However, the power requirements and stability at high pressures have been obstacles to achieving significant improvement. In this study, we explore the application of a novel class of atmospheric-pressure plasmas, microplasmas², for the conversion of hydrocarbon gases including CH₄ and CO₂. As carbon dioxide emissions increase globally, reactions consuming CO₂ may become a necessity. The reaction of CO₂ with CH₄, known as dry methane reforming, is endothermic and normally requires high temperature and pressure and a catalyst; however, a non-equilibrium microplasma could potentially carry it out at room conditions. Additionally, when coupled with a catalyst, plasmas in general have been shown to have a synergistic effect³ that improves conversion beyond that of just the plasma alone or catalyst alone.

In this study, CO₂ and CH₄ were introduced into a microplasma in varying feed ratios and flow rates. The effluent was characterized by simultaneous gas chromatography and mass spectrometry to identify and quantify products. Reactive intermediate species were monitored by optical emission spectroscopy and soot formation was detected by aerosol ion mobility measurements. Results for CO₂ and CH₄ conversion as well as selectivity to specific products such as CO, H₂, and higher order hydrocarbons will be presented, as well as the formation of soot.

References

[1] Fridman A, Gutsol A, and Rabinovich A. "Combustion-assisted Plasma in Fuel Conversion." J. Phys. D: Appl. Phys. **44** (2011).

[2] Mariotti D, and Sankaran R M. "Microplasmas for Nanomaterials Synthesis." J. Phys. D: Appl. Phys. **43** (2010).

[3] Chang M B, et al. "Review of Plasma Catalysis on Hydrocarbon Reforming for Hydrogen Production—Interaction, Integration, and Prospects." Applied Catalysis B: Environmental **85** (2008).

PS-TuP19 Multi-Peaked and Stepped Electron Velocity Distributions in RF-DC Discharge with Secondary Emission. *A. Khrabrov, I.D. Kaganovich*, Princeton Plasma Physics Laboratory, *P. Ventzek, L. Chen*, Tokyo Electron America

Hybrid RF-DC capacitively coupled discharges find important and growing applications in industrial processes. In such discharges, secondary electrons emitted from the electrodes undergo a complicated motion defined by acceleration in, and bouncing between a steady and an oscillating sheath. For the secondary electrons that return to, and impinge upon the RF electrode, the arrival energy is a non-monotonic function of the driving voltage phase at which they were emitted. This basic property leads to a velocity distribution with multiple peaks [1,2]. This effect may explain the multiple peaks in the electron energy distribution function measured in RF-DC system at RF electrode [2,3]. The energy dependence upon the phase of arrival can also be discontinuous (as the number of bounces between the sheaths changes by plus or minus one), which corresponds to a distribution containing steps. Further, the velocity distribution of secondary electrons is sensitive to variations in the bouncing time and may form additional peaks if a small high-frequency ripple is present in the RF sheath voltage [2]. We have found such features in numerical test-particle simulations of the discharge, and analyzed the observed structure of the electron distributions.

[1] D. Israel, K.-U. Riemann, and L.D. Tseng, J. Appl. Phys. **99**, 093303 (2006). [2] K.E. Orlov and A.S. Smirnov, Plasma Sources Sci. Technol. **10**, 541(2001). [3] L. Xu, L. Chen, M. Funk, A. Ranjan, M. Hummel, R. Bravenec, R. Sundararajan, D. J. Economou, and V. M. Donnelly, Appl. Phys. Lett. **93**, 261502 (2008).

PS-TuP20 Formation of Multi-Peak Electron Velocity Distribution Function by Two-Stream Instability in a dc Discharge. *D. Sydorenko*, University of Alberta, Canada, *I.D. Kaganovich, A. Khrabrov*, Princeton Plasma Physics Laboratory, *L. Chen, P. Ventzek*, Tokyo Electron America

Interaction of an electron beam with a plasma is of particular importance for hybrid dc-rf coupled plasma sources used in plasma processing. Electron acceleration by high-frequency waves may explain the low-energy peak in the electron energy distribution function measured in plasma processing devices [1]. In the present paper, the collisionless electron heating in a dc plasma source is studied using the particle-in-cell code EDIPIC [2,3]. In simulations, electrons emitted from the cathode surface are accelerated through a dc bias electric field and form an 800 eV electron beam entering the bulk plasma. The beam excites electron plasma waves via the two-stream instability. In the region of strong plasma oscillations bulk electrons can be accelerated to substantial energies. These energetic electrons are correlated with the peaks in the cedf described in [1]. In this presentation we discuss factors impacting peak energy and magnitude such as plasma profile. [1] L. Chen and M. Funk, Langmuir wave standing wave resonance

in DC/RF plasma, Proceedings of ICRP 2010. [2] D. Sydorenko, A. Smolyakov, I. Kaganovich, and Y. Raitses, *Phys. Plasmas*, **14**, 013508 (2007). [3] D. Sydorenko, I. Kaganovich, Y. Raitses, and A. Smolyakov, *Phys. Rev. Lett.*, **103**, 145004 (2009).

PS-TuP21 Electron Molecule Collisions with Methane. *W.J. Brigg*, University College London, UK, *A.I. Williams*, *S. Lopez-Lopez*, *D. Monahan*, Quantemol Ltd., UK, *J.C. Tennyson*, University College London, UK, *A. Dzarasova*, Quantemol Ltd., UK

Methane is of particular interest due to its use in diamond deposition processes, and presence in fusion and combustion plasmas. Methane is known to be a difficult molecule to simulate, combined with the difficulty of obtaining electronic excitation and dissociation for both theorists and experimentalists alike[1], this presents a relative lack of data for this important molecule.

Quantum-mechanical calculations can be the answer. The calculations presented use the R-Matrix method: where the configuration space is divided into two regions. There is an inner region, where the physics is complicated by exchange and correlation effects, and an outer region, where greatly simplified equations can be solved. The programs used to carry out these calculations are provided by the UKRmol suite. See Tennyson [2][3] for a detailed review of electron-molecule collisions using the R-matrix method. Quantemol-N provides an expert system for running these codes as well as adding extra functionality tailored to provide data for plasma models.

Using Quantemol-N, several different cross sections and properties were calculated for methane, including electron impact elastic, excitation, rotational excitation, differential, momentum transfer, ionisation, and dissociative attachment cross sections. This data can be converted in the reaction rates and used for modeling of plasma processes.

[1]: M. Ziolkowski et al., *J. Chem. Phys.*, **137**, 22A510 (2012)

[2]: J. Tennyson, *Phys. Rep.* **491**, 2-3 (2010)

[3]: J. Tennyson et al, *J. Phys. Conf. Series*, **86**, 012001 (2007)

PS-TuP22 A Comparative Study of New Algorithm for Fluid Simulation of High Density Plasma Discharges. *S.G. Oh*, *Y.J. Lee*, *J.H. Jeon*, *J.H. Seo*, *H. Choe*, Korea Aerospace University, Republic of Korea

The inductively coupled plasma or the capacitively coupled plasma reactors are typical ones in the material processes for the electronic device fabrications such as semiconductor, TFT-LCD, solar cell. Fluid simulation is one of the simulation method in transport modeling of these discharges, because the profiles of plasma quantities such as densities, temperatures, fluxes and potentials are easily obtained. It is known that there is a restriction on the simulation time step, because the shielding time scale of an electric field perturbation is very short. To overcome this limitation, semi-implicit methods are suggested for the solution of Poisson's equations. In this work, from the physical origin of restriction on simulation time step, a new method for larger time step in the steady-state fluid simulation of high density plasma discharge is suggested, and is explained. To study the differences and similarities, a simple comparison of the new method with previously known one is given.

PS-TuP23 Properties of a Magnetic Neutral-Loop Discharge. *W. Li*, *S. Kim*, *K. Mavrakakis*, *Z. Ling*, *H. Zhang*, *J. Bray*, *T. Griffin*, *M. Nichols*, University of Wisconsin-Madison, *B.-H. Moon*, *Y.M. Sung*, Kyungsoong University, Korea, *S. Banna*, Applied Materials Inc., *Y. Nishi*, Stanford University, *J.L. Shohet*, University of Wisconsin-Madison

The magnetic neutral-loop discharge (NLD) was developed in 1994.[1] In this work we designed an NLD reactor using a stainless-steel chamber, instead of the commonly used quartz chambers in previous work because of the need for such a system in microelectronic processing. The vacuum chamber lies in the middle of three sets of magnet coils. With DC currents flowing in the opposite direction in the middle set of coils, a circle on which magnetic field is zero, *i.e.* a neutral loop(NL), can be produced in the middle of the chamber. In order to generate plasma, 13.56 MHz RF is inductively coupled into the chamber with a spiral antenna, through a quartz window located on one end of the chamber. The reactor can be operated in two modes, (1) an NLD mode when there are oppositely directed DC currents in the magnet coils, or (2) an ICP mode when there are either no DC currents or same direction DC currents in the magnet coils. In the NLD mode, the plasma was observed to be brighter near the location of the NL than in the center. This difference was further confirmed with measurement of the optical spectrum using an OceanOptics spectrometer, which shows the relative plasma glow brightness at the NL is as twice high as from the center of the chamber, and about 10% higher than the ICP plasma mode.

By adjusting the ratio of the DC currents running in the magnet coils, the radius of the NL can be changed. Both experiment and simulation show that the glow follows the change of the NL radius, especially at low pressure

measured with a monochromator and photomultiplier and compared with that observed from the ICP mode as well as other reactors. Although the location of the argon peaks are the same, the relative heights of the peaks and their widths are strong functions of the operating pressure and r.f. power for both modes.

1. H Tsuboi, M. Itoh, M. Tanabe, T. Hayasi and T. Uchida, *Jpn. J. Appl. Phys* **34** 2476 (1995)

PS-TuP24 Size Effect of Hf Liquidous Nano-particles on PEPVD Growth of HfSiON on SiO₂/Si. *T. Haga*, *T. Kitajima*, *T. Nakano*, National Defense Academy of Japan

In the paper, we show the size effect of metal particles on PEPVD of high-k dielectric thin film for MOSFETs.

In the case of a fewer deposition of Hf, high density hafnium metal nano particles with 2-6 nm diameter are formed on SiO₂/Si surface and subsequent nitrogen plasma exposure (~10 min.) leads to the growth of HfSiON high-k dielectric film with a SiN interface layer. The exposure of atomic nitrogen and ions from the non-equilibrium plasma enables the introduction of N into the film and increases the interfacial reaction rate of Hf and SiO. Within the first 1 min., the Hf nano particles are oxynitrided with the N atoms from the plasma and the O atoms supplied from the lower interface judging from the XPS analysis. The nitridation rate is quite high and the quantitative measure shows the sticking of the N atom to the Hf nano particles reaches 1.0, while it is an order lower for thicker Hf layers more than 50 nm. A contact AFM survey of the Hf nano particles indicates the nano particles are liquidous due to Melting-point depression [2]. The following plasma exposure (~ 5 min.) enables the diffusion of Si atoms into the high-k film from the underlying SiO layer. Following N₂ ICP exposure continuously increases the N atom fraction in the film which is relatively slow compared to the initial stage. The XPS spectrum shows the sea incorporated is mostly nitrides in the film. The spectrum also indicates the interfacial SiO layer is nitrided and this leads to the minimized EOT of the high-k stack structure.

[1] H. Watanabe, *Appl. Phys. Lett.* **85**, 449 (2004).

[2] M. J. Stowell, *Proc. Roy. Soc. Lond. A.*, **318**, 231 (1970).

PS-TuP26 High Etching Rate of Lithium Niobate Substrate using BCl₃/Ar Mixture Gases by ICP-RIE. *C.M. Chang*, *P.L. Chen*, *J. Su*, *M.H. Shiao*, *C.-N. Hsiao*, National Applied Research Laboratories, Taiwan, Republic of China

In this study, Z-cut LiNbO₃ single crystal wafers were etched by the inductively coupled plasma reactive ion etching (ICP-RIE) technique by using the boron trichloride (BCl₃)/ Argon (Ar) mixture gases. Effects of the ICP power and RF power ranged from 100W to 400W of the ICP-RIE system were studied on the etching rate, surface roughness, and corresponding DC bias under two working pressures of 30 mTorr and 50 mTorr, respectively. Besides, photoresist and metallic nickel thin film were used as the etching mask, and the selective ratios of the two etching masks were also compared. From the experimental results, it can be found that the DC bias (-V) decreases with the working pressure, and increases with the ICP power and the RF power. The surface roughness of the etched LiNbO₃ substrate was decreased from 55 nm to 30 nm with increasing working pressure, but it increased when the ICP power and RF power were increased. The etching rate of the LiNbO₃ substrate was increased with increasing the ICP power and RF power under the two working pressure. It is noted that the etching rate was greater than 100 nm/min when the working pressure was controlled at 30 mTorr. The selective ratios of the photoresist and the nickel were calculated to be approximately 0.4 and 8, respectively. Under suitable processing parameters of ICP-RIE, the surface roughness less than 40 nm, structure depth greater than 2 μm, and sidewall angle greater than 70° of the LiNbO₃ substrate can be obtained within 20 min, which etching rate is greater than 80 nm/min.

PS-TuP27 Direct Liquid Injection into Low-Pressure Plasmas. *D. Ogawa*, Chubu University, Japan, *M.J. Goekner*, *L.J. Overzet*, The University of Texas at Dallas

What if a liquid is injected directly into low-pressure plasmas? The current material processing with low-pressure plasmas (< 100 Pa) requires the gas-phase precursors in many cases. The limitation is sometimes irritating. The technique we have proposed, *the direct liquid injection into low-pressure plasmas*, enables liquids for plasma processing without applying any heat. Also, this technique enables the injection of solids through a liquid. For example, one could control the number of nano-particles in a film that is produced with a plasma to change the mechanical property of the film. Or, one could leave the clusters of solids on a substrate by evaporating a liquid off to print a three-dimensional structure. It is also fine that one uses heat-sensitive materials such as proteins, or even bacterias because the

temperature of plasma processing is generally low. This technique definitely expands the possibility of material processing with plasmas.

With our best knowledge, not so many people researched the combination of direct liquid injection and low-pressure plasmas. Coppins suggested these kinds of plasmas to call as *misty plasmas*[i] [#_edn1] because one can consider that the droplets are another material state of particles. In contrast to dusty plasmas, misty plasmas can regulate the increase of particle temperature due to the droplet evaporation. Ward patented the configuration to realize the plasma processing in 2005.[ii] [#_edn2] However, our experiences showed that the configuration should create unstable plasma so that the process should be difficult.

This presentation shows the some investigations of the technique from some theoretical calculations and from the experimental observations. Our calculations shows that the evaporation time of droplets becomes half even at a plasma with 10^{10} cm^{-3} and 2 eV due to the contribution of three-vapor recombination on the droplet surface. On the other hand, our experimental results are far from the computational results because of our technical difficulties. Our time-resolved measurements of plasma density and optical emission intensity showed that a plasma dimmed due to the massive vapor at the first several milliseconds. This means that the plasma gives almost no contribution to the droplets' evaporation because the transport time of vapor is much shorter than that of droplets. This result indicates that the control of initial vapor plays a role to realize this technique. In the poster, we will summarize these results shown above with recent progresses.

[i] [#_ednref] M. Coppins, Phys. Rev. Let. **104**, 065003 (2010).

[ii] [#_ednref] Ward, US Patent No. 2005/0227018 A1.

PS-TuP28 Role of Heterogeneous Surface Reactions on the Evolution of O and N Atoms in N₂/O₂ Flowing Afterglows, J. Pregent, L. Stafford, Université de Montréal, Canada

The number density of N and O atoms in the flowing afterglow of a reduced-pressure N₂/O₂ plasma sustained by propagating electromagnetic surface wave in the microwave regime was determined using a NO titration method. While the density of O atoms increased monotonously with increasing percentage of O₂ in the N₂/O₂ gas mixture, the N population first increased with trace amounts of O₂ and then decreased as the concentration of O₂ increased above ~0.1 %. Introduction of either Teflon, aluminum, stainless steel, or copper surfaces in the afterglow chamber influenced both N and O populations. The more prominent decrease was observed for Cu; a result consistent with the high heterogeneous recombination coefficient of O and N atoms on such surfaces. For all materials, the O-to-N number density ratio increased sharply with the addition of O₂, suggesting either a competition for surface recombination sites between N and O or the blocking of adsorption sites by physisorbed O₂. This latter mechanism affects more N than O recombination. A similar behavior was deduced from the analysis of the NO-B and N₂-B emission. Assuming that NO-B levels are populated by N+O+M->NO-B+M and N₂-B levels by N+N+M->N₂-B+M, where M is a third body, the NO-B/N₂-B emission intensity ratio becomes proportional to the O/N number density ratio. Over the range of experimental conditions investigated, we found that the ratio increased with the injection of O₂ in N₂. A less prominent increase was observed in presence of wood samples placed in the afterglow chamber, which indicates that O heterogeneous recombination reactions are more strongly affected by reactor walls or substrate properties.

PS-TuP29 Synthesis of Small Organic Molecules from a CO₂/CH₄ Mixture by Dielectric Barrier Discharge (DBD): Gas Composition and Power Effect, A. Ozkan, G. Arnoult, T. Bieber, P. De Keyser, F.A.B. Reniers, Université Libre de Bruxelles, Belgium

Carbon dioxide is usually considered as an end-product in chemistry because of its high stability. Due to the high quantities of CO₂ produced, its conversion received more and more attention in the recent years [1]. The transformation of CO₂, with CH₄ as second reactant and using atmospheric plasma technology shows that in good conditions, both gases can be converted into valuable products [2-3].

The conversion of CO₂/CH₄ mixtures was performed using a dielectric barrier discharge atmospheric plasma using Argon as the main plasmagen gas. Gas Chromatography was used to determine the composition of the gas after plasma treatment and this treatment was carried out in a new type of reactor developed in the laboratory. We demonstrated that the synthesis of syngas (CO and H₂) and small organic molecules such as C₂H₆, C₂H₄ is totally possible in this type of discharge [Fig. 1].

The study is focused on the effect of the plasma parameters on the CO₂ and CH₄ conversion rate. The parameters which are evaluated in this work are the ratio of CO₂/CH₄ flow rates and the power supplied.

We demonstrated that the CO₂/CH₄ ratio in the mixture has an important impact on the conversion rate. However, there is no real interaction between active species of these two gases since oxygenated organic compounds have

only been detected at trace amounts. Nevertheless, the absence of oxygen after CO₂/CH₄ plasma is always obtained, suggesting that atomic oxygen is consumed in a plasma which contains only a few quantity of CH₄.

On the other hand, the effect of the power was clearly visible, showing a linear increase for both the CO₂/CH₄ conversion rates and the production of syngas according to the supplied power [Fig. 2]. This suggests that the number of electrons circulating between the electrodes has a huge impact on the conversion rate.

The detection of emitting species generated in the plasma (such as CO₂⁺ and CO₂ from the Fox, Duffendack and Barker's system, different peaks of H, OH, O...) was also carried out via optical emission spectroscopy (OES).

Finally, we observed a different effect of two plasmagen gases (Argon and Helium) on the conversion of CO₂ and CH₄. Indeed, the conversion of CH₄ is better when He is used as carrier gas compared to the use of Ar, whereas we observed an opposite effect for the conversion of CO₂.

[1] T. Sakakura, J.-C. Choi and H. Yasuda, *Chem. Rev.* **107** (2007) 2365–2387

[2] X. Tao, M. Bai, X. Li, H. Long, S. Shang, Y. Yin and Xiaoyan Dai, *Progress in Energy and Combustion Science* **37** (2011) 113-124

[3] A.-J. Zhang, A.-M. Zhu, J. Guo, Y. Xu and C. Shi, *Chemical Engineering Journal* **156** (2010) 601–606

PS-TuP30 Mechanisms of Silicon Nitride (SiN) Etching by Hydrofluorocarbon (HFC) Plasmas, K. Miyake, T. Ito, M. Isobe, K. Karahashi, Osaka University, Japan, M. Fukasawa, K. Nagahata, T. Tatsumi, Sony Corporation, Japan, S. Hamaguchi, Osaka University, Japan

Selective etching of silicon nitride (SiN) over silicon dioxide (SiO₂) and/or silicon (Si) is widely used in the microelectronics industry. For example, the formation of dual stress liners or etching of dual/triple hard masks (DHM/THM) for dual-damascene structures requires highly selective SiN etching technology. It has been known that the use of plasmas based on hydrofluorocarbon (HFC) gases such as CHF₃ and CH₂F₂ or hydrogen (H) /fluorocarbon (FC) gases can result in higher etching rates of SiN. The goal of this study is to clarify the etching mechanism of SiN and SiO₂ by HFC/FC plasmas. For this purpose we have performed molecular dynamics (MD) simulations of SiN and SiO₂ etching by HFC/FC ions with improved interatomic potential functions. In the new interatomic potential functions, electronegativity of fluorine (F) bonded with carbon (C) is taken into account. It has been found that, in MD simulation, electronegativity of F strongly affects the etch rates of SiN by FC ions. Since F is highly electronegative and tends to attract electrons more strongly than C does, the CC bond of C-C-F or C=C-F is weaker than that of C-C-H or C=C-H and the C-F bond of C-C-F or C=C-F is stronger than that of CF₄. The bond energy of Si-F is comparable with that of the C-F bond. Therefore, when C and F atoms are provided from the incident beam to a SiN surface, the formation of C-F and Si-F bonds takes place simultaneously and the balance between the C-F and Si-F formation rates determines the total sputtering yield. Since SiFx is a volatile species whereas CFx radicals can form a polymer, if more SiFx bonds are formed, etching proceeds more rapidly and, if more CFx radicals are formed, polymer deposition takes place. In this study, we evaluate the sputtering yields of SiN by HFC/FC ions and examine the surface atomic compositions and desorbed products. The results are also compared with data obtained from ion beam experiments. Sputtering yields obtained from MD simulations with the new interatomic potential functions with more accurate electronegative effects of F are found to be in good agreement with those obtained from ion beam experiments.

PS-TuP31 Novel TSV Etching Technologies using Spatial and Temporal Control Plasma, Y. Morikawa, T. Murayama, T. Sakuishi, K. Suu, NMEMS and ULVAC, Inc., Japan

The advantage of high pressure ICP process is lower self bias voltage than capacitive coupled plasma (CCP) to reduction of notching profile for via last process. And, the very high frequency CCP can cause a plasma uniformity issue due to the standing-wave effect. The plasma characteristics of inductive coupled plasma (ICP) source above 10Pa process operated with dual rf antenna coils with magnetic neutral loop discharge (NLD) plasma were investigated for thru silicon via (TSV) etching. Improved plasma characteristics such as higher plasma density and very uniform and high aspect ratio anisotropy TSV etching process were realized in 300mm wafer. Which plasma source is kind of planar type ICP or NLD. 13.56MHz or 2MHz of rf for dual antenna coils and low frequency rf bias can operate independently. Mechanism of Si etching is mainly fluorine radical reaction. High density plasma is need to get high etch rate. On the other hand, management of radical diffusion from around rf antenna is important for very uniform process of high aspect ratio TSV as well. Center gas injection on the rf window is induced instead of side gas injection to avoid of the rf electric field effect. Therefore, when Si was etched using dual rf antenna coil with SF₆ / O₂ / SiF₄ or SiCl₄ mixture gases injection from center of rf

window and outer side, the high etch rate and selectivity of Si over the photo-resist and very uniform process were observed. And, the combination of "spatial and temporal control of rf input power on dual rf antenna", and "gases inject apportionment each nozzles (center/outer)" can be controllable in large diameter substrate etching process. This method named "STEVIA" (Spatial and Temporal Control Plasma for Thru Silicon Via Etching).

PS-TuP32 State-Space Mapping of Plasma Tools via Coarse Mesh Tool Simulation, D. Monahan, Quantemol Ltd., UK, J.C. Tennyson, University College London, UK

The physical processes underlying low-pressure, low-temperature industrial plasma tools encompasses substantial ranges of space and time. This presents significant difficulty for simulation. Large processing tools produce atomic scale features with process times often exceeding 1000's of seconds while applied frequencies are typically in the MHz or even GHz range. Tractable simulations, therefore, must typically make a number of range limiting assumptions. An extreme simplification which is often employed when probing large parameter spaces is the "global-model" approximation, where volume-averaged chemistry balance equations are solved over the parameter space of interest. Though this may be regarded as an extreme approximation in view of the complexity of typical processing tool geometries, careful consideration of the transport and loss effects often yields surprising agreement with experiment. However, these models do have limited potential and cannot hope to account for spatially dependent phenomena, which may play a significant role in many industrial processes. Spatially resolved simulations, on the tool level, are much less commonly employed for state-space exploration and are often restricted to limited regions of parameter space, or significantly simplified chemistries. However, as the prevalence of multi-core desktop computers continues to grow rapidly, it is not unusual for an engineer to have easy access to a great many processing cores. Utilizing relatively coarse mesh tool simulations, in conjunction with such computer resources now makes spatially resolved state-space mapping tool simulations feasible for short term investigations. In this poster we will present the results of such a study with an SF6 etching chemistry done using the new Quantemol - Virtual Tool (Q-VT) plasma simulation package.

PS-TuP33 Development of ICP Etching Processes for Gallium Nitride HEMT, S. Uehara, T. Nishimiya, Y. Kusuda, M. Hiramoto, S. Motoyama, O. Tsuji, SAMCO Inc., Japan

Next-generation power devices fabricated from wide band-gap semiconductors, such as Gallium Nitride (GaN) or Silicon Carbide (SiC), have the advantages of less energy consumption and smaller device size compared to Silicon power devices, and therefore, are expected to see application in hybrid and electric vehicles, trains, wind or solar power generators, and smart grid technology. This paper reports our recent development of manufacturing processes for a GaN High-Electron-Mobility Transistor (HEMT).

A planar structure GaN-HEMT enables high-speed switching with a two-dimensional electron gas (2DEG), but it is a normally-on device while a normally-off device is preferable. To realize normally-off planar GaN-HEMTs, precise thickness control of the AlGaN layer at the gate is necessary. However, reproducible, stable thickness control of the AlGaN layer in the etching process is challenging when manufacturing normally-off GaN HEMTs. For this reason, we developed a slow etching process with low damage and high reproducibility, combined with in-situ thickness measurement using an optical interferometric film thickness monitor.

Manufacturing GaN-HEMTs with a triple channel (Camel) structure requires an etching process with high GaN to AlGaN selectivity on the p-GaN substrate. We developed an etching process with GaN to AlGaN selectivity of 60:1. We also applied interferometric film thickness monitoring for high etch process reproducibility. Another challenge in the Camel GaN-HEMT structure is to prevent current collapse, which prevents drain current, caused by electron traps on the interface of the AlGaN and insulation layers. We managed this issue by lowering the interface states of the AlGaN.

PS-TuP34 Study of the Substrate Heating in a Magnetron Sputtering Process, J.S. Restrepo, University of Mexico, S. Muhl, J. Cruz, Universidad Nacional Autonoma de Mexico

The substrate heating by the plasma on the magnetron sputtering process is a knowledge process that has not been extended studied such as involve complex effects like ion, excited and neutral surface bombardment and radiation heat from the plasma. To this end we have constructed a multi-point thermocouple to study the spatial variation of the substrate heating under a range of experimental conditions, plasma power and Ar gas pressure during DC magnetron sputtering of titanium. Additionally, we have studied the effect of allowing the thermocouples to be floating, connected to ground and reactive environment. The results showed that the

substrate temperature can reach temperature more than 200°C with a plasma power of 200W and that the highest temperature is localized in front at the race track due to a higher degree of particle bombardment.

**Synchrotron Analysis Focus Topic
Room: Hall B - Session SA-TuP**

Synchrotron Analysis Poster Session

SA-TuP1 Mesoscale and Microstructural Changes in HMX Measured with Synchrotron-Based USAXS and Microtomography, T.M. Willey, L. Lauderbach, T.W. van Buuren, I.C. Tran, Lawrence Livermore National Laboratory, J. Ilavsky, Argonne National Laboratory, H.K. Springer, Lawrence Livermore National Laboratory

HMX (octahydro-1,3,5,7-tetranitro-1,3,5,7-tetrazocine) is a relatively insensitive high explosive at room temperature. Mesoscale voids are thought to influence sensitivity and detonation properties in polymer bound explosive compositions, where HMX crystals are mixed with, for example, ~5% Viton. HMX molecular crystals undergo a solid-solid phase transition from the so-called beta- to delta- phases at elevated temperatures around 170 Celsius, an prior to this study, little was known about how this phase transition affected mesoscale voids and microstructure. We have measured the ultra-small angle x-ray scattering (USAXS) as the explosive was heated through this phase transition. The USAXS is sensitive to structure from about 10 nm to about 5, and shows how the porosity in these size regimes evolves during the phase change. X-ray computed microtomography was also performed before and after temperature cycling to observe changes on length scales larger than a micron. These results enable studies to determine how the mesoscale porosity affects detonation properties in heated HMX-based explosives.

This work performed under the auspices of the U.S. Department of Energy by Lawrence Livermore National Laboratory under Contract DE-AC52-07NA27344.

SA-TuP4 Grazing Incidence X-ray Fluorescence Analysis for the Characterization of Ge_{1-x}Sn_x Thin Films, P. Hönicke, Physikalisch-Technische Bundesanstalt, Germany, C. Fleischmann, IMEC, Belgium, P. Hermann, Physikalisch-Technische Bundesanstalt, Germany, S. Zaima, Nagoya University, Japan, B. Beckhoff, Physikalisch-Technische Bundesanstalt, Germany, O. Nakatsuka, Nagoya University, Japan

Crystalline GeSn alloys have triggered enormous research efforts in the last decade for future optoelectronic devices. The Ge_{1-x}Sn_x material system exhibits a tunable direct energy gap in the composition range 0 < x < 0.15, enabling its use in light emitting/absorbing components. In addition, GeSn alloys are predicted to show enhanced carrier mobility when compared to elemental Ge, a necessary prerequisite for high-speed semiconductor devices.

The growth of single crystalline GeSn thin films is very challenging due to the limited solubility of Sn in Ge and the large lattice mismatch. Progresses made in the last years using epitaxial growth techniques such as molecular beam epitaxy (MBE), GeSn thin films can be grown with high crystal quality and Sn concentrations above 1 at.% [1]. However, as these films are highly metastable with respect to their equilibrium conditions, sustaining their quality, and hence their electrical and optical properties upon further processing will be as demanding as their growth. As such, the applicability of GeSn in electronic devices will depend on their stability upon e.g. thermal treatment.

We report on the thermal stability of strained GeSn (4-6 at.% Sn) thin films grown by low-temperature MBE on Ge. We discuss degradation mechanisms observed in these layers and the thermal budget that can be derived from this. The samples were characterized using synchrotron-based, reference-free X-ray fluorescence analysis [2] in grazing incidence mode (GIXRF). This technique is based on the in-depth intensity variations within the X-ray Standing Wave (XSW) field which arises between primary and reflected beam. During a GIXRF measurement, the depth distribution of Sn is combined with the intensity distribution of the XSW field, resulting in a distribution specific angular fluorescence curve [3]. This method enables us to gain information about the *in depth* and the *integral changes* of the Sn concentration in the layer.

A relative comparison of GIXRF profiles recorded on pristine and annealed GeSn indicates significant diffusion of Sn and compositional changes in the GeSn layer for high annealing temperatures. Complementary analysis reveal morphological changes on the surface of the annealed films, e.g. the formation of large islands. IR-based scattering type scanning-near-field optical microscopy (s-SNOM) [4] measurements show that these islands exhibit distinctively different optical properties than the GeSn layer.

- [1] Shimura et al., *Thin Solid Films* **518** 2010
 [2] Beckhoff et al., *Anal. Chem.* **79**, 7873 2007
 [3] Hönicke et al., *Anal. Bioanal. Chem.* **396**, 2825 2010
 [4] Hermann et al., *Optics Express* **21**, 2913 2013

Surface Science

Room: Hall B - Session SS-TuP

Surface Science Poster Session

SS-TuP3 Scanning Tunneling Microscopy Study of Subsurface Atomic Activity in Heterogeneous Catalysis, *D.R. Killelea, J. Derouin, S. Heslop, D. Valencia, M. Farmer, J. Bender*, Loyola University Chicago

Subsurface species are an enigmatic source of energetic reagents in heterogeneous reactions catalyzed by metal surfaces. As adsorbed atoms in the selvage of a metal, they may be metastable with respect to atoms adsorbed to the surface or in the gas-phase, and so can leave the subsurface with excess energy. Furthermore, when subsurface atoms emerge from beneath adsorbed molecules new reaction geometries are enabled that are otherwise inaccessible between reactants co-adsorbed to a surface. Although believed to be important reactive intermediaries, a systematic study of their fundamental chemistry has yet to be undertaken. To address this, we will develop the basis for a more complete understanding by studying the dynamics of subsurface species. We have selected two model systems for study; hydrogen on Ni(111) and oxygen Ag(111) which will provide basic details of subsurface absorption and reactivity, and further provide guidance for utilization of these species to selectively control chemistry. For catalytic transformations in either system, subsurface atoms are key components of catalytic processes, but it remains unclear how they enhance reactions. To reveal the surface dynamics, scanning tunneling microscopy (STM) will image the surface, tracking the movement of individual atoms as they diffuse across and into the metal surfaces. The unique capabilities of STM to selectively energize and manipulate atoms on surfaces will also be used to further investigate the energetics of subsurface incorporation and emergence. To complement STM images, temperature programmed desorption and Auger electron spectroscopy will identify adsorbates and provide thermodynamic information. Our results will show mechanisms for subsurface migration and we will also probe the energetics of subsurface incorporation. Taken together, this new information seeks to narrow the gap our understanding between model and actual catalytic systems and enable chemists to accurately gauge the role of subsurface species in the transformation of plentiful feedstock into energy-rich chemicals over metal catalysts.

SS-TuP4 Photoelectron Spectroscopy Studies on the Superconducting NbC and MoC, *L. Huerta, R. Escamilla*, Universidad Nacional Autónoma de México, *M. Flores*, Universidad de Guadalajara, Mexico, *L. Rivera, M. Romero*, Universidad Nacional Autónoma de México

X-ray Photoelectron spectroscopy (XPS) and ultraviolet photoelectron spectroscopy (UPS) were used to investigate the binding energies and valence band for the NbC and MoC phases. The NbC and MoC polycrystalline samples superconducting were synthesized by arc melting. X-ray diffraction pattern showed that the samples were essentially single phase. The Nb 3d, Mo 3d and C 1s core levels associated to the chemical states of NbC and MoC were identified. Comparing the Nb 3d, Mo 3d and C 1s core levels with metallic Nb, Mo and C reference materials, we observed a positive chemical shift for Nb 3d and Mo 3d a negative chemical shift for C 1s in both samples. These results suggest that the charge transfer model based on the concept of electronegativity is applicable on the NbC and MoC compounds.

SS-TuP5 FTIR Spectroscopy of Water Clusters in Methane Matrix, *N. Ozawa, S. Takekuma, K. Yamakawa, I. Arakawa*, Gakushuin University, Japan

Water clusters have been investigated in terms of their geometric structures and electronic states for the last few decades [1]. One of the main purposes of these studies was to obtain information of hydrogen-bond interactions in water and ice. Experimentally, a matrix isolation technique, in which water clusters are prepared in a condensed film of chemically inactive species such as para-H₂, and rare gases, has also been a useful method for the cluster study because of high sample density [2][3]. It is worth noting that the cyclic water hexamer which has not been found in the gas phase was observed in para-H₂ matrices [4]. In the present study we investigated water clusters in the methane matrix by Fourier Transform Infrared Spectroscopy (FTIRS).

A vacuum chamber equipped with a liquid helium cryostat was evacuated and baked at 393 K for 24 hours, which resulted in the base pressure of 1×10^{-8} Pa. The methane matrix was deposited on the gold-coated oxygen-free copper substrate which was fixed on the cryostat and maintained at 6 K. Methane and water vapor were dosed from different gas lines through variable leak valves. The mole ratios of water to methane (H₂O/CH₄) were 0.026-0.053. Infrared spectra were measured in a reflection configuration using a FTIR spectrometer with a compartment of a liquid nitrogen cooled HgCdTe detector. The spectral range was 500-6000 cm⁻¹ and a resolution was set at 4 cm⁻¹ in the present experiment. The incident angle of infrared light on the substrate was 80°. The whole optical path was evacuated to eliminate infrared absorption due to carbon dioxide and water vapor in the atmosphere.

The infrared spectra of water clusters in methane matrices showed adsorption peaks at 3531 cm⁻¹, 3497 cm⁻¹, 3360 cm⁻¹, 3344 cm⁻¹ and 3216 cm⁻¹, all of which are attributed to vibrational modes of bonded OH, which forms a hydrogen bond with an oxygen atom of a neighboring water molecule. The peaks at 3531 cm⁻¹ and 3497 cm⁻¹ are due to the trimer and the peak at 3216 cm⁻¹ to the cage-hexamer. The other peaks at 3360 cm⁻¹ and 3344 cm⁻¹ may be attributed to pentamer and cyclic-hexamer, respectively. In addition to the variety of the absorption peaks, we found that the relative intensities of these peaks depended on the H₂O/CH₄ ratio, which was likely to reflect the size distribution of the water clusters.

- [1] A. Bankura et al., *Chem. Phys.* **400**, 154 (2012).
 [2] M. E. Fajardo et al., *J. Chem. Phys.* **115**, 6807 (2001).
 [3] S. Hirabayashi et al., *J. Chem. Phys.* **122**, 244501 (2005).
 [4] F. Huisken et al., *J. Chem. Phys.* **104**, 17 (1996).

SS-TuP6 Work Function Variation in Alkali Metal / W(110), *A.A. Padama, W.A. Diño, H. Kasai*, Osaka University, Japan

In surface systems, work function is an important property that indicates the required energy necessary to remove an electron from solid to vacuum. This property is essential for different applications that require electron emission such as in optoelectronic and thermionic devices and in ion productions for plasma application [1-3]. Low work function system is desired and is usually realized by introducing adsorbate which can modify the electronic properties of the surface under investigation [4-6]. It is therefore fundamental to understand the work function lowering and establish indicators that could possibly predict the changes in work function among materials.

In this present work, we investigated the variation of work function in alkali metal (Li, Na, K, Rb, Cs) / W(110) surface systems at different alkali metal coverage by performing density functional theory-based calculations. For all cases, work function rapidly decreases and reaches minimum value at an optimum coverage and rises again with further increase in alkali metal coverage (Fig. 1). The variation of work function values was analyzed using the density of states projected on the adsorbed alkali metal atoms. For K, Rb, and Cs, we observed that the minimum work function is achieved when the states corresponding to the interaction of the adsorbed alkali metals are partially occupied. Further increase in the coverage shifts the states to the occupied region and signifies the interaction among the adsorbed alkali metals which causes the increase in work function. For Li and Na which have smaller atomic radius, work function starts to increase when these states begin to shift in the occupied region. We conclude that the electronic profile of the system is a simple yet good indicator in predicting work function variation in alkali metal – W(110). The details of our work will be presented in the symposium.

References:

- [1] D. Otálvaro, T. Veening, G. Brocks, *J. Phys. Chem. C* **116** (2012) 7826-7837.
 [2] M. Bacal, *Chem. Phys.* **398** (2012) 3-6.
 [3] M. Lin, R. Jao, W. Lin, *J. Vac. Sci. Technol. B* **26** (2008) 821-825.
 [4] H. Nakanishi, H. Kasai and A. Okiji, *Surf. Sci.* **197**, 515 (1988).
 [5] H. Nakanishi, H. Kasai and A. Okiji, *Surf. Sci.* **216**, 249 (1989).
 [6] H. Ishida and K. Terakura, *Phys. Rev B* **36**, 4510 (1987).

SS-TuP7 The Analysis of an Asymmetric Peak of Infrared Absorption due to the Antisymmetric Stretching Vibration of CO₂ on TiO₂ Nanotubes, *K. Yamakawa*, Gakushuin University, Japan, *K. Fukutani*, University of Tokyo, Japan

The origin of asymmetric line shapes appearing in spectroscopy were first discussed in terms of interaction between a discrete state and continuous states by Fano [1]. Thereafter this Fano effect has been observed in a variety of systems including the adsorbate-surface system such as H / W(100), CO / Cu(100), and CO / Cu(111) [2, 3], where metal electronic states of a continuous spectrum interact with the vibrational state of the adsorbate. In

the present study we performed Fourier transform infrared spectroscopy (FTIRS) of CO₂ adsorbed on TiO₂ nanotubes to observe an asymmetric absorption peak in the range of the antisymmetric stretching vibration (ν_3). In contrast to previous studies on metallic substrates, the asymmetric peak was observed on a semiconductor substrate in this study.

TiO₂ nanotubes were synthesized following the way described in the literature [4]. For evaluation of the nanotubes Raman spectroscopy, infrared spectroscopy, scanning electron microscopy and transmission electron microscopy (TEM) were performed. From the TEM images the diameters of the tubes were estimated to be several nanometers. Then, the TiO₂ nanotubes dispersed in ethyl alcohol were sprayed on a CaF₂(111) surface, which was set on a liquid-nitrogen cooled cryostat in an ultra-high vacuum chamber with a base pressure of 2×10^{-8} Pa. Infrared spectra were recorded in a transmission configuration, using a FTIR spectrometer at a spectral resolution of 4 cm⁻¹ with a liquid-nitrogen cooled HgCdTe detector. The substrate temperature was kept at 81 K.

In the spectral range of ν_3 an absorption peak grew around 2340 cm⁻¹ first, as the exposure of CO₂ was increased. After this peak was saturated, a new absorption peak grew at 2350 cm⁻¹. Saturation of the latter peak was followed by formation of a CO₂ multilayer. Noting that the former peak appeared to be only a slight shoulder at the saturation of the latter peak, the former was assigned to ν_3 of CO₂ on oxygen vacancy sites, while the latter to that on terrace sites. Whereas the absorption peak at 2350 cm⁻¹ exhibited a normal absorption feature, the peak at 2340 cm⁻¹ revealed an asymmetric shape. Adsorption on defect sites is thought to play an important role for appearance of the asymmetric peak.

[1]U. Fano, Phys. Rev. **124**, 1866 (1961).

[2]Y. J. Chabal, Phys. Rev. Lett. **55**, 845 (1985).

[3]C. J. Hirschmugl et al., J. Electron Spectrosc. Relat. Phenom. **54**, 109 (1990).

[4]T. Kasuga et al., Adv. Mater. **11**, 1307 (1999).

SS-TuP8 Deposition of the Transparent and Conductive ZnO Film by an Atmospheric Pressure Plasma Jet, C.M. Hsu, S.T. Lien, Y.J. Yang, J.Z. Chen, I.C. Cheng, C.C. Hsu, National Taiwan University, Taiwan, Republic of China

In this work, deposition of transparent and conductive ZnO thin films using an atmospheric pressure plasma jet (APPJ) is presented. The film properties, namely morphology, crystal structure, conductivity, and transmittance, are examined using SEM, XRD, 2-probe measurement, and UV-Vis spectrometer, respectively. The APPJ is sustained by a pulsed power source with a repetitive frequency up to 25 kHz using N₂ or O₂ as plasma gases. Zinc chloride solution is used as the precursor and is nebulized and then sprayed into the downstream of the plasma jet to deposit thin films on glass or Si wafer substrates. It is found that upon exposure of the precursor to the plasma jet, sheet-like zinc hydroxide chloride is first formed, and is then converted to zinc oxide if the jet temperature is sufficiently high. Under an optimal condition, ZnO films with the resistivity of 0.9 Ohm-cm and the average transmittance between 400 and 800 nm of 80% can be obtained. This demonstrates a one-step and fast process without the need of post-annealing steps to fabricate transparent and conductive ZnO films.

SS-TuP9 Effect of Isothermal Aging on the Interfacial Reactions between Sn-58Bi Solder and ENEPIG, S.M. Lee, S.B. Jung, Sungkyunkwan University, Republic of Korea

The interfacial reaction between the Sn-58wt.% Bi solder and a surface finish of ENEPIG (Electroless Nickel Electroless Palladium Immersion Gold) were studied during isothermal aging at 125 °C. The thin uppermost layer of immersion gold was resolved into solders bulk and the intermetallic compound (IMC) as known as PdSn₄ was created between tin of solder and Pd-P layer, while the solder was reflowing. As aging time increased, the new IMC creation of Ni₃Sn₄ between Ni-P layer and tin of solder below PdSn₄ became dominant. As aging time increased more, the IMC of PdSn₄ was resolved out into solder bulk and the IMC of Ni₃Sn₄ remained. As aging time went further, Ni-P layer was consumed and pits happened on Ni-P layer made paths Ni₃Sn₄ through Cu layer, and the IMC of Ni₃Sn₄ was discontinuously growing. As result of Cu penetration through Ni-P layer, the IMC became into (Ni,Cu)₃Sn₄ and the new IMC of (Ni,Cu)₆Sn₅ under (Ni,Cu)₃Sn₄ was created and growing. As aging time increased over 500 hour, the main IMC is (Ni,Cu)₆Sn₅ and (Ni,Cu)₃Sn₄ between ENEPIG and 58wt.% Bi solder. In addition to Ni-P layer, presence of phosphorous made such as Ni₃P layer and NiSnP layer. Result of this study showed that the surface finish of ENEPIG layer acts as a diffusion barrier and be able to expect the IMC behavior for long term as low temperature solder.

SS-TuP10 Adsorption Properties of Ammonia on Defective Graphite Surfaces, R.S. Shibuya, M. Sakurai, Y. Saito, K. Kawarai, University of Tsukuba, Japan, T. Kondo, University of Tsukuba and PREST JST, Japan, J. Nakamura, University of Tsukuba, Japan

The graphite surface consists of the p conjugated system which originates from the resonance of the 2p_z electron orbital of the carbon atoms and it is well known as an inert surface. However, because of the perturbation of π conjugated system, the non-bonding π electronic states of the graphite-related materials such as graphene sheets and graphite are known to appear as the localized states at the carbon atoms around the zigzag edge,^{1,2} metal cluster,³ defects,⁴ and dopants. We have reported that localized non-bonding electronic states near the Fermi level in the unoccupied region at carbon atoms around point defects of graphite by scanning tunneling microscopy/spectroscopy (STM/STS). This localized state propagates with threefold symmetry perpendicular to the zigzag edges at the point defect. Considering that the carbon atoms with the localized state may act as an acid site, we have examined the ammonia adsorption properties on graphite surface with point defects. In this work, we have prepared the defect induced HOPG surface (Ar⁺/HOPG) by Ar ion bombardment (ion energy is 140 eV and coverage of defect is 1%). We investigated the ammonia adsorption properties on Ar⁺/HOPG by Temperature programmed desorption (TPD), Helium atom scattering (HAS), XPS, and STM/STS. From TPD and HAS, we found that ammonia weakly chemisorbed near the defects at 110 K. The detail of adsorption features will be discussed in the presentation with our STM/STS and XPS results.

1. M. Fujita, et al., J. Phys. Soc. Jpn., 65 (1996) 1920.

2. Y. Niimi, et al., Appl. Surf. Sci., 241 (2005) 43; Y. Kobayashi, et al., Phys. Rev. B 71 (2005) 193406.

3. T. Kondo, Y. Iwasaki, Y. Honma, Y. Takagi, S. Okada and J. Nakamura, Phys. Rev. B 80 (2009) 233408.

4. T. Kondo, Y. Honma, T. Machida, J. Oh, J. Nakamura, Phys. Rev. B 82 (2010) 153414

SS-TuP11 Photo-functional Property of TiO₂/Cu₂O and TiO₂/TiN/Cu₂O Thin Films by Reactive Magnetron Sputtering, T. Nakajima, I. Takano, Kogakuin University, Japan

Characteristics based on photo-inducement of TiO₂ have attracted various interests in many fields. TiO₂ has been known as one of a promising photocatalyst and is already used in various practical applications, such as the degradation of environmental pollutants and the self-cleaning of glasses. Furthermore, the most important characteristic as a photocatalyst of TiO₂ is well known that photo-excited state is very stable and does not cause self-decomposition. Therefore, the electrolysis of water is performed under ultra-violet (UV) light irradiation to TiO₂. However UV energy accounts for only a small fraction (~5%) of the sun's energy compared to the visible region (45%).

In this study, to improve the photo-functional property of TiO₂ the double layer films were fabricated by the constitution of the TiO₂ layer of an n-type semiconductor and the Cu₂O layer of a p-type semiconductor. Each arrangement of the film with TiO₂/Cu₂O was also investigated by optical permeability. Furthermore, to prevent diffusion of Cu from the Cu₂O layer to the TiO₂ layer, the TiN layer was inserted between the TiO₂ layer and the Cu₂O layer. As the following study, this Cu₂O layer was replaced to the Ag₂O layer. Those layers were fabricated by reactive magnetron sputtering. Composition and microstructure of these films were investigated by X-ray photoelectron spectroscopy and X-ray diffraction, respectively. Chromatic change of a methylene blue solution was applied for the photocatalytic evaluation. Light irradiation to the sample in a methylene blue solution was carried out using a commercial sterilizing lamp as ultraviolet light and an artificial sun lamp as visible light. Transmittance of a methylene blue solution was measured by a spectrophotometer after irradiation for 6 hours by each lamp.

The XRD pattern of the TiO₂/Cu₂O thin film showed the strong peak of the anatase-rutile TiO₂ from an upper layer and the weak peak of Cu₂O from a lower layer. The suitable photocatalytic effect was obtained by the constitution of TiO₂ with 300 nm and Cu₂O with 200 nm in thickness, when the photocatalytic effect showed about 31 % under an artificial sun lamp and about 90 % under a sterilization lamp. In the case of the TiO₂/TiN/Cu₂O film it was estimated that the diffusion of Cu atoms was almost prevented by inserting TiN from the XRD pattern, when the photocatalytic effect showed about 39 % under an artificial sun lamp and about 89 % under a sterilization lamp.

SS-TuP12 Characterization of Bimetallic Pt-Co Clusters and Surface Composition Effect on Catalyst Performance for Proton Exchange Membrane. A.S. Ahsen, Gebze Institute of Technology, Turkey, O.K. Ozdemir, Yildiz Technical University, Turkey, O. Ozturk, Gebze Institute of Technology, Turkey, H. Yan, R.P. Galhenage, D.A. Chen, University of South Carolina

Pt and Pt-Co bimetallic alloy clusters were grown both on commercial hydrophobic carbon paper substrate and on TiO₂(110) crystal. Pt and Pt-Co bimetallic surfaces were deposited on carbon paper substrate using dc magnetron sputtering to investigate electrocatalytic properties of Pt-Co interaction toward the oxygen reduction reaction in 0.5M H₂SO₄ solution by means of cyclic voltammetry (CV) and linear sweep voltammetry (LSV) on rotating disc electrode (RDE). Pt-Co alloy catalysts showed significant improvement on catalytic activity against the pure platinum catalysts. The increase of Co content leads to rise in the electrochemical active surface area (EASA) and improved Pt utilization. The improvement is closely related with the electronic interaction of Pt with Co and modification of the surface electronic structure using bimetallic alloy clusters. Pt-Co alloy surface as a catalyst improved also polymer electrode membrane fuel cell (PEM) performance and decreased Pt usage compared to pure Pt catalyst. Bimetallic clusters are investigated on TiO₂ crystal surface to clarify the Pt-Co interaction.

The growth, nucleation and chemical activity of bimetallic Pt-Co clusters on TiO₂(110) crystal have been investigated by using scanning tunneling microscopy (STM) and low energy ion scattering (LEIS). STM results demonstrate that the mobility of Pt atoms on TiO₂(110) crystal is higher than mobility of Co atoms. For equivalent coverage of Pt and Co the number of cluster density of Pt is higher than for Co. For clusters with a total coverage of 0.25 ML, the cluster density increases as the fraction of Co increases. Next, the surface compositions of Pt on Co and Co on Pt bimetallic clusters are studied using low energy ion scattering (LEIS). The bulk composition is ranging from 100% Pt to 75%, 50%, 25% Pt and 100% Co within total metal coverage of 0.25 ML. For all coverages the cluster surfaces are covered by Pt, which is relatively mobile compared to Co. This explains also the electrochemical improvement. After annealing to 900K all clusters become encapsulated by titania but for the bimetallic clusters the interaction of Co with Pt can be observed up to 600K.

SS-TuP14 Improvement of PIN-Type Amorphous Silicon Thin Film Solar Cell Performance with Phosphorus Light Doping in Intrinsic Layer. W.H. Son, S.K. Lee, T.G. Kim, S.H. Lee, S.Y. Choi, Kyungpook National University, Republic of Korea

In this paper, by investigating the effect of phosphorus light doping on an i-layer of the pin-type hydrogenated amorphous silicon (a-Si:H) solar cells, we confirmed that the incorporation of phosphorus in a-Si:H films has produced superior i-layer material for pin-type thin-films solar cells than the undoped i-layer material. The doped a-Si:H films with various phosphorus concentrations were fabricated by mixing phosphine (PH₃), silane (SiH₄) with hydrogen (H₂) during the i-layer deposition. All films of amorphous materials were deposited by 13.56 MHz plasma enhanced chemical vapor deposition (PECVD) method. The PH₃ flow rate in the reactive gas was modified from 0 to 4.2 sccm (standard cubic centimeter per minute). The phosphorus concentration of the i-layer was measured by secondary ion mass spectroscopy (SIMS). It has been shown from the experiments that a-Si:H film doped with about 2×10^{18} atoms/cm³ of phosphorus shows an n-type property at a flow rate of 0.9 sccm. The optical properties of the films were measured with UV-VIS-NIR spectrophotometer in the range of 380 - 2000 nm. The various values of open-circuit voltage (V_{oc}), short-circuit current density (J_{sc}), fill factor (FF) and conversion efficiency (Eff) were measured under 100 mW/cm² (AM 1.5) solar simulator irradiation. Finally, by applying this process, we were able to improve the all the electrical parameters (V_{oc}, J_{sc} and FF).

SS-TuP15 Experimental and Theoretical Investigation of Stress-induced Near-surface Compositional Redistribution on Si_{0.8}Ge_{0.2} Substrates for 2D Array Growth of Ge Quantum Dots. S. Ghosh, J. Bonilla, University of New Mexico, D. Kaiser, T.R. Sinno, University of Pennsylvania, S.M. Han, University of New Mexico

Long-range, ordered, three-dimensional micro-/nano-structures of Si/Ge heteroepitaxial systems possess unique electronic properties for a wide range of applications, including quantum computers, photodetectors, and solar cells. Herein, we use simulation to predict and experiment to demonstrate the compositional redistribution of Si and Ge in the near-surface region of Si_{0.8}Ge_{0.2} substrates by applying a spatially structured compressive stress to the substrate and thermally annealing the substrate under stress. The stress is applied by a mechanical assembly that presses a 2D array of Si pillars (40 nm diameter and 400 nm pitch) fabricated on a Si substrate against the Si_{1-x}Ge_x substrate. Based on energy dispersive x-ray spectroscopy, the compressed region shows Ge depletion (8%), while the surrounding areas show an increase in Ge concentration (3%). This

compositional variation in turn can be used to selectively grow a 2D array of Ge quantum dots upon Ge exposure. When the annealing temperature is above 950 °C, the compressive stress under each pillar (> 1 GPa) is found to generate plastic deformation, while no plastic deformation is observed below 950 °C. The depth of the plastically deformed regions increases from 15 to 30 nm as the annealing temperature, held constant for each annealing experiment, increases from 950 to 1000 °C. We attribute the plastic deformation to (1) the localized pressure applied to the substrate under the contact area (4.3 to 15 GPa), (2) the near-surface substrate stiffness decreasing with increasing substrate temperature, and (3) the tensile biaxial stress (86 to 135 GPa) under the compressed region due to different thermal expansion rates of Si vs. Si_{0.8}Ge_{0.2}. In particular, the biaxial stress exceeds the reduced Young's modulus (75.5 GPa) at the annealing temperature range. The compositional redistribution of Ge under purely elastic deformation conditions is also predicted, using a kinetic Monte Carlo simulation that accounts for the influence of composition, temperature, and stress on the diffusion kinetics of Ge in SiGe alloy. We will compare the prediction with experimental results in this presentation.

SS-TuP16 Characterization and Chemical Activity of Pt-Ru Clusters on HOPG: Vapor Deposition and Electroless Deposition. R.P. Galhenage, K. Xie, J.M.M. Tengco, J.R. Monnier, D.A. Chen, University of South Carolina

Bimetallic Pt-Ru clusters on highly oriented pyrolytic graphite (HOPG) have been studied as model systems for direct methanol fuel cell catalysts. Metal clusters deposited via vapor-deposition in ultrahigh vacuum have been compared with clusters prepared via electroless deposition (ED) of Ru onto existing Pt seed clusters. Cluster sizes and distributions are characterized by scanning tunneling microscopy (STM), while surface compositions are examined by low energy ion scattering (LEIS) and X-ray photoelectron spectroscopy (XPS). For the growth of 0.25 ML of pure Pt on HOPG, STM images show that large Pt clusters (average height 33 Å) are formed, and these clusters are located almost exclusively at the step edges. Ar ion sputtering was used to introduce defects and create nucleation sites for Pt clusters on the terraces; this treatment resulted in smaller cluster sizes (12 Å) and higher cluster densities (0.12×10^{12} cm⁻² vs. 2.25×10^{12} cm⁻²) compared to growth on the unmodified HOPG surface. When 0.5 ML of Ru was vapor-deposited onto 0.5 ML Pt clusters, the number of clusters did not increase, indicating that bimetallic clusters are formed by incorporation of Ru into the Pt seed clusters. Electroless deposition of Ru onto 0.5 ML Pt clusters on HOPG was carried out in solution using Ru(NH₃)₆Cl₃ with formic acid as a reducing agent at pH 3. LEIS experiments confirmed that Ru was deposited onto the Pt seed clusters, whereas no Ru was deposited on HOPG in the absence of the Pt seed clusters. STM images of the Pt-Ru clusters grown by ED indicate that the cluster densities and sizes are comparable to that of the vapor-deposited clusters. Methanol oxidation experiments will be carried out to study the activity of the Pt-Ru/HOPG surfaces in a recirculating loop reactor coupled to the vacuum chamber.

SS-TuP18 Molecular Control of Doping at a Topological Insulator Surface: F₄-TCNQ on Bi₂Se₃. J. Wang, A.S. Hewitt, D.B. Dougherty, North Carolina State University

The simplest 3D topological insulator is Bi₂Se₃, with a single almost perfectly-conical topological surface state. A challenge in the quest to characterize charge and spin transport in this unique surface state band is that samples are almost always heavily n-doped by Se vacancies when grown from the binary melt. Recently, the strong electron acceptor, F₄-TCNQ has been successfully employed to control doping in exfoliated Bi₂Se₃ and allowed access to surface transport properties [1]. This poster reports our characterization of F₄-TCNQ film growth on Bi₂Se₃ by combining Atomic Force microscopy, X-ray photoelectron spectroscopy, and angle-resolved UV photoelectron spectroscopy. We report evidence for a Stranski-Krastanov film growth mode and interfacial charge transfer effects. [1] D. Kim et al., Nat. Phys. 8, 460 (2012).

SS-TuP19 Tunneling Electron-induced Hopping Motion of CO on Ag(110) Surface. J. Oh, Y. Kim, RIKEN, Japan

Inelastic electron tunneling (IET) process can induce motion and reaction of a single molecule at metal surfaces. CO hopping phenomena on Pd(110) and Cu(110) surfaces have been achieved with tunneling electrons from the tip of a scanning tunneling microscope (STM) [1]. This phenomenon is initiated by the excitation of a high-frequency (HF) vibrational mode (C-O stretching mode, ~240 meV) with inelastic tunneling electrons from the tip of scanning tunneling microscopy. The CO hopping, however, cannot be induced on Cu(110), even though the hopping barrier is lower than that on Pd(110). This result ascribed as anharmonic coupling between low-frequency (LF, ~25 meV) modes and the HF mode combined with electron-hole pair creation. W. Ho *et al.* reported that CO molecules on Ag(110) surface always move when the tip-substrate bias voltage reached beyond

240 meV [2]. It is really interesting because Cu and Ag are very similar to each other in terms of vibrational mode coupling [3].

In this work, we have measured the hopping probability of CO molecule on Ag(110) surface by injecting tunneling electrons from STM tip as a function of sample bias (V_s) up to 320 meV. The probability shows sudden increases at 80 meV, even though there are no vibrational modes correspond to this energy. As one of possibilities, it is considered that direct excitation of either a frustrated rotation or translation mode causes the CO hopping on the Ag(110) surface. The detail of hopping mechanism at the low bias range will be discussed in the presentation.

References;

- [1] T. Komeda, Y. Kim, M. Kawai, B.N.J. Persson, H. Ueba, *Science***295**(2002)2055
- [2] H.J. Lee, W. Ho, *Science***286**(1999)1719
- [3] N. Lorente, H. Ueba, *Eur. Phys. J. D***35**(2005)341

SS-TuP20 Properties of Metal Coating Films on the Biodegradable Resin Irradiated by Ion Beam, R. Tan, I. Takano, Kogakuin University, Japan

Recently, biodegradable resin attracts attention as one of the effective use of resources on environmental measures. PGA (Polyglycolic acid) used in this study is categorized to a kind of polyester resin and is composed of hydrogen, carbon and oxygen. PGA shows a high gas barrier property, a high hydrolysis property and high mechanical strength. These characteristics are applied for sutures of surgery or multi-layer PET bottles, while there is hardly application in an electronic field. The usage of PGA in electronic parts such as a printed circuit board has the important role in environmental measures, however, there are some problems that have to be overcome.

In this study, the surface of PGA was modified by using an ion beam so that the durability of the PGA coated with metal films was improved. The ion beam cut off the bonding of molecules and as a result the surface of PGA turned to a carbon layer which was stable against heating or humidity. Metal films of Ti or Cu were deposited on the modified PGA by vacuum evaporation. The ion beam irradiation and vacuum evaporation were performed using the high current ion implanter with an electron beam evaporator. The ion beam was extracted from the bucket type ion source with multi-aperture electrodes.

The Ar^+ ion irradiation conditions were controlled at a current density of $20 \mu\text{A}/\text{cm}^2$, an acceleration voltage of 1 kV and irradiation time of 0-70 s. The deposition conditions of Ti and Cu were kept at deposition rate of 0.3 nm/s and a film thickness of 200 nm. The prepared samples were the metal coated PGA sample, the ion irradiated PGA sample and the metal coated sample on the irradiated PGA. The sample hardness was measured by a load-unloading method using micro-hardness tester with Knoop indenter. Friction coefficient and wear measurements were evaluated by reciprocating sliding test with load of 0.198N. The water contact angle was measured by using the $\theta/2$ method. Electrical conductivity of metal films was calculated from V-I characteristics measured using the four probe method. Hydrolysis test was evaluated in a distilled water of 100 ml of 30°C. Surface chemical-bonding state was investigated by X-ray photoelectron spectroscopy.

Knoop hardness of Ti or Cu coated samples on the Ar^+ ion irradiated PGA showed the maximum value around 50s in irradiation time. Mechanical properties of these samples were improved as compared with the metal coated PGA without Ar^+ ion irradiation. The measurement results of electrical conductivity suggested the possibility of PGA used as a printed circuit board.

SS-TuP21 Atomic Force Microscopy Studies of Charge Transport Properties of Strained and Indented Topological Insulator, J.H. Hwang, S. Kwon, KAIST, Republic of Korea, J. Park, Pohang University of Science and Technology, Republic of Korea, J. Lee, KAIST, Republic of Korea, J.S. Kim, Pohang University of Science and Technology, Republic of Korea, H.-K. Lyoo, Korea Research Institute of Standards and Science, Republic of Korea, J.Y. Park, KAIST, Republic of Korea

We investigated the correlation between electrical transport and mechanical stress in $\text{Bi}_2\text{Te}_2\text{Se}$ by using a conductive probe atomic force microscopy in an ultra-high vacuum environment. Uniform distribution of measured friction and current were observed over a single quintuple layer terrace, which is an indication of the uniform chemical composition of the surface. By measuring the charge transport of $\text{Bi}_2\text{Te}_2\text{Se}$ surface as a function of the load applied by a tip to the sample, we found that the current density varies with applied load. The variation of current density was explained in light of the combined effect of the changes in the in-plane conductance and spin-orbit coupling that were theoretically predicted. We suppose that the local density of states is modified by tip-induced strain, but topological phase still remains. We exposed a clean topological insulator surface by tip-induced indentation. The surface conductance on the indented $\text{Bi}_2\text{Te}_2\text{Se}$ surface was

studied, and the role of surface oxide on the surface conductance is discussed.

SS-TuP22 Silicon Rich Oxide Films Deposited with Different Flows: An Approximation of its Kinetics Growth, K. Monfil, D. Vázquez, G. Garcia, J.A.L Luna, Benemérita Universidad Autónoma de Puebla, Mexico, A. Morales, Centro de Investigación en Materiales Avanzados, Mexico, J. Carrillo, A. Benítez, Benemérita Universidad Autónoma de Puebla, Mexico

Recently silicon rich oxides have been a material important for optical functions. Various techniques can be used as Hot-fire Chemical Vapor Deposition (HFCVD). The SiO_x has shown to have a very good photoluminescence response and is also compatible with silicon technology. Therefore, in this works, SiO_x Films were obtained by hot fire chemical vapor deposition (HFCVD) with different deposit conditions and an approximation of its kinetics grown was realized. To realize this approximation with experimental data, the hydrogen flows were changing of: 50, 75, 100, and 125 and 150 sccm, and the range of deposit temperature were from 800 to 1000°C. This approximation was realized with Arrhenius's equation. The activation energies for SiO_x films were determined by Arrhenius's plot using the differences between weights before and after of the deposits. The slope of the plot describes us that our deposits have been due at the transport of the precursors. A more detailed analysis of the results is presented to confirm this.

SS-TuP24 A Review of the Current State and Usage of SIMS Libraries, M. Pacholski, The Dow Chemical Company

There are several databases and libraries of static SIMS data, however their utility in general problem solving is unclear. Many of these libraries are older, and use ion sources with comparatively low yields to today's sources. We have initiated a survey of the community and will present the results at the meeting. The questions probe which resources are used, approaches to interpretation of unknowns, how many people add their own data to the libraries, ideas for improvement to the tools and types of samples analyzed.

SS-TuP28 Ion-Modified MOS Structures, R. Shyam, E. Srinadhu, J.E. Harriss, W.R. Harrell, C.E. Sosolik, Clemson University

As-grown SiO_2 layers (50 nm to 200 nm) were exposed to incident beam of Na^+ ions with energies in the range of 100 eV to 10 keV. The oxide is analyzed post exposure by encapsulating the irradiated and pristine region under top metallic (Aluminum) contacts or within a finished MOS device. Characterization of the resulting ion-modified and pristine MOS devices involves the standard techniques of bias-temperature stress and high and low frequency capacitance-voltage (C-V) measurements. Our high frequency C-V data show flatband voltage shifts and changes in slope of the irradiated devices that are beam energy dependent. The flatband voltage shifts are greater than those expected for mobile charges only, implying an irradiation-dependent effect. Additionally, the interface trap density, extracted from the high and low frequency C-V measurements, increases by one order of magnitude over our incident beam energy. We model these effects with standard formalisms for MOS capacitance in the presence of interface defects, where SRIM is used to include ion implantation depth and damage within the oxide.

SS-TuP29 Adsorbate-induced Atomic Segregation Phenomena and Morphological Stability of Size- and Shape-Selected Octahedral PtNi Nanoparticles, M. Ahmadi, F. Behafarid, University of Central Florida, C. Cui, P. Strasser, Technical University Berlin, Germany, B. Roldan Cuenya, University of Central Florida

A study of the morphological and chemical stability of shape-selected octahedral PtNi nanoparticles (NPs) supported on highly-oriented pyrolytic graphite (HOPG) is presented. *In situ* X-ray photoelectron spectroscopy (XPS), *ex situ* atomic force microscopy (AFM) and transmission electron microscopy (TEM) measurements were used to monitor atomic segregation phenomena in PtNi NPs under vacuum, H_2 , and O_2 atmospheres. The initial oxidation state of the as-prepared NPs was found to play a pivotal role in the final surface composition of the NPs after the different thermal treatments. In particular, for these *ex-situ* synthesized NPs, Ni segregation to the NP surface was observed in all environments until all NiOx species were reduced. Enhanced Ni surface segregation was observed in the presence of oxygen, while Pt surface segregation took place in hydrogen and vacuum above 270°C.

SS-TuP34 Spin Crossover Transition in a Molecular Adsorbate. X. Zhang, S. Beniwal, University of Nebraska Lincoln, T. Palamarciuc, P. Rosa, J.F. Létyard, Université de Bordeaux, France, J. Liu, Northeastern University, E. Vega Lozada, F. Torres, L.G. Rosa, University of Puerto Rico – Humacao, B. Doudin, Université Louis Pasteur Strasbourg, France, A. Enders, P.A. Dowben, University of Nebraska Lincoln

We investigated the occupied and unoccupied electronic structure of ultra thin films of the spin crossover $[\text{Fe}(\text{H}_2\text{B}(\text{pz})_2)_2(\text{bipy})]$ complex (with $\text{H}_2\text{B}(\text{pz})_2 = \text{bis}(\text{hydrido})\text{bis}(1\text{H-pyrazol-1-yl})\text{borate}$ and $\text{bipy} = 2,2'$ -bipyridine) by ultraviolet photoelectron spectroscopy (UPS), inverse photoemission (IPES) and X-ray absorption spectroscopy (XAS). The XAS spectra clearly shows the change of iron L edge spectra associated with thermal induced spin crossover and the Raman spectra are consistent with the intact molecule – so the molecule can be evaporated and will form a thin molecule film on a variety of substrates. The shift of the unoccupied density of states seen in inverse photoemission is consistent with the thermally induced spin crossover transition for molecules deposited on the organic ferroelectric copolymer polyvinylidene fluoride with trifluoroethylene (PVDF-TrFE) as well as gold. Perhaps more significant is the fact that the spin crossover transition, and certainly the unoccupied electronic structure, is influenced by the ferroelectric polarization direction of PVDF-TrFE substrates at temperatures in the vicinity of the thermally driven spin crossover transition, if the $[\text{Fe}(\text{H}_2\text{B}(\text{pz})_2)_2(\text{bipy})]$ complex film is very thin 25 molecular layers or less. Combining the STM studies of different adsorbate coverage with the thickness dependent IPES results of the molecular adsorbate on gold substrates, we understand that the molecular thin film spin-states transition may well be affected by thickness of the film which significantly change the magnetic moment of the thin film based on the SQUID measurements.

SS-TuP35 Evaluating Influencing Factors on Nanofiltration and Reverse Osmosis Membrane Processes: A Computational Chemistry Approach to Modeling. A. Kennicutt*, J. Kilduff, L. Morkowchuck, C. Breneman, Rensselaer Polytechnic Institute

We have developed quantitative structure-property relationship (QSPR) models to assess the efficacy of water treatment processes for removal of endocrine disrupting compounds, pharmaceuticals, and personal care products (EDC/PPCPs). Data sets were developed from literature sources reporting nanofiltration and reverse osmosis membrane rejection. QSPRs were developed and implemented by relating compound properties to their removal in membrane water treatment processes. Properties were coded by descriptors capturing physical, chemical, and electronic molecular features. Descriptors were selected maximize model accuracy, sensitivity, and predictive ability. Individual descriptor importance was assessed using stability of descriptor weights across observations and sensitivity of model predictions across perturbations in descriptor values. Models were developed using Partial Least Squares and Support Vector Machine techniques, and were cross-validated and γ -scrambled to verify that results were not serendipitous.

Initial modeling work was done to primarily investigate influential characteristics of the contaminant compound. Descriptor sets were then expanded to attempt to capture membrane influences, including membrane surface chemistry, as well. Modeling was also broadened to develop predictive models based on mechanistic data, instead of a process-specific percent rejection value. Mechanistic parameters of EDC/PPCP fate and transport in membrane processes can be determined from a combined film and hydrodynamic model, a pore surface diffusion model (PSDM) for adsorption, and a steric, electric, and dielectric exclusion (SEDE) model.

Transparent Conductors and Printable Electronics

Focus Topic

Room: Hall B - Session TC-TuP

Transparent Conductors and Printable Electronics

Poster Session

TC-TuP2 A Universal Method of Producing Transparent Electrodes Using Wide-Bandgap Materials: Direct Ohmic Contact to p-AlGaIn. H.D. Kim, S.W. Kim, K.H. Kim, S.J. Kim, Korea University, Republic of Korea, M.D. Kim, Chungnam National University, Republic of Korea, T.G. Kim, Korea University, Republic of Korea

Indium-doped tin oxide (ITO) is the most popular transparent conductive electrodes (TCEs) used in flat screen displays and lighting technologies for decades. However, due to indium's limited supply and increasing cost, there

has been a big push for many years to find alternatives or replacements of ITO (i.e., indium-free TCEs); many scientist and engineers have been working with zinc oxide and other metal-oxide materials but this area still remains quite challenging. Here we worked towards something different, developing new ways to give a current path between the TCEs using ordinary wide-bandgap materials and p-(Al)GaIn layers via conducting filaments (CFs), which can be formed using electrical breakdown (or forming) processes, for ultraviolet light-emitting diodes (UV LEDs).

UV LED is one of the eco-friendly optical sources for different wavelengths in the UV A to C regimes (200–400 nm), useful for various applications including sterilization and high color rendering index lighting. However, currently, the external quantum efficiency of the UV LED, particularly in UV-C bands, is extremely low (3–11%). One of the primary reasons for this low efficiency is a large absorption in narrow-bandgap contact layers for ohmic contact. To fundamentally solve this problem, we should obtain a direct ohmic contact to the p-AlGaIn layers using UV-transparent conductive electrodes, as depicted in the right figure below. However, with conventional ohmic methods, it is almost impossible to make such contact and therefore no report has been made so far. In this article, we present a universal method of producing transparent electrodes with high conductivity and high optical transmittance in the UV A to C regimes (as well as visible-to-infrared regimes) using electrical breakdown to form CFs providing a current path between the TCEs and the semiconductor, which leads to a large reduction in their contact resistance. As a result, we found the contact resistance between the TCEs and the p-GaN layers (or p-AlGaIn layers) to be on the order of $10^{-5} \Omega\text{-cm}^2$ (or $10^{-3} \Omega\text{-cm}^2$) while optical transmittance was maintained at up to 95% for the AlN-based TCEs at 250 nm.

TC-TuP4 Bending Properties of In and Ga Doped Zinc Oxide Films Deposited on Plastic Substrates by Magnetron Sputtering. K. Nagamoto, K. Kondo, LINTEC Corporation, Japan, K. Ishii, Utsunomiya University, Japan

Transparent conductive oxides (TCO) on polymer substrates are prospected as a key material for next-generation devices such as flexible displays and photovoltaics. The advantages of polymer substrates include light-weight, low cost, a multiplicity of materials with tailored properties, shock absorption and highly flexibility. However, polymer substrates also have disadvantages such as low heat resistance and large thermal expansion coefficient compared with glass substrates. A main challenge for an efficient TCO on polymer substrate is not only to choose conductive oxide materials having capability of growing at low substrate temperature, but also to develop a deposition processes in order to obtain good electrical characteristics. Thus, in this study structural, electrical and optical properties of highly transparent conductive polycrystalline Ga-doped ZnO (GZO) and In, Ga-doped ZnO (IGZO) films deposited on plastic substrates at below 100 °C by magnetron sputtering were investigated. The dependences of crystal structure, electrical and optical properties of the GZO and IGZO films on plastic substrates have been systematically studied. The surfaces of plastic substrates and optically properties were controlled by coating buffer layers (CBLs).

The aim of this study is to investigate the effect of surface roughness of plastic substrates on characteristics of GZO and IGZO films of less than 150 nm thickness, such as structural and electrical characteristics. Then optically properties of GZO and IGZO films, for example transmittance, reflectance, yellow index, haze, a^* and b^* value, were depend on GZO and IGZO films thickness and CBLs. The GZO and IGZO films in the thicknesses range from 20 to 120 nm were prepared by magnetron sputtering. The resistivity and average transmittance in the visible wavelength region of GZO films of 120 nm thickness on plastic substrates were $1.0 \times 10^{-3} \text{ohm-cm}$ and more than 85 %, respectively.

TC-TuP5 Influence of Rapid Thermal Annealing Treatment on Various Properties of Texture-Etched Al- or Ga-Doped ZnO Thin Films Deposited by Magnetron Sputtering. T. Minami, J. Nomoto, T. Miyata, T. Yamanaka, Kanazawa Institute of Technology, Japan

This paper describes an investigation of the influence of a rapid thermal annealing (RTA) treatment on various properties of transparent conducting Al- or Ga-doped ZnO (AZO or GZO) thin films that was conducted in an effort to develop thin-film transparent electrodes suitable for thin-film solar cell applications. These doped ZnO thin films were deposited by an r.f. power superimposed d.c. magnetron sputtering deposition using AZO or GZO target : prepared with Al_2O_3 contents of 0.5–2 wt.% or Ga_2O_3 contents of 0.5–5.7 wt.%, respectively. The optical and electrical properties and texture-etched surface structures as well as the stability of electrical properties after use for long terms in moist environment in these thin films were found to be considerably influenced after heat treatment with RTA at 500°C for 5 min in air. In particular, the obtained electrical properties in these thin films were considerably dependent on the RTA treatment conditions as well as the kind and content of impurity doped into the films.

* Morton S. Traum Award Finalist

For example, the heat treatment with RTA always decreased the carrier concentration in both the AZO and GZO films, irrespective of the doped impurity content, whereas the resulting carrier concentration in as-deposited AZO and GZO thin films increased as the impurity content doped into the films was increased. In addition, the Hall mobilities in both the AZO and GZO films doped with impurity contents up to approximately 1.25 at.% always decreased after heat treatment with RTA, which is in contrast to the slight increase of the Hall mobilities exhibited in films doped with an impurity content above approximately 1.5 at.%. The etch pit size developed in AZO and GZO films that were surface textured by wet-chemical etching in 0.2 mol/l HCl at 25°C tended to increase as the content of impurity doped in the films was increased up to approximately 2.5 at.%; however, the etch pit size obtained in GZO films decreased as this content was increased further. It should be noted that the heat treatment with RTA resulted in considerably enhanced etch pit size in these films, irrespective of the kind and content of doped impurity. As a result, in the films that were wet-chemically etched after being heat treated with RTA, the transmittance and the haze value in the near infrared range of 800-1200nm both increased as the size of the etch pits increased. It should be noted that the improvement in the transmittance and the haze value obtained in texture-etched AZO and GZO thin films heat treated with RTA is sufficient to enable the use of the surface textured these films described above for thin-film transparent electrode applications in thin-film solar cells.

Tribology Focus Topic

Room: Hall B - Session TR-TuP

Tribology Poster Session

TR-TuP1 Study of Charge Separation and Relaxation during Friction between Metal and Plastics in a Vacuum and in Air, T. Miura, National Institute of Occupational Safety and Health, Japan

Electric charges generated by friction, i.e., triboelectricity, between industrial materials induce incendiary electrostatic discharges, such as a spark. In fact, many industrial accidents involving explosions and fires occur due to the electrostatic discharges. In this study, we focus on the elemental processes, e.g., charge separation and relaxation, during friction between metal and plastics. Measurement of the charge separation in a vacuum makes it clear that the real amount of triboelectrification between solid materials because of suppression of charge relaxation through gas discharge in a micro-gap interface of them. In air, we can obtain the relaxation efficiency for the initial charge separation.

The experimental equipment was constructed on the basis of pin-on-disk technique in a vacuum chamber. The pin was made of metal and the disk was made of plastic material. Amount of the separated electric charges between them during sliding friction was measured with an electrometer by connecting to the metal sample.

Experiment with a stainless steel pin and a poly-ethylene terephthalate (PET) disk was performed. The charge density on the rubbed surface of PET was calculated to be about -5×10^{-4} C/m² from the generated charges and the width of the friction track. In air, the charge accumulation was, however, one order of magnitude less than the value measured in a vacuum. This should be caused by the charge relaxation as a result of the micro-gap discharge [1].

[1] T. Miura and I. Arakawa, IEEE Transactions on Dielectric and Electrical Insulation, **14**, 560-565 (2007).

TR-TuP2 Development of Solid Lubricant Films for Smooth Motion at High Temperatures, A. Kasahara, M. Sasaki, M. Goto, H. Honda, H. Suzuki, M. Tosa, National Institute for Materials Science, Japan

Research on low friction materials has attracted considerable attention from the viewpoint of effective energy use for realizing a low carbon society, as these materials can substantially reduce energy loss in bearings, gears, and other mechanical drive parts. However a problem is an increase in friction due to the oxidation reaction in high-temperature environments.

We therefore tried to develop advanced high-temperature motion materials with excellent tribological properties (i.e.: little wear, low friction, good lubrication) in order to guarantee a smooth sliding motion over long periods. Our final purpose is to design coatings suitable for smooth sliding motion up to 1073K.

As a first step, In order to measure friction at high-temperatures exceeding 673K, we designed and manufactured a prototype of a high temperature tribological evaluation device. For this purpose high-temperature friction measurement system based on Bowden-Leben type system has been successfully developed that can evaluate sliding friction force under

changing load from 9.8N to 0.098N and under changing heat temperature from 1073K to room-temperature.

We have investigated solid lubricant coatings in order to develop high performance motion mechanism at high-temperature. In previous work, we developed high temperature lubricating coatings by precise control of coating processes using ceramics such as copper oxide, zinc oxide, boron nitride, etc. This time, we focused Cr₂O₃, since this material has been reported to be suitable at high-temperature, but not well been investigated for industrial application to sliding parts.

We have carried out basic study of SUS304, SUS440C and SUJ2 to find out suitable friction parameter at high-temperature from 973K to room-temperature. Their tribological characteristics at high-temperature was evaluated by high-temperature friction measurement system, abrasion measurements by Stylus Surface Profiler and Micro Slurry-jet Erosion.

TR-TuP3 Wear and Oxidation Behaviors of Ti(C, N, O) Coatings, J.H. Hsieh, Y.R. Cho, Ming Chi University of Technology, Taiwan, Republic of China

It has been known that the life time of Ti-based hard coatings is dependent on the oxidation rate of Ti. Here, Ti(C,N,O) coatings prepared by an unbalance magnetron sputtering were studied and compared using a static oxidation approach as well as a pin-on-disc tribometer. Ti(C,N,O) thin film prepared with different N₂/O₂ flow rates were deposited on M2 steel substrates. The films properties were analyzed by Raman spectroscopy, SEM and X-ray Diffraction. These samples then went through static oxidation and tribological testing. The surface morphology and the thickness of oxidation layer were obtained by using scanning electron microscopy (SEM).

In static oxidation, the formed titanium oxide (TiO₂) was found to have mainly anatase structure at temperatures between 500°C to 600°C and transform to rutile structure at temperature higher than 600°C. Through this study, oxidation rate and activation energy of oxidation for each sample were evaluated. It is found the samples exhibited higher activation energy could have higher oxidation resistance. These results are consistent with those obtained from wear testing.

TR-TuP4 Multi-Scale Simulation of Ohmic Contact Deformation in RF-MEMS, C.R. Freeze, X. Ji, B.E. Gaddy, D.L. Irving, North Carolina State University

“Ohmic” RF-MEMS are radio frequency Microelectromechanical Systems (RF-MEMS) switches relying on metal-metal contact. They are of great interest to the telecommunications and defense industries due to their potential for use in switching networks, low-noise/power circuits, portable wireless systems, phased arrays, filters, and antennas. Issues with reliability, however, have prevented widespread commercial use of these devices. In an effort to better understand important degradation mechanisms in the vicinity of the contact, we simulated the complicated environment at the electrical contact through implementation a multi-scale method. This method incorporates an overlay of a finite difference mesh on top of a traditional molecular dynamics simulation. Thermal and electric transport equations are solved via finite difference part of the method and the results are coupled to an underlying atomistic simulation. In this work, contact deformation of ohmic RF-MEMS was approximated as the indentation of a single-asperity on a variety of substrates. These substrates included polycrystalline gold, polycrystalline gold with a void and polycrystalline gold with a trapped pocket of contamination. Indentation was performed for a variety of pressures and applied voltages. The different structures of the substrate result in drastically different steady state thermal profiles when voltage was applied. This significantly affected the indentation depth as compared to room temperature no voltage cases. Flow stress calculations as a function of bulk temperature were used to provide insight into trends in indentation depths as a function of load and underlying structure of the substrate.

TR-TuP5 Effects TiN and TaN Barrier Layers on the Emergence of Ag and Cu Particles and the Subsequent Mechanical and Antibacterial Properties of TaN-(Ag,Cu) Nanocomposite Films, J.H. Hsieh, Y.R. Cho, Y.H. Lie, Ming Chi University of Technology, Taiwan, Republic of China

TaN-(Cu,Ag) nanocomposite films were deposited by reactive co-sputtering on Si(001) and M2 tool steels. Prior to annealing, the films were deposited with a barrier layer of TiN or TaN (with various thickness) in order to control the amount of emerged Ag and Cu particles. As a result, the tribological and anti-bacterial behaviors can be controlled. The films were then annealed using RTA (Rapid Thermal Annealing) at 200 °C–400 °C to induce the nucleation and growth of metal particles. These films’ structures, surface morphologies, and mechanical properties were analyzed. The samples were tested for their anti-wear and anti-bacterial behaviors against Gram-negative Escherichia coli, as function of barrier layer thickness. It is found that, through the application of diffusion barrier, the antibacterial

efficiency against E. coli as well as the tribological properties can be changed and controlled, depending on the layer thickness of TiN and TaN. In general, the films with TiN layer tended to allow more Ag and Cu particles to form on the surface.

TR-TuP6 Study of the Wear Mode in Tribocorrosion Tests of CoCrMo Alloys Coated with TiAlN/TiAl Multilayers, M. Flores, O. Jimenez, E. Rodriguez, Universidad de Guadalajara, México, C.E. Canto, E. Andrade, Universidad Nacional Autónoma de México

The tribocorrosion phenomenon is present in biomedical alloys that are used in artificial implants to replace natural joints. This damage limit the service life of such implants, the hard coatings can improve the resistance of wear and corrosion. The multilayers of TiAlN/TiAl were deposited on CoCrMo alloys by magnetron sputtering. The structure of coatings was studied by means of XRD and the composition by RBS and EDS techniques. The tribocorrosion behavior of CoCrMo alloys alone and coated with TiAlN/TiAl multilayers was studied in simulated body fluid. The tribocorrosion was performed using a ball on plate reciprocating tribometer, the test was conducted in a simulated body fluid at 37 °C of temperature. The loads used were between 0.25 N to 2N, the oscillating frequencies was 1Hz. The corrosion and tribocorrosion were studied using open circuit potential (OCP), potentiodynamic polarization, cyclic polarization and potentiostatic polarization measurements. The potentiodynamic polarization was used to estimate the change in the corrosion rate due to wear and the potentiostatic polarization in the passive region to measure the change in the wear rate due to corrosion. In order to study the wear mechanisms, the topography and composition of worn surfaces were analyzed by means of profilometry, SEM and EDS. For the CoCrMo alloy the corrosion augmentation factor was greater than the wear augmentation factor. The coatings improve the corrosion and tribocorrosion resistance of CoCrMo alloys.

TR-TuP8 Shape-dependent Adhesion and Friction on Au Nanoparticles Studied using Probing Atomic Force Microscopy, Y.J. Yuk, J.W. Hong, S.W. Han, J.Y. Park, KAIST, Republic of Korea

Shape control of metal nanocrystals has broad applications, including catalysis, plasmonics, and sensing. It was found that controlling the atomic arrangement on metal nanocrystal surfaces affects many properties, including the electronic dipole or work function. Tuning the surface structure of exposed facets of metal nanocrystals was enabled by shape control. We investigated the effect of shape on nanomechanical properties, including friction and adhesion forces. Two nanoparticles systems, high-index {321} and low-index {100}, were used as model nanoparticle surfaces. Scanning force microscopy was used to probe nanoscale friction and adhesion. Because of the abundant presence of high-density atomic steps and kinks, high-index faceted nanoparticles have a higher surface energy than low-index faceted cubic nanoparticles. Due to this high surface energy, high-index faceted particles have shown stronger adhesion and higher friction than low-index nanoparticles. We discuss the results in light of the differences in surface energy as well as the effect of capping layers in the measurement.

TR-TuP9 Effect of Plasma Nitriding Treatment Time on the Tribology of Tool Steels, P. Abraha, Meijo University, Japan, J. Miyamoto, Toba National College of Maritime Technology, Japan

The effect of the plasma treatment time on the formation of the hard but brittle compound layer and the subsequent change on the tribological properties of the tool steel surface were investigated. The nitriding of tool steel was performed in electron beam excited plasma using neutral and charged nitrogen species. The tribological experiments were carried out at room temperature using a pin on disc tribometer. The results show that the tool steel nitrided by neutral nitrogen species for six hours produced, based nitrided layer up to 40 μm, without altering the pretreatment surface finish, Ra=14nm. The specific wear rate was less than one hundredth, 4.3×10^{-7} mm³/Nm that of the untreated sample. On the other hand, the samples produced by the charged nitrogen species, ions, produced rough and brittle compound layer on the surface. Consequently, the friction coefficient of the former showed slightly lower friction coefficient compared to that of the latter. The results demonstrate that neutral species based nitriding is effective for high performance precision mechanical components that require better friction and wear performance while keeping the as finished pre-treatment dimensional accuracy, surface roughness and appearance of the sample.

Vacuum Technology

Room: Hall B - Session VT-TuP

Vacuum Technology Poster Session and Student-Built Vacuum System Poster Competition

VT-TuP1 A Study of Uncertainties at Calibration of Helium Leak Calibrator, Y.W. Lin, C.P. Lin, C.-N. Hsiao, F.Z. Chen, National Applied Research Laboratories, Taiwan, Republic of China

Helium leak calibrator is used throughout industry for calibration of leak detectors. A calibration system for helium leak calibrator is developed, and the range of calibration is from 10^{-6} to 10^{-7} std* cc/s. The origins of the entire system's uncertainty may be divided into two categories, type A and type B. Type A uncertainty can be determined by making use of a statistical methodology to treat the statistical data of normal distribution and come up with the average standard deviation. The measurement repetitiveness of a set of 35 acquired calibration data was evaluated and reported in the study, and the quantitative value is a measure for the system's stability. Type B uncertainty includes tracing back the national laboratory (national institute standards and technology, NIST), resolution of Helium leak calibrator, temperature effect, and impurities of working gas. The present estimate of the total uncertainty in the measured leak rate of this artifact at 23°C at the time of test is 5.2%. This includes a systematic uncertainty of 2.0% in flow meter of the NIST primary Leak standard and 3.2% random errors in the measured leak rate of this artifact. The errors represent three standard deviations. Declared is the relative expanded uncertainty (U) which resulted from the relative standard uncertainty multiplied by the coverage factor k=2. The uncertainty is calculated according to the "Guide to the Expression of Uncertainty in Measurement". In regular cases it can be assumed that the value of the measure lies with a level of confidence of approximately 95% within the specified interval. The present research has demonstrated the high stability and great efficacy of the calibration system for helium leak calibrator.

VT-TuP2 Performance Measurements of Scroll Pump, F.C. Hsieh, P.H. Lin, C.W. Chen, J.S. Kao, F.Z. Chen, National Applied Research Laboratories, Taiwan, Republic of China

Scroll pumps are widely used in solar-optic and semiconductor industry for backing purpose. The performance of scroll pump could affect significantly the performance of pumping station. Here, a condition monitoring of scroll pump was developed and monitored through LabVIEW. The pumping speed, acceleration, and noise level were measured for mass flow rate ranges from 50 to 200 sccm (standard cubic centimeter per minute). The pumping speed increases sharply and almost linearly when inlet pressure smaller than 0.307 mbar. The RMS magnitude of acceleration shows a maximum peak which occurs at about 30 Hz. Moreover, small peaks were observed in the spectrum because of the reciprocating motion of the pump. The noise level fluctuates obviously at inlet pressure approaches 1 mbar. The proposed measurements provide a considerable advancement in diagnosis development of pump.

VT-TuP4 Vacuum Thermal Oxidation of a Stainless Steel Vacuum Chamber Following Citric Acid Cleaning, T. Ha, S. Chung, C.D. Park, POSTECH, Republic of Korea

We perform vacuum thermal oxidation with a stainless steel vacuum chamber after citric acid cleaning to reduce the outgassing rate. Pure and dense chromium oxide layer on the surface of the stainless steel is considered to be a diffusion barrier for hydrogen atoms from the bulk. How to form such a high quality chromium oxide layer onto the surface is the key to reduce hydrogen outgassing and to reach extreme high vacuum with stainless steel vacuum systems. The vacuum thermal oxidation at 450°C in vacuum with low oxygen partial pressure is a proven treatment for that. We enhance the purity of the chromium on the surface of the stainless steel by citric acid cleaning before this vacuum thermal oxidation using the property that the citric acid is effective to reduce surface iron contents. The surface analysis results and the vacuum characteristics for this treatment are discussed in this paper.

VT-TuP5 Operation Status of the PLS-II Photon Absorbers, T. Ha, C.D. Park, POSTECH, Republic of Korea

The PLS-II storage ring photon absorbers are designed to accommodate the high heat load from the stored beam with 3 GeV beam energy and 400 mA beam current. Two temperature sensors are attached on the lower and upper part of the photon absorber body near to the thermally most severe point, which are placed inside the vacuum chamber. We report the operation status of the photon absorbers since the start of the commissioning in 2011. First, we compare the calculated temperature values with the measured ones during the beam stored up to 100 mA. From this results, we can estimate the

temperature of the photon absorbers with 400 mA beam current more accurately. Second, We estimate the electron beam position by measured temperature differences between the upper and lower sensors. The results are compared with the measured values from the beam position monitor.

VT-TuP8 Measurement of Low Outgassing Rates using Quadrupole Mass Spectrometers, D.L. Seymour, S. Davies, J.A. Rees, Hiden Analytical

Measurements of the total outgassing rates of UHV chambers are often limited to around 1×10^{-13} Torr-litres per sec by the outgassing rates of the vacuum gauges used to monitor the behaviour of the vacuum chamber and by possible thermal desorption caused by heating of the chamber walls by the gauges. The use of quadrupole mass spectrometer instruments to monitor the outgassing of vacuum chambers, including those used in plasma processing systems, is of interest both because the minimum measurable outgassing rate may be lower and because the mass spectrometer data provides partial outgassing rates for individual gas components. This more detailed description of the outgassing process gives a better historical record of the behaviour of a particular system, and can readily follow, for example, changes from outgassing dominated by water vapour to a regime where the dominant outgassing gas is hydrogen. Increased sophistication may be added to the mass spectrometric measurements by adopting threshold ionisation techniques in which the use of electron energies well below those normally employed in QMS instruments can be used to distinguish between gases, such as nitrogen and carbon monoxide, that have nominally the same mass peak at $m/q = 28$. New measurements carried out using a high sensitivity instrument are reported which illustrate the power of such procedures and, in particular, help resolve outstanding problems such as the identity and origins of the mass peak at $m/q = 19$ in RGA data for UHV systems.

Atom Probe Tomography Focus Topic

Room: 203 A - Session AP+AS+EM+MI+TF-WeM

APT Analysis of Semiconductor, Magnetic, and Oxide Materials

Moderator: T. Li, University of Sydney, Australia

8:00am **AP+AS+EM+MI+TF-WeM1 Progress in Planar-Feature Spatial Reconstruction for Atom Probe Tomography, D.J. Larson, B.P. Geiser, T.J. Prosa, T.F. Kelly, CAMECA**

In the last decade, the applicability of atom probe tomography (APT) has undergone a revolution [1] due to: 1) improved specimen preparation due to focused ion beam milling, 2) improved field of view due to the advent of a local electrode or other ion optical methods, and 3) reinvention of the use of lasers to induce field evaporation. This combination has created challenges in the area of spatial data reconstruction algorithms for APT for two reasons. Firstly, datasets collected at wider field of view are not accurately reconstructed using small angle approximation algorithms. Secondly, heterogeneous specimens containing multiple phases are more likely to yield, which creates challenges in reconstruction due to the non-hemispherical specimen shapes arising from field evaporation.

The most common algorithm for APT data reconstruction has been used with minimal changes for nearly twenty years [2] and has two main limitations: 1) the field evaporated surface is reconstructed as a hemispherical shape and 2) the atomic volume/depth increment is independent of X or Y. This abstract presents recent advances that have been made on APT data reconstruction, particularly in the areas of algorithm development and field evaporation simulation [3]. Various methods of improving APT reconstruction include: 1) post-reconstruction density correction [4], 2) methods which operate within the limits of the hemispherical projection, both pre- and post-reconstruction [5], and 3) methods which remove the hemispherical limitation, primarily based on simulation [6].

1. T. F. Kelly and D. J. Larson, *MRS Bull.* 37 (2012) 150
2. P. Bas et al., *Appl. Surf. Sci.* 87/88 (1995) 298.
3. B. P. Geiser et al., *Micro. Microanal.* 15(S2) (2009) 302
4. X. Sauvage et al., *Acta Mater.* 49 (2001) 389, F. Vurpillot, A. Cerezo and D. J. Larson, *Surf. Int. Anal.* 36 (2004) 552, F. DeGeuser et al., *Surf. Int. Anal.* 39 (2007) 268.
5. D. J. Larson et al., *J. Microscopy.* 243 (2011) 15, F. Vurpillot et al., *Ultramicroscopy* 111(8) (2011) 1286, B. Gault et al., *Ultramicroscopy* 111(11) (2011) 1619, D. J. Larson et al., *Micro. Microanal.* 17(S2) (2011) 740, M. Moody et al., *Micro. Microanal.* 17 (2011) 226, D. J. Larson et al., *Ultramicroscopy* 111(6) (2011) 506, B. P. Geiser et al., *Micro. Microanal.* (2013) in press,
6. D. J. Larson et al., *Micro. Microanal.* 18(5) (2012) 953, D. Haley et al., *J. Microscopy.* 244 (2011) 170.

8:20am **AP+AS+EM+MI+TF-WeM2 APT Analysis of Superlattices, Nanowires, and Non-Planar Heterostructures, L.J. Lauhon, Northwestern University** **INVITED**

I will describe pulsed laser atom probe tomography of semiconductors and semiconductor heterostructures in which the specimen or device geometry significantly limits the application of alternative analytical characterization techniques, thereby presenting unique opportunities for APT analysis. At the same time, geometry and other factors can complicate specimen preparation and APT interpretation. The talk will present both new scientific findings enabled by APT as well as challenges in data analysis, using three examples. First, I will describe the dopant distribution in semiconductor nanowires, for which APT studies have provided new understanding of dopant incorporation mechanisms. Additionally, advances in nanowire growth and design have enabled imaging of the entire nanowire diameter. Second, I will describe the analysis of InGaN/GaN superlattices extracted from light emitting diodes, for which APT is uniquely able to investigate fluctuations in indium mole fraction and the 3-D morphology of the InGaN quantum wells. In both GaN nanowires and thin-films, we have found that the surface polarity strongly influences the measured stoichiometry, but the indium mole fraction can be determined reliably. Finally, we have analyzed InGaN quantum wells grown on GaN nanowires. These are nonplanar heterostructures in which quantum wells are grown simultaneously on both polar and non-polar surfaces. Data from scanning transmission electron microscopy-based analytical methods will be compared with APT analysis, and the relative merits described. A

comparison of these 3 examples will provide insights into the influence of intrinsic materials properties as well as specimen geometry on the capabilities and limitations of APT.

9:00am **AP+AS+EM+MI+TF-WeM4 Atom Probe Analyses of Interfaces in Nd-Fe-B Permanent Magnets for Higher Coercivity, T. Ohkubo, H. Sepehri-Amin, K. Hono, National Institute for Materials Science, Japan** **INVITED**

Nd-Fe-B permanent magnets are one of the most important engineering materials that are used for traction motors of (hybrid) electric vehicles. For these applications, coercivity at an operating temperature around 200°C must be higher than the demagnetization field in motors; thus, Nd atoms in the Nd₂Fe₁₄B phase are partly substituted with heavy rare earth element (HREE). However, due to the limitation of natural resources of HREE, the development of high coercivity Nd-Fe-B magnets without HREE has become a new technical target in Japan. In order to understand the relationship between the microstructure and the coercivity, quantitative characterization of chemical compositions at various interfaces in Nd-Fe-B magnets have been needed. In this talk, we present how 3DAP analysis results of Nd-Fe-B magnets played crucial role in the development of high coercivity nanocrystalline anisotropy magnets with superior coercivity and comparable energy density.

One of the long-standing issues on the coercivity of Nd-Fe-B sintered magnets was the chemical and magnetic characteristics of the thin intergranular layer that emerge after the optimal post-sinter heat treatment. Although people thought that the intergranular layer is non-ferromagnetic, 3DAP analysis indicated it is ferromagnetic based on the concentration of the Fe within the phase [1]. We also found that the intergranular layer is formed by the Nd/NdCu eutectic reaction. This finding has been applied to nanocrystalline HDDR [2], melt-spun [3], and hot-deformed Nd-Fe-B magnets [4] to modify the grain boundary chemistry by the Nd-Cu eutectic diffusion process. Unlike the conventional HREE grain boundary diffusion process that has to be carried out above 900°C, this new low temperature process suppress the grain growth of the Nd₂Fe₁₄B phase. Employing this new eutectic diffusion process, we have succeeded in developing bulk Nd-Fe-B magnets with sufficiently high coercivity and the energy product comparable to that of the conventional (Nd,Dy)-Fe-B magnets. In this talk, we will emphasize the role of the multi-scale characterization using 3DAP, (S)TEM, and SEM in the development of high coercivity Nd-Fe-B magnets.

This work was in part supported by JST, CREST.

- [1] H. Sepehri-Amin, T. Ohkubo, T. Shima, K. Hono, *Acta Mater.* **60** (2012) 819.
- [2] H. Sepehri-Amin, T. Ohkubo, T. Nishiuchi, S. Hirose, K. Hono, *Scripta Mater.* **63** (2010) 1124.
- [3] H. Sepehri-Amin, D. Prabhu, M. Hayashi, T. Ohkubo, K. Hioki, A. Hattori, K. Hono, *Scripta Mater.* **68** (2013) 167.
- [4] H. Sepehri-Amin, T. Ohkubo, M. Yano, T. Shoji, A. Kato, T. Schrefl, K. Hono, submitted

10:40am **AP+AS+EM+MI+TF-WeM9 New Insights Into the Corrosion Behavior of Simulated Vitrified Nuclear Waste from Atom Probe Tomography, D.K. Schreiber, J.V. Ryan, J.J. Neeway, Pacific Northwest National Laboratory, S. Gin, CEA Marcoule, France**

Atom probe tomography (APT) is being used to study the corrosion and alteration layers formed in borosilicate glass samples during long-term (1–26 years) water corrosion. The water environment and glass composition (SON68 – the non-activated surrogate of the French nuclear waste form R7T7 glass) were selected to generate novel insights into the rate-limiting mechanisms of glass corrosion that are relevant to the long-term storage of high-level nuclear waste in a geologic repository. APT concentration profiles across the corroded/pristine glass interface reveal significantly different interfacial widths for B and Na (~2–5 nm) than for Li and H (~15–30 nm), which suggests that multiple element-specific degradation mechanisms are occurring in parallel. Furthermore, the measured interfacial widths are much sharper than were measured previously by energy-filtered transmission electron microscopy and NanoSIMS. Accurate compositional APT analysis of this 26-component complex glass is, however, quite difficult. The implications of these findings and also practical considerations and limitations when performing these experiments will be discussed in some detail.

11:00am **AP+AS+EM+MI+TF-WeM10 Advanced Applications in LEAP Microscopy**, *H.G. Francois-Saint-Cyr, R. Ulfzig*, CAMECA Instruments, Inc., *J. Valley, T. Ushikubo*, University of Wisconsin, Madison, *M. Miller*, Oak Ridge National Laboratory, *H. Takamizawa, Y. Shimizu*, Tohoku University, Japan, *L. Gordon, D. Joester*, Northwestern University, *A. Giddings, D. Reinhard, D. Lawrence, P. Clifton, D. Larson*, CAMECA Instruments, Inc.

The second revolution in atom probe tomography (APT), mainly due to the pursuit of sophisticated laser pulsed modes and focused ion beam based sample preparation, has broadened the range of new applications benefiting from three-dimensional, sub-nanometer compositional information [1]. Novel applications include dopant distribution analysis in metal-oxide-semiconductor (MOS) transistor, geological dating of zircon crystals, quantum dot (QD) assembly growth in Light-Emitting Diodes (LEDs), analysis of biological materials, and nano-scale phase behavior of metallic glasses using the LEAP 4000X®.

Elemental mapping from APT allows threshold voltage in 65 nm-node n-MOS transistors to be successfully correlated with the channel dopant concentration [2]. In geology, precipitates containing Y and Pb are visualized after APT reconstruction of zircon crystals and helped understanding the thermal history and mechanisms of mineral reaction, mineral exchange and radiation damage. Data analysis shows that $^{207}\text{Pb}/^{206}\text{Pb}$ ratios for nm-scale domains ($<2 \times 10^4$ atoms Pb) average 0.17 ± 0.04 and 0.43 ± 0.14 for 2.4 and 4.0 Ga zircons respectively [3], in agreement with SIMS ratios (0.1684 and 0.4269) derived from much larger analysis volumes (hundreds of μm^3 (10^{16} m 3)). In the pillar arrangement of the Quantum Dots (QDs), as imaged in InAs/GaAs multi-layers, the strain field from one QD layer influences the growth of subsequent layers, although the apparent helical distribution has never previously been reported [4]. In biology, spatially organized collagen fibers in the dentin of elephant tusks have been unveiled. Three-dimensional imaging of apatite-derived calcium and phosphate species, inorganic substituents, and carbon/nitrogen containing fragments of organic macromolecules sheds some light on the source of strength for these materials [5]. Metallic glass $\text{Fe}_{76}\text{Cu}_{13}\text{Si}_{13}\text{B}_{5.0}\text{P}_{8.7}\text{Cu}_{0.7}$ used for low-cost transformer applications shows phase separation into a -Fe precipitates, ultrafine spheroidal e -Cu-rich precipitates, silicon-depleted $\text{Fe}_3(\text{P,B,C})$, and Fe_3C after annealing for 30 minutes at 729 K [6].

1. T. F. Kelly and D. J. Larson, *Annual Reviews of Materials Research* 42 (2012) 1.
2. H. Takamizawa et al., *Applied Physics Letters* 100 (2012) 253504.
3. J. W. Valley et al., *Abstracts American Geophysical Union Fall Meeting* (2012) V12A-05.
4. A. D. Giddings et al., *Phys. Rev. B* 83 (2011) 205308.
5. L. M. Gordon, L. Tran and D. Joester, *ACS Nano* 6(12) 2012 10667.

Part of this research was sponsored by ORNL's Shared Research Equipment (ShaRE) User Facility, which is sponsored by the Scientific User Facilities Division, Office of Basic Energy Sciences, US Department of Energy.

11:20am **AP+AS+EM+MI+TF-WeM11 Gaining an Atomic Scale Understanding of Optoelectronic, Magneto- and Ionic-Transport in Nanostructured Materials using Cross-Correlative STEM and APT**, *B. Gorman, D. Diercks, R. Kirchhofer*, Colorado School of Mines **INVITED**
Atomic scale characterization of internal interfaces such as grain boundaries and thin films is needed in order to fully understand the electronic, ionic, mechanical, magnetic, and optical properties of the engineered material. High resolution analytical TEM has given a significant amount of new information about these interfaces, but lacks chemical sensitivity below ~1 at% as well as 3-D information and light element sensitivity. Atom probe tomography in inorganic solids has shown that atomic scale, 3-D characterization is possible with 10 ppm chemical resolution, but a thorough understanding of the laser assisted field evaporation process is needed. Previous studies of inorganic photovoltaic devices have shown that APT is capable of quantifying dopant distributions and interface roughness at resolutions where junction models can be directly correlated.

In ionic conductors, grain boundaries are particularly important as they frequently have conductivities at least two orders of magnitude less than the bulk. Therefore, being able to quantitatively characterize the grain boundary nature to ascertain the reasons behind the decreased conductivity is indispensable for guiding future improvements. In this work an oxygen ion conductor $\text{Ce}_{1-x}\text{Nd}_x\text{O}_{2-x/2}$ and a proton conductor $\text{BaCe}_{0.2}\text{Zr}_{0.7}\text{Y}_{0.1}\text{O}_{2.95}$ were analysed with particular emphasis on analysis of the grain boundary regions. In the Nd-doped ceria, cation and anion segregation at the grain boundary is quantifiable with sub-nm spatial resolution. The BCZY27 specimen was solid state reactive sintered using 2 wt% NiO and then operated in a reducing atmosphere for 1000 hrs. Most grain boundaries

were observed to be compositionally no different than the bulk, however, some pockets of NiO were found at and near some grain boundaries.

Ferroelectric oxides are used in a wide variety of applications including capacitors, transistors, piezoelectric transducers, and RAM devices. The perovskite family has proven to be especially useful, with materials such as lead zirconium titanate (PZT) and barium titanate (BT) becoming the industry standards in dielectric and multiferroic applications. Through substitutions of niobium or lanthanum for some of the lead, PNZT and PLZT relaxor ferroelectrics are created. They have extraordinarily high piezoelectric and electrostrictive coefficients, respectively making them useful in electromechanical applications. It has been proposed that relaxor ferroelectrics achieve their electrostrictive properties through nanoscale phase separation. APT analysis of these relaxors illustrates that nanoscale phase separation of the B-site cations does occur in volumes less than 20nm^3 .

Applied Surface Science

Room: 204 - Session AS+BI+IS-WeM

Ambient Ionization Mass Spectrometry

Moderator: C. Szakal, National Institute of Standards and Technology, K. Artyushkova, University of New Mexico

8:20am **AS+BI+IS-WeM2 Rapid Evaporative Ionization Mass Spectrometry - Principles and Applications**, *Z. Takats*, Imperial College, London, *J. Balog*, MediMass Ltd., Hungary **INVITED**

Development of ambient ionization methods lifted some of the constraints on the applications of mass spectrometry regarding sample pre-treatment and accessibility. However, even these techniques failed to offer a general solution for in-vivo analysis. Rapid Evaporative Ionization Mass Spectrometry (REIMS) has been developed to fill this gap and bring metabolic/lipidomic phenotyping into interventional medical environment. Origins of REIMS technique were based on the observation that thermal evaporation of tissues during surgical intervention produces gaseous ions corresponding to complex lipid species. Furthermore, these complex lipid fingerprints were found to show excellent histological specificity, similarly to those obtained by MALDI or DESI. Following the development of REIMS-based intra-surgical tissue identification technology, the mechanism of the technique was studied in details, and a wide variety of further applications were proposed. Observations strongly suggest that the REIMS technique – similarly to sonic spray ionization – transfers pre-formed ions from solution to gas phase. Electric current and power setting studies revealed minor dependence of the ionization efficiency on the AC frequency, while increasing power (and hence current) settings improved ion yield in the studied ranges. Studying the effect of atmospheric interface settings led to the conclusion that gaseous ionic species detected in the mass spectrometer are formed in the intermediate vacuum regime via cluster-surface collision phenomena. The assumption was further supported by cluster pick-up experiments where various parts of the ion optics were labelled with low volatility compounds (Rhodamine 6G, arginine) and surface re-ionization was studied during REIMS process. Based on these observations, a new type of atmospheric inlet was built, featuring a target surface for surface-induced dissociation of large molecular clusters accelerated by free jet expansion. The ions formed on collisions are collected by a ring electrode trap which is coupled to the ion optics of the mass spectrometer. Based on the results of mechanistic and earlier surgical studies, a number of new applications were developed ranging from the analysis of arbitrary liquid samples through identification of bacterial strains to imaging analysis.

9:00am **AS+BI+IS-WeM4 A Microplasma VUV Photoionization Source for Ambient Mass Spectrometry**, *J.M. Symonds, R.D. Gann, F. Fernández, T.M. Orlando*, Georgia Institute of Technology

Microplasma ionization sources have been shown to be simple, effective tools for ambient mass spectrometry. Microplasmas have the advantages of being cheap to operate and manufacture, and require only modest gas flows and power sources. One of the challenges in ambient mass spectrometry is to produce sample ions from a wide variety of sample molecules without excessive fragmentation. Due to the chemically-specific nature of ionization, this remains a challenge for any new source. In this work we attempt to mitigate both of these problems by using high energy photons to ionize our samples. We have created a microplasma source that employs a mixture of neon and hydrogen to produce vacuum ultraviolet (VUV) light which can ionize samples at atmospheric pressure. Traditionally, VUV light has been both difficult and expensive to produce, which limits its use for applications like ambient mass spectrometry. With the development of our microplasma VUV source, we are able to take advantage of the VUV

photon's capability as a broadly-applicable, low-fragmentation photoionization source, while retaining the low cost and simple operation which makes ambient mass spectrometry so appealing. By combining this ionization technique with laser desorption, we investigate the use of this source for mass spectrometric imaging.

This work was supported by the National Science Foundation under award number 0923179.

9:20am **AS+BI+IS-WeM5 Advances in Pulsed-Plasma Sources for Surface Analysis by Ambient Mass Spectrometry**, *J.W. Bradley, K. McKay, A. Bowfield*, University of Liverpool, UK, *T.L. Salter*, National Physical Laboratory, UK, *J.W. Walsh*, University of Liverpool, UK, *M.R. Alexander, D.A. Barrett*, University of Nottingham, UK, *I.S. Gilmore*, National Physical Laboratory, UK

The potential benefits of using atmospheric pressure "cold" plasma sources as a means of both desorption and ionisation of material in ambient mass spectrometric analysis of surfaces has been recognized by a number of researchers worldwide. Plasma sources include dielectric barrier jets (PADI [1] and LTP [2]) operating at mid-frequency and also RF corona needle discharges.

Here we develop further strategies to pulse modulate such sources (jet and needle) and investigate the influence of duty cycle on the production of chemical species in the source plasma and the composition of the ionised desorbed species from a range of test surfaces (polymeric, pharmaceutical and biological). For the plasma plume study we use a time resolved (5 μ s) Hidden Analytical molecular beam MS (HPR-60) unit, while detailed information on the spatial distribution of surface species from the chosen material samples was done using a Thermo Velos LTQ Orbitrap MS.

The influence of source-sample and sample-instrument distances on the signal intensities is investigated for both sources. We observe that as the duty cycle of the pulse is decreased the positive ion yield shifted towards higher mass clusters, due to a decrease in gas temperature enabling increased hydration reactions. The negative ions also display similar trends with the yield of larger negative ions increasing with shorter duty cycles. From time-resolved ion intensities it is clearly seen that positive ions are produced in the on-phase of the discharge, and decay in the off-phase. Negative ions, in contrast, are produced mainly in the off-phase of the discharge and decay during the on-phase. With increased distance between source and instrument we observe that the yield of large positive ions increases, at the expense of smaller positive ions which are lost before they reach the orifice. Negative ions, on the other hand, show an increase in yield as distance is increased.

Preliminary analysis of common pharmaceutical products suggest that a decreased duty cycle gives improved identification of negative ion surface compounds however, where surface compounds undergo ionisation to form positive ions, larger duty cycles allowed for better identification. The gas-phase plasma chemistry for different arrangements will be discussed.

1] Ratcliffe LV, Rutten FJ, Barrett DA, Whitmore T, Seymour D, Greenwood C, Aranda-Gonzalvo Y, Robinson S, McCoustra M, *Anal Chem.* (2007) 79 (16) 6094

2] Zhang, JI, Costa, AB, Tao, WA, Cooks, RG, *Analyst*, (2011), 136, 15, 3091

9:40am **AS+BI+IS-WeM6 Comparison of Ambient Pressure Ionization Sources by Determining Useful Yields of Forensic Compounds of Interest**, *T. Brewer, C. Szakal, E. Sisco, S. Muramoto, T. Forbes, G. Gillen*, NIST

The detection of illicit drugs and trace explosives represents one of the most significant challenges for law enforcement and forensic communities. Of particular interest to the forensic analyst is the ability to rapidly identify suspected illicit drug materials and explosives residues in their native state (powder, tablet or liquid form), under atmospheric conditions and with a high level of specificity and sensitivity. To that end there are numerous ambient pressure ionization techniques such as atmospheric pressure glow discharge (APGD), low temperature plasma (LTP), and desorption electrospray ionization (DESI) that can be used to interrogate forensic compounds. However, a method of comparing between the different ambient ionization sources does not exist. Here, useful yields are determined for a series of forensic compounds using different ambient pressure ionization sources as a means of comparison. Using a precision inkjet deposition system a well-defined array of microdroplets is produced with each deposit containing a known number of analyte molecules. The individual deposits were removed or desorbed until consumed while monitoring the integrated characteristic molecular secondary ions for each analyte. The ratio of integrated counts to the number of molecules in the deposit defines the useful yield of the experiments. The results here highlight a way to compare the different ambient ionization sources for the analysis of forensic compounds of interest.

10:40am **AS+BI+IS-WeM9 Atmospheric Pressure Ionization Mass Spectrometry: Fundamentals, Simulations, and Applications**, *Th. Benter*, University of Wuppertal, Germany **INVITED**

Almost for a century now, mass spectrometric instrumentation is generally designed to establish linear analyte concentration – ion signal responses. Deviations from linear relationships are tolerated to a certain extent but such observations usually raises doubts on the performance of the method applied. Surprisingly, Atmospheric Pressure Ionization (API) techniques have swiftly led to the frequent usage of terms such as "matrix effects", "ion suppression", or "non-linear response". This is particularly true for ambient ionization methods. In fact, the various API methods not only target different analyte properties, e.g. gas phase acidities, they also frequently generate new ion signals which are then somehow related to the neutral analyte precursor. On the other hand API mass spectra may also show unexpected fragmentation patterns – despite the often claimed "soft" nature of the ionization processes involved.

In this contribution we are attempting to highlight some of the key processes operating on the primarily generated analyte ion population en route from the origin of ion formation to the collision free analyzer region. For this purpose, we are defining *chemical domains* such as the initial reagent ion generation domain (in ambient ionization often plasmas), the chemical ionization domain, or the thermal ion transport domain, among others. These domains exhibit distinct features, which are significantly changing the chemical matrix in which ions and neutrals are moving towards the collision free - and thus chemically non-reactive - analyzer region.

Primary ionization pathways, subsequent thermal ion molecule chemistry, and electrical fields are discussed as potential drivers of chemical transformation processes, which may render the interpretation of API mass spectra quite difficult. This is particularly true for the analysis of complex mixtures using API MS without chromatographic pre-separation of the neutrals. Ambient ionization methods are generally designed to do exactly that: Analyze samples (e.g., human urine, drug tablets, surface contaminations, to name but a few) without sample preparation and preferentially in real time.

Examples are given to illustrate the extent of selected transformation processes. Among other issues it is discussed why the generation of Helium metastable atoms (He^M) results in protonation in API MS, or why aromatic hydrocarbons ionized with the exact same primary excitation scheme yield almost exclusively radical cations in classical mass spectrometers but often deprotonated molecules in API systems.

11:20am **AS+BI+IS-WeM11 Ambient Mass Spectrometry for Structural Analysis of Organic Monolayers**, *H. Zuilhof*, Wageningen University, Netherlands

For the analysis of covalently bound organic monolayers a variety of surface-sensitive techniques has been developed, including XPS, AES, IR, contact angle measurements and X-ray reflectivity. While each of these has its own merits, none of them provide **structural** information. In addition, via e.g. XPS it is sometimes possible to follow $A \rightarrow B$ reactions on a surface, but $A \rightarrow x\% B + y\% C$ is already nearly impossible to properly analyze. Similar restrictions apply to the study of diluted monolayers (e.g. 10% of a bioactive compound surrounded by 90% inert surface-covering monolayer), while dilution may actually be essential for the proper biological functioning of the monolayer! Therefore novel analysis techniques are still in demand, and here we present the application of DART ambient mass spectrometry as a generic and highly powerful technique for the analysis of such monolayers. Using a variety of tailor-made, covalently attached organic monolayers on silicon nitride and other substrates we show that MS can be used to study: 1) the progress of four sequential surface-bound organic reactions, 2) surfaces with a mixture of halogens on them, 3) the progress of incomplete reactions, and 4) the stability of biofunctional groups. In the current presentation we summarize our recently published work in this area (*ChemComm* 2013, 922) and present new, as of yet unpublished data that outline the tremendous potential of this novel analysis technique!

11:40am **AS+BI+IS-WeM12 Differentiation of Microbial Species & Strains in Coculture Biofilms by Multivariate Analysis of Laser Desorption Postionization Mass Spectra**, *C. Bhardwaj, Y. Cui*, University of Illinois at Chicago, *H.C. Bernstein, R.P. Carlson*, Montana State University, *L. Hanley*, University of Illinois at Chicago

The metabolic states of microbial biofilms vary with growth conditions such as host surface, culture media, or antibiotic concentration. 7.87 and 10.5 eV vacuum ultraviolet (VUV) photon energies were used in laser desorption postionization mass spectrometry (LDPI-MS) to analyze microbial biofilms comprised of binary cultures of interacting microorganisms grown on polymer membranes. Principal components analysis (PCA) was applied to the MS data to differentiate species in

Escherichia coli-*Saccharomyces cerevisiae* coculture biofilms. PCA of LDPI-MS also differentiated individual *E. coli* strains in a biofilm comprised of two interacting gene deletion strains, even though these strains differed from the wild type K-12 strain by no more than four gene deletions each out of approximately 2000 genes. PCA treatment of 7.87 eV LDPI-MS data separated the *E. coli* strains into two "pure" groups and a distinct mixed region. Furthermore, the "pure" regions of the *E. coli* cocultures showed greater variance by PCA when analyzed by 7.87 eV photon energies than by 10.5 eV radiation. Comparison of the 7.87 and 10.5 eV data is consistent with the expectation that the lower photon energy selects a subset of low ionization energy analytes while 10.5 eV is more inclusive, detecting a wider range of analytes. These two VUV photon energies therefore give different spreads via PCA and their respective use in LDPI-MS constitute an additional experimental parameter to differentiate the metabolite states of microbial biofilms growing on different surfaces.

Biomaterial Interfaces

Room: 201 B - Session BI-WeM

Cell-Surface Interactions

Moderator: M.R. Alexander, University of Nottingham, UK

8:00am **BI-WeM1 High-Throughput Discovery of Materials for Human Pluripotent Stem Cell Culture**, A.D. Celiz, J.G.W. Smith, A.K. Patel, University of Nottingham, UK, R. Langer, D.G. Anderson, Massachusetts Institute of Technology, D.A. Barrett, L.E. Young, C. Denning, M.C. Davies, M.R. Alexander, University of Nottingham, UK

A key hurdle in translating stem cell therapies from research to industrial scale and clinical application is to produce the necessary numbers of cells. For example, a major heart attack causes loss of 1 billion cardiomyocytes and similar cell numbers are lost during progression of other conditions such as multiple sclerosis and diabetes. To meet the demand for such high cell numbers, a defined growth substrate free of animal-derived components is desirable. To this end, we have employed polymer microarrays to screen for human pluripotent stem cell (hPSC) attachment and phenotype on polymers in a high-throughput manner. Polymer microarrays enable a large combinatorial chemical space to be interrogated on a single glass slide. Furthermore, since monomers can be robotically printed and polymerized on the slide via UV photo polymerization, rapid evolution of large numbers of polymers is facilitated. 'Hit' materials identified from the initial screen can be taken forward to a second generation array and mixed in a combinatorial manner to test hypotheses formed from the first generation array and this iteration continues until scaled up to plastic ware for automated culture protocols to achieve long-term expansion of hPSCs.

We have screened over 140 acrylate and acrylamide homopolymers in an array format for hPSC attachment in mouse embryonic fibroblast (MEF) conditioned medium and defined media including StemPro® and mTeSR™ after 24 hours in culture. Hit materials were then mixed to produce a second generation array of over 500 unique copolymers to optimise cell attachment. Polymer microarrays were characterized using time of flight secondary-ion mass spectrometry (ToF-SIMS), X-ray photoelectron spectroscopy (XPS), atomic force microscopy (AFM) and water contact angle (WCA) measurements. Multivariate analysis (MVA) was used to successfully predict material wettability and cell performance from the ToF SIMS data. Cell attachment was identified using DAPI (nuclei) staining and maintenance of pluripotency was confirmed by OCT-4 staining and imaged using automated fluorescence microscopy. This approach to materials discovery will provide a defined, synthetic growth substrate for hPSC culture that is amenable to scale up for industrial application and is a step toward xeno-free hPSC culture conditions necessary for clinical application.

8:20am **BI-WeM2 Toxicology of Antimicrobial Conjugated Electrolytes: Interactions with Mammalian Cells**, H.E. Canavan, K.N. Wilde, D.G. Whitten, University of New Mexico

Certain cationic phenylene ethynylene (CPE)-based polymers (PPEs) and oligomers (OPEs) exhibit dark- and light-activated antimicrobial activity. Until recently, it was unknown if they would also exhibit similar biocidal activity toward mammalian cells. Based on their biocidal activity and diversity of repeat unit number and functional groups, a variety of CPEs, PPEs, and OPEs were selected for these studies, and were examined for their toxicity toward mammalian cells at three levels: cytotoxicity testing of cell monolayers, skin irritation testing of tissues, and intracellular colocalization. As expected, concentration plays the largest role in determining viability. The lack of skin irritation for all substances alleviates initial safety concerns for products based on these CPEs and OPEs. In all

cases, the addition of light changed the effects of the compounds on the mammalian cells. The modes of action of these compounds appear to be governed primarily by length.

8:40am **BI-WeM3 In Situ ATR-FTIR of Human Mesenchymal Stem Cell Differentiation**, D.E. Barlow, P.A. Fulmer, T.J. O'Shaughnessy, K.P. Fears, J. Morabito, R. Stine, S.P. Mulvaney, B.R. Ringeisen, U.S. Naval Research Laboratory

Vibrational spectroscopies are valuable methods for non-destructive characterization of biochemical functionality and physiological changes in stem cells. To date, the primary approaches have almost exclusively used either Raman microscopy or Fourier transform infrared (FTIR) microscopy in transmission or reflection configurations. Another FTIR approach is the interfacially sensitive attenuated total reflectance (ATR) configuration which has often been used for in situ characterization of buried cell-substrate interfaces with live microorganisms such as bacteria. However, so far, the method has rarely been used with mammalian cells. Our approach provides a useful complimentary method for which multiple live specimens can be kept under controlled environmental conditions and analyzed by ATR-FTIR over multi-week periods. As a first step in employing in situ ATR-FTIR, we will present results demonstrating early detection of osteogenic differentiation of live human mesenchymal stem cells (hMSC's). In comparison to control hMSC spectra, hydroxyapatite related bands are clearly observed for cells in osteogenic media within 24 hours. Further hydroxyapatite formation and differentiation characteristics were observed over 2 week periods. Additional results will also be presented comparing interfacial spectra of live hMSC's on surfaces with varying properties, including poly-D-lysine/laminin coated substrates, graphene, and nanocrystalline hydroxyapatite.

9:00am **BI-WeM4 Do Cells Read Braille? High Throughput Screening of Surface Topography-Induced Cellular Responses**, J. De Boer, University of Twente, Netherlands **INVITED**

It is well known that cells can respond to diffusible molecules but it is less well known that they are also able to respond to patterned surface topographies. If we are able to understand how cells respond to these patterns, we can rationally design the surface of medical implants for optimized functionality. To unravel the secret Braille language of cells, we have designed and engineered the TopoChip platform, a library of surface topographies reproduced onto polymeric surfaces. Using high-content imaging, we are able to analyze the response of cells to thousands of different surface patterns simultaneously. Thus, we have found surfaces which induce expression of the early osteoblast marker alkaline phosphatase (ALP) in mesenchymal stromal cells to levels similar to that induced by classical osteoblast inducers such as dexamethasone. In addition to ALP staining, we have also stained the actin cytoskeleton and the nucleus, and using CellProfiler software, we have extracted nearly 300 morphological features for each cell on the TopoChip. Using machine learning algorithms, we are now able to predict ALP expression based on cell morphology alone, and further experiments are in progress to investigate a possible correlation between the actin cytoskeletal organization and ALP expression. In conclusion, using a high-throughput screening approach, we can now start to unravel the secret language of surface topographies and apply the hit surfaces to improve medical implants.

9:40am **BI-WeM6 Less is More: Enhancing the Effect of Fibroblast Growth Factor (FGF2) on Human Dermal Fibroblast Proliferation by Surface Modification**, J.D. Whittle, D.E. Robinson, University of South Australia

Often the materials selected for culture-ware, scaffolds or bandages are chosen for their bulk properties and low cost, rather than their suitability for cell culture. Consequently cell culture frequently requires relatively large quantities of expensive growth factors (GFs) and other supplements to be added to the culture medium. Cell response to surfaces is known to be heavily influenced by surface chemistry and topology, which may impact on cell attachment, proliferation or differentiation. These surface properties can affect the growth of cells, they do so by influencing the cellular microenvironment. Often this is by modulating the composition and conformation of adsorbed proteins.

A number of approaches to healing of chronic wounds involve the culture of patient cells on bandages or scaffolds for delivery direct into wounds. In this paper, we describe the approach we have taken in our lab to provide a suitable microenvironment for human dermal fibroblasts.

Inspired by the role of the extra-cellular matrix (ECM) in vivo, we use a plasma polymer surface to bind glycoaminoglycans (GAGs) which are able to capture the growth factor FGF2 from solution. By binding the GAG and growth factor to the culture surface, we achieve significantly higher cell proliferation rates at low serum concentrations than adding these components directly into the culture media. We show that binding GAG and

GF to the surface has a cooperative effect, in which the combination of these biomolecules is much more effective than either of them alone. In addition to better performance, the pre-loading of culture surfaces avoids the need to add these reagents to the culture medium and therefore reduces the cost of cell culture. We also show how this approach can be translated from 2d cultures to electrospun scaffolds to provide organised dermal structures of fibroblasts and keratinocytes.

10:40am **BI-WeM9 An Anionic Drug Delivery System using Lecithin Liposomes to Improve Oncolytic Viral Cancer Therapy.** *N. Mendez, V. Herrera, F. Hedjran, S.L. Blair, T. Reid, W.C. Trogler, A.C. Kummel*, University of California San Diego

Several treatment modalities such as surgery, radiation, and chemotherapy are effective for cancer treatment however also face several limitations. Alternatively, oncolytic viruses (OVs) can target multiple mechanisms of action while at the same time exploit validated genetic pathways known to be dysregulated in many cancers. In particular, the oncolytic virus TAV-255 has shown viral replication attenuation in normal cells while retaining cytolytic activity in tumor cells by taking advantage of defects in the p53-tumor suppressor pathway. Despite its several advantages, the utility of OVs for cancer therapy is limited by 1) neutralization by antibodies mediated by the immune system, 2) rapid clearance by the reticuloendothelial (RE) system in the liver, and 3) the lack of expression of surface receptors (CAR) in certain cancers necessary for OV transduction. Oncolytic viruses are promising agents to combine with nanoparticle delivery approaches because of the capacity for self-replication of the virus. In systemic delivery, targeting with nanoparticles may focus the viral load to the primary tumor cells as well as metastatic tumors to insure a productive initial infection. A non-toxic liposomal delivery system has been developed for delivery of the virus to tumor cells. Further, with the aim to overcome an immune response and to enhance its potential use to treat primary and metastatic tumors, an encapsulation method involving an anionic non-toxic liposome has been prepared by self-assembly of Lecithin around the viral capsid. The developed method has shown that encapsulated viruses retain their ability to infect cancer cells. Furthermore, an immunoprecipitation (IP) technique has shown to be a fast and effective method to extract non-encapsulated viruses and homogenize the liposomes remaining in solution. Extracting non-encapsulated viruses from solution may prevent an adverse immune response when used in an in vivo model and may enhance treatment for multiple administrations.

11:00am **BI-WeM10 Poly(*N*-isopropyl Acrylamide)-coated Surfaces: Investigation of Biocompatibility with Mammalian Cells.** *M.A. Cooperstein, H.E. Canavan*, University of New Mexico

Poly(*N*-isopropyl acrylamide) (pNIPAM) undergoes a conformation change in a physiologically relevant temperature range. PNIPAM is relatively hydrophobic above its lower critical solution temperature (LCST, ~32°C), and mammalian cells are easily cultured on pNIPAM-grafted surfaces. When the temperature is lowered below the LCST, the polymer's chains rapidly hydrate, and cells detach as intact sheets capable of being used to engineer tissues ("cell sheet engineering"). Although the NIPAM monomer is toxic, there are conflicting reports as to whether its polymerized form is toxic, as well. Very few (<10) studies exist that investigate the cytotoxicity of pNIPAM, and their results are conflicting. Furthermore, the published studies are not comprehensive. Before the cell sheets detached from pNIPAM can ultimately be used on humans, it is crucial to first assess the cytotoxicity of the surfaces from which they have been obtained. In this work, we present a comprehensive investigation of the cytotoxicity of pNIPAM-grafted surfaces. The relative biocompatibility of substrates prepared using different polymerization (free radical and plasma polymerization) and deposition (spin coating and plasma polymerization) techniques is evaluated using appropriate cytotoxicity tests (MTS, Live/Dead, plating efficiency). Four different mammalian cell types (endothelial, epithelial, smooth muscle, and fibroblasts) were used for the cytotoxicity testing. The pNIPAM-coated surfaces were evaluated for their thermoresponse and surface chemistry using X-ray photoelectron spectroscopy and goniometry. We find that while cell viability on pNIPAM surfaces decreases when compared to controls, the viability also seems to be deposition type dependent, with sol-gel-based pNIPAM surfaces being the least biocompatible. We attribute this difference to surface topography and chemistry. This work will have valuable insights into the cytotoxicity of pNIPAM-coated surfaces, and therefore into the applicability of cells grown on these surfaces for use in human subjects. In addition, the trends observed in the effect of polymer molecular weight, surface modification technique, and cell type may be extrapolated to other bioactive polymers of interest.

11:20am **BI-WeM11 Polymer Microarrays for the High Throughput Discovery of Novel Switchable Materials.** *A.L. Hook, C. Chang*, University of Nottingham, UK, *R. Langer, D.G. Anderson*, Massachusetts Institute of Technology, *P. Williams, M.C. Davies, M.R. Alexander*, University of Nottingham, UK

Polymer microarrays for the high throughput discovery of novel switchable materials

Andrew L. Hook^a, Chien-Yi Chang^b, Robert Langer^c, Daniel G. Anderson^c, Paul Williams^b, Martyn C. Davies^a, Morgan R. Alexander^a

^aLaboratory of Biophysics and Surface Analysis, University of Nottingham, UK

^bSchool of Molecular Medical Sciences, University of Nottingham, UK

^cDavid H. Koch Institute for Integrative Cancer Research, Massachusetts Institute of Technology, USA

Polymer microarrays have become a key enabling technology for high throughput materials discovery. This format has been applied to a broad range of biological systems, from stem cell attachment to the resistance of bacterial attachment.¹ Switchable materials have also been a focus of materials research as they provide temporal control of biological systems. Switchable materials are able to alter their surface or physical properties in response to an external specific signal such as a change in temperature, pH, or concentration of a signal molecule. This class of materials has been applied to drug delivery and controlled cell attachment.

We have applied polymer microarrays for the discovery of novel switchable materials that are able to temporally manipulate biological systems.^{2,3} Polymer microarrays were formed by printing mixtures of acrylate monomers, followed by UV curing and vacuum extraction. This enabled arrays of hundreds of unique materials to be produced. We screened these materials for switchable properties using AFM, WCA, optical microscopy and ToF-SIMS. The focus of this work was to identify materials with thermally induced changes in chemistry or topography.^{2,3} Using these methods we discovered novel materials with unique switchable properties. In particular, ToF-SIMS analysis provided insight into the conformational changes induced in the polymers by the change in temperature.² These were applied to investigate the attachment of bacteria to surfaces, where we were able to temporally control the interaction of bacteria with a polymer surface. These materials have potential application for regenerative filtration devices.

¹ Hook et al., *Biomaterials*, **2010**, 31, (2), 187-198.

² Hook et al., *Surface and Interface Analysis*, **2013**, 45, (1), 181-184.

³ Hook et al., *Soft Matter*, **2011**, 7, (16), 7194-7197.

11:40am **BI-WeM12 Antibacterial and Cells Proliferation Studies of Biodegradable Polymeric 3D Scaffolds.** *A. Pegalajar-Jurado, K.A. Wold, M.M. Reynolds, E.R. Fisher*, Colorado State University

Wounds caused by diseases or injuries often present complications, requiring medical intervention to restore biochemical processes needed for proper healing to occur. Several biodegradable polymeric materials have been applied to wounds for protection and to facilitate the healing. These materials, however, often do not inhibit bacterial infection nor support cell growth.

Development of therapeutic materials that release antimicrobial agent from a porous, polymeric fibers scaffold has been previously reported by our group, which was directly related to the release of nitric oxide (NO). These scaffolds showed a release of NO under physiological pH and temperature, and a log2 reduction in *Acinetobacter baumannii* was achieved using 15 mg/mL of NO releasing S-nitrosated poly(lactic-co-glycolic-co-hydroxymethyl propionic acid (PLGH)-cysteamine. However, fibroblast cells showed low viability when exposed to concentrations higher than 0.1 mg/mL of S-nitrated PLGH-cysteamine polymer. A log5 reduction in bacteria such as *Escherichia coli* and methicillin-resistant *Staphylococcus aureus* is required to be considered medically relevant. To achieve this goal, a multiple therapeutic strategy was implemented. The antimicrobial activity of silver nanoparticles against *E.coli* and *S.aureus* over short period of time is well established. To obtain a long term efficacy as well as local toxicity, silver nanoparticles were incorporated within the NO releasing scaffolds. This combination is expected to result in antibacterial activity against multiple strains included *E.coli* and MRSA.

Plasma processing has been used extensively to modify two-dimensional materials. Recently, however, plasma treatments have been used to successfully modify three-dimensional (3D) structures. Our preliminary data demonstrate that porous (ϵ -caprolactone) (PCL) scaffolds can be modified by plasma functionalization. Significant increase in the scaffolds' wettability was achieved by H₂O/NH₃ and H₂O/N₂ plasma treatments. XPS analysis corroborated changes in the surface chemistry throughout the 3D structure, with no significant changes in scaffold morphology after plasma treatments (SEM analysis). In addition, enhanced osteoblast proliferation

was observed in PCL scaffolds after plasma surface modification. These results support plasma surface modification as a viable technique to improve the surface properties of 3D materials to promote cell growth and ultimately aid in tissue engineering. In addition to these results, cell proliferation and the antimicrobial behavior of S-nitrated PLGH-cysteamine polymer after the incorporation of silver nanoparticles and plasma surface modification will be discussed.

Electronic Materials and Processing

Room: 102 A - Session EM+PS-WeM

Oxides and Dielectrics for Novel Devices and Ultra-dense Memory II

Moderator: J. Kim, The University of Texas at Dallas

8:00am **EM+PS-WeM1 Active Surfaces and Interfaces in Valence Change Memory Type Oxides**, R. Waser, R. Dittman, RWTH Aachen University, C. Lenser, Forschungszentrum Juelich GmbH, Germany

INVITED

Flash memories and DRAM are ubiquitous today. However, a potential leap beyond the limits of Flash (with respect to write speed, write energies) and DRAM (with respect to scalability, retention times) emerges from nanoionic redox-based switching effects encountered in metal oxides (ReRAM). A range of systems exist in which ionic transport and redox reactions on the nanoscale provide the essential mechanisms for memristive switching. One class relies on mobile cations which are easily created by electrochemical oxidation of the corresponding electrode metal, transported in the insulating layer, and reduced at the inert counterelectrode (so-called electrochemical metallization memories, ECM). Another important class operates through the migration of anions, typically oxygen ions, towards the anode, and the reduction of the cation valences in the cation sublattice locally providing metallic or semiconducting phases (so-called valence change memories, VCM). The electrochemical nature of these memristive effects triggers a bipolar memory operation. In yet another class, the thermochemical effects dominate over the electrochemical effects in metal oxides (so-called thermochemical memories, TCM) which leads to a unipolar switching as known from the phase-change memories. In all systems, the defect structure turned out to be crucial for the switching process.

The presentation will cover fundamental principles in terms of microscopic processes, switching kinetics and retention times, and device reliability of the VCM-type ReRAM variant. It will describe what can be learnt about the nature of the redox-based switching process on open surfaces (e.g. system with top electrodes removed) and embedded electrode interface.

Despite exciting results obtained in recent years, several challenges have to be met before these physical effects can be turned into a reliable industrial technology.

8:40am **EM+PS-WeM3 Resistive Switching and Interface Structure of Metal / Ga₂O₃ / Metal Heterostructures**, B. Zhao, X. Zheng, H. Pham, M.A. Olmstead, F.S. Ohuchi, University of Washington

Materials exhibiting reversible resistance changes are essential elements of resistance random access memory (R-RAM), which has a simpler structure, lower energy consumption, higher operating speed and higher endurance than conventional RAM. The monoclinic transparent conducting oxide β -Ga₂O₃ is a promising candidate for R-RAM due to its open-channel structure that enables large scale defect migration. The resistive switching mechanism in pulsed-laser-deposited Ga₂O₃ was investigated by combining electrical measurements with x-ray diffraction (XRD) and sputter-profiling x-ray photoemission spectroscopy (SP-XPS), revealing a strong correlation of oxide-metal interface conductance with electrically and thermally driven defect migration and agglomeration near the interface.

Electrically-activated reversible resistance switching is observed in thin-film Ni/Ga₂O₃/Ir, while irreversible changes can be observed upon annealing either single-crystal or thin film gallium oxide. Room-temperature Ni deposition on single crystal β -Ga₂O₃ results in a rectifying contact with barrier height \sim 0.8 eV and SP-XPS reveals no interface reaction; annealing this structure to 500°C irreversibly creates an ohmic contact, as well as oxidized Ni and reduced Ga at the interface.

A reversible resistance change can be triggered by an electrical pulse in polycrystalline gallium oxide films grown by pulsed laser deposition. Ni/Ga₂O₃/Ir heterostructures were fabricated and then investigated at different points in their electrical cycling history. Application of less than about 10 V across a 100 nm film (\sim 10⁶ V/cm) maintains the initial Schottky behavior; a 1 sec, 30 V electric pulse switches the metal/oxide contact from Schottky to Ohmic and increases the device conductance by two orders of

magnitude. X-ray diffraction shows the film recrystallizes into α and β phases of Ga₂O₃; further electric field treatment increases the β -phase fraction. Sputter-profiling XPS shows an increase in the near-surface Ga:O ratio and introduction of reduced Ga within 2 nm of the metal-oxide interface. The film remains Ohmic under low voltage cycling, but a high-voltage pulse with the opposite polarity both reverses the interface chemical changes and reverts the electrical characteristic to a Schottky contact. Further cycling between Ohmic and Schottky behavior continues with additional voltage pulses. The results are consistent with Ga interstitial migration and/or an interface redox reaction.

This project is supported by the National Science Foundation under DMR 1104628 and the Micron Foundation.

9:00am **EM+PS-WeM4 The Effect of High-Pressured N₂ Annealing in NiO_x based Resistive Random Access Memory**, D.H. Yoon, Y.J. Tak, J. Jung, S.J. Kim, H.J. Kim, Yonsei University, Republic of Korea

High pressure annealing (HPA) is known as an effective way to control the fundamentals of oxide system through the modification of stoichiometry, thermal decomposition, and compression.[1] Here, we report the effect of N₂ HPA on NiO_x based resistive random access memory (RRAM) device in terms of applied pressures in NiO_x system. In this research, the annealing temperature was fixed at 350 °C while the applied pressures were varied to 1, 20, and 50 atm. Pt was commonly used as bottom and top layer of metal-insulator-metal structure. As the N₂ pressure increased, the on- and off-resistance ratio was decreased from \sim 10⁵ to \sim 10⁴. However, the operation voltages (reset and set voltage) were reduced followed by increment of N₂ pressure. Specifically, the 50 atm HPA sample shows the lowest reset voltage of 0.95 V and set voltage of 2.12 V. This result implies that enhanced grain size was induced by the N₂ pressure as the grain boundaries are preference sites for conduction filament formation.[2] Furthermore, notable increment of non-lattice oxide component was confirmed which may cause the reduced driving voltages by x-ray photoelectron spectroscopy. These findings can enhance the understanding of low-power driving RRAM for next generation memory device.

References:

[1] Y. S. Rim, W. H. Jeong, D. L. Kim, H. S. Lim, K. M. Kim and H. J. Kim, *J. Mater. Chem.* **22**, 12491 (2012).

[2] S. Kim, D. Lee, J. Park, S. Jung, W. Lee, J. Shin, G. Choi, and H. Hwang, *Nanotech.* **23**, 325702 (2012).

9:20am **EM+PS-WeM5 Ionic Memory - Materials and Devices**, M.N. Kozicki, Arizona State University

INVITED

There is widespread agreement within the semiconductor industry that existing high density non-volatile memory technologies are reaching their scaling limits and will ultimately be replaced by some variant of resistive random access memory (RRAM). This paper discusses advances in ionic RRAM, which relies on ion transport and redox reactions in thin solid electrolyte/dielectric films. Emphasis is placed on a technology known as Conductive Bridging Random Access Memory (CBRAM), a recently commercialized ionic memory based on the Programmable Metallization Cell (PMC) platform. In this technology, metallic cations are typically the mobile species. An ion current will flow if (1) the electrolyte is placed between two conductive layers, at least one of which can supply ions, (2) the ion-supplying electrode is made positive with respect to the opposing electrode, and (3) a sufficient bias is applied to overcome the internal potential barrier. The ion current feeds the reduction reaction, resulting in the formation of a metallic filament within the electrolyte/dielectric. The filament has a conductivity that is much higher than the surrounding material and hence it allows the resistance of the structure to be reduced by several orders of magnitude. The resistance of the conducting filament depends on the total number of metal ions that are reduced, which in turn depends on the charge supplied by the external circuit. Thus, the on-state resistance can be controlled by programming current and time. Control over the on-state resistance means that it is possible to create multiple discrete resistances levels to represent more than one binary digit per cell. If one electrode is electrochemically inert, the resistance-change process can be reversed by applying an opposite bias to that used for programming which dissolves the conducting pathway via oxidation of the metal in the filament. It is this electrode asymmetry that allows the deposition/dissolution process to be cycled repeatedly. We have also studied stackable diode-isolated arrays, in which each cell has one resistive switching element and one integrated Zener diode formed by the junction of the Cu filament of the device on-state and a doped silicon (n-type) electrode. The diode reduces "sneak path" currents via low resistance on-state devices in an array, but the reverse breakdown of the Zener element allows the cells to be erased by reverse bias.

10:40am **EM+PS-WeM9 Electrode-bias Injection and Percolation Controlled Transport through Vacated O-atom Site Defects in Nanograin (ng-) TM Oxides and in Non-crystalline (nc-) Si(Ge)O₂.** D. Zeller, G. Lucovsky, North Carolina State University, J. Kim, University of Illinois at Urbana Champaign

Remote plasma CVD of thin film (i) non-crystalline nc-SiO₂ on Si substrates and (ii) nanograin ng-TM oxides thin-film dielectrics plasma processed Ge substrates combined removal of Ge-O and Ge-N layers by post-processing annealing presents new opportunities for devices.

Semiconductor conduction band edge states (CBES), and symmetries and singlet transport and/or trapping states of vacated O-atom defects are quantitatively different for nc-Si(Ge)O₂ and nano-grain (ng-) TM oxides. CBES in Si(Ge)O₂ and Si/Ge on a zinc-blende III-V semiconductors are "s-like" with high electron mobilities. Combined with intrinsic band edge triplets in SiO₂, energies of vacated O-atom singlet defect states are deeper into the band-gap. Injection into, and transport through singlet defects localized in 1 nm nc-SiO₂ clusters with "crystalline-like" medium range order (MRO) extends to self-organized symmetric dihedral angles. Hopping transport through vacated O-atom sites is determined by percolation. It is eliminated through nc-Si(Ge)O₂ interfacial transition regions by the 0.6 eV spectral extent of the intrinsic band edge triplets explaining the absence of bulk negative space-charge in devices, and after accelerated bias-controlled stress testing. CBES and vacated O-defects in X-ray absorption spectra (XAS).

Properties of nc-SiO₂ dielectrics and their semiconductor interfaces are the standard against which high-k TM gate dielectrics are evaluated. CBES are "d-like" with symmetries dependent on coordination, "t_{2g}-like" for 6-fold coordinated TiO₂ and Ti₂O₃ and Magneli-phase alloys, and "e_g-like" for 7- and 8-fold coordinated HfO₂ and ZrO₂. Jahn-Teller effects remove 3-fold t_{2g} and 2-fold e_g degeneracy in O K-edge XAS in thin films <2 nm in TiO₂ and <3 nm-HfO₂.

In thicker films O-vacancy singlet states are below CBES with bias-controlled injection and transport. Combined with metal gates, and n- and p-type doping, for Si, Ge and III-V semiconductor substrates, memory and switching functionality is established. 300° CVD devices are obtained in RPD ~2 nm thick TiO₂ or HfO₂ onto nitrided Ge substrates with ~0.5 nm of Ge-N detected by in-line AES. 400-500°C post-deposition annealing removes Ge-N bonds at nitrided interfaces, and provides a template for deposition of nc- and ng-dielectrics. Ne-HfSiON on Si-passivated and nitrided Ge (100) and ng-TiO₂ yield Dit levels of 2-5x10¹⁰ cm⁻². C-V characteristics are symmetric with respect to flat-band voltages, V_{FB} yielding fixed charge levels ~2-3x10¹¹ cm⁻³. J-V characteristics yield currents at 1 V > V_{FB} of 3-5x10⁻⁶ A-cm⁻². TiO₂ capacitors on Ge have EOT values of ~ 4.5 nm, as well as low values of Dit.

[1] G. Lucovsky, et al: Many-Electron Multiplet Theory Applied to O-Vacancies in (i) Nanocrystalline HfO₂ and (ii) Non-crystalline SiO₂ and Si Oxynitride Alloys, Progress in Theoretical Chemistry and Physics 23 (2010) 193-211.

[2] G. Lucovsky, D. Zeller, Remote Plasma Enhanced Chemical Deposition of Non-Crystalline GeO₂ on Ge and Si Substrates, Journal of Nanoscience and Technology 11 (2011) 7974-7981

[3] Y. Tanabe, S. Sugano, On the absorption spectra of complex ions, Journal of the Physical Society of Japan (1956) 11 (8) (1956) 864-877; 9(5) (1954) 9(5) 766-779.

11:00am **EM+PS-WeM10 Investigation of the Dominant Conduction Mechanisms in Metal-Insulator-Metal Tunnel Diodes with Ta₂O₅ and Nb₂O₅ Dielectrics Deposited by Atomic Layer Deposition.** N. Alimardani, J.F. Conley, Jr., Oregon State University

Thin film metal-insulator-metal (MIM) tunnel devices have seen renewed interest for high speed applications such as infrared (IR) detectors, optical rectennas for energy harvesting, and hot electron transistors. For many of these applications, desired properties include high asymmetry (η) and non-linearity (f_{NL}) of current vs. voltage (I-V) behavior and small turn-on voltage (V_{ON}). The standard approach to achieving these characteristics in tunnel devices is M₁IM₂ diodes - the use of electrodes with different workfunctions to induce a built-in field across the insulator. V_{ON} is influenced by the choice of the dielectric layer. In theory, small band-gap dielectrics with large electron affinity (χ) are desired to achieve small V_{ON} in tunnel diodes as they make small energy barriers with electrodes. Regarding this, Nb₂O₅ and Ta₂O₅ are widely considered to be promising candidates as tunnel dielectrics. In this work, we investigate Nb₂O₅ and Ta₂O₅ MIM diodes. Atomic layer deposition (ALD) was used to deposit 5 nm and 10 nm thick Nb₂O₅ and Ta₂O₅ tunnel barriers with sputtered amorphous bottom electrodes (ZrCuAlNi) and evaporated Al top electrodes. The I-V responses were found to be asymmetric for diodes made with 5 nm and 10 nm of either of these dielectrics. Although a lower V_{ON} was observed, the maximum asymmetry was 3 orders of magnitude smaller than what we previously reported for similar diodes with ALD Al₂O₃ as the

dielectric layer. High speed operation of MIM devices is typically based on Fowler-Nordheim tunneling (FNT). Conduction mechanisms were investigated as a function of temperature and electric field. By fitting I-V curves to FNT, Schottky emission (SE), and Frenkel-Poole (FP) emission plots, the dominant conduction mechanism in these diodes was found to be SE in the small bias regime (0.1 V to 0.3 V) and FP emission in the large bias regime (≥ 0.75 V). These assignments were confirmed by the close match of the optical dielectric constants extracted from the SE and FP plots with spectroscopic ellipsometry. Finally, Arrhenius plots show temperature dependence of current at both small and large bias regimes, indicating that tunneling is not the dominant conduction mechanism. In conclusion, we find that the small low-voltage asymmetric I-V behavior in MIM diodes made with Nb₂O₅ and Ta₂O₅ dielectrics is due to SE, rather than FN tunneling. A comparison will be made to bi-layer dielectric MIIM diodes, which we recently reported to show improved low voltage η and f_{NL} . This work indicates that the choice of dielectric is critical as high χ dielectrics may not exhibit conduction mechanisms appropriate for high speed applications of MIM tunnel diodes.

11:20am **EM+PS-WeM11 Mechanism of Light Emission and Optical Characteristics of Thin Film Metal Oxides.** Y. Kuo, C.-C. Lin, Texas A&M University

Currently, light emitting devices (LEDs) are made of inorganic or organic semiconductor materials prepared in crystalline thin films or nanocrystalline dots. They usually emit narrow band light due to the limit of the band gap energy of the semiconductor material. Commercial p-n junction or quantum well LEDs are fabricated with the MOCVD process involving toxic chemicals on the expensive single crystal substrate. Compared with the incandescent or the fluorescent light bulb, these LEDs have many advantages, such as the compact size, long lifetime, and low power consumption, but at the expense of the higher price, e.g., by more than one order of magnitude. On the other hand, the good-quality white light cannot be emitted from a single LED chip. It requires a set of three different LEDs or one LED in combination with a phosphor layer.

Recently, it has been reported that the broad band white light could be emitted from a new type of LED that has a MOS structure with a very thin amorphous metal oxide high-k dielectric layer (1,2,3). The complete device can be easily fabricated on the Si wafer using the IC compatible process at a low thermal budget. In this talk, authors will discuss 1) the light emission mechanism, which is from the thermal excitation of the conductive paths formed during the dielectric breakdown, 2) the optical characteristics, which covers the whole visible and part of the IR wavelength range of 400 nm to 1,000nm with a high color rendering index of 95, and 3) the lifetime, which is longer than 1,500 hours under the continuous operation at room temperature in the air. The unique physical structure and material properties of the sub 10 nm thick metal oxide layer are responsible for the light emitting phenomenon. Experimental results on this kind of device will be shown and discussed. In summary, this type of LED is applicable to a large range of industry, consumer, medical, etc. products.

(1) Y. Kuo and C.-C. Lin, *Appl. Phys. Lett.*, **102**, 031117 (2013).

(2) Y. Kuo and C.-C. Lin, *ECSSolid State Lett.*, **2(8)** Q59-Q61 (2013).

(3) Y. Kuo and C.-C. Lin, *Solid State Electronics*, accepted, August 2013.

Electronic Materials and Processing

Room: 101 B - Session EM1-WeM

Electrical Testing and Defects in III-V's

Moderator: C.L. Hinkle, University of Texas at Dallas

8:20am **EM1-WeM2 Formation and Properties of High-k/InGaAs Interfaces on Well-Controlled Surfaces.** P.C. McIntyre, Stanford University

INVITED

Electrically active defects that either trap carriers or act as centers of fixed charge are critically important in MOS devices. Their effects are particularly pronounced for arsenide-based semiconductors intended for NMOS devices because of 1) the relative ease of forming surface defects on these crystals, 2) the lack of an insulating native oxide (such as SiO₂) to inhibit tunneling of electrons from the substrate into near-interface defects in deposited gate dielectrics, and 3) the low density of states in the conduction band of the semiconductor that enhances the effect of charge traps on the measured capacitance compared to materials such as Si or Ge. Alloying GaAs with InAs reduces the band gap of the former by lowering the energy of the conduction band edge, reducing the overall density of defect states in the band gap and thus the density of interface traps. Further reduction in both bulk dielectric defect densities (e.g. border traps and fixed charge) and interface trap densities can be achieved by appropriate pre-

dielectric and post-dielectric processes. This presentation will review recent results on pre-atomic layer deposition defect passivation, including trimethyl aluminum and oxidant pre-dosing of initially clean and oxide-free InGaAs (100) surfaces, plasma treatments of initially air-exposed surfaces, and post-dielectric defect passivation using hydrogen. Reliable interface trap density measurements that combine capacitance-voltage and conductance-voltage analysis indicate trends in interface trap density across the band gap (down to $\sim 10^{12} \text{ cm}^{-2} \text{ eV}^{-1}$ near midgap) and in border trap density as a function of the different passivation treatments. Results obtained from MOS capacitors fabricated on As₂-decapped InGaAs (100) substrates are compared with reported density functional theory predictions and scanning probe measurements of InGaAs surface defect passivation.

9:00am **EM1-WeM4 Chemical Passivation of GaAs using Alkanethiols**, *P. Mancheno-Posso, A.J. Muscat*, University of Arizona

III-V semiconductors are among the most promising materials for low-power and high-speed electronic devices owing to their high electron mobility and high breakdown fields. For instance, their use as channel materials would enable an increase in performance without changing the transistor density. Despite these advantages, III-V materials lack a defect-free and stable native oxide that could be used as a dielectric in metal-oxide-semiconductor field-effect transistors (MOSFET). Moreover, the most widely studied III-V semiconductor, GaAs, contains interfacial oxides that detrimentally affect its electronic performance. Etching the oxides and depositing a passivation layer that hinders oxidation is one approach to incorporate III-V materials in high volume production. Chemical passivation layers containing S have shown particular promise and were deposited using the precursors Na₂S, (NH₄)₂S, and alkanethiols. The alkyl chain on the thiols can act as a diffusion barrier to prevent oxygen from reaching the III-V surface, if the thiol molecules can be closely packed. In this study, alkanethiols with chain lengths from 3-20 carbon atoms were deposited from the liquid phase on GaAs (100), and their effectiveness in preventing oxidation in ambient conditions was characterized using ellipsometry, X-ray photoelectron spectroscopy (XPS), and Fourier-transform infrared spectroscopy (FTIR). The C 1s XPS peak showed that thiols with longer carbon chains exhibited higher surface coverages, as well as reduced surface oxidation after ambient exposure. FTIR peaks at 2918±1 and 2850±1 cm⁻¹, corresponding to asymmetric and symmetric stretches of CH₂ moieties, demonstrated the formation of a well ordered monolayer for chains with 18 and 20 carbon atoms. In addition, XPS and temperature programmed desorption confirmed the successful desorption of the carbon chains of thiols after annealing in vacuum to 750 K. Atomic layer deposition (ALD) of Al₂O₃ using a TMA and water process showed that film nucleation and growth was reduced by a factor of about two on the thiol-passivated surface compared to the liquid-cleaned surface. Although the initial film growth was slowed, a thiol passivation layer could broaden the use of III-V semiconductors in device manufacturing.

9:20am **EM1-WeM5 Disorder Induced Gap States in III-V MOS Devices**, *E.M. Vogel*, Georgia Institute of Technology **INVITED**

Frequency dispersion is a commonly observed feature in the experimental capacitance-voltage characteristics of III-V MOS devices. This characteristic has been reported on a wide variety of III-V substrates in conjunction with many different dielectrics. The conventional interface state capacitance model, which works extremely well for Si devices, does not accurately model the frequency dispersion observed in III-V systems. Different models have been developed to explain the origin of this frequency dispersion. One model, disorder induced gap states (DIGS), attributes this dispersion to the tunneling of carriers into a disordered region caused by oxidation of the III-V substrate which is close to the interface between the III-V substrate and an insulator. A separate model attributes this dispersion to border traps located inside and associated with the high-k dielectric. In this talk, electrical characterization, modeling and physical characterization is used to demonstrate that the observed frequency dispersion must be due to the disruption of the crystalline III-V semiconductor during oxide deposition and not due to border traps located in the high-k dielectric.

10:40am **EM1-WeM9 III-V Frequency Dispersion in CV and Small Signal AC Transconductance Measurements**, *H.C. Lin*, IMEC, Belgium **INVITED**

High-Mobility n-MOSFET option with InGaAs channels are of intense interests. As the well-known interfacial trap (D_{it}) problem appears now contained, new challenges are emerging from above the interface. The evidence of oxide border traps (BT) in high-k dielectrics and its effect on the on-state performance of InGaAs n-MOSFETs are presented in this study through combined CV dispersion and AC transconductance analyses. Frequency dispersion in CV measurements can be associated with conductive losses of the MOS system. At different gate bias the conductive loss due to events such as minority carrier generation-recombination,

trapping/de-trapping at the dielectric/III-V interface and within the dielectrics can be observed. By carefully examine the multi-frequency CV and GV response we can establish the conductance spectroscopy of the MOS device. Frequency dispersion in strong accumulation can be the result of oxide trapping. By measuring the device at different temperatures we have observed strong temperature dependence in CV dispersion at accumulation. The AC transconductance (AC-gm) measurement resembles the conventional CV measurement except for the additional small drain bias applied to inject carriers across the channel. This small but crucial difference allows one to examine the effect of oxide border traps on carrier transport. Clear frequency dispersion is observed on both the CV and AC-gm response of the InGaAs MOSFET. The increase in AC frequency reduces both the trapping time constant and the charging of the border traps, resulting in lower capacitance and yet higher peak transconductance. The amount of frequency dispersion on the AC-gm curves reflects the border trap density close to the oxide-semiconductor interface and clearly shows the impact of the traps on carrier transport.

11:20am **EM1-WeM11 High-k Dielectric/InGaAs MOSCAPs with EOTs 0.7 nm and Low Interface Trap Densities**, *V. Chobpattana, S. Stemmer*, University of California, Santa Barbara

A major challenge for future high performance metal-oxide-semiconductor field effect transistors (MOSFETs) is the development of high-k dielectrics, such as Al₂O₃ and HfO₂. A large density of interface traps (D_{it}) is typical for highly scaled dielectrics on III-V semiconductor channels and causes inefficient Fermi level response or even Fermi level pinning. In this presentation, we show a novel surface preparation method using alternating cycles of nitrogen plasma and trimethylaluminum (TMA) pulse on III-V surface before atomic layer deposition (ALD) of HfO₂ gate stack. We show that nitrogen plasma cleaned stacks exhibit much reduced frequency dispersion in depletion that is due to midgap D_{it} even for highly scaled stacks. This technique allows for highly scaled HfO₂/n-In_{0.53}Ga_{0.47}As gate stacks with equivalent oxide thicknesses (EOTs) of less than 0.7 nm and midgap D_{it} values less than $4 \times 10^{12} \text{ cm}^{-2} \text{ eV}^{-1}$. Interface trap densities are characterized by capacitance-based and conductance methods. High-quality HfO₂ MOSCAPs exhibit accumulation capacitance densities above 2.5 $\mu\text{F}/\text{cm}^2$. We report on the interfacial layer thickness, analyze the interface chemistry and bonding, and discuss the reason for the improve performance of nitrogen plasma cleaned gate stacks.

11:40am **EM1-WeM12 Effect of Deposition Temperature on the Electrical Properties of ALD-HfO₂ Film on GaAs**, *S. Choi, Y.-C. Byun, Y. An, H. Kim*, Sungkyunkwan University, Republic of Korea

For the scaling of n-channel metal-oxide-semiconductor field-effect transistor (NMOSFET) down to a sub-10 nm-node, atomic layer deposition (ALD) of high-k gate dielectrics on III-V channel materials has been widely studied to achieve excellent dielectric quality comparable to that on Si. Nevertheless, there are still many remaining issues to be solved and the most important one is a poor interface quality. The high interface state density is believed to be closely associated with the existence of substrate element-related oxide bonds near the interface region [1]. In this presentation, we systematically investigated the electrical properties of ALD-HfO₂ films on both n-type and p-type GaAs substrates as a function of the ALD temperature and compared with those on Si substrates. Based on several physical and chemical probing methods, we tried to understand the identity of near-interface characteristics and to correlate with the resulting electrical properties. For the initial surface preparation before the ALD process, n- and p-type GaAs substrates were cleaned with HF and S-passivated using (NH₄)₂S solution. For the HfO₂ deposition, tetrakis (ethylmethylamino) hafnium/H₂O precursors were used, and the ALD temperature was varied from 200 °C to 300 °C. According to the high frequency capacitance-voltage measurement, the frequency dispersion in the accumulation region was somewhat decreased when the deposition temperature was lowered. The interface trap density (D_{it}) distribution across the GaAs bandgap was estimated based on the conductance measurements conducted on both n- and p-type GaAs samples. This also exhibited a decreasing trend with decreasing ALD temperature. Detailed discussion on various physical/chemical analysis results such as X-ray photoelectron spectroscopy and time of flight-secondary ion mass spectrometry will be presented and compared with the similar experimental results performed on the Si substrates.

[1] M. M. Frank, G. D. Wilk, D. Starodub, T. Gustafsson, E. Garfunkel, Y. J. Chabal, J. Grazul, and D. A. Muller, *Appl. Phys. Lett.*, **86**, 152904 (2005).

Thin Films for Energy

Moderator: G.T. Wang, Sandia National Laboratories

8:00am EN+SE+SS+TF-WeM1 ALD of Nanolayers and Nanoparticles for Photovoltaics and Other Clean Energy Technologies, W.M.M. Kessels, Eindhoven University of Technology, Netherlands INVITED

Atomic layer deposition (ALD) is well known for its ability to deposit ultrathin films with sub-nanometer growth control and with an excellent conformality over demanding 3D surface topologies. These films can be deposited in regular cycles in an ABAB-like fashion but also more complex cycles can be employed such as $(AB)_nC(AB)_n$ ($n \geq 1$) etc. In addition to binary thin film materials, such more complex (super)cycles also allow for the preparation of complex compound films and doped films with a high level of control of the film properties. Moreover, besides thin films, ALD can also be used to deposit nanoparticles by exploiting the poor wettability of several thin film materials, in particularly metals, on certain substrate materials. By carrying out only a limited number of cycles in the initial growth phase of the films nanoparticles can be deposited with accurate size control and a relatively narrow size distribution. These features make ALD a very attractive method to synthesize nanomaterials for clean energy technologies such as solar cells, batteries, and fuel cells. In this presentation, I will build on our previous work with respect to the deposition of nanolayers for surface passivation of silicon solar cells [1], the preparation of active films for Li-ion batteries [2], and the synthesis of noble metal nanoparticles for catalysis applications [3]. More particularly, I will report on $Al_2O_3/ZnO:Al$ stacks for passivating (tunnel) contacts in silicon solar cells, $LiCoO_2$ as cathode material in all-solid state Li-ion batteries, and Pt nanoparticles as counter-electrode in flexible dye-sensitized solar cells. Most ALD processes employed in this work go beyond the regularly employed ABAB-like cycles and this will be used to demonstrate the unique features of ALD.

[1] Status and prospects of Al_2O_3 -based surface passivation schemes for silicon solar cells, G. Dingemans and W.M.M. Kessels, *J. Vac. Sci. Technol. A* 30, 040802 (2012).

[2] Atomic layer deposition for nanostructured Li-ion batteries, H.C.M. Knoops et al., *J. Vac. Sci. Technol. A* 30, 010801-1 (2012).

[3] Supported Core/Shell Bimetallic Nanoparticles Synthesis by Atomic Layer Deposition, M.J. Weber et al., *Chem. Mater.* 24, 2973 (2012).

8:40am EN+SE+SS+TF-WeM3 Titanium Doped Tungsten Oxide (WO_3) Thin Films for Application in Photovoltaic Devices, A.P. Gutierrez, T. Wilson, E.J. Rubio, C.V. Ramana, The University of Texas at El Paso

Tungsten oxide (WO_3) is a fascinating material, which has potential for integration into a wide range of technological applications. Most recently, it has been considered for use in photoelectrochemical cells due to the associated photocatalytic properties. However, the optical, photochemical and electrical properties of W-oxide thin films grown from either chemical or physical vapor deposition methods are sensitive to the physical and chemical characteristics, which in turn depend on the processing conditions and precursor materials. In this work, titanium (Ti) doping into WO_3 has been considered to fabricate transparent conducting oxides (TCO) for photovoltaic devices. Ti-doped WO_3 (W-Ti-O) films were grown by sputter-deposition onto silicon, Si (100), and optical grade quartz wafers. Co-sputtering of Ti and W metal targets was performed in a wide growth temperature range (room temperature (RT)-500 °C). The thin films were deposited for 1 hour, resulting in a thickness ranging from 80-90 nanometers. The structure and optical properties were characterized by the X-ray diffraction (XRD), scanning electron microscopy (SEM) and the spectrophotometry measurements. The films are optically transparent and a correlation between the growth conditions and optical properties is derived. The XRD results show Ti-doped WO_3 films grown are amorphous and crystalline. A decrease in the peak intensity implies that the crystallinity decreases with an increase in titanium (Ti) along with a phase change at higher substrate growth temperatures. The optical results show the transparency of the films is well above 80% and the energy band gap is ~3 eV, which meet the criteria TCO parameters. The effect of Ti concentration on the structure and optical properties of W-Ti-O films grown at various temperatures is presented and discussed.

9:00am EN+SE+SS+TF-WeM4 Microstructural and Chemical Features Affecting the Reversible Lithiation of SiO_x , C. Ban, National Renewable Energy Laboratory, B.B. Kappes, Colorado School of Mines, Q. Xu, C. Engtrakul, National Renewable Energy Laboratory, C.V. Ciobanu, Colorado School of Mines, A.C. Dillon, Y. Zhao, National Renewable Energy Laboratory

We demonstrate the reversible lithiation of SiO_2 up to 2/3 Li per Si, and propose a mechanism for it based on molecular dynamics and density functional theory simulations. Our calculations show that neither interstitial Li (no reduction), nor the formation of Li_2O clusters and Si-Si bonds (full reduction) are energetically favorable. Rather, two Li effectively break a Si-O bond and become stabilized by oxygen, thus partially reducing the SiO_2 anode: this leads to increased anode capacity when the reduction occurs at the Si/ SiO_2 interface. The resulting Li_xSiO_2 ($x < 2/3$) compounds have electronic band gaps in the range of 2.0-3.4 eV. (Published in *Applied Physics Letters* 100 (2012) 243905.)

9:20am EN+SE+SS+TF-WeM5 Correlation of Thermoelectric Properties with Local Chemical Environments in Reduced Polycrystalline and Single Crystalline $Sr_xBa_{1-x}Nb_2O_6$, C.S. Dandeneau, Y. Yang, R.K. Bordia, M.A. Olmstead, F.S. Ohuchi, University of Washington

The excellent high-temperature stability of many oxide thermoelectrics (TEs) has led to the exploration of these materials for waste heat recovery applications. Of particular interest are oxides with a complex atomic structure involving random site occupation, which serves to decrease the thermal conductivity and improve the overall thermoelectric figure of merit. $Sr_xBa_{1-x}Nb_2O_6$ (SBN100x) has such a structure, and also exhibits a relaxor ferroelectric transition with an x -dependent Curie temperature near or above room temperature. In this work, the thermoelectric properties of reduced polycrystalline SBN fabricated via solution combustion synthesis (SCS) were compared with those of single crystal SBN. While reduction annealing increases the electrical conductivity (σ) and decreases the magnitude of the Seebeck coefficient (S), the conventional inverse relationship between S and σ with respect to temperature does not hold. In particular, the magnitude of S for SBN samples with various Sr:Ba ratios increases with temperature over the entire range of testing temperatures ($dS/dT > 0$), but $d\sigma/dT$ is positive between room temperature and ~ 350°C, and then becomes negative at higher temperatures. To better understand the obtained TE data, extensive X-ray photoelectron spectroscopy (XPS) analysis was carried out both "in-situ" during reduction and "ex-situ" so as to elucidate the site occupancy of Sr and Ba ions and determine the variation of Nb valence in the reduced tungsten bronze crystal structure. The SBN carrier concentration was estimated via changes in the niobium valence state and the findings were correlated with Hall effect measurements on the n-type oxides. During reduction, Nb^{5+} and Nb^{4+} ions and a single oxygen vacancy (V_o) may preserve the octahedral structure of SBN. However, once two oxygen atoms are missing from an octahedron and/or the central Nb cation is further reduced to Nb^{3+} or Nb^{2+} with a larger ionic radius, strong localized distortion counteracts the increased carrier density to decrease both mobility and S . A potential correlation between the ferroelectric and thermoelectric properties of SBN will also be discussed. This work is supported by a grant from the U.S. Department of Energy (DE-FE0007272).

9:40am EN+SE+SS+TF-WeM6 Engineering Energy Levels at the TiO_2 :P3HT Interface using Atomic Layer Deposition, J. Dorman, J. Weickert, M. Putnik, L. Schmidt-Mende, Universität Konstanz, Germany

It has been shown over the last two decades that conversion efficiencies up to 12% can be achieved using TiO_2 based solar cells, such as in the dye sensitized solar cell. Recently, there has been a push to replace these hazardous electrolytes with organic materials to create environmentally friendly devices with extended lifetimes. However, one of the limitation of these hybrid solar cells is electron-hole interaction across the metal-oxide and organic hole transporter interface.

In this work, we introduce core-shell nanostructured hybrid solar cells with a single crystal core in order to increase electron mobility and light scattering without additional recombination effects. Atomic layer deposition (ALD) was used to fabricate TiO_2 nanowires (NWs) in order to take advantage of the directed electric field within the structures. The TiO_2 NWs were grown in a template structure using titanium iso-propoxide and water as precursors, forming high aspect ratio arrays. During the growth process a Sn^{4+} dopant is introduced to create a doped $Sn:TiO_2$ nanostructured array with increased electron mobility. After the NW growth, an additional ALD step is used to deposit a TiO_2 layer, creating the core-shell structure. The dopant gradient within the core-shell structure causes the electrons to migrate toward the core of the nanowire due to the lower energy conduction band, potentially reducing electron-hole recombination at the TiO_2 :P3HT interface. The conduction band engineering has a similar effect as that seen with dipole modification of the interface. Additionally, the surface can be further modified with dye molecules. This doped core-shell structure has

resulted in a conversion efficiency of 2 % with a surface treatment of the squaraine dye SQ2. This increase in efficiency is due to the contribution of the P3HT in the photon conversion, which is limited in various dyes due injection of electrons caused by the conduction band offset. Furthermore, the engineered energy levels and interfacial modifiers have a significant effect on the external quantum efficiency and internal resistances, as determined using various characterization methods.

10:40am **EN+SE+SS+TF-WeM9 Electrical and Thermal Transport in Inorganic Nanowire/Polymer Nanocomposites**, *G.J. Szulczewski, K. Anderson, A. Yousuf, D. Wallace, K. Kreil, E. Ellingsworth*, University of Alabama

In this talk we will present results from a systematic study to understand charge and heat transport through polymer composites containing inorganic nanowires. Specifically we have synthesized tellurium and bismuth telluride nanowires of various diameter/length by controlling the synthesis conditions. We used the aqueous conducting polymer poly(3,4-ethylenedioxy-thiophene):polystyrene sulphonate, or PEDOT:PSS, due to its low thermal conductivity. Thin films of the nanocomposites were made by drop casting and annealing. The films were characterized by scanning electron microscopy, atomic force microscopy, x-ray photoelectron spectroscopy and Raman spectroscopy. In general we find that increasing the weight fraction of nanowires with respect to PEDOT:PSS increases both the electrical conductivity and Seebeck coefficient of the films. In addition, the electrical conductivity can be further increased by adding a secondary dopants without significant degradation of the thermopower factor. The spectroscopic measurements suggest that chemical and structural changes at the poly(3,4-ethylenedioxy-thiophene) segment/inorganic nanowire interface are responsible for the improved thermoelectric performance of the nanocomposite.

11:00am **EN+SE+SS+TF-WeM10 TOF-SIMS and AFM Studies of Morphology and Molecular Intermixing at Organic Thin Film Interfaces**, *A. Dolocan*, The University of Texas at Austin

Charge separation at small molecule organic donor/acceptor (D/A) interfaces is controlled, among other factors, by morphology and molecular packing. These buried interfaces are both crystalline and amorphous and exhibit a considerable degree of molecular intermixing. This combination prevents any single technique from solving the detailed picture of D/A interfaces. Here, a general methodology that combines Time-of-Flight Secondary Ion Mass Spectrometry (TOF-SIMS) and Atomic Force Microscopy (AFM) is shown. Since AFM is little sensitive to buried interfaces, it is employed here to investigate the surface after sequential profiling using TOF-SIMS. The unique combination of high (few nanometers) resolution depth profiling and ultra-high (parts-per-billion) chemical selectivity of TOF-SIMS and nanometer spatial resolution of AFM can assess the degree of molecular intermixing, local crystallinity and molecular packing at such interfaces. We will present results for two model interfaces: copper phthalocyanine/fullerene (CuPc/C₆₀) [1] and squaraine/fullerene (SQ/C₆₀) [2]. We find that both interfaces deviate considerably from the cartoon like picture with sharp interfaces. The CuPc/C₆₀ interfaces are characterized by an interdiffusion of the C₆₀ molecules as far as 6.5 nm into the CuPc amorphous regions. A similar interdiffusion scenario is found for SQ/C₆₀ interfaces that can be correlated with the resulting 60% increase in the external quantum efficiency (EQE).

References:

[1] Na Sai, Raluca Gearba, Andrei Dolocan, John R. Tritsch, Wai-Lun Chan, James R. Chelikowsky, Kevin Leung, and Xiaoyang Zhu, "Understanding the Interface Dipole of Copper Phthalocyanine (CuPc)/C₆₀: Theory and Experiment", *The Journal of Physical Chemistry Letters* 3, 2173 (2013).

[2] Jeremy D. Zimmerman, Brian E. Lassiter, Kai Sun, Andrei Dolocan, Raluca Gearba, Keith J. Stevenson, David Vanden Bout, and Stephen R. Forrest, "Control of interface order by inverse quasi-epitaxial growth of squaraine/fullerene thin film photovoltaics", submitted to *Proceedings of the National Academy of Sciences of the USA* (2013).

Exhibitor Technology Spotlight Room: Hall A - Session EW-WeM

Exhibitor Technology Spotlight IV Moderator: C. Moffitt, Kratos Analytical Limited, UK

10:00am **EW-WeM7 PREVAC's Solution for Scientific Software Needs**, *M. Czarnecki, J. Latkowski*, PREVAC sp. z o.o., Poland

Time used to integrate scientific equipment and get the various components of a complex system operating smoothly is time wasted. PREVAC has tackled this problem with a software platform that actually helps accelerate the scientific research process. RAPID SE (Rapid Scientific Environment) is a complete and versatile software environment which was developed after many year's experience of listening to and working with research labs worldwide. It is an intuitive, user-friendly environment which allows complex and interdependent scientific equipment to be operated from a single platform. Every aspect of a complete system, from pump-down and vent routines, sample manipulation, process recipe steps and data acquisition can be quickly and intuitively managed from the core RAPID SE platform. Rapid provides the following advantages:

- Real time synchronous data acquisition
- Fast, real time chart data preview
- Process automation with safety guard
- Visual system state presentation
- Process creation and control
- Extendable and reconfigurable during runtime (additional modules, connections, data presentations, etc.)
- Full system control from Graphical User Interface
- Fully customizable user interface
- Password protected user profiles
- Number of configurable working mode (eg. admin, scientist, student)
- Multi-screen support
- Graphical system state presentation
- Full system events log for system maintain and quick problem detection
- Email or SMS message notification on system events and errors
- Export collected data to various formats (real time data, archived data)
- PLC integration (option)

Examples of use: Data acquisition systems (data acquisition, system/devices control, failure detection and log) • Deposition systems (complete process and vacuum control, data acquisition, failure detection and log) • TDS (Thermal Desorption Spectroscopy Process Control) • UMS (Universal Mass Spectrometer) • VPC (Vacuum Pressure Control) • ASTS (Automation of The Sample Transfer System) • Vacuum Conditions Simulators

10:20am **EW-WeM8 Integrated AFM-Raman – Connecting Performance & Flexibility to Ease of Use & Reliability**, *M. Wall, M. Ibrahim*, Thermo Fisher Scientific

As the largest Raman instrument supplier in the world, Thermo Fisher Scientific is committed to continued innovations in Raman microscopy. The Thermo Scientific™ DXR™ family of Raman systems is known for making research performance Raman more accessible and useable by a wider number of users. **This year we extend our solutions to materials science research to include an integrated AFM-Raman solution that allows multifaceted analysis of advanced materials with nanoscale resolution.** Join us to briefly hear about instrument solutions for analysis of graphene and other advanced materials including Raman, co-localized Raman AFM, and TERS. Whether you're in academic or government research or an analytical laboratory in industry the DXR family can get you there faster.

Graphene and Other 2D Materials Focus Topic Room: 104 B - Session GR-WeM

2D Materials on Metallic Substrates

Moderator: U. Kaiser, University of Ulm, Germany, A. Pasupathy, Columbia University

8:00am **GR-WeM1 Growth of Graphene by Catalytic Dissociation of Ethylene on CuNi(111)**, *P. Tyagi, T.R. Mowll*, University at Albany-SUNY, *Z. Robinson*, Naval Research Laboratory, *C.A. Ventrice, Jr.*, University at Albany-SUNY

Copper foil is one of the most common substrates for growing large area graphene films. The main reason for this is that Cu has a very low carbon solubility, which results in the self-termination of a single layer of graphene when grown using hydrocarbon precursors at low pressure. Our previous results on Cu(111) substrates indicate that temperatures of at least 900 °C are needed to form single domain epitaxial films. By using a CuNi alloy, the catalytic activity of the substrate increases, which allows the catalytic decomposition of the hydrocarbon precursor at lower temperatures. In this study, the growth of graphene by the catalytic decomposition of ethylene on a 90:10 CuNi(111) substrate was attempted. The growths were done in an ultra-high vacuum system by either heating the substrate to the growth

temperature followed by introducing the ethylene precursor or by introducing the ethylene precursor and subsequently heating it to the growth temperature. The growth using the former method results in a two-domain epitaxial graphene overlayer. However, introducing the ethylene before heating the substrate resulted in considerable rotational disorder within the graphene film. This has been attributed to the deposition of carbon atoms on the surface at temperatures too low for the carbon to crystallize into graphene.

This research is supported in part by the NSF (DMR-1006411).

8:20am GR-WeM2 Energies and Lifetimes of Unoccupied Electronic States of Graphene on the Ru(0001) Surface, J. Guedde, N. Armbrust, P. Jakob, U. Hoefler, Philipps-University Marburg, Germany

We present the results of an investigation of energies, dispersion and lifetimes of initially unoccupied electronic states between Fermi and vacuum level of single graphene layers on Ru(0001) obtained by means of time- and angle-resolved two-photon photoelectron spectroscopy (2PPE) [1]. Graphene/Ru(0001) is a particular interesting system because of a relative strong geometrical corrugation of the graphene layer in form of a periodically rippled moiré superstructure caused by the interaction with the Ru surface. The high in-plane polarizability of the graphene sheet and the dissimilar graphene-Ru distances in the hill and valley areas of the moiré superstructure lead to a number of novelties referring to image-potential and interface states as compared to other adsorbate systems on metal surfaces.

In the experiment we identify three image-potential states close to the vacuum level and two interface states at energies of 0.91 and 2.58 eV above the Fermi level. The most strongly bound, short lived and least dispersing image-potential state is suggested to have some quantum-well character with a large amplitude below the graphene hills. The two other image-potential states are attributed to a series of slightly decoupled states. Their lifetimes and dispersions are indicative of almost free-moving electrons, predominantly located in the interconnected valley areas. The two interface states most likely originate both from a surface resonance of Ru(0001) and exhibit different confinement and energy shifts in the valley and hill areas.

These results will be compared with model calculations using a parametrized one-dimensional model potential for a varying graphene/metal distance. It will be shown that the strong attraction of graphene for electrons in combination with its low workfunction lead to the situation that the image-potential states typically originate from the graphene and are modified by the presence of the metal surface. This is in strong contrast to insulating adsorbates on metal surfaces where the adsorbate layer modifies the image-potential states of the metal. The observed interface states, on the other hand, are both assigned to a modified surface resonance of Ru. The different confinement in the hill and valley areas result in distinct energy shift of this resonance that resembles the Shockley surface state observed on the (111) surfaces of the noble metals. This will be underlined by comparing the present results with the energy shift observed for the Shockley surface state of the Ag(111) surface upon adsorption of polycyclic aromatic hydrocarbon layers.

[1] N. Armbrust, J. Guede, P. Jakob, and U. Höfer, Phys. Rev. Lett. **108**, 056801 (2012).

8:40am GR-WeM3 Low-Energy Electron Microscopy of Hexagonal Boron Nitride on Nickel, P. Mende, Q. Gao, M. Widom, R.M. Feenstra, Carnegie Mellon University, A. Ismach, H. Chou, R.S. Ruoff, University of Texas at Austin

Because of its structural similarity with graphene (~2% lattice mismatch), its atomically smooth surface, and lack of charge traps, hexagonal boron nitride (hBN) serves as an ideal candidate both as a substrate for graphene based devices, as well as an insulating layer in graphene-based heterostructures. Following the success achieved in the growth of graphene by chemical vapor deposition (CVD) on metal substrates, many investigators have pursued similar avenues in the synthesis of hBN. In this work, results are presented of low-energy electron microscopy and μ LEED studies of hBN grown on polycrystalline Ni substrates by CVD. Low-energy electron reflectivity (LEER) spectra are acquired from surface regions containing various thicknesses (1 – 6 monolayers) of hBN on Ni. Distinct differences in the spectra are found in the low energy (0 – 10 eV) range, with a series of reflectivity minima observed, and the number of such minima being correlated with the thickness of the hBN. These results are consistent with prior work on multilayer graphene, in which it was demonstrated that interlayer states localized between the graphene layers give rise to the reflectivity minima found in the LEER spectra [1]. Theoretical simulation of the spectra using a first-principles method [1] is used to provide a basis for interpreting the experimental results. With the LEER spectra, it is found that the number of layers in multilayer hBN can be confidently determined, and maps of the hBN thickness over the surface are thus obtained.

This work was supported by STARnet, a Semiconductor Research Corporation program sponsored by MARCO and DARPA.

[1] R. M. Feenstra, et al., Phys. Rev. B **87**, 041406(R) (2012).

9:00am GR-WeM4 Intercalation of C₆₀ at the Interface of CVD Graphene and Copper, E. Monazami, University of Virginia, P. Rudolf, L. Bignardi, University of Groningen, Netherlands, P. Reinke, University of Virginia

The unique properties of graphene are coveted for application in electronic devices but doping and opening of a bandgap while retaining the integrity of the Dirac cone, remains a challenge. The electronic properties of graphene can be modified through the interaction with adsorbates or the substrate, which has also been exploited to achieve moderate doping of the graphene layer. In our study we present the intercalation of fullerene molecules at the interface between copper and graphene as a method to electronically decouple graphene from the metal substrate, introduce a controlled strain field and create a topographic superlattice.

Our presentation focuses on the synthesis of the intercalated fullerene layer, and the local impact of intercalated fullerenes on the strain and deformation of the graphene layer. The intercalation is achieved by depositing 10-20 ML of C₆₀ on graphene, which was grown on a polycrystalline Cu-substrate. The C₆₀-graphene-Cu sandwich is annealed at 400-500° C in UHV and subsequently imaged with Scanning Tunneling Microscopy (STM) and Spectroscopy (STS) conductivity maps at room temperature. The graphene-Cu system was studied separately to ascertain that the impact of Cu crystallinity and annealing on graphene's topographic and electronic structure is minimal. The role of temperature and Cu-structure on the intercalation process will be discussed in detail, and we will introduce specific indicators in the STM and STS signature to ascertain C₆₀ intercalation. Recent experiments strongly suggest that a temperature around 400° C leads to the formation of regular, crystalline intercalated C₆₀ layer, while higher temperatures favor an irregular, amorphous arrangement of the molecules.

The intercalation of C₆₀ molecules leads to the modulation of the graphene topography due to the mechanical deformation and strain around a fullerene molecule. The graphene is detached from the Cu-substrate in the vicinity of C₆₀ molecules and the Fermi level is shifted with respect to the Dirac point indicating a local p-type doping at the graphene-fullerene contact. The local electronic properties are controlled by the intercalated molecules offering a new approach to manipulating of charge distribution in graphene. The intercalation leads to a considerable increase in the density of graphene wrinkles, which is attributed to the reduction of graphene adhesion. We will present a cohesive model, which integrates the impact of C₆₀ intercalation on graphene strain, adhesion, and electronic structure.

9:20am GR-WeM5 Controlled Synthesis of Heterostructures of 2D Materials, P.W. Sutter, Brookhaven National Laboratory INVITED

The ability to combine materials in heterostructures with controlled interfaces has become one of the foundations of modern materials science. Two-dimensional (2D) crystals, such as graphene, hexagonal boron nitride, and a family of metal dichalcogenides, represent a new class of systems that offer unique opportunities for materials integration. Heterostructures that combine different 2D materials in layer stacks or as several tightly interfaced components in a single, atomically thin membrane promise tunable properties and extended functionality, and raise fundamental questions on interface formation, intermixing, strain, polarity, etc., in a new context at reduced dimensionality.

I will discuss recent advances in developing the synthesis and processing of heterostructures of 2D materials on metal substrates, derived primarily from real-time observations by surface electron microscopy, complemented by high-resolution scanning probe microscopy and in-situ spectroscopy. Focusing on the integration of graphene [1,2] with hexagonal boron nitride [3], I will discuss progress toward meeting key challenges in the controlled formation of 2D heterostructures: Atomically precise thickness and stacking control in superlattices [4], and the creation of atomically sharp line interfaces in heterogeneous monolayer membranes [5]. Our combined findings establish a powerful toolset for the scalable fabrication of 2D heterostructures for research and applications.

References

- [1] P. Sutter, J.I. Flege, and E. Sutter, Nat. Mater. **7**, 406 (2008).
- [2] P. Sutter and E. Sutter, Adv. Funct. Mater. (2013), DOI: 10.1002/adfm.201203426 and references therein.
- [3] P. Sutter, J. Lahiri, P. Albrecht, and E. Sutter, ACS Nano **5**, 730 (2011).
- [4] P. Sutter, J. Lahiri, P. Zahl, B. Wang, and E. Sutter, Nano Lett. **13**, 276 (2013).
- [5] P. Sutter, R. Cortes, J. Lahiri, and E. Sutter, Nano Lett. **12**, 4869 (2012).

11:00am **GR-WeM10 Growth and Characterization of Single Layer MoS₂ and Mo₂S₃ on Cu(111): Toward an Inverted Catalyst**, *W. Lu, C.S. Wang, D. Sun, Q. Ma, D. Kim, J. Wyrick, J. Mann, Y. Zhu, L. Bartels, S. Bobek*, University of California, Riverside

Single layer MoS₂ can be exfoliated mechanically similar to graphene. This presentation shows an alternative avenue for the fabrication of MoS₂ monolayers at comparatively low temperature and mild conditions through sulfur loading of a copper substrate using thiophenol followed by the evaporation of Mo atoms and annealing. In addition, this method allows the growth of ordered Mo₂S₃ films and Mo₆S₆ nanowires. Using anthraquinone and formic acid as test molecules, we titrate the various MoS_x and copper-based structures presented on our substrate in order to determine their affinity for adsorbate interactions. We will also report on ongoing catalytic/TPD investigations of these films.

11:20am **GR-WeM11 Ultrafast Charge Transfer at Graphene Monolayers on Ni(111) and Other Substrates**, *D. Menzel*, Technical University Muenchen, Germany, *P. Lacovic*, Sincrotrone Trieste, Italy, *R. Larciprete*, CNR Inst. for Complex Systems, Italy, *M. Dalmiglio*, Sincrotrone Trieste, Italy, *K.L. Kostov*, Bulgarian Academy of Sciences, Bulgaria, *S. Lizzit*, Sincrotrone Trieste, Italy

The unique electronic properties of graphene (Gr) are being investigated vigorously with the entire arsenal of surface science. Nevertheless the dynamics of excited states remote from the Dirac cone range are still not well known, even though they should be important for photochemistry on Gr and for contact formation in electrochemistry. In a late breaking contribution at the AVS meeting last year we have reported our preliminary results on the investigation of ultrafast charge transfer at Gr monolayers on substrates with strongly varying coupling, using the well-established core-hole-clock method with adsorbed argon [1]. We have shown [2] that decoupled layers, irrespective of the way of decoupling, show the same rather slow charge transfer despite the high empty DOS at the relevant energies about 1.5 eV above the Dirac point. This slowdown has been tentatively explained by the local charge accumulation interfering with CT, similar to dynamical Coulomb blockade [3]. On Ru(0001) the much faster CT, graded depending on the location on the periodically buckled Gr layer, has been explained by the degree of hybridisation of Gr empty states with substrate states. The results on the Gr "hills" on Ru(0001) and on Pt(111), which are characterized by considerably faster CT than on the decoupled layers, show that these layers - often assumed to be essentially bound only by Van der Waals forces - must also exhibit considerable hybridisation. We have now extended our investigation to Gr on Ni(111) which, due to the good lattice match, is a flat layer and does not possess a Dirac cone, so that good coupling and fast CT should be expected. The results however, show CT much slower than on the Gr "valleys" on Ru, and about as fast as on the Gr "hills" on Ru. We will discuss this unexpected result in terms of hybridising states and the surface DOS. Another interesting finding is that oxygen intercalation acts very differently on Gr/Ni(111) from Gr/Ru(0001). While on Gr/Ru it fully decouples the Gr layer [2], for Gr/Ni much faster CT persists.

[1] See, e.g., D. Menzel, Chem. Soc. Rev. 37, 2212 (2008), and references therein.

[2] Lizzit et al., AVS-59, abstract #1538. S. Lizzit et al., ACS Nano (in press), DOI: 10.1021/nn4008862

[3] C. Brun et al., Phys. Rev. Lett. 108, 126802 (2012).

11:40am **GR-WeM12 Growth Kinetics of Monolayer Graphene on Pd(111)**, *H.S. Mok*, University of California at Los Angeles, *A. Ebnonnasir*, Colorado School of Mines, *S. Nie, N.C. Bartelt, K.F. McCarty*, Sandia National Laboratories, *C.V. Ciobanu*, Colorado School of Mines, *S. Kodambaka*, University of California at Los Angeles

Using *in situ* low energy electron microscopy (LEEM) observations along with density functional theory (DFT) calculations, we investigated the growth kinetics of monolayer graphene on Pd(111). All of our experiments were carried out on carbon-containing Pd(111) single crystals. Graphene layers were grown by cooling the sample to temperatures below 900 °C during annealing the sample in ultra-high vacuum. LEEM images and electron reflectivity data were acquired during graphene growth as a function of incident electron energy and annealing time. From the LEEM images, we measured the time-dependent changes in areas of graphene islands. From the electron reflectivity data, we determine the work functions of graphene-covered and graphene-free regions on the surface as a function of time. Interestingly, the work functions of graphene-free regions decrease (increase) during the growth (dissolution) of graphene. DFT calculations show that Pd work function can change due to the formation of metastable carbides and precipitation of C adatoms on the surface. Based upon our results, we suggest that graphene layers grow out of C atoms intercalated at the graphene-Pd interfaces.

Accelerating Materials Discovery for Global Competitiveness Focus Topic

Room: 202 B - Session MG+EM+MI+MS-WeM

Materials Discovery and Optimization through Iterative Approaches

Moderator: M.B. Holcomb, West Virginia University, S. Jones, National Science Foundation

8:40am **MG+EM+MI+MS-WeM3 Preparation of Ultra Stable Organic Glasses by Physical Vapor Deposition**, *J.J. de Pablo*, University of Chicago, *L. Yu, M.D. Ediger*, University of Wisconsin-Madison **INVITED**

There is considerable interest in identifying structure-property relations in glasses. Structural studies of glassy materials have benefited from insights provided by molecular simulations of model glass forming liquids. In particular, simulations have provided support for the existence of dynamic and mechanical heterogeneity at the level of small groups of molecules or particles. In general, however, the cooling rates employed in simulations have been many orders of magnitude faster than in experiments, thereby adding some level of ambiguity to direct comparisons between theory and experiment. Recently, experiments have shown that glasses of organic molecules having unusually large thermal and kinetic stability can be prepared by a vapor deposition process. Such glasses exhibit higher onset temperatures, higher densities, and higher mechanical constants than those of ordinary glasses. In particular, vapor-deposited glasses have been shown to exhibit relaxation times that are many orders of magnitude longer than those of ordinary glasses. Inspired by such experiments, we have devised a strategy that allows one to prepare highly stable glassy materials, *in silico*, having thermal and kinetic characteristics that are superior to those obtained by gradual cooling of liquid samples. In this presentation, we will describe current experimental efforts to produce and characterize stable glasses, along with an overview of available theoretical and computational strategies aimed at understanding their properties. Emphasis will be placed on recent attempts to identify the structural origins behind the extraordinary stability of vapor deposited glasses, with the goal of providing new insights for design of stable amorphous materials deep in the potential energy landscape.

9:20am **MG+EM+MI+MS-WeM5 Composition and Structure Manipulation for Energy Materials with Improved Properties**, *S. Lany, H. Peng*, National Renewable Energy Laboratory, *V. Stevanovic*, Colorado School of Mines

Ideally, materials for energy applications like photovoltaics, photo-electro catalysis, or thermoelectrics should have a high performance, but be earth-abundant and manufacturable by low-cost processes. Given such demanding constraints, the list of promising materials that could potentially fulfill all requirements often shrinks to a few hopefuls. Then, the question arises whether we can start from materials that have both good and bad features, and manipulate the composition and structure such to cure their deficiencies. The role of theory is to assess the properties and identify promising alloying approaches.

We are presenting two recent examples for this approach: As a photovoltaic material, Cu₂O suffers from a high absorption threshold due to a relatively large band gap and a forbidden optical transition. Also, the p-type doping is 1-2 orders of magnitude below the optimal level. Our theoretical work identifies alloying of Zn, S and Se as a promising route to improve the optical and electrical properties of Cu₂O. Strong dopant-defect interactions lead to the unusual situation that the isovalent (S, Se) alloying increases the electrical doping, whereas the aliovalent (Zn) alloying changes the optical properties. The second example of MnO-ZnO alloys is based on the prediction [Phys. Rev. B 85, 201202(R) (2012)] that MnO in a hypothetical tetrahedral structure (zinc-blende or wurtzite) should have a smaller band gap and superior carrier transport properties than the normal octahedral rocksalt structure. These features would make this hypothetical material interesting, e.g., for photo-electro-catalytic water-splitting. We predict that Mn_{1-x}Zn_xO alloys assume the wurtzite structure above x = 0.38, and that such alloys preserve the beneficial properties of the tetrahedral MnO phase. Thus, the alloy approach presents a viable path to realize desirable materials properties that were originally identified for a hypothetical material.

9:40am **MG+EM+MI+MS-WeM6 Accelerated Optimization of Solar Cell Materials**, *A. Zakutayev*, National Renewable Energy Laboratory, *V. Stevanovic*, Colorado School of Mines, *S. Lany, J. Perkins, D. Ginley*, National Renewable Energy Laboratory

The rate of progress in the field of solar cells has been historically limited by the need for materials with desired functionality. Two complementary high-throughput approaches that have potential to facilitate such innovation

are combinatorial thin-film experiments and predictive first-principles theory. Here we present examples of accelerated optimization of solar cell materials using the combined theoretical/experimental approach. The specific examples include (i) photovoltaic absorbers, and (ii) p-type contacts for solar cells

(i) PV absorbers are the key elements in any solar cells. Functionally, the absorbers are required to (1) absorb sunlight, and (2) facilitate extraction of charge carriers. We demonstrate accelerated progress towards (a) enhancement of optical absorption in Cu_2O , (b) improvement of electrical charge transport properties of Cu_3N , and (c) optimization of Cu-Sn-S material with respect to both optical and electrical properties. Our progress towards integration of these materials into thin film solar cell prototypes also will be discussed.

(ii) p-type contacts are needed for next-generation thin-film photovoltaics. Functionally such p-type contacts are required to (1) transmit sunlight, and (2) conduct holes. To accelerate the progress, we show (a) formulation of design principles (d6 oxide spinels) to guide the candidate selection [1, 2, 3], (b) down-selection of the most promising materials (Co_2ZnO_4 and Co_2NiO_4) from ~30 candidates using predictive theory [4], (c) optimization of the selected best-of-class materials (Co-Zn-O, Co-Ni-O) using thin-film combinatorial experiments [5], and (d) integration of the optimized materials (Zn-Ni-Co-O) as hole transport layers in organic photovoltaic devices [6].

In summary, combination of high-throughput theoretical and experimental methods demonstrated here can significantly accelerate the development of materials for thin film solar cells. This approach should be also suitable for discovery and optimization of materials for other technological applications.

This research is supported by U.S. Department of Energy, as a part of two NextGen Sunshot projects, an Energy Frontier Research Center, and a "Rapid Development" agreement.

- [1] V. Stevanovic et al Phys. Rev. Lett. 105, 075501 (2010)
- [2] V. Stevanovic et al J. Am. Chem Soc. 133, 11649 (2011)
- [3] J. Perkins, A. Zakutayev et al Phys. Rev. B 84, 205207 (2011)
- [4] T. Paudel, A. Zakutayev et al Adv. Func. Mat. 21, 4493 (2011)
- [5] A. Zakutayev et al Phys. Rev. B 85, 085204 (2012)
- [6] A. Zakutayev et al MRS Comm. 1, 23 (2011)

10:40am **MG+EM+MI+MS-WeM9 The "Materials Genome" Project: Accelerated and Large-Scale Materials Discovery through Computation. G. Ceder, MIT** **INVITED**

Novel materials design has become a critical capability to address several urgent societal problems. The need for novel materials is the technological Achilles Heel of our strategy to address the energy and climate problem facing the world, and over-reliance on critical elements has inspired large efforts to develop accelerated materials design strategies. The Materials Genome Project, originally started at MIT (www.materialsproject.com), has as its objective to use high-throughput first principles computations on an unparalleled scale to provide basic materials property data on all known and many potential new inorganic compounds, thereby facilitating the search for new materials.

I will show successful examples of high-throughput calculations in the field of lithium batterier, and show several new materials that have been discovered. I will discuss the public release version of the Materials Genome project which is making large quantities of computed data freely available to the materials community. The Materials Project is rapidly growing as a large collaborative environment for computed materials data.

11:20am **MG+EM+MI+MS-WeM11 Multifunctional Interfacial Materials by Design. C. Eom, University of Wisconsin-Madison** **INVITED**

Complex oxides materials have been fertile ground for new discoveries, due particularly to their wide-ranging electronic, optical, and magnetic properties. Interfaces between complex oxides and related materials create juxtapositions between different symmetries and ordered states, and it has become clear that these interfaces are new materials in their own right and lead to dramatically different properties from those in bulk. But interfacial materials encompass a virtually unexplored territory, one in which theory or experiment alone cannot be successful. New approaches must be implemented to understand basic principles, categorize competing interactions, and design and synthesize complex oxide interfaces with advanced functionalities. Our project focuses on an iterative cooperation between forefront theory and experiment that determines the fundamental principles controlling new physical phenomena at oxide interfaces, uses these principles to design couplings between multiple orders at interfaces to generate new functionalities, and experimentally synthesizes and investigates designed interfacial materials for novel electronic devices. These atomic-scale interfacial materials lead to, for example, new classes of electric-field controllable electronic and magnetic phenomena, and enable

the development of new technologically important devices that exploit these couplings. Using a predictive theory and modeling, and feedback to theory from experiments, we have designed and synthesized novel oxide hetero-interfaces that have unique properties not presently available. This work has been done in collaboration with M.S. Rzchowski, C.J. Fennie, E.Y. Tsybmal, L.Q. Chen, X.Q. Pan, S. Ryu, T. Hernandez, T. R. Paudel, H. Zhou and D. D. Fong.

Nanometer-scale Science and Technology
Room: 203 B - Session NS+AS+BI+SP-WeM

Nanoscale Imaging and Microscopy
Moderator: U.D. Schwarz, Yale University

8:00am **NS+AS+BI+SP-WeM1 Outcomes of and Materials for Two University-Level Courses on Atomic Force Microscopy, N.A. Burnham, Worcester Polytechnic Institute**

The outcomes of and materials for undergraduate and graduate courses on atomic force microscopy (AFM) in the Physics Department at Worcester Polytechnic Institute are described [1]. Given since 2001, the courses have been well received by over 150 students – from freshmen to emeritus professors – 45% of whom go on to use their AFM skills in subsequent studies or professions. Over half of the enrollees have been students external to the author's home department. The course materials that have been developed are: YouTube videos [2], instrument lab instructions, computer lab instructions and programs, instructions and programs for labs with a macroscopically sized cantilever, classroom materials including writing exercises, and notes for teaching assistants and lecturers. Still under development is a textbook with homework problems. Most materials are available upon request from the author in order to promote AFM courses at other institutions, with the intent to draw more students into the intriguing world of nanoscience.

1. Accepted for publication in J. Nano Education
2. <http://www.youtube.com/user/AtomicForceMicro/featured>

8:20am **NS+AS+BI+SP-WeM2 Imaging Li and B in a Glass Sample with 100nm Lateral Resolution Using NanoSIMS, Z. Zhu, Crum Northwest National Laboratory, Y. Wang, University of Florida, J. Crum, Pacific Northwest National Laboratory, Z. Wang, Chinese Academy of Science**

A widely used method to immobilize nuclear wastes is fusing them into glasses. These proposed glass waste forms are multicomponent complex material with the common components of Li and B compounds. During the fast cooling process, phase separation occurs in the form of 200-500 nm clusters and the glass matrix. It is difficult for commonly-used surface analysis tools (e.g., X-ray photoelectron spectroscopy (XPS), Auger electron spectroscopy, scanning electron microscope/energy dispersive spectroscopy (SEM/EDX), and transmission electron microscope/energy dispersive spectroscopy (TEM/EDX)) to characterize the distributions of ultra-light elements like Li and B in these two phases. For example, although TEM/EDX characterization can show mapping of heavy elements in the two phases, this technique is not ideal to identify the location of ultra-light elements, such as Li and B, because the sensitivity of EDX analysis for Li and B is poor. NanoSIMS can provide nano-scale spatial resolution (down to 50 nm) as well as excellent sensitivity for Li and B, making it a good candidate to image Li and B in the glass sample. We have used NanoSIMS to map Li and B in the glass sample with a lateral resolution of ≤ 100 nm. NanoSIMS images clearly show enrichment of both Li and B in the matrix phase.

8:40am **NS+AS+BI+SP-WeM3 Visualization of Subsurface Features in Soft Matrix using Atomic Force Microscopy Techniques, K. Kimura, K. Kobayashi, H. Yamada, Kyoto University, Japan**

Imaging of deeply buried subsurface features in soft matrices such as parasites in red blood cells [1], carbon nanoparticles in living cells [2], and buried electronic circuit in industrial products [3] have been demonstrated by heterodyne force microscopy [4] (HFM). Subsurface imaging using ultrasonic AFM (UAFM), which is a technique to evaluate contact stiffness with high sensitivity, has also been demonstrated in some papers. However, UAFM has been mainly applied for imaging subsurface features in hard matrices such as Si and metals, whose resolved maximum depth was typically less than 200 nm [5]. In this study, we visualized Au nanoparticles buried in a polymer matrix under 960 nm from the surface by using HFM and UAFM, which has never been achieved [6].

A dispersion of Au particles (50-nm-diameter) was dropped on a polyimide sheet (125-micro-meter-thick). After drying, a top-coat (photo polymer)

was spin-coated on it and annealed at 150°C. Top-coat thickness was estimated from the film coated on a Si wafer. We used a modified commercial AFM instrument (JEOL: JSPM 4200). The sample was directly glued on a piezoelectric plate, which was fixed on a tube scanner. Another piezoelectric plate for HFM was attached on a cantilever holder. The contact resonance frequency used for imaging was determined by measuring the thermal noise spectrum of the cantilever contacted on the sample. The schematic diagrams of HFM and UAFM are shown in Figs. 1 and 2 in the supplemental file.

We performed subsurface imaging for the samples with the top-coat thickness of up to 1 micro-meter. We found that the maximum depth of the subsurface features resolved by HFM and UAFM depends on the spring constant (k) of the cantilever. Figure 3 in the supplemental file shows subsurface images of Au particles buried under a top-coat of 900-nm-thick obtained by UAFM using a Si cantilever (k : 1.3 N/m), which we found the most suitable for subsurface imaging on the polymer matrix. We suppose that subsurface features in a soft matrix at least buried under 1 micro-meter from the surface affect surface viscoelasticity, which are detected by AFM techniques when a cantilever of suitable stiffness is used.

This work was supported by the Murata Science Foundation and Grant-in-Aids from the Japan Society for the Promotion of Science (JSPS).

- [1] G. S. Shekhawat et al., *Science* **310** (2005) 89.
- [2] L. Tetard et al., *Nature Nanotech.* **3** (2008) 501.
- [3] S. Hu et al., *J. Appl. Phys.* **109** (2011) 084324.
- [4] M. T. Cuberes et al., *J. Phys. D* **33** (2000) 2347.
- [5] Z. Parlak et al., *J. Appl. Phys.* **103** (2008) 114910.
- [6] K. Kimura et al., *Ultramicroscopy* (2013) in press (10.1016/j.ultramicro.2013.04.003).

9:00am **NS+AS+BI+SP-WeM4 Nanoscale Characterization Using Resonance Enhanced Infrared Spectroscopy**, *E. Dillon, M. Lo, C. Prater, K. Kjoller*, Anasys Instruments, *M. Belkin, F. Lu*, University of Texas at Austin

As current research focuses on shrinking the size of devices and the components that comprise these devices, the characterization of these systems becomes more and more challenging. The resolution of conventional IR spectroscopy techniques is diffraction limited to a practical resolution limit of $\sim 3 \mu\text{m}$. This length scale is too large to observe any potential nanoscale features on today's devices. Atomic force microscopy (AFM) is a widely used nanoscale imaging technique that provides the user with a high spatial resolution topographic map of a sample surface. When combined, the resulting AFM-IR can provide the high resolution topographic maps commonly associated with AFM with the addition of high spatial resolution IR spectroscopy and IR imaging. Currently, AFM-IR spectroscopy has the ability to collect IR spectroscopic information below the diffraction limit with a lateral resolution of $\sim 100 \text{ nm}$. However, there are still some limitations that prevent its use on many important nanoscale systems. One of the main limitations is the thickness of sample required for examination ($> 100 \text{ nm}$). Overcoming these limitations has a dramatic impact by enabling widespread use of nanoscale IR spectroscopy for spatially resolved chemical characterization. The use of a quantum cascade laser (QCL) as the IR source significantly increases the sensitivity of AFM-IR. The QCL has repetition rates 1000 times higher than previous lasers used for AFM-IR. This allows the ability to pulse the laser at the resonant frequency of the AFM cantilever giving rise to a high IR sensitivity mode referred to as resonance enhanced infrared nanospectroscopy (REINS). Due to the increased IR sensitivity, less laser power is required to generate a spectrum, meaning samples that were too thin or easily damaged using previous AFM-IR techniques can now be easily examined. Using REINS we have been able to collect nanoscale IR spectra and perform chemical imaging on films as thin as 10 nm. These advances in AFM-IR allow for the characterization of samples from a wide variety of applications, including, organic photovoltaic materials, materials for energy generation and storage, cellular biology, development of advanced polymeric materials and integrated circuit devices.

9:20am **NS+AS+BI+SP-WeM5 AFM-based Chemical and Mechanical Property Characterization of Low-k/Cu Interconnects**, *M. Lo*, Anasys Instruments, *S.W. King*, Intel Corporation, *E. Dillon, Q. Hu, R. Shetty, C. Prater*, Anasys Instruments

Infrared (IR) spectroscopy is a powerful technique for characterizing the chemical bonding in low dielectric constant (i.e. low-k) materials utilized in nano-electronic Cu interconnect structures. Combined with nanoindentation and other techniques, IR spectroscopy has enabled the structure-property relationships in these materials to be determined. However, such property analysis have been primarily limited to characterizing blanket films due to the spatial resolution of a typical IR measurements being diffraction limited to ca. 3 - 10 μm . Further advances in low-k materials and failure analysis

would be greatly enhanced by the ability to perform IR spectroscopy and other material property characterization on actual nanometer scale low-k/Cu interconnects. In this report, we demonstrate both AFM based IR chemical analysis and contact resonance mechanical analysis of a single layer 90 nm low-k/Cu interconnect structure.

To achieve better spatial resolution in IR spectroscopy measurements, a broadly tunable infrared laser was coupled to an atomic force microscope (AFM-IR). IR laser pulses at the wavelengths of the low-k materials characteristics absorption bands was utilized to create rapid thermal expansion that invoked vibrations in the AFM tip directly in contact with the sample. Amplitudes of the ringing motion of the AFM tip were recorded as the same tip scanned over the areas of interest. By detecting only the perturbations directly underneath the AFM tip, spatial resolution below the diffraction limits of IR radiation could therefore be achieved. In this manner, IR spectra and 2D images of a $< 1.5 \mu\text{m}$ wide interlayer dielectric (ILD) in a low-k/Cu interconnect were achieved.

To complement the AFM-IR technique and achieve nanometer scale structure property measurements, AFM-based contact resonance (CR-AFM) measurements were performed in parallel. The CR-AFM technique probes the relative mechanical property of different materials and has been previously demonstrated useful for characterizing the elastic properties of low-k material in similar Cu interconnect structures. For the current CR-AFM measurements, the resonant frequency of the AFM tip was controlled by modulating the alternating current going through a specialized ThermoLever™, which interacts with the magnetic field of a magnet nearby. As this tip scans from ILD to other metallic layers, the frequency of the AFM tip vibration changes due to the variations in the mechanical stiffness from one material to another. By combining the AFM-IR and CR-AFM techniques, both chemical and mechanical analysis of a low-k/Cu nano-electronic structure were achieved using an AFM at high spatial resolution.

9:40am **NS+AS+BI+SP-WeM6 Amino Acid Immobilization and Surface Diffusion of Copper**, *E. Iski*, University of Tulsa, *A.J. Mannix, B.T. Kiraly, M.C. Hersam*, Northwestern University, *N.P. Guisinger*, Argonne National Laboratory

The 2D-scale study of relevant biomolecules, like amino acids, is pertinent for a variety of applications from the origin of biological homochirality and the amplification of surface chirality to the examination of noncovalent supramolecular interactions. Importantly, the study of these molecules on a copper surface may also be significant to the medical community as the binding of amino acids/proteins to copper ions plays a major role in the development of neurodegenerative diseases, like Mad Cow's Disease and Alzheimer's. The need for pristine molecular resolution of these systems requires the use of ultra-high vacuum scanning tunneling microscopy (UHV STM) as the primary technique for these studies. Through the detailed examination of the self-assembly behavior of five amino acid molecules on a Cu(111) single crystal, a fascinating and unexpected phenomenon was discovered. All of the amino acids assisted in the immobilization of copper atoms on the surface. The energetic landscape of the surface as mediated by temperature and molecular coverage facilitated the growth of copper islands and clusters. The growth and size fluctuation of the islands offered an interesting snapshot of metal nanocluster diffusion that often occurs at time scales beyond the resolution of a given surface science technique. The presence of $\sim 1 \text{ ML}$ of molecules on the surface effectively trapped the metal atoms into localized islands. Elevated temperatures ($\leq 350 \text{ K}$) were used to promote further diffusion, coalescence, and extinction of the islands for a more detailed understanding of the coarsening and ripening mechanisms. In conclusion, while these systems provide insights into the chiral assembly of amino acids on Cu(111), they also provide a unique glimpse into metal surface diffusion and offer the ability to study the mass transport of metal atoms, which is important for the understanding of thin film growth and its morphological evolution.

10:40am **NS+AS+BI+SP-WeM9 Catalytic Model Systems Studied by High-Resolution, Video-Rate Scanning Tunneling Microscopy**, *F. Besenbacher*, Aarhus University, Denmark, *J. Kibsgaard*, Stanford University **INVITED**

For decades single-crystal surfaces have been studied under ultra-high vacuum (UHV) conditions as model systems for elementary surface processes. This "surface science approach" has contributed substantially to our understanding of the processes involved in especially catalysis.

In this talk I will show how STM can reveal fundamental processes in relation to catalysis, and how we can extract quantitative information on surface diffusion of adatoms and molecules. We use time-resolved, high-resolution STM images/movies to understand diffusion of vacancies, interstitials and molecules, e.g. water molecules on oxide surfaces, sintering and diffusion of nanoclusters on oxide surfaces, diffusion of intermediate species, and to identify active sites and to determine new nanostructures

with novel catalytic properties (see www.phys.au.dk/spm). The atomic-scale information obtained may even lead to the design of new and improved catalysts in certain cases.

11:20am **NS+AS+BI+SP-WeM11 Scanned Probe Based Nanofabrication on Silicon: Progress, Challenges and Technology Spin-Offs**, *J.W. Lyding**, University of Illinois at Urbana Champaign **INVITED**
Atomic-scale nanofabrication on Si(100) surfaces can be achieved by using hydrogen as an atomic layer electron resist. Electrons from a STM probe can create atomically precise patterns of clean silicon under ultrahigh vacuum conditions. These patterns can serve as templates for selective chemistry, including the atomically precise placement of molecules on the silicon surface. By performing these studies under UHV conditions it is also possible to obtain information about the hydrogen desorption process. Two desorption regimes are observed. The first involves the direct excitation of the bonding-to-antibonding transition and requires an electron energy of ~6.5 eV. In this regime a constant quantum desorption efficiency is observed irrespective of the electron current. At electron energies insufficient to excite the direct bonding-to-antibonding transition, desorption also occurs but with a strong current-dependent desorption efficiency. In this regime, the STM electrons inelastically excite the Si-H vibrational modes, which have a long lifetime of ~10 ns. Thus, if the excitation rate, which depends on the electron current, exceeds the quenching rate by the lattice, then the Si-H bond moves up its vibrational state ladder until desorption occurs from the hot ground state. Atomic resolution patterning is a side benefit of this vibrational heating process since tunneling electron energies are involved. Following a suggestion by Avouris, these experiments were extended to deuterated Si(100) surfaces where a giant kinetic isotope effect was observed. In the single-particle desorption regime, when excitation to the antibonding level occurs deuterium accelerates more slowly away from the silicon surface, thereby enhancing the probability that the bond will reform. Experimentally, deuterium is observed to be about two orders of magnitude more difficult to desorb than hydrogen. In the vibrational heating regime the deuterium desorption probability decreases by many orders of magnitude due to the short Si-D vibrational lifetime (< 1 ns). The STM isotope experiments set the stage for the discovery that deuterium can be used to dramatically reduce hot carrier degradation in silicon CMOS technology. Hot carriers at the transistor gate dielectric-silicon interface desorb the hydrogen used to passivate silicon dangling bonds. Deuterating the interface increases chip hot carrier lifetimes by more than an order of magnitude. Consequently, deuterium processing is now used in advanced chip manufacture. We have also developed a novel tip sharpening method for STM and AFM probes that results in sub-5 nm radii probe tips with ultra-hard conductive coatings.

Plasma Science and Technology Room: 104 C - Session PS-WeM

Fundamentals of Plasma Surface Interactions

Moderator: S.A. Vitale, MIT Lincoln Laboratory

8:00am **PS-WeM1 Examination of Atomistic Etching Control of SiO₂-Si-SiO₂ Multi-Layers Stacks Using Cyclic Ar/C₄F₈ Plasma**, *D. Metzler, G.S. Oehrlein*, University of Maryland, College Park, *S.U. Engelmann, R.L. Bruce, E.A. Joseph*, IBM T.J. Watson Research Center

There is great interest in establishing directional etching methods capable of atomic scale resolution for fabrication of highly scaled electronic devices. We report on controlled etching of sub-nm thick layers of silicon and SiO₂ using cyclic Ar/C₄F₈ plasma. The work was performed in an inductively coupled plasma reactor. Use of SiO₂-Si-SiO₂ multi-layers on a Si substrate enables precise examination of selectivity, etch stop, and modification using *in situ* ellipsometry. Controlled etching is based on deposition of a thin (<1 nm) reactive fluorocarbon (FC) layer on SiO₂-Si-SiO₂ layers using pulsed C₄F₈ flow. Subsequent Ar⁺ ion bombardment removes the FC layer along with SiO₂ from the surface. Ar⁺ ion bombardment energies were selected so that once the FC layer had been removed, etching ceased. If ion energies are too high, significant SiO₂ etching takes place and a self-limited process cannot be achieved. The impact of deposited FC layer thickness on SiO₂ etching and etch selectivity relative to Si is examined and quantified. Additionally, x-ray photoemission spectroscopy (XPS) studies are used to investigate surface chemistry at various stages of the cyclic surface etching and will be reported. We found that chamber condition, especially inadvertent fluorocarbon deposition on the chamber walls concurrent with ultra-thin FC layer deposition on the substrate surface, can have a strong

impact on the etch characteristics. The authors gratefully acknowledge financial support from National Science Foundation award CBET-1134273.

8:20am **PS-WeM2 Plasma Induced Surface Roughness of ArF Photoresist Examined by Plasma-Beam Processes**, *T. Takeuchi, Y. Zhang, K. Ishikawa, M. Sekine*, Nagoya University, Japan, *Y. Setsuhara*, Osaka University, Japan, *K. Takeda, H. Kondo, M. Hori*, Nagoya University, Japan

We report an observed relationship between chemical modifications and physical morphological roughness on a photoresist for ArF excimer laser photolithography in plasma beam irradiation. In fluorocarbon plasma, at the very beginning period, three stages of characteristics of chemical changes occurred upon surface roughening or wrinkling of the photoresist; (1) a rapid reduction of C=O bonds, (2) gradual formation of a fluorocarbon layer, and graphitic (sp²-C) or amorphous (sp³-C) carbon layer; (3) as elapsed incubation phase, i.e. lag, where reached a steady-state of chemical changes for fluorocarbon ion irradiation on the surface; finally morphological changes initiated. Those processes evolved within dose of 6 × 10¹⁵ cm⁻² for ion energy of a few hundred eV [1].

Furthermore, in hydrogen plasma, especially in annealing at approximately 160°C, the photoresist surface was corrugated with size of the order of microns as similar as the report about mechanically buckling [2]. Subsequently the roughen surface was treated by the plasma beam irradiation, the roughness was developed with a size of the order of nanometers as same as the previous report [1]. Therefore we are revisiting the roughening process on the plasma process [3], and we will discuss on the roughening phenomena on the photoresist during plasma processes.

References [1] T. Takeuchi *et al.*, J. Phys. D **46**, 102001 (2013). [2] H. Jiang *et al.*, PNAS **104**, 15607 (2007). [3] R. Bruce *et al.* J. Appl. Phys. **107**, 084310 (2010).

8:40am **PS-WeM3 Sidewall Polymer Deposition for Achieving Near 1:1 x:y Critical Dimension Shrinkage**, *N.A. Fox-Lyon, D. Metzler, A.J. Knoll*, University of Maryland, College Park, *T. Liu, D. Farber*, Texas Instruments, *G.S. Oehrlein*, University of Maryland, College Park

New methods for shrinking lateral features are required to extend current generation photoresist patterning to smaller structures for devices. One approach for this is deposition onto sidewalls of patterned features using plasma-etch equipment. Current issues with this method are creating significant and uniform (x,y dimensions) pattern shrinkage and minimizing roughness and deformation of patterned features. In this work, we explored shrinking circular/elliptical holes and lines in 248 nm photoresist and 193 nm films using plasma-enhanced deposition in combination with etching. Both hydrocarbon and fluorocarbon plasma mixtures with inert/reactive carrier gases were evaluated for deposition. Plasma parameters for shrinkage were chemistry (e.g., ratio of deposition gas to carrier gas flow), pressure, applied power, ion energy (by substrate biasing), and deposition time. Real-time *in situ* ellipsometry and x-ray photoelectron spectroscopy of deposited films and scanning electron microscopy of patterns were carried out for characterization. We report on the plasma parametric dependencies of top-down and sidewall deposition rates, along with optical density and chemical composition of the films. Cyclical deposition/etching and pulsed plasmas were also explored for achieving shrink and minimizing sidewall roughness. Statistical analysis of x:y shrink, top-down deposition to sidewall deposition, and sidewall/surface roughening was investigated. We find strong dependencies on sidewall shrink on feature size and aspect ratios. As feature sizes get below 50 nm, minimizing feature roughness/occlusion becomes more difficult for the plasma parameters explored. Achieving significant 1:1 x:y sidewall shrink requires fine control of the plasma parameters that can change during deposition. By fine-tuning plasma parameters we have achieved 10's of nm of 1:1 x:y sidewall shrink of circular/elliptical patterned photoresist features.

9:00am **PS-WeM4 Plasma Energy Partitioning and Influences on Surface Reactivity**, *J.M. Blechle, M.F. Cuddy, E.R. Fisher*, Colorado State University

The partitioning of energy within plasma systems is of vital importance to plasma chemistry as it provides insight into reactivity via possible formation and decomposition mechanisms as well as its significant contribution to surface reactivity. Here, such investigations are used to determine the internal and kinetic energies of species within a variety of inductively coupled plasma systems. To obtain this information, optical emission spectroscopy (OES), broadband absorption spectroscopy (BAS), and the imaging of radicals interacting with surfaces (IRIS) technique were utilized to determine species energetics (vibrational, rotational, and translational temperatures). Although comparisons will be made between internal energies of SiF in SiF₄ plasmas and CF in variety of fluorocarbon plasmas, a primary focus will be placed on nitric oxide plasma systems and the associated energies of NO gas species. These data are also correlated to

* NSTD Recognition Award

species surface reactivity data, and are used to demonstrate the relationship between internal temperatures and observed surface scatter coefficients (S), which is directly related to surface reactivity (R). One such comparison will be on the strong correlations measured between the vibrational temperatures (Θ_v) of NO and $S(\text{NO})$ as a function of applied plasma power. Such observations allow for unique insight into these plasma systems and the integral role energy partitioning plays in the assessment and understanding of complex plasma chemistry.

9:20am **PS-WeM5 $\text{H}_2/\text{D}_2/\text{Ar}$ Plasmas Interacting with Carbon-based Films: Plasma Distribution Functions, Etching and Applications**, N.A. Fox-Lyon*, A.J. Knoll, University of Maryland, College Park, J. Franek, West Virginia University, V. Demidov, Wright-Patterson Air Force Base, M. Koepke, West Virginia University, G.S. Oehrlein, University of Maryland, College Park

Prediction and control of plasma distribution functions in low temperature plasmas are important for control of plasma-materials interactions. Reactive impurity additions to inert plasmas are important due to their large effects on both plasma properties and role in plasma-surface interactions. H_2 and/or D_2 added to Ar is an increasingly large topic of interest. The addition of small amounts of H_2/D_2 to Ar cause a change from physical to chemical sputtering of etching surfaces. Sode *et al.* have shown that small additions of H_2 to Ar cause unpredicted distributions of ion composition and a large loss in plasma density [1]. We investigate the effect that addition of small amounts of H_2/D_2 has on the ion compositions and energy distributions, along with effects on the plasma electrical properties and neutral and metastable species. D_2 addition to Ar plasma causes a faster transition to predominant ArD^+ ions than H_2 addition causes transition to predominantly ArH^+ ions. We also report on the effect H_2/D_2 added to Ar plasma has on the Ar metastable concentration. We find that, like the effect on plasma density, the metastable concentration decreases rapidly with the introduction of H_2 impurities. We find measurable differences for these effects when using D_2 impurity instead of H_2 impurity. The effect of these changes to plasma properties by H_2/D_2 impurity addition is also reflected in the plasma material interactions with hydrocarbon films. While ion mass falls gradually with addition, etch rate and modification change drastically. Direct plasma and neutral-based etching experiments were performed for different chemistries to separate the effects of ion composition/mass and reactive neutrals generated in the plasma. The authors gratefully acknowledge financial support from US Department of Energy (DE-SC0001939).

[1] Sode *et al.* J. Appl. Phys. **113**, 093304 (2013)

9:40am **PS-WeM6 Molecular Dynamics Simulation for Hydrogen Plasma Processing of Graphene**, A. Davydova§§, E. Despiau-Pujo, G. Cunge, Cnrs/ujf/ Cea - Ltm, France, D.B. Graves, University of California, Berkeley, L. Magaud, L. Delfour, CNRS/UJF, Institut Néel, France

Graphene is a two-dimensional material with unique physical, chemical and mechanical properties, promising for novel applications in industrial scale. The successful development of graphene-based thin film technologies relies on the capability to grow and integrate this material into sophisticated devices, but the nm-scale control of graphene processing challenges current technology, especially in plasma treatment.

The main issue associated with plasma/graphene processes is the few- to mono-atomic thickness of the material: graphene is easily damaged upon exposure to reactive plasma. This precludes the use of conventional plasma technologies to clean, dope and pattern graphene layers in a controlled way as is done for other materials in the microelectronic industry. Pulsed inductively coupled plasmas (ICPs) could in principle alleviate this issue by reducing ion bombardment energy while retaining active radicals. Hydrogen plasma has been shown to be promising for graphene treatment with minimal damage, but little is known of the fundamental mechanisms.

In this work, we applied classical molecular dynamics (MD) simulations of H_2 plasma / graphene interaction to assist the development of two important processes: graphene surface cleaning (selective removal of polymeric PMMA residues from its surface) and graphene nanoribbon (GNR) patterning with well controlled edges. Using MD we investigate the impact of the graphene temperature and incident H species energy on nanoribbon modification. We found that on the ribbon basal plane, H species experienced a repulsive force due to delocalized π -electrons, which prevents them from chemisorption if their energy is below ~ 0.6 eV. By contrast, there is no barrier for H chemisorption on GNR edges and the graphene border can be rapidly hydrogenated by H radicals without damaging the basal plane. MD simulations further suggest that lateral etching will not occur unless the graphene temperature is raised above ~ 600 K and that etching probability slows above about 800K. This result is in good

agreement with experiments. We also show that exposure of graphene to energetic H above a threshold of ~ 12 eV leads to H penetration through graphene. Severe damage of the graphene basal plane (i.e. C-C bond breaking) is observed at incident H energies higher than ~ 15 eV. This suggests that ions and fast neutrals from pulsed ICPs, which impact surfaces at $\sim 1-10$ eV, may be well suited for graphene cleaning and GNR trimming. This result has now been confirmed experimentally. XPS, AFM, Raman and electrical measurements show that pulsed H_2 plasmas clean PMMA residues from graphene surface with almost no damage after annealing.

10:40am **PS-WeM9 Beam Studies of Plasma Etching Reactions**, K. Karahashi, S. Hamaguchi, Osaka University, Japan **INVITED**

For the development of highly integrated semiconductor devices, more precise control of etching processes is required for further progress. For this purpose, it is desirable to have full understanding of surface reaction mechanisms associated with the etching processes. However, in general, it is difficult to analyze such reactions in detail for plasma etching processes because a large number of reactions take place simultaneously. One way to tackle this challenge is use a beam system to examine specific beam-surface interactions that are likely to take place in actual plasma etching processes. Pioneering work by Coburn *et al.* [1] using beam experiments clearly showed that silicon etching reactions on fluorinated surfaces are enhanced by energetic inert ion bombardment. Many such studies have provided useful qualitative information on silicon etching by plasmas based on, for example, halogen gases. As new advanced semiconductor devices have been proposed, the variety of materials that require highly controlled etching and that of gases that are used for the reactive ion etching (RIE) processes have increased significantly. Therefore we believe that needs for such beam studies are higher than ever. Based on an earlier beam system [2], we have recently advanced our techniques to examine interactions of reactive ions and free radicals with material surfaces, using a multi-beam system. With this system, we have obtained detailed information on reactive etching and physical sputtering processes on various materials such as silicon, silicon oxide, silicon nitride, and metals including ferromagnetic materials. The multi-beam system is a mass-selected ion beam injector combined with supersonic molecular beam and effusive molecular beam sources. When a sample is irradiated with any combination of these beams, it exhibits a specific surface reaction that would take place in an actual plasma. Its surface analyses include *in-situ* chemical analyses by X-ray photoelectron spectroscopy and Fourier transform infrared spectroscopy and angular and time-resolved measurements of desorbing molecules by a rotatable QMS. In the presentation, a detailed account will be given of how such beam experiments unveil surface reaction mechanisms for RIE processes, based on examples of our recent studies on selective etching processes of Si-based materials and metals. [1] J. W. Coburn, H. F. Winters, and T. J. Chuang: J. Appl. Phys. **48**(1997) 3532. [2] K. Karahashi *et al.*: J. Vac. Sci. Technol. A **22**(2004) 1166

11:20am **PS-WeM11 Surface Cleaning for Enhanced Adhesion to Packaging Surfaces: Plasma and Free Radical Chemistries**, S. Gaddam, H. Kasi, J. Kelber, University of North Texas

In microelectronics device packaging, the removal of adventitious carbon and other contaminants, and the formation of a hydrophilic surface, are key steps to ensure adequate bonding to epoxy. This surface cleaning is commonly accomplished by oxygen plasma treatment, but the effects of such treatment on contaminant removal, surface composition and surface hydrophilicity are not well-understood. In-situ x-ray photoelectron spectroscopy (XPS) indicates that He, O_2 and NH_3 capacitively-coupled plasmas are equally effective at removing adventitious carbon from silicon nitride (Si_3N_4) and silicon oxynitride ($\text{Si}_x\text{O}_y\text{N}_z$) surfaces. O_2 or He plasma treatment, however, results in initial oxidation of Si_xN_y or $\text{Si}_x\text{O}_y\text{N}_z$ surfaces, and eventual formation of a SiO_2 -like overlayer. In contrast, exposure of either surface to thermal atomic O yields carbon removal, but only surface oxidation of Si_xN_y , and no further change in $\text{Si}_x\text{O}_y\text{N}_z$ surface composition. The data demonstrate that silica overlayer growth involves reaction of background O_2 or H_2O with reactive sites induced by ions or vacuum ultraviolet photons present in the plasma. In contrast, the exposure to NH_3 plasma results in negligible surface oxidation of the Si_xN_y or $\text{Si}_x\text{O}_y\text{N}_z$ surface, but with effective removal of the adventitious carbon. There is no formation of a SiO_2 overlayer even at higher exposure times. This indicates that the presence of H passivates or reduces reactive sites for SiO_2 formation at the Si_xN_y or $\text{Si}_x\text{O}_y\text{N}_z$ surfaces. Ex-situ contact angle measurements show that Si_xN_y and $\text{Si}_x\text{O}_y\text{N}_z$ surfaces exposed to oxygen plasma are initially more hydrophilic than surfaces exposed to NH_3 plasma, indicating that the O_2 plasma-induced SiO_2 overlayer is highly reactive towards ambient. At longer ambient exposures ($> \sim 10$ hours), however, surfaces treated by either method exhibit similar steady state contact angles, correlated with rapid uptake of adventitious C, as determined by XPS. These data demonstrate that O_2 or even He plasma cleaning of Si_xN_y or $\text{Si}_x\text{O}_y\text{N}_z$ surfaces results in unintended SiO_2 overlayer formation and that the use of NH_3

* Coburn & Winters Student Award Finalist

plasma can clean the substrates efficiently without the SiO₂ formation. The data also demonstrate that the hydrophilicity of such surfaces decreases rapidly upon ambient exposure, suggesting the potential advantage of in-situ surface passivation following plasma cleaning.

Acknowledgement: This work was supported by the Semiconductor Research Corporation under Task ID 2071.016. The authors thank Texas Instruments for providing the samples and the contact angle measurement capability, and thank Andy Burnett and Varughese Matthew for stimulating discussions.

Synchrotron Analysis Focus Topic

Room: 203 C - Session SA+AS+MI+SS-WeM

Synchrotron and Imagery: PEEM, Nano-ARPES and Others (8:00-9:40 am)/Synchrotron TXRF and Related Techniques (10:40 am-12:00 pm)

Moderator: M.C. Asensio, Synchrotron SOLEIL, France, J. Kawai, Kyoto University, Japan

8:00am **SA+AS+MI+SS-WeM1 LEEM, PEEM and ARPES Studies of Epitaxial Graphene on SiC(0001)**, *U. Starke*, Max Planck Institute for Solid State Research, Germany **INVITED**

Large area epitaxial graphene (EG) can be grown on SiC(0001) by heating in Ar atmosphere [1]. However, such graphene layers are *n*-doped due to the influence of a covalently bonded carbon interface layer. This influence can be completely eliminated and the graphene layers be decoupled from the substrate by atomic intercalation. The electronic structure can be tuned in various ways for these decoupled graphene layers. Detailed investigations of the π -band structure, the spatial arrangement, chemical bonding and local surface order are shown based on angle-resolved photoemission spectroscopy (ARPES), low-energy electron microscopy (LEEM), photoemission microscopy (PEEM) combined with microscopic X-ray photoelectron spectroscopy (μ -XPS) and low-energy electron diffraction (μ -LEED), as well as scanning tunneling microscopy (STM) experiments.

By annealing the EG samples in atmospheric H₂, atomic hydrogen reacts under the interface layer, so that the underlying SiC layer becomes passivated [2]. The interface layer alone transforms into a quasi-free standing monolayer while monolayers and bilayers turn into decoupled bilayers and trilayers [3,4]. As a result, charge neutral quasi-free standing graphene layers can be obtained. By intercalation of Germanium the graphene layers can also be decoupled. In this process both *p*- and *n*-doping can be produced, depending on the amount of Ge material intercalated. By preparing both phases in coexistence on the surface, lateral *p-n* junctions can be generated on a mesoscopic scale [5]. Intercalation of Cu induces a coincidence superstructure on top of the SiC surface, which originates from periodic regions of different bond configuration for the carbon atoms in the graphene layer. As a result, a long range periodic potential is imposed onto the graphene layer, which leads to a profound modification of its electronic spectrum. A surprisingly strong doping and the development of mini-Dirac cones are observed [6].

References:

- [1] K.V. Emtsev, et al., Nat. Mater. 8, 203 (2009).
- [2] C. Riedl, C. Coletti, T. Iwasaki, A.A. Zakharov, and U. Starke, Phys. Rev. Lett. 103, 246804 (2009).
- [3] S. Forti, K.V. Emtsev, C. Coletti, A.A. Zakharov, C. Riedl, and U. Starke, Phys. Rev. B 84, 125449 (2011).
- [4] C. Coletti, K.V. Emtsev, A.A. Zakharov, T. Ouisse, D. Chaussende, and U. Starke, Appl. Phys. Lett. 99, 081904 (2011).
- [5] K.V. Emtsev, A.A. Zakharov, C. Coletti, S. Forti, and U. Starke, Phys. Rev. B 84, 125423 (2011).
- [6] K.V. Emtsev, S. Forti, A.A. Zakharov, C. Coletti, and U. Starke, in preparation.

8:40am **SA+AS+MI+SS-WeM3 An Imaging NEXAFS Detector for Compositional and Structural Analysis**, *C. Weiland*, Synchrotron Research, Inc., *Z. Fu, C. Jaye, D. Fischer*, National Institute of Standards and Technology (NIST), *K. Scammon*, University of Central Florida, *P. Scobol, E. Principe*, Synchrotron Research, Inc.

We present the development of the second generation Large Area Rapid Imaging Analytical Tool (LARIAT MKII) for near edge x-ray absorption fine structure (NEXAFS) surface chemical and structural analysis. This analyzer utilizes magnetostatic electron optical elements to maintain the lateral distribution of electrons into a 16 mega channel detector, while

providing a near 180° collection angle for high collection efficiency enabling rapid parallel imaging. A series of electrostatic lenses can be used to tune the energy and depth sensitivity of the imaged electrons allowing for 3D analysis of the near surface region (<7nm). The first LARIAT MKII will be installed on the NIST SST beamline at NSLS II; initial testing is currently being performed at NSLS beamline U8B.

The first generation LARIAT has demonstrated capabilities in determining simultaneously the concentration and orientation of single-strand DNA micro array sensors, organic electronic combinatorial device arrays, and semifluorinated molecular gradients. Additionally, LARIAT MKI was used to identify cancerous versus non-cancerous dermal tissue through spectroscopic analysis. LARIAT MKII advances these capabilities by improving the lateral resolution of the analyzer to below 7 μ m and improving collection efficiency through a series of gridless electrostatic lenses. Here we will present an overview of LARIAT MKII and its capabilities, as well as some of the initial data recorded from the system.

9:00am **SA+AS+MI+SS-WeM4 Recent Advances in High Resolution Real and Reciprocal Space Photoelectron Emission Microscopy**, *K. Winkler, B. Kroemker*, Omicron NanoScience, Germany, *N.J. Weber, M. Escher*, FOCUS GmbH, Germany, *N. Barrett*, Cea Dsm Iramis Spesi, France

Conventional electron spectroscopy methods are limited in providing simultaneous real and reciprocal or k-space information from small areas under laboratory conditions. Therefore, the characterization of materials with only micron scale sample homogeneity requires new instrumentation. Recent improvements in aberration compensated energy-filtered photoelectron emission microscopy (PEEM) can overcome the known limitations in both synchrotron and laboratory environments.

We present first results from real and reciprocal space photoelectron emission microscopy (PEEM) e.g. on Ag (111) showing high k and high energy resolution using a laboratory based He I and II radiation at room temperature and temperatures below 40K. The combination of a recently developed LHe cooled sample stage with an improved aberration compensated energy-filter allows 30 meV energy resolution while a new type of event counting detector improves the signal to noise ratio of the detector.

9:20am **SA+AS+MI+SS-WeM5 Quantum Material Spectroscopy Center at the Canadian Light Source**, *S. Gorovikov, B. Yates*, Canadian Light Source, *A. Damascelli, H. Davis*, University of British Columbia, Canada, *R. Reininger*, Advanced Photon Source, *K.I. Blomqvist*, Consultant, *M. Sigrist, S. Chen, E. Hallin*, Canadian Light Source

We report on the concept and design features of the Quantum Material Spectroscopy Center (QMSC), a state-of-the art XUV and soft X-ray beamline facility currently under construction at the Canadian Light Source. The QMSC will operate within the photon energy from 15 to 1200 eV and is intended for spin- and angle-resolved photoemission spectroscopy (SARPES and ARPES).

A distinctive feature of the QMSC is the combination of two independent end stations dedicated to SARPES and ARPES experiments with a unique source consisting of a pair of 4 m long APPLE type undulators. The low- and high-energy undulators will be installed side by side in a switch yard arrangement and will provide the highest possible photon flux within this photon energy range. Complete polarization control in both linear and circular modes will be available. Moreover, the quasiperiodic magnetic structure of the low-energy undulator will result in optimized suppression of the higher order harmonics.

The optical design of the beamline is based on the Variable Line Spacing Plane Grating Monochromator (VLS PGM) design and will deliver 10¹² - 10¹³ photons/second at the experimental stations with a resolving power higher than 10⁴ over the full photon energy range.

The theoretical performance of the beamline will be presented. Research capabilities of the beamline will be illustrated.

9:40am **SA+AS+MI+SS-WeM6 Nano-ARPES Beamline at SOLEIL: A Powerful and Innovative Probe for Nanoscience**, *M.C. Asensio*, Synchrotron SOLEIL, France

Over the last decades, we have witnessed exponential advances in a wide diversity of new nanotechnologies. These advances, seen particularly in nanoelectronics, nanomagnetism and nanochemistry, among others, affect almost every aspect of our lives. Following the fundamental step in the creation of nano-objects and even if these "building blocks" have shown remarkable properties, they would have remained unexploited if, at the same time, we had not developed new tools capable of analyzing, viewing and scrutinizing objects on a wide range of scales, from a few microns to a few tens of nanometers.

Recently, great progress has been made as a result of the rapid expansion in the range of modern microscopies. However, if they have achieved nanometer spatial resolution, the challenge still remains to provide powerful high-energy-resolution spectroscopic tools for probing nano- and micro-areas. The challenge then, is to quantify and analyze the electronic properties of advanced materials on a nano- and mesoscopic-scale. For such a result, analysis of the electronic structure must be comprehensive, not only with regard to detection of core levels, but especially to study the structure of electronic states of the valence bands, directly responsible for chemical bonds, electrical transport and the thermal and mechanical properties.

In this presentation, the latest results of the ANTARES microscope beamline at the synchrotron SOLEIL will be disclosed. In particular, nano-ARPES findings describing the electronic band structure of mono-atomic thick graphene films grown on copper substrates by chemical vapor deposition will be presented. This end-station, with a spatial resolution of several tens of nanometers, has already been able to carry out direct imaging of core levels, their chemical shifts and the band electronic structures of several ordered materials. High precise Chemical images and valence band information of nano-objects like exfoliated graphene, granular materials and Nanowires will be reported.

1.- J. Avila et al., *Sci. Rep.* 2013, 14, August 3 : 2439 | DOI: 10.1038/srep02439

10:40am **SA+AS+MI+SS-WeM9 Grazing Incidence and Grazing Exit X-ray Spectroscopy of Ultra Shallow Arsenic Implants in Silicon, F. Meirer**, Utrecht University, Netherlands **INVITED**

Grazing incidence (GI) and grazing exit (GE) geometries exhibit exotic geometries in x-ray fluorescence (XRF) spectroscopy and are mainly used to restrict the information depth of the analysis to the sample surface. For samples with sufficiently small surface roughness, variation of the angle of incidence within the range of the critical angle of total (external) reflection of x-rays allows obtaining information about the depth distribution of elements within the sample's surface. In total reflection x-ray fluorescence analysis (TXRF) the effect of total reflection is utilized adjusting the measurement angle below the critical angle. TXRF offers excellent detection limits and is routinely used for chemical trace analysis and surface contamination control.

The use of synchrotron radiation (SR) is highly beneficial for TXRF and for angle-dependent XRF in general, because its properties (e.g., high intensity, linear polarization, small source size, and natural collimation) make it ideally matched to the requirements of these techniques. Furthermore, when using SR as x-ray source these methods can be combined with x-ray absorption spectroscopy (XAS) analyzing the local coordinate structure of an element of interest in the sample. This extends XAS to the trace element level (ppb) in samples where only small amounts are available or where the sample is confined in or on the surface of a substrate material.

In this presentation I will review strengths and weaknesses of SR induced TXRF, GI-XRF and GE-XRF and their combination with XAS on the basis of the analysis of state-of-the-art ultra shallow arsenic implants in silicon produced by plasma immersion ion implantation and deposition (PIIID) and subsequent LASER annealing.

11:20am **SA+AS+MI+SS-WeM11 Basic Principles and Applications of Time Resolved Grazing Incidence EXAFS Experiments for Surface Studies in the 50 ms Range, D. Lützenkirchen-Hecht, J. Stötzl, O. Müller, R. Frahm**, Bergische Universität Wuppertal, Germany

The surfaces of materials play a decisive role for many fundamental physico-chemical processes such as e.g. aqueous and gaseous corrosion, catalysis, or coating procedures. Many of those processes proceed in non-vacuum environments, so that classical surface analytical techniques like XPS or scanning electron microscopy are not suited for in-situ investigations. Furthermore, all of the above mentioned processes are strongly time dependent, so that fast surface sensitive in-situ probes are necessary to study the respective phenomena. EXAFS can be made surface sensitive by using the grazing incidence geometry: For incidence angles below the critical angle of total reflection, the penetration depth of the X-rays amounts to only some few nanometers, and the reflected X-ray beam only contains information about the near surface region of the studied samples. Here we have combined the grazing incidence geometry with the Quick-scanning EXAFS (QEXAFS) data collection. Recent experimental developments of QEXAFS have substantially improved the time resolution to about 50 ms for a single spectrum, thereby enabling completely new surface science experiments.

In this contribution, we will briefly discuss the experimental setup and present results obtained in-situ during the film deposition by sputtering. The growth of gold and copper thin films on float glass substrates and Si wafers were investigated as examples. We will show that the evolution of the film structure can be followed with a subsecond time resolution, and a detailed

modelling of the experimental data using the distorted wave Born approximation yields e.g. the film composition, thickness and roughness as a function of time. First experiments showed the need for an automated analysis, and we will also introduce appropriate software solutions for the processing of huge amounts of data acquired in a typical time resolved experiment with several thousands of spectra. Furthermore, we will also discuss the oxidation of the Cu thin films by their exposure to ambient air at different temperatures. The results clearly show that the dynamics of the oxidation are strongly depending on the actual temperature of the samples.

11:40am **SA+AS+MI+SS-WeM12 Portable versus Synchrotron TXRF Analysis, J. Kawai, Y. Liu, S. Imashuku**, Kyoto University, Japan

Total reflection X-ray fluorescence (TXRF) analysis is a micro (absolute amount is less than pg) and trace (relative concentration is less than ppb) analysis method. When synchrotron X-rays are used, the minimum detection limit becomes down to fg for transition metals. However the synchrotron radiation is an elemental selective method, and thus overall elements are not detectable. On the other hand, synchrotron radiation can eliminate the interference of elements whose analytical lines overlap, such as Ba and Ti, As and Pb. The TXRF spectrometers can be classified into three categories: (i) synchrotron radiation TXRF, (ii) high power X-ray tube (kW) TXRF, and (iii) low power (1-50 W) desk top TXRF. Type (i) achieves highest sensitivity, with WD-TXRF spectrometer (wavelength dispersive), down to fg, however ED (energy dispersive type) is also used, where polarization is additionally used to reduce the scattering of incident X-rays. Type (ii) is used for routine analysis of Si wafer analysis (ISO standard methods), but due to the recent progress of the semiconductor processing, the detection limit is not enough for the advanced semiconductor processing systems. Type (iii) is again classified into monochromatic and non-monochromatic types. Monochromatic type needs 50 W X-ray tube (cooling by fan), but non-mono type is possible only by 1 W X-ray tube. The sensitivity is comparable. Type (iii) is mainly used for environmental analysis, toxic elements analysis, and water quality analysis. We must also consider the sensitivity of elements for mass spectrometry such as SIMS and ICP-MS. These methods are sometimes more sensitive than synchrotron radiation TXRF. Most versatility method is the non-monochromatic X-ray tube (1 W) type portable TXRF spectrometer, by which we can analyze something toxic materials, whether it is truly toxic or not toxic. Several examples which show the ability of the low power TXRF, such as laboratory hazard analysis, will be presented.

Surface Science

Room: 202 A - Session SS+AS-WeM

Catalysis in Prebiotic Chemistry (8:00-10:00 am)/Environmental Interfaces (10:40 am-12:00 pm)

Moderator: A.J. Gellman, Carnegie Mellon University

8:00am **SS+AS-WeM1 Models for the Origin of Biological Homochirality, D.G. Blackmond**, The Scripps Research Institute **INVITED**

The single chirality of biological molecules has fascinated scientists and laymen alike since Pasteur's first painstaking separation of the enantiomeric crystals of a tartrate salt over 150 years ago. In the past decade, a number of theoretical and experimental investigations have helped to delineate models for how one enantiomer might have come to dominate over the other from what presumably was a racemic prebiotic world. Our work has highlighted mechanisms that include either chemical or physical processes, or a combination of both. While much of the scientific driving force for this work arises from an interest in understanding the origin of life, research focusing on mechanisms for the enantioenrichment of chiral molecules has the potential to impact a wide range of applications, most notably in the synthesis and formulation of pharmaceuticals.

8:40am **SS+AS-WeM3 A New Catalytic RNA for the RNA World, J.E. Moretti, G.F. Dolan, U.F. Müller**, University of California San Diego **INVITED**

The RNA world hypothesis describes a stage in the early origin of life in which RNA molecules served as genome and as the major genome-encoded catalyst. RNA world organisms must have existed more than 3.5 billion years ago, which makes it unlikely that direct evidence of them can be found. In contrast, researchers are trying to recapitulate these early stages of life in the lab. These efforts identified processes that can generate nucleosides under prebiotically plausible conditions, and have generated catalytic RNAs that are able to polymerize RNAs from nucleoside 5'-triphosphates. The latter would be the central activity in a self-replicating RNA organism. However, it has not been shown how nucleosides can be converted to nucleoside 5'-triphosphates in an RNA World scenario. Here

we describe a new catalytic RNA that generates RNA 5'-triphosphates from RNAs with 5'-hydroxyl groups, using trimetaphosphate. Trimetaphosphate is a prebiotically plausible compound because it can be generated by volcanic processes and by the erosion of phosphide minerals. The catalytic RNAs were obtained by *in vitro* selection and work with pseudo-first order rate constants $> 0.01 \text{ min}^{-1}$. We are currently trying to identify variants of these catalytic RNAs that are able to triphosphorylate single nucleosides in multi-turnover reactions. In summary, our results show that catalytic RNAs can triphosphorylate RNA 5'-hydroxyl groups with trimetaphosphate and further the efforts to re-surrect RNA world organisms.

9:40am **SS+AS-WeM6 Chemical Mapping of Minerals and Meteorites for Origins of Life Research**, *R.D. Gann, C. Pirim, T.M. Orlando*, Georgia Institute of Technology

Surface analytical techniques such as Raman, x-ray photoelectron spectroscopy, and two-step laser desorption/ionization stand to shed considerable light on the chemistry that occurs on mineral surfaces and the surfaces of meteorites. The results of Raman and XPS analysis of the meteorite schreibersite, for instance, show a rich surface with phosphate and several impurity metals. Because this surface is potentially prebiotic, the chemistry involved has implications for the origins of life, and recent results within our center show it is capable of phosphorylation of relatively simple molecules. Analysis of other potentially prebiotic minerals such as pyrite are also under investigation with these techniques. Toward this goal, we have built a xenon tripling cell for vacuum-ultra-violet (10.5 eV) photoionization and a basic rastering UV desorption laser for direct detection of organic molecular analytes over 40 amu photons. The rastering allows spatial resolution for investigation of different domains of a mineral. This provides a nondestructive means for meteorite chemical analysis without the intervention of wet chemistry, which would potentially introduce molecules via reactions that would not otherwise happen. It also allows for detection of extremely small amounts of mass analytes.

This work was jointly supported by NSF and the NASA Astrobiology Program, under the NSF Center for Chemical Evolution, CHE-1004570

10:40am **SS+AS-WeM9 Water at Interfaces under Realistic Conditions**, *A. Nilsson*, SLAC National Accelerator Laboratory **INVITED**

I will present two classes of systems involving water at interfaces probed using ambient pressure XPS, water on BaF_2 and the interaction of oxygenated species during electrocatalysis. The structure of thin-film water on a $\text{BaF}_2(111)$ surface under ambient conditions was studied using Auger electron detected x-ray absorption spectroscopy (XAS) from ambient to supercooled temperatures at relative humidity up to 95 %. No ice-like structure was observed in spite of the expected templating effect of the lattice-matched (111) surface. The XAS spectrum of liquid thin-film water on BaF_2 exhibits, at all temperatures, a strong resemblance to that of high-density ices for which the observed spectroscopic features correlate linearly with the density. Molecular dynamics simulations indicate that the first layer water on $\text{BaF}_2(111)$ is indeed in a unique local structure that resembles high-density water, with a strongly collapsed second coordination shell.

The performance of fuel cells is limited by the sluggish kinetics of the oxygen reduction reaction (ORR) at the Pt cathode. An improved understanding of the catalytic steps of the ORR is thus essential for overcoming these limitations. By means of a PEM fuel cell designed to be compatible with our APXPS system, we have been able to identify the oxygenated intermediates of the ORR through their specific O 1s chemical shifts. Using XPS studies of well-defined model systems as spectroscopic references, we differentiate two types of OH intermediates whose population depends on cell voltage: hydrated and non-hydrated OH. We also establish that non-hydrated OH is the dominant surface species on a Pt cathode during ORR at high partial pressures of $\text{O}_2(g)$. With the assistance of DFT calculations, we show that the reduction of non-hydrated OH requires less overpotential than that of hydrated OH. This indicates that tuning OH hydration through cathode or electrolyte design will be crucial for enhancing ORR activity.

11:20am **SS+AS-WeM11 pH Dependent Behavior of Ammonia and Ammonium at the Liquid-Vapor Interface of Aqueous Solutions**, *M.H.C. Van Spyk, A.M. Margarella, K.A. Perrine*, University of California, Irvine, *B. Winter*, Helmholtz-Zentrum Berlin für Materialien und Energie/Elektronenspeicherring BESSY II, Germany, *J.C. Hemminger*, University of California, Irvine

The distribution of solutes near the air/water interface is known to affect chemical reactions occurring at the surface of aqueous atmospheric aerosols. Ammonia is a basic gas which is introduced into the air both naturally and biogenically, and is important for atmospheric reactions. Solvated ammonia (NH_3) is in equilibrium with the protonated cation ammonium (NH_4^+), and variation of the $\text{NH}_4^+/\text{NH}_3$ ratio with pH for **bulk** solutions is reasonably well known. In contrast, little is known about the

$\text{NH}_4^+/\text{NH}_3$ ratio at the liquid/vapor interface, or how it varies with bulk solution pH. Understanding the interfacial chemistry of ammonia solutions is important because the $\text{NH}_4^+/\text{NH}_3$ ratio may differ at the air/water interface leading to changes in reactivity that can influence air quality.

Liquid jet X-ray photoelectron spectroscopy (LJ-XPS) was used to investigate the interfacial behavior of aqueous ammonia in relation to pH at a solution temperature of 5 °C. For these studies, aqueous ammonium solutions were generated by dissolving ammonium hydroxide or ammonium chloride in water, and the pH was varied using hydrochloric acid or sodium hydroxide, respectively. A continuously renewed jet of solution was probed using photoelectron spectroscopy with synchrotron radiation which was tuned to produce various photoelectron kinetic energies corresponding to the desired sampling depth. Spectra were collected from the bulk solution by generating photoelectrons with high kinetic energies (600 eV) in which case the electron mean free path in solution is sufficiently large so that the experiment probes the bulk solution. Spectra were collected from the near-surface region by exciting photoelectrons with low kinetic energy (150 eV) so that signal from the bulk is attenuated. Nitrogen (N1s) and oxygen (O1s) photoelectron spectra were collected at two kinetic energies to study the relative amounts of each species at the surface versus the bulk for different bulk pH values. The N1s spectra were deconvoluted into three peaks from aqueous NH_4^+ , and NH_3 , and gaseous NH_3 , and since the spectra were recorded at the magic angle, the ratios of the integrated peak areas provide a comparison of the relative amounts of each species. It is observed that the $\text{NH}_4^+/\text{NH}_3$ ratio decreases with increasing bulk solution pH for the surface and bulk of solution, and there is a reduction of the $\text{NH}_4^+/\text{NH}_3$ ratio at the surface, compared to the bulk. The titrations of ammonium chloride and ammonium hydroxide may be contrasted to understand the impact of chloride concentration. This study illustrates that interfacial aqueous ammonia experiences a different equilibrium than that in the bulk.

11:40am **SS+AS-WeM12 Hydrogen Bonding – Probing its Role in Electron-promoted Desorption from Icy Films**, *D. Marchione, M.P. Collings, M.R.S. McCoustra*, Heriot-Watt University, UK

Previous work has demonstrated the efficiency of long range exciton transport to the vacuum/ice and substrate/ice interfaces in electron irradiation of solid water [1]. Building on this work, we have reported substantial enhancement of the cross-section for electron-promoted desorption (EPD) of benzene (C_6H_6) that we know to interact with the surface through a weak form of hydrogen-bonding (π -hydrogen bonding which is found to be common in biological systems) [2,3]. To probe the role of the hydrogen-bonding network in solid water in promoting the large enhancement of the EPD cross-section, we have undertaken studies on solid methanol (which possesses a one-dimensional hydrogen bonding network) and a simple ether, diethyl ether ($\text{C}_2\text{H}_5\text{OC}_2\text{H}_5$), which present a similar electronic environment for exciton formation under electron irradiation yet have decreasing degrees of hydrogen bond interaction. We will report on our studies of the basic surface science of these thin films investigated using a combination of temperature programmed desorption (TPD) and reflection-absorption infrared spectroscopy (RAIRS) and our C_6H_6 EPD measurements from these thin films. Comparisons with solid water as a substrate will be drawn.

[1] N.G. Petrik, and G.A. Kimmel, *J. Chem. Phys.* 123 (2005) 054702.

[2] J. D. Thrower, M. P. Collings, F. J. M. Rutten, and M. R. S. McCoustra, *Chem. Phys. Lett.* 505 (2011) 106.

[3] J. D. Thrower, A. G. M. Abdulgalil, M. P. Collings, M. R. S. McCoustra, D. J. Burke, W. A. Brown, A. Dawes, P. D. Holtom, P. Kendall, N. J. Mason, F. Jamme, H. J. Fraser and F. J. M. Rutten, *J. Vac. Sci. Technol. A* 28 (2010) 799.

Surface Science

Room: 201 A - Session SS+NS-WeM

Nanostructures: Reactivity & Catalysis

Moderator: I. Lyubinetsky, Pacific Northwest National Laboratory

8:00am **SS+NS-WeM1 Structure Sensitivity of Glycerol Oxidation Catalyzed by Pt/SiO₂ under Mild Conditions**, *Y. Li, F. Zaera*, University of California, Riverside

The surface structures of catalysts have in some instances a large impact on their catalytic properties. On the other hand, historically, mild reactions are not considered to be surface structure sensitive. In this work we report on our observation that both the size and the shape of Pt nanoparticles strongly affect the selectivity of glycerol oxidation, a reaction that can proceed at room temperature and under atmospheric pressures. In a series of

experiment using Pt/SiO catalysts with average particle sizes varying from 3.9 to 6.2nm, it was determined that selectivity toward primary carbon oxidation increases as the proportion of larger particles increases. Aside from this size effect, supported tetrahedral Pt and cuboctahedral Pt also exhibit different selectivity and kinetic behavior from the regular Pt catalysts. (See Fig. 1&2) We propose that these selectivity differences are due to the different adsorption state of the surface species. Dihydroxyacetone (the product of dehydrogenation on secondary carbon) is thermodynamically more stable than glyceraldehyde (the product of dehydrogenation on primary carbon) but with larger steric hindrance effect in the dehydrogenation process. While on the edge and corner parts of the Pt surface, the steric hindrance could be largely reduced comparing to smooth Pt surface, therefore dihydroxyacetone is more favored on smaller particles. (See Fig. 3) Further characterization of the catalysts and their detailed kinetic behavior is currently under way.

8:20am SS+NS-WeM2 Heats of Adsorption and Surface Reaction for CO and O₂ on Pd Nanoparticles by Single Crystal Adsorption Microcalorimetry, S. Schauer mann, M. Peter, J.M. Flores-Camacho, J.-H. Fischer-Wolfarth, S. Adamovski, H.-J. Freund, Fritz-Haber-Institut der Max-Planck-Gesellschaft, Germany

Establishing the correlation between the energetics of adsorbate-surface interaction and the structural properties of a catalyst is an important fundamental issue and an essential prerequisite for understanding the realistic catalytic processes. We apply a newly developed microcalorimetry set up to determine the adsorption heats of carbon monoxide and oxygen on Pd nanoparticles supported on a well-defined Fe₃O₄/Pt(111) film. We systematically vary the Pd cluster size in the range of ~ 100 to 5000 Pd atoms to address the energetics of CO and O interaction with the nanoparticles of different dimensions. Particularly, two major structural factors were identified that determine the CO and oxygen binding energy on Pd: the local configuration of the adsorption site, and the particle size. We show that the change of the binding site from a three-fold hollow site at Pd(111) to the edges of Pd nanoparticles results in a strong increase of the oxygen binding energy, while this effect is absent for CO adsorption, pointing to the adsorbate-specific nature of this factor. In contrast, the decreasing particle size was shown to result in strongly decreasing binding energies for both adsorbates. In case of oxygen, these both counteracting trends were found to give rise to a non-monotonous dependence of the oxygen adsorption energy on the particle size [1,2].

[1] J.-H. Fischer-Wolfarth, J.A. Farmer, J.M. Flores-Camacho, A. Genest, I.V. Yudanov, N. Rösch, C.T. Campbell, S. Schauer mann, H.-J. Freund, Phys. Rev. B, 81, 2010, 241416(R)

[2] M. Peter, J. M. Flores Camacho, S. Adamovski, L.K. Ono, K.-H. Dostert, C.P. O'Brien, B. Roldan Cuenya, S. Schauer mann, H.-J. Freund, Angew. Chem. Int. Edit. DOI: 10.1002/anie.201209476

8:40am SS+NS-WeM3 Size-dependent Correlations between Supported Cluster Electronic Properties and Catalytic/Electrocatalytic Activity, S.L. Anderson, University of Utah INVITED

We prepare model catalysts or catalyst-decorated electrodes by depositing size-selected Pd_n and Pt_n clusters on planar supports, including TiO₂(110), alumina/Ta(110), alumina/Rh(0001) as well as glassy carbon and ITO/glass electrodes. The samples are prepared in UHV and characterized *in situ* by a combination of X-ray and UV photoelectron spectroscopy (XPS, UPS), and low energy He⁺ ion scattering (ISS). The activity of the model catalysts for gas-surface reactions such as CO oxidation is studied using mass spectrometric methods, such as temperature-programmed reaction/desorption (TPR, TPD). Electrochemistry is done in an attached UHV antechamber fitted with a three electrode cell that can be sealed against the sample surface, allowing electrochemistry to be done both without, and with prior exposure to laboratory air. Electrocatalytic activity is drastically altered by air exposure. Results will be presented for CO oxidation over various M_n/oxide catalysts, and for electrochemical reactions observed under conditions appropriate for oxygen reduction or ethanol oxidation. One interesting result seen in many of these systems is a size-dependent anti-correlation between activity as oxidation catalysts, and shifts in the catalytic metal core level binding energies. Potential reasons for this correlation, and related studies of valence level shifts with UPS, will be discussed.

9:20am SS+NS-WeM5 Characteristics of Sulfur-Vacancy Clusters in Single Layer MoS₂: Insights from *ab initio* Calculations, D. Le, T.B. Rawal, T.S. Rahman, University of Central Florida

Single-layer MoS₂ is proving itself to be a versatile material for a wide variety of electronic, optical and chemical applications. Sulfur depletion, without destabilization of the single-layer, is considered a prudent way for making the basal plane of the layer catalytically active. We will present results of our density-functional-theory based examination of vacancy

structures on one side of a MoS₂ layer which point to their structural stability and chemical reactivity. We will show that the formation energy per sulfur vacancy is lowest (energetically favorable) when the vacancies form a row, and that the longer the row, the lower the formation energy. In addition, we will show that the lowest energetic barrier for spoiling these row structures by exchanging a vacancy with a nearby sulfur atom is 0.79 eV, and that this barrier increases as the row elongates. Furthermore, the presence of vacancy clusters will be shown to make the system thermodynamically facile for alcohol synthesis from syngas. (Work supported in part by DOE grant DE-FG02-07ER15842.)

9:40am SS+NS-WeM6 A New Effect of Nanoconfinement on Chemical Equilibrium: Theory and Experimental Evidence, L. Rubinch, M. Polak, Ben-Gurion University of the Negev, Israel

Recently¹ we predicted that when a reaction involving a small number of molecules occurs in a nanometric-scale domain entirely segregated from the surrounding media, the nanoconfinement can shift the position of equilibrium toward products via reactant-product reduced mixing. In this talk, we demonstrate how most-recently reported single molecule fluorescence measurements of partial hybridization of ssDNA confined within nanofabricated chambers provide the first experimental confirmation of this entropic nanoconfinement effect. Thus, focusing separately on each occupancy-specific equilibrium constant, quantitatively reveals extra stabilization of the product upon decreasing the chamber occupancy or size.² Namely, the DNA hybridization under nanoconfined conditions is significantly favored over the identical reaction occurring in bulk media with the same reactant concentrations. This effect, now directly verified for DNA, can be relevant to actual biological processes, as well as to reactions occurring on nanoparticle surfaces, and within molecular capsules, nanotubes, or other functional nanospaces.

1. Polak, M.; Rubinch, L. Nano Lett. 2008, 8 (10), 3543–3547.

2. Rubinch, L.; Polak, M. Nano Lett. 2013, DOI: 10.1021/nl4008198.

10:40am SS+NS-WeM9 Encapsulation of Noble-Metal Clusters on ZnO(10-10) and Its Impact on Catalytic Reactivity, Z. Zhang, F. Liu, Louisiana State University, L. Liu, Texas A&M University, E.W. Plummer, P.T. Sprunger, R.L. Kurtz, Louisiana State University

Supported metal clusters on ZnO are important catalysts for industrial synthesis of methanol from syn-gas. The active site of this reaction has long been debated. We have employed model single crystal catalysts and surface characterization tools to elucidate key aspects of the cluster structure and reactivity. Specifically, we have probed the CO oxidation reaction at high pressure (tens of Torr). In the case of Cu/ZnO(10-10), both LEIS and EELS show an encapsulation of the cluster with an ultrathin layer of ZnO which is thermally driven (up to 725 K) and promoted with oxygen exposure. Other spectroscopies, including XPS and UPS, suggest a self-limiting ZnO film (thickness of 1 – 2 ML). UPS measurements on the bare (un-annealed) Cu/ZnO clusters show that CO adsorbs molecularly at 85K while it dissociates on an encapsulated cluster at the same temperature, indicating that the ZnO coating is crucial to reactivity. Similarly CO₂ reacts strongly with the encapsulated Cu clusters indicating that the ultra-thin ZnO is participating in the adsorption process. High-pressure studies at 50 Torr at RT show that there is a greatly enhanced reactivity for CO oxidation for the encapsulated clusters compared to either the bare ZnO substrate or the un-encapsulated clusters. Similar results have been seen in the case of Au clusters on ZnO(10-10) and corresponding encapsulation, however differences in reactivity and structure exist. These results offer a new understanding of the “support” role of ZnO on this heterogeneous catalyst system, and may lead to new means to drive the mechanism of methanol synthesis and help to develop new designs of this important industrial catalyst.

11:00am SS+NS-WeM10 ALD ZnO 3D Hierarchical Nanostructures for Enhanced Photocatalytic Dye Degradation Kinetics, J. Zhao, A. Bagal, Q. Yang, X. Zhang, C.-H. Chang, M.D. Losego, G.N. Parsons, North Carolina State University

ZnO has been used as photocatalyst to degrade organic compounds, such as phenol, phenol derivatives, naphthalene, anthracene, and dye molecules. In order to overcome the limitation of ZnO nanosurfaces, immobilized photocatalyst with high S/V ratio nanostructure is needed. Previously, ZnO-nanowire-decorated pore-array films, polymer fiber mats and ZnO nanoplates have been fabricated and reported with enhanced photocatalytic properties. However, diffusion of dye molecules into nanostructures was found to limit the photocatalytic performance. Since the structures of these photocatalysts were not made periodic or uniform in size, the effects of nanostructure dimension could not be investigated. Periodic 3D nanostructures with tunable sizes are therefore needed.

A series of ZnO hierarchical 3D nanostructures were fabricated for photocatalytic applications. Nano-pillars were patterned on photoresist

(Pfi88A7) using interference lithography, and were coated with a conformal ZnO seed layer (~40nm) using atomic layer deposition (ALD). ZnO nanowires were grown onto the nano-pillars via hydrothermal synthesis. With varied growth time, we decorated the ALD ZnO coated nano-pillars with ZnO nanowires of different lengths (60~150nm). Scanning electron microscopy confirmed the 3D hierarchical nanostructures. Photodegradation kinetics of methyl orange was measured to characterize the photocatalytic property of the ZnO nanostructures. Apparent first order rate constant (k_{app}) of dye degradation was improved by 35% with ALD ZnO coated nano-pillars, compared with ZnO flat film catalyst. By decorating the nano-pillars with ZnO nanowires of 120 nm length, k_{app} was further increased by 88% to 1.75 h⁻¹. We compared the photocatalytic property of our nanostructures with varied sizes. We will show how the nanostructures controlled the diffusion rate of dye molecules and affected the overall photocatalytic performance.

11:20am **SS+NS-WeM11 Phase/Catalytic Activity Correlations of TiO₂ ALD Functionalized Nanoporous Gold**, *M. Bagge-Hansen*, Lawrence Livermore National Laboratory, *A. Wichmann*, University Bremen, Germany, *J.R.I. Lee*, *T.M. Willey*, Lawrence Livermore National Laboratory, *A. Wittstock*, University Bremen, Germany, *J. Biener*, Lawrence Livermore National Laboratory, *M. Bäumer*, University Bremen, Germany, *M. Biener*, Lawrence Livermore National Laboratory

Nanoporous metals have many promising technological applications, such as catalysts, photo-catalysts, and electrodes in batteries, but their practical use is often limited by their tendency to coarsen at elevated temperatures. Here we demonstrate that atomic layer deposition (ALD) of nanometer-thick TiO₂ films can drastically improve the thermal stability and mechanical properties of nanoporous gold (np-Au) while further adding functionality—such as dramatically improved catalytic activity. Aerobic CO oxidation was used to test the effects of annealing on the catalytic activity of the TiO₂/npAu hybrid materials, and the observed changes in catalytic activity will be discussed in terms of annealing induced morphology and phase changes. We characterized these annealing-induced changes of morphology and phase composition by cross-sectional scanning electron microscopy (xSEM), x-ray photoemission spectroscopy (XPS), and near-edge x-ray absorption fine structure (NEXAFS). The Ti L_{2,3}-edge in NEXAFS is well known to exhibit exceptional sensitivity to Ti coordination and structure. Amorphous, anatase and rutile polymorphs of TiO₂ can be clearly distinguished and reveal a smooth and strong variation in the predominant TiO₂ phase as a function of annealing. Our results provide new insights into the thermal stability of functionalized electrodes for energy storage and harvesting applications.

This work was performed under the auspices of the US DOE by LLNL under Contract DE-AC52-07NA27344

11:40am **SS+NS-WeM12 Nanostructured Gold Model Catalysts on Oxygen-Free Substrates**, *L. Liu*, Texas A&M University, *F. Womack*, Louisiana State University, *Z. Zhou*, Texas A&M University, *M. Patterson*, Louisiana State University, *B. Habenicht*, *Y. Xu*, Oak Ridge National Laboratory, *P.T. Sprunger*, *R.L. Kurtz*, Louisiana State University

A new class of nanostructured gold model catalysts has been synthesized by depositing gold on single-layer graphene and boron nitride (BN) thin films formed on refractory metals. These thin films, which are oxygen-free and devoid of strong adsorption sites in themselves, develop moiré superstructures due to lattice mismatch with the metal substrates, which present periodic, identical traps on the potential energy surface for possible cluster nucleation. STM studies have shown that gold atoms forms two-dimensional (2-D) islands on graphene/Ru(0001) but small monodisperse clusters on BN/Rh(111). The electronic structures of these gold nanostructures have been characterized by electron energy loss spectroscopy (EELS) and angle resolved photoemission spectroscopy (ARPES), and the geometric structures have been studied by scanning tunneling microscopy (STM). CO and O₂ are used to probe the activity of these gold model catalysts. On 2-D gold islands, adsorbed CO molecules demonstrate a stretching frequency characteristic of anionic Au and can be titrated by O₂ molecules. On gold clusters on BN/Rh(111) substrates, both CO and O₂ chemisorption is demonstrated in temperature programmed desorption (TPD). Furthermore, density function theory (DFT) calculations have been used to elucidate the adsorption sites and adsorption configurations for CO and O₂ on the two different gold model catalysts. Our findings illustrate the critical importance of size to the reactivity of gold catalysts and the exciting possibility of corrugated thin films such as graphene and BN moirés functioning as templates to form model nano-catalysts.

Transparent Conductors and Printable Electronics Focus Topic

Room: 102 B - Session TC+EM+TF-WeM

Oxide and Flexible Electronics

Moderator: G. Exarhos, Pacific Northwest National Laboratory, L.M. Porter, Carnegie Mellon University

8:00am **TC+EM+TF-WeM1 Characterization of Thermal Plasma.....**, *M. Kinsler*, *K. Teh*, *R. Harrison*, San Francisco State University

A low-vacuum thermal plasma system is designed and developed to enable plasma-enhanced chemical vapor deposition and rapid plasma annealing of metal oxide thin films within the same system. Using this system, we have successfully synthesized optically transparent and electrically conductive, nanocrystalline zinc oxide (ZnO) thin films, with average grain sizes of between 75 nm and 150 nm at substrate temperatures ranging from 550C to 600C. Prior to synthesis, argon and oxygen are first introduced into the synthesis vessel, consisting of a quartz tube positioned in the center of an inductive copper coil, at 42 sccm and 0.07 sccm, respectively, with a background vacuum level of 1.15 PSIA. During synthesis, pure solid zinc precursor is melted and ionized by thermal plasma, and reacted with oxygen to form ZnO which is deposited on the substrate. Keeping the vessel pressure and substrate temperature constant, the growth rate of the ZnO films is approximately 15 nm/min. Using the same system, the ZnO-coated substrate can next be mounted on a different fixture and be annealed by thermal plasma at temperatures from 300C to 800C (0.25 to 0.38 T_m of ZnO) in a pure argon environment at 1.15 PSIA background pressure. Comparing the as-synthesized and annealed samples using techniques such as scanning electron microscopy (SEM), x-ray diffraction (XRD), UV-Vis spectroscopy, and four-point probe sheet resistance measurements, we observed improvements in the properties of the post-annealed ZnO films in the following ways: 1) ZnO grain size increased from approximately 50 nm to 100 nm, 2) the number of grains decreased and hence the number of grain boundaries decreased, 3) grain morphology became smoother possibly indicating less internal strain, and 4) sheet resistance of the film decreased. We hypothesize the improved electrical properties are attributed to the reduction in both grain boundaries and internal stress—both of which are known to reduce electron mobility. Synthesizing and annealing metal oxides, such as ZnO, in the same system would reduce overall turnaround time as moving samples between systems is avoided. Ultimately, this method could pave the way for the production of high-quality, optically transparent, and electrically conductive metal oxide semiconductor thin films in a single, rapid operation within a low-cost, small-footprint benchtop system.

8:20am **TC+EM+TF-WeM2 Effects of High Pressure on InGaZnO Thin Film**, *S.H. Yoon*, *Y.J. Tak*, *D.H. Yoon*, *U.H. Choi*, *H.J. Kim*, Yonsei University, Republic of Korea

Since Hosono et al presented amorphous oxide semiconductor (AOS) thin film transistor (TFTs) in 2004, AOS TFTs have been attracting attention from many researchers for a decade [1]. AOS TFTs have high enough mobility for organic light emitting diodes, and high resolution display. One of the technologies for improving electrical characteristics is high pressure annealing [2,3]. We studied pressure effects on AOS TFTs without additional annealing process. We applied pressure on inverted staggered InGaZnO (IGZO) TFTs. IGZO layer (50nm) was deposited by sputtering. SiO₂ layer (200 nm) was deposited by plasma enhanced chemical vapor deposition (PECVD) as a gate insulator and an etch stop layer, respectively. MoW (200 nm) was deposited by sputtering as a gate metal, and Mo was deposited by sputtering as source/drain metal. Applied gas was N₂, and applied pressures varied 1MPa, 3 MPa, and 5 MPa for 2 hours, respectively. Figure 1 shows transfer curves on different pressure, and mobility and sub-threshold swing were improved. References:

[1] K. Nomura, H. Ohta, A. Takagi, T. Kamiya, M. Hirano, and H. Hosono, *Nature* **432**, 488-492 (2004).

[2] K.H. Ji, J.-I. Kim, H.Y. Jung, S.Y. Park, R. Choi, U.K. Kim, C.S. Hwang, D. Lee, H. Hwang, and J.K. Jeong, *Appl. Phys. Lett.* **98**, 103509 (2011).

[3] R.S. Rim, W.H. Jeong, D.L. Kim, H.S. Lim, K.M. Kim, and H.J. Kim, *J. Mater. Chem.* **22**, 12491-12497 (2012).

8:40am **TC+EM+TF-WeM3 Surface Chemistry of Amorphous InGaZnO₄ Films**, *B. Flynn*, Oregon State University, *S.A. Thevuthasan*, Pacific Northwest National Laboratory, *H. Bluhm*, Lawrence Berkeley National Laboratory, *G.S. Herman*, Oregon State University

Thin film transistors (TFT) utilizing amorphous InGaZnO₄ (a-IGZO) have multiple applications in high performance electronic devices, from flat-panel displays and integrated circuits to non-volatile memories. A-IGZO enables low processing temperatures, while retaining large electron mobilities, and low operation voltages and off currents. These stable carrier transport and electrical characteristics are crucial for many applications, and can be strongly affected by backchannel surface chemistry of a-IGZO TFTs. Understanding the chemistry of adsorbed species and their effect on the electronic structure of a-IGZO is critical to improve the stability of these TFTs, while reactions at the metal/a-IGZO interface strongly influences switching characteristics of resistive random access memories. In this study we have characterized sputter-deposited thin films of a-IGZO using in-situ x-ray photoelectron spectroscopy (XPS). Both standard Al K α and synchrotron-based radiation were used to investigate chemical changes at the a-IGZO surface. We have observed surface segregation and desorption of oxygen containing impurities for anneals up to 300 °C in ultra-high vacuum (UHV). The O 1s spectra were very sensitive to the local chemistries at the surface, and we used these spectra to characterize the interaction of molecular oxygen and water with well-defined a-IGZO surfaces for a wide range of temperatures and exposures. It was found that water adsorbs both molecularly and dissociatively at temperatures below 200 K, with corresponding downward band bending of ~0.15 eV for >20 Langmuir exposures. Oxygen did not appreciably affect the XPS spectra for the temperatures and exposures studied. We have also characterized the initial growth of platinum metal films on a-IGZO. The XPS characterization of chemical state differences of the elements and band bending due to surface effects will be discussed along with the film processing conditions.

9:00am **TC+EM+TF-WeM4 UV Radiation Effect on Electrical Characteristics of Passivated IGZO TFTs**, *Y.J. Tak*, *D.H. Yoon*, *S.H. Yoon*, *U.H. Choi*, *H.J. Kim*, Yonsei University, Republic of Korea

Ultraviolet (UV) radiation effects have been intensively researched in oxide thin film transistors (TFTs). In general, UV radiation induces the increase of off-current and the existence of hump effect.[1] These changes of electrical properties in non-passivated oxide TFTs are almost recovered to original states.[2] However, back surface of oxide TFTs is sensitive to oxygen and humidity, passivation is key layer for stability and reliability on device. For this reason, we investigated the effects of post UV treatment on the SiO₂ passivated indium gallium zinc oxide (IGZO) TFTs, specifically by irradiating UV spectrum of different wavelength, intensity, and treatment time. We performed light treatment of wavelength of 365 nm and 185 nm. And then varied power intensities were performed 64.66 mW/cm², 0.9375 mW/cm² respectively. These UV experiments were carried out with various treatment time of 10 min, 20 min, 30 min, and 60 min. As a result, the increment of off-current was shown which was higher in 185 nm radiated one than that of 365 nm, and increase of the intensity and treatment time led to increase in off-current and hump effect. Also, these changes were not restored to its original state after relaxation period. The result of experiment indicated that SiO₂ passivated-TFTs need to block the UV radiation because of incompletely vanished hump effect that causes degradation on the devices.

9:20am **TC+EM+TF-WeM5 Processing Water-based TFT Materials**, *D.A. Keszler*, Oregon State University **INVITED**

High-quality semiconductor and dielectric films can readily be deposited from aqueous solutions containing polynuclear metal nonoclusters. To support the continued development of the films and their use, new techniques have been developed to remove residual mobile ions associated with hydroxide. Examples of incorporation of the resulting films into TFTs and MIM devices will be described.

10:40am **TC+EM+TF-WeM9 Printed Circuits and Sensing Systems**, *G.L. Whiting*, *T. Ng*, *D.E. Schwartz*, *B.J. Van Tassell*, Palo Alto Research Center, *A.M. Gaikwad*, University of California, Berkeley, *D.A. Steingart*, Princeton University, *J. Veres*, Palo Alto Research Center **INVITED**

Low-temperature processable, mechanically compliant materials and the use of printing as a manufacturing technique enables fabrication of flexible electronic systems over large areas at low-cost, potentially allowing for novel applications and more widespread use of such systems. In this report recent developments made in printed systems technology will be presented, including examples of printed complementary circuits, sensors and power sources fabricated using techniques such as ink-jet, screen and gravure printing; as well as integration of these devices into functional printed systems.

Circuits in this work are based on ink-jet printed complementary organic field-effect transistors (FETs), which benefit from simplified design in comparison with unipolar circuits. Design rules for these devices have been determined and models describing the characteristics of these FETs have been developed to aid in designing circuits that can tolerate variation in the performance of printed transistors. In addition to ink-jet, devices have also been fabricated using a gravure method, providing a potential route to large-scale production of printed electronics. Flexible, printed batteries suitable for driving these systems have also been developed and will be described.

11:40am **TC+EM+TF-WeM12 Low Temperature Integration of Metal Oxide Thin Films for Flexible Electronic Applications**, *P. Joshi*, *M. Shao*, *K. Xiao*, *S. Killough*, *P. Kuruganti*, *C. Duty*, Oak Ridge National Laboratory

In the last few years, there has been growing interest in the development of flexible electronics to meet the manufacturing technology demands of higher functionality, reduced material usages and device dimensions, and lower consumption of products. Metal oxide thin films are attractive for multifunctional flexible system development due to their very low cost, tunable properties, and simple electronic interface. Low temperature processing of metal oxides thin films is critical to exploit their unique structural, optical, and electrical properties for a wide range of active and passive device applications, such as flat panel displays, organic electronics, RFIDs, antennas, inductors, capacitors, sensors, batteries and energy harvesting devices. In the present paper, we report on the pulse thermal processing (PTP) processing of metal oxide thin films integrated on flexible substrates. The PTP technique is being explored for the development of cost-effective, high yield, and high quality integrated thin films and devices on low temperature substrates. This technology offers the ability to expose large areas of material to an extremely high energy flux (up to 20 kW/cm²) during a very short period of time (as low as 30 microseconds) meeting the demands of roll-to-roll manufacturing technology. The details of the PTP processing of metal oxide thin films with specific examples related to single and multilayer thin film structures incorporating ZnO and ITO thin films are presented in this paper. The influence of the low processing temperature (<100°C) on the thin film growth and properties has been investigated in terms of process-structure-property correlation study. The impact of the substrate on the thin film growth and properties has also been analyzed. The low thermal budget PTP processing significantly impacts the microstructural, optical, and electrical characteristics on low temperature flexible substrates. The combination of low temperature deposition techniques and low thermal budget PTP processing show promise for multifunctional thin film material and device integration for flexible electronics.

Thin Film

Room: 102 C - Session TF+MI-WeM

Magnetic Thin Films and Nanostructures

Moderator: S. Gupta, The University of Alabama

8:00am **TF+MI-WeM1 Recent Advances and Challenges in Magnetic Recording Media**, *M. Desai*, *C. Pappasoi*, *K. Srinivasan*, *R. Acharya*, Western Digital Corporation **INVITED**

For perpendicular magnetic recording (PMR) beyond areal density of 700 Gb/in², signal to noise ratio (SNR) and write-ability improvements are becoming extremely challenging to realize. The present exchanged coupled composite (ECC) recording medium has become quite complex and consists of multiple magnetic layers. To enable 1Tb/in² areal density, it is required to (i) improve grain isolation for SNR (ii) increase magnetic anisotropy for thermal stability and (iii) reduce all the dimensions, such as thicknesses of the magnetic layers and media grain size. Improvement in grain isolation with maintaining magnetic anisotropy poses challenges on material selection and process optimization and higher anisotropy materials limits the write-ability of the media. It was estimated that the media grain size <8nm can achieve higher SNR due to reduced jitter and transition noise. However, for last several years, the media grain size has hardly changed in optimized PMR media. The increased inter-granular exchange coupling in small grain size media degrades recording media noise characteristics. Also, thermal stability is compromised on media with small grain size. Here, we discuss recent developments and efforts on perpendicular recording media with small grain size and will present our major findings in terms of SNR, write-ability and thermal stability characteristics. We will also discuss advanced ECC media structure with multiple exchange break layers that offers advantages towards enabling reduced grain size. We also describe advanced characterization methods to quantify the effect of inter granular interactions and their relation with materials and sputtering processes.

8:40am **TF+MI-WeM3 FePt Nanopillars for Advanced Media by Glancing Angle Deposition**, *H. Su, A. Montgomery, S. Gupta*, The University of Alabama

Granular $L1_0$ FePt films are leading candidates for next generation magnetic recording, for instance, heat assisted magnetic recording (HAMR). This is due to its high magnetocrystalline energy constant ($\sim 7.0 \times 10^7$ erg/cm³), which can maintain thermal stability even with a reduced grain size of 3nm [1]. However, post-deposition annealing at high temperatures or substrate heating during deposition is required to obtain the $L1_0$ phase. Meanwhile, glancing angle deposition (GLAD) is a physical vapor deposition method in which the incoming flux from the source impinges on the substrate at oblique angles, causing increased shadowing and forming nanorods and other nanostructured films [2-5]. Herein we report for the first time the fabrication of FePt, utilizing glancing angle deposition (GLAD) with lower annealing temperatures to obtain $L1_0$ phase FePt. The samples were co-sputtered using elemental iron and platinum targets. X-ray diffraction (XRD), scanning electron microscopy (SEM), transmission electron microscopy (TEM), and alternating gradient magnetometry (AGM) were employed to characterize the structural and magnetic properties. SEM micrographs indicated that the nanorods were approximately 12 nm in diameter, the angle between the substrate plane and the growth direction was about 78 degrees, while the lengths of the nanorods varied, depending on deposition time. The angles between the substrate plane and incident flux ranged from 47 degrees to 82 degrees as the substrate presented itself at different angles to the target during the planetary deposition. After annealing, M-H loops showed that the planetary GLAD samples had higher coercivity than that of normally deposited samples. XRD confirms the $L1_0$ structure for FePt. Our preliminary results indicate a novel and promising approach to $L1_0$ -phase FePt for HAMR that is the subject of intense research in the data storage industry.

Acknowledgements

This work was supported by National Science Foundation Grant ECCS-0901858, "GOALI: Nanopatterned Graded Media". The authors acknowledge the Central Analytical Facility (CAF) and Microfabrication Facility (uamicro) for their support and facilities.

Reference

- [1] J.Chen, C. Sun and G. M. Chow, *Int. J. Product Development*, **5**, 238(2008)
- [2] M. M. Hawkeye and M. J. Brett, *J. Vac. Sci. Technol. A* **25**, 1317 (2007).
- [3] T. Smy, D.Vick, M.J.Brett, S. K. Dew, A.T. Wu, J. C. Sit and K. D. Harris, *J. Vac. Sci. Technol. A* **18**, 2507(2000).
- [4] J. Wang, H. Huang, S. V. Kesapragada and D. Gall, *Nano Lett.* **5**, 2505(2005)
- [5] A. Dolatshahi-Pirouz, D. S. Sutherland, M. Foss, F. Besenbacher, *Appl. Surf. Sci.* **257**, 2226(2011)

9:00am **TF+MI-WeM4 Mössbauer Study of Disordering in Thin Sputtered FeCo-SiO₂ and FeCo Films**, *S.S. Maklakov, S.A. Maklakov, I.A. Ryzhikov*, Institute for Theoretical and Applied Electromagnetics, Russian Federation, *V.A. Amelichev, K.V. Pokholok, M.V. Lomonosov* Moscow State University, Russian Federation, *K.N. Rozanov, A.V. Osipov, A.N. Lagarkov*, Institute for Theoretical and Applied Electromagnetics, Russian Federation

Thin ferromagnetic films possess perspective applications for a data recording devices, magnetic field sensors, and microwave devices^[1]. Thin nanocomposite films, which are prepared of a dielectric matrix and ferromagnetic filler, show interesting magnetic properties. In the case, magnetic properties are determined by exchange interactions and dipole-dipole interactions between ferromagnetic nanoparticles. Among the other techniques, magnetron sputtering results in the composite films with high uniformity. The report demonstrates structural modification in a solid solution $Fe_{70}Co_{30}$ which is caused by additional energy flux towards the substrate during a $(Fe_{70}Co_{30})_{95}(SiO_2)_5$ composite growth comparing with the metal film growth.

Thin metal films ($h = 130$ nm) were deposited via DC magnetron sputtering onto a PET substrate; the DC magnetron operating regime (time, pressure and discharge parameters) was identical during the composite synthesis. To sputter SiO_2 , a RF magnetron was applied; both magnetrons were sputtering simultaneously. To derive structure information, a Mossbauer spectroscopy, X-ray diffraction (GIXD) and electron microscopy data were gathered. Magnetic properties were studied using VSM and a coaxial line technique for a microwave permeability.

Thin $Fe_{70}Co_{30}$ and $(Fe_{70}Co_{30})_{95}(SiO_2)_5$ films show differently broadened Mossbauer sextet. Composite film possess unusually high effective field at iron nuclei $H_e = 371(3)$ kOe. We propose a model which describes H_e values depending on environment of a reference iron atom^[2]. With this

construction, $Fe_{70}Co_{30}$ solid solution possesses higher $CsCl$ -type ordering degree when in form of the composite. Such modification is the result of surface processes during film growth. SiO_2 injection also decreases FMR frequency from 10 to 3 GHz, depending on a composition.

The results reported may be applied to design thin film microwave devices.

Literature

1. S.S. Maklakov, S.A. Maklakov, I.A. Ryzhikov, K.N. Rozanov, A.V. Osipov. Thin Co films with tunable ferromagnetic resonance frequency. // *J. Magn. Mater.* **324** (2012) 2108-2112
2. S.S. Maklakov, S.A. Maklakov, I.A. Ryzhikov, V.A. Amelichev, K.V. Pokholok, A.N. Lagarkov. Mossbauer study of disordering in thin sputtered $FeCo-SiO_2$ and $FeCo$ films. // *J. Alloys. Compd.* **536** (2012) 33-37

9:20am **TF+MI-WeM5 Comparing Deep Reactive Ion Etching vs. Ion Milling for Block Copolymer Templating for Bit Patterned Media**, *A. Owen, S. Gupta, A. Highsmith, A. Montgomery, H. Su, R. Douglas*, University of Alabama

Block copolymer templating has been used to pattern perpendicular magnetic anisotropy Co/Pd multilayers.¹ A multilayer stack of Ta 5Pd 5/[Co 0.3/Pd 1]₂₀/Pd 5 nm nanolayers was sputter deposited onto a bare silicon wafer. The block copolymer used was polystyrene polyferrocenyldimethylsilane² (PS-b-PFS). This was spin coated onto the wafer and annealed to cause phase separation.² The wafer was ashed in an oxygen plasma to remove the polystyrene matrix and reveal the PFS nanospheres. The Co/Pd multilayer films were subsequently etched using an ion mill and a deep reactive ion etching tool.³ In order to optimize the size tuning of the PFS nanospheres and the coercivity of the magnetic films, response surface methodology was performed to optimize the power, etching times and ashing time of the block copolymer mask and magnetic film. This statistical Design of Experiments was used for both ion milling and deep reactive ion etching. We will discuss some of the shapes of the resulting nanopillars from the different etching techniques. Magnetometry was taken to characterize the films before and after patterning, showing a significant improvement in the coercivity, increasing from 1.5 kOe to 3.6 kOe.

Acknowledgements

NSF ECCS 0901858 "GOALI: Nanopatterned Graded Media" is acknowledged for partial support. The UA Microfabrication Facility and the Central Analytical Facility are acknowledged for support and use of facilities.

References

1. O. Hellwig, J. K. Bosworth, E. Dobisz, D. Kercher, T. Huet et al. *Appl. Phys. Lett.* **96**, 052511 (2010)
2. Joy Y. Cheng, Feng Zhang, Henry I. Smith, G. Julius Vancso, and Caroline A. Ross, *Adv. Mater.*, **18**, 597,(2006)
3. Xiao Li, Z.R. Tadisina, S. Gupta, G. Ju, *J. Vac. Sci. Technol. A* **27**, 1062, (2009)

10:40am **TF+MI-WeM9 Atomic Layer Deposition Enabled Synthesis of Nanostructured Composite BiFeO₃/CoFe₂O₄ Thin Films for Multiferroic Applications**, *C. Pham, J.P. Chang*, University of California at Los Angeles

Multiferroic materials are a class of material which exhibit two or more forms of ferroic order such as (anti)ferroelectricity, (anti)ferromagnetism, or ferroelasticity and have been proposed for use in future devices in which magnetism is switched upon the application of an electric field. While the existence of intrinsic multiferroic materials, such as $BiFeO_3$, have been demonstrated, composite multiferroics offer improved switching performance, consisting of a piezoelectric and a magnetostrictive material coupled together via interfacial strain. In addition, nanoscale composites have been shown in literature to have even greater coupling when compared to other composites. For this project, atomic layer deposition (ALD) is used to enable the precise control of the composition and thickness by manipulating the pulsing sequence of the precursors. In addition, two approaches to multiferroic composites emphasize the flexibility of the ALD technique; for a 2D composite approach, the ability to deposit nanoscale laminates; while for a 3D composite approach, the ability to uniformly coat films over a nanoscale porous template.

In this work, $BiFeO_3$ (BFO) and $CoFe_2O_4$ (CFO) were deposited by ALD to synthesize 2D nanoscale multiferroic composite multilayers. The ALD processes used the metallorganic precursors $Bi(tmhd)_3$, $Co(tmhd)_2$, and $Fe(tmhd)_3$ alongside oxygen atoms produced from a microwave atomic beam source. The ALD BFO and CFO films were able to be grown with a stoichiometric ratio Bi:Fe close to unity and Co:Fe close to 1:2, respectively, and with a controlled linear growth rate. The ALD BFO and CFO processes were then combined to deposit multilayer nanolaminates which repeated between the two oxides at varying thicknesses between 5-20

nm and number of repeating layers. Additionally, ALD BFO was integrated with a 3D mesoporous CFO template consisting of approximately 14 nm diameter pores, which was synthesized using a di-block copolymer self-assembly technique. The conformal aspect of ALD deposition was demonstrated by covering the pores at varying thicknesses until the pores were completely filled.

To compare the material performance of the ALD enabled BFO/CFO films to previously reported benchmarks, measurements of magnetic and ferroelectric properties were accomplished using SQUID magnetometry and Sawyer-Tower circuit methods, respectively. For the 3D mesoporous composite, SEM and XPS confirmed that BFO was able to be deposited onto the nanoscale high aspect-ratio structure of the CFO conformally. The magnetoelectric coupling properties in the composite films were studied by taking magnetic measurements with and without an *ex-situ* electric poling.

Thin Film

Room: 104 A - Session TF+VT-WeM

Thin Film Permeation Barriers and Encapsulation

Moderator: L.W. Rieth, University of Utah

8:00am **TF+VT-WeM1 Tuning the Composition and Water Vapor Permeation Properties of the Silica-Like Films Deposited in Atmospheric Pressure High Current Dielectric Barrier Discharge, S.A. Starostin, H. de Vries, FUJIFILM Manufacturing Europe B.V, Netherlands, M. Creatore, Eindhoven University of Technology, Netherlands, M.C.M. van de Sanden, Dutch Institute for Fundamental Energy Research (DIFFER), Netherlands**

Atmospheric pressure plasma enhanced thin film deposition is new and rapidly developing technology strongly beneficial regarding equipment costs, footprint size and possibilities of in-line processing. However the main characteristics of the deposition process as well as the properties of synthesized coatings are not known as good as for the traditional low pressure PECVD. Moreover the control over large area plasma at atmospheric pressure imposes serious scientific and engineering challenges. Recently we demonstrated the possibility to produce high quality silica layers using ambient air as a process gas [1] and to synthesize films with ultra-smooth morphology [2].

In this contribution we present study on the thin film properties deposited in high current diffuse dielectric barrier discharge between cylindrical electrode system in industrially relevant roll- to-roll configuration on polymeric PEN and PET webs. As the model case the silica-like films were synthesized from cost efficient gas mixture of N_2/O_2 and TEOS as organosilicon precursor. Film composition and molecular network structure was analyzed by ATR-FTIR and XPS methods. Gas permeation properties were controlled by MOCON and Ca-test.

The energy spent per precursor molecule as well as the substrate temperature were recognized as important parameters influencing thin films composition and gas permeation characteristic. The increased incorporation of nitrogen was detected for good performing gas diffusion barrier layers. An unusual power law dependency of WVTR on the film thickness was found for the 20 nm – 120 nm thick films. It was shown that atmospherically deposited silica like thin films can provide excellent overall WVTR barrier of $7.5 \cdot 10^{-4} \text{ g/m}^2 \text{ day}$ at 40 °C and 90% RH which can be extrapolated using experimental activation energy value down to $6 \cdot 10^{-5} \text{ g/m}^2 \text{ day}$ at standard conditions of 20 °C /50% RH. The measured intrinsic barrier value at 20 °C /50% RH was as good as $3 \cdot 10^{-5} \text{ g/m}^2$.

[1] S.A. Starostin, P. Antony Premkumar, H. de Vries, R.M.J. Paffen, M.Creatore, and M.C.M. van de Sanden; Appl. Phys. Lett. 96, 061502 (2010)

[2] P. Antony Premkumar, S.A. Starostin, H. de Vries, M. Creatore, P.M. Koenraad, M.C.M. van de Sanden; Plasma Processes and Polymers 10, 313 (2013)

8:20am **TF+VT-WeM2 Measuring the Diffusion Coefficient of Water in High Quality Permeation Barrier Layers, B. Visweswaran, Princeton University, P. Mandlik, J. Silvermail, R. Ma, Universal Display Corporation, J.C. Sturm, S. Wagner, Princeton University**

Deposited thin film permeation barriers are of great interest for the protection of flexible organic light-emitting diode (OLED) displays. Water can permeate on three pathways into such barrier coated devices: 1. Diffusion through the bulk of the barrier; 2. Permeation through defects in the barrier; and 3. Permeation along the barrier/substrate interface. During research on new barrier materials, permeation through defects and along interfaces can easily dominate permeation through the bulk of the barrier. This makes evaluation of the inherent permeability of a new barrier material

difficult. We present two fast turnaround techniques that measure the diffusion of water in flexible barrier films that have ultra-low permeability: electrical capacitance, and mechanical stress. These techniques are calibrated against the results of secondary ion mass spectrometry (SIMS). Capacitance is measured on layers sandwiched between electrodes on glass substrates. Stress is measured from the curvature of barrier films deposited on silicon wafers. Both the capacitance and the stress technique measure very low diffusion coefficients. All three techniques are applied to one specific type of ultra-low permeability barrier film prepared by the plasma oxidation of hexamethyl disiloxane. Films are exposed to water between 65°C and 200°C, including D_2O and H_2O^{18} for SIMS. From the accelerated diffusion data we extrapolate barrier lifetimes at room temperature. Lifetime is defined as the time required for the permeation of one monolayer of water.

SIMS provides values of H, D, O^{16} and O^{18} concentrations and their depth profiles. We use these to calibrate the concentrations in the capacitance and stress measurements, and to identify the diffusion mechanism. Capacitance is highly sensitive to the in-diffusion of water because of its high dielectric constant (liquid H_2O : 80 vs. SiO_2 : 3.9). Mechanical stress also is highly sensitive because the barrier swells as water diffuses in. Each exposure to water produces a change of capacitance and stress from which diffusion coefficients are extracted. We assume that capacitance and stress are linear with water content of the barrier.

For samples exposed to water at 100°C, the diffusion coefficient determined from SIMS is $4.4 \cdot 10^{-15} \text{ cm}^2/\text{s}$, from capacitance $5.6 \cdot 10^{-15} \text{ cm}^2/\text{s}$, and from stress $4.2 \cdot 10^{-15} \text{ cm}^2/\text{s}$. The close agreement suggests that any one of the three techniques will yield reliable results. The activation energy for the diffusion coefficient is 0.7 eV and that for water solubility is -0.2 eV. At 30°C and 100% relative humidity, one monolayer of H_2O will diffuse through a 2.5 micrometer thick barrier layer in 20 years.

8:40am **TF+VT-WeM3 Improving the Reliability of Electronics Using ALD Barrier Films, S. Graham, H. Kim, A. Sharma, D. Samet, A. Bulusu, Georgia Institute of Technology** **INVITED**

The development of ultra barrier films has been seen as an enabling technology for the packaging and reliability of organic electronic devices. While a number of technologies exists for creating ultra barrier coatings, atomic layer deposition has been viewed as a leading technology for creating single layer and nanolaminate barriers with molecular level control of the film thickness and composition. Such control allows for the creating of barriers with multiple functionality that can be utilized in organic electronics and extended to other electronic platforms. In this talk, we will discuss the development of ALD ultra barrier films based on several oxides that are targeted for packaging organic electronics as well as creating highly stable interfaces for their improved lifetime and stability. Methods to control or enhance the nucleation of these films on polymer and metallic surfaces with the aid of surface functionalization groups will be discussed. The mechanical properties of the ALD films in terms of their onset cracking strain and its impact on the limitations of flexible electronics will be discussed. Finally, the stability of these barrier films when exposed to harsh environmental conditions including damp heat and aqueous solutions will be presented. Stability of the films was determined through a variety of methods including photoluminescence, XPS, UPS, and atomic force microscopy. Films showing superior stability in these environments will be demonstrated through the coating of both organic and inorganic electronics and showing improvements in their stability in harsh environments.

9:20am **TF+VT-WeM5 Long-term Performance of Atomic Layer Deposited Al_2O_3 and Parylene Bi-layer Encapsulation for Utah Electrode Array Based Neural Interfaces, X. Xie, L.W. Rieth, F. Solzbacher, University of Utah**

Encapsulation of three dimensional neural interfaces with complex geometries and tight gaps between components is one of the greatest challenges to achieve long-term functionality and stability. We present a novel encapsulation scheme that combines atomic layer deposited (ALD) Al_2O_3 and Parylene C for biomedical implantable. Our approach is composed of the highly effective moisture barrier properties of ALD alumina, and Parylene as a barrier to many ions and for preventing contact of alumina with liquid water.

Different configurations of Utah electrode array (UEA) based devices were used to test the encapsulation performance from three different aspects: long-term impedance stability, current drawing level, and long-term wireless signal strength and frequency shift. 52 nm of Al_2O_3 was deposited by plasma-assisted (PA) ALD on assembled UEAs at 120 °C. A 6- μm thick Parylene-C layer was deposited by CVD using Gorman process on top of Al_2O_3 and A-174 (Momentive Performance Materials), an organosilane, was used as adhesion promoter.

Hybrid methods were used to de-insulate the tips of the UEAs in order to interact with neurons for recording and stimulation. First, 200 laser pulses

with fluence of 1400 mJ/cm² were used to remove the Parylene C layer. 3 minutes of oxygen plasma etching was added to remove the carbon residue on the tips from laser de-insulation. Then the alumina layer was removed by dipping the array into buffered oxide etch (BOE) for 10 minutes. Parylene C acted as a mask layer for BOE etching and only alumina in the area where Parylene was removed by laser was etched away. The tip exposure was ~ 35 μm. The devices were then put into saline solution for soak testing.

The median tip impedance of the bi-layer encapsulated wired Utah electrode array increased from 60 kΩ to 160 kΩ during the 960 days of equivalent soak testing at 37 °C. The loss of tip metal iridium oxide and etching of silicon in PBS solution contributed to the increase of impedance. Also bi-layer coated fully integrated Utah array based wireless neural interfaces had stable power-up frequencies at ~910 MHz and constant RF signal strength of -50 dBm during the 1044 days of equivalent soaking time at 37 °C. Bi-layer coated Utah arrays had steady current drawing of about 3 mA during 228 days of soak testing at 37 °C. The relatively stable tip impedance, constant power-up frequencies and signal strengths, and low current drawing suggested that the alumina and Parylene C bi-layer coating is very suitable for encapsulating chronic implantable devices.

9:40am **TF+VT-WeM6 On the Role of Nanoporosity in Moisture Permeation Barrier Layers**, *A. Perrotta, G. Aresta, W. Keuning*, Eindhoven University of Technology, Netherlands, *M.C.M. van de Sanden*, Eindhoven University of Technology; *DIFFER*, Netherlands, *W.M.M. Kessels, M. Creatore*, Eindhoven University of Technology, Netherlands

Although satisfactory results in term of moisture permeation barrier performance have been achieved for the encapsulation of organic electronic devices, a deeper understanding of the relation between barrier properties and permeation pathways is still necessary. This contribution focuses on the role of the residual nanoporosity in the inorganic layer in controlling its barrier performance.

Plasma-assisted atomic layer deposition (PA-ALD) and plasma-enhanced chemical vapor deposition (PECVD) inorganic (i.e. Al₂O₃ and SiO₂) barrier layers have been extensively analyzed by means of IR spectroscopy, spectroscopic ellipsometry, Rutherford backscattering spectroscopy and elastic recoil detection. The calcium test has been performed to determine the intrinsic water vapor transmission rate (WVTR), i.e. by excluding the local white spot development, as well as the effective WVTR values. Ellipsometric porosimetry (EP) has been applied to determine the open porosity and pore size range of the layers. Two different adsorptives have been adopted as probe molecules, i.e. trivinyltrimethylcyclotrisiloxane (d_{V3D3} = 1 nm) and water (d_{H2O} = 0.3 nm). A correlation between the residual nanoporosity and the intrinsic barrier properties of moisture barriers has been found, regardless the chemistry of the layer and deposition technique used. Pores larger than 1 nm with a relative content above 1% have been found responsible for poor barrier layers characterized by a WVTR in the range of 10²-10³ gm²day⁻¹. Furthermore, the pore size range of [0.3-1] nm and its relative content have been found to drive the transition in WVTR from 10⁴ to 10⁵-10⁶ gm²day⁻¹, highlighting the role of the residual nanoporosity in controlling the intrinsic barrier properties.

Electrochemical impedance spectroscopy (EIS) has also been adopted as novel technique in the evaluation of the moisture barrier properties. Water diffusion through the barrier has been followed as a function of the variation of the electrochemical properties and related to the layer porosity.

The control at nanoporosity level has also been addressed by coupling a mediocre PECVD SiO₂ barrier layer with an ultra-thin (2 nm) PA-ALD Al₂O₃ layer. The decrease in WVTR by three orders of magnitude in the SiO₂/Al₂O₃ system has been attributed to the filling of the residual nanoporosity in the SiO₂ layer by Al₂O₃. This result is supported by angle-resolved XPS analysis and explained on the basis of the molecular dimension of the Al₂O₃ deposition precursor, i.e. trimethylaluminum (d_{TMA} = 0.65 nm), able to penetrate pores larger than 1 nm.

10:40am **TF+VT-WeM9 Atomic Density and Nano-Porosity Thresholds for Nanoscale Low-k Moisture Diffusion Barrier Materials**, *S.W. King, E. Mays, J.D. Bielefeld, D. Jacob, B. Colvin, D. Vanleuven, J. Kelly*, Intel Corporation, *M. Liu, D. Dutta, D. Gidley*, University of Michigan

As the semiconductor industry strives to keep pace with Moore's Law, new materials with extreme properties are increasingly being introduced and tighter control of these material properties is being demanded. Low dielectric constant (i.e. low-k) Cu and moisture diffusion barrier materials are one specific example. Low k diffusion barrier materials are desired to replace the relatively high-k SiN_x:H (k = 7.0) material currently utilized as both a moisture and Cu diffusion barrier layer in order to reduce resistance-capacitance (RC) delays in nano-electronic Cu interconnect structures. Typical methods for producing low-k materials consist of introducing controlled levels of nano-porosity via intentional incorporation terminal organic (CH_x) groups during plasma enhanced chemical vapor deposition

(PECVD) of SiO₂ and SiN_x:H network materials. However while lowering k, the introduction of nano-porosity can seriously compromise the performance of such materials as potential moisture and metal diffusion barriers. In this presentation, we will demonstrate that critical thresholds in nano-porosity exist for the diffusion of water and solvents through low-k materials. Specifically, we utilize Fourier Transform Infra-Red (FTIR) spectroscopy, to show that the concentration and size of nano-pores formed in low-k a-SiN(C):H dielectric materials is controlled by the concentration of terminal Si-CH₃ bonding versus Si-N network bonding. We further combine moisture / solvent diffusivity measurement with x-ray reflectivity (XRR) and positron annihilation lifetime spectroscopy (PALS) to demonstrate that low-k a-SiN(C):H dielectrics become poor moisture diffusion barriers at mass densities < 2.0 g/cm³ and when the pore size approaches that for the molecular diameter of water. Similarly, we show that low-k materials become easily penetrable by solvents and metals when the pore diameter approaches the size of these species. The implications of these critical nano-porosity thresholds on the performance of low-k materials as diffusion barriers and potential limitations on thickness scaling in the presence of defects will also be discussed.

11:20am **TF+VT-WeM11 Low Stress Carbon Films as Gas Barrier Layers**, *J. Rowley, R.C. Davis, L. Pei, R.R. Vanfleet*, Brigham Young University, *S. Liddiard, M. Harker, J. Abbott*, MOXTEK Incorporated

A low stress, flexible hydrogenated sp² carbon film(a-C:H) was developed using reactive sputtering of a graphite target in an ethylene/argon gas mixture. This resulted in a corrosion resistant layer. The carbon film was characterized by a series of techniques including Raman, EELS, AFM, XPS, and CHN analysis. An ethylene to argon gas ratio of 0.1 resulted in a film with 83.9% carbon, 5.0% hydrogen and 10.6% oxygen by weight fraction. This corresponds to a mole fraction of hydrogen to carbon of 4:6, a large hydrogen fraction. The films are dominantly sp² as seen by Raman and EELS. Bulge testing determined a low elastic modulus and strength. The 4:6 a-C:H, 100 micron films showed a stress of 200 MPa(compressive) which is much lower than what has been reported previously for sputtered carbon films.

11:40am **TF+VT-WeM12 The Effective Control of Surface Profile and Arc Discharge during Amorphous Carbon Layer Deposition Process**, *I.-S. Kim, J. Park, J.H. Lee, M.J. Kim, Y.B. Choi, H.-G. Kim, S.H. Lee, J.W. Hong, J.L. Lee, M.W. Kim, G. Choi, H.-K. Kang, E.S. Jung*, Samsung Electronics Co., LTD., South Korea

Amorphous carbon layer (ACL) has been introduced to the hard mask material for dry etch process under sub 20 nm devices, due to the optical transparency, easy removal and proper mechanical properties. With the shrinkage of device scales, thickness uniformity of hard mask is critically related to the next etch performance, such as etch depth or profile uniformity. Furthermore, in case of thicker ACL deposition for high aspect ratio etch process, the arc discharge is frequently occurred due to the high conductivity of carbon film.

In this study, ACL was deposited by plasma enhanced chemical vapor deposition (PECVD), which consists of capacitive coupled plasma(CCP) at 13.56 MHz, by using the propylene(C₃H₆-Carbon source). The multi-zone gas distributor and partially controlled heater were applied to control the surface profile, resulting in ~1% of thickness uniformity. In addition, the thickness profile was freely controlled from convex surface to concave surface shape, which results in easier and better process integrations for the following etch steps.

During the thick ACL (over 1μm) deposition, the arcing discharge is frequently occurred inside chamber and damaged to the wafers or hardware of equipment. The arc discharge was effectively controlled by introducing various ground paths and modified hardware. As the ground paths were integrated into the chamber, the RMS voltage which is applied to the chamber was decreased while the RMS current was increased. As a result, these tendencies induced to the decrease of impedance in process plasma, avoiding arc discharges. Not only more stable glow discharge is generated, also process efficiency is improved.

Vacuum Technology

Room: 202 C - Session VT-WeM

Pumps, Accelerators and Large Vacuum Systems

8:00am **VT-WeM1 Recent Innovation in Dry Pumping Technology**, *A.D. Chew, I. Stones, N. Schofield*, Edwards, UK **INVITED**

Dry pump technologies have become routinely utilized in, and for, a wide range of vacuum based applications. Some of the most recent significant developments in dry technologies, including scroll, screw, roots-claw and

turbo-molecular, will be discussed with reference to improved operation and productivity, maintenance and minimised environmental impact and cost of ownership. Specific examples will include semiconductor and flat panel production, mass spectrometry and chemical processing.

8:40am **VT-WeM3 Novel Approaches in the Pumping Speed Characterization of NEG, SIP and their Combination in UHV Systems**, *F. Siviero, A. Bonucci, A. Conte, L. Caruso, T. Porcelli, L. Viale, G. Bongiorno, E. Maccallini, P. Manini*, SAES Getters, Italy

Thanks to their compactness and large pumping speed for H₂ and oxygenated gases Non Evaporable Getter (NEG) pumps are effective solutions in a variety of applications from particle accelerators to surface science equipment, scanning/transmission electron microscopes and other analytical systems or sealed off devices. The quest for more compact, efficient and performing UHV pumping systems, is however pushing towards the development of new and innovative pump designs. A deeper understanding of the pumping mechanisms and the development of suitable pumping speed characterization techniques, is key to achieve this objective. In the present paper we update on the activities being carried out at SAES R&D Labs on the characterization of getter and ion pumps performances, either tested separately or in combination. In particular we provide highlights on the experimental methodology and data analysis which have been introduced to overcome some limitations coming from the use of the well-known ASTM F798-97 standard method for the measurement of sorption curves at constant pressure. At the heart of this approach, is the extensive use of the quadrupole mass spectrometry which allows to identify and separate the different gas sorption/desorption mechanisms taking place during the simultaneous operation of NEG and SIP. A better understanding of the actual pumping speed for gases, as well as synergies or interference in a NEG/SIP structure is therefore possible.

9:20am **VT-WeM5 Symbiotic Relation between High Energy Accelerators and Advanced Medical Treatments**, *J.R. Noonan, D.R. Walters*, Argonne National Laboratory **INVITED**

High energy particle accelerators have been essential to developing fundamental knowledge of the nature of matter and energy¹. Even from the early history of accelerators, accelerators have applications in materials science, biology, and medical therapies. Over 70% of accelerators in operation are for industrial and medical applications. Medical treatment can be categorized into therapeutic and diagnostic applications. External beam radiation therapy refers to radiation sources that are non-invasive. Intensity Modulated Radiation Therapy in which multi-MeV electrons strike a tungsten target to make x-rays is the largest application. Cyberknife is a "pencil beam" of electrons is focused on a small target to make a narrow x-ray beam source. High energy proton and heavy ion beams are used for precise radiation delivery. However, because of the expense, there are only a limited number of proton (heavy ion) beam centers. External beam radiation therapy (mostly x-rays) has significantly improved cancer survivability. Electron beams are focused directly on tumors in Intraoperative Radiation Therapy. The electrons beam is used after a tumor is surgically removed. Accelerators are also used to produce radioactive isotopes that are used in diagnostic imaging. Proton cyclotrons and linacs are the most used accelerators. However, electron linacs are used for special isotopes. Nuclear reactors are currently the dominant sources for isotopes; however, because of nuclear security, accelerators for isotope production are being developed. The presentation will discuss how the accelerators are used in medicine and the long lead time before accelerator advances are incorporated into medical therapy. The presentation will also give examples of advanced accelerator technology for radiation therapy.

1. Accelerators for America, Washington, D.C., (editors W. Hennig and C. Shank, DOE, June 2010)

11:00am **VT-WeM10 LHC Experimental Beam Pipe Vacuum Chambers Characterization and Validation**, *G. Lanza, G. Bregliozzi, V. Baglin, J.M. Jimenez*, CERN, France

The LHC experiments ATLAS, CMS and LHCb will profit of the LHC Shutdown 1 (years 2013- 2014) to improve and upgrade their detectors including the vacuum beam pipes.

The new chambers and modules positioned in the central core of the detector have been designed and optimized following the experiment specification. The material used for the chamber walls are aluminium, beryllium, copper or inox in order to grant the required transparency for the radiation. The internal wall NEG coating is a fundamental characteristic to reach the ultrahigh vacuum pressure required to lower the detector background.

Several vacuum chambers and modules have been tested and validated to grant their efficiency after the installation in the cavern. The validation tests of the uncoated components included: leak tightness, ultimate vacuum pressure, material outgassing, and residual gas composition. The validation

tests of the NEG coated elements included also the NEG pumping speed for different gases and the sticking coefficient measurement. The integration of new pumping components on the vacuum modules have been studied, simulated and tested as well.

In this paper the motivation for the beam pipe upgrade, the validation test and the results are illustrated and commented.

11:20am **VT-WeM11 Commissioning of NSLS-II Vacuum Systems**, *H.-C. Hseuh, A. Anderson, W. DeBoer, C. Hetzel, S. DiStefano, S. Leng, K. Wislon, H. Xu, D. Ziggrosser*, Brookhaven National Laboratory

The National Synchrotron Light Source II is a synchrotron radiation facility designed with ultra-high-flux and -brightness. It consists of a 200-MeV Linac, a 3-GeV Booster and a 3-GeV, 792-meter circumference storage ring. The Booster vacuum system is made of thin-wall stainless steel chambers and is pumped with ion pumps. The Linac and Booster vacuum systems are completed and have reached ultrahigh vacuum. The storage ring vacuum chambers are mainly made of extruded aluminium with ante-chamber. The synchrotron radiation from the bending magnets in the storage ring is intercepted at discrete photon absorbers made of GlidCop. NEG strips in the ante-chamber provide the distributed pumping, while lumped ion pumps and titanium sublimation pumps at photon absorbers remove the desorbed gas. The 250 long aluminium chambers were manufactured by extrusion, bending, machining and welding. They are assembled with pumps, photon absorbers and diagnostic components, integrated into magnet girders and installed in the storage ring tunnel. All 30 DBA cells with 210 chambers have been connected with RF bellows, pumped down, in-situ baked and have reached 10⁻¹¹ mbar. The narrow gap insertion device chambers are to be coated with NEG, and are currently under fabrication. This paper describes conditioning, installation, integrated testing and commissioning of the NSLS-II vacuum systems. Experience from the large scale production, testing and lesson learned will be summarized.

*Work performed under the auspices of U.S. Department of Energy, under contract DE-AC02-98CH10886.

11:40am **VT-WeM12 Higher Order Mode RF Absorbers for Cornell ERL Superconducting Cavity Cryo-Module**, *Y. Li, Y. He, J.V. Conway, R.G. Eichhorn*, Cornell University

As a part of continuing R&D efforts toward to Cornell Energy Recover LINAC based hard X-ray light sources, a superconducting RF (SRF) cavity cryo-module (the so-called horizontal test cryo-module or HTC) has been designed and constructed, and a series of tests has been carried out during the past year to evaluate performance of the SRF cavities. One of the key and challenging components, which are still in development, is the higher order mode (HOM) RF absorber. The UHV compatibility is essential for these HOM RF absorbers, as they form part of electron accelerator beampipes adjacent to the SRF cavities. The out-gassing rates of various HOM RF absorber materials were measured by a throughput method. In the presentation, we report vacuum out-gassing measurements on various candidate HOM absorber materials, including two promising materials, namely SiC and AlN. We will also discuss several joint designs (such as vacuum brazing and shrink-fit) for the absorbers to ensure that the assembly is not only UHV compatible, but also works properly from bakeout temperature (150C) to cryogenic temperature (80K).

Wednesday Lunch, October 30, 2013

Exhibitor Technology Spotlight

Room: Hall A - Session EW-WeL

Exhibitor Technology Spotlight V

Moderator: C. Moffitt, Kratos Analytical Limited, UK

12:20pm **EW-WeL2 High-Sensitivity, Quadrupole Mass Spectrometry Method for Measuring Water Vapour Transmission Rate (WVTR) of Barrier Membranes to 10^{-6} g/m²/Day using Deuterium Oxide (D₂O), S. Swann, M.P. Dobson, N. Singh, VGScienta Ltd., UK**

We present a vacuum-enabled measurement technique and equipment utilising mass spectrometry and deuterium oxide combined with a novel calibration method, enabling traceability to national standards. This method incorporated in the VacuTRAN™ instrument allows measurements to 10^{-6} g/m²/day WVTR and the ability to measure multiple species simultaneously. The sensitivity of the UHV system with respect to residual gases and D₂O proton-exchange reactions are discussed.

12:40pm **EW-WeL3 High Efficiency, High Capacity, and Economical "Point of Use" Gas Abatement, S. Yee, CS Clean Systems Inc., D.K. Prasad, CS Clean Systems, Inc.**

Air pollution regulations, employee health concerns, and growing awareness of toxic agents from semiconductor processes demand increased improvements in exhaust gas conditioning. The NOVASAFE® Dry Scrubber reduces the hazards associated with flammable, toxic or corrosive gases and vapors. NOVASAFE® effluent gas scrubbers offer an extremely safe and efficient way to treat toxic and corrosive gases resulting from hazard processes. This scrubber is a technologically advanced dry chemical scrubber containing approximately 2.5 gallons (9.5 liters) of scrubbing media. The scrubber is suitable for use in production and general laboratory environments. Operating passively at ambient temperature, chemical resins in the canister react on contact with process gases and by-products, converting them to non-volatile inorganic solids. NOVASAFE combines high efficiency and high capacity in a compact, in-situ solution providing compliance with appropriate exhaust gas regulations and protocol NOVASAFE is a passive abatement solution for semiconductor, vent gas, R&D and Lab instruments application. As a zero footprint scrubber, the NOVASAFE can be easily integrated with your vacuum pump system. Effluents are abated with the NOVASAFE to sub-TLV levels from roughing pumps and cryopumps. There are no moving parts. Change-outs are accomplished easily and have minimal impact on operations. With its compact and low impact design, the NOVASAFE is the ultimate uptime and economical abatement solution. Typical applications include; Etch, CVD, Implant, MOCVD, ALD, and advanced processes such as III-V Etch. The majority of semiconductor processes gases can be safely abated, including challenging gases such as; AsH₃, SiH₄, Cl₂, F₂, MO's as examples.

1:00pm **EW-WeL4 AFM and Raman Spectroscopy: Correlated Imaging and TERS, I. Armstrong, Bruker**

The desire to identify materials and their properties to understand complex systems and better engineer their functions has been driving scanning probe microscopies since their inception. Both atomic force microscopy (AFM) and Raman spectroscopy are techniques used to gather information about the surface properties and chemical information of a sample. There are many reasons to combine these two technologies, and this presentation discusses both the complementary information gained from the techniques and how a researcher having access to a combined system can benefit from the additional information available.

1:20pm **EW-WeL5 Can Your AFM Do This—Advanced Characterization with Asylum AFM Accessories, A. Labuda, R. Proksch, A. Moshar, Asylum Research, an Oxford Instruments company**

Asylum Research, an Oxford Instruments company, will discuss the performance and results from a variety of AFM accessories used for advanced characterization for MFM, stress and strain measurements, and imaging in fluid. We'll show our Variable Field Module 2 that applies in-plane magnetic fields of more than ± 0.8 Tesla (8,000G) and offers ~ 1 G field resolution. Our NanoRack™ Stretching Stage applies symmetric tensile or compressive loading to samples about a central area that can be simultaneously observed with the AFM. Finally, we'll discuss the blueDrive™ Photothermal Excitation capability for Cypher™, the highest resolution fast scanning AFM. blueDrive enhances the performance of AC (tapping) mode imaging by providing extremely clean tunes in both air and water.

1:40pm **EW-WeL6 Nanofabrication Below 10nm Using He and Ne Ions, D. Elswick, B. Singh, Carl Zeiss Microscopy**

Ion microscopy using helium or neon beams created from a gas field ion source (GFIS) shows great potential and flexibility for many imaging and nanofabrication applications. With helium or neon, sub-10 nm structures can be routinely fabricated in a variety of materials including sensitive materials such as graphene. Additionally, the beam-sample interaction dynamics of helium/neon ion beams offer unique contrast and stunning surface detail at sub 0.5nm lateral resolution.

The helium ion beam introduces a unique opportunity for high precision patterning in graphene. High aspect ratio nanoribbons have been machined down to 5 nm without damage. Due to the nature of imaging with the helium ions, non-destructive imaging of graphene with excellent surface sensitivity can be achieved both before and after patterning. Helium and neon beams have also been used for a diverse range of other nanofabrication applications. Solid state nanopores for DNA sequencing devices with holes down to 3 nm in diameter and aspect ratios greater than 10:1 have been created in a variety of materials. In plasmonic applications, dislocation damage to surrounding structural elements is greatly reduced compared to gallium FIB when using helium or neon, thus allowing work on delicate and sensitive membranous materials. Plasmonic devices with nearly vertical sidewalls have been patterned in films demonstrating machining precision of better than 5 nm. Direct write lithography using commercial resists HSQ and PMMA resulted in line features as narrow as 4 nm. Finally, the use of helium and neon ions beams for circuit edit applications is being developed. Deposition of conducting and insulating materials creates features smaller than those obtained with gallium FIB and with better electrical properties due to the absence of gallium.

A gallery of helium ion microscopy imaging and nanofabrication results will be presented to showcase the capability and performance of this novel microscope.

Wednesday Afternoon, October 30, 2013

Atom Probe Tomography Focus Topic

Room: 203 A - Session AP+AS+MI+NS+SS-WeA

APT and FIM Analysis of Catalysts and Nanoscale Materials

Moderator: P.A.J. Bagot, Oxford University, UK

2:00pm **AP+AS+MI+NS+SS-WeA1 Atom Probe Tomography Characterization of Engineered Oxide Multilayered Structures**, S.A. Thevuthasan, M.I. Nandasiri, A. Devaraj, D.E. Perea, T. Varga, V. Shuthanandan, Pacific Northwest National Laboratory

There has been growing interest in developing materials which possess high oxygen ionic conduction at low temperatures for solid oxide fuel cell applications. In our group, we have been developing trivalent element doped ceria/zirconia multilayer thin film structures for this purpose. We have grown (i) multilayers of high quality samaria doped ceria (SDC) and scandia stabilized zirconia (ScSZ) films, and (ii) samaria and gadolinia co-doped high quality ceria films using oxygen plasma-assisted molecular beam epitaxy (OPA-MBE). These films exhibit significantly higher oxygen ionic conduction at intermediate temperatures in comparison to bulk materials. Although we have demonstrated that these structures possess high oxygen ionic conduction at low and intermediate temperatures, we haven't established the mechanisms associated with the enhancement in oxygen ionic conduction through these engineered heterogeneous interfaces.

Atom Probe Tomography (APT) can provide quantitative three-dimensional chemical analysis of materials with lateral and depth resolutions in the order of 0.2-0.3 nm and chemical sensitivity up to parts-per-million levels with field-of-view on the order of $100 \times 100 \times 100 \text{ nm}^3$. Although APT has been extensively used to characterize metals, it is in its infancy in characterizing oxides and insulators. In addition, multilayer structure adds additional complications to the characterization of the doped ceria/zirconia multilayers. In this study, we have synthesized high quality SDC and ScSZ multilayers and used surface impedance spectroscopy to carry out detailed analysis of oxygen ionic conductivity as a function of individual layer thickness and dopant concentration. As a part of this study we attempted coupled scanning transmission electron microscopy and atom probe tomography to study the oxygen vacancy and dopant distributions along with the inter-diffusion and dopant segregation at the interfaces. These STEM/APT findings are correlated to the conductivity measurements and these results will be discussed.

2:20pm **AP+AS+MI+NS+SS-WeA2 Correlative Atom Probe Tomography and Transmission Electron Microscopy of Metal-Dielectric Composites**, A. Devaraj, R.J. Colby, D.E. Perea, S.A. Thevuthasan, Pacific Northwest National Laboratory **INVITED**

Metal-dielectric composite materials are ubiquitous in several important engineering applications ranging from catalysis to semiconductor devices. The technological advances in such fields heavily depend upon the development of three-dimensional characterization capabilities that can accurately identify composition and structure at sub-nanometer spatial resolution and ppm-level composition sensitivity. Atom probe tomography (APT) has already demonstrated its potential in three-dimensional characterization of bulk metals and alloys, however the theoretical understanding of the evaporation behavior of dielectrics and metal-dielectric composites, as well as possible artifacts during laser assisted APT, is still at its infancy. 3D transmission electron microscopy (TEM) tomography on the other hand is currently restricted by long acquisition times and reconstruction artifacts. A correlative TEM-APT approach can help in extending the applicability of APT analysis and TEM beyond the current boundaries by providing not only complementary information but also a deeper understanding of the possible artifacts. This presentation will focus on such a correlated TEM-APT approach to investigate the field evaporation behavior of metal dielectric composites with metallic nanoparticles embedded inside oxides as well as planar structures with metallic thin films on single crystalline oxide substrates. Aberration-corrected TEM high angle annular dark field scanning transmission electron microscopy (HAADF-STEM) were used to image the APT samples before and after APT analysis. STEM imaging after interrupted APT analysis was used to capture snapshots of evolving tip shape. Such understanding, when combined with novel APT reconstruction processing, can greatly aid in expanding the capabilities of APT analysis to novel complex heterogeneous metal-dielectric composite materials.

3:00pm **AP+AS+MI+NS+SS-WeA4 High Temperature In Situ Diffusion Studies of Gas – Solid Reactions with Atom Probe Tomography**, S. Dumpala, S.R. Broderick, Iowa State University, P.A.J. Bagot, University of Oxford, UK, K. Rajan, Iowa State University

The diffusion couples of in-situ metal-oxygen reactions are analyzed through laser pulsed atom probe tomography (APT) reactions and experiments. Using ternary metal compounds, the relative diffusion and segregation of the different species with oxidation is assessed. This provides a further level of information beyond typical diffusion profiles by considering relative changes in metallic species, providing basic material descriptions at a higher resolution than ever previously measured.

The oxidation experiments were performed in-situ and at temperatures of $\sim 450^\circ\text{C}$ and at 10^{-3} torr pressures. Given atom probe's atomic scale spatial resolution, chemical diffusion over a nanometers wide range across the chemical interface is assessed with exceptional accuracy, and the identification of compound formation is quantified. By performing all reactions within an in-situ APT reaction cell along with initial (in-situ) cleaning of the samples, any effects due to native oxidation or contamination are eliminated, which is particularly important when considering atomic scale spatial resolution and femto-scale chemical resolution. The challenges associated with performing in-situ reactions and the potential of this new experimental set-up to study a far wider range of treatment conditions, particularly when coupled with a laser-pulsed APT are discussed.

3D results of binary and ternary catalytic alloys are presented and the advancements in studying catalytic reactions are discussed. Aluminum and silicon samples were also oxidized and chemically-mapped atomic scale imaging of the material were processed to identify the preferred stoichiometry of aluminum oxides as a function of the distance from the aluminum-oxygen interface. This demonstrated ability of the APT to simultaneously image and chemically quantify gas-metal interactions at the atomic level enables us to systematically quantify these interactions as a function of material chemistries, crystallographic orientations and important microstructural features.

Acknowledgments : The authors acknowledge the support from Air Force Office of Scientific Research grants: FA9550-10-1-0256, FA9550-11-1-0158 and FA9550-12-0496; NSF grants: ARI Program CMMI-09-389018 and PHY CDI-09-41576; and Defense Advanced Research Projects Agency grant N66001-10-1-4004.

4:00pm **AP+AS+MI+NS+SS-WeA7 Atomic Scale Characterisation of Catalyst Material**, T. Li, P.A.J. Bagot, S.C.E. Tsang, G.D.W. Smith, Oxford University, UK **INVITED**

Bimetallic heterogeneous catalysts have proven remarkably successful in catalysing a wide range of important processes, in fuel-cells, exhaust emission control and in hydrocarbon processing. However, the effects of the operating environment on the surface composition, structure and stability of the noble metal catalysts are poorly understood at the atomic-scale. This knowledge will be required to produce the improved catalysts needed for future energy- and materials-efficient technologies.

Atom probe tomography offers a unique method for studying these materials, offering atomic-scale chemical identities of the catalyst surfaces and chemisorbed species. We have used APT to show a rich variety of behaviour in Pt-based alloys, investigating the effects of high temperature/pressure oxidation. These reveal pronounced surface segregation behaviour, strongly dependent on the treatment conditions, crystallographic plane and alloy composition. Furthermore, while subsequent reduction treatments remove formed oxides, the marked changes to the metallic surface compositions remain. Such results suggest using sequential oxidation and reduction treatments as an alternative synthesis method for designing and preparing nano catalysts with controlled surface compositions.

Another aspect of our work focuses on the investigation of the use of APT for characterizing catalyst nanoparticles either in colloidal dispersions or on the carbon supports. It is very challenging to fully characterize these complex 3D architectures by conventional electron microscope technique. In this work, we have for the first time demonstrated the use of APT for the analysis and characterization of such materials in atomic detail. Alongside a description of the preparations, we will also present a range of results from these catalysts materials, highlighting the correction between catalytic efficiency and the atomic-scale chemical/structural information uniquely provided by APT.

4:40pm **AP+AS+MI+NS+SS-WeA9 From Field Ion Microscopy of Tips to 3D Atom Probe Tomography of Real Catalyst Nanoparticles, N. Kruse**, Université Libre de Bruxelles, Belgium **INVITED**

This contribution will address some major achievements made in the application of Field Ion Microscopy (FIM) and 1D/3D Atom-Probe (AP) techniques to study catalysis-related problems. In particular, we shall demonstrate the unique capabilities of FIM to image reaction-induced morphological reshaping of single metal nanoparticles conditioned in the form of tips. As an example, we show how a nearly hemispherical Rh nanoparticle is transformed into a polyhedral morphology in the presence of oxygen gas.

In a second example, we shall inspect the use of 1D AP as a tool to provide a detailed kinetic analysis of adsorption/thermal desorption processes. As an example, measurements of the mean life time of NO molecules adsorbing on ~ 60 atomic sites of a (111) Pt facet will be presented. A quantitative evaluation of the data in terms of activation energies for desorption along with pre-exponential factors becomes possible by temperature variation.

Third, we shall consider the combined approach of FIM and 1D AP in imaging the dynamics of surface reaction processes while mapping the local chemistry during these processes. As an example, we shall present results of the catalytic reaction between oxygen and hydrogen on the surface of a Rh nanoparticle. Moving reaction fronts are followed here by using video techniques. The observed patterns demonstrate a strong non-linearity merging into oscillating reaction behavior between oxygen and hydrogen. 1D atom-probe measurements during oscillations allow distinguishing between oxygen- and hydrogen-covered surface patches. They also indicate the participation of sub-surface oxygen species in a feedback process. The oscillatory behavior has been successfully modeled using theoretical models of non-linear processes along with DFT.

Finally, we show that 3D AP can also be used for a chemical mapping of single nanosized grains of real catalysts. Using focused ion beam techniques, "CoCuMn" real catalyst particles as used for the selective production of 1-alcohols from synthesis gas (CO/H₂), can be conditioned in the form of tips. A 3D AP analysis of a single catalyst grain demonstrated the occurrence of a core-shell structure with Co forming the core. Interestingly, all three metals are found to be present in a 2nm thick shell which is otherwise dominated by large amounts of Cu. Such information is most important when it comes to establish relationships between catalytic activity/selectivity and surface chemical composition.

5:20pm **AP+AS+MI+NS+SS-WeA11 NO₂ Reduction over Pt and Rh Single Nanoparticles: Imaging with Nanometric Lateral Resolution, C. Barroo***, S. Lambeets, Y. De Decker, F. Devred, T. Visart de Bocarmé, N. Kruse, Université Libre de Bruxelles, Belgium

Nitric oxides (NO_x) emissions from vehicles are harmful to human beings and may cause severe health issues. NO_x abatement is therefore highly desirable, but the development of viable solutions still represents a major challenge for catalyst makers, especially in the case of lean-driven vehicles. NO is known to be oxidized to NO₂ under lean-burn conditions in automotive engines, and subsequently reduced into N₂ during the rich-burn regime. In this work, we have investigated the catalytic reduction of NO₂ over platinum and rhodium field emitter tips by means of Field Emission Microscopy (FEM). Real-time FEM is a powerful method for studying the dynamics of catalytic reactions that take place on the surface of the top of a nanosized metal tip, which acts as a catalytic particle. These studies are performed during the ongoing catalytic reaction which can be imaged in real time and space. Nanoscale resolution is achieved, providing a local indication of the instantaneous surface composition. Reaction-induced structural changes of the catalyst's surface can also be assessed with step-site resolution. FEM is based on the emission of electrons from the sample which can be affected by the presence of various adsorbates. Local variations of the work function are reflected in the form of a brightness pattern and the surface composition of the sample can be qualitatively investigated during the ongoing catalytic process, allowing for the determination of the elementary processes involved.

The microscope is run as an open nanoreactor, through a constant supply of gaseous reactants and constant gas-phase pumping of the reaction chamber, ensuring that the system is kept far from thermodynamic equilibrium. This may lead to non-linear dynamics. Among others, oscillating phenomena observed during the NO₂ reduction by H₂ over both Pt and Rh nanocrystal (whose diameter is ≈40 nm) are presented.

Data have been characterized by Fourier transforms, temporal autocorrelations and dynamical attractors that demonstrate the existence and robustness of the kinetic oscillations. Furthermore, the optimal parameters obtained for the reconstruction of the dynamical attractor from the experimental time series, give important information that can lead to a

better understanding of the mechanism of the catalytic reduction of NO₂ over PGM nanoparticles.

5:40pm **AP+AS+MI+NS+SS-WeA12 Quantitative Three-Dimensional Compositional Analysis of Geologic Minerals using Atom-Probe Tomography, J. Liu, D.E. Perea, R.J. Colby, B. Arey, O. Qafoku, A. Felmy**, Pacific Northwest National Laboratory

Carbon capture and sequestration within deep geological formations has become one of the most important options to mitigate the ever-growing environmental CO₂ emissions. The olivine group of minerals, X₂SiO₄ where X = Mg or Fe, hold promise as potential media to sequester carbon. Upon reaction of supercritical CO₂ (sc-CO₂) with fayalite (Fe₂SiO₄) or forsterite (Mg₂SiO₄), various oxide and carbonate phases result accompanied by a complex change in surface morphology. A combination of atom probe tomography (APT) and scanning transmission electron microscopy (STEM) is being used to map the complex composition across various site-specific interfaces in order to better understand the complex phases that form upon reaction with sc-CO₂. The advantage of APT analysis is that it can provide a unique 3-D atomic-scale compositional map with a part-per-million sensitivity to allow tomographic mapping of low-level impurities such as Li. Optimization of the APT analysis conditions will be discussed leading to the optimal stoichiometric composition. The results demonstrate the viability of using APT analysis to study the composition geological minerals for energy and environmental applications.

Applied Surface Science

Room: 204 - Session AS-WeA

Developments in Electron Spectroscopies for Non-Ideal Samples 2

Moderator: A. Herrera-Gomez, CINVESTAV-Queretaro, Mexico

2:00pm **AS-WeA1 Albert Nerken Award Lecture - Photocathodes for Future X-ray Light Sources, H.A. Padmore†**, Lawrence Berkeley National Laboratory **INVITED**

Synchrotron sources of x-rays have revolutionized many areas of materials science. From the 1st generation synchrotrons of the 1970s to the 3rd generation of storage ring-based machines of today, the brightness has increased by around 6 orders of magnitude. Measurements that were formerly done at the mm spatial scale have become routine at sub 100 nm spatial resolution. New methods such as ptychography are taking us now to nm resolution. Storage rings can be pushed further, and sources with full transverse coherence are planned, increasing the brightness again by 2 - 3 orders of magnitude. Over the last 10 years, there has been a parallel development of Free Electron Lasers (FELs), that push the peak brightness up again by a further factor of 10¹⁰ and reduce pulse length to the few femtosecond range. These machines complement quasi cw synchrotrons and are the tool of choice for studying ultrafast dynamics. I will briefly review some of these historical developments, and then focus on a key enabling technology for MHz repetition rate FELs, the production of ultrafast pulses of electrons from photocathodes. I will review our current work in the synthesis of high efficiency alkali antimonide based cathodes, and cathodes based on non-linear photoemission from plasmonic structures.

2:40pm **AS-WeA3 Monochromatic Ag L_α for XPS – A Practical High Energy X-ray Source, S.J. Coultas, J.D.P. Counsell, S.J. Hutton, A.J. Roberts, C.J. Blomfield, C. Moffitt, D. Surman**, Kratos Analytical Limited, UK

The concept of high energy X-ray sources for laboratory based XPS analysis has been around for a long time. The often cited work by Yates and West was published thirty years ago [1]. However, it is still rare to find data in the literature recorded using X-ray sources other than Al K_α or Mg K_α. In this paper we attempt to illustrate the usefulness of the Ag L_α source for a variety of sample types.

After Al K_α, Ag L_α is probably the most practical monochromatic source for standard laboratory based XPS instrumentation as it utilises the second order diffraction of the same quartz crystals as used for Al K_α. This allows it to be easily accommodated on a modern spectrometer.

The photon energy of Ag L_α is 2984.2 eV, approximately twice that of Al K_α (1486.6 eV). This greater energy leads not only to the excitation of additional, higher binding energy, core lines for some elements (Table 1) but also the possibility of analysis of deeper layers due to the decrease in

* NSTD Student Award Finalist

† Albert Nerken Award Winner

attenuation length with increasing photoelectron energy [2]. For example, the inelastic mean free path (IMFP) of C 1s, binding energy 285 eV, using Al K α X-rays is 3.14 nm at a kinetic energy (KE) 1201 eV, but for Ag L α this is increased to 5.89 eV at KE 2699 eV [3].

In this work we present examples of sample analysis where the consequences of using a higher energy excitation source have been exploited. Examples of using higher binding energy core lines, such as Si 1s and Hf 3d, are presented together with applications utilising the greater information depth available from the source. We have studied samples using both spectroscopy and imaging and explored the depth dimension by ARXPS and depth profiling.

Table 1: Elements with core line binding energies in the range of Ag L α X-rays but not Al K α (*at least one half of doublet)[4]

Core Line Element

1s	Al Si P S Cl
2s	As - Mo
2p	Br - Ru
3s	Pr - Re
3p*	Sm - Tl
3d*	Tm - Rn

References

- [1] K Yates & RH West, *Surf. Interface Anal.*, 1983, **4**, 5
- [2] MP Seah & WA Dench, *Surf. Interface Anal.*, 1979, **1**, 2
- [3] www.nist.gov/srd/nist71.cfm
- [4] X-Ray Data Booklet LBNL/PUB-490 Rev.2 Jan 2001

3:00pm AS-WeA4 Industrial Applications of Auger Electron Spectroscopy (AES) in GE Research and Development Laboratory, H. Piao, L. Le Tarte, General Electric Co., D.F. Paul, Physical Electronics Inc.

Auger Electron Spectroscopy (AES) is one of the most widely used techniques for quantitative surface analysis. AES is the dominant technique in numerous applications in industries. The advantage of high spatial resolution in AES makes it an attractive technique over XPS in solving new types of problems in a diverse range of technologies that are growing in importance. The presentation gives an emphasis on unique advances in surface analysis using AES, including the application of TEM specimen preparation techniques (FIB, microtome and ion-milling). We also demonstrate high energy resolution applications for chemical states analysis by the concept of the sample biasing method [1].

Keywords: AES, energy resolution, chemical states

- [1] D.S. Watson, P.E. Larson, D.F. Paul and R.E. Negri, *Surf. Interface Anal.* 44 (2012) 121.

4:00pm AS-WeA7 Developing Electron Spectroscopy to Meet the Characterization Needs of Modern Materials – Past, Present and Future Challenges, D.R. Baer, Pacific Northwest National Laboratory

INVITED

As surface analytical methods, Auger electron and x-ray photoelectron spectroscopies (AES and XPS) are now approximately fifty years old and both are in wide use. Based on the rapidly growing number of publications, XPS has become the most widely applied method for surface chemical analysis. Although analysis is now mostly routine and quantitative as applied to many types of samples, it has taken considerable effort by many in the research and vendor communities to establish the instrument quality and implement new technologies and to establish the fundamental understanding and relevant physical data needed to develop the accurate approaches to analysis that are now available. However, many modern materials have significant characterization requirements that extend beyond those available using many of the standard measurement and analysis approaches in routine use and as supplied by instrument vendors. In this talk we will look at the types of advances that have taken place over the past four decades and explore some of the issues that were identified that needed to be addressed along the way. Although many of these are now transparent to instrument users, some of them highlight the types of unexpected challenges that can arise when careful analysis is required. The roles that AES, XPS and other methods may play in meeting the significant analysis challenges presented by a new generations of organic, composite and other nanomaterials will be discussed. Among the issues that need to be considered are: sample preparation, mounting and analysis damage; *in situ* and time-dependent analysis; three dimensional structure information; rapid imaging; multimodal and functional characterization; coating uniformity and thickness; surface functionality; analysis speed and cost, and the nature and presence of very minor amounts of contamination. Many of these issues are not new, but the advanced materials now capable of being synthesized

exaggerate some of the challenges and raise additional problems still to be addressed.

This talk has evolved from research programs, research conducted as part of the EMSL User Program (www.EMSL.PNL.gov), and interactions with colleagues from around the world. Portions of this work were performed using EMSL, a national scientific user facility sponsored by the Department of Energy's (DOE) Office of Biological and Environmental Research (BER) and located at PNNL. Aspects of the work have been supported by the DOE's Offices of Basic Energy Science (BES) and Biological and Environmental Research (BER) and the NIEHS under Center grant U19 ES019544.

4:40pm AS-WeA9 Quantifying the Oxidation of Artificially Aged Elastomers with Multivariate Analysis and Imaging NEXAFS, J.A. Ohlhausen, M.H. Van Bentem, M.C. Celina, Sandia National Laboratories

Elastomers made of organic polymers are used in forms such as O-rings, gaskets and electrical wire insulation. Changes in oxidation can lead to significant performance changes as mechanical properties are affected; therefore it is important to be able to directly measure oxidation of these materials. Elastomers have been found to exhibit diffusion limited oxidation whereby the edges are preferentially oxidized over the interior of the part. Much work has been done to characterize ideal elastomer systems; that is, elastomers with no fillers. Fillers, such as oxides and carbon black, confound most chemical analyses. While studies with non-filled elastomers reveal much about the chemistry and mechanical properties in an aged state, the measurement of the oxidation in "real" systems has often involved modulus profiling but much less chemical analyses. We are developing a method that promises to be effective for measuring the oxidation of filled polymer systems based on intrinsic chemical signatures.

Imaging Near Edge X-ray Absorption Fine Structure (NEXAFS) has been found to be a technique that overcomes the major limitations encountered in filled systems. Located at the National Synchrotron Light Source (NSLS) at Brookhaven National Laboratories (BNL), imaging NEXAFS is uniquely capable of measuring the local bonding of elements over large length scales. Thus, the oxidation of these polymers can be directly measured using this technique. We are developing the methods to acquire and process data from samples, ultimately providing a direct chemical measure of oxidation.

In this talk, the results from multivariate analysis of the data are used to calculate oxidation. Specific materials, aging conditions, sample preparation, data acquisition, multivariate analysis and results will be discussed.

**Sandia National Laboratories is a multi-program laboratory managed and operated by Sandia Corporation, a wholly owned subsidiary of Lockheed Martin Corporation, for the U.S. Department of Energy's National Nuclear Security Administration under contract DE-AC04-94AL85000.

5:00pm AS-WeA10 Quantitative Characterization of Corrosion Oxides on Metal Alloy Surfaces Exposed to High Temperature Water, M.C. Burrell, J.T. Orr, T.K. Nolan, M.J. LeClair, Bechtel Marine Propulsion Corporation

Corrosion of metal alloys in high temperature (~500 °F) water results in the formation of a retained oxide film and the preferential release of metal ions into solution. Quantification of the composition and mass of the retained oxide is required to determine the amount of base alloy consumed, and the identity and quantity of released metal ions. We have characterized the oxide formed on a series of steels, nickel-based alloys, and a cobalt-chromium alloy (Stellite-6B) using a combination of surface analysis, microscopy, and gravimetric methods. These oxide films range from a few tens of angstroms up to several microns in thickness. Electron Spectroscopy for Chemical Analysis (ESCA) depth profiling provides a measure of the relative proportion of metal ions in the oxide film and changes in near-surface composition of the metal; oxide film mass is ideally determined gravimetrically using a chemical dissolution method. In the case of the thin, resistant oxide formed on Stellite, the gravimetric approach was not satisfactory, and the oxide thickness was determined using electron microscopy. This presentation will describe the challenges encountered in the characterization of these complex surfaces, and some general trends in the corrosion behavior as related to alloy composition and surface finish.

5:20pm AS-WeA11 Surface Preparation for Multitechnique Surface Analyses, A.E. Wright, P. Mack, T.S. Nunney, A. Bushell, Thermo Fisher Scientific, UK

Surface analysis using multiple techniques is becoming increasingly common in materials characterisation, where the desire for more detailed chemical and structural information is complemented by increasing functionality and automation in instrumentation. It is now often possible to use a single instrument to analyse a sample using four or more techniques in quick succession.

X-ray Photoelectron Spectroscopy (XPS) has become routine in many laboratories, while related techniques such as Auger Electron Spectroscopy (AES), Ultraviolet Photoelectron Spectroscopy (UPS), Ion Scattering Spectroscopy (ISS) and Reflected Electron Energy Loss Spectroscopy (REELS) are being used more frequently to supplement XPS analyses.

Any sample that has been exposed to the ambient environment will typically have a thin (1-2 nm or more) covering of hydrocarbons and other contaminants, and may also have oxidised, hydrated or undergone other reactions. These surface deposits can have a significant effect on the results of surface analytical techniques.

The aforementioned techniques can provide a wealth of complementary information from the surface and near-surface regions of a material, but they have differing susceptibilities to the common surface modifications and contaminants. This presentation evaluates samples including polymers, metals and semiconductors, and examines methods of overcoming the contamination issues with particular focus on the use of monatomic and gas cluster ion beams for surface cleaning.

5:40pm AS-WeA12 Interface Analysis of ALD Grown Oxides using Tunable HAXPES, J. Church, J. Krajewski, R. Opila, University of Delaware, C. Weiland, National Institute of Standards and Technology (NIST)

The roadmap for the development electronic device world follows Moore's law. New challenges appear at with each node. Presently there is a need to find effective ways to characterize a few monolayers of material. In this study, Atomic Layer Deposition (ALD) thin films of ZrO₂ and Nb₂O₅ films have been studied using high-energy synchrotron-based x-ray photoemission spectroscopy, performed at the NIST beamline at the National Synchrotron Light Source. ALD permits precise control of oxide composition, thickness, and coverage. As a result, thin high dielectric constant materials, which are routinely deposited by ALD, are seeing more applications. Given the unique beam energy tuning ability of synchrotron based sources the x-rays are able to effectively probe the interface of ZrO₂ and Nb₂O₅ layers with their respective substrates. Binding energy shifts associated with the chemical environment at the interface of up to 1.4 eV and 1.1 eV for the ZrO₂ and Nb₂O₅ films respectively have been found. These energy shifts suggest significant charge transfer at the interface between the high-k oxide and the Si. In addition, the composition and chemistry of the films as a function of thickness has been determined non-destructively by converting a series of spectra taken with different incident x-ray energies (and simultaneously, different photoelectron sample depths) to depth profiles using Bayesian analyses.

Biomaterial Interfaces

Room: 201 B - Session BI+AI+AS+BA+IA+NL+NS+SP-WeA

Characterization of Biointerfaces

Moderator: A. Rosenhahn, Ruhr-University Bochum, Germany

2:00pm BI+AI+AS+BA+IA+NL+NS+SP-WeA1 Barrier Properties of the Three Layers of the Stratum Corneum to Metal Ions Analyzed by TOF-SIMS, I. Ishizaki, ULVAC-PHI, Inc., Japan, J.S. Hammond, Physical Electronics Inc., A. Kubo, H. Kawasaki, K. Nagao, Keio University, Japan, Y. Ohashi, ULVAC-PHI, Inc., Japan, M. Amagai, A. Kubo, Keio University, Japan

The stratum corneum (SC) is the outermost barrier protecting the mammalian body from desiccation and foreign insults. Congenital SC barrier insufficiencies, i.e., filaggrin deficiency, are hypothesized to predispose patients to atopic diseases. The insoluble nature of the SC has hampered in-depth-analysis of its barrier function by conventional cell biological methods. Here, we applied time-of-flight secondary-ion-mass-spectrometry (TOF-SIMS) imaging technology to analyze the SC in skin sections of wild type and filaggrin knockout mice.

TOF-SIMS enabled the visualization of the distribution of natural substances and the infiltration of externally applied molecules directly without any staining procedure. The distribution of potassium (K) and arginine revealed that the SC consists of three sharply demarcated layers. K was concentrated in the upper layer, while arginine, a major component of the filaggrin-derived natural moisturizing factors, was specifically concentrated in the middle layer and markedly decreased in the filaggrin knockout SC. When skin was soaked in water, K of the upper layer disappeared. When the mice tails were soaked in solutions of K or hexavalent chromium before cross-sectioning, the TOF-SIMS line scan data indicates that the upper layer of the SC allowed the influx of these ions,

suggesting that this layer acts like a "sponge" allowing the passive influx and efflux of exogenous ions. The middle layer blocked the influx of K and hexavalent chromium ions, but failed to block the influx of trivalent chromium ions, which was blocked at the lower layer. Therefore the middle and lower layers have distinct barrier properties depending on each metal. Filaggrin deficiency resulted in the abrogation of the lower layer barrier, allowing trivalent chromium to permeate through the SC to viable epidermal layers. These results, obtained by TOF-SIMS analyses, reveal that the SC consists of three layers of distinct functional properties and demonstrate the loss of barrier properties for particular metal ions in filaggrin deficient SC samples.

2:20pm BI+AI+AS+BA+IA+NL+NS+SP-WeA2 Imaging Hydrated Schewanella p. Biofilm in a Microfluidic Reactor by ToF-SIMS, X.Y. Yu, M. Marshall, B. Liu, Z. Zhu, L. Yang, E. Hill, S. Belchik, Pacific Northwest National Laboratory

We recently developed a microfluidic interface that enables direct probing of liquid surface in vacuum using ToF-SIMS and SEM. The device contains a 100 nm thick silicon nitride (SiN) membrane as the detection area (1.5 × 1.5 mm²) and the microchannels fabricated from polydimethylsiloxane (PDMS) using soft lithography. The unique aspect of our approach is that the detection window is an aperture of 2-3 μm diameter, which allows direct detection of the liquid surface and use surface tension to hold the liquid within the aperture. Its application in ToF-SIMS as an analytical tool was evaluated. In this paper, we present new results of using the microfluidic flow cell to grow *Schewanella p.* biofilm and characterize the biofilm subsequently using ToF-SIMS in the hydrated environment. Depth profiling was used to drill through the SiN membrane and the biofilm grown on the substrate. A controlled media sample was used to compare with the wet biofilm sample. In addition, dry samples deposited on clean silicon wafer were studied to show the difference between wet and dry samples. Multivariate statistical analysis including Principle Component Analysis was used to investigate observations. Our results indicate that imaging biofilm in the hydrated environment using ToF-SIMS is possible using the unique microfluidic device for the first time. Moreover, characteristic biofilm fragments were observed in the wet sample than in dry sample, illustrating the advantage of imaging biofilm in the hydrated state.

2:40pm BI+AI+AS+BA+IA+NL+NS+SP-WeA3 High-resolution Secondary Ion Mass Spectrometry Imaging of Distinct Lipid Species in the Plasma Membranes of Mammalian Cells, M.L. Kraft, University of Illinois at Urbana Champaign INVITED

The plasma membrane is the selectively permeable lipid bilayer that separates every cell from its surroundings. In mammalian cells, the plasma membrane contains domains of differing protein composition. Growing evidence suggests that each different lipid species and cholesterol are also organized into compositionally and functionally domains within the plasma membrane. Domains that are enriched with cholesterol and sphingolipids, which are often referred to as lipid rafts, are hypothesized to be present in the plasma membrane and influence its functions. Despite this potential importance, the organizations of cholesterol and sphingolipids in cell membranes are poorly understood. Until recently, the distributions of most lipid species could not be directly imaged without the use of fluorophore labels, which may alter the distributions of the lipid molecules that they label. We have combined high-resolution SIMS, which is performed with a Cameca NanoSIMS 50, with metabolic stable isotope labeling in order to visualize the organizations of rare isotope-labeled lipids in the plasma membrane by mapping their distinctive isotope enrichments. Here, the details of this approach and its application to imaging the distributions of metabolically incorporated ¹⁵N-sphingolipids and ¹⁸O-cholesterol in the plasma membranes of fibroblast cells will be presented. Use of this approach to evaluate hypotheses concerning the mechanisms that regulate lipid organization within the plasma membrane will also be discussed.

4:00pm BI+AI+AS+BA+IA+NL+NS+SP-WeA7 Analysis of Breast Cancer Tumors with ToF-SIMS, L.J. Gamble, M. Robinson, University of Washington, F. Morrish, D. Hockenbery, Fred Hutchinson Cancer Research Center

Tumor metabolism plays a large role in cancer onset and progression, and its causes and effects are under intense scrutiny. Recently, the lipid metabolism in tumors has been looked at as a factor in tumor type and treatment. Time-of-flight secondary ion mass spectrometry (ToF-SIMS) is well suited for analysis of the lipid distribution in tumors. In this study, frozen breast cancer tissue specimens from patients were cut using a cryomicrotome at a thickness of 4μm and deposited on silicon wafers. Serial tissue slices were stained with hematoxylin and eosin (H&E) and were used to determine from which structures the various chemical signatures originated. SIMS tissue sample data were acquired on an IONTOF TOF-SIMS V using Bi₃⁺ in both high mass and high spatial resolution

modes on both ER+ and ER- human breast tumor tissue samples. Mass fragments spectra from multiple spots and tissue slices for the ER+ and ER- tissue samples can be separated from one another using PCA within a 95% confidence interval. Key differences between tissue types are abundance of cholesterol and triacylglycerides/diacylglycerides (TAGs/DAGs). Imaging ToF-SIMS of these samples show variances for different fatty acids (saturated versus unsaturated) that correlate with model studies using similar cancer cell types.

4:20pm **BI+AI+AS+BA+IA+NL+NS+SP-WeA8 Tools For TOF-SIMS Image Analysis**, *D.J. Graham, L.J. Gamble, D.G. Castner*, University of Washington

The use of time-of-flight secondary ion mass spectrometry (ToF-SIMS) for imaging has increased in recent years. This is due to the improvements in spatial resolution and ion yields from modern primary ion sources. These improvements have made ToF-SIMS attractive for cell and tissue imaging, especially due to the fact that ToF-SIMS can detect and identify a wide range of membrane lipids and other cellular components, and can potentially image these in both 2D and 3D. Characterization of tissues and cells by ToF-SIMS often requires advanced data collection and analysis methodologies including the use of stage rastering for large area analysis and 3D depth profiling. It is also often of interest to localize specific areas within a cell or tissue and carry out region of interest (ROI) analysis. Finally, ToF-SIMS image analysis presents challenges due to the sheer size of the data sets. In order to deal with these large, complex data sets, we have created a set of Matlab toolboxes for multivariate analysis of both images and spectra. This talk will highlight new tools in the NBtoolbox that enable the user to process stage raster images, overlay images, and extract ROI images based off of image masks created from any imported image.

For example, the stage raster tools enable the user to import and run PCA on an entire stage raster image, or to dice the stage raster into separate image tiles that can then be analyzed individually. The ROI generation tools enable the user to import any image to be used as a ROI mask. Examples will be shown using fluorescent images from confocal microscopy as masks to extract ROI from ToF-SIMS images of mouse muscle tissue. Tools are also included for image alignment, and image cropping. All data processed with these tools can be analyzed using PCA, MAF or MCR.

4:40pm **BI+AI+AS+BA+IA+NL+NS+SP-WeA9 How Hydration Affects Mechanical Anisotropy, Nano-Topography and Fibril Organization of Osteonal Lamellae**, *A. Faingold, S.R. Cohen*, Weizmann Institute of Science, Israel, *R. Shahar*, Koret School of Veterinary Medicine, The Hebrew University of Jerusalem, *S. Weiner, H.D. Wagner*, Weizmann Institute of Science, Israel

Water serves a central role in physiological systems. Even bone, a relatively "dry" component, has high water content: cortical (also known as compact) bone contains about 20% water by volume. The water content varies with age, and influences the structural and mechanical properties of the bone, from the level of mineralized fibrils up to osteonal lamellae. Many studies on mechanical properties of bone are performed on bone which has been dehydrated to some degree, whereas the relevant physiological state is wet. In this work, atomic force microscopy, nanoindentation, and microindentation have been applied to wet and dry bone samples in order to investigate the influence of hydration at different hierarchical levels; the mineralized fibril level (~100nm), the lamellar level (~6µm); and the osteon level (up to ~30µm). Measurements were made both in directions parallel and perpendicular to the osteonal axis by cutting appropriate slices from a metacarpal bone of a 5 year old male horse. "Dry" samples were obtained by allowing the polished sample to stand under ambient conditions for 24 hours. "Wet" samples were measured under deionized water, or PBS solution in which they were incubated between 1 - 18 hours prior to measurement. We note that under these conditions, the wet samples contained 12% water whereas dry samples contained 9% water. Nonetheless, significant differences between the two states were observed: (1) Dry samples were both stiffer and harder than the wet samples in both directions studied, and at all length scales. (2) The anisotropy ratio, ratio of modulus or hardness along vs. perpendicular to the osteonal axis, was larger in the dry samples than for the wet ones. (3) These mechanical changes are accompanied by marked variation in the sample topography as observed by atomic force microscopy. These results will be presented in the context of related work. A model we developed based on differences in the fibril orientation between dry and wet states provides a good rationale for the observed behavior.

5:00pm **BI+AI+AS+BA+IA+NL+NS+SP-WeA10 AFM of Supported Lipid Bilayers: From Critical Point Behaviour to Actin Polymerization**, *G.R. Heath, S.D. Connell, S.D. Evans*, University of Leeds, UK

In this study we create supported lipid model membranes which display phase separation into liquid-ordered and liquid disordered domains and use

atomic force microscopy (AFM) to observe critical phenomena and protein interactions with the aid of stable and precise temperature control. The regions of criticality were determined by accurately measuring and calculating phase diagrams for the 2 phase L_d -L_o region, and tracking how it moves with temperature, then increasing the sampling density around the estimated critical regions. Compositional fluctuations were observed above the critical temperature (T_c) and characterized using a spatial correlation function. From this analysis, the phase transition was found to be most closely described by the 2D Ising model, showing it is a critical transition. The region of critically fluctuating 10-100 nm nanodomains has been found to extend a considerable distance above T_c to temperatures within the biological range, and seem to be an ideal candidate for the actual structure of lipid rafts in cell membranes. Although evidence for this idea has recently emerged, this is the first direct evidence for nanoscale domains in the critical region.

Ponticulin is a 17KDa integral membrane protein with multiple membrane spanning beta strands and glycosylphosphatidylinositol (GPI) lipid anchor at its C-terminus. Ponticulin has been shown to be the major high affinity link between the plasma membrane and the cortical actin network in *D. discoideum* (Wuestehube and luna, 1987; Chia et al., 1991). This protein is thought to reside in cholesterol-rich lipid microdomains ('lipid rafts') with the transmembrane domain apparently lying outside the lipid raft with the raft localization being dependant upon the GPI anchor at the C-terminus of the protein. We test the hypothesis of localization and show for the first signs of GPI-anchored membranes proteins preferentially locating to boundaries between the L_o and L_d phase. This may provide a potential mechanism by which the cytoskeleton can influence lipid organization.

Cationic lipids have been previously shown to adsorb actin from a non polymerizing solution, induce its polymerization, and form a 2D network of actin filaments, in conditions that forbid bulk polymerization. We show this phenomenon on supported lipid bilayers using high resolution AFM and QCM-D, investigating various factors such pH, charge concentration and lipid mobility which affect the actin structures formed. We then go on to mathematically model this process to show 2 different polymerization mechanisms depending on the lipid diffusion.

5:20pm **BI+AI+AS+BA+IA+NL+NS+SP-WeA11 Investigating Reversible Dye Adsorption on TiO₂: A QCM-D Study**, *H.K. Wayment-Steele, L.E. Johnson*, Pomona College, *M.P. Dixon*, Biolin Scientific, *M.S. Jhal*, Pomona College

Understanding the kinetics of dye adsorption on semiconductors is crucial for designing dye-sensitized solar cells (DSSCs) with enhanced efficiency. Harms et al. (2012) have recently demonstrated the applications of QCM-D to show in-situ dye adsorption on flat TiO₂ surfaces. QCM-D provides adsorption measurements in real time and therefore determination of the kinetics of the process. In this work, we examine reversible, non-covalent binding of N3, a commercial RuBipy dye, using the native oxide layer of a titanium sensor to simulate the TiO₂ substrate of a DSSC. To isolate the weak binding mode, we deactivated the carboxylate groups of N3 by forming methyl esters, thus disabling chelation to TiO₂. Improved understanding of the weak binding mode provides insight into dye aggregation and the relative contributions of chelation versus non-covalent processes.

5:40pm **BI+AI+AS+BA+IA+NL+NS+SP-WeA12 Combined Raman Systems for Biological Imaging and Analysis**, *A.J. King*, Renishaw Inc, *T. Prusnick*, Renishaw Inc., *M. Canales*, Renishaw Inc

Raman microscopy has become a routine tool for many materials, but the need for this molecular imaging and analysis technique in biological research has become essential. The ability probe the chemical and molecular structure of biological materials is obtained directly without the need for any dyes or markers. These systems can be utilised to generate chemical images of cells, tissue, bone and bio-compatible materials with very high spatial resolution. It has been employed for cancer diagnosis, stem cell differentiation, skin treatments, protein structure analysis, bio-diagnostics, bacterial identification and green energy.

This Raman instrumentation can also be combined with environmental chambers, scanning probe techniques, scanning electron microscopes and in-vivo probes; to provide in-situ and co-localised measurements. This talk will provide an introduction to Raman microscopy with biological materials; the instrumentation required for these techniques; and, will highlight some applications where Raman microscopy is making the biggest impact with biological materials.

Spectroscopic Ellipsometry Focus Topic

Room: 101 A - Session EL+AS+EM+SS+TF-WeA

Spectroscopic Ellipsometry: Perspectives and Novel Applications

Moderator: T. Hofmann, University of Nebraska-Lincoln, S. Zollner, New Mexico State University

2:00pm **EL+AS+EM+SS+TF-WeA1 Optical Hall Effect - Detection of Symmetric and Anti-Symmetric Landau-Level Transitions in Multilayer Epitaxial Graphene on C-face SiC**, *P. Kühne**, Univ. of Nebraska-Lincoln, *V. Darakchieva*, Linköping Univ., Sweden, *J.L. Tedesco*, ABB, Inc, *R.L. Myers-Ward*, *C.R. Eddy, Jr.*, *D.K. Gaskill*, U.S. Naval Research Lab, *C.M. Herzinger*, *J.A. Woollam Co., Inc.*, *M. Schubert*, *T. Hofmann*, Univ. of Nebraska-Lincoln

We report on polarization sensitive, magneto-optic, reflection-type Landau level (LL) spectroscopy at low temperatures by using the optical-Hall effect in the mid-infrared spectral range (from 600 to 4000 cm^{-1}) on epitaxial graphene grown on C-face silicon carbide by thermal decomposition. In contrast to transmission measurements, our reflection-type ellipsometry setup allows simultaneous detection of Landau level transitions, and the classical Drude-type magneto-optic free charge carrier contribution throughout the full mid-infrared spectral range, including the opaque Reststrahlen band of the SiC substrate. In this region, we observe a multitude of LL transitions that can be assigned to single-, bi- and Bernal stacked (ABA) tri-layer graphene.¹² For the first time, we observe symmetric and anti-symmetric signatures due to non-polarizing, i.e., isotropic, and polarizing, i.e., anisotropic Landau level transitions, respectively. Isotropic polarization behavior is found for LL transitions exhibiting a square-root dependence on the magnetic field, typical for stacks of decoupled graphene mono-layers. Anisotropic polarization behavior is observed for LL transitions with a sub-linear to linear dependence on the magnetic field, indicative for bi- and ABA stacked tri-layer graphene. We present a dielectric model describing contributions from the substrate, Drude-type free charge carrier and symmetric and non-symmetric Landau level transitions. Model parameters as the average velocity of Dirac fermions $c = (1.01 \pm 0.01) 10^6$ m/s and interlayer coupling constant $\gamma = (3150 \pm 50) \text{ cm}^{-1}$ are found to be in excellent agreement with previously reported values.

[1] M. Koshino and T. Ando, Phys. Rev. B **77**, 115313 (2008).

[2] M. Orlita, C. Faugeras, R. Grill, C. Berger, W. A. de Heer, G. Martinez, M. Potemski, et al., Phys. Rev. Lett. **107**, 216603 (2011).

2:20pm **EL+AS+EM+SS+TF-WeA2 A Physical Model Dielectric Function for Graphene from the THz to the UV**, *A. Boosalis†‡§*, University of Nebraska-Lincoln, *W. Li*, *R. Elmquist*, *M. Real*, *N.V. Nguyen*, National Institute of Standards and Technology (NIST), *M. Schubert*, University of Nebraska-Lincoln, *R. Yakimova*, *V. Darakchieva*, Linköping University, Sweden, *R.L. Myers-Ward*, *C. Eddy*, *D.K. Gaskill*, Naval Research Laboratory, *T. Hofmann*, University of Nebraska-Lincoln

Graphene has been the focus of much recent research due to its unique electronic and optical properties, with potential for high performance electronics, tunable ultra-fast lasers, and transparent electrodes. Further development of graphene requires a complete understanding of graphene's optical properties. Once thought to be trivially related to the lattice constant, it has become clear that graphene's dielectric response contains distinct absorption features at ~4.5 and ~6 eV. However, the scientific community currently lacks consensus as to the origin of each feature [1,2].

In order to determine the physical origin of both absorption features, we have carried out spectroscopic ellipsometry measurements from 0.75 to 9 eV on graphene grown by CVD on Cu and by high-temperature Si sublimation from SiC. CVD grown graphene was transplanted to a fused silica substrate prior to measurement, while measurements conducted on SiC included 3C and 6H SiC polymorphs, before and after hydrogen intercalation.

Experimental data were analyzed with a biaxial model dielectric function which is dependent on the graphene joint density of states and modified by the Fano configuration interaction to account for exciton absorption [3]. Physical parameters include the electron next-neighbor hopping energy, the exciton resonant energy, the exciton absorption affinity, and the graphene optical thickness. All parameters are varied until the lowest mean squared error between model dielectric function and experimental spectra is achieved.

* **Spectroscopic Ellipsometry Graduate Student Award Finalist**

Our results show that the absorption ~4.5 eV is excitonic, while the absorption ~6 eV is an interband transition arising from the saddle point at the M position in the graphene band structure, a similar result to optical properties predicted by density functional theory [4]. The strain in the graphene lattice can be estimated from the next-neighbor hopping energy, and our results demonstrate relaxation in the graphene lattice after hydrogen intercalation of graphene on SiC. Epitaxial graphene on SiC also shows a higher affinity for exciton production and a lower exciton binding energy than graphene grown by CVD.

References:

[1] Mak et al., Phys. Rev. B. **106**, 046401 (2011)

[2] Santos et al., Phys. Rev. B. **84**, 081403 (2011)

[3] Chae et al., Nano. Lett. **11**, 1379 (2011)

[4] Yang et al., Phys. Rev. Lett. **103**, 186802 (2009)

2:40pm **EL+AS+EM+SS+TF-WeA3 Spectroscopic Ellipsometry – A Perspective**, *D.E. Aspnes*, North Carolina State University **INVITED**

Since its initial development in the early 1970's, spectroscopic ellipsometry (SE) has become the primary technique for determining optical properties of materials. In addition to the other historic role of ellipsometry, determining film thicknesses, SE is now widely used to obtain intrinsic and structural properties of homogeneous and inhomogeneous materials in bulk and thin-film form, including properties of surfaces and interfaces. Its nondestructive capability for determining critical dimensions has made SE indispensable in integrated-circuits technology. The presentation is directed toward those who are unfamiliar with SE but may feel that it could provide useful information in specific situations. Accordingly, I give some background and basic theory, then illustrate capabilities with a variety of applications. Probable directions for the future are also discussed.

4:00pm **EL+AS+EM+SS+TF-WeA7 The First Report of Meta-SIMS with Bismuth Over Layers**, *M.R. Linford*, *N. Madaan*, Brigham Young University

The low ionization yields of many sputtered moieties is a bottleneck for completely exploiting the tremendous potential of ToF-SIMS. Among the many procedures for improving ionization efficiencies in SIMS, a significant amount of work has been directed towards metal assisted SIMS (Meta-SIMS). In this procedure a thin film (ca. 2 nm) of a metal (Au or Ag) is deposited on a sample surface before SIMS analysis. The resulting secondary ion yields have been shown to increase substantially for many polymers, where the yield enhancement is found to be fragment specific and also to depend on the type of primary ion and sample used. In our work we are studying Meta-SIMS on spin coated polyethylene glycol surfaces using thin layers of bismuth. To be best of our knowledge, Meta-SIMS with Bi over layers has not previously been reported. In particular, we are striving to incorporate spectroscopic ellipsometry (SE) as a tool to accurately find the thickness of deposited metal so that we can best understand the correlation between Bi film thickness and ionization yield enhancements. When a QCM crystal is used to monitor the thickness of a film of a deposited metal on a sample surface, one assumes that the sticking coefficient of the evaporated metal is the same for both the QCM crystal and the sample surface. However, it has now been shown that the sticking coefficient on a polymer surface can be $1/10^{\text{th}}$ of that on the QCM crystal. Thus a different film measurement technique is needed to more accurately allow us to determine the thicknesses of metal films on polymer surfaces. To best determine our Bi thicknesses by SE (from ca. 200 – 1000 nm) we have used the interference enhancement technique – a ca. 500 nm oxide on silicon substrate. Of course SE is also a very fast and non-invasive technique for film thickness determination compared to AFM or XPS. Unlike Au, Bi and Ag appear to form a thin oxide layer that may chemically affect the SIMS ionization process. Accordingly, we compare the Meta-SIMS of polyethylene glycol films using Au, Bi, and Ag with all thicknesses determined by SE. XPS is used in parallel to determine the amount of oxide on the metals and to confirm their deposition.

4:20pm **EL+AS+EM+SS+TF-WeA8 Spectroscopic Ellipsometry of Thin Films for Archival Optical Data Storage and for Microfabricated Thin Layer Chromatography Plates**, *M.R. Linford*, *A. Diwan*, *S. Kanyal*, *H. Wang*, *N. Madaan*, Brigham Young University, *A. Dadson*, Diamond Analytics, *R.C. Davis*, *B. Lunt*, Brigham Young University, *N. Podraza*, The University of Toledo

Our group is focused on the synthesis and characterization of new materials and over the years this interest has led us into different research areas. Of late we have focused on developing and understanding the materials for archival optical data storage and for separations science (chromatography). In particular, we have recently helped spin out a company from the university that is selling a DVD that has been shown to last for more than 1000 years – see www.mdisc.com. Another company has licensed our

technology to microfabricate thin layer chromatography (TLC) plates – see www.diamond-analytics.com.

In this talk we discuss the important role that spectroscopic ellipsometry (200 – 1000 nm) has played in the development and understanding of the materials in these devices. For many of these measurements we use interference enhancement to break the correlation between film optical constants and thicknesses. Some of our measurements have been fairly routine. For example, the thicknesses and optical properties of the ca. 35 nm alumina barrier layers in our microfabrication of TLC plates are easily modeled using a Cauchy dispersion relationship. In other cases the analyses have been challenging, e.g., the thin, ca. 6 nm, Fe films used to make TLC plates appear to be completely oxidized, but thicker Fe films show increasing metallic (Drude) character. An understanding of the optical properties of our bismuth-tellurium-selenium (BTS) write layers on Mylar tape for optical data storage has also been nontrivial. These films show high levels of roughness by AFM, significant void fractions by RBS, and moderately high levels of oxidation by XPS and SIMS, which mandated the use of a roughness layer and optimization of the depolarization factor in the effective medium approximation that described the film. AFM and SEM were also used to characterize these materials, and our final SE analysis of this material might not have been reasonable without the extra information these techniques provided. Both the BTS write layer and Fe films for TLC have been monitored over an extended period of time by SE. The resulting plots of psi and delta vs. several wavelengths reveal the long-term stabilities of these materials. At present we are also attempting to determine the optical constants of the carbon nanotube forests used as templates in TLC plate microfabrication. We believe that the resulting optical constants of these materials, which should show a considerable degree of anisotropy, will be of interest to the community.

4:40pm **EL+AS+EM+SS+TF-WeA9 Optical Properties of Nanoscale Nanoelectronic Materials, A.C. Diebold**, College of Nanoscale Science and Engineering **INVITED**

Nanoscale dimensions clearly alter the optical properties of materials. All too often, changes in key optical properties such as direct gap transitions are attributed to quantum confinement. The origin of changes in optical properties depends on several factors including crystal structure (polycrystalline vs single crystal), material type (metal, semiconductor, or dielectric) and temperature. Temperature dependent determination of the dielectric function of ultra-thin silicon on insulator films show that electron-phonon interactions alter optical transitions. Thus changes in the phonon dispersion will alter room temperature optical properties. These changes can be due the films that surround the nanolayer. Other examples include silicon fins and silicon fins topped with Si(1-x)Ge_x layers. The Si fins are confined in two dimensions. Here the need for understanding anisotropic optical properties is described. The optical properties of metal films also show dimensional effects. The origin of the thickness dependence of the optical properties of polycrystalline metal films can be traced to grain size. In this talk, the impact of nanoscale dimensions will be explored using examples that include ultra-thin silicon films, thin silicon “fin” structures, and polycrystalline thin metal films.

5:20pm **EL+AS+EM+SS+TF-WeA11 Optical Constants of Ni_{1-x}Pt_x Silicides from Spectroscopic Ellipsometry, L.S. Abdallah*, S. Zollner**, New Mexico State University, C. Lavoie, A. Ozcan, IBM, M. Raymond, GLOBALFOUNDRIES

Nickel silicides are widely used in semiconductor manufacturing as contacts in CMOS device processing to achieve highly stable low-resistance contacts between copper back-end metallization and front-end silicon transistors. We provide a comprehensive analysis of the dielectric function and optical conductivity for nickel platinum silicides with different platinum concentrations (0 to 30 at.% Pt). Our goal is in-line process control of Ni-Pt alloy deposition and silicide formation using spectroscopic ellipsometry.

Previously, we determined the optical constants of Ni_{1-x}Pt_x metal alloys. We deposited 100 Å Ni_{1-x}Pt_x alloy films with different Pt compositions (0 to 25 at.% Pt) on a thick layer of SiO₂ to prevent the reaction between the metal and the silicon. Ellipsometric measurements were performed on these samples from 0.6 to 6.6 eV using a broad range of angles of incidence (20 to 80°). Using a thick transparent layer of SiO₂ as well as using a broad range of angles of incidence, we vary the optical path length and thus obtain more information about our metal films.

After determining accurate optical constants of Ni_{1-x}Pt_x alloys with the same thickness were deposited directly on Si to study the optical constants of silicides. Ellipsometric measurements were performed over the same photon energy range (0.6 to 6.6 eV), but using a smaller range of incident

angles because of the absence of SiO₂ underneath the metal (no sharp interference fringes).

During Ni_{1-x}Pt_x deposition on Si, some metal atoms will diffuse into the Si substrate even at room temperature, creating a metal-rich silicide. Annealing the samples at 500° C for 30 s creates a monosilicide layer with a thickness of about 200 Å. No unreacted metal remains. We include a 10 Å layer of SiO₂ as a native oxide in our model. To obtain the correct silicide thickness, we tried different thicknesses (all around 200 Å) and then we picked the thickness that eliminates Si substrate artifacts.

The imaginary part of the resulting dielectric function of monosilicides shows metallic Drude behavior with two additional peaks at 1.5 eV and 4.5 eV due to interband electronic transitions. Our results will be compared to previous measurements and electronic structure calculations on NiSi and PtSi. In our results, absorption peaks broaden with increasing Pt content in the silicides, similar to our earlier results for Ni_{1-x}Pt_x metal alloys.

5:40pm **EL+AS+EM+SS+TF-WeA12 Anisotropic Bruggeman Effective Medium Approaches for Slanted Columnar Thin Films, D. Schmidt, E. Schubert, M. Schubert**, University of Nebraska-Lincoln

Two different formalisms for the homogenization of composite materials containing ellipsoidal inclusions based on Bruggeman’s original formula for spherical inclusions can be found in the literature [1,2]. Both approximations to determine the effective macroscopic permittivity of such an idealized composite assume randomly distributed dielectric particles of equal shape and differ only in the definition of the depolarization factors. The two approaches are applied to analyze ellipsometric Mueller matrix spectra acquired in the visible and nearinfrared spectral region from metal and semiconductor slanted columnar thin films. Furthermore, the effective dielectric function tensor generated by the two Bruggeman formalisms is compared to effective major axes dielectric functions individually determined with an assumption-free homogeneous biaxial layer approach.

Best-match model parameters of all three model approaches are discussed and compared to estimates from scanning electron microscope images. It was found that all three optical model equivalents for slanted columnar thin films agree well with the imaging technique and that no preference can be given to any one of the two Bruggeman formalism in terms of structural properties determination.

Application of the effective medium approximation models will be highlighted on the example of in-situ monitoring of dielectric and metal conformal coating growth onto slanted columnar thin films by atomic layer deposition.

[1] D. Polder and J. H. van Santen, *Physica* 12, 257 (1946).

[2] Mackay and Lakhtakia, *J. Nanophoton.* 6, 069501 (2012).

Electronic Materials and Processing

Room: 102 A - Session EM+AS+NS+SS-WeA

Semiconductor Heterostructures/Heusler Alloys

Moderator: J. Hilton, Mantis Deposition

2:00pm **EM+AS+NS+SS-WeA1 New Directions in GaN Material Research: Thinner and Smaller, J. Han**, Yale University **INVITED**

The past two decades have witnessed phenomenal progress in optoelectronic display and illumination devices enabled by AlGaInN (III-N). As the technology of conventional devices enters commercial maturity, innovation is called for continual advances in device applications.

In this talk we will discuss the possibility of extending III-N devices in the directions of flexible and large-area applications. Our recent work in using electrochemical etching to achieve layer slicing will be presented with preliminary device demonstrations. We envision new possibilities in the manufacture of ultrathin and flexible GaN devices. To circumvent the difficulty in the growth of GaN on silicon, we investigated the concept of evolutionary growth combining modern fabrication techniques with epitaxy to provide new freedoms in tackling this grand challenge. The result of preparing high quality GaN on SiO₂ will be reported.

2:40pm **EM+AS+NS+SS-WeA3 A Comparison of Phase Invariant and Mosaic Crystal Models for Dynamical Diffraction from InGaAs/GaAs (001) Heterostructures Containing Dislocations, P.B. Rago, J.E. Ayers**, University of Connecticut

In previous work an approximate phase invariant dynamical diffraction model (PIDDM) has been developed for the analysis of high-resolution x-ray rocking curves from metamorphic semiconductor heterostructures containing threading dislocations. In principle, use of the PIDDM allows depth profiling of composition, strain, and dislocation density in device

* **TFD James Harper Award Finalist**

structures. It accounts for the broadening of diffraction linewidths through the use of an effective deviation parameter, which includes the angular mosaic spread and lattice spacing mosaic spread of a crystal distorted by dislocations. Although the PIDDM correctly predicts the linewidth broadening of diffraction profiles, it is unable to account for some features of the rocking curves from metamorphic structures, such as the suppression of the Pendellosung fringes and the extinction behavior of layers with high dislocation densities. To address these issues, we have developed a refined model for dynamical diffraction from dislocated semiconductor heterostructures, the Mosaic Crystal Dynamical Diffraction Model (MCDDM), which includes phase variations between blocks of the mosaic crystal. In this paper, we compare the PIDDM and MCDDM for the case of metamorphic InGaAs/GaAs (001) heterostructures, and illustrate the situations in which the more complex MCDDM needs to be applied.

3:00pm **EM+AS+NS+SS-WeA4 Lattice Relaxation and Misfit Dislocations in Sublinearly Graded $\text{In}_x\text{Ga}_{1-x}\text{As}/\text{GaAs}$ (001) and $\text{GaAs}_{1-y}\text{P}_y/\text{GaAs}$ (001) Heterostructures**, T. Kujofsa, J.E. Ayers, University of Connecticut

Metamorphic devices such as high electron mobility transistors (HEMTs), heterojunction bipolar transistors (HBTs), light-emitting diodes (LEDs), laser diodes, and solar cells have been fabricated on GaAs substrates using graded buffer layers. These metamorphic buffer layers usually employ linear grading of composition, and materials including $\text{In}_x\text{Ga}_{1-x}\text{As}$ and $\text{InAs}_{1-y}\text{P}_y$ have been used. The most important function of the linearly-graded buffer layer is to minimize the threading defect density by enhancing the mobility and glide velocity of dislocations, thereby promoting long misfit segments with relatively few threading arms. In general, there are three features of graded buffers which reduce the thread density: (i) a misfit dislocation free zone (MDFZ) near the substrate interface which reduces pinning interactions with substrate defects, (ii) a second MDFZ near the surface which reduces pinning interaction near the device layer; and (iii) a large built-in strain in the top MDFZ which enhances glide of dislocations to sweep out threading arms. However, non-linear grading may be beneficial for better control of the widths of the MDFZs and for higher built-in strain in the surface MDFZ. In this work, we present minimum energy calculations for sublinearly graded heterostructures, with logarithmic and power law grading, and compare the cases of cation (Group III) and anion (Group V) grading. We show that differences in the elastic stiffness constants give rise to significantly different behavior in these two commonly-used buffer layer systems. Moreover, the use of different grading profiles for sublinear buffer layers allows for correlation of a sublinearity factor to the width of dislocated region and peak misfit density.

4:00pm **EM+AS+NS+SS-WeA7 Heteroepitaxial III-V/Si for Advanced Multijunction Photovoltaics**, S.A. Ringel, T.J. Grassman, J.A. Carlin, C. Ratcliff, D. Chmielewski, The Ohio State University **INVITED**

The integration of III-V semiconductors with Si through epitaxial methods is receiving renewed interest, due to recent advances in mitigating defects related to the complex III-V/Si growth interface. In photovoltaics, a resultant III-V/Si heteroepitaxial solar cell would address the key technological barriers related to III-V solar cells, namely cost, manufacturing scalability and weight, and it would also address Si wafer photovoltaic concerns related to approaches that increase efficiencies of Si solar cells. This presentation will focus on our recent efforts regarding the achievement of high-quality, heterovalent epitaxy of GaP on (100)-oriented Si substrates in which all nucleation-driven defects have been eliminated. Device quality GaP/Si interfaces are an enabling pathway for the creation of III-V/Si multijunction photovoltaic devices in which the Si growth substrate can simultaneously act as a near-ideal sub-cell when epitaxially integrated beneath a metamorphic GaInP/GaAsP solar cell structure in which the GaInP, GaAsP and Si, having respective bandgap energies of ~ 2 eV/1.55 eV/1.1 eV, create a nearly ideal, Si-based, triple junction solar cell design. This presentation will focus on the heteroepitaxy of GaP/Si using both molecular beam epitaxy (MBE) and metalorganic chemical vapor deposition (MOCVD) methods. We have very recently transitioned our earlier MBE work on achieving nucleation-defect-free GaP/Si to the MOCVD environment (Grassman, et al., Applied Physics Letters 102, 142102, 2013) and this presentation will focus on this MBE to MOCVD transition in which all such defects (anti-phase domains, stacking faults and microtwins) have been simultaneously and totally avoided. Four main topics will be presented: (1) GaP/Si(100) grown by MOCVD free of antiphase domains and stacking defects; (2) growth, fabrication, and testing of GaP/active-Si sub-cells utilizing the GaP as an effective passivation layer on Si sub-cells created by two methods - in-situ (i.e. in the III-V MOCVD growth system) and ex-situ (i.e. using high efficiency pre-processed Si sub-cells as growth substrates for III-V/GaP/Si integration); (3) MOCVD-grown GaAsP/Si multijunction structures having target lattice constants and bandgaps for high efficiency, and (4) comparative interface studies of nucleation-defect-free MBE- and MOCVD-grown III-V/GaP/Si. The

presentation will capture the overall III-V/Si advances for multijunction III-V/active-Si photovoltaics.

4:40pm **EM+AS+NS+SS-WeA9 Why All the Interest in Heusler Alloys?**, C.J. Palmstrom, University of California at Santa Barbara **INVITED**

Heusler alloys have received a lot of attention because of their large range of properties, which include electronic, piezoelectric, magnetic, thermoelectric and shape memory. Their properties depend on the number of valence electrons per formula unit and have been predicted to be semiconductors, metals, ferromagnets, antiferromagnets, half metals, superconductors and topological insulators. Similar to compound semiconductors, the band structure and lattice parameters of Heusler alloys can also be tuned through alloying but over a much larger range of properties. Magnetic tunnel junctions using Heusler alloys that are predicted to be half metals have shown record tunneling magnetoresistance. They can be lattice matched to most compound semiconductors and have also been used for spin injecting contacts. This presentation will emphasize the molecular beam epitaxial growth on III-V semiconductors and tuning of their properties with examples for spintronic, semiconductor, topological insulator and shape memory applications.

5:20pm **EM+AS+NS+SS-WeA11 Spin Injection and Detection in Epitaxial $\text{Co}_2\text{MnSi}/\text{GaAs}$ (001) Heterostructures**, S. Patel, University of California, Santa Barbara, K. Christie, C. Geppert, University of Minnesota, B.D. Schultz, University of California, Santa Barbara, P. Crowell, University of Minnesota, C.J. Palmstrom, University of California, Santa Barbara

High spin polarization ferromagnets, including half-metallic ferromagnets, are attractive choices for use as spin injectors into semiconductors as well as other spintronic devices. Co_2MnSi is predicted to be half-metallic [1], and with a lattice constant of 5.65\AA , is almost perfectly lattice-matched to GaAs (0.06% mismatch), and a strong candidate for use as a spin-injector in the ferromagnet/GaAs system. We demonstrate the growth of epitaxial Co_2MnSi films directly on GaAs (001) by molecular beam epitaxy (MBE) for use as a spin injector, as well as successful spin injection and detection. In addition, we observe a growth temperature dependence of spin injection/detection in three-terminal lateral transport devices on GaAs. X-ray diffraction studies verify near lattice matching of Co_2MnSi films to GaAs. We employ the use of a shuttered growth technique to initiate Co_2MnSi growth on GaAs. This technique allows for the initial deposition of either a full Co monolayer or a full MnSi monolayer, influencing the interfacial ordering of the ferromagnet/semiconductor interface. In order to study the effects of interfacial ordering, scanning transmission electron microscopy (STEM) and x-ray diffraction techniques, as well as electrical measurements of spin injection and transport are used. Magnetic hysteresis measurements show extremely low coercivities of grown films, as well as uniaxial anisotropy with an easy axis in the [110] direction. Co_2MnSi has been grown at growth temperatures varying from 180°C to 320°C , and a layer-by-layer growth mode has been confirmed for this temperature range by the presence of intensity oscillations in reflection high energy electron diffraction (RHEED) patterns. The Co_2MnSi layers have also been studied by low energy electron diffraction (LEED), scanning tunneling microscopy (STM), and scanning tunneling spectroscopy (STS). The STM and STS studies have been carried out at room temperature, and at 4.5K at which atomic resolution was obtained. STS has been performed with both a Nb tip and a W tip at room temperature and 4.5K to study the local density of states. In addition, we demonstrate a growth temperature dependence of spin injection/detection in three-terminal lateral transport devices on GaAs. These methods were used to better understand the growth mechanisms and electronic properties of the films.

This work was supported by the MRSEC Program of the National Science Foundation under Award Number DMR-0819885 and by the Semiconductor Research Corporation under award number 2011-IN-2153.

[1] S. Picozzi, A. Continenza, and A. J. Freeman. Phys. Rev. B 69 (9), 094423 (2004)

Electronic Materials and Processing

Room: 101 B - Session EM-WeA

III-V Devices and Tunnel FETs

Moderator: P.C. McIntyre, Stanford University, E.M.

Vogel, Georgia Institute of Technology

2:40pm **EM-WeA3 Plasma Enhanced ALD of High-k Dielectrics on GaN and AlGaIn: Interface Formation, Growth, and Electronic States.** *R.J. Nemanich, B.S. Eller, J. Yang, Arizona State University* **INVITED**

The disparate polarization at AlGaIn/GaN heterostructures engenders a 2D electron gas (2DEG) that effectively reduces on-resistance and power loss, resulting in a high electron mobility ideal for high-frequency, high-temperature, and high-voltage requirements associated with HFETs and HEMTs. Since GaN and AlGaIn are characterized by a large spontaneous polarization, there is a large polarization bound surface charge (2.2×10^{13} and 3.2×10^{13} charges/cm²) that must be compensated presumably by states near the dielectric-GaN or dielectric-AlGaIn interface. While specific failure mechanisms have yet to be identified, it is clear that these states may play a role in gate leakage and current collapse. Recent efforts to improve performance of high power devices have focused on the role of a high-k dielectric as a gate oxide between the gate metal and AlGaIn/GaN and as a surface passivation layer between the gate and source-drain contacts. The use of a specific dielectric requires a large band gap and band offsets that confine carriers in the semiconducting layers. Moreover, the concentration of the 2DEG is directly affected by the presence of interface states and defect states associated with the dielectric. In this research, we have employed remote plasma enhanced ALD (PEALD) and *in-situ* photoemission spectroscopy to prepare and characterize different dielectric layers on GaN and AlGaIn surfaces. The *in-situ* x-ray and UV photoemission (XPS and UPS) measurements provide insight into the interface bonding, presence of impurities, band alignment, and band bending, which indicate the presence of defects. This report will concentrate on the properties of PEALD Al₂O₃ and HfO₂ layers on AlGaIn and GaN on both the Ga-face and N-face. Results establish that the band alignment is relatively independent of processing and may be described by the charge neutrality level model. In contrast, the band bending is dependent on processing and can be directly related to the presence of charged defect states at the interface and in the dielectric. The wet chemical and *in-situ* surface cleaning processes and the PEALD growth affect the band bending, resulting in similar band bending regardless of the surface polarization. This consistency indicates the presence of interface states that compensate the polarization charge on Ga- and N-face surfaces even though the polarization charge is opposite in sign and for GaN and AlGaIn surface where the polarization charge increases by a factor of two. The interplay of polarization and the defect states and the 2DEG properties are discussed for the different dielectric layers and processing approaches.

Research is supported by ONR through DEFINE MURI.

4:00pm **EM-WeA7 Graphene-based Vertical Heterostructures and Tunneling Field Effect Transistors.** *K. Lee, K. Kim, B. Fallahzad, S. Larentis, M.S. Points, E. Tutuc, The University of Texas at Austin* **INVITED**

We discuss the realization of vertical heterostructures consisting of two-dimensional materials, such as graphene and transition metal dichalcogenides, using a layer-by-layer transfer approach. We demonstrate double layer heterostructures consisting of two graphene layers separated by a thin hexagonal boron nitride dielectric, with layer mobilities as high as 200,000 cm²/Vs. We discuss the in-plane electron transport as a function of temperature and in magnetic fields, as well as the tunneling between the two layers, which can be used as basis for vertical field-effect transistors.

4:40pm **EM-WeA9 Quantum Mechanical Corrections for Accurate and Rapid Analysis of III-V/High-k MOS Devices.** *R. Galatage, C.L. Hinkle, University of Texas at Dallas, E.M. Vogel, Georgia Institute of Technology*

The measurement, modeling, and extraction of MOS relevant parameters from high-k on III-V semiconductors is significantly more challenging than that for Si gate stacks. Oxidation of the III-V material during high-k deposition leads to an extremely high interface trap density (D_{it}) as well as tunneling of carriers into defects further away from the interface. Additionally, the exact band structure of III-V semiconductors is a matter of ongoing research,¹ and the effects of band non-parabolicity and quantization have not been thoroughly investigated. Each of these considerations is crucial in the proper analysis of III-V MOS devices.

Due to the high electric fields, quantum mechanical effects have a significant impact on the electrical properties of scaled MOS devices. In

accumulation and inversion, quantization results in the splitting of the once continuous energy bands into discrete subbands and moves the charge centroid away from the semiconductor/dielectric interface. Both of these effects reduce the inversion and accumulation charge density at a given gate bias resulting in both a threshold and flatband voltage shift, as well as a reduction in the inversion and accumulation capacitances. Therefore, it is imperative that quantum mechanical effects be considered to accurately extract the EOT, V_{fb} , and D_{it} when researching these devices. Full Schrodinger/Poisson solvers are available to calculate the carrier concentration in a physically accurate and self-consistent manner. However, these calculations take considerable computation time and cannot be used to extract parameters from an experimental data set.

In this work, we implement quantum mechanical corrections to *rapidly extract* relevant III-V MOS C-V parameters by approximating the quantization effects as an effective increase in the semiconductor bandgap in accumulation and inversion in a manner similar to that of van Dort for Si.^{2,3} When coupled with non-parabolic energy bands, these approximations are shown to be quite accurate in modeling and extracting the characteristics of III-V/high-k devices. These approximations have been rigorously tested against experimental III-V devices as well as benchmarked with full Schrodinger/Poisson solutions to ensure their accuracy. This implementation allows for the rapid assessment of III-V parameters.

This work is sponsored by the SRC Global Research Corporation.

1 T. P. O'Regan, et al., *Applied Physics Letter*, 96,103705, 2010.

2 M. J. Van Dort, *Solid-State Electronics*, 37, 411, 1994.

3 E. M. Vogel, et al., *Solid State Electronics*, 47, 1589, 2003.

5:00pm **EM-WeA10 The Physics and Challenges of Realizing High Performance Group IV Tunnel Transistors.** *J.C.S. Woo, H.-Y. Chang, B. Adams, P.-Y. Chien, J. Li, University of California at Los Angeles* **INVITED**
Reducing the standby power ($I_{OFF} \cdot V_{DD}$) and operation power ($C_g V_{DD}^2 \cdot f$) are crucial for low power application in MOSFET scaling. Hence, it becomes essential to lower I_{OFF} and to scale V_{DD} , and therefore devices with steep subthreshold swing (SS) are highly desired in low power application [1].

In conventional MOSFETs, the subthreshold swing is limited by thermal diffusion current (≥ 60 mV/dec at $T=300$ K). To overcome this limit, novel devices based on the band-to-band tunneling mechanism, namely tunnel FET (TFET), is proposed. It has been reported that TFETs can achieve ultra-high I_{ON}/I_{OFF} under reduced V_{DD} and steep SS (<60 mV/dec), which makes it a competitive candidate for low power application [2-3]. However, reported results so far show that TFET can only provide small I_{ON} and achieve steep SS under low current level. These short comes may prevent TFET from entering main stream.

To resolve these challenges, it is important to understand the physics of TFET. Based on these insights, small band-gap materials such as SiGe and Ge have been proposed to improve carrier tunneling by lowering the tunnel barriers [4-5]. It is also critical to improve carrier tunneling (that is, reducing the tunneling distance) by enhancing lateral electric field across the tunneling junction. TFETs with dopant pocket between source and channel are reported as one of the devices to achieve small tunneling distance [6]. In this talk, n-i-p Si TFET with p⁺ pocket source fabricated by laser annealing is proposed and investigated. By the application of source pocket in TFET, the tunneling distance is reduced due to enhanced electric field across the tunneling junction. The steep SS (46 mV/dec), excellent I_{ON}/I_{OFF} ratio ($>10^7$) and improved output characteristics are observed in the experiment data at $T=300$ K. The device performance of this TFET under low temperature measurement is also used to confirm the band-to-band tunneling mechanism. Finally, compared to other TEFTs, the TFET with source pocket is one of the most promising structures to improve the device characteristics of TFETs.

[1] R. Jhaveri et al., *Trans. Elec. Dev.*, vol. 58, no. 1, pp. 80-86, 2011.

[2] F. Mayer et al., *IEDM Tech. Dig.*, 2008, pp. 163-166.

[3] K. Jeon et al., *VLSI Symp. Tech. Dig.*, 2010, pp. 121-122.

[4] D. Kazazis et al., *Appl. Phys. Lett.*, vol. 94, no. 26, pp. 263508-1 - 263508-3, 2009.

Graphene and Other 2D Materials Focus Topic
Room: 104 B - Session GR+AS+EM+NS+SS-WeA

Dopants, Defects and Interfaces in 2D Materials

Moderator: B.J. LeRoy, University of Arizona, A. Sinitskii, University of Nebraska-Lincoln

2:00pm **GR+AS+EM+NS+SS-WeA1 Atomic Force Acoustic Microscopy Detecting Defects in Graphene-Substrate Interface, Q. Tu, Z. Parlak, R. Ferris, S. Zauscher, Duke University**

Graphene has extraordinary mechanical and electrical properties and has been demonstrated wide applications in flexible electronics and sensors. Most of the graphene-based devices functionalizes with graphene on a substrate. The conformation of graphene to the substrate and the bonding between graphene and substrate[1] will influence the electronic properties of graphene[2] and the stress transferred from the substrate to graphene, which is a big issue of device stability. Herein we show that the defects in graphene-substrate interface could be nondestructively detected by atomic force acoustic microscopy (AFAM), which is a dynamic AFM technique sensitive to the tip-sample contact stiffness. The contact stiffness mapping indicates that the graphene covered silicon was softer than uncovered area, which contradicts that graphene is the stiffest material ever known. This is due to the cavity and water molecules present in the graphene-substrate interface. With the topography data, a layered structure model is built up and the simulated contact stiffness mapping matches the experiment well. In addition, graphene was transferred to a substrate with patterned surface chemistry and the contact stiffness in hydrophobic area is higher than that in hydrophilic area, which indicates that reducing water molecules in the interface would increase the graphene-substrate contact.

[1] L. H. Liu and M. D. Yan, "Simple Method for the Covalent Immobilization of Graphene," vol. 9, pp. 3375-3378, Sep 2009.

[2] M. Lafkioti, B. Krauss, T. Lohmann, U. Zschieschang, H. Klauk, K. von Klitzing, and J. H. Smet, "Graphene on a Hydrophobic Substrate: Doping Reduction and Hysteresis Suppression under Ambient Conditions," vol. 10, pp. 1149-1153, Apr 2010.

2:20pm **GR+AS+EM+NS+SS-WeA2 Polarization Induced p-type Doping in the H-intercalated Epitaxial Graphene on SiC(0001), S. Rajput, M. Chen, Y.Y. Li, M. Weinert, L. Li, University of Wisconsin Milwaukee**

Hydrogen intercalation at the epitaxial graphene/SiC(0001) interface was achieved by annealing in hydrogen atmosphere at 800 °C. Raman spectroscopy, scanning tunneling microscopy and spectroscopy measurements were performed to determine the electronic and structural properties of the H-intercalated graphene. We find that while the as-grown graphene is n-type with the Dirac point at -0.35 eV below Fermi level, the H-intercalated graphene is p-type with a Dirac point +0.2 eV above the Fermi level. These results are explained by density functional theory calculations, which indicate that the carrier type and concentration in H-intercalated graphene/SiC are determined by the spontaneous polarization of the hexagonal SiC substrate.

2:40pm **GR+AS+EM+NS+SS-WeA3 Engineering Chemical Dopants in Monolayer Graphene, A. Pasupathy, Columbia University INVITED**

Chemical doping is a promising route to achieve control over the carrier concentration in graphene. I will describe recent experiments on the growth of graphene that is chemically doped using nitrogen and boron atoms. Using a combination of scanning tunneling microscopy, Raman and x-ray spectroscopies, we are able to obtain a picture of the chemical and electronic structure of doped graphene from the atomic to the macroscale. At the atomic scale, I will describe the local bonding of nitrogen and boron dopants and their effect on free carrier concentration in the graphene sheet. At larger length scales, I will show that nitrogen dopants avoid edges and grain boundaries of the graphene film over length scales that can be as large as a micron. I will also discuss dopant clustering and show that nitrogen and boron behave very differently in this respect. Understanding these various effects requires us to consider both the mechanism by which graphene grows by chemical vapor deposition, and the interaction between the dopant atoms and the underlying substrate during growth.

4:00pm **GR+AS+EM+NS+SS-WeA7 Water-Induced Splitting of Epitaxial Graphene and Resulting Graphene Flake, X. Feng*, M.B. Salmeron, Lawrence Berkeley National Laboratory**

Epitaxial graphene on metal substrates has been demonstrated to be a promising route for graphene synthesis. The produced graphene is however typically polycrystalline, with defects that can affect its properties. The impact of defects might be critical when graphene interacts with gas molecules due to their enhanced reactivity, so there is a need to understand the adsorption of environmentally abundant molecules (such as water and oxygen). Here we report a study of water adsorption on epitaxial graphene on Ru and Cu substrates using scanning tunneling microscopy (STM). We found that on Ru(0001), graphene line defects are extremely fragile towards chemical attack by water, which splits the graphene into numerous fragments at temperatures as low as 90 K, followed by water intercalation under the graphene [1]. On Cu(111) water can also split graphene but far less effectively, indicating that the chemical nature of the substrate strongly affects the reactivity of C-C bonds in epitaxial graphene.

The graphene splitting produced many graphene flakes that were displaced onto the first graphene layer on Ru. These flakes show very facile translational and rotational motions between commensurate initial and final states at temperatures as low as 5 K. The motion is initiated by a transition of the flakes from a commensurate to an incommensurate registry with the underlying graphene (the superlubric state), followed by a rapid sliding until another commensurate position is reached [2]. We also studied the electronic screening effects in stacked graphene flakes on Ru. The screening affects the apparent STM height of each flake in successive layers reflecting the density of states near the Fermi level and thus the doping level. It is revealed in this way that the strong doping of the first graphene layer on Ru(0001) is attenuated in the second one, and almost eliminated in the third and fourth layer [3].

References:

[1] X. Feng, S. Maier and M. Salmeron. *J. Am. Chem. Soc.* **134**, 5662–5668 (2012).

[2] X. Feng, S. Kwon, J. Y. Park and M. Salmeron. *ACS Nano* **7**, 1718–1724 (2013).

[3] X. Feng and M. Salmeron. *Appl. Phys. Lett.* **102**, 053116 (2013).

4:20pm **GR+AS+EM+NS+SS-WeA8 STS Observation of Landau Levels on the Flat Area of Nitrogen-doped HOPG Surface under the Zero Magnetic Fields, T. Kondo, D. Guo, T. Sikano, T. Suzuki, M. Sakurai, J. Nakamura, University of Tsukuba, Japan**

The charge carriers in graphene are known to follow a relativistic Dirac equation and behave as massless Dirac fermions [1]. In a magnetic field, massless Dirac fermions in graphene exhibit a relativistic Landau-level quantization and an anomalous quantum Hall effect [2,3]. The Landau-level energy sequence in graphene (single layer) shows a square-root dependence on both the magnetic field and the Landau index n , where a zeroth Landau level appears at the Dirac point. However, we have recently reported based on the scanning tunneling spectroscopy (STS) that the Landau levels of massless Dirac fermions generate in the absence of an external magnetic field on a partially potassium-intercalated highly oriented pyrolytic graphite (K-HOPG) surface [4]. The observation of the Landau levels of massless Dirac fermions indicates appearance of the graphene characters in K-HOPG. The generation of the Landau levels is ascribed to a vector potential induced by the perturbation of nearest-neighbour hopping, which may originate from a strain or a gradient of on-site potentials at the perimeters of potassium-free domains. There are other reports that the strain of graphene induces the Landau levels generation under the zero magnetic fields [5-8]. Here, we report the generation of the Landau levels of massive Dirac fermions on a nitrogen-doped graphite (N-HOPG) surface without strain under the zero magnetic fields. The pseudomagnetic fields are estimated to be as much as 60 T. Landau levels are observed at the flat area of the N-HOPG surface and thus the strain can be excluded as the possible origin of the perturbation of nearest-neighbour hopping. According to XPS, STM, and STS, our N-HOPG sample was found to consist mainly of the graphitic-N species which has a positive charge and modulates a potential on the surface [9]. Therefore, the generation of the Landau levels on N-HOPG is probably originated from a gradient of on-site potentials of carbon across the domain of the equipotential contour induced by the dopant graphitic-N species of N-HOPG.

[2] K.S.Novoselov, *et al.* Nature 438, 197 (2005).

[3] Y. Zhang, *et al.*, Nature **438**, 201 (2005).

[4] D.Guo, T.Kondo, J.Nakamura *et al.*, Nature Communications **3**, 1068 (2012).

[5] N.Levy, *et al.* Science **329**, 544 (2010).

*** Morton S. Traum Award Finalist**

- [6] H. Yan, et al., Phys. Rev. B 85, 035422 (2012).
 [7] K.K.Gomes, et al., Nature, 483, 306 (2012).
 [8] J. Lu, A.H. C. Neto and K.P.Loh, Nature Communications 3, 823 (2012).
 [9] T.Kondo, S.Casolo, J.Nakamura, et al., Phys. Rev. B 86, 035436 (2012).

4:40pm **GR+AS+EM+NS+SS-WeA9 X-ray Photoelectron Spectroscopy Investigation of the Band Alignment at h-BN/Graphene/High-k Dielectric Interfaces**, *M. Paquette, J. Otto*, Univ. of Missouri-Kansas City, *S.W. King, J.D. Bielefeld, M. Jaehnig, M. French, B. French, M. Kuhn*, Intel Corp., *B. Nordell, A.N. Caruso*, Univ. of Missouri-Kansas City, *Y. Song*, MIT, *R. Caudillo*, Intel Corp., *J. Kong*, MIT
 Due to a wide band gap (~ 6 eV), close lattice matching (< 2%) and atomic planarity, hexagonal boron nitride (h-BN) is of interest as a potential substrate and gate dielectric in graphene channel transistor devices. A key property for the success of h-BN as a gate dielectric in such devices is its interfacial band alignment with graphene, the gate contact metallization and the surrounding insulating dielectric materials. In this regard, we have utilized x-ray photoelectron spectroscopy (XPS) to determine the Schottky barrier and valence band offsets present at the interfaces between plasma enhanced chemically vapor deposited amorphous h-BN:H and a variety of materials including graphene, Cu, SiO₂, a-SiN_x:H, a-SiC:H, and Si. In combination, we have also investigated the valence band alignment between graphene and various high-k dielectrics including Al₂O₃, HfO₂, ZrO₂, and TiO₂. Combined with reflection electron energy loss spectroscopy measurements of the band gaps for the respective dielectric materials, we have also been able to determine the conduction band offset at these interfaces. We show that in many instances the valence and conduction band offsets are significant (> 2 eV) and favorable for a variety of possible h-BN/graphene transistor devices.

5:00pm **GR+AS+EM+NS+SS-WeA10 Epitaxial Graphene Bands and Adsorption of FePc for Stepped SiC-Si Surfaces**, *J.E. Rowe, D.B. Dougherty, A.A. Sandin*, North Carolina State University, *A. Al-Mahboob, J.T. Sadowski*, Brookhaven National Laboratory

We have conducted a number of experimental measurements of the adsorption system FePc on stepped and unstepped graphene surfaces which may become important for spin-dependent electronics. Our studies were partially conducted using the PEEM beamline as NSLS, the Brookhaven synchrotron facility and we studied epitaxial graphene grown in UHV on 6H and 4H Si surfaces of SiC. In addition, we have measured changes in graphene bands using local area angle-resolved photoemission spectroscopy (ARPES) and normal emission PES for these surfaces both before and after adsorption of Iron Phthalocyanine (FePc). This is to understand the interactions of the FePc as an alternate approach to spin injection into graphene by the use of planar organic molecules as interfacial layers to enhance spin injection. Since weak intermolecular interactions can be comparable in size to molecule-substrate interactions for planar aromatics on graphene, high quality film growth is more likely. We have studied using PEEM, LEEM and STM the growth of iron phthalocyanine (FePc), a chemically-robust paramagnet, on epitaxial graphene on SiC(0001)-Si for the above mentioned surfaces. Ordered monolayer films are obtained on all surfaces with exposure and post-deposition annealing. Stepped surfaces introduces some preferred orientation domain formation as expected. Details of the PES and ARPES studies are discussed as well as LEEM images that clearly show step-flow growth of graphene.

5:20pm **GR+AS+EM+NS+SS-WeA11 Atomic Collapse in Graphene: Exploring Tunable Charge Impurities at the Nanometer Scale**, *M.F. Crommie, Y. Wang, D. Wong*, University of California, Berkeley, *V.W. Brar*, California Institute of Technology, *H.-Z. Tsai, S. Choi, W. Regan*, University of California, Berkeley, *R. Kawakami*, University of California, Riverside, *A.V. Shytov*, University of Exeter, UK, *A. Zettl, S.G. Louie*, University of California, Berkeley, *L.S. Levitov*, Massachusetts Institute of Technology

INVITED

Graphene has unique electronic properties that arise from its 2D honeycomb structure and which cause novel behavior at the atomic scale. This can be seen in graphene's response to charged impurities, where graphene's ultra-relativistic nature leads to impurity states that are unlike those found in any other material. The physics of Coulomb impurities on graphene is divided into two regimes: subcritical and supercritical. In the subcritical regime no bound states form around the impurity. When the impurity charge exceeds the threshold for supercritical behavior, however, "atomic collapse" states are predicted to emerge. Such states are different from semiconductor impurity states in that their wave functions are composed of a near-field collapsing electron-like component that is coupled via Klein tunneling to a far-field hole-like component that escapes to infinity. We have explored such impurity states across different impurity-charge regimes by building charge centers (i.e., "artificial nuclei") atom-by-atom at the surface of

graphene devices and probing them via scanning tunneling microscopy. New results on this topic, including the observation of "atomic collapse" [1], will be discussed.

References:

- [1] Y. Wang, D. Wong, A. V. Shytov, V. W. Brar, S. Choi, Q. Wu, H.-Z. Tsai, W. Regan, A. Zettl, R. K. Kawakami, S. G. Louie, L. S. Levitov, M. F. Crommie, "Observing Atomic Collapse Resonances in Artificial Nuclei on Graphene", *Science*, DOI:10.1126, March 7, 2013.

Accelerating Materials Discovery for Global Competitiveness Focus Topic

Room: 202 B - Session MG+EN+MS-WeA

Education for Interactive R&D & Industrial Implementation

Moderator: C. Eom, University of Wisconsin-Madison, B. Nelson-Cheeseman, University of St. Thomas

2:00pm **MG+EN+MS-WeA1 21st Century Skills and Educating the Next Generation Workforce for Expedited Innovation and Deployment**, *C.C. Broadbridge*, Southern Connecticut State University **INVITED**

The goal of the Materials Genome Initiative [MGI] is to expedite materials discovery, innovation and deployment via the development of new approaches to materials research that exploit interdisciplinary collaboration and innovation. Successful implementation will require a workforce possessing 21st Century Skills including critical thinking, problem solving, communication, collaboration, technological fluency and creativity. To address the need for US competitiveness in a global economy, educational reform has been initiated at the K-12 level with the development of 21st Century Skills Standards [1], Common Core Standards [2] and the Next Generation Science Standards [3]. Similar reform is needed at the university and post-graduate [PG] professional development levels to assure the optimal development of a STEM educational pipeline. At the university level, reform has been initiated with the development of novel approaches to all university [non-major] requirements as well as courses and programs for majors (e.g., [4,5]). For the effective implementation of the MGI, it is important to realize the natural synergies that exist between these efforts and those within the materials science education and research communities. Arguably, individuals acquire and refine these necessary skills best via exposure to, and active participation in, authentic science research. NSF funded Materials Research Science and Engineering Centers [MRSECs] support interdisciplinary and multidisciplinary materials research and outreach components that effectively integrate the collaborative and innovative aspects of materials research. Components are developed and implemented at the K-PG levels and also include programs that educate the general public. For this presentation, educational reform at all levels will be reviewed with an emphasis on approaches with the greatest potential positive impact on the implementation of the MGI. In particular, an interdisciplinary team-based approach to materials research effectively leveraging programs within the Center for Research on Interface Structures and Phenomena (CRISP) MRSEC will be described that integrates materials science education and research while maximizing on the attainment of the 21st Century Skills necessary for successful implementation of the MGI.

1. <http://www.p21.org/overview/skills-framework/351>
2. <http://www.corestandards.org/>
3. <http://www.nextgenscience.org/>
4. <http://www.aacu.org/resources/generaleducation/index.cfm>
5. <http://www.tms.org/pubs/journals/jom/0910/thornton-0910.html>
6. <http://www.mrsec.org/>

2:40pm **MG+EN+MS-WeA3 High-Performance Ceramics – Challenges for Next Generations**, *W. Rossner, S. Lampenscherf*, Siemens AG, Germany **INVITED**

Ceramics play an important role in system engineering for demanding industrial applications because they provide functionality of key components that are critical for overall system performance and operational benefit. The continuous development of high performance ceramics over the last decades was aiming mainly towards 'better' properties and 'deeper' understanding of material behaviour.

For today's applications in areas such as power engineering, medicine, automotive, aircraft and high-end electronics the time-to-market aspect is an important success factor. Product cycles become shorter while R&D cycles

especially including materials development are not able to keep up with such pace. The complex relationship between ceramic performance and processing plays a special role for accelerating the R&D process. An additional time-consuming factor is the need for extensive qualification and testing of high-performance ceramics to guarantee functionality and reliability under desired operation conditions.

Based on the very much improved understanding of the dependencies of processing, performance and application as well as the availability of advanced computational methods and tools materials engineering can be a vital part to overcome today's limitations for accelerating materials development and product implementation.

In the talk we discuss these aspects in the context of current industrial examples for next generation high performance ceramics.

4:00pm MG+EN+MS-WeA7 Educating for High-Impact Computation - Skills vs. Acceptance, W.E. Windl, The Ohio State University INVITED

As an integral part of the Materials Genome Initiative (MGI), the task of materials computation, in concert with experiment and theory, is to help accelerate the discovery and maturation of new materials by at least a factor of two. During the first rounds of MGI-related solicitations, two major groups of challenges that always existed became very evident. For one, the obvious question about the skill set available in the Materials Research community to actually perform the necessary computations. Secondly, and much less apparent on the surface, was the frequent lack of acceptance of computational work as a valid input, maybe foremost in the experimental community, which can lead to awkward situations, missed opportunities, and frustration in collaborative projects. Beginning with the 2012-2013 academic year, The Ohio State University has moved from a quarters-based academic calendar to a semesters-based calendar. As part of this change, the Department of Materials Science and Engineering has elected to revise degree program curricula in a significant manner. A key objective in our revision was to respond to the challenges in skill set and acceptance of computational work from Integrated Computational Materials Engineering and MGI described above. We have developed a curriculum that attempts to integrate congruently database use, visualization, simulation and computational approaches in materials science with other core educational content. At the undergraduate level, our goal was to produce graduates who are cognizant of the broad range of computational tools available to materials engineers and what they can do to solve engineering problems, and who are able to use a number of those tools proficiently to solve problems of practical importance themselves. The MSE core curriculum includes 9 credit hours (four courses), or 20% devoted to these topics. Students may take an additional 4 credit hours (two courses) in elective content on computational methods in materials science. In this presentation, details will be presented on the specific course offerings, course content, exercises, and software packages used. How the courses are postured in the curriculum will also be addressed. The experiences, challenges, and recommendations resulting from the first year of teaching will finally be discussed, where the author was involved in four different courses relying on different combinations of traditional teaching with reverse and peer teaching approaches as well as with significant fractions of active-learning work.

4:40pm MG+EN+MS-WeA9 MGI in the Laboratory: Closing the Feedback Loop in Aerospace Materials Design and Development, E. Sapper, P. Kinlen, Boeing Research & Technology INVITED

The aerospace industry has continuously driven major developments in material science as technology has evolved from wood and fabric to lightweight metal alloys and advanced polymer composites. Future aerospace materials systems will require even more advanced technologies, such as those afforded by smart and responsive systems like electroactive polymers and composites. The unique properties of these materials provide the ability to construct intelligent systems which produce a defined, predictable response to an input.

Concurrent with state-of-the-art chemical technology, the increasing availability of high-performance computing power has facilitated the entry of various computational simulation and modelling methods into the research and development production cycle. Quantum mechanics, molecular dynamics, and multi-scale simulation approaches, developed and applied within a Materials Genome Initiative paradigm, are providing insight into aerospace material properties of interest, such as species-specific transport rates, electrochemical response, service lifetime prediction, material color and appearance, and quantitative structure-property relationships.

The ultimate goal of a coupled experimental-computational approach is the closed and tightened feedback loop between laboratory results and computational predictions. This leads to the incorporation of more theory into experimental practice as well as more heuristics into computational method development, expressed in the form of semi-empirical models and empirically-pinned property response surfaces. This presentation will

review some of the challenges involved in applying advanced computational methods alongside state-of-the-art laboratory procedures. The development of novel, more environmentally friendly aerospace coatings that release site-specific corrosion inhibitors on-demand will be presented as a case-study in closed-loop computation-experimentation.

5:20pm MG+EN+MS-WeA11 Condensed Matter Physics in an Age of Computation, M. Marder, University of Texas at Austin INVITED

Condensed matter physics and materials physics have grown so enormously that no one can hope to know everything done in the last five years let alone the last fifty. This does not relieve researchers of the charge of educating new generations of students. I will discuss the balance between acquisition of skills and acquisition of knowledge, and the way that computing power changes what is taught and how.

**Nanometer-scale Science and Technology
Room: 203 B - Session NS+BI+EM-WeA**

Nanopatterning and Nanolithography

Moderator: P.E. Sheehan, Naval Research Laboratory

2:20pm NS+BI+EM-WeA2 Tunneling Electron Induced Adsorption of Copper Phthalocyanine on the Cu(111) Surface, T. Stock*, J. Nogami, University of Toronto, Canada

The adsorption of up to one monolayer (ML) of copper phthalocyanine (CuPc) molecules on a room temperature Cu(111) surface has been studied using scanning tunneling microscopy (STM) and scanning tunneling spectroscopy (STS). Below 1 ML the molecules are in a fluid state and are highly mobile on the surface. At 1 ML coverage the molecules coalesce into a highly ordered 2D crystal phase. At sub-ML coverages, adsorption of individual CuPc molecules can be induced through exposure to tunneling electrons at a bias voltage exceeding a threshold value. This tunneling electron induced adsorption effect allows for a novel variety of molecular STM lithography, and permits probing of the mechanisms involved in the adsorption of individual molecules.

2:40pm NS+BI+EM-WeA3 STM Study of Pyramid Structures on Ge(110) Formed by Argon Ion Sputtering, M.S. van Zijll, S. MacIntyre, S. Chiang, University of California, Davis

Defects often act as nucleation points for island growth on surfaces. Earlier studies found that sputtering surfaces of silicon and germanium could create ordered arrays of dot and ripple structures. As a result of the sputtering and annealing cleaning procedures on Ge(110), we had previously observed the formation of pyramid structures, which could serve as engineered defects for island growth. Although these structures had some similarities to the dot patterns observed by other groups, the better defined shapes and the larger separation between the pyramid structures were striking. In an effort to better understand and control the formation of these defects, we used scanning tunneling microscopy (STM) under ultra high vacuum (UHV) conditions to measure the shapes, sizes, and spatial distribution of the observed pyramid structures on Ge(110) as a function of the argon ion sputtering energy. The samples were sputtered with low-energy ions ranging from 200eV to 500eV at an incident angle of 34°. The bases of the pyramids are rhombuses due to the 16x2 reconstruction of the Ge(110) surface. The lengths of the rhombuses range from 10 to 80nm, and the side-walls slant upward at ~4° from the horizontal. A Monte Carlo simulation of the sputtering process is used to determine the dependence of the sputtering yield on the binding energy of the surface atoms and on the incident ion energy, thereby giving insight into the process of pyramid formation.

3:00pm NS+BI+EM-WeA4 Enhanced Electrical Conductivity by Au Nanoparticle Islands Deposited from Solution, F. Jiang, A.J. Muscat, University of Arizona

Colloidal Au nanoparticles (NPs) capped with tetraoctylammonium bromide (TOAB) were synthesized using the Brust method, and deposited on oxidized p-type Si(100) covered by either 3-aminopropyltrimethoxysilane (APTMS) or 3-mercaptopropyltrimethoxysilane (MPTMS). Dip coating was used to deposit the Au NPs with nominal diameters of 5-20 nm using the linker 1,2-ethanedithiol (EDT). One coating cycle consisted of immersion in the Au NP colloid for 1 h, rinsing in toluene, immersion in EDT for 1 h, and rinsing in toluene. Deposits were made of one half-cycle (NPs only) up to 9 complete cycles. After deposition the samples were annealed for 1 h at 300°C in flowing N₂, which removed at least 85% of the organic

*** NSTD Student Award Finalist**

compounds based on FTIR. SEM and cross-sectional TEM showed that after 9 cycles, 40% of the surface was covered with small islands consisting of clusters of Au NPs that were 10-20 nm in diameter and 20-30 nm apart from one another. AFM showed that the heights of the islands were also 20-30 nm. FTIR also showed that EDT replaced only half of the TOAB on the surface, suggesting that island growth is caused by TOAB ligands blocking binding sites. Current-voltage (IV) measurements were made by clamping two Cu terminals with a contact area of 6 mm² to the surface of a sample, separated by a distance of 10 mm. The film stack consisted of a) p-type Si substrate, b) 1.6 nm silicon oxide layer, c) 0.7-3 nm silane layer, and d) Au islands. A control experiment in which the Au NP islands were replaced by two 20 nm thick e-beam deposited Au films separated by a 10 nm gap yielded a sigmoidal IV curve due to current flow through the p-type Si substrate and possibly to lateral charge transfer through the APTMS monolayer. The Au NP islands increased the current flow at negative bias relative to the control. The Au NP islands could reduce the contact resistance or electrons could hop or tunnel between islands, through the underlying silane layer. Compared to the nanometer scale 1D Au NP arrays on BNNTs reported in the literature, electron transfer over such a large area found in this study could be used to scale up the class of semiconductor-free transistors that operate based on electron tunneling and could contribute to other applications that require effective local charge transfer, such as the seed layer for electro- and electroless deposition.

4:00pm NS+BI+EM-WeA7 Nanoimprinted Amorphous Metals for Energy Applications, J. Schroers, A.D. Taylor, R.C. Sekol, Yale University, G. Doubek, IPEN, Brazil, G. Kumar, Texas Tech University, M. Carmo, Forschungszentrum Jülich GmbH, Germany, F. Gittleson, N. Hardesty-Dyck, Yale University, S. Mukherjee, University of North Texas
INVITED

Here we report a unique CMOS compatible approach using bulk metallic glass Pt₅₈Cu₁₅Ni₅P₂₂ (Pt-BMG) [1] to create high performance fuel cell catalysts. We have shown that these materials can be nanoimprinted into ~10 nm diameter rods with aspect ratio up to 200 [2]. A nanoporous Al₂O₃ was used as a template to create the nanorod surface. The Pt-BMG is heated into the supercooled liquid region where it softens and can be thermoplastically imprinted. Under an applied pressure (ca. 50 MPa) the Pt-BMG fills the nanopores. An additional step can separate the nanorods from the reservoir [3]. The uniformly vertical nanorods are well-isolated and parallel to one another.

Our results show that these materials are highly active with lower onset potentials for CO, methanol, and ethanol oxidation [4]. In this talk we will demonstrate how these BMG systems can also serve as a platform for stategically designed catalyst systems. As a proof of concept we have modified the surface of a Pt-BMG by depositing ruthenium using underpotential deposition. We show that this approach facilitates the fabrication of multicomponent nanowires having elements outside of the glass formability with enhanced methanol oxidation beyond the initial Pt-BMG.

References:

1. Schroers, J. and W.L. Johnson, *Highly processable bulk metallic glass-forming alloys in the Pt-Co-Ni-Cu-P system*. Applied Physics Letters, 2004. **84**(18): p. 3666-3668.
2. Kumar, G., H.X. Tang, and J. Schroers, *Nanomoulding with amorphous metals*. Nature, 2009. **457**(7231): p. 868-872.
3. Schroers, J., Q. Pham, and A. Desai, *Thermoplastic forming of bulk metallic glass - A technology for MEMS and microstructure fabrication*. Journal of Microelectromechanical Systems, 2007. **16**(2): p. 240-247.
4. Carmo, M., et al., Bulk Metallic Glass Nanowire Architecture for Electrochemical Applications. *ACS Nano*, 2011. **5**(4): p. 2979-2983.

4:40pm NS+BI+EM-WeA9 Submicron Cylindrical Gratings for Rotation Sensors, J. Laukkanen, University of Eastern Finland, S. Tonchev, Y. Jourlin, S. Reynaud, CNRS, France, H. Hirshy, S.G. Scholz, Cardiff University, UK, O. Parriaux, CNRS, France

We demonstrate a production chain for making submicron gratings on the wall of a cylinder. Gratings of this kind can be used, for example, in rotation sensors. We have converted a conventional 2D interference lithography setup into 3D setup by using a circularly symmetrical planar high index phase mask [1]. With this method, a lot smaller period is achieved than with CNC tools, which are commonly used for similar structures.

A planar phase mask was made in CVD-grown silicon nitride (Si₃N₄) on top of a quartz mask plate using electron beam lithography and reactive ion etching. Silicon nitride was chosen as a grating material because of its high refractive index and therefore ability to cancel zeroth order transmission [2]. In photolithography, a specially made glass cylinder was used as a substrate and it was coated with photoresist by dip coating. The phase mask was

illuminated with radially polarized light in oblique incidence creating an interferogram on the resist coated wall of a cylinder. The produced stitchingless grating lines were over one millimeter long.

In order to be able to mass produce these cylindrical gratings a nickel mold was done using electroforming like in LIGA process [3]. The nickel mold can then be used in injection molding. With this fabrication method, we can control the exact number of lines and spaces and have a constant period over the whole round of the cylinder, which is crucial for high precision rotation sensors.

[1] S. Tonchev, Y. Jourlin, C. Veillas, S. Reynaud, N. Lyndin, O. Parriaux, J. Laukkanen, and M. Kuittinen, "Subwavelength cylindrical grating by holistic phase-mask coordinate transform," *Optics Express*, **20**, 7946-7953 (2012).

[2] E. Gamet, A. V. Tishchenko, and O. Parriaux, "Cancellation of the zeroth order in a phase mask by mode interplay in a high index contrast binary grating," *Applied Optics*, **46**, 6719-6726 (2007).

[3] W. Bacher, W. Menz, J. Mohr, "The LIGA technique and its potential for microsystems-a survey," *Industrial Electronics, IEEE Transactions on*, **42**, 431 (1995).

5:00pm NS+BI+EM-WeA10 DNA Assembly on Nanopatterns Created by Electron Beam Lithography, A.K. Pradhan, Norfolk State University

A major goal of nanotechnology is to couple the self-assembly (SAMs) of molecular nanostructures with conventional micro as well as nanofabrication, for instance the so-called bottom-up and top-down fabrication methods would enable us to register and recognize individual molecular nanostructures in order to integrate them electronically into functional devices. However, the integration of top-down (lithographic pattern) with bottom-up (functionalizing with synthetic chemical) approaches remains a central challenge in nanofabrication. We demonstrate that the selective self-assembly of DNA nanostructures can happen on electron beam lithographically patterned surfaces at lower energy. The fluorescent dye coupled amine modified DNA nanostructures were selectively attached to the patterned glass substrates. The optimized binding interaction between self-assembled DNA nanostructures occurred preferably at lower beam energy due to the attractive energy between the pattern and DNAs. Patterns containing self-assembled DNA molecules with dimensions as small as 2 nm in height and 68 nm in width have been successfully demonstrated. The periodicity in DNA self-assembly was observed. This technology of combination of "top-down" fabrication and "bottom-up" self-assembly may find use wherever there is a need to attach self-assembled DNA molecules in a nanometer scale patterned surface for various applications.

5:20pm NS+BI+EM-WeA11 Organic Resist Materials for sub-20 nm Patterning: Robust Materials Enabled by Crosslinking Based Designs, C. Henderson, R. Lawson, A. Cheshmehkhani, Georgia Institute of Technology

Future scaling of integrated circuits (IC) is in jeopardy due to a number of challenges related to both future material and process requirements that are needed to allow for fabrication of sub-20 nm IC devices. One of the most critical challenges is that of developing patterning technologies that can allow for formation of sub-20 nm patterned structures in a fast and economically viable manner. Extreme Ultraviolet Lithography (EUVL) is poised to be the successor to current 193 nm optical lithography for high volume manufacturing (HVM) of integrated circuits. However, problems in developing sufficiently bright exposure sources for EUVL have hindered its ramp into HVM. Now that source power difficulties appear to be on a path to being addressed, the other critical problem of developing resist materials that are capable of being patterned with EUV radiation and which can produce the desired sub-20 nm patterned features must be addressed. Current chemically amplified resist material designs will be incapable of satisfying all of the patterning requirements for EUVL, and this alternative resist material designs will be needed to enable successful integration of EUVL.

The goal of our work has been to develop novel organic resist materials that can enable sub-20nm patterning using EUVL. One of the critical challenges for producing sub-20 nm organic material patterns is that conventional positive tone polymeric resists exhibit poor mechanical stability at such dimensions and are thus prone to pattern collapse during development and drying. Furthermore, photoacid diffusion in conventional positive chemically amplified resists limits their resolution. As a result, one of our design strategies has been to explore the use of molecular resists that can either be crosslinked upon to exposure to operate in a negative tone manner or which can be crosslinked and depolymerizes upon exposure to operate in a positive tone fashion. We will present our latest results on these two families of materials and will show examples of organic resists that are capable of resolving 10 nm features using 100 keV e-beam lithography and

sub-20 nm features using EUVL. The detailed materials design and mechanisms underlying these capabilities will be discussed.

Plasma Science and Technology Room: 104 C - Session PS-WeA

PSTD at AVS60: Looking Back and Moving Forward

Moderator: C.A. Wolden, Colorado School of Mines

2:00pm **PS-WeA1 The Origins of the AVS Plasma Science and Technology Division.** *H.F. Dylla*, American Institute of Physics **INVITED**
The AVS Plasma Science and Technology Division (PSTD), from its origins the mid 1980's through the present, has been a significant international forum for both the science and technology associated with the interaction of low temperature plasmas with materials. This talk will trace the origins of the PSTD from the formation of the Fusion Technology Division (FTD) in the late 1970's. The FTD's topical interests concerned both magnetic and inertial fusion devices that were undergoing rapid development at the time. Initial interests included the important plasma surface interactions that influenced the behavior of boundary plasmas and were used to condition the vacuum vessels of magnetic fusion devices or to prepare the multi-layer targets used in inertial fusion experiments. This concentration on plasma surface interactions laid the groundwork for broadening the FTD to the wider interests of the application of low temperature plasma for materials processing, and for rebranding the division to reflect its expanded focus.

2:40pm **PS-WeA3 The Emergence of Plasma Processing.** *M.A. Lieberman*, University of California, Berkeley **INVITED**
Plasma processing is a crucial technology for fabricating trillions of nanometer-size transistors on a silicon wafer [1]. It evolved from humble beginnings in the early 1900's: the silver-coating of mirrors by physical sputtering in dc glow discharges. The late 1950's - early 1960's saw extensive studies of physical and reactive sputtering in capacitive rf reactors. Isotropic plasma etching, mainly for photoresist stripping, was developed in the late 1960's - early 1970's, and etching of many other important materials was demonstrated. Three key advances in the late 1970's made plasma processing technology indispensable: (a) the discovery of ion-enhanced (anisotropic) etching [2]; (b) the development of SiO₂ etching with high SiO₂/Si selectivity [3]; and (c) the controlled etching of passivating films, e.g., Al₂O₃ over Al [4]. Etching discharges evolved from a first generation of "low density" reactors capacitively driven by a single source, to a second generation of "high density" reactors having two power sources, such as ICP's (rf inductive-driven) and ECR's (microwave-driven), in order to control independently the ion flux and ion bombarding energy to the substrate. A third generation of "moderate density" reactors, driven capacitively by multiple frequency sources, is now used, and there is increasing use of pulsed discharges to further control processing characteristics. The inductive reactors were invented 129 years ago [5], while the ECR's and the pulsed technology emerged in the aftermath of World War II [6]. Amazing challenges lie ahead as scale-down of transistor critical dimensions proceeds.

Supported by the Department of Energy Office of Fusion Energy Science Contract DE-SC0001939; special thanks to J.W. Coburn.

- [1] H. Abe, M. Yoneda and N. Fujiwara, "Developments of Plasma Etching Technology for Fabricating Semiconductor Devices," *Jpn. J. Appl. Phys.* **47**, 1435 (2008).
- [2] N. Hosokawa, R. Matsuzaki and T. Asamaki, "RF Sputter-Etching by Fluoro-Chloro-Hydrocarbon Gases," *Jpn. J. Appl. Phys. Suppl. 2*, Pt. 1, 435 (1974).
- [3] R.A.H. Heinecke, "Control of Relative Etch Rates of SiO₂ and Si in Plasma Etching," *Solid State Electronics* **18**, 1146 (1975).
- [4] S.I.J. Ingrej, H.J. Nentwich, and R.G. Poulsen, "Gaseous Plasma Etching of Al and Al₂O₃," USP 4,030,967 (filed 1976).
- [5] W. Hittorf, "About the Conduction of Electricity Through Gases," *Wiedemanns Ann. Phys.* **21**, 90 (1884).
- [6] H. Margenau, F.L. McMillan Jr, I.H. Dearnley, C.S Pearsall and C.G. Montgomery, "Physical Processes in the Recovery of TR Tubes," *Phys. Rev.* **70**, 349 (1946).

4:00pm **PS-WeA7 The Virtual World of Modeling Plasma Processing.** *M.J. Kushner*, University of Michigan **INVITED**
Modeling of plasma processes has significantly advanced during the tenure of the AVS with benefits to investigating fundamental science issues and to technology development. Modeling's contributions to plasma processing

science have been facilitated by a series of milestone contributions, including development of accessible particle-in-cell simulations, use of molecular dynamics for investigation of surface processes, hybrid techniques which have expanded the variety of plasmas investigated, multi-phase models for dusty plasmas, technology relevant profile simulation, on-demand computation of cross sections, and now state-of-the-art algorithms embedded in commercially available modeling platforms. Although model development has been closely tied to applications, a collaborative development of fundamental theories has been exceedingly important to formulating proper and relevant technology focused models. The variety and dynamic range of plasma processing applications, from low pressure magnetrons to atmospheric pressure jets and now to liquids, has both challenged and benefited modeling. In other fields of applied physics, and other sub-fields of plasmas, the dynamic range of interest is markedly smaller and so resources have been concentrated on advancing modeling in more focused areas. Plasma processing, with its greater dynamic range, has been less focused with the unexpected benefit of finding more common ground between what appears to be quite different sub-fields of plasma processing. With this virtual capability, the plasma processing community has embraced computational experimentation as a necessary and beneficial tool. In this talk, a perspective will be provided of modeling's impact on science and technology development in plasma processing, and on future opportunities.

*Work supported by the Semiconductor Research Corp., DOE Office of Fusion Energy Science, National Science Foundation, Agilent Research Labs and HP Research Labs.

4:40pm **PS-WeA9 Innovations in Diagnostics for Non-Thermal Plasma.** *N.St.J. Braithwaite*, The Open University, UK **INVITED**

Internal electrical diagnostics of plasmas date back to the early days of plasma physics. The first innovation was the realisation that drawing currents between wires placed in a plasma does not measure conductivity - the current depends mainly on the non-neutral space charge sheaths around the wires. In 1926 Langmuir and Mott-Smith reported this in a systematic analysis. Langmuir and coworkers were then able to link the form of collected currents to the density of charged species and to the mean energy of the electrons. Their equipment was inexpensive and uncomplicated; their analysis was state of the art for the 1930s and could take up to an hour between measurement and quantitative result. Since then electrostatic (Langmuir) probes have been a standard tool for investigating low-temperature plasmas. The chief innovations in the Langmuir probe method have come from incremental improvements in the analysis of probe data and refinements of the method. Self-consistent analysis of particle collection, the inclusion of collisional factors and the Druyvesteyn method that yields electron energy distributions have now been truly popularized by the digital revolution, enabling sophisticated data acquisition and rapid processing: quantitative sub-ms plasma parameters in real time. Nevertheless, autonomous systems still have not mastered the insight of real experts. Less obvious, but equally important in opening up access to probe methods, was the development of vacuum compatible, ceramic epoxies. Many imaginative variations of electrostatic probes now deliver data on potentials, densities, energies and fluxes. These innovations were awaiting 'need' more than 'technology'. For instance, probes for plasma environments involving RF or electronegative gases were slow to evolve until the semiconductor manufacturing industry found both scenarios to be indispensable. The simplicity of Langmuir's probe is both an advantage (anyone can make one) and a disadvantage (the models for analysis are contentious and restrictive). A similar challenge has been faced by electromagnetic probes based on resonances and transmissions of microwave signals in and around low temperature plasmas with ns resolution, in real time. Microwave methods also owe a great deal to advances in materials and data acquisition, driven by the technological need for robust, minimally intrusive probing of plasmas as a dielectrics. Thus, C21, user-friendly, finite element methods have opened up microwave techniques for probing low pressure plasmas, long after fast oscilloscopes and programmable microwave sources had made them attractive options to the electrically minded plasma diagnostician.

5:20pm **PS-WeA11 Plasma Surface Interactions and How They Limit Semiconductor Plasma Processing.** *R.A. Gottscho, K.J. Kanarik, S. Sriraman*, Lam Research Corp **INVITED**

Semiconductor growth continues at a brisk pace, driven by consumer electronics. Meanwhile, the semiconductor industry is evolving and facing unprecedented technology and economic hurdles. Limits imposed by planar technology and a stalled lithographic roadmap threaten to slow down the rate at which density, cost, and speed improvements can be made. More intricate device designs hold the promise of extending Moore's Law, but they increasingly rely on high-precision plasma processes of deposition and etching. This means that deposited films must be conformal and atomically smooth; and formation of the FinFET structure requires atomic-scale etch

precision across not only the wafer but also from wafer to wafer and fab to fab. Precision process solutions are already known but making them cost-effective is difficult as they are prone to inefficiencies in plasma surface interactions. In this paper, we will review fundamental plasma surface interactions such as the kinetics and dynamics of transport, adsorption, and desorption. These interactions will be discussed in relation to the performance of processing equipment, and how the resulting limitations can be overcome with clever process solutions.

Advanced Surface Engineering

Room: 203 C - Session SE+PS-WeA

Atmospheric Pressure Plasmas

Moderator: H. Barankova, Uppsala University, Sweden

2:00pm **SE+PS-WeA1 Tailoring Surfaces using Atmospheric Plasma Technologies : Examples, Challenges, Limits, Future, F.A.B. Reniers,** Université Libre de Bruxelles, Belgium

INVITED

Atmospheric plasma present nowadays numerous applications in the treatment of surfaces. They can be used for the cleaning of metals, for the reduction of surface oxides, to increase the adhesion of polymers, to deposit a wide variety of coatings from anticorrosion ones to biocompatible ones, including hybrid multifunctional coatings. They also have an effect on the surface roughness. Although the principles of the main technologies used (dielectric barrier discharge, RF discharges,...) are well known, the mechanisms involved in the different processes are still partly to be determined. Through a few detailed examples, the talk will try to go deeper in the understanding of what is going on in the process. The current limitations of atmospheric plasma technologies (what can be done, and what cannot be done (yet)) will conclude the talk.

Some detailed examples :

- Understanding the mechanisms for etching PTFE by atmospheric plasma to make it superhydrophobic. Through a combined study of the gas phase and the polymer by optical emission spectrometry, dynamic water contact angle, AFM, XPS and weight measurements, we will evidence the selected effect of atomic oxygen, metastable helium and UV photons on the etching process. The etching study is extended to a range of other polymers, ranging from PE to PTFE, with an increasing number of fluorinated atoms. Different mechanisms are proposed.

- The deposition of atmospheric plasma coatings usually leads to coatings exhibiting a good adhesion to the substrate. This adhesion, evidenced by peeling test, can be studied at the molecular level. The case of poly-AMA coatings and Silane coatings on aluminum will be presented.

- Plasma polymerization is strongly influenced by the chemical reactivity of the precursor molecule. A wide selection of molecules of precursor molecules, liquid at room temperatures have been injected in dielectric barrier discharge (from pure C_xH_y , to C_xCl_y and C_xF_y , and esters such as nPIB, nPMA, AMA). We will show the effect of the double bonds on the final chemical structure of a coating, and on the deposition rate. We will also show that double bonds known to be unreactive in conventional polymerization can easily be activated in plasma. The effect of halogenated atoms present on the precursor is also studied

Finally, some perspectives regarding the future applications of atmospheric plasma will be discussed. Geometrical aspects, frequency range, hybrid coatings, microtexturing, deposition rates, will be approached.

2:40pm **SE+PS-WeA3 Defining Atmospheric Pressure Air Plasma Treatment Parameters for Bonding Sheet Molding Compound, L.P. Haack, A.M. Straccia,** Ford Motor Company

Sheet molding compound (SMC) is used in the automotive industry for constructing body closure panels, typically on vehicles of low volume where tooling costs can be kept to a minimum. SMC is a reinforced composite material consisting of dispersed strands of chopped glass fibers in a polyester/polystyrene blended resin along with surface additives and inorganic fillers. The SMC body panels are typically constructed with an inner structure and an outer skin that are mated by adhesive bonding. Epoxy adhesives are used to join the panels. Although the resin chemistry should allow for a strong covalent bond with the epoxy adhesive, instead poor bonding is often noted in production. This is mostly attributed to the use of internal and external mold release agents. Physical sanding will help improve bonding, but the process creates substantial amounts of dust and debris and is prone to human error. Atmospheric pressure air plasma is therefore being evaluated as an alternative to prepare the surfaces for bonding. Plasma was shown to improve bond reliability at low to moderate levels of treatment. Interestingly, it also yielded impeccable bond durability at high to extremely high levels of treatment; conditions that would be

deleterious to many plastics, especially polyolefins that can revert treatment at elevated temperatures. Measurements were conducted in an attempt to elucidate how this material interacts with the plasma to produce a surface exceedingly robust to bonding at an unexpectedly wide range of treatment conditions. Atomic force microscopy measurements gave insight into the amount of surface roughness created by the plasma treatments, while chemistry was determined by surface energy measurements and X-ray photoelectron spectroscopy (XPS). Dyne level testing was unable to accurately discern varying treatment levels since measurements reached 72 dynes/cm (the wetting point of water) even at lower treatment levels, while robust bonding occurred at still considerably higher dosage levels. Solvent wiping experiments along with XPS measurements revealed that, under the time constraints of the automotive manufacturing process, plasma treatments essentially achieve a condition of steady state that will remove material and yet still present a highly oxidized surface that is conducive to bonding. Thus, in practice, a condition of overtreatment is essentially unattainable.

3:00pm **SE+PS-WeA4 Correlation of Spectral Emissions of a He-O₂ RF Atmospheric Plasma Discharge with Polymer Surface Activation, V. Milosavljevic, M. Donegan,** University College Dublin, Ireland, *P.J. Cullen,* Dublin Institute of Technology, Ireland, *D.P. Dowling,* University College Dublin, Ireland

Atmospheric pressure non-thermal helium plasma jets are increasingly used in many processing applications due to their combination of inherent plasma stability and excellent reaction chemistry. Despite their widespread usage, it remains largely unknown whether cold atmospheric plasma jets maintain characteristics, such as gas temperatures and particle flux, when they breakdown while arcing or whether they possess different operating modes. From an application point of view, the activation of polymer surfaces can help to overcome the chemical inertness and low surface energy generally associated with these types of materials. Polymers, such as PET, are thermally damaged at relatively low temperatures and so a delicate balance must be reached where surface activation of the polymer is maximised, while thermal damage is prevented.

The atmospheric plasma system employed generates plasma using He-O₂ (in the range of 100-200 W), operates at a frequency of 27.12 MHz and uses a 5 cm wide beam applicator. The input variables on this system were: helium gas at a constant flow rate of 30 l/min, while secondary gas input: plasma power ratios are set by the manufacturer.

This work employs optical emission spectroscopy as a diagnostic technique for the measurement of atomic and molecular spectral emissions generated using the plasma jet system. The OES of neutral atomic spectral lines and molecular bands are investigated over a range of plasma process parameters. Wavelength resolve optical emission profiles suggest that the emission of helium's spectral lines shows that the high energy electrons have a larger influence than helium metastables on the overall spectral emission. Furthermore, the experimental data indicates that the use of high helium flow rates limits the significance of air impurities, e.g. N₂, for the creation and sustainability of plasma discharges in He-O₂ gas chemistry. The level of polymer surface activation was evaluated based on changes to the water contact angle of PET samples after plasma treatment. For the first time a direct correlation was obtained between polymer water contact angle changes and the OES measurement of the atomic hydrogen Balmer H α and molecular OH line emission intensities. Further work will be presented how the high helium flow rate is used in an attempt to minimize the ratio of gas convection to chemical reaction time scale (recombination). This is also favours the rapid transport of newly created radicals and excited species to the surface under treatment.

This work was funded by SFI under the Precision cluster, the 'Fresh-Pack' project funded by the National Development Plan of Republic of Ireland and grant OII71006.

4:00pm **SE+PS-WeA7 Atmospheric Plasma Polymerization Enhanced by Simultaneous UV Irradiation, N. Vandecasteele, J. Bossert,** Université Libre de Bruxelles, Belgium, *A. Kakaroglou,* Vrije Universiteit Brussel, Belgium, *B. Nisol,* Université Libre de Bruxelles, Belgium, *H.A. Terry,* Vrije Universiteit Brussel, Belgium, *F.A.B. Reniers,* Université Libre de Bruxelles, Belgium

Plasma polymerization is now commonly used to deposit a wide variety of films for various applications (corrosion protection, biocompatibility, ultrahydrophobic layers...). Atmospheric plasma polymerization is a very promising technique for thin film deposition in industry. Indeed it does not require the use of organic solvent and it is not limited by vacuum requirement. Furthermore the high reactivity of the plasma medium allows for a rapid deposition of a large number of molecules on virtually any kind of substrate.

However there are still some issue remaining: the degree of crosslinking is not always sufficient to ensure good barrier and mechanical properties of

the films. In some instance the adhesion of the films to the substrate is not strong enough. In this study we looked at the plasma polymerization of Allyl methacrylate on gold substrate using a high frequency (17 kHz) dielectric barrier discharge (DBD). The effects of the classical plasma polymerization parameters (monomer concentration, power, deposition time...) are studied as well as the effect of in situ ultra violet (UV) irradiation. The UV source is a mercury discharge lamp commonly used to cure polymers. Our experimental setup consists of a 2 mm thick quartz plate (acting as the dielectric) covered with a stainless steel grid (diameter 0.018 mm, spacing 0.045 mm) acting as the powered electrode. The second electrode is made of a grounded copper plate. It is separated from the powered electrode by a 3mm gap. The UV lamp is placed directly above the quartz electrode, illuminating the sample through the grid. Argon is used as the plasma gas. Its flow ranges from 1 to 3 liter per minute (LPM). The precursor vapor is carried in the plasma by a secondary argon line with flow ranging from 1 to 3 LPM. The total gas flow is kept constant at 4 LPM.

Three separate cases are studied: plasma polymerized films (pp-film) without UV irradiation, pp-films with post plasma UV irradiation and finally pp-films with UV irradiation during the plasma polymerization.

The pp-films are characterized by FTIR, XPS, contact angle and ellipsometry. Differences between the pp-film compositions have been evidenced for the 3 types of treatments. Increased O/C ratios have been observed for the films exposed to UV irradiation. The FTIR spectra are also strongly affected by the presence of UV irradiation. Changes in the C=O/C-C peaks ratio are observed for the 3 types of treatments. This allows us to conclude that the irradiation during the films growth leads to different results than the usual UV post treatment (UV curing).

4:20pm SE+PS-WeA8 Plasma Polymerization of (3-aminopropyl) Trimethoxysilane using a Micro-plasma Printing Setup, J.R.G. Schalken, Eindhoven University of Technology; InnoPhysics B.V., Netherlands, A.A.E. Stevens, P. Verhoeven, InnoPhysics B.V., Netherlands, M. Creatore, Eindhoven University of Technology, Netherlands

Amino-functionalities are introduced in biosensors in order to specifically bind proteins using biomolecules for the detection of diseases from human blood samples. Plasma polymerization of amine-containing precursor molecules such as (3-aminopropyl) trimethoxysilane (APTMS) can be used to deposit films with amino-functionalities.

The μ PlasmaPrint technique utilizes a pin-to-plate dielectric barrier discharge at atmospheric pressure. A dielectric substrate is placed on a high-voltage plate electrode. An array of needles is moved above the substrate, while individual needles are allowed to move towards the surface and back based on a digital pattern. According to the Paschen law, a reduction of the distance between a grounded needle electrode and the high-voltage substrate holder from about 800 μ m to 200 μ m can lead to the ignition of a plasma. Within a millisecond the plasma is turned off by moving the needles up again. The dot-wise exposure of the surface to short micro-plasmas enables a local plasma treatment with a minimum feature size of 100 μ m.

Thin films of plasma polymerized APTMS have been deposited on a fluorinated ethylene propylene copolymer (FEP) using the μ PlasmaPrint technique. The thickness of the deposited films varied in the range of 5 to 100 nm. The surface characteristics and ageing behavior of the films have been investigated by X-ray photoelectron spectroscopy (XPS), fluorescence microscopy and water contact angle measurements, respectively. Depending on the number of print repeats of the μ PlasmaPrint system, the concentration of amino-functionalities in the deposited film as derived from XPS peak analysis varied from 9.1% for a single print repeat, down to 4.7% for 20 print repeats.

Water contact angle measurements showed an increase from 10° for a single print repeat up to 40° for 20 print treatments, while the water contact angle of the FEP substrate was measured to be 110°. The increase in water contact angle with increasing print repeats suggested a reduction of polar components at the surface and was therefore consistent with the relative reduction of amino-functionalities as measured with XPS.

Based on the experimental results, a polymerization process of APTMS is proposed. It is suggested that polymerization mainly takes place by the abstraction of methyl- and methoxy- groups to develop siloxane chains. For an increased number of print repeats, which results in a prolonged plasma exposure, it is proposed that the creation of reactive sites for the cross-linking of APTMS polymer chains also takes place in the aminopropyl chains, resulting in a decreased concentration of amino-functionalities.

4:40pm SE+PS-WeA9 Evaporative Coating at Atmospheric Pressure (ECAP), Y.L. Wu, J. Hong, D. Peterson, J. Zhou, T.S. Cho, D.N. Ruzic, University of Illinois at Urbana Champaign

Recently, the Center for Plasma-Material Interaction (CPMI) has developed innovative coating method of Evaporative Coating at Atmospheric Pressure (ECAP). This new idea is an atmospheric pressure based process following the similar concept as the Laser Pressure LAPCAP purely at Atmospheric Pressure (LAPCAP) [1], the material captured by the plasma plume is atomic in nature (the evaporated metal atom) and should therefore end up deposited molecule-by-molecule in a PVD fashion. By using the thermal energy from the microwave plasma solid 99.99%+ purity aluminum are evaporated and then produce a PVD-like alumina coating on a workpiece. The Aluminum target is inserted in the center of the microwave torch feeding a melt pool and evaporates into the surrounding plasma plume. A bottle neck was made in the antenna and could reduce the heat loss by 84%. The film was deposited as Al₂O₃ using oxygen from the environment. Alpha and other metastable phases of aluminum oxide were found on the deposited films. Deposition rate was around 2 μ m/min. Gas flow rate around the antenna tip was about 0.9 m/s, and temperature of the plasma was about 1400°C at 1350W input power from simulations. Gas shield was used to keep the work gas pure. A much higher thermal energy of the plasma plume will make a superior coating microstructure as compared to a purely evaporated film.

Reference:

[1] Laser-assisted plasma coating at atmospheric pressure: production of yttria-stabilized zirconia thermal barriers, Zihao Ouyang *et al* 2011 *J. Phys. D: Appl. Phys.* 44 265202

5:00pm SE+PS-WeA10 Selection of an Atmospheric Plasma Source for 450mm Backside Wafer Cleaning, F.T. Molkenboer, J. Van Veldhoven, Y.L.M. Creyghton, O. Kievit, T.W. Versloot, N.B. Koster, TNO Technical Sciences, Netherlands

TNO is working on the selection and development of a non-thermal atmospheric plasma source for backside wafer cleaning. This selection started with a theoretical comparison of the potential candidates. Main criteria for the selection are cleaning speed, the amount of contamination that can be removed in a certain time and plasma temperature. Further criteria are the dependency of plasma homogeneity on substrate conductivity, the distance between the plasma source and the substrate as well as scalability of the source up to a 450 mm wide cleaner. Backside wafer cleaning is important for the semiconductor industry to enable the transition from 300 mm wafers to 450 mm wafers. Contamination on the backside of a wafer can lead to printing errors and can negatively influence post lithography processing like metal deposition.

The selection of the plasma source is part of a TNO project that has the objective to build and deliver a complete backside wafer cleaner to the 450 mm pilot line to be installed at IMEC, Belgium. The final selection will be made on the basis of a series of experiments. Candidates already tested are surface- and volume- dielectric barrier discharge (SDBD and VDBD) plasma sources.

In this presentation we will report the outcome of our selection of the plasma source, supported by the validated source inventory and experimental results.

This work is funded by the ENIAC Joint Undertaking and AgentschapNL. It has the goal to enable the European semiconductor industry to make the transition to 450mm wafers

5:40pm SE+PS-WeA12 Rapid Atmospheric Pressure Plasma Jet Treatment on ZnO for rf-sputtered MgZnO/ZnO Heterostructures, S.T. Lien, H.C. Li, Y.J. Yang, C.C. Hsu, I.C. Cheng, J.Z. Chen, National Taiwan University, Taiwan, Republic of China

MgZnO/ZnO heterostructures have shown great potential for optoelectronic device applications. The polarization field at MgZnO/ZnO heterojunction can induce charge accumulation at the interface to form two-dimensional electron gases (2DEGs). This has been observed in high quality materials grown by molecule beam epitaxy (MBE) or pulse laser deposition (PLD) as well as in defective MgZnO/ZnO heterostructure system deposited by rf-sputtering. Although high quality MgZnO/ZnO is desirable for its high electron mobility, the required deposition technique such as MBE or PLD is not suitable for the processing of large-area electronics. In regard to large-area deposition, rf-sputtering technique is the preferred process in spite of the more defective nature of the deposited materials. In our previous studies, we have demonstrated that the electron Hall mobility of ~40 cm²V⁻¹s⁻¹ and field-effect mobility of ~84 cm²V⁻¹s⁻¹ in the rf-sputtered Mg_{0.4}Zn_{0.6}O/ZnO heterostructure and the top-gated Mg_{0.2}Zn_{0.8}O/ZnO thin film transistor, respectively. The mobility exceeds the typical value (6 to 9 cm²V⁻¹s⁻¹) of a-InGaZnO TFT, which is the most promising technique for large-area oxide electronics nowadays.

One key step to obtain 2DEGs in the *defective rf-sputtered* MgZnO/ZnO heterostructures is the thermal annealing process on ZnO prior to the deposition of MgZnO material. This paper reports that atmospheric pressure plasma jet (APPJ) treatment can be used for the same purpose with a much shorter processing time. A thirty-second APPJ anneal on ZnO with a maximum temperature of 340 °C can replace a 30 min, 400 °C furnace-anneal to promote the formation of 2DEGs in the rf-sputtered MgZnO/ZnO heterostructure. The APPJ treatment also increases the crystallinity of ZnO films and releases the compressive residual stresses, verified by XRD and UV-Vis transmission measurements. The ultra-short processing time is attributed to the synergy of plasma reactivity and temperature of APPJ.

Surface Science

Room: 202 A - Session SS+AS+NS+SP-WeA

Single Molecules at Surfaces: Structure and Dynamics

Moderator: A.L. Utz, Tufts University

2:00pm **SS+AS+NS+SP-WeA1 Probing the Interface of Organic Coatings on Metals**, H.A. Terryn, VUB/TU Delft, Belgium, T. Taheri, TU Delft, the Netherlands, T. Hauffman, VUB, Belgium, O. Ozkanat, J.A. Mol, TU Delft, the Netherlands

During the functional lifetime of coated metals, interfacial bonds at polymer/(oxyhydr)oxide/metal joints have to withstand high mechanical forces and corrosive attack. Therefore, it is crucial to control and understand the bonding mechanism originating at polymer/(oxyhydr)oxide/metal interfaces in order to achieve long-term stability. While the type of bonding contributes to the strength of adhesion, the nature of the interface depends on both functionality present in the organic molecules of the coating and the nature of the oxide film e.g. hydration, hydroxyl content, oxide thickness, surface morphology and chemical composition. Those properties might be extremely sensitive to the small changes in the environmental conditions, such as ageing and humidity.

Studying the bonding properties of the polymeric coating to the metal surface is experimentally difficult, because the interface is hard to be reached by analytical techniques due to the relatively high thickness of the polymer coatings. Consequently, the interfacial bonding can be modeled through adsorption of functional groups -representative interfacial adhesive molecules- on differently pretreated surfaces by means of bonding mechanism (FTIR) and affinity (XPS) studies. Furthermore, the buried interface and delamination mechanisms at this location can be studied by Scanning Kelvin Probe (SKP) measurements.

Recent References

In situ study of buried interfacial bonding mechanisms of carboxylic polymers on Zn surfaces, *Journal of Physical Chemistry C*, Volume: 117, N° in volume: 7, pp: 3374 - 3382, 2013, Taheri p., Flores J., Hannour F., de Wit J., Terryn H., Mol J.

Effects of Zinc Surface Acid-Based Properties on Formation Mechanisms and Interfacial Bonding Properties of Zirconium-Based Conversion Layers, *Journal of Physical Chemistry C*, Volume: 116, pp: 8426 - 8436, 2012, Taheri p., Lill K., de Wit J., Mol J., Terryn H.

A comparison of the interfacial bonding properties of carboxylic acid functional groups on zinc and iron substrates, *Electrochimica Acta*, Volume: 56, pp: 1904 - 1911, 2011, Taheri p., Wielant J., Hauffman T., Reyes Flores J., Hannour F., de Wit J., Mol J., Terryn H.

Role of surface oxide properties on the aluminum/epoxy interfacial bonding, *Journal of Physical Chemistry C*, Volume: 117, N° in volume: 9, pp: 4480 - 4487, 2013, Salgin B., Ozkanat O., Mol J., Terryn H., Rohwerder M.

Bonding mechanisms at buried interfaces between carboxylic polymers and treated zinc surfaces, *Journal of Physical Chemistry C*, Volume: 117, N° in volume: 6, pp: 2780 - 2792, 2013, Taheri p., Ghaffari M., Flores J., Hannour F., de Wit J., Mol J., Terryn H.

2:20pm **SS+AS+NS+SP-WeA2 Ultra-High Vacuum Tip-Enhanced Raman Spectroscopy with Molecular-Resolution Scanning Tunneling Microscopy**, N. Jiang, J. Klingsporn, E. Pozzi, M.C. Hersam, R.P. Van Duyne, Northwestern University

The study of ultrahigh vacuum (UHV) tip-enhanced Raman spectroscopy (TERS) has been raised to an unprecedented level. By using ex-situ laser focusing and Raman collection optics, optimization of the optical path is achieved without compromising UHV. All sample preparation and tip degassing are performed in-situ, maintaining atomically clean surfaces, greatly enhancing the stability of the tip-sample junction, and ensuring minimal contamination in the field enhancement region beneath the STM

tip. At 292K, multiple vibrational modes for copper phthalocyanine (CuPc) adlayers on Ag (111) have been resolved in TER spectra obtained concurrently with molecular resolution UHV Scanning tunneling Microscopy (STM). Then Rhodamine 6G (R6G) molecules were studied as they have larger Raman cross-section. The sample was cooled down to 19 K to decrease the diffusion of R6G on surface at very low coverage. Single R6G molecules and clusters were observed using STM. For the first time, TERS vibrational modes for a few R6G molecules on Ag (111) have been resolved with concurrent molecular resolution STM images at 19 K. In comparison with the TER spectra at 292 K, the sharpening of TERS peaks and the existence of new peaks at 19 K demonstrates the utility of UHV-TERS towards obtaining site-specific chemical information about adsorbed molecules. This study sets the stage for Raman vibrational fingerprinting and correlated sub-molecular resolution topography of site-specific binding of molecules on solid surfaces.

2:40pm **SS+AS+NS+SP-WeA3 High Resolution STM-IETS Characterization for Single Molecule on Metal Surface**, C. Xu, C. Jiang, Y.N. Zhang, R.Q. Wu, W. Ho, University of California, Irvine

Inelastic electron tunneling spectroscopy (IETS) with the scanning tunneling microscope (STM) has been regarded as the ultimate tool to identify and characterize single molecules adsorbed on solid surfaces with atomic spatial resolution. With the improvement of energy resolution obtained at ~600 mK, STM-IETS is able to resolve the lowest vibrational energies and reveal subtle interactions between the molecule and its environment which were previously not possible at higher temperatures. Here we demonstrate the capability of sub-Kelvin STM on detecting the influence of the tip as well as the anisotropy of the reconstructed Au(110) surface on the low energy hindered vibrational motions of single adsorbed CO molecule.

3:00pm **SS+AS+NS+SP-WeA4 Electronic Structure of H₂Pc on Ultrathin NaCl Films with Various Thickness**, M. Imai, The University of Tokyo, Japan, H. Imada, T.K. Shimizu, RIKEN, Japan, M. Kawai, The University of Tokyo, Japan, Y. Kim, RIKEN, Japan

We have investigated thickness dependence of electronic states of single metal-free Phthalocyanine (H₂Pc) on NaCl insulating films on Au(111), using scanning tunneling microscopy (STM) and scanning tunneling spectroscopy (STS). Our aim is to understand how the thickness of NaCl films affect the molecular properties using the well-known and widely studied molecule.[1] NaCl films are known to weaken the molecular-metal interaction,[2] but we found the electronic properties of the H₂Pc adsorbed on 2 ML and 3 ML-thick NaCl are indeed different. Isolated H₂Pc molecules are adsorbed on both 2 ML and 3 ML thick NaCl islands, which are grown from Au(111) step edges. Appearances of H₂Pc are similar for both islands, four-lobe or eight-lobe depending on bias voltages. STS spectra acquired at the centers of molecules on both islands show one peak in occupied and one in unoccupied states. By visualizing spatial distribution of density of states at the peak bias, we found that these two peaks corresponded to the highest occupied molecular orbital (HOMO), and degenerated lowest unoccupied molecular orbitals (LUMO and LUMO+1). A difference between 2ML and 3 ML is the peak position of degenerated LUMO and LUMO+1 states and thus HOMO-LUMO gap. Our observation implies that the effect of NaCl is not just to decouple metal electronic states, but it indeed affects the electronic states of adsorbed molecules, which might arise from the metal-insulator interaction such as interfacial dipole.

[1] T. Komeda, H. Isshiki, and J. Liu, *Sci. Tech. Adv. Mater.***11**, 054602 (2010).

[2] J. Repp, G. Meyer, S. Stojković, A. Gourdon, and C. Joachim, *Phys. Rev. Lett.***94** (2005).

4:00pm **SS+AS+NS+SP-WeA7 Species-Selective Atomic Resolution Imaging with Scanning Probe Methods**, H. Monig, University of Muenster, Germany, M. Todorovic, Universidad Autónoma de Madrid, Spain, M.Z. Baykara, Bilkent University, Turkey, J. Goetzen, O.E. Dagdeviren, Yale University, T.C. Schwendemann, Southern Connecticut State University, L. Rodrigo, Universidad Autónoma de Madrid, Spain, E.I. Altman, Yale University, R. Perez, Universidad Autónoma de Madrid, Spain, U.D. Schwarz, Yale University

INVITED

Despite the evolution of scanning probe microscopy (SPM) into a powerful set of techniques that image surfaces and map their properties down to the atomic level, significant limitations in both imaging and mapping persist. Currently, typical SPM capabilities qualitatively record only one property at a time and at a fixed distance from the surface. Furthermore, the probing tip's apex is chemically and electronically undefined, complicating data interpretation. To overcome these limitations, we started to integrate significant extensions to existing SPM approaches. First, we extended noncontact atomic force microscopy with atomic resolution to three dimensions by adding the capability to quantify the tip-sample force fields

near a surface with picometer and piconewton resolution. Next, we gained electronic information by recording the tunneling current simultaneously with the force interaction. We then moved on to study the influence of tip chemistry and asymmetry on the recorded interactions. Through a combination of experimental work and theoretical analysis, we show how specific atomic species can be selectively imaged in both the force and the current channels depending on the choice of imaging parameters and tip chemistry. Applications to metal oxides are shown. From this platform, we present our vision of a method capable of characterizing full atomic-scale chemical and electronic properties.

4:40pm **SS+AS+NS+SP-WeA9 Surface Morphology of Chemisorbed N on Pt(111)**, Z. Liang*, University of Illinois at Chicago, H. Yang, Y. Kim, RIKEN, Japan, M. Trenary, University of Illinois at Chicago

The surface morphology of chemisorbed N on a Pt(111) surface has been studied at the atomic level with low temperature scanning tunneling microscopy (LT-STM). At high coverages, two phases, p(2×2)-N and (√3×√3)R30°-N, are found to coexist at temperatures between 360 and 400 K. For both phases nitrogen occupies fcc-hollow sites. At temperatures of 400 K and slightly above, only the p(2×2)-N phase is present on the surface. At temperatures above 420 K, nitrogen starts to desorb. The p(2×2)-N phase shows a honey-comb structure in STM images with three nitrogen and three platinum atoms forming a six-member ring, which can be attributed to the strong nitrogen binding to the underlying Pt atoms. At low coverages, incomplete (2×2) patches of N, but no (√3×√3)R30° structure, are observed on the surface. When N and O are coadsorbed on the surface, they form a mixed (2×2) overlayer of N+O at high coverages. N and O can be clearly distinguished from each other by their appearance in the STM images.

5:00pm **SS+AS+NS+SP-WeA10 Relative Stability of Thiols and Selenols SAMs on Ag(111) – Exchange and Desorption Experiments**, J.W. Ossowski, J. Rysz, Jagiellonian University, Poland, A. Terfort, Goethe University, Germany, P. Cyganik, Jagiellonian University, Poland

The stability of chemical bonding between molecule and substrate is one of the key factor considering diverse applications of Self-Assembled Monolayers (SAMs). Addressing this issue experimentally or theoretically is difficult considering complex interplay of the molecule-substrate and molecule-molecule interactions in SAMs. So far most of experiments have been performed for thiol based SAMs on Au(111) substrate and far less is known for equally important Ag(111) substrate.

In this presentation we report exchange and desorption experiments probing the effect of S to Se substitution on stability of molecule-substrate interface in SAMs on Ag(111) substrate by using two homologue series of molecules in the form BPNs/Ag(111) (CH₃-(C₆H₄)₂-(CH₂)_n-S-Ag, n = 2-6) and BPNSe/Ag(111) (CH₃-(C₆H₄)₂-(CH₂)_n-Se-Ag, n = 2-6).¹ Such experiments were possible since both analogs form similar structures on Ag(111) substrate² and thus observed differences in stability between these two types of SAMs could be related to the molecule-substrate interface stability. Quantitative control of the exchange process was obtained using IRRAS (Infrared Reflection Absorption Spectroscopy). Additionally, ion-induced desorption experiments by means of SIMS (Secondary Ion Mass Spectrometry) were performed. Obtained results will be discussed together with analogical experiments³⁻⁵ performed previously for Au(111) substrate enabling comparison of molecule substrate-interface stability for thiol and selenol based SAMs on Ag(111) and Au(111) substrates.

References

- (1) J. Ossowski, P. J. Rysz, A. Terfort and P. Cyganik *in preparation*.
- (2) T. Weidner, A. Schaporenko, J. Muller, M. Schmid, P. Cyganik, et al. *J. Phys. Chem. C* **2008**, *112*, 12495.
- (3) K. Szlagowska-Kunstman, P. Cyganik, et al. *Phys. Chem. Chem. Phys.* **2010**, *12*, 4400.
- (4) F. Vervaecke, S. Wyczawska, P. Cyganik, et al. *ChemPhysChem(Communication)* **2011**, *12*, 140. (5) S. Wyczawska, P. Cyganik, A. Terfort, P. Lievens, *ChemPhysChem(Communication)* **2011**, *12*, 2554.

5:20pm **SS+AS+NS+SP-WeA11 Formation Mechanism of van der Waals Interface between a π-conjugated Molecule and Au(111)**, J. Jung, RIKEN, Japan, J.-H. Kim, The University of Tokyo, Japan, K. Tahara, Y. Tobe, Osaka University, Japan, M. Kawai, The University of Tokyo, Japan, Y. Kim, RIKEN, Japan

Van der Waals (vdW) force is one of the most abundant interactions in nature, and thus it plays a pivotal role in determining architectures of molecular and biological systems or in constructing interfaces between chemically non-reactive materials. Understanding interfacial electronic and

geometric structures at organic-metal contacts formed by the vdW interactions is, in particular, of great importance in order to finely control the functions of organic electronic and photovoltaic devices. Nevertheless, fundamental insights into a formation mechanism of vdW interface have not yet been fully achieved due to the weak adsorption characters. Here, we propose a detailed description on formation mechanisms of interfacial electronic and geometric structures at vdW interface between a π-conjugated hydrocarbon (π-CHC) molecule and the noblest Au surface, using vdW density functional (vdW-DF) calculations based on atomically-resolved scanning tunneling microscopy (STM) imaging and scanning tunneling spectroscopy (STS) at a cryogenic temperature. Based on the first direct observation of adsorption geometry of an isolated π-CHC molecule on Au(111) and an efficient computational approach, we revealed that the interfacial electronic structures form in a way to maximize the interfacial orbital interaction between a π-CHC molecule and the noble Au surface through processes of *interlocking–dragging–splitting* induced by the local splitting of the Au d state due to electronic coupling with the molecular π-state. Furthermore, the orbital interaction between a π-CHC molecule and the Au surface can play a decisive role in constraining adsorption geometry, i.e., both horizontal orientation and adsorption distance, even in the archetypal vdW adsorption system. Considering that the overlap of the frontier electronic states is important in a charge-carrier path at the organic-metal contact, our observations provide not only deeper insight into the weak adsorption process but also new perspectives to organic electronics using π-CHC molecules on the Au electrodes.

5:40pm **SS+AS+NS+SP-WeA12 Scanning Tunneling Microscopy/Spectroscopy Studies of Indolo[2,1-b]quinazolin-6,12-dione (tryptanthrin) and its Analogs Adsorbed at the Solution-HOPG Interface**, J. Olson, J.C. Baum, M. Novak, K. Sriraman, Florida Institute of Technology

Tryptanthrins represent a class of compounds of interest for their anti-parasitic properties. Particularly, they have shown in-vitro efficacy versus organisms that cause malaria, leishmania, trypanosomiasis, tuberculosis, and fungal infections. However, little is known of their mode(s) of action at the molecular level. To investigate their geometric and electronic behavior, STM has been used to observe molecular monolayers of these compounds. Sub-molecular resolution has allowed the direct observation of individual lobes of the HOMO and LUMO states. The parent compound forms rows that alternate in contrast (light/dark), which is attributed to adsorption-induced stereoisomerization, with each row comprised of one enantiomer. Also excellent lobe-to-lobe resolution is observed for the LUMO of the parent compound as well as the HOMO of 8-fluorotryptanthrin (which similarly displays adsorption-induced stereoisomerization). Additionally, the authors have undertaken measurements of the tunneling barriers of these molecules, with a quantitative structure-activity relationship (QSAR) correlation as the goal. Sub-molecular quantitative measurements of the tunneling barriers have been accomplished for the parent compound, and show an interesting correlation to its known chemistry. Also, preliminary correlations of biological efficacy and molecular barrier heights have been observed over several analogs. Generally speaking, increased anti-parasitic efficacy corresponds to lower measured barrier heights, which is consistent with a possible tunneling mechanism.

Surface Science

Room: 201 A - Session SS+EM-WeA

Semiconductor Surfaces and Interfaces

Moderator: M.A. Hines, Cornell University

2:00pm **SS+EM-WeA1 Monte Carlo Simulation Studies of Ge(100)-2 × 1 Surface Chemistry**, B. Shong††††, S.F. Bent, Stanford University

Organic functionalization of semiconductor surfaces is of interest due to its possibilities for forming tailorable organic-inorganic interfaces. The (100) surface of Si or Ge reconstructs to a highly ordered 2 × 1 pattern under proper vacuum preparation. On these surfaces, only a few possible two-dimer configurations exist [1], and such a simple geometry allows facile introduction of stochastic simulations. However, to date, such methods have not been well utilized in organic functionalization studies. In this talk, we will introduce recent results in the integration of Monte Carlo (MC) simulations with other widely used techniques, and will show that the addition of MC simulations leads to deeper understanding of many coverage-dependent behaviors.

In the first example, self-assembly of two small organic building block molecules, ethylene and methanol, on the Ge(100) surface is explained through MC simulations based on density functional theory (DFT) calculations [2]. Characteristic one-dimensional adsorbate patterns along

* **Morton S. Traum Award Finalist**

the rows of Ge(100) were observed in previous scanning tunneling microscope (STM) studies, where the dimers linearly aligned within the same rows are the nearest neighbor sites on Ge(100). Our DFT calculations show that the adsorption of ethylene is hindered next to another ethylene, whereas adsorption of methanol is facilitated by the presence of an adjacent methanol. Kinetic MC simulations based on the DFT-calculated adsorption probabilities predict adsorbate patterns that agree well with the experimental observations.

In another example, the adsorption of a bifunctional molecule, 1,3-benzenediol, is explored by a similar MC approach. Whether dual or single reaction occurs during attachment of bifunctional molecules is critical, since dual binding adsorbates terminate the reaction site. Fourier transform infrared (FTIR) spectroscopy experiments as well as DFT calculations show that 1,3-benzenediol adsorbed on Ge(100) assumes only one type of dual binding configuration. This limitation simplifies the geometrical dimension of the adsorption phenomena. The fraction of singly bound adsorbates increases nonlinearly with increasing coverage according to X-ray photoelectron spectroscopy (XPS) measurements. This behavior is explained through MC simulations showing that unreacted functionalities appear on the reactive surface due to limitations in available adjacent sites. In conclusion, we demonstrate the potential of combining MC simulations with other techniques in studies of semiconductor surface chemistry.

1. B. Shong, K.T. Wong, S.F. Bent, *J. Phys. Chem. C* 116, 4705 (2012).

2. B. Shong, S.F. Bent, *J. Phys. Chem. C* 117, 949 (2013).

2:20pm SS+EM-WeA2 Structural Instability in the Adatom Vacancy on Si(111)- $\sqrt{3}\times\sqrt{3}$ Surface: An STM/S Study, D. Eom, C.-Y. Moon, J.-Y. Koo, Korea Research Institute of Standards and Science, Republic of Korea
We report a direct probe of the structural instability in the adatom vacancy on heavily boron doped Si(111)- $\sqrt{3}\times\sqrt{3}$ surfaces by using a low-temperature scanning tunneling microscopy/spectroscopy (STM/S). Three dangling bonds (DBs) are generated inside an adatom vacancy on Si(111)- $\sqrt{3}\times\sqrt{3}$ surface, each of which is located at one of three second layer Si atoms with Si(111)-1x1 spacing. The conductance maps of this triple DBs exhibit dissimilar spatial distributions with varying eigenenergies, indicating that the electronic coupling between three DBs is significant due to the proximity. Also, the reduced C_{3v} symmetries of ground and excited states' wavefunctions of triple DBs, which are probed at -0.25 eV below and +0.3 eV above the Fermi level respectively, contrast to C_{3v} symmetry of underlying 1x1 lattice and are ascribed to Jahn-Teller type instability accompanying degenerate orbital configurations. More detailed analysis of multi-electron configurations and structural instabilities in triple DBs will be reported.

2:40pm SS+EM-WeA3 Sunlight-Driven Hydrogen Formation by Membrane-Supported Photoelectrochemical Water Splitting, N. Lewis, California Institute of Technology
INVITED

We are developing an artificial photosynthetic system that will only utilize sunlight and water as the inputs and will produce hydrogen and oxygen as the outputs. We are taking a modular, parallel development approach in which the three distinct primary components—the photoanode, the photocathode, and the product-separating but ion-conducting membrane—are fabricated and optimized separately before assembly into a complete water-splitting system. The design principles incorporate two separate, photosensitive semiconductor/liquid junctions that will collectively generate the 1.7-1.9 V at open circuit necessary to support both the oxidation of H₂O (or OH⁻) and the reduction of H⁺ (or H₂O). The photoanode and photocathode will consist of rod-like semiconductor components, with attached heterogeneous multi-electron transfer catalysts, which are needed to drive the oxidation or reduction reactions at low overpotentials. The high aspect-ratio semiconductor rod electrode architecture allows for the use of low cost, earth abundant materials without sacrificing energy conversion efficiency due to the orthogonalization of light absorption and charge-carrier collection. Additionally, the high surface-area design of the rod-based semiconductor array electrode inherently lowers the flux of charge carriers over the rod array surface relative to the projected geometric surface of the photoelectrode, thus lowering the photocurrent density at the solid/liquid junction and thereby relaxing the demands on the activity (and cost) of any electrocatalysts. A flexible composite polymer film will allow for electron and ion conduction between the photoanode and photocathode while simultaneously preventing mixing of the gaseous products. Separate polymeric materials will be used to make electrical contact between the anode and cathode, and also to provide structural support. Interspersed patches of an ion conducting polymer will maintain charge balance between the two half-cells. The modularity of the system design approach allows each piece to be independently modified, tested, and improved, as future advances in semiconductor, polymeric, and catalytic materials are made. Hence, this work will demonstrate a feasible and functional prototype and blueprint for an artificial photosynthetic system, composed of only

inexpensive, earth-abundant materials, that is simultaneously efficient, durable, manufacturably scalable, and readily upgradeable.

4:20pm SS+EM-WeA8 Dual Passivation of the In_{0.53}Ga_{0.47}As (001)-(2x4) Surface with TMA and an Oxidant, T. Kent, M. Edmonds, E. Chagarov, University of California San Diego, R. Droopad, Texas State University, A.C. Kummel, University of California San Diego

III-V semiconductors are expected to be used as the channel material in future metal oxide semiconductor field effect transistors (MOSFETs) due to their intrinsically higher electron mobilities. Previous work has shown that the InGaAs (2x4) surface reconstruction has promising CV characteristics and is a viable choice for use as the channel[1], but there is a fundamental problem with this surface. Edmonds et al. showed that all In/GaAs (2x4) surfaces contain at least 8% α_2 -(2x4) unit cells and when alloying In/Ga to form InGaAs that number jumps to a minimum of 48%. [2] The α_2 -(2x4) unit cell is missing one As-As dimer on the row which results in metallic In-Ga bonds. These metallic bonds cause bond angle strain in the edge As atoms which prefer to be in tetrahedral sp³ bonding configuration. This strain causes a conduction band edge state in the (2x4) density of states (DOS), and prevents the Fermi level from being efficiently modulated without proper passivation techniques. In order to improve III-V based MOSFET performance it is crucial to passivate the intrinsic α_2 -(2x4) defect unit cells. Trimethylaluminum (TMA) does not react with the defect unit cells; therefore, in order to achieve an ideal interface a dual passivation scheme is necessary. In this study density functional theory (DFT) was used to show that there is a conduction band (CB) edge state associated with the defect unit cells. By inserting -OH, -SH, or -NH₂ into the metallic In-Ga bonds and to the edge In/Ga dangling bonds after TMA passivation, it is possible to fully passivate the CB edge state. Scanning tunneling microscopy and spectroscopy (STM/STS) was utilized to show that it is possible selectively passivate the α_2 -(2x4) by dosing H₂O (g) and maintain an unpinned Fermi level. Subsequently TMA was dosed to passivate the β_2 -(2x4) unit cells, STM shows an atomically ordered surface exists and ALD of Al₂O₃ was nucleated in each unit cell. STS showed that by using this dual passivation technique the Fermi level remained unpinned. Using the optimized oxidant dosing temperatures, the McIntyre group at Stanford has shown this dual passivation technique results in superior CV characteristics in MOSCAPs consistent with the dual passivation technique improving InGaAs based MOSFETs.

1)Hwang, Y, et al., *Influence of trimethylaluminum on the growth and properties of HfO[sub 2]/In[sub 0.53]Ga[sub 0.47]As interfaces*. Applied Physics Letters, 2011. 98(5): p. 052911.

2)M. Edmonds, W.M., T. Kent, E. Chagarov, A. C. Kummel, ECS Transactions, 2012. 50(4): p. 129-140.

4:40pm SS+EM-WeA9 Specific Attachment of Ethylenediamine on Modified Si(111) Surfaces, T. Peixoto, Y.J. Chabal, University of Texas at Dallas

Silicon nitridation is of fundamental interest to the microelectronics, biotechnology and nanotechnology communities, with its ability to act as an oxygen diffusion barrier for devices while concurrently optimizing the effective dielectric constant. The Si-N bond plays a key role in the stability of silicon nitride layers, used in devices due to its durability and thermal stability; amine groups aid in additional functionalization of surfaces enabling the attachment of quantum dots, nanoparticles, and biological molecules allowing for development of new surfaces/devices. The incorporation of nitrogen groups on the silicon surface thus allows for the creation of modified surfaces with expanded properties and extensive tailorability. Despite these advantages, a clear understanding of the underlying mechanisms towards well controlled nitride and amino group attachment on Si surfaces, is not completely developed.

To uncover the reaction mechanisms, we have performed experiments with several different Si(111) surfaces terminations (SiH, SiF, and SiCl) and reacted with the bifunctional molecule ethylenediamine (NH₂-CH₂-CH₂-NH₂). With its amine termination on ends of the molecule, ethylenediamine makes it possible to obtain amine functionality following Si-N attachment on the surface. Our results indicate that ethylenediamine only physisorbs on hydrogen-terminated Si(111) surfaces, as evidenced by the intensity and high wavenumber of the (N-H) deformation and stretch modes and the binding energy of the main N1s peak in XPS. When exposed to a 1/3 nanopatterned Si(111)-F surface, the intensities of the stretch and deformation modes are consistent with a 1/3 coverage, and their frequencies associated with interacting amine groups expected of an ordered monolayer. Importantly, XPS shows a component of the N1s core level that is associated with direct bonding to silicon. In contrast, ethylenediamine molecules appear to adsorb by bridge configuration on fully chlorine-terminated Si surfaces, indicating that both NH₂ ends dissociate and react, as evidenced by a dominance of Si-N bonds in XPS and undetectable (N-H) deformation and stretch in IR spectra.

These results provide a means to controlling amine functionalization of silicon surfaces, and further understanding of the reaction mechanism for nitrogen group attachment on F, Cl, H terminated Si(111) surfaces.

5:00pm SS+EM-WeA10 Lowering the Density of Electronic Defects on Organic-Functionalized Si(100) Surfaces, W. Peng, W.J. De Benedetti, S. Kim, University of Texas at Dallas, M.A. Hines, Cornell University, Y.J. Chabal, University of Texas at Dallas

The integration of self-assembled monolayers (SAM) with semiconductor surfaces helps to provide the functionality necessary for various application possibilities, ranging from molecular electronics, hybrid optoelectronics to chemical sensing. So far, Si(111) surfaces have been the most explored systems mainly due to the fact that atomically flat hydrogen terminated Si(111) surfaces can be easily prepared for further chemical functionalization. Recently a method to produce quasi atomically flat H-Si(001) surfaces has been developed¹ and the surface structure carefully studied with FTIR analysis, STM imaging and kinetic Monte Carlo simulations.

In this work, we compare the density of interface electronic states after organic functionalization (hydrosilylation) on both atomically rough and atomically flat Si(100) surfaces. Although differences in surface morphology are not detectable with FTIR or XPS, conductance voltage measurements² are able to detect a clear difference in interface state densities D_{it} (i.e., defect densities). Specifically, atomically flat Si(100) surfaces functionalized with $C_{11}H_{23}$ monolayers have D_{it} values three times lower than those of rough functionalized surfaces, leading to D_{it} values very close to our previous results on atomically-flat Si(111) surfaces functionalized with the same molecule.² These findings open the way for integrating common functionalization methods using the technologically important Si(100) surfaces to meet the needs of critical applications.

¹M. A. Hines, M. F. Faggin, A. Gupta, B. S. Aldinger, and K. Bao, J. Phys. Chem. C **116** (35), 18920 (2012).

²W. Peng, O. Seitz, R. A. Chapman, E. M. Vogel, and Y. J. Chabal, Appl. Phys. Lett. **101** (5) (2012).

5:20pm SS+EM-WeA11 Monolayer Doping via Arsenic Acid Grafting on Silicon Surfaces, A. Vega, W. Cabrera, R. Longo, Y. Lu, The University of Texas at Dallas, P. Thissen, Karlsruhe Institute of Technology, Germany, Y.J. Chabal, The University of Texas at Dallas

Density scaling and subsequent device dimension reduction continue to drive significant advances in the materials, processing, and architecture of advanced transistors. As gate lengths approach the sub-10 nm regime, junction doping has become an increasing concern due to its importance in controlling short channel effects. Source/drain junction depths must be extremely shallow and abrupt, typically around 1/3 of gate length (L_g). Unfortunately, the conventional technique for junction doping, ion implantation and anneal, is incapable of producing uniform and abrupt junctions shallower than 10 nm in depth due to random dopant fluctuations and ion-induced damage leading to broadened dopant profiles. Monolayer doping (MLD) is a promising technique for creating ultra-shallow junctions (USJs). The self-limiting nature of self-assembled monolayers (SAMs) of MLD provides uniform coverage of a specific quantity of dopant containing molecules. Subsequent high temperature anneals drive the dopant atoms into the semiconductor via diffusion mechanism.

In this work we explore how methyl arsonic acid molecules can be grafted on H-terminated Si(111) surfaces. This approach has recently been demonstrated for alkylphosphonic acids by Longo et al.¹, showing that the weak link of a molecule such as octadecylphosphonic acid (ODPA), is the P-C bond, with typical release of the carbon ligand around 500°C. First-principles calculations predict that the dissociation of the As-C bond occurs at lower temperature (barrier is 1 eV lower) and shallower junctions can be achieved due to the lower diffusion rate of arsenic compared to phosphorus. We have further used infrared absorption spectroscopy to determine the extent of chemisorption of the methyl arsonic acid molecules by quantifying the amount of H remaining and directly detecting the monolayer-Si bond (Si-O-As) at $\sim 1080\text{cm}^{-1}$. The final stage of the process (dopant diffusion) is characterized in-situ with Low Energy Ion Scattering (LEIS) with angstrom resolution, and supported by first-principles calculations.

(1) Longo, R. C.; Cho, K.; Schmidt, W. G.; Chabal, Y. J.; Thissen, P. Advanced Functional Materials 2013.

5:40pm SS+EM-WeA12 Defect Engineering in Metal Oxides via Control of Surface-Bulk Defect Interactions, P. Gorai, E. Ertekin, E.G. Seebauer, University of Illinois at Urbana Champaign

Control of native oxygen defects in transition metal oxides like ZnO plays an important role in photovoltaic, catalytic, photonic and gas sensing applications. The interaction chemistry between bulk point defects and reactive sites on clean semiconductor surfaces is comparable in richness to

the reactions of gases with surfaces. Surfaces of semiconducting metal oxides can be used to manipulate the concentrations and spatial distributions of oxygen defects, particularly oxygen vacancies. Such surface-based defect engineering methods should play an especially important role in nanostructured devices where the surface to volume ratio is high. The present work discusses a novel mechanism of bulk defect interaction with c-axis polar ZnO surfaces that enables control of oxygen defect injection. Oxygen diffusion rates were measured by exposing natural-abundance single-crystal c-axis wurtzite ZnO to isotopically-labeled oxygen ($^{18}\text{O}_2$) gas. The resulting diffusion profiles were measured by secondary ion mass spectrometry (SIMS) and modeled with mass transport equations for the reaction and diffusion of mobile and stagnant oxygen point defect species. The effective oxygen diffusivity is determined by fitting this model to experimental diffusion profiles. In addition, first principles calculations based on density functional theory (DFT) were performed to identify the elementary-step oxygen defect injection mechanism for active site exchange. Influence of the surface polarity on defect injection rates was also investigated. Gas-solid exchange experiments coupled with continuum and *ab initio* modeling will help us understand mechanistically the effect of each of the elementary steps on the defect injection rates at polar ZnO surfaces.

Transparent Conductors and Printable Electronics

Focus Topic

Room: 102 B - Session TC+EM+EN+TF-WeA

Transparent Conductors and Photovoltaics

Moderator: G.S. Herman, Oregon State University, G.L.

Whiting, Palo Alto Research Center

2:00pm TC+EM+EN+TF-WeA1 Metal Nanowires-based Composite Transparent Electrodes for Photovoltaics, J. Moon, A. Kim, Y. Won, Yonsei University, Republic of Korea

INVITED

To fabricate cost-effective solar cells, it is imperative to develop a low cost transparent electrode with low resistivity and high transparency. Although crystalline indium tin oxide (ITO) has been widely adopted as a transparent electrode in solar cells, it is an undesirable material for use in low cost solar cells because of the scarcity of indium and its high deposition cost. Silver nanowires (AgNWs) network films have recently attracted substantial interest as a transparent conducting material. Transparent electrodes composed of random AgNW networks can be readily achieved by simple and scalable solution processing such as spin coating and rod coating from AgNWs dispersion. However, the AgNWs film is easy to undergo local oxidation and melting on a heated substrate, which adversely affects the conductivity of the AgNWs film. In addition, the low carrier collecting efficiency of AgNW films could pose another hurdle. The limited contact area of AgNWs with *n*-type or buffer layers is incapable of effectively collecting the charge carrier generated at the *p-n* junction. Here, we propose a sandwich composite electrode structure of Al doped ZnO (AZO)/AgNWs/AZO fabricated by all solution processes. The AZO/AgNW/AZO composite structure is suitable for cost-effective large area fabrication, because it involves relatively low-cost materials, and it is prepared by scalable solution processes instead of high-vacuum process. The AgNWs inserted in AZO layers reduced sheet resistance dramatically of a solution processed AZO layer, and the density of AgNWs plays an important role in determining the film conductivity and optical transparency. The AZO underlayer acts as an *n*-type buffer layer as well as a surface flattener against the absorber layer, while the upper layer prevents the AgNWs from local melting-induced disconnection. As a result, the thermal stability of the AgNWs was enhanced and the adhesion of AgNWs to the substrate was improved. Such a composite electrode is also capable of effective charge carrier collection due to filling the empty space unoccupied by AgNWs with AZO materials as well as resulting in a better surface smoothness. We applied the AZO/AgNW/AZO composite electrode on the CIGS thin film solar cells and observed the power conversion efficiency of 11% comparable to reference ITO used solar cells. We also demonstrated the similar approach involving copper nanowire (CuNW) in form of AZO/CuNW/AZO. Our low temperature processed AZO/CuNW/AZO composite electrode at 70°C exhibited highly transparency (> 88%) and low sheet resistance (< 25 ohm sq^{-1}) as well as good thermal oxidation stability against the exposure to air and flexibility.

2:40pm **TC+EM+EN+TF-WeA3 Modeling and Characterization of Ag Nanowire-Based Transparent Conductors: Towards Optimization of Electrical and Optical Properties**, *S. Narayanan, C. Treacy, M.R. Bockstaller, L.M. Porter*, Carnegie Mellon University

Many contemporary devices, including displays, solar cells and LEDs, employ transparent conducting films. The traditional materials for transparent conductors are transparent, conductive metal oxides, primarily tin-doped indium oxide (ITO). However, due to the increased cost of indium and other challenges with ITO, significant effort has been devoted to develop alternatives that are cheaper, flexible, and compatible with a variety of substrates. One alternative is based on random networks of solution-processed silver nanowires (Ag-NWs). While being comparable to ITO in their electrical and optical properties, the high variability in films of Ag-NWs fabricated by solution-processing is a major concern for scalability and reproducibility. The variability in NW coverage can be attributed to instability of the NWs in solution, which can be addressed by the use of polymer additives and modified solution chemistries. For example, we found that composites of Ag-NWs and poly(ethylene dioxythiophene):poly(styrene sulfonate) (PEDOT:PSS) can be deposited more uniformly and reproducibly than films comprised of Ag-NWs only. Ag-NW films that were spun-cast from solution showed bulk-like electrical resistivities ($\sim 2\text{-}50 \text{ } \Omega/\text{sq}$) while being highly transparent ($\sim 70\text{-}90\%$). The films show a variability in NW coverage of $\sim 15\%$, owing to aggregation. Spun-cast films of the Ag-NW/PEDOT:PSS composites show similar transmittances and resistivities but with significantly reduced variability in NW coverage of $<5\%$. Composites with higher aspect ratios (smaller NW diameters) also show similar resistivities at transmittance values approximately 5% higher, thus showing great potential for use as transparent conductors. Additionally, by obtaining similar resistivities at lower Ag-NW coverage densities, the composites effect a lowering of the threshold for percolative conduction.

In order to understand how the processing and physical conditions affect the electrical and optical properties of these NW networks, we have also modeled NW-networks under conditions similar to those of the experimental system. Both simulation and experiment show that the percolation threshold of these networked conductors can be shifted towards lower NW densities via parameters such as the nature of the NW dispersion, the composition of the network, and the NW geometry. In this presentation, we discuss results how each of these parameters affects the electrical and optical properties of Ag-NW networks, including their reproducibility, on the way towards achieving optimized characteristics for their use in devices.

3:00pm **TC+EM+EN+TF-WeA4 Surface Modification of ZTO/Al/ZTO Stack Structure using Inductively Coupled Plasma**, *H.S. Kim*, Chung-Ang University, Republic of Korea, *J.C. Woo*, ETRI, Republic of Korea, *Y.H. Joo, K.R. Choi, Y.S. Chun, C.I. Kim*, Chung-Ang University, Republic of Korea

Transparent conductive oxide (TCO) is material which simultaneously possesses the properties of electrical conductivity and optical transmission. TCO is a doped metal oxide thin film mainly used in optoelectronic applications such as transparent electrodes in touch panels, flat panel displays (FPDs), and other future devices. Among the new TCO, Zinc tin oxide (ZTO) is a one of very promising candidate. ZTO has the advantage of good stability at high temperature and unlike other popular TCOs such as ITO and Cd-Sn-O, ZTO films do not contain expensive or toxic elements. Another advantage of ZTO is its low sensitivity towards visible light. Moreover, Conductivity of ZTO thin films can be increased by doping of ZTO with aluminum. In many organic and hybrid devices al-doped ZTO thin films are used as the anode or hole transport layer. In order to get excellent device characteristics in OLED applications, efficiency of hole injection is important factor. In this study, the effects of various gases employed of plasma treatments of al-doped ZTO anode surfaces have been studied in an Inductively Coupled Plasma (ICP). The surface modification of al-doped ZTO was studied as a function of the process parameters, including a RF power, a process time and a process pressure. By modifying the surface properties of the al-doped ZTO, the work function of the anode can be considerably varied to alter the hole-injection energy barrier. The work function of the treated al-doped ZTO thin film was investigated by Surface Analyzer (AC-2). The analysis of X-ray Photoelectron Spectroscopy (XPS) was carried out to investigate the chemical reactions between the surface of al-doped ZTO thin films and etch species. Surface morphology of the treated al-doped ZTO was characterized using Atomic Force Microscope. As a result of XPS and AFM analysis, plasma treatment reduces the carbon contamination of al-doped ZTO surface and increases the work function of it.

4:00pm **TC+EM+EN+TF-WeA7 Printing Photovoltaics**, *M.F.A.M. van Hest, S. Habas, H. Platt, R. Pasquarelli, J. Fields, D. Ginley*, National Renewable Energy Laboratory

INVITED

Photovoltaics are becoming an increased part of the energy supply mix, however the cost is currently too high. In order to reduce the cost, moving towards non-vacuum production routes is very attractive because of the low capital equipment cost. Non-vacuum processes can be used in several steps of the photovoltaic cell and module manufacturing process, for both wafer based and thin film photovoltaics. The different components can be deposited and processed using one of many non-vacuum techniques, e.g. inkjet printing, aerosol jetting, slot coating and spray coating. Details about these techniques will be discussed. Since non-vacuum techniques use a chemical route to the end product, inks are the key to success. Inks have been developed for metallization grids, e.g. Ag, Cu, Ni, and Al, but also for absorbers, e.g. CIGS and organics. These materials can be processed under atmospheric conditions and have properties similar to their vacuum deposited counterparts. Aside from the absorber and the metallization, transparent conductors are an intrinsic part of thin film photovoltaic devices, however transparent conductive oxides have only been deposited and processed from inks with moderate success. Research to overcome this last hurdle is under way and focuses on chemical routes to oxides as well as alternatives, i.e. metal nanowires, with the latter showing potential. Several details of non-vacuum processing of the various components of photovoltaic cells will be addressed.

5:00pm **TC+EM+EN+TF-WeA10 Interfacial Layer Engineering of Transparent Conductive Oxides for Optoelectronic Device Application**, *I.T. Martin, H.M. Lemire, K.A. Peterson, M.S. Breslau, K.D. Singer, R.H. French*, Case Western Reserve University

Transparent conductive oxides (TCOs) have widespread utility as electrical contacts in photovoltaic (PV) and other optoelectronic devices, such as display screens and organic light emitting diodes (OLEDs). The TCO surface chemistry can be tailored through the addition of interfacial layers (IFLs), such as polymers, covalently bonded organofunctional silanes, and chemisorbed small molecules. These IFLs can be used to optimize rates of charged carrier transfer, and increase the compatibility of the polar TCO with nonpolar materials used in OPVs and OLEDs. Understanding the interactions between these materials and the TCO interfaces is essential to controlling device performance. For example, PEDOT:PSS (poly(3,4-ethylenedioxythiophene) poly(styrenesulfonate)), a polymer commonly used in OLED and OPV devices, functions as an electron blocking layer for the TCO anode, improving device efficiency. However, the polymer is highly acidic and can be corrosive to the TCO layer; in the case of organic PV devices, this can limit their lifetime.

We used organofunctional silanes, including allyl triethoxy silane (ATES), octa-decyl-trichloro silane (OTS), 3-aminopropyl-triethoxy silane (APTES) and 3-aminopropyl-dimethyl-ethoxy silane (APDMES), to modify indium tin oxide (ITO), aluminum doped zinc oxide (AZO) and fluorine doped tin oxide (FTO). We characterized the electrical and optical properties and surface energies of the silanized TCOs, and compared the results to a standard OPV polymer, PEDOT:PSS. Results demonstrate that varying the functionality and deposition conditions of the silane is a simple method of tuning and customizing the surface energy of the hydrophilic TCO; water contact angles ranging from 57° (APDMES) to 94° (OTS) are achieved without affecting the TCO transparency or conductivity. Additionally, both bare and silanized ITO, AZO and FTO were exposed to damp heat (DH, 85°C , 85% relative humidity) for up to 1000 hours. After each exposure a standard cleaning process was used and the TCOs' electrical and optical properties and surface energies were determined. Using contact angle measurements with multiple fluids, the surface energies of the TCOs were tracked, and the largest change in total surface energy was found for AZO, then ITO, with FTO remaining essentially unchanged for the conditions studied. In preliminary degradation studies of TCO/silane stacks, ATES was found to delay and reduce the resistivity increase of ITO in damp heat. Further degradation data of TCO/silane stacks, with and without encapsulation will be presented.

5:20pm **TC+EM+EN+TF-WeA11 Growth and Characterization of Epitaxial $(\text{Al}_x\text{Ga}_{1-x})_2\text{O}_3$ Alloy Films**, *B. Krueger*, University of Washington, *N. Nguyen, T. Chikyow*, National Institute for Materials Science, Japan, *F.S. Ohuchi, M.A. Olmstead*, University of Washington

Gallium oxide is a transparent semiconductor ($E_g \sim 4.8 \text{ eV}$) that exhibits n-type conductivity; it has been proposed for a variety of uses ranging from "solar-blind" conductive coatings to chemical sensing. An intriguing possibility is development of transparent, high power transistors based on carrier accumulation at an epitaxial Ga_2O_3 - $(\text{Al}_x\text{Ga}_{1-x})_2\text{O}_3$ alloy interface. Using pulsed laser deposition, combinatorial $(\text{Al}_x\text{Ga}_{1-x})_2\text{O}_3$ thin films were fabricated on a variety of substrates, including sapphire, GaN, SrTiO_3 and LaAlO_3 , with x varying smoothly across the surface. Position-dependent X-ray diffraction revealed [-201]-oriented Ga_2O_3 on hexagonal GaN (0001)

surfaces (5% lattice mismatch) and predominantly [-201]-oriented on c-plane sapphire (8% mismatch). Alloy $(\text{Al}_x\text{Ga}_{1-x})_2\text{O}_3$ films remain in the $\beta\text{-Ga}_2\text{O}_3$ phase for $0 < x < 0.15$ on GaN and $0 < x < 0.35$ on sapphire, with negligible lattice expansion; a new alloy phase is observed for $0.15 < x < 0.35$ on GaN. Photoemission spectroscopy shows core and valence levels both shift to higher binding energy with increasing Al concentration, and the work function decreases, consistent with a widening band gap.

This work was supported by the National Science Foundation under DMR 1104628 and OISE 1209856 and by the Micron Foundation.

5:40pm **TC+EM+EN+TF-WeA12 Weakly Bounded Zn Atoms in Polycrystalline ZnO Thin Films caused by Ga Doping, H. Makino, H. Song, T. Yamamoto**, Kochi University of Technology, Japan

Ga-doped ZnO (GZO) is promising candidate for alternative to ITO as transparent electrodes. We have reported that thermal desorption of Zn from polycrystalline GZO films starts at a little low temperature of 150 °C, which is close to the deposition temperature [1]. The amount of desorbed Zn from GZO films showed strong correlation with carrier concentration [1]. The Zn desorption also appeared in epitaxially grown GZO films deposited on sapphire substrates. In this paper, we reports thermal desorption of Zn in comparison between GZO films and ZnO films deposited on glass substrates.

The 150 nm thick GZO and ZnO films were deposited on glass at a substrate temperature of 200 °C using ion plating with DC arc discharge. The oxygen gas was introduced to the deposition chamber during the deposition process. The oxygen gas flow rate (OFR) was varied between 5 sccm and 25 sccm. Thermal desorption spectroscopy (TDS) was employed to evaluate characteristics of Zn desorption.

The TDS of Zn for the ZnO film deposited at 10 sccm showed a dominant desorption peak at 450 °C and a shoulder peak at 500 °C. The intensities decreased with increasing the OFR, and the peak at 500 °C disappeared with increasing the OFR to 20 sccm. On the other hand, the TDS of Zn for the GZO films deposited at the OFR of 10 sccm showed two peaks at 300 and 400 °C. The intensity of peak at 300 °C decreased with increasing the OFR, and the peak at 400 °C shifted to high temperature with increasing the OFR. Then, the TDS result of GZO deposited at 25 sccm showed one peak at 450 °C, which is similar to the dominant peak observed in the undoped ZnO films. The lower temperature of TDS peak of Zn suggests existence of weakly bounded Zn atoms in the GZO films. The weakly bounded Zn atoms are obvious in the GZO films deposited at low OFR conditions. It is possible to say that the weakly bounded Zn atoms were caused by high density of Ga doping to ZnO.

[1] H. Makino, Y. Sato, N. Yamamoto, T. Yamamoto, *Thin Solid Films* **520**, 1407 (2011).

Thin Film

Room: 104 A - Session TF+AS+BI+EM+SE+SS-WeA

Applications of Self-Assembled Monolayers and Nano-Structured Assemblies

Moderator: M.R. Linford, Brigham Young University, H. Zuilhof, Wageningen University, Netherlands

2:00pm **TF+AS+BI+EM+SE+SS-WeA1 Enhanced Multiphoton Processes for Molecule Localization on Plasmonic Nanostructures, J. Shumaker-Parry**, University of Utah **INVITED**

Plasmonic nanostructures produce enhanced optical near fields as a result of localized surface plasmon resonances (LSPRs). Tailoring of the nanostructure size, shape, and inter-structure spacing provides tuning of the LSPR properties including the near field behavior. We use two approaches to produce plasmonic architectures with enhanced fields. First, we have developed an asymmetric functionalization process to create nanoparticle assemblies by controlling the localization of molecules on the surface of the nanoparticles. The spatial localization of the molecules on the Janus-like particles lead to controlled assembly and direction of molecules into regions of enhanced near fields, a process that can be monitored through enhanced spectroscopy. The second approach we use is based on nanosphere template lithography to fabricate uniquely-shaped plasmonic nanoantennas. One example is the nanocrescent which exhibits polarization dependent LSPR responses across a broad spectral range, from the visible through the mid-infrared regions. Simulations of the LSPR response predict localized, inhomogeneous near fields around the nanocrescent antennas. We mapped the local fields of nanocrescents through an enhanced multiphoton photopolymerization process. Local cross-linking of a photopolymer provides evidence of the near field behavior and confirms the predicted polarization-

depend enhanced fields. Localized photopolymerization can be used to spatially localize molecules at the nanoscale through these enhanced fields created by the plasmonic nanoantennas.

2:40pm **TF+AS+BI+EM+SE+SS-WeA3 A Path towards Single-Electron Devices, P. Campbell**, University of Texas at Dallas, *L. Caillard, O. Pluchery*, University of Pierre and Marie Curie, France, *Y.J. Chabal*, University of Texas at Dallas

As the minimum feature size in CMOS technology continues to decrease, quantum effects begin to dominate the operation of the transistors. In order to compensate for these effects, we require a new transistor design that operates based on the quantum effects present at the nanoscale. Single-electron transistors present a viable option to create smaller, more efficient transistors but a high-yield process has not yet been developed for their manufacturing.

In addition to the increasing effect of quantum mechanics, current lithographic methods face challenges in scaling below the 10 - 20 nm scale. Several proposed lithographic methods, such as direct write methods, can provide high resolution lithography, enabling the creation of transistors in the sub-10 nm region. However, direct write methods require extensive development of multi-tip approaches to achieve throughput comparable to optical lithography.

A chemical method to fabricate devices can create high performance transistors with a high throughput. The first step of this process is the deposition of a monolayer of organic molecules on a hydrogen-passivated silicon surface. Second, mono-dispersed gold nanoparticles are deposited on the surface to form a tunnel junction. The electrical properties of the sample are determined by probing the surface with scanning tunneling microscopy (STM). This results in a double-tunnel junction. By properly tailoring the nanoparticle size, organic molecule size, and STM tip-sample distance, a Coulomb staircase can be observed in the I-V curve of the junction [1].

Using a 1.7 nm thick organic molecule, evidence consistent with a Coulomb staircase is observable on a small number of spectroscopy curves. However, the electronic response of each nanoparticle is not consistent. This suggests that thermal and electronic noise play a significant role in the measurement and behavior of double-tunnel junctions. As well, the properties of the junction are influenced greatly by the quality of the interface between the substrate and organic layer and the organic layer itself. By exploring the chemistry of varying length molecules on the surface and characterizing the quality of attachment and durability of the organic layer, optimization of the samples is possible to create more reliable double tunnel junctions.

References:

[1] K. Mullen, E. Enjacob, R.C. Jaklevic, Z. Schuss. I-V Characteristics of Coupled Ultrasmall-Capacitance Normal Tunnel-Junctions. *Phys. Rev. B* **37** (1988) 98-105.

3:20pm **TF+AS+BI+EM+SE+SS-WeA5 Chemical and Electronic Interface Formation between a Monolayer and Cobalt, S. Pookpanratana, H.-J. Jang, L.K. Lydecker, C.A. Richter, C.A. Hacker**, National Institute of Standards and Technology (NIST)

Organic-based electronics are attractive for next-generation applications because of the wide range of possibilities in tailoring the chemical structure of molecules for a desired functionality. An emerging field is to combine the flexibility of organic materials into spintronics. While the self-assembly of molecular layers onto Au is well-studied, self-assembly does not form as readily between molecules and a ferromagnetic metal due to the lack of control of the interface composition (i. e., oxide formation). Conventional approaches to fabricate hybrid organic-metal interfaces have relied on vacuum-based physical vapor deposited organic molecules since the metal-organic interface can be better controlled. However, vacuum-based deposition of organic materials limits the manufacturing and applications of such hybrid systems making solution-based processes attractive for organic-based electronics. We have explored self-assembled monolayers (SAM) on a template-stripped Co surface to understand the molecular-metal interface from a structural, chemical, and electronic point of view.

Template-stripped Co is a method to prepare consistent surfaces that can be used in ambient conditions. First, Co is evaporated onto a molecular layer-treated Si (tSi) surface, and then the Co surface is laminated to a plastic substrate. The plastic/Co surface is stripped off of the tSi and immediately placed into SAM solution. We chose octadecanethiol (ODT) and mercaptohexadecanoic acid (MHA) as “fruit fly” molecules to self-assemble onto Co. This hybrid molecule-metal interface is investigated by using microscopy, infrared spectroscopy, and photoelectron spectroscopy to provide details of the physical, chemical, and electronic structure at that interface.

The self-assembly of ODT and MHA are directly confirmed by infrared spectroscopy and X-ray photoelectron spectroscopy (XPS). The absorbance intensities of the C-H stretches of ODT and MHA on Co are comparable to

those on Au, which indicates similar packing density on both surfaces. MHA has the added complexity with both the -SH and -COOH functional groups are able to bond. Moreover, the -COOH groups also affect the Co surface by reducing the native oxide as shown by XPS. Molecular electronic junctions formed on Si by flip-chip lamination [1] show that electron transport is heavily influenced by the MHA/Co interface or Co electrode when compared to a Si/MHA/Au control device. Preliminary results suggest that SAMs on Co surfaces are a promising route for controlling the organic-ferromagnet interface for next generation devices.

[1] M. Coll et al., *J. Am. Chem. Soc.* 2009, 131, 12451-12457.

4:00pm **TF+AS+BI+EM+SE+SS-WeA7 Stability of the Molecule-Substrate Interface in SAMs Probed by SIMS – Experiments and Simulations**, *J.W. Ossowski, J. Rysz, D. Maciazek*, Jagiellonian University, Poland, *M. Krawiec, Maria Curie-Sklodowska University*, Poland, *Z. Postawa*, Jagiellonian University, Poland, *A. Terfort*, Goethe University, Germany, *P. Cyganik*, Jagiellonian University, Poland

Self-Assembled Monolayers (SAMs) play nowadays a key role in many aspects of nanotechnology ranging from patterning and molecular electronics up to biocompatible materials. One of the key requirements for successful use of SAMs in all of these applications is a control of their stability at the molecule-substrate interface. Analysis of this interface is however extremely difficult for technologically relevant, and therefore, more complicated SAMs. In this presentation we report extensive static secondary ion mass spectrometry (SIMS) studies on series of thiols and selenols on Au(111) substrates where structure and stability of molecule-substrate interface were systematically modified.¹ Correlating SIMS data with our previous microscopic^{2,3}, spectroscopic⁴ and neutral mass spectrometry studies^{5,6} we show that, SIMS can be successfully applied to monitor fine changes in the molecule-substrate interface stability of these model SAMs. To reveal the possible mechanism of ion-induced desorption sensitivity to the SAM-substrate interface energetics we discuss also results of our molecular-dynamic (MD) simulations of the desorption process for this system with starting structure calculated by DFT calculations.¹ Our data show that a new approach for probing the stability of molecule-substrate interface in SAMs can be proposed by using such relatively popular and fast technique as SIMS, which can be applied for virtually all complicated and technologically relevant SAMs.

References

- (1) J. Ossowski, P. J. Rysz, D. Maciazek, M. Krawiec, Z. Postawa, A. Terfort and P. Cyganik *submitted*.
- (2) P. Cyganik, K. Szlagowska-Kunstman, et al. *J. Phys. Chem. C* **2008**, *112*, 15466.
- (3) M. Dendzik, A. Terfort, P. Cyganik *J. Phys. Chem. C* **2012**, *116*, 19535.
- (4) K. Szlagowska-Kunstman, P. Cyganik, et al. *Phys. Chem. Chem. Phys.* **2010**, *12*, 4400.
- (5) S. Wyczawska, P. Cyganik, A. Terfort, P. Lievens, *ChemPhysChem(Communication)* **2011**, *12*, 2554.
- (6) F. Vervaecke, S. Wyczawska, P. Cyganik, et al. *ChemPhysChem(Communication)* **2011**, *12*, 140.

4:20pm **TF+AS+BI+EM+SE+SS-WeA8 Controlled Modification of Protein-Repelling Monomolecular Films by Ultraviolet Light: The Effect of Wavelength and Implications for Lithography**, *Y.L. Jeyachandran*, University of Heidelberg, Germany, *A. Terfort*, Frankfurt University, Germany, *M. Zharnikov*, University of Heidelberg, Germany

Advanced lithographic techniques applied to monomolecular resists enable the fabrication of well-defined patterns of functional biomolecules, above all proteins, and specific receptors, which are the key elements of biosensors, bio-fouling analysis assays, cell studies, and tissue engineering applications. An essential element of such patterns is a protein-repelling "background" surrounding the pre-selected sensing areas and preventing non-specific adsorption of proteins beyond these regions. Here we use protein-repelling oligo(ethylene glycol) (OEG) terminated alkanethiolate (AT) monolayers on gold as matrix for the preparation of such patterns. Exposure of this matrix to ultraviolet (UV) light results in the damage of the OEG chains and photooxidation of the thiolate headgroups, which can be used for controlled tuning of protein-repelling properties within so-called UV direct writing (UVDW) approach or for the preparation of mixed OEG-AT/specific-receptor films by so-called UV-promoted exchange reaction (UVPER). Using several model systems, we studied the effect of the wavelength (254 – 390 nm) on the course and efficiency of the UVDW and UVPER processes applied to different OEG-AT matrices. The cross sections of the UV induced damage were found to decrease significantly with increasing wavelength of UV light. In accordance with this behavior, the efficiencies of both UVDW and UVPER were maximal at a wavelength of 254 nm, somewhat lower at 313 and 365 nm, and lowest at 390 nm. Both UVDW and UVPER allowed a fine tuning of protein affinity for non-

specific and specific adsorption, respectively, but UVDW did not occur below a certain, wavelength-dependent threshold dose. Performing UVPER below this dose enables to suppress possible non-specific adsorption of proteins even in the case of non-complete exchange of the UV-damaged molecules of the primary OEG-AT matrix by receptor-bearing moieties. The obtained results are of direct relevance for the preparation of high-quality mixed OEG-AT/specific-receptor films and the fabrication of complex protein patterns.

4:40pm **TF+AS+BI+EM+SE+SS-WeA9 The 2D Self-Assembly of Strongly Dipolar Molecules**, *A. Enders, D. Kunkel, S. Beniwal, P.A. Dowben*, University of Nebraska Lincoln, *S. Simpson, E. Zurek*, State University of New York at Buffalo

The self-assembly of organic molecules on flat metal surfaces can differ considerably from the well-known solution-based supramolecular chemistry. Substrates may set limits to the mobility of molecular adsorbates, and interactions across the organic/inorganic interface may perturb the electronic structure of the molecules and the substrate considerably. As a result, their diffusivity, the strength of chemical bonds, charge, protonation and deprotonation may all be dependent on the substrate itself. This can be exploited to engineer unique structures and properties that may not exist naturally in the respective crystalline phase.

One of the central questions in organic self-assembly is the role of an intrinsic molecular electric dipole and how the resulting electrostatic interaction competes with other chemical bonds. We studied small molecules with large intrinsic electrical dipole as model system for molecular films adsorption on surfaces for altering the interface dipole screening. For instance, we investigated the self-assembly and interface properties of zwitterionic molecules of type C6H2(...NHR)2(...O)2 (R = H, ...), adsorbed on Cu(111), Ag(111), Au(111) surfaces with scanning tunneling microscopy in UHV [1]. These molecules carry positive and negative charges on opposite parts of the molecule, resulting in a huge electric dipole of typically 10 Debye. We find that the dipole of the surface-supported molecule is decreased with respect to free species and of order of 1 - 2 Debye, depending on the substrate material. The molecules self-assemble into 2D structures upon adsorption, where the substrate-dependent strength of the dipolar interactions between the adsorbed molecules can dictate the network architecture. DFT calculations were performed to analyze adsorption geometry, charge transfer and dipole moment. By systematic comparison of the self-assembly of those molecules on different metal substrates we were able to show that the intrinsic dipole mainly plays a role in the structure formation if the interaction strength with the substrate is very weak, otherwise epitaxial fit to the substrate dictates the molecular arrangement.

5:00pm **TF+AS+BI+EM+SE+SS-WeA10 Quasicrystalline Ordering in Small-Molecule Self-Assembly**, *N.A. Wasio, R.C. Quardokus, R.P. Forrest, C.S. Lent, S.A. Corcelli, J.A. Christie, K.W. Henderson, S.A. Kandel*, University of Notre Dame

Scanning tunneling microscopy was used to study self-assembly of carboxylic acid monolayers. In most cases, the formation of two strong hydrogen bonds results in dimer formation; in some others, linear catemer chains are formed. We report the observation of a five-membered catemer ring, stabilized by additional CH...O interactions available in the cyclic structure. We confirm the existence of CH...O hydrogen bonding, both with density functional theory calculations and by observing the disappearance of pentamers when molecules without suitable CH donors are used. Long-range assembly of pentamers results in a two-dimensional quasicrystalline lattice, the first observation of such structure from small-molecule self-assembly.

5:20pm **TF+AS+BI+EM+SE+SS-WeA11 Unexpected Behaviour of Liquid Wetting at the Limit of Small-Scale Surface Topography**, *J. Knauf*, Advanced Molecular Films GmbH and RWTH Aachen University, Germany, *L. Reddemann*, Advanced Molecular Films GmbH and Universität zu Köln, Germany, *A. Böker*, RWTH Aachen University and DWI an der RWTH Aachen e.V., Germany, *K. Reihls*, Advanced Molecular Films GmbH, Germany

The size of topographic surface structures that affect wetting can be as small as sub-nanometer dimensions. As a model system we prepare monolayer from binary mixtures of 1H,1H,2H,2H-perfluoroalkyl thiols of different chain lengths on gold. Detailed characterization by static secondary ion mass spectrometry and ellipsometry confirm binary monolayer of randomly mixed constituents. Owing to their stiff helical conformation such perfluoroalkyl chains create topographic features of well-characterized sub-nanometer dimensions. As a result, surface topographies of randomly distributed long and short chains of a height difference of 1.2 Å per CF₂ group and a next neighbor distance of 5.8 Å are obtained.

We present comprehensive investigations of wetting properties of such binary monolayers of various molar fractions and chain length differences. As an example, a binary mixed monolayer from 1H,1H,2H,2H-perfluorodecyl and 1H,1H,2H,2H-perfluorododecyl thiols, thus differing by two CF₂ groups increase the advancing water contact angle from 116.0° for either one of the single component monolayer by about 2° to 117.7° for a surface of an equimolar composition of the two constituents. Such increase is considerably less than expected from simple thermodynamic models. Wenzel's equation of wetting on rough surfaces predicts an advancing angle difference of 7°. Results of contact angles of different liquids on various sub-nanometer size topographies will be presented and discussed assuming an apparent effective reduction of surface energy at short length scales similar to results obtained from grazing-incidence X-ray scattering experiments [1].

[1] S. Mora *et al.*, Phys. Rev. Lett. **90**, 216101 (2003)

5:40pm **TF+AS+BI+EM+SE+SS-WeA12 The Balance between Transparency and Roughness on a Superhydrophobic Coating.** C. Wang, A. Wu, R. Lamb, University of Melbourne, Australia

High orders of interfacial roughness are known to scatter light; as a result, superhydrophobic surfaces, which are inherently rough, generally appear opaque. Therefore, an ideal range of roughness that can provide both superhydrophobicity and low light scattering in the visible light spectrum is a highly attractive challenge. The use of self-assembling nanoparticles is a popular choice to generate the required roughness for superhydrophobicity. While such systems offer ease of fabrication and processing, coating thickness is generally kept to a minimum to reduce light scattering, below the light scattering threshold, typically in the sub-micron scale. The degree of roughness in a sol-gel synthesized coating can be manipulated using differences in solvent polarity and vapor pressures. There is a clear trend in solvent-particle and particle-particle interaction under polar and non-polar solvents, resulting in a difference in nanoparticle cluster size^[1], which contributes to light scattering. Changes in vapor pressure can also result in surface morphology formation during the drying process. We demonstrate that a simple change in solvent polarity on a sol-gel system can increase the optical transparency of a coating of thickness > 1 μm from 82-96% to 93-100% transparent in the visible spectrum. Meanwhile, the increased drying temperature from 100°C to 350°C can transform the coating's hydrophobicity to superhydrophobicity.

1. Khan, S.A. and N.J. Zoeller, Journal of Rheology, 1993. (6): p. 1225-1235.

Thin Film

Room: 102 C - Session TF+AS+NS+SE-WeA

Beam and Glancing Angle Deposition (GLAD) Techniques

Moderator: T. Karabacak, University of Arkansas at Little Rock

2:40pm **TF+AS+NS+SE-WeA3 GLAD-ALD Core-Shell Nanorod Arrays for Solar Cell Applications.** N. Biyikli, C. Ozgit-Akgun, A. Haider, Bilkent University, Turkey, H. Cansizoglu, M.F. Cansizoglu, T. Karabacak, University of Arkansas at Little Rock

In a nanostructured photovoltaic cell, one should take into consideration the competing effects of enhanced light absorption and shorter carrier collection lengths that both lead to improved photo-conversion efficiencies, and negative effects due to the larger amounts of surface recombination events. However, a key limitation to systematically investigating this in detail originates from the disordered random network nature and the wide particle size distribution of nanostructured geometries studied in the past. In addition, most of the nanofabrication methods that can produce uniform nanostructure geometries are limited to certain material systems. Therefore, it is essential to develop innovative low-cost solar cell fabrication approaches that can provide semiconductor nanostructures of a variety of materials with uniform and optimized geometries for improving cell efficiencies. In this work, we demonstrate a novel nanostructured solar cell fabrication method using core-shell radial junction nanorod arrays, which can potentially offer superior conversion efficiencies compared to conventional planar designs. Nanorod arrays of metallic/semiconductor materials (core) were produced by utilizing glancing angle deposition (GLAD) technique. GLAD metallic nanorods were made of molybdenum (Mo) and semiconducting ones were indium sulfide (In₂S₃). For the fabrication of proof-of-concept nanostructured photovoltaic cells, we conformally coated GLAD nanorods with semiconducting metal-oxide layers (shell) of zinc oxide (ZnO) and titanium dioxide (TiO₂) using atomic

layer deposition (ALD) method. Our preliminary structural, optical, electrical, and solar cell characterization results are presented.

3:00pm **TF+AS+NS+SE-WeA4 Branched Nanostructured Anodes for Dye-Sensitized Solar Cells.** W. Alayashi, K. Robbie, Queen's University, Canada

The nanostructured metal oxide layer, typically TiO₂, that is part of the conductive electrode (anode) is the most puzzling component of Dye Sensitized Solar Cells (DSSCs). While the sponge-like morphology of the sintered-powder electrode improves efficiency by providing a high surface area scaffold for adsorption of light-absorbing dye molecules, the convoluted transport paths for photo-generated charge carriers ultimately limit achievable efficiency. Its morphology has been identified as an important efficiency-limiting aspect of TiO₂ films. A DSSC is composed of a conductive electrode (anode), a nanoporous metal oxide film such as TiO₂, an organic sensitizing dye, a redox electrolyte, and a cathode electrode. Behaviour of the porous anode is strongly influenced by several factors: the open structure of the electrode that permits electrolyte penetration through the entire electrode, the small size of the individual colloidal particles that prevents accumulation of a large space charge, and the low intrinsic conductivity of TiO₂. I will present a demonstration of a new type of DSSC nanostructured oxide layer based on a fractal structure (branched tree-like morphology) for the metal oxide anode, and the effect of this morphology on electron transport and thus the overall efficiency of DSSC. Different thicknesses of the tree-like morphology films are fabricated to find their influence on photovoltaic performance. The result includes a comparison of the DSSCs efficiencies that are made by Glancing angle deposition technique, conventional nanoparticulated DSSCs and highly ordered nanotube arrays.

4:40pm **TF+AS+NS+SE-WeA9 Thermal Annealing Study of Nickel Nanorod Arrays.** E. Alrashid, D. Ye, Virginia Commonwealth University

Nickel nanorods arrays were prepared on silicon (100) substrates using the glancing angle deposition (GLAD) technique. The nanorods with different lengths were then annealed in a split-top tube furnace in vacuum with Argon background. The annealing temperature was maintained at 500 °C for 30 minutes, or varied from 300 – 600 °C at a step of 100 °C. After the thermal processing, the nanorods were studied by scanning electron microscopy (SEM) and X-ray diffraction (XRD) studied. It was found that with increasing annealing temperatures, the intensity of XRD peaks for both Ni (111) and Ni (200) increased, which indicates that re-crystallization occurs after annealing, leading to the formation of larger grain sizes. In the temperature dependent study, we found that surface melting is dominant at temperatures lower than 500 °C while coalescence of nanorods happens at 600 °C, resulting significant morphology change at high annealing temperature. The well-separated nickel nanorods join together to create a porous continuous film with interconnected pores after coalescence, which is potentially useful in the applications of catalyst support, fuel cells, and electrodes for battery.

5:00pm **TF+AS+NS+SE-WeA10 Gas Assisted Nanofabrication Using He and Ne Ion Beams: Toward Ultimate Resolution.** H.M. Wu, D. Ferranti, L.A. Stern, D.Y. Xia, Carl Zeiss

Focused ion beam systems combined with gas precursors for deposition and enhanced, selective material removal have led to many important applications. The gas field ion source (GFIS) has demonstrated its capabilities as an ultrahigh resolution (< 0.5 nm) imaging as well as a sub-10 nm nanofabrication technique using helium ion beam. Recently, the new Zeiss Orion-NanoFab microscope provides three ion beams (helium, neon and gallium) into one platform and promotes the further studies of He and Ne induced deposition and etching procedures to compare with a Ga ion beam. Because of the mass difference between He, Ne and Ga ions, the interactions of ions with precursor molecules result in different sputtering rates, implantation and deposition yields. This presentation gives an overview of our current studies using this new platform to deposit or mill nano structures with sub-10 nm resolution.

He and Ne ion beam induced metal and dielectric deposition using different precursors have been investigated extensively in our lab. The dimensions and electrical properties of these deposits are strongly dependent on the ion beam type, beam conditions and precursor gas flux. To improve the properties of deposits and minimize the ion implantation, we have been optimizing deposition conditions to increase the deposition purity and to maximize the deposition yield. We will discuss the factors that determine the ultimate resolution of deposits using He and Ne ion beams and the beam chemistry that influences the choice of gas precursors for a particular procedure and how to select between the He and the Ne ion beams to achieve the best result.

Removing material by direct He ion sputter (milling) has a resolution of a few nanometers, but a low sputter yield. The Ne ion beam offers precise

nanofabrication capabilities, and 30 times higher sputter yields than the He ion beam. The implementation of chemical etching further increases the material removal process substantially and reduces the ion implantation. The effects of the ion beam conditions and etchant gas flux on the milling rate and on the gas assisted etching (GAE) enhancement have been studied and 10x enhancement has been achieved so far, compared with direct ion beam sputter.

5:20pm **TF+AS+NS+SE-WeA11 A New Type of Super Intense Cluster Beam Source based on Matrix Assembly**, R.E. Palmer, L. Cao, W.D. Terry, F. Yin, University of Birmingham, UK

Atomic clusters are attracting a great deal of attention because of their remarkable size-dependent properties and the corresponding potential applications which arise, e.g. in catalysis, nanomaterials, biochips [1][2]. However, the advancement of this field is limited by the low cluster fluxes, ~ 1nA, currently available [3]. Here we demonstrate a radical new instrument, the Matrix Assembly Cluster Source (MACS), with the potential to produce size-selected clusters in great abundance (up to ~1A, i.e. an increase of 9 orders of magnitude). In this new approach, the atoms of the desired cluster material (e.g. Au or Ag) are trapped in a thin matrix of condensed rare gas atoms (e.g. Ar). Clusters are then produced by collisions in the matrix which are driven by an atomic ion beam (such as Ar⁺) in the transmission sputtering regime.

The transmission sputtering of the matrix is monitored in real time by ion-induced luminescence while the noble metal clusters produced and deposited are analyzed by aberration-corrected scanning transmission electron microscopy (STEM): the number of cluster atoms is measured by the integrated HAADF intensity [4][5]. The results demonstrate the production of Au and Ag clusters by the new method and show that the distribution of cluster size, even before mass selection, is narrow under certain experimental conditions. We find the mean size of the clusters is mainly determined by the concentration of metal atoms in the condensed rare gas matrix. The size distribution and flux of clusters also depends on the ion beam energy.

[1] J. V. Lauritsen, J. Kibsgaard, S. Helveg, H. Topsøe, B.S. Clausen, E. Laegsgaard and F. Besenbacher, *Nature Nanotechnology*, **2**, 53 (2007)

[2] R.E. Palmer, C. Leung, *Trends Biotechnol.*, **25**, 48, (2007)

[3] S. Pratontep, S. J. Carroll, C. Xirouchaki, M. Streun, R. E. Palmer, *Rev. Sci. Instrum.* **76**, 045103 (2005)

[4] Z.Y. Li, N.P. Young, M. Di Vece, R.E. Palmer, A.L. Bleloch, B.C. Curley, R.L. Johnston, J. Jiang, J. Yuan, *Nature*, **451**, 46, (2008)

[5] Z. W. Wang, R. E. Palmer, *Nano Letters*, **12**, 91, (2012)

Corresponding Author: R.E.Palmer@bham.ac.uk

Vacuum Technology

Room: 202 C - Session VT+AS+SS+TF-WeA

Surface Science for Accelerator Applications

Moderator: Y. Li, Cornell University

4:00pm **VT+AS+SS+TF-WeA7 Growth and Characterization of High Quantum Efficiency Photocathodes for the Cornell ERL R&D Project**, L. Cultrera, I. Bazarov, B. Dunham, Y. Li, X. Liu, A. Bartnik, K. Smolenski, S. Karkare, W. Schaff, T. Moore, Cornell University **INVITED**

Electrons generated by photoemission process are nowadays recognized as the brightest beams source to drive X-ray Free Electron Lasers or Energy Recovery Linacs. Part of the Cornell University ERL R&D project is aimed at developing photocathodes for electron guns that can support the production of very high brightness beams with high average current for extended periods of time

We focused our studies to III-V semiconductors activated to negative electron affinity and to alkali antimonide semiconductors.

Both classes of materials show high quantum efficiency on the visible part of the spectrum but are extremely sensitive to poor vacuum conditions. Because of this a dedicated apparatus consisting of different interconnected UHV chambers has been realized in the photocathode lab. This allows transferring samples from preparation to analysis chamber while keeping them under UHV. A movable vacuum suitcase is used to transfer selected samples from the photocathode lab to the photoinjector.

The procedure and challenges for preparing high quantum efficiency photocathodes will be illustrated as well as the characterization performed in photocathode lab and by using them in the photoinjector.

Aiming at a better understanding of the photoemission process we recently developed a Monte Carlo code to simulate the photoemission from GaAs

activated to negative electron affinity. This tool will eventually guide us in engineering new photocathode materials.

Perspectives for further development on the generation of high brightness electron beams will be discussed.

5:00pm **VT+AS+SS+TF-WeA10 Photocathode Materials Able to Sustain High Currents**, Z. Li, K. Yang, L. Wang, J. Riso, R.A. Lukaszew, The College of William and Mary

We will present preliminary work on photocathode materials able to sustain high currents, pertinent to the technology of accelerators and associated systems and essential to develop strategies and technologies for next generation nuclear physics accelerator capabilities. To this end, metallic photocathodes offer several clear advantages over semiconductor photocathodes because they are robust against degradation due to surface contamination and against damage resulting from conditioning or heating and can withstand high electric surface fields present at the cathode in RF accelerators. Other advantages include their very short response time (less than picoseconds) and their very long lifetime (years or longer), which is much longer than of other types of photocathodes (hours to months). However, the main problem with metallic photocathodes is the rather low quantum efficiency (QE), even for UV radiation. A possibility to improve the QE of metallic photocathodes is to exploit surface plasmon resonance using adequate geometries for the intended application, as well as possible cap layers able to lower the metal work function. In this way, metal photocathodes designed to support surface plasmons could produce high electron yields by enhancing their QE. We will show design criteria for such platform for this application as well as our preliminary results.

5:20pm **VT+AS+SS+TF-WeA11 Quantum Efficiency and Divergence from Metal Photocathodes**, T. Vecchione, D.H. Dowell, SLAC National Accelerator Laboratory, J. Feng, W. Wan, H.A. Padmore, Lawrence Berkeley National Laboratory

Quantum efficiency and divergence are key parameters for measuring photocathode performance. This work presents new theoretical expressions for each quantity and experimental confirmation of each expression with respect to excess energy. Novel instrumentation and analysis techniques developed are described in detail. The data obtained from polycrystalline metal thin films matches reasonably well to that which is theoretically predicted.

Thursday Morning, October 31, 2013

Applied Surface Science

Room: 204 - Session AS+BI+EM+NL+NS+SS-ThM

Nanoparticle Surface Chemistry

Moderator: H. Zuilhof, Wageningen University, Netherlands, D.Y. Petrovykh, International Iberian Nanotechnology Laboratory, Portugal

8:00am **AS+BI+EM+NL+NS+SS-ThM1 Surface Analysis as a Critical Step in Translating Nanomaterials to Technologies**, *D.W. Grainger*, University of Utah **INVITED**

Difficulties assessing human exposure, safety, and possible toxicity from nanotechnologies have prompted questions about how to characterize nanomaterials in various experimental test beds for predictive use. While little consensus is published about human risk/benefit analysis, this is confounded by lack of accepted, sensitive and reliable characterization methods of practical value for nanomaterials in physiological milieu. Relatively few studies are conducted on these materials in biologically relevant media to understand their surface properties and physical states (i.e., sedimentation, aggregation) prior to in vitro or in vivo exposures. Few studies have standard reference materials and analytical protocols established for comparisons to other studies. The current understanding of the fate of nanomaterials of most any size and shape, both in cell culture media with serum or inside the mammalian body, is poor at best. Additionally, the collective published scientific record documenting fate of nanomaterials in vivo is consistent with long known tissue-based particle filtration for micro-colloids, with far less success deliberately targeting particles to specific tissue or disease sites (i.e., <5% of a nanoparticle dose reaches a disease site).

To date, most data suggest that size reductions to the nanometer dimension have not significantly changed how nanomaterials interact with physiological systems in vivo, despite in vitro distinctions observed with proteins and in cell cultures. Connecting nanomaterials properties with how they interact with proteins and cells in vitro to affect their biodistribution in vivo allows a more rational approach to designing nanomaterials with specific biomedical and toxicity properties, and to avoid the ubiquitous non-specific tissue scavenging. This is related to materials interactions with whole blood components, including platelets, cells, and plasma proteins, producing fluid transport to tissue sites, particle binding, opsonization and aggregation. However, analytical methods for nanomaterials are not sufficiently sensitive to study these effects in vivo to alter nanomaterials biodistribution patterns. Additionally, understanding how surface coatings, ligands and contaminants change physiological behavior requires careful analysis.

The nanotechnology field must develop improved, sensitive analytical tools and methods to drive a consensus for how nanomaterials (1) should be fully and reliably characterized for biological and biomedical purposes, and (2) how different nanomaterials properties produce either beneficial (i.e., therapeutic) or toxic responses inside complex physiological systems.

8:40am **AS+BI+EM+NL+NS+SS-ThM3 Molecular Surface Characterization of Individual Nano-objects**, *C.-K. Liang, S.V. Verkhouturov, E.A. Schweikert*, Texas A&M University

The importance of surface characterization of nano-objects in dimensions below 50 nm is well recognized. Indeed the most pronounced changes in chemical reactivity are expected to occur on the smallest size nano-objects. Yet, as their size shrinks, measurement techniques are lagging. A further concern, when seeking insight into size-composition-reactivity relationships, is population heterogeneity. We present here a technique for assaying individual nano-objects. The method involves bombarding dispersed nano-objects one-by-one with nanoprojectiles specifically Au₄₀₀⁴⁺, at hypervelocity. Their impact causes abundant emission of ionized ejecta which are identified individually for each impact by time-of-flight mass spectrometry. We will describe the characterization of surfaces and environments of nano-objects as revealed by selected grazing projectile impacts.

9:00am **AS+BI+EM+NL+NS+SS-ThM4 Towards the Effective Combination of Static and Dynamic SIMS for Nanoparticle and Biological Analyses**, *C. Szakal*, National Institute of Standards and Technology

Static SIMS and dynamic SIMS experiments, protocols, instrumentation, and laboratory groups have largely developed in separate paths. As a result, it is common to think of certain application areas for a specific SIMS

analysis, such as semiconductor depth profiling with dynamic SIMS and molecule-specific imaging with static SIMS. However, a combination of the two SIMS methodologies could generate a more complete data set by utilizing the surface-sensitive characteristics of ToF-SIMS with the enhanced signal dynamic range of large geometry (LG) dynamic SIMS. Benefits and potential pitfalls of such a combined analysis are discussed for nanoparticle surface chemistry vs. bulk measurements along with other biological application areas.

9:20am **AS+BI+EM+NL+NS+SS-ThM5 Quantitation of Protein Adsorption to Gold Nanoparticles**, *C. Minelli, N.C. Bell, A.G. Shard*, National Physical Laboratory, UK

The ability to quantitatively describe protein coronas of nanoparticles in biological fluids is highly sought for to understand protein corona formation, nanoparticle fate and their interaction with biological systems. A quantitative description of the nanoparticle biomolecular interface is challenging and chemical information along with structural and biofunctional characterization requires the use of complementary techniques.

The parallel use of different techniques provides in fact a range of complementary information of the materials under study, each technique being based on a specific physical principle. Here, we combine the use of liquid-based size measurement techniques such as Dynamic Light Scattering (DLS), Nanoparticle Tracking Analysis (NTA) and Differential Centrifugal Sedimentation (DCS), with vacuum techniques such as X-ray Photoelectron Spectroscopy (XPS) to provide quantitative information of core/shell nanoparticle systems.

We used a set of spherical gold nanoparticles having diameters from 20 nm to 80 nm and coated with different amount of Immunoglobulin G (IgG) antibodies as a model system. The shift of the nanoparticle Localized Surface Plasmon Resonance (LSPR) frequency measured by UV-Vis spectroscopy is known to relate to the amount of molecules adsorbed at nanoparticles' interface. We measured the LSPR shifts along with the nanoparticle sizes in liquid by using DLS, NTA and DCS. When the nanoparticles had a complete protein shell, shell thickness measurements were consistent for all the techniques. DCS sedimentation times showed excellent correlation with LSPR frequency shifts, indicating that analytical centrifugation can provide precise measurement of the thickness of complete protein shells on nanoparticles. However, in the low coverage regime, NTA and DLS techniques provided the best correlation with LSPR frequency shifts. By combining the information from the different techniques we estimated the amount of IgG molecules per nanoparticle as a function of the IgG concentration in solution. Data analysis in the high concentration regime suggested that nanoparticle curvature strongly influences the ability of a surface to allow the further adsorption of IgG.

Core/shell nanoparticle systems were also characterized by XPS. A methodology for the preparation of nanoparticle samples for analysis in vacuum was developed. XPS data was collected from nanoparticles of different core size and analysis provided quantitative chemical information of the nanoparticle. The combined use of XPS with liquid-based techniques for particle characterization provided quantitative chemical and structural information of core/shell nanoparticle systems.

9:40am **AS+BI+EM+NL+NS+SS-ThM6 Surface Characterization of Protein Functionalized Gold Nanoparticles**, *Y.-C. Wang, A. Rafati, D.G. Castner*, University of Washington

Nanoparticles exhibit unique surface properties and require well-controlled surface properties to achieve optimum performance in complex biological or physiological fluids. Thus, there is a need to develop rigorous and detailed surface analysis methods for their characterization. The surface chemistries of oligo(ethylene glycol) (OEG) self-assembled monolayers (SAMs) on Au nanoparticle (AuNP) surfaces were characterized with x-ray photoelectron spectroscopy (XPS), time-of-flight secondary ion mass spectrometry (ToF-SIMS), Fourier transform IR spectroscopy and high-sensitivity, low-energy ion scattering (HS-LEIS). The size, shape, and size distribution of the AuNPs was determined by transmission electron microscopy (TEM).

Both methoxy (CH₃O-) and hydroxyl (HO-) terminated OEG SAMs with chains containing 11 methylene and 4 ethylene glycol units were examined. ToF-SIMS clearly differentiates the two OEG SAMs based on the C₃H₃O⁺ peak attributed to the CH₃ terminated SAM, while XPS didn't detect a significant difference between the two SAMs on the same surface. However, XPS did show a significant difference between the same SAM on different sized AuNPs. Both OEG SAMs were more densely packed on the 40 nm diameter AuNPs compared to the 14 nm diameter AuNPs. FTIR experiments indicates the methylene backbone groups are well-ordered on

all gold surfaces, but the OEG groups are more ordered on the 40 nm diameter AuNPs. Together the XPS and FTIR results suggest the OEG SAMs form a thicker and/or higher density SAMs on the 40 nm AuNPs compared to the 14nm AuNPs. HS-LEIS experiments showed the OEG SAMs on the 40 nm AuNPs were significantly thicker (2.6 nm) than the OEG SAMs on the 14 nm AuNPs (2.0 nm) and the flat Au surface (1.9 nm). The 2.6 nm thickness measured on the 40 nm AuNPs is consistent with thickness expected for a well-order OEG SAM (2.7 nm). TEM showed the 40 nm AuNPs had a larger size distribution and were less spherical compared to the 14 nm AuNPs, suggesting the shape of the AuNPs can have a significant effect on the structure and thickness of the OEG SAMs.

Protein G was immobilized onto the HO-terminated OEG SAMs via carbonyl diimidazole chemistry. ToF-SIMS analysis showed the relative intensities of characteristic amino acid fragments from Protein G varied with both the protein solution concentration and the type of surface.

10:40am **AS+BI+EM+NL+NS+SS-ThM9 Optical Rotation Measurements of Enantioselective Separation on Chiral Au Nanoparticles**, N. Shukla, N. Ondeck, N. Khosla, A.J. Gellman, Carnegie Mellon University

Adsorption of chiral compounds on chiral surfaces is the initial step in enantioselective processes such as separations and catalysis. There has been a significant effort over the past decade aimed at the preparation of chiral nanoparticles based on metallic cores modified by chiral ligands. In principle, these can serve as the basis for enantioselective chemical processing. In this work we demonstrate a simple measurement of enantioselective adsorption on chiral metal nanoparticles using a method that can yield quantitative measures of the enantiospecific adsorption equilibrium constants [1].

The surfaces of chemically synthesized Au nanoparticles have been modified with D- or L-cysteine to render them chiral and enantioselective for adsorption of chiral molecules. Their enantioselective interaction with chiral compounds has been probed by optical rotation measurements when exposed to racemic propylene oxide. The ability of optical rotation to detect enantiospecific adsorption arises from the fact that the specific rotation of polarized light by R- and S-propylene oxide is enhanced by interaction Au nanoparticles. This effect is related to previous observations of enhanced circular dichroism by Au nanoparticles modified by chiral adsorbates. More importantly, chiral Au nanoparticles modified with either D- or L-cysteine selectively adsorb one enantiomer of propylene oxide from a solution of racemic propylene oxide, thus leaving an enantiomeric excess in the solution phase. Au nanoparticles modified with L-cysteine (D-cysteine) selectively adsorb the R-propylene oxide (S-propylene oxide). A robust method based on optical rotation data has been developed that allows extraction of the enantiospecific equilibrium constants for R- and S-PO adsorption on the chiral Au nanoparticles.

[1] N. Shukla, M.A. Bartel, A.J. Gellman "Enantioselective separation on chiral Au nanoparticles" *Journal of the American Chemical Society*, 132(25), (2010), 8575–8580

11:00am **AS+BI+EM+NL+NS+SS-ThM10 Monitoring the Citric Acid Content on Dialyzed Gold Nanoparticle**, V. Spampinato, R. La Spina, D. Gilliland, L. Calzolari, G. Ceccone, F. Rossi, EC-JRC-IHCP, Italy

Gold nanoparticles (GNPs) are probably the most investigated metal nanomaterials due to their interesting properties. In fact, GNPs are applied in a several areas including material sciences, catalysis and biomedical diagnostics.^[1] Most of the applications of GNPs in the medical and biosensing fields require the development of careful purification to obtain afterwards a more efficient surface functionalization.^[3,4] The process of purification is usually obtained by filtration, centrifugation and/or dialysis of the GNPs solution to remove part of the citrate or other stabilizing agents.^[5,6] The citrate reduction Au(III) in water, known as Turkevich method, is one of the most used synthesis process to produce monodispersed and stable GNPs.^[8] In this synthesis, the citrate is either the reducing agent and the stabilizer and it is used in large excess in comparison to the amount of gold.^[9] In this work, we have investigated the stability and effect of dialysis on citrate stabilized GNPs by quantifying the content of citrate by Nuclear Magnetic Resonance (¹H-NMR), and by characterizing the GNPs/citrate interface chemistry using X-ray Photoelectron Spectroscopy (XPS) and Time of Flight Secondary Ion Mass Spectrometry (ToF-SIMS). In these studies, 15 nm gold nanoparticles stabilized with the citrate have been synthesized via the Turkevich process and the content of citrate was monitored at several or different cycles of dialysis against ultrapure water. These systematic studies showed a decreasing of the citrate content with the dialysis cycles. In particular, XPS and ToF-SIMS show that for low dialysis cycles the ratio Au/Na and Au/CHO increase almost linearly, while after 9 dialysis cycles a plateau is reached. A similar trend is observed by ¹H-NMR where the amount of citrate is quantified against an internal standard. The behavior of the GNPs at different dialysis cycles was

also monitored by Centrifuge Particle Separation (CPS) and Dynamic Light Scattering (DLS) and UV-Vis spectra, revealing that several dialysis cycle result in a partial aggregation of the nanoparticles.

- [1] P-J Debouttière, et al., *Adv. Funct. Mater.*, **2006**, 16, 2330
- [3] N. L. Rosi, et al., *Science*, **2006**, 312, 1027
- [4] C. Murphy et al., *Acc. Chem. Res.*, **2008**, 41 (12), 1721
- [5] S. Techane, et al., *J Phys Chem C*, **2011**, 115(19), 9432
- [6] S. Sweeney et al., *J. Am. Chem. Soc.*, **2006**, 128 (10), 3190
- [7] C. Chen, et al. *Nano Lett.*, **2006**, 6 (4), pp 611–615
- [8] J. Turkevich, et al., *Discuss. Faraday Soc.*, **1951**, 11, 55
- [9] M. Doyen, et al., *J. Coll. Int. Sci.*, **2013**, 399, 1

11:20am **AS+BI+EM+NL+NS+SS-ThM11 Comparison of the Structure and Solution Behaviors of 20nm Silver and 20nm Silver-Shell-Gold-Core Nanocomposites in Aqueous Biological Media**, P. Munusamy, Pacific Northwest National Laboratory, S. Chen, L.B. Yen, Imperial College London, UK, C.W. Wang, M. Engelhard, Pacific Northwest National Laboratory, A. Porter, Imperial College London, UK, D.R. Donald, Pacific Northwest National Laboratory

Different synthesis routes have made it possible to produce silver nanoparticles with variety of structure properties such as size, shape, and surface functionality. Synthesizing or processing silver nanoparticles under different conditions can impart variations in properties and reactivity which can influence the biological end points. In this study we have examined how silver nanoparticles of nearly identical size, as measured by dynamic light scattering, but produced with and without gold core behave in the biological media RPMI 1640 with FBS, the cell culture media used in our laboratory for in vitro nanotoxicity studies. The initial physico-chemical characterization of citrate capped nanoparticles using DLS size and surface charge measurement showed particles of average size 27nm with negative surface charge. Structure and compositional analysis using STEM and XPS confirmed the presence of gold core of size ~7nm in one set of particles. The detailed structure of the pure silver and the core-shell particles differ significantly. Based on TEM images and XRD measurements, the pure silver particles are highly crystalline, made up of ~ 15-20 nm crystallites with well-defined grain boundary or slip plane defect structures. The silver surrounding the gold core is made up of smaller highly disordered crystallites. After 24h incubation in culture media, STEM images showed that the particles with Au core dissolved significantly and non-uniformly indicating solution attack down to the gold core. In contrast, pure silver particles underwent more uniform dissolution with some indication of varying rates for different crystal faces. In addition to the dissolution of the primary particles of both types, new smaller "daughter" silver particles were observed both nearby or some distance away from the initial nanoparticles. Centrifugation followed by ICP-MS analysis of the supernatant was used to quantify the amount of dissolved silver. The dissolution extent for core-shell particles in 24h was 3 times higher than that for pure Ag. These results highlight the significance of synthesis route and sample structure on the solution behavior of similar nanoparticles in biologically relevant environmental conditions.

11:40am **AS+BI+EM+NL+NS+SS-ThM12 Influence of Carrier Gas on the Nucleation and Growth of Nb Nanoclusters Formed Through Plasma Gas Condensation**, K.R. Bray, C.Q. Jiao, UES, Inc., J.N. DeCervo, Air Force Research Laboratory

The synthesis and characterization of metallic nanoclusters is a growing field of research due to their promising catalytic, electrical, magnetic, mechanical, and optical properties. These properties generally differ from the bulk material and can be tuned by varying the nanocluster size. Transition metal clusters have received considerable interest due to their wide range of applications. Niobium has attracted attention due to observations of ferroelectric properties at low temperature. In this work, Nb nanoclusters are deposited using a plasma gas condensation process which involves the sputtering of a Nb target to create a dense metallic vapor where clusters are formed. The concept of a temperature dependent nucleation zone in conjunction with classical nucleation theory is used to describe nanocluster nucleation and growth. Changes in the nanocluster nucleation and growth are influenced through modifications of the process parameters such as carrier gas flow rate, sputter source ion current, and aggregation length. Initial data show a novel dual peak cluster distribution under select process conditions, with the smaller cluster diameter near 1 nm and the larger cluster diameter varying from 4 to 10 nm. The larger cluster appears to be a simple condensation product while data suggest the smaller cluster may be a structured cluster with a different nucleation and growth mechanism. The effects of differing argon and helium carrier gas ratios on cluster formation in conjunction with varying sputter source currents and aggregation lengths will be discussed. These results provide the opportunity for a broader understanding into the nucleation and growth of nanoclusters

as well as insights into how process parameters interact during deposition. This knowledge will enhance the ability to create nanoclusters with desired size dispersions.

Biomaterial Interfaces

Room: 201 B - Session BI+NL+NS+SS-ThM

Bio/Nano Interfaces

Moderator: G.J. Leggett, University of Sheffield

8:20am **BI+NL+NS+SS-ThM2 Utility of Lipid Membranes Assembled on Nanoparticles for Measuring Protein Membrane Interactions, S.M. Reed**, University of Colorado Denver

Nanoparticles (NPs) provide a well-defined template for preparing supported lipid membranes with controlled curvature. We have coated supported lipid bilayers and hybrid membranes on silica and gold nanoparticles. The localized surface plasmon resonance (LSPR) of gold NPs can be used to monitor the assembly of lipid layers on NPs and to monitor protein lipid interactions. The gold LSPR is very sensitive to the immediate surroundings of the nanoparticle surface and therefore provides a method to monitor the coating of lipids and subsequent conversion of a supported bilayer to a hybrid membrane after the addition of hydrophobic alkanethiols. We demonstrate that both long chain (decanethiol) and short chain (propanethiol) anchors are able to form hybrid membranes and that these membranes allow for LSPR based detection of protein binding events at the membrane surface.

While many materials have been used as membrane supports, there are unmet needs in the development of membrane mimics and it remains challenging to monitor the coating process and to control the curvature of a membrane. Recent work has demonstrated that quantum dots, silica NPs, and gold NPs can be used as templates for membranes providing an opportunity to control curvature. Here, we have exploited the local refractive index sensitivity of the gold LSPR to observe the process of lipid-coating, structural rearrangement of supported membranes into hybrid membranes, and finally the binding of protein. The introduction of phosphatidylcholine (PC) to the gold NPs results in a rapid binding evidenced by a change in the wavelength of the LSPR, however, the interaction with gold is weak and the gold is not completely covered by the lipid. By adding a hydrophobic alkanethiol anchoring group, the lipids bind closer to the gold NP surface resulting in increased stability. This stability is achieved at different concentrations for short and long hydrophobic chains. When propanethiol was used it was possible to destabilize and remove the lipid coating by adding the hydrophilic thiol, beta-mercaptoethanol. This loss of membrane is observed through changes to the LSPR and increased permeability of the membrane to ions.

8:40am **BI+NL+NS+SS-ThM3 Primitive Osmosensing by Phospholipid Membranes, K. Oglecka**, Nanyang Technological University, Singapore, *J. Sanborn, D. Gettel*, University of California, Davis, *R. Kraut, B. Liedberg*, Nanyang Technological University, Singapore, *A.N. Parikh*, University of California, Davis

INVITED

This talk describes experimental observations of the response of multicomponent vesicles to osmotic gradients. We find that giant vesicles, consisting of phase separating lipid mixtures, immersed in hypertonic bath exhibit a Rayleigh-Plateau like pearling instability paving for elemental mechanical process of vesicular self-reproduction. When immersed in hypotonic bath, however, the response of giant vesicles comprise an unusual transitory state, characterized by damped, periodic oscillations between a microscopically phase-separated state and a uniform one. We find that this unusual oscillatory phase separation is synchronized with the cyclical patterns of membrane tension and poration, producing swell-burst cycles. Swelling, which is caused by the influx of water, raises membrane tension, thus promoting the appearance of microscopic domains. Bursting, which facilitates solute leakage, relaxes the membrane tension, breaking up large domains into those below the optical limit. This autonomous self-regulatory response – in which an external osmotic perturbation is managed by a co-ordinated and cyclical sequence of simple physical mechanisms. These mechanisms allow vesicles to sense (by domain formation) and regulate (by solute efflux) osmotic differences across their compartmental boundaries in a negative feedback loop producing a primitive form of a quasi-homeostatic regulation in a synthetic system, generated from simple components, namely, water, osmolytes, and lipids.

9:20am **BI+NL+NS+SS-ThM5 Ultrathin Poly(ethylene glycol) Films as Flexible Platform for Plasmonics and Lithography and as Precursors for Free-Standing Nanomembranes, N. Meyerbröker, M. Zharnikov**, University of Heidelberg, Germany

We present a novel approach to prepare ultrathin, biocompatible films based on cross-linking of multi-functionalized, star-branched poly(ethylene glycols) (STAR-PEGs) with tunable film thicknesses of 4 – 200 nm. A two-component mixture of amine- and epoxy-terminated four-arm STAR-PEGs was spin-coated on a flat substrate and cross-linked chemically by gentle heating, resulting in a stable, hydrogel-like film with a density close to that of bulk PEG material. The films revealed pronounced swelling behavior, which was fully reversible and could be precisely controlled. Additionally, they provided a high affinity to citrate-stabilized gold nanoparticles (AuNP) that could be adsorbed with high densities into the PEG matrix from an aqueous solution. These novel PEG/AuNP composite films offer interesting and potentially useful optical properties. Controlling the accessibility, swelling behavior, and biorepulsive properties of the PEG films lithographically, we prepared nanocomposite patterns of metal nanoparticles and fluorophores imbedded into the PEG matrix as well as protein-affinity patterns in protein-repelling background. Further, using electron beam lithography, we succeeded to fabricate wettability patterns and to sculpture complex 3D microstructures on the PEG basis. Finally, we demonstrated that the PEG films can be separated from the substrate and exist as ultrathin, biocompatible, free-standing membranes. These membranes possess high stability and exceptional elasticity. They can be used in transmission electron microscopy experiments on sensitive biological targets and as a new type of support for the characterization of nanoparticles.

9:40am **BI+NL+NS+SS-ThM6 Miniaturized Localized Surface Plasmon Resonance Sensing with Single Nanoparticle Arrays, S. Chen, M. Svedendhal, T. Antosiewicz, M. Käll**, Chalmers University of Technology, Sweden

Ultrasensitive biosensing is one of the main driving forces behind the dynamic research field of plasmonics. I will show that the sensitivity of single metal nanoparticle plasmon spectroscopy can be greatly enhanced by enzymatic amplification of the refractive index footprint of individual protein molecules, so called plasmon-enhanced ELISA. The technique, which is based on generation of an optically dense precipitate catalyzed by horseradish peroxidase at the metal surface, allowed for colorimetric analysis of ultralow molecular surface coverages with a limit of detection approaching the single molecule limit. In addition I will show that by combining large arrays of well-separated gold nanoparticles fabricated by electron beam lithography (EBL) with hyper spectral imaging, spectral responses of up to 700 LSPR particles can be simultaneously studied. This allows us to obtain enough statistical significant number of spectra to further study the inhomogeneous broadening of the sensing properties of individual particles. This includes how variation in electric field enhancement over the surface of a single particle and variation in size and morphology of the enzymatic precipitate could affect the uncertainty in determining the number of enzyme molecules per particle. By combining the electromagnetic simulations with the measurements we could conclude that main sources of uncertainty come from variations in sensitivity across the surface of individual particles and between different particles. There is also a considerable uncertainty in the actual precipitate morphology produced by individual enzyme molecules. I will also discuss the possible improvement that can be done to achieve digital responses from the enzymatic amplified single particle sensing.

10:40am **BI+NL+NS+SS-ThM9 Design of Nanoscale Bionterfaces by Self-Assembly of Genetically Encoded Peptide Polymers, A. Chilkoti**, Duke University

INVITED

This talk will cover work in my laboratory over the past decade on the self-assembly of genetically encoded stimulus responsive elastin-like polypeptides (ELPs). We have exploited ELPs to create stimulus responsive nanostructures via three approaches. In the first approach, we have designed diblock ELPs with two ELP blocks with different hydrophobicity's that self-assemble into spherical micelles with an increase in temperature about the critical micellization temperature of the diblock polymer. Building on this architecture, we have incorporated histidine residues in the hydrophobic block to create a diblock ELP that self-assembles into spherical micelles with an increase in temperature, while a small drop in pH from 7.4 to 6.4 leads to micelle disassembly. In a second –chemical attachment triggered self-assembly– approach, we have shown that the attachment of multiple copies of small molecule hydrophobes to the multiple cysteine (C) residues of an ELP with the sequence (VPGXG)_n(CGG)_s can drive their self-assembly into spherical micelles. In a third approach, we replace the Cys (C) with W, Y, or F, and find that oddly, this leads to the formation of stimulus responsive worms and vesicles depending on the specific residue.

These are the first examples of stimulus responsive worms and vesicles in peptide polymers.

11:20am **BI+NL+NS+SS-ThM11 Label-Free Mapping of Protein/Peptide Interactions in Complex Arrays Using Core/Shell Nanoparticle-Based Biosensors**, *H.O. Guvenc*, University of Heidelberg, Germany, *C. Schirwitz, F. Breitling*, Karlsruhe Institute of Technology, Germany, *F.R. Bischoff*, German Cancer Research Center Heidelberg, Germany, *A. Nesterov-Mueller*, Karlsruhe Institute of Technology, Germany, *V. Stadler*, PEPPERPRINT GmbH, Heidelberg, Germany, *J. Wagner, R. Dahint*, University of Heidelberg, Germany

The detailed analysis of biospecific interactions is of crucial importance in biomedicine, biotechnology, and pharmacology. Important applications range from medical diagnosis and drug development to the screening of the human genome and proteome. In recent years, array concepts have become very popular and powerful tools to allow for highly parallel, rapid identification of binding events. These arrays contain a multitude of different probe molecules immobilized at specific locations of an underlying substrate.

Interaction analysis is usually facilitated by labelling the potential binding partners with additional markers. Today, many of such techniques are well-established yielding considerably low detection limits and high lateral resolution. Yet, they suffer from the fact that labelling procedures are usually costly and time-consuming, that the labelling efficiency needs to be properly controlled for quantitative analysis, and that the marker itself can affect the original functionality of the molecules being studied. Moreover, the detection of low-affinity binding events is often hampered as additional washing steps and (bio)chemical reactions are required in-between the interaction and detection processes. To overcome those obstacles, strong efforts have been made to establish label-free detection schemes for interaction analysis. However, marker-free, sensitive readout of high-density arrays is still a technological challenge.

Here we report recent experiments on the label-free detection of protein/peptide interactions in complex arrays based on surface plasmon imaging with core-shell nanoparticle monolayers. Upon reflection of white light, these films exhibit a pronounced extinction spectrum which shifts to higher wavelength upon molecule binding, thus, providing a simple, sensitive and label-free detection mechanism. Variants of HA (human influenza hemagglutinin A) and FLAG epitopes with permuted amino acid sequence are synthesized in array format by means of combinatorial chemistry using a novel laser printing approach. After array preparation, the pattern is cleaved from the carrier and transferred to a biosensor surface consisting of core-shell nanoparticle films. By this means, the arrays are purified from synthesis artefacts caused by incomplete coupling reactions in the synthesis without the loss of spatial resolution. The interaction of the different peptides with their respective antibodies is quantified by the wavelength shift observed for individual peptide spots and compared to fluorescence-based interaction analysis. Based on the data we conclude on relevant amino acid sequences for an efficient antibody/epitope binding.

11:40am **BI+NL+NS+SS-ThM12 Graphene for Biosensing and Surface Functionalization**, *P.E. Sheehan*, Naval Research Laboratory, *R. Stine*, Nova Research, *S.P. Mulvaney, J.T. Robinson, C.R. Tamanaha*, Naval Research Laboratory

Graphene, a one-atom thick sheet of sp^2 carbon, offers many intriguing possibilities in the field of molecular sensing. Its unique combination of large areas with nanometer thickness and high electrical conductivity could enable small scale device sensitivity with large scale production methods. A major benefit of using graphene is the large toolbox of well-established chemistries for incorporating chemical functionalities or specific recognition elements at the device surface. Here, we will discuss our efforts to develop graphene-based biological field-effect transistors (BioFETs), which offer sensitivity comparable to sensors made with other nanoscale materials (carbon nanotubes, nanowires), but with greatly simplified production methods common in the semiconductor industry. Devices utilizing both graphene and graphene oxide will be covered, and surface spectroscopic studies of the material modification will be discussed. Successful results for the detection of specific DNA hybridization using graphene BioFETs will also be presented. We will further discuss our efforts to use graphene as a bifunctionalized interface for a number of materials, from polymers to dielectrics to semiconductors, of interest to the biosensing community. Graphene's ultrathin nature allows its inclusion in more traditional sensing platforms as a non-intrusive functionalization layer, discreetly lending its chemical flexibility to other, more inert materials without significantly impacting the sensing device.

Spectroscopic Ellipsometry Focus Topic
Room: 101 A - Session EL+AS+EN+PS+SS+TF-ThM

Spectroscopic Ellipsometry for Photovoltaics and Instrument Development

Moderator: M. Creatore, Eindhoven University of Technology, Netherlands

8:00am **EL+AS+EN+PS+SS+TF-ThM1 Application of Spectroscopic Ellipsometry for the Characterization of Various Solar Cell Devices**, *H. Fujiwara*, Gifu University, Japan **INVITED**

To establish new structural characterization methods for Si-based and $CuInGaSe_2$ (CIGS)-based solar cells, we have developed spectroscopic ellipsometry (SE) techniques that can be applied for the analysis of various textured structures used in the solar cell devices. In particular, our SE analyses allow the structural characterization of (i) hydrogenated amorphous silicon (a-Si:H) and microcrystalline silicon (μ c-Si:H) tandem-type solar cells, and (ii) a-Si:H/crystalline Si (c-Si) heterojunction solar cells, both fabricated on textured substrates. For the determination of a-Si:H and μ c-Si:H properties, optical databases in which the optical constants of a-Si:H and μ c-Si:H are described by micro-structural factors have been constructed.^{1,2)} Furthermore, by developing a new optical model, we have confirmed that the high-precision analysis of a-Si:H/ μ c-Si:H multilayer stacks can be performed even on textured substrates having sub-micron size rough surface. On the other hand, to determine the thickness and properties of a-Si:H layers incorporated into textured a-Si:H/c-Si solar cells, SE with a tilt angle measurement configuration^{3,4)} has been employed. In this technique, samples are tilted so that the specular light reflection on the texture facets is measured. From this technique, we have succeeded in characterizing the properties of quite thin a-Si:H layers (5 nm) on the c-Si textures. Recently, we have applied the SE technique further to establish the structural characterization method for CIGS-based solar cells.⁵⁾ For the SE analysis, we have constructed an optical database in which the CIGS dielectric function can be calculated as functions of the Ga composition $x=Ga/(In+Ga)$ and Cu composition $y=Cu/(In+Ga)$. By using the constructed optical database, we have demonstrated that the structure and compositions of CIGS-based thin films can be determined accurately.

1) Kageyama et al., Phys. Rev. B 83, 195205 (2011), 2) Yuguchi et al., J. Appl. Phys. 111, 083509 (2012), 3) Saenger et al., Thin Solid Films 518, 1830 (2010), 4) Watanabe et al., Appl. Phys. Express 3, 116604 (2010), 5) Minoura et al. J. Appl. Phys. 113, 063505 (2013).

9:00am **EL+AS+EN+PS+SS+TF-ThM4 Real-Time and Through-the-Glass Mapping Spectroscopic Ellipsometry for Analysis of CdS/CdTe Coated Superstrates and Correlations with Solar Cell Performance**, *P. Koirala, J. Chen, X. Tan, R.W. Collins*, The University of Toledo

In-situ real-time spectroscopic ellipsometry (RT-SE) from the film side has been applied along with ex-situ spectroscopic ellipsometry through the glass (TG-SE) toward the analysis of the different stages of CdS/CdTe solar cell fabrication in the superstrate configuration. The RT-SE studies of the CdS and CdTe layers deposited on transparent conducting oxide (TCO) coated glass superstrates provide information on the CdS growth, its surface roughness evolution, as well as overlying CdTe interface formation and bulk layer growth. Such information is very useful for developing a realistic optical model for the as-deposited layer structure in TG-SE mapping analysis over the full 15 cm x 15 cm superstrate area. In the mapping analysis, a mask is used to measure all 256 points where 0.125 cm² area dot cells are to be made. Because the as-deposited superstrate/film-structure undergoes additional processing steps, however, in order to complete the solar cell devices, three sets of TG-SE data maps are collected that characterize the superstrate/film-structure in the (i) as-deposited, (ii) CdCl₂-treated, and (iii) back-contact patterned states. With the optical database that has been established for both the as-deposited and CdCl₂ treated CdS and CdTe, each of the three TG-SE data maps has been analyzed based on an optical model deduced from RT-SE studies of the CdS and CdTe depositions. By using these SE techniques, we have been able to quantify the spatial dependence of the changes that occur in the superstrate/film-structure as a result of the different processing steps. In order to corroborate the layer structure determined by TG-SE, comparisons with cross-sectional transmission electron microscopy (XTEM) have been performed for selected states of the superstrate/film-structure and for selected locations. The results have been found to validate the overall RT-SE and TG-SE approach and analysis results. Finally, the layer parameters as determined from the TG-SE analyses have been correlated statistically with the device performance of the 256 dot cells fabricated over the final 15 cm x 15 cm superstrate/film-structure. The resulting correlations expedite solar cell optimization.

9:20am **EL+AS+EN+PS+SS+TF-ThM5 Expanded Beam Spectroscopic Ellipsometry for In-line Monitoring of Thin Film Process, M. Fried,** Hungarian Academy of Science, Hungary **INVITED**

Non-destructive analysing tools are needed at all stages of thin film process-development, especially photovoltaic (PV) development, and on production lines. In the case of thin films, layer thicknesses, micro-structure, composition, layer optical properties, and their uniformity are important parameters. An important focus is to express the dielectric functions of each component material in terms of a handful of wavelength independent parameters whose variation can cover all process variants of that material. With the resulting database, spectroscopic ellipsometry coupled with multilayer analysis can be developed for on-line point-by-point mapping and on-line line-by-line imaging.

This talk will try to review the investigations of different types of PV-layers (anti-reflective coating, transparent-conductive oxide (TCO), multi-diode-structure, absorber and window layers, backreflector) showing the existing dielectric function databases for the thin film components of CdTe, CIGS, thin Si, and TCO layers.

Off-line point-by-point mapping can be effective for characterization of non-uniformities in full scale PV panels in developing labs but it is slow in the on-line mode when only 15 points can be obtained (within 1 min) as a 120 cm long panel moves by the mapping station. Last years [1, 2], a new instrumentation was developed that provides a line image of spectroscopic ellipsometry (wl=350-1000 nm) data. Upto now a single 30 point line image can be collected in 10 s over a 15 cm width of PV material [3, 4]. This year we are building a 30 and a 60 cm width expanded beam ellipsometer which speed will be increased by 10 X. Then 1800 points could be mapped in a 1 min traverse of a 60*120 cm PV panel or flexible roll-to-roll substrate. Another enhancement is the switch-over to rotating compensator measuring principle.

[This work was supported by the ENIAC E450EDL and KMR_12_1_2012_0225 projects]

[1] C. Major, G. Juhasz, Z. Horvath, O. Polgar, M. Fried, *PSS (c)*, **5**, 5 (2008).

[2] G. Juhász, Z. Horváth, C. Major, P. Petrik, O. Polgar and M. Fried, *PSS(c)*, **5**, 5 (2008).

[3] M. Fried, G. Juhász, C. Major, P. Petrik, O. Polgár, Z. Horváth, A. Nutsch, *Thin Solid Films* **519**, 2730 (2011).

[4] M. Fried, G. Juhasz, C. Major, A. Nemeth, P. Petrik, O. Polgar, C. Salupo, Lila R. Dahal, R. W. Collins, *Mater. Res. Soc. Symp. Proc.* **Vol. 1323**, DOI: 10.1557/opl.2011.820. (2011).

10:40am **EL+AS+EN+PS+SS+TF-ThM9 Materials Characterization using THz Ellipsometry and THz Optical Hall Effect, T. Hofmann,** University of Nebraska-Lincoln **INVITED**

Ellipsometry in the THz spectral range has been demonstrated to be a very versatile tool for the investigation of semiconductor heterostructures, meta-materials, 2D electron gases (2DEG), and even graphene.

In this talk, instrument development with particular emphasis on frequency-domain, rotating optical element THz ellipsometry will be reviewed and recent progress on THz optical Hall-effect systems, which encompasses generalized ellipsometry in magnetic fields, will be discussed.

The application of THz ellipsometry for the accurate measurement of complex optical constants of isotropic and anisotropic bulk materials and thin films will be illustrated briefly. The progress on THz generalized ellipsometry investigations of 3D metal nanostructured thin films will be reported in detail. The investigated films exhibit a strong anisotropic optical response in the THz spectral range. It will be demonstrated that the anisotropic optical response of 3D nanostructures changes drastically as the function of the dielectric properties of the ambient. Applications for 3D metal nanostructured thin films as THz optical sensors will be discussed.

In addition, recent results on application of THz optical Hall-effect measurements will be reported. Exemplarily, temperature-dependent THz optical Hall-effect investigations of AlGaIn/GaN high electron mobility transistors structures are shown. Our findings indicate that the 2DEG sheet density is independent of the sample temperature. The mobility and effective mass, however, strongly depend on the sample temperature. The mobility shows a strong increase with decreasing temperature largely due to the reduction of LO phonon scattering. The opposite behavior is observed for the effective mass and explained by the reduction of the 2DEG confinement, i.e., the wave function penetration of the AlGaIn with increasing temperature.

11:20am **EL+AS+EN+PS+SS+TF-ThM11 A History of Early Ellipsometry and Polarimetry, R.A. Synowicki,** J.A. Woollam Co., Inc.

This work surveys the early history of polarimetry and ellipsometry. Special consideration is given to the time period between Drude's original work in the late 1880's and the work of Rothen in the mid 1940's.

Snell determined the refractive index of water in 1621. Isaac Newton followed in the 1660's with the prism minimum deviation technique. In the late 1880's August Kundt measured the optical properties of very thin metal films by minimum deviation, but a better technique was needed for absorbing materials.

The polarimeter was invented around 1840. Early polarimetry was used to measure the rotation of polarized light through solutions of sugar, and used in customs offices at seaports for taxation of sugar shipments. In 1845 the Faraday effect showed rotation of polarization by a magnetic field, a result later explained by James Clerk Maxwell's electromagnetic theory.

Paul Drude applied Maxwell's theory to describe the internal structure of materials. To experimentally determine optical properties Drude developed ellipsometry as an analytical technique between 1885 and 1890. Null ellipsometry techniques were originally used, but in the following decades half-shade techniques with improved accuracy became common.

Ellipsometry remained a popular technique after the time of Drude. A surprising amount of this early ellipsometry work was spectroscopic. By 1910 R.S. Minor, A.Q. Tool, and L.R. Ingersoll used ellipsometry to determine the optical constants of metals over a wide spectral range from 226 nm in the ultraviolet to 2250 nm in the infrared.

11:40am **EL+AS+EN+PS+SS+TF-ThM12 Vibrational Properties of Lanthanum Aluminate and Magnesium Aluminate Spinel Using Fourier Transform Infrared Ellipsometry, T. Willett-Gies,** New Mexico State University, *C.J. Zollner*, Cornell University, *E. DeLong*, *S. Zollner*, New Mexico State University

Using FTIR ellipsometry, we have determined the dielectric function of twinned single-crystalline lanthanum aluminate (LaAlO_3) and spinel (MgAl_2O_4) wafers which are often used as substrate materials for oxide epitaxy. Measurements were taken at 300 K in the region of lattice vibrations between 250 and 1000 cm^{-1} . LaAlO_3 is a rhombohedrally distorted perovskite with two formula units per unit cell, leading to eight IR-active phonon modes [1]. Two of these eight are below our spectral range, one is very weak, and two are nearly degenerate [1]. We thus expect four TO peaks in the imaginary part of the dielectric function. The polar character of LaAlO_3 also causes strong LO-TO splittings. Unlike previously published FTIR reflectance studies (which require a Kramers-Kronig analysis to determine the TO/LO phonon peaks), our FTIR ellipsometry measurements allow the direct determination of TO and LO phonon energies as peaks in the dielectric function ϵ and the loss function $1/\epsilon$, respectively.

Magnesium aluminate spinel (MgAl_2O_4) belongs to the cubic O_h^7 space group and has two formula units per primitive cell. Of its 39 optic modes, factor group analysis [2] shows that there are only four IR-active modes with T_{1u} symmetry. The lattice dynamics of spinel has long been controversial and differences have been found between natural crystals (which are believed to be fully ordered) and synthetic crystals (which often contain a small amount of Mg/Al disorder).

A good description of the dielectric functions of these materials can be found using a sum of Lorentz oscillators (for the TO phonons in our spectral range) and two poles for electronic and low-energy phonon absorption outside of our spectral range. A factorized model [3] with LO/TO phonon pairs and a UV pole yields even better agreement with the data. The classical Lorentz model assumes a frictional force proportional to the velocity of the atoms resulting in a single broadening parameter, while the Lowndes model [3] takes into account the anharmonic phonon decay and assigns independent broadening parameters to the LO and TO phonons. Our FTIR ellipsometry measurements yield LO and TO parameters (energies, broadenings, and oscillator strengths) with unprecedented accuracy, far exceeding those from previous FTIR reflectance results. We will compare our experimental phonon energies with those obtained from *ab initio* density-functional theory for both LaAlO_3 and MgAl_2O_4 .

[1] P. Delugas, V. Fiorentini, and A. Filipetti, *Phys. Rev.* **B71**, 134302 (2005).

[2] A. Chopelas and A.M. Hofmeister, *Phys. Chem. Minerals* **18**, 279 (1991).

[3] R. P. Lowndes, *Phys. Rev.* **B1**, 2754 (1970).

Electronic Materials and Processing

Room: 101 B - Session EM+AS+EN+TF-ThM

Hybrid and Organic Electronics

Moderator: A.J. Muscat, University of Arizona, J.R.

Engstrom, Cornell University, J. Xue, University of Florida

8:00am EM+AS+EN+TF-ThM1 **When the Sequence of Thin Film Deposition Matters: Examination of Organic-on-Organic Heterostructure Formation using Molecular Beam Techniques and *In Situ* Real Time X-ray Synchrotron Radiation**, E.R. Kish, R.K. Nahm, A.R. Woll, J.R. Engstrom, Cornell University

Over the past several years significant advances have been made concerning our understanding of the growth of crystalline small molecule organic thin films consisting of a single component. An important challenge in organic electronics is to develop and improve methods to integrate both *p*-type and *n*-type small molecule organic semiconductors into the same device microstructure. Thus, developing an understanding of the molecular scale events that lead to heterojunction formation is essential. In this work we present results concerning nucleation and growth of a series of *n*-type organic semiconductors: PTCDI- C_n , where the length of the alkyl tail (C_n) attached to the perylene core of these molecules has been varied from $n = 5, 8$ and 13. In addition to examinations of the growth of these molecules themselves, we have also examined the growth of these molecules on ultrathin films of the *p*-type semiconductor pentacene, and vice-versa, the growth of pentacene on layers of PTCDI- C_n . In this work we make use of molecular beam techniques to deliver PTCDI- C_n and/or pentacene, and growth of these layers is monitored *in situ* and in real time using X-ray synchrotron radiation, and *ex situ* using atomic force microscopy. Concerning the growth of PTCDI- C_n on 1 monolayer (ML) of pre-deposited pentacene we find substantial differences between the C_5 and C_{13} variants of this molecule: X-ray intensity oscillations at the anti-Bragg scattering condition, signifying layer-by-layer (LbL) growth, are *much* more extended for the C_5 variant. Interestingly, despite the extended nature of LbL growth for this molecule, the thin film crystallinity formed from C_5 is significantly reduced when compared to the C_{13} variant, suggesting that the molecular interactions that provide the driving forces for crystallization, may also contribute to higher barriers for step-edge crossing events—highly crystalline but rough thin films. More dramatic differences emerge as we examine the sequence of deposition. While each perylene variant grows approximately layer-by-layer on 1 ML of pentacene for several layers of PTCDI- C_n , when this order is reversed, and pentacene is grown on 1 ML of PTCDI- C_n , dramatic changes occur: growth is immediately 3D, and a very rough morphology is formed. *Ex situ* analysis using AFM reveals that the thin film morphology is rougher than what would be formed from simple random deposition. Examination of multilayer structures, e.g., A/B/A/B... where A is PTCDI- C_n and B is pentacene, shows that the growth of roughness tends to reflect this asymmetry, where the pentacene cycle tends to roughen the vacuum/film interface, while the PTCDI- C_n cycle tends to smoothen the interface.

8:20am EM+AS+EN+TF-ThM2 **Scanning Tunneling Microscopy and Spectroscopy Study of Sliding Defects in α -6T Films on $C_{60}/Au(111)$** , D.B. Dougherty, J. Wang, North Carolina State University

Compared to the Si-based traditional inorganic electronics, mechanical flexibility is a tremendous advantage for organic electronics. The origin of mechanical flexibility is the relatively weak intermolecular interactions. In addition to flexibility, these weak interactions can also lead to structural disorder in organic thin films that has a significant impact on carrier transport in organic electronic devices [1]. A recent example can be seen in the analysis of the temperature dependence of carrier mobility in 2D α -sexithiophene (α -6T) field effect transistors (FET's) [2] which differ from 3D counterparts due to different sources of disorder.

In an effort to understand the origin of disorder in sexithiophene films relevant to 2D FETs, we have grown single layer α -6T films on top of a C_{60} monolayer on Au (111). By utilizing Scanning Tunneling Microscopy and Spectroscopy, structural disorder effects in the α -sexithiophene layer have been observed. Sexithiophene molecules form islands on C_{60} monolayer with apparent height about equal to the length of one single molecule. The α -6T molecules assemble into "dimer strips" indicating the competition between interactions present in the α -6T bulk crystal and interactions with C_{60} substrate. Random apparent height variations are observed that can be explained by vertical sliding defects in the layer, similar to other standing molecular films [3]. Remarkably, these defects have a minimal effect on the HOMO energy level, which is instead only strongly influenced by random STM tip variations. This shows that intrinsic structural disorder in α -6T films does not have a strong electronic impact.

*This work was funded by NSF CAREER award DMR-1056861.

[1] Tessler et al., Adv. Mater. 21, 2741 (2009).

[2] Brondijk et al., Phys. Rev. Lett. 109, 056601 (2012).

[3] Kang et al., Appl. Phys. Lett. 86, 152115(2005).

8:40am EM+AS+EN+TF-ThM3 **Organic-Organic Heterostructures for Organic Electronics**, F. Schreiber, University of Tuebingen, Germany
INVITED

Functional organic materials and devices are becoming increasingly complex. Their preparation and growth is, not surprisingly, similarly complex, and the resulting structure will be determined by a competition between kinetics and thermodynamics, which is not trivial to predict in particular for multi-component systems. We discuss general concepts [1] and recent examples [2,3] of organics-based heterostructure growth in the context of kinetic effects compared to thermodynamic (equilibrium) structure.

These include unconventional roughening and smoothing behavior at interfaces as well as unconventional structural motifs, such as a frozen-smectic structure formed in a blend of organic semiconductors which form conventional crystals as pure compounds [4].

Particular attention is paid to the case of kinetically limited phase separation of a donor-acceptor pair (DIP:C60) used in organic photovoltaics [5]. This leads to asymmetric domain sizes near bottom vs top electrode due to the time (thickness) dependent phase separation with important implications for device modeling [1,6].

We also discuss the associated optical properties and the question of coupling between donor and acceptor components [7,8]. Finally, we comment on the implications for the optical and electronic properties as well as possible device applications with focus on organic photovoltaics [1,6].

Contributions by A. Hinderhofer, C. Frank, K. Broch, F. Anger, J. Novak, R. Banerjee, A. Gerlach, and S. Kowarik, are gratefully acknowledged.

[1] A. Hinderhofer and F. Schreiber, Organic-organic heterostructures: Concepts and applications, ChemPhysChem, 13 (2012) 628

[2] A. Hinderhofer et al., Templating effect for organic heterostructure film growth: Perfluoropentacene on diindenoperylene, J. Phys. Chem. C 115 (2011) 16155

[3] A. Hinderhofer et al., Structure and morphology of co-evaporated pentacene-perfluoropentacene thin films, J. Chem. Phys. 134 (2011) 104702

[4] A. Aufderheide et al., Mixing-induced anisotropic correlations in molecular crystalline systems, Phys. Rev. Lett. 109 (2012) 156102

[5] R. Banerjee et al., Evidence for kinetically limited thickness dependent phase separation in organic thin film blends, Phys. Rev. Lett. (2013)

[6] J. Wagner et al., High fill factor and open circuit voltage in organic photovoltaic cells with diindenoperylene as donor material, Adv. Funct. Mater. 20 (2010) 4295

[7] K. Broch et al., Optical evidence for intermolecular coupling in mixed films of pentacene and perfluoropentacene, Phys. Rev. B 83 (2011) 245307

[8] F. Anger et al., Photoluminescence spectroscopy of pure pentacene, perfluoropentacene and mixed thin films, J. Chem. Phys. 136 (2012) 054701

9:20am EM+AS+EN+TF-ThM5 **Importance of Interfaces in Graphene Transfer to Polymers**, E.H. Lock, Naval Research Lab, D. Delongchamp, National Institute of Standards and Technology (NIST), M. Laskoski, Naval Research Lab, M. Baraket, Lab de Chimie Inorganique et Biologique, France, S.P. Mulvaney, S.C. Hernandez, P.E. Sheehan, J.T. Robinson, Naval Research Lab, C. Jaye, D.A. Fisher, NIST, S.G. Walton, Naval Research Lab

Organic materials are widely used because they are cost effective and have excellent physical and mechanical properties. The polymers of interest in this work are polystyrene (PS) and ultra-high molecular weight polyethylene (UHMW PE). PS has been successfully used as electronics and biosensors platforms. UHMW PE is the material in lightweight high strength Dyneema and Spectra fibers for personal armor. However, to enable production of flexible and wearable electronic devices we need to transform the inherently low thermal and electrical polymer conductance. In order to maintain low cost it is technologically beneficial to modify only the surface of the polymer while preserving the bulk properties. This approach leads to development of hybrid materials. We recently reported production of graphene/polystyrene (Gr/PS) hybrid material using a dry transfer print method [1]. Graphene is an excellent "coating" for a polymer because it is flexible and has high thermal and electrical conductivity. Furthermore, its remarkable chemical stability and low permeability allows for applications as barrier coating for plastics.

However, production of graphene/polymer hybrids is not trivial because graphene has to be transferred from the growth substrates (e.g. copper foil, SiC) to polymers without introducing chemical and structural defects. In this talk we will show that there may be a “trade off” between the use of attachment chemistries to ensure good transfer, and the resultant performance of the transferred graphene. More aggressive attachment chemistries ensure transfer success at the cost of compromising the transport properties of graphene. Different interface preparation approaches may prove to be optimal for different applications, depending on whether transfer yield or surface conductivity is more important. This work was supported by the Naval Research Laboratory Base Program. S. C. Hernandez and M. Baraket were postdoctoral National Research Council fellows during the completion of this work.

[1] E. H. Lock, et. Al. ”High-quality uniform dry transfer of graphene to polymers”, Nano Letters 12, 102 (2012).

9:40am **EM+AS+EN+TF-ThM6 Towards Organic Electronics: Methods for the Selective Deposition of Semiconductors and Metals**, Z. Shi, J. Yang, K. Borner, A. Ellsworth, A.V. Walker, University of Texas at Dallas

Robust methods for the chemically selective deposition of metals, semiconductors, biomolecules and other substances are developed and applied in the construction of complex two- and three-dimensional structures. This work has important applications in molecular and organic electronics, sensing, biotechnology and photonics. These methods are easily parallelized, afford precise nanoscale placement and are compatible with photolithography. This work has important applications in photovoltaics, molecular and organic electronics, sensing, photonics and other technologies.

Several recent developments in our laboratories are discussed including the chemical bath deposition (CBD) and atomic layer deposition (ALD) of ZnO and the formation of Cu and Cu₂S “wires” on micron-scale patterned surfaces. We demonstrate that the deposition selectivity and film morphology can be controlled by the deposition technique, the experimental conditions and the underlying substrate chemistry. Optimization and further development of these techniques requires a detailed understanding of the reaction pathways involved in the interaction of organic thin films with metals, organometallic compounds, ions, and other compounds.

11:00am **EM+AS+EN+TF-ThM10 Organic Thin-Film Transistors Manufactured by Vacuum-Evaporation in a Roll-to-Roll Web-Coater Exploiting a Flash-Evaporated Polymer Gate Dielectric**, Z. Ding, G. Abbas, H. Assender, University of Oxford, UK, D.M. Taylor, E. Patchett, A. Williams, Bangor University, UK, J. Morrison, S. Yeates, University of Manchester, UK, L. Lin, University of Leeds, UK

We have developed a process to make bottom gate top contact organic thin-film transistors (OTFTs) in a roll to roll vacuum web coater environment. The vacuum based all-evaporated process allows a solvent-free deposition to make organic/inorganic multilayer structures for thin-film electronic devices on a flexible substrate, at high speed. The polymeric gate dielectric layers have been fabricated by flash evaporation of acrylic monomers followed by radiation curing of E-Beam or Plasma onto a polymer film with pre-patterned metal gates. We now report our work on improving the performance of OTFTs by including modification of the dielectric surface, using new dielectric materials and new semiconductors. With a non-polar dielectric surface, charge carrier mobility of 1cm²/Vs; on/off current ratio of 10⁸, sub-threshold slope of 0.3V/decade and saturated output curve was routinely achieved in DNTT transistors. The devices showed good stability in ambient environment with no need of encapsulation. Inverters and ring oscillators based on these transistors were fabricated successfully. The effect of mechanical deformation; aging time and aging environment on these thin-film devices were also investigated in this work.

11:20am **EM+AS+EN+TF-ThM11 Interface Science of Emerging Thin Film Photovoltaic Technologies: The Role of Interface Composition on Charge Harvesting Efficiencies**, N.R. Armstrong, University of Arizona
INVITED

Organic solar cells, while still not at the efficiencies of more mature PV technologies, are improving in efficiency at the fastest rate of all PV technologies. There are nevertheless significant technical and scientific challenges to be overcome before OPVs can be a legitimate energy conversion technology. This talk will review our recent work in understanding the role that electrical contacts play in determining the performance characteristics of OPVs. We discuss both the role of the contact/active layer interface, and the roles of electron- or hole-selective interlayer materials in modifying the properties of the contact, for both small molecule and polymer based OPVs.

We will focus first of all on the characterization small molecule systems (correlating UPS, conducting tip AFM, and device performance), where the contact can dictate the efficiency of charge harvesting through specific interactions between small molecule components and the contact. We find that for several systems orientation, charge redistribution, heterogeneity of charge harvesting, local fields and leakage currents are all influenced by these interactions.

We secondly deal with electron-selective interlayers (e.g. ZnO, TiO₂), and the role of surface/interface composition in controlling their selectivity. Interlayer materials, typically with thicknesses of 10-50 nm, are increasingly required to ensure efficient and selective charge harvesting in bulk-heterojunction polymer and small molecule based organic solar cells (OPVs) and even in solar cells based on nanocrystalline semiconductors. Selectivity is typically achieved by choosing band edge energies in interlayer materials which provide for efficient collection of only one charge carrier and minimization of surface recombination velocities. New approaches to oxide interlayers will be shown, using conventional (sol-gel) and sputtering approaches, and chemical vapor deposition, focusing on the surface characterization of electronically relevant defect states which appear to control charge selectivity, sub-micron heterogeneity in charge collection, and OPV efficiency.

Electronic Materials and Processing

Room: 102 A - Session EM+AS+PS+TF-ThM

Materials and Process for Advanced Interconnects I

Moderator: S.W. King, Intel Corporation, E. Mays, Intel Corporation

8:00am **EM+AS+PS+TF-ThM1 Measurement of the Bandgap Energies in Low-k Organosilicates**, M. Nichols, University of Wisconsin-Madison, Q. Lin, IBM T.J. Watson Research Center, S. Banna, Applied Materials Inc., Y. Nishi, Stanford University, J.L. Shohet, University of Wisconsin-Madison

The experimental measurements of the electronic band gap of low-k organosilicate dielectrics are presented and discussed. The measurement of bandgap energies of organosilicates was made by examining the onset of inelastic energy loss in core-level atomic spectra using x-ray photoelectron spectroscopy (XPS). This energy serves as a reference point from which many other facets of the material can be understood, such as the location and presence of defect states in the bulk or at the interface. In order to measure the spectra due inelastic energy loss, a suitable primary photoelectron peak must be chosen. Although in principle any core-level spectra will exhibit the same inelastic losses, the measured photoelectron intensity must be large enough so that a sufficient signal to noise ratio can be achieved with suitably high resolution. It was determined that the O 1s peak is dominant for both SiO₂ and for the organosilicate films used in this work.

To find the bandgap energy, a linear fit is made to the measured loss spectra curve near the approximate location of onset of inelastic losses. The energy corresponding to the onset of inelastic losses, is found by extrapolating the linear fit line and calculating its intersection with the “zero” level. The bandgap energy is equal to the difference between the core level peak energy and the onset of inelastic losses. For SiO₂ this method yields a bandgap energy of 8.8 eV which is in excellent agreement with the established value of 8.9 eV. Bandgap energies were measured for 644 nm k=2.75 as-deposited SiCOH films using the linear extrapolation method, yielding a bandgap energy of E_g = 7.0 eV. For 500 nm thick k=2.65 SiCOH the bandgap energy was found to be 7.7 eV while for a 325 nm thick, k = 2.75 photopatternable low-k (PPLK) dielectric, the bandgap was found to be 8.25 eV.

This work has been supported by the Semiconductor Research Corporation under Contract No. 2012-KJ-2359 and by the National Science Foundation under Grant CBET-1066231.

8:20am **EM+AS+PS+TF-ThM2 Complementary Porosity Metrologies for Porous Ultra Low-k Material**, D. Yang, R. Opila, University of Delaware, V. Pallem, Air Liquide, D. Dutta, D. Gidley, University of Michigan, N. Bhargava, University of Delaware

As transistor density on integrated circuits doubles as driven by Moore’s Law, propagation delays from interconnections at the back-end-of-line (BEOL) have begun to contribute significantly. Low dielectric constant (k) materials, e.g. organosilicate glasses (SiCOH), have been introduced to replace silicon oxide to reduce power consumption and capacitive signal delay. It has been generally agreed that decreasing material density by incorporating porosity is the most feasible means to achieve ultra low k.

However, when a higher portion of porogen is introduced, pores tend to aggregate and interconnect, especially when porosity is above percolation threshold. The pore interconnectivity may lead to degradation of mechanical and thermal properties and permit intrusion of moisture, chemical species and sequestering of cleans byproducts. Therefore, characterization and understanding of porosity and pore interconnectivity are important to optimize porous low-k materials. In this work, three non-destructive porosimetry techniques, **Positron Annihilation Lifetime Spectroscopy (PALS)**, **Ellipsometric Porosimetry (EP)** and **X-ray Reflectivity (XRR)**, are applied to characterize porous SiCOH low-k dielectric thin films of different porosity and pore interconnection, results will be analyzed and compared to highlight each technique's advantage and limitation for characterizing porous low-k materials. This study will provide valuable guidance for future porosity characterization, data comprehension, porosity understanding and further structural optimization of porous low-k materials.

The results showed that ellipsometric porosimetry (EP) provides information on open meso-pores accessible to organic solvents but may underestimate porosity without probing pores smaller than the probing organic molecule³; Positron Annihilation Lifetime Spectroscopy (PALS), which probes the amount of free surface and is able to detect micropores but with limitations on analyzing multiple pore size distribution within pore interconnection length; PALS also has unique feature to quantify pore interconnection length by depth-profiling; X-ray Reflectivity(XRR) gives absolute overall porosity in terms of film density but tends to overestimate porosity and provides few details on pore size distribution.

After comparison, we conclude that each porosimetry technique shows their strengths and limitations due to different physical principles. Information derived from any single porosimetry technique is not sufficient to reveal comprehensive pore information without bias. Therefore, metrology must be carefully selected and complementary techniques are required in order to acquire a full picture of pores.

8:40am **EM+AS+PS+TF-ThM3 Future of Ultra Low-k Materials**, W. Volksen, T. Magbitang, K. Lioni, G. Dubois, IBM Almaden Research Center

INVITED

Integration of porous low dielectric constant materials constitutes a major roadblock in the reliable manufacturing of back end of the line (BEOL) wiring for advanced technology nodes [1]. The two main issues for Ultra low-k (ULK) materials are their low mechanical properties and high sensitivity to plasma induced damage (PID). We have developed a new class of bridged oxycarbosilane (OCS) type materials with unique stiffness [2-4], and a novel process to enable their integration [5,6]. The Post Porosity Plasma Protection (P4) consists of refilling the pores of the fully cured porous ULK with an organic material prior to patterning, integrating the protected ULK and thermally removing the filler at the end of the process. We demonstrate the enormous potential of our integrated solution (materials at $k < 2.4$ and P4 process) on blanket films and its compatibility with integration.

- [1] W. Volksen, R. D. Miller, G. Dubois, *Chem. Rev.* 2010, *110*, 56-110.
- [2] G. Dubois, W. Volksen, T. Magbitang, R. D. Miller, D. M. Gage, R. H. Dauskardt, *Adv. Mater.* 2007, *19*, 3989-94.
- [3] G. Dubois, W. Volksen, T. Magbitang, M. H. Sherwood, R. D. Miller, D. M. Gage, R. H. Dauskardt, *J. Sol-Gel Sci. Technol.* 2008, *48*, 187-93.
- [4] M. S. Oliver, G. Dubois, M. Sherwood, D. M. Gage, R. H. Dauskardt, *Adv. Funct. Mater.* 2010, *20*, 2884-92.
- [5] T. Frot, W. Volksen, S. Purushothaman, R. Bruce, G. Dubois, *Adv. Mater.* 2011, *23*, 2828-32.
- [6] T. Frot, W. Volksen, S. Purushothaman, R. Bruce, T. Magbitang, DC Miller, VR. Deline, G. Dubois, *Adv. Funct. Mater.* 2012, *22*, 3043-3050.

9:20am **EM+AS+PS+TF-ThM5 Porosity Scaling Strategies for Low-k Films**, D.J. Michalak, J.M. Blackwell, A. Sengupta, J.S. Clarke, D. Pantuso, Intel Corporation

Mechanical properties of highly porous low-k films are a key manufacturing concern area. Next generation ILD materials will need to be carefully crafted in order to deliver a needed reduction in dielectric constant while also delivering needed mechanical and chemical stability concerns. We have generated a backbone and porogen system with high chemical stability that allows us to control porosity from 0% to 60% volume and achieve dielectric constant values ranging from 3.4 to 1.6. At a given porosity, Young's modulus values are higher than typical PECVD films, but the amount of improvement decreases as porosity increases. The high porosity and mechanical strength were achieved by tuning the number of reactive crosslinking sites on our oligomeric backbone precursor. Our data are evaluated in light of percolation theory, which sets a theoretical maximum porosity limit for materials made from random mixes of backbone and porogen. Ways around this maximum limit are proposed. Finite Element Modeling of the 0-60% porosity films yielded calculated

Young's modulus values very close to observed values when experimental inputs of porosity, pore size, and pore shape were used. Up to 4x improvement in Young's modulus is observed for hypothetical structures containing controlled pore size, shape, and order. Stress contour mapping allows a rapid visualization of the mechanisms at play. Material needs for the next generation ILDs will be discussed in light of these data.

9:40am **EM+AS+PS+TF-ThM6 Ellipsometric Porosimetry Surface Characterization of Oxygen Plasma Damage and κ Repair on Ultra Low κ Dielectrics**, Z. Sun, GLOBALFOUNDRIES U.S. Inc., A. Bondaz, T. Karpowicz, Semilab, V. Seshachalam, S. Srivathanakul, H. Liu, GLOBALFOUNDRIES U.S. Inc.

Due to its intrinsic weakness of high levels of carbon-containing compounds and open pores, an ultra low- κ film is prone to Back End of Line (BEOL) downstream damage from processes such as ashing, reactive ion etching, wet processing and CMP. With continued scaling beyond the 14nm technology node, κ repair processes become required as an ultimate solution in restoring the dielectric properties and keeping the low κ benefit of low capacitance and power consumption.

Oxygen plasma is widely used in the ashing process of photo resist striping, which degrades low- κ material and cause dielectric loss. In this study, Ellipsometric Porosimetry (EP) has been applied to characterize the ultra low- κ surfaces, which are damaged by oxygen plasma and repaired by subsequent hydrocarbon-sourced plasma. The results of the pore size measured by EP shows 1.1nm pore size for a pristine film, 0.4nm for a repaired film and no pores for a damaged film. The conclusion from these readings indicate that the damaged film has a dense crust on the top of the film which prevents adsorption of the solvent used in EP. The repair process reopens the pore but not completely since it shows a significantly smaller pore size than the pristine film. When low- κ films undergo a heating process, the pristine film shows an approximate linear behavior of thermal expansion, while the damaged film shows thickness shrinkage, which could be explained by the desorption of the -OH containing species formed due to oxygen plasma exposure. The repaired film shows the same trend as the pristine film, with the same extracted Coefficients of Thermal Expansion (CTE) as the pristine film. The penetration of plasma repair has been identified as deep as 30nm through film stack model fitting.

This extensive study proves the κ repair process is taking effect as well as proving Ellipsometric Porosimetry is capable and sensitive enough to measure the film property changes statically and dynamically.

10:40am **EM+AS+PS+TF-ThM9 Pore Stuffing to Enable Interconnect Scaling**, J.D. Bielefeld, M. Chandhok, J.S. Clarke, C.J. Jezewski, K. Singh, A.M. Myers, J.M. Torres, R. Turkot, Intel Corporation

To lower interconnect signal delay, the industry continues to work on the integration of low-k interlayer dielectrics (ILD). Momentum has slowed in recent years due to the challenges of working with porous thin films. The pores in the ILD can lead to damage and increased roughness during patterning, and can allow precursor penetration during the metal barrier deposition. Low-k ILDs ($k \sim 2.0$) exhibit 40-50% porosity with interconnected pores with pore size at approximately 2nm+. These challenges are currently reducing interconnect reliability and inhibiting combined capacitance and resistance scaling.

Two approaches have been investigated to mitigate the integration issues with porous dielectrics. The first is pore sealing, in which a non-porous layer is added to the porous ILD's surface to enhance adhesion and to prevent metal penetration during barrier deposition. The down-side of pore sealing is that it does not address the issue of damage and profile roughness during the patterning process.

The second approach is pore stuffing, in which a sacrificial material is infiltrated into the pores of a fully cured ILD. This process generates a non-porous material with increased mechanical properties. The benefits of a non-porous material are utilized during both patterning and metallization. Once the metallization process is complete the sacrificial material is removed to restore the properties of the low-k ILD.

In this paper, we will discuss the challenges of finding a pore stuffing material that can fill the pores of the ILD, that can remain in place during dual damascene processing and that can be removed low-k ILD post metal deposition. Next we will show step by step how pore stuffing improves trench profiles, enhances resistance to wet cleans damage, and eliminates metal precursor penetration. Finally the successful implementation of this process into a dual damascene process flow will be shown.

11:00am **EM+AS+PS+TF-ThM10 Molecular Layer Deposition of Organic Films for Nanoelectronics Applications**, S.F. Bent, Stanford University

INVITED

Many challenges exist in forming the nanostructured materials that will be needed for future electronics technologies. New approaches are required in

both the materials and the processing methods to achieve the required atomic-scale level of control. This presentation will focus on the potential for molecular layer deposition (MLD) to solve some of the technological challenges in nanoelectronics applications. MLD, like the analogous process of atomic layer deposition, utilizes an alternating sequence of self-limiting reactions, and it can be used to deposit conformal, tunable organic films with controllable thicknesses down to the sub-nanometer scale. In our studies, a variety of nanoscale organic films have been deposited by MLD via urea coupling chemistry and other related coupling chemistries. Different backbones have been used to tune the properties of the organic films, which are attached covalently to the underlying substrate. Incorporation of blended and nanolaminate films, which can allow for the films properties to be optimized at a molecular level, has also been explored, and the films have been characterized by a variety of experimental techniques.

A potential application for MLD films is for advanced interconnects. To meet the aggressive demands of interconnect scaling, future devices will require ultrathin, smooth, conformal copper diffusion barriers and seed layers, motivating the development of new barrier layer materials. Organic films are one promising class of materials that have received interest as a possible solution. We have explored the use of MLD to form nanoscale organic thin films for barrier layer applications. The technique allows tailoring of the film properties to optimize desirable barrier properties, such as density, copper surface adhesion, thermal stability, and low copper diffusion. We will describe the copper diffusion barrier properties of the nanoscale organic films as tested by adhesion, annealing, and microscopy studies. Other applications of the MLD films for nanoelectronics, including use as resist materials for extreme ultraviolet (EUV) lithography and as surface modification layers for subsequent materials deposition, will also be presented.

11:40am **EM+AS+PS+TF-ThM12 Surface Photoconductivity of Low-k Organosilicates Induced by Plasma Vacuum Ultraviolet Radiation**, *H. Zheng, D. Pei, M. Nichols*, University of Wisconsin-Madison, *S. Banna*, Applied Materials Inc., *Y. Nishi*, Stanford University, *J.L. Shohet*, University of Wisconsin-Madison

Charging during plasma processing of VLSI/ULSI devices can cause degradation of dielectrics and is a leading cause of damage in semiconductor devices. Thus, a search for a proper method to limit and deplete charge in dielectric materials, especially low-k dielectric materials, (SiCOH) has received great interest. In this work, the temporary increase in the surface conductivity of SiCOH during exposure to vacuum-ultraviolet radiation is investigated and compared with similar measurements for SiO₂¹. To measure this, patterned titanium "comb structures" were deposited on thin SiCOH films and exposed to synchrotron radiation. VUV-induced currents along the surface of the layer between the titanium fingers of the comb structure were measured by biasing the comb structure through electrical connections from the test structure to outside circuitry. By measuring the I-V characteristics of the comb test structure under a constant flux of VUV light, we determined that, for low electric fields, the measured current density and applied electric field are linearly proportional. However, because the SiCOH samples used here are relatively thin, as the electric field increases, the photoinjection current from the substrate becomes large and then dominates the measured VUV-induced current. Hence, it is possible to generate a self-consistent VUV-induced IV characteristic only by using low applied electric fields. Based on these measurements, the surface conductivity can be found. Specifically, under VUV radiation with photon energies between , the surface conductivity of the SiCOH films materials increases by at least one order of magnitude compared with the surface conductivity in the absence of radiation. This increase can be beneficial in limiting charging damage of dielectrics by depleting the plasma-deposited charge, which holds the potential to decrease processing-induced plasma damage to semiconductor devices significantly.

¹ C.Cismaru, J.L. Shohet and J.P. McVittie, *Applied Physics Letters*, **71** 2191 (2000).

This work was supported by the Semiconductor Research Corporation under Contract 2012-KJ-2359 and by the National Science Foundation under Grant CBET-1066231.

Graphene and Other 2D Materials Focus Topic Room: 104 B - Session GR+AS+NS+SS-ThM

2D Materials: Nanostructures

Moderator: T.F. Heinz, Columbia University, D. Xiao, Carnegie Mellon University

8:00am **GR+AS+NS+SS-ThM1 Density Functional Theory Studies of Mechanical and Electronic Properties in 2-D Superlattices Made of Carbon and Boron Nitride Domains**, *C.V. Ciobanu*, Colorado School of Mines

Using density functional theory approaches, we have studied the energies and stresses for edges of SiC and BN nanoribbons and for domain boundaries of graphene-BN superlattices. The SiC and BN armchair nanoribbons show pronounced edge relaxations, which obliterate the 3-family oscillatory behavior of the edge stress reported for graphene. Our calculations show small boundary stresses in graphene-BN superlattices, suggesting that such domain boundaries will not experience severe deformation. We have also found that the C-terminated and Si-terminated zigzag edges in SiC nanoribbons have different compressive stresses which results in different rippling behavior of these edges. Furthermore, we have studied the spin-dependent bandgap in superlattices and investigated its dependence, for each spin component, on the domain width and magnitude and direction of applied strains. These investigations suggest the possibility of opening of a bandgap in one spin component but not the other, a behavior which could be controlled by the synthesizing domains with different widths and by applying strains of prescribed magnitude and directions

8:20am **GR+AS+NS+SS-ThM2 Enclosing, Isolation and Electron Microscopy of Encapsulated Microscopic Objects Using Graphene Oxide Membranes**, *A. Yulaev, A. Kolmakov*, Southern Illinois University Carbondale

We report on a new drop casting technique for facile and gentle encapsulation of micro and nano objects at arbitrary substrates by electron (photon) transparent graphene oxide membranes. The encapsulation is based on a droplet formation around the encapsulated object and relies on the effect of facile water permeability through the surface segregated quasi 2D network of graphene oxide microflakes. The process of encapsulation was studied using a set of model objects and micro-structured surfaces such as nanowires, inorganic droplets, micro-bubbles, pollen and micro-organisms. Two specific regimes of encapsulation, such as wrapping and isolating, can be realized via controlling the hydrophobicity of the substrates. Several specific phenomena, such as object compression, primary and secondary encapsulation were observed. Finally, the electron microscopy and analysis of the encapsulated objects, image contrast formation mechanism, beam broadening and attenuation are discussed. The technique can find an application in forensic science, histology and environmental remediation.

8:40am **GR+AS+NS+SS-ThM3 "Princess and the Pea" at the Nanoscale: Wrinkling and Unbinding of Graphene on Nanoparticles**, *M. Yamamoto*, University of Maryland, *O. Pierre-Louis*, Univ. Lyon 1-CNRS, France, *J. Huang*, University of Maryland, *M.S. Fuhrer*, University of Maryland & Monash University, Australia, *T.L. Einstein, W.G. Cullen*, University of Maryland

Thin membranes exhibit complex responses to external forces or geometrical constraints. A familiar example is the wrinkling instability, exhibited by human skin, plant leaves, and fabrics, resulting from the relative ease of bending versus stretching. We have carried out a systematic study of the wrinkling instability of graphene membranes supported on SiO₂ substrates with randomly placed silica nanoparticles [1]. At small nanoparticle density, monolayer graphene adheres to the substrate and is highly conformal over the nanoparticles, detached only in small regions around them. With increasing nanoparticle density, and decreasing nanoparticle separation to about 100 nm, graphene's elastic response dominates substrate adhesion, and the elastic stretching energy is reduced by the formation of wrinkles which connect the protrusions. Above a critical nanoparticle density, the wrinkles form what is evidently a percolating network across the sample. As the graphene membrane is made thicker, delamination from the substrate is observed. Since the wrinkling instability acts to remove inhomogeneous in-plane elastic strains through out-of-plane buckling, our results can be used to place limits on the possible in-plane strain magnitudes that may be created in graphene to realized strain-engineered electronic structures.

Work at UMD supported by NSF under MRSEC Grant DMR 05-20471 and Grant DMR 08-04976

[1] M. Yamamoto et al., *Phys. Rev. X* 2 (2012) 041018.

9:00am **GR+AS+NS+SS-ThM4 Chemical Properties of Ultrathin MgO(100) Films: The Role of Interfaces and Dopants, T. Risse**, Freie Universität Berlin, Germany, A. Gonchar, Fritz-Haber-Institut der MPG, Germany

The ideal (100) surface of MgO being the prototype of an ionic oxide is considered rather inert with respect to chemical interactions. Recent theoretical and experimental evidences show that this perception may have to be significantly altered if ultrathin films of only a few monolayer in thickness or transition metal doped systems are considered.¹⁻³

To address these questions thin and ultrathin single crystalline MgO(100) films grown on Mo(100) were investigated. On the one hand we will discuss the properties of ultrathin MgO films between 4 and 10 ML thickness focusing on the adsorption properties of molecular oxygen. While molecular oxygen is thought to be weakly physisorbed on bulk stoichiometric MgO(100) surfaces, the stoichiometric surfaces of the thin films bind oxygen much stronger, showing a desorption only above 300 K. In addition, electron spin resonance spectroscopy done under ultrahigh vacuum conditions show that these oxygen molecules are in fact O₂- radical species on the surface, being created by a charge transfer from the metal substrate onto the oxygen molecule. Spectroscopic evidence for structural modifications of the MgO surface namely polaronic distortions will be discussed.

The situation on the ultrathin film will be compared to transition metal doped MgO(100) films, which are thick enough (typically around 20 ML) to ensure that charge transfer from the metal substrate does not occur. We will discuss the geometric and electronic properties of the transition metal dopants focusing on Mo ions and discuss their impact on the redox chemistry which occurs on the MgO(100) surface.

References

- [1] Hellman, A.; Klacar, S.; Grönbeck, H. J. Am. Chem. Soc. 2009, 131, 16636
- [2] Frondelius, P.; Häkkinen, H.; Honkala, K. Phys. Chem. Chem. Phys. 2010, 12, 1483.
- [3] Stavale, F.; Shao, X.; Nilus, N.; Freund, H. J.; Prada, S.; Giordano, L.; Pacchioni, G. J. Am. Chem. Soc. 2012, 134, 11380.

9:20am **GR+AS+NS+SS-ThM5 The Self-assembly of Carbon Atoms on Catalyst Surface—Mechanism of Carbon Nanotube and Graphene Chemical Vapor Deposition (CVD) Growth, F. Ding**, The Hong Kong Polytechnic University, Hong Kong Special Administrative Region of China **INVITED**

Carbon nanomaterials, such as fullerene, carbon nanotubes (CNT) and graphene have drawn great interests due to their intriguing properties and the unlimited applications. Although the technologies of their synthesizing and using them for many applications have been greatly advanced, their formation mechanisms are still not very clear to us. In this talk, I will address two issues regarding (i) the chirality control in SWCNT growth and (ii) the epitaxy of graphene chemical vapor deposition (CVD) growth: (i) Encouraged by the dream of synthesizing carbon nanotubes (CNTs) with identical chiral indexes (n,m), the growth mechanism of CNTs has been overwhelming explored both theoretically and experimentally for nearly two decades. By developing a new version of potential energy surface (PES) and a hybridized atomic simulation method, we are able to simulate the nucleation and growth of perfect SWCNTs and the kinetics that controls the chirality assignment in CNT growth has been revealed. Based on this understanding, two strategies that may lead to chirality control in SWCNT synthesis, using high melting solid catalysts and varying the SWCNT's chirality during growth, are proposed. (ii) The epitaxial CVD growth on catalyst surface is the most promising method of synthesizing high quality, large area graphene. The key issue that how the orientation of the synthesized graphene is determined is crucial for both experimental design and growth control. Here three modes of graphene CVD growth, on terrace, near metal step, and the embedded growth are proposed and explored by the ab initio method. It is revealed that CVD graphene tends to be embedded on soft catalyst surfaces (e.g., Cu and Au) while the on terrace growth dominates the growth on the rigid catalyst surface (e.g., Ru, Ir, Rh). The graphene grown via on terrace mode may align along with different orientations while the graphene grown via the embedded mode or near metal step mode has only two potential orientations. Based on this understanding, many experimental puzzles are well understood and the strategies of growing high quality graphene on various catalyst surfaces are proposed.

10:40am **GR+AS+NS+SS-ThM9 Graphene Nanostructures: Top-down vs. Bottom-up Approaches, A. Sinitskii**, University of Nebraska-Lincoln **INVITED**

Graphene, a two-dimensional carbon allotrope, is often considered as a complement or even replacement for silicon in many electronics

applications. However, the absence of an electronic bandgap in graphene prevents its use in logic devices. According to the theoretical studies, a bandgap compared to that in silicon (1.1 eV) could be found in narrow graphene nanoribbons (GNRs) that have atomically precise armchair edges and widths less than 2 nm. Different top-down approaches, such as a combination of electron-beam lithography and dry etching, sonochemical method, nanowire lithography, and unzipping of carbon nanotubes, typically yield ribbons with widths > 10 nm and have a limited control over the edge structure in GNRs. Several recent studies have also focused on the development of bottom-up chemical approaches for narrow GNRs. Most of these methods are based on a polymerization of pre-synthesized molecular precursors followed by a cyclodehydrogenation. The reported bottom-up techniques could yield narrow atomically-engineered GNRs that are currently unachievable by any top-down approach, stimulating further research and development of new synthetic methods for GNRs. However, several problems still need to be solved, such as a limited length of synthetic GNRs, their poor solubility, difficulties with their precise placement on dielectric substrates for device fabrication, etc.

In this talk I will review recent efforts to synthesize GNRs with an emphasis on a comparative analysis of top-down and bottom-up approaches. I will also discuss a recently developed bottom-up approach for gram quantities of narrow GNRs that are less than 2 nm wide and have atomically precise armchair edges. These GNRs could be conveniently deposited from solution on any substrate, such as Si/SiO₂, mica and Au(111), for further studies. The GNRs were characterized by different techniques, including NMR, UV-vis-NIR and Raman spectroscopy, XPS, EDX, PES/IPS, SEM, AFM and STM. These data suggest that GNRs obtained by this novel synthetic approach could be promising for applications in field-effect transistors with high on-off ratios. Also, since these GNRs could be synthesized in gram quantities and at a very high yield, they could be used for bulk applications, including coatings, composites and photovoltaic devices.

11:20am **GR+AS+NS+SS-ThM11 Exfoliation, Sorting, and Applications of Few Layer Graphene Sheets, X. Chen**, Northwestern University

Graphene is one of the strongest, lightest and most conductive materials known so far. The common approach to prepare single layer graphene sheets is the reduction of graphene oxide which is made with well-known Hummer method. Due to the high level of the defects, the conductivity and the mechanical strength are significantly decreased comparing to the pristine graphene sheets. CVD growth is a very promising method to prepare large scale and high quality of graphene. It is still a challenge to transfer the sheet to insulate substrates. The liquid exfoliation of graphite without chemical modification is still desired for the electronics-grade graphene sheets. We are developing a simple and efficient exfoliating method to produce high quality and large scale graphene material.

The starting material is expandable graphite. This material is a product of flake graphite reacting with intercalation reagents in order to migrate between the graphene layers in a graphite crystal and remain as stable species. The materials were heat treated and then dispersed in N-Methyl-2-pyrrolidone (NMP). After the sonication and centrifuge process, the graphene sheets have been characterized by SEM, TEM, AFM, XPS, and Raman.

The material was treated at 450 °C for 30 min in nitrogen atmosphere and was changed to be very fluffy. The XPS shows that the carbon has a narrow peak and it indicates the fraction of bonding to oxygen is negligible. The result shows that most graphite is pristine and not oxidized by the intercalation process. The exfoliated graphene sheets have been observed with AFM and TEM. The result shows that the majority of the sheets are several layer thick and submicrometer to several micrometers long. The Raman measurement was also carried out on these few layer sheets and the result shows the D band is negligible and it indicates that these graphene sheets have little defects. Besides the electronics applications of these few layer graphene sheets, they also have potential applications in conductive composite. The result of the composite of graphene sheets and polystyrene will also be discussed.

11:40am **GR+AS+NS+SS-ThM12 Interaction of Copper Nanoparticles with Graphene Membrane, L.W. Huang, C.S. Chang**, Academia Sinica, Taiwan, Republic of China

We obtained atomically clean graphene membrane by annealing free-standing graphene in ultra-high vacuum transmission electron microscopy (UHV-TEM). Copper (Cu) nanoparticles formed by in-situ e-beam deposition of Cu atoms onto the clean graphene surface. The interaction between individual metal nanoparticles and this exceptional clean suspended graphene membrane was demonstrated by the stabilization and uniform distribution of Cu nanoparticles on the graphene surface. After carefully analyzing, we report the individual metal nanoparticle induced local strain field on the graphene membrane. The result is crucial to

understand the structural effect and charge transfer between graphene and Cu nanoparticles.

Helium Ion Microscopy Focus Topic Room: 203 A - Session HI-ThM

Basics of Helium Ion Microscopy

Moderator: A. Gözlhäuser, Bielefeld University, Germany

8:40am **HI-ThM3 Imaging with Helium Ions - A New Detector Regime with New Challenges and New Opportunities**, *J.A. Notte*, Carl Zeiss Microscopy **INVITED**

The helium ion microscope (HIM) is now accepted as a valuable instrument on par with the SEM, the TEM, and Gallium FIB within the family of charged particle microscopes. The introduction of the HIM was sparked by the successful commercialization of the gas field ion source (GFIS), and several scientific papers have already addressed its principles of operation. However, at the opposite end of this instrument, secondary electron (SE) detector has received relatively little attention despite several interesting characteristics. This presentation will give an overview of the HIM's SE detector and the unique circumstances in which it is used.

The SE detector on the HIM commonly operates under conditions and regimes that are distinctly different from the SEM. First, the overall efficiency is of prime importance since the excessive beam currents or excessive averaging often induce undesired sputtering or implantation in some samples. Generally, the areal dosages (measured ions / cm²) that are required must be kept to a minimum, sufficient to achieve the minimum required signal to noise ratio (SNR) and the necessary field of view (FOV). Second, the probe current that is used in the HIM is commonly as small as 0.5 pA or less. While such small currents are adequate for high magnification imaging, the ions arrive infrequently with long intervals wherein no meaningful information is acquired. In contrast, for most charged particle microscopes the incident particles arrive so frequently that their resulting signals overlap. Third, when the incident ions do arrive, each one produces an abundance of secondary electrons - usually three or more - and substantially more for glancing angles. Thus, the amplitude of the detected signal conveys more information than the frequency of the pulses.

While some of these three conditions present challenges for the instrument and for the operator, they also represent a new regime for signal acquisition. Towards that end, a variety of new techniques have been tested with computer simulations and with real experiments. For example, pulse counting has been implemented with somewhat surprising results. Signal integration (as opposed to simple averaging) has also been thoroughly investigated on the instrument with very favorable results. Finally, a new imaging technique called 'quotient mode' has been investigated and seems to offer a unique advantage of a significantly improved SNR available to the HIM.

9:20am **HI-ThM5 Interaction of Energetic Ions and Electrons with Two-Dimensional Materials**, *A.V. Krasheninnikov*, Aalto University and University of Helsinki, Finland **INVITED**

The experiments (see [1,2] for an overview) on the bombardment of 2D materials with energetic particles indicate that irradiation can have beneficial effects on such targets and that electron or ion beams can serve as tools to change the morphology and tailor the properties of such materials. It is also evident from the experimental and theoretical data obtained so far that the conventional theory of defect production in bulk materials not always works at the nanoscale or it requires considerable modifications. In this talk, our latest theoretical results on the response of graphene [3-6] and inorganic 2D materials like BN [7] and dichalcogenides (MoS₂, etc) [8] to electron and ion irradiation will be presented, combined with the experimental results obtained in collaboration with several groups [5,6,8-11]. I will also touch upon applications of time-dependent density-functional theory (TD-DFT) to ion electronic stopping calculations. I will show that combining TD-DFT with Ehrenfest dynamics and PAW approach, one can calculate electronic stopping power from first principles for a specific trajectory and different charge states of the projectile, and the results of calculations are in an excellent agreement with the experimental data.

1. A. V. Krasheninnikov, K. Nordlund, JAP 107 (2010) 071301.
2. A.V. Krasheninnikov and F. Banhart, Nature Materials, 6 (2007) 723.
3. O. Lehtinen et al., PRB 81 (2010) 153401.
4. E. H. Åhlgren, et al., APL 100 (2012) 23310.
5. J. Kotakoski, et al., PRL 106 (2011) 105505.
6. J.C. Meyer et al., PRL 108 (2012) 196102.

7. N. Berseneva, et al., PRL 107 (2011) 035501.
8. H.-P. Komsa, et al., PRL 109 (2012) 035503.
9. R. Nair, et al., Nat. Phys. 8 (2012) 199.
10. M. Kalbac et al., Advanced Materials 25 (2013) 1004.
11. S. Standop et al., Nano Letters (2013) in press.

10:40am **HI-ThM9 Imaging of Graphene Films by Helium Ion Microscope**, *S. Ogawa, T. Iijima, S. Nakaharai, M. Hayashida, S. Sato*, National Institute of Advanced Industrial Science and Technology (AIST), Japan

The helium ion microscopy is a unique technology for observation of soft materials such as low-k materials and photo resist patterns for LSI fabrication [1] and for nm order patterning. Graphene, a two-dimensional sheet of carbon atoms [2], is a promising channel material for next-generation transistors, and we have shown an on-off gating of current through a graphene nano-ribbon which was etched down by the helium ion nano beam using the helium ion microscope (HIM) [3] and by controlling electrical properties of the graphene films themselves by the helium ion dose [4]. On the other hand it is difficult to characterize whether the graphene films on the silicon oxide layer were single layers or not.

Graphene flakes were mechanically exfoliated from a crystal of HOPG using adhesive tape, and then deposited on a silicon wafer with a 300-nm-thick surface thermal oxide layer. The number of graphene layers was identified by sight with an optical microscope based on interference color and then characterized by HIM using brightness ratio of the graphene films and the silicon oxide surface. Brightness of the surface of the silicon oxide showed linear dependency to beam currents but with some offset for different HIM contrast conditions, and to normalize the brightness ratio at several imaging conditions, the brightness was compensated by the offset. HIM images show higher brightness ratio for single layer graphene films with darker brightness than multi-layer graphene films and much higher spatial resolution than the optical microscope, while it is not sufficient to determine layer numbers of the films so far. Helium ions dose higher than 1E16/cm² decreased the brightness ratio. Detail of the brightness ratio and its dependency on the layers of the graphene films will be discussed.

This work was partly supported by JSPS through the "FIRST Program," initiated by CSTP, Japan.

- [1] S. Ogawa, et al., Jpn. J. Appl. Phys., 49 (2010) 04DB12, [2] K. Novoselov, et al., Science 306, 666 (2004), [3] S. Nakaharai, et al., Appl. Phys. Express 5 015101 (2012), [4] S. Nakaharai, et al., 2012 IEEE International Electron Devices Meeting (IEDM), Technical Digest p.72 (2012)

11:00am **HI-ThM10 Secondary Electron Contrast for Few Layer Graphene in Helium Ion Microscope**, *Y. Zhou, H. Zhang*, Trinity College Dublin, Ireland

The one layer, atomic thin graphene has attracted numerous interests since its discovery, and reveals great potential application in the fields of nano-devices. However, the electrical structure for few layer graphene will be influenced by the layer thickness, thus the device performance will also be affected. As a result, the determination of graphene layer thickness becomes important. Recently, graphene secondary electron (SE) contrast in scanning electron microscope (SEM) provides a new method to determine graphene layer thickness. However, the mechanism of graphene SE contrast is still unclear, which limits the application and needs further exploration.

The recent developed Helium Ion Microscope offers a new and effective tool to investigate the mechanism of graphene SE contrast. The ultimate small source size, small energy dispersion and high gun brightness of HIM brings out a sub-nanometer resolution for graphene metrology. Meanwhile, HIM also has a lower SE energy distribution than SEM. thus SEs in HIM will be more surface sensitive. All the advantages of HIM reveal that it is an effective tools to study the SE emission in graphene from a new aspect, and may help us to clarify some uncertainty of the contrast mechanism.

Here, we used a Carl Zeiss Orion Helium Ion Microscope to investigate graphene SE contrast at the typical acceleration voltage of 30KV. Exfoliated few layer graphene flakes on silicon oxide substrates exhibited higher SE yield (brighter contrast) than substrates. Graphene layers could also be clearly distinguished for more than five layers with almost linear SE contrast dependence. An ultra large SE yields more than 200% was measured from the free-standing graphene. Thus we attributed the SE emissions in HIM and low voltage SEM to the SE emission from graphene itself, with very little contribution from substrate SE attenuations. Similar SE contrast variation and high SE yields for few layer graphene flakes could be observed in SEM at very low acceleration voltages below 0.2KV. We also observed the influence of graphene work function to the SE contrast for graphene flakes less than four layers.

The results could help us to understand the graphene SE contrast mechanism more clearly. The linear layer dependence SE contrast also offered an effective method to determine the graphene layer thickness.

11:20am **HI-ThM11 Monte Carlo Simulations of Helium and Neon Ions Beam Induced Deposition and Etching.** *R.T. Timilsina*, The University of Tennessee Knoxville, *D.A. Smith, P.D. Rack*, The University of Tennessee Knoxville and Oak Ridge National Laboratory

The new Gas Field Ion Microscope is able to deposit and etch material at the nanoscale in a highly controlled manner, but in order to exploit this capability it is necessary to have a detailed quantitative model of the process. A Monte Carlo simulation for He⁺ and Ne⁺ ion beam induced deposition (and etching) has been developed which provides data in excellent agreement with the observed experimental results over a wide range of experimental conditions. The ion beam induced nanoscale synthesis of Pt_x (where x~5) using the trimethyl (methylcyclopentadienyl)platinum(IV) (MeCpPt^{IV}Me₃) precursor is investigated by performing Monte Carlo simulations of helium and neon ions integrated with a gas handling routine to mimic the precursor adsorption and decomposition. The simulation results show that the helium beam leads to more lateral growth relative to the neon beam because of its larger interaction volume. The lateral growth of the nanopillars is dominated by molecules deposited via secondary electrons in the both simulations. Using a low precursor residence time of 70µs resulting in an equilibrium coverage of ~4%, the neon simulation has a lower deposition efficiency (3.5%) compared to that of the helium simulation (6.5%). At larger residence time (10ms) and consequently larger equilibrium coverage (85%) the deposition efficiencies of helium and neon increased to 49% and 21%, respectively; which is dominated by increased lateral growth rates leading to broader pillars. The nanoscale growth is further studied by varying the ion beam diameter at 10 ms precursor residence time. The study shows that total SE yield decreases with increasing beam diameters for the both ion types. Finally, experimentally we have shown that He ion deposited material has a larger room temperature resistivity (~3.5x10⁴ - 2.2x10⁵ µΩ-cm) and temperature dependent transport behavior consistent with a granular material in the weak intergranular tunnel coupling regime. Conversely Ne ion deposited material has a much lower room temperature resistivity (~600 - 3.0x10³ µΩ-cm) and temperature dependent electrical behavior representative of strong intergranular coupling. The Ne ion deposited nanostructure has larger platinum nanoclusters, which is rationalized via Monte-Carlo ion-solid simulations that show the neon energy density deposited during growth is much larger due to the smaller ion range as shown in The observed platinum grain coarsening and subsequently lower resistivity for the Ne ions beam induced deposits is correlated to the enhanced platinum mobility via the enhanced nuclear stopping of the Neon ions.

11:40am **HI-ThM12 Helium Ion Microscope; a Single Beam for Imaging and Fabrication.** *E. van Veldhoven, N.B. Koster, F.T. Molkenboer, D.J. Maas*, TNO Technical Sciences, Netherlands, *H.W. Zandbergen, P.F.A. Alkemade*, TU Delft, Netherlands

At TNO, we focus on imaging novel materials and developing new nanofabrication applications for mainly the semiconductor and solar industry. The helium ion microscope (Orion plus Zeiss) creates new opportunities for exploration [1]. The microscope provides a sub nanometer spot size with ions that hardly scatter back. For the secondary electron image, it produces only low energy SE. The obtained image has an unique contrast, which contains information about the morphology and often grain and material contrast are clearly present. The SE's appear only from a very local interaction volume which gives a high surface sensitivity. Single layers, small particles and thin layers of contamination can be made relative easily visible even on charging surfaces which are of great interest in the semiconductor and solar industry.

The small interaction volume created by charged species is unique and opens new ways for nanofabrication. Novel recipes are being developed to obtain high, small and dense deposition yields for Pt-precursor and small and dense high etching yields with the XeF₂-precursor. With the Oxford OmnigisTM and the Raith Elphy MultibeamTM. A wide set of parameters like beam current, acceleration voltage, refreshment rates, gas flows, writing patterns are being included in our research for true 3D-nanofabrication. Direct sputtering of materials for thin films are highly promising since no helium can stay trapped in the bulk material [2]. Recently we showed that it is possible to perform incisions into bulk material without any helium trapping yielding in high quality TEM samples [3]. The HIM enables a novel way for dense and high resolution nanofabrication and imaging.

[1] D Maas, E van Veldhoven, P Chen, V Sidorkin, H Salemkink, E van der Drift, P Alkemade; Proceedings. of SPIE 7638 (2010)

[2] M. M. Marshall, J. Yang, A.R. Hall, Scanning, 34, 2 (2012), 101-106

[3] M. Rudneva, E van Veldhoven, S.K. Malladi, D.Maas, H.W. Zandbergen. J. Mat. Sci., 28, 8, (2013), 1013-1020

In Situ Spectroscopy and Microscopy Focus Topic Room: 203 B - Session IS+AS+SS-ThM

Ambient Pressure XPS from Sophistication to Reality Moderator: A. Thissen, SPECS Surface Nano Analysis GmbH

8:40am **IS+AS+SS-ThM3 Ambient Pressure XPS Observation of Electrode Surfaces during Electrochemical Reactions.** *H. Sanchez Casalongue, S. Kaya, D.J. Miller, D. Friebe, A. Nilsson, H. Ogasawara*, SLAC National Accelerator Laboratory **INVITED**

The sluggish kinetics in oxygen reduction reaction (ORR) is one of key challenges in polymer electrolyte membrane fuel cells (PEMFCs). Understanding the ORR mechanism under operating conditions is essential to isolate parameters that allow for high PEMFC efficiencies. Through the use of ambient pressure photoemission spectroscopy (APXPS) at Stanford Synchrotron Radiation Lightsource (SSRL) [1], we identified the surface speciation of the fuel cell Pt cathode under different operating conditions. We also established that the species on the electrode change drastically depending on the oxygen pressures. We used this knowledge to clarify that the favored ORR pathway is dependent on the operating conditions, thus identifying a key parameter to be controlled in high efficiency fuel cells [2].

1. S. Kaya, H. Ogasawara, L.-A. Nasdlsund, J.-O. Forsell, H. Sanchez Casalongue, D.J. Miller, A. Nilsson, Ambient-pressure photoelectron spectroscopy for heterogeneous catalysis and electrochemistry, Catalysis Today 205 (2013) 101.

2. H.S. Casalongue, S. Kaya, V. Viswanathan, D. Miller, D. Friebe, J.K. Noskov, A. Nilsson, H. Ogasawara, Direct observation of the oxygenated species during oxygen reduction reaction on a Pt fuel cell cathode, submitted.

9:20am **IS+AS+SS-ThM5 Ambient Pressure Photoelectron and Electron Spectro-Microscopy Using Electron Transparent Membranes.** *A. Yulaev*, Southern Illinois University Carbondale, *M. Amati, L. Gregoratti*, Sincrotrone Trieste, Italy, *S. Guenther*, Technical University Muenchen, Germany, *M. Kiskinova*, Sincrotrone Trieste, Italy, *I. Sgura, B. Bozzini*, University of Salento, Italy, *A. Kolmakov*, Southern Illinois University Carbondale

Truly *in situ* (photo-) electron spectroscopy and microscopy under ambient pressure conditions in different environments such as electrolytes, water, reactive liquids and gases would provide a nanoscopic access to processes taking place at solid-liquid-gas interfaces. However this exciting line of research still remains a challenging experimental task but is strongly demanded by a variety of active research directions *i.e.* in fuel cells, batteries, catalysis, (bio-) medical, automotive, geological, forensic *etc.* To address these needs a number of designs have been developed since nineties to probe the samples in liquid state or gases at sub-atmospheric pressure. In particular, the elevated pressure XPS at liquid solid and liquid-gas interfaces have been demonstrated via development of advanced differentially pumped lens systems for the electron energy analyzer or via liquid micro jets and droplet "trains" methods.

Novel quasi-2D materials such as graphene and its derivatives currently constitute the active source of innovations in electronics, optics, energy harvesting/storage, catalysis and bio-medical applications. When isolated as ultrathin (~0.3-1 nm) membranes, graphene sheets have thicknesses comparable to the effective attenuation length of 200-1000 eV electrons. In addition, these membranes are chemically stable, gas impermeable and mechanically robust. Based on this unique combination of properties and on recent developments in fabrication and transfer protocols we demonstrate the capability to perform XPS and electron microscopy studies of the processes taking place at liquid-solid interface through graphene-based membranes.

9:40am **IS+AS+SS-ThM6 Surface Chemistry over Inverse Model Catalysts under Near-Ambient Pressure.** *A. Baber, K. Mudiysenselage, S. Senanayake, J. Rodriguez, D. Stacchiola*, Brookhaven National Laboratory

The importance of metal-oxide interfaces has long been recognized, but the molecular determination of their properties and role is only now emerging. Atoms with properties ranging from metallic to ionic are available at the metal-oxide interface and create unique reaction sites. We have shown that the activation of an efficient associative mechanistic pathway for the water-gas shift reaction by an oxide-metal interface leads to an increase in the catalytic activity of ceria nanoparticles deposited on Cu(111) or Au(111) by

more than an order of magnitude. *In situ* near ambient pressure X-ray photoelectron spectroscopy (NAP-XPS) experiments demonstrated that a carboxy species formed at the interface is the critical intermediate in the reaction. To obtain a complete picture of the morphological and chemical changes occurring during catalytic processes, we investigated the reduction of $\text{Cu}_2\text{O}/\text{Cu}(111)$ under NAP of CO by a combination of *in situ* scanning tunneling microscopy (STM) and XPS to provide insight into the highly reducing environment of the water gas shift reaction on a model oxide surface. Systematic studies allow us to identify intermediate structures and determine how reaction fronts propagate across a surface with atomic scale resolution. Traditionally, STM is used to monitor surface structures and electronic properties, but here we show the surface oxide species can be identified with atomic-scale detail under near ambient pressures.

10:40am **IS+AS+SS-ThM9 Ambient Pressure Photoelectron Spectroscopy using Tender X-ray**, *S. Ananda, E.J. Crumlin, R. Chang, B. Mao*, Lawrence Berkeley National Laboratory, *W. Stolte*, Lawrence Berkeley National Laboratory, **INVITED**

The ambient pressure x-ray photoelectron spectroscopy (AP-XPS) endstations based on differentially pumped electron energy analyzers have been recognized by scientific communities as an important in-situ tool to study water, environmental science, catalysis and many other important fields.

Multiple new AP-XPS endstations are currently under planning or development at US and international synchrotron light sources. Recently we have installed a new hard x-ray AP-XPS endstation at ALS Beamline 9.3.1 (2.5keV- 5keV). By using tender X-ray up to 5KeV, we can perform AP-XPS at a pressure up to 110 torr. The probing depth of photoelectrons also increases to >10 nm, which will allow us to study not only the gas/solid interface but also the liquid/solid interface. In this meeting, we will present results of our in-situ study on the electrolyte/electrode interface of a working model electrochemical cell.

We believe the successful development of hard X-ray APXPS endstation will provide energy research community a powerful in-situ tool to directly study the electrolyte/electrode interface of many important electrochemical devices.

11:20am **IS+AS+SS-ThM11 Novel Developments in Near Ambient Pressure XPS – The Route Towards Standard Analysis Tools in Laboratory Environments**, *A. Thissen, S. Bahr*, SPECS Surface Nano Analysis GmbH, Germany

Modern devices are often only functional in environments far away from ultrahigh vacuum, still being the standard operation conditions for all Surface Science techniques. In parallel the importance of surfaces for the correct device operation is continuously increasing due to miniaturization down to the nanoscale. To contribute to advanced materials analysis in future means using Photoelectron spectroscopy combined with Scanning Probe Microscopies and related techniques in the generic or near generic device environments. This means high, elevated or near ambient pressures of defined working gas mixtures, liquid media, potentials or magnetic fields applied. Also extremely low or high temperatures might be necessary. In past all standard Surface Science Techniques did not work under these extreme environments. As a route to in situ sample analysis Near Ambient Pressure XPS has already been used for a longer time with tremendous success. Nowadays steps are made to utilize this analysis technique not only at synchrotrons and in academic environments, but also as standard analysis tools in user friendly laboratory systems. This work summarizes and presents existing solutions nowadays and future development routes to new instruments and materials analysis methods being functional under these working conditions. Opportunities and limits will be discussed. from the perspective of a supplier of scientific instruments. Finally applications, examples and results from existing In situ methods like high pressure treatments cells, complete High Pressure or Near Ambient Pressure Photoelectron Spectroscopy or Scanning Probe Microscopy Systems (NAP-PES or NAP-SPM), liquid and electrochemical cells, Liquid sample “manipulators”, and concepts and status of equipment working in highest or lowest temperatures, high magnetic fields and static or dynamic potentials will be demonstrated.

Accelerating Materials Discovery for Global Competitiveness Focus Topic

Room: 202 B - Session MG+MI+NS-ThM

Theoretical and Computational Methods

Moderator: K. Cook-Chennault, Rutgers, the State University of New Jersey, L. Madsen, National Science Foundation (NSF)

8:40am **MG+MI+NS-ThM3 Application of Computational Methods to Material Design and Discovery**, *S.B. Sinnott*, University of Florida **INVITED**

Modeling of materials is an integral component in the design and discovery of materials as outlined in the Materials Genome Initiative. Illustrative examples are discussed where computational methods are used in conjunction with cutting-edge experimental methods. In the first example, electronic-structure, density functional theory calculations and empirical, atomic-scale simulations are used in conjunction with experimental synthesis and characterization to identify the features of Pt electrode/PbTiO₃ dielectric interfaces that lead to the degradation of devices. The results specify how the microstructure of the interface might be designed to improve performance. In the second example a combination of simple, electrostatic calculations, high-through-put experiments, and materials informatics is used to investigate the tribological properties of inorganic materials. The results are used to design a simple model to identify material properties that are indicative of solid-state lubrication. This work is supported by the National Science Foundation under grant DMR-1207293 and the Office of Naval Research

9:20am **MG+MI+NS-ThM5 New Ferroelectrics and Antiferroelectrics by Design**, *K.M. Rabe*, Rutgers, the State University of New Jersey **INVITED**

I will describe our work on the design and discovery of new classes of ferroelectric and antiferroelectric materials using a combined crystallographic database / first principles approach. For ferroelectrics, using the design principle that any polar structure type can have ferroelectric representatives if the barrier to switching is lowered by appropriate chemical variation, we have recently identified a new family of ferroelectrics in the intermetallic LiGaGe structure type. For antiferroelectrics, we used a design principle based on the close relationship between ferroelectrics and antiferroelectrics to identify a previously unrecognized class of antiferroelectrics, related to the LiGaGe-type ferroelectrics, in the MgSrSi structure type. The further development of design principles and their application will be discussed. The discovery of new classes of antiferroelectrics is expected to open the way to increased recognition and application of antiferroelectrics as functional materials.

10:40am **MG+MI+NS-ThM9 Disruptive Design Strategies for Emergent Ferroics**, *J.M. Rondinelli*, Drexel University

There are two main routes to accelerate materials discoveries for advanced electronic and sustainable energy technologies: serendipitous realization through conventional synthesis or computationally guided growth of novel materials through, *e.g.*, artificial structuring of bulk compounds at the atomic scale. Recently, the launch of the Materials Genome Initiative (MGI) at the national level has reinvigorated the search for new routes to accelerate the discovery of advanced materials for rapid deployment—the aim being to evolve a “hunter and gatherer” discovery paradigm into the cultivation of materials by design. This discovery process may be accelerated by merging applied theoretical crystallography, where the objective is transformed into (i) identifying suitable topologies – approximate geometric arrangements of structural building units – that lift particular symmetries, with electronic structure methods to (ii) search for microscopic mechanisms and external conditions that energetically stabilize those geometries. Such information may guide experimental explorations, whereby the synthetic efforts are focused on a more manageable (and largely reduced) structural data set by the theoretical (symmetry) considerations.

Here, we describe report an Ensemble Computation Materials Protocol (ECMP) with predictive capability to design and accelerate the discovery of a new class of A-site cation-ordered perovskite ferroelectrics from combinations of the centric, non-polar, transition metal–oxygen octahedra that form the perovskite framework. First, we describe the microscopic origin for the loss of inversion symmetry and the electric polarization in layered $(A,A')\text{BO}_3$ perovskite oxides. We then show that the mechanism can be translated to $A_nB_n\text{O}_{3n+1}$ ($n=1,2$) Ruddlesden-Popper (RP) oxides with disconnected layers of corner-sharing octahedra. We use the group theoretical methods to enumerate the structural criteria required to remove

the mirror symmetry elements. Feasible chemistries are proposed using Bayesian inference methods. We then evaluate the stability of the possible ground state structures with density functional theory (DFT) calculations. We predict that ordering of divalent and trivalent cations in a layered RP manganite leads to a polar phase, space group $Pca2_1$, with a sizeable polarizations, which are supported by preliminary experimental. We anticipate that these findings and methodology will contribute to our understanding of not only new ferroic materials, but also that this general approach of physical properties by atomistic structure design within the MGI is immediately amenable to other material functionalities.

11:00am **MG+MI+NS-ThM10 Computational Design of Materials for Catalysis: Interface Matters**, *T.S. Rahman*, University of Central Florida **INVITED**

An important ingredient in computational design of functional materials is back and forth feedback between theory and experiment, which necessarily involves modeling of realistic environments, using accurate methods. In this talk, I will present results of our density functional theory based calculations which together with experimental observations help isolate catalyst descriptors for specific reactions, in particular for supported nanoparticles. For example, for methanol oxidation on Au nanoparticles on titania [1], the higher activity of interfacial sites can be traced to charge-transfer-induced Coulomb interaction among the gold, reactant, and reducible TiO₂ support, brought about through the formation of an ionic O–Au bond between gold and methoxy in such sites, which turns the participating perimeter gold atom cationic. A direct result of such charge-transfer-induced repulsive interaction between cationic gold and positively charged C moiety of methoxy is activation of the positively charged C moiety of methoxy, as manifested by the pronounced elongation of O–C bond length and the tilting of the methoxy axis, which facilitate reaction of methoxy through C–H scission with the bridge oxygen atoms that are readily available from the reducible support. I will use the above guidelines to predict the reactivity of several titania supported metallic/bimetallic nanoparticles for oxidation of organic molecules with the structure of R–O–R', where R and R' are (saturated) hydrocarbons. Similarly, I will analyze the role of the interface (with the support) for a set of nanometer and sub-nanometer sized Pt nanoparticles on titania and alumina and point to the variations in the physical and chemical characteristics as a function of size, shape, and chemical environment (H and OH coverage). Through detailed comparison with XANES data [2], I will provide an understanding of the descriptors that control specific nanoparticle property.

[1] S. Hong and T. S. Rahman, J. Am. Chem. Soc., dx.doi.org/10.1021/ja4010738 (2013)

[2] F. Behafarid, L. K. Ono, S. Mostafa, J. R. Croy, G. Shafai, S. Hong, T. S. Rahman, Simon R. Bare and B. Roldan Cuenya, Phys. Chem. Chem. Phys., 2012, **14**, 11766–11779

*Work supported in part by DOE under grant DE-FG02-07ER15842.

Plasma Science and Technology

Room: 102 B - Session PS+AS+NS+SS-ThM

Plasma Synthesis of Nanostructures

Moderator: R.M. Sankaran, Case Western Reserve University

8:00am **PS+AS+NS+SS-ThM1 Nanoscale Interface Engineering of Silicon Nanocrystals by Non-equilibrium Microplasma**, *V. Svrcek*, Advanced Industrial Science and Technology (AIST), Japan **INVITED**

Silicon nanocrystals (Si-ncs) created vast interests and Si-ncs interfaces are at the basis of application in water splitting, for bio-imaging and may open up great opportunities for the development of most advanced technologies. For instance, in photovoltaic community enormous interests is mainly due to their enhanced multiple exciton characteristics. The fundamental aspects of exciton dissociation are highly important to improve the efficiency of solar cells and therefore the employment of Si-ncs in a range of applications requires careful investigation on the surface conditions. Indeed, the interplay of quantum confinement with surface effects reveals a complex scenario, which can strongly affect of Si-ncs properties and prediction of their corresponding behaviour. In this context, a variety of carefully surface-engineered Si-ncs are highly desirable both for understanding of Si-ncs photo-physics and for their successful integration in application devices. Surface surfactant free functionalization techniques that can assess the functionalities of the Si-ncs interface need to be developed so that efficient charge transport and excitons dissociation could be achieved. In this talk we firstly highlight a selection of theoretical efforts and experimental surface engineering approaches. Secondly we present our results on surfactant free

surface engineering of Si-ncs, which have utilized novel microplasma-liquid interactions. The possibilities of surface engineering and tuning overall Si-ncs properties by two independent techniques will be pointed out. Particularly, we will show that the atmospheric pressure RF and DC microplasmas in liquid media offer a wide range of opportunities for Si-ncs surface engineering due to multiple mechanisms induced by the microplasma process and more efficient electron driven non-equilibrium liquid chemistry. The flexibility and results on superior capabilities of the microplasma-based surface engineering approach will be presented. Then, an influence of Si-ncs surface engineering on photovoltaic based devices and the possibilities of enhancement optical density and role of Si-ncs surface engineering on integration within nanotubes will be shown. Finally the potential for scaled-up to achieve large scale surface engineering as would be required for industrial applications will be discussed as well.

8:40am **PS+AS+NS+SS-ThM3 Single Step Plasma Synthesis of Core-shell Group IV Nanoparticles**, *R.P. Chaukulkar**, Colorado School of Mines, *K. de Peuter*, Eindhoven University of Technology, Netherlands, *P. Stradins*, National Renewable Energy Laboratory, *S. Agarwal*, Colorado School of Mines

There has been an increased interest in group IV nanoparticles (NPs) for a variety of applications including photovoltaics, lithium ion batteries, and bio-imaging. The properties of these quantum-confined NPs are governed by their size as well as the surface passivating layer. Si NPs, 3-7 nm in size, were synthesized in a tubular, capacitively-coupled, radio-frequency SiH₄/Ar plasma at pressures ranging from 5-8 Torr. The H-terminated surface of the as-synthesized Si NPs is highly reactive, and requires surface passivation to prevent oxidation. We have developed a single-step synthesis and in-flight surface passivation technique wherein we use a dual-plasma setup, which consists of a second capacitively-coupled C₂H₂ plasma, downstream from the SiH₄/Ar synthesis plasma. The Si NPs can be coated with amorphous carbon (*a*-C) to obtain core-shell nanostructures, with a thin SiC interface between Si and *a*-C. These core-shell NPs are transported by flow into a surface analysis chamber, which is equipped with *in situ* attenuated total reflection Fourier transform infrared and photoluminescence spectroscopy setups to determine the surface composition and the optical band gap of the NPs, respectively. The NPs are also extensively characterized using *ex situ* x-ray diffraction, Raman spectroscopy, and transmission electron microscopy (TEM). The thickness of the coating, determined from TEM, is ~2-4 nm. We have also studied the effect of varying the C₂H₂ plasma parameters on the structure and composition of the *a*-C coating and the SiC interface. This plasma synthesis and passivation technique has been extended to other group IV NPs such as Ge and Sn, which are less likely to have a carbide interface.

9:00am **PS+AS+NS+SS-ThM4 On the Structure of Non-Thermal-Plasma Produced Nanocrystals**, *T. Lopez*, *L. Mangolini*, University of California, Riverside

The use of continuous flow non-thermal plasma reactor for the formation of silicon nanoparticles has attracted great interest because of the advantageous properties of the process [1]. Despite the short residence time in the plasma (around 10 milliseconds), a significant fraction of precursor, silane, is converted and collected in the form of nanopowder. The structure of the produced powder can be tuned between amorphous and crystalline by adjusting the power of the radio-frequency power excitation source, with high power leading to the formation of crystalline particles [2]. Numerical modelling suggests that higher excitation power results in a higher plasma density, which in turn increases the nanoparticle heating rate due to interaction between ions, free radicals, and the nanopowder suspended in the plasma [3]. An understanding of the mechanism that leads to the crystallization of the powder while in the plasma is lacking. In this work, we present an experimental investigation on the crystallization kinetic of plasma-produced amorphous powder. Silicon nanoparticles are nucleated and grown using a non-thermal plasma reactor similar to the one described in [1], but operated at low power to give amorphous nanoparticles. The particles are then extracted from the reactor and flown through a tube furnace capable of reaching temperatures up to 1000°C. Raman and TEM have been used to monitor the crystalline fraction of the material as a function of the residence time and temperature. A range of crystalline percentages can be observed from 750 °C to 830 °C. We have also used *in-situ* FTIR to monitor the role of hydrogen on the crystallization kinetic. It has been proposed that that hydrogen induced crystallization is the mechanism for deposition of microcrystalline silicon thin films in PECVD systems. We find that the plasma-produced amorphous silicon powder is rich with surface SiH_x species, but no detectable signature from bulk Si-H bonds has been observed. A discussion of particle growth and plasma-

* **Coburn & Winters Student Award Finalist**

particle interaction will be presented with its relation to the overall effect on crystallization mechanisms.

1. Mangolini, L.; Thimsen, E.; Kortshagen, U., *High-yield plasma synthesis of luminescent*

silicon nanocrystals. *Nano Letters* **2005**, *5* (4), 655-659.

2. O. Yasar-Inceoglu, T. Lopez, E. Farshihagro, and L. Mangolini, *Silicon nanocrystal*

production through non-thermal plasma synthesis: a comparative study between silicon

tetrachloride and silane precursors. *Nanotechnology*, **23**(25): p. 255604.(2012)

3. Mangolini, L.; Kortshagen, U., Selective nanoparticle heating: another form of

nonequilibrium in dusty plasmas. *Physical review E* **2009**, *79*, 026405 1-8.

9:20am **PS+AS+NS+SS-ThM5 Detection of Nanometer Scale Ni Clusters Formed in an Atmospheric Pressure DC Microplasma by Ion Mobility Spectrometry**, *C.J. Hogan*, University of Minnesota, *A. Kumar*, Case Western Reserve University, *S. Kang*, *C. Larriba-Andaluz*, *H. Ouyang*, University of Minnesota, *R.M. Sankaran*, Case Western Reserve University

Using a high resolution differential mobility analyzer (1/2-mini DMA, Nanoengineering) coupled to a Faraday cage electrometer for ion mobility spectrometry, we have investigated the formation of Ni clusters in a DC atmospheric pressure Ar microplasma. To produce Ni clusters, nickelocene (bis(cyclopentadienyl)nickel) vapor was continuously introduced into the microplasma by sublimation of a heated solid powder into an Ar gas flow. Particles were nucleated, grown, and rapidly quenched to limit their diameter to less than ~10 nm. Prior to mobility measurement, a steady-state charge distribution of the aerosol particles was achieved via diffusion charging with background gas ions produced in a Kr-85 source (TSI, Inc.). Both positive and negative mobility distributions were measured. A background high intensity peak around ~0.75 nm equivalent "mobility diameter", corresponding to the ions produced by the Kr-85 source, was always observed. The introduction of nickelocene vapor in the microplasma resulted in a lower intensity distribution of particles, spanning from the peak corresponding to Kr-85 generated ions to 10 nm in mobility size. Under all circumstances, the mobility distribution from the ion peak to the largest produced particles was continuous, indicating the microplasma reactor can form stable Ni clusters below 2.0 nm in size. To obtain structure-mobility relationships, density functional theory and gas molecule scattering calculations were carried out. The nanoparticles were also collected by electrostatic precipitation and further characterized by atomic force microscopy to confirm their size and distribution. These results confirm a that a continuous distribution of particles is formed in microplasma processes down to less than 1.0 nm which could have both fundamental and technological implications ranging from the study of particle formation in the vapor phase to novel applications of quantum confined materials.

9:40am **PS+AS+NS+SS-ThM6 One-step Synthesis of Gold Bimetallic Nanoparticles with Various Metal Compositions**, *M.A. Bratescu*, *N. Saito*, Nagoya University, Japan

In our group, Solution Plasma Processing (SPP) is a useful and simple method for metal NPs (nanoparticles) synthesis [1, 2]. In the present work, we demonstrate a special merit of the SPP method for the fabrication of bimetallic NPs using a combination of the reduction reaction of the metal (M) ion to the neutral state, while simultaneously eroding the electrodes during the discharge, which generates the second metal in the structure of the bimetallic NPs [3].

The gold bimetallic NPs were synthesized by alloying gold with various types of metals, which are divided in four categories: (i) divalent *sp* metals, Zn and Cd, (ii) trivalent *sp* metals, Ga and In, (iii) *3d* metals Fe, Co, Ni, and Cu, and (iv) *4d* metals Pd and Ag. We used SPP between two gold electrodes immersed in a nitrate solution of the corresponding metal M. We studied the optical properties of the gold nanoalloys, as well as their crystallinity, composition, size and morphology, and we have evaluated the interaction of various gold bimetallic NPs with free radicals for possible consideration as catalysts. SPP characterization has been done using electrical and optical probes. We found that the properties of the gold bimetallic NPs are connected with the category to which the metal belongs. We analyzed that the amount of the intermetallic compound in the composition of the gold bimetallic NPs depends on the electrochemical potential and the electron density of the Wigner-Seitz cell. The obtained gold bimetallic NPs using one step in Solution Plasma have sizes in the range from 5 to 20 nm. The difference in electronegativity between gold and the other metal was the main reason for the formation of the intermetallic compounds found in the composition of the gold bimetallic

NPs. This work was supported in part by Kakenhi, Challenging Exploratory Research, JSPS, Japan.

[1] M.A. Bratescu, et al., *J. Phys. Chem. C* **115** (2011) 24569.

[2] S.P. Cho, et al., *Nanotechnology* **22** (2011) 455701.

[3] M.A. Bratescu, et al., *J. Alloys and Compounds* **562** (2013) 74.

10:40am **PS+AS+NS+SS-ThM9 Synthesis of Platinum Nanoparticles on Carbon Powder by the Means of an RF Plasma Torch for Fuel Cells Applications**, *D. Merche*, *T. Dufour*, Univ. Libre de Bruxelles, Belgium, *L. Devant*, Facultés Univ. Notre Dame de la Paix, Belgium, *F. Deschamps*, Univ. de Liège, Belgium, *J.-J. Pireaux*, *L. Housiau*, Facultés Univ. Notre Dame de la Paix, Belgium, *N. Job*, Univ. de Liège, Belgium, *F.A.B. Reniers*, Univ. Libre de Bruxelles, Belgium

The grafting of noble metal nanoparticles on porous carbon supports has attracted a great interest over the last few years, due to potential applications in Proton Exchange Membrane Fuel Cells (PEMFC). Plasma processes for the synthesis of such electrodes could be a major asset for the production of the fuel cell elements at lower cost.

In this study, Pt nanoparticles are synthesized from the decomposition of Platinum (II) acetylacetonate [Pt(acac)₂] and deposited on porous carbon by the means of an RF atmospheric plasma torch running with argon in an open air environment. This one single step technique is very simple, fast and robust. It also presents substantial economic advantages, such as the non requirement of a high-vacuum and the possibility to easily implement this process in a continuous production line. The Pt nanoparticles were principally grafted on carbon-black powder. Some tests were also conducted on Carbon Xerogel matrices presenting well-controlled porosity.

The organometallic-carbon powder mixture pressed on a copper tape was treated in the post-discharge of the Ar plasma torch. A kinetic study has been carried out by XPS to evaluate the optimal exposure time to the post-discharge required for synthesizing a significant amount of Pt nanoparticles. 6% of Pt was detected after only 30 seconds of plasma treatment, and 14% after 600 seconds. According to the fitting of the Pt XPS peaks, the most intense component of the Pt for the sample treated by plasma was the Pt(0). 68% of the platinum was under metallic form after 30 seconds of plasma treatment, and 78 % after 600 seconds.

The effect of the distance between the powder and the torch, and the addition of a small quantity of hydrogen to the vector gas was studied by XPS regarding the elemental composition and the oxidation state of the platinum nanoparticles. A comparison with Pt synthesized in a controlled atmosphere was also realized. For a study more focused on the PEMFC applications, the powder mixture was overlaid on a Gas Diffusion Layer (GDL), namely Carbon Toray Paper (CTP), before being exposed to the Ar post-discharge.

The size and the dispersion of the nanoparticles grafted on carbon black powder or on carbon Xerogel were observed by a FEG-SEM and by TEM.

11:00am **PS+AS+NS+SS-ThM10 Growth of Nanocomposites on Heat-Sensitive Polymers using Cold, Dielectric Barrier Discharges at Atmospheric Pressure**, *J. Profili*, Université Paul-Sabatier, France and Université de Montreal, Canada, *N. Gherardi*, CNRS-LAPLACE, France, *L. Stafford*, Université de Montreal, Canada

Cold, atmospheric-pressure plasmas have already demonstrated their potential for homogeneous thin film deposition in polymers functionalization. In order to achieve multifunctional properties, a new challenge is the plasma-assisted deposition of nanocomposite coatings. This contribution is focused on the growth of nanocomposites based on TiO₂ nanoparticles embedded in a silica-like matrix with the objective of synthesizing barrier layers with improved resistance to UV irradiation. Experiments were carried out in a parallel plate dielectric barrier discharge with the substrate placed on the bottom electrode. The gas mixture is composed of either N₂ or He as the carrier gas, a mixture of hexamethyldisiloxane, and either nitrous oxide (for experiments in N₂) or O₂ (for experiments in He) for the growth of the SiO₂ matrix, and TiO₂ nanoparticles which are introduced by nebulizing stable colloidal solutions. Preliminary results show that TiO₂ nanoparticles can successfully be incorporated in the film. In addition, as in low-pressure plasma conditions, electrostatic forces were found to play a very important role on the transport of nanoparticles in the discharge. As a result, an appropriate tuning of the applied voltage waveform (shape, amplitude and frequency) was found to directly impact the spatial distribution of nanoparticles in the film.

11:20am **PS+AS+NS+SS-ThM11 Fabrication of Asymmetric Nanopores by Pulsed PECVD**, *S.S. Kelkar*, *C.A. Wolden*, Colorado School of Mines

The field of nanopore fabrication has attracted a lot of attention recently due to their potential application in DNA sequencing, ionic field effect

transistors, and detection and separation of biomolecules and nanoparticles. The objective of our research is to develop a simple approach for large area fabrication of nanopores (pore size ~ 1–10 nm) with atomic level precision. In this work, we first employ relatively large template structures (~ 100–250 nm) produced by track-etching or e-beam lithography. The pore size is then refined to the desired level by deposition of material using pulsed plasma enhanced chemical vapor deposition (PECVD). Pulsed PECVD has been developed as an alternative to atomic layer deposition (ALD) to deliver self-limiting growth of oxides like alumina and silica. Pulsed PECVD has two growth components that act sequentially: ALD-like growth during the plasma off step ($\gamma \sim 0$); and PVD-like growth during the plasma on step ($\gamma \sim 1$), where γ is the reactive sticking probability. The ALD contribution is constant at $\sim 1 \text{ \AA/pulse}$ whereas the PECVD contribution can be typically varied from 0.5 - 5 \AA/pulse by appropriate control of operating conditions. The degree of conformality in pulsed PECVD can be engineered by controlling the relative contribution of these 2 growth components. As such this technique can produce novel morphologies that are distinct from those produced by conventional deposition processes. We have developed feature scale models to predict the pore closure phenomenon in pulsed PECVD. This model successfully predicts experimentally observed profiles in features such as trenches and cylinders. The model findings will enable us to determine optimal operation conditions for obtaining the desired nanopore opening and geometry. Flux experiments on nanopore-based membranes are further employed to validate the feature scale models. Such well-defined nanopores can serve as an ideal platform for rigorous evaluation of hindered transport at the nanoscale.

11:40am **PS+AS+NS+SS-ThM12 Microplasma Reduction of Metal-Organic and Metal-Polymer Films for Single-Step Fabrication of Flexible, Conductive Patterns**, S. Ghosh, R. Yang, C.A. Zorman, P. X.-L. Feng, R.M. Sankaran, Case Western Reserve University

In situ approaches to synthesizing metal nanoparticles from metal-organic or metal-polymer films have recently emerged as a simple and viable method to fabricating flexible, conductive patterns.^{1,2} In general, a metal precursor is mixed or reacted with an organic or monomer, cast as a film, and exposed to ultraviolet, laser, heat, or electron beam (e-beam). Recently, we have demonstrated that an atmospheric-pressure microplasma can be similarly used to initiate reduction of metal ions and formation of metal nanoparticles in polymer films.³ In this study, we present electrical characterization of the reduced lines and show that conductive patterns are achieved similar to other methods including e-beam irradiation.

Polymer films containing ionic metal precursors were prepared by first dissolving metal salts [e.g., silver nitrate (AgNO_3), palladium acetate ($\text{Pd}(\text{OAc})_2$] with polymers [e.g., polyvinyl alcohol (PVA), polymethylmethacrylate (PMMA)] in solution. The solvent was chosen according to the metal salt-polymer system. For AgNO_3 and PVA, we used a 1:1 ratio of water:ethanol, and for $\text{Pd}(\text{OAc})_2$ and PMMA, acetonitrile was used. The mixed metal-organic solutions were drop cast or spin coated onto Si substrates to form thin films (100nm–1 μm thick). The films were dried in vacuum and then exposed to the microplasma process. An Ar microplasma was formed by applying DC power to a stainless steel capillary tube and the substrate holder. Patterns were generated by scanning the microplasma at constant discharge current. After exposure, the films were peeled off from the substrate and transferred to a glass substrate. The conductivity was measured using a two point probe method. The as-prepared films were also characterized by scanning electron microscopy (SEM) and energy-dispersive spectroscopy (EDX) to confirm metallization (*i.e.*, reduction) over the exposed areas.

Our results show that plasma exposure leads to conductive patterns on a free-standing flexible substrate. SEM and EDX confirm the reduction of metal ions to metal nanoparticles. We have also compared these results with exposure to an e-beam. In the case of the plasma, the polymer is removed, probably due to oxidation, whereas the e-beam causes conformational changes to the polymer. The effects of annealing following exposure to increase the conductivity of the films will also be discussed.

References:

1. B. Radha et al., J. Am. Chem. Soc. 133, 12706–12713 (2011).
2. S. W. Lee et al., Adv. Funct. Mater. 21, 2155–2161 (2011).
3. S. W. Lee et al., Macromolecules 45, 8201–8210 (2012).

Plasma Science and Technology Room: 104 C - Session PS-ThM

Plasma Modeling

Moderator: D.J. Economou, University of Houston

8:00am **PS-ThM1 Molecular Dynamics Analysis of Si Etching in HBr-based Plasmas: Ion Incident Energy and Angle Dependence**, N. Nakazaki, Y. Takao, K. Eriguchi, K. Ono, Kyoto University, Japan

Profile anomalies and surface roughness are now critical issues to be resolved in the plasma etching of nanometer-scale microelectronics devices, which in turn requires a better understanding of the effects of the ion incident energy and angle on surface reaction kinetics. For example, the line edge and line width roughness on feature sidewalls and the roughness on bottom surfaces of the feature are assumed to be caused by the angular distribution of incident ions onto feature surfaces. In addition, incident neutral radicals also affect the surface reaction kinetics and thus etching characteristics achieved. This paper presents a classical molecular dynamics (MD) simulation of Si etching in HBr-based plasmas with different ion incident energies and angles, by using an improved Stillinger-Weber interatomic potential model for Si/H/Br system interactions. Emphasis is placed on the surface structure and the yield and stoichiometry of products depending on the ion incident energy, angle, and neutral radical-to-ion flux ratio.

In the MD simulation, a target substrate Si(100) was placed in the simulation cell, which was a square 32.58 \AA on a side and initially contained 1440 Si atoms ($6.78 \times 10^{14} \text{ atom/cm}^2$) in a depth of 26 \AA . Energetic ions and low-energy neutral radicals were injected toward the surface from randomly selected horizontal locations above the target. We assumed that the plasma of interest consisted of HBr^+ ions and H and Br neutrals. The ion incident energy was in the range $E_i = 20\text{--}300 \text{ eV}$ and the incident angle was in the range $\theta_i = 0\text{--}90^\circ$. The neutral radical-to-ion flux ratio was $\Gamma_n/\Gamma_i = 0$ and 100. In addition, we sometimes added a layer of Si atoms at the bottom of the simulation cell, to maintain the number of target atoms during etching. The yield and stoichiometry of products, and the surface structures were analyzed by averaging more than 1000 impacts after the surface and etching characteristics had become statistically stable.

Numerical results indicated that the thickness of the surface reaction layer (SiH_xBr_y layer) decreases with increasing θ_i , because of decreased penetration depth of incident ions at large θ_i , which is less significant for $\Gamma_n/\Gamma_i = 100$ than for $\Gamma_n/\Gamma_i = 0$ at each E_i incidence, owing to increased desorption of reaction products therefrom at increased Γ_n/Γ_i as a result of enhanced etching reactions. Moreover, the Si yield is larger for $\Gamma_n/\Gamma_i = 100$ than for $\Gamma_n/\Gamma_i = 0$, and correspondingly, the amount of volatile etch products containing H atoms is larger for $\Gamma_n/\Gamma_i = 100$ than for $\Gamma_n/\Gamma_i = 0$.

8:20am **PS-ThM2 MD Simulations of Pulsed Chlorine Plasmas Interaction with Ultrathin Silicon Films for Advanced Etch Processes**, P.D. Brichon, E. Despiiau-Pujo, G. Cunge, M. Darnon, O. Joubert, Cnrs/ujf/ Cea - Lim, France

Due to high ion bombardment energies and significant fragmentation rates, conventional continuous-wave plasma processes are not able to selectively etch ultrathin films without damaging the active layers of advanced nanoelectronic devices (e.g. FDSOs, FinFETs). In order to achieve a uniform/smooth etching of sub-nm thick materials, one possible alternative is to use pulsed-plasma discharges which exhibit lower average ion energies, thus minimizing surface damage when necessary. Pulsing the plasma consists in switching on and off the RF power, which introduces two additional parameters, the pulsation frequency and the duty cycle, *i.e.* the ratio between the pulse on-time and the total pulse duration. This latter has been shown to control the dissociation rate of the plasma *i.e.* the proportion of atomic species (Cl , Cl^+) relative to that of molecular species (Cl_2 , Cl_2^+). However, the interactions between reactive pulsed plasmas and surfaces are so complex that the efficient development of new processes requires numerical simulations. Therefore, we propose to develop Molecular Dynamics (MD) simulations to study the silicon-chlorine system under pulsed plasma conditions. These simulations can help to understand the precise role of the ion energy in plasma-surface interactions, as well as the relationship between the flux/energy of reactive species (ions, radicals) bombarding the surface and its structural/chemical modifications. To understand the impact of the dissociation rate in pulsed plasma processes, we first compare the effects of atomic (Cl , Cl^+) versus molecular species (Cl_2 , Cl_2^+) bombardment on the silicon substrate. All simulations show an initial rapid chlorination of the surface followed by the formation of a stable SiCl_x mixed layer and a constant etch yield at steady state. Regarding the role of the ion energy, it appears that for most etch features (chlorine uptake, SiCl_x layer thickness, nature of etch products), bombarding the surface with X eV Cl^+ is equivalent to bombarding it with $2X \text{ eV Cl}_2^+$. This

mathematical relation does not hold for the etch rate, which is larger for atomic bombardment (Cl^+) at low energy (5-10eV) but more important for molecular bombardment (Cl_2^+) at high energy (50-100eV). Comparisons with experiments and mechanisms responsible for these behaviors will be discussed during the presentation. The influence of both the ion-to-radical flux ratio and the duty cycle on the dynamics/characteristics of the etch (yield, products) and on the surface evolution (structure, chemical composition) will also be presented.

8:40am **PS-ThM3 Control of SiO_2 Etch Properties by Pulsed Capacitively Coupled Plasmas Sustained in $\text{Ar}/\text{CF}_4/\text{O}_2$.** *S.-H. Song, M.J. Kushner*, University of Michigan

In the fabrication of microelectronics devices, the performance and quality of the devices are ultimately determined by the energy distribution of charged particles and radicals in the plasma. High aspect ratio dielectric etching in microelectronics fabrication using dual frequency capacitively coupled plasmas (DF-CCPs) continues to be challenged to optimize the fluxes and energy distributions of radicals and ions to the wafer. Pulsed power is one technique being investigated to achieve these goals. In one configuration of DF-CCP, the high frequency (HF) power is applied to the upper electrode and low frequency (LF) power is applied to the lower electrode serving as the substrate which is serially connected through a blocking capacitor generating self dc bias. In this presentation, ion energy distributions, fluxes to the wafer, and SiO_2 etch properties in a pulsed DF-CCP sustained in $\text{Ar}/\text{CF}_4/\text{O}_2$ are discussed with results from 2-dimensional plasma hydrodynamics and feature profile models. The ion energy distribution (IED) can be uniquely manipulated by either pulsing the LF or HF power for a given size of the blocking capacitor (BC). During the pulse, the dc-bias can have a time variation – small BC produces more time variation than large BC. This time variation in the dc bias provides an additional control mechanism for the IED. In this paper we report on a computational study of IEDs and SiO_2 etch profiles in DF-CCPs. To investigate this coupling we applied a pulsed format for HF and LF power with different duty cycles and blocking capacitances. We found that high energy ions are dominant when pulsing HF power and low energy ions are dominant when pulsing LF power. Smaller BC generally broadens the IED. We also found that the ratio of F/CF_x ($x = 1 - 3$) fluxes increases by pulsing either the HF or LF however the effect is more sensitive to pulsing HF power. Control of etch profiles will be demonstrated by combinations of pulsing HF and LF power, and BC. For example, bowing and undercut may occur when pulsing HF while these effects are suppressed by pulsing LF. The propensity for twisting is less when pulsing LF.

* Work supported by the Department of Energy Office of Fusion Energy Sciences, the Semiconductor Research Corp. and National Science Foundation.

9:00am **PS-ThM4 Accuracy of the Step Sheath Approximation.** *M.A. Soblewski*, NIST

In modeling plasma sheaths, it is useful to approximate the electron density profile by a sharp, step-like drop between a neutral (or quasineutral) region and an electron-free region. This approximation allows rapid and efficient numerical calculations of sheath properties, and, when combined with other assumptions, allows predictions for sheath properties to be calculated analytically. Nevertheless, the approximation must result in some loss of accuracy. Here, the accuracy of the step approximation was investigated by comparisons with exact solutions for Poisson's equation in the sheath and with experimental measurements of current and voltage waveforms and ion energy distributions. The measurements were performed in pure argon gas and argon mixtures in a radio-frequency (rf) biased, inductively coupled plasma reactor. Experimental conditions were chosen to cover the intermediate-frequency regime, where the rf period is comparable to ion transit times and the ion current oscillates strongly during the rf cycle. In general, the errors introduced by the step approximation were small but not negligible. The displacement current and time-dependent ion current were both affected by the step approximation, resulting in errors that are more apparent in the phase of the sheath impedance than in its magnitude. The effects on ion energy distributions are most noticeable in the amplitude of the low-energy peak, which is sensitive to the choice of boundary conditions on the plasma side of the step. Using the exact Poisson solution in place of the step approximation results in a modest improvement in the agreement with experiment.

9:20am **PS-ThM5 Multi-dimensional Modeling of Industrial Plasma Processing Systems.** *S. Rauf, J. Kenney, A. Agarwal, A. Balakrishna, M.-F. Wu, K. Collins*, Applied Materials Inc.

INVITED

Plasma processing is widely used in the semiconductor industry for thin film etching and deposition, modification of near-surface material, and cleaning. Several factors have made plasma modeling critical for plasma processing system design in recent years including the necessity to generate

uniform plasmas over large substrates while fabricating sub-20 nm devices, increased plasma system cost and complexity, and reduced development time-scales. Using examples from recent design and analysis work, this paper describes the current status of multi-dimensional plasma modeling in the semiconductor industry. Areas warranting further research are also discussed. Most industrial design work is done using fluid plasma models due to their maturity, robustness, and computational speed relative to other techniques. Hybrid codes with Monte Carlo simulation of kinetic phenomena (e.g., secondary and beam electrons) are also utilized. Several examples of the use of these fluid plasma models to industrial hardware and process design are discussed, including analysis of the effect of azimuthally asymmetric components on plasma non-uniformity in capacitively coupled plasmas (CCP), the effect of magnetic field on plasma non-uniformity in magnetized CCPs, and the dynamics of synchronously pulsed inductively coupled plasmas. With growing use of very high frequency radio-frequency sources and increasing plasma dimensions, electromagnetic effects have become pronounced in plasmas. A related issue is modeling of the strong influence of the distributed external electromagnetic circuit (e.g., transmission line, antenna feed) on the plasma and its spatial structure. Computational techniques that are used to treat electromagnetic effects in multi-dimensional plasma models along with examples are discussed. Many plasma processes use pressures < 1 Pa. At these low pressures, fluid assumptions break down and kinetic effects become important. An important unsolved problem is how to model these low pressure plasmas accurately in fluid plasma models. Fully kinetic models are more accurate, but their computational cost and lack of robustness remain an issue. Initial efforts at improving fluid plasma models through comparison with particle-in-cell modeling results and experiments are described.

10:40am **PS-ThM9 Self-Consistent Simulations of the Radial Line Slot Antenna Plasma Source.** *P. Ventzek*, Tokyo Electron America, *R. Upadhyay*, Esgee Technologies Inc., *M. Aita, J. Yoshikawa, T. Iwao, K. Ishibashi*, Tokyo Electron Ltd., *L. Raja*, University of Texas at Austin

The radial line slot antenna plasma source couples microwave power through a slot antenna structure and window to a plasma characterized by a generation zone adjacent to the window and a diffusion zone that contacts a substrate. The diffusion zone is characterized by a very low electron temperature. This property renders the source useful for soft etch applications and thin film processing for which low ion energy is desirable. Frequently simulations of the source employ a quasi-neutral plasma model. These are unable to represent the impact of an rf bias applied to a substrate. Furthermore the presence of a time-varying biased potential impacts the transport of charged particles from the zone in which they are created through the diffusion zone to the wafer. At some pressures and powers secondary plasmas may be created. In this presentation we report self-consistent simulations of the source employing a drift-diffusion approximation or variants of this approximation. A test particle Monte Carlo simulation will be used to illustrate the evolution of the electron energy distribution function at different locations in the source. We relate the test particle experiments to electron energy distribution functions derived from solutions of the Boltzmann Equation.

11:20am **PS-ThM11 Feature Profile Simulator with Atomic Mono-Layer Resolution Capability.** *P. Moroz*, Tokyo Electron US Holdings

Theoretical and experimental understanding of plasma interactions with solid materials has led to development of 2D and 3D feature profile simulators. Different approaches have been used for over 40 past years for that. Our simulator, FPS3D [1-2], is a general code which uses a cellular model for representing solid materials and uses Monte Carlo pseudo-particles for representing all incoming fluxes of reactive species. Those particles are launched such that statistically they represent the angle-energy distribution of fluxes coming to the wafer from the plasma. Each particle typically contains many molecules, but preferentially significantly less than the number of molecules in a full cell. FPS3D is very different in many ways from other feature profile simulators, most importantly in the way how it represents gaseous and solid materials and how it represents interactions of reactive gaseous species with solids. The algorithms applied enable simulation of very large span of models ranging from large features of hundreds of microns to very small ones of a few nanometers where a cell size is approaching to the size of a single molecule. Regimes with application of beams, plasmas, or just reactive gases could be conveniently simulated. Interaction with solids is described very differently for low-energy and high-energy particles. While the low-energy gaseous species interact only with the surface layers of the cells, the energetic particles such as ions or fast neutrals could penetrate into the body of the cells, and could even go through the cells. The finite penetration depth of a fast particle into a solid material is a key factor dictating the regime of interaction. When an energetic particle moves through a cell, it loses energy there on collisions and bond breaking between atoms. The energetic particle finally stops and implants in a solid material. The deposited energy might be enough for

some molecules to diffuse to other cells or go through upper layers. This way, etching through polymer layers could be simulated. Correspondingly, FPS3D can simulate etching, deposition, and implantation processes going on at the same time. Also among new developments to be presented is the capability of considering multi-step (or multi-recipe) processes, when each step could have different fluxes to the surface and different chemistry. Another new development in FPS3D is a possibility of simulating pulsed-plasma effects. Examples are mainly based on a case of HARC etching of SiO₂ by the fluorocarbon-argon-oxygen plasma.

[1] P. Moroz, ECS Transactions, 35 (20) 25 (2011).

[2] P. Moroz, IEEE Transactions of Plasma Science, 39 (11) 2804 (2011).

11:40am **PS-ThM12 Feature Profile Evolution in Plasma Processing using On-Wafer Monitoring System**, *T. Kubota*, Tohoku University, Japan, *M. Sato*, Harada Corporation, Japan, *T. Iwasaki*, Mizuro Information & Research Institute, Inc., Japan, *K. Ono*, Mizuho Information & Research Institute, Inc., Japan, *S. Samukawa*, Tohoku University, Japan

Plasma etching is widely used for the fabrication of semiconductor devices and MEMS. However, irradiation damage and etching profile anomalies are severe problems for the plasma processes. We are developing a system to predict the etching profile and plasma irradiation damage by using a combination of the process monitoring on the sample stage of the plasma chamber (on-wafer monitoring) and a computer simulation, and are promoting the commercialization of this system [1]. We have already developed a sensor to measure the differential charge-up between the top and bottom of the high-aspect-ratio hole structure (on-wafer charge-up sensor) and have presented a concept of the charge-up simulation [2]. Here, we developed a calculation based on the on-wafer charge-up sensor measurement that enables for the fusion of the measurement and simulation.

The calculation was performed in two steps. First, a calculation is conducted to determine the situation in the sensor. Here, we developed a calculation to obtain the incidence condition of the ions and electrons from the measured value of the charge-up voltage. A high-speed algorithm (ICCG method) is used to obtain the electric field distribution because the calculation needs iteration to converge the charge-up voltage into the measured value. Second, subsequent calculations are conducted to obtain the charge-up voltage and ion trajectory of an arbitrary etching profile using the ion/electron incident condition obtained from the first calculation.

An on-wafer charge-up sensor with an aspect ratio of 10 was used for the plasma measurement. Then, the calculation was performed. As a result, it was predicted that etching is possible up to aspect ratio of 30, but the etching profile would be anomalous if the aspect ratio is more than 20.

This indicates that the etching profile of an arbitrary structure can be predicted based on a measurement and computer simulation.

[1] <http://www.mizuho-ir.co.jp/solution/research/semiconductor/fabmeister/onwafer/index.html> (in Japanese)

[2] H. Ohtake et al., Jpn. J. Appl. Phys. 49, 04DB14 (2010), B. Jinnai et al., J. Appl. Phys. 107, 043302 (2010)

Advanced Surface Engineering

Room: 203 C - Session SE+PS-ThM

Pulsed Plasmas in Surface Engineering (8:00-10:00 am)/Atmospheric Pressure Plasmas (10:40 am-12:00 pm)

Moderator: H. Barankova, Uppsala University, Sweden, J.

Klemberg-Sapieha, Ecole Polytechnique de Montreal, Canada

8:00am **SE+PS-ThM1 A 60 Year Perspective on Developments in Plasma Assisted PVD Processes for Enhanced Surface Engineered Performance**, *A. Matthews*, University of Sheffield, UK **INVITED**

Over the past 60 years there have been many developments in PVD technology which have contributed to the successful emergence of the technological discipline which we now know as Surface Engineering. There now exist many products which could not even function without these developments, and other products whose performance so far-exceeds what was previously possible that they can offer improvements in measures such as productivity which are many hundreds (if not thousands) of times better than previously achievable. We can see these benefits in all major industrial sectors, especially aerospace, automotive, energy and healthcare. This paper highlights how these product enhancements have been achieved through a combination of plasma process developments and materials systems developments. The plasma processes have included ionisation enhancing

systems such as thermionic assistance, magnetic confinement and pulsed-plasmas, and the materials developments have included multi-layered and nanocomposite combinations of phases which have allowed the creation of surfaces with mechanical and chemical properties which were previously unachievable. We can now even create "duplex" engineered surfaces which combine plasma assisted diffusion treatments with optimised coatings, which allow the use of substrate materials (such as titanium and aluminium alloys) which were previously considered unsuitable for heavily-loaded tribological contacts in arduous conditions. The progress in process and performance enhancements is charted with examples from each decade over the past 60 years.

8:40am **SE+PS-ThM3 Optimized Magnetic Field Configuration for High Power Impulse Magnetron Sputtering**, *P. Raman*, *L. Meng*, *H. Yu*, *D.N. Ruzic*, University of Illinois at Urbana Champaign, *M. Schilling*, Dexter Magnetic Technologies, Inc, *S. Armstrong*, Kurt J. Lesker Company

Magnetic field design is critical in magnetron sputtering systems as it affects the plasma parameters and film quality. Most magnetic field configurations are designed for DC sputtering and they suffer from low target utilization, non-uniform ionized metal atoms, etc. High Power Pulsed Magnetron Sputtering (HIPIMS) discharge has high degree of ionization of the sputtered material with very high peak power on the target [1]. Therefore HIPIMS is an ideal candidate for the next generation magnetron sputtering systems. There are no magnetic field configurations that are optimized for HIPIMS discharge. It has been confirmed from our previous work on HIPIMS that a spiral-shaped magnetic field design on 36 cm diameter copper target was able to produce superior plasma uniformity on the substrate in addition to improved target utilization without the need for magnet rotation [2]. Commercial 4 inch sputter cathodes are very popular as they function with a wide variety of target materials and they can be operated with DC, RF and Pulsed-DC power supplies. These 4 inch cathode guns typically have a conventional circular magnetic field design (old). To optimize the magnet field configuration in HIPIMS for the 4 inch cathode gun, the spiral design (new) from the 36mm target was shrunk in size to produce the same magnetic field on the 4 inch target surface. In order to understand the effects of new magnet field configuration, the old and new magnet field configurations were tested in HIPIMS, Z-pulsed and DC power supplies side by side using two 4 inch guns for deposition rate, film density, film uniformity and film stress. Plasmas from each power supply were diagnosed (ne, Te, ionization fraction) for the new and old magnet filed configuration in order to understand the pulsing parameters for better plasma control.

References

1. J. Bohlmark, J. Alami, C. Christou, A. P. Ehiasarian and U. Helmersson, J. Vac. Sci. Technol. A, 23, 18 (2005).

2. He Yu, Liang Meng, Matthew M. Szott, Jake T. McLain, Tae S. Cho and David. N. Ruzic, Investigation and Optimization of Magnetic Field Configuration in High Power Impulse Magnetron Sputtering, Plasma Sources Sci. Technol (Submitted).

9:20am **SE+PS-ThM5 HiPIMS Deposition of Semiconducting ZnO Thin Films**, *A.N. Reed*, *P.J. Shamberger*, Air Force Research Laboratory, Wright Patterson Air Force Base, *C. Muratore*, University of Dayton, *J.E. Bultman*, University of Dayton Research Institute, *A.A. Voevodin*, Air Force Research Laboratory, Wright Patterson Air Force Base

High power impulse magnetron sputtering (HiPIMS) was demonstrated for the first time on semiconducting zinc oxide thin films for use as a transistor channel material. Nanocrystalline ZnO thin film transistors are of interest for integrated RF devices due to their high mobilities ($110 \text{ cm}^2\text{V}^{-1}\text{s}^{-1}$) and high on-off ratios (up to 10^{12}) [1]. These electrical transport properties are critically dependent on film microstructure, defect densities, crystal orientation, surface roughness and grain size. Due to a highly ionized flux, HiPIMS allows for control of thin film microstructure, while simultaneously producing high quality crystalline films on unheated substrates. However the use of HiPIMS for the growth of oxide semiconductors and their resulting electrical transport properties remain largely unexplored.

In this study, we investigate the interrelationship between the plasma characteristics, resulting film microstructure, and the electrical transport properties of nanocrystalline ZnO thin films. HiPIMS was used to deposit thin (~100 nm) ZnO films from ceramic ZnO and metallic Zn targets onto substrates heated to 150 °C. In both non-reactive and reactive cases, the resulting films had stronger crystallinity, more highly aligned (002) texture and lower surface roughness than films grown with pulsed DC sputtering, as determined by XRD, SEM and AFM measurements. The degree of alignment in the films was strongly dependent on the target potential, gas pressure and pulsing parameters. Film I-V characteristics were compared alongside microstructures to correlate electrical transport properties with specific aspects of microstructure (grain size, crystallinity, texture).

Similarly, time-resolved current measurements of the target and ion energy distributions, determined using energy resolved mass spectrometry, were correlated to film microstructure in order to investigate the effect of plasma conditions on film nucleation and growth. Finally, we will compare ZnO films grown by HiPIMS against those grown by other techniques (pulsed DC sputtering, pulsed laser deposition) and will critically evaluate the capability of HiPIMS for the deposition of electronic oxide films.

[1] B. Bayraktaroglu, K. Leedy, R. Neidhard. Microwave ZnO Thin Film Transistors. IEEE Electronic Device Letters V 29 Iss. 9, 1024-1026 2008

9:40am **SE+PS-ThM6 Si₃N₄ Spacers Etching in Synchronized Pulsed CH₃F/O₂/He/SiF₄ Plasmas**, R. Blanc, STMicroelectronics, France, M. Darnon, G. Cunge, O. Joubert, LTM – MINATEC – CEA/Leti, France

Gate spacers are used in submicron metal oxide semiconductor field effect transistor (MOSFET) in order to precisely define the channel length with abrupt junction geometry and eventually to tailor the electrical characteristics of the MOSFET transistors. Therefore, spacer etch process is considered to be one of the most critical processes of CMOS technologies. The Si₃N₄ spacer etching process requires a high etch selectivity to Si so that Si₃N₄ etching can be stopped on the Si surface without silicon substrate consumption in source/drain (S/D) regions of the MOSFET transistor. Silicon loss in S/D regions during spacer etching causes substrate bias dependent leakage and etch induced damage in the silicon surface raises the resistance of ultra-shallow junctions. More recently, the introduction of an ultra-thin Si channel in 28 nm FDSOI technology brought more aggressive requirements in terms of Si consumption. At the same time, plasma etch processes are reaching their limits regarding etch selectivity and profile control at the nanometer scale. In this study, we investigate the combination of synchronized pulsed plasma technologies and the addition of a Si-containing gas, SiF₄, with the objective to improve spacer etch process performance.

The experiments are performed in a 300mm AdvantEdge™ etch tool from Applied Materials. The inductively coupled plasma is sustained by two RF generators (13.56 MHz) to create the plasma and to polarize the wafer, using synchronous pulsing at different frequencies and duty cycles. Moreover, a Theta300 angle resolved XPS system from Thermo Scientific is connected under vacuum, allowing quasi in-situ analysis of etched samples.

In this work, we investigate the effect of SiF₄ addition in a synchronized pulsed CH₃F/O₂/He plasma. In a previous study, we have already shown that high Si₃N₄/Si selectivity is obtained by oxidizing the silicon surface during the landing of the nitride etching process on the silicon surface. When the plasma is pulsed at 1 kHz with a duty cycle of 10%, spacer profiles are improved and the oxidized thickness is significantly reduced but still generates a Silicon recess of 0.5 nm. With 5sccm SiF₄ added to the plasma gas phase, we observe a SiO_x deposition at the Si surface without any Si consumption, showing that the etch stop is obtained by the deposition of a SiO_x layer originated from the plasma gas phase.

10:40am **SE+PS-ThM9 CO₂ Conversion to CO and O₂ by DBD Plasma at Atmospheric Pressure**, G. Arnoult, T. Bierber, A. Ozkan, P. De Keyser, F.A.B. Reniers, Université Libre de Bruxelles, Belgium

Because of its high thermodynamical stability, carbon dioxide is usually considered as a waste, unavoidable end-product of many industrial processes. It is therefore necessary to develop technologies able to reuse it. In this objective, dry reforming of carbon dioxide by plasma has attracted significant interest to generate carbon monoxide which has an interesting energetic value^{[1],[2]}.

We present here a study of the plasma assisted conversion of CO₂ into CO and O₂ in a Dielectric Barrier Discharge plasma device operating at atmospheric pressure. We focus on determining the influence of several parameters on the conversion efficiency: the input power, the flow rate and finally the use or not of an additional plasmagen gas (argon or helium) in the mixture. Gas chromatography and mass spectrometry at atmospheric pressure are used to determine the composition of the gas after plasma treatment. Conversion rates for CO₂ can then be extracted.

The conversion rate increases with the power, suggesting an effect of the electron density (Fig.1 and Fig.2). On the other hand, the conversion rate drops with increasing flow rate from 0.1 L/min to 10 L/min. Indeed since the flow rate is inversely proportional to the residence time of the gas in the reactor, increasing it means that the gas spends less time in the plasma. Furthermore the addition of a plasmagen gas increases the conversion rate.

Optical emission spectroscopy and electrical measurements are also performed in order to have a better comprehension of the physical and chemical processes leading to the observed results.

[1] R. Li, Q. Tang, S. Yin, et T. Sato, « Plasma catalysis for CO₂ decomposition by using different dielectric materials », *Fuel Processing Technology*, vol. 87, n° 7, p. 617–622, 2006.

[2] S. Paulussen, B. Verheyde, X. Tu, C. De Bie, T. Martens, D. Petrovic, A. Bogaerts, et B. Sels, « Conversion of carbon dioxide to value-added chemicals in atmospheric pressure dielectric barrier discharges », *Plasma Sources Science and Technology*, vol. 19, p. 034015, 2010.

11:00am **SE+PS-ThM10 Cold Atmospheric Plasma Assisted Production of Hydrogen**, L. Bardos, H. Baránková, Uppsala University, Sweden

Experimental study of submerged cold atmospheric plasma generated in water and in water-based mixtures has been carried out. A hermetic stainless steel reactor with an originally designed coaxial plasma source immersed in the tested liquid has been used both with and without additional gas transported into the plasma zone. The reactor has been equipped with a pH meter, conductivity meter, thermometer, a simple pressure gauge, and a quartz fiber optics for optical emission spectroscopy of the submerged plasma. A sensor measuring the hydrogen content has been installed at the outlet of the reactor after rotameter tube measuring the outlet gas flow. The gas outlet has been provided also by a simple jet for gas flammability tests. Several types of the power generators have been tested for ignition and maintenance of the submerged plasma in the water and in water mixtures with ethanol. Preliminary experiments have confirmed production of the hydrogen containing synthesis gas that can be enhanced by adding ethanol admixtures. Very short dc pulses with average power of less than 50 W led to spontaneous formation of gas bubbles and flammable outlet gas with more than 50 % H₂.

11:20am **SE+PS-ThM11 Optical Emission Spectroscopy of He Dielectric Barrier Discharges at Atmospheric-Pressure Applied to the Functionalization of Wood Surfaces**, L. Stafford, R.K. Gangwar, O. Levasseur, Université de Montreal, Canada, N. Gherardi, CNRS-LAPLACE, France, N. Naudé, Université Paul-Sabatier, France

Application of dielectric barrier discharges (DBD) to the modification of “novel” materials such as nanostructured polymers is much more challenging than for conventional substrates such as Si or SiO₂. This can be attributed not only to the highly anisotropic nature of this polymer which can introduce spatial inhomogeneities of the electric field near the substrate surface, but also to its highly porous microstructure which can release impurities either from plasma-substrate chemical reactions or from sample outgassing. In this work, a porous wood sample (sugar maple, acer saccharum) was placed on the bottom electrode of a DBD operated in nominally pure helium to examine the influence of plasma-wood interactions and substrate outgassing on the evolution of the plasma properties. Optical emission spectroscopy revealed strong emission from N₂, N₂⁺, O and OH impurities. While the nitrogen and oxygen emission can be attributed to air outgassing, the OH emission was ascribed to etching of the weak boundary layer and humidity desorption from wood. We have calculated various line ratios from the time-resolved optical emission spectra. The He-588 nm-to-He-707 nm line ratio, I_{588/707}, was found to decrease from when going from right after ignition of the first few discharges where substrate outgassing is important to longer treatment times where “pumping” of the wood samples is nearly complete. Assuming that the He 3D and 3S levels (L•S coupling) giving rise to the emission at 588 and 707 nm are populated by stepwise excitation through the most populated metastable He 3S1 level and are lost by spontaneous emission, the I_{588/707} line ratio becomes link to the ratio of the rate for stepwise excitation of the He 3D and 3S levels, which is only a function of the electron temperature T_e. Accounting for collisional energy transfer reactions between the He 3D, 3P, and 3S states in atmospheric-pressure plasmas and using the set of cross sections reported in literature for stepwise excitation, energy transfer reactions, and collisional quenching, it was found that the observed decrease of I_{588/707} can be ascribed to a decrease of the electron temperature. Further analysis of the time evolution of the emission spectra and of the current-voltage characteristics indicated that the release of products from the wood substrate also yields to a significant quenching of He metastables. This method was further used to examine the detailed influence of hexamethyldisiloxane (HMDSO) and titanium isopropoxide (TTIP) injection on the plasma characteristics during plasma enhanced chemical vapor deposition of functional, nanostructured coatings on wood.

11:40am **SE+PS-ThM12 Substitution of ThO₂ by La₂O₃ for Tungsten Electrodes used in Atmospheric Plasma Spraying**, M. Heissl, C. Mitterer, Montanuniversitaet Leoben, Austria, T. Granzer, T. Schroeder, M. Kathrein, PLANSEE Composite Materials GmbH, Germany

ThO₂ additions are commonly used in tungsten-based electrodes for plasma spraying due to the excellent electron emissivity, improved arcing behavior, higher strength, and better machinability. Because of their radioactive potential, which makes handling, use, recycling, and disposal more difficult, alternative additives are required that provide the same advantages as thoriated tungsten, but without environmental hazards. Within this work,

tungsten cathodes with 2 wt.% ThO₂ and 1 wt.% La₂O₃ were compared with respect to their arc ignition behavior, plasma stability and arc erosion. Both, cyclic and continuous plasma spraying experiments were carried out. In addition, structure and mechanical properties of Al₂O₃ coatings sprayed on Mo substrates were evaluated. La₂O₃ is characterized by a similar plasma ignition and operation behavior as well as a comparable coating quality with respect to ThO₂ additions. Further, La₂O₃ additions caused a reduced degradation of the cathode material, which is attributed to the lower cathode temperature, giving rise to an expected longer lifetime.

Scanning Probe Microscopy Focus Topic

Room: 202 C - Session SP+AS+BI+MI+NS+SS-ThM

Advances in Scanning Probe Imaging

Moderator: S. Allen, The University of Nottingham, UK,
A.P. Li, Oak Ridge National Laboratory

8:00am **SP+AS+BI+MI+NS+SS-ThM1 Inelastic Imaging of Single Molecule Dynamics**, *W. Ho*, University of California, Irvine **INVITED**

A greater part of chemistry is designed to probe the encounter of reactants to form products through a sequence of reaction steps that involve reaction complexes as intermediates. The detection of these complexes is an important step to reveal the reaction mechanisms and advance our understanding and control of chemistry. While sophisticated spectroscopic techniques have been developed to provide properties of the complexes in the energetic and temporal domains, much less is known about the spatial properties. Advances made over the last 15 years in scanning tunneling microscopy (STM) have led to direct characterization and imaging of reaction complexes that are formed by controlled manipulation of the reacting molecules to separate from each other at distances from non-interaction to those approaching the transition state. Changes in their vibrational properties can be monitored as a function of the spatial separation by inelastic electron tunneling spectroscopy (IETS) with the STM. Both spectroscopic information (vibrational energies, intensities, and lineshapes) and inelastic images can be obtained by STM-IETS. These results provide sub-THz spectral characterization and spatial visualization of chemical reactions with sub-Angstrom spatial resolution.

8:40am **SP+AS+BI+MI+NS+SS-ThM3 Tunneling Resonances Into Engineered Nanoscale Cavities on a Noble Metal Surface**, *A. DiLullo, D. Acharya*, Ohio University, *N. Takeuchi*, Universidad Nacional Autónoma de México, *S.-W. Hla*, Ohio University

Variations in surface topologies such as step edges and surface defects are known to alter the electrochemical properties of the surfaces. The ability to directly alter surface topologies on the nanoscale in order to achieve desired properties is useful. We report on the direct modification of local surface topologies and the resulting changes in local electronic properties. Surface vacancies on a Ag(111) surface are created by probe manipulations using a scanning tunneling microscope operated at 78 K. Tunneling resonances, found at certain probe-sample biases, are determined by analysis of spatial height-differential mapping (dz/dV). The resonances, when considered over paths crossing the induced surface vacancies, significantly shift when comparing clean terraces to vacancy positions. These resonances originate as a result of field emission where the emitted electron has greater energy than the surface potential (work function) at the probe lateral position. By fitting these resonances to the Gundlach equation describing resonant tunneling it is possible to extract the tip work function, sample work function at probe position, and absolute tip height from the sample. The shift in resonances at vacancy locations is related to the variation in the work function due to local topology. It is important to be able to tune the work function as it plays a large role in many surface processes and properties. The created surface vacancies may then be considered local wells having work functions differing from the supporting substrate, with resonances tunable by probe manipulations, and may be useful for nanotechnological applications.

9:00am **SP+AS+BI+MI+NS+SS-ThM4 Real-space Spectroscopy and Microscopy of Tunneling Electron Induced Light Emission from Single Gold Nanoclusters**, *S.W. Li, A.X. Yu, G. Czap, W. Ho*, University of California, Irvine

Historically, gold has been treasured for its beauty and permanence. In the quantum regime, gold nanoclusters gain even more reputation from their unique power as photocatalysts. To better understand the optical properties of nanoclusters, we investigated Scanning Tunneling Spectroscopy and tunneling electron induced light emission of single Au nanoclusters deposited on Al₂O₃ / NiAl(110) surface. In this electron-in-light-out

experiment, optical phenomena are probed with sub-Ångström spatial resolution.

9:20am **SP+AS+BI+MI+NS+SS-ThM5 Spatial Mapping of Surface Plasmons in Nanoscale Ag Islands on Graphite using Scanning Probe Energy Loss Spectroscopy**, *K. Bauer, S. Murphy, L. Tang, R.E. Palmer*, University of Birmingham, UK

A scanning STM tip operated at high voltage can be used to obtain localized spectroscopic information from surfaces via energy loss measurements [1]. In this technique, known as Scanning Probe Energy Loss Spectroscopy (SPELS), the STM tip is used as a localized source of field-emitted electrons, which, upon backscattering from a surface, are analyzed by an energy-dispersive detector to obtain localized energy loss spectra. Characteristic surface excitations such as plasmons and excitons (as well as secondary electrons) can be probed with a spatial resolution below 50 nm and an energy resolution approaching 0.3 eV [2].

We report the development of a new generation SPELS instrument utilizing a 400-channel electron detector. This allows sufficiently fast sampling of the energy loss spectra to obtain 2D spatially-resolved maps of energy loss features in a reasonable timeframe. We demonstrate the new instrument by mapping plasmons in (thermally evaporated) Ag nano-islands on the surface of graphite and illustrate the various mechanisms give rise to the contrast obtained in the energy-resolved maps.

[1] A. Pulisciano, S.J. Park and R. E. Palmer, Appl. Phys. Lett. 93, 213109 (2008).

[2] F. Festy and R. E. Palmer, Appl. Phys. Lett. 85, 5034 (2004).

9:40am **SP+AS+BI+MI+NS+SS-ThM6 Development of a Synchrotron X-Ray Assisted STM**, *H. Kersell, S.-W. Hla*, Ohio University, *N. Shirato, V. Rose*, Argonne National Laboratory

Scanning tunneling microscopy (STM) yields substantial information about surface properties of conductive materials by probing the electronic properties of samples under investigation. However, the nature of STM's reliance on the sample density of electronic states often limits the elemental contrast of resulting images. By targeting samples with high energy X-rays, such as those generated by a synchrotron light source, core level electrons may be excited and subsequently measured as a contribution to the tunneling current in STM. Since core level energies are chemically specific, this technique can be used to gain elemental sensitivity in STM imaging, providing enhanced understanding of molecule-substrate and intermolecular interactions. We present the development of a synchrotron-assisted STM (SXSTM), for this purpose.

10:40am **SP+AS+BI+MI+NS+SS-ThM9 High-Speed AFM Studies of Cell Membrane Dynamics**, *A. Slade, S.C. Minne*, Bruker Nano Inc.

Bacterial membranes have a much more complex structure than mammalian cell membranes. As such, knowledge of bacterial membrane composition and organization, as well as characterization of the molecular-level responses to drug interactions, is critical to the development and assessment of effective antibacterial drug formulations. Cellular drug responses involve highly dynamic processes. However, the ability to image live cells with nanometer resolution on timescales relevant to dynamic cellular events has proven challenging. With traditional AFM systems, the typically longer image acquisition times required to obtain a single high-resolution image (~minutes) has limited the ability to investigate dynamic biological processes. While recent years have shown significant progress in the development of high-speed atomic force microscopy (HS-AFM), the nature of the instrumentation that has been developed has several drawbacks in specimen size, requiring small scan sizes and flat sample surfaces. As such, the majority of biologically-related HS-AFM studies have concentrated on imaging single biomolecules with little focus on using HS-AFM to examine cellular processes. With the rapidly growing antibiotics crisis, antimicrobial peptides (AmP) are increasingly being investigated as therapeutic alternatives. Key to their success is an understanding of the mechanisms by which AmPs interact with the cell membrane and facilitate cellular death. Using HS-AFM, we have obtained the first high-resolution time sequence images of the native structure of a bacterial outer membrane, obtained directly on the surface of live *Escherichia coli* cells. The increased time resolution of HS-AFM allowed us to observe dynamic changes in the nanoscale structure of the outer membrane in direct response to the AmP CM15, at timescales relevant to the mechanism of AmP-induced cell death. To understand how CM15 interacts with the bacterial inner membrane, we also conducted HS-AFM imaging on supported model membranes that mimic the composition of the inner membrane of *E. coli*. Our results revealed the formation of circular, pore-like defects within specific lipid domains upon exposure to the AmP. The results of these HS-AFM studies have provided the first opportunity to resolve the dynamics of AmP-mediated cell death in a native cell membrane environment in real-time and with nanoscale resolution.

11:00am **SP+AS+BI+MI+NS+SS-ThM10 Photothermal Excitation for Reliable and Quantitative AFM**, A. Labuda, D. Walters, D. Bocek, M. Rutgers, J. Cleveland, R. Proksch, Asylum Research, an Oxford Instruments Company

Since the advent of atomic force microscopy, cantilevers have predominantly been driven by piezos for AC imaging and data acquisition. The ease of use of the piezo excitation method is responsible for its ubiquity. However, the well-known “forest of peaks”, which is clearly observed while tuning a cantilever in liquids, renders AC imaging in liquids problematic because the peaks move around with time (see Figure). Effectively, these shifting peaks result in a setpoint that changes with time causing stability problems while AFM imaging. Furthermore, the same “forest of peaks” prevents the quantitative interpretation of forces in liquids[1], air[2], and vacuum environments[3], even if the cantilever tune looks clean. Dissipation studies in all these environments have especially suffered due to piezo excitation of the cantilever.

Photothermal excitation is an alternative method for exciting a cantilever by heating/cooling the base of the cantilever to drive the cantilever. Photothermal excitation results in a repeatable, accurate and time-stable cantilever tunes, as seen in the Figure. Therefore, the setpoint remains truly constant while imaging, preventing tip crashes, or unwanted tip retractions. A true atomic resolution image of calcite in water, shown in the inset of the Figure, were made for hours with no user intervention, testifying to the stability of photothermal excitation. Unlike other specialized drive methods, photothermal excitation is compatible with almost any cantilever and with all AFM techniques. The introduction of a blue laser into the AFM also enables several other functionalities, such as tuning the temperature of the cantilever. Furthermore, because the photothermal tune represents the true cantilever transfer function, existing AFM theories can be applied to accurately recover conservative and dissipative forces between the tip and the sample. This is especially important for force spectroscopy, dissipation studies, as well as the frequency modulation AFM techniques.

Our recent developments in perfecting photothermal excitation [4] and its benefits to the AFM community will be discussed in this talk.

- [1] A. Labuda, K. Kobayashi, *et al.* AIP Advances **1**, 022136 (2011)
- [2] R. Proksch and S. V Kalinin, Nanotechnology **21**, 455705 (2010)
- [3] A. Labuda, Y. Miyahara, *et al.* Phys. Rev. B **84**, 125433 (2011)

11:20am **SP+AS+BI+MI+NS+SS-ThM11 Minimally Invasive AFM for Imaging Biomolecules in Liquid**, B.W. Hoogenboom, University College London, UK **INVITED**

Atomic force microscopy (AFM) is a unique tool in combining nanometre spatial resolution and high temporal resolution with the ability to visualise biological molecules in their native environment, i.e., aqueous solution. Its ultimate resolution on such samples depends on the strength of the interaction between the sample and the AFM probe: Too weak an interaction means low contrast, too high an interaction usually results in molecules being distorted or dislodged. I will discuss our recent work on minimising the invasiveness of AFM in liquid, resulting among others in the first observation of the DNA double helix on a single molecule in aqueous solution [Nano Lett. 2012, 12(7), pp. 3846-3850].

Surface Science

Room: 201 A - Session SS+EN-ThM

Photocatalysis and Photochemistry at Surfaces

Moderator: G.A. Kimmel, Pacific Northwest National Laboratory

8:00am **SS+EN-ThM1 Hinderer Influence of Oxygen Vacancies for Photoactivity on TiO₂(110)**, I. Lyubintsky, Z.T. Wang, Pacific Northwest National Laboratory, N.A. Deskins, Worcester Polytechnic Institute, M.A. Henderson, Pacific Northwest National Laboratory

In photoinduced processes, surface point-defects are expected to act as charge trapping and/or recombination centers. However, the direct impact of surface defects on photoreactivity is not well explored. We present the first observation of a suppressing effect of oxygen vacancy (V_O) defects on photoreactivity of TiO₂(110). Direct scanning tunneling microscopy imaging reveal a pronounced site-selectivity in the hole-mediated photooxidation of trimethyl acetate (TMA) on TiO₂(110) upon ultra-violet light irradiation, wherein the reaction readily occurs at regular Ti sites but is completely inhibited at V_O defects. Utilizing electron energy loss spectroscopy and density functional theory, we show that the lack of reactivity of TMA groups adsorbed at V_O 's cannot be attributed to either a less active adsorption conformation or electron transfer from the V_O defect.

Instead, we propose that the excess unpaired electrons associated with the V_O promptly recombine with photoexcited holes approaching the surface, effectively ‘screening’ TMA species at V_O site. We also show that this screening effect is spatially short-ranged, being predominately localized at the V_O , and only mildly affecting TMA's at adjacent Ti sites. The direct impact of O vacancies on TMA photoreactivity over TiO₂(110) is expected to have similar implications for other hole-mediated (e.g., photooxidation) reactions in which adsorption at or near electronic point-defects is possible. Furthermore, the localized influence of these defects on hole-mediated chemistry offers opportunities for additional study of site-selective photocatalysis on TiO₂. The presented results also demonstrate that structure–reactivity relationships, a customary subject in heterogeneous catalysis, are clearly relevant to photocatalysis.

8:20am **SS+EN-ThM2 Anisotropic Photochemical Reactivity of Rutile (110)**, A. Song, D. Jing, M.A. Hines, Cornell University

The surface chemistry of nanocrystalline titanium dioxide has garnered a tremendous amount of attention over the past decade due to a number of high-profile applications, including dye-sensitized solar cells and photoactivated self-cleaning or environmentally-remediating surfaces. Since most surface science investigations study pristine surfaces in ultrahigh vacuum conditions, little is known about the photoreactivity of surfaces in aqueous solutions. In particular, do certain sites on the surface dominate reactivity or are all sites equally reactive? To gain insight into the site specificity (or chemical anisotropy) of the reactions, we have used *ex situ* scanning tunneling microscopy to investigate the reaction of aqueous solutions of H₂O₂ with rutile (110). Contrary to naïve expectation, above band gap radiation appears to suppress certain chemical reactions while also increasing reaction anisotropy. This finding suggests that some sites on the surface are more photoreactive than others. A mechanism that explains this anisotropy will be proposed.

9:20am **SS+EN-ThM5 Energy Transfer and Photostimulated Desorption of Atoms and Molecules Co-adsorbed with Oxygen on TiO₂(110) Surface**, N.G. Petrik, G.A. Kimmel, Pacific Northwest National Laboratory

Titanium dioxide is a widely used photocatalyst. However, fundamental aspects of the photochemistry, including the role of molecular oxygen in photooxidation reactions, are still actively debated. Here, we use weakly bound (i.e. physisorbed) atoms and molecules, such as Ar, Kr, Xe, CO₂ and N₂, to probe the photochemical interactions of O₂ on rutile TiO₂(110). UV irradiation of chemisorbed O₂ along with the physisorbed probe species lead to photon-stimulated desorption (PSD) of the probe species. Without O₂, the PSD yields of the probe species are very low or not observable. However, the Ar, Kr and N₂ PSD yields increase with increasing coverage of chemisorbed O₂. No PSD was observed for CO₂, and the PSD yield for Xe is very low compared to the other probe atoms or molecules. The angular distribution of the photo-desorbing Kr, which is broad and cosine, is quite different from the O₂ PSD angular distribution, which is sharply peaked along the surface normal. We propose a mechanism for the observed phenomena, where the chemisorbed O₂ serve as photoactive centers, excited via electronic excitations (electrons and/or holes) created in the TiO₂ substrate by UV photon irradiation. The photo-excited O₂ may transfer its energy to neighboring co-adsorbed atoms or molecule resulting in their desorption. Simple momentum transfer considerations suggest that heavier adsorbates (like Xe) and adsorbates with higher binding energy (like CO₂) would desorb less efficiently according to the proposed mechanism.

9:40am **SS+EN-ThM6 Adsorption and Photo-induced Decomposition of Formate on Rutile TiO₂ (110)**, A. Mattsson, S. Hu, K. Hermansson, L. Österlund, Uppsala University, Sweden

Adsorption of formic acid on rutile TiO₂ (110) were studied with reflection absorption infrared spectroscopy (RAIRS) in UHV with both s- and p-polarized IR light, incident along either the <001> or <1-10> direction. Experiments were conducted on surfaces prepared with different pre-treatments to obtain stoichiometric (s-TiO₂), oxidized (o-TiO₂) and reduced (r-TiO₂) surfaces. Experiments were compared with density functional theory (DFT) calculations as implemented in the Vienna ab initio simulation package (VASP).

With p-polarized light, transmission and absorption peaks are observed due to the symmetric and asymmetric O-C-O stretch and C-H wagging modes in formate bonded to the Ti-atoms between the bridging oxygen rows in the <001> direction, in agreement with the measurements made by Hayden and co-workers.[1] This orientation of the formate molecule is dominant on for all surface preparations studied here. Employing s-polarized light reveals that the C-H wagging occurs in the plane of the molecule, since it is only seen with s-polarized light incident in the <1-10> direction. In the earlier work by Hayden, weak absorption peaks were observed with p-polarized light incident in the <1-10> direction, and attributed to a minority specie,

oriented perpendicular to the majority specie, and bonded to bridging oxygen vacancies. This interpretation is at variance with our results for s-polarized light, and furthermore an equally weak band is seen regardless of the surface preparation. We attribute this to rapid hydroxylation of the bridging oxygen vacancies in good agreement with recent STM studies, which show that bridging oxygen vacancies become hydroxylated within a few minutes at pressures of 3×10^{-10} mbar.[2] DFT calculations support the above assignments, and in particular show that the minority species inferred from RAIRS is due to formate bonded to OH groups and not to bridging oxygen vacancies. We discuss the implications of our results for the photo-induced decomposition of formic acid on $\text{TiO}_2(110)$.

[1] B.E. Hayden, A. King, M.A. Newton, *Journal of Physical Chemistry B* **103** (1999) 203-208.

[2] S. Wendt, *et. Al. Surf. Science* **598** (2005) 226-245.

10:40am **SS+EN-ThM9 TiO_2 Nanoparticle Arrays Functionalized with Pt Photodeposition: Studies Using X-ray Spectroscopies under *In Situ* Heating and Hydrogen Annealing.** Y. Liu, J. Taing, University of California, Irvine, C.-C. Chen, Argonne National Laboratory, H. Bluhm, Z. Liu, Lawrence Berkeley National Laboratory, M. Veenendaal, Argonne National Laboratory, T. Devereaux, SLAC National Accelerator Laboratory, J.C. Hemminger, University of California, Irvine

Using ambient pressure x-ray spectroscopies, we report the electronic and surface structures of TiO_2 nanoparticle arrays with and without Pt photodeposition under *in-situ* heating and hydrogen annealing. X-ray absorption and transmission electron microscopies indicate that the TiO_2 nanoparticles are in the rutile phase, but the anatase phase also can exist after Pt photodeposition. Valence photoemission results demonstrate a band gap narrowing when Pt is loaded onto the surface of TiO_2 nanoparticles. Upon heating the samples, surface defects and oxygen vacancies are formed, which could prevent the recombination of electron-hole pairs. Heating also enhances the occupation of metallic Pt on top of the TiO_2 . In contrast, introducing hydrogen at high temperature would enhance the Pt^{4+} species related to the strong metal support interaction. The reduced band gap and the increased contact surface in the Pt-photodeposited TiO_2 nanostructures can potentially enhance the performance of these materials in solar absorption and photocatalysis applications.

Reference:

Taing, J.; Cheng, M. H.; Hemminger, J. C., Photodeposition of Ag or Pt onto TiO_2 Nanoparticles Decorated on Step Edges of HOPG. *ACS Nano* **2011**, *5*, 6325-6333.

Liu, Y.; Taing, J.; Chen, C.-C.; Sorini, A. P.; Cheng, M. H.; Margarella, A. M.; Bluhm, H.; Devereaux, T. P.; Hemminger, J. C., Narrowing of Band Gap in Thin Films and Linear Arrays of Ordered TiO_2 Nanoparticles, to be submitted to *ACS Nano*.

11:00am **SS+EN-ThM10 Carrier Dynamics on Oxide Surfaces Studied by Time-resolved Soft X-ray Photoelectron Spectroscopy.** S. Yamamoto, R. Yukawa, The University of Tokyo, Japan, M. Emori, Sophia University, Japan, K. Ozawa, Tokyo Institute of Technology, Japan, M. Ogawa, K. Fujikawa, Sh. Yamamoto, R. Hobaru, I. Matsuda, The University of Tokyo, Japan

Photocatalytic reactions on semiconductor oxide surfaces can be divided into four processes: (i) photon absorption, (ii) electron-hole pair formation, (iii) transport of photo-excited carriers from bulk to surface, and (iv) surface redox reactions. It is important to understand the dynamics of photo-excited carriers in order to make more efficient photocatalysts. Despite of its importance, little is known about transient electronic structures of photo-excited semiconductor surfaces.

Photoelectron spectroscopy (PES) has been successful in providing direct access to electronic structures of materials with surface sensitivity. The extension of PES to time-domain, or time-resolved PES, is now realized by the use of brilliant short pulse (several tens ps) x-ray available at the state-of-the-art synchrotron radiation facilities [1]. This allows us to study transient electronic structures of materials.

In this talk we will introduce the newly developed time-resolved PES system at the high-brilliance soft x-ray beamline BL07LSU at SPring-8 [2]. In the time-resolved PES measurements, the transient electronic structures after optical excitation by fs-laser pump pulses are monitored by ps soft x-ray probe pulses. The time-resolved PES studies on the relaxation of surface photovoltage effect on oxide surfaces such as $\text{SrTiO}_3(001)$ and $\text{ZnO}(0001)$ will be presented.

References

[1] S. Yamamoto, I. Matsuda, *J. Phys. Soc. Jpn.*, **82**, 021003 (2013).

[2] M. Ogawa, S. Yamamoto, Y. Kousa, F. Nakamura, R. Yukawa, A. Fukushima, A. Harasawa, H. Kondoh, Y. Tanaka, A. Kakizaki, I. Matsuda, *Rev. Sci. Instrum.*, **83**, 023109 (2012).

11:20am **SS+EN-ThM11 Atomic Scale Photochemistry with STM.** A.X. Yu, S.W. Li, G. Czup, Y.N. Zhang, H.Y. He, R.Q. Wu, W. Ho, University of California, Irvine

The STM has proven to be an invaluable tool for studying surface chemistry at the atomic and molecular scale, such as bond formation, bond breaking, and photo-catalysis. Here we present STM studies on photon-induced desorption of H_2 molecules from Au (110) surface. Upon laser irradiation, H_2 is found to desorb from Au surface. We attribute the desorption mechanism to excitation of molecular vibrational modes by photon-induced hot electrons. We also study the photo-induced desorption and reaction of CO and O_2 on Al_2O_3 / NiAl (110) surface. We hope to have a better understanding of various mechanisms for photon mediated reactions and effects of plasmon modes in nearby nanoparticles on chemical reactions.

11:40am **SS+EN-ThM12 Atomic Structure and Catalytic Activity of Size-Selected MoS_2 Nanoclusters for Water Splitting.** R.E. Palmer, M. Cuddy, K. Arkill, Z.W. Wang, N.V. Rees, University of Birmingham, UK

The green production of hydrogen by photocatalytic splitting of water molecules requires the catalyst both to absorb solar photons and to supply excited carriers of the correct energy to split water. MoS_2 is a new and abundantly available candidate catalyst material with a layered structure in the bulk; it is believed that quantum confinement in MoS_2 nanoparticles will allow the band gap and energy levels to be tuned to maximize the efficiency of water splitting. Here we report the atomic structure of size-selected nanoparticles (clusters) of MoS_2 , generated by magnetron sputtering of a bulk target and condensation in helium gas, then size selection with a novel lateral time-of-flight mass filter [1] prior to deposition onto carbon supports. X-Ray Photoelectron Spectroscopy (XPS) of cluster ensembles confirms that approximately stoichiometric compound clusters, with average formula $\text{MoS}_{1.95}$, are produced (although we find they are somewhat sensitive to oxygen).

Atomic-scale imaging of the deposited MoS_2 clusters by aberration-corrected Scanning Transmission Electron Microscopy (STEM) [2] of the MoS_2 clusters shows layered nanoparticle structures (as opposed to e.g. fullerene structures), presenting ordered hexagonal arrays of Mo atoms. The cluster growth is remarkably anisotropic, such that as cluster size increases from 150-1000 MoS_2 units (always mass selected) the lateral diameter of the clusters increases but the mean vertical height (2.3 ± 1.0 layers) remains constant. These clusters demonstrate efficient electrocatalytic activity in the hydrogen evolution reaction, probably at edge sites, confirming these new nanosystems as intriguing candidates for water splitting.

[1] S. Pratontep, S. J. Carroll, C. Xirouchaki, M. Streun, and R. E. Palmer, *Review of Scientific Instruments* **76**, 045103 (2005).

[2] Z. W. Wang and R. E. Palmer, *Nano Letters* **12**, 91 (2012).

Surface Science

Room: 202 A - Session SS-ThM

Chirality & Enantioselectivity on Surfaces

Moderator: J. Millunchick, University of Michigan

8:20am **SS-ThM2 Creation of Local Chiral Surface Environments via the Adsorption of Propylene Oxide on achiral Pt(111) Surfaces.** S. Karakalos, F. Zaera, University of California, Riverside

The efficient development of enantiomeric separations has become increasingly important, especially in the pharmaceutical industry, as optical isomers often show different biological behavior, some detrimental to physiological functions. Two-dimensional (2D) molecular surface science aims at understanding molecular recognition, the nature and consequences of intermolecular interactions. The identical alignment of molecules due to adsorption on 2D surfaces, imposes a directionality among lateral interactions. In this study, temperature programmed desorption (TPD), molecular beam (MB) experiments, and Monte Carlo (MC) simulations have been carried out to investigate how propylene oxide (PO), a small chiral molecule, can act as a seed to induce enantioselective adsorption on Pt(111) single-crystal surfaces. TPD results showed that the adsorption of a small initial amount of enantiopure PO on Pt(111) leads to differences in the coverages of a second adsorbate such as enantiopure propylene oxide or propylene (Py), as probed by using a third molecule. Additional studies of isotope exchange on the Pt(111) surface by coadsorbing regular and deuterated PO showed significant replacement of the initially adsorbed PO by the incoming molecules. By using deuterated Py with regular PO, it was also possible to assess the contribution of each molecule on the total coverage on the surface and establish that the induced chirality from the seeding PO plays a crucial role in the final surface coverage. The sticking probabilities of Py, measured by MB experiments on clean Pt(111) and on

various PO/Pt(111) systems, identified differences in the adsorption kinetics indicating that the adsorbed chiral PO can lead to desired enantioselective reactions. Initial Monte Carlo simulations have shown promise in their ability to reproduce these sticking probabilities.

8:40am **SS-ThM3 Enantiospecific Adsorption and Decomposition of Aspartic Acid on Cu(hkl)^{R&S} Surfaces**, *A.J. Gellman, Y. Yun, B.S. Mhatre*, Carnegie Mellon University

One of the key experimental challenges in the study of enantioselective surface chemistry is the development of tools or methods that can distinguish one enantiomer from the other. For two reasons we have identified aspartic acid (HO₂CCH(NH₂)CH₂CO₂H) as an ideal chiral probe for studying enantioselective surface chemistry on naturally chiral Cu single crystal surfaces. Firstly, it exhibits extremely highly enantiospecific surface reaction rates because of the fact that it decomposes by an explosive mechanism with highly non-linear kinetics. Secondly, it is an amino acid and as a consequence we are able to use *L-aspartic acid-1,4-¹³C₂ (*L-Asp) which can be distinguished from D-aspartic acid (D-Asp) using mass spectrometry. These have been studied on the achiral Cu(110) and chiral Cu(3,1,17)^{R&S} surfaces. Decomposition of Asp on the Cu(110) and chiral Cu(3,1,17)^{R&S} surfaces yields CO₂ and CH₃-C¹³N as primary products. Not surprisingly, ¹³C labeling in *L-aspartic acid-1,4-¹³C₂ shows that the ¹³CO₂ comes only from the carboxylate end-groups while labeling of other atoms shows that the CH₃-C¹³N product arises only from the C2 and C3 carbon atoms. Exposure of a racemic mixture of *L-Asp and D-Asp has been used to establish enantiospecific adsorption equilibria on the Cu(3,1,17)^{R&S} surfaces. During exposure to the racemic mixture, the enantiomer with the higher binding energy is capable of displacing the more weakly bound enantiomer to establish a non-racemic adsorbed layer. In other words, exposure of the Cu(3,1,17)^{R&S} surfaces to the racemic mixture in the gas phase results in a separation and enrichment of one of the two enantiomers on the surface. This can be measured quantitatively to determine the ratios of the enantiospecific adsorption equilibrium constants; $K_S^D/K_R^D = K_R^L/K_S^L = 2.29 \pm 0.17$. These translate into an enantiospecific difference in free energies of adsorption of $\Delta\Delta G = 3.15 \pm 0.29$ kJ/mol. This favors adsorption of L-Asp on the Cu(3,1,17)^R surface and D-Asp on the Cu(3,1,17)^S surface. Although the adsorption energetics of D-Asp and *L-Asp on the Cu(3,1,17)^{R&S} surfaces are enantiospecific, the decomposition kinetics are not. However, on the Cu(643)^{R&S} surfaces the decomposition kinetics exhibit extremely high enantioselectivity. This arises from the non-linear kinetics of the explosion decomposition mechanism.

9:00am **SS-ThM4 Imaging a Surface Explosion: Autocatalytic Desorption of Tartaric Acid from Cu(110)**, *T.J. Lawton**, Tufts University, *B.S. Mhatre, V. Pushkarev, B.S. Holsclaw, A.J. Gellman, Carnegie Mellon University, E.C.H. Sykes*, Tufts University

Autocatalytic reactions occur in a variety of fields and are characterized by an initiation event causing the rate of a reaction to increase non-linearly until it ceases. In addition to occurring in ambient environments, this type of reaction has been observed in a growing number of systems on single crystal surfaces (sometimes called surface explosions) under ultra high vacuum conditions but the mechanism for this process has not been fully determined. These well-controlled model surfaces allowed us to study the progression of an autocatalytic reaction, the thermal decomposition of tartaric acid (TA) on a Cu(110) single crystal surface, with molecular resolution imaging using scanning tunneling microscopy (STM) and temperature programmed reaction spectroscopy (TPRS). Using STM we progressively anneal the tartaric acid system and obtain the first molecular-scale images during a surface explosion to determine the changes occurring as a function of temperature. From these images we determine that the density of molecules slightly decreases until a critical threshold is reached when the molecules can decompose then desorb. We also observe, for the first time, a new phase of TA complexed with Cu adatoms that may play a role in the surface explosion as it occurs at the onset of the explosion. One area in which an understanding of autocatalytic reactions could be exploited is the separation of enantiomers from a heterogeneous catalyst. In this example a more complete separation of enantiomers could be achieved compared to normal desorption kinetics.

9:20am **SS-ThM5 Exploring Enantioselectivity on Chirally Modified Surfaces in Ultrahigh Vacuum**, *W.T. Tysoe*, University of Wisconsin Milwaukee

INVITED

The mode of operation of heterogeneous chiral modifiers can be classified into those operating as templates, where several modifier molecules act in concert to define a chiral adsorption site, or one-to-one modifiers that form a docking complex between the modifier and a prochiral reactant. Enantioselectivity is measured by adsorbing chiral probe molecules onto

chirally modified surfaces. Templating is illustrated using aminoacids on Pd(111). Scanning tunneling microscopy (STM) reveals that some aminoacids form tetrameric units, and others form dimers. Only those aminoacids that form tetramers are enantioselective implying that the tetramers act as templates.

Naphthylethylamine (NEA) is proposed to act as a one-to-one modifier. The interaction between NEA and a prochiral reactant, methyl pyruvate, is explored using STM. Possible docking complexes are identified using density functional theory and the simulated images are compared with experimental images.

10:40am **SS-ThM9 Spin-dependent Electron Transmission through Helical Organic Molecules**, *B. Goehler, M. Kettner*, University of Muenster, Germany, *T.Z. Markus, R. Naaman*, Weizmann Institute of Science, Israel, *H. Zacharias*, University of Muenster, Germany

Since more than a decade the field of spintronics deals with the manipulation of the electron spin to facilitate electronic operations. For such devices spin-dependent electron transfer processes (namely spin filters) are needed, which are usually realized using either magnetic materials or systems containing heavy atoms to make use of spin-orbit coupling. Here we present spin-selective electron transmission through organic molecules with helical symmetry of quite high filtering efficiencies.

The work is based on "electron dichroism", an effect that describes different interactions of longitudinally spin-polarized electrons with chiral molecules. Experiments in the mid-90s showed that spin-polarized electron beams, guided through vapor of chiral molecules, are attenuated differently, depending on the longitudinal spin polarization of the electrons and the enantiomer of the molecules.

Studying the transmission of low-energy photoelectrons through ordered self-assembled monolayers of chiral molecules on gold, an intensity dichroism was observed between the excitation with circularly polarized light of opposite helicity, which has been interpreted as a spin-dependent transmission through these ordered layers. We extend these studies by directly measuring the electron spin polarization using a calibrated Mott detector [1]. The observed spin selectivity at room temperature is extremely high as compared to other known spin filters. A systematic study on DNA monolayers shows that the spin filtration efficiency depends on the length and organization of the adsorbed molecules: single-stranded DNA molecules, which form a rather floppy instead of an ordered layer, show almost no spin-filtering effect. Recently, the spin transmission studies have been extended to bacteriorhodopsin membrane protein physisorbed on gold and aluminum surfaces. Spin polarization measurements yield up to 15% spin polarization for transmitted electron ensembles with a minor dependency on the preparation scheme. Results obtained using an Al substrate yield that the high spin-orbit coupling of the Au substrate used in former experiments does not influence the effect. Because of the low atomic numbers of the constituents (P, C, H) of the organic molecules adsorbed on the surface, spin-orbit-coupling is not sufficient to explain the observation of the quite large spin-specific interaction. Even though very recently different models were published aiming to rationalize the observed effect, it is not understood so far.

[1] Science, 331, 894 (2011)

11:00am **SS-ThM10 Coverage Dependent Self-Assembled Structures of Glutaric Acid on Cu(110)**, *E.H. Park, S. Kim*, KAIST, Republic of Korea

We have investigated the adsorption structure of glutaric acid (HOOC-(CH₂)₃-COOH) on the Cu(110) surface as a function of coverage using Scanning Tunneling Microscopy and Reflection-Absorption IR Spectroscopy. At low coverage, glutaric acid molecules diffuse freely on Cu(110) surface at room temperature, thus they can't form ordered structures at this coverage. However, novel structures have been formed under continuous scanning of the tip. We suggest that this new structure can be created by the field-induced self-assembly. As increasing coverage, glutaric acids are self-assembled by annealing at 450K. At 0.25ML, glutaric acid adsorbs with a bi-glutarate (-OOC(CH₂)₃-COO-) configuration producing a racemic conglomerate of coexisting mirror domains. Although the molecule is achiral, it forms chiral domains on the surface from adsorption-induced asymmetrization. At 0.5ML, two distinct adsorption configurations are observed which are chiral each other. Overall, the heterochiral structure with chiral chains alternating each other is created at this coverage forming zigzag structure, and still glutaric acid adsorbs with a bi -glutarate configuration. Finally, at 1ML, glutaric acid adsorbs with a mono-glutarate configuration forming close packed structures.

11:20am **SS-ThM11 Enantioselective Decomposition of L and D Tartaric Acid on Copper Surface Structure Spread Single Crystals.** A. Reinicker, B.S. Mhatre, B.S. Holsclaw, A.J. Gellman, Carnegie Mellon University

The role of atomic surface structure in catalytic reactions requires a fundamental understanding to develop new catalysts. Surface Structure Spread Single Crystals (S⁴Cs) expose a continuous distribution of crystal planes across their surfaces. Each point on the S⁴Cs has a different local crystallographic orientation that can be determined from the shape of the S⁴Cs and the orientation of its bulk crystal lattice vectors. The majority of crystal planes on these S⁴Cs contains terraces, monatomic steps, and kinks and can be described as chiral with an R or an S orientation. When coupled with spatially resolved surface analysis techniques, S⁴Cs can be used to study the effects of surface chirality on surface chemistry across a broad, continuous distribution of crystal planes. In this work, the enantioselectivity of the explosive decomposition of L and D tartaric acid was studied using Cu(100)±10°, Cu(110)±10°, and Cu(111)±10° S⁴Cs. We used Isothermal Temperature Programmed Desorption (TPD) in which each sample was held at a temperature >20 K below the temperature of peak decomposition observed in a standard (TPD) experiment until the decomposition reaction occurred. Spatially resolved X-ray Photoelectron Spectroscopy (XPS) was performed to determine which crystal planes on each S⁴C had undergone explosive decomposition after quenching the temperature of each sample at the decomposition peak during an isothermal TPD. It was found that D-tartaric acid decomposes before L-tartaric acid on R oriented surfaces and L-tartaric acid decomposes before D-tartaric acid on S oriented surfaces on all three Cu S⁴Cs.

11:40am **SS-ThM12 Stereodirecting Interactions and Stereodynamics on Chirally Modified Pt(111).** Y. Dong, G. Goubert, Y. Zeng, P.H. McBreen, J.-C. Lemay, Laval University, Canada

The stereocontrol of chemical reactions on surfaces is a challenging task. STM imaging coupled with DFT calculations provides a powerful method for studying asymmetric induction on chirally modified catalysts. In combination, these techniques can be used to observe and define transient pre-organization complexes formed by binding the prochiral substrate to the chemisorbed chiral modifier. We present sub-molecularly resolved regiospecific and stereospecific data for isolated bimolecular and termolecular complexes formed at chiral sites on Pt(111). The measurements provide new insight on both the stereodirecting interactions involved and the dynamics of chiral selection.

Thin Film

Room: 104 A - Session TF+AS+EM+NS+SS-ThM

Thin Film: Growth and Characterization I

Moderator: S.M. Rossnagel, IBM Research Division, T.J. Watson Research Center

8:00am **TF+AS+EM+NS+SS-ThM1 Understanding Strongly Correlated Complex Oxides through Epitaxial Control.** T.Z. Ward, Oak Ridge National Laboratory **INVITED**

The strong electronic correlations arising from overlapping spin-charge-orbital order parameters in complex oxides are of fundamental importance to many desirable characteristics such as the metal-insulator transition, colossal magnetoresistance, and high T_C superconductivity. By selectively tuning the elastic energy in manganite films through epitaxial strain and noble ion implantation, we investigate the influence of isotropic and anisotropic stress/strain on each of the three crystal axes. From this, we can gain a much deeper understanding of how orbital overlaps and occupation act to drive emergent mesoscopic behaviors. We will discuss recent work on La_{1-x}Sr_xMnO₃ (LSMO) and La_{0.5/0.8-x}Pr_xCa_{0.3/0.8}MnO₃ (LPCMO) single crystal thin films in which we find many different avenues to tune critical temperatures and magnetoresistive properties by controlling lattice deformations. Quantum Monte Carlo and percolation models are presented as a means of understanding the role of orbital degeneracy and electronic phase competition in driving macroscopic electron transport and magnetization. These open the door to bridging fundamental discoveries to creation of functional devices. Supported by the US DOE Office of Basic Energy Sciences, Materials Sciences and Engineering Division.

8:40am **TF+AS+EM+NS+SS-ThM3 Tracing the History of Inorganic Thin Films from ~2500 BC to the Early 1900s AD.** J.E. Greene, University of Illinois, Linköping University, National Taiwan University of Science and Technology **INVITED**

Gold was likely the first metal discovered by man, more than 11,000 years ago. However, unlike copper (~9000 BC), bronze (~3500 BC), and wrought iron (~2500-3000 BC), it was too soft for use as tools and weapons. Instead, gold was used for decoration, religious artifacts, and commerce. The earliest documented inorganic thin films were gold layers, < 3000 Å thick, produced chemi-mechanically by Egyptians more than 5000 years ago. Examples, gilded on statues and artifacts (requiring interfacial adhesion layers), were found in early stone pyramids dating to ~2650 BC in Saqqara, Egypt. Spectacular samples of embossed Au sheets date to at least 2600 BC. Fatty-acid-based monolayers were deposited in King Hammurabi's time (~1800 BC, Mesopotamia); modern experiments were carried out much later by Ben Franklin, Lord Rayleigh, and Irving Langmuir. Although there is forensic archeological evidence for electroplating as early as the first few centuries BC, no written evidence survived. The earliest published electroplating experiments were ~1800 AD following the invention of the dc electrochemical battery by Volta. Chemical vapor deposition (CVD) of metal films was reported in 1649. Sols were produced in the mid-1850s (Faraday) and sol-gel films synthesized in 1885.

Vapor phase film growth including sputter deposition (Grove, 1852), arc deposition ("deflagration," Faraday, 1857), atmospheric plasmas (Siemens, 1857), plasma-enhanced CVD (1869, Berthelot), and evaporation (Stefan, Hertz, and Knudsen, 1873-1915) all had to wait for the invention of vacuum pumps whose history ranges from ~1650 for mechanical pumps through ~1865 for mercury pumps that could produce ballistic pressures in small systems. The development of the science of crystallography, leading to Miller indices (1839) for describing orientation and epitaxial relationships in modern thin film technology, was already well advanced by the 1780s. The starting point for the development of heterogeneous thin film nucleation theory was provided by Thomas Young (contact angle equation) in 1805.

While an historical road map tracing the progress of thin film technology is interesting in itself, the stories behind these developments are even more fascinating and provide insight into the evolution of scientific reasoning.

9:20am **TF+AS+EM+NS+SS-ThM5 Metal-Insulator Transition Induced in SrVO₃ Thin Films.** M. Gu, S.A. Wolf, J.W. Lu, University of Virginia

Metal-insulator transition (MIT) in strongly correlated oxides has been an intriguing topic of condensed matter physics over many decades. SrVO₃ (SVO) with a 3d¹ electronic configuration for vanadium is a typical strongly correlated system for studying MIT. High quality epitaxial SVO thin films of various thicknesses were grown on (001)-oriented LSAT single crystal substrates by using a novel pulsed electron-beam deposition (PED) technique. Thick SVO films (~25 nm) exhibited metallic behavior with the electrical resistivity following the T² law that corresponds to a Fermi liquid system, the resistance ratio R(300K)/R(2K) was ~1.6. We observed a temperature driven MIT in SVO films with thicknesses below 6 nm. The emergence of this MIT can be attributed to the reduction in the effective bandwidth due to a crossover from a three-dimensional metal to a two-dimensional insulator. We also synthesized SrTi_{1-x}V_xO₃ (0 ≤ x ≤ 1) thin films with thicknesses of ~15 nm to study the chemical doping of Ti⁴⁺ ions in the SVO system. The films with high vanadium content (x > 0.7) were metallic following the T² law, and the films with low vanadium content (x < 0.7) were semiconducting following the variable range hopping mechanism. The x = 0.7 film showed a temperature driven MIT at ~100K. The observed MIT induced by the substitution of Ti⁴⁺ ions for V⁴⁺ ions could be interpreted by the induced Anderson localization that trapped the electrons below a mobility edge.

9:40am **TF+AS+EM+NS+SS-ThM6 Bi-Chromatic Far-Field Optical Probing the Percolative Metal-Insulator Transition in VO₂ Thin Film.** L. Wang, I. Novikova, The College of William and Mary, J.M. Klopff, S. Madaras, Thomas Jefferson National Accelerator Facility, E. Madaras, NASA Langley Research Center, G.P. Williams, Thomas Jefferson National Accelerator Facility, R.A. Lukaszew, The College of William and Mary
Vanadium dioxide (VO₂) is a prototype of a highly correlated electron material exhibiting a metal-insulator transition (MIT) that can be thermally, electrically or optically controlled. Using near field optical techniques it has recently been shown that the thermally induced MIT in VO₂ thin films is initiated by nucleation of nanoscale metallic puddles in the insulating host. Here we exploit these microscopic changes in phase-composition at the onset and during the MIT on a VO₂ thin film sample by observing their effect on the optical properties using far-field infrared (IR) and broadband coherent Terahertz (THz) light optical techniques. We model the transition and are able to accurately describe it particularly regarding the different

temperatures recorded at the onset of the MIT depending on the probe used. Further, we compare the optical and DC transport responses, and our findings and modeling settle the question regarding the different transition temperatures observed in each case on the same sample under thermally induced MIT. Finally, we show that Mie scattering explains the observed wavelength scaling dependence of the optical response as function of temperature near the MIT.

10:40am **TF+AS+EM+NS+SS-ThM9 Magnetron Deposition of IGZO Thin Films Utilizing dc, Pulsed dc and Bipolar Power Supply.** *P. Baroch, J. Rezek, J. Houska*, University of West Bohemia, Czech Republic, *P. Ozimek, A. Klimczak*, Huettinger Electronic

Transparent semiconducting amorphous indium gallium zinc oxide (IGZO) films have attracted great attention due to their excellent electrical properties and possible utilization in thin film transistors or in photovoltaic applications. It is known that the properties of IGZO films prepared by magnetron sputtering are highly sensitive to process parameters, especially to oxygen partial pressure. In this study we have focused on the comparison of various types of power supplies with precise control of process parameters in order to optimize electrical and optical properties of the IGZO thin films. We employed dc and pulsed dc power supplies for single magnetron sputtering and bipolar and mid frequency sine wave power supplies for dual magnetron sputtering. All power supplies were equipped with advanced process stabilization solutions, ultra-fast arc management characterized by very low stored energy, and a digital control platform enabling highly flexible software algorithms design. Magnetrons were equipped either with ceramic InGaZnO targets or with metallic InGaZn targets. A novel fast process control system was used in order to precisely control deposition conditions during reactive magnetron sputtering of IGZO films from metallic targets. It is shown that the electrical resistivity can be effectively controlled in the wide range from 10^{-3} to 10^5 Ω .cm and the field effect mobility can reach values up to 40 $\text{cm}^2/\text{V}\cdot\text{s}$ at a film thickness of 270 nm. In parallel to the difference between individual power supplies (sputtering techniques), the effect of the discharge power and the oxygen partial pressure on deposition rate, optical and electrical properties and film structure will be discussed in detail.

11:00am **TF+AS+EM+NS+SS-ThM10 Structure and Optical Properties of Nanocrystalline Hafnium Oxide Thin Films Made by Sputter-Deposition.** *M. Vargas, C.V. Ramana*, University of Texas at El Paso

Hafnium oxide (HfO_2) is a unique material characterized by excellent chemical and physical properties. It is a wide band gap (5.5 eV) material, which makes it attractive for optoelectronics since it transparent from the ultraviolet to the mid-infrared region. Being a promising high- k dielectric, HfO_2 has a strong potential to replace silicon oxide as the insulator in CMOS devices. HfO_2 exhibits various polymorphs; the thermodynamic stability and phase existence depends on the temperature and pressure conditions. Controlled growth and manipulation of specific crystal structures of HfO_2 at the nanoscale dimensions has important technological implications. The present work entails a detailed analysis of growth behavior, microstructure, and optical properties of monoclinic HfO_2 films as a function of growth temperature. In addition, the effect of post-deposition annealing temperature was also studied. HfO_2 thin films were grown by RF magnetron sputtering onto silicon (100) and quartz substrates by keeping power, pressure, and flow of Ar and O_2 and their ratio (70:30) constant, but varying growth temperature from room temperature to 600 C. A thorough characterization was performed through scanning electron microscopy (SEM), transmission electron microscopy (TEM), atomic force microscopy (AFM), and grazing incidence x-ray diffraction (GIXRD). Optical properties were evaluated using spectrophotometric and ellipsometry measurements. GIXRD data revealed a well oriented structure along (-111) as temperature increases, and an evident crystallization temperature at 300 C. The grain sizes measured were in the range of 15 to 20 nm; grain sizes increased with temperature. While SEM and AFM analyses also indicate the grain size with increasing temperature, roughness of the films exhibits a decreasing tendency with increasing temperature. Optical data revealed a double band gap for temperatures higher than RT as well as an increase in band gap with increasing growth temperature. The band gap for at HfO_2 thin films grown at RT was found to be 5.7 eV. The band gap increased to values of ~ 6.2 eV with increasing growth temperature. A correlation between growth conditions, microstructure and optical properties of nanocrystalline HfO_2 thin films is discussed.

11:20am **TF+AS+EM+NS+SS-ThM11 Studies of Electrical and Surface Properties of High-k Dielectric Gate formed by Al_2O_3 , HfO_2 , $\text{Al}_x\text{Hf}_y\text{O}_z$ and AlHFON on Silicon via Atomic Layer Deposition.** *V. Ou, Y.S. Lin, R. Candler, S. Franz*, UCLA

In order to meet the increasing demand for high frequency electronic devices, the physical dimensions of MOSFETs have been continuously

scaled down to nanoscale. However, one of the bottlenecks we encountered during the down-scaling process is the tunneling current leakage at gates. SiO_2 , the most commonly used traditional gate dielectric experiences an appreciable amount of tunneling current when gate thickness is below 1 - 1.2 nm. The leakage greatly degrades the performance of nanoelectronics. Therefore, we propose using high- k dielectrics to replace SiO_2 , which can effectively limit the tunneling leakage without losing the current control at gates. Our research has mainly focus on Al_2O_3 , HfO_2 and $\text{Al}_x\text{Hf}_y\text{O}_z$ deposit on silicon via Atomic Layer Deposition. The Aluminum to Hafnium ratio in the oxide is tuned to maximize the electrical and physical properties of the film. We expect $\text{Al}_x\text{Hf}_y\text{O}_z$ to have a better interface than HfO_2 and an intermediate band-gap between Al_2O_3 and HfO_2 , as well as better thermal stability. The electrical properties of each oxide will be characterized by fabricating transistors with gate oxide thicknesses of 5 , 10 , and 15 nm. In addition to the C-V and I-V measurements for capacitors and transistors, the films will be characterized by XPS, AFM, and spectroscopic ellipsometry. To improve the electrical property of the film, we will incorporate N into the high-dielectric films using Plasma ALD. Finally, the effects of various annealing and deposition temperatures at the silicon-oxide interface will be studied using TEM.

11:40am **TF+AS+EM+NS+SS-ThM12 TiO_2 Film Crystallization by Post-Deposition Annealing.** *A. Henegar, T. Gougousi*, University of Maryland, Baltimore County

Optical and electrical properties of TiO_2 thin films are largely effected by film morphology. TiO_2 usually crystallizes into anatase or rutile phase. The rutile phase is generally stable while the anatase phase is difficult to produce in pure form through annealing. TiO_2 thin films were grown by atomic layer deposition (ALD) on Si (100) surfaces using tetrakis(dimethylamino) titanium (TDMAT) and H_2O . Films were grown at every 50°C increment from 100 to 300°C approximately 100 nm thick, determined by nominal growth rates derived from spectroscopic ellipsometry (SE) measurements. The growth rate varied from $0.4\text{\AA}/\text{cycle}$ at the ALD optimal temperature of 200°C to $1.2\text{\AA}/\text{cycle}$ at 300°C . Films were annealed post-deposition at temperatures of 500°C , 700°C and 900°C for 3 , 5 and 10 minutes in an argon environment using a rapid thermal annealer. Characterization was completed using Fourier transform infrared spectroscopy (FTIR), X-ray diffraction (XRD), scanning electron microscopy (SEM), transmission electron microscopy (TEM) and atomic force microscopy (AFM). FTIR measurements indicate that the as-deposited films have an amorphous structure. Annealed films exhibit various crystallization to rutile phase, anatase phase, or a mixture of the two phases, depending on the deposition and post-deposition annealing conditions, as confirmed by XRD. Specifically, TiO_2 films grown at 100°C and annealed for 10 minutes at 900°C exhibit only amorphous and anatase phase TiO_2 . It is shown that TiO_2 crystallinity can be tuned between amorphous, anatase and rutile phases by controlling the deposition temperature and post-deposition annealing parameters.

Thin Film

Room: 102 C - Session TF+PS-ThM

Advanced CVD Methods

Moderator: R.C. Davis, Brigham Young University

8:00am **TF+PS-ThM1 Non-destructive Spectroscopic Analysis of Gradient Hydrocarbon/Fluorocarbon Thin Films to Demonstrate the Formation of a Stable Gradient Structure during PECVD Film Growth.** *B.D. Tompkins, E.R. Fisher*, Colorado State University

Thin films that have a continuous change in composition in one or more dimensions have a wide variety of potential applications, including biomimetic materials, barrier films, adhesion interlayers, and optical coatings. These gradient film structures are valuable for their ability to direct processes within a film or along a surface; the ability to tailor these materials allows for unprecedented control over such a process. We have developed a plasma enhanced chemical vapor deposition (PECVD) system capable of fabricating a range of arbitrary gradient film structures using dynamic mixing of C_3F_8 and H_2 . We used time resolved optical emission spectroscopy (TR-OES) to characterize the PECVD process and found that the relative gas-phase density of key radical species change reproducibly based on the $\text{C}_3\text{F}_8/\text{H}_2$ ratio at any given time. Although the $\text{C}_3\text{F}_8/\text{H}_2$ composition can be varied continuously, verifying that a stable continuous gradient composition has been fabricated presents a more complicated analysis problem. Recently, we have adapted standard non-destructive spectroscopic analysis techniques to elucidate the structure within a gradient film. A series of homogenous films and model gradient films were examined using x-ray photoelectron spectroscopy (XPS), variable angle

spectroscopic ellipsometry (VASE), and infrared spectroscopy (FTIR). By examining the shift in CF_2 binding energy from XPS, dielectric constant from VASE, and the shift in $\nu(\text{CF}_2)$ from FTIR, we demonstrate that stable confined layers with high fluorocarbon content remain incorporated into the gradient material when fabrication is complete. The ability to tailor surface composition and properties through programmed deposition will also be discussed.

8:20am TF+PS-ThM2 CVD Infiltration of Carbon into Carbon Nanotube Forests for Templated Microfabrication. *R.R. Vanfleet, W. Fazio, J.M. Lund, K. Zufelt, T. Wood, D.D. Allred, R.C. Davis, B.D. Jensen,* Brigham Young University

Chemical Vapor Deposition (CVD) of materials into patterned frameworks of carbon nanotube forests can be used to create precise high-aspect-ratio (up to 200:1) microstructures. We call this process carbon nanotube templated microfabrication (CNT-M). The "as grown" CNT forests are very low density (at 0.009 g/cc the forest is ~1% carbon and 99% air) and not useful as mechanical materials themselves because they are extremely fragile, due to their low density and weak intratube bonding. However, when we replace the air spaces between tubes in the forest with a filler material by atomistic deposition, the infiltrated CNT framework becomes a robust microstructure consisting mostly of the filler material. We have used various deposition techniques to infiltrate the CNT framework with a range of materials. This presentation will focus on the fabrication and characterization of structures using CVD of carbon into the nanotube forest. A range of characterization has been applied to the materials and resulting structures from high resolution electron microscopies of the base materials to bending and failure tests of full structures. The materials consist of nanocrystalline graphitic carbon coated on multiwalled carbon nanotubes. The complete structures exhibit fairly low Young's modulus (5-15 GPa), and ultimate strength (100-200 MPa) with a resulting high maximum strain of over 2%.

8:40am TF+PS-ThM3 Initiated Chemical Vapor Deposition of Functional Polymers onto Porous Materials and Liquid Surfaces. *M. Gupta,* University of Southern California **INVITED**

This talk will present the mechanism, kinetics, and potential applications associated with the vapor phase deposition of functional polymers onto structured materials and liquid surfaces. Vapor phase deposition eliminates the need for organic solvents and thereby offers a safer and cleaner alternative to liquid phase polymer processing. We will demonstrate our ability to pattern functional polymers onto structured materials such as microfluidic devices, porous materials, and pillar arrays. We will also present our recent work demonstrating deposition onto liquids with negligible vapor pressures such as ionic liquids (ILs) and silicone oils. We will demonstrate that the polymer morphology at the liquid/vapor interface is controlled by surface tension interactions. The ability to controllably tailor polymer morphology at the interface allows for the design of ultrathin free-standing polymer films, micron-scaled particles, and core-shell particles. We will also demonstrate that polymerization can occur within the liquid layer allowing for the fabrication of polymer/IL composite films.

9:20am TF+PS-ThM5 Ultrasonic Spray Deposition of Mesoporous WO_3 Films Displaying 100% Optical Modulation. *C.-P. Li,* Colorado School of Mines, *C. Engtrakul, R.C. Tenent,* National Renewable Energy Laboratory, *C.A. Wolden,* Colorado School of Mines

Smart windows employing electrochromic materials to reversibly modulate optical transmission and reflection can significantly improve building energy efficiency. However, further improvements in both performance and cost reduction are required for widespread implementation of electrochromic windows. Mesoporous films comprised of nanocrystalline domains can provide both high performance and good durability. Sol-gel chemistries combined with sacrificial templating agents is a well-established technique to introduce controlled porosity, but conventional techniques for film formation such as spin/dip coating are not amenable to large scale production. Ultrasonic spray deposition (USD) is an attractive technique for large scale, low cost thin film manufacturing of nanostructured thin films. USD provides high materials utilization and the use of benign solvents enables deposition under ambient conditions. Piezoelectric nebulizer technology addresses the quality and uniformity issues that were a concern with conventional pressure driven sprays. In this work mesoporous WO_3 films were deposited by adapting sol-gel chemistry to ultrasonic spray deposition. The sol was formed by dissolving WCl_6 and an organic templating agent (P123) in ethanol. The dynamics of both sol preparation and hydrolysis were investigated by UV-Vis spectroscopy. Electrochromic performance is strongly correlated to both the annealing conditions and the sol composition. Optimized films produced world record coloration efficiency ($68 \text{ cm}^2/\text{C}$), resulting in never before achieved 100% optical modulation across the visible spectrum during cycling. The films also displayed good switching kinetics, producing a 75% change in absolute

transmission in 4 and 19 s during coloration and bleaching, respectively. Achievement of optimum electrochromic performance could be achieved by controlling the sol concentration and/or the number of spray passes in this robust process. The films were smooth and uniform, and the excellent performance is attributed to the nanocrystalline nature of the films, which provides high specific surface area ($>100 \text{ m}^2/\text{g}$) for efficient lithium ion intercalation.

9:40am TF+PS-ThM6 Preparation and Characterization of CVD & ALD Tungsten & Molybdenum Thin Films for CNT-M Metallic Microstructures. *D.D. Allred, R.R. Vanfleet, J.K. Anderson, C. Brown, R.S. Hansen,* Brigham Young University, *D. McKenna,* University of Notre Dame, *R.C. Davis,* Brigham Young University

Microelectromechanical systems (MEMS) fabrication traditionally uses the same limited methods and materials as those used in the silicon-based microelectronics industry. In order to make MEMS out of a much richer suite of materials, such as metals, Brigham Young University researchers are investigating chemical vapor infiltration and atomic layer infiltration of patterned carbon nanotube (CNT) forests, using the surface of the carbon nanotubes as nucleation sites for the metal deposition. Our goal has been to fill in the spaces between CNTs by atomistic deposition, thus creating a CNT-composite material possessing the original pattern of the CNT forest. We have investigated two metals: tungsten and molybdenum and 3 precursors: tungsten carbonyl, molybdenum carbonyl and tungsten hexafluoride with hydrogen. molybdenum carbonyl proved to be more successful than tungsten carbonyl for infiltration. As deposited the materials are not pure metals, but contain substantial amounts of carbon and oxygen. As deposited the materials are not pure metals, but contain substantial amounts of carbon and oxygen. Efforts to remove impurities as well as the electrical and mechanical properties of the resulting composite material will be reported. Most recently tungsten fluoride via both CVI and ALI has been used to deposit purer tungsten structures.

10:40am TF+PS-ThM9 Silica Structures by Plasma-enhanced Chemical Vapor Infiltration of a Carbon Nanotube Template. *J.M. Lund, B.D. Jensen, R.C. Davis, R.R. Vanfleet,* Brigham Young University

This work investigates the advantages of infiltrating carbon nanotube structures with silica by plasma-enhanced chemical vapor deposition (PECVD). Carbon nanotube (CNT) forests have unique porous structures created through CNT interaction during the growth process. It is possible to coat individual nanotubes with silicon oxide using a PECVD process. Oxidation of the carbon nanotubes then removes the initial CNT template, resulting in a uniquely structured silica material. One application of this work is the fabrication of ultra-low thermal conductivity films. Measurements indicate a thermal conductivity less than $0.05 \text{ W/m}\cdot\text{K}$. However, with this particular process the coating is invariably thicker near the top surface and the silica typically penetrates no more than $17 \mu\text{m}$ into the CNT forest. The current challenge in this work is to keep the structures as porous as possible while coating enough at the base to keep the structure continuous and attached to the substrate. Some investigation is made into the parameters influencing, and possible uses of, the infiltration depth. This includes the usefulness in capping or sealing porous structures so they can be planarized in preparation for other films and structures.

11:00am TF+PS-ThM10 High Deposition Rate and Uniformity of Silicon Thin Films Deposited Via Efficient, Low-Damage Surface Wave Plasma Source. *J. Peck, P.S. Zonooz, D. Currelli,* University of Illinois at Urbana Champaign, *M. Reilly, R. Stubbers, B. Jurczyk,* Starfire Industries, LLC, *D.N. Ruzic,* University of Illinois at Urbana Champaign

An innovative surface wave plasma source provided by Starfire Industries, LLC has been tested by the Center for Plasma-Material Interactions at the University of Illinois Urbana-Champaign. Operating in the microwave range, the source efficiently generates high-density ($10^{11-12} \text{ cm}^{-3}$) and low electron temperature ($\sim 1 \text{ eV}$) plasmas. Thin silicon films were deposited with the interest of characterizing a cost-effective PECVD process for high quality silicon photovoltaics. Parameters of interest included substrate temperature, total operating pressure, silane dilution, RF power, discharge gap width, and process gas flowrate. Through a SiH_4/H_2 discharge, films were deposited and subsequently analyzed via profilometry, SEM, Raman microscopy, and X-ray diffraction. For a 15 cm source, consistent radial uniformity was maintained across a 12 cm diameter from $2.0 \pm 0.4 \text{ nm/s}$ up to $3.5 \pm 0.9 \text{ nm/s}$ at a 2.5 cm discharge gap. Well-formed films were produced with substrate temperatures above 285°C . With decreasing operating pressure and increasing flowrate, area of coverage is shown to increase without compromising speed of film growth. An assessment on deposition rate optimization, film uniformity, and large-area scalability is presented.

11:20am **TF+PS-ThM11 Ab-initio and Classical Molecular Dynamics Study of Diffusion of Ti and N Adatoms on the TiN(001) Surface.** *D.G. Sangiovanni, D. Edström, L. Hultman*, Linköping University, Sweden, *I.G. Petrov, J.E. Greene*, University of Illinois at Urbana Champaign, *V. Chirita*, Linköping University, Sweden

We carry out *ab-initio* and classical molecular dynamics (MD) simulations to investigate fundamental atomistic processes and surface properties responsible for TiN surface evolution during thin film growth. We find that Ti adatoms are highly mobile on TiN(001) terraces where they diffuse between fourfold hollow sites primarily via $\langle 100 \rangle$ channels. $\langle 110 \rangle$ diffusion via atop N terrace atoms, double and triple $\langle 100 \rangle$ jumps are also observed, and their occurrence is a function of TiN(001) temperature. When placed on TiN/TiN(001) islands, Ti adatoms funnel toward cluster edges and corners, where they rapidly descend by either direct hopping or push/out-exchange. Ti and N adatoms diffusion on square islands is anisotropic and results in preferential channels for mass transport. N adatoms, considerably less mobile than Ti adatoms, can form strong chemical bonds with underlying terrace or island N atoms. As an effect of this bonding, N adatoms can diffuse on TiN(001) terraces by exchange with N terrace atoms. At high temperatures, the rapid lattice vibrations assist the desorption of N_2 (N-adatom/N-terrace) dimers, and anion vacant sites are produced in the TiN(001) terrace. When placed on square TiN/TiN(001) clusters, N adatoms can pull Ti corner atoms onto the island to form TiN dimers which descend via direct hop over the island edge. Both N and Ti adatoms slowly diffuse along island edges. In contrast, due to the high degree of ionicity in Ti-N bonds, Ti and N adatoms easily diffuse around island corners of the same chemical type via 1D push-out/exchange due to electrostatic repulsion. Corners of opposite chemical type are rapidly rounded by direct diffusion. Finally, we combine the Arrhenius plots obtained from classical, and quantum-mechanical simulations to determine, with high accuracy, Ti and N adatom diffusion energy barriers and diffusion coefficients on TiN(001). The excellent agreement between empirical and *ab-initio* methods results further demonstrates the ability of classical interaction potentials for accurate, fully-deterministic, simulations of thin films deposition.

11:40am **TF+PS-ThM12 Quantum Chemistry Analysis of the Role of Radicals in Plasma Assisted Atomic Layer Deposition of Silicon Nitride Films.** *J. Yoshikawa, N. Fukiage, S.Y. Kang*, Tokyo Electron Ltd., *P. Ventzek*, Tokyo Electron America, *H. Ueda*, Tokyo Electron Ltd.

Silicon nitride films are well known as important dielectric components for semiconductor device fabrication because of their good physical and electrical properties for 3D structure device construction. High quality silicon nitride film deposition has been demonstrated in high density plasma sources by using RLSA™ in which a nitrogen and hydrogen containing plasma nitrates a silicon surface deposited by a thermal adsorption process. [1] A typical precursor for the silicon component is Dichlorosilane (DCS), used in thermal CVD of silicon nitride. [2] In plasma assisted atomic layer deposition of silicon nitride films, silicon nitride deposition is effected by alternating deposition and nitridation steps. The film quality, defined by the 0.5% DHF solvent wet chemical etching ratio, is a function of many process parameters. It has been shown experimentally that hydrogen radicals produced in this plasma are important for film quality. The exact film growth mechanism in plasma assisted deposition processes is, as yet, not fully clarified and most studies are related to thermal CVD. *Ab-initio* studies focusing on the role of radicals are rare. In this presentation a quantum chemistry analysis (Gaussian 09) of the film formation mechanism in Atomic layer Deposition sequence is presented. Hexachlorodisilane (HCD) is used as a model surface in the study. We revealed the role of H as a critical precursor for the growth of high quality films. Un-dissociated ammonia or hydrogen interacts with Si-Cl to liberate chlorine from silicon. Hydrogen liberates H from the new NH_2 structure. Silicon containing structures with dangling bonds interact with the structure then complete the formation of Si-N-Si bonding. Hydrogen and NH_3 limit restoration of the Si-Si chain.

[1] T. Karakawa, M. Oka, N. Fukiage, H. Ueda, T. Nozawa, PS+TF-ThM1 AVS Symposium Nashville (2011) [2] A. A. Bagatur'yants, K. P. Novoselov, A. A. Safonov, L. L. Savchenko, J. V. Cole and A. A. Korkin, Materials Science in Semiconductor Processing 23, 3 (2000)

Thursday Afternoon, October 31, 2013

Applied Surface Science

Room: 204 - Session AS+BI+EM+NL+NS+SS-ThA

Nanoparticle Surface Chemistry II

Moderator: N. Kruse, Université libre de Bruxelles, Belgium

2:00pm **AS+BI+EM+NL+NS+SS-ThA1 Fundamental Explorations of Chemical Bonding and Surface Chemistry at Graphene Interfaces**, *B.J. Schultz, V. Lee, R. Dennis, J. Aldinger, S. Henderson, S. Banerjee*, University at Buffalo, The State University of New York **INVITED**

The distinctive 2D sp^2 -hybridized structural framework of graphene gives rise to a unique electronic structure characterized by conical valence and conduction bands touching at the Dirac point with linear energy dispersion within ± 1 eV of the Fermi level. Given the entirely surficial geometric structure of graphene, the extent of manifestation of true Dirac physics in this material is substantially modulated by perturbations of the electronic structure as a result of interactions with charged impurities, coupling to the underlying substrate, orbital hybridization with deposited contacts, and buckling/corrugation of graphene sheets. I will focus on the results of our combined X-ray absorption spectroscopy, Raman microprobe analysis, and density functional theory studies of graphene/metal and graphene/dielectric interfaces. Depending on the nature of the transition metal and the proximity of the graphene surface, physisorption or covalent chemical bonding is observed. Studies of the hybridization of single-crystalline metal surfaces with graphene suggest clear facet selectivity. We further evidence the potential for anisotropically functionalizing only one surface of planar graphene. For dielectric interfaces, charge transfer is observed without formation of carbidic bonds. Next, I will discuss our recent results on nitrogen incorporation within graphene oxide achieved through chemical reduction or annealing under a NH_3 atmosphere. Using near-edge X-ray absorption fine structure spectroscopy in conjunction with electrical transport measurements, we have developed a detailed picture of the recovery of the electronic structure of graphene oxide upon chemical or thermal defunctionalization. I will further discuss the design of graphene—polyetherimide nanocomposites based on engineered graphene interfaces that endow remarkable corrosion protection to low alloy steel upon application as thin films.

2:40pm **AS+BI+EM+NL+NS+SS-ThA3 Structure-dependent Trends in Adsorption of CO, O₂, and H₂ on Pd and Pt Nanoparticle Catalysts**, *H. Mistry, F. Beharfarid, B. Roldan Cuenya*, University of Central Florida

Many important catalytic reactions have shown striking dependence on particle size and shape. Therefore, understanding structure-dependent adsorption processes using model nanoparticles is key to designing highly active and selective catalysts. Temperature-programmed desorption and x-ray absorption fine structure spectroscopy were used to study the interaction of adsorbates with Pt and Pd nanocatalysts. The binding strength of oxygen and carbon monoxide adsorbed on Pd nanoparticles supported on $SiO_2/Si(111)$ was shown to increase with decreasing particle size. In addition, pressure-dependent changes in hydrogen coverage and structure of size- and shape- selected $Pt/\gamma-Al_2O_3$ nanoparticles were investigated.

3:00pm **AS+BI+EM+NL+NS+SS-ThA4 CO-induced Scavenging of Oxide-Supported Platinum Nanoclusters**, *N. Chaabane*, INSTN, CEA, France, *R. Lazzari, J. Jupille*, INSP, UPMC and CNRS, France, *G. Renaud*, INSC, CEA, France, *E.A. Soares*, ICEx-IFMG, Belo Horizonte MG, Brazil

The efficiency of oxide-supported catalysts frequently relies on the dispersion of the metallic particles whereas the optimization of the proportion of active atoms of the often precious metals involved in catalysts is an economic issue. Beyond the achievement via synthesis processes of the optimum morphology that accounts for the combination of those constraints, a great attention is paid to the phenomena which drive changes in shape, size and structure of the clusters of catalysts in running conditions. Aside the capability to resist high temperature aging, a main concern is the sustainability of catalyst particles upon exposure to reactive atmospheres. A prototypical case is the effect of CO on transition metals catalysts, of which supported platinum is a thoroughly studied example because it combines a strong practical relevance with puzzling stability behavior in the presence of CO [1]. Under CO exposure, disruption and agglomeration of supported Pt clusters were simultaneously evidenced by extended x-ray absorption fine structures, scanning tunneling microscopy and infrared spectroscopy. However, those parallel phenomena are not explained yet.

In the present work, changes in size and shape of $MgO(100)$ -supported Pt nanoclusters were tracked *in situ* by Grazing Incidence Small-Angle X-Ray

scattering (GISAXS) at CO pressures ranging from 10^{-6} to 10^3 Pa [2]. MgO has been chosen as an archetype of non-reducible support giving rise to abrupt interfaces with platinum [3]. Between 300 K and 470 K, Pt particles smaller than a critical size of 1 nm were shown to disrupt at CO pressure as low as 10^{-1} Pa. Once formed, the disrupted particles - suggested to be carbonyl moieties - underwent scavenging by clusters larger than the critical size. Disruption and agglomeration are both consistent with a CO-driven ripening mechanism [4]. An additional agglomeration mechanism was evidenced. Upon annealing up to the desorption temperature of CO, CO-covered Pt clusters of size ranging between the critical value and 2 nm were seen to agglomerate by diffusion; this is discussed in terms of an adsorbate-induced weakening of the cluster-support bonding. Similar CO-induced mechanisms (ripening and cluster diffusion) are suggested to hold for other supported metal catalysts such as Ru, Rh and Ir.

[1] Y. Nagai et al., *Catal. Today* 175 (2011) 133.

[2] N. Chaabane, R. Lazzari, J. Jupille, G. Renaud and E.A. Soares, *J. Phys. Chem. C* 116 (2012) 23362.

[3] J. Olander, R. Lazzari, J. Jupille, B. Mangili, J. Goniakowski and G. Renaud, *Phys. Rev. B* 76 (2007) 075409.

[4] R. Ouyang, J.-X. Liu and W.-X. Li, *J. Am. Chem. Soc* 135 (2013) 1760.

3:40pm **AS+BI+EM+NL+NS+SS-ThA6 Adsorption Energies of Cu Nanoparticles on CeO_{2-x}(111) Supports Studied by Microcalorimetry**, *T.E. James, S.L. Hemmingson, C.T. Campbell*, University of Washington

The increasing demand for energy has accelerated the need to develop new and improved catalysts for existing and alternative technologies. Heterogeneous catalysts consisting of transition metal nanoparticles dispersed across oxide supports are found in solar cells, fuel cells, industrial chemical production and environmental cleanup. Fundamental understanding of these supported catalysts, such as the bond energies between the metal clusters and their supports, which is crucial to understand the sintering behavior and catalytic reactivity, is still largely missing. This work uses Cu clusters and a single-crystal ceria support as a well-defined model system to study the bond energies between metal clusters and the oxide support as a function of particle size. The adsorption energies and growth morphologies of Cu on $CeO_{2-x}(111)$ (where $x=0.05, 0.1$ or 0.2) at 100 and 300 K were investigated using single crystal adsorption microcalorimetry together with x-ray photoelectron spectroscopy (XPS), ion scattering spectroscopy (ISS), Auger electron spectroscopy (AES), low energy electron diffraction (LEED), and sticking probability measurements. Ceria thin films (~4nm) were grown on Pt(111) single crystal. The initial heat of Cu adsorption decreased with the extent of reduction of the ceria surface. The measured heat of adsorption increases with additional Cu deposition until it reaches the Cu bulk heat of sublimation ($\Delta H_{sub} = 337$ kJ/mol) at > 4 monolayers coverage. Interestingly, the Cu coverage required to reach ΔH_{sub} decreases as the ceria surface is reduced. These results indicate that Cu adsorbs more strongly to ceria terraces than to oxygen vacancy sites, since the primary defect for reduced ceria surfaces is oxygen vacancies, but weakens the Cu-Cu bond for particles nucleated at terraces. The growth modes of Cu on $CeO_{2-x}(111)$ was also studied by XPS, ISS and AES. It was found that Cu grows as three dimensional particles on ceria. At 100 K the Cu particle density increased compared to 300K with a similar initial heat of adsorption, but took longer to reach the Cu heat of sublimation. The sticking probability was near unity for Cu adsorption on all these surfaces.

4:40pm **AS+BI+EM+NL+NS+SS-ThA9 Complimentary XPS and AES Analysis of MoS₃ Solid Lubricant Coatings**, *J.R. Lince*, The Aerospace Corporation, *S.S. Alnabulsi, D.F. Paul, J.F. Moulder, J.S. Hammond*, Physical Electronics Inc.

Molybdenum disulfide (MoS_2) nanoparticles are an ideal additive in solid coating for lubricating mechanisms in vacuum environments, with widespread application in the spacecraft industry. The formation of these nanoparticles can be complex, and the use of MoS_3 nanoparticles, which are produced using a simple wet chemical synthesis is being explored as an alternate approach.¹ The use of MoS_3 as a tribological material has not been explored beyond its use as an oil additive.² There is new interest in investigating its potential for use in solid lubricant coatings.

To aid in the evaluation of the tribological performance of a MoS_3 -formulated coating compared to MoS_2 based coatings, X-ray photoelectron spectroscopy (XPS) and Auger electron spectroscopy (AES) are utilized as complimentary techniques for the surface characterization of the contact wear regions created on the coating surface.

The unique scanning micro-focused monochromatic x-ray source was used to provide x-ray excited secondary electron images that help reveal

topographical and surface chemical information which aid in resolving and pinpointing the analysis area of interest within the contact region of the wear track that is 50 μm to 100 μm wide. The micro-XPS results provided quantitative chemical characterization that complement high spatial resolution imaging AES analysis of the sub 100 nm molybdenum sulfide particles.

Tribometer testing showed the MoS₃-formulated coating perform similar to the MoS₂-based coatings, with similar coefficients of friction and endurance in dry nitrogen. MoS₃ nanoparticles produced using simple wet chemical synthesis, and the tribology of resin-bonded MoS₃ nanoparticle coating is comparable to similarly prepared bonded coatings containing MoS₂. The surface analysis results show a lubricating effectiveness that is consistent with the production of a thin film of MoS₂ in the contact region, with an increase in the presence of sulfide relative to polysulfide in the wear track and surface segregation of lubricating species.

We will present results of micro-area XPS and AES surface analyses on worn coatings to reveal changes in composition and chemical state of the coating surface, which might explain the observed friction results of the mechanical testing.

References

P. Afanasiev, "Synthetic approaches to the molybdenum sulfide materials," *Comptes Rendus Chimie*, 11(1-2) (2008) 159-182.

O.P. Parenago, V.N. Bakunin, G.N. Kuz'mina, A.Yu. Suslov, and L.M. Vedeneva, "Molybdenum Sulfide Nanoparticles as New-Type Additives to Hydrocarbon Lubricants," *Doklady Chemistry*, 383(1-3) (2002) 86-88.

Biomaterial Interfaces

Room: 102 B - Session BI+AS+BA+NS+SS-ThA

Biomolecules at Interfaces

Moderator: S.M. McArthur, Swinburne University of Technology, Australia

2:00pm **BI+AS+BA+NS+SS-ThA1 The Protein Resistance Properties of Hydroxy- and Methoxy-terminated Oligo(ethylene oxide) (OEO) Self-Assembled Monolayers (SAMs) to Membrane Proteins, M. Walker, National Institute of Standards and Technology (NIST), A. Vaish, D. Vanderah, National Institute of Standards and Technology (NIST) and Institute of Bioscience and Biotechnology Research**

Spectroscopic ellipsometry was used to evaluate the resistance to protein adsorption of self-assembled monolayers (SAMs) of HS(CH₂)₃O(CH₂CH₂O)_nM and [HS(CH₂)₃]₂CHO-(CH₂CH₂O)_nM, where M = CH₃ or H, on Au. The SAMs were exposed to fibrinogen, a soluble protein frequently used to evaluate surface protein resistance properties, and rhodopsin, an integral membrane protein. We show that the nature of the oligo(ethylene oxide) end group governs the extent of protein adsorption resistance of OEO SAMs to integral membrane proteins.

2:20pm **BI+AS+BA+NS+SS-ThA2 A Bottom-up Approach for Creating Biomimetic Surfaces with Defined Nanotopographic Structure and Surface Chemistry, N.P. Reynolds, K.E. Stryan, C. Easton, CSIRO Materials Science & Engineering, Australia, R. Mezzenga, ETH Zürich, Switzerland, B. Muir, P. Hartley, CSIRO Materials Science & Engineering, Australia**

Interactions of tissue cells with their local microenvironment (the extracellular matrix) can be split into three distinct categories: 1) Physical interactions, such as cellular responses to elasticity or stiffness, 2) chemical interactions, with specific epitopes contained within the extracellular matrix, and 3) topographical interactions with the nanoscale fibrous proteins that make up the majority of the extracellular matrix. In order to study how these interactions affect cell physiology *in vitro*, biomimetic substrates can be designed to reproduce these interactions. Whilst there have been multiple examples of substrates that accurately mimic chemical and physical interactions, the effects of truly biomimetic topographies are less well explored.

We show for the first time it is possible to use networks of self-assembled amyloid fibers as templates for the deposition of plasma polymers under high vacuum conditions. The nanoscale topography of the underlying amyloid networks is replicated on the top surface of the polymers with remarkable fidelity, resulting in a chemically homogenous surface with well-defined nanoscale surface features that mimic the topography of the extracellular matrix. The culture of fibroblast cells on these substrates resulted in an increased cell attachment and spreading compared to flat polymer films. We show evidence that the increase in favorable cell spreading was caused by a stabilization of adsorbed serum proteins

(including fibronectin) by the nano-topography. Thus, we hypothesize that the reduced denaturation of proteins on the nano-topographical substrates results in matrix adhesion moieties (e.g. the RGD sequence) being presented to the cell membrane in a more physiological orientation. This templating technique allows for the rapid and reproducible fabrication of substrates with nanoscale biomimetic topography. We believe that such surfaces will have applications in the development of new biomaterials that will allow the routine investigation of physiological nanoscale morphology on cellular phenotype.

N.P. Reynolds et. al., "Nano-topographic surfaces with defined surface chemistries from amyloid fibril networks can control cell attachment" *Biomacromolecules*, 2013, DOI: 10.1021/bm400430t.

2:40pm **BI+AS+BA+NS+SS-ThA3 Nanoscale Imaging of Peptide-Membrane Interactions, P.D. Rakowska, National Physical Laboratory, UK**

Antimicrobial peptides (AMPs) are attracting growing attention as efficient anti-infective agents in the post-antibiotic era. However, the detailed molecular mechanisms of their action and precise rationale for their selectivity remain poorly understood.

Here we will present our recent findings, highlighting specific membrane-mediated mechanisms of AMPs, which we probed using a de novo designed archetypal AMP and imaged using a combination of Atomic Force Microscopy (AFM) and high-resolution Secondary Ion Mass Spectrometry (NanoSIMS). This approach provides unique information on the topography of peptide-treated membranes, obtained from AFM images, suggesting membrane changes as a result of peptide structuring and pore formation. The data is complemented by chemical imaging performed on the same samples with NanoSIMS, which revealed the precise localization of peptide molecules in the membranes.

This comparative topographical and chemical imaging gives the first evidence of antimicrobial pore expansion that was further strengthened by AFM imaging in real time in liquid, and supported by microbiological and biophysical studies as well as molecular dynamic simulations.

Relevant publication:

Rakowska, P. D., Jiang, H., Ray, S., et al. Nanoscale imaging reveals laterally expanding antimicrobial pores in lipid bilayers. *Proc. Natl. Acad. Sci. USA*, 2013, 110, in press.

3:00pm **BI+AS+BA+NS+SS-ThA4 Development of Molecular Modeling Capabilities in LAMMPS Specifically Designed for the Efficient and Accurate Simulation of Biomolecule-Surface Interactions, R.A. Latour, Clemson University, C.D. Lorenz, King's College-London, UK**

The ability to understand and predict the interactions of tethered or adsorbed biomolecules (e.g., protein, DNA, carbohydrates) at material interfaces represents a critical need for many applications in bionanotechnology and biomedical engineering. Experimental methods alone are typically very limited in terms of their ability to probe the molecular level of detail needed to quantitatively understand these types of complex interfacial interactions. As a result, biomaterial systems must often largely be designed by trial-and-error approaches. Molecular simulation methods provide an excellent means to complement experimental studies to provide theoretical assessment and predictive capability of the behavior of biomolecules at interfaces with atomic-scale resolution. These methods, however, must be specifically designed and developed for biomaterial applications. The Latour group has focused on the development of molecular simulation methods for the efficient and accurate simulation of protein-surface interactions over the past two decades, mostly involving the CHARMM molecular simulation program. Over the past year, we have focused on transitioning from CHARMM to the LAMMPS molecular simulation program for our continued development work in collaboration with the Lorenz group at King's College-London. LAMMPS (Large-scale Atomic/Molecular Massively Parallel Simulator) is a fast, versatile, and highly parallelizable molecular simulation program with excellent capabilities for materials modeling. It is also freely available for download from the primary developer's website (Sandia National Laboratory, <<http://lammps.sandia.gov/>>). Over the past year, we have been developing new LAMMPS modules that are specifically being designed to support the efficient and accurate simulation of protein-surface interactions, with planned extension to other biomolecule systems. In this presentation, we will provide an overview of the developed capabilities in the LAMMPS program, with demonstrated applications to simulate protein-surface interactions at the atomic level. The development of these molecular simulation modules in LAMMPS has the potential to revolutionize current capabilities to accurately simulate, predict, and understand mechanisms governing biomolecule interactions at material interfaces and to serve as a valuable tool for system design.

3:40pm **BI+AS+BA+NS+SS-ThA6 Dynamic Nanomaterials for Diagnostics and Drug Delivery.** *P. Stayton*, University of Washington
INVITED

Our group develops stimuli-responsive nanomaterials that utilize dynamic structural and architectural transitions to enable new drug delivery and diagnostic functionalities. For drug delivery applications we are focused on opening the intracellular target universe to biologic drugs. Biologic drugs such as DNA, RNA and proteins have significant therapeutic potential, but effectively formulating and delivering them remains a widely recognized challenge. Barriers include drug stability, tissue penetration and transport, but cytoplasmic entry is a widespread barrier for those that function against intracellular disease targets. We have been developing synthetic polymeric carriers that mimic the highly efficient intracellular delivery systems found in pathogenic viruses and organisms. Another important aspect of these polymeric carriers is the development of controlled polymerization techniques to streamline bioconjugation of targeting agents and therapeutics, as well as to generate controlled carrier architectures. The carriers might open up new families of peptide, antibody or nucleic acid drug candidates that attack previously inaccessible intracellular targets. For diagnostic applications we are addressing the technology gap for making clinical assays faster and more sensitive, as well as the need for simple yet efficient sample handling techniques that concentrate dilute biomarkers for point-of-care (POC) tests. We have developed a new stimuli-responsive magnetic nanoparticle reagent system for achieving both of these goals. These new bioanalytical systems are being applied to clinical lab assays, lab card disposable devices and for non-instrumented lateral flow diagnostic platforms.

4:20pm **BI+AS+BA+NS+SS-ThA8 Determination of Orientation and Tertiary Structure of Adsorbed Protein on Material Surfaces by Chemical Modification and Peptide Mapping.** *A.A. Thyparambil, Y. Wei, R.A. Latour*, Clemson University

Chemical modification of targeted amino acid residues with peptide mapping via mass spectrometry (MS) is a promising technique to provide highly detailed information on the structural shifts and orientation of adsorbed protein by revealing adsorption-induced changes in amino acid solvent accessibility. A decrease in amino acid labeling (i.e., decreased solvent accessibility) is indicative of adsorbed orientation while an increase is indicative of tertiary unfolding. However, the potential of this method for the study of adsorbed protein structure is largely undeveloped at this time. The objective of our research was therefore to develop chemical modification and peptide mapping techniques that would help identify the dominant configuration of adsorbed protein on a material surface for a range of amino acid types. By directly comparing the extent of amino acid modification (profiles) from separate batch experiments targeting different types of amino acids, a fairly detailed picture of adsorption-induced changes in adsorbed protein structure can be obtained. In our current study, when unmodified segments of the protein without the targeted amino acid from the MS results was used as an internal standard for each of the batch experiments, a common baseline to directly compare the profiles of different amino acids could be obtained. Under these conditions, the configuration of hen egg white lysozyme (HEWL) when adsorbed on fused silica glass (glass), high density polyethylene (HDPE), and poly(methyl-methacrylate) (PMMA) was mapped by directly comparing the profiles of arginine (Arg), lysine (Lys), tryptophan (Trp), and carboxylic groups (Asp, Glu, C-terminus). For each of the targeted amino acid groups, the labeling procedure did not induce significant structural shifts, which was verified by circular dichroism spectropolarimetry. The resulting quantitative differences in the profiles of targeted amino acid residues in HEWL on different surfaces under different conditions correspond to different configuration of HEWL on each adsorbent surface. The developed technique has the potential for broad application and to be expanded to other targeted amino acids, thus providing highly detailed information on the adsorbed state of protein on any given surface.

4:40pm **BI+AS+BA+NS+SS-ThA9 Exploring the Formation, Lifetime and Dissociation Statistics of Acid-Amine Bonds.** *S. Raman, M. Valtiner*, Max Planck Institute für Eisenforschung GmbH, Germany

Acid-amine interactions are non-covalent, long-range interactions, contributing to the structural integrity in manmade adhesives and to serve complex life functions in several biological systems. Understanding how these interactions develop and alter over time in an aqueous environment, especially when presented across an interface, is vital when it comes to designing functional surfaces for biomedical applications. We use single molecule force spectroscopy to investigate the contact dynamics of molecular bonds under near-physiological conditions. We explore the interactions of NH₂/COOH bonds that are presented across the atomic force microscopy (AFM) tip-surface interface, with much focus on the dissociation of these bonds by studying specific signatures obtained during the force measurements[#]. Since the approach permits us to have an exquisite

of control over the interface, a number of experimental parameters are varied such as the number density of the molecules, ionic strength of the surrounding medium and extension/retract speed of the tip to vary the loading rate. A statistical evaluation of the interactions and contact dynamics is discussed to assess the influence of the experimental parameters on the bond dissociation. The transition rate under zero-load conditions is calculated combining the detachment statistics and Kramer-Evans theory. Our results provide new insights into the binding regime and dissociation behavior of acid-amine bonds from non-equilibrium to near-equilibrium conditions as a function of the loading rate on a logarithmic scale in aqueous environments of varying ionic concentration.

[#] M Valtiner, SH Donaldson, MA Gebbie, JN Israelachvili, *J. Am. Chem. Soc.*, 2012, 134, pp 1746-1753.

5:00pm **BI+AS+BA+NS+SS-ThA10 Thiolene Reaction Applied to Different Metal Oxide Surfaces: Role of Short and Long PEG-terminated Chains on Biomolecules Solution Adsorption.** *A. Galtayries, A. Dellinger*, Chimie ParisTech, France, *V. Semetey*, Institut Curie, France

The control of biomolecules adsorption (such as proteins) and other microorganisms is of high interest for various fields of biotechnology, such as bioanalytics, cell biology, tissue engineering and biomaterials. A simple and efficient method to control adsorption includes the use of the thiolene chemistry to form self-assembled monolayer (SAM) from commercial long (poly(ethylene glycol)) and short (oligo-ethylene glycol) terminated chains, applied on metal oxide surfaces [1].

Both on silicon, titanium and iron-chromium substrates, we selected two polymers either with short or long chains: one is adhesive, the other one is non-adhesive once in interaction with solutions of biomolecules. As regards short-chain molecules, the adhesive O-(2-Mercaptoethyl)-O'-methyl-hexa(ethylene glycol) and the adhesive O-(2-Carboxyethyl)-O'-(2-mercaptoethyl) heptaethylene glycol further activated by reaction with N-hydroxysuccinimide (NHS) were selected for grafting strategies implying full surface grafting or adhesive/non adhesive patterning (100 micrometer-large bands or half-moon surfaces). Similarly, as long-chain molecules, poly(ethylene glycol) methyl ether with an average molecular weight of 5,000 have been used, adhesive ones being NH₂-terminated.

With such molecular selection, we performed a systematic study using surface characterization techniques such as X-ray Photoelectron Spectroscopy (XPS), Time of Flight Secondary Ion Mass Spectrometry (ToF-SIMS) and Infra-Red Surface Spectroscopy (ATR-IRFT or PM-IRRAS): at different steps of the grafting process, as well as after interaction with protein solutions, surface qualitative as well as quantitative information were obtained to discuss the efficiency of these molecular strategies to build biointerfaces on metal oxide surfaces.

[1] "A Facile and Versatile Approach to Design Self-Assembled Monolayers on Glass using Thiol-ene Chemistry", B. Oberleitner, A. Dellinger, M. Déforet, A. Galtayries, A.-S. Castanet, V. Semetey, *Chemical Communication*, 49, 1615-1617 (2013).

5:20pm **BI+AS+BA+NS+SS-ThA11 Immobilization of Peptide-Based Stimuli-Responsive Biomolecules on Silica Surfaces.** *L. Li, O. Im, J. Harris, W. Han, A. Chilkoti, G.P. López*, Duke University

The immobilization of stimuli-responsive biomacromolecules onto silica surfaces is often performed the development of silica-based biosensors, protein microarrays and supramolecular assemblies. The R5 silaffin peptide, derived from *Cylindrotheca fusiformis*, is of current interest because of its capacity to induce and regulate silica precipitation at ambient conditions. In this study, we found that a fusion protein comprised of a synthetic silaffin R5 peptide and elastin-like polypeptide (ELP) bound reliably to silica particles and flat silica-based surfaces. ELPs are a class of stimuli-responsive polypeptides that undergo a reversible lower critical solution temperature (LCST) phase transition. In silaffin-ELP fusion proteins, the R5 peptides serve as silica-binding domains that immobilize ELPs onto silica, allowing its surface properties to be modulated upon change in temperature through the LCSTs of the ELPs. The attachment of silaffin-ELP to silica particles was confirmed by temperature- and time-dependent turbidity, zeta potential, and dynamic light scattering measurements. As demonstrated through zeta potential measurements, the positively charged silaffin-ELPs neutralized the negative charge on the silica particles, confirming the binding of silaffin-ELPs. Dynamic light scattering experiments revealed an increase in particle size after surface modification. The sizes of surface-modified particles also changed in response to temperature. We also investigated the absorption of silaffin-ELP on oxidized silicon wafers. The elemental composition of the protein-modified surfaces was characterized by X-ray photoelectron spectroscopy. We also used ellipsometry and atomic force microscopy (AFM) to test the thickness and roughness of the protein bound surfaces. Contact angle measurements were performed to examine the temperature-responsive nature of the surfaces. Furthermore, we demonstrated that GFP-ELP fusion protein can be adsorbed to silaffin-ELP

modified silica surface through co-aggregation above their LCSTs. A thermally triggered aggregation behavior of fluorescently-labeled silica particles was also visualized using confocal fluorescence microscopy. The results of this study demonstrated that a silaffin tag can be used to immobilize ELPs on silica surfaces such as silica particles, silicon wafers and glass slides, and that these protein-modified surfaces can be used to capture and immobilize ELPs and ELP-fusion proteins reversibly onto their surfaces. This system has potential uses in bioseparations, biomaterials, and biosensors.

5:40pm **BI+AS+BA+NS+SS-ThA12 Microfluidic Extraction and Labeling of Methylated DNA from Small Cell Populations for Single-Molecule Analysis, J. Benitez, J. Topolancik, H. Tian, C. Wallin, V. Adiga, P. Murphy, J. Hagarman, P. Soloway, H.G. Craighead,** Cornell University

We describe a microfluidic device for the extraction, labeling, and purification of human chromosomal DNA from single cells and small cell populations. The extracted and labeled material was quantified using single-molecule fluorescence analysis in nanofluidic channels. A two-dimensional array of micropillars in a microfluidic polydimethylsiloxane (PDMS) channel was designed to capture cells. Megabase-long DNA strands released from the cell upon lysis are trapped in the micropillar array and stretched under optimal hydrodynamic flow conditions. Chromosomal DNA is immobilized in the array, while other cellular components are washed away from the channel. To assess DNA methylation, genomic DNA from different cell types was extracted using the device and labeled on-chip with methyl-CpG binding domain 1 (MBD1) protein. MBD1-bound DNA was released from the device and directly transferred to a nanofluidic channel for single-molecule detection of MBD1 molecules. Individual DNA fragments and MBD1 proteins were driven electrophoretically through the nanofluidic channels. The photon counts obtained from each MBD1 detection event are directly proportional to the total number of MBD1 molecules. By quantifying the amount of bound MBD1 molecules, the DNA methylation abundance of each cell type can be assessed and compared. This methodology provides a means for epigenetic fluorescence analysis of small cell populations with single-molecule resolution, extendable to single cells.

Electronic Materials and Processing

Room: 101 B - Session EM2-ThA

Non-traditional Inorganic Semiconductors

Moderator: S. Durbin, University at Buffalo-SUNY, D.O. Scanlon, University College London, UK

2:00pm **EM2-ThA1 Electronic Structure and Defect Chemistry of II-IV-V₂ Semiconductors, D.O. Scanlon,** University College London, UK
INVITED

The drive to replace indium in optoelectronic devices, and to move away from toxic materials such as CdTe in photovoltaics has focused attention on semiconductors featuring affordable and abundant elements. Recently, both ZnSnP₂ and ZnSnN₂ have emerged as leading candidates for earth abundant photovoltaics.[1,2] In this presentation we discuss the electronic structure and defect chemistry of these two materials, and specifically the role of intrinsic defects in controlling the native conductivity. The possibility of tuning the polarity of the conductivity by varying growth environments or via incorporation of extrinsic impurities will also be discussed.

- [1] D. O. Scanlon and A. Walsh, "Bandgap engineering of ZnSnP₂ for high efficiency solar cells", *Applied Physics Letters*, 100, 251911 (2012)
- [2] N. Feldberg, B. Keen, J. D. Aldous, D. O. Scanlon, P. A. Stampe, R. J. Kennedy, R. J. Reeves, T. D. Veal and S. M. Durbin, "ZnSnN₂: A new earth-abundant element semiconductor for solar cells", *Photovoltaic Specialists Conference*, 38, 002524 (2012)

2:40pm **EM2-ThA3 The Role of Native Defects in the Electrical Conductivity of Metal-Oxide Semiconductors, A. Janotti,** University of California, Santa Barbara
INVITED

Oxide semiconductors exist in a variety of crystal structures, exhibiting a wide range of bonding environments and electronic behavior. For instance, ZnO (wurtzite), In₂O₃ (bixbyite), and SnO₂ (rutile) all support high levels of *n*-type conductivity and are highly transparent to visible light, making them excellent transparent conductors. TiO₂ (rutile and anatase) and SrTiO₃ (STO, perovskite) are prototype wide-band-gap transition-metal oxides, widely studied for catalysis and, in the case of STO, often used as a substrate for high-T_c superconductors and other oxides. STO is also at the core of recently fabricated complex-oxide-based heterostructures that display two-dimensional electron gases (2DEGs) with high carrier densities.

As in any semiconductor, native defects are expected to greatly influence the electronic properties of these oxides. In particular, oxygen vacancies have been invariably invoked as a source of unintentional *n*-type conductivity, based on annealing experiments. In this talk, the role of native defects in oxide semiconductors will be revisited from the perspective of first-principles calculations. The donor or acceptor character, the likelihood of defects to form as a function of Fermi-level position and chemical potential, and defect-related optical transitions will be discussed. The possibility of *p*-type doping will also be addressed.

This work was performed in collaboration with C. G. Van de Walle, J. L. Lyons, M. Choi, L. Bjaalie, and J. B. Varley, and supported by ARO and NSF.

3:40pm **EM2-ThA6 Electronic and Lattice Dynamical Properties of II-IV-N₂ Semiconductors, W.R. Lambrecht, A. Panya,** Case Western Reserve University
INVITED

An overview will be presented of our recent results on the electronic band structures and lattice dynamical properties of the II-IV-N₂ semiconductors. The electronic band structure of ZnSiN₂, ZnGeN₂, ZnSnN₂ and CdGeN₂ were obtained using the quasiparticle self-consistent GW approximation using the full-potential linearized muffin-tin orbital method for the orthorhombic wurtzite based structure. They are found to span band gaps from the red to the UV with CdGeN₂ having a gap in the green region of the spectrum. Zero point motion corrections of the band gap were estimated as well as exciton binding energies. Comparisons with experimental data are discussed. We also studied the band structure of ZnSnN₂ in a few alternative structures and find that the gap can be strongly reduced if besides tetrahedrons of two Zn and two Sn, also tetrahedrons with 1 Zn and 3 Sn or vice versa occur. The splittings of the valence band maximum and the effective masses and generalized Kohn-Luttinger parameters were determined. Spin-orbit splittings are found to be very small. The band offsets between ZnGeN₂, ZnSnN₂, GaN and ZnO were calculated from interface calculations for different interfaces and indicate an interesting type-II alignment between ZnGeN₂, GaN and ZnO. The vibrational spectra were obtained using density functional perturbation theory in a previous series of papers. Infrared and Raman spectra were predicted and compared with the available experimental data. In ZnGeN₂ besides the expected peaks for first-order allowed Raman, some additional features are seen in the experimental spectra. We show that these can either be due to disorder induced Raman scattering or to forbidden LO modes and further experimental work using resonant Raman spectroscopy would be useful to distinguish between the two cases. Preliminary results on native point defect calculations will be presented. The difference in energy of formation of the Ge₃N₄ and Sn₃N₄ changes the allowed window for chemical potentials of Zn and Ge or Sn. These in turn may have an important effect on the dominant point defects. The prospects for *p*-type doping are given particular attention. Z_NGe₂ antisites, V_{Zn} and V_{Ge} are all three found to behave as acceptors while Ge_{Zn} and V_N are donors. The relative stability of Ge₃N₄ together with the requirement to stay on the N-rich line, implies that one cannot make the samples very Ge-rich. This is however favorable for doping Ga on Ge sites which is a potential route to effective *p*-type doping.

4:20pm **EM2-ThA8 Novel Nitrides and Bismides: Growth and Optical Properties, T.D. Veal,** University of Liverpool, UK
INVITED

Recent research on the growth by MBE and optical properties of two classes of novel highly mismatched semiconductor will be presented, namely, dilute nitride antimonides and dilute bismide antimonides. These have potential applications ranging from thermophotovoltaics within the 2-4 micron range to night vision in the 8-14 micron IR transmission window. The incorporation of N in GaSb, GaInSb and InSb as a function of temperature and growth rate is investigated using x-ray diffraction, secondary ion mass spectrometry and kinetic modelling. For GaNSb, the optical properties are studied by absorption spectroscopy. In addition to providing evidence of the well-known band anticrossing interaction between the N localized states and the host GaSb conduction band, a strong influence of both lifetime broadening and N pair states is apparent. Meanwhile, incorporation of Bi is a little-explored approach to band gap and lattice constant tuning for GaSb and related materials, in spite of intensive recent studies of GaAsBi and sporadic study of InSbBi over the last thirty or so years. Alloying with Bi offers the potential to reduce the band gap more effectively than with indium (and may even be used in conjunction with N alloying), enabling greater valence band offsets for enhanced hole confinement and also increased spin orbit splitting. Here, MBE growth is reported of GaSbBi with Bi occupying in excess of 3% of the group V sublattice, as estimated from the increase in lattice constant determined by x-ray diffraction. This contrasts markedly with previous reports of GaSbBi MBE growth where lattice contraction was observed upon Bi incorporation and the maximum Bi content, from Rutherford backscattering, was only 0.7%. Our MBE growth study explores the Bi incorporation dependence upon the Bi flux, substrate temperature and

growth rate and is compared to our Ga(In)NSb results. The influence of the Bi alloying on the band gap is also reported from Fourier transform infrared optical absorption measurements. The results are compared with predictions of both the lattice parameters and band gaps from our density functional theory calculations employing hybrid functionals. This research is performed principally in collaboration with the University of Warwick, UK, and University College London and is supported by EPSRC grant EP/G004447/2.

5:00pm **EM2-ThA10 Single Crystal Growth of ZnSnN₂ by Molecular Beam Epitaxy**, *N. Feldberg, J.D. Aldous*, University at Buffalo, *W.M. Linhart, T.D. Veal*, University of Liverpool, UK, *P.A. Stampe, R.J. Kennedy*, Florida A&M University, *D.O. Scanlon*, University College London, UK, *L.F.J. Piper*, Binghamton University, *L. Schweidenback, A. Petrou, S. Durbin*, University at Buffalo

Over the past decade indium has experienced significant price fluctuations due to limited supply and increasing demand; these factors have motivated the search for alternative semiconductor materials based on earth-abundant elements. Such materials should still have a direct tunable bandgap similar to existing indium-containing semiconductor compounds. One candidate which may exhibit these desirable properties is ZnSnN₂. In addition to the abundance and low price of the constituent elements, Zn and Sn benefit from a well-established recycling infrastructure. Little is known about the properties of this material, however it is predicted to have a band gap near 2.0 eV. This band gap should be tunable through alloying with either wider or narrower band gap members of the Zn-IV-N₂ family, making it attractive for a range of optoelectronic device applications. The crystal structure of ZnSnN₂ is derived from that of InN through an ordered substitution of Zn and Sn on the In sublattice. The resulting structure is predicted to be orthorhombic due to the different metal-N bond lengths distorting the wurtzite structure of InN.

A series of ZnSnN₂ films have been grown via plasma-assisted molecular beam epitaxy (PAMBE) on (111)-oriented yttria-stabilized zirconia and LiGaO₂(001) substrates. Regardless of substrate type and growth conditions, all films exhibit a monoclinic structure based on x-ray diffraction (XRD) and supported by reflection high energy electron diffraction (RHEED). The crystallization in a monoclinic structure can be explained by the existence of a disordered cation sublattice. Similar lattice arrangements have been observed to occur in related compounds ZnGeN₂ [1] and ZnSnP₂ [2] in the presence of varying degrees of cation ordering. We have found that growth of high quality single crystal epitaxial films is dependent on having a high Zn:Sn flux ratio. Single crystal films were observed for flux ratios in excess of 20:1. The need for such an extremely large overpressure of Zn is expected due to the significant difference in vapor pressures between Zn and Sn. Hall effect and optical absorption suggest a variation in band gap energy as a function of crystal quality beyond expectations for Moss-Burstein and band gap renormalization effects, which is consistent with density functional theory predictions.

This project is supported by NSF grant DMR1244887 (Program Director Charles Ying), and EPSRC grant EP/G004447/2.

1. I. W. R.L. Lambrecht, E. Alldredge, and K. Kim, Phys. Rev. B **72** (2005) 155202.
2. D.O. Scanlon and A. Walsh, Appl. Phys. Lett. **100** (2012) 251911.

5:20pm **EM2-ThA11 Growth and Characterization of Zn-IV-Nitride Semiconductors**, *K. Kash, P. Quayle, E. Blanton*, Case Western Reserve University

INVITED

The Zn-IV-nitrides, Zn(Si,Ge,Sn)N₂ form a family of three ternary semiconductors that, although closely related to the III-nitrides AlN, GaN and InN, have elicited relatively little interest until recently. One reason is surely the great success of the III-nitrides as optoelectronic materials. In addition, while the two higher-bandgap members of the family, ZnSiN₂ and ZnGeN₂, were first synthesized over four decades ago, it was not until the last couple of years that ZnSnN₂, the low-bandgap analogue to InN, was reported. Further investigation of these materials has several motivations, including the promise of strategies for circumventing some of the lingering problems associated with the III-V materials, as well as predictions of interesting properties that are markedly different, in potentially useful ways, from those of the III-V materials. In this talk, we will describe the results of vapor-liquid-solid growth of ZnGeN₂ and ZnSnN₂, using either ammonia or plasma-activated nitrogen as the nitrogen source. These growth methods have produced high quality polycrystalline material that has made possible the investigation of some of the fundamental properties of these materials, including precise experimental determinations of their band gaps. The investigations have also yielded information relevant to the phase diagrams of the Zn-IV-N systems. In particular, conditions under which Zn₃N₄, Sn₃N₂, or ZnSnN₂, separately, are produced, have been defined. Finally, the characteristic Raman spectra of both ZnSnN₂ and ZnGeN₂ show evidence of varying degrees of phonon localization that correlate with the occurrence of

“exchange defects”; that is, the exchange of ions between the group II and group IV sublattices, detected through their influence on the x-ray diffraction spectra. For ZnGeN₂, we show that the degree of II-IV sublattice disorder--the density of these exchange defects--can be controlled via the choice of growth conditions.

This work was done in collaboration with Jie Shan, Keliang He, Hongping Zhao and Lu Han.

Electronic Materials and Processing Room: 102 A - Session EM-ThA

Materials and Process for Advanced Interconnects II Moderator: S.W. King, Intel Corporation, E. Mays, Intel Corporation

2:00pm **EM-ThA1 Electrically Detected Magnetic Resonance of Deep Level Centers in SiCN:H Dielectrics**, *M. Mutch, P.M. Lenahan*, Penn State University, *S.W. King*, Intel Corporation

SiCN:H films have great promise as etch stop layers in interlayer dielectric structures [1]. Unfortunately, very little is known about the physical mechanisms of electronic transport in these materials. In this study we have utilized variable field electrically detected magnetic resonance (EDMR) almost certainly via spin-dependent trap-assisted tunneling (SDT) in variable range hopping [2]. Our results are of significance for several reasons. First, they demonstrate that SDT/EDMR is sensitive enough to detect defects involved in transport within these films. The simple observation of an EDMR spectrum undoubtedly links the defects responsible for the spectrum to electronic transport. Secondly, they provide information about the physical and chemical nature of the defects involved of transport within the films.

The films studied were deposited via PECVD and have a composition of 45% Si, 29% C, 23% N and 3% O. The SDT/EDMR measurements were taken on a home-built X-band (≈ 9.5 GHz) EDMR spectrometer at room temperature utilizing specially thinned SiCN:H films deposited on p-type silicon with titanium electrode. We observe quite strong SDT/EDMR traces with a zero crossing of $g = 2.003$ and a peak-to-peak line width of 14 Gauss. (The g is determined by the expression $g = hv/(\mu_B B)$, where h is Planck's constant, ν is microwave frequency, μ_B is the Bohr magneton and B is the magnetic field at resonance. We find that the SDT/EDMR response is quite strongly voltage dependent and find a fractional contribution of the SDT/EDMR response to be highly asymmetric, with a much larger $\Delta I/I$ corresponding to negative gate polarity. It is clear that the paramagnetic sites observed to not involve electron wave function primarily localized on either hydrogen or nitrogen as both of these nuclei have virtually 100% abundant isotopes with nuclear moments [3]. The zero crossing of $g = 2.003$ and a 14 G line width are essentially a perfect match with the well characterized EPR spectrum of K-centers, silicons back-bonded to three hydrogens. The K-centers have been studied extensively in silicon nitride [4, 5]. We thus tentatively assign the observed EDMR to K-centers and also tentatively conclude that the K-centers are important defects in transport in SiCN:H films under study.

- [1] J. Martin et. al, IEEE Proceedings, vol., no., pp. 42, 44 (2002).
- [2] J.T. Ryan et. al, J. Appl. Phys., vol 108, 064511 (2010).
- [3] J. Weil et. al, **Electron Paramagnetic Resonance**. Wiley-Interscience (1994).
- [4] D.T. Krick et. al, J. Appl. Phys. **64**, 3558 (1988)
- [5] P. M. Lenahan et. al, Appl. Surf. Sci. **39**, 392 (1989).

2:20pm **EM-ThA2 Effect of Hybrid Cleaning in Mitigating Low-k Damage for Critical BEOL Applications at 20 nm Node and Beyond**, *N. Mohanty, J. Stillahn, Y.P. Feurprier, T. Yoshida, T. Yamamura, L. Wang, Y. Chiba, K. Kumar, D.M. Morvay, P. Biolsi*, TEL Technology Center, America, LLC, *S. Mishra, W. Hwang, M. Wang*, GLOBALFOUNDRIES U.S. Inc.

Integration of low-k dielectrics ($k \leq 2.7$) into the fabrication of interconnects in integrated circuits has enabled the reduction of RC time delays, opening the path for continued scaling. Typical porous low-k dielectrics are formed by plasma-enhanced chemical vapor deposition and contain a significant amount of Si-CH_x groups. For the ubiquitous trench-first metal hard mask dual damascene scheme, etching of the via holes into the low-k dielectric is mostly achieved using a fluorocarbon chemistry, after which a cleaning step is needed for concomitant in-situ removal of etch residues as well as the top organic mask for subsequent underlying trench pattern transfer. The cleaning step can either be reductive (N₂, H₂ containing feed gas) or oxidative (O₂, CO₂, CO containing feed gas).

Owing to their higher reactivity, mild oxidative chemistries comprised of CO₂ feed gas have been the predominant chemistry of choice industry-wide, which minimizes the depletion of -CH_x groups known as low-k damage while maintaining reasonable etch rates. However, as the industry moves on to advanced technology nodes (sub 20 nm nodes), even minor damage during the cleaning step becomes highly undesirable due to increased RC delay and diminished reliability. This talk will present the successful mitigation of low-k damage as compared to standard cleaning processes through the use of a novel two-step hybrid cleaning strategy. This two-step hybrid cleaning strategy leverages unique hardware solutions with the reactive ion etching efforts for reducing low-k damage.

2:40pm EM-ThA3 Cu Interconnects at 1x Node - Challenges & Approaches, S. Kesapragada, K. Shah, Applied Materials, Inc. INVITED

While much attention is focused on transistor innovation, it is interconnect performance that is

also now challenging Moore's law because of its performance and scaling limitations. The last

time interconnects were overhauled for performance reasons was more than 15 years ago when

aluminum was replaced with copper interconnects fabricated in the revolutionary dualdamascene

architecture.

Copper dual-damascene interconnects provided superior lower resistance, and the incorporation

of porous low-k dielectrics into this architecture drove down the capacitance – together these two

materials have reduced RC delay and reduced energy consumption. However, the reduction of

the low-k dielectric constant has slowed in recent years. As they become more porous, these

dielectric materials become fragile, unable to cope with the mechanical stress that chips undergo

during packaging. They are not robust enough to maintain their low-k properties through the

dual-damascene process integration steps. In addition, the resistance of the interconnect is rising

dramatically because of three main factors: (i) the conventional tantalum nitride/tantalum highresistance

metallic barriers that block copper diffusion and prevent oxidation are taking up a

larger fraction of the metal interconnect cross-section, (ii) surface scattering increases as the

critical dimensions of the wires become smaller than the bulk mean free path of the electrons,

and (iii) grain boundary scattering increases as the copper grain size scales approximately with

the critical dimensions of the wires in dual-damascene fabricated interconnects. Hence, the RC

delay for interconnects has started to rise dramatically as the node shrinks beyond 22nm, driven

by the rise in resistivity for conventional damascene copper interconnects. This presentation

looks at process and integration-level inflections that promise to limit RC delay increase while

also achieving void-free gap fill in nano-scale interconnects.

3:40pm EM-ThA6 Selective Deposition of Cu Film in Recessed Features using a Hollow Cathode Magnetron Physical Vapor Deposition Source, A. Dulkin, I. Karim, H. Qiu, E. Ko, R. Tarafdar, K. Colinjivadi, J. Hahn, K. Leeser, K. Ashtiani, Lam Research Corp

Copper filled vias and trenches in dielectrics are the building blocks of the dual damascene interconnect metallization in VLSI. The fill is traditionally done with electroplating, which is preceded by physical vapor deposition (PVD) of a Cu seed layer. PVD film is known to have poor conformality within a recessed structure, with the top of the feature sidewall getting thicker coverage than the bottom. The resulting film coverage profile is not favorable for subsequent plating. Advances in iPVD technology have improved conformality; however, as the size of the features decreased below 40nm, achieving conformal seed coverage became increasingly undesirable. Conformal deposition increases the effective aspect ratio (AR) of the features, thereby making the subsequent electrofill process more challenging. Hence, bottom-up film growth which forms a seed profile with

a thick bottom and continuous but not too thick sidewall coverage is desired. We have demonstrated the feasibility of depositing such profile by balancing deposition, surface diffusion, and film resputtering using the Lam hollow cathode magnetron (HCM[®]) PVD source. Necessary conditions were obtained by utilization of extremely low operating pressure, Cu self-sputtering, and strong magnetic confinement of plasma in the entire volume of the deposition module. The novel configuration of the magnetic field ensured that the metal ion/neutral ratio was uniform across a 300mm wafer. With the proper metal ion/neutral ratio, more than 70% of the volume of a small feature could be filled while larger features were lined with Cu film. Thus, the aspect ratio of small features was significantly reduced, resulting in void free electrofill. PVD film is characterized by small grains which attribute to high resistivity, especially inside small features. We demonstrated that the grain size can be increased with post-deposition anneal, which resulted in improved line resistance. Deposition in very large CD and AR features, such as through-silicon vias (TSV), benefited as well. The metal ion-rich deposition formed a continuous seed on the TSV sidewall with 3-5 times less flux required than with standard PVD.

4:00pm EM-ThA7 Analysis of Grain Structure and Electrical Resistivity of 17 nm Half-Pitch Copper Wires, J.S. Chawla, K.J. Ganesh, B.J. Krist, J.S. Clarke, H.J. Yoo, Intel Corporation

We report electrical resistivity, copper grain size, and grain orientation distribution for 17-51 nm drawn wires fabricated with Cu/Ta, Cu/Ru and CuMn/Ru based processes on 300 mm Si wafer platform. Interconnects containing those structures measured in this study were fabricated using patterning and metallization schemes described earlier [1, 2]. The grain structure and size are characterized using a recently developed technique [3, 4], which couples diffraction-scanning transmission electron microscopy (D-STEM) configuration with precession electron diffraction (PED). Electrical resistivity and *conducting* cross section area of each wire is obtained by a four-point probe resistance measurement at various temperatures (25-75 °C) and lengths of wire (25-100 μm). The *geometrical* cross sectional area is measured using transmission electron microscopy (TEM), and shows the *conducting* cross sectional area for both Cu/Ru and Cu/Ta wires equals the *geometrical* Cu cross-sectional area. This result indicates neither Ru or Ta liner contribute to conduction, owing to their high resistivity compared to Cu at these dimensions.

The wires studied for this report have a *conducting* cross-sectional area ranging from 150 to 1100 nm². The resistivity of Cu/Ru and Cu/Ta wires at *conducting* cross-sectional area of 200 nm² is 4.6 and 7.7 μΩ-cm, respectively. The resistivity of the Cu/Ru wire is 40% lower than that of the Cu/Ta wire, and can be attributed to a larger (2x) median Cu grain area for the Cu/Ru, thus resulting in reduced electron scattering at grain boundaries. The resistivity delta between Cu/Ru and Cu/Ta wires decreases from 3.1 μΩ-cm to 0.8 μΩ-cm as area increases from 200 nm² to 900 nm². This is attributed to a combination of respective increase in grain size, and reduction in electron scattering at surfaces with increasing dimensions. The resistivity of a CuMn/Ru wire with 200 nm² *conducting* cross-sectional area is 9.9 and 10.3 μΩ-cm with and without annealing, respectively. The higher resistivity for the CuMn/Ru wire is attributed to the Mn dopant, which increases impurity scattering. The electrical resistivity data is also consistent with the combined Fuchs-Sondheimer and Mayadas-Shatzkes expression.

References:

- [1] M. van Veenhuizen et al., IEEE International Interconnect Technology Conference (IITC), 2012
- [2] J. S. Chawla et al., IEEE International Interconnect Technology Conference (IITC), 2013
- [3] K. J. Ganesh et al., *Microscopy and Microanalysis*, 16 (5), 2010
- [4] K. J. Ganesh et al., *Nanotechnology*, 23 (13), 2012

4:20pm EM-ThA8 The Role of Gas-phase Reaction during Co-CVD using Amidinate Precursor for ULSI-Cu Liner Application, Y. Suzuki, H. Shimizu, T. Momose, Y. Shimogaki, University of Tokyo, Japan

Reaction mechanism of chemical vapor deposition (CVD) for Co using amidinate precursor was examined by introducing multi-scale analysis using cold-wall reactor equipped with macrocavity. We thereby found that Co film growth by direct surface decomposition of the source precursor was negligible and the intermediate species generated by gas-phase reaction was the major species.

Ongoing shrinkage of ULSI devices manifests EM/SIV reliability issues originated from poor adhesion between Cu and underlying material. The higher effective resistivity caused by the shrinkage of Cu lines is another concern. These issues suggest the necessity of more adhesive and conductive material for Cu liner/barrier layer instead of conventional Ta/TaN bi-layer. We proposed Co(W) monolayer film as a hopeful candidate to solve these issues [1]. The poor step coverage of PVD is also a

problem in future technology. We, therefore, worked on the CVD of Co(W), and proved better barrier property and lower resistivity than Ta/TaN. This paper is focusing on Co-CVD kinetics from Co(BuNC(Et)NEt)₂ (Co-amidinate) [2] and NH₃ as a basis of Co(W)-CVD.

We firstly used cold-wall chamber to focus on the surface reaction kinetics. Arrhenius plot of deposition rate showed two slopes corresponding to surface-reaction- and diffusion-limited regime. Mass transfer coefficient estimated from the growth rate under diffusion-limited regime has 200 times lower than that from fluid dynamics. This suggested that major deposition species was not the precursor itself, but intermediate species generated from the precursor near by the heated substrate. Deposition rate dependence on precursor partial pressure was then studied under reaction-limited condition, which showed Langmuir-Hinshelwood reaction kinetics. Surface reaction rate constants were finally extracted.

Gas-phase reaction kinetics were analyzed by macrocavity installed in the cold-wall chamber. Macrocavity consists of two facing substrates with variable spacing. The spacing of the macrocavity controls surface to volume ratio, which in turn changes the contributions of gas-phase reaction over surface reaction [3]. Film thickness profile within the macrocavity was compared with that by finite element simulation of diffusion equations coupled with the experimentally obtained surface reaction kinetics. We could finally obtained gas-phase reaction rate constant.

As a summary, we successfully analyzed reaction mechanism of Co-CVD using amidinate precursor, which enables to design the wafer-scale reactor. Our results show the importance of controlling gas-phase reactions when we use this precursor for CVD-Co as ULSI-Cu liner application.

4:40pm **EM-ThA9 Copper Reflow Modeling**, *P. Stout*, Applied Materials

A copper reflow model implemented in a feature profile evolution model will be discussed. The barrier/seed/plating process flow is being challenged as the metal interconnects shrink in size. The barrier and seed deposition are requiring more of the total volume within the interconnect via and trench structures. Copper reflow is being explored as a means to fill via and trench structures for back end of line interconnects. The wafer is raised in temperature to allow copper to move, shift around, or "reflow" within the feature. The feature model used for the study is a 3D Monte Carlo model. The reflow model implemented here assumes Cu transport during reflow is due to surface diffusion. The surface diffusion depends on the wafer temperature, the material Cu is diffusing on (i.e., Cu, Ta, SiO₂, etc.), and the local morphology of the surface. The implemented surface diffusion model is a hopping model. A probability matrix is constructed to determine the next surface "hop" location as the Cu moves around on the surface. The hopping Cu will settle into surfaces which minimize surface energy. In this model that translates to Cu preferring higher coordination number (CN) sites. Depending on the temperature and material parameters the minimal surface morphology can change. If hopping probabilities are similar between CNs the surface will roughen and become more dendritic. If there are large hopping probability differences the surfaces will become more faceted with low energy crystalline planes exposed. Using a simple hopping surface diffusion model, reflow behavior is shown. The model predicts the initial reflow causes rounding of the Cu surfaces and a shrinking of the opening as the surfaces round to a more minimal surface configuration. The end result for the successful reflow cases is a filled feature which is concave at the feature bottom or flat once the field is reached. The main issue with the reflow process is pinch-off at the feature opening causing void formation in the feature. For vias the model is predicting mostly void formation. One reason vias are more prone to void formation (vs trench) is the different CN distributions for a flat (trench) vs rounded (via) surface. Thus, the movement (i.e., hopping) of the Cu is different for these surfaces. Another reason is trenches are closing in on the opening from only two sides whereas the via is closing in from all sides. Once a void forms it is unlikely to breach the field and have more copper enter the feature. Smaller voids move more quickly about the feature vs large voids given the smaller amount of Cu needed to shift in the small void for the void center to change position.

5:00pm **EM-ThA10 Chemical Mechanical Polishing of Gold**, *G. Karbasian, H. Xing, A.O. Orlov, P.J. Fay, G.L. Snider*, University of Notre Dame

In today's IC technology, the size of the transistors is constantly shrinking and interconnect RC delay is a dominant factor in determining the speed of circuits. Gold is a promising replacement for copper and aluminum due to its low resistivity and high chemical stability. A key feature of a successful Au CMP is the use of a relatively soft adhesion layer beneath the gold, along with proper slurry additives. Ni is a soft metal compared to other common adhesion layer metals such as Ti and Cr, and was therefore used as the adhesion layer. Ultra Sol A20 from Eminess Technologies Inc., an alumina based slurry with added potassium iodide, was used to polish the

Au/Ni metal overlay on the patterned dielectric substrate. The slurry, at pH=4, was modified by adding hydrogen peroxide as an oxidizer. Previously, Ishii et al.[1] observed that adding 30% H₂O₂ to an alumina based slurry with added potassium iodate at pH=4, in 1:1 ratio resulted in the maximum polish rate of gold, and proposed it as the optimum concentration. However, this slurry composition results in high static etch rate, i.e. chemical dissolution, of gold, approximately 95nm/min. This high static etch rate increases edge recess and dishing in the interconnect trench as shown in Figure1. Moreover, this concentration of H₂O₂ exceeds the optimal oxidizer concentration needed for the highest Ni removal rate[2]. The lower polish rate of adhesion layer compared to gold, which was lowest for Cr and highest for Ni due to their different hardness, made adhesion layer removal the limiting factor in determining the total polish time. Our experiments show that reducing the concentration of 30% H₂O₂ solution from 50% to 25% improves the selectivity between the adhesion layer and gold such that at this concentration, Ni is polished approximately 3 times faster than gold, and this allows us to reduce the total polish time by a factor of 3. Additionally, the chemical etch rate of gold dropped from 90nm/min to 30nm/min, which reduces the dishing of Au during the Ni removal step.

Adding SDS and PVP enhanced the stability of the colloidal slurry that was otherwise prone to agglomeration leading to nonuniform polishing and microscratches. A combination of H₂O₂ and UltraSol A20 in 1:3 volume ratio along with added SDS and PVP resulted in a stable slurry giving a successful CMP Damascene process, Figure2, with 37nm of dishing across a 150 μm wide contact pad.

We have also studied the evolution of the coefficient of friction during the CMP process, and observed a decrease in this parameter when the metal overlay is polished away, suggesting that this can be used for end-point detection.

5:20pm **EM-ThA11 Effect of Nucleation Layer on Electrical Properties of W-contact in Sub 2x nm Flash Devices**, *K.H. Lee, S.W. Kim, K.S. Lee, T.H. Kim, S.S. Lee, S.H. Kim, J.H. Won*, Samsung Electronics, Republic of Korea

With the continuous scaling down of integrated circuits, the diameter of a contact plug decreases. This causes an increase of contact plug resistance, which is not desirable for high-speed transistor operation. Since metal Tungsten (W) has good filling capability and electrical properties, it has been widely used in semiconductor device area such as gate, metal contact, and via. Tungsten deposition process consists of two steps of nucleation which is for seed layer and bulk step that is for contact filling by CVD process. B₂H₆ based W nucleation layer technology has been widely used to realize low resistive W film. [1,2]

In this study, the effects of W-nucleation layer using a B₂H₆ gas as a reducing agent of WF₆ gas on electrical properties of W-contact in sub 2x nm flash devices was investigated. CVD-W films using CVD reaction of WF₆ and H₂ gas were deposited on different thickness of nucleation layer. The resistivity of CVD-W film was not changed as thickness of nucleation layer increase because the thickness of nucleation layer is too thin to affect resistivity of CVD-W film. In order to decrease resistivity of CVD-W film, B₂H₆ treatment was carried out after nucleation process. It caused decrease of resistivity as B₂H₆ treatment cycle increased grain growth due to increase of grain size resulted from additional Boron atom. WF₆ reacts with adsorbed boron preferentially causing a formation of β-W phase of amorphous phase W film which decelerates the nucleation with α-phase W film formed by H₂ reaction, which result in larger size grains and low resistive W film as B₂H₆ post-treatment cycle increases.

In addition, the resistivity of CVD-W deposited on three different thickness nucleation layers is not variable, which means the final grain size of CVD-W film is similar. The contact resistance increases (~12 %) when W nucleation cycle increases from x to x+4 cycles. In general, contact resistance on gate is associated with the resistivity of the total film stack related to final grain size. However, this result reveals that the resistivity of W nucleation layer also affects the contact resistance of CVD-W film although the resistivity of bulk-W film is dominant factor to define a contact resistance.

[1] A. Buerke et al., *Material Research Society AMC XXI*, p239 (2006).

[2] S. Smith et al., *Microelectronic Engineering* **82**, 261 (2005).

Graphene and Other 2D Materials Focus Topic Room: 104 B - Session GR+AS+BI+PS+SS-ThA

Plasma Processing, Surface Chemistry, Functionalization, and Sensor Applications of 2D Materials

Moderator: P.E. Sheehan, Naval Research Laboratory

2:00pm **GR+AS+BI+PS+SS-ThA1 Carbon Monoxide-induced Reduction and Healing of Graphene Oxide, S.L. Weeks, B. Narayanan, B.N. Jariwala, Colorado School of Mines, B. Macco, J.W. Weber, Eindhoven University of Technology, Netherlands, M.C.M. van de Sanden, Eindhoven University of Technology; DIFFER, Netherlands, C.V. Ciobanu, S. Agarwal, Colorado School of Mines**

Reduction of graphene oxide (GO) has recently generated intense research interest due to the possibility of using this method to inexpensively produce large quantities of graphene. Current reductive processes rely on thermal or chemical removal of oxygen functional groups from the surface. While reduction has been demonstrated, a certain fraction of residual oxygen remains after processing with current techniques. Furthermore, the use of high process temperatures in the reduction of GO leads to the generation of defects through the loss of carbon atoms from the basal plane of graphene. The ultimate improvement in the electronic, optical, or mechanical properties of graphene that can be achieved through reduction of GO is limited by defect formation and the residual oxygen remaining after reduction through present reported methods. Here, we report the facile removal of oxygen functional groups from the surface of GO through reduction in a carbon monoxide atmosphere. Common oxygen-containing functional groups on the basal plane of GO (epoxides, hydroxyls, and ketone pairs) are removed from the surface due to the reducing action of CO. First, we have used molecular dynamics simulations and density functional theory calculations to elucidate the mechanisms of removal of these surface species by CO, and show that this reduction process proceeds without degradation of the underlying graphene sheet; CO₂ and H₂O are the only surface reaction products. We also show that the corresponding activation energy barriers for these reactions are easily surmounted at low temperatures. Second, the removal of oxygen-containing functional groups from GO by CO is confirmed experimentally using *in situ* attenuated total reflection Fourier transform infrared spectroscopy, indicating the reduction of the GO surface with CO is consistent with our atomistic-level calculations. Third, through controlled generation of defects into an otherwise pristine graphene sheet, we show that exposure to CO results in near-complete healing of the sheet as demonstrated with *ex situ* Raman spectroscopy. Thus, our results indicate CO induced reduction of GO not only proceeds without damaging the underlying sheet, but also heals defects that are produced in the production of GO via exfoliation of oxidized graphite.

2:20pm **GR+AS+BI+PS+SS-ThA2 Plasma Enhanced ALD of Hafnium Oxide on Graphene Layer with Plasma Pretreatment, T. Kitajima, T. Nakano, National Defense Academy of Japan**

Graphene is the candidate of the future generation semiconductor material due to its high mobility of electrons and ultimately thin feature of the 2D structure. The use of graphene for CMOS technology to replace current silicon devices requires matching of each interface between the substrate, electrodes, channel, and dielectrics. Among these, growth of high dielectric constant film growth over graphene is not successful due to the chemically inert nature of the graphene surface. In order to have reactive chemical bond on graphene surface, there are trials of oxidation with ozone, etc.

Here, the effect of the oxygen plasma pretreatment on the graphene surface is examined in this study.

Graphene layer is prepared by peeling method from HOPG using adhesive tape. The domain size is 1 micron in width. (AFM topograph is shown in Fig.1) The pretreatment of the graphene surface is the exposure of O₂ ICP at 30 Pa for less than 1 min. This atomically modifies the topography (fig. 2), and the chemistry of the surface (fig. 3). The XPS analysis indicates the many of the graphene 2D bonds are replaced by C-O or C-OH bond and the defects are increased.

The growth sequence of Hafnium oxide ALD consists of the exposure of metal precursor (Tetrakis Ethyl Methyl Amino Hafnium : TEMAH) with N₂ buffer flow, N₂ purge, and O₂ ICP at 30 Pa.

The chemical composition from XPS shows the film thickness is specifically controlled by ALD cycle number and it saturates at 4th cycle owing to the limited mean free path of photoelectrons.

The initial growth stage of the film with and without plasma pretreatment is compared for 2nd ALD cycle sample. (AFM in fig. 4 and 5). With

pretreatment, the surface consists of 2-5 nm width dispersed nano-islands and 20 nm width HfO₂ mesa (film) of 1nm height. Mesas are separated by base graphene surface by 10 nm pitch. Without pretreatment, the surface is covered by closely packed 5-10nm width nano-islands, around 1nm of height. This comparison indicates the oxygen bonds introduced by O₂ plasma pretreatment contribute to the chemisorption of the precursor and successful 2D growth of HfO₂ in the initial stage. In contrast, inert graphene surface without pretreatment prohibits the interconnection of the physisorbed precursor with the surface and 3D island growth is preferred.

In summary, although the domain size of the HfO₂ is limited to around 20 nm, 2D mode growth is enabled by the introduction of O₂ plasma pretreatment. Further progress is necessary on the increase of the coverage of the film, minimizing the oxidation of the base graphene layer, and reducing nano-sized islands on the film.

2:40pm **GR+AS+BI+PS+SS-ThA3 Detection of Uranium and Plutonium by Graphene-Based Nanosensors, G. Sandi, Argonne National Laboratory, A. Bobadilla, Texas A&M University, A.V. Sumant, L. Ocola, Argonne National Laboratory, J. Seminario, Texas A&M University, C. Mertz, M. Kaminski, Argonne National Laboratory**

The design and fabrication of arrays of electronic molecular devices as sensors for plutonium and uranium at the nanoliter volume will be discussed. Computational calculations performed at Texas A&M University and experiments performed at Argonne National Laboratory (Center for Nanoscale Materials and Chemical Sciences and Engineering Division), will be presented. In particular, we are studying graphene, which is a vibronic, plasmonic, and electronic material for molecular circuits and sensors. The idea is to use the plasmonic features of graphene molecules in order to transfer the electrical, magnetic, vibrational, and optical characteristics of nuclear agents into the graphene plasmon, which produces an enhancement (amplification) of observable quantities as successfully done with chemical and biological agents. For nuclear agents, we have additional possibilities due to their radiation features. Theoretical simulations have shown the possible use for sensors to identify single molecules with high selectivity and sensitivity that will contribute to the miniaturization, as well as efficient transport and processing of signals using graphene based devices. It is expected that this approach will allow us not only to sense targeted agents, but also to perform chemical recognition using molecular potentials, which have become the signature at the nanoscale, perfectly suitable for detection and identification of atoms and small molecules. Maps of the molecular potentials around complexes of U and Pu allows us to distinguish their main signatures similar to those observed in biological systems where receptors are able to distinguish to its transmitters or when a donor of electrons is able to match with an acceptor. The information obtained, especially following a supercritical nuclear event, would severely limit the list of potential actors and provide critical information to guide a proper and timely response.

Acknowledgments

Use of the Center for Nanoscale Materials was supported by the U. S. Department of Energy, Office of Science, Office of Basic Energy Sciences, under Contract No. DE-AC02-06CH11357.

The submitted manuscript has been created by U Chicago Argonne, LLC, Operator of Argonne National Laboratory ("Argonne"). Argonne, a U.S. Department of Energy Office of Science laboratory, is operated under Contract No. DE-AC02-06CH11357. The U.S. Government retains for itself, and others acting on its behalf, a paid-up nonexclusive, irrevocable worldwide license in said article to reproduce, prepare derivative works, distribute copies to the public, and perform publicly and display publicly, by or on behalf of the Government.

3:00pm **GR+AS+BI+PS+SS-ThA4 Damage-free Etching of Graphene using Oxygen Neutral Beam towards Edge State Control, T. Okada, K. Igarashi, S. Samukawa, Tohoku University, Japan**

The band gap of graphene needs to be controlled for electronic device applications because it is a zero band gap semiconductor. Narrow width graphene, which is called graphene nanoribbon (GNR), has an effective band gap and solves several problems. Although there are several approaches to fabricating GNRs, top-down lithographic patterning is the most attractive method for the well-arranged GNRs required for large-scale device integration. However, conventional plasma etching always produces high density defects around the edges of the GNRs due to UV irradiation. This makes it difficult to obtain a sufficiently large band gap and the high mobility necessary for GNR-based FETs using wide GNRs (>10 nm). We developed an etching process using a damage-free neutral beam (NB) to fabricate the GNRs that can eliminate the UV irradiation to overcome this issue. We compared oxygen neutral beam etching to oxygen plasma etching within the same flux and energy conditions to clarify the defect generation mechanism at the edges of graphene.

Graphene sheets were extracted by micromechanical cleaving them from the HOPG and depositing them onto the substrate. The graphene was then etched using a stencil mask. The laser spot for taking the Raman measurement was shifted step by step to measure the defects at the edges. The Raman peaks at approximately the D-band and G-band were examined.

At the edges, the D/G ratio was increased, indicating that the defects were not generated on the plane but on the edge of the graphene. We also found that the D/G ratio on the edge etched by using oxygen NB was extremely lower than that for plasma. These results suggest that high-quality graphene edges can be easily fabricated using NB etching. The defects on the edges from the plasma etching were caused by UV radiation. Several studies have reported this defect generation on materials by high-energy UV photons during the plasma processing. Since UV photons have a non-orientation, they irradiated to the edges during etching. In contrast, in the case of neutral beam etching, damage-free etching was possible because the UV radiation was suppressed.

We concluded that NB etching is a promising candidate for GNR fabrication for high-mobility graphene transistors. In addition, this damage-less etching technique can be used for defect free formation of graphene nano structures, like nano dots and its periodic array when using the top-down process.

3:40pm **GR+AS+BI+PS+SS-Tha6 Controlling the Chemistry of Graphene.** *S. Hernández, E.H. Lock, Naval Research Laboratory, C. Bennett, Nova Research, C. Junkermeier, F. Bezares, S. Tsoi, Naval Research Laboratory, R. Stine, Nova Research, J.T. Robinson, J. Caldwell, T. Reinecke, P.E. Sheehan, C.R. Tamana, S.G. Walton, Naval Research Laboratory*

Graphene has attracted widespread interest because of its unique structural and electronic properties. Given its pure two dimensional nature, adsorbates have a strong impact on these properties and so global chemical modification provides opportunities towards homogeneous control of graphene films. However, control over the spatial distribution of chemical moieties provides an even greater functionality in that the properties can be manipulated locally, opening up a wealth of opportunities in biosensing, plasmonics, catalysis, smart surfaces, and heterojunction devices.

Global and spatial chemical functionalization of graphene using electron beam generated plasmas will be discussed. The resulting chemical, structural, and electrical properties of the functionalized graphene as they originate for -oxygen, -fluorine, and -nitrogen functionalities will be demonstrated. This work is supported by the Naval Research Laboratory Base Program.

4:00pm **GR+AS+BI+PS+SS-Tha7 Covalent Functionalization of Graphene with Fluorine by Plasma Treatment.** *G. Mordì, S. Jandhyala, S. McDonnell, R.M. Wallace, J. Kim, The University of Texas at Dallas*

As the performance of graphene based devices has continued to improve over the years (mobility, contact resistance, transconductance), the realization of novel logic devices as the BiSFET (Bi-layer Pseudospin Field-Effect Transistor) for ultra-fast switching speeds and ultra-low power consumptions may not be far off. One of the challenges in realizing BiSFET¹ is the integration of a thin (1-2 nm), low-k (~2) dielectric material which can electrically isolate the two graphene layers in which a condensate is formed and at the same time act as a tunnel barrier.

One approach for obtaining a low-k dielectric is using two dimensional materials similar to graphene which can be manufactured independently and transferred on top of graphene. Covalent functionalization of graphene is a process of adding functional groups which covalently bind to the graphene network, changing its structure from sp^2 to sp^3 hybridization resulting in opening of a band gap. Fluorination among other processes (graphene oxide¹, graphane²) can be used to covalently functionalize graphene. Fluorinated graphene (GrF) is an interesting material because of its atomically thin nature, thermodynamically more stable compared to graphene oxide and graphane, has a wide band gap (~3-7.5 eV) and a potentially low-k dielectric (expected to have dielectric constant of ~2)².

In this study we utilized fluorine based plasma (CF₄) to covalently functionalize graphene films. We established suitable CF₄ plasma exposure parameters and then investigate the conduction mechanisms across GrF based devices. Raman spectroscopy studies showed the evolution of Raman active D (~1350 cm⁻¹), G (~1595 cm⁻¹), D' (1620 cm⁻¹) and 2D (~2680 cm⁻¹) peaks as function of plasma exposure (fluorination) time. XPS studies revealed the type of bonding that exists between fluorine and carbon atoms of the graphene lattice. Conductive atomic force microscopy (C-AFM) showed the *out-of-plane* conductivity on the GrF films were significantly small compared to non-fluorinated films. *In-plane* transport characteristics of GFETs displayed two minima (or Dirac points) for short CF₄ exposures possibly attributed by both ionic and covalent doping effects simultaneously. Longer exposures result in a single minimum conductivity point possibly due to dominant covalent functionalization effects.

References

1. J.P Eisenstein and A.H MacDonald, *Nature* **432** 691-694 (2004)
2. V. Georgakilas, M. Otyepka, A. B. Bourlinos, V. Chandra, N. Kim, K. C. Kemp, P. Hobza, R. Zboril and K. S. Kim, *Chemical Reviews* **112** (11), 6156-6214 (2012).
3. F. Karlicky, R. Zboril and M. Otyepka, *Journal of Chemical Physics* **137** (3) (2012).

4:20pm **GR+AS+BI+PS+SS-Tha8 Field Effect Control of Carrier Conduction in Helium Ion Irradiated Graphene.** *S. Nakaharai, T. Iijima, S. Ogawa, AIST, Japan, S.-L. Li, K. Tsukagoshi, NIMS, Japan, S. Sato, N. Yokoyama, AIST, Japan*

We demonstrate the gate control of carrier conduction in graphene which is functionalized by Helium ion beam irradiation in a Helium Ion Microscope (HIM) [1]. Carrier conduction control is important for graphene application to electronics, but it has long been an obstacle to realization of graphene electronics. We found that an appropriate amount of He ion dose to graphene induced point defects which enabled gate bias control of current with an on-off ratio of two orders of magnitude at room temperature.

Helium ions were applied to graphene with ion doses from 2.2×10^{15} ions/cm² to 1.3×10^{16} ions/cm². The induced defect density was estimated by numerical calculation to be 0.2% to 1.3% [2]. The introduction of defects was confirmed by the D-mode peak of Raman spectroscopy. A series of samples with different ion doses exhibited a drastic decay of current by more than five orders of magnitude as the defect density increased from 0.2% to 1.3%. In spite of such a drastic change in current, the basic structure of graphene remained, as evidenced by G-mode peak of the Raman spectra. Room temperature current switching with an on-off ratio of two orders of magnitude was realized at a moderate defect density of 0.9%. We also found that the current exhibited an exponential decay as the irradiated region length increased from 5 to 50 nm. These results suggest that the carriers in graphene are spatially localized due to interference of waves which are scattered at the randomly distributed defect sites. A theoretical investigation of localization in a defective graphene has predicted that 1% point defects will cause a strong localization of carriers [3], which shows good agreement with our experimental results. Therefore, it should be argued that the gate control of carrier conduction is realized by a transport gap which is generated by defect-induced localization.

Since the presented technique of graphene functionalization is a "top-down" process, it is easily introduced to the fabrication process of future electron devices. We will also present the application of our ion irradiation technique to the channel of graphene transistors [4] which achieved nearly four orders of magnitude on-off ratio at 250 K.

This research is granted by JSPS through FIRST Program initiated by CSTP.

- References: [1] S. Nakaharai, *et al.*, *ACS Nano* **7**, 5694 (2013), [2] M. C. Lemme, *et al.*, *ACS Nano* **3**, 2674 (2009); D. Bell, *et al.*, *Nanotechnology* **20**, 455301 (2009), [3] A. Lhebier, *et al.*, *Phys. Rev. B* **86**, 075402 (2012). [4] S. Nakaharai, *et al.*, *IEEE Tech. Dig. IEDM2012*, p.72 (2012).

5:00pm **GR+AS+BI+PS+SS-Tha10 Epitaxial Graphene Oxide.** *E. Riedo, A. Bongiorno, Georgia Institute of Technology, Y.J. Chabal, University of Texas at Dallas, C. Berger, Georgia Institute of Technology, C. Aruta, CNR*

INVITED

Graphene and graphene-based materials hold great promise for the next generation of nanodevices. One of the most pressing issues for the technological use of graphene is the possibility to control physical and chemical properties by means of ad hoc functionalization. Thermal, chemical and optical reduction of graphene oxide have been explored as a route to produce graphene-based materials with the desired electron transport, mechanical and optical properties. Here, we demonstrate the ability to reduce graphene oxide at the nanoscale by using hot AFM tips (thermochemical nanolithography, TCNL). The resulting nanostructures have a conductivity that can be tune over 4 orders of magnitude [1]. Graphene oxide is indeed a material of great interest for its potential applications in nanoelectronics, nanoelectromechanical system, sensors, polymer composites, catalysis, energy storage devices and optics. However, the chemistry of graphene oxide and its response to external stimuli such as temperature and light are not well understood and only approximately controlled. This understanding is crucial to enable future applications of this material. We have carried over a combined experimental and density functional theory study [2] which shows that multilayer graphene oxide produced by oxidizing epitaxial graphene through the Hummers method is a metastable material whose structure and chemistry evolve at room temperature with a characteristic relaxation time of about one month. At the quasi-equilibrium, graphene oxide reaches a nearly stable reduced O/C ratio, and exhibits a structure deprived of epoxide groups and enriched in hydroxyl groups. This study shows that the structural and chemical changes

are driven by the availability of hydrogen in the oxidized graphitic sheets, which favors the reduction of epoxide groups and the formation of water molecules. Furthermore, we have discovered that a mild chemical oxidation of multilayer epitaxial graphene produces uniform oxidized films showing no propensity to exfoliate. XRD measurements show that the epitaxial graphene oxide films are extremely well ordered with an interlayer distance of 10 Å [3].

[1] Z. Q. Wei, D. Wang, S. Kim, Y. Hu, M. K. Yakes, A. Laracuate, Z. Dai, S. Marder, C. Berger, W. P. King, W. A. de Heer, P. E. Sheehan, and E. Riedo, "Nanoscale Tunable Reduction of Graphene Oxide for Graphene Electronics," *Science*, 328, 1373-1376, (2010).

[2] S. Kim, S. Zhou, Y. Hu, M. Acik, Y. J. Chabal, C. Berger, W. de Heer, A. Bongiorno, and E. Riedo "Room Temperature Metastability of Multilayer Epitaxial Graphene Oxide", *Nature Materials*, 11, 544, (2012).

[3] L. Aruta, Y. Chabal, E. Riedo, A. Bongiorno, (2013).

Graphene and Other 2D Materials Focus Topic Room: 101 A - Session GR+EM+NS+SS+TF-ThA

Beyond Graphene: Other 2D Electronic Materials and their Heterostructures

Moderator: J.A. Robinson, The Pennsylvania State University, A. Turchanin, University of Bielefeld, Germany

2:00pm **GR+EM+NS+SS+TF-ThA1 Functionalization of MoS₂ Surfaces for High-k Atomic Layer Deposition.** S. McDonnell, A. Azcatl, C. Buie, N. Lu, J. Kim, C.L. Hinkle, M.J. Kim, R.M. Wallace, University of Texas at Dallas

The transition metal dichalcogenide (TMD) family of materials are 2-D bulk crystals similar to graphite that can be exfoliated to yield single-layer analogs to graphene. The materials can be metallic or semiconducting with bandgaps that are tunable with thickness. Recent publications have focused on devices fabricated with MoS₂ or WSe₂ channels and the deposition of thick gate oxides was carried out by atomic layer deposition (ALD) without any functionalization suggesting that these surfaces may be more reactive than graphene.^{1,2}

Preliminary results have shown that the direct deposition of HfO₂ using tetrakis (dimethylamino) hafnium (TDMA-Hf) and H₂O precursors on MoS₂ is not a scalable process. The deposition of films less than 15 nm in thickness is three-dimensional, with pinholes reaching the MoS₂ surface. Ozone functionalization of graphene, as well as the deposition of seed layers by e-beam, has been previously shown to allow the subsequent uniform growth of high-k materials by ALD.^{3,4}

Presented here will be a comparative study of ozone and e-beam seed-layer based functionalization. X-ray photoelectron spectroscopy will be used to probe the interfaces for any chemical reactions. Atomic force microscopy, inelastic ion scattering, and transmission electron microscopy will be used to monitor the film uniformity. The band offsets of the resultant heterostructures will also be presented.

This work was supported in part by the Center for Low Energy Systems Technology (LEAST), one of six centers supported by the STARnet phase of the Focus Center Research Program (FCRP), a Semiconductor Research Corporation program sponsored by MARCO and DARPA. C. L. Hinkle acknowledges support from the Nanoelectronic Research Initiative (NRI SWAN Center).

1 B. Radisavljevic *et al.*, "Single-layer MoS₂ transistors," *Nature nanotechnology* 6 (3), 147-150 (2011).

2 H. Fang *et al.*, "High-Performance Single Layered WSe₂ p-FETs with Chemically Doped Contacts," *Nano letters* 12 (7), 3788-3792 (2012).

3 B. Lee *et al.*, "Characteristics of high-k Al₂O₃ dielectric using ozone-based atomic layer deposition for dual-gated graphene devices," *Applied Physics Letters* 97, 043107 (2010).

4 B. Fallahzad *et al.*, "Dielectric thickness dependence of carrier mobility in graphene with HfO₂ top dielectric," *Applied Physics Letters*, 97, 123105 (2010).

2:20pm **GR+EM+NS+SS+TF-ThA2 Silicene: From Single Sheets to Multilayers.** G. Le Lay, A. Resta, Aix-Marseille University, France

Born in 2012 on a silver plate [1], artificially created by epitaxy on silver (111) substrates since it does not exist in nature, silicene, graphene's silicon cousin, offers many exciting promises. This is due, typically, to its Dirac fermions with trigonal or hexagonal wrapping and very high Fermi velocity, its two-dimensional topological insulator character, a hint for high-

temperature superconductivity, and, last but not least, its direct compatibility with current silicon-based electronics.

However, the significant task to isolate free-standing silicene sheets has not yet been achieved. We will present a first step in this endeavor, since we have succeeded in growing silicene multi-layer stacks, which host massless Dirac Fermions, as demonstrated by the cone-like dispersion in Angle-Resolved PhotoElectron Spectroscopy measurements [2]. We could further characterize this novel silicon allotrope by comparing simultaneously acquired nc-AFM and STM observations in conjunction with transport measurements revealing sheet resistance.

In my talk, I will present these last results and draw perspectives for future research and potential applications.

*guy.lelay@univ-provence.fr

[1] "Silicene: Compelling Experimental Evidence for Graphenelike Two-Dimensional Silicon" P. Vogt, P. De Padova, C. Quaresima, J. Avila, E. Frantzeskakis, M. C. Asensio, A. Resta, B. Ealet and G. Le Lay, *Phys. Rev. Lett.*, 108, 155501 (2012).

[2] "Evidence of Dirac fermions in multilayer silicene" P. De Padova, P. Vogt, A. Resta, J. Avila, I. Razado-Colambo, C. Quaresima, C. Ottaviani, B. Olivieri, T. Bruhn, T. Hirahara, T. Shirai, S. Hasegawa, M. C. Asensio and G. Le Lay, *Appl. Phys. Lett.*, 102, 163106 (2013).

[3] "Sheet resistance of multilayer silicene" P. Capiod, M. Berthe, A. Resta, P. De Padova, T. Bruhn, P. Vogt, G. Le Lay and B. Grandidier, submitted.

2:40pm **GR+EM+NS+SS+TF-ThA3 Topological Valleytronics in Monolayers of Group-VI Dichalcogenides.** D. Xiao, Carnegie Mellon University **INVITED**

In many crystals the Bloch bands have inequivalent but degenerate energy extrema in the momentum space, known as valleys. The valley index constitutes a well-defined discrete degree of freedom for low-energy carriers that may be used to encode information. This has led to the concept of valleytronics, a new type of electronics based on manipulating the valley index of carriers. In this talk, we show that, when inversion symmetry is broken, a pair of valleys which are equivalent by time-reversal are distinguishable by their magnetic moment and Berry curvature. These quantities give rise to valley Hall effect and circularly-polarized valley optical selection rule both in graphene and in monolayer group-VI transition metal dichalcogenides. Moreover, in monolayer dichalcogenides, we find that the electrons and holes at the band edges are described by massive Dirac Fermions with strong spin-valley coupling, which further results in valley and spin dependent optical selection rule, and coexistence of valley Hall and spin Hall effects. These phenomena pave the way towards dynamic control of valley and spin by electric and optical means for device applications in monolayer dichalcogenides. We will report photoluminescence studies on dichalcogenide thin films, which show the first evidence on valley optical selection rule and optical valley pumping.

3:40pm **GR+EM+NS+SS+TF-ThA6 Controlled Scalable Synthesis of Uniform High-quality Monolayer and Fewlayer MoS₂ Films.** L. Cao, North Carolina State University **INVITED**

Two dimensional (2D) materials with a monolayer of atoms represent an ultimate control of material dimension in the vertical direction. Molybdenum sulfide (MoS₂) monolayers, with a direct bandgap of 1.8 eV, offer an unprecedented prospect of miniaturizing semiconductor science and technology down to a truly atomic scale. Recent studies have indeed demonstrated the promise of 2D MoS₂ in fields including field effect transistors, low power switches, optoelectronics, and spintronics. However, device development with 2D MoS₂ has been delayed by the lack of capabilities to produce large-area, uniform, and high-quality MoS₂ monolayers. Here we present a self-limiting approach that can grow high quality monolayer and few-layer MoS₂ films over an area of centimeters with unprecedented uniformity and controllability. This approach is compatible with the standard fabrication process in semiconductor industry. It can pave the way for the development of practical devices with 2D MoS₂ and opens up new avenues for fundamental research.

4:20pm **GR+EM+NS+SS+TF-ThA8 Electronic and Optical Properties of MoS₂ at Monolayer Thickness.** T.F. Heinz, Columbia University **INVITED**

Inspired by the fascinating properties and application potential of graphene, interest within the community has extended to a broader class of stable, atomically thin materials. In this paper, we will discuss recent advances in the study of atomically thin layers of MoS₂ as representatives of the class transition metal dichalcogenides. Although the structure of the monolayer of MoS₂ is similar to that of graphene, the A and B sublattice are occupied either by Mo atoms or by a pair of S atoms, rather than just by C atoms. This difference in symmetry allows MoS₂ to be a semiconductor with a significant band gap. Through characterization of the optical properties of

the material as a function of thickness, we show that quantum confinement effects lead to a crossover in MoS₂ from an indirect gap semiconductor in the bulk to a direct gap semiconductor at monolayer thickness.

As expected for lower-dimensional materials, excitonic effects are very strong in monolayer MoS₂. This allows for the existence of charged exciton with binding energies sufficient to produce stable states even at room temperature. Another distinctive feature of this material is the possibility of creating long-lived valley polarization in which one of the two inequivalent, but energetically degenerate K and K' valleys is populated in preference to the other. We demonstrate how this can be achieved using optical excitation with circularly polarized radiation and monitored through the retention of the polarization in fluorescence emission. The pronounced change in symmetry from the non-centrosymmetric monolayer to the centrosymmetric bilayer has also been examined through its influence on the production of valley polarization and of optical second-harmonic radiation.

5:00pm **GR+EM+NS+SS+TF-ThA10 Low Energy Ion Scattering Studies of the Surface Termination and Structure of Bismuth Selenide**, W. Zhou, X. He, Z.Y. Wang, J. Shi, J.A. Yarmoff, University of California, Riverside

Topological insulator (TI) materials are electrically conductive through unique two-dimensional surface states that are characterized by a Dirac cone, while they are insulators in the bulk. TIs have garnered great attention because of their potential use in next generation electronic devices. One of the concerns with TIs, however, is that their surface transport can degrade over time, which has been dubbed the "aging" effect. The transport is dependent on the detailed surface structure and how it changes over time, but this is not completely understood.

Low energy ion scattering (LEIS), which can measure the composition and atomic structure at the surface of a solid, was used to show that the surface termination can change after *in situ* cleaving, which might be related to aging effect [1]. LEIS spectra were collected from Bi₂Se₃, the prototypical TI material, after cleaving a bulk single crystal in ultra-high vacuum. Bi₂Se₃ has a layered structure with a fundamental quintuple layer (QL) unit composed of five atomic layers ordered as Se-Bi-Se-Bi-Se. While the atoms within each QL are covalently bonded, the QLs are attached to each other by relatively weak van der Waals forces. It has thus been assumed that the material cleaves between QLs resulting in a Se-terminated surface. Surprisingly, however, spectra collected at room temperature using 3 keV Na⁺ ions in a double-alignment orientation, which is sensitive only to the outermost atomic layer, show scattering from Bi and none from Se. It was thus hypothesized that the material initially cleaves between QLs, but a thermally activated process induces a termination change. When cleaved at low temperature (80 K), the process is slowed and LEIS measurements are able to monitor the termination change in real time, consistent with the hypothesis.

We will discuss conditions that lead to the termination change, the stability of the Bi-terminated structure and the mechanisms involved. To quantitatively ascertain the atomic structure of the top few atomic layers, additional LEIS spectra were collected as a function of orientation and compared to the results of simulations.

[1] X. He, W. Zhou, Z. Y. Wang, Y. N. Zhang, J. Shi, R. Q. Wu and J. A. Yarmoff, Phys. Rev. Lett. **110**, 156101 (2013).

5:20pm **GR+EM+NS+SS+TF-ThA11 Electronic Activity of Silicene Boundaries, Edges, and Defects**, A.J. Mannix, B.T. Kiraly, M.C. Hersam, Northwestern University, N.P. Guisinger, Argonne National Laboratory

Recent experimental evidence suggests that silicene, the silicon analog to graphene, exhibits a Dirac cone band structure[1,3], low temperature superconductivity[2], and Dirac Fermion chirality[3]. These discoveries highlight silicene's potential as a platform for novel electronics and physical phenomena. Depending on the growth parameters, silicon deposition on Ag(111) produces several distinct monolayer silicene phases corresponding to different silicon buckling configurations. Although these phases are well documented, their defect structure remains uninvestigated. Using ultra-high vacuum scanning tunneling microscopy (UHV STM), the structural and electronic properties of edges and defects within these various silicene phases were probed. Several highly-buckled phases are shown to exhibit electronically active domain boundaries, edges, and/or point defects, but do not show evidence of scattering. On the other hand, the lightly buckled honeycomb phase demonstrates clear, bias-dependent electronic scattering from edges and point defects. These contrasting behaviors suggest fundamental differences in charge transport properties that are of great interest to further silicene development. Additional insight is derived from the structure and electronic characteristics of the 0D and 1D defects, which often play a dominant role in determining material properties.

[1] Vogt, P., De Padova, P., Quaresima, C., Avila, J., Frantzeskakis, E., Asensio, M., ... Le Lay, G. (2012). Silicene: Compelling Experimental

Evidence for Graphene-like Two-Dimensional Silicon. *Physical Review Letters*, 108(15), 155501. doi:10.1103/PhysRevLett.108.155501

[2] Chen, L., Feng, B., & Wu, K. (2013). Observation of a possible superconducting gap in silicene on Ag(111) surface. *Applied Physics Letters*, 102(8), 081602. doi:10.1063/1.4793998

[3] Feng, B., Li, H., Liu, C., Shao, T.-N., Cheng, P., Yao, Y., Wu, K. (2013). Observation of Dirac Cone Warping and Chirality Effects in Silicene. *ACS Nano*. doi:10.1021/nn403661h

5:40pm **GR+EM+NS+SS+TF-ThA12 A Large Scale Epitaxial Growth of h-BN and Graphene Hybrid Structures (BNCs) on 6H-SiC (0001) Controlled a Ratio of h-BN and Graphene by Annealing Temperature**, H.-C. Shin, S.J. Ahn, B.G. Shin, J.-R. Ahn, Sungkyunkwan University, Republic of Korea

Since the hexagonal boron nitride (h-BN) and graphene lateral hybrid structures (BNCs) were successfully fabricated on Cu foil, methods of BNCs synthesis were studied due to theoretically expected interesting electronic, magnetic and transport properties of BNCs, especially on metallic surfaces. However, for device application, it is required to transfer from metallic surfaces to insulating surface. We demonstrate direct growth of large scale epitaxial BNCs controlled a ratio of h-BN and graphene from perfect h-BN to perfect graphene by annealing temperature on 6H-SiC (0001) wafer. The electronic structures and the growth mechanism of BNCs on SiC were investigated by using low energy electron diffraction (LEED), angle resolved photoemission spectroscopy (ARPES) and scanning tunneling microscopy (STM). We found that grown graphene domains gradually replaced initially grown h-BN domains and increased by h-BN decomposition and silicon sublimation at above 1150 degree Celsius. Interestingly, although graphene conventionally grown on 6H-SiC (0001) rotate 30 degrees from substrate, BNCs included both initially grown h-BN and finally grown graphene have 0 degree rotation angle from SiC. Therefore, h-BN and graphene are connected at an atomic scale.

Helium Ion Microscopy Focus Topic Room: 203 A - Session HI-ThA

Imaging and Lithography with Helium Ions

Moderator: G. Hlawacek, University of Twente, Netherlands

2:00pm **HI-ThA1 Imaging of Biological Cells and Carbon Nanomembranes with Helium Ion Microscopy**, A. Beyer, Bielefeld University, Germany **INVITED**

In my talk, I will present a helium-ion microscopy (HIM) study of biological cells and carbon nanomembranes (CNMs). The cells were imaged without conductive coating and the attainable high resolution allowed imaging of extremely small features at the cell surface. Charging of these specimens was effectively compensated by the electron flood gun.

HIM is also a very efficient imaging tool for characterizing CNMs which exclusively consist of surface-near atoms. These 1 nm thick membranes yield a high secondary electron signal, provided that charging is absent. This condition is fulfilled by choosing a suitable beam current or employing the electron flood gun.

Aspects of helium ion beam lithography will also be discussed. In particular, I will show the fabrication of patterned CNMs by local cross-linking of aromatic self-assembled monolayers with helium ions.

2:40pm **HI-ThA3 Patterning of Sub-10 nm Optical Apertures on Single Crystal Metallic Films with the Helium Ion Microscope**, D. Pickard, Unaffiliated, H.F. Hao, V. Viswanathan, National University of Singapore, M. Bosman, IMRE, A*STAR, J. Dorfmueller, H. Giessen, University of Stuttgart, Germany, A.S. Yusuf, Z.K. Ai, Y. Wang, M. Mahmoudi, National University of Singapore **INVITED**

Metallic nanostructures, resonant at optical frequencies, provide controlled enhancement and concentration of electromagnetic energy in the near-field. One example is the enhanced transmission and field localization through sub-wavelength C-apertures on thin metallic films, where transmission gains of 6x and field enhancements of 550x have been reported by others.

[1] [#_fn1]^[2] [#, _fn2] Typically, the critical dimensions of optical apertures are on the order of tens of nanometers (for low-order structures in the near-IR). These dimensions are accessible with conventional focused gallium ion beam patterning, and this has traditionally been the technique used for fabrication. However, for patterning dimensions smaller than 30 nm (typical of visible and ultraviolet structures, or higher order resonant structures), gallium based systems have not performed as successfully. The most critical

shortcomings of Ga⁺ patterning in this regime are the degradation of the fine structure by etching with the beam's tail, and the shift in the optical characteristics or quenching of the resonant metal's properties due to gallium implantation. gallium implantation [3] [#_ftn1].

We have employed the Helium Ion Microscope to directly pattern high order, sub-10 nm optical fractal apertures (free of implanted metal impurities) through optically thick, polycrystalline metallic films and single crystal metal nanoplatelets. Our experimental measurements of the near-field mode profiles with electron energy loss spectroscopy (EELS) demonstrate tight field confinement in multiple modes as predicted by FDTD simulations. This has resulted in extremely high fidelity, optically-active resonant structures (down to 10 nm critical dimension). Controlled fabrication of structures on this size scale opens fascinating prospects for engineering complex multi-modal structures which were previously unrealizable by other techniques. We report our investigations in this arena and detail a variety of novel structures that are now accessible with this technique.

- [1] X.L. Shi, L. Hesselink, *J. Opt. Soc. Am. B* **21**, 13 (2004)
[1] B. Lee, I.M. Lee, S. Kim, D. Ho Oh, L. Hesselink, *J. Mod. Optic.* **57**, 19 (2010)
[1] J.B. Leen, P. Hansen, Y.T. Cheng, L. Hesselink, *OptLett* **33**, 23 (2008)

3:40pm **HI-ThA6 Characterization of 2D Materials by using Scanning Helium Ion Microscopy.** *H.X. Guo, J.H. Gao, D. Fujita*, National Institute for Materials Science, Japan

Two dimension(2D) materials, such as graphene or hexagonal boron nitride (h-BN), have layer structures which are different from bulk materials [1]. Normally, different layers of the 2D materials were combined by a weak band compared with the interlayer chemical bands. This makes the 2D materials special in physical and chemical properties such as optical properties or band structures. Many methods have been applied to research 2D materials, such as Raman microscopy, scanning probe microscopy, transmission electron microscopy and others.

In this presentation, we will show our investigation of 2D materials with scanning helium ion microscopy(SHIM) and other methods. The BN nano sheets and quasi-free standing graphene were synthesized by BN and carbon segregation on surface of metallic substrate [2]. We characterized the number and morphology of the h-BN by using scanning electron microscopy(SEM) and SHIM. On the basis of the interaction between the scanning particles (electrons and helium ions) and h-BN nanosheets, we interpreted an exponential relationship between the intensities of images and the number of layers. Inelastic mean free paths (IMFP) of electrons and helium ions in h-BN nano sheets were calculated approximately. The quasi-free standing graphene on metallic substrate was characterized by scanning kelvin probe microscopy, scanning Auger microscopy, SEM and SHIM. The SHIM images of such samples show high surface sensitivity and space resolution. The advantage of different characterization were interpreted in this presentation.

- [1] Mingsheng Xu, Tao Liang, Minmin Shi, and Hongzheng Chen, *Chem. Rev.* DOI: 10.1021/cr300263a.
[2] Mingsheng Xu, Daisuke Fujita, Hongzheng Chen, and Nobutaka Hanagata, *Nanoscale*, **3**, 2854(2011)

4:00pm **HI-ThA7 Helium Ion Microscopy of CVD-grown Films: Transition Metals and Catalytically Active Transition Metal Oxides.** *H. Vieker, A. Beyer, Z.-Y. Tian, P. Mountapmbeme Kouotou, A. El Kasmî, K. Kohse-Höinghaus, A. Götzhäuser*, Bielefeld University, Germany

Pulsed spray evaporation – chemical vapor deposition (PSE-CVD) is a cheap and scalable route to prepare specifically engineered layers, e.g. metallic and metal oxide films. The latter type is a promising class of materials for developing new efficient catalysts. Such developments require a detailed analysis of the surface morphology which significantly affects the catalytic activity. Among other methods, we employed helium ion microscopy to investigate such films. The high resolution and the high depth of focus are very advantageous in imaging these highly corrugated surfaces. We revealed extremely small surface structures which yield new insights in the morphology of these films. In this study, changes in the morphology of metallic as well as metal oxide PSE-CVD layers by varying the deposition temperature, precursor type, pressure and composition were investigated which leads to a better understanding of the involved growth processes and the catalytic activity.

4:20pm **HI-ThA8 Helium Ion Microscopy of Blood Clot Microstructure.** *S.A. Boden*, University of Southampton, UK, *G. Mills, P.A. Evans*, Morriston Hospital, UK, *M. Bagnall, H.N. Rutt*, University of Southampton, UK

In addition to a smaller probe size and so higher resolution imaging, a key advantage of the helium ion microscope (HIM) is the large depth-of-field (DOF) it provides, typically five times larger than that of a scanning electron microscope [1]. Here we exploit the high resolution and large DOF of the HIM in a study of how diluting blood affects the resulting blood clot microstructure.

Blood clot formation involves the polymerization of fibrinogen into fibrin, forming a fibrous mesh which binds the clot together. Clinicians are looking for better ways of determining what effect dilution has on clot formation to improve the management of fluid replacement therapy. One such method being developed is a rheological technique that measures the gel point (GP) of clotting blood and the incipient clot microstructure complexity at the gel point (the fractal dimension, D_f) [2]. In this study, HIM is used to characterize fully matured clots to demonstrate that variations in the haemorheological properties measured during clotting (D_f), as a result of diluting with isotonic saline, can be correlated with changes in the resulting microstructure of the mature clots. Demonstrating the link between D_f of the incipient clot and the resulting clot microstructure is an important step in developing D_f as a biomarker for use in management of fluid replacement therapy and potentially as a point of care test.

HIM is used to image blood clots formed from samples diluted by isotonic saline to various degrees (0 – 60% dilution), so that the average fibril width can be measured and compared to the D_f of the sample. The large DOF of the HIM (due to its small beam convergence angle) is particularly useful when imaging blood clot microstructure because of their inherent 3D nature and high degree of surface topography. A large number of fibrils appear in focus within one image and so a large number of width measurements can be extracted. Furthermore, the large DOF allows the capture of high quality stereopairs from which the 3D structure of the fibrin network can be analyzed. In addition, the HIM enables imaging of the uncoated fibril surface at a higher resolution compared to SEM which could lead to a deeper understanding of the effects of dilution on blood clot fibril structure.

- [1] B. W. Ward, J. A. Notte, and N. P. Economou, *Journal of Vacuum Science and Technology B*, vol. 24, no. 6, pp. 2871–2874, 2006.
[2] P. A. Evans, K. Hawkins, R. H. K. Morris, N. Thirumalai, R. Munro, L. Wakeman, M. J. Lawrence, and P. R. Williams, *Blood*, vol. 116, no. 17, pp. 3341–6, Oct. 2010.

4:40pm **HI-ThA9 Formation of “Ridge” like Structures for Possible Suppression of Secondary Electron Emission on Cu and Al Surfaces.** *V. Shuthanandan, S. Manamdhara, M.I. Nandasiri, A. Devaraj, D.E. Perea, S.A. Thevuthasan, D.M. Asner*, Pacific Northwest National Laboratory, *D. Rubin, W.H. Hartung, Y. Li*, Cornell University

The performance of future high intensity positron and proton accelerators is likely affected by the electron cloud (EC) generated by the secondary electrons yield (SEY) created from the inner wall of vacuum chambers. One of the promising techniques for suppressing EC formation in regions with magnetic fields is the use of modified surfaces such as longitudinally grooved chamber surfaces to help suppress the escape of secondary electrons from the walls into the central volume of the vacuum chamber. However, the use of macroscopic structures in chambers increases the vacuum chamber impedance and can adversely impact a high intensity beam, particularly if the beam motion has a significant component perpendicular to the direction of the structures. A possible way to obtain the same “geometric” suppression of the electron cloud with less impact on the particle accelerator beams of interest is to prepare the vacuum chamber surfaces with microstructures produced by ion bombardment. In this project we have investigated the secondary electron yield from the ion beam modified Cu and Al surfaces, which are typically employed in high energy positron/electron circular accelerators, and correlate the yield to the chemical and structural properties of the microstructures generated by the high energy ion beam and their interfaces. “Ridge” like structures were generated by irradiating the surfaces using 1 MeV gold, copper and aluminum ions at 60 degrees or more from the normal to the surface. Modified sample surfaces were investigated using Rutherford backscattering spectrometry (RBS), X-ray photoelectron spectroscopy imaging (XPS), Helium ion microscopy (HIM), Atomic Force Microscopy (AFM), high-resolution transmission electron microscopy (HRTEM) and Atom probe tomography (APT). HIM micrographs obtained from the as implanted samples show that the surface of the implanted region underwent substantial rearrangement and formed “ridge” like structures at higher ion fluence. These “ridge” like structures are formed throughout the implanted region with an average height of 1 to 2 microns. The measured secondary electron yield from these structures will be correlated to the microstructures and the combined results will be presented.

5:20pm **HI-ThA11 Towards SIMS on the Helium Ion Microscope: Detection Limits and Experimental Results on the ORION**, *T. Wirtz, D. Dowsett*, Centre de Recherche Public – Gabriel Lippmann, Luxembourg, S. Sijbrandij, J.A. Notte, Carl Zeiss Microscopy

The ORION Helium Ion Microscope (HIM) has become a well-established tool for high resolution microscopy [1] and nanofabrication [2]. The source can operate with both helium and neon [3]. While secondary electrons are used for high-resolution high-contrast imaging, some compositional information can be obtained from backscattered He/Ne ions.

In order to get chemical information with much higher sensitivity, we have investigated the feasibility of performing Secondary Ion Mass Spectrometry on the HIM [4]. In order to reach these objectives, the secondary ion formation process under He⁺ and Ne⁺ bombardment has been investigated and optimized along with the experimental beam parameters such as spot size and dwell time [5]. We have determined experimentally secondary ion yields under helium and neon bombardment for a range of semiconductor and metal samples. While basic yields are low due to the use of noble gas primary ions, they may be enhanced by several orders of magnitude for both negative and positive secondary ions by caesium and oxygen flooding respectively [6]. Measurement of yields has allowed us to determine detection limits for these samples under typical ORION imaging conditions.

More recently an extraction and detection system for secondary ions has been developed for the Helium Ion Microscope by the CRP - Gabriel Lippmann. We have investigated secondary ion emission for semiconductor (Si, InP and GaAs) and metal (Cu, Ni) samples on the ORION. Both total secondary ion depth profiles and secondary ion images have been obtained under helium and neon bombardment.

The obtained results are very encouraging and the prospects of performing SIMS on the ORION are very interesting. In this paper we will present an overview of our results to date and first experimental results of secondary ion detection on the Helium Ion Microscope.

References

- [1] L. Scipioni, C.A. Sanford, J. Notte, B. Thompson, and S. McVey, *J. Vac. Sci. Technol. B* 27, 3250 (2009)
- [2] D. Winston et al, *Nano Letters* 11 4343 (2011)
- [3] F. Rahman et al., *Scanning* 33 (2011) 1
- [4] T. Wirtz, N. Vanhove, L. Pillatsch, D. Dowsett, S. Sijbrandij and J. Notte, *Appl. Phys. Lett.* 101 041601 (2012)
- [5] D. Dowsett, T. Wirtz, N. Vanhove, L. Pillatsch, S. Sijbrandij and J. Notte, *J. Vac. Sci. Technol. B* 30 06F602 (2012)
- [6] P. Philipp et al., *Int. J. Mass Spectrom.* 253 (2006) 71

5:40pm **HI-ThA12 Blunt Tungsten Tip Cleaning with Nitrogen Gas Reaction in Ultra-high Vacuum**, *I.-Y. Park, B. Cho, C. Han, J. Kim, S.J. Ahn*, KRISS, Republic of Korea

The ultra-sharp tips are an essential part for probing and charged particle beam generation in current high resolution microscope. There are a lot of required conditions of tip fabrication and preparation for the high performance of microscopes. Among them, tip cleanliness is very important for the stable and high charged particle current. Here, we describe a simple and efficient method to clean the tungsten tip under UHV (ultra-high vacuum).

Tungsten is preferably adopted for tip material because extremely sharp tip can be easily obtained through electrochemical etching and has higher evaporation field value than ionization field value of rare gases. However, the drawback is poor resistance to surface oxidation; also the surface is contaminated during etching and exposure to atmosphere. In order to eliminate the contaminants, a proper annealing treatment in UHV can remove the contaminant from the tip surface and field evaporation (desorption) can eliminate intensively in the vicinity of the tip apex. In case of annealing, the tip is generally cleaned at approximately 1000 K for several seconds or minutes. However, high temperature could induce the surface diffusion which causes atoms to migrate from the tip apex to tip shank, thereby increasing the radius of tip [1]. Field evaporation cleaning method needs the ultra-sharp tip to produce the field enhancement at the end of tip with a few kV, otherwise it is difficult due to breakdown of high voltage. The nitrogen gas reaction with tungsten surface can sharpen the tip until atomically defined level [2], so we adopted this phenomenon to clean the tip which rarely occur field evaporation with less than 10 kV due to large radius of tip. Firstly, we annealed the tip about 700 K for a few seconds. After that, we inject the nitrogen gas around 10⁻⁸ mbar and helium gas up to 10⁻⁵ mbar to observe directly the cleaning process through an atomic-scale FIM (field ion microscope) in real time. We can monitor the cleaning and sharpening process simultaneously with FIM. This whole process starts from a base pressure in the low 10⁻¹⁰ mbar range; during the cleaning, the chamber is back filled with 10⁻³ mbar. On this, vacuum pressure returns to the 10⁻¹⁰ mbar with pumping system. The technique

considered here can find applications in blunt tip cleaning and making from blunt tip to the few atom tip sequentially in UHV condition.

In Situ Spectroscopy and Microscopy Focus Topic
Room: 203 B - Session IS+EN+SP+SS-ThA

In Situ Studies of Electrochemical Interfaces and Processes

Moderator: A. Kolmakov, Southern Illinois University Carbondale

2:00pm **IS+EN+SP+SS-ThA1 Direct In Situ Probe of Electrochemical Processes in Operating Fuel Cells**, *S.S. Nonnenmann, R. Kungas, J.M. Vohs, D.A. Bonnell*, University of Pennsylvania

Many strategies for advancing energy related processes involve high temperatures and reactive environments. Fuel cell operation, chemical catalysis, and certain approaches to energy harvesting are examples. Scanning probe microscopy boasts a versatile toolbox of local and often atomic resolution measurements of phenomena at a scale that enables understanding of complex processes involved in many systems. Applying these techniques to the realistic conditions under which these processes operate inherently poses significant experimental design challenges. To overcome this, we have developed a system allowing SPM at temperatures to 600°C in reactive gas environments. Here the characterization of an operating fuel cell serves as the first demonstration. Solid oxide fuel cells (SOFCs) offer the highest conversion efficiencies with operating temperatures ranging from 400°C - 1000°C and operate under variable gaseous fuel environments – H₂-based environments (anode side) and O₂-based environments (cathode side). Topography and the influence of the local ionic chemical potential on the surface potential are observed along the electrode/electrolyte interface while under operation. While not (yet) at atomic levels of spatial resolution, these probes are at the scale to examine local interface properties.

2:20pm **IS+EN+SP+SS-ThA2 Ex Situ Lift-Out of Specimens for In Situ TEM Studies**, *L.A. Giannuzzi*, L.A. Giannuzzi & Associates LLC, Z. Yu, M.P. Harmer, Lehigh University

In-situ transmission electron microscopy (TEM) of grain boundaries at elevated temperature requires accurate manipulation of electron transparent specimens to site-specific carbon films patterned on heating membranes measuring only ~5-10 micrometers in diameter. Ex-situ lift-out (EXLO) of focused ion beam (FIB) prepared or other electron transparent specimens (e.g., fibers, particles, platelet precipitates) is advantageous for accurate manipulation of specimens to these membranes because it is fast, reproducible, and avoids deleterious ion implantation into the specimens while FIB imaging during the in-situ lift-out method. The ex-situ lift-out technique for this application will be described and in-situ TEM results will be presented.

2:40pm **IS+EN+SP+SS-ThA3 In Situ Characterization of Thermal Degradation of LiNi_{0.8}Co_{0.15}Al_{0.05}O₂ Cathode Materials for Lithium Ion Batteries: Insights from Combined Synchrotron XRD, XAS and Environmental Microscopy Studies**, *E. Stach, S. Hwang, S.-M. Bak, K.-W. Nam*, Brookhaven National Laboratory, *W. Chang*, Korean Institute of Science and Technology, *X. Yu, E. Hu, K.-B. Kim*, Brookhaven National Laboratory, *K.-Y. Chung*, Korean Institute for Science and Technology, *X.-Q. Yang*, Brookhaven National Laboratory

INVITED

Li-ion batteries have seen widespread application as secondary batteries in numerous applications in consumer electronics, and have attracted recent attention for various forms of electric vehicles. One particularly attractive material for the cathode is the Ni-rich system of LiNi_{0.8}Co_{0.15}Al_{0.05}O₂. These materials are being explored as a replacement to LiCoO₂, as they offer several performance improvements, including higher energy density and lower cost. However, these materials have demonstrated a significant increase in impedance and capacity fade during aging, or upon cycling at elevated temperatures. Additionally, when in highly delithiated states, the reduction of Ni ions during thermal cycling releases oxygen from the crystal structure, which can lead to both thermal runaway and violent reactions with the flammable electrolyte.

We have utilized a variety of in-situ characterization methods to understand the mechanisms associated with the thermal degradation of LiNi_{0.8}Co_{0.15}Al_{0.05}O₂ materials, as a function of their delithiation / charge state. By combining time-resolved synchrotron x-ray diffraction and mass spectrometry, we have directly shown that these materials undergo a specific sequence of phase transformations - from layered to disordered spinel to rock salt - as a function of temperature, and directly correlate these

phase transformations with the evolution of oxygen from the microstructure. In-situ observations in an environmental transmission electron microscope confirm these global average measurements on the nanoscale, and allow us to kinetically track the evolution of oxygen from the surfaces of the nanoparticles into their bulk. In-situ spectroscopic results - from XAS and EELS - allow correlation between electronic structure changes and the resulting phase transformations. Finally by performing these same thermal treatments in-situ to the TEM and in the presence of excess oxygen, we show that it is possible to suppress these phase transformations to significantly higher temperatures, thereby suggesting that methods to protect the surfaces from oxygen evolution could lead to significant enhancements in the safety performance of these materials. Throughout the presentation, the insights gained from complementary in-situ techniques will be highlighted.

3:40pm **IS+EN+SP+SS-ThA6 In Situ Measurement and Control of Interaction Forces at Electrified Softmatter | Metal Interfaces**, **M. Valtiner**, Max Planck Institut für Eisenforschung GmbH, Germany, *S.H. Donaldson, K. Kristiansen, M.A. Gebbie, J.N. Israelachvili*, University of California, Santa Barbara

Redox-active interfaces are ubiquitous in the realms of natural and technological systems. For instance, prevention of corrosive delamination at metal|oxide|paint interfaces, or bio-mimicry of adhesive bonding in natural systems (e.g. mussel glues) rely on a fundamental understanding of interaction forces at electrified and/or redox-active solid|liquid|softmatter interfaces. Recently, we developed a newly designed electrochemical surface forces apparatus setup (EC-SFA) that allows control and measurement of both surface potentials and interfacial electrochemical reactions with simultaneous measurement of normal interaction forces and the absolute distances between (similar or dissimilar) apposing surfaces [1], [2].

To quantify both oxide growth and interaction forces between asymmetric apposing softmatter and metal surfaces we performed normal force measurements across atomically smooth polarized gold electrodes facing PEGolated lipid bilayers with different head-group chemistries. Switching electrochemical potentials allowed us to quantitatively and qualitatively identify, rationalize, and therefore control, which interaction forces dominated between the electrode surfaces and a surface coated with differently end-functionalized polyethylene glycol (PEG) polymers. In particular, the manipulation of *surface potentials and the oxidation of the gold have profound and very strong influences on the measured interaction forces*. Moreover, our measurements allowed us to *in-situ quantify the Au-oxide thickness with Ångstrom accuracy*. Here, we will discuss in detail, how (1) electric double layer potentials, (2) change of surface chemistry (e.g. oxide growth, oxide thickness) as well as (3) polymer chemistry (functional groups and backbone chemistry) influence specific and non-specific interaction forces (electrostatic, hydrophobic and Van der Waals forces, see also [3]) across electrified softmatter|metal interfaces.

[1] Valtiner, M., Kristiansen, K., Greene, G. W. et al. in *Advanced Materials* 23, 2294 (2011).

[2] Valtiner, M., Banquy, X., Kristiansen et al. in *Langmuir* 28, 13080-13093 (2012).

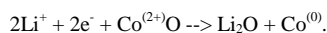
[3] Valtiner, M., Donaldson, S. H., Jr., Gebbie, M. A. et al. in *Journal of the American Chemical Society* 134, 1746-1753 (2012).

4:00pm **IS+EN+SP+SS-ThA7 In Situ Studies of Strain Evolution in Graphene on Ir(111) and Interplay with Magnetic Few Layer Cobalt Films**, **A. N'Diaye**, Lawrence Berkeley National Laboratory **INVITED**

Graphene's transport properties make it a promising component of spintronic applications and logic circuitry operating at gigahertz frequencies or as a support for nanocatalysts. Understanding graphene's interplay with the substrate is key to understanding and tailoring its properties. Here we show how thermal compression leads to few nanometer wide and micrometer long elongated wrinkles on single layer epitaxial graphene on Ir(111) to partially relieve compressive strain in the graphene layer. The strain relief process can be followed in-situ with spot profile analysis low energy electron diffraction (SPA-LEED) and low energy electron microscopy (LEEM). We show that micrometer wide regions of graphene slide over substrate and that the residual strain is spatially inhomogeneous. An other example for the interplay of graphene with its support is the enhancement of the perpendicular magnetic anisotropy in thin Cobalt films intercalated between graphene and Ir(111). We use spin-polarized LEEM (SPLEEM) to study the thickness induced spin reorientation transition in the graphene/Co/Ir(111) system and produce a phase diagram of an in-plane state, an out-of-plane state, and a partially canted state. This work was supported by the U.S. Department of Energy under Contract No. DE-AC02-05CH11231, by the French ANR contract ANR-2010-BLAN-1019-NMGEM and by the Alexander von Humboldt Foundation.

4:40pm **IS+EN+SP+SS-ThA9 The Lithium-Induced Conversion Reaction of CoO Thin Film Battery Materials in Ultra-High Vacuum**, **R. Thorpe**, *S. Rangan, M. Sina, F. Cosandey, R.A. Bartyński*, Rutgers University

Lithium-ion conversion batteries can store 2-3 times more charge than intercalation batteries by utilizing the full range of oxidation states of their constituent divalent or trivalent transition metal compounds during discharge. A prototypical conversion compound is CoO, which follows the reaction



Cobalt oxide and other transition metal oxides are attractive for use as Li-ion anodes in portable electronics due to their high charge storage capacity and moderate voltage versus Li^+/Li^0 . However, the cycling stability of conversion electrodes is poor, and capacity losses have thus far prevented their implementation.

In order to understand phase progression during the conversion reaction of CoO, high-purity CoO thin films grown in UHV were sequentially exposed to atomic lithium. The electronic structure of the pristine films and of the products of lithiation was studied using x-ray photoemission spectroscopy (XPS), UV photoemission spectroscopy, and inverse photoemission spectroscopy. The crystal structure and film reorganization were probed in parallel with transmission electron microscopy (TEM) and scanning tunneling microscopy.

The amount of CoO reduction for a given Li dose was observed to be highly dependent upon the temperature at which lithiation was performed. At 150°C, Li mobility in the active material was sufficient to allow full reduction of the CoO film as confirmed by XPS. Consistent with electrochemically lithiated CoO electrodes, precipitation of Co nanoparticles in a Li_2O matrix was observed in TEM images. However, at room temperature, the Li-rich overlayers that formed on the CoO film after initial lithiations inhibited further Li diffusion. This could be due to the intrinsically poor kinetic properties of Li_2O or to the formation of Li_2O_2 and/or LiOH passivating films.

The reactivity of CoO films was also found to depend on the orientation of the film. CoO(100) films exhibited a higher degree of conversion for a given Li exposure than polycrystalline films. STM and angle-resolved XPS of these films have been used to investigate the differences between these two film morphologies upon exposure to Li.

Accelerating Materials Discovery for Global Competitiveness Focus Topic

Room: 202 B - Session MG-ThA

Theory, Computation and Data-Enabled Scientific Discovery

Moderator: T. Mueller, Johns Hopkins University

2:00pm **MG-ThA1 High-throughput Quantum Chemistry and Virtual Screening for Materials Solutions**, **M.D. Halls**, *D.J. Giesen, H.S. Kwak, A. Goldberg, T.F. Hughes, Y. Cao*, Schrödinger Inc.

For the past 20 years the standard approach to drug discovery has been the automated computational screening of chemical structure libraries to identify lead systems for further investigation and experimental development. Recent advances in the power of computational resources and the improvements in the efficiency and stability of first-principles simulation packages has made it possible to apply this paradigm to challenges in material science. It is now possible for multi-step property calculations using accurate quantum-based methods to be executed automatically for diverse chemical libraries, with the results collected in a growing data record. This record can then be sorted and mined to identify exemplary candidates and establish critical structure-property limits within a chemical design space. To date very few studies have been reported in which quantum chemical calculations are carried out in a high-throughput fashion to compute properties and screen for optimal materials solutions, however with time virtual screening will become central to advanced materials chemistry research.

In this presentation, the use of high-throughput quantum chemistry to analyze and screen a chemical structure library is demonstrated for key materials applications including organic light-emitting diode (OLED) and organic photovoltaic (OPV) materials, and precursors for optimal thin film deposition in semiconductor device fabrication.

2:20pm **MG-ThA2 Computational Materials Design: Precious Material Free Catalyst for NO Dissociation**, *H. Kasai, A.A. Padama*, Osaka University, Japan

We entered the 21st Century witnessing remarkable progress in Science and Technology. Novel materials and devices that were once considered the stuffs of *science fiction* are becoming a reality. It would not be an exaggeration to say that we are coming to the **Age of Designer Materials**. **Complex materials** are designed to have desired properties, with both basic and technological applications. A **Designer Material** has to be **Functional**. To realize this and to test the concepts and principles developed for realizing designer materials, we use **Surfaces** as our testing ground. These give access to the appropriate reduced dimensionality and means to manipulate the degree of complexity, and emergence of function.

Specifically, we were able to design catalyst for NO dissociation that is free from precious materials. NO is emitted from the combustion of fossil fuels and converts to nitric acid in the atmosphere which leads in the formation of acid rain. The dissociation of NO is known to be the rate limiting process for its reduction due to the strong N-O bond [1]. Precious metals such as Rh, Pd and Pt are efficient catalysts for such purpose but their high cost prohibits their massive production [2]. Through first principles investigation, we were able to confirm that Cu-based surface is capable of dissociating NO molecule [3, 4]. The analysis is made with reference to a clean Cu surface. In Cu(111), dissociation of NO is accompanied by a large activation barrier and NO desorption is more likely to happen. This is due to the filled d states of the Cu atoms which limits their interaction with the adsorbate. In the contrary, the local density of states profile of the d orbital of the Cu atoms in Cu₂O(111) shows that the states are shifted to the Fermi level region which explains the good adsorption and easy dissociation of NO. We also found that the reaction path of NO on Cu₂O surface is comparable with that of Rh surface which is characterized by a transition state lying below the reference level (surface and NO_{gas}) [5]. Nevertheless, the activation barrier for NO dissociation is lower in Cu₂O indicating the easier dissociation of NO on the alternative catalyst. Furthermore, the adsorption energy of N and O atoms from the dissociated molecule is also lower on Cu₂O which is desirable for the succeeding steps in the reduction process.

References:

- [1] S. Gonzalez et al., *J. Catal.* 239 (2006) 431.
- [2] H.J. Kwon et al., *Chem. Eng. Sci.*, 62 (2007) 5042.
- [3] A.A.B. Padama et al., *J. Phys.: Condens. Matter*, 24 (2012) 175005.
- [4] H. Kishi et al., *J. Phys.: Condens. Matter*, 24, 262001 (2012).
- [5] H. Kasai et al., *J. Jpn. Petroleum Institute*, (2013) *accepted for publication*.

2:40pm **MG-ThA3 Computer-aided Design of Materials for CO₂ Utilisation**, *N.H. de Leeuw*, Unaffiliated, *A. Roldan, N. Hollingsworth, J. Goodall*, University College London, UK **INVITED**

Despite the high thermodynamic stability of CO₂, biological systems are capable of both activating the molecule and converting it into a range of organic molecules, all of which under moderate conditions. It is clear that if we were able to emulate Nature and successfully convert CO₂ into fuel or useful chemical intermediates, without the need for extreme reaction conditions, the benefits would be enormous: One of the major gases responsible for climate change would become an important feedstock for the fuel, chemical and pharmaceutical industries!

Iron-nickel sulfide membranes formed in the warm, alkaline springs on the Archaean ocean floor are increasingly considered to be the early catalysts for a series of chemical reactions leading to the emergence of life. The anaerobic production of acetate, formaldehyde, amino acids and the nucleic acid bases - the organic precursor molecules of life - are thought to have been catalyzed by small cubane (Fe,Ni)₄S clusters which are structurally similar to the surfaces of present day sulfide minerals such as greigite (Fe₃S₄) and mackinawite (FeS).

Contemporary confirmation of the importance of sulfide clusters as catalysts is provided by a number of proteins essential to modern anaerobic life forms, e.g. ferredoxins or (de)hydrogenases, all of which retain cubane (Fe,Ni)₄S clusters with a greigite-like local structure, either as electron transfer sites or as active sites to metabolise volatiles such as H₂, CO and CO₂.

We have used a combination of computation, synthesis and electrochemistry to mimic Nature and produce Fe-S and Ni-doped Fe-S nanoparticles to catalyse the conversion of CO₂. Careful and sensitive testing of the computationally designed materials, prepared through novel synthesis routes, shows that the nanoparticles have the power to adsorb CO₂ and reduce it to formic acid - a useful chemical intermediate. A particularly promising aspect is that the catalytic conversion of CO₂ takes place at room

pressure and temperature and at the sort of low voltages that could be obtained from solar energy, thus making it a sustainable process.

3:40pm **MG-ThA6 Surface Technology Solutions: Materials Design for Aero-Engine Gas Turbine Applications**, *J.R. Rodgers*, Toth Information Systems Inc., Canada **INVITED**

Erosion damage of aero-engine compressor gas path components occurs to aircraft operating in sandy environment. Erosion can lead to gradual changes in surface finish and component geometry, which consequently alters the dynamic response characteristics of compressor airfoils, causing premature failure. One of the approaches to deal with erosion problems in gas turbine engines is to apply protective hard coating on the component surface. Hardness and ductility are two of the key values for the design and characterization of materials that are used for surface protection. These key values largely depend on the elastic properties of the material, as described by the elastic stiffness tensor. Materials informatics approaches and high-throughput computational materials science methods have been employed, to explore chemistry and property space, to aid the prediction, synthesis, characterization and property optimization of promising candidate materials, for protective hard coatings systems, with enhanced erosion resistance for application to gas turbine airfoils. These generic methods have been employed to explore multidimensional property space, at a previously unavailable level of detail and to rapidly calculate thermophysical properties that are difficult to measure. Given these vast resources of structure and property data it is possible to extract trends on the structure of materials and their properties and use these results at the materials selection and design stages. These informatics approaches, coupled with *ab initio* quantum mechanics methodologies, provide many of the tools needed to guide materials selection via computational experiments. Examples for the application of these methods coupled with the use of experiments for the design of materials for industrial applications will be presented. The results presented will highlight the potential of this combined - informatics, theoretical and experimental - research strategy to aid the manufacturing process.

4:20pm **MG-ThA8 Exploring Electronic Structure in the Search for New Functional Materials**, *M. Klintonberg*, Uppsala University, Sweden **INVITED**

The Electronic Structure Project (ESP/ELSA)[1-3] is an initiative that dates back to 2001 [4,5] and today contain tens of thousands of materials that have been investigated using robust and high accuracy electronic structure methods (all-electron full-potential linear muffin-tin orbital approach, FP-LMTO). A short history of the project, the present capabilities of ESP/ELSA including some examples of successful studies using ESP as well as future developments and outlook will be presented.

- [1] <http://www.materialsgenome.se> (re-directed to <http://gurka.fysik.uu.se/esp>).
- [2] A high accuracy fermi-surface database can be found at <http://gurka.fysik.uu.se/esp-fs>
- [3] "Data mining and accelerated electronic structure theory as a tool in the search for new functional materials", C. Ortiz, O. Eriksson and M. Klintonberg. *Comput. Mater. Sci.* 44, 1042-1049 (2009)
- [4] "A systematic search for new scintillators using electronic structure calculations", M. Klintonberg, S. E. Derenzo and M. J. Weber, *Nanotech.* 2, 427 (2002). Technical Proceedings of the 2002 International Conference on Computational Nanoscience and Nanotechnology, <http://www.nsti.org/procs/ICCN2002/16/W62.11>
- [5] "Potential new scintillators identified by electronic structure calculations", M. Klintonberg, S. E. Derenzo and M. J. Weber, *Nucl. Inst. Meth. A*, 486, 298 (2002), <http://www.sciencedirect.com/science/article/pii/S0168900202007234>

5:00pm **MG-ThA10 Data-Driven Discovery of Physical, Chemical, and Pharmaceutical Materials**, *B.A. Jones*, IBM Almaden Research Center **INVITED**

Data-driven insights have aided materials discovery in the pharmaceutical and related chemical areas for some years now, with even commercial products available. I will describe some successes in these areas, and derive lessons which might be applicable to the areas of condensed matter and polymeric materials. Three points which I will be emphasizing are that a) Just as experiment, theory, and computation must guide each other for MGI to succeed, a triangle of inter-relationships, for MGI it is really a tetrahedron, with computer science forming the fourth vertex. I will discuss the benefits which modern computer science can bring in the areas of modern data mining, machine learning, and big data analytics techniques. The volume of data on materials is fast-growing and scattered across many sources. While new tools and platforms have allowed the processing of vast volumes of data, our ability to integrate heterogeneous and unstructured

data sets is still developing. The ability to correlate data from multiple sources deepens the value of data and allows new insights to emerge. b) The elements of accelerated materials discovery are different in the different scientific fields. Pharmaceutical discovery involves extracting chemical constituents and structures from patents; polymer data is scattered, unstructured, statistical and often ambiguous; and in condensed matter we tend to look at materials properties as a function of some parameter such as doping or temperature, often in graph form. Understanding the needs of both soft and hard condensed matter will help common tools and synergies to develop. c) There are many challenges ahead in fully incorporating data-enabled scientific discovery, as well as learning on both computer science and materials science sides. Getting scientific insights from both computer scientists and from data mining and databases is not yet common, and requires some work ahead in both communities to familiarize themselves with opportunities and to optimize the tools needed for future materials by design.

Nanoparticle-Liquid Interfaces Focus Topic

Room: 201 B - Session NL+AS+BI-ThA

Nanoparticles with Proteins and Cells: Modelling and Measurement

Moderator: D.G. Castner, University of Washington

2:00pm NL+AS+BI-ThA1 **Nanoscale Interface Between Engineered Matter and Living Organisms: Understanding the Biological Identity of Nanosized Materials.** *K. Dawson*, University College, Dublin **INVITED** Nanoscale materials can interact with living organisms in a qualitatively different manner than small molecules. Crucially, biological phenomena such as immune clearance, cellular uptake and biological barrier crossing are all determined by processes on the nanometer scale. Harnessing these endogenous biological processes (for example in creation of new nanomedicines or nanodiagnostics) will therefore require us to work on the nanoscale. This ensures that nanoscience, biology and medicine will be intimately connected for generations to come, and may well provide the best hope of tackling currently intractable diseases. These same scientific observations lead to widespread concern about the potential safety of nanomaterials in general. Early unfocussed concerns have diminished, leaving a more disciplined and balanced scientific dialogue. In particular a growing interest in understanding the fundamental principles of bionanointeractions may offer insight into potential hazard, as well as the basis for therapeutic use. Whilst nanoparticle size is important, the detailed nature of the nanoparticle interface is key to understanding interactions with living organisms. This interface may be quite complex, involving also adsorbed proteins from the biological fluid (blood, or other), leading to a 'protein corona' on the nanoparticle surface that determines its "biological identity." We discuss how this corona is formed, how it is a determining feature in biological interactions, and indeed how in many cases can undermine efforts at targeting nanoparticles using simple grafting strategies. Thus, nanoparticle interactions with living organisms cannot be fully understood without explicitly accounting for the interactions with its surroundings, i.e. the nature of the corona.

·Monopoli, M. P.; Aberg, C.; Salvati, A.; Dawson, K. A. Biomolecular Coronas Provide the Biological Identity of Nanosized Materials. *Nature Nanotechnology* **2012**, *7*, 779-786.

Kim, J. A.; Aberg, C.; Salvati, A.; Dawson, K. A. Role of Cell Cycle on the Cellular Uptake and Dilution of Nanoparticles in a Cell Population. *Nature Nanotechnology* **2012**, *7*, 62-68.

·Monopoli, M. P.; Walczyk, D.; Campbell, A.; Elia, G.; Lynch, I.; Baldelli Bombelli, F.; Dawson, K. A. Physical-Chemical Aspects of Protein Corona: Relevance to in Vitro and in Vivo Biological Impacts of Nanoparticles. *Journal of the American Chemical Society* **2011**, *133*, 2525-2534.

·Cedervall, T.; Lynch, I.; Lindman, S.; Berggard, T.; Thulin, E.; Nilsson, H.; Dawson, K. A.; Linse, S. Understanding the Nanoparticle-Protein Corona Using Methods to Quantify Exchange Rates and Affinities of Proteins for Nanoparticles. *Proceedings of the National Academy of Sciences* **2007**, *104*, 2050-2055.

2:40pm NL+AS+BI-ThA3 **In Silico Modelling and Prediction of the Biological Effects of Nanoparticles.** *D.A. Winkler, V.C. Epa, F.R. Burden*, CSIRO Materials Science & Engineering, Australia, *C. Tassa, R. Weissleder*, Harvard Medical Center, *S. Shaw*, Massachusetts General Hospital and Harvard Medical School **INVITED**

Products are increasingly incorporating nanomaterials because of their superior properties. It is estimated that 50,000 products will contain nanomaterials by 2015. However, we have a poor understanding of their

potential adverse effects on workers, the public, and the environment. To assess risk, regulatory authorities need more experimental testing of nanoparticles. Computational models play a complementary role to experiments in allowing rapid prediction of potential toxicities of new and modified nanomaterials. We have generated quantitative, predictive models of cellular uptake and apoptosis induced by surface modified metal iron oxide nanoparticles for several cell types using sparse feature selection and optimal machine learning methods. We illustrate the potential of computational methods to make a contribution to nanosafety.

3:40pm NL+AS+BI-ThA6 **Quantitative Characterization of Bacterial Cell Loading with Nanoparticles.** *C. Sousa, D. Sequeira, P.M. Martins*, University of Minho, Portugal, *Y.V. Kolen'ko*, International Iberian Nanotechnology Laboratory, Portugal, *S. Lanceros-Méndez*, University of Minho, Portugal, *D.Y. Petrovykh*, International Iberian Nanotechnology Laboratory, Portugal

The primary analytical challenge in characterizing bacterial cells loaded with nanoparticles (NPs) is that the various methods that are traditionally used to measure cells or NPs separately are not readily applied to the mixed samples. These complex samples may contain, for example, a mixture of free NPs, NP-loaded cells, and cells without NPs, while the relative concentrations of NPs and cells or the average number of NPs loaded in one cell is not always known or readily established. Accordingly, methods for separating the different sample components have to be developed and validated before the component of interest (NP-loaded cells in most cases) can be characterized. The final challenge is determining the localization of NPs in and around the cells, as for some applications in sensing and nanomedicine NPs bound to cells externally can be the goal, whereas for exploiting physical properties of NPs, e.g., to induce hyperthermia, maximizing the internalization of NPs by cells can be advantageous.

Our approach to investigating these complex analytical challenges is based on using model systems that are amenable to quantitative characterization by complementary methods, both separately and when mixed as indicated above. Specifically, we are using *Staphylococcus aureus* as model bacterial cells, in part because the typical 500 nm diameter of *S. aureus* cells is within the size range of NP aggregates or large NPs, therefore, the same microscopy and spectroscopy methods can be applied to both components of mixed cell-NP samples. We use gold NPs as the primary model NPs because the strong plasmon peak enables their characterization in solution, while the high density and atomic number of gold can be helpful during separation and for characterization by electron microscopy and spectroscopy. Superparamagnetic iron-oxide NPs with different organic shells are used as a second type of model NPs. We will describe the use of multiple complementary microscopy and spectroscopy techniques for developing, validating, and quantifying protocols for cell-NP separation and for characterization of cell loading by NPs.

4:00pm NL+AS+BI-ThA7 **Protein-Corona: A New Gateway to Disease Therapeutics.** *K. Giri, P. Mukherjee, M. Zimmermann, S. Khader, B. Madden, D. McCormick*, Mayo Clinic

Nanomedicine is a burgeoning field with immense potential in disease therapeutics, diagnosis and imaging. However, an inevitable phenomenon regarding the use of nanoparticles (NPs) *in vivo* is the adsorption of proteins to its surface to form a layer called the "protein corona". The concept of synthetic vs. biological identity of the NPs has emerged. Studies have reported that the acquired biological identity of NPs due to its protein corona influences not just the interaction of the NPs with its targets but also its fate. Among all the NPs that are currently being investigated in nanomedicine, gold nanoparticles (GNPs) are unique in that they possess strong affinity to bind to SH and NH₂ containing molecules. Therefore, proteins by virtue of having cysteine and lysine residues function as unique substrates to bind to GNPs. We hypothesize that the proteome and secretome of cancer cells may include low abundance proteins that escape detection by conventional methods. Enrichment and identification of these proteins may play a critical role in understanding the pathophysiology of disease development and open new avenues for treatment. Our aim was to study the formation of protein corona on GNP surface as a unique way to enrich and identify low abundance proteins that can serve as new therapeutic targets for ovarian cancer. Understanding the interaction of proteins on GNP surface is important as it will guide modulation of protein corona formation for protein enrichment based on physicochemical properties and structure. Here, we present a systematic study of protein corona using 20 nm GNPs. We studied the binding of proteins from lysates derived from two ovarian cell lines, namely OSE (non-cancerous) and A2780 (cancerous). We followed the evolution of the corona for 24 hrs to account for the dynamic and competitive binding of proteins on the NP surface. We characterized the corona at 5 mins, 15 mins, 1hr, 6hrs and 24 hrs using UV-vis spectroscopy, dynamic light scattering, electron microscopy and ζ -potential measurements and identified corona constituents by mass spectroscopy. We focused on understanding what drives protein

adsorption to the NP surface. Lastly, we identified low abundance proteins from the A2780 cell line that were enriched on GNP surface as a proof of concept study to demonstrate that protein corona can be effectively utilized for study of disease and its therapeutics.

Plasma Science and Technology

Room: 104 C - Session PS-ThA

Low Damage Processing

Moderator: E. V. Johnson, LPICM-CNRS, Ecole

Polytechnique, France

2:00pm PS-ThA1 Damage Control: Electron Beam Generated Plasmas for Low T_c Processing, S.G. Walton, Naval Research Laboratory INVITED

The advantages of plasma-based materials processing techniques are numerous. The capability to modify large ($> 10^3 \text{ cm}^2$) areas with precision down to the nanoscale is one reason plasmas are widely used in the materials and surface engineering communities. However, with the rapidly evolving demand for new materials in applications ranging from organic and nanoelectronics to biosensors, some of the limitations of conventional plasma sources are becoming apparent. The lack of process control and excessive ion energies in the processing of soft or very thin materials are examples.

The Naval Research Laboratory (NRL) has developed a processing system based on an electron beam-generated plasma. Unlike conventional discharges produced by electric fields (DC, RF, microwave, etc.), ionization is driven by a high-energy ($\sim 2 \text{ keV}$) electron beam. This approach provides a solution to many of the problems associated with conventional plasma processing systems, making it potentially useful in the development of a wide variety of novel materials. Importantly, high plasma densities (10^{10} - 10^{11} cm^{-3}) can be produced in electron beam generated plasmas, while the electron temperature remains between 0.3 and 1.0 eV. Accordingly, ions leaving the plasma impact surfaces with energies in the range of 1 to 5 eV. This provides the ability to slowly etch and/or controllably engineer both the surface morphology and chemistry, critically important features for applications requiring atomically thin or smooth materials.

An overview of NRL's research efforts in developing this technology with a focus on source development, plasma characterizations, and materials processing will be presented. Particular attention will be given to current efforts in the processing of polymers and 2-d materials such as graphene, where we take advantage of the unique attributes of electron beam generated plasmas to engineer the surface properties of these materials for electronic and sensing applications. This work is supported by the Naval Research Laboratory base program.

2:40pm PS-ThA3 Numerical Simulation of Oxidation Process in Silicon by O₂ Gas Cluster Beam, K. Mizotani, M. Isobe, S. Hamaguchi, Osaka University, Japan

A surface modification process based on a gas cluster ion beam (GCIB) is known to be less damaging to the surface than that based on an ordinary atomic or molecular ion beam. In a GCIB process, several thousands of atoms or molecules aggregated by Van der Waals interactions form a gas cluster and such gas clusters are ionized and accelerated up to a high kinetic energy (typically in the range of several keV) toward a surface that is to be processed. Although the total acceleration energy for each cluster can be very high, each atom or molecule has relatively low kinetic energy. Therefore a GCIB process is essentially a low energy beam process. In this study, we use molecular dynamics (MD) computer simulations to examine surface oxidation processes for silicon (Si) by oxygen-molecule GCIBs at various incident energies and compare the results with those of earlier experimental studies. Especially in this study, we focus on extremely low energy processes, where incident oxygen molecules in gas clusters have kinetic energies close to thermal energy at room temperature. It has been found in MD simulations that only the top surface layer of the substrate can be oxidized with little damage to the surface in GICB processes. This is in contrast with oxygen molecular-ion beam processes, where oxygen hardly sticks to the Si surface when the beam kinetic energy is sufficiently low (so that the chemical bond of O₂ cannot be broken). If the kinetic energy is high, then the surface can be oxidized but the beam impact causes surface damage. It has been observed that, in the case of low-energy gas cluster beam incidence, each gas cluster sticks to the Si surface for dozens of picoseconds until the gas cluster is sublimed by heat transport from the substrate. While a cluster remains on the substrate surface, a large number of oxygen molecules with a solid density are directly exposed to the substrate surface, which increases the probability for the formation of Si-O bonds only on the top surface.

3:00pm PS-ThA4 Ultra-low k Dielectric and Plasma Damage Control for Advanced Technology Nodes (10-nm and Below), F. Lazzarino, IMEC, Belgium, M. Krishtab, KU Leuven, Belgium, S. Tahara, TEL, Belgium, M. Baklanov, IMEC, Belgium

The continuous decrease of the critical dimension together with the introduction of new porous low-k materials (k-value lower than 2.5) make plasma etch more and more challenging. Besides the morphological aspect (profile of the structure or bottom roughness), the degradation of the dielectric properties of the low-k film is another important point that needs to be understood and well-controlled. In this work, we compare and analyze the damage (loss of Si-CH₃ groups and moisture absorption) caused by different types of fluorocarbon-based chemistries and we propose a new damage-free chemistry to pattern advanced low-k materials identified for the most advanced technology nodes.

In the first part of the study, the low-k film is exposed to a selection of few conventional C₄F₈-based chemistries. In all cases, a significant level of damage is observed and is mainly attributed to the diffusion of fluorine radicals coming from the fluorocarbon polymer layer deposited on the low-k surface. As fluorine cannot be suppressed from the discharge, two options are considered to reduce its concentration in the passivation layer. First, a less polymerizing gas like CF₄ is used to replace C₄F₈ then a carbon-free molecule like NF₃ is considered to fully modify the nature of the passivation layer. Both approaches led to a very low level of damage. However, all CF₄-based chemistries show very low etch rate and exhibit a poor selectivity towards masking layers like TiN. In contrast, a much higher etch rate and a greater selectivity is observed when NF₃ is used to replace C₄F₈. Concerning the damage, an extremely thin ($\sim 1 \text{ nm}$) but very hydrophilic carbon depleted layer is formed at the low-k surface and a rough surface appears while the etch front progresses. We characterized and understood these issues using FTIR spectroscopy, Auger analysis and AFM and we fixed both instabilities together by slightly adapting the chemistry. The optimized chemistry leads to a very low level of water absorption within an extremely thin and smooth damaged layer. Finally, a comparative study including k-value, surface roughness and composition of the damage layer using TOF-SIMS is presented applying our best C₄F₈-, CF₄- and NF₃-based chemistries on two potential low-k candidates for the 10-nm technology node.

To conclude, it is shown that a very low level of damage is obtained by using a C-free NF₃-based chemistry. The two side effects like the surface roughness and the high moisture uptake were characterized and the chemistry was tuned in order to overcome both issues. This new chemistry is rated as the best candidate to pattern ultra-low k dielectrics for the most advanced technology nodes.

3:40pm PS-ThA6 High Temperature Etching of GaN Preserving Smooth and Stoichiometric GaN Surface, R. Kometani, K. Ishikawa, K. Takeda, H. Kondo, M. Sekine, M. Hori, Nagoya University, Japan

Plasma etching of GaN is necessary for fabricating high performance GaN devices, however plasma exposure generates defects and produces residues, which results in degradation. It is strongly required that the damage induced by plasma etching should be reduced. Post annealing can recover damages, however, preferentially N lost causes Ga-rich surface. The stoichiometric surface was reported to be deteriorated under annealing of 200 to 1000°C after N₂⁺ sputtering at room temperature.¹ We have revisited the surface reactions at high temperature (HT).

We constructed a high-temperature plasma reactor,² where a CCP was generated by 13.56-MHz rf power to the substrate electrode. Ion bias energy was determined about 250 eV. SiC sample stage can be rapidly heated up to 800°C by an IR lamp as fast as 100°C/s.

As the GaN was exposed to Ar plasma at 600°C, a rough surface appeared with a root-mean-squared (RMS) value of 9.88 nm in AFM image. By XPS analysis of the shoulder peak at 18.9 eV in the Ga 3d region, it revealed Ga metallic state or Ga cluster formation. In contrast, no significant increase of roughness (1.46 nm) was observed after N₂ plasma exposure even at 600°C.

On the other hand, for Cl₂ plasma, the etch rate increased at HT, from 293 to 534 nm/min for 300 to 600°C, and hexagonal pits were formed for 600°C etching. These mean that the heating would prompt the chemical reaction. The optical properties were investigated for YL (deep level defects such as N vacancy), BE (GaN band gap emission), and their ratio indicates crystal quality. Ar plasma exposure increased the YL/BE. It means crystal quality deterioration and deep level defects generation. The shallow level defects were also increased and not only YL but also lower energy side of BE increased. However, the crystal quality after Cl₂ plasma etching was much better than that of Ar plasma.

In Cl₂ plasma, no metallic gallium at any temperature, etch rate increasing and smooth surface was retained at HT except the hexagonal pits formation at 600°C. Consequently, HT etching is effective to enhance the surface chemical reaction and reducing plasma damages.

This work was supported by the Knowledge Cluster Initiative (Second Stage), MEXT, Japan.

1 Y. H. Lai et al., *J. Phys. Chem. B* 105, 10029 (2001).

2 R. Kometani et al., *Appl. Phys. Express* 6 (2013) 056201.

4:00pm **PS-ThA7 Investigation of Surface Roughness in III-V Semiconductors After an *In Situ* Hydrogen Plasma Clean Prior to PEALD**, E. Cleveland, NRL-ASEE, L. Ruppalt, B. Bennett, S.M. Prokes, NRL

III-V compound semiconductors, such as GaSb, are attracting widespread attention as an alternative to Si in advanced complementary metal-oxide-semiconductor (CMOS) technologies; their high electron and hole mobilities, as well as relatively narrow bandgaps, makes them particularly well-suited for high-speed, low power applications. However, for high-performance device realization, the quality of the interface between the III-V semiconductor and the gate-oxide is crucial. Most III-V semiconductors have a highly reactive surface and unlike SiO₂, the native oxides are complex in structure and composition leading to the formation of heavily defected interfaces that pin the semiconductor Fermi-level near midgap and degrades device performance. A significant effort has been focused on surface preparations prior to ALD that removes the native oxide and passivates the III-V atoms in order to ensure the best possible interface. Current approaches typically rely upon wet-chemical etches to remove the defect-prone native oxide layer prior to dielectric deposition; however, this technique typically suffers from a lack of reproducibility, as well as potential interface contamination between processing steps.

Recently, we demonstrated the use of an *in situ* hydrogen plasma treatment prior to the deposition of plasma enhanced ALD (PEALD) Al₂O₃ on GaSb. Samples demonstrating good electrical characteristics correlated to the elimination of Sb-oxide, a decrease in elemental Sb, as well as an increase in Ga₂O₃ as determined by XPS. While using plasma has been shown to produce good quality interfaces and subsequent dielectric films, a significant amount of surface roughening can take place across the semiconductor surface. Although surface roughness may not greatly influence the capacitance modulation of a MOS capacitor, it could significantly hamper charge mobility within a field-effect transistor (FET). Therefore, we investigated the surface roughness of a GaSb surface after exposure to hydrogen plasma as a function of select plasma parameters: rf-power, substrate temperature, and exposure time. Surfaces were characterized using atomic force microscopy, transmission electron microscopy, as well as, electrical measurements. Furthermore, we investigated the surface roughness across GaAs samples of different facets when exposed to a hydrogen plasma prior to PEALD in order to gain a better understanding of surface interactions during plasma assisted ALD.

4:20pm **PS-ThA8 Fabrication of GaAs/AlGaAs Nano-Pillars using Bio-Template Combined with Neutral Beam Defect-Free Etching**, C. Thomas, Y. Tamura, A. Higo, Tohoku University, Japan, N. Okamoto, I. Yamashita, Nara Institute of Science and Technology, Japan, S. Samukawa, Tohoku University, Japan

Quantum dot (QD) lasers have been extensively studied in the last few decades due to their device characteristics benefits. However, fabrication of a high density and uniform two-dimensional array of QDs is still a big challenge. We have developed the first damage-free top-down process for creating GaAs QDs by combining a high-density bio-template [1] and a neutral beam (NB) etching process [2]. The bio-template consists of a high-density (about $7 \times 10^{11} \text{ cm}^{-2}$), two-dimensional array of cage-shaped proteins called ferritins with encapsulated metal oxide nanoparticles (NPs). After removal of the protein shell, 7 nm in diameter iron (Fe) or cobalt (Co) oxide NPs were used as etching masks. The NB etching consists of an inductively coupled plasma chamber separated from the process chamber by a carbon electrode with a high-aspect-ratio aperture array. As a result, the charged particles are efficiently neutralized whereas almost no UV photons can reach the sample.

A thin oxide layer was deposited on top of the single quantum well (GaAs, with Al_{0.3}GaAs barrier layer) samples grown by using metal organic vapor phase epitaxy after removing the native oxide. Then, deposition of the 2D-array etching masks was conducted. An oxygen treatment was carried out to remove the protein shell, followed by a hydrogen radical treatment to remove the remnant oxide layer. Etching was performed using the NB technique. Defect-free nano-pillars [3] were obtained using both etching masks. It appeared that the nano-pillars with Co masks had a better etching profile than those with Fe masks. Indeed, the nano-pillars formed using Co NPs as the etching masks presented a vertical sidewall whereas the ones formed by using Fe NPs presented an etching profile with tapered angles of about 82°. Moreover, we have successfully achieved 15-nm-in-diameter and over 100-nm-high pillars by NBE process. The average height of the nano-pillars was larger when the Co masks were used. These results suggest that the etching selectivity of Co NPs is higher than that of Fe NPs. The

maximum density of the nano-pillars was up to $5 \times 10^{10} \text{ cm}^{-2}$ and did not seem dependent on the chemical nature of the etching mask. The most important parameter for achieving high density, over that of conventional QDs grown by molecular beam epitaxy, is the interaction between the cores and the GaAs surface rather than the etching selectivity. The results showed that III-V compound nanodisk devices can be realized by this defect free top-down nanoprocess.

[1] I. Yamashita et al., *Biochim. Biophys. Acta* 1800 (2010) 845

[2] S. Samukawa et al., *Jpn. J. Appl. Phys.* 40 (2001) L997

[3] X. Y. Wang et al., *Nanotechnology* 22 (2011) 365301.

4:40pm **PS-ThA9 Conductive Carbon Film Formation at Low Temperature (R. T.) using Neutral-Beam-Enhanced Chemical-Vapor-Deposition**, Y. Kikuchi, Tohoku University and Tokyo Electron, Japan, S. Samukawa, Tohoku University, Japan

Conductive carbon material such as graphite film is one of the primary materials used as an alternative for metal electrodes in various devices. However, it is difficult to precisely control their properties at low temperature depositions using conventional plasma-enhanced chemical vapor deposition (PECVD). We have developed a neutral-beam-enhanced chemical vapor deposition (NBECVD) process as an alternative to the conventional PECVD process for forming conductive carbon film to solve this problem. NBECVD can almost completely eliminate the irradiation of UV photons and electrons on the substrate surface by using a carbon aperture, resulting in a damage-free deposition process. Moreover, the NBECVD can form a film through the surface polymerization caused by the bombardment of an energy-controlled Ar neutral beam on a surface with absorbed precursors. We previously proposed controlling the molecular-level structures in SiOCH film by using the NBECVD process, which can control the film properties (k-value and modulus). Since the bombardment energy of the neutral beam can be precisely controlled, selective dissociation of the weak chemical bonds in the precursors is possible, which enables us to control the precursor structure when designing the film structure.

In this study, we used toluene as the precursor to grow an aromatic hydrocarbon structure in the film to obtain the conductive properties. As a result, we formed highly conductive carbon films using a low temperature process.

5:00pm **PS-ThA10 Numerical Simulation of Total Processes of Neutral Beam Etching from Generation of Neutral Beam by Collision of Ions against Graphite Sidewall to 3-dimensional Etching Profile**, N. Watanabe, S. Ohtsuka, Mizuho Information & Research Inst., Japan, S. Mochizuki, Mathematical Systems, Japan, T. Kubota, Tohoku Univ., Japan, T. Iwasaki, Y. Iriye, K. Ono, Mizuho Information & Research Inst., Japan, S. Samukawa, Tohoku Univ., Japan

Neutral beam is an indispensable technology for fabrication of future nano-devices. Especially, a neutral beam source developed by Prof. Samukawa can achieve high neutralization efficiency, controllable energy, and realistic flux. It can perform damage-free processes and is expected to be used in mass production. To achieve production of such future devices, etching simulation is indispensable.

To construct the etching simulation by the neutral beam, simulations of (1) neutral beam generation process by collision of ions from plasma against graphite aperture wall, (2) energy and angular distributions and trajectories of ions and neutral beams passing through the aperture, (3) surface reactions such as etching and deposition, and (4) 3-dimensional etching profile evolution are needed. We performed these simulations and combined into an etching simulation.

First principles calculation was performed to simulate the neutralization process of chlorine ions. By using a larger unit cell, a planar electronic state which is located about 0.4 nm apart from the graphene sheet was found. Also, it was found that electrons emitted from chlorine particles were absorbed by the planar electronic state. It seems that the state plays an important role in a neutralization process. We have calculated neutralization efficiencies as a function of incident energy, incident angle, and number of collisions.

Based on the result, energy and angular distributions of neutral beam were calculated. In the stage of surface reaction simulation, reactions such as radical adsorption, desorption of products, beam-assisted reaction, physical sputtering, carbon adsorption, and so on were considered. Finally 3-dimensional etching simulator was developed by these results. By using the simulator we could reproduce the experimental results such as aperture aspect ratio dependence and bias dependence.

A part of this work was supported by the New Energy and Industrial Technology Development Organization (NEDO).

5:20pm **PS-ThA11 Controlling the Attributes of Electron Beam Generated Processing Plasmas**, D.R. Boris, E.H. Lock, R.F. Fernster, S.G. Walton, Naval Research Laboratory

Electron beam generated plasmas have a variety of unique features that make them distinctive plasma sources for materials processing. They are characterized by high plasma density, very low electron temperature, and unique gas phase chemistries that distinguish them from discharge based plasmas. This work presents measurements from suite of diagnostics (RF impedance probes and Langmuir probes, optical emission spectroscopy (OES), and energy resolving mass spectrometer) used to characterize the unique features of electron beam generated plasmas. The focus will be on the important role that gas chemistry plays in determining plasma parameters (kT_e , V_p , ion energy distribution) and the resulting flexibility of the processing system.

5:40pm **PS-ThA12 Time-resolved Discharge Observation of an Argon Plasma Generated by Commercial Electronic Ballast for Remote Plasma Removal Process**, T. Cho, Y. Sen, R. Bokka, S. Park, D. Lubomirsky, S. Venkataraman, Applied Materials Inc.

Recently, a remote plasma reactor has been widely used to clean the wafer surface and especially for the removal of the silicon dioxide or silicon nitride over silicon with high selectivity in semiconductor manufacturing industry. In a remote plasma process, plasma is generated within a plasma reactor and delivers only radicals to the process chamber. Absence of plasma in the process region decreases the physical damages of the substrate by ion bombardment and the radicals created by the plasma results in chemical reactions at wafer surface. For a stable supply of radicals to process chamber, a plasma reactor has to be designed very carefully. In Applied Materials, Inc, the plasma reactor adopting a hollow cathode type electrode is being used as a remote plasma source. An argon plasma generated between the cone-shaped electrode powered by commercial electronic ballast and grounded plane electrode has been investigated. Since the electronic ballast has positive and negative cycle in a period, two different discharge modes of remote plasma reactor - the normal glow discharge mode and the hollow cathode discharge mode - have been observed. The hollow cathode discharge mode has wider operation window in gas pressure than the glow discharge one. The glow discharge started to be extinguished at higher pressure than 4.1 Torr and turned suddenly to another hollow cathode discharge mode in the holes on ground plate, while the hollow cathode discharge mode kept growing until 10 Torr. These results show that the stable operation window of the system could be defined by the glow discharge mode rather than the hollow cathode discharge mode and could be improved by optimizing the applied voltage waveform and electrode configuration.

Advanced Surface Engineering

Room: 203 C - Session SE+NS+TF-ThA

Nanostructured Thin Films and Coatings

Moderator: C. Mitterer, Montanuniversität Leoben

2:00pm **SE+NS+TF-ThA1 John A. Thornton Memorial Award Lecture - Control of Micro- and Nanostructure in Hard Coatings: Recent Advances**, I.G. Petrov*, J.E. Greene, L. Hultman, University of Illinois at Urbana Champaign and Linköping University, Sweden **INVITED** Polycrystalline TiN and related transition-metal nitride (TMN) thin films are typically deposited by reactive magnetron sputter deposition and employed as diffusion barriers in microelectronics as well as hard, wear-, and corrosion-resistant coatings in mechanical and optical applications. We use a combination of HR-XRD, TEM, HR-XTEM, AFM, and STM analyses to characterize micro- and nanostructures. We will review the fundamental film growth processes - nucleation, coalescence, competitive growth, and recrystallization - and their role in thin film microstructure evolution as a function of substrate temperature. Special attention will be paid to in-situ substrate treatment by ion-irradiation and its effect on film microstructure and adhesion. Using spontaneous natural patterning processes, we show that self-organized nanostructures consisting of commensurate nanolamellae, nanocolumns, nanospheres, and nanopipes can be synthesized to further extend the range of achievable properties. All of these structures are a result of kinetic limitations and require low growth temperatures combined with low-energy (less than the lattice atom displacement potential), very high flux, ion irradiation during deposition. Quantitative information of adatom transport and surface site energies required for the models are obtained from in-situ high-temperature STM

and LEEM analyses. In addition, we use classical molecular dynamics and the modified embedded atom method formalism to investigate the dynamics of atomic-scale transport and film growth on a low-index model compound surface, TiN(001). This approach allows us to gain insight in kinetics of the pathways of Ti, N, and TiN_x ($x = 1 - 3$) adspecies on terraces and single-atom-high TiN(001) in the picosecond regime which are not accessible by state of the art atomistic experimental techniques or by static DFT calculations. We will also review recent advances in the selective use of metal ions during HIPIMS co-sputtering to extend the attainable structures and properties in metastable TMN with examples of $Ti_{(1-x)}Al_xN$, $Ti_{(1-x)}Si_xN$, and $Ti_{(1-x)}Ta_xN$.

2:40pm **SE+NS+TF-ThA3 High Pressure and High Temperature Stabilization of Cubic AlN in $Ti_{0.60}Al_{0.40}N$** , N. Norrby, H. Lind, Linköping University, Sweden, G. Parakhonskiy, University of Bayreuth, Germany, M.P. Johansson-Jöesaar, F. Tashádi, Linköping University, Sweden, L.S. Dubrovinsky, N. Dubrovinskaia, University of Bayreuth, Germany, I.A. Abrikosov, M. Odén, Linköping University, Sweden

As-deposited cubic $Ti_{0.60}Al_{0.40}N$, mainly used as a hard coating on metal cutting tools, decomposes in two steps at elevated temperatures and ambient pressure. The first step is a spinodal decomposition where coherent nanostructured cubic TiN- and AlN-rich domains are formed, after which a transformation of cubic AlN into hexagonal AlN is followed. In the present work, the decomposition of arc evaporated $Ti_{0.60}Al_{0.40}N$ at elevated temperatures and quasi hydrostatic pressures has been studied both experimentally and by first-principles calculations. High pressure and high temperature treatment of the samples was realized using the multi anvil press and diamond anvil cell techniques. The products of the HPHT treatment of $Ti_{0.60}Al_{0.40}N$ were investigated using x-ray diffractometry and transmission electron microscopy. Complimentary calculations show that both hydrostatic pressure and high temperature stabilize the cubic phase of AlN which is in excellent agreement with the experimental results. In addition, the experimental results suggest that the presence of Ti in the system serves to increase the stability region of the cubic AlN phase. The results are industrially important as they show that $Ti_{0.60}Al_{0.40}N$ coatings on cutting inserts do not deteriorate faster under pressure due to the cubic AlN to hexagonal AlN transformation.

3:00pm **SE+NS+TF-ThA4 Surface Chemistry and Interaction with Polymers of TiAlNO Protective Coatings Deposited by HPPMS**, C. Kunze, S. Waschke, University of Paderborn, Germany, M. Baben, D. Music, J.M. Schneider, RWTH Aachen University, Germany, G. Grundmeier, University of Paderborn, Germany

Plasma deposited coatings of TiAlN and TiAlNO are a promising approach to decrease wear and friction of tools within polymer processing such as extrusion and injection molding. Up to now the mechanisms defining the interaction between the protective coating and the polymer melt are not well understood.

An experimental approach is presented that analyzes the surface chemistry of TiAlN and TiAlNO films as a function of film composition and deposition parameters by means of X-ray photoelectron spectroscopy (XPS). The investigated coatings were synthesized via high power pulsed magnetron sputtering (HPPMS) under varying plasma compositions.

It could be shown that the surface composition of TiAlNO films significantly differs from the integral film composition due to a passivation of the surface near region upon contact with ambient atmosphere or residual gas immediately after deposition[1]. These effects have to be taken into account considering adhesion phenomena and interaction with the polymer melt.

The formation of the passive layer on TiAlN was monitored *in-situ* by time resolved XPS spectroscopy with a time resolution of several seconds. It could be shown that the kinetics of the oxidation reaction is quite fast and occurs within a few minutes even at low oxygen partial pressures of less than $1 \cdot 10^{-8}$ mbar. The experimentally observed preferential oxidation reaction of a single element (Ti vs. Al) is compared to DFT based simulations.

The interaction of the TiAlNO passive layer with polymers (polypropylene and polycarbonate) was studied towards a technical application within plastics processing. Besides the passive layer a native contamination film consisting of low-weight (hydro-)carbon species adsorbed from the environmental atmosphere has to be discussed when considering the adhesion to the polymer phase.

To investigate the role of the surface contaminations, an approach using a model adsorbate which carries a marker element (such as P or F) was chosen. TiAlNO coatings with model adsorbate surface layers were brought into contact with the polymer melt. The interface between the coating and the polymer was cleaved under high vacuum conditions to avoid recontamination from the atmosphere. It could be shown that the adsorbate layer remains on the TiAlNO coating even during contact with the polymer

* John A. Thornton Memorial Award Winner

melt. Thus the native contamination layer also has to be carefully considered for the interaction and adhesion to the polymer.

[1] C. Gnoth, C. Kunze, M. Hans, M. to Baben, J. Emmerlich, J. M. Schneider, G. Grundmeier, *Surface chemistry of TiAlN and TiAlNO coatings deposited by means of high power pulsed magnetron sputtering*, J. Phys. D., 46, 2013.

3:40pm SE+NS+TF-ThA6 Oxidation Resistant Zr/Hf-Si-B-C(-N) Films with High Electrical Conductivity, P. Zeman, S. Proksova, J. Kohout, P. Mares, R. Cerstvy, J. Vlcek, University of West Bohemia, Czech Republic
Zr-B-C and Hf-B-C films prepared in our laboratories by nonreactive magnetron sputtering have showed very interesting properties, such as an enhanced hardness (~37 GPa), high electrical conductivity (~ $2 \times 10^6 \Omega\text{m}$) and resistance to oxidation up to 600°C in synthetic flowing air.

In the present paper, the effect of Si and N addition on high temperature behavior of Zr/Hf-Si-B-C(-N) films is systematically investigated with aim to extend oxidation resistance to higher temperatures while keeping the films electrically conductive. The Zr/Hf-Si-B-C(-N) films with hardness ranging from 20 to 30 GPa were deposited on Si(100) substrates by dc pulsed magnetron co-sputtering of a single B₄C-Zr/Hf-Si target (with a fixed 15% Zr/Hf fraction in the target erosion area) in argon or nitrogen-argon gas mixtures. The Si and N content in the as-deposited films was varied in a wide range by the Si fraction in the target erosion area and by the N₂ fraction in the nitrogen-argon gas mixtures, respectively. Oxidation resistance of the Zr/Hf-Si-B-C(-N) films was investigated in synthetic air using a symmetrical high-resolution Setaram TAG 2400 thermogravimetric system. Changes in the structure, elemental composition and surface morphology of the films subjected to oxidation tests were analyzed by X-ray diffraction, Rutherford backscattering spectroscopy and optical microscopy. Electrical resistivity of the as-deposited and annealed films was measured by a standard 4-point method and mechanical properties by microindentation.

The results obtained show that an addition of Si positively affects oxidation resistance of the films resulting in a reduction of their mass gains. The Zr-Si-B-C films deposited with the 20% Si fraction in the target erosion area are oxidation resistant up to 650°C and the mass gain detected at 800°C is less than 0.01 mg/cm². An addition of N into the Zr-Si-B-C films results in a further shift of the onset of oxidation to higher temperatures. The films deposited with the 20% Si fraction in the target erosion area and with the 15% N₂ fraction in the gas mixture are oxidation resistant at least up to 1000°C. As-deposited electrical conductivity and hardness of the Zr-Si-B-C-N films is maintained up to 900°C after dynamical heating in air for the 5% and 10% N₂ fractions in the gas mixture. Preliminary data on the Hf-Si-B-C and Hf-Si-B-C-N films deposited at the same process parameters show even better oxidation behavior and thermal stability of electrical conductivity and hardness. These results will be discussed as well.

4:00pm SE+NS+TF-ThA7 Interfacial and Inter-Diffusion Studies of Epitaxial TiN/Cu Layers on MgO(001), M. Mühlbacher, F. Mendez Martin, Montanuniversität Leoben, Austria, B. Sartory, Materials Center Leoben Forschung GmbH, Austria, J. Keckes, Montanuniversität Leoben, Austria, J. Lu, L. Hultman, Linköping University, Sweden, C. Mitterer, Montanuniversität Leoben, Austria

Interface-controlled materials are widely applied in microelectronics as thin conductive or isolating layers and as diffusion barriers. Degradation of such barrier layers by segregation or diffusion typically results in failure of the device. Thus, as the basis for further enhancement of their reliability, a fundamental understanding of diffusion in these interface-controlled layer materials is necessary.

The Cu/TiN thin film system investigated in the present study is of particular technological relevance, with Cu layers being used as interconnectors and TiN as a diffusion barrier material. TiN layers were grown on (001) oriented MgO substrates by unbalanced DC magnetron sputter deposition at a substrate temperature of 700°C in an Ar/N₂ atmosphere. Subsequently, within the same deposition run, Cu top-layers were deposited at 50°C in pure Ar. To investigate the efficiency of the TiN barrier layer against in-diffusion of Cu, these bi-layer samples were then annealed in vacuum for 60 minutes at 600 and 900°C, respectively.

Pole figures and electron back-scatter diffraction orientation maps indicate that both layers in the as-deposited state are single-crystalline with a cube-on-cube epitaxial relationship with the substrate. This epitaxial relationship is confirmed by selected area electron diffraction patterns. The interfaces were studied on an atomic scale by a combination of high-resolution transmission electron microscopy (HRTEM) and laser-assisted three-dimensional atom probe tomography (3D-APT). HRTEM confirms the single-crystalline structure of each layer and atomically sharp interfaces between both Cu-TiN and TiN-MgO. 3D-APT and energy dispersive X-ray spectroscopy mappings were used to determine the elemental distribution

over the interface in the as-deposited and annealed state, enabling to illuminate the inter-diffusion behavior.

4:20pm SE+NS+TF-ThA8 The Effect of Si Alloying on the Thermal Stability of Al₂O₃ Films Deposited by Filtered Cathodic Arc, F. Nahif, D. Music, S. Mráz, H. Bolvardi, L. Conrads, J.M. Schneider, RWTH Aachen University, Germany

The effect of Si additives on the phase transformation sequence and phase formation temperatures was investigated for filtered cathodic arc deposited Al₂O₃ thin films.

The here obtained XRD data suggest that by addition of Si the transformation of γ - to δ - and θ -Al₂O₃ is restrained by 100°C extending the thermal stability range of the δ - and θ -phase by $\geq 200^\circ\text{C}$ with respect to the unalloyed Al₂O₃ thin film. The formation of α -Al₂O₃ is restrained by 200°C upon addition of Si. Furthermore, the formation of orthorhombic mullite is observed at $\geq 1300^\circ\text{C}$ for the Si alloyed samples, while single phase α -Al₂O₃ is obtained for the unalloyed films at 1100°C.

According to the experimentally observed stabilization of the metastable γ - to δ - and θ -Al₂O₃ phases and the restrained α -Al₂O₃ phase formation upon Si addition the presence of amorphous SiO₂ at the grain boundaries, which may impede mass transport and hence crystalline growth, appears to be the cause of the here reported stabilization. Inconsistency of the Si bonding data obtained by XPS with the notion of a solid solution of Si in the alumina lattice suggests that this cannot serve as an explanation for the stability enhancement.

4:40pm SE+NS+TF-ThA9 A Multitechnique Study of the Interfacial Reaction between TiO₂ Surfaces and Molybdenum, X. Noirfalise, University of Mons, Belgium, D. Cossement, Materia Nova, J.-F. Paul, Université Lille, France, F. Renaux, Materia Nova, R. Snyders, University of Mons, Belgium

Recently, TiO₂ surfaces supporting metals, used in numerous fields of application, have generated a lot of works because of the relationship between the morphology of the deposit and the electronic interactions at the TiO₂/metal interface. As an example, oxygen deficient MoO_x compound supported on TiO₂ substrates demonstrate interesting catalytic properties. Accordingly, the growth of ordered MoO_x nanostructures (nano-particles or ultrathin films) on TiO₂ is of particular importance. Until now, the influence of the chemistry of the support on the deposit morphology is mainly studied. No systematic studies of the impact of the crystallographic constitution of the TiO₂ substrates on the morphology of ultrathin (< 5 nm) Mo films have been reported yet. The objective of this work is to address this question.

We grew, by non-reactive DC sputtering of a metallic Mo target, MoO_x films on home-made (reactive sputtering) and standard TiO₂ supports. The TiO₂ supports differ by their crystallographic constitution (amorphous, anatase and rutile). A particular attention is made on the influence of the TiO₂ properties on the diffusion mechanism and oxidation process at the interface TiO₂/MoO_x using XPS and ToF-SIMS measurement. Periodic DFT calculations have been performed to support the experimental data.

XPS measurements showed that the interfacial reaction between the TiO₂ surface and the deposited Mo is affected by the crystalline properties of the TiO₂ support. The strong oxidation of the first monolayer of the deposited Mo is evidenced. Differences were found in the electronic exchange and, as a consequence, in the growth mode for the three TiO₂ substrates. The emphasis is made with the Cabrera-Mott theory, namely the dependence of the interface reaction on the bulk electronic structure of the three phases.

The data are supported by ToF-SIMS depth profile measurements revealing the substrate-dependent diffusion of oxygen at the interface with appearance of a more or less important oxygen depleted zone at the surface of the TiO₂ support. Additional measurements performed with Ti¹⁸O₂ substrates as well as DFT calculations support the initial conclusion.

The growth mechanisms were estimated from the analysis of the peak and background shapes of the XPS signal by using the "QUASES" software. Due to the differences of the electronic exchange at the interface, a layer-by-layer growth mode is observed for Mo deposited on the (110)-rutile substrate, a Volmer-Weber growth mode is observed on the (101)-anatase substrate and a Stranki-Krastanov growth on the amorphous one.

5:00pm SE+NS+TF-ThA10 Ordered Arrays of Solid and Nanoporous Nanostructures: Particles, Alloy Particles, Pillars, Composites - From Design to Applications, P. Schaaf, D. Wang, Y. Yan, A. Herz, TU Ilmenau, Germany

INVITED

Nanostructured materials gained attention for many applications due to their size effects on both physical and chemical properties and the effects of increased surface area. Modern nanotechnologies can fabricate nanostructured materials in different forms and with different structures, compositions and phases. Furthermore, a combination of different methods

in nanotechnologies provides even more possibilities to design nanostructured materials with more diversity and complexity. Here, some examples will be presented. Metallic nanostructures are very interesting in catalysis and plasmonics. Ordered arrays of pyramidal pits were structured into the Si substrate by using nanoimprint lithography. After deposition of a thin Au film on a pre-patterned substrate, a dewetting process leads to the formation of ordered arrays of nanoparticles. Dewetting is a simple method to form metallic nanoparticles by reducing the surface energy. Structured substrates can modulate the chemical potential during dewetting, so that the ordered arrays of nanoparticles can result from the dewetting on pre-patterned substrates. By dewetting of bi-layers with two different types of metals, alloy nanoparticles can be formed. By tuning the layer thickness ratio and the total layer thickness, the particle size and composition of the particles can be well controlled. For example, the ordered arrays of Au-Ag alloy nanoparticles are fabricated by a combination of nanoimprint lithography and dewetting of Au/Ag bi-layers. By that, ordered arrays of nanoporous gold nanoparticles can be realized by combining a further process step of dealloying. Dealloying is a selective removing process, and nanoporous gold particles are formed by removing the Ag out of the Au-Ag alloy particles via submerging the sample in a HNO₃ solution. The plasmonic property of the porous gold nanoparticles is clearly different from the solid gold nanoparticles with similar particle size.

Ordered arrays of single crystalline nanoporous Si nanopillars are fabricated by a combination of nanoimprint lithography and metal-assisted chemical etching. The pillar structure is first defined on the Si wafer via nanoimprint lithography, and then a thin Au film is deposited on the wafer. The metal-assisted chemical etching is performed in a solution consisting of HF and H₂O₂, and the Au film acts as catalyst for the etching process. The etching process with highly doped p-type Si leads to the formation of porous pillars. By combining a further process step of biomimetic synthesis, porous Si/TiO₂ core/shell nanocomposite pillars are successfully produced. Besides, the TiO₂ is N-doped and also partially filled in the porous Si core.

5:40pm **SE+NS+TF-ThA12 Silicone Nanofilaments as a Novel Carrier Material for Catalysts**, *G.R. Meseck, S. Seeger*, University of Zurich, Switzerland

Immobilization of molecular and nanoparticulate catalysts on carrier materials is crucial to facilitate their handling and recycling as well as to minimize environmental and health risks. While ceramic and oxidic carrier materials provide stability under rough working conditions, engineering possibilities and applications are restricted to extruded or pressed shapes. We introduce silicone nanofilaments (SNFs) as a promising alternative because they can be grown as a thin film on a variety of substrates such as glass, metals and polymers of different composition and shape. A surface bound carpet of SNFs is formed which induces a high surface roughness and conveys the unique physico-chemical properties of a silicone polymer to the coated surface. The procedure uses easily available silane precursors and proceeds via either vapor deposition or solvent based routes. The shape and size of the single filaments within the carpet is tunable and they typically show a high aspect ratio with diameters from 50 to 100 nm and lengths on the micrometer scale. To exploit SNFs as a carrier material we applied deposition-precipitation (DP) to finely disperse titania nanoparticles (TiO₂-NPs) along the filaments. The thus obtained easily recyclable composite of SNFs and TiO₂-NPs showed photocatalytic performance in the degradation of methylene blue which was superior to TiO₂-NPs on a flat reference. While DP can in principle be used to deposit a variety of powerful catalysts, we also investigated physical vapor deposition as a complementary approach. Here, SNFs were uniformly coated with platinum metal via sputter coating. In the hydrogenation of 4-Nitrophenol we proved that this composite material represents a recyclable and easy to handle alternative to nanoparticle based systems.

Scanning Probe Microscopy Focus Topic

Room: 202 C - Session SP+AS+BI+EM+MI+NS+SE+SS-ThA

Probe-sample Interactions, Nano-manipulation and Emerging Instrument Formats

2:00pm **SP+AS+BI+EM+MI+NS+SE+SS-ThA1 Antibody Movement on Regular Antigen Clusters: Fab Arms are Made for Walking**, *J. Preiner*, Johannes Kepler Univ. & Ctr for Adv. Bioanalysis GmbH, Austria, *N. Kodera*, Kanazawa Univ., Japan, *J. Tang*, Chinese Academy of Sciences, *A. Ebner*, Johannes Kepler Univ., Austria, *M. Brameshuber*, Vienna Univ. of Tech., Austria, *D. Blaas*, Medical Univ. of Vienna, Austria, *N. Ilk*, Univ. of Natural Resources & Applied Life Sci. Vienna, Austria, *H.J. Gruber*, Johannes Kepler Univ., Austria, *T. Ando*, Kanazawa Univ., Japan, *P. Hinterdorfer*, Johannes Kepler Univ. & Ctr for Adv. Bioanalysis GmbH, Austria **INVITED**

Antibodies are key molecules for the immune system of vertebrates. The Y-shaped IgGs exhibit C₂-symmetry; their Fc stem is connected to two identical Fab arms binding antigens. The Fc part is recognized by the complement system and by phagocytic cells. Antibodies can be considered molecular calipers; bivalent binding of the two Fab arms to adjacent antigens can only occur within a distance of roughly 6 to 12 nm. This leads to much higher avidity and slower dissociation rates as compared to monovalent binding. Here we show that antibodies exhibit "bipedal" walking on antigenic surfaces and static binding of both Fab arms of an antibody may hold true only for a time scale of ~ 0.04 s. The walking speed depends on the lateral spacing and symmetry of the antigens. On 2D-crystalline surfaces, such as found on bacteria and viruses, steric strain thus appears to be the main reason for short-lived bivalent binding. Importantly, the collision between randomly walking antibodies was seen to reduce their motional freedom. It leads to formation of transient antibody clusters even at low antibody density. Interestingly, such assemblies are known nucleation sites for docking of the complement system and/or phagocytes.

2:40pm **SP+AS+BI+EM+MI+NS+SE+SS-ThA3 Development of a Novel Single-Molecule Force Based Approach for Fragment Screening**, *G.A. Milson*, University of Nottingham, UK

The discovery and development of new chemical entities is complex and time consuming, and of great expense to the pharmaceutical industry¹. High throughput screening (HTS) is the main method used for lead identification, allowing significant numbers of compounds to be tested. However, productivity levels are still below those desired². Due to this, interest in a relatively new process termed fragment based drug discovery (FBDD) has developed³. The FBDD process starts from small, efficiently binding fragments elaborated to more drug-like molecules⁴. However, with fragments being smaller components of the traditionally screened small molecules they have lower affinities and as a result require sensitive detection systems⁵.

It has been proposed that the atomic force microscope (AFM) could be used as a novel system in fragment screening. The AFM benefits from the ability to probe single molecular interactions⁶ using only small volumes of solution that need not be of high purity. Single molecule force recognition spectroscopy (SMFRS) is the commonly termed process where an AFM tip is functionalised with probe molecules that are known to recognise specific target molecules on the opposing surface. Fragments can theoretically be screened against their potential target on the surface and if they bind will block the natural ligand on the tip from occupying the active site.

Here, the well-characterised interaction between streptavidin and biotin was used as a model in which fragments of biotin were screened using an AFM probe functionalised with a biotin-mimetic peptide. It was seen that the AFM was capable of measuring the specific interaction between the biotin mimetic peptide and streptavidin. Each competition assay worked well, with the peptide-streptavidin interaction being blocked by fragments in a concentration dependent manner. Analysis of the percentage adhesion-versus-concentration data resulted in a ranking of the fragments, which matched their known or measured affinities to streptavidin. Despite the fact that this is still in the early stages of development, the results are promising and it is hoped that with further development the approach will be introduced into drug discovery fragment screening methods.

References:

1. Murray, C. W. & Rees, D. C. T., 187-192, (2009).
2. Campbell, S. F., 255-260, (2000).
3. Chessari, G. & Woodhead, A. J., 668-675, (2009).
4. Schulz, M. N. & Hubbard, R. E., 615-621, (2009).
5. Murray, C. W., Verdonk, M. L. & Rees, D. C., 224-232, (2012).

3:00pm **SP+AS+BI+EM+MI+NS+SE+SS-ThA4 Popping Nano-Balloons on TiO₂(110) Surface with the STM Tip, D.V. Potapenko, Z. Li, R.M. Osgood, Columbia University**

Argon-filled subsurface nano-cavities can be created on TiO₂ rutile(110) surface by the means of Ar-ion bombardment combined with temperature treatment of the sample. The presence of the nano-cavities is manifested by the elliptical protrusions on the surface up to 1 nm high and 5 – 30 nm wide. We have developed a micromechanical model that can predict the shape and the depth of individual nano-cavities from the geometry of the corresponding protrusions. To evaluate the validity of the model 7 – 9 V, 1 – 10 ms voltage pulses from the STM tip were used to cause controllable explosions of the nano-cavities, thus allowing the direct independent measurements of their depth. The explosions are caused by the combination of local heating due to the voltage pulse and the high mechanical strain of the TiO₂ crystal lattice in the volume of the protrusion. We discuss the general mechanisms of the nanoscale surface modification produced by voltage pulses from the STM tip and show that at certain conditions the mechanical contact between the tip and the surface occurs. This work is an example of an unusual application of scanning probe microscopy for deep subsurface exploration.

3:40pm **SP+AS+BI+EM+MI+NS+SE+SS-ThA6 Manipulating Magnetism One Atom at a Time, S. Loth, Center for Free-Electron Laser Science, Germany INVITED**

Magnetic materials consist of atoms that interact very locally – often on atomic length scales. In nanoscopic systems the details of these interactions become increasingly important. We use scanning tunneling microscopy to test how far classical concepts of magnetism can be extended into the nanoworld and how they emerge from the quantum mechanical behavior of individual spins.

We have developed a complete toolset to explore magnetization dynamics in artificial few-atom nanostructures:

Magnetic atoms can be assembled into precisely defined arrays by atom manipulation with the STM tip. The atomic spins interact with each other and form collective magnetic states that can be tailored by modifying the atomic arrangements. Elastic and inelastic electron tunneling spectroscopy is used to quantify magnetic properties such as excitation energies, anisotropy barriers and spin-polarization as the nanostructure is being built up [1]. Crucial information on the stability of a nanostructure and influence of the environment can be obtained from the spin system's dynamical response to an external stimulus. For this purpose we use an all-electronic pump probe measurement scheme that excites the nanostructure repeatedly by spin-transfer torque and measures its response by spin-polarized tunneling [2].

With this technique we identified a new route to create stable magnetic states using antiferromagnetic spin-spin interaction. While individual Fe atoms exhibit a spin relaxation time on the order of 1 ns, linear antiferromagnetic chains with as few as eight Fe atoms show magnetic states that are stable for several minutes [3]. This dramatic change in dynamic behavior is indicative of a cross-over from quantum mechanical spin states to a ground state with classical magnetic order.

These experiments show a promising route towards rapid prototyping of quantum magnetic spin structures with control over static and dynamic properties by atom assembly in the STM.

[1] C. F. Hirjibehedin, C.-Y. Lin, A. F. Otte, M. Ternes, C. P. Lutz, B. A. Jones, A. J. Heinrich, *Science* 317, 1199 (2007).

[2] S. Loth, M. Etzkorn, C. P. Lutz, D. M. Eigler, A. J. Heinrich, *Science* 329, 1628 (2010).

[3] S. Loth, S. Baumann, C. P. Lutz, D. M. Eigler, A. J. Heinrich, *Science* 335, 196 (2012).

4:20pm **SP+AS+BI+EM+MI+NS+SE+SS-ThA8 High-speed AFM with a Light Touch, M. Miles, R. Harniman, D.J. Phillips, L.M. Picco, O. Payton, M. Antognozzi, S. Simpson, S. Hanna, D.J. Engledew, University of Bristol, UK, G. Gibson, R. Bowman, M.J. Padgett, University of Glasgow, UK INVITED**

AFM offers unique characteristics amongst microscopy techniques, and offers many benefits such as high-resolution 3D imaging in many environments including liquids. However, there are three areas in which conventional AFM has limitations: (i) a low imaging rate, (ii) the probe-sample force interaction, and (iii) the planar nature of the sample. We are developing two high-speed force microscopy techniques to overcome the first two of these, (i) and (ii).

(i) One high-speed AFM (HS AFM) technique is a DC mode in which an automatic feedback mechanism essentially arising from the hydrodynamics

of the situation maintains a tip-specimen separation of about 1 nm. This technique routinely allows video-rate imaging and has achieved imaging at over 1000 fps. Damage to specimens resulting from this high-speed DC-mode imaging is surprisingly less than at normal speeds. The behavior of the cantilever and tip at these high velocities has been investigated and super lubricity is a key component in the success of this technique [1,2].

(ii) The second high-speed force microscope is a non-contact method based on shear-force microscopy (ShFM). In this HS ShFM, a vertically-oriented, laterally-oscillating probe detects the sample surface at about 1 nm from it as a result of the change in the mechanical properties of the water confined between the probe tip and the sample. With this technique, very low normal forces are applied to the specimen. Information on the molecular water layers as a function of position [3,4].

(iii) AFMs require planar samples because the probe scans in a plane. The tip only 'sees' the sample from above. We have overcome this limitation by steering the tip of a nanorod in a three dimensional scan with six degrees of freedom using holographically generated traps such that it is possible to scan around a sample from any direction. We use various probe types: including silica nanorods, rod-like diatoms, and two-photon polymerized 3D structures [5,6].

1. Payton, OD, et al., *Nanotechnology* 23 (2012) Art. No. 265702.

2. Kalpetek, P, et al., *Measurement Sci. & Technol.*, 24 (2013) Art. No. 025006.

3. Harniman RL, et al., *Nanotechnology* 23 (2012) Art. No. 085703.

4. Fletcher, J, et al., *Science* 340 (2013) online April 11th.

5. Phillips DB, et al., *Nanotechnology* 22 (2011) Art. No. 285503.

6. Olof SN et al., *Nano Letters* 12 (2012) 6018-6023.

5:00pm **SP+AS+BI+EM+MI+NS+SE+SS-ThA10 Multimodal and Multispectral Nano-imaging: Accessing the Structure Underlying the Function of Polymers, organic Photovoltaics, and Biomaterials, M.B. Raschke, University of Colorado at Boulder INVITED**

The properties of many functional soft-matter systems, including polymer heterostructures, organic photovoltaics, and biomembranes are typically defined on the mesoscopic few nm to sub-micron scale. Scattering scanning near-field optical microscopy (s-SNOM) has demonstrated its ability to access the relevant spatial regime. In combination with IR-vibrational spectroscopy s-SNOM provides molecular structural information. However, a yet higher degree of specificity, sensitivity, and selectivity with respect to specific molecular functional features is desired. We will discuss the combination of scattering scanning near-field optical microscopy (s-SNOM) with other nano-optical and scanning probe modalities. That together with the multi-spectral features of different coherent and incoherent IR sources including tunable continuous-wave lasers, femtosecond sources, broadband synchrotron radiation, and thermal near-field radiation provides the desired enhanced dynamic range to probe at the level of the intra- and intermolecular interaction. This results in a unprecedented degree of specificity, sensitivity, and selectivity with respect to specific molecular functional features, as we will discuss for several specific block-copolymer, organic photovoltaic, protein, self-assembled monolayer, and biomineral systems we investigated.

5:40pm **SP+AS+BI+EM+MI+NS+SE+SS-ThA12 Mapping Local Dipole Domains within Two-Dimensional Plastic Lattices, J.C. Thomas, J.J. Schwartz, H.S. Auluck, G. Tran, J. Gilles, S. Osher, University of California at Los Angeles, C.A. Mirkin, Northwestern University, P.S. Weiss, University of California at Los Angeles**

We have observed aligned dipoles forming two-dimensional plastic lattices in self-assembled monolayers of carboranethiols on Au{111}. We have used scanning tunneling microscopy (STM) and simultaneously acquired local barrier height images of 9,12-dicarba-*closo*-dodecaborane *o*-9-carboranethiol (**O9**) monolayers on Au{111} at 4K in extreme high vacuum to determine the local structures and dipole orientations within the monolayers. The molecular structure of **O9** is that of a symmetric cage; a two-dimensional plastic lattice of aligned dipoles is formed through favorable intermolecular dipole-dipole interactions after chemisorption. Local barrier height images juxtaposed with the simultaneously recorded topography reveal directional dipole offsets within domains. New imaging analysis methods were used to overlay the multimodal data and determine molecular dipole orientations. We employ Monte Carlo simulations to model the dipole-dipole interactions, and to predict alignment at low temperature. We compare and contrast topographic and simultaneously acquired local barrier height images of 1,7-dicarba-*closo*-dodecaborane *m*-1-carboranethiol (**M9**) on Au{111} in which the largest dipole is due to the sulfur-gold bond (as opposed to the cage) and is aligned to topographic maxima in STM images.

Organic Layers on Surfaces

Moderator: A.J. Gellman, Carnegie Mellon University

2:00pm **SS1-ThA1 Stability Reversal and Superstructure Formation of Photochromic Diarylethene on Noble Metals**, *T.K. Shimizu, J. Jung, H. Imada, Y. Kim*, RIKEN, Japan

We have studied using scanning tunneling microscopy (STM) and density functional theory calculations one of the diarylethene molecules [1] adsorbed on Au(111) and Cu(111). Two isomers of this molecule, open-form and closed-form, are known to be thermally stable, and its isomerization reactions are induced by irradiation of UV and visible light for the cyclization and cycloreversion reaction, respectively, in solution and single crystalline. Based on STM measurements after deposition of either form of the isomer as well as with and without annealing process, we found that the closed-form was more stable than the open-form on both Au(111) and Cu(111), which is opposite to gas phase. We expect that the stability reversal upon adsorption could arise from the partial ionization of the molecule due to the charge transfer between the molecule and the substrate metal, which stabilizes the closed-form isomer more than the open-form. It is also revealed that while small clusters are formed on clean metallic surfaces, a largely extended 2D superstructure can be fabricated when NaCl is co-deposited on Cu(111). Similar to earlier studies of other organic molecules [2,3], x-ray photoelectron spectroscopy data can be reasonably explained by assuming Na ion incorporation into the superstructure and Cl diffusion into the bulk. We propose a superstructure model where a Na ion binds fluorine and sulfur atoms of the adjacent molecules.

[1] M. Irie, S. Kobatake and M. Horichi, *Science* 291, 1769 (2001).

[2] Ch. Wackerlin et al., *Chem. Commun.* 47, 9146 (2011).

[3] D. Skomski et al., *J. Am. Chem. Soc.* 134, 14165 (2012).

2:20pm **SS1-ThA2 Transient Effects in Optical Properties of Organic Semiconductor Blends Observed in Real Time during Growth and Their Connection to Film Structure**, *K. Broch, A. Gerlach, C. Lorch, J. Dieterle, J. Novak, A. Hinderhofer, F. Schreiber*, University of Tuebingen, Germany

As possible active layers in optoelectronic devices, binary blends of organic semiconductors are of high relevance for applications. A detailed understanding of the structure-property relation in these complex systems is crucial for device optimization, but due to the variety of film structures and associated optical properties also a challenge for fundamental research [1,2]. In particular for vacuum deposited thin films, post growth studies are often not sufficient for a detailed characterization due to possible pronounced transient effects observable during film growth [3]. These effects can include film thickness dependent changes in the average molecular tilt angle or intermolecular spacing, which may result in significant variations in the relative intensities or energy position of specific peaks in the absorption spectra [3].

Using organic molecular beam deposition we prepare thin mixed films of the prototypical organic semiconductors perfluoropentacene (PFP, C₂₂F₁₄) and diindenoperylene (DIP, C₃₂H₁₆) and follow the film growth in situ in real-time simultaneously using grazing incidence X-ray diffraction and optical spectroscopy. We discuss the result of the competing effects of strong and favourable donor-acceptor interaction and steric incompatibilities due to the size mismatch of PFP and DIP on the structure formation in mixed films, concentrating on the size of coherently scattering islands, which is related to the structural order within the films. By exploiting the advantages of a simultaneous measurement of structural and optical properties of the samples we are able to relate pronounced changes in the relative intensities of specific peaks in the optical absorption spectra to the observed changes in the structural order. The results of these experiments give insight in the complex mechanisms of structure formation and structure-property relations in mixed systems and point towards the possibility to tune the structural and optical properties for the optimization of opto-electronic devices.

[1] A. Hinderhofer and F. Schreiber, *ChemPhysChem*, **13**, 628 (2012),

[2] A. Aufderheide et al., *Phys. Rev. Lett.*, **109**, 156102 (2012),

[3] U. Heinemeyer et al., *Phys. Rev. Lett.*, **104**, 257401 (2010),

2:40pm **SS1-ThA3 Charge Transfer between Donor-Acceptor Molecular Networks and Metal Surfaces**, *K. Lauwaet*, IMDEA-Nanociencia, Spain, *J. Rodríguez Fernández, M.R. Reliño, S. Díaz-Tendero, M. Alcamí*, Universidad Autónoma de Madrid, Spain, *N. Martín*, Universidad Complutense de Madrid, Spain, *F. Martín*, Universidad Autónoma de Madrid, Spain, *J.M. Gallego, R. Otero, R. Miranda*, IMDEA-Nanociencia, Spain

Organic charge-transfer (CT) complexes are molecular compounds mixing two species with different electron affinities: an electron donor (D) and an electron acceptor (A). Charge transfer processes between D-A complexes and metallic electrodes are at the heart of novel organic optoelectronic devices such as solar cells [1]. In contrast with the existing exhaustive study of the bulk properties of CT solids, very little is known about the thin-film behaviour. The transition from bulk D-A complexes to ultra-thin films of monolayer thickness deposited on metals introduces a new phenomenology related to the organic-inorganic interface [2]. Effects like hybridization, CT with the surface and molecular level alignment become factors that may govern the electronic transport. Hence, the adsorption of an ultra-thin D-A layer on a metal opens a new field of research for the potential application of CT complexes as devices in the nanoscale.

Simultaneous characterization of the interdependent structural and electronic properties is required for a thorough understanding of the D-A complexes under study [3]. Here, by combining both Scanning Tunnelling Microscopy (STM) and X-ray Photoelectron Spectroscopy (XPS) *in situ*, we can study the delicate balance that exists between intermolecular and molecule-substrate interactions, as well as the hybridization, and the charge transfer taking place in model donor-acceptor assemblies at metal-organic interfaces.

We will show that the metal surface allows us to expand the variety of such D-A networks, permitting the design of D-A metal-organic frameworks with the formulation of D_mA_n (m,n ≥ 1). By controlling the stoichiometry between tetrathiafulvalene (TTF, electron-donor) and tetracyanoethylene (TCNE, electron-acceptor), we can tune the both the structural and the electronic properties of a donor-acceptor system on Ag(111). We show that this system exhibits various structural phases, depending on the stoichiometry, each leading to different levels of charge transfer. These results demonstrate that atomistic studies on the growth of organic thin films under ultrahigh vacuum (UHV) conditions can lead to the kind of accurate control needed in order to optimize device characteristics.

[1] L. Bartels, *Nat. Chem.*, **2**, 87 (2010).

[2] N. Gonzalez-Lakunza, I. Fernández-Torrente, K. J. Franke, N. Lorente, A. Arnau, and J. I. Pascual, *Phys. Rev. Lett.*, **100**, 156805 (2008)

[3] D. G. de Oteyza, J. M. García-Lastra, M. Corso, B. P. Doyle, L. Floreano, A. Morgante, Y. Wakayama, A. Rubio, and J. Enrique Ortega, *Adv. Funct. Mater.*, **19**, 3567 (2009)

3:00pm **SS1-ThA4 Extending Crystalline Organic Nanostructures at Surfaces into Multilayer Films**, *S.L. Tait, D. Skomski, C. Tempas*, Indiana University

Application of self-assembly strategies to complex, organic-based devices requires fabrication of many-layered architectures from multiple organic species. Recent advances in studies of organic adsorbates and supramolecular self-organization have provided examples of two-dimensional crystalline organic assemblies in the first molecular layer. Here, we demonstrate the extension of highly ordered organic layers into multiple layers away from a metal surface. High-resolution scanning tunneling microscopy and X-ray photoelectron spectroscopy are used to study structure and chemistry in these layers. Interfacial organic layers (IOLs) at the metal interface hold promise for the extension of supramolecular self-organization towards the multilayer regime, an area of surface assembly that had been insufficiently explored up to now. IOLs may enable the propagation of highly-ordered 2D supramolecular structure at the surface into the third dimension, thus enabling programmable, crystalline organic films. We illustrate that complex carboxyl and thiophene species can be self-assembled with atomic precision on top of a metal-templated IOL, even though the species are chemically unstable or do not form periodic structures when deposited directly onto the metal. In addition to yielding more complex architectures, the IOL decouples the organics from direct interactions with the metal surface, thereby protecting the species from metal-catalyzed degradation. We have also observed examples of crystalline film growth of up to 10 layers in thickness using STM and atomic force microscopy. These results provide new strategies to achieve long-range self-assembly of well-ordered complex molecular species incorporating technologically-relevant functional groups, which will be of interest in organic electronics and catalysis.

3:40pm **SS1-ThA6 Interface Formation and Nanocrystallization in Molecular Semiconductor Films.** *J. Reutt-Robey*, University of Maryland
INVITED

Molecular materials have a natural tendency toward polymorphism due to the highly anisotropic nature of intermolecular interactions. Because crystal structure dictates key material properties, such as solubility and charge transport, crystallographic phase control is of intense interest to applications ranging from pharmaceuticals to organic electronics. In this talk we describe the kinetic assembly of molecular semiconductors into controlled arrangements. We show how crystalline monolayer films of pentacene (P) and titanyl phthalocyanine (TiOPc) can be produced with varied packings and orientations through controlled deposition. We subject metastable film structures to chemical (fullerene adsorption) tests to create charge-separating interfaces expected in OPV devices. Low-density molecular films rearrange spontaneously under C_{60} (and C_{70}) deposition, yielding new co-crystalline phases with distinctive electronic features; whereas dense films generally yield abrupt semiconductor interfaces. We further show how highly polarizable fullerenes respond to the electrostatic contours of oriented molecular semiconductor films to form unexpected fullerene arrangements. Structure evolution in functionalized fullerenes further demonstrate how electrostatics impact phase selection. C_{60} - and C_{70} -PCBM molecular ordering is monitored from a glassy monolayer phase, produced by pulsed delivery of solute PCBM from a liquid microaerosol, to neat hcp crystalline arrangements inaccessible through homogeneous PCBM crystallization. We relate kinetic barriers for molecular ordering to solvent expulsion and PCBM reorientation, determining the critical PCBM surface density needed to induce nanocrystallization.

Acknowledgement: Portions of this work have been supported by the National Science Foundation Division of Chemistry-MSN and Division of Materials Research DMR-05-20471.

4:20pm **SS1-ThA8 Donor-to-Acceptor Core-level Shift in Molecular Blend/Metal Interfaces.** *P. Borghetti, A. El-Sayed*, Material Physics Center (MPC), Spain, *E. Goiri*, Donostia International Physics Center (DIPC), Spain, *C. Rogero*, MPC, Spain, *L. Floreano*, CNR-IOM, Lab Nazionale TASC, Italy, *D. Mowbray, J.L. Cabellos-Quiroz*, DIPC, Spain, *Y. Wakayama*, International Center for Materials Nanoarchitectonics (WPI-MANA), Japan, *A. Rubio*, Univ. del País Vasco, Spain, *J.E. Ortega*, Univ. del País Vasco, Spain, *D.G. De Oteyza*, DIPC, Spain

Self assembled donor-acceptor complexes on metallic electrodes are at the heart of novel organic optoelectronic applications such as solar cells. In these devices, the organic/metal interface is of fundamental importance, since it defines the charge injection barrier that determines the ultimate device performance. Despite the dramatic progress of the organic electronic field so far, the ability to accurately model and predict the electronic properties at interfaces is still inadequate, thereby hampering the translation of organic thin film growth into an established technology. One of the key issues is how the molecule/metal interaction plus the intermolecular interactions affect the energy-level alignment, i.e., how do the Highest Occupied Molecular Orbital, HOMO, and the Lowest Unoccupied Molecular Orbital, LUMO, align with respect to the metal Fermi energy. However, the HOMO and LUMO alignment is not easy to elucidate in complex multi-component, molecular/metal systems. Here we demonstrate that core-level photoemission from donor-acceptor/metal interfaces can straightforwardly and transparently determine molecular level alignment. We focus on 2D crystalline networks, and carry out a systematic investigation over a number of donor-acceptor/metal systems. In particular, we use Au(111), Cu(111) and Ag(111) as substrates, perfluorinated copper-phthalocyanine (F_{16} CuPc) and perfluoropentacene (PFP) as aromatic acceptors, and copper-phthalocyanine (CuPc) and pentacene (PEN) as electron donors. For each combination, XPS spectra show a characteristic binding energy shift in core-levels as a function of molecular donor/acceptor ratio, irrespectively of the molecule or the metal. Such shift reveals how the level alignment at the molecule/metal interface varies as a function of the donor-acceptor stoichiometry in the contact blend. We also show that the energy level alignment is barely affected by donor-to-acceptor charge transfer, and majorly determined by the electron potential created by donor (high attractive potential) or acceptor (low attractive potential) molecules in their vicinity, i.e., by the average change in work function.

4:40pm **SS1-ThA9 Morphology of Submonomolecular Layers of PTCDI-C8 on (16x2) Reconstructed Si(110).** *K. Lament, P. Mazur, S. Zuber, W. Kaminski, A. Ciszewski*, University of Wrocław, Poland

Organic nanostructures on semiconductor surfaces offer a variety of applications in modern electronic such as light emitting diodes, transistors, solar cells, etc. In most cases well-ordered interfaces are required. Therefore interest in interfaces between organic molecules and inorganic semiconductors surface and the phenomenon of self-organization is still increasing. The growth of thin molecular films with a commensurate structural relationship to the substrate needs substrates that exhibit template

structure into which the molecules can be locked. We apply STM, STS, XPS, UPS, and LEED techniques to study adsorption of PTCDI-C8 (N, N'-Dioctyl-3,4,9,10-perylenedicarboximide) on Si(110). The adsorbate of an average thickness from a fraction of monomolecular layer (ML) up to 1.3 ML was vapor deposited on (16x2) reconstructed surface of n-type, Sb-doped substrate. The reconstruction, typical for clean Si(110) surface, shows a stripe-like structure with alternately spaced lower and higher terraces lying along the [-112] and [1-12] directions. The distance between adjacent raised stripes is about 5 nm and the width of the stripes is about 0.2 nm.

We have found out that the PTCDI-C8 molecules are bound to the surface through oxygen atoms. We have measured the changes of electron affinity of the surface as a function of the average adsorption layer thickness. We were able to observe single molecules of the adsorbate for the layers of the thickness up to 0.6 ML. For these coverage values template effect of the substrate on the PTCDI-C8 ad-layer structure is clearly visible. The molecules form chains along the [-112] and [1-12] directions of the substrate. Conclusions are drawn concerning the chain structure and, with the help of model calculations, the topography of adsorption site for a single molecule in the chain.

5:00pm **SS1-ThA10 Passivation of Metallic Al Surface with Monolayer Organic Adsorbates.** *T. Yamada, R. Sato*, RIKEN, Japan, *K. Watanabe*, Science University of Tokyo, Japan, *M. Kawai*, The University of Tokyo, Japan

We performed a surface-scientific investigation on adsorption of hydrocarbon thiols and fluorocarbon thiols on clean aluminum (111) in order to realize passivation of metallic Al towards air oxidation. Passivation of Al surfaces with oxide-free ultimately thin layers, that is, molecular monolayers, is a prerequisite in nanofabrication with Al entities, such as planar nano-patterned devices and nano-particles. We newly surveyed the adsorption of organic thiol molecules to form densely-packed monolayers, which are suitable for blocking O_2 gas molecules. We found hydrocarbon thiols can readily adsorb on clean Al(111) and form monolayers at room temperature by exposure to vapor from liquid ($n-C_nH_{2n+1}SH$, ($n \leq 12$)) or by sublimation ($(n-C_nH_{2n+1}SH, (n > 12)$ and 4-biphenylthiol). The hydrocarbon parts were proven to be intact after adsorption by the electron spectroscopies (XPS and vibrational analysis byHREELS). The SH species was not detected vibrationally, indicating that S is anchoring the hydrocarbon part on Al. Blocking of O_2 oxidation of Al substrate was effective in the O_2 pressure range below 10^{-5} Torr. At higher pressures ranging up to 1000 Torr, a multilayer of Al_2O_3 was formed underneath the organic monolayer, even for $n-C_{18}H_{37}SH$ monolayer. The ability to block O_2 oxidation was remarkably enhanced by curing these organic monolayers with electron beam. We irradiated a shower of 100 eV electron ($\sim 1 \text{ mC cm}^{-2}$) onto these monolayers, and the rate of Al substrate oxidation decreased to less than one tenth of that of the clean Al(111) in the atmospheric pressure of O_2 . It was seen that the irradiation of electron beam introduces unsaturated C-C bonds with a nearly complete loss of C-H bonds from the monolayer, both from alkane and aromatic thiols. A quasi-graphitic monolayer is anticipated to be formed by electron irradiation. The thickness of this layer is ~ 1 nm. The electron-bombarded monolayers of this type exhibited a substantial robustness towards oxidation in ambient O_2 . [1,2] Linear fluoroalkane thiols, $n-C_nF_{2n+1}C_2H_4SH$ ($n=4,8$), form monolayers at room temperature with a full coverage smaller than the alkanethiols. When the adsorption process was made at substrate temperatures higher than 100°C , the uptake of carbon exceeded the monolayer amount of the precursor molecule, and substantial loss of F from the adlayer was observed. The adlayer seemed to be composed of polymerized fluorohydrocarbon, and exhibited a substantial strength against oxidation. These robust monolayers will bring about a better utility of metallic Al in nanotechnology in general. [1] S. Nomura et al., *Chem. Lett.* **39** (2010) 1297. [2] T. Yamada, Japan Patent Application 2011-168725.

5:20pm **SS1-ThA11 Selenium: The Better Anchor Group for Self-Assembled Monolayers (SAMs) on Gold?** *A. Terfort*, University of Frankfurt, Germany, *M. Zharnikov*, University of Heidelberg, Germany, *P. Cyganik*, Jagiellonian University, Poland

Self-assembled monolayers (SAM) became a very powerful tool in the materials sciences, biochemistry, and engineering. In particular SAMs of thiolates are renowned for their ease of formation, their stability and their high order. Nevertheless, not all thiols can form densely packed monolayers and for some cases even the best thiolate monolayers are not well ordered enough.

Based on the idea that a softer anchoring atom would fit better to the soft gold atoms (according to Pearson's HSAB principle), we prepared a number of selenium-containing precursors and studied their assembly on gold (and in some cases on silver). Data obtained by surface infrared spectroscopy, different photo-electron spectroscopies, and STM hint on the formation of very stable monolayers with improved order.[1-4]

In this talk we will present the preparation methods for the starting materials and the respective monolayers, give details on the surface characterisation, and offer explanations for the superior behaviour of the selenolate SAMs.

References

- [1] Szelągowska-Kunstman, K.; Cyganik, P.; Schüpbach, B.; Terfort, A. *Phys. Chem. Chem. Phys.* **12**, 4400-4406 (2010)
- [2] Weidner, T.; Shaporenko, A.; Müller, J.; Schmid, M.; Cyganik, P.; Terfort, A.; Zharnikov, M. *J. Phys. Chem C* **112**, 12495–12506 (2008)
- [3] Cyganik, P.; Szelągowska-Kunstman, K.; Terfort, A.; Zharnikov, M. *J. Phys. Chem C* **112**, 15466-15473, (2008)
- [4] Shaporenko, A.; Müller, J.; Weidner, T.; Terfort, A.; Zharnikov, M. *J. Am. Chem. Soc.* **129**, 2232-2233 (2007)

Surface Science

Room: 202 A - Session SS2-ThA

Surface Dynamics and Non-adiabatic Processes

Moderator: R.A. Bartynski, Rutgers University

2:00pm SS2-ThA1 Angle-Resolved Dissociative Sticking Coefficients of Light Alkanes on Pt(111) Measured with Effusive Molecular Beams, J.K. Navin, S.B. Donald, I.A. Harrison, University of Virginia

Angle-resolved dissociative sticking coefficients (DSCs) were measured for a series of small alkanes on Pt(111) using effusive molecular beams. Measurements relevant to both thermal equilibrium ($T_g = T_s$) and non-equilibrium ($T_g \neq T_s$) conditions were obtained. A precursor mediated microcanonical trapping (PMMT) model was useful in analyzing and comparing different kinds of experiments. The thermal DSC for methane dissociative chemisorption on Pt(111) at 700 K varied sharply around the direction of the surface normal as $S(700\text{ K}, \varphi) = 8.2 \times 10^{-5} \cos^{14.5}(\varphi)$. Successful modeling of this methane DSC behavior, consistent with existent supersonic molecular beam experiments involving rotationally cold molecules, required that translation parallel to the surface and rotations be treated as a spectator degree of freedoms and that the vibrational efficacy relative to normal translational energy be $\eta_v=0.4$. Across the series of alkanes, methane, ethane, and propane, the angular distributions of the thermal DSCs broadened significantly. The only angle-dependent energy that promotes thermal dissociative chemisorption of alkanes is molecular normal translational energy, $E_n = E_t \cos^2(\varphi)$, which should become less important as the vibrational energy of the impinging molecules increases with increasing molecular size. The bounds that the thermal angle-resolved DSCs place on theoretical models of alkane reactivity will be discussed.

2:20pm SS2-ThA2 Thermal Non-Equilibrium Desorption of $^{13}\text{CO}_2$ Formed by the Decomposition of Formate on Cu Surfaces, J. Quan, T. Kondo, M. Sakurai, J. Nakamura, The University of Tsukuba, Japan

It is well known that formate (HCOO^*) specie is the important intermediate for methanol synthesis by hydrogenation of CO_2 on copper catalysts. Because the formate synthesis by reaction of CO_2 with adsorbed hydrogen atom has been suggested to be an Eley – Rideal type mechanism^[1], we try to clarify the dynamics of formate decomposition on Cu (110), Cu (100) and Cu (111) surfaces in this study. That is, both formate synthesis and formate decomposition are expected to be thermal non-equilibrium processes. We have thus measured angle-resolved temperature programmed desorption (AR-TPD) of CO_2 formed by decomposition of formate. Formate was prepared by decomposition of ^{13}C -formic acid (H^{13}COOH) on oxygen pre-adsorbed or oxygen-free Cu(110), Cu(100) and Cu(111) surfaces. AR-TPD experiments were then carried out for $^{13}\text{CO}_2$. The signal intensity of $^{13}\text{C}^{16}\text{O}_2$ in distribution was plotted for each polar angle in the range -80° to 80° (5° as interval angle) from TPD spectrum. It is found that identical sharp distributions of $^{13}\text{CO}_2$ were observed Cu(110), Cu(100) and Cu(111) surfaces, showing distribution normal to the surfaces with the function of $\cos^8\theta$. These results indicate that the decomposition of formate is a thermal non-equilibrium process, in which CO_2 molecules desorb with hyper-thermal energy due to a repulsive force from the surfaces. It is also suggested that the local structures just before the CO_2 desorption near the transition states (TS) are the same on Cu (110), Cu (100) and Cu (111). That is, ^{13}C of ^{13}COO is bound with a hydrogen adatom, while the O-Cu bond has been already broken just before the CO_2 desorption. The TS structures may be free to rotate and therefore desorbed $^{13}\text{CO}_2$ distribution is insensitive to the surface structure. The structure insensitivity is consistent with that measured for the kinetics of formate synthesis. Density functional theory (DFT) calculations are also consistent with the proposed model. [1] H. Nakano, J. Nakamura et al., *J. Phys. Chem. B*, 105 (2001) 1355-1365.

2:40pm SS2-ThA3 RRKM Simulation of Hydrogen Dissociation on Cu(111): Addressing Dynamical Biases, Surface Temperature, and Tunneling, S.B. Donald, I.A. Harrison, University of Virginia

The effects of dynamics, surface temperature, and tunneling on the dissociative chemisorption of hydrogen on Cu(111) are explored using a dynamically-biased precursor mediated microcanonical trapping (d-PMMT) model. Transition state vibrational frequencies were taken from recent GGA-DFT electronic structure calculations and the model's few remaining parameters were fixed by optimizing simulations to a limited number of quantum-state-resolved associative desorption experiments. The d-PMMT model reproduces a diverse variety of dissociative chemisorption and associative desorption experimental results, and, importantly, largely captures the surface temperature dependence of quantum-state-resolved dissociative sticking coefficients. Molecular translational energy parallel to the surface was treated as a spectator degree of freedom. The efficacy of molecular rotational energy to promote dissociation, relative to normal translational energy, varied monotonically from -45% to 33% as the rotational energy increased. The molecular vibrational and surface phonon efficacies were 60% . Efficacies did not vary with isotope change from H_2 to D_2 . The thermal dissociative sticking coefficient for $\text{H}_2/\text{Cu}(111)$ is predicted to vary as $S(T) = S_0 \exp(-E_a/RT)$ where $S_0 = 0.075$ and $E_a = 49.2$ kJ/mol over the $300\text{ K} \leq T \leq 1000\text{ K}$ temperature range. Dynamical effects are significant and suppress $S(T)$ by ~ 2 orders of magnitude as compared to statistical expectations. For thermal dissociative chemisorption of $\text{H}_2/\text{Cu}(111)$ at 1000 K , a temperature of catalytic interest, normal translational energy is calculated to provide 74% of the energy necessary to react, surface phonons 17% , molecular rotation 5% , and vibration 4% . Tunneling is calculated to account for 13% of $S(T)$ at 1000 K , but more than 50% at temperatures below 400 K .

3:00pm SS2-ThA4 Ultrafast Probing of Chemical Reactions using X-rays from a Free-Electron Laser, J.L. LaRue, SLAC National Accelerator Lab, M. Dell'Angela, Univ. of Hamburg, Germany, M. Beye, HZB für Mat. und Energie/Elektronenspeicherung BESSY II, Germany, R. Coffee, SLAC National Accelerator Lab, A. Föhlisch, HZB für Mat. und Energie/Elektronenspeicherung BESSY II, Germany, J. Gladh, Stockholm Univ., Sweden, T. Katayama, S. Kaya, J.A. Sellberg, SLAC National Accelerator Lab, A. Møgelhøj, Technical Univ. of Denmark, D. Nordlund, J.K. Nørskov, SLAC National Accelerator Lab, H. Öberg, Stockholm Univ., Sweden, H. Ogasawara, SLAC National Accelerator Laboratory, H. Öström, L.G.M. Pettersson, Stockholm Univ., Sweden, W.F. Schlotter, SLAC National Accelerator Lab., W. Wurth, Univ. of Hamburg, Germany, M. Wolf, Fritz-Haber-Institut der Max-Planck-Gesellschaft, Germany, A. Nilsson, SLAC National Accelerator Lab.

The femtosecond dynamics of CO adsorbed on a Ru(0001) surface after excitation by an optical laser have been studied using the Linac Coherent Light Source (LCLS) free electron x-ray laser. Changes in the occupied and unoccupied electronic structure were monitored using ultrafast soft x-ray absorption and emission spectroscopy. We found that the CO molecules, upon excitation by the optical laser, are excited to a weakly adsorbed precursor state occurring on a time scale of >2 ps, and at longer timescales, desorbed from this precursor state. Ab initio molecular dynamics simulations of CO adsorbed on Ru(0001) were performed at 1500 and 3000 K providing insight into the desorption process. Within the first couple picoseconds, the metal-adsorbate coordination is initially increased due to hot-electron-driven vibrational excitations. This process is faster than, but occurs in parallel with, the transition into the precursor state. With resonant x-ray emission spectroscopy, each of these states can be selectively probed and the optical laser fluence dependent transient populations can be determined. At high optical laser fluences, a large fraction of the molecules (30%) were trapped in the transient precursor state that precedes desorption. We observed electronic structure changes that are consistent with a weakening of the CO interaction with the substrate. About half the molecules in the precursor state desorbed from the surface while the other half return to the chemisorbed state. We calculated the free energy of the molecule as a function of the desorption reaction coordinate using density functional theory, including van der Waals interactions. Two distinct adsorption wells - chemisorbed and precursor state separated by an entropy barrier - explain the anomalously high prefactors often observed in desorption of molecules from metals.

3:40pm SS2-ThA6 Dynamics of Electron Transfer and Exciton Formation at Interfaces, M. Wolf, Fritz-Haber-Institut der Max-Planck-Gesellschaft, Germany

INVITED

We have studied the ultrafast dynamics of photoinduced electron transfer and solvation processes at the water ice-metal interface and focus here on the effect of co-adsorbed alkali ions (Na, K, Cs). Femtosecond time-resolved two-photon-photoemission (2PPE) spectroscopy provides direct access to elementary processes like electron injection and the subsequent solvation dynamics which competes with the electron transfer back to the

Cu(111) substrate. In particular, we study the electronic structure changes and ultrafast dynamics for the build-up of a solvation shell (up to 6 water molecules) around individual alkali atoms at the metal surface and compare with electronic structure calculations. For ice multilayers doped with alkali ions we observe the formation of long-lived electron alkali-water complexes.

As an example for a hybrid system of inorganic and organic semiconductors we investigate the electronic structure and dynamics at the ZnO(10-10) surface and the influence of hydrogen and pyridine adsorption. Hydrogen termination leads to the formation of a metallic surface band, whereas pyridine adsorption results in a quite substantial work function reduction (up to 2.9 eV), which may be useful for controlling the energy level alignment at inorganic/organic interfaces. Furthermore we directly monitor the ultrafast relaxation of hot photocarriers in the ZnO conduction band and the subsequent formation of an excitonic state at the ZnO surface on ps timescales.

4:20pm **SS2-ThA8 Single Molecule Spectroscopy and Reactions at Surfaces**, *M. Kawai*, The University of Tokyo, Japan, *Y. Kim*, RIKEN, Japan, *N. Takagi*, The University of Tokyo, Japan **INVITED**

Ultimate spatial resolution of scanning tunneling microscope (STM) enables us to observe the inner electronic, vibrational [1-6] and spin [7-9] structures of a molecule adsorbed on solid surfaces. Vibrational spectrum of a single molecule provides useful information not only for the chemical identification of the molecule [1] but also for investigating how molecular vibrations can couple with the relevant dynamical processes [2-6], where the response of vibrationally mediated molecular motion to applied bias voltage, namely an "action spectrum", can reveal vibrational modes that are excited through STM inelastic tunneling processes, because the molecular motion is induced only *via* the inelastic tunneling processes [3-5]. Molecular spin can couple with electrons of metal substrates. Depending on the strength of the coupling spin state of the molecule changes. Examples are given for Iron phthalocyanine (Fe-Pc) adsorbed on Cu, Au and Ag. With strong coupling with Cu(110) the spin is completely killed whereas if decoupled as on Cu(110) 2x1-O, spin survives with change in the direction of easy axis [7]. On Au weak coupling leads to appearance of Kondo state, where a competition between the RKKY interaction affects the spin state [8]. Kondo state of FePc on Au depends on the adsorption site, where the difference was originating from the coupling with the substrate electrons [9-10].

References :

- [1] Y. Kim, T. Komeda, and M. Kawai, *Phys. Rev. Lett.* **89** (2002) 126104.
- [2] S. Katano, M. Trenary, Y. Kim and M. Kawai, *Science* **316** (2007) 1883.
- [3] T. Komeda, Y. Kim, M. Kawai, et al., *Science* **295** (2002) 2055.
- [4] Y. Sainoo, Y. Kim, T. Okawa, et al., *Phys. Rev. Lett.* **95** (2005) 246102.
- [5] M. Ohara, Y. Kim and M. Kawai, *Phys. Rev. Lett.* **100** (2008) 136104.
- [6] K. Motobayashi, Y. Kim, H. Ueba and M. Kawai, *Phys. Rev. Lett.* **105** (2010) 076101.
- [7] H.-J. Shin, J. Jung, K. Motobayashi, S. Yanagisawa, Y. Morikawa, Y. Kim and M. Kawai, *Nature Materials* **9** (2010) 442-447.
- [8] N. Tsukahara, K. Noto, M. Ohara, S. Shiraki, N. Takagi, Y. Takata, J. Miyawaki, M. Taguchi, A. Chainani, S. Shin and M. Kawai, *Phys. Rev. Lett.* **102** (2009) 167203.
- [9] N. Tsukahara, S. Shiraki, S. Itou, N. Ohta, N. Takagi, and M. Kawai, *Phys. Rev. Lett.* **106** (2011) 187201.
- [10] E. Minamitani, D. Matsunaka, N. Tsukahara, N. Takagi, M. Kawai, Y. Kim, *e-J. Surf. Sci. Nanotech.* **10** (2012) 38.
- [11] E. Minamitani, N. Tsukahara, D. Matsunaka, Y. Kim, N. Takagi, and M. Kawai, *Phys. Rev. Lett.* **109** (2012) 086602.

5:00pm **SS2-ThA10 The Role of Vibrationally Hot Precursors in Methane Activation on Ir(111) and Ir(110)**, *A.L. Utz*, *E. Peterson*, *E. Dombrowski*, *E. High*, Tufts University

Vibrationally excited molecules can play an important role in methane activation on transition metal catalysts. This talk will focus on the reactivity of vibrationally excited methane molecules physisorbed to the surface. Under thermal reaction conditions typical in a steam reforming reactor, over half of the methane molecules are vibrationally excited, but their average translational energy is low enough that their trapping probability is significant. We use seeding techniques and molecular beam scattering methods to control the translational energy of the methane molecules incident on the surface, and infrared laser excitation of molecules in the molecular beam to control the amount and type of vibrational excitation. We find that vibrationally hot molecules can undergo reaction on low-index Ir surfaces via a precursor-mediated mechanism even in the presence of efficient vibrational quenching channels on the metal surface. In another set

of experiments we explore how methane molecules in the ground vibrational state are activated while physisorbed to a hot surface.

In contrast to prior suggestions, this work suggests that an increase in reactivity with gas temperature may not be an automatic signature for a direct reaction mechanism where methane dissociates in a single collision. High gas temperatures also result in significant populations of vibrationally excited molecules whose additional internal energy may enhance their precursor-mediated reactivity. Our ability to control independently the translational and vibrational energy of the methane reagent and the surface temperature allows us to deconvolute these contributions to reactivity and more clearly reveal the mechanistic basis for methane activation under conditions typical in thermal processing.

5:20pm **SS2-ThA11 Vibrational Efficacy in Methane Dissociative Chemisorption Dynamics**, *S.B. Donald*, *I.A. Harrison*, University of Virginia

Dynamics play an important role in the activated dissociative chemisorption of methane and can modulate the thermal reactivity by about an order of magnitude as compared to statistical expectations based on energetics alone. A dynamically-biased precursor mediated microcanonical trapping (d-PMMT) model of activated dissociative chemisorption has sufficed to quantitatively replicate the behavior of methane interacting with a number of metal surfaces (M) for a variety of non-equilibrium and thermal equilibrium experiments. It was found that molecular translation parallel to the surface and rotations are spectator degrees of freedom and vibrational energy is typically less efficacious than translational energy directed along the surface normal in promoting reactivity [e.g., the vibrational efficacy relative to normal translational energy is $\eta_v = 0.4$ for CH₄/Pt(111)]. This latter kind of dynamical effect is well-documented for gas-phase atom + diatomic molecule reactions where it is codified by the "Polanyi rules" which state that "early" transition state barriers are preferentially surmounted by translational energy and "late" barriers by vibrational energy. The threshold energy for chemisorption, E_0 , and the thermally state averaged vibrational efficacy, η_v , derived from d-PMMT analysis of different CH₄/M experiments are shown to have interesting and systematic correlations with the results of GGA-DFT electronic structure calculations of CH₄/M transition state properties as M is varied. The Polanyi rules apparently extend well to the CH₄/M chemistry and may thereby serve to guide ab initio predictions of experimental dissociative sticking coefficients.

5:40pm **SS2-ThA12 NO Formation in Eley-Rideal Reactions with Hyperthermal N Atoms**, *T. Zaharia*, Materials innovation institute (M2i), Netherlands, *A.W. Kley*, University of Amsterdam, Netherlands, *M.A. Gleeson*, FOM Institute DIFFER, Netherlands

Almost all chemical reactions at surfaces proceed via the Langmuir-Hinshelwood mechanism. In such a reaction all reactants equilibrate to the surface before meeting by diffusion and reacting. By contrast, Eley-Rideal reactions are prompt reactions occurring on impact of an atom or molecule from the gas phase. In environments where hyperthermal reactive atoms are present such as on spacecraft, such Eley-Rideal type reactions can be expected. However, these have not yet been observed under well-defined conditions for heavy atoms such as nitrogen. Only for hydrogenic reactions Eley-Rideal reactions have been demonstrated under UHV conditions. In this work we present results of a systematic study into the importance of such reactions and report the first observations thereof.

In the experiments an effusive beam of hyperthermal nitrogen atoms is aimed at a Ru(0001)-O(2x1) surface at an angle of 60 degrees from the surface normal. Measurements of the angular distribution for Argon scattering under the same conditions have revealed that this surface is atomically flat and uncorrugated. Upon N-atom impact hyperthermal (4 eV) NO is detected. The angular distribution is peaked in the forward direction with a peak at 30 degrees from the normal, indicating that part of the N-atom parallel momentum is conserved in the NO forming collision. These are strong signatures of a prompt surface reaction.

To check the efficiency of the reaction, the time-of-flight spectra of the NO produced were measured for successive intervals. It became clear that fast NO was no longer produced, even though NO is still present in the back ground. From the decay of the NO production rate as a function of time the reactive cross section for the N+O=> NO reaction could be determined. It is about 2 Å². Such a high cross section is another evidence for an Eley-Rideal reaction.

Prompt reactions can be used to specifically remove adsorbates from surfaces. We will demonstrate that not only O-atoms but also N-atoms can be removed from surfaces.

Thin Film

Room: 104 A - Session TF+EM+NS+SS-ThA

Thin Film: Growth and Characterization II

Moderator: C. Vallee, LTM - MINATEC - CEA/LETI, France

2:00pm **TF+EM+NS+SS-ThA1 Comparison of Al₂O₃ Deposited via Prompt Inorganic Condensation vs. Atomic Layer Deposition**, S.W. Smith, W. Wang, D.J. Matthews, D.A. Keszler, J.F. Conley, Oregon State University

Due to the purge separated pulsing of precursor and oxidation gases combined with self-limiting surface reactions, atomic layer deposition (ALD) enables the synthesis of dense conformal thin films with atomic scale control. In terms of sustainable manufacturing however, ALD suffers from slow deposition rates, precursor waste, and the requirement of a vacuum system. Solution-based thin-film deposition methods are attractive because they allow for deposition at atmospheric pressure and with shorter processing times. However, traditional solution based approaches often involve organometallic sol-gels with bulky ligands. High temperature post deposition anneals are required to drive off these ligands resulting in a dramatic change in physical dimensions as the films are densified. The resulting films are thus often porous and exhibit poor electrical properties. More recently, a novel solution processing technique known as prompt inorganic condensation (PIC) enables the deposition of dense, smooth, high-quality films through the use of aqueous metal-inorganic precursors.

In this work we compare the electrical and physical properties of Al₂O₃ films produced by ALD and PIC. ALD of Al₂O₃ was performed using trimethyl-aluminum and H₂O at 300°C. PIC of Al₂O₃ was performed using an aqueous aluminum hydroxide nitrate solution at room temperature in atmosphere. Post deposition anneals were performed following PIC to convert the hydroxide to an oxide and densify the films. Al/Al₂O₃/Si MOS capacitors were used for electrical measurements. For 10 nm thick films, 300°C annealed PIC Al₂O₃ shows higher leakage, and lower breakdown strength than ALD Al₂O₃. After a 500°C anneal, the PIC Al₂O₃ shows lower leakage current density at fields >2.5 MV/cm and equivalent breakdown strength to ALD Al₂O₃. Conduction mechanisms will be discussed. Capacitance vs. voltage data showed that PIC films have a lower dielectric constant than ALD films and an anneal temperature dependent flat band voltage shift. X-ray reflectivity indicates that as-deposited PIC films have a low density which increases with increasing anneal temperature to approach that of the ALD films. Finally, X-ray photoelectron spectroscopy and transmission electron microscope data are used to examine the Al₂O₃/Si interfacial region. Differences in interfacial layer formation may explain the reduced leakage current observed in the lower density PIC films. Our results show that PIC is promising method for deposition of thin (~10 nm) Al₂O₃ films on silicon.

2:20pm **TF+EM+NS+SS-ThA2 Static Mode CVD at Low Temperatures: Highly Conformal and Smooth Films in Deep Structures**, A.N. Cloud, J.L. Mallek, K.A. Arpin, P.V. Braun, G.S. Girolami, J.R. Abelson, University of Illinois at Urbana Champaign

Chemical vapor deposition can afford smooth and conformal films in high aspect ratio structures in the limit of high precursor pressure and low substrate temperature. Under those conditions, adsorbed precursor molecules cover the growth surface, react to deposit film at useful rates, but also block active sites such that the effective sticking coefficient is reduced. The result – a conformal film in trenches deeper than 30:1 – can be competitive with ALD. This is not surprising, given the underlying kinetic principle, surface site-blocking, is the same.

We report the successful implementation of the most extreme parameters: we perform static CVD in an unpumped glass tube that is pre-filled with precursor up to its vapor pressure and slowly ramped to temperature in a clamshell furnace. The slow heating ramp at maximum possible precursor pressure affords remarkably uniform film nucleation, excellent conformality and surface smoothness. Based on the coating of deep trenches, silica-based synthetic opals, and aerogels, we estimate an effective sticking coefficient < 10⁻⁵. Many substrates can be loaded into the tube such that the throughput is good in batch mode. The precursor utilization is excellent (~ 25 %), unlike the case of flowing CVD in which most of the precursor is wasted under conformal growth conditions.

Static CVD is demonstrated for the conformal growth of HfB₂ and elemental Fe films. HfB₂ is an electrically conductive refractory material with high mechanical hardness, excellent tribological properties, and excellent diffusion barrier properties against Cu. The precursor, Hf(BH₄)₄, has a remarkably high vapor pressure of 15 Torr at 25°C. This pressure both promotes conformal film growth and provides a large gas density sufficient

to deposit 100 nm of film in a single cycle. The precursor is reactive toward O₂ and H₂O and acts as a gas-phase getter for potential contaminants. Thus, despite the rough vacuum apparatus, the films have O and C impurity contents < 1 at. % as evaluated by AES. The film composition is stoichiometric despite the buildup of reaction products. This implies that the growth surface has no net reactivity towards these products.

Fe films are deposited from the precursor Fe(CO)₅. Typically CVD Fe films grown from this precursor have faceted surfaces and are not conformal. Here, the film smoothness and conformality is excellent. The O and C impurity contents are ~ 1 at. %.

We will discuss the prospects for coating other materials by static CVD, as well as simple modifications that have the potential to afford thicker films and avoid impurity contamination in cases where the byproduct reactions are not negligible.

2:40pm **TF+EM+NS+SS-ThA3 Growth of Nanocomposite and Epitaxial Nitride and Oxide Thin Films by Magnetron Sputtering for Thermoelectric Applications**, B. Paul, S. Kerdsonpanya, P. Eklund*, Linköping University, Sweden

In this invited talk, we first review our recent work on ScN-based thin films for thermoelectrics and correlated theoretical studies. The anomalously high thermoelectric power factor of ScN can be explained in terms of the band structure, with vacancy and impurity states introducing sharp features near the Fermi level yielding a large power factor. We further present results on calcium cobalt oxide thin films grown on Al₂O₃(0001) substrate by co-sputtering from Ca and Co-targets by reactive rf-magnetron sputtering in presence of 1.5 % O₂. As-deposited films were found to be amorphous. Subsequent ex-situ annealing in O₂-atmosphere well crystallized highly c-axis-oriented Ca₃Co₄O₉ films were obtained. For higher annealing temperature of 800 °C, the films are found to be single-phase epitaxial Ca₃Co₄O₉. X-ray diffraction and pole figure XRD analyses reveal the films are having (001)-orientation. Furthermore, altering the nominal starting composition of the as-deposited films yielded Ca₃Co₄O₉-based nanocomposite films with cobalt oxide inclusions, which may act as phonon scatterers for potential reduction of thermal conductivity in a thermoelectric application.

3:40pm **TF+EM+NS+SS-ThA6 Atomic Layer Deposition of Pb(Zr,Ti-x)O₃ Thin Films**, D. Chien, T. Kim, J. Choi, J.P. Chang, UCLA

Lead zirconate titanate at its morphotropic phase boundary composition, Pb(Zr_{0.52}Ti_{0.48})O₃, exhibits strong coupling between electrical and mechanical energies, making it a promising material for piezoelectric MEMS. As MEMS continue to scale down to smaller sizes with more complex topography, the ability to deposit high quality PZT thin film conformally over high aspect ratio 3D structures and surfaces that are not in line-of-sight of deposition sources becomes an enabling factor. Atomic layer deposition (ALD) is a promising method because it is a surface-reaction controlled process based on alternating self-limiting reactions which can obtain superior uniformity and conformality over complex surface structures. Another challenge is to deposit (001) oriented PZT because it has a higher piezoelectric constant than (111) oriented PZT.

In this work, a (100) textured ALD PbTiO₃ (PT) seed layer was used to attain (100) oriented PZT on platinumized silicon substrates. The PT and PZT thin films were synthesized by depositing alternating layers of PbO, ZrO₂, and TiO₂ using Pb(TMHD)₂, Zr(TMHD)₄, and Ti(Oi-Pr)₂(TMHD)₂ as metal precursors and H₂O as the oxidant. The growth sequence consisted of a(Pb-O)-b(Ti-O)-c(Pb-O)-d(Zr-O) where a:b:c:d ratio of local cycles and global cycles were regulated to achieve the desired stoichiometry and thickness, respectively. To tailor the composition of PT and PZT by ALD, the incubation time of depositing one constituent oxide on another on KBr crystal disks was quantified by *in-situ* FTIR. The IR absorption spectrums of one metal oxide layer deposited on another were acquired after each ALD cycle until specific stretching vibration mode of the target metal oxide was observed to indicate the required incubation time to initiate the target oxide growth. These results were used to guide the design and synthesis of PT and PZT with precise composition control. The stoichiometry and crystallinity of PbTiO₃ and PZT films were confirmed by XPS and XRD, respectively.

To assess the feasibility of ALD P(Z)T films for piezoMEMS application, ALD PZT thin films were deposited on ALD PbTiO₃ seed layer and fabricated into simple capacitors with platinum as the top electrode. The dielectric and ferroelectric properties of ALD PZT thin films were characterized via CV measurements and PE hysteresis loops, which are sensitive to the composition of PZT. The (100) oriented ALD PZT thin film was poled to attain the desired (001) oriented PZT film, for which the effective transverse piezoelectric coefficient, e_{31,f}, was quantified via the

* Paul Holloway Award Winner

wafer flexure method. The conformality of 15nm ALD PZT films were confirmed over 300nmx700nm hollow Si₃N₄ cylinders.

4:20pm **TF+EM+NS+SS-ThA8 Aluminum Nitride Thin Films Deposition, Properties and Applications, L. le Brizoual, J. Camus, K. Ait Aissa, Q. Simon, P.Y. Jouan, M.A. Djouadi, Univ. de Nantes - CNRS-IMN, France, Y. Cordier, E. Frayssinet, M. Chmielowska, M. Nemoz, P. Vennéguès, S. Chenot, CRHEA-CNRS, France, N. Defrance, M. Leseq, P. Altuntas, A. Cutivet, A. Agboton, J.C. De Jaeger, Univ. de Lille - CNRS-IEMN, France** **INVITED**

Aluminum nitride (AlN) is a wide bandgap semiconductor and showing intrinsic properties such as high thermal conductivity, high electrical resistivity, good mechanical hardness and efficient piezoelectricity. Due to its intrinsic properties, single-crystalline AlN is a promising III-V semiconductor for applications in high power electronics and optoelectronics such as HEMTs, UV light-emitting diodes and acoustic waves devices. AlN films are grown on a variety of substrates using different deposition methods including chemical vapor deposition techniques and molecular beam epitaxy, laser ablation and reactive sputtering techniques. Among these methods, sputtering techniques permit to obtain *c*-axis oriented AlN films with small surface roughness at relatively low temperatures. Both modes of Magnetron Sputtering are presented: the DC mode and the HiPIMS mode (High Power Impulsed Magnetron Sputtering) for reactive AlN synthesis. HiPIMS for deposition of insulating AlN thin films were used and compare to the DC mode. The processes are optimized for working with Aluminum targets in a reactive atmosphere (Ar-N₂). As the plasma characterization of the ionized species is necessary in order to understand pulsed plasma process, time-resolved investigations were carried out using Optical Emission Spectroscopy and Mass Spectrometry was used for quantifying the ionic and neutral species reaching the substrate and the results are compared to the DC case. The AlN film stress was measured by the substrate curvature technique. The AlN film quality was characterized and by X-ray diffraction analysis (XRD), UV Raman spectrometry and Ellipsometry. The first purpose of this contribution consists to compare the structural and microstructural properties of AlN films deposited by DCMS and HiPIMS, in particular, in order to study the influence of the ionic bombardment resulting from the different discharges. Then, from the first deposition optimization study, we developed the epitaxial growth of AlN on a specific buffer layer on Silicon (111) and its electrical characterizations are presented. This AlN epitaxial layer obtained by magnetron sputtering was used to re-grow a thick GaN film in order to obtain HEMT device. This original structure exhibits a low drain current collapse which may be attributed to the enhanced thermal dissipation properties of the structure.

The present study has been supported by the French National Research Agency under grant ANR-2010-EMMA-030 CREATIVEPI.

5:00pm **TF+EM+NS+SS-ThA10 Atomic Layer Deposition of Tungsten Nitride Thin Films — Initial Surface Reactions, K. Bernal Ramos, The University of Texas at Dallas, R.K. Kanjolia, SAFC Hitech, Y.J. Chabal, The University of Texas at Dallas**

Tungsten nitride (WN_x) films have been reported to form amorphous or amorphous-like phases that are desirable to be used as a diffusion barrier for copper metallization or other contact materials in microelectronics applications. The properties of tungsten nitride, such as high melting temperature, relatively low resistivity and chemical inertness, make it an attractive material for a variety of applications. Its deposition using Atomic Layer Deposition (ALD) is however poorly understood, hindering a wider use.

This work focuses on the ALD of WN_x using a novel tungsten-based ALD precursor, dicarbonyl(methylcyclopentadienyl)nitrosyl tungsten (MeCpW(CO)₂(NO)) and hydrazine as its co-reactant. We first examine the reactivity of MeCpW(CO)₂(NO) with OH-terminated oxidized silicon surfaces (O₂Si-OH) in order to better understand and control thin film deposition. In situ infrared (IR) absorption spectroscopy is used to uncover the film growth mechanisms. The spectra indicate that, at a substrate temperature range of 200-300 °C, there is a nucleation period of 5-6 cycles, after which tungsten nitride begins to grow through an expected ligand exchange mechanism, with appearance of N-H vibrational modes at ~3280 and ~1600 cm⁻¹ after the hydrazine pulse. X-ray photoelectron spectroscopy (XPS) provides additional information on impurity concentration, such as carbon and oxygen, in addition to confirmation of the growth chemistry. XPS results indicate a low concentration of C impurities in the film bulk.

This study provides insight into the surface chemistry of the precursor's initial reactions necessary to enable future process development and deposition of W-based materials for a wide range of applications.

5:40pm **TF+EM+NS+SS-ThA12 Metal Oxide Growth, Characterization and Spin Precession Measurement in CVD Graphene, A. Matsubayashi, University at Albany-SUNY, J. Abel, Intel Corporation, D. Sinha, J. Lee, V.P. LaBella, University at Albany-SUNY**

Thin metal oxide layers deposited on graphene can be utilized as dielectric barriers between metals and graphene to help isolate a metal contact from the graphene channel. This is important for graphene based spintronic devices as dielectric layers between the ferromagnetic electrode and graphene have been shown to increase the spin relaxation time measured utilizing non-local detection and spin precession measurements. However, simply depositing metal oxide layers such as aluminum oxide on graphene results in non-uniform film lowering the quality of the interface barrier. We will present a systematic study of aluminum oxide layers grown on CVD (chemical vapor deposition) graphene under ultra-high vacuum conditions with and without titanium seed layers. The aluminum oxide layers with the titanium seed layers showed reduced surface roughness. The chemical and structural composition determined by XPS (X-ray photoelectron spectroscopy) will be also presented that shows full oxidation of the aluminum and partial oxidation of the titanium. The results on the spin precession measurements in CVD graphene will be also presented.

Thin Film

Room: 102 C - Session TF-ThA

Energetic Thin Films

Moderator: D.P. Adams, Sandia National Laboratories

2:00pm **TF-ThA1 Reactive Foil Ignition Threshold Dependence on Laser and Foil Properties, R.D. Murphy, Sandia National Laboratories, J.P. McDonald, Dow Corning Corporation, D.P. Adams, Sandia National Laboratories**

It has been shown that forced mixing of reactive layers (foils) leads to an exothermic release of energy after initiation of mixing by forced impact or pulsed laser irradiation. In this work, in order to understand the ignition of foils initiated by laser irradiation, we present laser ignition thresholds of Al/Pt multilayer reactive foils prepared by sputter deposition. It will be shown that the single-pulse ignition threshold is dependent on both the length of the laser pulse and properties of the foil such as bilayer thickness. The laser pulse length is varied from 100 fs to 100 ns and the bilayer thickness is varied from 20 nm to 200 nm. Models will be presented to account for the dependence of the ignition thresholds on diffusion and laser pulse - foil interaction mechanisms such as melting and ablation. Sandia is a multi-program laboratory managed and operated by Sandia Corporation, a wholly owned subsidiary of Lockheed Martin Company, for the United States Department of Energy's National Nuclear Security Administration under Contract DE-AC04-94AL85000.

2:20pm **TF-ThA2 Direct Visualization of Atomic Diffusion Distances after Self-Propagating Reactions in Zr/Al Multilayers, D.P. Adams, R.V. Reeves, P.G. Kotula, Sandia National Laboratories**

It is generally assumed that the diffusion distance for heterogeneous reactive materials is defined simply as half of the characteristic dimension of the constituent materials. In a powder system, this assumption results in the diffusion distance being equivalent to the particle radius, and, in a lamellar system, the diffusion distance would be half of the thickness of a single layer of material. This assumption is important as it is used to estimate overall reaction times and heat release rates. In this study, the validity of this assumption was investigated in sputter deposited multilayers of Zr/Al composition with a single Zr layer replaced by a Hf marker layer. Hafnium was selected as the marker material because Zr and Hf have similar chemical behavior. This is due to lanthanide contraction, which causes Hf and Zr to have very nearly identical electronegativities and atomic radii. Hafnium and zirconium also react with Al to form intermetallic compounds with similar structures, including di-aluminide line compounds. These similarities between Zr and Hf allow the reaction to progress with little detrimental effect from the Hf inclusion. Multilayers containing a single marker layer were converted to product phases (nominally ZrAl₂/HfAl₂) in the self-propagating reaction mode. Both unreacted and reacted foils were then cross-sectioned and imaged in an aberration-corrected transmission electron microscope. Energy dispersive spectroscopy (EDS) was performed to quantitatively identify the elemental distribution in both reacted and unreacted multilayers. EDS results clearly showed that the Hf atoms spread to over ten times the assumed diffusion distance. The results are in strong disagreement with the general assumption of diffusion distance and indicate that the atoms can remain mobile, even after complete mixing has occurred.

Sandia National Laboratories is a multi-program laboratory managed and operated by Sandia Corporation, a wholly owned subsidiary of Lockheed Martin Corporation, for the U.S. Department of Energy's National Nuclear Security Administration under contract DE-AC04-94AL85000.

2:40pm **TF-ThA3 Analysis and Modeling of Self-Propagating Reactions in Ni/Al and Ru/Al Nanoscale Thin Film Multilayers.** C. Rebolz, University of Cyprus, I.E. Gunduz, Northeastern University, K. Fadenberger, University of Cyprus, K. Woll, Johns Hopkins University, C.C. Doumanidis, University of Cyprus

Reactive nanoscale multilayer films/foils represent a relatively new class of materials which have recently received considerable attention for use in joining applications. However, due to the fast reaction rates in these foils (between 1 and ~ 20 m/s for the Ni/Al system) much of the understanding of the reactions is derived from comparing before and after states of the samples.

In this work, reaction characteristics of nanoscale multilayer foils of Nickel (Ni) and Aluminum (Al) and Ruthenium (Ru) and Al were investigated using a numerical model based on sequential diffusion limited growth with diffusivity values obtained from previous diffusion experiments. The model makes use of percentages of each phase that can exist at each grid point, which simplifies the enthalpy calculations and incorporation of phase changes. Obtained results show excellent agreement with measured velocity values, observed *in-situ* morphology of the thermal fronts and temperatures for both Ni/Al and Ru/Al multilayer foils, obtained using high-speed optical camera and infrared thermometry in combination with fast high resolution *in-situ* XRD.

3:00pm **TF-ThA4 Combustion Characterization of Blade Cast Magnesium and Manganese Dioxide.** K. Meeks, M.L. Pantoya, Texas Tech University, C.A. Appletr, Sandia National Laboratories

There is a current need for low cost heat sources for a variety of applications, from local joining and welding, to providing local heat for power sources. In this work, powders of magnesium and manganese oxide were mixed with a fluoropolymer or paraffin binder and blade cast onto a stainless steel foil substrate. The three binder-solvent systems investigated were Methyl Pyrrolidone (NMP) and Polyvinylidene Fluoride (PVDF), Acet one and Viton A, as well as Paraffin and Xylene. Films were prepared by mixing the energetic composites with the binder and solvent to create a 40% solids content suspension, and then casting onto stainless steel foil to a 200um wet film thickness. In this study, binder content and type was varied, and calorific output and open flame propagation speed was investigated for each mixture ratio. It was found that calorific output increased with increasing binder content, to a maximum observed value of 954 calories per gram, indicating participation of the binder in the exothermic reaction. Flame speed was shown to decrease with increasing binder content, with a maximum recorded value of 0.14 m/s for unconfined tests. This may reflect the lower heat transfer of the binder, or some mechanism that blocks propagation with increasing binder content. Confined tests were also conducted for the PVDF/NMP system, with a maximum recorded flame speed of 3.46 m/s. High speed video of the flame propagation shows significant gas generation ahead of the flame front, which may explain the observed difference between confined and open burn speeds, as the ejecta plume preheats the material in advance of the flame front.

3:40pm **TF-ThA6 Reactive Nano Laminates with Tailored Yield.** J.-P. Maria, E.J. Mily, H. Akyildiz, North Carolina State University **INVITED**

In this presentation we report on a series of reactive oxygen exchange nanolaminates between an oxygen source, CuO, and a reactive metal oxygen sink where the propensity for energy release is tailored by material selection and by multilayer geometry. These results suggest it is possible to create a class of energetic materials whose yield can be tailored for specific applications.

We demonstrate that by considering anion transport in the terminal oxide, we can produce multilayers that are unstable at room temperature, or those which require substantial thermal energy to ignite. We first explored this terminal phase hypothesis by comparing CuO-metal laminates with the reactive metals: Mg, Zr, and Al. Zr-CuO laminates were the least stable, owing to the fast oxygen transport through the ZrO₂ terminal oxide, while CuO-Al laminates were the most stable, owing to the excellent diffusion barrier properties associated with Al₂O₃. A second demonstration is made for laminates of CuO and Al_{1-x}Ti_x where x is varied systematically between the pure end members. We identify a composition of ~ 35% Ti, above which the laminates react at room temperature and below which thermal energy in the range of 300 °C and above is required to initiate oxygen exchange. Calorimetry analysis is used to measure effective activation energies for each material combination in order to better understand the material property / energy release relationships.

In addition, we report the use of *in situ* XPS analysis to explore, with sub nm resolution, the interface chemistry of as deposited nanolaminates precursors to identify the limitations of interface abruptness in the as-prepared state. We find that in all cases CuO/reactive metal interfaces have an unavoidable minimum oxide thickness but this thickness depends on a number of factors including thermodynamic driving force for oxygen exchange, wetting, and oxygen diffusivity.

4:20pm **TF-ThA8 A Novel Method of Managing Joint Stress, in a Metallic Bond Made Using Reactive Multilayer Foils, at a User Selected Temperature.** G.J. Matteau, Indium Corporation

Previously we have presented a joining method whereby materials of widely differing CTE were successfully bonded with no deformation at room temperature using reactive multilayer foils as the local heat source. This is unique in as far as creating a metallic bond with any other technique results in significant deformation upon cooling back to room temperature. For many large area applications this deformation results in having to use mechanical methods to flatten these surfaces to their original shape, which is highly undesirable as such techniques are unpredictable and do cause yield loss when used. When reactive multilayer foils are used in the bonding process, no such deformation of materials occurs resulting in assemblies that can be effectively used as soon as they are bonded.

Critical to the use of parts at higher temperature is the need to minimize/manage joint stress in assemblies at a particular application temperature. This paper will demonstrate how this can be done effectively, with the use of a reactive multilayer foil in creating the bond.

Applied Surface Science

Room: Hall B - Session AS-ThP

Applied Surface Science Poster Session

AS-ThP1 Wide-Range Parallel XPS Imaging for Feature Identification. *T.S. Nunny, A.E. Wright, P. Mack*, Thermo Fisher Scientific, UK

X-ray Photoelectron Spectroscopy (XPS) is a well-established technique for surface-sensitive measurements of the elemental and chemical-state composition of a material. Naturally, there has been a drive to allow imaging methods with XPS, so that chemical distributions can be obtained with high spatial resolution.

One such method, parallel XPS imaging, allows for the simultaneous acquisition of the entire image at a single energy, with high spatial resolution. Conventionally, acquiring such images in small energy steps across a photoelectron peak of interest yields a spectroscopic image, where each pixel contains a spectrum.

Typically, such spectroscopic images are acquired across a single peak region, such as C1s. This minimizes acquisition time, and generates more manageable data sets that are conceptually similar to region spectra in conventional XPS. On a modern XPS instrument, it is possible to acquire a full-range spectroscopic image, where each pixel contains a survey spectrum. This is rarely done, mainly due to acquisition times, and the fact that a point survey spectrum from the imaged area will usually give the elemental composition without need for survey images. However, there are advantages to the method, namely the ability to retrospectively generate spectra from arbitrary parts of the imaged area, to identify composition at any location.

In this presentation, the extension of the parallel XPS imaging technique to wider energy ranges will be discussed, showing how in some situations the use of wide-range spectroscopic imaging can provide information that is difficult or impossible to gain using single-point spectroscopy or region spectroscopic imaging analyses.

AS-ThP3 Evaluating the Stability of Li-O₂ Battery Components on Cathode/Electrolyte Interface by XPS. *E. Nasybuln, M. Engelhard, W. Xu, J. Zhang*, Pacific Northwest National Laboratory

The development of rechargeable Li-O₂ batteries is a fast growing research field. Scientific interest is driven not only by high theoretical energy density of Li-O₂ batteries (3,500 Wh kg⁻¹ including masses of lithium and oxygen) but also by many aspects of material science and engineering involved in the development. At the current stage, Li-O₂ batteries suffer from poor rechargeability because of the wide variety of side reactions between battery components (electrolyte solvent, electrolyte salt, and electrode materials – Li anode, cathode substrate, binder, catalyst) and reduced oxygen species (O₂[•], O₂²⁻) generated during the discharge. These side reactions predominantly happen at the cathode/electrolyte interface simultaneously with the reversible formation/oxidation of Li₂O₂ during the discharge/charge processes. Unlike Li₂O₂, the side products are difficult to decompose and accumulate with cycling forming an insulating layer at the interface and eventually leading to the battery failure. Therefore, analysis of side products is important to evaluate the stability of battery components and may suggest new robust materials for the application in Li-O₂ batteries. Considering the side products form only a thin layer on the interface, characterization of these products by bulk methods is problematic. X-ray photoelectron spectroscopy (XPS) is a powerful surface sensitive technique which is probably the most suitable for the analysis of such interfaces. In the present study, XPS is applied to evaluate the stability of various components of Li-O₂ batteries, including electrolyte solvents, electrolyte salts, polymer binders and organic catalyst on the surface of carbon-based cathodes during the discharge process of the Li-O₂ batteries. With the support from other techniques, the most stable components are identified and suggested for the rechargeable Li-O₂ batteries. Decomposition pathways are proposed for a number of components based on their decomposition products. Contributions from the degradation of various battery components to the overall failure of Li-O₂ batteries are estimated. It is demonstrated that the chemical and electrochemical stability of the components has a drastic effect on the discharge capacity and cycling stability of Li-O₂ batteries. Details of this study will be reported in the presentation.

AS-ThP4 Surface Modification of Multiferroic BiFeO₃ Ceramic by Argon Sputtering. *P. Wang, M. Guttag*, Bradley University, *C. Tu*, Fu Jen Catholic University, Taiwan, Republic of China

Films fabricated by sputtering deposition are extensively used in semiconductor, optical and optoelectronic industries. Since the sputtering is the key to physically deposit the films onto substrates, its effect on the target materials is needed to investigate in order to fabricate films successfully. In this study, multiferroic bismuth ferrite, BiFeO₃ (BFO) with 5 mole% BaTiO₃ target was sputtered by using 3 keV argon ions continuously after various time intervals. The X-ray Photoelectron Spectroscopy (XPS) was applied to examine the cleanliness and the chemical environment of the elements on the sample surface after each sputter time interval. The carbon contaminant was almost completely removed after 5120 s sputtering, but the sputtering induced metallization of the bismuth and two-component oxygen spectra were also observed. It was found that the oxidation states of bismuth from dominant 3+ state changed to equally weighted 3+ state and 0 state. The changes of the valence electrons of bismuth induced by the argon sputtering on the BFO target inevitably alter the film compositions deposited onto the substrate; however, it was found that the non-stoichiometric BFO films can be corrected by sputtering under partial oxygen pressure *via* the re-oxidation of bismuth metal.

AS-ThP5 In Situ Plasma Cleaning of Samples Prior to XPS and ToF-SIMS Analysis. *V. Smentkowski, H. Piao*, General Electric Global Research Center

Most samples submitted for surface analysis using Auger electron spectroscopy (AES), x-ray photoelectron spectroscopy (XPS) and/or time of flight secondary ion mass spectrometry (ToF-SIMS) that are generated in an industrial laboratory are exposed to ambient air, or harsher conditions. The spectra of the as received material is often dominated by carbon and oxygen or hydrocarbon species when analyzed by AES/XPS or ToF-SIMS respectively. These surface contaminants frequently attenuate the signal from the underlying surface of interest and can complicate accurate analysis of the sample. Such surface contaminants are often removed from samples using in-situ ion beam sputtering however sputtering is an energetic process which can modify the surface of interest. In this work, we demonstrate the benefits of using in-situ, low power, RF plasmas to clean a variety of samples for both XPS and ToF-SIMS analysis.

AS-ThP6 Spectral Chemical State Imaging with High Spatial Resolution Scanning Auger. *D.F. Paul*, Physical Electronics Inc.

Recent improvements of field emission scanning Auger instruments have led to the ability to provide elemental imaging of surfaces with a spatial resolution better than 8 nm. The PHI 710 now provides the capability to combine high energy resolution spectra with high spatial resolution chemical state imaging with a CMA analyzer. The system software also provides LLS separation of different chemical states from the Auger imaging data.

A semiconductor structure with multiple silicon chemical states will be presented. The 0.1% energy resolution spectra for silicide, silicon, and silicon oxynitride are extracted from the scanning Auger image. These basis spectra are then used to create the different chemical state images. The resulting image overlays demonstrate the ability of the CMA analyzer to image different chemical states at high energy resolution without topographical artifacts.

AS-ThP7 Laser Induced Breakdown Spectroscopy for Surface Mapping of Thin Polymer Films. *C.Y. Chou*, National Taiwan University, Taiwan, Republic of China, *P.R. Chou*, Chinese Culture University, Taiwan, Republic of China, *J. Lee*, Optimization Solutions Asia Engineering Co. Ltd., Taiwan, Republic of China, *R.B. Lin*, Chinese Culture University, Taiwan, Republic of China, *C.C. Hsu*, National Taiwan University, Taiwan, Republic of China

Laser Induced Breakdown Spectroscopy (LIBS) is a technique for elemental analysis on inorganic and organic materials. It uses a pulsed laser beam to ablate the surface of the target materials and generate plasma. By analyzing the optical emission spectra emanating from the plasma, information related to the ablated material composition can be obtained. The key features for LIBS include fast analysis, simultaneous multiple element detection, analysis under ambient atmosphere, and no or very little need for sample preparation. In this presentation, LIBS analysis on thin film samples is performed with the goal of understanding its capability to detect polymer thin film materials and to perform surface mapping. The LIBS system (Insight, TSA) is equipped with a pulsed laser and a charge-coupled device (CCD). LIBS systems equipped with 266 and 1064 nm laser sources are tested under air and argon atmosphere. The polymer films tested are

fluorocarbon (FC) thin films coated on silicon wafer and glass substrates. Results show that when the 1064 nm system is used, clear C- and F-emissions can be observed for FC coated substrates with a coating thickness down to 100 nm. While using the 266 nm laser, rather poor signal to noise ratio is obtained for F- and C-emissions. Substrates patterned with 500 nm wide stripes FC thin films are then tested to obtain spatially resolved information for the patterned surfaces. By using the 1064 nm laser source, spatial resolution of approximately 100 nm can be obtained. This demonstrates the capability using LIBS as the spatially-resolved surface mapping of polymer films for thin films. This work was supported by National Science Council of Taiwan, the Republic of China (101-2221-E-002-163-MY2)

AS-ThP8 Variables Affecting Fabric Water-Repellency: Enabling Property Correlations through the use of Secondary Ion Mapping Coupled with Multivariate Statistical Analysis. *K.G. Lloyd, S. Brown, L. Zhang, J.R. Marsh, D.E. Davidson*, DuPont Corporate Center for Analytical Sciences, T. Madeleine, DuPont

Water and soil repellency confer a distinct advantage to apparel. A number of processing steps are required to produce water-repellent fabrics. The original fiber spin finish is needed for fabric weaving but then must be removed (though rarely completely) prior to water-repellent treatment. The composition of water-repellent formulations varies among different formulators and even from a single formulator over time. In addition to fluorocarbons with different polymer backbones and different fluorocarbon tail lengths/distributions, water-repellent formulations may also include so-called "extenders" or performance enhancers. Drying and curing steps are typically required.

Surface characterization plays a critical role in understanding water repellency. This presentation will focus on the surface analytical methodologies developed to help correlate formulation and processing variables to repellency performance. These include the use of multivariate statistics with ToF-SIMS mapping data to quantify fluorocarbon coverage as well as to understand the effect of "uncoated" surface character. These results will be combined with fabric surface energetics measurements to yield a more complete picture of the fabric treatments.

AS-ThP9 Enhanced TOF-SIMS Analysis of Polymers and Biological Samples. *R. Price, G.L. Fisher, S.R. Bryan, J.S. Hammond*, Physical Electronics Inc., *I. Ishizaki, S. Iida, T. Miyayama*, ULVAC-PHI, Inc., Japan
Five synergistic performance characteristics of the new PHI nanoTOF to improve the analysis of polymer and biological samples will be discussed. These desired characteristics are the ultimate spatial resolution, mass resolution, mass range, insensitivity to topographical artifacts and ultimate abundance sensitivity. A new LMIG has been developed which can simultaneously achieve a typical spatial resolution of 400 nm and a mass resolution greater than 10,000 m/Δm. When combined with the nanoTOF analyzer, topographical features within a depth of field of 200 μm can be imaged. To extend the molecular sensitivity beyond the traditional static SIMS limit of 1013 incident ions/cm², the use of voxel analysis can be used. For voxel analysis, an image is acquired to the static limit, followed by the removal of the damaged surface layer with Gas Cluster Ion Beam (GCIB) source, followed by additional cycles of LMIG acquisition and GCIB damage removal. By integrating signal intensities as a function of GCIB depth of removal, three dimensional voxels of data can be acquired with much higher molecular sensitivities than data only acquired to the static SIMS limit.

Data from a mixed phase polymer sample, micron sized organic contamination features on a failure analysis sample and images of biological samples will be discussed. Retrospective quantitative line scans and spectra from these samples will demonstrate the advantages of these new capabilities for TOF-SIMS polymer and biological sample analyses.

AS-ThP12 XPS and ToF-SIMS Sputter Depth Profiling of OLEDs using Ar Cluster Ion Sources. *M. Bruns, K. Peters, P. Scharfer, W. Schabel*, Karlsruhe Institute of Technology, Germany, *H. Hummel*, Philips Technologie GmbH, Germany, *T.S. Nunney*, ThermoFisher Scientific, UK, *E. Tallarek*, Tascon GmbH, Germany, *S. Kayser*, ION-TOF GmbH, Germany

Research on organic light-emitting diodes (OLEDs) has gained much attention due to the potential for cheap and ultrathin illumination sources with high color range. In multilayer OLEDs the carrier injection efficiency from the electrodes into the light emitting layer is improved by layers for hole or electron transport and blocking. Vacuum evaporation is the standard method to produce precisely defined interfaces, but it is an expensive process with high material usage. Alternatively, the wet chemical processing has advantages in production cost, deposition rate and area, but shows problems with the intermixing of the subsequently coated functional layers. The specific nature of small molecules used for OLEDs with their

high mobility for diffusion in combination with low dry film thicknesses of only a few nanometers is challenging. For a better understanding of the physical limitations of liquid-phase processed multilayer OLED structures, the possibility to characterise the material mixing between two layers during coating and drying, and the comparison to evaporated layers is crucial.

The present study focusses on the surface analytical characterization of OLED multilayer films using X-ray photoelectron spectroscopy (XPS) and complementary time-of-flight secondary mass spectrometry (ToF-SIMS). In the case of (bio-) organic materials, both methods provide the chemical composition of the topmost layer, XPS mostly in a non-destructive manner. However, information on the in-depth distribution of the constituents in multilayer OLED systems, e.g. to prove chemistry and sharp interfaces, is unavailable via sputter depth profiling when using monoatomic Ar⁺ (XPS) and Cs⁺ (ToF-SIMS) ion sources for material erosion. Here the high fluence of even low energy monoatomic ions with a projected range in all cases greater than the XPS/ToF-SIMS sampling depth causes decomposition of the organic material. But since the recent introduction of high mass Ar cluster ion sources for both XPS and ToF-SIMS, enabling sputter depth profiling of organic materials while preserving the chemical/molecular information, this drawback can be overcome [1,2]. We present quantitative in-depth information on the desired OLED structures and, moreover, compare results achieved from monoatomic and cluster ion source depth profiling.

V. S. Smentkowski, G. Zorn, A. Misner, G. Parthasarathy, A. Couture, E. Tallarek and B. Hagenhoff, J. Vac. Sci. Technol. A 31 (2013) 030601.

P. J. Cumpson, J. F. Portoles, N. Sano, and A. J. Barlow, J. Vac. Sci. Technol. B 31 (2013) 021208.

This work was carried out with the support of the KNMF, a Helmholtz Research Infrastructure at KIT.

AS-ThP13 Depth Profiling of OLED and OPV Materials by Cluster Ion Beams. *K.D. Bomben, J.S. Hammond, J.F. Moulder, S.S. Alnabulsi, S.N. Raman*, Physical Electronics Inc., *N.C. Erickson, R.J. Holmes*, University of Minnesota

Cluster ion beam technologies, in particular the use of C₆₀ and Ar gas cluster ion beams (GCIB), are increasingly being used for the depth characterization of organic materials to provide information that is not available from monoatomic ion beams such as Ar⁺. For surface analysis applications, these cluster sources are used for a wide range of organic materials, including multi-layer organic thin films and organic light emitting diodes (OLEDs), including metal capped devices.

Improvements in the efficiencies for OLED structures have recently focused on the incorporation of more effective organic materials and the on the development of novel structures for arranging these organic materials. Multi-layer devices, graded composition devices, and novel electrical contact layers to the organic materials are all being rapidly developed. The need for analytical techniques that allow the elucidation of the organic thin film structure as a function of device fabrication and lifetime studies is extremely important.

In combination with GCIB sputtering, XPS and TOF-SIMS are being used for quantitative chemical as well as molecular depth profiling techniques for OLED structures. The ability to accurately identify the chemistry at an interface using a co-sputtering protocol involving conventional argon ions and an argon cluster will be discussed. Quantitative compositional depth profiling of graded composition multilayer OLED films and other OPV devices will be demonstrated.

AS-ThP15 Selective Chemistry for the Atomic Layer Deposition (ALD) of Alumina Oxide on Silicon Surfaces. *L. Guo, F. Zaera*, University of California, Riverside

In search for a way to modify SiO₂-based surfaces to prepare them for selective film deposition, silylation and UV/ozonolysis treatments were tested on different silicon oxide and ultra-low k SiCOH surfaces. The chemical behavior of surfaces treated with hexamethyldisilazane (HMDS) and octadecyltrichlorosilane (ODTS), two common silylation agents, was first investigated by contact angle measurements and attenuated total reflection infrared absorption spectroscopy (ATR-IR). Silylation with agents such as these are expected to block the surface hydroxyl sites believed to act as nucleation sites for film growth. Addition of the silanes was confirmed by ATR, after which the contact angle of the silicon surfaces became larger. This indicates an increase in hydrophobicity, which means that most if not all of the surface hydroxyl groups become covered and unavailable for atomic layer deposition (ALD) film growth. These and other hydrophobic surfaces were then treated with a combination of ozone and ultraviolet (UV) light for up to 45 min in order to return their hydrophilicity and to reactivate them for film deposition. Indeed, these treatments led to a decrease in contact angle with exposure time, which was varied from 5 to

35 min; no further changes in the contact angle were seen after exposures for more than 35 min. The silane-coated silicon samples exposed to the silylation agents and to the UV/ozone treatment are currently being tested for the selective ALD of metal oxide films.

AS-ThP16 Analysis of Doped Amorphous Carbon Film for Heat-assisted Magnetic Recording Application. R.Y. Zheng, R. Ji, L. Lu, H.L. Seet, Data Storage Institute, Singapore

Heat-assisted magnetic recording (HAMR) uses a laser-magnetic head integrated system to rapidly heat a localized recording area of the medium above its Curie temperature in order to reduce its coercivity below that of the applied magnetic field during the recording process.^{1,2} Unlike perpendicular recording, HAMR is not limited by the superparamagnetic effect associated with magnetic particle instability and low signal-to-noise ratio.² However, localized laser heating may affect the thermal stability of the protective carbon coating on the hard disk.^{1,2,3} To examine the effect of heating on carbon film stability, three types of a-C films of 5nm thickness have been studied; (1) single layer a-CH film (2) single layer a-CN film and (3) double layer a-CN/CH film. This paper discusses the relationship between thermal heating and structural evolution of the carbon films. XPS was employed to investigate the sp^2 and sp^3 carbon formation related to heating. The variation in sp^2/sp^3 content and the dispersion of D and G peaks in Raman spectra both prove that there is a structural change in the carbon films after heat. Differences in sp^2/sp^3 ratio shows that the carbon structure of a-CN/CH film is thermally more stable than a-CH and a-CN films. TOF-SIMS results reveal that the top a-CN capping layer of the double layer a-CN/CH film structure is able to preserve the C-H bonding within the a-CH under layer. This result in the carbon structure of double layer a-CN/CH film exhibiting better thermal stability compared to single layer a-CH film.

Reference:

- 1 N. Wang and K. Komvopoulos, IEEE Transactions on Magnetics 47, 2277 (2001)
- 2 S.N. Piramanayagam and K.Srinivasan, J. Magnetism and Magnetic Materials 321, 485 (2009)
- 3 W. Zhang, Y. Xia, J. Ju, Y. Fan, Z. Fang, L. Wang, Z. Wang, Solid State Communication 123, 97 (2002)

AS-ThP18 Application of Dye-Sensitized Solar Cells using ZnO Nanoparticles and Nanorods. S.-H. Nam, J.-H. Boo, B. Hong, Y. Kim, Sungkyunkwan University, Republic of Korea

One-dimensional metal oxide nanorods show improved electrical and optical properties in the photoelectrodes of dye-sensitized solar cells (DSSCs). They can provide straight moving paths for electrons and reduced the electron hole recombination. In this study, ZnO nanoparticles and nanorods were synthesized by the spray-pyrolysis and thermal evaporation method. The effect of the ZnO nanostructure morphology on the photovoltaic performance of a DSSC is investigated. The ZnO nanoparticle-based solar cell are 3.74 mA/cm² and 0.771 V, while the ZnO nanorod-based solar cell has Jsc of 2.48 mA/cm² and Voc of 0.751 V. This difference could be due to the difference in absorption behavior and surface area between the two types of ZnO nanostructures. At the IPCE data, the recombination of the nanoparticle/electrolyte interface occurs much lower than that at the nanorods/electrolyte interface.

AS-ThP19 Generation of White Light from Sr₂SiO₄ Doped with Lanthanides. M.A. Tshabalala, O.M. Ntwaeaborwa, H. Swart, University of the Free State, South Africa

In recent years, the study of the synthesis and characterization of white light emitting phosphors for use in white light emitting diodes (LEDs) has generated attention worldwide. In white light LEDs, white light can be generated by combination of light of three primary colors (red, green and blue) emitted from different LED chips¹ or combination of blue LED with yellow-emitting phosphor materials.^{2,3} The problems with these traditional white LEDs is that the yellow YAG:Ce³⁺ phosphor has been reported to show high thermal quenching and poor colour rendition, and that the efficiency of the blue emission is often affected by re-absorption by the red or green phosphor in the three converter system. It is important to find a phosphor that can be excited under near-ultra-violet and the blue region³. In recent studies it has been established that white light can be generated by doping one or more activator(s) in one matrix. For example, in this study white photoluminescence was generated when Sr₂SiO₄ single doped with Dy³⁺ or co-doped with Tb³⁺ and Eu³⁺ was excited using a monochromatized xenon lamp. The structure, particle morphology, chemical composition and oxidation states, photoluminescence (PL) and decay properties of the phosphor were analyzed using X-ray diffraction (XRD), scanning electron microscopy (SEM), X-ray photoelectron spectroscopy and PL spectroscopy, respectively. The XRD patterns showed that a monoclinic phase of Sr₂SiO₄

was crystallized. The decay characteristic data showed that the phosphor consist of single exponential decay curves. The X-ray diffraction data confirmed that.

References

- (1) Yanmin, Q.; Xinbo, Z.; Xiao, Y.; Yan, C.; Hai, G.; *Journal Rare Earths* **2009**, 27(2), 323
- (2) J.K. Park, M.A. Lim, C.H. Kim, H.D. Park *Applied Physics Letters* **2003**, 82(5), 683
- (3) Yao, S.; Chen, D.; *Central European Journal of Physics* **2007**, 5(4), 558

AS-ThP21 Thermally-Induced Evolution of Hydrogenated Amorphous Carbon Surfaces. R.W. Carpick, F. Mangolini, J. Hilbert, J.R. Lukes, University of Pennsylvania

Hydrogenated amorphous carbon (a-C:H) thin films are amongst the strongest, smoothest, and most lubricious coatings in existence. The impressive properties of these materials have resulted in their use in a wide range of applications. In particular, thin a-C:H films are employed as lynchpin materials to protect computer hard disks from corrosion and wear. Even though amorphous carbon-based materials have been studied for more than two decades, there is significant ambiguity regarding the mechanisms by which they transform in response to temperature or other energetic inputs. Quantifying the energetics and specifying the physical pathways of thermally-induced structural transformations have proven difficult. Progress has been limited by the challenges associated with the experimental investigation of the structure and bonding configuration of these materials in their thin film configurations, calling for the development of advanced analytical methods.

In this work, new insights into the thermally-induced structural evolution of a-C:H were gained by coupling experiments and molecular dynamics (MD) simulations. A new experimental methodology for quantitatively determining the bonding configuration of carbon in the near-surface region of a-C:H thin films was developed on the basis of X-ray photoelectron spectroscopy (XPS) and X-ray induced Auger electron spectroscopy (XAES) and allowed the *in situ* XPS and XAES investigation of the thermally-induced structural evolution of a-C:H. Upon high vacuum annealing, three thermally-activated processes with an assumed Gaussian distribution of activation energies with mean value E and standard deviation σ occur in a-C:H: a) ordering and clustering of sp^2 -hybridized C ($E=0.18$ eV; $\sigma=0.05$ eV); b) scission of sp^3 C-H bonds with formation of sp^2 -hybridized C ($E = 1.7$ eV; $\sigma = 0.5$ eV); and c) direct transformation of sp^3 - to sp^2 -hybridized C ($E = 3.5$ eV; $\sigma = 0.5$ eV). This first XPS-based study both demonstrates the low absolute energy barrier for clustering of the sp^2 phases, and indicates that hydrogen enables conversion to sp^2 hybridization in these films.

The experimental results were compared with the outcomes of MD simulations performed using the adaptive intermolecular reactive bond order potential. The atomic composition was chosen to match experiments, and the resulting structure was relaxed to the measured density. This enabled the direct visualization of the structure of a-C:H and its evolution as a function of temperature and time. We will discuss the comparison between the simulation and experimental results, emphasizing the insights gained from the fully atomistic picture provided by the atomistic simulations.

AS-ThP22 Contact-free Pyroelectric Measurements using X-ray Photoelectron Spectroscopy. H. Cohen, D. Ehre, The Weizmann Institute of Science, Israel

A novel application of x-ray photoelectron spectroscopy (XPS) is presented, measuring pyroelectricity in a non-contact mode.¹ We demonstrate, as a proof of concept, how the XPS-derived surface potential^{2,3} of Lithium Tantalate crystals provides a direct and simple probe of the desired property, free of all top-contact related difficulties. An experimentally challenging feature, the increase in Lithium Tantalate spontaneous polarization under cooling, is thus evaluated, proposing insight on the roll of surface contaminants and the control over trapped surface charge at the XPS vacuum environment. Our approach can be extended to other non-contact probes, as well as to measuring additional electrical properties, such as piezoelectricity and ferroelectricity.

References:

1. Ehre and Cohen, *Appl. Phys. Lett.*, in press.
2. Cohen, *Appl. Phys. Lett.*, 85, 1271 (2004).
3. I. Doron Mor et al., *Nature* **406**, 382 (2000).

Spectroscopic Ellipsometry Focus Topic

Room: Hall B - Session EL-ThP

Spectroscopic Ellipsometry Poster Session

EL-ThP2 Electronic and Vibrational Properties of Nickel Oxide using Spectroscopic Ellipsometry, C.M. Nelson, T. Willett-Gies, L.S. Abdallah, S. Zollner, New Mexico State University

Nickel oxide (NiO) is an interesting material, because it is a Mott-Hubbard charge-transfer insulator and also displays antiferromagnetic ordering of electron spins [1]. Spectroscopic ellipsometry is able to investigate the electronic structure of NiO (from the visible and UV portions of the spectra) and also its lattice dynamics (using infrared ellipsometry). Our interest in the NiO optical constants is also of a practical nature, to model ellipsometry spectra of bulk Ni and Ni thin films with a native oxide of NiO.

We measured the ellipsometric angles ψ and Δ for single-side polished bulk NiO from 0.8 to 6.5 eV with angles of incidence from 65 to 75° to determine the dielectric function. A dispersion model for the optical constants was built using two Tauc Lorentz oscillators; one with a Lorentz oscillator resonance energy at 3.96 eV and a second one with a much smaller amplitude at 6.40 eV. These peaks are in agreement with reflectance data analyzed using Kramers-Kronig transforms [2]. Our model also included a surface roughness layer with 40 Å thickness. Atomic force microscopy measurements confirmed this layer, showing an RMS roughness of 42.5 Å. We will report accurate dielectric function data for NiO from 0.8 to 6.5 eV.

FTIR ellipsometry was also performed on bulk NiO from 290 to 1000 cm⁻¹ to study the lattice vibrations. TO phonons were found at 392 cm⁻¹ and 551 cm⁻¹, with the corresponding LO modes at 592 cm⁻¹ and 545 cm⁻¹. The weak TO mode at 551 cm⁻¹ results from the antiferromagnetic ordering of NiO, which doubles the unit cell and causes zone folding, making a zone-edge TO mode infrared-active. Previous FTIR absorption measurements of NiO [3] did not report the infrared-active zone-edge phonon. Usually, antiferromagnetic ordering is only observed using neutron scattering, not with FTIR optical methods.

[1] G.A. Sawatzky and J.W. Allen, Phys. Rev. Lett. **53**, 2339 (1984).

[2] R.J. Powell and W.E. Spicer, Phys. Rev. B **2**, 2182 (1970).

[3] R. Newman and R.M. Chrenko, Phys. Rev. **114**, 1507 (1959).

* This work was supported by the National Science Foundation (DMR-1104934) and performed, in part, at the Center for Integrated Nanotechnologies, an Office of Science User Facility operated for the U.S. Department of Energy (DOE) Office of Science by Sandia National Laboratory (Contract DE-AC04-94AL85000).

EL-ThP3 Properties of Sm Doped CeO₂ Thin Films Prepared by Liquid Solution Deposition, K.N. Mitchell, C.A. Rodriguez, T. Willett-Gies, Y. Li, S. Zollner, New Mexico State University

Cerium(IV) oxide, also known as CeO₂ or ceria, is a transparent (insulating) oxide of the rare earth metal cerium. It is an ionic conductor with applications in fuel cells, as a catalyst, or for photovoltaic water splitting (hydrogen production). Thin films of ceria produced by RF magnetron sputtering on sapphire at 770C have been studied extensively by Arwin's group (S. Guo et al., J. Appl. Phys. **77**, 5369, 1995). They found changes in grain size, surface morphology (visible in AFM images), and optical constants varying with the film thickness. By contrast, we report analysis results for relatively thick (300-500 nm) ceria films prepared by liquid solution deposition (dip-coating) followed by annealing. We also investigate the effect of samarium doping (up to 20at.%) of ceria. The rare earth metal samarium usually forms a sesquioxide Sm₂O₃. Therefore, doping ceria with Sm is expected to lead to the formation of oxygen vacancies, which enhances the ionic conductivity of ceria. Our ellipsometry spectra (ellipsometric angles and depolarization) can be described very well in the transparent region (below 3 eV) using a Tauc-Lorentz dispersion model for ceria, if small amounts of surface roughness and thickness non-uniformity across the wafer are taken into account. Once these thickness parameters have been determined for our films, we obtain the optical constants of CeO₂:Sm using a basis spline expansion. We find the typical dispersion expected for an insulator with a direct band gap near 3.7 eV. Samarium doping causes a significant decrease of the refractive index in the transparent region. Most likely, the films with high Sm content are less dense (have more voids, perhaps due a smaller crystallite size) than pure ceria films. An increase in disorder due to Sm doping was also found in x-ray diffraction studies of electrodeposited ceria films (Phok and Bhattacharya, phys. status solidi (a) **203**, 3734, 2006). As expected from Kramers-Kronig consistency, we find a significant reduction of the height of the main absorption peak at 4 eV. The direct band gap, however, remains at 3.7 eV, independent of Sm content. There is, however, a significant

decrease in the slope of the onset of absorption with increasing Sm content. In addition to ellipsometry results, we will also report AFM, XRD, Raman, and (perhaps) FTIR ellipsometry results for our Sm-doped ceria films.

Electronic Materials and Processing

Room: Hall B - Session EM-ThP

Electronic Materials and Processing Poster Session

EM-ThP1 Hot Fire Chemical Vapor Deposited Silicon-rich Oxides: Its Optical and Compositional Properties, A. Benítez, J.A.L Luna, G. García, D. Vázquez, J. Carrillo, K. Monfil, Benemérita Universidad Autónoma de Puebla, Mexico, A. Morales, Centro de Investigación en Materiales Avanzados, Mexico

Silicon Rich oxides have been considered as a material to overcome the drawbacks of silicon to achieve optical functions. Various techniques can be used to produce it, including Hot-fire Chemical Vapor Deposition (HFCVD). Obtain silicon compatible material with an optimal photoluminescence response is important for to have optoelectronic functions. The SiO_x has shown to have a very good photoluminescence response and is also compatible with silicon technology. In this works, SiO_x Films were obtained by hot fire chemical vapor deposition (HF-CVD) with different deposit conditions. The hydrogen flows were changing of: 50, 75, 100, and 125 and 150 sccm, and the range of deposit temperature were from 800 to 1000°C. The compositional and optical properties of the SiO_x films were obtained using fourier transformed infrared spectroscopy (FTIR), photoluminescence (PL), Transmittance and perfilometer. The IR absorption spectrum shows the presence of three typical Si-O-Si vibrations modes in SiO₂ also the change of the morphology. At 75 and 100sccm showed the most intense PL. Transmittance spectra showed a wavelength shift of the absorption border from 350 to 450nm. We have analyzed the dependence of PL on the composition of non-stoichiometric SiO_x films.

EM-ThP2 Effect of Co-implantation of Nitrogen and Fluorine on the Total Dose Radiation Response of the Buried Oxide Layer of SOI Materials, Z.S. Zheng, Institute of Microelectronics of Chinese Academy of Sciences, China

In order to suppress the total dose radiation response of the buried oxide layer of silicon-on-insulator (SOI) materials, the method of co-implantation of nitrogen and fluorine into the buried oxide is used by fluorine implantation into the nitrogen-implanted buried oxide. The total dose radiation response of the modified buried oxide layer is characterized by the capacitance-voltage (C-V) technique after irradiation using a Co-60 source. The results show the radiation hardness differences between the co-implanted buried oxide layers and the nitrogen-implanted ones, and the improved radiation tolerance for the modified buried oxide layer under some conditions, compared to the unmodified one. It is also found that there is a negligible annealing effect for the co-implanted buried oxide at a temperature of 150°C after irradiation. All the results have been discussed and analyzed.

EM-ThP3 The Effects of Water Uptake on the Mechanical Properties of Low-k Organosilicate Glass, X. Guo, University of Wisconsin-Madison, J. Jakes, USDA Forest Service Forest Products Laboratory, M. Nichols, University of Wisconsin-Madison, S. Banna, Applied Materials Inc., Y. Nishi, Stanford University, J.L. Shohet, University of Wisconsin-Madison

Water uptake in porous low-k dielectrics has become a significant challenge for both back-end-of-the-line integration and circuit reliability. The influence of absorbed water on the mechanical properties of PECVD organosilicate glasses (SiCOH) was investigated with nanoindentation. The roles of physisorbed (α -bonded) and chemisorbed (β -bonded) water were examined separately through annealing at different temperatures. Nanoindentation measurements were made on dehydrated organosilicate glass (SiCOH) during exposure to different humidity conditions. The indentation results at shallow depth show that for as-deposited SiCOH, the elastic modulus and hardness were all intimately linked to the concentration of the absorbed water in the dielectric bulk and qualitatively held the same evolution mechanism with in-diffused water concentration. After annealing, the water-concentration-related film mechanical property changes were shown to be reversible. UV curing of SiCOH was shown to lower water-induced mechanical property variation effectively by depopulating the hydrophilic chemical groups in SiCOH. A high-load indentation test shows that in-diffusion of water at the film/substrate interface can degrade the hardness of a SiCOH/Si film stack significantly, while showing less effect on the elastic modulus.

This work was supported by the Semiconductor Research Corporation under Contract 2012-KJ-2359 and by the National Science Foundation under Grant CBET-1066231.

EM-ThP4 Study of Phosphorus-doped Polysilicon Films using Si₃H₈ by Ultra-high Vacuum Chemical Vapor Deposition. *B. Kim, H. Jang, D.-S. Byeon, S. Koo, D.-H. Ko*, Yonsei University, Republic of Korea

In situ phosphorus-doped polysilicon films grown on silicon oxide layers using trisilane (Si₃H₈) and phosphine (PH₃) as precursors were investigated as a function of Si₃H₈/PH₃ gas flow ratio and growth temperature. At high flow rate of Si₃H₈ the deposition process was controlled by the rate of desorption of hydrogen molecules on the surface, which has an activation energy of 1.13 eV, in the temperature range of 600 ~ 700 °C. In comparison, the deposition was limited by the diffusion of Si₃H₈ gas to the surface in the case of low Si₃H₈ flow rate for growth temperatures of > 650 °C. The presence of phosphorus decreased the crystallization temperature of polysilicon layers during growth. In addition, the ratio of phosphorus incorporated into the polysilicon at the same Si₃H₈/PH₃ ratio decreased with increasing growth temperature. The results of sheet resistance measurements suggest that the resistivity of phosphorus-doped polysilicon films decreased with increasing deposition temperature at the same phosphorus concentration, indicating that the use of a high growth temperature results in an enhancement in the activation of phosphorus in the polysilicon films during growth.

EM-ThP5 Electrical Properties of Atomic-Layer-Deposited Al-doped TiO₂ Films on p-type GaAs. *Y. An, Y.-C. Byun, S. Choi, H. Kim*, Sungkyunkwan University, Republic of Korea

For the development of high speed III-V-based metal-oxide-semiconductor field-effect transistors (MOSFETs) in replacement of current Si-based devices, high-*k* gate dielectric is the most crucial component and, especially, atomic layer deposition (ALD) technique has been acknowledged to be the ultimate solution in acquiring high electrical quality such as low leakage current and equivalent oxide thickness (EOT). In order to achieve a sub-1nm EOT value, many researchers have tried to introduce TiO₂ film due to its much higher *k* value than Al₂O₃ and HfO₂ [1, 2]. However, one major drawback in adopting TiO₂ is relatively high leakage current due to its small band gap (~3.1 eV) [1]. As an effort to reduce the leakage current, recently, Kim *et al.* employed Al-doped TiO₂ (ATO) films for memory capacitor application and demonstrated promising electrical performance [1]. More recently, Mahata *et al.* tried (TiO₂)_x(Al₂O₃)_{1-x} alloy film on In_{0.53}Ga_{0.47}As as a gate insulator [2].

In this study, we deposited various ATO films on S-passivated p-type GaAs substrates and characterized their electrical properties, while varying the Al₂O₃ doping concentration and film thickness. The nanolaminating ALD process for the formation of ATO films utilized trimethylaluminum, titanium tetrakis-isopropoxide, and H₂O precursors at a deposition temperature of 250 °C. After MOS capacitor fabrication, various electrical properties including capacitance-voltage, interface state density, and leakage current were evaluated. The dependency of these electrical properties on the ATO film composition will be discussed and correlated with various interface and film characterization results.

[1] S. K. Kim, G.-J. Choi, S. Y. Lee, M. Seo, S. W. Lee, J. H. Han, H.-S. Ahn, S. Han, and C. S. Hwang, *Adv. Mater.* 20, 1429 (2008).

[2] C. Mahata, S. Mallik, T. Das, C. K. Maiti, G. K. Dalapati, C. C. Tan, C. K. Chia, H. Gao, M. K. Kumar, S. Y. Chiam, H. R. Tan, H. L. Seng, D. Z. Chi, and E. Miranda, *Appl. Phys. Lett.* 100, 062905 (2012).

EM-ThP6 Surface Deactivation of SiO₂ using Octadecyltrichlorosilane Based Self-Assembled Monolayers. *A. Hinckley, A.J. Muscat*, University of Arizona

Self-assembled monolayers (SAMs) of octadecyltrichlorosilane (OTS) were investigated as a deactivation technique for SiO₂ surfaces. Liquid phase chemisorption of OTS has been previously described as a surface modification technique for prevention of atomic layer deposition in selective areas. However, the development of an OTS monolayer with the appropriate density required to fully deactivate the SiO₂ surface is extremely sensitive to multiple experimental parameters, including the ambient humidity. This study presents a liquid phase chemisorption method of forming deactivating SAMs in the absence of humidity control. SAMs were deposited both using OTS alone as well as co-adsorbed with trimethylchlorosilane (TMCS) monomers to repair defects in the OTS SAM which might have formed. Monolayers were deposited as a function of solution concentration, solvent, substrate temperature prior to deposition, and hydroxylating solution. Ellipsometric and goniometric results showed that the ideal OTS SAM thickness (26 Å) and water contact angle (110°) were achieved. X-ray photoelectron spectroscopy was used to probe monolayers for defects in conjunction with TiO₂ atomic layer deposition. High resolution Ti 2p XPS spectra showed that no titanium was bonded to

oxygen for up to 100 ALD deposition cycles. In addition, monolayers which initially showed evidence for titanium deposition were passivated via another exposure to the SAM process. This evidence suggests that a fully-deactivated SiO₂ surface can be achieved via the use of a secondary TMCS deposition step without the necessary humidity control. Future work includes the use of SAMs in patterned structures and the deposition of an OTS SAM from the vapor phase.

EM-ThP7 Investigation of Dual-Active-Layered Zinc-Tin-Oxide/Indium-Gallium-Zinc-Oxide Thin-Film Transistors with the Durability of the Chemical Damage. *C.H. Kim, H.J. Kim*, Yonsei University, Republic of Korea

Amorphous-indium-gallium-zinc-oxide (a-IGZO) as channel materials of thin-film transistors (TFTs) has attracted attention as alternative of amorphous silicon (a-Si) for the backplanes of next-generation active-matrix organic light-emitting diode (AMOLED) displays and active-matrix liquid-crystal displays (AMLCDs) due to advantages such as high field-effect mobility, flexibility, good uniformity, transparency in visible light, and low temperature process. However, IGZO thin film has an activated chemical reaction in the bulk of wet etchants for patterning source/drain (S/D) electrodes. Therefore, the process using IGZO film as a channel layer should adopt the protection layer (mainly insulator), that is high cost process due to accessional lithography process and causes a large parasitic capacitance due to the misalignment margin among the gate, the protection layer, and the S/D. So as to improve the above disadvantages, we applied Zn-Sn-O (ZTO) to the protection layer. ZTO has higher chemical stability than IGZO owing to its SnO₂ content, and provides very lower contact resistance compared to that of insulator due to the semiconductor property. The dual-active-layered IGZO/ZTO (DALZI) has the IGZO layer under ZTO layer, which is the protection layer that shield IGZO layer from damage by the aluminum etchant. The DALZI TFT was successfully shielded by ZTO layer during soaking in aluminum etchant, whereas the IGZO TFT was readily damaged or removed. As the above reason, the electrical performance of the DALZI TFT could be preserved after exposure to aluminum etchant compared with that of the IGZO TFT. Hence, the DALZI structure could grant IGZO-based oxide semiconductor the first option for next-generation active-matrix switch device due to low cost.

EM-ThP9 Comparison of Properties of FTO and ITO Films with Different Concentrations. *J.A.L Luna, M. Meneses, J. Carrillo, F. Flores, A. Morales, J. Martínez, J. Sosa, E. Gómez, K. Monfil, A. Benítez*, Benemérita Universidad Autónoma de Puebla, Mexico

Transparent conductive oxides (TCO) have become increasingly important in a large variety of applications due to demands as transparent and conductive materials. Applications of these devices include thin-film solar cells, display devices, optoelectronic devices, polymer-inorganic composite solar cells, gas sensors, and frost-resistant surfaces [1-4]. ITO is an n-type semiconductor where indium oxide (In₂O₃) has been doped with tin oxide in order to improve many of the material's properties, including its electrical conductivity [5]. Also, FTO is an ideal candidate for applications requiring TCO due to its ability to adhere strongly to glass, resistance to physical abrasion, chemical stability, high optical visible transparency, and electrical conductivity. FTO is frequently used as an alternative to ITO when chemical and electrical stability at elevated temperatures is required for device fabrication or application. FTO is more thermally stable because it does not depend on oxygen vacancies to provide charge carriers. As a result, when exposed to elevated temperatures, FTO does not experience the characteristic decrease in conductivity seen in the ITO system. Therefore, as device size continues to decrease, the potential use of nanoscaled structures of these TCOs grows, and a study for these TCO's is necessary. In this work, Spray pyrolysis automatized technique was used to deposit FTO and ITO films on glass corning. This technique allows us to obtain a better control on thin FTO and ITO films, with different properties just by varying the concentration of the fluorine. The structural and optical properties of the FTO and ITO films were obtained using X-ray Diffraction and scanning electronic microscopy, photoluminescence (PL), Transmittance and profilometer. The diffractograms shows the presence of preferential planes of the FTO and ITO. SEM images showed the formation of different agglomerates. All films showed different intensities PL and transmittance spectra showed a wavelength shift of the absorption border. With Hall Effect we obtain some electrical properties.

Acknowledgements: This work has been partially supported by CONACyT-154725 and VIEP-BUAP-2013.

EM-ThP10 Optical Monitoring of Vapor Induced Phase Separation During Spin Coating of PVDF. *N. Dawson, K. Malloy*, University of New Mexico

Poly(vinylidene fluoride) has been studied extensively owing to both its ferroelectric properties and its usefulness as a porous membrane. Its large

polarization response makes PVDF a promising material for electrical applications in digital memory, super capacitors, and electrocaloric coolers. These and other applications of PVDF require high quality thin films. While there are different ways to deposit thin polymer films, spin coating is particularly attractive due to its affordability and ubiquitous use in industry. Understanding the processes occurring under varying conditions during spin coating of PVDF is therefore important. Humid environments have been shown to affect the morphology and crystallinity of spin coated PVDF films. In this presentation we use *in situ* optical reflectance to present evidence that film formation during spin coating in a humid environment is controlled by liquid-liquid and solid-liquid phase separation similar to the demixing seen in the vapor induced phase separation and immersion techniques used to create PVDF membranes. This enables real-time identification of the film formation processes, suggesting that monitoring of optical reflectivity is a basis for process control during spin coating and hence tailoring of film morphology for specific applications.

EM-ThP12 High-efficiency Semipolar GaN-based Light Emitting Diodes Fabricated by Wet Chemical Etching, *S. Jung*, Chonbuk National University, Republic of Korea, *S.-N. Lee*, Korea Polytechnique University, Republic of Korea, *H. Kim*, Chonbuk National University, Republic of Korea

Semipolar GaN semiconductors have become significantly important owing to their potential applications to high-efficiency optoelectronic and electronic devices, especially for the light-emitting diodes (LEDs) with a quantum-confined Stark effect free by eliminating the polarization-induced internal electric fields in the active regions. Another feature of semipolar GaN planes is weaker chemical inertness against chemical solutions compared to the polar (0001) c-plane, indicating that wet etching can be practically used. Indeed, several previous studies have revealed that the wet etching of semipolar GaN planes can form peculiar surface textures such as striated trigonal prisms by exposing specific crystallographic planes. These features are quite interesting in terms of the fabrication of more energy-efficient and cost-competitive LEDs. For example, first, the mesa of LEDs having semipolar orientations can be made using a wet etching process instead of conventional dry etching. Second, the crystallographic surface textures formed after wet etching can act as excellent light scatters or exits for the guided mode caused by the large mismatch of the refractive indices of GaN and the environment (air), implying that the extraction efficiency can be significantly improved. Furthermore, wet etched surfaces were found to be much more efficient in making ohmic contacts, as will be discussed in our study for the first time. These findings suggest that wet etching can be practically used in the fabrication of LEDs. In this regard, we demonstrate the first semipolar GaN-based LEDs fabricated by a wet etching process, which led to better device performance than reference LEDs.

It was shown that the wet etching of semipolar GaN was a reaction-limited process with an E_a of 11.3 kcal mol⁻¹, exhibiting etching rates as high as 530 Å/min under 4M-KOH solution at 90°C. In particular, the wet etched surfaces exhibited the typical trigonal prism cell structure with a (0001) c-plane and [10-10] m-planes. Notably, the ohmic contact could be better formed on the wet etched surface, which could be attributed to the enhanced carrier transport through local shallow barriers associated with the exposed crystallographic structure. The LEDs fabricated by wet etching showed excellent output performance at 1.89 times higher than that of the reference LEDs. This could be due to the role of the textured surfaces. These findings suggest that wet chemical etching can be potentially important to semipolar or nonpolar-plane LEDs, which open new ways to achieve brighter and cost-competitive lighting engines for solid state lighting.

EM-ThP13 Characterization of Non-Stoichiometric Zinc Tungstate Thin Films, *S.T. King*, *E.M. Dinauer*, *J.S. Krueger*, *B.R. Zink*, *Z.C. Koop*, University of Wisconsin - La Crosse

Zinc tungstate (ZnWO₄) has recently gained much attention for its possible uses in photocatalysis and photovoltaic applications [1,2]. While many studies have focused on the fabrication and characterization of nanoscale structures of this material, few have investigated the properties of zinc tungstate thin films. Fewer have explored the properties of non-stoichiometric zinc tungstate materials.

The current study presents preliminary results on the structural, optical, and electronic properties of non-stoichiometric zinc tungstate thin-films fabricated using reactive DC sputter deposition. Such Zn_{1-x}W_xO₄ have been investigated in the parameter space from x = 0 to 0.5. The initial results of these studies suggest that the properties of zinc tungstate are strongly dependent on the quantity of W incorporated into the film. Therefore, the physical properties of zinc tungstate may be tailored for specific applications by employing such non-stoichiometric materials.

References:

- [1] C. J. Spengler and S. O'Hara, *Applied Optics*, 3,1084-1085 (1964)
- [2] J. Lin, J. Lin, and Y. Zhu, *Inorg. Chem.*, 46, 8372-8378 (2007)

EM-ThP17 Development of Chalcogenide Materials for Inline Phase Change Switches (IPCS) for RF Applications, *M.R. King*, *B.P. Wagner*, *E.B. Jones*, *N. El-Hinnawy*, *S.R. McLaughlin*, *P. Borodulin*, *J.S. Mason, Jr.*, *R.S. Howell*, *R.M. Young*, *M.J. Lee*, Northrop Grumman ES

Recently the digital memory industry has exploited chalcogenide materials for their distinct phase-dependent electrical properties, where the large resistivity difference between crystalline and amorphous states is used to create efficient memory platforms.

Digital applications primarily require large DC on/off ratios; RF switches on the other hand require very low on-resistance (R_{on}) and off-capacitance (C_{off}). These requirements are often mutually exclusive, where gains in one come at the expense of the other. Chalcogenide phase change materials represent a unique solution to this dilemma. With PCM devices, not only is it possible to obtain a very low R_{on} concomitant with very low C_{off} , but one can also achieve zero prime power consumption during steady state operation.

This presentation will detail the development of phase change materials that enable world class RF switch performance. Specifically a chalcogenide inline phase change switch (IPCS) utilizing GeTe has been fabricated for the first time utilizing a 3rd terminal for controlling an independent resistive heater to accomplish the thermal actuation of the phase change material. An on-state resistance of 6 Ω (0.06 Ω-mm), with an off-state capacitance and resistance of 33fF and 1 MΩ were measured, respectively, resulting in an RF switch figure-of-merit cut-off frequency (F_{co}) of 0.7 THz and a switching on/off ratio of 10⁵. The power required to change the GeTe from amorphous to crystalline was as low as 0.5W, with zero power consumption during steady state operation, making it a non-volatile RF switch. To the authors' knowledge, this is the first reported implementation of an RF phase change switch in a traditional, 3-terminal, in-line configuration.

In order to achieve such a high level of performance, significant material development efforts were undertaken. GeTe films were deposited using the DC magnetron sputtering technique and a power-pressure matrix was utilized to minimize sheet resistivity (R_s) and maximize the on-off ratio. Morphological features were evaluated using XRD, SEM and FIB-based cross sections. Electrical properties of as-deposited GeTe films were evaluated using 4-point probe measurements and a heated stage. The combined effect of sputtering power and pressure on film morphology and material properties will be presented.

In addition to wide ranging morphological and R_s variations with deposition parameters, it was found that the sputtering process significantly affects the chemical susceptibility of the films. An optimized fabrication scheme will be presented, in which high quality GeTe films were capable of being processed without a capping layer.

Graphene and Other 2D Materials Focus Topic
Room: Hall B - Session GR-ThP

Graphene and Other 2D Materials Poster Session

GR-ThP4 Characterization of Coatings for Tribological and High Temperature Applications, *S. Vijayalakshmi*, *V. Thippesamy*, *M.R. Sridhar*, *K.A. Harsha*, *R. Roshan*, GE Global Research, India, *B.A. Record*, GE

Metal Matrix Composite Coatings as wear resistant coatings and thermal barrier coatings play a crucial role in the life of current tribological and high temperature applications. Understanding the surface of these coatings in terms of its material structure, porosity, composition, mechanical strength, and bond strength is crucial. These properties essentially govern the final tribological and thermal properties and thereby dictate the life of the coatings. Various characterization techniques have been employed in studying the properties of the coatings. Proper choice of the characterization techniques; tools and method of evaluation are critical for distinguishing coating with very similar properties. This article presents the use of selected characterization techniques like Micro hardness, Scanning electron microscopy coupled with EDS, Image analysis, XRD and Surface Profilometry to analyze the mechanical, material and surface properties and understand the structure property correlation of coatings of varied microstructures with different volume fraction of ceramic particles embedded in metallic matrix.

GR-ThP5 Plasma Treatment of Thin Film Coated with Graphene Flakes for Sheet Resistance Reduction, *S.H. Kim*, *J.S. Oh*, *G.Y. Yeom*, Sungkyunkwan University, Republic of Korea

Recently, study of transparent electrode using graphene flake has been attracted in this field. The advantage of graphene flake is the high productivity, scalability, and the flexibility on using various substrate

materials. However, a thin film coated with graphene flakes generally showed a high sheet resistance due to the defects existed within graphene edges, domains, residual oxygen contents, etc. In this study, the effect of plasma treatment to thin film coated with graphene flake on the improvement of electrical properties was investigated. Graphene flake films were coated on the polyethylene terephthalate (PET) film by the spray coating system. By using a Cl_2 plasma treatment, the sheet resistance was decreased with the increase of treatment time. However, when the thin film was treated too long, the sheet resistance was again increased with the increase of the treatment time. The optimum treatment time was related to the thickness of the thin film. In this experiment, at an optimum condition, it was observed that the surface resistance of the graphene film could be decreased higher than 50 %. The detailed mechanism on the change of graphene sheet resistance & structure will be presented.

GR-Thp6 Characterisation of Mo Oxidation States in MoO_x and MoS_x Layer Materials Using X-ray Photoelectron Spectroscopy, A.J. Roberts, Kratos Analytical Limited, UK, N.A. Fairley, CasaXPS, UK, B. Mendoza-Sánchez, Trinity College Dublin, Ireland, C. Moffitt, Kratos Analytical Limited, UK

The characterisation of layered materials has been dominated by graphene in recent years. There are however other examples of layered materials which retain stability down to a single monolayer and whose properties are complementary to graphene. Of these materials both MoS_2 and α -phase MoO_3 are of interest due to electronic and optical properties which may lead to applications as diverse as optoelectronics and light emitting devices for the former material or energy storage and catalysis for the latter. The chemical state and therefore electronic structure of these materials is readily characterised using x-ray photoelectron spectroscopy. In the case of MoO_3 , which may be reduced quite easily, there are a number of stable phases where the Mo becomes progressively reduced until reaching the stable dioxide with the formal oxidation state Mo(IV). Here we present a study of electrochemically reduced MoO_3 where a mixture of lower valence oxides have been generated with concentrations varying as $\text{Mo(V)} > \text{Mo(IV)} > \text{Mo(VI)}$ with MoO_2 as the main component created below 0.185 V (vs Ag/AgCl). The stability of α - MoO_3 under x-ray irradiation has also been studied with particular focus on the possibility of x-ray / in-vacuo reduction of Mo(VI) causing misinterpretation of the valance of the samples generated electrochemically. To complement the work on the oxide material we also present a study of the oxidation state of MoS_2 where the Mo(IV) disulphide has been reduced in ultra-high vacuum by preferential sputtering of the sulfur. This relatively aggressive form of reduction leads to the creation of Mo(0) metallic-like molybdenum and demonstrates the extreme care required for in-vacuum sputter cleaning of layered materials.

GR-Thp7 Development of Field Effect Transistors Based on Graphene using Dielectrophoretic Deposition and Tantalum Nitride Electrodes, A.M. Pascon, J.A. Diniz, L.R.C. Fonseca, J.F. de Souza, University of Campinas, Brazil

For devices based on graphene, non-refractory metallic electrodes of Ti/Au or Ti/Pd are frequently used. However, to reduce the contact resistance between metal electrodes and graphene, an annealing step in vacuum at a temperature of 700° C is generally required, which is incompatible with non-refractory metals [1]. On the other hand, refractory metal electrodes, such as tantalum nitride (TaN), can tolerate the annealing step but are less studied. Furthermore, the many techniques established to obtain graphene and to build high quality devices based on graphene are severely limited for large scale integration (LSI). Here we attempt a new approach to reach LSI. In our approach, graphene was obtained in large quantity from dielectrophoretic (DEP) assembly [2] of a few layers of insulating graphene oxide followed by thermal reduction at 450°C. Next, for the metal contacts with graphene we used tantalum nitride (TaN) electrodes deposited by DC reactive sputtering in N_2/Ar environment. FET devices were obtained with the graphene sheets deposited between TaN electrodes, which are employed as source and drain, and laying on top of a TaO_x high-k gate dielectric deposited on an n+ silicon substrate used as the back electrode. To improve the contacts between graphene and TaN, ac signals were applied between electrodes, followed by annealing at 700° C in high vacuum to prevent electrode oxidation.

Scanning electronic microscopy and current-voltage (I-V) measurements were carried out to obtain the physical and electrical characteristics of our devices, respectively. The resistance values measured before and after annealing differ by five orders of magnitude, in agreement with [2], resulting in good contact characteristics.

In parallel, *ab initio* calculations were performed to investigate the nature of graphene/TaN interface employing two models for the interface. While this simulation effort is still ongoing, we have found that for the Ta/N-rich TaN surface and for the Ta-rich TaN surface the absence of the Dirac cone in the BL for each case is not due the BL roughness caused by the strong interaction with the TaN surface, especially for the Ta/N-rich surface, but

due to metal surface states induced in the BL. Because in graphene the inter-layer separation is large, the electronic properties of the second graphene sheet are graphene-like, displaying a clear linear dispersion near the Dirac point.

[1] Souza, J. F., Development of Materials and Methods of Fabrication of Chemical/Biochemical Sensors based on Silicium and Carbon Nanostructures (ISFET, CNTFET and GrafET), PhD, University of Campinas, 2012;

[2] Burg B R et al, Appl. Phys, Lett. 94 053110 (2009);

GR-Thp8 An Infrared Sensor using a Multi-walled Carbon Nanotube Sheet, D. Jung, M. Han, G.S. Lee, The University of Texas at Dallas

Carbon nanotubes (CNTs) have a potential capacity to be efficient infrared (IR) sensing materials due to their outstanding electronic and optical properties. There are many reports on the IR photo-response in the conductivity/resistance of single-walled carbon nanotube (SWCNT). Although theoretical and experimental development toward individual SWCNT based IR sensor has been reported, several obstacles disturb the further progress of SWCNT based IR sensors. Firstly, SWCNTs still have some issues in their purification, separation, and dispersion in a liquid/polymer used to enhance their electrical and optical properties. It is difficult to modify the density and thickness of the SWCNTs causing reduction in their production efficiency. Secondly, there is no a reliable and efficient transfer way to reproducibly fabricate SWCNT based sensors up to now. Lastly, how to make large scale and uniformly aligned films for mass production by using SWCNT. In this paper, spin-capable multi-walled carbon nanotube (MWCNT) is proposed to fulfill the above three challenges. The IR detector fabricated by MWCNT sheet, which pulled out from spin-capable MWCNT forest has large surface area and well aligned individual MWCNT. By investigating theoretical analysis with experimental results, we focused on which factors can affect the sensitivity and response time of MWCNT IR detectors, which gives help for further design for practical applications. We've founded that the extremely low heat capacity per unit area of MWCNT in sheet enabled a fast IR response of the MWCNT IR detectors. Experiments by acid treatment and increasing the surface area of CNT films have been carried out to improve the sensitivity and response time of the CNT film detector. We've observed that the MWCNT IR sensor exhibits shows a 16 % resistance change with a fast response time of 10 ms under 10 mW/mm² of IR illumination at room temperature.

GR-Thp9 The Robustness of the Electronic Structures of the Quasi-Free Standing Graphene Layers Upon Deposition of the Strong Hole-Doping Materials, W. Kim, Korea Research Institute of Standards and Science, Republic of Korea, G.-E. Yang, J. Kim, Y. Park, Kyung Hee University, Republic of Korea, B.-G. Park, Pohang Accelerator Laboratory, Republic of Korea

We investigated the change in the electronic structure of the quasi-free standing epitaxial graphene(QFEG) layers upon deposition of strong hole doping materials by using angle-resolved photoemission spectroscopy(ARPES). To produce the QFEG layers, we tried hydrogen intercalation into a zero-layer graphene grown on the 4H-SiC(0001) surface, and confirmed the successful formation of the QFEG layers, judging from the coincidence of the Dirac point and Fermi levels in the ARPES spectra of the hydrogen-intercalated graphene layers. Then we monitored carefully the change of the position of Dirac point in ARPES spectra during the deposition of strong hole-doping materials such as Bi atoms and tetrafluoro-tetracyanoquinodimethane (4F-TCNQ) molecules, both of which are known to induce the significant shifts of the Dirac point to the Fermi level in the conventional epitaxial graphene layers. However, for the QFEG layers, we could not find any measurable shifts of Dirac point upon the deposition of Bi atoms or 4F-TCNQ up to the 1 ML thickness. The overall shape of graphene π -bands also remained almost same, unlikely the results for the conventional epitaxial graphene layers which show significant blurring of band width near 1 ML thickness. This robustness of the electronic structure of QFEG layer upon deposition of Bi atoms and 4F-TCNQ molecules implies that more sophisticated approach is required to understand the hole-doping effect in the conventional epitaxial graphene and QFEG layers grown on the SiC(0001) surface.

GR-Thp12 Structural Stability and Electronic Structure of Boron- or Nitrogen-Doped Graphene, T. Umeki, J. Nakamura, The University of Electro-Communications (UEC-Tokyo), Japan

Graphene, a two-dimensional form of carbon with atoms arranged in a honeycomb lattice, has attracted enormous attention because of its unique electronic structures. To realize graphene-based electronics, modulation techniques of its electronic properties are indispensable. The most fundamental approach to tailor the electronic properties of graphene is doping. Nitrogen atoms can be doped into graphene using chemical vapor

deposition or NH₃ plasma exposure [1,2]. It has been confirmed that the nitrogen-doped graphene exhibits an n-type behavior [1,2]. However, there exists little knowledge about the well-defined atomic arrangements of nitrogen-doped graphene. In this work, we have investigated the energetic stability of boron- or nitrogen-doped graphene using first-principle calculations within the local density functional theory.

We have calculated the interaction energy between two substitutional N atoms. A (4 × 4) supercell for graphene is employed, in which two C atoms are replaced by N atoms. The interaction energy has been found to decrease with increasing distance between N atoms. It should be noted that N atoms prefer to locate at the third nearest neighbors with each other, as shown in the previous report [3].

Next, we have investigated the interaction energy for the homogeneously-arranged N-doped graphene using (*n* × *n*) and (*n*√3 × *n*√3)-R30 unit cells (*n*: integer), where substitutional N atoms form triangle or honeycomb grids on the graphene basal plane. It has been found that the interaction energy decreases with decreasing density of N atoms. However, anomalous stabilization is confirmed for the honeycomb-arranged N-doped graphene with N:C=1:3. We will also report on the band structures of N-doped and B-doped graphene.

[1] D. Wei et al., *Nano Lett.* **9**, 1752 (2009)

[2] Y.-C. Lin et al., *Appl. Phys. Lett.* **96**, 133110 (2010)

[3] Z. Hou et al., *Phys. Rev. B* **85**, 165439 (2012)

Helium Ion Microscopy Focus Topic

Room: Hall B - Session HI-ThP

Aspects of Helium Ion Microscopy Poster Session

HI-ThP2 Imaging Nascent Soot Particles: Tiniest Soot Particles are Not Structurally Homogeneous. *M. Schenk*, Bielefeld University, Germany, *S. Lieb*, University of Southern California, *H. Vieker*, *A. Beyer*, *A. Götzhäuser*, Bielefeld University, Germany, *H. Wang*, University of Southern California, *K. Kohse-Höinghaus*, Bielefeld University, Germany
Structural and morphological probing of nascent soot has been a challenging problem historically. Transmission electron microscopy (TEM) shows that mature soot is usually composed of stacks of polycyclic aromatic hydrocarbons arranged in a turbostratic fashion with a certain degree of microscopic crystallinity. Whether this observation can be extrapolated to nascent soot undergoing rapid mass and size growth in a flame remains an open question. In particular, recent studies show converging evidence that nascent soot may have an aromatic core-aliphatic shell structure not seen from previous TEM studies. The aliphatic component in the shell appears to be weakly bound among itself and with the aromatic core. In TEM probing, the possibility of high-energy electron beam damage or structural modification particles also remains an open question. Evidence of this possibility emerged as early as the mid 1980s when Iijima (S. Iijima, *J. Electron Microscop.* **34** (1985) 249-265) demonstrated the structural instability of gold nanoparticles ~3 nm in diameter under electron beam irradiation in a TEM. Sample damage can arise from electron beam induced chemical bond breaking and/or evaporation of the aliphatic component along with structural change and crystallization of the remaining particle material.

To explore the aforementioned problems and to find more suitable techniques, we report here results of two “softer” microscopic techniques: Helium Ion Microscopy (HIM) and phase imaging Atomic Force Microscope (AFM). In comparison to TEM, both techniques present far less sample damaging during imaging. The present study focuses on the HIM imaging of nanometer-sized soot particles sampled from a stagnation-point ethylene-oxygen-argon flame, under the conditions of Abid et al. (A. D. Abid, *Combust. Flame* **154** (2008) 775-788).

HI-ThP3 Helium Ion Microscopy as a Tool to Investigate Thin Layer Thicknesses. *H. Vieker*, *K. Rott*, *U. Werner*, *A. Beyer*, *G. Reiss*, *A. Götzhäuser*, Bielefeld University, Germany

The recently developed helium-ion microscope allows remarkable surface resolution with the secondary-electron (SE) detector. Simultaneously, backscattered ions can be detected that allow imaging with a substantially higher elemental contrast. This Rutherford backscattered ion (RBI) contrast depends mainly on the elemental composition of the investigated sample surface. The escape depth of backscattered ions is much larger than for secondary electrons. Thus whole layers with a wide range of thicknesses will contribute to a RBI image, whereas the SE image is far more surface sensitive.

In this contribution we examine RBI imaging as a tool to characterize thickness variations of layered samples with well defined compositions. The homogeneity of gold layers on silicon substrates is investigated and compared to simulations. The achievable spatial resolution as well as the use of reference samples to measure layer thicknesses will be addressed.

HI-ThP4 Helium Ion Microscopy and Ionoluminescence of Defects. *G. Hlawacek*, *V. Veligura*, *R. van Gastel*, *H.J.W. Zandvliet*, *B. Poelsema*, University of Twente, Netherlands

Defects are an unavoidable and often unwanted side product of Helium Ion Microscopy (HIM). We will discuss the role of defects and try to show examples of their useful application.

Point defects created using HIM can be analyzed in-situ using ionoluminescence. However, such point defects can also be exploited to create areas with specific optical properties, in particular areas that either absorb light or emit light of a certain wavelength when excited.

Going beyond normally used ion doses allows to investigate defect agglomeration, blister formation and the subsequent surface restructuring. We present examples of materials modification at doses starting from 1 × 10¹⁷ cm⁻² up to 1 × 10²² cm⁻². Examples of surface structures formed under extreme ion fluencies at different temperatures will be presented for a wide range of materials including technological relevant materials for nuclear applications.

This research is supported by the Dutch Technology Foundation STW, which is the applied science division of NWO, and the Technology Programme of the Ministry of Economic Affairs.

In Situ Spectroscopy and Microscopy Focus Topic

Room: Hall B - Session IS-ThP

In Situ Microscopy and Spectroscopy Poster session

IS-ThP1 Scanning Tunneling Microscopy of the Topological Crystalline Insulator SnTe. *D. Zhang*, *J. Ha*, NIST and University of Maryland, *H. Baek*, NIST and Seoul National University, Republic of Korea, *Y. Kuk*, Seoul National University, Republic of Korea, *J.A. Stroscio*, Center for Nanoscale Science and Technology, NIST

Recently, the topological classification of electronics states has been extended to a new class of matter called topological crystalline insulators. In contrast to topological insulators characterized by time reversal symmetry protected surface states with an odd number of Dirac cones, topological crystalline insulators arise from crystal symmetry and are characterized by surface states with an even number of Dirac cones. Here, we report *in-situ* low temperature scanning tunneling microscopy study of SnTe (001) surfaces grown by molecular beam epitaxy. SnTe high symmetry surfaces have been recently predicted and experimentally confirmed as hosting topological crystalline insulator surface states [1-3]. The growth of SnTe on multilayer graphene/SiC substrates is shown to produce SnTe (001) nanoplates with varying densities of Sn vacancies. The topological surface states on the SnTe (001) surface in these nanoplates were probed by scanning tunneling spectroscopic mapping. In this poster we discuss the spectroscopic mapping results in terms of scattering in Fermi surface contours of the topological surface states.

[1] T. H. Hsieh, *et al.*, *Nat. Comm.* **3**, 982 (2012).

[2] Y. Tanaka, *et al.*, *Nat. Phys.* **8**, 800 (2012).

[3] S.-Y. Xu, *et al.*, *Nat. Comm.* **3**, 1192 (2012).

IS-ThP2 In Situ Electrostatic and Thermal Manipulation of Suspended Graphene Membranes. *W. Bao*, *K. Myhro*, *Z. Zhao*, *Z. Chen*, *W. Jang*, *L. Jing*, *F. Miao*, *H. Zhang*, *C. Dames*, *C.N. Lau*, University of California, Riverside

Graphene is nature's thinnest elastic membrane, and its morphology has important impacts on its electrical, mechanical, and electromechanical properties. Here we report manipulation of the morphology of suspended graphene via electrostatic and thermal control. By measuring the out-of-plane deflection as a function of applied gate voltage and number of layers, we show that graphene adopts a parabolic profile at large gate voltages with inhomogeneous distribution of charge density and strain. Unclamped graphene sheets slide into the trench under tension; for doubly clamped devices, the results are well-accounted for by membrane deflection with effective Young's modulus $E = 1.1$ TPa. Upon cooling to 100 K, we observe buckling-induced ripples in the central portion and large upward buckling of the free edges, which arises from graphene's large negative thermal expansion coefficient.

Poster Session

SE-ThP1 Gas Barrier Properties of Hydrogenated Amorphous Carbon Films Synthesized by Atmospheric Pressure Plasma on Nitrogen-Plasma-Treated Polyethylene Terephthalate Substrates, Y. Futagami, T. Hirako, M. Noborisaka, A. Shirakura, T. Suzuki, Keio University, Japan

Gas barrier properties of hydrogenated amorphous carbon (a-C:H) films synthesized at atmospheric pressure have been investigated for applications to packaging materials. In this study, a-C:H films were synthesized on N₂-plasma-treated polyethylene terephthalate (PET) substrates by atmospheric pressure plasma enhanced chemical vapor deposition method. PET substrates were treated with various plasma treatment time at atmospheric pressure prior to synthesis of 500-nm-thick a-C:H films. The effects of N₂ plasma treatment on the properties of PET surface and a-C:H/PET were investigated in terms of chemical binding structure, surface free energy, roughness, adhesion and oxygen transmission rate (OTR). Formation of new C-N bonds were observed on the PET surfaces by N₂ plasma treatment from X-ray photoelectron spectroscopy analysis, and the adhesion strength between a-C:H films and PET substrates was improved in tape tests. As the plasma treatment time increased from 0 to 5 s, OTR of the a-C:H films on N₂-plasma-treated PET substrates decreased from 5.6 to 3.1 cc/(m²·24h·atm), which is five times less OTR than those of uncoated PET substrates. However by increasing the plasma treatment time from 5 to 40 s, the surface roughness of PET substrate and OTR of a-C:H/PET were increased to 10.5 nm and 4.2 cc/(m²·24h·atm). This result indicates that the proper time of N₂ plasma treatment on PET substrates is effective for improving adhesion and gas barrier properties of a-C:H films.

SE-ThP2 Recycling and Diffusion of Ions in High Power Impulse Magnetron Sputtering Plasmas, L. Meng, P. Raman, H. Yu, D.N. Ruzic, University of Illinois at Urbana Champaign

PLEASE NOTE THAT D. RUZIC CANNOT BE THE PRESENTER. HE IS ALREADY AN INVITED SPEAKER AND YOU MAY PRESENT ONE PAPER (ORAL OR POSTER) IN THE SYMPOSIUM In high power impulse magnetron sputtering (HiPIMS), ions either diffuse towards the substrate for the deposition or are recycled to sputter or self-sputter the target. Both processes were studied here to further understand the underlying mechanisms. For the diffusion, plasma across the entire chamber was characterized using a 3D scanning triple Langmuir probe. An obvious plasma expansion originated from the "race track" region was observed. The expansion speed and orientation varied with both pulsing parameters and magnetic field strength. These parameters were also found to affect the metal ionization fraction on the substrate. A lower magnetic field strength gave a higher ion fraction (e.g. up to 60% for Cu in a 200 Gauss field while about 30% in an 800 Gauss field) despite a lower plasma density. The corresponding lower plasma potential drop across the bulk plasma was accounted for the effect. Then, the fluxes of plasma species towards the cathode were directly measured through an orifice on the target. Quartz crystal microbalance and current collecting plate behind grid filters were used to determine the fluxes of argon ions, metal ions, and metal atoms. The self-sputtering effect during HiPIMS was supported by a higher fraction of metal ions obtained at a higher pulse peak current. A delayed detection of ion flux for 10 to 40 μs from the onset of pulse likely supported the theory of localization of ionization zone during the HiPIMS ignition.

SE-ThP3 Mechanical Properties and Impact Resistance of CrAlSiN and TiAlSiN Coatings, Y.Y. Chang, Y.C. Yang, Y.K. Chou, J.X. Liu, National Formosa University, Taiwan, Republic of China

The extension of the tool life is a considerable goal for high speed precision forming tools. Therefore, it is interested to reduce the friction and wear for such tools. The employment of hard coatings, in form of metal and ceramic, increases the production and maintenance costs. In this study, CrAlSiN and TiAlSiN coatings have been deposited on cemented carbide tools by using cathodic-arc evaporation with plasma enhanced duct equipment. Titanium, TiAl, TiSi and CrAlSi alloy cathodes were used for the deposition. The alloy content of the deposited coating was correlated with the evaporation rate of cathode materials. The microstructure of the deposited coatings was characterized by using a field emission gun high resolution transmission electron microscope (FEG-HRTEM, FEI Tecnai G² 20 S-Twin), equipped with an energy-dispersive x-ray analysis spectrometer (EDS), operated at 200 keV for high-resolution imaging. Glancing angle X-ray diffraction was used to investigate the microstructure and phase identification of the films. The composition and depth profile were assessed by wavelength-dispersive x-ray spectroscopy (WDS). Mechanical properties, such as the hardness and elastic modulus, were measured by means of nanoindentation. To evaluate the

correlation between impact fracture resistance and hardness/elastic modulus ratio of the deposited coatings, an impact test was performed using a cyclic loading device with a tungsten carbide indenter as an impact probe. The design of CrAlSiN and TiAlSiN coatings is anticipated to inhibit the grain growth, and leads to grain refinement effect, which expected to increase the hardness and impact resistance of coatings.

SE-ThP4 Preferential Growth of Oxide Nanorods on Multicomponent TiAlSiN Coated Stainless Steels after Thermal Oxidation, Y.Y. Chang, Y.C. Yang, National Formosa University, Taiwan, Republic of China

Transition metal nitrides, such as TiN and CrN, have been used as protective hard coatings due to their excellent tribological properties. Recently, multicomponent TiAlSiN coatings have been developed in order to possess high hardness and good thermal stability at temperature exceeding 800 °C. In this study, a series of TiAlSiN coatings with different alloy contents (Ti_{0.67}Al_{0.32}Si_{0.01}N, Ti Al Si N, and Ti_{0.85}Al_{0.05}Si_{0.12}N) were deposited onto an SS304 substrate by using cathodic arc evaporation. Cathodes of Ti, TiAl (50 at.% of Al and 50 at.% of Si) and Ti_{0.8}Si_{0.2} (80 at.% of Al and 20 at.% of Si) alloy targets were used. The as-deposited films were annealed at 800 °C for different time from 20 minutes to 100 minutes in air to analyze the different preferential oxidation behaviors of TiAlSiN coatings. The surface morphology and microstructure of the deposited and oxidized coatings was investigated by field emission scanning electron microscopy (FESEM) equipped with an energy-dispersive x-ray analysis spectrometer (EDS). X-ray diffractometry was performed using PANalytical X'pert Pro diffractometer with a high resolution ψ goniometer and Cu radiation in both glancing angle and high-angle configurations for phase identification. The correlation between the preferential growth of oxide nanorods and the deposited multicomponent TiAlSiN coatings was discussed. During the oxidation process, Ti, Al, and Si would diffuse outward to form oxidative layers of Al₂O₃, TiO₂, and SiO₂ at high temperature. The Ti_{0.67}Al_{0.32}Si_{0.01}N with higher Al content ratio showed that needle-like α -Al₂O₃ oxides preferentially grow from the macroparticle defect sites. Oxide nanorods were uniformly found on the oxidized Ti_{0.8}Al_{0.17}Si_{0.03}N with smaller content of Al. The Ti_{0.85}Al_{0.05}Si_{0.12}N with the highest Si and the lowest Al contents showed only short TiO₂ nanorods uniformly grow on the surface. Therefore, the kinetic oxidation behavior of TiAlSiN coatings varied with the alloy content and phase segregation via high temperature oxidation.

SE-ThP5 Oxidation Resistance and Hardness of CrAlN based Films Deposited by the Arc Ion Plating Method, T. Mori, T. Suzuki, Keio University, Japan

In the field of hard coatings, oxidation resistance and high hardness of the coatings are among the main concerns. In this study, CrAlSiYN films with various silicon content were synthesized and investigated their oxidation resistance and hardness. The films were deposited on cemented carbide, silicon and SUS304 substrates by the arc ion plating method. X-Ray Diffraction results showed that the CrAlSiYN films had NaCl-type structure. With increasing the silicon content, the lattice parameter *r*s for cubic CrAlSiYN films decreased from 0.416 nm to 0.413 nm. The solid solubility limit of silicon into CrAlYN film was about 3 at. %. Hardness of CrAlSiYN films was measured using conventional micro-Vickers hardness tester and the result showed that CrAlSiYN films with high Si content exhibited high hardness (about 30 GPa). Using the flow discharge optical emission spectrometry depth profiling method, an oxygen peak was only observed around surface of films after annealed at 1000°C for 1 hour in air. The cross-sectional transmission electron microscopy observation of oxide layer of CrAlSiYN films showed that yttrium stimulated the formation of amorphous oxide, and its silicon or yttrium oxide prevented diffusion of oxygen and metal such as chromium. Incorporation of silicon and yttrium maintained the stable oxidation layer of Cr₂O₃ or Al₂O₃ produced at the surface under high temperature and improved oxidation resistance of CrAlN films.

SE-ThP7 Structure and Mechanical Properties of Tungsten-Yttrium Based Coatings, G. Martinez, C.V. Ramana, University of Texas at El Paso

The challenging environment associated with a fusion reactor will require the utilization of advanced materials in order to enable successful development of fusion energy for the future. Tungsten(W)-based materials have been considered for nuclear reactor applications for its outstanding properties such as high melting point, low vapor pressure, high thermal conductivity, and low thermal expansion coefficient. However, pure W exhibits low fracture toughness at all temperatures and a high ductile to brittle transition, which depends on the chemical and microstructure. The present work was focused on the W-Y based alloy coatings grown by sputter-deposition. The sputtering was performed using a W-Y target to fabricate coatings on to MgO(100) substrates. W-Y coatings were made at various growth temperatures (T_g) ranging from room temperature to 500 °C. The structural and mechanical properties of the coatings were evaluated as a

function of T_c . While the ultimate goal is to investigate the performance of W-Y coatings as a structural material in the next generation nuclear reactors, preliminary results obtained on the crystal structure, composition, stress evolution and mechanical properties of the coatings are presented and discussed.

SE-ThP8 A New Testing Method for Surfaces Subjected to Combined Impact and Sliding Loads, P. Epaminonda, C. Rebholz, University of Cyprus

There are a large number of factors involved in wear processes (e.g. mechanical, physical and chemical properties, surface topography, loading), making the precise theoretical and quantitative approach of wear a challenge even for “simple” tribo-systems. Many of these factors are hard to measure, may vary with time and space, and there is not yet a general theory available of how to link the basic properties with the tribological response. Several well established testing methods (e.g. pin-on-disk, fretting and impact tests) have been widely used to study treated surfaces and coatings on various substrates. However, many of these existing techniques have limitations in their ability to characterize materials, since they mainly focus on a single mode of loading and wear (e.g. only impact or sliding).

In this study, a new Dynamic Impact and Sliding Test (DIST) for the tribo-mechanical evaluation of surfaces under complex loading conditions is presented, where the surfaces are simultaneously subjected to sliding and impact loading. Such modes exist in many critical applications, from biomedical (e.g. hip/knee implants) to automotive applications (e.g. diesel injectors, engine valves, cam shafts), in cutting tools, general machine parts and systems, etc. Instruments and techniques for combined loading situations (such as the proposed DIST) are a feasible way for fast, economical and reliable evaluation of complex tribo-systems with high practical and industrial interest. Expected benefits include the time and cost effective evaluation of various surfaces and the better understanding of their peculiarities under such multi mode loading conditions. Some of the unique characteristics of the DIST (e.g. combined impact and sliding testing; wear area in a single point; pre-setting of desired maximum wear depth possible; evaluation of materials’ properties and behavior in a single run) are presented.

SE-ThP9 Exploring Crater Roughness for Durable Sol-Gel Derived Superhydrophobic Coatings, B. Dyett, A. Wu, R. Lamb, The University of Melbourne, Australia

Characterized as exhibiting water droplet contact angles $> 150^\circ$ and sliding angles $< 5^\circ$, superhydrophobic films have attracted considerable research attention as a result of their remarkable non-wetting properties and potential applications in self-cleaning, anti-fouling and anti-icing. The combination of hydrophobic chemistry and surface roughness necessary for imparting such non-wetting characteristics presents a challenge towards industrial applicability due to the intrinsic frail nature of highly rough surfaces.[1] Sol-gel synthesis offers a versatile and scalable means for producing superhydrophobic films. However, traditional sol-gel approaches are often reliant on ‘needle-like’ aggregations of nanoparticles to impart surface roughness. This surface structure, whilst ideal for minimizing solid-water interactions is inherently fragile.[2, 3] Upon contact, high aspect-ratio asperities experience excessive pressures usually exceeding the mechanical properties of the material[4], consequently such superhydrophobic films are very easy to abrade and damage. To overcome this challenge a templating method was used to engineer more robust structures. Discrete polymer spheres were embedded within an alkoxysilane sol-gel to form a continuous, robust, thin film. Roughness was then engineered into the film by thermally degrading the polymer spheres within the gel network, leaving behind crater-like structures with durability far exceeding its predecessor’s. The resultant crater-like films exhibited pencil hardness exceeding 4H, eclipsing traditional films’ pencil hardness, typically of the order 8B – HB. This avenue may provide a scalable approach for controlling roughness features in durable superhydrophobic films and allow for large scale application in areas of self-cleaning and anti-fouling.

References

1. Verho, T., et al., *Advanced Materials*, 2011. (5): p. 673-678.
2. Nakajima, A., K. Hashimoto, and T. Watanabe, *Monatshfte für Chemie/Chemical Monthly*, 2001. (1): p. 31-41.
3. Nakajima, A., et al., *Thin Solid Films*, 2000. (1–2): p. 140-143.
4. Bhushan, B. and M. Nosonovsky, *Acta materialia*, 2003. (14): p. 4331-4345.

SE-ThP10 Abrasion Resistance and Adhesion Promotion for SiOC(-H) / Polycarbonate System using Nanosilica Contained Acrylic Intermediate Layers, T. Masuko, M. Noborisaka, T. Mori, A. Shirakura, T. Suzuki, Keio University, Japan

SiOC(-H) films were synthesized on polycarbonate substrates from mixture of trimethylsilane (TrMS) and O_2 gases by radio frequency plasma enhanced chemical vapor deposition (RF-PECVD) method to improve the abrasion resistance of polycarbonate substrates.

In order to improve the adhesion to polycarbonate substrates, we applied the acrylic intermediate layer prepared by ultraviolet curing method between SiOC(-H) films and polycarbonate substrates. The nanosilica particles were mixed with pentaerythritol triacrylate and pentaerythritol tetraacrylate at various concentrations to control the hardness of the intermediate layer.

The scratch resistance of SiOC(-H) films deposited on polycarbonate substrates with the intermediate layer was improved as the pencil hardness of the intermediate layer increased. After the taber abrasion tests of the SiOC(-H) films deposited on polycarbonate substrates with the intermediate layer, the occurrence of delamination was inspected by digital microscope. The delamination was confirmed to be markedly suppressed as the hardness of the intermediate layer increased.

The haze difference (ΔH_{haze}) between before and after the abrasion tests exhibited sufficient abrasion resistance of 3.5% after 1000 revolutions when the 500 nm thick-SiOC(-H) film was deposited on polycarbonate substrates with the intermediate layer contained 25 wt.% nanosilica particles.

SE-ThP11 Highly Conformal and Size-Controlled Nanofabrication of Macro-scale Three-Dimensional Biotemplated Inorganic Nanonetworks, H. Ceylan, C. Ozgit-Akgun, T.S. Erkal, I. Donmez, R. Garifullin, F. Genisel, A.B. Tekinay, A.K. Okyay, M.O. Guler, N. Biyikli, Bilkent University, Turkey

By combining organic and inorganic nanomaterials using two different material growth techniques (self assembly and atomic layer deposition), we demonstrate a facile and reliable fabrication method for TiO_2 and ZnO semiconductor nanonetworks. Self-assembled peptide-amphiphile nanofibers are used as three-dimensional organic nano-templates, whereas subsequently atomic layer deposited metal-oxide films formed the conformal inorganic functional nano-coatings. Apart from the traditional organic templates, we used a fully dried, three-dimensional (cm-scale), highly interconnected peptide nanofibrous network template, which enabled atomic layer deposition (ALD) precursors to be homogeneously deposited with exceptional conformity. The wall thickness of the inorganic nanotubes can be precisely controlled by simply altering the number of ALD cycles. TiO_2 and ZnO nanonetworks demonstrated superior performance compared to the unstructured TiO_2 and ZnO substrates in photocatalytic activity because of the enhanced specific surface area of the photocatalysts with nanostructured morphology. Importantly, immobilization of the photocatalysts on a solid support enabled recycling of the material, which can dramatically reduce the treatment cost and prevent secondary contamination of the water sources with inorganic materials. Furthermore, we discovered that there is an optimal wall thickness for gaining photocatalytic advantage through nanostructuring for both TiO_2 and ZnO. This optimum nanotube wall thickness was found to be around ~ 8 nm for both TiO_2 and ZnO. These results demonstrate significant potential of using peptide-based organic templates to fabricate high-quality TiO_2 and ZnO nanostructures not only for photocatalysis, but for several applications where increased surface area plays a crucial role: chemical/gas sensing, dye synthesized solar-cells, etc. Further studies can be extended to other transition-metals and their compounds, such as oxides, nitrides, and sulfides. As a result of the rapid and convenient scaling of the peptide nanofibers into macro-size networks, new opportunities could be available for fabrication of a wider range of inorganic materials.

**Scanning Probe Microscopy Focus Topic
Room: Hall B - Session SP+AS+BI+NS-ThP**

Scanning Probe Microscopy Poster Session

Moderator: S. Allen, The University of Nottingham, UK,
A.P. Li, Oak Ridge National Laboratory

SP+AS+BI+NS-ThP1 Vision Sensing Based Drift Measurement and Compensation in Real Time for Atomic Force Microscope, Y. Wang, Beihang University, China, H. Wang, The Ohio State University, S. Bi, Beihang University, China

Atomic force microscope (AFM) is unique in its capability in measuring deformation and force in subnanometers and has been a crucial tool in nanoscale science and technology since its invention. However, mechanical

drift between AFM cantilevers and sample surfaces limits its applications, especially for some biological experiments which require long time measurement. In this study, the mechanical drift is obtained in real time by simultaneously measuring the z position of AFM cantilevers and sample surfaces through an off-focus image processing based vision sensing method. In this method, the z position of a micro bead is measured by processing the off-focus images of the bead with an optical microscope. To get the z position of an AFM cantilever, the cantilever is first fabricated with focused ion beam (FIB) and a micro bead is attached to the end of the cantilever. Another bead is placed on a transparent sample substrate. The z positions of the AFM cantilever and the sample surface can be simultaneously obtained through measuring the z position for the beads at end of the AFM cantilever and the sample surface, respectively. The mechanical drift between the cantilever and sample surface can be obtained and then compensated in real time.

SP+AS+BI+NS-ThP2 Rapid Near-Field Infrared Spectroscopy Using an External Cavity Quantum Cascade Laser. *I.M. Craig, M.S. Taubman, M.C. Phillips, A.S. Lea*, Pacific Northwest National Laboratory, *M.B. Raschke*, University of Colorado at Boulder

Scattering scanning near-field optical microscopy (s -SNOM) is an apertureless superfocusing technique that uses the antenna properties of a conducting atomic force microscope (AFM) tip to achieve infrared spatial resolution below the diffraction limit. The instrument can be used either in imaging mode, where a fixed wavelength light source is tuned to a molecular resonance and the AFM raster scans an image, or in spectroscopy mode where the AFM is held stationary over a feature of interest and the light frequency is varied to obtain a spectrum. In either case, a strong, stable, coherent infrared source is required. Here we demonstrate the integration of a broadly tunable external cavity quantum cascade laser (ECQCL) into a s -SNOM and use it to obtain infrared spectra of microcrystals adsorbed onto gold substrates.

Residues of explosive compounds PETN, RDX, and tetryl were deposited onto gold substrates. s -SNOM experiments were performed in the 1260–1400 cm^{-1} tuning range of the ECQCL, corresponding to the NO_2 vibrational fingerprint region. Chemical imaging with fixed wavelength tuned to a molecular resonance allows mapping of species distributions a spatial resolution of 25 nm. Vibrational infrared spectra are then collected on individual chemical domains with a collection area of 500 nm^2 . Acquisition times of less than 6 min with SNR of >50 and 0.2 cm^{-1} spectral resolution are possible. Spectra are compared to ensemble averaged far-field infrared reflection-absorption spectroscopy (IRRAS) results.

SP+AS+BI+NS-ThP3 Ferritin-based Magnetic Force Microscopic Probe with Very High Resolution. *N. Chung*, Korea Research Institute of Standards and Science, Republic of Korea, *D.H. Kim, J.W. Park*, Pohang University of Science and Technology, Republic of Korea

A single-molecule ferritin picking up process was realized with the use of AFM, which was enhanced by employing controlled dendron surface chemistry. The approach enabled the placement of a single ferritin protein molecule at the very end of an AFM tip. When used for magnetic force microscopy (MFM) imaging, the tips were able to detect magnetic interactions of approximately 10 nm sized magnetic nanoparticles. The single ferritin tip also showed the characteristics of a “multifunctional” MFM probe that can sense the magnetic force from magnetic materials as well as detect the biomolecular interaction force with DNAs on the surface. The multifunctional tip enabled us not only to investigate the specific molecular interaction but also to image the magnetic interaction between the probe and the substrate, in addition to allowing the common capability of topographic imaging. Because the protein engineering of ferritin and the supporting coordination and conjugation chemistry are well-established, we envisage that it would be straightforward to extend this approach to the development of various single magnetic particle MFM probes of different compositions and sizes.

Thin Film

Room: Hall B - Session TF-ThP

Thin Films Poster Session

TF-ThP1 Enhancement of Structural, Optical and Electrical Properties through Post-Annealing of N-doped ZnO Thin Films Grown by Reactive Magnetron RF-Sputtering. *L.A. Hernández-Hernández*, ESFM-IPN, Mexico, *A. Hernández-Hernández*, CINVESTAV-IPN, Mexico, *F. De Moure-Flores*, UAQ, Mexico, *J.S. Arias-Cerón*, CINVESTAV-IPN, Mexico, *J.G. Quiñones-Galván*, ININ, Mexico, *J. Aguilar-Hernández*, *G. Contreras-Puente*, ESFM-IPN, Mexico, *M. Meléndez-Lira*, CINVESTAV-IPN, Mexico

Nitrogen doped zinc oxide thin films were grown on glass and silicon substrates by reactive magnetron RF sputtering of zinc in a N_2O -Ar atmosphere, post-annealing treatment of samples was made in a nitrogen reactive atmosphere. We report a comparative study of as-grown and post-annealing treatment of N-doped ZnO thin films properties carried out by structural, optical, electrical and spectroscopic techniques. The characterization measurements allow us to confirm the improvement of crystalline quality, a higher incorporation of N, and the apparition of luminescence emission at room temperature and photoresponse in the visible range due to the post-annealing treatment of the samples.

† : partially funded by CONACyT-Mexico.

TF-ThP2 Fabrication of Sub-micron Structure by Thermal Lithography Technology with GSSO Thin Films. *C.M. Chang*, National Taiwan University, Taiwan, Republic of China, *D. Chiang, M.H. Shiao, P.L. Chen, M.J. Huang*, National Applied Research Laboratories, Taiwan, Republic of China, *W.J. Hsueh*, National Taiwan University, Taiwan, Republic of China

In this study, sub-micron structures of hole and line patterns on 4-inch silicon wafer were fabricated by thermal lithography technique using the wavelength of 405 nm laser. Fixed thickness of 80 nm of Quaternary Materials of Ge-Sb-Sn-O (GSSO) thin films were deposited on silicon wafer and glass substrate by magnetron sputter deposition system. The oxygen flow rate ranged from 0 SCCM to 15 SCCM of the sputter deposition process under working pressures of 10 mTorr were studied on the GSSO thin film optical properties of transmittance (T), reflectance (R), absorption (A). Besides, the extinction coefficient (k) of GSSO thin film was controlled between 0.35-1. Furthermore the hole and line structures were made on the GSSO surface with two different laser power ranges of 0.08 mW - 0.3 mW and 0.44mW - 0.88 mW, respectively. The silicon wafer substrate was immersed in Tetramethyl ammonium hydroxide ($\text{N}(\text{CH}_3)_4\text{OH}$) solution of 2.38 wt% for 30 seconds.

From the experimental results, it can be found that the depth and sidewall shape of the structure were varied with the extinction coefficient (k) of GSSO thin film and the laser power. The diameter of hole and line width of line structures were varied proportional to the extinction coefficient of GSSO thin film when the laser power was fixed at 0.18 mW and 0.66 mW, respectively. When the oxygen flow rate of 0 SCCM, the laser lithography process is unable to produce a pattern on the GSSO thin film surface since it resulted a pure metal thin film. When the oxygen flow rate increases, and the extinction coefficient GSSO thin film is decrease. When the extinction coefficient of GSSO thin film was fixed at 0.4, the V shape was presented in the hole and line structures when the laser powers were less than 0.13 mW and 0.44 mW, respectively. Besides, the structure presented as U shape when the laser power was higher than 0.18 mW for hole structure and 0.66 mW for line structure which the extinction coefficient of GSSO thin film was greater than 0.65. Finally the diameter and line width of two structures can be controlled between 350-700 nm, and the sidewall angle greater than 80° can be produced under suitable processing parameters.

TF-ThP4 Titanium-Aluminum Oxynitride (TAON) as New Gate Dielectric for 3D MOS Technology. *J. Miyoshi, J.A. Diniz, A.R. da Silva, I. Doi*, Universidade Estadual de Campinas, Brazil

The next generation of CMOS technology requires gate insulators with dielectric constant higher than 40, resulting in an Equivalent Oxide Thickness (EOT) thinner than 1 nm. Titanium-aluminum oxynitride (TAON) has been used as high-k gate dielectric for planar MOS devices. Thus, planar MOS capacitor and transistors were fabricated and characterized by TEM and EDS analyses, and C-V and I-V measurements, and the results have confirmed that these films can be used as gate dielectric for planar MOS technology. But, for future 3D device technology application, these films have been not investigated. So, 3D MOS capacitors with Al/TAON/Si (as control sample) and TiN/TAON/Si gate structures for 3D technology were fabricated. Al/TAON and TiN/TAON layers on 3D gate region must present conformal coverage, which is mandatory

requirement for 3D transistors, such as FinFET. In this work, Titanium-aluminum oxynitride (TAON) were fabricated by 0.75 Titanium (Ti) and 0.25 Aluminum (Al) subsequently deposition by vacuum e-beam evaporation of 99.9999% of Ti and Al metals, respectively, without any substrate heating. The evaporation pressure was 3.10^{-8} Torr, and the Ti and Al evaporation rates were of $0.1 \text{ nm}\cdot\text{s}^{-1}$. ECR plasma oxynitridation process was carried out at different $\text{O}_2/\text{N}_2/\text{Ar}$ flow ratios (3:10:20 sccm). Physical characteristics of this MoS₂ structure by ellipsometry and x-ray photoelectron spectroscopy (XPS) were performed to confirm the physical film thickness and define the composition of the film. C-V curves of these structures were performed at 1 MHz.

TF-ThP5 Influence of Microstructure, Surface Morphology and Optical Properties of the WO₃C Film by DC Reactive Magnetron Sputtering. *C.-T. Lee, D. Chiang, C.-Y. Su*, ITRC, NARL, Taiwan, Republic of China, *M.-C. Liu, C.-C. Jaing*, Minghsin University of Science and Technology, Taiwan, Republic of China

The WO₃C film was deposited on an ITO glass substrate at room temperature by DC reactive magnetron sputtering with W and C target. Effects of carbon concentration on the microstructure, surface morphology and optical properties of WO₃C film were investigated by X-ray diffraction, field emission scanning electron microscopy, atomic force microscopy and spectrometer. X-ray diffraction analysis reveals that all of the as-deposited films are amorphous. The surface roughness of the WO₃C film was increased with increasing carbon content from 0.73 nm to 1.29 nm. The average transmittance of coloured WO₃C film in the visible region (400-700 nm) was decreased with increased carbon content from 0 at.% to 9.35 at%. The optimum average transmittance of about 76.2% and 7.9% during bleaching and coloration states in the visible light region (400-700 nm) with +3V and -3V applied.

TF-ThP6 Fabrication of Al₂O₃ Gate pH-ISFET for Continuous Monitoring. *S.K. Lee, W.H. Son, S.H. Lee, Y.S. Moon, T.Y. Lee, S.Y. Choi*, Kyungpook National University, Republic of Korea

The sensing membrane of the pH-ion-sensitive field-effect transistor (pH-ISFET) is a very important element in order to measure continuous monitoring of pH in systems. The Al₂O₃ film among the sensing membrane materials is well-known as a chemically stable dielectric material that has low leakage current, however, it is classified to be poor sensing materials because of their low sensitivity than other sensing membrane materials. The atomic layer deposition (ALD) method meets the good characteristics the Al₂O₃ film, because it is possible for deposition of high density, low impurity level, uniform thickness, and low pinhole density. Also, the pH-sensitivity of the pH-ISFET can be improved by thermal annealing at high-temperatures in O₂ ambient after ALD deposition. In this paper, to apply continuous monitoring, the pH-ISFET with the Al₂O₃ sensing membrane deposited by ALD was fabricated, and its characteristics were investigated.

The n-channel field effect transistor (FET) designed for using the pH-ISFET was fabricated by the CMOS-processing technology. The thermal temperature annealing process of the Al₂O₃ film was carried out using a conventional furnace system in O₂ ambient for 40 min at 500, 600, 700 and 800 °C. All the measurements of pH-ISFET were carried out in a standard pH solution. The conventional reference of Ag/AgCl and liquid-junction filled with 3 M KCl electrode was used to establish the pH solution potential. The null balance circuit, which maintained constant the drain current and the drain voltage, was used to measure continuous monitoring. In the operation of pH-ISFET sensor, the change of electrochemical potential between the surface of sensing membrane and a reference electrode is generated by the establishment potential with chemical response in the pH solution. In order to ensure the shift of V_T of pH-ISFET with the Al₂O₃ sensing membrane, the I_{DS}-V_{GS} curves were measured in pH 4, pH 7 and pH 10 at a constant 600 °C, these are shown in Fig. 1. From measured results, we confirmed that the V_T of the pH-ISFET was shifted from the pH values which changed the surface potential on the Al₂O₃ sensing membrane. In accordance with experiment results, we measured the shift of the V_T on the pH-ISFETs with Al₂O₃ sensing membrane with respect to the difference of thermal annealing temperatures. Those results are shown in Fig. 2. Through the results of our experiments, we ascertained that the sensitivity of the pH-ISFETs with Al₂O₃ sensing membranes annealed at 500, 600, 700 and, 800 °C are about 56.7, 55.2, 50.3, and 33 mV/pH, respectively.

TF-ThP8 Effect of Tungsten Incorporation on the Structure and Optical Properties of β-Gallium Oxide Thin Films. *E.J. Rubio, C.V. Ramana*, The University of Texas at El Paso

Gallium oxide (Ga₂O₃) finds attractive applications in luminescent phosphors, hightemperature sensors, antireflection coatings, and solar cells. With a band gap of ~5eV, Ga₂O₃ has been recognized as a deep ultraviolet transparent conducting oxide, which makes the material a potential candidate for transparent electrode applications in UV optoelectronics. The

present work was performed to study the effect of tungsten (W) incorporation on the crystal structure, chemical composition, surface morphology and optical properties of Ga₂O₃ films. Films were grown by co-sputtering keeping the sputtering power to Ga₂O₃-target constant (100 W) while varying the sputtering-power (PW) to W-target in a wide range (50-100 W) in order to vary W-concentration in the films. The samples were deposited on to Si(100) and quartz substrates in a growth temperature range of 500-800 °C. It is seen that increasing W concentration alters the electronic structure of Ga₂O₃ while the crystal structure of β-Ga₂O₃ phase is retained. Spectrophotometry analysis indicates that the W-doped Ga₂O₃ films are single phase and transparent. Due to substitutional nature, W ions incorporated form donor levels and, thus, allowing band gap reduction and conductivity enhancement of Ga₂O₃. The band gap showed a red-shift from ~5 eV to ~4 eV with highest concentration of W-incorporation into β-Ga₂O₃ films. The structure-property relationship as a function of W-concentration in Ga₂O₃ films is established.

TF-ThP9 Effect of Growth Temperature and Post-Deposition Annealing on the Structure and Optical Properties of Yttrium Oxide Thin Films. *C.V. Ramana, L. Sanchez*, University of Texas at El Paso, *V. Atuchin, A.V. Rzhavov* Institute of Semiconductor Physics, Russian Federation, *V.N. Kruchinin*, Institute of Semiconductor Physics, Russian Federation, *I.P. Prosvirin*, Boreskov Institute of Catalysis, Russian Federation

Yttrium oxide (Y₂O₃) has received significant attention in recent years in view of its possible integration into a wide range of scientific and technological applications. Y₂O₃ films exhibit excellent electronic properties such as transparency over a broad spectral range (0.2–8 μm), high dielectric constant (~14–18), high refractive index (~2), large band gap (~5.8 eV), low absorption (from near-UV to IR), and superior electrical break-down strength (>3 MV/cm). These properties make Y₂O₃ films interesting for various electrical, optical and electro-optic devices. Therefore, controlled growth and manipulation of microstructure, particularly at the nanoscale dimensions, has important implications for the design and applications of Y₂O₃ films. The present work was performed on the growth and optical characterization of nanocrystalline Y₂O₃ films made by magnetron sputter-deposition. The Y₂O₃ thin films were grown onto Si(100) substrates using reactive magnetron sputter-deposition at temperatures (T_s) ranging from room temperature (RT) to 500 °C. In addition, post-depositon annealing (T_a) in air was also performed in the temperature range of 500-1000 °C. The effect of T_s and T_a on the microstructure and optical properties of Y₂O₃ films were investigated. The structural studies employing X-ray diffraction (XRD) and reflection high-energy electron diffraction (RHEED) indicate that the films grown at room temperature (RT) are amorphous while the films grown at T_s=300-500 °C are nanocrystalline. Depth profiling has been produced with Ar⁺ ion bombardment and XPS analysis. Spectroscopic ellipsometry measurements indicate that the size-effects and ultra-microstructure were significant on the dispersive optical constants. A significant enhancement in the index of refraction (n) (from 2.03 to 2.25) is observed in well-defined Y₂O₃ nanocrystalline films compared to that of amorphous Y₂O₃. The changes in the optical constants were explained on the basis of increased packing density and crystallinity of the films with increasing T_s. The optical properties of Y₂O₃ films were also found to be affected upon annealing due to structural transformation and/or interfacial compound formation.

TF-ThP10 Fabrication and Electrical Properties of Nanocrystalline Yttrium-Doped Hafnium Oxide Thin Film Capacitors. *A. Kongu*, University of Texas at El Paso, *S. McPeak, S. Kotru*, The University of Alabama, *C.V. Ramana*, University of Texas at El Paso

Hafnium oxide (HfO₂) has emerged as the most promising high-k dielectric for Metal-Oxide-Semiconductor (MOS) devices and has been highlighted as the most suitable dielectric materials to replace silicon oxide because of its comprehensive performance. In the present research, yttrium-doped HfO₂ (YDH) thin films were fabricated using RF magnetron sputter deposition onto Si (100) with a variable thickness. Electrical properties such as capacitance-voltage (C-V), current-voltage (I-V), leakage and breakdown characteristics of YDH films were studied. YDH films that were relatively thin (<1500 Å) crystallized in monoclinic phase while thick films crystallized in cubic phase. The band gap (E_g) of the films was calculated from the optical measurements using linear regression. The band gap was found to be ~5.60 eV for monoclinic YDH films while it is ~6.05 eV for cubic. Cross-sectional SEM and Filmetrics were used to measure the thickness of the films. The thicknesses of the films range from 700 Å to 7500 Å. Frequency dependence of the electrical resistivity (ρ_{ac}) and the total conductivity of the films were measured. Resistivity decreased (by three orders of magnitude) with increasing frequency from 100 Hz to 1 MHz, attributed due to the hopping mechanism in YDH films. Whereas, while ρ_{ac}~1 Ω-m at low frequencies (100 Hz), it decreased to ~E-4 Ω-cm at higher frequencies (1 MHz). Aluminum electrodes were deposited to

fabricate a thin film capacitor with YDH layer as dielectric film thereby employing Al–YDH–Si capacitor structure. The results indicate that the capacitance of the films decrease with increasing film thickness. A detailed analysis of the electrical characteristics of YDH films is presented.

TF-ThP11 Electrochemical Corrosion of Thin Ferromagnetic Fe-N Films in Neutral Solution, S.S. Maklakov, S.A. Maklakov, A.S. Naboko, I.A. Ryzhikov, Institute for Theoretical and Applied Electromagnetics, Russian Federation

Energy and information transfer is an actual task in biosensors. Thin ferromagnetic films are widely used as antennas and magnetic field sensors^[1]. The study of corrosion behavior in neutral solutions serves fundamental interest and practical applications.

Corrosion behavior is reported for Fe-N films ($h = 150$ and 300 nm) deposited onto polymer (*Fe-PET*) and glass (*Fe-glass*) substrates via DC magnetron sputtering (90 % Ar - 10 % N₂ gas mixture). Polarization curves are obtained in 0.1 M Na₂SO₄ under ongoing Ar bubbling.

Film's surface is covered with an oxide layer. *Fe-PET* films show lesser free surface energy in comparison with *Fe-glass* films (H₂O wetting angle is $\theta = 77 \pm 5^\circ$ and $\theta = 87 \pm 2^\circ$, which gives adhesion energy $W_a = 89.1 \cdot 10^{-3}$ J/m² and $W_a = 76.6 \cdot 10^{-3}$ J/m², respectively). Initial corrosion stage for films on the rigid substrate goes slower than for the polymer substrate: corrosion currents for oxide dissolution and stationary potentials are $i_{corr} = 5 \cdot 10^{-7}$ A/cm², and $E_0 = -0.050$ V (vs SHE) for *Fe-glass*; $i_{corr} = 7 \cdot 10^{-6}$ A/cm², and $E_0 = -0.465$ V for *Fe-PET*.

Film's thickness influences corrosion rate, but rigidity of substrate does not. Increase in thickness results in increase in corrosion current: $i_{corr} = 1 \cdot 10^{-5}$ A/cm² for $h = 150$ nm, and $i_{corr} = 8 \cdot 10^{-5}$ A/cm² for $h = 300$ nm. Stationary, passivation and repassivation potentials for Fe-N films after oxide layer removal are $E_0 = -0.575$ V, $E_{pass} = -0.500$ V, and $E_{repass} = +1.350$ V. In the case of $h = 150$ nm, films show localized corrosion. In a passive state, *Fe-glass* films are more stable than *Fe-PET* films.

The phenomena observed are probably the results of a mechanical stresses within metal film^[2]. In the case of flexible and plastic substrate these stresses are partially decreased due to sample bend. The rigid substrate produces mechanical stress excess which increases oxide layer thickness and increase initial corrosion durability.

The results reported are of practical interest for thin film devices.

Literature

1. S.S. Maklakov, S.A. Maklakov, I.A. Ryzhikov, K.N. Rozanov, A.V. Osipov, A.S. Naboko, V.A. Amelichev, S.V. Kulikov. The structure and microwave permeability of thin cobalt films. // *Nanotechnologies in Russia*. 7 (2012) 255-261
2. A.V. Agaponova, I.V. Bykov, S.A. Maklakov, S.S. Maklakov, A.A. Pukhov, I.A. Ryzhikov, M.V. Sedova, E.E. Shalygina, I.T. Yakubov. Visualization of the domain structure of ferromagnetic films using the magnetochemical effect. // *Physics of the Solid State*. 53 (2011) 1013-1016

TF-ThP12 Chemical Bonding in Silicon Nitride Films Deposited with SiH₄/N₂ by Very High Frequency Plasma-Enhanced Chemical Vapor Deposition, S. Kobayashi, Tokyo Polytechnic University, Japan

Hydrogenated amorphous silicon nitride (a-SiN_x:H) films are useful for microelectronic and optoelectronic applications such as passivation layers and antireflection layers. These films are usually deposited by plasma-enhanced chemical vapor deposition (PECVD) using a SiH₄/NH₃ gas mixture. However, in order to obtain low-hydrogen-content a-SiN_x:H films at a low substrate temperature for passivation and/or barrier applications, it is advantageous to use N₂ instead of NH₃ as the nitrogen source. I obtained transparent a-SiN_x:H films with an optical bandgap about 5.0 eV by very high frequency (VHF: 150 MHz)-PECVD using a SiH₄/N₂ gas mixture in a conventional diode-type reactor at 50 °C. The films were examined with a Fourier transform infrared spectrophotometer (FTIR). The Si-N stretching frequency increases upon increasing VHF power. This shift is induced by the H atom, which is more electronegative than Si, back-bonded to the N atom of the Si-N bonds. Films were stored in an FTIR system containing dry air for 3 months. The changes in local structure in the films during storage deduced from FTIR spectra will be discussed.

TF-ThP13 Optical and Structural Properties of GaN Thin Films as Grown by Closed-Space Vapor Transport, L.A. Hernández-Hernández, J. Aguilar-Hernández, F. De Moure-Flores, A. Escamilla-Esquível, ESFM-IPN, Mexico, M. López-López, CINVESTAV-IPN, Mexico, G. Santana-Rodríguez, IIM-UNAM, Mexico, M. Meléndez-Lira, A. Hernández-Hernández, CINVESTAV-IPN, Mexico, J.G. Quiñones-Galván, ININ, Mexico, O. De Melo-Pereira, UH, Cuba, G. Contreras-Puente, ESFM-IPN, Mexico

We report in this work the structural and optical properties of GaN films grown by the Closed-Space Vapor Transport (CSVT) technique. The samples were deposited on quartz substrates using GaN powder as the starting material source, which were contained inside a semi-hermetic cell made of graphite in a low pressure atmosphere. We present the characterization carried out by X-Ray Diffraction (XRD), Scanning Electron Microscopy (SEM), Energy Dispersive Spectroscopy (EDS) and Photoluminescence (PL) measurements. XRD results exhibit the growth of low quality hexagonal GaN, while SEM image shows GaN clusters over the entire substrates surface. Concerning EDS measurements they indicated that non-stoichiometric GaN films with non-intentional carbon (C) impurification were obtained. Finally, PL measurements under UV excitation (He:Cd laser $\lambda=325$ nm), present PL emission at room temperature. We observed the presence of different emission bands in the visible region: the yellow (YL) at 2.20 eV and the blue (BL) at 2.7-3.0 eV bands are related to undoped and C-doped GaN, while, the green (GL-2) band at 2.36 eV is related to Ga-rich GaN.

† : partially funded by CONACyT-SENER, ICyTDF and DGAPA-UNAM PAPIIT.

TF-ThP15 Patterning of Nonwoven Fiber Mats by Atomic Layer Deposition, W.J. Sweet, C.J. Oldham, G.N. Parsons, North Carolina State University

The ability to pattern substrates is an integral part of many industries, from integrated circuit manufacturing to newspaper printing. To apply features for flexible electronics, techniques such as screen printing, inkjet printing, or shadow masking are available. Alternatively, features can be created by a negative etch if the patterned areas can be sufficiently protected. However, these methods do not offer the ability to use patterning to produce conformally coated 3D structures on complex substrates. Nonwoven fiber mats are an example of a complex substrate, which offers highly tunable properties such as fiber chemistry, diameter and geometry, all of which can be produced in high volumes at very low cost.

In this work, we demonstrate a new method using Atomic Layer Deposition to selectively pattern features on nonwoven fiber mats, allowing for the creation of conformally coated 3D patterns. By compressing the sample between two patterning plates we are able to restrict precursor diffusion in the compressed region, but allow ALD to occur in the exposed portion of the sample, imparting the pattern on the substrate. By stacking multiple layers of substrate in the patterning plates, the 3D pattern that is created can easily be seen by deconstructing the layers or by cutting the sample to view a cross section of the feature. The impact of substrate chemistry (polypropylene, nylon, cotton) and structure (woven vs. nonwoven) as well as fiber diameter (microfibers vs. nanofibers) is examined. In addition the impact of deposition conditions (temperature, precursor exposure) and coating chemistry (Al₂O₃ and ZnO) is investigated. This technique will enable new applications for ALD coatings on flexible substrates; applications in gas and liquid sensors as well as flexible electronics will be discussed.

TF-ThP16 Low Temperature Plasma-assisted Atomic Layer Deposition of Copper Studied using In Situ Reflection-Adsorption Infrared Spectroscopy, S. Agarwal, R.P. Chaukulkar, Colorado School of Mines, N.F.W. Thissen, Eindhoven University of Technology, Netherlands, V.R. Rai, Colorado School of Mines

Cu interconnects in modern integrated circuits are fabricated using an electroplating process, which requires an ultrathin, conformal, and continuous Cu seed layer. The resulting interconnect performance depends significantly on the quality of this seed layer. Atomic layer deposition (ALD) is a thin film growth technique, which is widely used to deposit highly conformal, high-purity films with digital control over the thickness. This technique has been successfully implemented to deposit a variety of metals. To enable new deposition chemistries, and to achieve better control over existing ones, it is important to understand the surface reaction processes that occur during film growth. *In situ* infrared spectroscopy has been shown to be an excellent technique to study surface reactions in an ALD processing environment. However, due to free electron absorption in metals, traditional infrared techniques based on transmission and internal reflection cannot be used to study metal ALD processes beyond the very initial nucleation stage. In this study, we have designed and implemented an *in situ* reflection-absorption infrared spectroscopy (RAIRS) setup to study

the surface reactions during the deposition of Cu from Cu(hfac)₂ and a remote H₂ plasma at a substrate temperature of 80 °C. We specifically report on the surface reactive sites, and the mechanism for Cu(hfac)₂ chemisorption on an oxide (Al₂O₃) surface. Unlike previous studies, we propose a detailed surface reaction mechanism, which does not require the presence of hydroxyl groups on the oxide surface. Lastly, using RAIRS, we also report results with the use of reducing agents other than atomic H, and report on their efficacy.

TF-ThP17 Mo/Si Multilayer Film with 4 nm Bandwidth for EUV Mirrors by RF Magnetron Sputtering, C.-T. Lee, Y.-C. Yeh, W.-H. Cho, H.-P. Chen, P.-K. Chiu, C.-N. Hsiao, ITRC, NARL, Taiwan, Republic of China, S.W. Lin, P.-J. Wu, National Synchrotron Radiation Research Center
Most applications of Mo/Si bilayers mirrors in extreme-ultraviolet lithography (EUVL) require a high normal-incidence reflectivity. This work represents our effort to design and prepare the Mo/Si multilayer film with 4 nm bandwidth at 13.5 nm wavelength. The Mo/Si multilayer film was deposited on a Si substrate at room temperature by RF magnetron sputtering with Ar gas. The optimum simulation reveals that normal-incidence average reflectivity of Mo/Si multilayer film with 4 nm bandwidth at 13.5 nm was 14%. Effects of RF power and working pressure on the microstructure, surface morphology and EUV reflectivity of Mo/Si multilayer film were investigated by X-ray diffraction, atomic force microscopy and high resolution transmission electron microscopy (HRTEM). It was found that the surface roughness of Mo/Si multilayer film was significantly improved under 0.2 nm at low RF power and work pressure. In addition, HRTEM lattice fringe revealed that Mo film was polycrystalline and Si film was amorphous. The resulting EUV bandwidth of this Mo/Si multilayer film is 4 nm ($\lambda=13.5$ nm, $\alpha=15^\circ$).

TF-ThP18 Thin-Film and Crystalline Properties of Silicon Deposited Using a Novel, Low-Damage, Surface Wave Plasma Source, P.S. Zonooz, J. Peck, D. Currelli, D.N. Ruzic, University of Illinois at Urbana Champaign, M. Reilly, B. Jurczyk, R. Stubbers, Starfire Industries, LLC
A novel surface wave plasma device has been developed by Starfire Industries, LLC to deposit amorphous and micro-crystalline silicon at high deposition rates (>2 nm/s) and low defect densities for large-area processing. Testing of this device has been carried out by the Center for Plasma Material Interaction at the University Illinois at Urbana-Champaign. Operating in the microwave frequency range, the surface wave generates a high density ($>10^{12}$ cm⁻³), low temperature (<2 eV) plasma with excellent uniformity over the excitation area. Using SiH₄-H₂ as the gas, the surface wave plasma has demonstrated deposition along a continuum between purely amorphous and highly crystalline silicon films. The film phase and quality are controlled by modifying process parameters e.g., RF power, dilution ratio, substrate temperature, substrate-plasma gap distance and gas flow rate. The films were analyzed using Raman Spectroscopy and Microscopy, SEM and X-Ray Diffraction. Using these diagnostics, the parameter space is explored to demonstrate control over deposited silicon phase applicable for photovoltaics. Trends show the relationship between substrate temperature, power density and flow rate with respect to film crystallinity and electrical properties.

TF-ThP19 Ar⁺ Ion Sputter Processing of Monolayer MoS₂ Films, Q. Ma, P.M. Odenthal, J. Mann, C.S. Wang, Y. Zhu, University of California, Riverside, D. Sun, Columbia University, T. Chen, K. Yamaguchi, T. Tran, M. Wurch, J.L. McKinley, M. Isarraraz, K. Magnone, University of California, Riverside, T.F. Heinz, Columbia University, R. Kawakami, L. Bartels, University of California, Riverside
Low-energy Argon sputtering can selectively reduce the Sulfur contents of single-layer MoS₂ films while not removing Molybdenum, as shown by XPS analysis. Even after removing ¼ of the total S, the Mo 3d states' XPS features remain virtually unchanged and sharp, suggesting that the Mo oxidation states are unchanged and that widespread reconstruction of the film does not take place. Concurrent measurement of the PL yield shows a rapid decay of the PL signal independent of the substrate temperature between 175 and 300K. A basic model describes the data near quantitatively and suggests very short exciton diffusion lengths.

TF-ThP20 Atomically Thin Molybdenum Sulphoselenide Films with Tunable Band Gaps, J. Mann, E. Preciado, V. Klee, K. Yamaguchi, S. Bobek, M. Isarraraz, D. Barroso, A. Nguyen, E. Bonilla, S. Naghibi, M. Wurch, L. Bartels, University of California, Riverside
We demonstrate the growth of atomically thin (mono to few layer) alloys of Molybdenum Sulphoselenide films with the use of organic sulfur and organic selenium precursors. Changing the ratio of these precursors allows us to tune the value of the band gap continuously between 1.87 eV and 1.54 eV, the band gaps of MoS₂ and MoSe₂, respectively. Our growth technique yields mm scale films on SiO₂/Si (300 nm oxide layer) substrates. The films

are characterized with Raman spectroscopy, X-ray photoelectron spectroscopy, photoluminescence measurements, and atomic force microscopy

TF-ThP21 Optimization of Diamond-Like Carbon (DLC) Films as Anti-Reflection Coatings, R. Takahashi, T. Akutsu, National Astronomical Observatory of Japan, Y. Saito, High Energy Accelerator Research Organization, Japan, N. Sakamoto, ICS Corporation, Japan
Laser interferometer gravitational wave telescopes need baffles to avoid stray light in UHV. The surface of baffles should be treated with anti-reflection coatings without scattering light and increasing outgassing. Diamond-like Carbon (DLC) films are suitable for this aim. The reflectivity of DLC films on SS304 was less than 1% at minimum for 1064nm in wavelength. We could optimize the thickness of the film so that the reflectivity can be less than 20% for any polarization, wide incident angle, and large inhomogeneity of thickness.

TF-ThP22 Fabrication of Distributed C60 Molecules Reinforced Al Nano-composite Thin Films and Their Mechanical Properties, A.M. Matsumuro, Aichi Institute of Technology, Japan
Fabrication of distributed C60 molecules reinforced Al nano-composite thin films was carried out on Si(100) wafer substrate using a conventional vacuum evaporation method. The evaporation sources were separated between C60 molecule powder and Al powder in order to prevent from the reaction between different original powders. The concentration of C60 molecule powder was changed ranging from 0.1 to 40 wt%. The structure analyses of all nano-composite films prepared by X-ray diffraction method showed aluminum crystalline structure and FT-IR analysis clarified the existence of C60 molecules contained in Al thin films. Cross-section TEM observations were carried out to evaluate the structure of the composite thin film. This result showed the uniform microstructure inside the composite films. From above results the uniform distribution of C60 molecules was obtained in Al matrix film. Nano-indentation studies showed that the hardness of Al-1wt %C60 increased up to 3 times larger than that of Al film. The present result clearly indicates that high-strength nanocomposite thin metallic films reinforced by distributing C60 molecules should be developed.

TF-ThP23 Plasma Polymerization of the Inner Wall of a Long, Narrow Tube under Atmospheric Pressure, T.H. Lin, Y.J. Yang, C.C. Wang, C.C. Hsu, National Taiwan University, Taiwan, Republic of China
Coating in the lumen surface of long and thin tubes has been highly desired yet challenging. In this work, generation of stable plasmas in a long thin tube and the use of such plasmas to perform plasma polymerization in the lumen surface of the tube are presented. By inserting a specially designed long thin electrode into the tube, stable Ar or He discharges can be sustained in tubes with the inner diameter down to 0.26 mm and the length up to 1 m under atmospheric pressure using an AC power source. This system is then used to perform plasma polymerization in the lumen surface of a tube 1 mm in inner diameter. When allylamine is used as the precursor, carried by Ar gas flow, films containing NH₂ can be obtained through plasma polymerization. The film composition is examined by ATR-FTIR. The spectra show the absorption at 3274 cm⁻¹, which is attributed to NH₂, and the absorption at 1658cm⁻¹, contributed by C=N, C=C, or N-H. Further analyses using SEM, XPS, and AFM show that smooth film with NH₂-bonded surface can be obtained. Such an approach offers a promising approach in various fields such as biomaterial application.

TF-ThP24 Vapor Phase Polymerization onto Liquid Substrates, L.C. Bradley, M. Gupta, University of Southern California
We will present our work demonstrating polymer deposition onto ionic liquid (IL) substrates. ILs have recently attracted significant interest as an environmentally-friendly alternative to traditional volatile organic solvents because ILs are non-volatile, non-flammable, and can be easily recycled. The low volatility of ILs allows for their use in vacuum processing. The immobilization and encapsulation of ILs is important to implementing ILs in commercial processes to bypass issues caused by their high viscosity. We will demonstrate the encapsulation of IL droplets in polymer shells and the integration of ILs into layered polymer films. Our encapsulation method uses a liquid marble technique to deposit a continuous polymer shell on the entire area of IL droplets. Polymer shells composed of 1H,1H,2H,2H-perfluorodecyl acrylate crosslinked with ethylene glycol diacrylate (P(PFDA-co-EGDA)) were found to be stronger than the respective homopolymers. We also studied the immobilization of IL in layered polymer films made by sequential and simultaneous depositions of soluble and insoluble monomers. We found that the polymerization of soluble monomers within the bulk IL leads to the integration of the IL into the polymer films and that the order in which the monomers are introduced into

our polymerization process significantly affects the structure of the layered films.

TF-ThP25 Performance of WSe₂ Thin Film Photovoltaic Devices as Determined by Numerical Modeling. *H. Kyureghian, J.D. Banninga, N.J. Ianno, R.J. Soukup*, University of Nebraska-Lincoln

Recently the promise of thin film solar cells has begun to be realized on a commercial scale with the introduction of CdTe and CuInGaSe modules in the market place. Although these materials yield cost-effective modules from a dollar/watt aspect they present environmental and possibly long term availability issues. In view of this a great deal of interest is being focused on environmentally safe earth abundant materials including iron sulfide (FeS₂) in the pyrite phase, and tin sulfide (SnS). While promising, iron sulfide is presenting serious material science challenges, while work on SnS is just beginning. In addition the band gaps of these materials are less than the optimal value of 1.36 eV. Another excellent candidate for an earth abundant absorber material is WSe₂ which can be directly grown as a p-type semiconductor with a band gap near 1.4 eV. In view of this we have evaluated the performance of WSe₂ in photovoltaic devices by means of numerical modeling. The model is based on thin film material properties obtained from the literature as well as those measured in our laboratory. These results will be compared to those obtained for FeS₂ where it will be shown that WSe₂ has a significantly higher potential for yielding devices with efficiencies in the 20% range.

TF-ThP27 Passivation Effect of MPTMS Monolayer for Ag Thin Films. *M. Kawamura, T. Hirose, Y. Abe, KH. Kim*, Kitami Institute of Technology, Japan

Ag thin films with excellent physical properties have been used as electrode, optical reflector, and so on. It is necessary to prevent degradation of the Ag films in air or humid atmosphere. We pay attention to sub-nanometer thick layer of 3-mercaptopropyltrimethoxysilane (MPTMS), as a protective coating. If the MPTMS monolayer is formed at the surface of Ag thin films, a strong bond between them may bring an effective passivation of the Ag films.

Ag thin films (10nm) were deposited on clean glass substrates by vacuum evaporation. Then monolayer of MPTMS was formed over the Ag thin films by solution method. The samples were kept in a constant temperature and humidity chamber (40 degree celsius and 80 RH%) for a week. The electrical resistance, surface morphology, optical transmittance were measured before and after the test. Ag film without the monolayer was also examined for comparison.

The surface roughness (rms) of the Ag film modified with the monolayer was increased from 2.1 nm to 3.8 nm after the test. However, that of Ag film without the monolayer drastically increased from 3.7 nm to 12.4 nm. As a result, passivation effect of the MPTMS monolayer for Ag films was confirmed. By the measurement of electrical resistivity, it was found that increase in the resistivity after the test was very much suppressed in the Ag film with MPTMS monolayer. In addition, optical transmittance measurement showed that spectrum of Ag films with the monolayer did not change after the test. These results accord with film morphology change. Consequently, we found modification of Ag films with MPTMS monolayer can improve durability of the Ag films.

TF-ThP28 Photoluminescence Characterization of Polythiophene Doped with Metallophthalocyanines whose Central Metals Contain 3d, 4d and 5d Electrons. *H. Kobe, R. Sakamoto, H. Kato, S. Takemura, k. Shimada, T. Hiramatsu, K. Matsui*, Kanto Gakuin University, Japan

Conducting polymer polythiophene (PT) films doped with zinc phthalocyanine (ZnPc), tin phthalocyanine (SnPc) and lead phthalocyanine (PbPc) were synthesized and characterized by photoluminescence measurements (PL) and time-correlated single photon counting (TCSPC) measurements in order to obtain fundamental PL properties of various PT-phthalocyanine complexes prepared by different solvents. PT films were electrochemically synthesized on an indium tin oxide (ITO) substrate with a resistivity of 30 Ω / cm² in an electrochemical cell utilizing the voltage controlled method. Electrochemical polymerization was performed in acetonitrile containing 0.05 M thiophene monomer and 0.1 M of the supporting electrolyte (Et)₄NBF₄ in a N₂ atmosphere. The ITO substrate was used as a working electrode (anode) for polymerization. A platinum mesh and Ag/AgCl electrode were used as a counter and reference electrodes, respectively. Typically, 3.5 V versus the reference electrode was applied to the anode for 300 sec for the PT film synthesis. BF₄⁻ anions were doped in the as-grown films. Injection of PcMs into the PT films was performed by a diffusion method. PcMs molecules were diffused into the PT films by dipping as-grown PT films in phthalocyanine dissolved acetonitrile or toluene. Phthalocyanine was dissolved until it was saturated. The wavelength of PL emission peaks and lifetimes drastically changed with the used solvent in the doping process and the central metals. In the PL

measurement, in the case of ZnPc doped films, emission peaks were observed in both Soret and Q band regions using both solvents in the doping process. In the case of SnPc doped films, using acetonitrile in the process, the observed PL emission peaks were originated from Soret and Q bands whereas the PL emission peaks were assigned to only Q band-origin in the case of toluene used as a solvent. In the case of PbPc doped films, emission peaks were observed in only Soret band region using both acetonitrile and toluene. In the TCSPC measurements, the lifetime values ranged from several ten nsec to several hundred nsec. Calculated averaged lifetime value of each compound showed almost the same value among these three compounds. Typically, the averaged lifetime was around 190 nsec. However, ZnPc-doped PT acetonitrile-processed sample and SnPc-doped PT toluene-processed sample yielded a different lifetime profile which gave a short lifetime value. The lifetime depended not only on the central metals of the doped phthalocyanine but also on the solvent used in the doping process. This work was aided by MEXT-supported Program for the Strategic Research Foundation at Private Universities.

TF-ThP30 Chemical Composition on the Top of a Surface Characterized with the Evolution of Surface States. *D. Luh*, National Central University, Taiwan, Republic of China

Epitaxial growth continuously plays an indispensable role in both fundamental and applied research in nanotechnology. The detailed characterization of epitaxial growth provides essential knowledge to control the construction of nanostructures. A novel technique to characterize a surface will be demonstrated in this presentation. On monitoring the evolution of surface states with angle-resolved photoemission spectroscopy, not only the chemical properties associated with the surface states are explored, but also the chemical elements in the topmost layer of the nanostructures on which the surface states reside can be identified. The technique was applied to the epitaxial growth of Cu on Ag(111); our results indicate that the chemical element on top of the Cu islands on Ag(111) with the (9x9) reconstruction was not Cu but Ag.

TF-ThP34 Combinatorial ALD to Accelerate Integration of New Materials for Nanomanufacturing. *F. Greer, W. Zhu, E. Adhiprakasha, R. Lindulpaiboon, J. Watanabe, C. Lang*, Intermolecular, Inc.

New materials and new device architectures have created an increasing need for Atomic Layer Deposition (ALD) of nano-scale conformal films to be incorporated into the manufacturing process flow. The conformality of ALD films is required to form some of the functional layers in today's leading-edge planar IC devices, and in three-dimensional (3D) multi-gate CMOS devices such as "finFETs." However, especially at the beginning of an R&D evaluation, ALD research involves expensive and exotic precursors that may only be available in small quantities. Therefore, there is a need to be as efficient as possible when exploring the potential use of a new ALD precursor for commercial manufacturing.

This drive towards efficiency often leads research in the direction of small volume, "coupon"-based reactors to attempt initial learning. Unfortunately, often results don't translate from small reactors to full 300mm diameter silicon wafers, and this problem is only expected to become worse as the industry transitions to 450mm diameter wafers. In addition, performing experimentation at 300mm allows for integration of ALD films with other state-of-the-art processes to generate the stacks of materials necessary to extract the key electrical data necessary to evaluate device performance. Therefore, there is a pressing need for a more efficient approach that allows ALD R&D to occur on full 300mm diameter wafers.

One such approach is to use a high productivity combinatorial (HPCTM) platform—such as that developed by Intermolecular, Inc.—to dramatically accelerate R&D of integrated ALD films by 10-100x relative to traditional methods. Combinatorial ALD can be integrated with combinatorial processes for wet-etching/cleaning and physical vapor deposition/chemical vapor deposition (PVD/CVD) to engineer interfaces and multilayer stacks for optimal device performance.

In one Collaborative Development Program with an Intermolecular customer, the initial design-of-experiments to integrate an ALD film with novel substrates, overlayers, and annealing resulted in over 3500 required tests to completely explore the potential solutions-space. It was estimated that a conventional R&D approach would have taken 2 years while using the HPC platform allowed the team to identify a combination of materials with the desired properties in just 7 months with a 75% reduction in raw materials expenses for ALD precursors and wafers.

This presentation will detail the concepts and physics behind combinatorial ALD and provide case studies on how Intermolecular has used integrated combinatorial methods to solve problems of interest to leading device manufacturers and materials suppliers.

TF-ThP35 The Effect of BN Coating on the Hydrogen Permeation through Stainless Steel. *M. Tamura*, The University of Electro-Communications, Japan

Hydrogen cracking of steels is a major concern in steel processing and service, and occurs in several applications, such as cracking of rolled steel products, cold cracking of welds, and as a result of corrosion in H₂S environments.

Low-permeation thin films can be used as hydrogen permeation barriers. When coated on stainless steel they can reduce the rate of hydrogen transport. And they might be useful for sterling engines, tritium containment, or components of hydrogen fuel cells.

The hydrogen permeation behavior of BN-coated SUS316L stainless steel was investigated. The c-BN (cubic boron nitride) coating, deposited by magnetically enhanced plasma ion plating, was effective to reduce the rate of hydrogen permeation through stainless steel. The c-BN coating is also known as high-performance coating for cutting tools at high temperature.

This can be used for high-temperature and wear-resistant applications as hydrogen permeation barriers.

TF-ThP38 Development and Application of Novel Precursors for Atomic Layer Deposition. *T.M. Chung*, Korea Research Institute of Chemical Technology, Republic of Korea, *B.K. Park, D.J. Deon, S.S. Lee, K.-S. An, C.G. Kim*, Korea Research Institute of Chemical Technology, Republic of Korea

Advanced electronic industries have highly required novel materials due to the continuous shrinking dimensions of the related devices. The preparation and use of metal compounds as precursors for electronic areas has been extensively focused on application to electronic devices. The systematic development of metal complexes with excellent properties such as thermal stability, volatility, and air sensitivity are highly important in the vacuum deposition field of chemical vapor deposition. Among the properties of metal precursors, volatility is most important in vacuum technology because the transportation of precursor from canister to substrate in chamber is necessary to deposit the metal containing materials. Generally, metal complexes of inorganic ligands such as halides, nitrate, and sulfate are not volatile enough to be used in the vacuum technology although there are some except compounds – titanium tetrachloride, tin tetrachloride, tungsten hexafluoride. Organic ligands attached on the metals afford definite effects to the volatility property of the metal precursors. To improve of the volatile character of metal precursors, various ligands have been applied with preparation of the metal complexes. In this talk, we will discuss the development of a wide variety of metal compounds through molecule level design to be applicable in vacuum deposition technology such as metal organic chemical vapor deposition (MOCVD) and atomic layer deposition (ALD). Recent results on ALD of metal sulfide, metal oxide, and metal using metal precursors such as nickel, tin, ruthenium, and tungsten synthesized in our group will be disclosed.

Friday Morning, November 1, 2013

Electronic Materials and Processing

Room: 101 B - Session EM+NS+SS+TF-FrM

Growth and Characterization of Group III-Nitride Materials

Moderator: N. Dietz, Georgia State University, I.T. Ferguson, University of North Carolina at Charlotte

9:00am **EM+NS+SS+TF-FrM3 Photoluminescence and Kelvin Probe Studies of Mg-doped GaN, J.D. McNamara, A.A. Baski, M.A. Reshchikov, Virginia Commonwealth University**

High-quality p-type gallium nitride (GaN) can only be achieved by doping with magnesium (Mg). However, some unidentified point defects are also present in this material and detrimentally affect the properties of GaN thin films and related devices. Analyzing the photoluminescence (PL) spectra of GaN thin films provides valuable information regarding point defects in GaN. Additionally, the Kelvin probe method supplies complementary information about the electrical and optical properties of GaN near the surface. We have demonstrated in the past that simple phenomenological models based on rate equations are able to describe the results obtained in PL and Kelvin probe experiments. In particular, the concentrations of defects, their carrier-capture parameters, and energy levels can be found from PL measurements. The Kelvin probe method allows us to accurately determine the conductivity type for GaN thin films where Hall effect measurements are ambiguous. Temperature-dependent surface photovoltage (SPV) studies provide useful data about the surface band bending in dark, during illumination and the subsequent restoration after illumination. Using these methods, we have studied Mg-doped p-type GaN samples grown by various techniques. Interestingly, the PL spectra at low temperatures for several different samples contain different dominant bands – the ultraviolet luminescence (UVL), blue luminescence (BL) and green luminescence (GL) bands – which are all related to different defects. In some samples, the UVL band is quenched abruptly at a characteristic temperature (between 100-200 K) which can be tuned by excitation intensity. In other samples, the UVL band demonstrates no tunable quenching and a much faster decay (orders of magnitude) after pulsed excitation in time-resolved PL experiments. Our temperature-dependent Kelvin probe measurements show a conversion of the conductivity type at low temperatures under UV illumination. The temperature of the change in conductivity type varies between the samples and is also tunable with excitation intensity. This is consistent with PL results and can be explained by a switch in the majority charge carrier. These results are indicative of some special features of the nonradiative defects in p-type GaN (deep donors which have large capture cross-sections for both carriers). Although all the samples are Mg-doped and have comparable p-type conductivity, we assume that unidentified point defects in Mg-doped GaN are responsible for the diverse behaviors which have been observed. By modeling and comparing data from PL and Kelvin probe studies, we can acquire a better understanding of the properties of p-type GaN materials.

9:20am **EM+NS+SS+TF-FrM4 Surface Structure, Polarity and Surface Kinetics of InN Grown by Plasma – Assisted Atomic Layer Epitaxy: A HREELS Study, A. Acharya, Georgia State University, N. Nepal, C. Eddy, Naval Research Laboratory, B. Thoms, Georgia State University**

The surface bonding configuration and kinetics of hydrogen desorption from InN grown on Si (100) by plasma-assisted atomic layer epitaxy have been investigated. High resolution electron energy loss spectra exhibited loss peaks assigned to a Fuchs-Kliewer surface phonon, N-N and N-H surface species. The observation of N-H but no In-H surface species suggests N-polar InN. Isothermal desorption data was best fit by the first-order desorption kinetics with an activation energy of 0.88 ± 0.06 eV and pre-exponential factor of $(1.5 \pm 0.5) \times 10^5$ s⁻¹. The lower activation energy, the first-order desorption kinetics and surface N-N vibrations are attributed to surface defects.

9:40am **EM+NS+SS+TF-FrM5 A Vertical Superatmospheric Pressure MOCVD Reactor for InGaN Growth, A.G. Melton, P. Davis, M. Uddin, E.B. Stokes, University of North Carolina at Charlotte**

Thermodynamic calculations have predicted that elevated nitrogen pressure over the In_xGa_{1-x}N growth surface will suppress indium evaporation, thus enabling growth at higher temperature. This is expected to result in both better adatom mobility on the growth surface and improved pyrolyzation efficiency of ammonia (thus reducing nitrogen vacancies). These two effects are expected to result in improved internal quantum efficiency of

high indium In_xGa_{1-x}N materials. A vertical, rotating susceptor MOCVD reactor capable of superatmospheric growth pressures (up to 3 bar, absolute) has been designed and built at UNC Charlotte. The intended application of this reactor is to explore the use of elevated growth pressure in suppressing nitrogen vacancies, indium desorption, and phase separation in high-indium In_xGa_{1-x}N alloys, such as those within the “green gap”. The reactor is capable of growth on a single 2” diameter wafer at a time and has been designed to minimize turbulence using computational fluid dynamics simulations. The reactor design and results from early growth runs will be presented here. X-ray diffraction and confocal photoluminescence are used to evaluate macroscopic and spatially resolved phase separation, respectively, as well as composition and crystal quality.

10:00am **EM+NS+SS+TF-FrM6 Atomic Layer Epitaxy of III-N Semiconductors, C.R. Eddy, Jr., U.S. Naval Research Laboratory, N. Nepal, American Association for Engineering Education, N.A. Mahadik, U.S. Naval Research Laboratory, L.O. Nyakiti, American Association for Engineering Education, S.B. Qadri, M.J. Mehl, J.K. Hite, U.S. Naval Research Laboratory**

The synthesis of III-nitride semiconductors by atomic layer epitaxy (ALE) is explored to reveal that growth temperatures for high-quality crystalline layers are less than half that of conventional growth methods and that the new parameter space can lead to previously unrealized phases and stoichiometries of III-N binaries and ternaries.

ALE is a method in which the precursors for growth are introduced in a sequence of gas pulses added to an inert carrier gas flow at temperatures sufficient to promote either homo- or hetero-epitaxial growth. Here, we use alternating pulses of traditional group III metalorganics and plasma-activated nitrogen carried on an ultra-high purity argon carrier gas. A variety of substrates (silicon, sapphire, GaN templates on sapphire, etc.) are subjected to the pulse sequences at temperatures from 150°C to 500°C in a customized Cambridge Nanotech, Inc. Fiji plasma-assisted ALD reactor.

With proper surface preparations, high quality, wurtzitic AlN is grown at 500°C. These thin films (~36 nm) demonstrated smooth surfaces (~0.7 nm rms roughness for 10x10 mm² scan area) and a (0002) peak rocking curve width of 630 arc-sec [1,2], but contained a high fraction of carbon (8%) and small fraction of oxygen (0.6%). Similar results are demonstrated for GaN films grown between 350 and 450°C. For InN, two growth regimes were defined. One between 175 and 185°C, in which a new cubic phase of InN was realized, and a second regime between 220 and 260°C for which quality wurtzitic materials (262 arc-sec for (0002) reflection) were grown. As with AlN, both films contained high fractions of carbon (3%), but little-to-no oxygen (0.1%). Finally, initial efforts to grow ternaries of InAlN were conducted using a digital alloying approach where quality, crystalline ternaries were realized over the entire stoichiometric range. These early results suggest great potential for ALE growth of III-N semiconductors.

[1] T. Koyama et al., Phys. Stat. Sol. (a) 203, 1603 (2006). MBE (1.58 micron, 420 arc-sec).

[2] K. Balakrishnan et al., Phys. Stat. Sol. (c) 3, 1392 (2006). MOCVD (2 micron, 400 arc-sec).

10:20am **EM+NS+SS+TF-FrM7 Advances in Ternary Group III-Nitrides for Advanced Solid State Lighting, Photovoltaics and Thermoelectric Applications, B. Kuckgok, B. Wang, M. Oroc, A.G. Melton, N. Lu, I.T. Ferguson, University of North Carolina at Charlotte**
INVITED

The ternary group III-Nitrides have demonstrated great promise in becoming the universal III-V compound semiconductor material for electronic, optoelectronic and other applications. This talk will show that the III-Nitrides can provide a possible solution for many applications that traditionally used III-V materials and associated devices. The development of wide-band gap compound semiconductors materials and devices, in particular III-Nitrides, are leading a revolution in energy related areas of light emitting diodes (LEDs) and, more recently, solar cells and thermoelectric applications. However, a sound understanding of the appropriate material properties of III-Nitride for these diverse applications is needed as well as the understanding the compromises that are needed in the corresponding device structures. For example, the use of LEDs in general illumination, known as solid state lighting, incorporate InGaN in such a way that it shows large compositional fluctuations in the active region of the device. This physical phenomenon has been associated with bright emission from these devices despite the high defect density in the material. Moreover, these first generation devices typically have poor color rendering capability, in addition to poor correlated color temperature associated with gaps in the power spectrum. The group III-Nitride technology is also the basis for the development of a new generation of

highly efficient solar cells. Wide-band gap InGaN is one of the few materials that can provide bandgaps in the 2.4-2.9 eV range for multi-junction photovoltaics devices to achieve efficiencies greater than 50%. Single phase InGaN with indium compositions up to 30% (2.5 eV band gap) are needed for these applications including understanding their absorption characteristics and ability to p-type dope. Another emerging application for the group III-Nitrides is high temperature (>700°C) thermoelectric applications for waste heat harvesting. Recent measurements of the thermoelectric properties of InGaN; including the Seebeck coefficient, the electrical conductivity, and the power factor, etc., show promising results for this application. However, the effects of point and extended defects on thermoelectric properties, in particularly the Seebeck coefficient, are not well understood and need further investigation.

11:00am **EM+NS+SS+TF-FrM9 InGaN Epilayer Growth using Migration-enhanced, Remote-Plasma MOCVD**, *R.L. Samaraweera, F. Gueth, J.K.S. Nanayakkara, M.K.I. Senevirathna, N. Dietz*, Georgia State University

Group III-nitrides possess a number of attractive physical, optical, and electronic properties that allow the fabrication of novel materials and device structures as presented in numerous reviews over the last two decades. However, encountered ternary and quaternary materials stabilization and integration problems under presently deployed processing conditions limit the indium incorporation to a narrow composition range. Potential pathways to stabilize group III-nitride alloys with higher indium content, include the pressure dependency of the surface chemistry, as well as kinetic stabilized growth concepts such as plasma-assisted MBE. Recent advances in remote-plasma-enhanced CVD and RF microwave plasma assisted MOCVD for the growth of group III-nitrides, demonstrate the epitaxial growth of InN and InGaN at growth temperatures of 450°C - 650°C with growth rates that are comparable to MOCVD.

In this contribution, we will present first results on epitaxial InGaN growth under migration-enhanced, remote-plasma MOCVD (MERP-MOCVD). The growth system is based on a rotating turbo-disc showerhead configuration with added provisions for the spatial and temporal control of plasma, metalorganic (MO) and hydride precursor injections, as well as real-time optical monitoring to study the evolution of surface chemistry processes as function of the process parameter. A remote plasma is generated by a nitrogen/hydrogen mixture injected in a hollow cathode, sustained by a 50W and 600W rf-power source. The reactive nitrogen species (e.g. N⁺/NH⁺/H⁺ fragments) in the after glow regime of a remote plasma are directed to the growth surface using the after glow regime of the remote plasma.

Data will be presented and discussed for the GaN and InN process window as function of nitrogen/hydrogen plasma mixture, reactor pressure, substrate temperature, and rf-power setting. The layers have been characterized by x-ray diffraction (XRD), Raman spectroscopy, Fourier transform infrared (FTIR) reflectance and optical absorption spectroscopy.

11:20am **EM+NS+SS+TF-FrM10 The Growth and Structural Properties Analysis of Indium-rich InGaN Epilayers**, *S. Gamage, J.K.S. Nanayakkara, M.K.I. Senevirathna*, Georgia State University, *A.G. Melton, I.T. Ferguson*, University of North Carolina at Charlotte, *N. Dietz*, Georgia State University

The large band gap tunability possible in ternary InGaN alloys opens new avenues in the field of advanced optoelectronics device structures. However, the stabilization of indium-rich InGaN epilayers is still a big challenge due large differences in the partial pressures and lattice parameters between the binaries InN and GaN, respectively. As a potential pathway to stabilize ternary InGaN alloys in a larger composition range and to reduce the temperature gap, we explore the growth of InGaN epilayers under super atmospheric pressures of up to 15 bars.

Starting from InN, we report in this contribution on the growth of indium-rich ternary In_{1-x}Ga_xN epilayers (with 0 ≤ x < 0.4) and study the influence of the pulse separations on the phase purity and stability of indium-rich In_{1-x}Ga_xN epilayer and resulting structural and optical layer properties. The structural InGaN epilayers are characterized by x-ray diffraction, Raman spectroscopy, and by infrared (IR) reflectance. The free carrier concentrations have been estimated by analyzing the IR-reflectance spectra and by Raman A1(LO) mode line shape analysis.

11:40am **EM+NS+SS+TF-FrM11 ALD Sidewall Passivation for Dark Current Reduction in GaN Avalanche Photodiodes**, *J. Hennessy, L.D. Bell, S. Nikzad*, Jet Propulsion Laboratory, California Institute of Technology, *P. Suvarna, F. Shahedipour-Sandvik*, College of Nanoscale Science and Engineering, University at Albany

The detection of ultraviolet light has important applications in planetary imaging and spectroscopy, communications, and defense-related photosensing. One major challenge facing UV detection is visible-rejection,

as UV photons in bands of interest are often greatly outnumbered by visible photons, effectively reducing the signal-to-noise ratio. Conventional systems for these detection applications include high-gain photomultiplier tubes and microchannel plate systems, which tend to be large, fragile, and require high-voltage operation. For these reasons, a more reliable all-solid-state alternative such as an avalanche photodiode (APD) is a desirable replacement option. III-N APDs based on the GaN/AlGaN material system are one candidate that can potentially offer high gain as well as visible-blind operation.

Significant materials challenges remain in order to improve the performance of AlGaN/GaN APDs, including the optimization of both bulk and surface defects. Sidewall-related defects in GaN APDs have often been observed to contribute to undesirable current components such as those produced by defect-related microplasmas. Although several approaches have been reported to address edge leakage issues, device repeatability and reliability remains a concern. In this work we investigate the effect of sidewall Al₂O₃ deposited by atomic layer deposition (ALD) as an alternative to more typical approaches like SiO₂ deposited by plasma-enhanced chemical vapor deposition (PECVD). ALD is an attractive option for III-N sidewall passivation due to the ease in depositing potentially more compatible materials with the AlGaN system, as well the ability to conformally coat three dimensional structures like mesa diodes.

The use of ALD Al₂O₃ as a sidewall passivation layer was observed to result in the reduced occurrence of premature breakdown in mesa p-i-n GaN APDs when compared to devices fabricated with a more common SiO₂ passivation deposited by PECVD. Mesa APDs with diameters ranging from 25 to 100 μm show a significant reduction in median dark current for the ALD-passivated devices. The reduction in median dark current was most significant for the smallest devices, showing an order of magnitude improvement at reverse biases near avalanche. The interfacial effect of ALD Al₂O₃ was investigated by fabricating MOS capacitors which show a large reduction in both slow trapping and faster interface states compared to PECVD SiO₂ devices.

Electronic Materials and Processing

Room: 102 A - Session EM+NS+TF-FrM

Nanoelectronic Interfaces, Materials, and Devices/Crystalline Oxides on Semiconductors

Moderator: A. Demkov, University of Texas at Austin, K. Kavanagh, Simon Fraser University, Canada, S. Zollner, New Mexico State University

8:20am **EM+NS+TF-FrM1 Growth and Properties of MoS₂ and MoX_y (X=S,Se and alloys thereof, y=1.5...2) on SiO₂ and Cu(111)**, *L. Bartels*, University of California, Riverside **INVITED**

I will present experimental methods for the preparation of MoS₂ and MoX_y (X=S,Se and alloys thereof, y=1.5...2) on SiO₂ and Cu(111). We investigated the films' structures by low energy electron microscopy and variable temperature scanning tunneling microscopy. The optical properties were probed in the range between room temperature and 5K. For sulfur-selenium alloys, we find an optical bandgap that is tunable between the values observed for pure MoS₂ and MoSe₂ monolayers. Investigation of the chemical properties of the materials show high affinity of the sulfur-deficient materials for adsorption of oxygenate species.

9:00am **EM+NS+TF-FrM3 Tuning Thermoelectric Power Factor in Pnictogen Chalcogenides through S and Cl Doping**, *R.J. Mehta, F. Devender*, Rensselaer Polytechnic Institute, *R.P. Ramprasad*, University of Connecticut, *D. Parker, D.J. Singh*, Oak Ridge National Laboratory, *T. Borca-Tasciuc, G. Ramanath*, Rensselaer Polytechnic Institute

High figure of merit (ZT) thermoelectric materials are attractive for solid state refrigeration of nanoelectronic devices. ZT enhancement is an exacting challenge because it entails achieving high Seebeck coefficient α, high electrical conductivity σ and low thermal conductivity κ, while these properties are usually unfavorably coupled. We recently demonstrated 25-250% ZT increases in pnictogen chalcogenides [1] by combining sub-atomic percent S doping-induced power factor α²σ increases [2], and nanostructuring-induced decrease in κ. Here, we show that S and Cl doping alter the electronic band structure near the Fermi level, impacting carrier concentration and mobility pnictogen chalcogenides. In Sb₂Te₃, we find that S doping increases α by suppressing Sb-antisite defect formation. In our quest for optimizing S concentration, we discovered that adventitious Cl confounds the trend between S doping and α²σ. Synthesis with Cl-free precursors eliminates this effect and we obtain the remarkable result of both α and σ increasing with S content, contrary to the usually observed inverse

correlation between σ and α . Additionally, we find that Cl doping at a fixed S content result in maxima of these properties at slightly different concentrations. Extended X-ray absorption fine structure analyses reveal that Cl occupies interstitial sites while S occupies Bi sites. We show that these results, together with first principles calculations, provide a framework for obtaining $ZT > 1.5$ by optimizing doping and stoichiometry in pnictogen chalcogenides through the manipulation of the electronic structure near the Fermi level.

1. R.J. Mehta, Y. Zhang, C. Karthik, B. Singh, R.W. Siegel, T. Borca-Tasciuc, G. Ramanath, *Nat. Mater.* 11, 233-240 (2012).

2. R.J. Mehta, Y. Zhang, H. Zhu, D.S. Parker, M. Belley, D. J. Singh, R. Ramprasad, T. Borca-Tasciuc, G. Ramanath, *Nano Lett.* 12, 4523-4529 (2012).

9:20am **EM+NS+TF-FrM4 From High-k Dielectrics to Functional Oxides on Silicon: Find More than Moore in More Moore, J. Fompeyrine, IBM Research - Zurich INVITED**

Research on oxide materials is a field of intense investigations, in particular for Information and Communication Technologies. This research has been driven since many years from a scientific and a technological perspective.

25 years ago, a scientific community did nucleate around high-Tc superconductivity, and expanded its research interest towards other materials. The motivation remained to understand the fundamentals of the properties of oxides thin films. To reach such an ambitious goal, physical phenomena had to be studied in clean systems, because of the strong coupling between properties and microstructure in oxide thin films. Rather than focusing on obtaining "bulk like" properties, it is more important to control their microstructural characteristics. To that respect, molecular beam epitaxy (MBE) is a well suited technique, although requiring specific design and components.

In a second recent phase, the quest for a replacement gate dielectric in transistors has been a powerful driver to investigate high quality oxide thin films. Replacing SiO_2 with HfO_2 in MOSFETs was a breakthrough for the microelectronic industry. This research is not over, since the replacement of silicon with compound semiconductors could take place within the next years. It will require changes on the materials structure and sequence to be used in dielectric stacks. Nevertheless, because of its ability to control interfaces and to easily combine analytical capabilities with deposition reactors, MBE is also a powerful learning tool to understand the chemistry of interfaces between oxide and semiconductors [2].

The motivation to *understand* or to *exploit* the physical properties of oxide thin films is quite different, but there is clearly cross-fertilization between the various communities. The best example one can give is the development of single crystalline oxides grown directly on semiconductor surfaces. Initially stimulated by the quest for a new gate dielectric, researchers are now able to grow high quality epi-oxide films onto silicon, that can be used as nucleation layers for other "functional" oxides. As expected, the combination of silicon microfabrication techniques with the capability to grow crystalline directly on silicon opens up perspectives for devices exploiting oxide properties with an improved efficiency [3].

The goal of my presentation is to review selected examples of the three phases mentioned, and to highlight exciting research directions in this domain.

[1] J.-P. Locquet et al, *Nature* **394**, 453 (1998)

[2] M. El Kazzi et al, *Appl. Phys. Lett.* **99**(5), 052102 (2011)

[3] S. Abel et al, accepted for *Nature Communications* (2013)

10:00am **EM+NS+TF-FrM6 High Performance Infrared Sensing Using Colloidal Quantum Dots Monolithically Integrated with a Silicon Readout IC, J.S. Lewis, E.J.D. Klem, C.W. Gregory, G.B. Cunningham, S. Hall, D.S. Temple, RTI International, A. D'Souza, E. Robinson, DRS Sensors and Targeting Systems, N. Dhar, Darpa, Mto, P.S. Wijewarnasuriya, Army Research Laboratories**

Low cost is frequently cited as a driver for hybrid and organic electronic devices, but in fact very few applications allow a sacrifice in performance. Here we present a hybrid organic/inorganic device that rivals high performance InGaAs detectors for short wave infrared (SWIR) imaging, and show that the hybrid devices based on colloidal quantum dots (CQDs) offer substantial benefits with respect to wavelength range, integration with Si readout integrated circuits (ROICs), and of course cost. We will present the results for detectors fabricated on passive Si substrates as well as for 320 x 10 arrays fabricated on ROICs. We will discuss recent advances in device architecture and processing that resulted in measured dark currents of 3 nA/cm² at room temperature, with sensitivity to 1.7 μm . We will show other devices with spectral sensitivity that extends from UV to 2.2 μm . For the ROIC-integrated devices we will show dark currents <10 nA/cm². The most significant advantage of the CQD technology is ease of fabrication. The

devices are fabricated directly onto the ROIC substrate at low temperatures compatible with ROICs, and arrays can be fabricated at wafer scale. This combination of high performance, dramatic cost reduction, and multi-band sensitivity makes the technology attractive for a variety of applications, which we will discuss.

10:20am **EM+NS+TF-FrM7 Epitaxial Integration of Magnetic Insulators on Silicon, A. Posadas, University of Texas at Austin INVITED**

In recent years, there has been remarkable progress in the growth of complex magnetic oxides in thin film form. Many novel physical properties such as colossal magnetoresistance, multiferroicity, tunneling magnetoresistance effects, and room-temperature ferromagnetism in dilute magnetic oxides have emerged and are ongoing sources of new ideas and systems for applications in the manipulation of the spin of the electron. Part of this field of complex magnetic oxides are materials that are both ferromagnetic and electrically insulating, a relatively rare combination compared to conducting magnetic materials. Such materials are envisioned to serve as spin filtering tunnel barriers, selectively allowing one particular spin to pass through over the other. In this talk, we will focus on insulating ferromagnets with particular emphasis on their growth on silicon substrates. Three insulating ferromagnetic materials systems will be described including the challenges of growing them in epitaxial form on silicon: EuO, strained LaCoO_3 , and Co-substituted SrTiO_3 . First we describe the use of Eu metal to form a chemical template on Si, similar to the use of 1/2 monolayer of Sr for the growth of SrTiO_3 on Si. We then describe various paths for the growth of EuO on this Eu template. We then describe the use of SrTiO_3 on Si as a pseudo-substrate for growing LaCoO_3 , normally non-magnetic but which becomes ferromagnetic as a result of epitaxial strain, onto silicon. Strain-coupled magnetoresistivity modulation of such $\text{LaCoO}_3/\text{SrTiO}_3/\text{Si}$ heterostructures will be described. Finally, we describe the growth on Si and properties of Co-substituted SrTiO_3 , a ferromagnetic insulator at room temperature that may find potential application in spintronics devices. We discuss the effect of Co concentration on the structural and magnetic properties and also describe theoretical calculations indicating magnetism resulting from cobalt-oxygen vacancy centers.

11:00am **EM+NS+TF-FrM9 Understanding the Origin of the Dead-layer at the $\text{La}_{0.66}\text{Ca}_{0.33}\text{MnO}_3/\text{SrTiO}_3$ Interface: A Grazing Incidence X-ray Diffraction and Hard X-ray Photoelectron Spectroscopy Study, J. Rubio-Zuazo, SpLine Spanish CRG beamline at the European Synchrotron Radiation Facility, France, A. de Andres, Institute Materials Science of Madrid-CSIC, Spain, G.R. Castro, SpLine Spanish CRG beamline at the European Synchrotron Radiation Facility, France**

$\text{La}_{1-x}\text{Ca}_x\text{MnO}_3$ -type perovskite-manganese oxides exhibit a wide variety of interesting physical properties which originate from mutual coupling among spin, charge and lattice degrees of freedom. The perovskite-manganese oxides have, in the Ca doping range between 0.15 and 0.5, a ferromagnetic-paramagnetic (F-M) phase transition accompanied by a metal-insulator (M-I) transition that results in a colossal magneto-resistance behaviour. In bulk $\text{La}_{0.66}\text{Ca}_{0.33}\text{MnO}_3$ (LCMO), the transition temperature T_C , T_M rises for 33% Ca doping level reaching values close to room temperature. We have studied a series of epitaxial LCMO films with thickness between 2.4 and 27 nm grown on $\text{SrTiO}_3(001)$ (STO). The magnetic measurements show a severe decrease of T_C as the film thickness is reduced below 2.4 nm. The atomic structure, as obtained by grazing incidence X-ray diffraction shows that the LCMO films adopt the substrate STO in-plane lattice parameter (1% mismatch) inducing a pseudomorphic growth. The 27 nm film presents a bulk-like crystal structure and space group, but also magneto-transport bulk behavior, while the 2.4 nm film shows a different crystallographic space group and the film is an insulator within the whole temperature range (i.e., no T_C transition is present). The structure, also observed at the LCMO-STO interface of thicker LCMO films, is based on an anti-correlation between Mn-O octahedra along the three crystallographic directions. This could explain the origin of anomalous magneto-transport or dead-layer behavior in LCMO hetero-structures. These results evidence the strong influence of the interface. The mismatch may be accommodated by the formation of facets, by structural defects or by diffusion-induced changes in stoichiometry or oxygen vacancies. However, in our study no facets were found, but bi-dimensional in-plane reciprocal space maps show a clear lattice relaxation of about 1% suggesting the existence of a stoichiometry change as strain relaxation mechanisms. To understand the relaxation mechanisms a non-destructive compositional depth profile analysis was performed using the Hard X-ray Photoelectron Spectroscopy (HAXPES). The data was fitted with a model in which the La is diffused into the interface, while the Ca is segregated to the surface. The substitution of the Ca^{2+} cation for La^{3+} results in an LCMO lattice enlargement reducing the mismatch between LCMO and STO. Hence, the first La enriched layer close to the interface will grow pseudomorphic, and in the successive layer Ca concentration increase and consequently a lattice parameter reduction

until the bulk lattice parameter is achieved, without energy strain accumulation.

11:20am **EM+NS+TF-FrM10 Monolithic Integration of Rare-Earth Oxides and Semiconductors for On-Silicon Technology**, *R. Dargis, A. Clark, F.E. Arkun, D. Williams, R. Smith, Translucent Inc., A. Demkov, A. O'Hara*, University of Texas at Austin **INVITED**

Increasingly there is a need to integrate functional semiconductors such as III-V's or III-N with low cost manufacturing attainable through existing silicon based technology. Scalability is one of the main issues here, because the cost savings from the Si processing can be only realized if 150-200 mm diameter substrates are used. This could be achievable by formation of the semiconductor layers on the silicon substrates. However, direct growth of the device-grade layers on silicon in many cases is impossible due to difference in crystal structure, huge lattice and thermal expansion mismatch or even chemical reactivity of the compounds. The most of the problems can be solved by introduction of buffer layers that help for stress management. Among the materials of consideration, epitaxial rare - earth oxides have several benefits: beside their crystallographic properties that allow them to be used for stress managing layers, their electrical, optical and thermal properties (good balance between bandgap and electrical permittivity, moderate refraction index, reasonable thermal conductivity) make them useful for additional functions such as electric field suppression layers, high reflectivity heterostructures, optically active heterostructures. In this presentation, some approaches of integration of the epitaxial rare-earth oxides into the emerging advanced semiconductor on silicon technology will be demonstrated. Engineering of the interface between the oxides and the substrate from single crystal to amorphous by controlling the epitaxy process parameters opens way for formation of relaxed or pre-stressed structures that can be used as a template for the growth of III-N semiconductors on silicon. Polymorphism of some of the rare-earth oxides allows to manipulate their crystal structure from cubic to hexagonal and to grow buffer layers that can be used for germanium on insulator on silicon. Additionally, multilayer silicon-oxide distributed Bragg reflectors with high reflectivity at designed wavelength can be grown with only several pairs of the layers and can be used for light emitting devices.

Graphene and Other 2D Materials Focus Topic

Room: 101 A - Session GR+EM+MS+NS+SP-FrM

2D Materials: Device Physics & Applications

Moderator: L. Cao, North Carolina State University, E. Riedo, Georgia Institute of Technology

8:20am **GR+EM+MS+NS+SP-FrM1 Epitaxial Graphene Electronics**, *J.A. Robinson*, The Pennsylvania State University **INVITED**

Graphene demonstrates exceptional properties such as high charge carrier mobility and high saturation velocity. Such attributes make graphene a promising candidate for radio frequency (rf) applications. However, one of the key limitations to the realization of graphene's full potential comes from its interaction with dielectric overlayers and metal contacts, which act to limit the excellent charge transport properties of graphene. We have directly demonstrated the importance of buffer elimination at the graphene/SiC(0001) interface where enhanced carrier mobilities of $>3000 \text{ cm}^2/\text{Vs}$ across large scale wafers is possible. Additionally, we have developed a robust method for forming high quality ohmic contacts to graphene, which improves the contact resistance by $>1000\times$ compared to untreated metal/graphene interfaces. We have also developed methods for ultra-thin gate oxides, and will discuss integration and the importance on improved interfaces between the graphene and dielectric. Each of these developments have provided a means to achieve graphene transistors with current saturation values $>1.5 \text{ A/mm}$, transconductance $> 400\text{mS}$, impressive *extrinsic* current gain response of epitaxial graphene transistors ($>30 \text{ GHz}$), and *intrinsic* current gain nearing 150 GHz . Additionally, we analyze the third order intermodulation product, gain compression and high frequency noise performance of graphene transistors for low noise amplifier applications and benchmark the graphene transistors with other RF device technologies. The graphene amplifier (un-matched) exhibits an output third order intercept (OIP3) of 19dBm and input 1dB gain compression ($P_{in,1\text{dB}}$) of 5.6dBm . Finally, the performance of a graphene mixer will be discussed and evidence is provided that matched graphene mixers can outperform current state-of-the-art technologies.

9:00am **GR+EM+MS+NS+SP-FrM3 Direct Transfer of Graphene Devices on Arbitrary Substrates**, *Z. Razavi Hesabi, C.A. Joiner, T. Roy, E.M. Vogel*, Georgia Institute of Technology

The wide-ranging high performance electronic properties of graphene and its ability to be roll-to-roll manufactured, provides an interesting platform for developing high performance, multifunctional electronics on arbitrary substrates such as paper or plastic. However, these substrates are not compatible with conventional high-temperature semiconductor processing. In this work, graphene devices are fabricated on as-synthesized graphene on copper foil using conventional semiconductor device processing techniques. The fully fabricated devices are then transferred onto the substrate of interest (glass, paper, or plastic) using a conventional PMMA-based wet transfer method. The effect of devices designs and processing conditions such as metal contact area and type (top contact versus mixed edge/top contact) on graphene device performance is investigated. The obtained results show that for top contacts, the Dirac point cannot be observed, while for mixed edge/top contacts, the Dirac point is observed. The obtained results suggest metal doping and edge contact can significantly shift the Dirac point. Overall, the results demonstrate a novel method for fabricating high performance graphene devices on arbitrary substrates.

Key words: Graphene, Field Effect Transistor (FET), Direct Transfer

9:20am **GR+EM+MS+NS+SP-FrM4 1/f Noise in Epitaxial Graphene Field Effect Transistors using Al_2O_3 and HfO_2 High k -Dielectrics**, *H.K. Chan*, Newcastle Univ., UK, *V.D. Wheeler*, U.S. Naval Research Laboratory (NRL), *V.K. Nagareddy*, Newcastle Univ., UK, *L.O. Nyakiti*, NRL, *A. Nath*, George Mason Univ., *R.L. Myers-Ward*, *Z. Robinson*, *N.Y. Garces*, NRL, *M.V. Rao*, George Mason Univ., *J.P. Goss*, *N.G. Wright*, Newcastle Univ., UK, *C.R. Eddy, Jr.*, NRL, *A.B. Horsfall*, Newcastle Univ., UK, *D.K. Gaskill*, NRL

It has been shown that graphene has substantially low $1/f$ noise, a characteristic potentially advantageous for electronic sensor applications. Most reports have been from studies of devices on flakes, which lack the desirable scale-up potential for practical applications. Here, we report the $1/f$ noise behavior for gated graphene devices formed on SiC substrates using low pressure sublimation (LPS) of Si in an Ar ambient. In general, we found that the $1/f$ characteristics of LPS graphene to be similar to or superior to all prior studies.

The LPS graphene was synthesized in an Aixtron VP508 reactor on $\sim 2.5 \text{ cm}^2$ nominally on-axis 6H(0001) semi-insulating substrates from the same boules. The process was designed to produce nominally 1 ML of graphene on the terraces of the samples; the samples should be identical as the synthesis process has been demonstrated to be uniform and run-to-run reproducible. Samples were processed using typical photolithographic methods before dielectric deposition; a Ti/Au stack was used for ohmic and gate contacts. High-k dielectric deposition was accomplished via a two-step process that includes functionalization of graphene by Fluorine followed by atomic layer deposition (ALD) of 20 nm thick Al_2O_3 and HfO_2 . Previously, we have shown that F-functionalization results in pinhole-free coverage of dielectrics and the films possess Dirac voltage shifts of 0.5V and 1.5V and dielectric constants of 9 and 18, for Al_2O_3 and HfO_2 , respectively. The $1/f$ noise data was acquired using a fast Fourier transform analyzer coupled with low noise amplifier and was averaged over 5 different samples on the same substrate for each oxide case; V_{GS} was controlled forward and reverse in the range -3 to 2V .

The $1/f$ noise magnitude, S_f/I^2 , was found to scale with channel dimension and was comparable or smaller in magnitude to reports by others on graphene flakes thus suggesting that the underlying SiC and interface layer does not add an appreciable number of noise generation sites. Comparing samples with a gate oxide to those processed identically but without oxide shows the noise magnitude was similar implying that the F-functionalization-based ALD process does not degrade the graphene channel by inducing interfacial traps. For the gated samples, the composition of the gate oxide had a minor effect on the channel noise magnitude relative to non-gated samples. For HfO_2 devices having an oxide surface coverage of $20 \times 4 \text{ m}^2$, $S_f/I^2 = 4 \times 10^{11} \text{ Hz}^{-1}$ (at 20 Hz). For gated measurements, the $1/f$ noise magnitude were not flat but showed a slight (20%) dependence on V_{GS} . Both oxides showed noise hysteresis ($\sim 15\%$) although it was more pronounced for the HfO_2 devices.

9:40am **GR+EM+MS+NS+SP-FrM5 MoS_2 MOSFETs: Dielectrics, Metal Contacts and Scaling**, *P.D. Ye*, Purdue University **INVITED**

The discovery of graphene has unveiled another material family with layered structures, which includes boron nitride, topological insulators such as Bi_2Te_3 and Bi_2Se_3 , and transition metal dichalcogenides like MoS_2 , WS_2 , and NbSe_2 . Though graphene, a fascinating two-dimensional (2D) crystal, has shown a superior carrier mobility of up to $200,000 \text{ cm}^2/\text{V}\cdot\text{s}$, its zero bandgap property limits its application to logic devices as graphene transistors cannot have high on/off ratios. As opposed to the semi-metal

graphene, transition metal dichalcogenides (such as MoS₂), as another type of layered structure material, have shown great potential in device applications due to their satisfied bandgaps, thermal stability, carrier mobility, and compatibility to silicon CMOS process. In order to realize high performance MoS₂ MOSFETs [1], three major issues must be solved: 1) how to deposit a high-quality dielectric on 2D crystal, 2) the fabrication of low-resistivity metal-semiconductor junction to be used as device contacts, and 3) the elimination of short channel effects. [2,3] In this talk, I will review the recent progress in this field about these three device aspects and discuss the fundamental physics, chemistry, and possible solutions on these challenges.

The work is in close collaborations with H. Liu, A.T. Neal, and Y.C. Du. The authors appreciate SRC GRC for the support.

[1] Radisavljevic, B.; Radenovic, A.; Brivio, J.; Giacometti, V.; Kis, A. Single-Layer MoS₂ Transistors, *Nat. Nanotechnol.* 2011, 6, 147 – 150.

[2] Liu, H.; Neal, A.T.; Ye, P.D. Channel Length Scaling of MoS₂ MOSFETs, *ACS Nano* 2012, 6, 8563-8569.

[3] Liu, H.; Ye, P.D. MoS₂ Dual-Gate MOSFET with Atomic-Layer-Deposited Al₂O₃ as Top-Gate Dielectric, *IEEE Electron Device Lett.* 2012, 33, 546-548.

10:20am **GR+EM+MS+NS+SP-FrM7 Broad Band Dielectric Functions of Graphene and MoS₂**, W. Li, G. Cheng, National Institute of Standards and Technology (NIST), Y. Liang, Peking Univ., China, K. Xu, NIST, A. Boosalis, Univ. of Nebraska-Lincoln, P.D. Ye, Purdue Univ., A.R. Hight Walker, NIST, X. Liang, Peking Univ., China, T. Hofmann, Univ. of Nebraska-Lincoln, C.A. Richter, D.J. Gundlach, N.V. Nguyen, NIST

Graphene and MoS₂ are among the most promising candidates for next generation of electronic and photonic devices. Accurate optical properties provide key information necessary for electronic and photonic device design. Here, we report the results of a broad band optical measurement of the dielectric function by spectroscopic ellipsometry (SE) of graphene and MoS₂ grown by chemical vapor deposition (CVD). With the extended spectral range, we are able to observe new higher energy interband absorptions in MoS₂ and a red shift of graphene excitons.

Monolayer graphene grown on a copper foil was transferred onto a fused silica substrate by solvent method; two and three graphene layers were formed by the sequential transfer of each monolayer. MoS₂ was directly grown on sapphire. Raman spectroscopy was performed on each sample. Both the exciton peak (around 4.8 eV) and another absorption peak (around 6.3 eV) were observed from the absorption spectra of graphene. In the IR range, both refractive index (n) and k increase with longer wavelength which is consistent with the reported results.^(a) It is notable that n increases whereas k decreases as the number of graphene layers increases. This is most likely due to the relatively weak interaction between transferred graphene monolayers. More importantly, we observe a red shift of the exciton peak for two layer graphene (0.04 eV shift) and three layer graphene (0.07 eV shift) relative to that of monolayer graphene, which we attribute to the interlayer screening effects. The theory predicts^(b) the transmittance of monolayer graphene to depend solely on the universal fine structure constant $a = e^2/hc$, which is related to the graphene's opacity. We find opacity to linearly increase for each of added layer. For example, at 550 nm the transmittance of one, two, and three layers of graphene are 96.9%, 93.6%, and 90.3%, respectively. Raman studies on MoS₂ confirm the presence of 3 layers, consistent with the three layer model derived from ellipsometry. The MoS₂ dielectric function exhibits the well-known A (1.86 eV) and B (2.02 eV) strong excitons which arise from the direct d-d transitions separated by a spin-orbit splitting. A series of higher energy interband transitions are clearly seen at 2.8, 3.1, 4.7 eV of which the 2.8 eV peak is the strongest absorption peak ever reported for MoS₂.

(a) F. J. Nelson, et al., *Appl. Phys. Lett.* 97, 253110 (2010)

(b) A. B. Kuzmenko, E. van Heumen, F. Carbone, and D. van der Marel, *PRL* 100, 117401 (2008); R. R. Nair, P. Blake, A. N. Grigorenko, K. S. Novoselov, T. J. Booth, T. Stauber, N. M. R. Peres, A. K. Geim, *Science* 320, 1308 (2008).

10:40am **GR+EM+MS+NS+SP-FrM8 Measurement of Charge Doping of Graphene in a Metal/Graphene/Dielectric Sandwich Structure by C-1s Core Level X-ray Photoelectron Spectroscopy**, A. Dahal, M. Batzill, R. Addou, H. Coy-Diaz, J. Lallo, University of South Florida

The contact resistance between graphene and metals critically affects device operations. In most realistic graphene device structures, graphene is supported on an insulating substrate and metals are deposited on top of graphene to make electrical contacts. Thus we should evaluate the contact resistance of a metal/graphene/dielectric sandwich structure rather than just a metal/graphene interface. A critical component for evaluating the contact resistance is the Fermi-level shift in graphene underneath the metal contact. We show that this Fermi-level shift relative to the graphene's Dirac point,

can be measured from C-1s core level x-ray photoelectron spectroscopy (XPS). In XPS of solids the binding energy is referenced to the Fermi-level, consequently measurement of C-1s core level of graphene allows us, in the absence of chemical shifts, to determine the Fermi-level of graphene at metal/graphene interfaces as well as at metal/graphene/dielectric interfaces. We show that the Fermi-level shift for metal/graphene interfaces of the weakly interacting metals such as Pt, Ir, Al, and Cu agrees well with previously reported DFT calculations (ref.1). However, the Fermi-level shift of graphene is strongly altered if graphene is sandwiched between a metal and a dielectric oxide. This behavior can be explained by a modified Schottky contact model. In metal/graphene/oxide sandwich structure, metal is replaced by a graphene/metal heterostructure and thus charges in the Schottky contact will be located on the graphene. A simple capacitor model for graphene/oxide interfaces predicts the difference in charge doping for graphene on a metal compared to graphene sandwiched between a metal and dielectric as $\Delta E_F \approx 0.2 \times (\Phi_{\text{metal}} - \Phi_{\text{dielectric}})$, in good agreement with our measurements.

Key words: Interface, Doping, Fermi-level, Spectroscopy, Schottky contact

Ref(1) G. Giovannetti, P. A. Khomyakov, G. Brocks, V. M. Karpan, J. van den Brink, and P. J. Kelly, *Physical Review Letters* 101, 026803 (2008).

In Situ Spectroscopy and Microscopy Focus Topic Room: 203 B - Session IS+AS+SP-FrM

Evolving In Situ Microscopic and Spectroscopic Techniques and Applications

Moderator: G. Zhou, Binghamton University

8:20am **IS+AS+SP-FrM1 In Situ Atomic-Scale Observations of the Oxidation of Metals**, G. Zhou, L. Luo, L. Li, State University of New York, Binghamton University, J. Ciston, Lawrence Berkeley National Laboratory, E. Stach, Brookhaven National Laboratory, J. Yang, University of Pittsburgh **INVITED**

Transmission electron microscopy (TEM) has evolved dramatically in recent years and allows for temperature-, time-, and pressure-resolved imaging of gas-surface reactions at the atomic scale. This is accomplished by differentially pumped environmental TEM (max pressures of several Torr) and the incorporation of aberration correction techniques. Here we describe how dynamic, atomic-scale TEM observations of terraces and steps during oxidation of Cu surfaces demands revisions in the current held oxidation mechanism. The canonical description of oxide formation in metals involves a solid-solid transformation proceeding with initial oxygen chemisorption induced reconstructions followed by oxygen subsurface incorporation. Such a mechanism has been inferred from idealized experiments that are primarily restricted to planar surfaces under ultrahigh vacuum conditions. In practice, however, metallic surfaces are seldom perfect. Rather, they contain a high density of low-coordinated surface sites. Thus, in order to gain a detailed understanding of the mechanism of oxide formation under realistic conditions, the role of surface defects during surface oxidation must be elucidated under practical environments. By observing the coordinated step retraction and oxide propagation on surface terraces in real time with in-situ TEM, we demonstrate that the oxide grows via an adatom process, in which Cu atoms detach from step edges and diffuse in along the surface terrace. This process involves neither reconstructive oxygen adsorption nor oxygen subsurface incorporation and is rather different from the mechanism of solid-solid transformation of bulk oxidation that is most commonly postulated. These results demonstrate that the presence of surface steps can promote the development of a flat metal-oxide interface by kinetically suppressing subsurface oxide formation at the metal-oxide interface.

9:00am **IS+AS+SP-FrM3 X-ray Analysis of Ultrastructure of Vitrified Biological Objects**, A.R. Buck, T. Gormiak, T.M. Senkbeil, Karlsruhe Institute of Technology, Germany, V.M. Haramus, Helmholtz-Zentrum Geesthacht, Germany, K. Hilpert, University College London, UK, A. Rosenhahn, Ruhr-Universität Bochum, Germany

Cryogenic sample environments allow investigations in the X-ray 'water window' of 284 – 540 eV which is of tremendous interest for microscopy and coherent scattering due to the high contrast of organic matter with respect to the aqueous background. In addition, no fixatives and stains are required and thus real in-situ analysis becomes possible. We present coherent diffractive imaging and X-ray micrographs of bacteria and compare the data against small angle X-ray scattering on large ensembles. Most measurements have been conducted at the synchrotron BESSY II, U49 PGM2 with our dedicated scattering chamber HORST. As example for

the approach, ultrastructure changes in bacteria induced by stress conditions such as different environmental conditions and biocides. We show that imaging and scattering provide complementary results as latter provides information averaged over thousands of cells and can thus provide insights of a very high statistical quality.

9:20am **IS+AS+SP-FrM4 Recent Advances in the Electrochemical Surface Forces Apparatus**, *K. Kristiansen*, University of California, Santa Barbara, *M. Valtiner*, Max Planck Institut für Eisenforschung GmbH, Germany, *X. Banquy*, Université de Montréal, Canada, *G.W. Greene*, University of Deakin, Australia, *J.N. Israelachvili*, University of California, Santa Barbara

We present a newly designed electrochemical Surface Forces Apparatus (EC-SFA) that allow control of surface potential and interfacial electrochemical reactions with simultaneous measurements distances between apposing surfaces (with 0.1 nm resolution), normal interaction forces (with nN resolution), and friction forces (with μN resolution). We will describe three applications of the EC-SFA:

(1) Oxide growth of a gold surface. Applying a high positive electrical potential on a metal surface will lead to an oxide growth. Using the EC-SFA we compared the measured thickness of the anodic gold oxide layer and the charge consumed for generating this layer which allowed the identification of its chemical structure as a hydrated $\text{Au}(\text{OH})_3$ phase formed at the gold surface at high positive potentials.

(2) The evolution of the friction forces at a metal-ceramic contact as a function of the applied electrochemical potential.

(3) The phenomenon of “pressure solution”. We have found an intimate relationship between dissolution rate and the surface potential difference across interfaces of dissimilar materials that are immersed in brine solution. For example, using the EC-SFA we have visualized and measured the dissolution of silica glass surfaces close to a gold electrode surface, which is on the order of 0.1 nm/hr. This is similar to geological samples of sandstones.

References:

Valtiner M, Banquy X, Kristiansen K, Greene GW, and Israelachvili JN, *Langmuir*, **28** (2012) 13080-13093.

Kristiansen K, Valtiner M, Greene GW, Boles JR, and Israelachvili JN, *Geochimica et Cosmochimica Acta*, **75** (2011) 6882-6892.

Valtiner M, Kristiansen K, Greene GW, and Israelachvili JN, *Advanced Materials*, **23** (2011) 2294-2299.

9:40am **IS+AS+SP-FrM5 Emerging Mesoscale Phenomena in Energy Conversion/Storage Characterized by In Situ Soft X-ray Spectroscopy**, *J.-H. Guo*, Lawrence Berkeley National Laboratory **INVITED**

Advanced technology arises from the understanding in basic science, and both rest in large on in-situ/operando characterization tools for observing related physical and chemical processes directly at the places where and while reactions occur. In energy science, experimental insight into physical and chemical processes has been largely limited to information obtain with in a framework of thermodynamic and kinetic concepts or atomic and nanoscale. In many important energy systems such as energy conversion, energy storage and catalysis, advanced materials and fundamental phenomena play crucial roles in device performance and functionality due to the complexity of material architecture, chemistry and interactions among constituents within. To understand and ultimately control the interfaces in energy conversion and energy storage application calls for in-situ/operando characterization tools. Soft x-ray spectroscopy may offer some unique features. This presentation reports the development of in-situ reaction cells for soft x-ray spectroscopic towards the studies of photosynthesis and catalytic reactions in recent years. The challenge has been that soft x-rays cannot easily peek into a high-pressure catalytic cell or a liquid photoelectrochemical cell (PEC). The unique design of the in-situ cell has overcome the burden. Some of the instrumentation design and fabrication principle are to be presented, and a number of experimental studies of nanocatalysts are given as the examples, also the recent experiment performed for studying the hole generation in a specifically designed photoelectrochemical cell under operando conditions.

10:20am **IS+AS+SP-FrM7 Changes to the Microstructure of Fibrous Collagen Hydrogels formed under Different Physicochemical Parameters and Upon Cross-Linking with Non-Toxic Reagents are Detected with In Situ Multiphoton Microscopy Imaging**, *Y.J. Hwang*, *X. Lang*, *J.G. Lyubovitsky*, University of California, Riverside

This presentation will highlight the knowledge developed by our laboratory regarding the microstructure of 3D collagen hydrogels detected in situ with multi-photon imaging while employing second harmonic generation (SHG) and two-photon fluorescence (TPF) contrasts. The materials were prepared

under different physicochemical parameters and independently stabilized with non toxic cross-linkers. The effects of collagen solid content, incubation temperature and ionic strength as well as cross-linking with genipin and carbodiimide (EDC) on 3D collagen hydrogel microstructure will be addressed. Second Harmonic generation (SHG) contrast was employed to follow modifications and/or evolutions of the hydrogels' microstructure in real time and two-photon fluorescence (TPF) was beneficial in monitoring the extent of the chemical reaction between collagen and genipin as well as spatial locations of the newly induced fluorescent fibers. The induced microstructures differ dramatically upon changing collagen solid content, incubation temperature or ionic strength. For example, short lag time, fast assembly rates and short, tightly connected fibers were detected upon assembly from 30 mM phosphate buffer. In 0.9 M NaCl adjusted 30 mM phosphate buffer only unconnected one micron fiber nuclei with low second harmonic generation contrast formed. Fiber width and length was somewhat similar upon assembly of collagen fibers from 30 mM phosphate buffer adjusted with 0.3 M or 0.6 M NaCl while pore structure depended on the polymerization temperature. Non-zero-length cross-linker genipin induced formation of long aggregated fluorescent strands throughout hydrogels. The SHG imaging suggested that modification with genipin partially disaggregated initial collagen microstructure within hydrogels at the expense of forming these new fluorescent fibers. On the other hand, zero-length cross-linker EDC, even with an addition of N-Hydroxysuccinimide (NHS), does not affect microstructures. Imaging of the interactions of these important materials with embryonic stem cells induced to differentiate into a neural lineage and implication for tissue engineering will be discussed as well.

10:40am **IS+AS+SP-FrM8 In Situ Atomic Scale Observation of Catalyst Surface and Carbon Nanotube Cap Interplay during the Lift-Off**, *M. Picher*, *P.A. Lin*, University of Maryland, College park, *J. Winterstein*, FEI Co, *R. Sharma*, National Institute of Standards and Technology

Catalytic chemical vapor deposition (C-CVD), using a transition metal catalyst (Ni, Fe, Co, etc.) on an SiO_2 , Al_2O_3 , or MgO support and a carbon-containing precursor (C_2H_2 , C_2H_4 , CH_4 , CO, etc.), is commonly employed for large-scale synthesis of carbon nanotubes (CNTs). However, synthesis of CNTs with the desired structure and morphology for a specific application has still not been demonstrated. Understanding the atomic-scale interplay between catalyst structure and CNT nucleation will aid us in determining the reaction conditions suitable for selective synthesis, especially for single walled CNTs (SWCNTs). During the last decade, the environmental scanning transmission electron microscope (ESTEM) has been successfully employed to reveal the structural, chemical and morphological changes occurring in catalyst nanoparticles during CNT growth. However, the mechanisms of CNT cap formation are yet to be revealed under normal growth conditions: the SWCNT nucleation and growth process is too fast to be captured at currently available video frame rates (30 s^{-1}). We have successfully addressed this problem by slowing the kinetics of the process using a Co-Mo/MgO catalyst system and low pressures of acetylene (C_2H_2) and ethanol ($\text{C}_2\text{H}_5\text{OH}$) as carbon precursors. Our direct observations show that the CNT cap preferentially nucleates on certain surfaces and first finds two surfaces as suitable anchor points before lift-off. The detailed interplay of catalyst surface structure, cap formation, incubation period, and lift-off will be presented using atomic-resolution videos recorded under these novel CVD conditions. Our observations provide direct insight into the mechanisms of SWCNT growth and open up possibilities for diameter and chirality control.

11:00am **IS+AS+SP-FrM9 Operando FTIR-MS Studies of Methanol on WO₃/SBA-15: How Stable Are Methanol Species on Oxide?**, *Y. Yang*, Pacific Northwest National Laboratory, *C. Mims*, University of Toronto, Canada, *C. Peden*, Pacific Northwest National Laboratory, *J. Kwak*, Ulsan National Institute of Science and Technology, Korea

Methanol adsorption and desorption are important on many oxide surfaces, for instance, as probe molecules of surface active sites. In this study, atomic layer deposited (ALD) tungsten oxide on silica was used as oxide sample and dimethyl ethylene (DME) synthesis was observed by operando FTIR-mass spectroscopy (IR-MS). Methanol adlayer, which contains both methanol and methoxy, was formed by exposing the sample with methanol at low partial pressure (~ 1 torr) with carrier inert gas at ~ 1 bar. The stability of the adlayer molecules was observed under two conditions: a) exposed to pure argon purging at different temperatures up to 300 C overnight; b) with constant methanol partial pressure (1 torr) in ambient flow while DME synthesis processed. The kinetics study here requires isotopic deuterated methanol exchange ($\text{CD}_3\text{OH}/\text{CH}_3\text{OH}$). Operando IR results shows under condition a), the majority of the adlayer, both methanol and methoxy species, remained on the surface overnight after the highest temperature treatment. Methanol stability is even stronger than methoxy. Temperature dependent IR results show an isosbestic point between the

surface water and Methanol species which is direct evidence of water replacement by methanol adsorption. These results further confirms other earlier studies reported. However, under condition b), both replacements transient of surface methanol and methoxy species by deuterated flow are by far much faster. As expected, only CD₃/CH₃ group exchange was observed upon isotope switch in IR and MS results. Measured replacement time constant for Methoxy was ~1000 s and that for methanol was ~2000 s. These surface species transients are compared with simultaneous MS data of gas products with the similar scale of the surface species. These preliminary results indicate that the methanol and methoxy are by far more active on a crowded surface with gas phase methanol exposing comparing a surface with slightly lower coverage and no gas phase exposure. This is a good example of reactivity strong dependence on the surface coverage.

11:20am **IS+AS+SP-FrM10 Coupling Environmental High Resolution Transmission Electronic Microscopy and Raman Spectroscopy: Toward a More Comprehensive *In Situ* Characterization.** *M. Picher, R. Blankenship, S. Mazzucco, R. Sharma*, National Institute of Standards and Technology

In situ imaging, using an environmental scanning transmission electron microscope (ESTEM), has been successfully used to reveal and better understand the crucial chemical and physical processes occurring at the nanoscale, e.g. oxidation/reduction, coalescence, Ostwald ripening, surface reconstruction, substrate/catalyst interaction... However, the relevance of such ETEM studies can be diminished if the following two questions cannot be satisfactorily answered: i) Do high energy electrons affect the reaction mechanism? In other words: is the probed area representative of what is happening on the whole sample? ii) What is the sample temperature in the gaseous environment? Here, we present unique instrumentation that helps to solve these two issues by collecting Raman data during ETEM observation. We can now combine and compare the structural information and kinetics obtained from large (micrometer-scale) areas by the Raman spectrometer with the local information collected by the ETEM at the nanoscale. This system also enables us to simultaneously monitor the actual temperature of the probed material by analyzing shifts in Raman peak frequency. Moreover, this versatile optical setup can be used i) to investigate light/matter interactions (the current 532 nm laser can be easily replaced by any IR/Vis/UV wavelength) ii) as a heating source: the sample can be heated up to 1000°C at 15 mW with a 532 nm laser, iii) for general spectroscopy (absorption, photoluminescence, cathodoluminescence...).

This combined approach is made possible by the insertion of a parabolic mirror in between the sample holder and the lower pole piece of the microscope (Fig1. in Supp Info). It focuses a laser on the sample and collects the scattered Raman photons. A set of optics then carries the Raman signal to the spectrometer.

11:40am **IS+AS+SP-FrM11 New Tools for *In Situ* Chemical and Structural Analysis: Raman and Photoluminescence Go Inside the Vacuum Chamber.** *A.J. King*, Renishaw Inc.

Micro-Raman systems have become very popular tools for analysing novel materials in a wide variety of application areas. Their ease of use has driven them to be employed routinely with carbon materials (graphene, carbon nanotubes, diamond, diamond-like-carbon (DLC)); semiconductors (silicon, germanium, III-V and II-VI materials); photovoltaics (silicon, CIGS, CdTe, CZTS); Chalcogenides (MoS₂, Bi₂Te₃, Bi₂Se₃); as well as oxides, nitrides and carbides. This technology enables researches to probe the molecular structure for phase identification, stress and crystal quality. It can also be used for reaction and catalysis monitoring.

New demands are now being made that require the use of in-situ techniques with very high sensitivity. The ability to conduct measurements inside the vacuum chamber has been enabled with highly efficient optical probes and spectrometer technology to give the required performance in these demanding applications. This talk will cover the basic concepts of Raman spectroscopy, the instrumentation required for these measurements, and highlight some of the applications where in-situ Raman and photoluminescence can increase the understanding of vacuum processes and how they can be optimised to improve quality and yield.

Accelerating Materials Discovery for Global Competitiveness Focus Topic

Room: 202 B - Session

MG+AS+EM+NS+SA+SE+SP+SS+TF-FrM

Novel Synthesis Approaches and Innovative Characterization Techniques Coupled with Theory & Computations

Moderator: E.B. Svedberg, The National Academies, M.B. Holcomb, West Virginia University

8:20am **MG+AS+EM+NS+SA+SE+SP+SS+TF-FrM1 MWCT and Piezoelectric Thick Film Composites that Incorporate Graphene Electrodes.** *K. Cook-Chennault, S. Banerjee, R. Kappera, M. Chhowalla*, Rutgers University

Three-phase, PZT-Epoxy- Multi-walled Carbon-Nanotube (MWCNT) flexible thick films prepared by a combination of solvent and spin coating technique were prepared, where materials were spin coated onto flexible substrates. The substrates investigated included; stainless steel, graphene and graphene with PMMA. Graphene and graphene/PMMA films which were grown by a chemical vapor deposition process, and the film thicknesses were ~ 200 μm. The volume fraction of the MWCNTs was varied from 1% to 6%, while the PZT volume fraction was held constant at 30%. The strain coefficient and capacitance were measured as a function of the MWCNT volume fraction and used to determine the effective dielectric constant. Samples that incorporated graphene electrodes rendered higher dielectric properties in comparison to samples with graphene-PMMA. The maximum values of dielectric constant were ~ 4353, ~1945 and ~ 61, for samples with graphene, graphene/PMMA and no electrode respectively. Sample surface morphology and sample composition were observed using SEM and measured using Raman Spectroscopy respectively. Improved dielectric properties observed for samples with graphene coatings are due to graphene's high carrier mobility and its ability to readily conform to the surface of the sample.

8:40am **MG+AS+EM+NS+SA+SE+SP+SS+TF-FrM2 Morphological and Structural Characterization of Size-Selected Pt NPs Supported on TiO₂(110) and SiO₂/Si(111) via Polarized Total Reflection Fluorescence XAS in UHV.** *F. Behafarid, L.R. Merte*, University of Central Florida, *R. Gordon*, Argonne National Laboratory, *B. Roldan Cuenya*, University of Central Florida

A combination of polarized total reflection x-ray absorption spectroscopy (XAS) and atomic force microscopy (AFM) data have been used to determine the morphological properties of the size-selected micelle-prepared Pt nanoparticles (NPs) supported on TiO₂(110) and SiO₂/Si(111) in an ultrahigh vacuum (UHV) environment. The Pt NPs were cleaned in UHV using an O₂-plasma followed by annealing in O₂ (1x10⁻⁶ mbar) at 600°C after the *ex situ* sample transfer. Extended X-ray absorption fine-structure (EXAFS) measurements were carried out at Argonne National Laboratory in fluorescence mode. Measurements along different orientations, namely one perpendicular and two parallel to the sample surface were carried out on the Pt NPs supported on TiO₂(110). Our analysis revealed that while the Pt NPs on SiO₂ remained spherical, the NPs on TiO₂ wetted the substrate and adopted an epitaxial relationship with the support. It will be shown that the first shell EXAFS analysis of the data acquired along different directions provides valuable information regarding the size and aspect ratio of the NPs as well as the degree of disorder and strain in their structure. FEFF simulations were carried out on model NP shapes and the theoretical data compared with experimental EXFAS data.

9:00am **MG+AS+EM+NS+SA+SE+SP+SS+TF-FrM3 Materials Control on a Nanoscale: Artificial Oxide Structures.** *D.H.A. Blank*, MESA+Institute for Nanotechnology, University of Twente **INVITED**

In general, nanotechnology provides the tools for controlling key parameters for thin films performance: chemical composition (and crystalline structure at nano-sized domains), thickness and topography (including nano-scale patterning of thin films' surface) and controlled interfaces at the nanoscale.

As research in nanotechnology develops, new characterization and production tools, new materials and process models as well as more computational power will become available. Nanotechnology is giving a new boost to thin films' application development.

Pulsed Laser Deposition (PLD) is one of the attractive research tools for complex materials because it is fast and one can easily investigate a wide range of different materials and compositions. Currently, a major issue in the growth of oxide materials with PLD is the control of the surface

morphology. For most materials it is necessary to control the thickness and roughness of the thin films down to an atomic scale. Such well-controlled growth can also be used to manufacture artificially layered structures. In this way it is possible to create a whole new class of materials.

Much effort is put in the deposition of excellent textured layers without grain boundaries. In general the properties of highly oriented films approximate the properties of single crystals. Single or multi-layer structures require a well-conditioned process technique. The deposited layers must have a large homogeneity with well-defined material properties, smooth surfaces, and, in the case of oxides, the correct oxygen stoichiometry. Important is the possibility to combine PLD with standard *in-situ* diagnostic techniques, like *high pressure* Reflecting High Energy Electron Diffraction (RHEED).

With our development of pulsed laser deposition with control at atomic level we are able to control the growth of complex materials and to introduce new growth manipulations, like pulsed laser interval deposition. At present, new superlattices can be synthesized that exhibit rare properties, like multiferroics. Extremely sharp and homogeneous interfaces can be realized and this is, for example, yet utilized in SrTiO₃-LaAlO₃ interfaces and artificial ferroelectric structures. In this presentation I like to show this unique technique and their use in obtaining complex materials systems 'on demand'.

9:40am **MG+AS+EM+NS+SA+SE+SP+SS+TF-FrM5 Catalytic Micro-Nano- Motors Propelled by Bubbles**, *M.T. Manjare**, University of Georgia, Athens, *B. Yang*, University of Texas, Arlington, *Y.P. Zhao*, University of Georgia, Athens

Catalytic Micromotors are micro- or nano- objects that use catalytic reaction, most commonly H₂O₂ → H₂O + 1/2 O₂, to propel themselves in fluid environment. The motion of the motors can be controlled by designing different motor geometries and functionalizations and to perform variety of tasks such as cargo towing and biosensing. One of the mechanisms by which the motors move is bubble propulsion, i.e., the O₂ generated in the reaction forms bubbles and propel the motors by ejecting or bursting the bubbles. Bubble propulsion is proven to be the most efficient and fastest way to drive the motors. Here we report our new discoveries on bubble propelled catalytic motors. For spherical particles, electron beam evaporation method is used to coat half of their surface with Pt and to make them as Janus motors. A new bubble propelled quasioctilatory translational motion is observed only for big motors. The motion coincided with bubble growth and burst resulting from catalytic reaction. A physical model was proposed which explained that bubble growth imparts a growth force on the motor to move it forward and instantaneous local pressure depression due to bubble burst causes the motor to move backward. The competition of the two processes generates a net forward motion. The bubble propulsion mechanism involves hydrodynamics, growth kinetics, and mass/momentum transport. In order to understand the detailed mechanism, we have investigated the mass transport in microtubular jet engines, a major bubble propelled motor. A one dimensional mass transport model using basic principles of diffusion and reaction is built to explain the effect of environmental factors such as fuel concentration and of geometry on the motion. Numerical investigations of the motion-related parameters, such as O₂ flux, bubble generation rate and frequency, and average speed of the microjet motors during bubble growth, are found to depend closely on the length and opening radius of the microjet and the concentration of H₂O₂ in the surrounding environment. The theoretical results are in good agreement with the motion of Graphene oxide tubular microjet motors we have fabricated.

10:00am **MG+AS+EM+NS+SA+SE+SP+SS+TF-FrM6 Erosion Resistant Physical Vapor Deposition Coatings for High Temperature Polymer Matrix Composites Applications**, *S. Dixit*, *M. Chin*, *R. Dixit*, Plasma Technology Inc.

The advantages of replacing metals in aircraft turbine engines with High-Temperature Polymer Matrix Composites (HTPMC's) include weight savings accompanied by high strength to weight ratio, and lower manufacturing costs. Most of the nacelle of a modern aero gas turbine is made of HTPMC, a component that accounts for approximately 25% of the weight and 20% of the cost of the power plant. Unfortunately, they are limited to applications where they are not exposed to high-temperature oxidizing atmospheres and/or particulates from ingested air. This is because oxidation and erosion occur on the surface, leading to weight loss, and/or cracking on the surface and a consequent decline of mechanical properties over time. Resistance to surface erosion is one rarely reported property of HTPMC's in engine applications because HTPMC's are generally softer than metals and their erosion resistance suffers.

* **TFD James Harper Award Finalist**

Although prior research has shown that oxidation can be slowed down when metallic or ceramic coatings are applied onto HTPMC's, there remains a need for erosion-resistant coatings that protect HTPMC's from high-velocity particulates in the engine flow path. These erosion-resistant coatings could extend the life of polymer composites and also reduce the overall cost of the turbine assembly. Hence in this paper we report the development of coating materials that are compatible with HTPMC's such as Avimid N and AFR-PE-4 using Cathodic Arc Physical Vapor Deposition (CAPVD). We report the feasibility of applying multilayer PVD TiN coatings onto the HTPMC substrates and characterize their adhesion, microstructure and erosion resistance. We also show the effectiveness of duplex process of thermal spray and PVD to enhance the overall adhesion of the multilayer coating.

10:20am **MG+AS+EM+NS+SA+SE+SP+SS+TF-FrM7 Poking Tips at Surfaces: Mechanical and Electronic Properties of Atomically Defined Interfaces**, *P. Grutter*, McGill University, Canada **INVITED**

How does stuff break? An important step in this process is inelastic deformation of the material, the formation of a first dislocation. We report on the for the first experiments which due to the small size and atomic scale control of the indenter allow a direct quantitative comparison with molecular dynamics simulations and state-of-the-art electronic transport theory.

We have studied the formation of the smallest permanent indentation in the Au(111) model surface by a combination of scanning tunneling microscopy (STM) and atomic force microscopy (AFM) in ultrahigh vacuum (UHV). We use field ion microscopy (FIM) to characterize the nanometer scale spherical apex of the W(111) indenter in UHV prior to the indentation experiments [1,2]. Knowledge of the indenter geometry is necessary to extract quantitative parameters such as contact pressures and stresses within the sample during indentation.

Traditional nanoindentation measures depth to high precision, but typically does not possess the force resolution (nN) to detect initial plastic events [3]. Indentation with standard AFM allows for excellent force resolution, but large piezo displacements required to load the contact with a soft cantilever hamper the extraction of true indentation depth because of quantitative optical beam deflection calibration issues (beam placement, sensitivity to mode shape, etc.) and piezo creep. I will describe how our set-up overcomes these limitations and allows us to quantitatively assess elastic and plastic behaviour in an indentation curve.

We report on the transition from elastic to plastic deformation in the indentation of Au(111). This is done by producing arrays of indentations to forces near the plastic yield point and examining the resulting force-displacement curves for both elastic and plastic indentation sites. Plasticity can be identified by features in the force displacement curves, such as the sudden displacement excursions of the tip (pop-ins), the work done by the indenter, and the sink-in depth measured at mild repulsive loads. These indicators of plasticity can also be correlated with the permanent impressions in the surface imaged by STM. The measured forces at the initial yield points correspond to shear stresses lower than those expected for the homogeneous dislocation nucleation. We suggest that heterogeneous nucleation involving surface effects and atomic scale indenter roughness is likely to play a role in the observed plastic behaviour.

[1] W. Paul et al. Nanotechnology 23, 335702 (2012) [2] D. J. Oliver et al., PNAS 109, 19097 (2012) [3] Minor et al., Nature Materials 5, 697 (2006)

11:00am **MG+AS+EM+NS+SA+SE+SP+SS+TF-FrM9 Functionalized Shape Memory Polyester Biomaterials**, *V. Sheares Ashby*, University of North Carolina at Chapel Hill **INVITED**
Functionalized Shape Memory Biomaterials

Valerie Sheares Ashby

*University of North Carolina at Chapel Hill, Department of Chemistry
Chapel, Hill, NC 27599*

919-962-3663(Phone); 919-9625467(Fax)

ashby@email.unc.edu

Shape memory polymers (SMPs) are a class of smart materials that can change their shape in a predetermined fashion when exposed to the appropriate external stimulus. Since Langer and Lendlein first demonstrated the tremendous potential of SMPs in biomedical applications there has been a growing interest in utilizing these materials as intelligent medical devices and minimally-invasive implants. Our research focuses on several areas: micro- and nanotopography, reactive functionality and switching stimuli. Recently, we have developed thermally responsive micro-patterned poly(ϵ -caprolactone) (PCL) shape memory films to examine the interaction of human mesenchymal stem cells (hMSCs) with dynamic surface patterns using PRINTTM (pattern replication in non-wetting templates). We have also begun research on novel polymer structures containing functionality with the goal of developing SMPs capable of micro- or nanoscopic shape

memory and post-functionalization. Finally, there have been several examples of dual (one temporary shape) and triple shape memory (two temporary shapes). Our efforts focus on the synthesis of novel bifunctional monomers and biodegradable prepolymers containing photo-responsive side groups (cinnamamide or cinnamate) using a polycondensation method to allow uniform repeat units each possessing a photo group, followed by end-functionalization and crosslinking to create networks with photo and thermal shape memory switches. The synthesis of these materials, which has led to shape memory polymers with switching temperatures near physiological temperature and unique functionality, in addition to characterization of thermal and shape memory properties, will be presented. Fabrication of the patterned surfaces, initial cytotoxicity and cellular response to dynamic shape switching will also be discussed.

Nanoparticle-Liquid Interfaces Focus Topic

Room: 201 B - Session NL+AS+BI+SA-FrM

Emerging Methods to Identify and Measure Nanomaterials in Biological Environments

Moderator: G. Ceccone, European Commission, Joint Research Centre, IHCP, Italy

8:20am **NL+AS+BI+SA-FrM1 3D Views of Hydrated Biological Cells with Soft X-ray Tomography, C.A. Larabell**, University of California, San Francisco **INVITED**

SXT is similar in concept to the well-established medical diagnostic technique, computed axial tomography (CAT), except SXT is capable of imaging with a spatial resolution of 50 nm, or better. We examine whole, hydrated cells (between 10-15 μm thick), eliminating the need for time-consuming and potentially artifact-inducing embedding and sectioning procedures. Cells are rapidly frozen then imaged using photons with energies between the K shell absorption edges of carbon (284 eV, $\lambda=4.4$ nm) and oxygen (543 eV, $\lambda=2.3$ nm). In this energy range, photons readily penetrate the aqueous environment while encountering significant absorption from carbon- and nitrogen-containing organic material. Consequently organic material absorbs approximately an order of magnitude more strongly than water, producing a quantifiable natural contrast image of cellular structures. By collecting images from multiple angles through 360 degrees of rotation, SXT reconstructions yield information at isotropic resolution.

Images are formed using unique optics called zone plates (ZP). An X-ray ZP optic consists of a number of concentric nanostructured metal rings, or zones, formed on a thin X-ray transmissive silicon nitride membrane. The width of the outermost ring determines the spatial resolution of the ZP lens, whereas the thickness of the rings determines the focusing efficiency. In our microscope, we use a condenser ZP lens with an overall diameter of 1 cm and an outer zone width of 50 nm. The high-resolution objective ZP lens has a diameter of 63 μm , 618 zones, a focal length of 650 μm at 2.4 nm wavelength, and an outer zone width of 50 nm.

Because SXT is fast (~ 5 min per tomographic data set), we can examine large numbers of cells. Since organic material absorbs approximately an order of magnitude more strongly than water, a unique and quantifiable natural contrast image of cellular structures is generated. X-ray absorption follows Beer's Law, therefore the absorption of photons is linear and a function of the biochemical composition at each point in the cell. As a result, a linear absorption coefficient (LAC) value of each voxel can be calculated. For example, lipid drops with high concentrations of carbon are more highly absorbing ($\text{LAC}=0.7 \text{ mm}^{-1}$) than fluid-filled vesicles ($\text{LAC}=0.2 \text{ mm}^{-1}$). We can determine the position of specific molecules by overlaying fluorescence microscopy signals on cell structures obtained with x-ray imaging. In addition, we can directly determine the locations and numbers of metal probes throughout the cell.

9:20am **NL+AS+BI+SA-FrM4 Ultrathin Electron Transparent Membranes as a Platform for Scanning Electron and Photoelectron Imaging and Spectroscopy of Fully Hydrated Nanoparticles, X.M. Ma, J. Geisler-Lee**, Southern Illinois University Carbondale, **M. Amati, L. Gregoratti**, Sincrotrone Trieste, Italy, **S. Guenther**, Technical University Muenchen, Germany, **M. Kiskinova**, Sincrotrone Trieste, Italy, **A. Kolmakov**, Southern Illinois University Carbondale

The increased use of engineered nanoparticles (ENPs) in biomedical applications and their inevitable release into the environment has prompted considerable need to study of their uptake, accumulation and transport inside biological tissue and in plants. This is particularly true for addressing the ENPs fate on a cellular level which inevitably requires the microscopy approach. For long time optical microscopy with the resolution in the order

of 100 nm was the major tool available. Better resolution can be readily achieved with traditional transmission (TEM) or scanning (SEM) electron microscopy. However, it requires histological sample treatments such as fixation, staining, dehydration, freezing etc which excludes *in vivo* (*in situ*) modes of observations and can alter their native morphology, functionality and living cycles. Different from standard environmental SEM, where the near sample pressure is limited by ca few tens of Torr, we are actively working on fabrication and tests of electron transparent membranes for ambient pressure electron spectromicroscopy and its application to fully hydrated samples for phytotoxicity, and materials research. Such enclosed environmental cells, equipped with 50-100 nm windows transparent for 10-20 keV electrons, can maintain the sample at atmospheric pressure and/or fully hydrated. This approach is beneficial compared with dry methods since *in vivo* SEM/TEM observations at nanoscale can be performed. Using this methodology, we were able to image the uptake of silver (Ag) NPs by living Arabidopsis roots on a cellular level. It was shown that NPs with the sizes larger than 20 nm accumulate preferably on the surface of the cellular walls and do not to traverse the plant cell membrane.

Recent developments in high yield fabrication and handling protocols of ultrathin (~1 nm) membranes, such as graphene or graphene oxide sheets with thicknesses comparable to the effective attenuation length (EAL) of 200-1000 eV electrons opened the opportunity to perform traditional XPS (X-ray Photoelectron Spectroscopy) and AES (Auger Electron Spectroscopy) at the interfaces between the membrane and fully hydrated samples. Using model water solutions and NPs, we report here on major design principles of such cells as well on first spectral demonstrations, advantages and limitations of this new technique.

9:40am **NL+AS+BI+SA-FrM5 Small-angle X-ray Scattering Investigation of Functional Materials at Inorganic-Macromolecular Interfaces, T.W. van Buuren, T.M. Willey, J.R.I. Lee, I.C. Tran, M. Bagge-Hansen**, Lawrence Livermore National Laboratory

Development in nanoscale engineering has enabled bioelectronics that can mimic and/or interact with the biological systems. Lipid bilayer-functionalized Si nanowires are considered as a promising candidate for the construction of bioelectrochemical devices. These biomimetic lipid bilayers serve as a general host matrix for bio-functional components such as membrane proteins. Though meaningful technological advancement of these materials has been made, critical questions about their structural and chemical composition remain. Small angle x-ray scattering (SAXS) experiments are used to investigate the structure of the lipid bilayers on Si nanowires, which provide information on the overall 1-D bilayer structure, the effect of substrate curvature on the lipid packing and local self-organization. The SAXS derived lateral-averaged characterizations are then corroborated with local arrangements of lipid bilayers on Si nanowires revealed by Scanning Transmission X-ray Spectroscopy (STXM). The results provide insights into a number of unresolved questions that are crucial for the comprehensive understanding this class of materials.

This work performed under the auspices of the U.S. Department of Energy by Lawrence Livermore National Laboratory under Contract DE-AC52-07NA27344.

Advanced Surface Engineering

Room: 203 C - Session SE+EN-FrM

Surface Engineering for Energy Conversion and Harvesting

Moderator: A.A. Voevodin, Air Force Research Laboratory, **M. Stüber**, Karlsruhe Institute of Technology, Germany

8:20am **SE+EN-FrM1 Nanoscale Thermal Transport, G. Mahan**, Penn State University **INVITED**

Nanoscale materials and devices are usually composed of materials whose bulk thermal conductivity has been measured and is well understood. However, new effects arise when they are components of nanoscale materials: (i) The thermal boundary (Kapitza) resistance at each interface is often the largest component of the thermal resistance of the nanomaterial. Experimental and theoretical values for these boundary resistances are scarce; (ii) Phonon mean-free-paths are also nanometers, and diffraction effects from the nanostructure are important. (ii) The interfaces and nanostructures themselves will have new phonon modes. We briefly review recent work on this field. We also discuss some of our own work on calculations of Kapitza resistances at two kinds of boundaries: (i) metal-insulator, and (ii) liquid solid.

- 1) G.D. Mahan, *Nanoscale and Microscale Therm. Eng.* 12, 294 (2008)
- 2) G.D. Mahan, *Phys. Rev.* B79, 075408 (2009)
- 3) G.D. Mahan, *Appl. Phys. Lett.* 98, 132106 (2011)
- 4) S. Neogi and G.D. Mahan, in press

9:00am **SE+EN-FrM3 Electrical and Thermal Properties and Understanding Interface Chemistry and Structure of Metal-Pnictogen Chalcogenide Interfaces**, *F. Devender, T. Borca-Tasciuc, G. Ramanath, I. Seshadri*, Rensselaer Polytechnic Institute

Thermoelectric materials are attractive for realizing eco-friendly solid-state refrigeration, and waste heat recovery and harvesting [1]. In addition to obtaining materials with high thermoelectric figure of merit ZT, it is key to tailor the electrical and thermal properties of interfaces of these materials with metals through control of interface structure and chemistry for high performance device applications [2]. Here, we describe the properties of interfaces comprised of two high figure-of-merit pnictogen chalcogenides, namely, n-Bi₂Te₃ and p-Sb₂Te₃ and Cu, Ni, Ti and Ta. Our results show that the thermal interface conductance of structures is insensitive to the majority charge carrier type. Cu shows the highest thermal conductance, which is about tenfold higher than that of the other interfaces studied. However, we find that interfaces of Ni and Ta with p-type materials show more than tenfold higher electrical conductivities than their interfaces with n-type materials. In order to understand these trends, we embarked on a study of the interface chemistry and structure using a combination of Rutherford Backscattering Spectrometry (RBS) and X-Ray Diffractometry (XRD). Our results from XRD analysis show that all the four metals studied tend to form interfacial phase with Tellurium in different stoichiometric amounts. RBS analysis show that just after 150 °C annealing for 30 minutes Cu diffuses significantly in both n-Bi₂Te₃ and p-Sb₂Te₃, whereas Ni shows significant compositional changes in p-Sb₂Te₃ while retaining the multilayer structure with n-Bi₂Te₃. Ti and Ta maintain multilayer structure with both n-Bi₂Te₃ and p-Sb₂Te₃. We will discuss our findings and our inferences of the interface chemistry/structure property relationships. Our results will be important for designing metal contacts to any thermoelectric material based device and especially for applications like spot cooling in electronics chips where interfacial properties have become the bottleneck for realizing high-efficiency thermoelectric cooling.

References

- 1) S.B. Riffat, and X.L. Ma, "Thermoelectrics: A review of present and potential applications," *Applied Thermal Engineering*, vol. 23, 2003, pp. 913-935.
- 2) G. Chen, M.S. Dresselhaus, G. Dresselhaus, J.P. Fleurial, and T. Caillat, "Recent developments in thermoelectric materials," *International Materials Reviews*, vol. 48, 2003, pp. 45-66.

9:20am **SE+EN-FrM4 Imaging of Electron-Phonon Interaction on the Atomic Scale**, *A.A. Voevodin, I. Altfeder*, Air Force Research Laboratory, *K.A. Matveev*, Argonne National Laboratory

The control of thermal transport through coupled metal and non-metal interfaces is critical for many applications, including electronic device operation, photovoltaic power generation, sensors, and many others. For design and engineering of such interfaces, the energy coupling between electrons and phonons for heat transfer needs to be assessed. An atomic level thermometer was developed to experimentally study interfacial thermal conductivity on a single molecular scale using an inelastic electron tunneling spectroscopy (IETS) combined with scanning tunneling microscopy (STM). The IETS-STM had led to a discovery of vacuum phonon tunneling across nanometer contact gaps as it can probe electron-phonon coupling at atomic scale [1]. The further development of the STM-based spectroscopic imaging technique discussed here provides direct real-space imaging of electron-phonon coupling parameter [2]. This is demonstrated using the combination of STM and IETS for thin Pb islands epitaxially grown on 7x7 reconstructed Si(111). Electron-phonon interaction increases when the electron scattering at the Pb/Si(111) interface is diffuse and decreases when the electron scattering becomes specular. The effect is driven by transverse redistribution of the electron density inside a quantum well.

References:

- [1] I. Altfeder, A. A. Voevodin, A. K. Roy, *Physical Review Letters*, 105 (2010) 166101.
- [2] Igor Altfeder, K. A. Matveev, A. A. Voevodin, *Physical Review Letters* 109, 166402 (2012).

9:40am **SE+EN-FrM5 Generation of Cu₂S Nanoparticles via Cluster Beam Deposition for Bulk Heterojunction Photovoltaics**, *M.W. Majeski, I. Bolotin, L. Hanley*, University of Illinois at Chicago

Hybrid inorganic-organic based nanocomposite films are prepared by cluster beam deposition for photovoltaic applications (F.D. Pleticha, *et al.*, *J. Phys. Chem. C* 116: 2012, 21693). Semiconducting copper(I) sulfide (Cu₂S) nanoparticles are co-deposited into an organic matrix, pentacene, to create a bulk heterojunction where p-type Cu₂S is expected to behave as an electron acceptor and pentacene behaves as a donor. Generation of Cu₂S nanoparticles are achieved by pulsed DC reactive magnetron sputtering of a Cu target with argon while forming compound clusters via introduction of reactive hydrogen sulfide gas. Reactive sputtering occurs in a gas aggregation source in which Cu₂S nanoclusters are allowed to nucleate and grow for subsequent deposition onto a substrate. Pulsing the DC power at 20 kHz allows for stable process parameters with an absence of arcing and has been shown previously to improve the quality of the deposited films. Finally, Cu₂S-pentacene nanocomposite films are also prepared with low energy acetylene ion assisted deposition. Film properties and nanoparticle stoichiometry are analyzed with X-ray photoelectron spectroscopy, transmission electron microscopy, and high angle annular dark field scanning transmission microscopy. Photovoltaic properties of these Cu₂S-pentacene nanocomposite films will be discussed.

10:00am **SE+EN-FrM6 Fabrication of Water-Splitting Photocatalytic Electrodes by "Particle-Transfer" Processing**, *T. Minegishi, T. Yamada, N. Nishimura, J. Kubota, K. Domen*, The University of Tokyo, Japan

We developed a process of fabricating planar electrodes from photocatalytic powder, and observed a high photo-electrocatalytic activity of LaTiO₂N for H₂O splitting in aqueous solutions. This technology, hereafter we call the "particle transfer (PT) method", is applicable for various kinds of photoactive semiconducting powder catalysts. We first prepare powder catalysts with a maximum grain size of a few μm. A thin layer of the powder (thickness < 0.5 μm) is spread on a planar substrate using a suspension in organic solvent. Then this layer is over-coated with a thin Nb layer and then a thick Ti layer by means of radio-frequency magnetron sputtering. The metallic Nb layer makes a good mechanical and electric contact between the grains and the Ti layer, which serves as a good electric conductor. Finally this multilayer is peeled off onto another glass substrate using an adhesive (such as epoxy resin), and a conductive electrode covered by the catalytic grains is completed. In this work we used LaTiO₂N powder loaded with 5 wt% IrO₂. The LaTiO₂N powder was synthesized by NH₃ flow gas treatment at 1223 K on La₂Ti₂O₇ prepared by a molten salt method [1]. The purity of LaTiO₂N was checked by X-ray diffraction. This material exhibits absorption of visible light shorter than 600 nm and can potentially utilize about a half of the solar energy. The cross sectional view of this electrode by EDX-aided scanning electron microscopy indicates the left-over grains of LaTiO₂N mostly in firm contact with the Nb layer laminating the Ti conducting layer. The grains formed monolayer in most of places, laterally interlocking one another.

This electrode was subjected to potential-versus-current measurement in 1 M Na₂SO₄ solution (pH 13.5) under illumination of AM 1.5D solar simulator. The anodic photocurrent reached ~ 2 mA cm⁻² at 1.0 V vs RHE, which is ~100 times higher than that on a LaTiO₂N powder-coated conductive glass substrate [2]. This is attributed to the well-controlled grain-substrate contact by the Nb layer. Similar effects were observed by replacing Nb with Ta, Zr or Ti. Furthermore, the gas products (O₂ from this electrode, H₂ from the counter Pt electrode) was detected in two-vessel electrochemical system separated by a glass filter. From the PT LaTiO₂N electrode, O₂ gas bubbled out at a rate (~ 0.1 μmol cm⁻² min⁻¹) exactly matching the photo-anodic current. Evidently, the PT method makes a breakthrough in the efficiency of solar hydrogen generation in water splitting, making use of the diversity of semiconductor powder catalysts.

- [1] P. A. Fuiere *et al.*, *J. Am. Ceram. Soc.* **74** (1991) 2876.
- [2] H. Hashiguchi *et al.*, *Bull. Chem. Soc. Jpn.* **82** (2009) 401.

Scanning Probe Microscopy Focus Topic

Room: 202 C - Session SP+AS+EM+GR+MI+NS+SS-FrM

Probing Electronic and Transport Properties

Moderator: S. Allen, The University of Nottingham, UK

8:20am **SP+AS+EM+GR+MI+NS+SS-FrM1 STM Mapping of Thermoelectric Power on Graphene across Defects and Boundaries, J. Park,** Oak Ridge National Laboratory, *G. He, R.M. Feenstra,* Carnegie Mellon University, *A.P. Li,* Oak Ridge National Laboratory

We present the spatially resolved thermoelectric power on epitaxial graphene on SiC by a scanning tunneling microscopy (STM) method. A thermovoltage is induced by a temperature difference between tip and sample and variations of thermovoltage are distinguished at defects and boundaries with atomic resolution. The epitaxial graphene shows a high thermoelectric power of 42 $\mu\text{V/K}$ with a big change (9.6 $\mu\text{V/K}$) at the monolayer-bilayer boundary. Also, the thermopower is modified by Friedel oscillations of the charge density in graphene. Besides the change at the monolayer and bilayer graphene boundary, the thermopower also provides spectroscopy maps which reveal domain structures induced by collapsed graphene wrinkles that not obvious in STM images. The thermopower distribution measurement with STM thus allows probing the electronic, thermoelectric, and structural properties down to the individual defect level.

8:40am **SP+AS+EM+GR+MI+NS+SS-FrM2 New Milestones in Scanning Probe Microscopy: Graphene on Rh(111) Studied by DFT, STM and NC-AFM, A. Thissen,** SPECS Surface Nano Analysis GmbH, Germany

Graphene and its interface with metallic substrates is proposed to be used in many technological applications. It can act as a protection layer for the underlying substrate, as a spin-filtering material separating two layers of a ferromagnetic material, or, in case of its growth on a lattice mismatched surfaces [for example, Ir(111), Rh(111), or Ru(0001)], as a template for the preparation of ordered arrays of clusters.

For graphene on Rh(111) [Fig.1(a-c)] several regions of different arrangements of carbon atoms above a Rh(111) substrate can be found: ATOP [A; carbon atoms are above Rh(S-1) and Rh(S-2) atoms], HCP [H; carbon atoms are above Rh(S) and Rh(S-2) atoms], FCC [F; carbon atoms are above Rh(S) and Rh(S-1) atoms], and BRIDGE [B; Rh(S) atoms bridge the carbon atoms]. These places are marked in Fig.1(a) by circle, down-triangle, square, and stars, respectively. Among them, the BRIDGE positions are expected to be the most energetically favorable for the nucleation of deposited atoms on top of a graphene layer.

In this contribution we present the combined study of the graphene/Rh(111) system via application of the state-of-the-art DFT calculations, STM, and NC-AFM. The calculated imaging contrast for STM between all high-symmetry positions for graphene/Rh(111) is in very good agreement with experimental results and this contrast does not depend on the sign of the bias voltage applied between a tip and the sample. As opposed to the latter observation, the imaging contrast in atomically-resolved AFM measurements depends on the frequency shift of the oscillating tip that can be understood on the basis of measured force-spectroscopy curves.

For this the KolibriSensor™, a new quartz sensor that excels in its performance reliability is used either for RT to HT studies in an SPM Aarhus 150 or for LT studies in the new Tyto™ scan head mounted into a JT-SPM. It is controlled by the Nanonis Control System.

9:00am **SP+AS+EM+GR+MI+NS+SS-FrM3 Electric Field Tuning of 2-dimensional Electrons in Graphene and Topological Insulators, J.A. Stroscio, J. Ha,** National Institute of Standards and Technology **INVITED**

The recent advances in classification of matter in terms of topological band theory have spurred a great deal of interest in synthesizing new materials demonstrating new topologically related properties. In a large class of these materials there are robust surface states on the spatial boundaries with vacuum. These surface states possess linear dispersive bands with chiral properties, similar to graphene. In this talk I will review our scanning tunneling spectroscopy measurements of graphene in applied electric field and magnetic fields [1-4] and compare them to some new results of applying electric fields in tunneling spectroscopy measurements of topological insulators [5,6].

Gate mapping tunneling spectroscopy has proved to be a powerful probe of the 2-dimensional electron system in graphene. In the presence of moderate disorder the charging of graphene quantum dots localized in the disorder potential has been observed with graphene on SiO₂ [1]. Intrinsic many body effects were observed in the renormalization of the dispersion velocity

when substrate disorder was reduced using boron nitride spacer layers between graphene and SiO₂ [4]. In contrast, removing the substrate and creating suspended graphene membranes was seen to generate pseudomagnetic fields localizing the carriers in response to the strain generated from the forces between the probe and graphene membrane [3].

In the topological insulator Sb₂Te₃, we achieved gate tunable devices which are suitable for low temperature scanning tunneling microscopy (STM) studies by designing sample holders with back gating capability [5]. Thin films are epitaxially grown on pre-patterned SrTiO₃ substrates which are mounted on the specially designed sample holders. This allows *in-situ* gating on epitaxial films without any *ex-situ* processing of the sample [5]. In 3 QL thick Sb₂Te₃ films we observe a gap opening at the Dirac point due to the coupling of the top and bottom surface states [6]. More importantly, the gap is found to be tunable by the gate field, indicating the possibility of observing a topological phase transition in this system. A comparison of the data with an effective model of 3D topological insulators suggests that 3QL Sb₂Te₃ belongs to the quantum spin Hall insulator class.

- [1] S. Jung *et al.*, *Nature Physics* **7**, 245 (2011).
- [2] G. M. Rutter *et al.*, *Nature Physics* **7**, 649 (2011).
- [3] N. N. Klimov *et al.*, *Science* **336**, 1557 (2012).
- [4] J. Chae *et al.*, *Phys. Rev. Lett.* **197**, 116802 (2012).
- [5] T. Zhang *et al.*, *Phys. Rev. B* **87**, 115410 (2013).
- [6] T. Zhang *et al.*, arXiv:1304.3661.

9:40am **SP+AS+EM+GR+MI+NS+SS-FrM5 SPM: Manipulating Spin to Operating Molecular Nanomachines, S.-W. Hla,** Argonne National Laboratory **INVITED**

We combine scanning tunneling microscopy (STM) imaging, manipulation and spectroscopy to investigate and manipulate magnetic, electronic, and mechanical properties of atoms and molecules on surfaces. This talk will highlight advances achieved by STM studies at atomic and molecular scale [1-3]. In spintronic area, we will present imaging and manipulation of atomic spin using a spin-polarized STM tip [1]. Here, individual cobalt atoms assembled as a chain on a Mn monolayer on W(110) surface appear different shapes due to their spin directions. In nanoscale superconductivity area, donor-acceptor type (BETS)₂GaCl₄ molecular clusters on a Ag(111) surface opens up the possibility to explore superconducting phenomena locally [2]. In this part, electronic structure evolutions at molecule-metal boundaries and manipulation of superconducting clusters will be presented. Quenching of surface state electrons due to the molecular superconducting state will also be discussed. Finally, operations of complex molecular motors using STM manipulation on a Au(111) surface will be shown. Interestingly a selective tunneling into specific rotor arms result in a controlled directional rotation of the motor. The inherent molecular design is critical to achieve such directional control. These innovative experiments are tailored to address several critical issues covering both for fundamental understanding, and for demonstration of novel molecule based nanodevices on materials surfaces.

- [1] D. Serrate, P. Ferriani, Y. Yoshida, S.-W. Hla, M. Menzel, K. von Bergmann, S. Heinze, A. Kubetzka, and R. Wiesendanger. *Imaging and manipulating the spin direction of individual atoms.* *Nature Nanotechnology* **5**, 350-354 (2010).
- [2] K. Clark, A. Hassanien, S. Khan, K.-F. Braun, H. Tanaka, and S.-W. Hla. *Superconductivity in just four pairs of (BETS)₂-GaCl₄ molecules.* *Nature Nanotechnology* **5**, 261-265 (2010).
- [3] U.G.E. Perera . F. Ample, H. Kersell, Y. Zhang, G. Vives, J. Echeverria, M. Grisolia, G. Rapenne, C. Joachim, and S.-W. Hla. *Controlled clockwise and anticlockwise rotational switching of a molecular motor.* *Nature Nanotechnology* **8**, 46-51 (2013).

10:20am **SP+AS+EM+GR+MI+NS+SS-FrM7 New Experiments and Applications Made Possible by a Low Temperature 4-Tip STM with UHV-SEM Navigation, A. Bettac, B. Guenther, J. Chrost, J. Hilton, J. Koebel, A. Feltz,** Omicron NanoScience, Germany

A major challenge in the development of novel devices in nano- and molecular electronics is their interconnection with larger scale electrical circuits required to control and characterize their functional properties. Local electrical probing by multiple probes with STM precision can significantly improve efficiency in analyzing individual nano-electronic devices without the need of a full electrical integration. Recently we developed a microscope stage that merges the requirements of a SEM navigated 4-probe STM and at the same time satisfy the needs for high performance SPM at low temperatures.

Besides SEM/STM probe fine navigation and imaging with atomic resolution at temperatures of T<5K, the pm-stability of the LT NANOPROBE expands applications to tunneling spectroscopy and even the creation or modification of nanostructures or single atoms by a sharp and

precise SPM probe. A further milestone in the development of the instrument was the implementation of the Qplus- NC-AFM mode for imaging on insulating surfaces. The Qplus measurement becomes important if nanowires/nanostructures are deposited on an insulating substrate for a better electrical decoupling of the nanowire from the substrate. In this case the Qplus sensor can be employed to locate the nanostructures and, after finding the structure, to carry out conductance measurements.

In this contribution we will present first Qplus results obtained with the LT Nanoprobe at low temperatures. Furthermore we will focus on measurements that prove the performance level of the instrument as well as on tunneling spectroscopy and atom manipulation experiments on Ag(111) at temperatures of $T < 5K$.

10:40am **SP+AS+EM+GR+MI+NS+SS-FrM8 Electrical Characterization of GaAs Nanowires with a 4-tip STM.** *B. Voigtlaender, S. Korte, V. Cherepanov, Peter Grünberg Institut (PGI-3), Forschungszentrum Jülich, Germany, M. Steidl, W. Zhao, P. Kleinschmidt, T. Hannappel, TU Ilmenau, Germany, W. Probst, University of Duisburg-Essen, Germany*

III-V semiconductor nanowires are promising building blocks for novel semiconductor devices in future electronic and opto-electronic applications such as solar cells. In this context the distribution of the dopant over the nanowires is of great importance. Resistance profiles of as-grown freestanding GaAs nanowires were measured with a multitip scanning tunneling microscope (STM) used as nanoprobe. Four point probe resistance measurements were performed along the nanowire. The dopant induced carrier concentration along the wire was determined from the resistance measurements and geometrical data. It was found that in the high temperature growth region (450°C) the carrier concentration is about one order of magnitude lower than in the low temperature regime (400°C). The NWs exhibit high mechanical elasticity, they can be deformed by the STM tips and revert to their original shape when released. Even extreme bending of a NW did not show a significant influence on its conductivity. These measurements were performed using a multi-tip scanning tunneling microscope (STM) in which four independent STM units are integrated on a diameter of 50 nm, resulting in an unsurpassed mechanical stability, enabling atomic resolution imaging with each tip. The heart of this STM is a new type of piezoelectric coarse approach called KoalaDrive. The coarse positioning of the tips is done under the control of an SEM. This multi-tip instrument is suited to perform electrical measurements such as local potential measurements at the nanoscale.

11:00am **SP+AS+EM+GR+MI+NS+SS-FrM9 Atomic and Electronic Structure of an Alloyed Topological Insulator $Bi_{1.5}Sb_{0.5}Te_{1.7}Se_{1.3}$.** *W. Ko, I. Jeon, H.W. Kim, H. Kwon, Samsung Advanced Institute of Technology, Republic of Korea, S.-J. Kahng, Korea University, Republic of Korea, J. Park, J.S. Kim, Pohang University of Science and Technology, Republic of Korea, S.W. Hwang, H. Suh, Samsung Advanced Institute of Technology, Republic of Korea*

The alloyed compound $Bi_{2-x}Sb_xTe_{3-y}Se_y$ has been argued to exhibit both topological surface states and insulating bulk states, but not yet been studied with local probes on the atomic scale. Here we report on the atomic and electronic structures of $Bi_{1.5}Sb_{0.5}Te_{1.7}Se_{1.3}$ studied using scanning tunneling microscopy (STM) and spectroscopy (STS). Although there is significant surface disorder due to the alloying of constituent atoms, cleaved surfaces of the crystals present a well-ordered hexagonal lattice in STM topographs with 10 Å high quintuple layer steps. STS results reflect the band structure and indicate that the surface state and Fermi energy are both located inside the energy gap. In particular, the surface states do not show any electron back-scattering; due to their topological nature they are extremely robust. This finding demonstrates that alloying is a promising route to achieve full suppression of bulk conduction in topological insulators whilst keeping the topological surface state intact.

11:20am **SP+AS+EM+GR+MI+NS+SS-FrM10 Schottky Barrier Height Measurements of Cu/Si(001), Ag/Si(001), and Au/Si(001) Interfaces Utilizing Ballistic Electron Emission Microscopy and Ballistic Hole Emission Microscopy.** *R. Balsano, V.P. LaBella, College of Nanoscale Science and Engineering*

The Schottky barrier heights of both n and p doped Cu/Si(001), Ag/Si(001), and Au/Si(001) diodes were measured using ballistic electron emission microscopy (BEEM) and ballistic hole emission microscopy (BHEM), respectively. Measurements using both forward and reverse BEEM and BHEM injection conditions were performed. The Schottky barrier heights were found by fitting to a linearized Bell-Kaiser and Prietsch-Ludeke model. The sum of the n-type and p-type barrier heights are in good agreement with the band gap of silicon and independent of the metal utilized. These findings may help to improve models for Schottky barrier heights of non-epitaxial diodes.

11:40am **SP+AS+EM+GR+MI+NS+SS-FrM11 A STM Study of a Self Assembled Cu-Si Nanoisland on Si(110).** *P.K. Ng, University of Illinois at Chicago, B. Fisher, N.P. Guisinger, Argonne National Laboratory, C.M. Lilley, University of Illinois at Chicago*

The surface of a self-assembled copper-silicide (Cu-Si) nanoisland on a silicon (Si) substrate with (110) orientation was studied using surface tunneling microscopy (STM). Self-assembled Cu-Si nanostructures on Si are of technological interest because of their potential use in nanoscale devices. Self-assembled Cu-Si nanoislands were fabricated by electron beam evaporation of Cu onto a 600°C annealing Si substrate in ultrahigh vacuum (UHV) environment. In prior work, we used transmission electron microscopy (TEM) to analyze material composition of Cu-Si nanostructures via x-ray energy dispersive spectroscopy (XEDS) [1]. The XEDS data of a Cu-Si nanowire show a Cu_3Si phase [2]. The size of these nanostructures was on the scale of hundreds of nanometers and high resolution analysis was focused on the cross-sectional (or bulk) material. However, the surface of these self-assembled Cu-Si nanoislands has not yet been studied. Figure 1(a) in the attached supplemental document (and all the referring figures therein) shows a scanning tunneling microscopy (STM) micrograph of a self assembled Cu-Si nanoisland on Si(110). The facets on the nanoisland indicates a single crystal. As seen in Figs. 1(b)-(c), a higher resolution scan and analysis on the same nanoisland indicates a surface periodicity between scan points A to B of ~ 6.8 Å. These results corroborate that the faceted nanoisland is a single crystal. The surface of the nanoisland appears to have unknown adsorbates, possibly from water or hydrogen contaminations, see Fig. 1(b). Interestingly, some of these adsorbates do not randomly form on the surface but also in a periodical manner. As such, the surface may have a periodical affinity for certain adsorbates. A full discussion of this study will be presented in the AVS proceeding.

[1] P. K. Ng, B. Fisher, K. B. Low, A. Joshi-Imre, M. Bode, and C. M. Lilley, "Comparison between bulk and nanoscale copper-silicide: Experimental studies on the crystallography, chemical, and oxidation of copper-silicide nanowires on Si(001)," *Journal of Applied Physics*, vol. 111, pp. 104301-7, 2012.

[2] P. K. Ng, B. Fisher, K. B. Low, R. E. Cook, and C. M. Lilley, "Crystallographic studies of self assembled Cu-Si nanowires on Si(001), Si(110), and Si(111)," in preparation, 2013.

Surface Science

Room: 201 A - Session SS-FrM

Oxides and Semiconductors: Structure and Reactivity

Moderator: G.A. Kimmel, Pacific Northwest National Laboratory

8:20am **SS-FrM1 Oxidation of Pd Supported on Au(111) and Single Crystal ZnO Supports.** *J. Lallo, M. Batzill, University of South Florida*

Supported palladium catalysts are involved in many important catalytic reactions, such as steam reforming of methanol and methane combustion. Palladium oxide has been discovered to play an important role in these reactions, and the conditions and mechanisms involved for PdO formation are of great interest. In this work we investigate the role of substrates in palladium oxidation. Thin films of Pd, < 10nm, are grown on Au(111) and different crystallographic orientations of ZnO substrates under UHV conditions. The films are exposed to high pressure $O_2 > 1 \times 10^{-3}$ Torr, at temperatures above 300°C. Post exposure XPS is used to determine the conditions required for stable PdO formation. Angle resolved XPS is used to determine the location of the initial oxidation, either at the film surface or interface. The conditions for oxide formation on single crystal Pd(111) will be compared to the thin Pd-deposits on gold and for different ZnO-terminations. The formation of stable PdO is found to depend on the thickness of the initial Pd film. This study provides insight in the role of the support on the oxidation/reduction of Pd catalysts.

8:40am **SS-FrM2 Zinc Oxide Surface Chemistry.** *J. Whitten, University of Massachusetts Lowell*

Zinc oxide is one of the most-studied and technologically relevant metal oxides and is particularly interesting because its nanoparticles are inherently photoluminescent. A variety of surface science techniques, including X-ray and ultraviolet photoelectron spectroscopies (XPS and UPS), have been used to investigate the adsorption of molecules on zinc oxide single crystal and nanoparticle surfaces. Adsorbates that have been studied include thiols, sulfur dioxide and nitrogen dioxide, and the effects of coadsorbates, such as water, have been evaluated. The effects of adsorption on the photoluminescence spectrum of ZnO have also been investigated.

Applications of this research for electronic materials, heterogeneous catalysis, and dye-sensitized solar cells are discussed.

9:00am SS-FrM3 Variations in the Orientation and Thermal Stability of the Carbonate Reaction Intermediate with the Surface Structure and Stoichiometry of Cerium Oxide Thin Films, P.M. Albrecht, D.R. Mullins, Oak Ridge National Laboratory

Carbonate, $[\text{CO}_3]^{2-}$ is a stable intermediate in the water-gas shift reaction ($\text{CO} + \text{H}_2\text{O} \rightarrow \text{H}_2 + \text{CO}_2$) over inverse $\text{CeO}_x/\text{Au}(111)$ catalysts, relevant to efficient H_2 production [1]. In addition, carbonate has recently been proposed as the high-temperature (600-700 K) intermediate in the dehydrogenation of methanol [2], and possibly in the complex reaction of acetaldehyde, on $\text{CeO}_2(100)$.

Here, we probe the formation and reaction of the carbonate species on $\text{CeO}_x(100)$ as a function of temperature and Ce oxidation state by adsorbing CO_2 at 180 K. There is a marked variation in the stability of the carbonate species with the crystallographic orientation of the ceria thin film. Temperature-programmed desorption (TPD) identifies CO_2 as the sole product, with desorption states at 230 K, 410 K, 510 K, and 655 K in the case of stoichiometric $\text{CeO}_2(100)$. On $\text{CeO}_2(111)$, carbonate desorbs entirely as CO_2 by 300 K [1, 3].

On $\text{CeO}_2(100)$, soft X-ray photoelectron spectroscopy (sXPS) confirms the persistence of carbonate up to 600 K. Near-edge X-ray absorption fine structure (NEXAFS) at the C *k*-edge shows a strong angular dependence that becomes more pronounced at higher temperature (lower coverage). The excitation of the π^* resonance at grazing incidence indicates that the carbonate is lying flat on $\text{CeO}_2(100)$.

For partially reduced $\text{CeO}_{1.67}(100)$, we observe: (1) A substantial decrease in low-temperature (< 250 K) desorption, (2) The appearance of an intense CO_2 desorption peak at higher temperature (765 K), and (3) The absence of well-defined peaks in the CO_2 desorption between 300 K and 600 K.

The integrated intensity of the $[\text{CO}_3]^{2-}$ peak in the C 1s spectrum following CO_2 adsorption on $\text{CeO}_{1.67}(100)$ at 180 K is a factor of two greater than that for fully oxidized $\text{CeO}_2(100)$. On the reduced surface there is also no loss of this initial intensity upon heating to 300 K. At 700 K the carbonate coverage on the reduced surface is one-third of its starting value, whereas on the oxidized surface complete desorption (as CO_2) has occurred. Furthermore, resonant photoemission spectroscopy (RPES) indicates negligible re-oxidation of the $\text{CeO}_{1.67}(100)$ surface. In contrast, an RPES study of CO_2 on reduced $\text{CeO}_x(111)$ demonstrated partial re-oxidation at temperatures as low as 300 K [4].

Research sponsored by the Division of Chemical Sciences, Geosciences, and Biosciences, Office of Basic Energy Sciences, US Department of Energy.

- [1] S. D. Senanayake et al., *J. Catal.* **271**, 392 (2010).
- [2] P. M. Albrecht and D. R. Mullins, *Langmuir* **29**, 4559 (2013).
- [3] S. D. Senanayake and D. R. Mullins, *J. Phys. Chem. C* **112**, 9744 (2008).
- [4] T. Staudt et al., *J. Catal.* **275**, 181 (2010).

9:20am SS-FrM4 Atomic Structure of the Anatase $\text{TiO}_2(001)$ Surface, Y. Xia, K. Zhu, Baylor University, T.C. Kaspar, Pacific Northwest National Laboratory, B. Birmingham, K.T. Park, Z. Zhang, Baylor University

Understand the atomic surface structure of well-defined anatase $\text{TiO}_2(001)$ surface is critical for deciphering site-specific thermal and photo- reaction mechanisms on anatase TiO_2 — the most reactive polymorph of TiO_2 . We have studied anatase $\text{TiO}_2(001)$ epitaxial thin films grown *ex-situ* by oxygen-plasma-assisted molecular beam epitaxy using UHV scanning tunneling microscopy (STM). Large (~30 nm) coexisting (4×1) and (1×4) reconstructed terraces are observed. The atomic corrugation on bright rows of the surface shows a strong bias voltage dependence and is not uniform. High resolution images resolve the atomic structure of the bright row. We propose a modified ad-molecule model for the anatase $\text{TiO}_2(001)$ surface structure.

9:40am SS-FrM5 Study of Low Density Sites on Planar Silicon Dioxide Surfaces using Fluorescent Probes, J.M. McCrate, J.G. Ekerdt, University of Texas at Austin

Characterization of low density sites on planar oxide surfaces remains a challenging task. Such sites are believed to play an important role in catalysis and particle/film nucleation, although the inability to directly observe these sites limits our understanding of these processes. We have developed a technique that enables detection of low density sites on planar surfaces using fluorescent probe molecules. Derivatives of perylene, a high quantum yield fluorophore, with various functional groups are used to titrate surface sites in vacuum. The functional group is chosen to chemically bind to the desired site and *in situ* photoluminescence (PL) measurements

are used to determine the density of sites and learn about their distribution. An estimated detection limit of $< 10^{10}$ sites / cm^2 is possible with this technique. We will discuss our work using fluorescent probes to study sites on the silica surface. In particular, results of our studies of strained siloxane with perylene-3-methanamine and oxygen vacancy defect (OVD) sites with 3-vinyl perylene will be presented.

10:00am SS-FrM6 Functionalization of Vicinal Silicon Surfaces: Insight into Si Nanoparticle Reactivity, W.J.I. DeBenedetti, University of Texas at Dallas, M.D. Halls, Schrodinger Inc., Y.J. Chabal, University of Texas at Dallas

Semiconductor nanoparticle (NP) surface chemistry has long been recognized as central to the development and optimization of opto-electronic devices (based on NPs photoluminescence properties). Much attention has been directed to group II-VI quantum dots (QDs) for a variety of targeted applications, although their toxicity renders them incompatible with biological systems. Consequently, there is a renewed interest in nanostructured silicon that is more compatible with existing technology and more biologically friendly. Silicon NPs are capable of exhibiting high quantum yield emission and are considered environmentally adventurous compared to current Cd or Pb alternatives, but the origin of Si NP photoluminescence remains elusive. A significant advantage of using Si NPs is the ability to covalently modify their surface rather than employing datively bound ligands that can over time lead to aggregation, i.e. loss of opto-electronic properties. Though covalent surface modification of Si NPs has been realized, the mechanism of hydrosilylation at defect sites (steps) remains unknown, suggesting that work on model step surfaces could bring much needed insight.

Herein we report the functionalization of vicinal silicon (111) surfaces with both monohydride and dihydride step edges using a 9° off orientation in the (-1-12 & 11-2) directions, respectively. Two reactions are studied as a function of immersion time on both model surfaces: i) thermal hydrosilylation with a terminal alkene (known to be concerted on flat surfaces) and ii) nucleophilic addition using small molecule (methanol). It is found that the nucleophilic system reacts preferentially at the step edge forming a bridge complex between the bridge and lower terrace hydrogen atoms (initial transition structure shown in Figure 1), while the alkene reacts with all terrace and step (mono- and di-hydride) sites. Such selectivity opens the door for nanopatterning and provides important insight into the behavior of Si NPs.

10:20am SS-FrM7 Gallium Nitride Surface Preparation for ALD Deposition of Aluminum Oxide, A.J. Kerr, S. Gu, T. Kaufman-Osborn, E. Chagarov, University of California, San Diego, S. Madiseti, University at Albany-SUNY, P. Asbeck, University of California, San Diego, S. Oktyabrsky, University at Albany-SUNY, A.C. Kummel, University of California, San Diego

Gallium nitride metal oxide semiconductor field-effect transistors (MOSFET) are promising candidates for high-speed and high-power circuits due to their voltage handling capability and high electron mobility. For these devices to function optimally, the oxide-semiconductor interface must have a low density of interfacial traps which can degrade performance and reliability. This study correlates the electrical properties and chemical bonding of deposited amorphous Al_2O_3 on $\text{GaN}(0001)$ prepared using ammonium sulfide solutions followed by in-situ atomic hydrogen cleaning.

A baseline CV measurement was made using simple TMA predepositing in the ALD system to reduce native oxide (Fig 1a). The ex-situ sulfide solution cleaning prior to cyclic atomic H and TMA predepositing resulted in improved C-V characteristics illustrated by decreased dispersion across the frequency spectrum. The greatest improvement in dispersion, however, was achieved when combining the ex-situ wet sulfur treatment with in-situ when atomic hydrogen plasma cleaning (Fig 1b.). To understand the role of the ex-situ wet sulfur treatment and in-situ atomic H cleaning, XPS, LEED, and SIMS were performed. Following wet sulfur treatment, in-situ XPS and LEED studies showed that heating to typical ALD temperatures (285°C) both removed the sulfur and produces a 1x1 LEED pattern consistent with less than a monolayer of disorder at the surface. SIM experiments upon the full oxide/ GaN structures confirmed minimal sulfur at the buried oxide-semiconductor interface consistent with the main role of sulfur being to protect the surface against oxidation in air instead of providing a chemical passivation at the oxide/semiconductor interface. Angle resolved XPS studies of the ALD nucleation layers showed the primary role of the in-situ atomic hydrogen was to increase the initial growth rate of the gate oxide thereby increasing the ALD nucleation density consistent with previous reports demonstrating that atomic hydrogen completely removes native oxide. Density Functional Theory Molecular Dynamics (DFTMD) calculations (Fig. 2 and 3) were performed to compare the bonding of the amorphous Al_2O_3 gate oxide to a bulk terminated $\text{GaN}(0001)$ versus a $\text{GaN}(0001)$ surface with a Ga adlayer. The bonding of the amorphous Al_2O_3 gate oxide directly to the bulk terminated $\text{GaN}(0001)$ was most consistent

with the experimental results since this interface had bulk-like charge states for the interfacial atoms and a very low density of band gap states compared to even the clean GaN(0001) surface.

10:40am **SS-FrM8 Monolayer-induced Electronic Structure of Crystalline Semiconductor Surfaces**, *A.J. Mäkinen, C.-S. Kim, G.P. Kushto*, Naval Research Laboratory

Directly grafted organic monolayers on Si and Ge surfaces offer an interesting opportunity to explore aspects of surface passivation and control of electrical properties, namely, *molecular gating*, of semiconductor surfaces. We report our study of the interfacial electronic structures of *n*-, and *p*-type of Si(111), Si(100) and Ge(111) surfaces that have been chemically modified with various organic monolayers. The investigated monolayers include octadecane, attached via hydrosilylation and hydrogermylation of 1-octadecene at Si and Ge surfaces, as well as para-substituted phenyl rings, attached by diazonium activation of hydrogenated Si and Ge surfaces. X-ray photoelectron spectroscopy of the modified Si and Ge surfaces, together with four-probe measurements of ultrathin (20-40 nm) silicon-on-insulator channels, functionalized with the monolayer structures, indicate that there is downward band bending, up to 200 meV, associated with assembling these organic monolayers on the semiconductor substrates. This band bending does not directly correlate with the dipole moment or electron withdrawing or donating character of the molecular moieties, pointing to the critical roles of the nature and quality of the self-assembled monolayer, and the intrinsic electronic structure of the semiconductor material in defining the interfacial electronic structure of the passivated Si and Ge surfaces.

11:00am **SS-FrM9 Probing Shallow Trapped Electrons in TiO₂ with UHV-IRRAS**, *H. Sezen, M. Buchholz, A. Nefedov, C. Natzeck, S. Heissler*, Karlsruhe Institute of Technology, Germany, *C. Di Valentin*, Università di Milano-Bicocca, Italy, *C. Wöll*, Karlsruhe Institute of Technology, Germany

Understanding photochemistry on oxide surfaces, a topic of pronounced importance in the context of solar fuel synthesis, includes tracking the path of the charge carriers photoexcited in the bulk to the surface where both, the electron and the hole, may induce chemical transformations in adsorbed molecular species. Shallow trap states which in the case of TiO₂ are known to store charge over extended periods of time (several hours) have a pronounced influence on this bulk-to-surface processes.[1-2] In this contribution we demonstrate that grazing-incidence IR-spectroscopy can be used to probe electrons localized in such states. Loading was carried out by either irradiation with UV-light or exposure to atomic hydrogen. For both, powders as well as a (110) oriented single crystal substrate of rutile titanium dioxide (r-TiO₂), distinct IR absorption features were observed at around 940 and 970 cm⁻¹. For the single crystal substrates, the IR absorption bands arising from an excitation of the trapped electrons into higher lying final states, are substantially sharper and, in addition, two new bands are resolved at 1205 cm⁻¹ and 1375 cm⁻¹. On the basis of this new high-resolution data we propose that the trap state has to be described as a polaron state and that the final states correspond to hydrogenic states within the polaron potential.

[1] M. Xu, Y. Gao, E. M. Moreno, M. Kunst, M. Muhler, Y. Wang, H. Idriss, C. Wöll, *Phys. Rev. Lett.* **106**, 138302 (2011).

[2] D. A. Panayotov and J. T. Yates Jr, *Chem. Phys. Lett.* **436**, 204 (2007).

11:20am **SS-FrM10 Dependence on Experimental Ambient of Surface Photovoltage Transients in Nanostructured Oxide Surfaces and Interfaces**, *Y.M. Strzhemechny, N.R. Chapagain, A. Nemashkalo, S. Pant, E.S. Davis*, Texas Christian University

Kelvin probe-based surface photovoltage (SPV) measurements were employed to monitor super-bandgap transients in nanostructured oxide specimens placed in different environments – high vacuum, He gas, N₂ gas, etc. In general, contactless SPV transient experiments in semiconductors and insulators can provide information about surface/subsurface state densities and their cross sections, and these experiments sometimes reveal intricate illumination-mediated charge recombination mechanisms, especially in materials with a complex microstructure. The SPV time-domain response of the surface/subsurface states could also be significantly affected by the experimental environment, which was addressed in this work. Light-dark transient SPV were studied in several oxide systems with nanostructured morphologies at room temperature using a white light source: a nanoporous silicon permeated with Ni and Co nanoparticles, ZnO thin films on Si, as well as sol-gel samples on Si substrates containing titania/zirconia/silica mixed with noble metal nanoparticles. Some of the latter samples were also irradiated with a flux of Ti⁺ ions. In most of these systems we observed nontrivial dynamics of charge redistribution in response to illumination changes and a strong dependence on the ambient. E.g., in the nanoporous Si samples, sharp ‘light on’/‘light off’ voltage spikes were detected in the He and N₂ gas environments, indicating several

distinct charge exchange mechanisms occurring on dissimilar time scales. However, experiments on these specimens in high vacuum revealed a very different, albeit nontrivial response. On the other hand, for the multicomponent sol-gel thin films, a significant distinction was observed between the as-received and ion-irradiated samples. While for the as-received films the saturation curves in the N₂ and vacuum environments were similar, the irradiated samples yielded a much slower charge dynamics in vacuum compared to that in the N₂ atmosphere. We discuss possible mechanisms responsible for the observed SPV dynamics, related to the complex microstructure and its interaction with the environment.

Thin Film

Room: 104 A - Session TF+EM+NS+SS-FrM

Thin Film: Growth and Characterization III

Moderator: M.R. Davidson, University of Florida

8:40am **TF+EM+NS+SS-FrM2 Atomically Controlled, Self-Limiting Procedures for Growth of Aluminum Oxide on SiC-on-Si to Yield an Atomically Sharp Interface**, *P. Morgen, R. Dhiman, J. Hvam*, University of Southern Denmark, *A. Gomes Silva*, Universidade Nova de Lisboa, Portugal, *K. Pedersen*, Aalborg University, Denmark, *Z. Li*, Aarhus University, Denmark

Electronic devices fabricated from SiC- or SiC/Si epitaxial wafers will need surface passivation and insulating coatings. In earlier work [1], we described a procedure for forming thin (1 nm) Al-oxide layers on Si surfaces, at processing temperatures of around 600°C or slightly higher, resulting in an atomically sharp interface and no silicate formation.

We have adopted the same procedures to a system of SiC/Si, formed by a remote CH₄ plasma interacting with heated Si surfaces in UHV [2]. After growing the SiC/Si system (SiC thickness between 0.5 and 25 nm; polycrystalline) a self-limiting Si-oxide layer was grown on the surface, with a thickness of around 1 nm, at 700°C. On top of this layer we deposited approximately 1 nm of Al with a Knudsen atomic source (all steps in UHV) and then reacted it thermally (at 600°C) with the Si-oxide. We monitored all the process steps and the resulting structures of the layers and the interface using synchrotron radiation induced core level photoemission at ASTRID, Aarhus, Denmark. We found similar qualities with this procedure, as for Si, i.e. an atomically sharp interface between Al-oxide and SiC, which is better than for conventional ALD. This reaction scheme offers self-limiting behavior both of the oxidation to create Si-oxide, and of the conversion into Al-oxide, which only needs a sufficient amount of Al to affect the total conversion of the Si-oxide, while excess Al will leave the system at sufficiently elevated temperatures.

[1] Nanostructured Materials in Different Dimensions for Sensing Applications, *Per Morgen, Joanna Maria Drews, Rajnish Dhiman, and Peter Nielsen*, in: NATO Science for Peace and Security Series B: Physics and Biophysics, Vol. 2011, Nr. 8, 2011, 257-273.

[2] Growth of thin SiC films on Si single crystal wafers with a microwave excited plasma of methane gas, *Rajnish Dhiman, and Per Morgen*, Thin Solid Films, in press 2013, [<http://dx.doi.org/10.1016/j.tsf.2013.03.090>]

9:00am **TF+EM+NS+SS-FrM3 Understanding Growth Mechanisms of Pyrolytic Graphite by Chemical Vapor Deposition**, *K. Yu, C. Hayman*, Case Western Reserve University, *W. Fan*, Momentive Performance Materials, Inc., *I.T. Martin, H. Martin, R.M. Sankaran*, Case Western Reserve University

Pyrolytic graphite (PG) is a semi-crystalline form of carbon with wide-ranging electronic and thermal applications.^{1,2} The unique anisotropic and unparalleled electronic and thermal properties of PG stem from the alignment of its planar graphite sheets. A variety of structural forms of PG are currently commercially produced by high temperature (>1500 °C) hot-wall chemical vapor deposition (CVD). The degree of alignment (*i.e.* crystallinity) of the graphite in three dimensions and the growth rate, both of which affect the material properties and cost, depend discretely on process conditions, including growth temperature, gas chemistry, flow geometry, and pressure.

We have recently built a laboratory-scale, high-temperature vacuum reactor to study PG growth. Mixtures of methane and hydrogen gas are reacted to deposit as a carbon film on a heated substrate (1100-2000 °C). Solid carbon deposition under different conditions has been examined to understand the interplay of gas-phase chemistry and substrate nucleation. As-deposited materials are characterized by a suite of analytical techniques. Cross-sectional SEM provides visualization of the interaction of the carbon film with the substrate. The degree of alignment is assessed by micro Raman spectroscopy and X-ray diffraction (XRD). The Raman intensity ratio of the

disordered carbon (D) to graphitic carbon (G) bands, an indicator of defects, decreases with increasing deposition temperature, consistent with commercial samples. Perfect Bernal stacking is only found for PG deposited at >2000 °C, as revealed by the 2D band. XRD also reveals the crystallite size through a Scherrer analysis of the peak widths. Smaller crystallite size and larger d-spacing are observed for PG samples deposited at lower temperature. In this talk, we will use discussion of these results to provide a picture of the mechanisms behind graphite nucleation and the PG growth during thermal CVD.

1. *Materials for Aircraft, Missiles and Space Vehicles; Symposium on Materials for Aircraft, Missiles, and Space Vehicles*; the 4th Pacific Area National Meeting: Los Angeles, 1962.

2. Flynn, S. B. *Using Annealed Pyrolytic Graphite in Conduction Cooled Electronics Cooling Applications*; Carleton University: Canada, 2006.

9:20am **TF+EM+NS+SS-FrM4 Characterization of the Thin Films in the Microfabrication of Carbon-Nanotube Templated Thin-Layer Chromatography Plates**, S. Kanyal, A. Diwan, Brigham Young University, D.S. Jensen, A. Dadson, M. Vail, Diamond Analytics, M.R. Linford, Brigham Young University

We have recently described the microfabrication of planar separation devices (thin layer chromatography plates).¹⁻³ These devices are created through the following steps, where silicon wafers are used as the substrates: deposition of 35 nm of alumina, deposition of ca. 6 nm of Fe, annealing of the Fe under a reducing environment to make Fe nanoparticles, carbon nanotube (CNT) growth, conformal coating of the CNTs with SiO₂, oxidative removal of the CNTs, and hydration of the SiO₂ surface. To understand our materials, we have exhaustively characterized them by a suite of characterization techniques. Spectroscopic ellipsometry has taught us about the optical properties of the materials, e.g., thicker Fe films are found to be more metallic than thinner Fe films and alumina films can be well parameterized by a Cauchy dispersion model. ToF-SIMS shows that as surface hydration became more effective, the SiOH⁺/Si⁺ ratio increases. Indeed, the SIMS results are correlated to the more commonly used FTIR analyses, but they appear to have greater predictive power for highly hydrated surfaces. ToF-SIMS also suggests an interesting even/odd effect in ion yields from the CNTs. Rutherford backscattering suggests an interesting potential channeling phenomenon in the CNT forests. XPS shows that the thinner Fe films are completely oxidized and that the CNT surfaces are entirely carbon with only slight oxidation/contamination one year after their fabrication. TEM confirms the deposition of inorganic materials around individual CNTs. AFM shows that the size of the Fe nanoparticles increases with increasing Fe thickness.

1. Jensen, D. S.; Kanyal, S. S.; Gupta, V.; Vail, M. A.; Dadson, A. E.; Engelhard, M.; Vanfleet, R.; Davis, R. C.; Linford, M. R., 195-203.

2. Kanyal, S. S.; Jensen, D. S.; Miles, A. J.; Dadson, A. E.; Vail, M. A.; Olsen, R. E.; Fabien, S.; Nichols, J.; Vanfleet, R.; Davis, R.; Linford, M. R., (3), 031203.

3. Song, J.; Jensen, D. S.; Hutchison, D. N.; Turner, B.; Wood, T.; Dadson, A.; Vail, M. A.; Linford, M. R.; Vanfleet, R. R.; Davis, R. C., (6), 1132-1139.

9:40am **TF+EM+NS+SS-FrM5 A Carbon/Ternary Alloy/Carbon Optical Stack on Mylar as an Optical Data Storage Medium to Potentially Replace Magnetic Tape**, H. Wang, R. Gates, B. Lunt, M. Asplund, Brigham Young University, S. Vaithiyalingam, Pacific Northwest National Laboratory, R.C. Davis, M.R. Linford, Brigham Young University
We have prepared a novel write-once-read-many (WORM) optical stack on Mylar tape as a replacement for magnetic tape. This approach has the potential to substantially increase the longevity of tape data storage, which is extremely important for many large organizations. This work follows our efforts to develop an archival DVD that will last 1000 years (see www.mdisc.com). This optical tape is modified with a ca. 40 nm write layer prepared by co-sputtering bismuth and a tellurium-selenium alloy target to prepare a bismuth-tellurium-selenium (BTS) write layer. This film is sandwiched between thin, protective films of reactively sputtered carbon. The adhesion of this stack to the substrate has been confirmed. Film thicknesses were determined by AFM step height measurements and film composition, morphology, and chemistry were confirmed by RBS, XPS, ToF-SIMS, and SEM. Sub 3 um marks can be made on the Mylar/C/BTS/C tape using 532 nm laser pulses. No marks are observed on the uncoated (control) Mylar substrate under identical conditions. Marks, which showed craters/movement of the write material, were characterized by optical microscopy and atomic force microscopy (AFM). The threshold power for marking the tape was explored as a function of film thickness. Interestingly, the threshold power is higher for either thinner or thicker films and lowest for films of intermediate thicknesses. These results are attributed to a

tradeoff between lower optical absorption by thinner films and the requirement of higher powers to melt thicker films. The BTS films appear to be quite stable to storage in the air. The effects of the microscope objective in our home-built apparatus were explored and smaller, higher quality marks could be made with the 60X objective compared to the 40X. The write process to the film was modeled by COMSOL, and the simulation was consistent with experimental results.

10:00am **TF+EM+NS+SS-FrM6 Toughness Enhancement in Hard Single-crystal V_{0.5}Mo_{0.5}N/MgO(001) Thin Films**, H. Kindlund, J. Lu, Linköping University, Sweden, I.G. Petrov, J.E. Greene, University of Illinois at Urbana Champaign, L. Hultman, Linköping University, Sweden

Hardness is an essential property for a wide range of applications, while for some purposes one also needs ductility to avoid film failure in ceramic films exposed to high stresses. Using VN as a model system, we demonstrate that VMoN alloys exhibit not only enhanced hardness, but impressive increased ductility, i.e. toughness, and study the effect of N vacancies on mechanical properties of pseudobinary NaCl-structure transition metal nitride, VMoN.

V_{0.5}Mo_{0.5}N_x thin films with 0.55 ≤ x ≤ 1.03, as determined by RBS, are deposited on MgO(001) substrates by dual reactive magnetron sputtering. For the entire N composition range x, we obtain single-crystal B1-structure V_{0.5}Mo_{0.5}N_x, as determined by XRD and TEM analyses. RLM results indicate that the films are relaxed with lattice parameters varying from a = 4.12 Å for x = 0.55 to a = 4.19 Å for x = 1.03, increasing with increasing N content. The nanoindentation hardness H increases as N-vacancy concentration increases, from H = 18 GPa (x=1.03), to 20 GPa (x=0.94), 21 GPa (x=0.72), to 26 GPa (x=0.55), while the elastic modulus is maintained essentially constant. In addition, while nanoindented VN and TiN reference samples suffer from severe cracking typical of brittle ceramics, V_{0.5}Mo_{0.5}N_x films do not crack. Instead, they exhibit material pile-up around nanoindenters, characteristic of plastic flow in ductile materials.

10:20am **TF+EM+NS+SS-FrM7 Manganese-based Thin Films Growth on Silicon Oxide Substrates**, H. Sun, X. Qin, F. Zaera, University of California, Riverside

The growth of manganese-based films on silicon oxide substrates via the chemical vapor decomposition of two Mn metalorganic precursors, methylcyclopentadienylmanganese(I) tricarbonyl, MeCpMn(CO)₃, and bis(N,N') diisopropylpentylamidinato)Mn(II), was characterized and contrasted by X-ray photoelectron spectroscopy (XPS). MeCpMn(CO)₃ proved to be much less reactive than the acetamidinate, even if gas-phase activation was used to promote the growth of Mn films at lower temperatures in the first case. The acetamidinate precursor does show high reactivity, affording the deposition of Mn at reasonable rates, higher at higher temperatures, but also leads to the incorporation of approximately 15% of nitrogen and additional carbon in the grown Mn(0) films. In both depositions, a nonstoichiometric mixture of MnOx + SiOx and Mn silicate is formed first, possibly followed by the formation of a thin subsurface Mn silicide layer. Mn(0) metallic films can be grown on top of the combined Mn silicate/Mn silicide structure, which serves as an effective diffusion barrier. The Mn(0) species deposited on top of those initial layers could be oxidized by N₂O or O₂, during which the organic ligands could be effectively removed from the surface. As a result, manganese-based thin films growth could be achieved by repeating this deposition-oxidation process.

10:40am **TF+EM+NS+SS-FrM8 Properties of Epitaxial VN_x/MgO(001) (0.70 < x < 1.36) Layers Grown by Reactive Magnetron Sputter Deposition**, A.R.B. Mei, University of Illinois at Urbana Champaign, D.G. Sangiovanni, H. Kindlund, Linköping University, Sweden, B. Howe, Air Force Research Laboratory, E. Broitman, V. Chirita, L. Hultman, Linköping University, Sweden, A. Rockett, J.E. Greene, I.G. Petrov, University of Illinois at Urbana Champaign

Ceramic coatings are, despite their high hardness, often limited in use by their brittleness. Under high stress conditions, brittle hard coatings, such as transition metal (TM) nitride thin-films, fail prematurely through crack nucleation and growth. In order to extend the longevity and broaden the applications of ceramic hard coatings, they must be toughened: their capacity for absorbing elastic energy prior to fracture must be increased. Here, we report on the toughening of under-stoichiometric VN_x, deposited on MgO(001) in ultra-high-vacuum by reactive magnetically-unbalanced magnetron-sputter deposition. X-ray diffraction (XRD), transmission electron microscopy (TEM), scanning transmission electron microscopy (STEM), and selected area electron diffraction (SAED) indicate that the films are fully-dense single-phase epitaxial VN_x(001). Hardness values of VN_x(001), determined from nanoindentation measurements according to the Oliver and Pharr method, increase with off-stoichiometry from H = 14.0±0.8 GPa (x = 1) to 17±0.76 GPa (x = 0.77) and 16.7±0.1 GPa (x =

1.20). Scanning electron micrographs (SEM) of nanoindentations performed with a sharp cube-corner tip reveal the presence of cracks in $VN_x(001)$ overlayers with $x > 0.95$; four cracks were observed in each film with $x > 1.23$, two in films between $1.06 < x < 1.10$, and one for $0.95 < x < 1.00$. Cracks were not observed in $VN_x(001)$ with $x < 0.88$. The resilience of highly under-stoichiometric $VN_x(001)$ films to fracturing, as indicated by the absence of cracks, is evaluated via crystal orbital overlap populations (COOP) analysis using *ab initio* density functional theory (DFT) calculations. The results indicate that the toughening is of electronic origin and due to the strengthening of V-V bonds along the slip direction.

11:00am **TF+EM+NS+SS-FrM9 Sandwiched Antibacterial Layers Topped by Thin Polymeric Coatings and Deposited in Thin Capillaries**, G.F. Franz, F.S. Schamberger, Munich University of Applied Sciences, Germany

Bottom-down strategies for nanostructures require tailoring techniques for very thin layers. One of the film-building polymers which cannot be deposited with ALD is poly-p-xylylene, commonly known as polyparylene, which has evolved to generate universally employable layers with unique properties. As known from growth theory, very thin layers below 100 nm in thickness are necessarily porous which reduces the property of preventing diffusion. This feature, however, is required to control the process of dissolution from metallic silver to silver ions of a layer lying beneath. The silver layer is used as a long-term depot for the generation of silver ions which exhibit an antibacterial conduct. The silver ions break through the cell walls of the bacteria, causing them to die.

To deposit very thin layers of polyparylene, the conventional Gorham method has been improved. We present a completely new method to control the growth of these very thin layers with defined porosity for which exact knowledge of vapor pressure and evaporation rate is required [1]. To tailor this long-term property above the death-causing threshold, the porosity (i. e. hole density) is:

(i) quantitatively determined with a digital evaluation procedure of the micrographs gained with AFM as function of the parameters of deposition.

and (ii) has been correlated with the breakdown voltage and the capacitance which can both easily applied to the samples (electro impedance spectroscopy, EIS).

This makes the hole density a quantitative measure to rate the degree of permeability for silver ions. Applying ICP-OES, the concentration of silver ions in the adjacent liquid around the silver spots is measured. This concentration depends on the thickness of the films of polyparylene. With standard biological procedures, this is correlated to the lethal impact on bacteria. Whereas layer growth upon open surfaces is controlled by the density of reactive particles (surface polymerization), the density becomes locally dependent for coating of narrow holes which occurs as a diffusive process with losses due to deposition. In a series of experiments, the growth behavior in thin, narrow pipes with an aspect ratio between 10 and 30 has been obtained, and a theoretical model is presented which reflects the crossover of these two transport mechanisms as function of chamber pressure and temperature.

[1] G. Franz et al., German patent disclosure DE 2012 014 915.8

11:20am **TF+EM+NS+SS-FrM10 Wurtzite Phase Stable $Mg_xZn_{1-x}O$ Epilayers with High Mg Compositions for High Performance Ultraviolet Photodetectors**, M. Wei, R.C. Boutwell, University of Central Florida, N. Faleev, Arizona State University, A. Osinsky, R. Miller, Agnitron Technology Inc., W.V. Schoenfeld, University of Central Florida

Wide band gap semiconductors such as $Mg_xZn_{1-x}O$ represent an excellent choice for making optical photodetectors and emitters operating in the UV spectral region. High crystal and optical quality $Mg_xZn_{1-x}O$ thin films were grown epitaxially on c-plane sapphire substrates by plasma-assisted Molecular Beam Epitaxy. ZnO thin films with high crystalline quality, low defect and dislocation densities, and sub-nanometer surface roughness were achieved by applying a low temperature nucleation layer. The critical growth conditions were discussed to obtain a high quality film: the sequence of Zn and O sources for initial growth of nucleation layer, growth temperatures for both ZnO nucleation and growth layers, and Zn/O ratio. Resultant epitaxial ZnO films demonstrated a root-mean-square surface roughness of 0.373nm for $1\mu m \times 1\mu m$ atomic force microscope images with clear hexagonal shaped terrace steps. The x-ray diffraction FWHM for (0002) peak was measured to be 13 arc sec for ZnO. By tuning Mg/Zn flux ratio, wurtzite $Mg_xZn_{1-x}O$ thin films with Mg composition as high as $x=0.46$ were obtained without phase segregation. The steep optical absorption edges were shown with a cut-off wavelength as short as 278nm, indicating of suitability of such material for solar blind photo detectors. Consequently, Metal-Semiconductor-Metal photoconductive and Schottky barrier devices with interdigital electrode geometry and active surface area of 1 mm^2 were fabricated and characterized. Photoconductor based on $Mg_{0.46}Zn_{0.54}O$ showed $\sim 10^2$ A/W peak responsivity at wavelength of $\sim 260\text{nm}$. The spectral

cutoff of the devices was close to 315nm with more than two orders of magnitude visible rejection ratio ($R_{260\text{nm}}/R_{400\text{nm}}$) these devices good candidates for solar blind applications.

11:40am **TF+EM+NS+SS-FrM11 Self-assembling Monolayers on Oxides: Utopia?**, T. Hauffman, A. Hubin, H.A. Terry, Vrije Universiteit Brussel, Belgium

Self-assembling monolayers are one of the most innovative ways to functionalise and change material surface' properties on the nanoscale. The adsorption of thiols on gold has proven the feasibility to build such well-ordered, compact monomolecular organic structures. However, gold is industrially less relevant and the variety of organic moieties that can be deposited in this way on the noble substrate is very limited.

Therefore, an interesting approach is outlined in literature, involving the deposition of monolayers on oxide films. In particular, the adsorption of phosphonic acids on aluminium oxides is proposed. In this presentation, we address the adsorption of n-octylphosphonic acids from aqueous and ethanolic solutions. It could be proven that not only the adsorbed layer should be characterised, but that the bare sample and the solvent play a crucial role as well. Furthermore, interactions between the oxide, the solvent and the individual molecules should be considered.

In this work, a strong focus laid on the in situ, real time monitoring of the dynamic adsorption of the organic molecules. Therefore, a methodology including in situ AFM, in situ, visual ellipsometry and Odd Random Phase Electrochemical Multisine Impedance Spectroscopy is outlined. Ex situ complementary techniques, such as XPS and FE SEM were included.

As such, it could be proven that in polar solvents, molecules adsorb in a fast and Stranski-Krastanov way. Moving to less polar solvents, such as ethanol, provoke deterioration of the oxide surface. The phosphonic acids adsorb on the surface, giving rise to condensed water on the surface. The acid molecules dissolve in this water, creating a hazardous environment for the oxide film.

In general, we state that it is impossible to form a SAM on aluminium oxide through an acid base elimination condensation reaction using organic molecules that are soluble in water [1-5]. Moreover, conformation and density issues are to be expected when using longer, non water soluble phosphonic acid.

References

1. T. Hauffman, Y. Van Ingelgem, T. Breugelmanns, E. Tourwé, H. Terry, A. Hubin, *Electrochimica Acta*, accepted for publication.
2. T. Hauffman, A. Hubin, H. Terry, *Surface and Interface Analysis* DOI 10.1002/sia.5150.
3. T. Hauffman, T. Breugelmanns, Y. Van Ingelgem, E. Tourwé, H. Terry, A. Hubin, *Electrochemistry Communications* 22 (2012) 124-127.
4. T. Hauffman, L. Van Lokeren, R. Willem, A. Hubin, H. Terry, *Langmuir* 28 (2012) 3167-3173.
5. T. Hauffman, O. Blajiev, J. Snauwaert, C. Van Haesendonck, A. Hubin, H. Terry, *Langmuir* 24 (2008) 13450-13456.

Authors Index

Bold page numbers indicate the presenter

— A —

Abbas, G.: EM+AS+EN+TF-ThM10, 181
Abbott, J.: TF+VT-WeM11, 147
Abbott, P.J.: VT-MoM1, **26**
Abdallah, J.: MS+AS+EL+EM+PS+TF-TuA4, 89
Abdallah, L.S.: EL+AS+EM+SS+TF-WeA11, **156**;
EL-ThP2, 234
Abe, Y.: TF-ThP27, 245
Abel, J.: TF+EM+NS+SS-ThA12, 229
Abelson, J.R.: EM+MI+NS+SS+TF-TuA10, 82;
TF+EM+NS+SS-ThA2, **228**
Ablett, J.: SA+AS+MG+SS-TuA9, 95
Abraha, P.: TR-TuP9, **121**
Abrahamson, J.T.: EN+PS+TF-MoM4, 9
Abrijo, M.: BI-TuP4, **101**
Abrikosov, I.A.: SE+NS+TF-ThA3, 220
Acharya, A.: EM+NS+SS+TF-FrM4, **247**
Acharya, D.: SP+AS+BI+MI+NS+SS-ThM3, 194;
SS-MoA6, 47
Acharya, R.: TF+MI-WeM1, 144
Achkar, A.: IA+BA-TuA12, 86
Adamovski, S.: SS+NS-WeM2, 142
Adams, B.: EM-WeA10, 158
Adams, D.P.: TF-ThA1, 229; TF-ThA2, **229**
Adamska, L.: GR+EM+NS+PS+SS+TF-MoM9, **12**
Addou, R.: GR+EM+MS+NS+SP-FrM8, 251
Adelmann, C.: EM+PS-TuM10, **58**;
SA+AS+MG+SS-TuA9, 95; TF+AS+SE+SS-
MoA9, 50
Adhiprakasha, E.: TF-ThP34, 245
Adiga, V.: BI+AS+BA+NS+SS-ThA12, 205
Agarwal, A.: PS-ThM5, 191
Agarwal, S.: GR+AS+BI+PS+SS-ThA1, 209;
PS+AS+NS+SS-ThM3, 188; TF-ThP16, **243**
Agboton, A.: TF+EM+NS+SS-ThA8, 229
Aguilar-Hernández, J.: TF-ThP1, 241; TF-ThP13,
243
Ahmadi, M.: SS-TuP29, **118**
Ahn, J.-R.: GR+EM+NS+SS+TF-ThA12, 212
Ahn, S.J.: GR+EM+NS+SS+TF-ThA12, 212; HI-
ThA12, 214
Ahsen, A.S.: SS-TuP12, **117**
Ai, C.F.: PS-TuP16, 111
Ai, Z.K.: HI-ThA3, 212
Ait Aissa, K.: TF+EM+NS+SS-ThA8, 229
Aita, M.: PS-ThM9, 191
Aiyar, A.: PS2-TuM11, 68
Akarvardar, K.: PS2-TuM9, 68
Akbar, S.: AS-TuM6, 54
Akdogan, N.: MI-TuP2, 104
Akutsu, T.: TF-ThP21, 244
Akyildiz, H.: TF-ThA6, 230
Al Salik, Y.: AC+AS+EN-TuA8, 77
Al Shankitil, I.: AC+AS+EN-TuA8, 77
Alamgir, F.: NS+AS+EN+SS-TuA11, 90
Alayashi, W.: TF+AS+NS+SE-WeA4, **173**
Albrecht, P.M.: SS-FrM3, 259; SS-MoA10, 48
Alcami, M.: GR+AS+EM+MI+MN-TuM1, 59
Alcami, M.: SS1-ThA3, 224
Aldinger, J.: AS+BI+EM+NL+NS+SS-ThA1, 202
Aldous, J.D.: EM2-ThA10, 206
Alexander, C.: BI+AS+IS+NL-MoM2, 6
Alexander, M.R.: AS+BI+IS-WeM5, 125;
BI+AS+IS+NL-MoM10, 7; BI+AS+IS+NL-
MoM2, 6; BI+AS+IS+NL-MoM8, 7; BI-
WeM1, 126; BI-WeM11, 127; EW-TuA6, 85
Alimardani, N.: EM+PS-WeM10, **129**
Alkemade, P.F.A.: HI-ThM12, 186
Allam, N.K.: NS+AS+EN+SS-TuA11, 90
Allen, G.C.: AC+AS+SS-TuM1, **53**
Alles, M.: BI-TuP7, **101**
Allred, D.D.: MN+AS+SS-MoM4, 15;
MN+AS+SS-MoM5, 15; TF+PS-ThM2, 200;
TF+PS-ThM6, **200**

Al-Mahboob, A.: GR+AS+EM+NS+SS-WeA10,
160
Alnabulsi, S.S.: AS+BI+EM+NL+NS+SS-ThA9,
232; AS+BI-MoM2, **3**; AS-ThP13, 232
Alrashid, E.: TF+AS+NS+SE-WeA9, 173
Al-Saidi, W.A.: SS+AS-TuM5, 69
Altfeder, I.: SE+EN-FrM4, 256
Altman, E.I.: SS+AS+NS+SP-WeA7, 166
Altuntas, P.: TF+EM+NS+SS-ThA8, 229
Amagai, M.: BI+AI+AS+BA+IA+NL+NS+SP-
WeA1, 153
Amasaki, S.: PS2-TuA11, 94
Amati, M.: IS+AS+SS-ThM5, 186;
NL+AS+BI+SA-FrM4, 255
Amelichev, V.A.: TF+MI-WeM4, 145
Armstrong, S.: SE+PS-ThM3, 192
An, K.-S.: TF-ThP38, 246
An, Y.: EM1-WeM12, 130; EM-ThP5, **235**
Ande, C.K.: TF+AS+SE+SS-MoA3, **49**
Anders, A.: PS1-TuM11, **67**
Andersen, A.S.: BI-TuP2, **100**
Anderson, A.: VT-WeM11, 148
Anderson, C.: PS-MoM3, 20
Anderson, D.G.: BI+AS+IS+NL-MoM10, 7;
BI+AS+IS+NL-MoM8, 7; BI-WeM1, 126; BI-
WeM11, 127
Anderson, E.H.: MI+AS+NS+SP-TuA11, 87
Anderson, J.K.: TF+PS-ThM6, 200
Anderson, K.: EN+SE+SS+TF-WeM9, 132
Anderson, S.L.: SS+NS-WeM3, **142**
Ando, T.: SP+AS+BI+EM+MI+NS+SE+SS-ThA1,
222
Andrade, E.: TR-TuP6, 121
Andreas, B.: VT-MoM9, 27
Andreev, A.V.: AC+AS+EN-TuA7, 77
Andrieu, S.: MI+EM-TuM1, **61**
Angelova, A.: GR+EM+NS+PS+SS+TF-MoM8,
12
Antognozzi, M.:
SP+AS+BI+EM+MI+NS+SE+SS-ThA8, 223
Antonov, P.V.: TR+AS+NS+SS-MoA9, **51**
Antony, A.: SS-MoA3, 47
Antosiewicz, T.: BI+NL+NS+SS-ThM6, 177
Anwar, S.: EM-MoA3, **32**
Aoki, T.: AS-MoA10, 30
Apblett, C.A.: TF-ThA4, 230
Appy, D.: SS+AS+NS-MoM11, **23**
Arakawa, I.: SS-TuP5, 115
Arena, D.: NS+AS+EM-MoA1, 41; NS+AS+EM-
MoA2, 42
Aresta, G.: TF+VT-WeM6, 147
Arey, B.: AP+AS+MI+NS+SS-WeA12, 151
Arias-Cerón, J.S.: TF-ThP1, 241
Arjad, A.B.: SS+AS+NS-MoM1, **21**
Arkill, K.: SS+EN-ThM12, 196
Arkun, F.E.: EM+NS+TF-FrM10, 250
Armbrust, N.: GR-WeM2, 133
Armstrong, C.T.: TF-TuA9, 97
Armstrong, I.: EW-WeL4, **149**
Armstrong, N.R.: EM+AS+EN+TF-ThM11, **181**
Arnadottir, L.: SS-TuA1, **96**
Arnold, J.C.: MS+AS+EL+EM+PS+TF-TuA9, 89
Arnold, P.C.: VT-MoM8, **27**
Arnoult, G.: PS-TuP29, 113; SE+PS-ThM9, **193**
Arpin, K.A.: TF+EM+NS+SS-ThA2, 228
Artyushkova, K.: AS-TuM6, **54**
Aruta, C.: GR+AS+BI+PS+SS-ThA10, 210
Asbeck, P.: EM+TF-MoM11, 9; SS-FrM7, 259
Asensio, M.C.: SA+AS+MI+SS-WeM6, **139**
Ashtiani, K.: EM-ThA6, 207
Askew, H.J.: BI-TuP5, **101**
Asner, D.M.: HI-ThA9, 213
Asplund, M.: TF+EM+NS+SS-FrM5, 261
Aspnes, D.E.: EL+AS+EM+SS+TF-WeA3, **155**
Assender, H.: EM+AS+EN+TF-ThM10, 181
Ast, Chr.R.: MI-MoM8, 14

Asthagiri, A.: SS-MoA3, 47
Astier: MS+AS+BA+BI+PS+TF-TuM3, 63
Atsuro, I.: NS-TuP1, **106**
Atuchin, V.: TF-ThP9, 242
Auciello, O.: MN+NS-TuM1, **62**
Auluck, H.S.: SP+AS+BI+EM+MI+NS+SE+SS-
ThA12, 223
Avasarala, B.: PS2-TuA8, **94**
Awschalom, D.: MI+EM-TuM3, **61**
Axnanda, S.: IS+AS+SS-ThM9, 187
Aydil, E.S.: EN+PS+TF-MoM10, 11; EN+PS+TF-
MoM4, **9**; EN+PS+TF-MoM9, 10
Ayers, J.E.: EM+AS+NS+SS-WeA3, 156;
EM+AS+NS+SS-WeA4, 157
Azcatl, A.: EM+TF-MoM5, 8;
GR+EM+NS+SS+TF-ThA1, 211

— B —

Baben, M.: SE+NS+TF-ThA4, 220
Baber, A.: IS+AS+SS-ThM6, **186**
Babor, P.: GR+AS+NS+SP+SS-TuA9, 85
Babson, D.: BI+AI+BA+IS-MoA3, 31
Backus, E.H.G.: IA+AI+BI+IS+NL+SS-MoA3, 37
Bae, D.: MS+AS+EL+EM+PS+TF-TuA9, 89
Baehr-Jones, W.: MN+NS-MoA1, **40**
Baek, H.: IS-ThP1, 238
Baer, D.R.: AS-WeA7, **152**
Bagal, A.: SS+NS-WeM10, 142
Bagge-Hansen, M.: NL+AS+BI+SA-FrM5, 255;
SS+NS-WeM11, 143
Baglin, V.: VT-WeM10, 148
Bagnall, M.: HI-ThA8, 213
Bagot, P.A.J.: AP+AS+MI+NS+SS-WeA4, 150;
AP+AS+MI+NS+SS-WeA7, 150
Bagus, P.S.: AC+AS+SS-TuM3, **53**; SS+AS-
TuM12, 71
Bahr, S.: IS+AS+SS-ThM11, **187**
Bai, J.: MS+AS+BA+BI+PS+TF-TuM3, 63
Bai, Q.: MS+AS+BA+BI+PS+TF-TuM1, 63
Baik, S.: TF-TuM5, 71
Bailey, S.: MS+AS+BA+BI+PS+TF-TuM11, 63
Baimpos, T.: IA+AI+BI+IS+NL+SS-MoA11, **38**
Baio, J.E.: BA+AI+AS+BI+IS+NL-MoM5, **5**
Bak, S.-M.: IS+EN+SP+SS-ThA3, 214
Baker, L.: TF+EN-MoM11, 25; TF-TuM9, 72
Bakker, H.J.: IA+AI+BI+IS+NL+SS-MoA3, 37
Baklanov, M.: PS-MoA9, 46; PS-ThA4, 218
Balachander, N.: NS+EM+EN-TuM11, 65
Balakrishna, A.: PS-ThM5, 191
Balandin, A.A.: GR+AS+EM+MI+MN-TuM2, 60;
GR+EM+NS+SP+TF-MoA7, **36**
Balasubramanian, T.: MI-MoM11, 14
Balchandran, P.: MI+EM+MG-MoA10, 39
Balog, J.: AS+BI+IS-WeM2, **124**
Balsano, R.: SP+AS+EM+GR+MI+NS+SS-
FrM10, **258**
Ban, C.: EN+SE+SS+TF-WeM4, 131
Banerjee, S.: AS+BI+EM+NL+NS+SS-ThA1, **202**;
MG+AS+EM+NS+SA+SE+SP+SS+TF-FrM1,
253
Banik, A.: MS+AS+EL+EM+PS+TF-TuA9, 89;
PS2-TuM11, 68
Banna, S.: EM+AS+PS+TF-ThM1, 181;
EM+AS+PS+TF-ThM12, 183; EM-ThP3, 234;
PS1-TuA7, 91; PS1-TuM6, 66; PS-TuP13, 110;
PS-TuP17, 111; PS-TuP23, 112
Banninga, J.D.: TF-ThP25, 245
Banquy, X.: IS+AS+SP-FrM4, 252
Bao, P.: BI-TuP10, **102**
Bao, W.: GR+EM+NS+SP+TF-MoA1, 36; IS-
ThP2, 238
Baraket, M.: EM+AS+EN+TF-ThM5, 180
Baran, N.: BI+AS+IS+NL-MoM3, 6
Baránková, H.: SE+PS-ThM10, 193
Barback, C.: BI-TuP3, 100
Barcaro, G.: SS+AS-TuM9, 70

- Bardos, L.: SE+PS-ThM10, **193**
- Barja, S.: GR+AS+EM+MI+MN-TuM1, 59
- Barlow, A.: AS+BI-MoM1, 3; AS-MoA9, 30; AS-TuM5, **54**
- Barlow, D.E.: BI+AI+BA+IS-MoA3, 31; BI-WeM3, **126**
- Baroch, P.: TF+AS+EM+NS+SS-ThM9, **199**
- Barrett, D.A.: AS+BI+IS-WeM5, 125; BI-WeM1, 126
- Barrett, L.: MN+AS+SS-MoM5, **15**
- Barrett, N.: SA+AS+MG+SS-TuA3, 94; SA+AS+MI+SS-WeM4, 139
- Barroo, C.: AP+AS+MI+NS+SS-WeA11, **151**
- Barroso, D.: TF-ThP20, 244
- Barry, S.T.: TF+AS+SE+SS-MoA4, 49
- Bartels, L.: EM+NS+TF-FrM1, **248**; GR-WeM10, 134; TF-ThP19, 244; TF-ThP20, 244
- Bartelt, N.C.: GR-WeM12, 134
- Bartis, E.J.: PS+AS+BI+SE-MoM11, **19**
- Bartnik, A.: VT+AS+SS+TF-WeA7, 174
- Barton, D.: MN+AS+SS-MoM5, 15
- Bartynski, R.A.: EN+AS+NS+SS-MoA10, 35; EN-TuP7, 103; IS+EN+SP+SS-ThA9, 215; VT+EN+TF-TuA7, 98
- Baryshev, S.: EN+PS+TF-MoM10, 11
- Baski, A.A.: EM+NS+SS+TF-FrM3, 247
- Basov, D.N.: GR+AS+EM+MI+MN-TuM9, **60**
- Batarseh, A.: EN+AS+NS+SS-MoA10, 35
- Bates, R.L.: PS2-TuA9, **94**
- Batista, E.: AC+AS+EN-TuA10, 78
- Batzill, M.: GR+EM+MS+NS+SP-FrM8, 251; GR+EM+NS+PS+SS+TF-MoM9, 12; SS-FrM1, 258
- Bauer, G.E.W.: MI+EM-TuM11, **62**
- Bauer, K.: SP+AS+BI+MI+NS+SS-ThM5, **194**
- Bauer, S.: BI+AI+BA+IS-MoA2, **31**; NS+EM+EN-TuM9, 64
- Baum, J.C.: SS+AS+NS+SP-WeA12, 167
- Bäumer, M.: SS+AS-TuM11, 70; SS+NS-WeM11, 143
- Baxter, J.B.: EN+AS+NS+SS-MoA4, 35
- Baykara, M.Z.: SS+AS+NS+SP-WeA7, 166; TR+AS+NS+SS-MoA11, **52**
- Bazarov, I.: VT+AS+SS+TF-WeA7, 174
- Beach, J.: EN+PS+TF-MoM5, 10
- Beard, M.: PS-MoA3, 45
- Beckhoff, B.: SA-TuP4, 114
- Behafarid, F.: AS+BI+EM+NL+NS+SS-ThA3, 202; MG+AS+EM+NS+SA+SE+SP+SS+TF-FrM2, **253**; SS-TuP29, 118
- Béland, A.E.: EN+PS+TF-MoM9, 10
- Belchik, S.: BI+AI+AS+BA+IA+NL+NS+SP-WeA2, 153
- Belfort, G.: BI+AS+BA+NL-TuM10, 56
- Belkin, M.: NS+AS+BI+SP-WeM4, 136
- Bell, A.: EN-TuM5, **59**
- Bell, L.D.: EM+NS+SS+TF-FrM11, 248
- Bell, N.C.: AS+BI+EM+NL+NS+SS-ThM5, 175
- Belmonte, A.: EM+PS-TuM5, 57
- Belu, A.: AS+BI-TuA3, 80
- Bender, J.: SS-TuP3, 115
- Benítez, A.: EM-ThP1, **234**; EM-ThP9, 235; SS-TuP22, 118
- Benitez, J.: BI+AS+BA+NS+SS-ThA12, **205**
- Beniwal, S.: SS-TuP34, 119; TF+AS+BI+EM+SE+SS-WeA9, 172
- Bennett, B.: PS-ThA7, 219
- Bennett, C.: GR+AS+BI+PS+SS-ThA6, 210
- Bennowitz, R.: TR+SE-TuM9, **74**
- Bent, S.F.: EM+AS+PS+TF-ThM10, **182**; SS+EM-WeA1, 167; TF-TuM6, 72
- Benter, Th.: AS+BI+IS-WeM9, **125**
- Bentley, S.: MS+AS+EL+EM+PS+TF-TuA9, 89
- Berg, Ch.: VT-MoA6, **52**
- Berger, C.: GR+AS+BI+PS+SS-ThA10, 210
- Bergersen, H.: EW-TuL5, **76**
- Berman, D.: TR+SE-TuM11, **74**
- Bernal Ramos, K.: TF+EM+NS+SS-ThA10, **229**
- Bernal-Ramos, K.: EM+TF-MoM10, 9
- Bernard, L.: AS+BI-MoM6, 4
- Bernstein, H.C.: AS+BI+IS-WeM12, 125
- Berry, I.: PS-MoM6, 21
- Bersuker, G.: EM+MI+NS+SS+TF-TuA3, **82**
- Bertran, F.: MI+EM-TuM1, 61
- Bertrand, P.: PS+AS+BI+SE-MoM5, 18
- Besenbacher, F.: NS+AS+BI+SP-WeM9, 136
- Bettac, A.: SP+AS+EM+GR+MI+NS+SS-FrM7, **257**
- Beye, M.: SS2-ThA4, 226
- Beyer, A.: HI-ThA1, **212**; HI-ThA7, 213; HI-ThP2, 238; HI-ThP3, 238
- Bez, R.: MS+AS+EM+NS+PS+TF-MoA8, **41**
- Bezares, F.: GR+AS+BI+PS+SS-ThA6, 210
- Bhardwaj, C.: AS+BI+IS-WeM12, 125; AS-MoA3, 29
- Bhargava, N.: EM+AS+PS+TF-ThM2, 181
- Bhattacharya, A.: MI+EM+MG-MoA10, 39
- Bi, S.: SP+AS+BI+NS-ThP1, 240
- Bieber, T.: PS-TuP29, 113
- Biedermann, L.B.: SS+AS-TuM1, 69
- Bielefeld, J.D.: EM+AS+PS+TF-ThM9, 182; GR+AS+EM+NS+SS-WeA9, 160; TF+VT-WeM9, 147
- Biener, J.: SS+NS-WeM11, 143
- Biener, M.: SS+NS-WeM11, 143
- Bieber, T.: SE+PS-ThM9, 193
- Biffinger, J.C.: BI+AI+BA+IS-MoA3, 31
- Bignardi, L.: GR-WeM4, 133
- Binek, C.: MI+EM-TuM9, 61
- Bingaman, D.: EW-TuA5, **85**
- Biolsi, P.: EM-ThA2, 206; PS1-TuM5, 66; PS2-TuA8, 94; PS2-TuM12, 69; PS-MoA1, 45; PS-MoM11, 21
- Birmingham, B.: SS-FrM4, 259
- Bischoff, F.R.: BI+NL+NS+SS-ThM11, 178
- Bittencourt, C.: NS+AS+EM-MoA4, 42
- Biyikli, N.: SE-ThP11, 240; TF+AS+NS+SE-WeA3, **173**
- Blaas, D.: SP+AS+BI+EM+MI+NS+SE+SS-ThA1, 222
- Blackledge, R.: AS+BI-TuA4, 80
- Blackmond, D.G.: SS+AS-WeM1, **140**
- Blackwell, J.M.: EM+AS+PS+TF-ThM5, 182
- Blair, S.L.: BI-TuP3, 100; BI-WeM9, 127
- Blanc, R.: PS1-TuA7, 91; SE+PS-ThM6, **193**
- Blank, D.H.A.: MG+AS+EM+NS+SA+SE+SP+SS+TF-FrM3, **253**
- Blankenship, R.: IS+AS+SP-FrM10, 253
- Blanton, E.: EM2-ThA11, 206
- Blechle, J.M.: PS-WeM4, **137**
- Blomfield, C.J.: AS+BI-MoM4, 3; AS-MoA6, 29; AS-WeA3, 151; EW-TuL3, **76**
- Blomqvist, K.L.: SA+AS+MI+SS-WeM5, 139
- Bluhm, H.: IA+AI+BI+IS+NL+SS-MoA10, 38; SS+EN-ThM9, 196; TC+EM+TF-WeM3, 144
- Blum, I.: AP+AS+SS-TuA10, **79**; AP+AS+SS-TuA12, 79
- Bo, T.C.: PS-MoA11, 47
- Bobadilla, A.: GR+AS+BI+PS+SS-ThA3, 209
- Bobek, S.: GR-WeM10, 134; TF-ThP20, 244
- Bocek, D.: SP+AS+BI+MI+NS+SS-ThM10, 195
- Bochmann, J.: MN+NS-MoA6, **40**
- Bockstaller, M.R.: TC+EM+EN+TF-WeA3, 170
- Boden, S.A.: HI-ThA8, **213**
- Boffard, J.B.: PS1-TuA11, 92; PS-TuP14, 110
- Böker, A.: TF+AS+BI+EM+SE+SS-WeA11, 172
- Bokka, R.: PS-ThA12, 220
- Bol, A.A.: EN+AS+NS+SS-MoA9, 35; TF+EN-MoM10, 25; TF-TuM12, 72
- Boland, K.: AC+AS+EN-TuA10, 78
- Bolotin, I.: SE+EN-FrM5, 256
- Bolvardi, H.: SE+NS+TF-ThA8, 221
- Bomben, K.D.: AS-ThP13, **232**
- Bondaz, A.: EM+AS+PS+TF-ThM6, 182
- Bonecutter, A.: NS+AS+EN+SS-TuA11, 90
- Bonell, F.: MI+EM-TuM1, 61
- Bongers, W.: EN+AS+PS-TuA11, 84
- Bongiorno, A.: GR+AS+BI+PS+SS-ThA10, 210
- Bongiorno, G.: VT-WeM3, 148
- Bonilla, E.: TF-ThP20, 244
- Bonilla, J.: SS-TuP15, 117
- Bonn, M.: BA+AI+AS+BI+IS+NL-MoM10, 5; BA+AI+AS+BI+IS+NL-MoM5, 5; IA+AI+BI+IS+NL+SS-MoA3, **37**
- Bonnell, D.A.: IS+EN+SP+SS-ThA1, 214; NS+BI+EM-MoM9, **17**; NS+EM+EN-TuM3, 64; SS+AS-TuM5, 69
- Bonucci, A.: VT-WeM3, 148
- Boo, J.-H.: AS-ThP18, **233**
- Boosalis, A.: EL+AS+EM+SS+TF-WeA2, **155**; GR+EM+MS+SP-FrM7, 251
- Booth, J.-P.: PS+TF-MoA1, 43; PS1-TuA2, **91**
- Borca-Tasciuc, T.: EM+NS+TF-FrM3, 248; NS+EM+EN-TuM11, 65; SE+EN-FrM3, 256
- Bordia, R.K.: EN+SE+SS+TF-WeM5, 131
- Borg, A.: SS-MoA9, 48
- Borghetti, P.: SS1-ThA8, **225**
- Boris, D.R.: PS-ThA11, **220**
- Borner, K.: EM+AS+EN+TF-ThM6, 181
- Borodulin, P.: EM-ThP17, 236
- Bosman, M.: HI-ThA3, 212
- Bossert, J.: SE+PS-WeA7, 164
- Bostwick, A.: MI+AS+NS+SP-TuA7, 87
- Boswell, R.: AS-MoA1, 29
- Boufnichel, M.: PS2-TuA3, 93; PS-TuP1, 109
- Boutaud, B.: PS2-TuA4, 93
- Boutwell, R.C.: TF+EM+NS+SS-FrM10, 262
- Bowden, M.E.: SS+AS-TuM6, 70
- Bower, S.: MS+AS+BA+BI+PS+TF-TuM11, 63
- Bowfield, A.: AS+BI+IS-WeM5, 125
- Bowman, R.: SP+AS+BI+EM+MI+NS+SE+SS-ThA8, 223
- Boxford, W.: AS+BI-MoM4, 3
- Bozzini, B.: IS+AS+SS-ThM5, 186
- Bradley, J.: AC+AS+EN-TuA10, 78
- Bradley, J.W.: AS+BI+IS-WeM5, **125**
- Bradley, L.C.: TF-ThP24, **244**
- Braithwaite, N.St.J.: PS1-TuA7, 91; PS-WeA9, **163**
- Brameshuber, M.: SP+AS+BI+EM+MI+NS+SE+SS-ThA1, 222
- Brar, V.W.: GR+AS+EM+NS+SS-WeA11, 160
- Bratescu, M.A.: PS+AS+NS+SS-ThM6, **189**
- Braun, P.V.: TF+EM+NS+SS-ThA2, 228
- Bray, J.: PS-TuP23, 112
- Bray, K.R.: AS+BI+EM+NL+NS+SS-ThM12, **176**
- Bregliozzi, G.: VT-WeM10, 148
- Brehmer, F.: EN+AS+PS-TuA11, 84; PS1-TuA12, 92
- Breit, S.: PS-MoA7, 46
- Breitling, F.: BI+NL+NS+SS-ThM11, 178
- Breneman, C.: SS-TuP35, 119
- Brennan, B.: EM+TF-MoM10, 9; EM+TF-MoM5, 8
- Brennen, R.: MS+AS+BA+BI+PS+TF-TuM1, 63
- Brenner, D.: TR+AS-MoM6, 26
- Breslau, M.S.: TC+EM+EN+TF-WeA10, 170
- Brewer, T.: AS+BI+IS-WeM6, **125**
- Brichon, P.D.: PS-ThM2, **190**
- Brierley, M.: AC+AS+EN-TuA11, **78**
- Brigg, W.J.: PS-TuP21, 112
- Briggs, E.: MN+AS+SS-MoM10, 15
- Brihoum, M.: PS1-TuA7, 91; PS2-TuM3, 68
- Brink, M.: MS+AS+BA+BI+PS+TF-TuM3, 63; PS-MoA6, 45
- Brizzi, S.: EM+PS-TuM10, 58
- Broadbridge, C.C.: MG+EN+MS-WeA1, **160**
- Broch, K.: SS1-ThA2, **224**
- Broderick, S.R.: AP+AS+MI+NS+SS-WeA4, 150
- Brodsky, M.J.: PS2-TuM11, 68
- Broitman, E.: TF+EM+NS+SS-FrM8, 261; TR+SE-TuM4, **73**
- Brongersma, H.: GR+AS+NS+SP+SS-TuA9, 85
- Brown, C.: TF+PS-ThM6, 200
- Brown, S.: AS-ThP8, 232
- Brown, T.M.: TF+EN-MoM6, 24

- Bruce, R.L.: MS+AS+BA+BI+PS+TF-TuM3, 63; PS-MoA8, **46**; PS-MoM2, 20; PS-WeM1, 137
- Bruemmer, S.M.: AP+AS+SS-TuA9, 79
- Bruener, P.: GR+AS+NS+SP+SS-TuA9, 85
- Bruneau, B.: PS+TF-MoA1, 43
- Bruns, M.: AS-ThP12, **232**
- Bryan, S.R.: AS+BI-MoM5, **3**; AS-ThP9, 232
- Buchholz, M.: SS-FrM9, 260
- Buck, A.R.: IS+AS+SP-FrM3, **251**
- Budinska, Z.: SS+AS+NS-MoM9, 23
- Buffière, M.: NS+AS+EM-MoA4, 42
- Buie, C.: EM-MoA3, 32; GR+EM+NS+SS+TF-ThA1, 211
- Bultman, J.E.: SE+PS-ThM5, 192
- Bulusu, A.: TF+VT-WeM3, 146
- Burand, A.: AS+BI-TuA3, 80
- Burden, F.R.: NL+AS+BI-ThA3, 217
- Burkett, S.L.: MN-TuP6, 105
- Burnham, N.A.: NS+AS+BI+SP-WeM1, **135**
- Burns, S.: PS2-TuM11, 68
- Burrell, M.C.: AS-WeA10, **152**
- Bushby, R.J.: BI-TuP10, 102
- Bushell, A.: AS-WeA11, 152
- Bussmann, K.: GR+EM+NS+PS+SS+TF-MoM3, 11
- Butler, J.: MS+AS+BA+BI+PS+TF-TuM11, 63
- Buttery, L.: BI+AS+IS+NL-MoM2, 6
- Byeon, D.-S.: EM-ThP4, 235
- Byun, Y.-C.: EM1-WeM12, 130; EM-ThP5, 235
- C —
- Cabellos-Quiroz, J.L.: SS1-ThA8, 225
- Cabral, C.: PS-MoA6, 45
- Cabrera, W.: EM+TF-MoM10, **9**; SS+EM-WeA11, 169
- Cahill, D.G.: EN-TuM3, **58**
- Cai, X.: BA+AI+AS+BI+IS+NL-MoM8, 5
- Caillard, L.: TF+AS+BI+EM+SE+SS-WeA3, 171
- Calaza, F.: SS-MoA11, 48
- Caldwell, J.: GR+AS+BI+PS+SS-ThA6, 210
- Calleja, F.: GR+AS+EM+MI+MN-TuM1, 59
- Callow, J.A.: BI+AI+BA+IS-MoA2, 31
- Callow, M.E.: BI+AI+BA+IS-MoA2, 31; BI-TuP7, 101
- Calusine, G.: MI+EM-TuM3, 61
- Calzolari, L.: AS+BI+EM+NL+NS+SS-ThM10, 176
- Cammarata, A.: MI+EM+MG-MoA10, 39
- Campbell, C.T.: AS+BI+EM+NL+NS+SS-ThA6, 202; SS-MoA2, 47; SS-TuA3, **96**; SS-TuA8, 36
- Campbell, P.: TF+AS+BI+EM+SE+SS-WeA3, **171**
- Campbell, S.A.: EN+PS+TF-MoM4, 9
- Camus, J.: TF+EM+NS+SS-ThA8, 229
- Canales, M.: BI+AI+AS+BA+IA+NL+NS+SP-WeA12, **154**
- Canavan, H.E.: BI-WeM10, 127; BI-WeM2, **126**
- Candler, R.: TF+AS+EM+NS+SS-ThM11, 199
- Cansizoglu, H.: TF+AS+NS+SE-WeA3, 173
- Cansizoglu, M.F.: TF+AS+NS+SE-WeA3, 173
- Canto, C.E.: TR-TuP6, 121
- Cantone, J.: PS2-TuM9, 68
- Cao, G.X.: MI-MoM10, 14; MI-MoM9, 14; NS+EM+EN-TuM4, 64
- Cao, J.: PS-TuP11, **110**
- Cao, L.: GR+EM+NS+SS+TF-ThA6, **211**; TF+AS+NS+SE-WeA11, **174**
- Cao, W.: EM-TuA7, 83
- Cao, Y.: BI-TuP9, 101; MG-ThA1, 215; MI+EM-TuM9, 61
- Carlin, J.A.: EM+AS+NS+SS-WeA7, 157
- Carlson, R.P.: AS+BI+IS-WeM12, 125
- Carmo, M.: NS+BI+EM-WeA7, 162
- Carpick, R.W.: AS-ThP21, 233; TR+AS-MoM10, 26; TR+AS-MoM11, 26; TR+AS-MoM5, 25; TR+AS-MoM8, **26**
- Carr, L.: MS+AS+BA+BI+PS+TF-TuM1, **63**
- Carraro, C.: MN+AS+SS-MoM8, 15
- Carrillo, J.: EM-ThP1, 234; EM-ThP9, 235; SS-TuP22, 118
- Cartas, W.: SS+AS-TuM11, 70
- Caruso, A.N.: GR+AS+EM+NS+SS-WeA9, 160
- Caruso, L.: VT-WeM3, 148
- Castner, D.G.: AS+BI+EM+NL+NS+SS-ThM6, **175**; BI+AI+AS+BA+IA+NL+NS+SP-WeA8, 154
- Castro, G.R.: EM+NS+TF-FrM9, **249**; SA+AS+MG+SS-TuA4, **95**
- Caubet, P.: EM+PS-TuM2, 57; PS+TF-MoA8, 44
- Caudillo, R.: GR+AS+EM+NS+SS-WeA9, 160
- Cavallo, F.: GR+EM+NS+SP+TF-MoA2, 36
- Cavanagh, A.S.: TF+EN-MoM11, **25**; TF-TuM9, 72
- Caymax, M.: EM+TF-MoM2, 8
- Ceccone, G.: AS+BI+EM+NL+NS+SS-ThM10, **176**
- Ceder, G.: MG+EM+MI+MS-WeM9, **135**
- Celina, M.C.: AS-WeA9, 152
- Celiz, A.D.: BI-WeM1, **126**
- Cerstvy, R.: SE+NS+TF-ThA6, 221
- Ceylan, H.: SE-ThP11, 240
- Cha, S.: TF+EN-MoM1, **23**
- Chaabane, N.: AS+BI+EM+NL+NS+SS-ThA4, 202
- Chabal, Y.J.: EM+TF-MoM10, 9; GR+AS+BI+PS+SS-ThA10, 210; SS+EM-WeA10, 169; SS+EM-WeA11, 169; SS+EM-WeA9, 168; SS-FrM6, 259; TF+AS+BI+EM+SE+SS-WeA3, 171; TF+EM+NS+SS-ThA10, 229
- Chabert, P.: PS1-TuA2, 91
- Chae, S.: EM+TF-MoM8, 9
- Chagarov, E.: EM+TF-MoM11, 9; SS+EM-WeA8, 168; SS-FrM7, 259
- Chait, B.T.: BI+AS+BA+NL-TuM10, 56
- Chaker, M.: PS-MoM8, 21
- Chakrapani, V.: PS2-TuA8, 94
- Chamberlin, S.E.: SS+AS-TuM10, 70; SS+AS-TuM6, **70**
- Chambers, S.A.: MI+EM+MG-MoA2, 38; SS+AS-TuM10, 70; SS+AS-TuM6, 70
- Chan, B.T.: MS+AS+EM+NS+PS+TF-MoA6, 41
- Chan, C.K.: SS+AS-TuM1, **69**
- Chan, H.K.: GR+EM+MS+NS+SP-FrM4, 250
- Chandhok, M.: EM+AS+PS+TF-ThM9, 182
- Chang, C.: BI+AS+IS+NL-MoM8, 7; BI-WeM11, 127
- Chang, C.-H.: SS+NS-WeM10, 142
- Chang, C.M.: PS-TuP26, 112; TF-ThP2, **241**
- Chang, C.S.: GR+AS+NS+SS-ThM12, 184
- Chang, H.-Y.: EM-WeA10, 158
- Chang, J.P.: PS2-TuA7, 93; PS-MoM10, 21; TF+EM+NS+SS-ThA6, 228; TF+EN-MoM4, 24; TF+MI-WeM9, 145
- Chang, N.: EM+MI+NS+SS+TF-TuA10, 82
- Chang, R.: IS+AS+SS-ThM9, 187
- Chang, W.: IS+EN+SP+SS-ThA3, 214
- Chang, Y.Y.: SE-ThP3, **239**; SE-ThP4, 239
- Change, I.: TF+EN-MoM1, 23
- Chao, W.: MI+AS+NS+SP-TuA11, 87
- Chapagain, P.R.: SS-FrM10, 260
- Chaukulkar, R.P.: PS+AS+NS+SS-ThM3, **188**; TF-ThP16, 243
- Chawla, J.S.: EM-ThA7, **207**
- Cheetham, M.: BI-TuP10, 102
- Chen, C.: EM+TF-MoM8, 9
- Chen, C.-C.: SS+EN-ThM9, 196
- Chen, C.W.: VT-TuP2, 121
- Chen, D.: SA+AS+MG+SS-TuA10, 95
- Chen, D.A.: SS-TuA11, **96**; SS-TuP12, 117; SS-TuP16, 117
- Chen, F.Z.: VT-TuP1, 121; VT-TuP2, 121
- Chen, H.-P.: TF-ThP17, 244
- Chen, H.Y.: PS+AS+BI+SE-MoM4, 18
- Chen, H.-Y.: EM+MI+NS+SS+TF-TuA11, 83
- Chen, J.: EL+AS+EN+PS+SS+TF-ThM4, 178
- Chen, J.-B.: NS+AS+EM-MoA3, 42
- Chen, J.H.: PS-MoA3, 45
- Chen, J.Z.: SE+PS-WeA12, **165**; SS-TuP8, 116
- Chen, K.: PS2-TuA7, **93**; PS-MoM10, 21
- Chen, L.: PS1-TuM1, **65**; PS-TuP19, 111; PS-TuP20, 111; SS-MoA6, 47
- Chen, M.: GR+AS+EM+NS+SS-WeA2, 159
- Chen, P.L.: MN-TuP1, **104**; PS-TuP26, 112; TF-ThP2, 241
- Chen, P.-L.: MN-TuP2, 105
- Chen, P.-L.: MN-TuP3, 105
- Chen, S.: AS+BI+EM+NL+NS+SS-ThM11, 176; BI+NL+NS+SS-ThM6, **177**; SA+AS+MI+SS-WeM5, 139
- Chen, T.: TF-ThP19, 244
- Chen, X.: GR+AS+NS+SS-ThM11, **184**; NS+BI+EM-MoM9, 17; TF+EN-MoM3, 23
- Chen, Y.Y.: EM+PS-TuM5, 57
- Chen, Z.: IS-ThP2, 238
- Chen, Z.Y.: PS1-TuM1, 65
- Cheng, C.: PS+TF-MoA3, 44
- Cheng, G.: GR+EM+MS+NS+SP-FrM7, 251
- Cheng, I.C.: SE+PS-WeA12, 165; SS-TuP8, 116
- Cheng, Y.L.: PS-MoA11, **47**
- Chenot, S.: TF+EM+NS+SS-ThA8, 229
- Cheong, S.-W.: MI+AS+NS+SP-TuA12, 88
- Cherepanov, V.: SP+AS+EM+GR+MI+NS+SS-FrM8, 258
- Chernomordik, B.D.: EN+PS+TF-MoM9, **10**
- Cheshmehkhami, A.: NS+BI+EM-WeA11, **162**
- Cheung, D.: PS-MoM6, 21
- Chew, A.D.: VT-WeM1, **147**
- Chew, S.A.: EM+PS-TuM10, 58
- Chhowalla, M.: MG+AS+EM+NS+SA+SE+SP+SS+TF-FrM1, 253
- Chi, M.: NS+AS+EM-MoA8, 43
- Chiang, D.: TF-ThP2, 241; TF-ThP5, **242**
- Chiang, S.: NS+BI+EM-WeA3, **161**
- Chiappe, D.: EM-MoA1, 32
- Chiba, Y.: EM-ThA2, 206; PS2-TuA8, 94; PS-MoA1, 45
- Chien, D.: TF+EM+NS+SS-ThA6, **228**
- Chien, P.-Y.: EM-WeA10, 158
- Chikyw, T.: TC+EM+EN+TF-WeA11, 170
- Chilkoti, A.: BI+AS+BA+NS+SS-ThA11, 204; BI+NL+NS+SS-ThM9, **177**
- Chin, M.: MG+AS+EM+NS+SA+SE+SP+SS+TF-FrM6, 254
- Chiou, P.W.: PS-TuP8, 110
- Chirita, V.: TF+EM+NS+SS-FrM8, 261; TF+PS-ThM11, 201
- Chitre, K.P.: EN+AS+NS+SS-MoA10, 35
- Chiu, P.-K.: TF-ThP17, 244
- Chiu, S.Y.: MN-TuP4, 105
- Chmielewski, D.: EM+AS+NS+SS-WeA7, 157
- Chmielewska, M.: TF+EM+NS+SS-ThA8, 229
- Cho, B.: HI-ThA12, 214
- Cho, G.: TF+EN-MoM1, 23
- Cho, J.: TF+EN-MoM4, **24**
- Cho, M.R.: NS+BI+EM-MoM3, **16**
- Cho, T.: PS-ThA12, **220**
- Cho, T.S.: SE+PS-WeA9, 165
- Cho, W.-H.: MI-TuP1, 104; TF-ThP17, 244
- Cho, Y.-J.: TF-TuM5, 71
- Cho, Y.R.: TR-TuP3, **120**; TR-TuP5, 120
- Chobpattana, V.: EM1-WeM11, **130**
- Choe, H.: PS-TuP22, **112**
- Choi, C.H.: NS+AS+EM-MoA4, 42
- Choi, E.C.: EN-TuP3, **103**; EN-TuP4, 103
- Choi, G.: TF+VT-WeM12, 147
- Choi, J.: TF+EM+NS+SS-ThA6, 228
- Choi, K.R.: TC+EM+EN+TF-WeA4, 170
- Choi, S.: EM1-WeM12, **130**; EM-ThP5, 235; GR+AS+EM+NS+SS-WeA11, 160
- Choi, S.Y.: SS-TuP14, 117; TF-ThP6, 242
- Choi, U.H.: TC+EM+TF-WeM2, 143; TC+EM+TF-WeM4, 144
- Choi, Y.B.: TF+VT-WeM12, 147
- Chou, C.C.: PS-TuP8, 110
- Chou, C.Y.: AS-ThP7, **231**
- Chou, H.: GR-WeM3, 133

- Chou, L.-W.: NS+BI+EM-MoM8, 17; SS+AS+NS-MoM2, 22
- Chou, P.R.: AS-ThP7, 231
- Chou, Y.K.: SE-ThP3, 239
- Christie, J.A.: TF+AS+BI+EM+SE+SS-WeA10, 172
- Christie, K.: EM+AS+NS+SS-WeA11, 157
- Christophis, C.: BI+AS+IS+NL-MoM3, 6; BI-TuP7, 101
- Chrost, J.: SP+AS+EM+GR+MI+NS+SS-FrM7, 257
- Chu, N.: MS-TuP2, 106
- Chu, Y.-H.: SA+AS+MG+SS-TuA10, 95
- Chun, Y.S.: TC+EM+EN+TF-WeA4, 170
- Chung, K.-Y.: IS+EN+SP+SS-ThA3, 214
- Chung, N.: SP+AS+BI+NS-ThP3, **241**
- Chung, S.: VT-TuP4, 121
- Chung, T.M.: TF-ThP38, **246**
- Chung, T.-Y.: PS+AS+BI+SE-MoM11, 19
- Church, J.: AS-WeA12, **153**
- Cinquanta, E.: EM-MoA1, 32
- Ciobanu, C.V.: EN+SE+SS+TF-WeM4, 131; GR+AS+BI+PS+SS-ThA1, 209; GR+AS+NS+SS-ThM1, **183**; GR-WeM12, 134
- Cirigliano, N.: TF+EN-MoM4, 24
- Ciston, J.: IS+AS+SP-FrM1, 251
- Ciszewski, A.: SS1-ThA9, **225**
- Clancey, J.: TF+EN-MoM11, 25; TF-TuM9, **72**
- Clark, A.: EM+NS+TF-FrM10, 250
- Clarke, J.S.: EM+AS+PS+TF-ThM5, 182; EM+AS+PS+TF-ThM9, 182; EM-ThA7, 207
- Cleland, A.N.: MN+NS-MoA6, 40
- Cleveland, E.: PS-ThA7, **219**
- Cleveland, J.: SP+AS+BI+MI+NS+SS-ThM10, 195
- Clifton, P.: AP+AS+EM+MI+TF-WeM10, 124
- Clima, S.: EM+PS-TuM5, **57**
- Cloud, A.N.: TF+EM+NS+SS-ThA2, 228
- Cobas, E.: MI+EM-TuM5, 61
- Coffee, R.: SS2-ThA4, 226
- Coffey, G.: NS-TuP12, 108
- Cohen, H.: AS-ThP22, **233**
- Cohen, P.I.: GR+EM+NS+PS+SS+TF-MoM1, **11**
- Cohen, S.R.: BI+AI+AS+BA+IA+NL+NS+SP-WeA9, **154**
- Cohn, A.W.: SS+AS-TuM6, 70
- Colburn, M.E.: MS+AS+EL+EM+PS+TF-TuA4, 89
- Colby, R.J.: AP+AS+MI+NS+SS-WeA12, 151; AP+AS+MI+NS+SS-WeA2, 150; AP-TuP1, 100; MI+EM+MG-MoA2, 38
- Cole, C.: MS+AS+EL+EM+PS+TF-TuA9, 89
- Cole, J.: PS-TuP18, **111**
- Colinjivadi, K.: EM-ThA6, 207
- Collings, M.P.: SS+AS-WeM12, 141
- Collins, K.: PS-ThM5, 191
- Collins, R.W.: EL+AS+EN+PS+SS+TF-ThM4, 178
- Colombo, L.: MS+AS+EM+NS+PS+TF-MoA1, **41**
- Colvin, B.: TF+VT-WeM9, 147
- Comes, R.B.: MI+EM+MG-MoA11, 39
- Conard, T.: SA+AS+MG+SS-TuA9, 95
- Conboy, J.: IA+BA-TuA7, **86**
- Conklin, D.: NS+BI+EM-MoM9, 17
- Conley, J.F.: TF+EM+NS+SS-ThA1, 228
- Conley, Jr., J.F.: EM+PS-WeM10, 129
- Connell, S.D.: BI+AI+AS+BA+IA+NL+NS+SP-WeA10, 154
- Conrad, E.H.: GR+EM+NS+PS+SS+TF-MoM1, 11
- Conrads, L.: SE+NS+TF-ThA8, 221
- Conte, A.: VT-WeM3, 148
- Contreras-Puente, G.: TF-ThP1, 241; TF-ThP13, 243
- Conway, J.V.: VT-WeM12, 148
- Cook-Chennault, K.: MG+AS+EM+NS+SA+SE+SP+SS+TF-FrM1, **253**
- Cooperstein, M.A.: BI-WeM10, **127**
- Corcelli, S.A.: TF+AS+BI+EM+SE+SS-WeA10, 172
- Cordier, Y.: TF+EM+NS+SS-ThA8, 229
- Corely, S.D.: TR+AS-MoM6, 26
- Corkery, R.: IA+AI+BI+IS+NL+SS-MoA7, 37
- Cosandey, F.: IS+EN+SP+SS-ThA9, 215
- Cossement, D.: SE+NS+TF-ThA9, 221
- Cotte, J.: MS+AS+BA+BI+PS+TF-TuM3, 63
- Coults, S.J.: AS-MoA6, 29; AS-WeA3, **151**
- Counsell, J.D.P.: AS+BI-MoM4, 3; AS-MoA6, **29**; AS-WeA3, 151
- Coy-Diaz, H.: GR+EM+MS+NS+SP-FrM8, 251
- Coyle, J.: TF+AS+SE+SS-MoA4, 49
- Crabtree, G.: MS+AS+EM+EN+NS+TF-MoM1, **16**
- Craig, I.M.: SP+AS+BI+NS-ThP2, 241
- Craighead, H.G.: BI+AS+BA+NS+SS-ThA12, 205
- Creator, M.: EN+AS+NS+SS-MoA9, 35; SE+PS-WeA8, 165; TF+EN-MoM6, **24**; TF+VT-WeM1, 146; TF+VT-WeM6, 147
- Cremer, P.S.: IA+BA-TuA3, **86**
- Creyghton, Y.L.M.: SE+PS-WeA10, 165
- Crommie, M.F.: GR+AS+EM+NS+SS-WeA11, **160**
- Crookes-Goodson, W.J.: BI+AI+BA+IS-MoA3, **31**
- Crowcombe, W.E.: VT+EN+TF-TuA9, 98
- Crowell, P.: EM+AS+NS+SS-WeA11, 157
- Crum, J.: NS+AS+BI+SP-WeM2, 135
- Crumlin, E.J.: IS+AS+SS-ThM9, 187
- Cruz, J.: PS-TuP34, 114
- Cuddy, M.: SS+EN-ThM12, 196
- Cuddy, M.F.: PS-WeM4, 137
- Cui, C.: SS-TuP29, 118
- Cui, Y.: AS+BI+IS-WeM12, 125; AS-MoA3, **29**
- Cullen, P.J.: SE+PS-WeA4, 164
- Cullen, W.G.: GR+AS+NS+SS-ThM3, 183
- Cultrera, L.: VT+AS+SS+TF-WeA7, **174**
- Culver, C.L.: PS1-TuA11, 92
- Cumpson, P.: AS+BI-MoM1, **3**; AS-MoA9, **30**; AS-TuM5, 54
- Cunge, G.: PS1-TuA7, **91**; PS-ThM2, 190; PS-WeM6, 138; SE+PS-ThM6, 193
- Cunningham, G.B.: EM+NS+TF-FrM6, 249
- Curreli, D.: PS-TuP12, 110; TF+PS-ThM10, 200; TF-ThP18, 244
- Currie, M.: GR+EM+NS+PS+SS+TF-MoM3, 11
- Cutivet, A.: TF+EM+NS+SS-ThA8, 229
- Cyganik, P.: SS+AS+NS+SP-WeA10, 167; SS1-ThA11, 225; TF+AS+BI+EM+SE+SS-WeA7, **172**
- Czap, G.: SP+AS+BI+MI+NS+SS-ThM4, 194; SS+EN-ThM11, 196
- Czarnecki, M.: EW-WeM7, **132**
- Czerwinski, A.: AP-TuP2, 100
- **D** —
- da Silva, A.R.: TF-ThP4, 241
- Dadson, A.: EL+AS+EM+SS+TF-WeA8, 155; TF+EM+NS+SS-FrM4, 261
- Dagdeviren, O.E.: SS+AS+NS+SP-WeA7, 166
- Dahal, A.: GR+EM+MS+NS+SP-FrM8, **251**
- Dahint, R.: BI+NL+NS+SS-ThM11, **178**
- Dai, S.X.: VT-MoA8, 52
- Dalmiglio, M.: GR-WeM11, 134
- Daly, S.: AC+AS+EN-TuA10, 78
- Damascelli, A.: SA+AS+MI+SS-WeM5, 139
- Dames, C.: IS-ThP2, 238
- Dandeneau, C.S.: EN+SE+SS+TF-WeM5, **131**
- Daniels, S.: PS1-TuA1, 91
- Darakchieva, V.: EL+AS+EM+SS+TF-WeA1, 155; EL+AS+EM+SS+TF-WeA2, 155
- Dargis, R.: EM+NS+TF-FrM10, **250**
- Darnon, M.: PS1-TuA7, 91; PS-ThM2, 190; SE+PS-ThM6, 193
- Davidson, D.E.: AS-ThP8, 232
- Davies, M.C.: BI+AS+IS+NL-MoM10, 7; BI+AS+IS+NL-MoM8, 7; BI-WeM1, 126; BI-WeM11, 127
- Davies, S.: VT-TuP8, 122
- Davis, E.S.: SS-FrM10, 260
- Davis, H.: SA+AS+MI+SS-WeM5, 139
- Davis, J.: AS+BI-MoM8, 4
- Davis, P.: EM+NS+SS+TF-FrM5, 247
- Davis, R.C.: EL+AS+EM+SS+TF-WeA8, 155; MN+AS+SS-MoM4, 15; MN+AS+SS-MoM5, 15; TF+EM+NS+SS-FrM5, 261; TF+PS-ThM2, 200; TF+PS-ThM6, 200; TF+PS-ThM9, 200; TF+VT-WeM11, 147
- Davissou, M.L.: AS+BI-TuA1, 80
- Davydova, A.: PS1-TuA7, 91; PS-WeM6, **138**
- Dawson, K.: NL+AS+BI-ThA1, **217**
- Dawson, N.: EM-ThP10, **235**
- de Andres, A.: EM+NS+TF-FrM9, 249
- De Battice, L.: BI+AS+BA+NL-TuM5, 56
- De Benedetti, W.J.: SS+EM-WeA10, 169
- De Boer, J.: BI-WeM4, **126**
- De Decker, Y.: AP+AS+MI+NS+SS-WeA11, 151
- De Geyter, N.: PS1-TuA8, 225
- De Jaeger, J.C.: TF+EM+NS+SS-ThA8, 229
- De Keyser, P.: PS-TuP29, 113
- De Keyzer, P.: SE+PS-ThM9, 193
- de Leeuw, N.H.: MG-ThA3, **216**
- De Marneffe, J.-F.: PS-MoA9, 46
- De Melo-Pereira, O.: TF-ThP13, 243
- De Moure-Flores, F.: NS-TuP3, 106; NS-TuP4, 107; TF-ThP1, 241; TF-ThP13, 243
- De Oteyza, D.G.: SS1-ThA8, 225
- de Pablo, J.J.: MG+EM+MI+MS-WeM3, **134**
- de Peuter, K.: PS+AS+NS+SS-ThM3, 188
- de Souza, J.F.: GR-ThP7, 237
- de Vries, H.: TF+VT-WeM1, 146
- de Weerd, M.-C.: AS+BI-TuA9, 81
- Dean, C.: NS+EM+EN-TuM1, **64**
- DeBenedetti, W.J.I.: SS-FrM6, **259**
- DeBoer, W.: VT-WeM11, 148
- DeCerbo, J.N.: AS+BI+EM+NL+NS+SS-ThM12, 176
- Deconihout, B.: AP+AS+SS-TuA10, 79; AP+AS+SS-TuA12, 79
- Deeks, C.: AS+BI-TuA4, 80
- Defrance, N.: TF+EM+NS+SS-ThA8, 229
- Degraeve, R.: EM+PS-TuM5, 57
- Delabie, A.: TF+AS+SE+SS-MoA9, 50
- Delattre, P.A.: PS+TF-MoA1, 43
- Delcorte, A.: PS+AS+BI+SE-MoM5, 18
- Delfour, L.: PS-WeM6, 138
- Deligiannis, D.: EN+AS+NS+SS-MoA9, 35
- Dell'Angela, M.: SS2-ThA4, 226
- Dellinger, A.: BI+AS+BA+NS+SS-ThA10, 204
- DeLong, E.: EL+AS+EN+PS+SS+TF-ThM12, 179
- Delongchamp, D.: EM+AS+EN+TF-ThM5, 180
- Demidov, V.: PS-WeM5, 138
- Demirci, E.: MI-TuP2, 104
- Demkov, A.: EM+NS+TF-FrM10, 250
- Deng, D.D.: EN+PS+TF-MoM9, 10
- Denning, C.: BI+AS+IS+NL-MoM10, 7; BI-WeM1, 126
- Dennis, R.: AS+BI+EM+NL+NS+SS-ThA1, 202
- Deon, D.J.: TF-ThP38, 246
- Derouin, J.: SS-TuP3, 115
- Desai, M.: TF+MI-WeM1, **144**
- Deschamps, F.: PS+AS+NS+SS-ThM9, 189
- Deskins, N.A.: SS+EN-ThM1, 195
- Despiau-Pujo, E.: PS1-TuA7, 91; PS-ThM2, 190; PS-WeM6, 138
- Devant, L.: PS+AS+NS+SS-ThM9, 189
- Devaraj, A.: AP+AS+MI+NS+SS-WeA1, 150; AP+AS+MI+NS+SS-WeA2, **150**; AP-TuP1, 100; HI-ThA9, 213; NS-TuP12, 108
- Devashayam, A.: PS-TuP12, 110
- Devender, F.: EM+NS+TF-FrM3, 248; SE+EN-FrM3, 256
- Devereaux, T.: SS+EN-ThM9, 196
- Devred, F.: AP+AS+MI+NS+SS-WeA11, 151
- Dhar, N.: EM+NS+TF-FrM6, 249
- Dhiman, R.: TF+EM+NS+SS-FrM2, 260
- Di Valentin, C.: SS-FrM9, 260
- Dianoux, R.: AS+BI-MoM6, 4
- Diao, Z.: MN+NS-MoA3, 40; MN+NS-MoA4, **40**

- Diaz, C.: GR+AS+EM+MI+MN-TuM1, 59
Díaz-Tendero, S.: SS1-ThA3, 224
Dickey, E.R.: TF-TuA7, 97
Diebold, A.C.: EL+AS+EM+SS+TF-WeA9, 156
Diercks, D.: AP+AS+EM+MI+TF-WeM11, 124
Dieterle, J.: SS1-ThA2, 224
Dietz, N.: EM+NS+SS+TF-FrM10, 248;
EM+NS+SS+TF-FrM9, 248
Dietzel, D.: TR+SE-TuM12, 74
Dillon, A.C.: EN+SE+SS+TF-WeM4, 131
Dillon, E.: NS+AS+BI+SP-WeM4, 136;
NS+AS+BI+SP-WeM5, 136
DiLullo, A.: SP+AS+BI+MI+NS+SS-ThM3, 194
DiMeglio, J.: EN+AS+PS-TuA3, 84
Dinauer, E.M.: EM-ThP13, 236
Ding, F.: GR+AS+NS+SS-ThM5, 184
Ding, Z.: EM+AS+EN+TF-ThM10, 181
Diniz, J.A.: GR-ThP7, 237; TF-ThP4, 241
Diño, W.A.: SS-TuP6, 115
DiStefano, S.: VT-WeM11, 148
Dittman, R.: EM+PS-WeM1, 128
Diwan, A.: EL+AS+EM+SS+TF-WeA8, 155;
TF+EM+NS+SS-FrM4, 261
Dixit, R.: MG+AS+EM+NS+SA+SE+SP+SS+TF-
FrM6, 254
Dixit, S.: MG+AS+EM+NS+SA+SE+SP+SS+TF-
FrM6, 254
Dixon, M.P.: BI+AI+AS+BA+IA+NL+NS+SP-
WeA11, 154
Djouadi, M.A.: TF+EM+NS+SS-ThA8, 229
Dobrovitski, V.V.: MI+EM-TuM3, 61
Dobson, M.P.: EW-WeL2, 149
Dohnalek, Z.: SS-MoA6, 47
Doi, I.: TF-ThP4, 241
Doi, K.: NS-TuP7, 107
Dolan, G.F.: SS+AS-WeM3, 140
Dolocan, A.: EN+SE+SS+TF-WeM10, 132
Domagala, J.Z.: AP-TuP2, 100
Dombrowski, E.: SS2-ThA10, 227
Domen, K.: SE+EN-FrM6, 256
Donald, D.R.: AS+BI+EM+NL+NS+SS-ThM11,
176
Donald, S.B.: SS2-ThA1, 226; SS2-ThA11, 227;
SS2-ThA3, 226
Donaldson, S.H.: IS+EN+SP+SS-ThA6, 215
Donath, M.: MI-MoM1, 13; MI-MoM8, 14
Donegan, M.: SE+PS-WeA4, 164
Dong, H.: EM+TF-MoM10, 9; EM+TF-MoM5, 8
Dong, Y.: SS-ThM12, 198; TR+AS-MoM11, 26
Donmez, I.: SE-ThP11, 240
Donnelly, V.M.: PS1-TuA9, 92; PS1-TuM3, 65;
PS1-TuM4, 66
Dorfmueller, J.: HI-ThA3, 212
Doris, B.: PS2-TuM9, 68
Dorman, J.: EN+SE+SS+TF-WeM6, 131
Dorrestein, P.C.: BP+AS-SuA1, 1
Doubek, G.: NS+BI+EM-WeA7, 162
Doudin, B.: SS-TuP34, 119
Dougherty, D.B.: EM+AS+EN+TF-ThM2, 180;
GR+AS+EM+NS+SS-WeA10, 160; SS-TuP18,
117
Doughty, B.: BA+AI+AS+BI+IS+NL-MoM1, 5
Douglas, R.: TF+MI-WeM5, 145
Doumanidis, C.C.: TF-ThA3, 230
Dowben, P.A.: MI+EM-TuM9, 61; SS-TuP34,
119; TF+AS+BI+EM+SE+SS-WeA9, 172
Dowell, D.H.: VT+AS+SS+TF-WeA11, 174
Dowling, D.P.: SE+PS-WeA4, 164
Dowsett, D.: HI-ThA11, 214
Drake, C.N.: BI+AI+BA+IS-MoA3, 31
Droopad, R.: EM+PS-TuM3, 57; EM+PS-TuM9,
57; SS+EM-WeA8, 168
D'Souza, A.: EM+NS+TF-FrM6, 249
Du, K.: NS+AS+EM-MoA4, 42
Du, Y.: MI+EM+MG-MoA2, 38
Dubois, G.: EM+AS+PS+TF-ThM3, 182
Dubois, J.-M.: AS+BI-TuA7, 80
Dubrovinskaia, N.: SE+NS+TF-ThA3, 220
Dubrovinsky, L.S.: SE+NS+TF-ThA3, 220
Dufour, T.: PS+AS+BI+SE-MoM5, 18;
PS+AS+NS+SS-ThM9, 189
Dufresne, C.: BI+AS+IS+NL-MoM4, 6; EW-
TuA6, 85
Duke, A.S.: SS-TuA11, 96
Dukovic, G.: EN+AS+NS+SS-MoA6, 35
Dulkin, A.: EM-ThA6, 207
Dumpala, S.: AP+AS+MI+NS+SS-WeA4, 150
Dunham, B.: VT+AS+SS+TF-WeA7, 174
Dunn, B.: TF+EN-MoM4, 24
Dunn, M.: BI+AI+BA+IS-MoA11, 32
Dupuy, E.: PS2-TuM3, 68
Durand, C.: AP+AS+SS-TuA12, 79
Durbine, S.: EM2-ThA10, 206
Dussart, R.: PS2-TuA1, 93; PS2-TuA4, 93; PS-
TuP1, 109
Dutta, D.: EM+AS+PS+TF-ThM2, 181; TF+VT-
WeM9, 147
Duty, C.: TC+EM+TF-WeM12, 144
Dyett, B.: SE-ThP9, 240
Dylla, A.G.: SS+AS-TuM1, 69
Dylla, H.F.: PS-WeA1, 163; VT-TuM11, 75
Dzarasova, A.: PS-TuP21, 112
— E —
Easton, C.: BI+AS+BA+NS+SS-ThA2, 203
Ebert, H.: MI+AS+NS+SP-TuA7, 87
Ebner, A.: SP+AS+BI+EM+MI+NS+SE+SS-
ThA1, 222
Ebnonnasir, A.: GR-WeM12, 134
Economou, D.J.: PS1-TuA9, 92; PS1-TuM3, 65;
PS1-TuM4, 66
Eddy, C.: EL+AS+EM+SS+TF-WeA2, 155;
EM+NS+SS+TF-FrM4, 247;
GR+EM+NS+PS+SS+TF-MoM3, 11
Eddy, Jr., C.R.: EL+AS+EM+SS+TF-WeA1, 155;
EM+NS+SS+TF-FrM6, 247;
GR+EM+MS+NS+SP-FrM4, 250
Ediger, M.D.: MG+EM+MI+MS-WeM3, 134
Edley, M.E.: EN+AS+NS+SS-MoA4, 35
Edmonds, M.: EM+PS-TuM9, 57; SS+EM-WeA8,
168
Edström, D.: TF+PS-ThM11, 201
Egan, P.: VT-MoM3, 27
Egberts, P.: TR+AS-MoM11, 26
Ehre, D.: AS-ThP22, 233
Eichhorn, R.G.: VT-WeM12, 148
Einstein, T.L.: GR+AS+NS+SS-ThM3, 183;
SS+AS+NS-MoM3, 22
Eisenthal, K.B.: BA+AI+AS+BI+IS+NL-MoM1, 5
Eizenberg, M.: EM+TF-MoM2, 8
Ekerdt, J.G.: SS-FrM5, 259
Eklund, P.: TF+EM+NS+SS-ThA3, 228
El Kasmi, A.: HI-ThA7, 213
El Mel, A.: NS+AS+EM-MoA4, 42
El-Hinnawy, N.: EM-ThP17, 236
El-Khoury, P.: NS-TuP12, 108
Eller, B.S.: EM-WeA3, 158
Ellies, L.G.: BI-TuP3, 100
Ellinger, C.R.: TF-TuA3, 97
Ellingsworth, E.: EN+SE+SS+TF-WeM9, 132
Elliott, S.D.: TF+AS+SE+SS-MoA3, 49
Ellsworth, A.: EM+AS+EN+TF-ThM6, 181
Elmqvist, R.: EL+AS+EM+SS+TF-WeA2, 155
El-Sayed, A.: SS1-ThA8, 225
Elsener, B.: AS-TuM12, 55
Elswick, D.: EW-WeL6, 149
Emori, M.: SS+EN-ThM10, 196
Enderes, R.: VT-MoM9, 27
Enders, A.: SS-TuP34, 119;
TF+AS+BI+EM+SE+SS-WeA9, 172
Engel, L.: MN+AS+SS-MoM6, 15
Engelhard, M.: AS+BI+EM+NL+NS+SS-ThM11,
176; AS-ThP3, 231
Engelmann, S.U.: PS-MoA8, 46; PS-MoM2, 20;
PS-WeM1, 137
Engeln, R.: EN+AS+PS-TuA11, 84; PS1-TuA12,
92
Engledew, D.J.: SP+AS+BI+EM+MI+NS+SE+SS-
ThA8, 223
Engstrom, J.R.: EM+AS+EN+TF-ThM1, 180
Engtrakul, C.: EN+SE+SS+TF-WeM4, 131;
TF+PS-ThM5, 200
Enochson, L.: BI+AS+BA+NL-TuM6, 56
Eom, C.: MG+EM+MI+MS-WeM11, 135
Eom, D.: SS+EM-WeA2, 168
Epa, V.C.: BI+AS+IS+NL-MoM8, 7; NL+AS+BI-
ThA3, 217
Epaminonda, P.: SE-ThP8, 240
Epuri, S.R.: SS+AS-TuM11, 70
Ercolano, G.: TF-TuA9, 97
Erdemir, A.: TR+SE-TuM11, 74
Erdemir, O.: MI-TuP2, 104
Erickson, N.C.: AS-ThP13, 232
Eriguchi, K.: PS-MoM1, 19; PS-ThM1, 190
Erkal, T.S.: SE-ThP11, 240
Erkovan, M.: MI-TuP2, 104
Ertekin, E.: SS+EM-WeA12, 169
Erten, A.: MN+AS+SS-MoM10, 15
Escamilla, R.: SS-TuP4, 115
Escamilla-Esquivel, A.: TF-ThP13, 243
Escher, M.: SA+AS+MI+SS-WeM4, 139
Estrada-Raygoza, I.C.: MS+AS+EL+EM+PS+TF-
TuA4, 89; PS2-TuM9, 68
Eun, C.: PS+AS+BI+SE-MoM3, 18
Evans, J.E.: AP-TuP1, 100
Evans, J.W.: AS+BI-TuA10, 81
Evans, P.A.: HI-ThA8, 213
Evans, S.D.: BI+AI+AS+BA+IA+NL+NS+SP-
WeA10, 154; BI-TuP10, 102
Eymerly, J.: AP+AS+SS-TuA12, 79
— F —
Fadenberger, K.: TF-ThA3, 230
Fadida, S.: EM+TF-MoM2, 8
Fadley, C.S.: MI+AS+NS+SP-TuA7, 87
Faingold, A.: BI+AI+AS+BA+IA+NL+NS+SP-
WeA9, 154
Fairley, N.A.: GR-ThP6, 237
Faken, D.: PS-MoA7, 46
Faleev, N.: TF+EM+NS+SS-FrM10, 262
Falk, A.L.: MI+EM-TuM3, 61
Fallahzad, B.: EM-WeA7, 158
Fan, W.: TF+EM+NS+SS-FrM3, 260
Fanciulli, M.: EM-MoA1, 32
Fantauzzi, M.: AS-TuM12, 55
Fantini, A.: EM+PS-TuM5, 57
Faradzhev, N.S.: VT+EN+TF-TuA7, 98
Farah, S.: MS+AS+BA+BI+PS+TF-TuM11, 63
Farber, D.: PS-WeM3, 137
Farmer, M.: SS-TuP3, 115
Farrar, P.: MS+AS+EM+NS+PS+TF-MoA10, 41
Farstad, M.H.: SS-MoA9, 48
Faubel, M.: IA+AI+BI+IS+NL+SS-MoA10, 38
Fay, P.J.: EM+TF-MoM8, 9; EM-ThA10, 208
Fazio, W.: TF+PS-ThM2, 200
Fears, K.P.: BI-WeM3, 126
Fedchak, J.A.: VT-MoM5, 27
Feenstra, R.M.: GR-WeM3, 133;
SP+AS+EM+GR+MI+NS+SS-FrM1, 257
Feldberg, N.: EM2-ThA10, 206
Feldman, L.C.: GR+EM+NS+PS+SS+TF-MoM1,
11
Feldmann, M.: TR+SE-TuM12, 74
Felmy, A.: AP+AS+MI+NS+SS-WeA12, 151
Feltz, A.: SP+AS+EM+GR+MI+NS+SS-FrM7,
257
Feng, J.: VT+AS+SS+TF-WeA11, 174
Feng, P. X.-L.: MN+NS-MoA8, 40; MN+NS-
TuM6, 63; PS+AS+NS+SS-ThM12, 190
Feng, X.: GR+AS+EM+NS+SS-WeA7, 159
Fennie, C.J.: MI+AS+NS+SP-TuA12, 88
Ferguson, I.T.: EM+NS+SS+TF-FrM10, 248;
EM+NS+SS+TF-FrM7, 247
Fernández, F.: AS+BI+IS-WeM4, 124
Fernandez, M.C.: PS2-TuA3, 93
Fernsler, R.F.: PS-ThA11, 220
Ferranti, D.: TF+AS+NS+SE-WeA10, 173
Ferris, R.: GR+AS+EM+NS+SS-WeA1, 159
Feurprier, Y.P.: EM-ThA2, 206; PS-MoA1, 45

- Fields, J.: TC+EM+EN+TF-WeA7, 170
 Filler, M.A.: NS+AS+EM-MoA8, 43;
 NS+BI+EM-MoM8, 17; SS+AS+NS-MoM2,
 22
 Finlay, J.: BI+AI+BA+IS-MoA2, 31
 Fischer, D.: SA+AS+MI+SS-WeM3, 139
 Fischer, P.: MI+AS+NS+SP-TuA11, 87
 Fischer-Wolfarth, J.-H.: SS+NS-WeM2, 142
 Fisher, B.: GR+EM+NS+PS+SS+TF-MoM6, 12;
 SP+AS+EM+GR+MI+NS+SS-FrM11, 258
 Fisher, D.A.: EM+AS+EN+TF-ThM5, 180
 Fisher, E.R.: BI-WeM12, 127; NS+AS+EM-
 MoA10, 43; PS+AS+BI+SE-MoM10, 19; PS-
 WeM4, 137; TF+PS-ThM1, 199
 Fisher, G.L.: AS+BI-MoM5, 3; AS-ThP9, 232
 Fitz-Gerald, J.M.: MI+EM+MG-MoA11, 39
 Flatt, J.: MS+AS+BA+BI+PS+TF-TuM11, 63
 Fleischmann, C.: SA+AS+MG+SS-TuA9, 95; SA-
 TuP4, 114
 Floreano, L.: SS1-ThA8, 225
 Flores Gracia, F.J.: EN-TuP8, 103
 Flores, F.: EM-ThP9, 235
 Flores, M.: SS-TuP4, 115; TR-TuP6, 121
 Flores-Camacho, J.M.: SS+NS-WeM2, 142
 Floro, J.A.: MI+EM+MG-MoA11, 39
 Flynn, B.: TC+EM+TF-WeM3, 144
 Föhlisch, A.: SS2-ThA4, 226
 Pompeyrine, J.: EM+NS+TF-FrM4, 249
 Fonseca, L.R.C.: GR-ThP7, 237
 Forbes, T.: AS+BI+IS-WeM6, 125
 Forrest, R.P.: TF+AS+BI+EM+SE+SS-WeA10,
 172
 Fortunelli, A.: SS+AS-TuM9, 70
 Foucher, M.: PS1-TuA2, 91
 Fouchier, M.: PS2-TuM3, 68
 Fournée, V.: AS+BI-TuA9, 81
 Fox-Lyon, N.A.: PS-WeM3, 137; PS-WeM5, 138
 Frahm, R.: SA+AS+MI+SS-WeM11, 140
 Francois-Saint-Cyr, H.G.: AP+AS+EM+MI+TF-
 WeM10, 124
 Franek, J.: PS-WeM5, 138
 Frank, C.W.: BI+AS+BA+NL-TuM11, 56
 Franz, G.F.: TF+EM+NS+SS-FrM9, 262
 Franz, S.: TF+AS+EM+NS+SS-ThM11, 199
 Frayssinet, E.: TF+EM+NS+SS-ThA8, 229
 Fredricks, Z.: TR+AS+NS+SS-MoA4, 51
 Freeman, M.R.: MN+NS-MoA3, 40; MN+NS-
 MoA4, 40
 Freeze, C.R.: TR-TuP4, 120
 French, B.: EM+MI+NS+SS+TF-TuA2, 82;
 GR+AS+EM+NS+SS-WeA9, 160
 French, M.: GR+AS+EM+NS+SS-WeA9, 160
 French, R.H.: TC+EM+EN+TF-WeA10, 170
 Frenken, J.W.M.: TR+AS+NS+SS-MoA9, 51
 Freund, H.-J.: SS+AS-TuM12, 71; SS+NS-WeM2,
 142
 Friddle, P.: PS2-TuM9, 68; PS-MoA3, 45
 Friebe, D.: IS+AS+SS-ThM3, 186
 Fried, D.: PS-MoA7, 46
 Fried, M.: EL+AS+EN+PS+SS+TF-ThM5, 179
 Friedman, A.L.: MI+EM-TuM5, 61
 Friend, C.M.: NS+AS+EN+SS-TuA3, 90;
 NS+AS+EN+SS-TuA4, 90
 Fritz, E.C.: VT+EN+TF-TuA9, 98
 Fritz, G.: PS-MoA6, 45
 Fröhlich, J.: BA+AI+AS+BI+IS+NL-MoM10, 5
 Frontini, P.M.: TR+SE-TuM4, 73
 Frost, R.: BI+AS+BA+NL-TuM5, 56
 Fu, D.: TR+AS+NS+SS-MoA10, 52
 Fu, Z.: SA+AS+MI+SS-WeM3, 139
 Fuchs, H.: TR+SE-TuM12, 74
 Fuhrer, M.S.: GR+AS+NS+SS-ThM3, 183
 Fujii, M.: AS-MoA10, 30
 Fujikawa, K.: SS+EN-ThM10, 196
 Fujimori, S.: AC+AS+EN-TuA3, 77
 Fujita, D.: HI-ThA6, 213
 Fujiwara, H.: EL+AS+EN+PS+SS+TF-ThM1, 178
 Fukasawa, M.: PS-MoM1, 19; PS-TuP30, 113
 Fukiage, N.: TF+PS-ThM12, 201
 Fukidome, H.: GR+EM+NS+PS+SS+TF-MoM4,
 11
 Fukutani, K.: SS-TuP7, 115
 Fuller, N.: PS-MoA8, 46
 Fulmer, P.A.: BI-WeM3, 126
 Funk, M.: PS1-TuM1, 65
 Furuta, H.: NS-TuP9, 108
 Futagami, Y.: SE-ThP1, 239
 — G —
 Gaddam, S.: MI+EM-TuM9, 61; PS-WeM11, 138
 Gaddy, B.E.: TR-TuP4, 120
 Gahan, D.: PS1-TuA3, 91; PS1-TuA7, 91
 Gai, Z.: MI-MoM10, 14; MI-MoM9, 14
 Gaikwad, A.M.: TC+EM+TF-WeM9, 144
 Gaillard, A.: AP+AS+SS-TuA10, 79
 Galatage, R.: EM-WeA9, 158
 Galhenage, R.P.: SS-TuA11, 96; SS-TuP12, 117;
 SS-TuP16, 117
 Gallego, J.M.: SS1-ThA3, 224
 Galoppini, E.: EN+AS+NS+SS-MoA10, 35
 Galtayries, A.: BI+AS+BA+NS+SS-ThA10, 204
 Gamage, S.: EM+NS+SS+TF-FrM10, 248
 Gaman, C.: PS1-TuA1, 91
 Gamble, L.J.: BI+AI+AS+BA+IA+NL+NS+SP-
 WeA7, 153; BI+AI+AS+BA+IA+NL+NS+SP-
 WeA8, 154
 Gamelin, D.R.: SS+AS-TuM6, 70
 Ganesh, K.J.: EM-ThA7, 207
 Gangwar, R.K.: SE+PS-ThM11, 193
 Gann, R.D.: AS+BI+IS-WeM4, 124; SS+AS-
 WeM6, 141
 Gao, J.H.: HI-ThA6, 213
 Gao, Q.: GR-WeM3, 133
 Gao, Y.: NS+EM+EN-TuM4, 64
 Garces, N.Y.: GR+EM+MS+NS+SP-FrM4, 250
 Garcia, G.: SS-TuP22, 118
 Garcia, G.: EM-ThP1, 234
 Garcia-Alonso, D.: TF+EN-MoM6, 24; TF-
 TuM12, 72
 Garifullin, R.: SE-ThP11, 240
 Garnica, M.: GR+AS+EM+MI+MN-TuM1, 59
 Gaskill, D.K.: EL+AS+EM+SS+TF-WeA1, 155;
 EL+AS+EM+SS+TF-WeA2, 155;
 GR+EM+MS+NS+SP-FrM4, 250;
 GR+EM+NS+PS+SS+TF-MoM3, 11
 Gassilloud, R.: PS+TF-MoA8, 44
 Gates, R.: TF+EM+NS+SS-FrM5, 261
 Gaudry, E.: AS+BI-TuA9, 81
 Gebbie, M.A.: IS+EN+SP+SS-ThA6, 215
 Geeson, D.A.: AC+AS+SS-TuM4, 53
 Geiger, F.: BA+AI+AS+BI+IS+NL-MoM3, 5
 Geiser, B.P.: AP+AS+EM+MI+TF-WeM1, 123
 Geisler-Lee, J.: NL+AS+BI+SA-FrM4, 255
 Gellman, A.J.: AS+BI+EM+NL+NS+SS-ThM9,
 176; SS-ThM11, 198; SS-ThM3, 197; SS-
 ThM4, 197
 Geng, Y.: MI+AS+NS+SP-TuA12, 88
 Genisel, F.: SE-ThP11, 240
 George, S.M.: TF+AS+SE+SS-MoA8, 50;
 TF+EN-MoM11, 25; TF+EN-MoM5, 24; TF-
 TuM9, 72
 Geppert, C.: EM+AS+NS+SS-WeA11, 157
 Gerlach, A.: SS1-ThA2, 224
 Gerou, H.: MN+AS+SS-MoM3, 14
 Gerson, Y.: MN+AS+SS-MoM3, 14
 Gerty, D.: VT-MoM3, 27
 Gettel, D.: BI+NL+NS+SS-ThM3, 177
 Gherardi, N.: PS+AS+NS+SS-ThM10, 189;
 SE+PS-ThM11, 193
 Ghibaud, G.: EM+PS-TuM2, 57
 Ghosh, S.: EM-MoA8, 33; PS+AS+NS+SS-
 ThM12, 190; SS-TuP15, 117
 Gianchandani, Y.: PS+AS+BI+SE-MoM3, 18
 Giannuzzi, L.A.: IS+EN+SP+SS-ThA2, 214
 Gibbs-Davis, J.M.: IA+AI+BI+IS+NL+SS-MoA6,
 37
 Gibson, B.A.: MN-TuP4, 105
 Gibson, D.: MS+AS+BA+BI+PS+TF-TuM11, 63
 Gibson, G.: SP+AS+BI+EM+MI+NS+SE+SS-
 ThA8, 223
 Giddings, A.: AP+AS+EM+MI+TF-WeM10, 124
 Gidley, D.: EM+AS+PS+TF-ThM2, 181; TF+VT-
 WeM9, 147
 Giesen, D.J.: MG-ThA1, 215
 Giessen, H.: HI-ThA3, 212
 Gignac, M.S.: AS+BA+BI+PS+TF-TuM3, 63
 Gillen, G.: AS+BI+IS-WeM6, 125
 Gilles, J.: SP+AS+BI+EM+MI+NS+SE+SS-
 ThA12, 223
 Gilliland, D.: AS+BI+EM+NL+NS+SS-ThM10,
 176
 Gilmore, I.S.: AS+BI+IS-WeM5, 125; AS+BI-
 MoM9, 4; AS-MoA7, 30
 Gin, S.: AP+AS+EM+MI+TF-WeM9, 123
 Ginley, D.: MG+EM+MI+MS-WeM6, 134;
 TC+EM+EN+TF-WeA7, 170
 Giri, K.: NL+AS+BI-ThA7, 217
 Girolami, G.S.: EM+MI+NS+SS+TF-TuA10, 82;
 TF+EM+NS+SS-ThA2, 228
 Gittleson, F.: NS+BI+EM-WeA7, 162
 Gladh, J.: SS2-ThA4, 226
 Gleeson, M.A.: SS2-ThA12, 227
 Go, D.B.: PS+AS+BI+SE-MoM1, 18;
 PS+AS+BI+SE-MoM6, 18
 Goeckner, M.J.: PS-TuP7, 112
 Goede, A.P.H.: EN+AS+PS-TuA11, 84
 Goehler, B.: SS-ThM9, 197
 Goeke, R.S.: VT-MoA8, 52
 Goetzen, J.: SS+AS+NS+SP-WeA7, 166
 Goiri, E.: SS1-ThA8, 225
 Golaszewska, K.: AP-TuP2, 100
 Gold, J.: BI+AS+BA+NL-TuM6, 56
 Goldberg, A.: MG-ThA1, 215
 Goldblatt, M.S.: AS+BA+BI+PS+TF-TuM3, 63
 Goldfarb, S.R.: VT-TuM9, 75
 Goli, P.: GR+AS+EM+MI+MN-TuM2, 60
 Gölzhäuser, A.: GR+EM+NS+PS+SS+TF-MoM8,
 12; HI-ThA7, 213; HI-ThP2, 238; HI-ThP3,
 238
 Gomes Silva, A.: TF+EM+NS+SS-FrM2, 260
 Gómez, E.: EM-ThP9, 235
 Gonchar, A.: GR+AS+NS+SS-ThM4, 184
 Gong, B.: TF+AS+SE+SS-MoA6, 49
 Gonzalez, D.L.: SS+AS+NS-MoM3, 22
 Gonzalez, P.A.: GR+AS+EM+MI+MN-TuM3, 60
 Goodall, J.: MG-ThA3, 216
 Gorai, P.: SS+EM-WeA12, 169
 Gordon, L.: AP+AS+EM+MI+TF-WeM10, 124
 Gordon, R.: AS-MoA3, 29;
 MG+AS+EM+NS+SA+SE+SP+SS+TF-FrM2,
 253
 Gorman, B.: AP+AS+EM+MI+TF-WeM11, 124
 Gorniak, T.: IS+AS+SP-FrM3, 251
 Gorovikov, S.: SA+AS+MI+SS-WeM5, 139
 Goss, J.P.: GR+EM+MS+NS+SP-FrM4, 250
 Goss, M.: PS2-TuM9, 68
 Gosset, N.: PS-TuP1, 109
 Goto, M.: TR-TuP2, 120
 Gottscho, R.A.: PS-WeA11, 163
 Goubert, G.: SS-ThM12, 198
 Gougousi, T.: TF+AS+EM+NS+SS-ThM12, 199;
 TF+AS+SE+SS-MoA7, 50
 Gouma, P.: MS+AS+EL+EM+PS+TF-TuA10, 89
 Goux, L.: EM+PS-TuM5, 57
 Govoreanu, B.: EM+PS-TuM5, 57
 Graetzel, M.: EN+AS+NS+SS-MoA11, 35
 Graham, D.J.: BI+AI+AS+BA+IA+NL+NS+SP-
 WeA8, 154
 Graham, S.: TF+VT-WeM3, 146
 Graham, W.S.: PS-MoM2, 20
 Grainger, D.W.: AS+BI+EM+NL+NS+SS-ThM1,
 175
 Grande, P.L.: AS-MoA4, 29
 Granzer, T.: SE+PS-ThM12, 193
 Grassman, T.J.: EM+AS+NS+SS-WeA7, 157
 Graswinkel, M.: EN+AS+PS-TuA11, 84

- Graves, D.B.: PS+AS+BI+SE-MoM11, 19; PS-WeM6, 138
- Gray, A.X.: MI+AS+NS+SP-TuA7, **87**
- Grazianetti, C.: EM-MoA1, 32
- Green, I.X.: SS-MoA2, 47
- Green, R.: IA+BA-TuA12, 86
- Greene, G.W.: IS+AS+SP-FrM4, 252
- Greene, J.E.: SE+NS+TF-ThA1, 220; TF+AS+EM+NS+SS-ThM3, **198**; TF+EM+NS+SS-FrM6, 261; TF+EM+NS+SS-FrM8, 261; TF+PS-ThM11, 201
- Greene, J.N.: VT+EN+TF-TuA11, 99
- Greer, F.: TF-ThP34, **245**
- Gregoratti, L.: IS+AS+SS-ThM5, 186; NL+AS+BI+SA-FrM4, 255
- Gregorczyk, K.: TF+AS+SE+SS-MoA11, **50**; TF+EN-MoM3, 23
- Gregory, C.W.: EM+NS+TF-FrM6, 249
- Grehl, T.: GR+AS+NS+SP+SS-TuA9, **85**
- Greiner, K.: PS-MoA7, 46
- Grierson, D.S.: TR+AS-MoM10, 26; TR+AS-MoM5, 25
- Griffin, T.: PS-TuP23, 112
- Gronheid, R.: MS+AS+EM+NS+PS+TF-MoA6, **41**; PS-MoA9, 46; TF+AS+SE+SS-MoA9, 50
- Grubbs, R.K.: VT-MoA8, 52
- Gruber, H.J.: SP+AS+BI+EM+MI+NS+SE+SS-ThA1, 222
- Grundmeier, G.: SE+NS+TF-ThA4, 220
- Grunze, M.H.: BI-TuP7, 101
- Grueter, P.: MG+AS+EM+NS+SA+SE+SP+SS+TF-FrM7, **254**
- Gu, M.: TF+AS+EM+NS+SS-ThM5, **198**
- Gu, S.: EM+TF-MoM11, 9; SS-FrM7, 259
- Gudmundsson, J.T.: PS+TF-MoA9, **44**
- Guedde, J.: GR-WeM2, **133**
- Guenther, B.: SP+AS+EM+GR+MI+NS+SS-FrM7, 257
- Guenther, S.: IS+AS+SS-ThM5, 186; NL+AS+BI+SA-FrM4, 255
- Gueth, F.: EM+NS+SS+TF-FrM9, 248
- Guglietta II, G.W.: EN+AS+NS+SS-MoA4, 35
- Gullorn, M.: MS+AS+BA+BI+PS+TF-TuM3, 63
- Guisinger, N.P.: GR+EM+NS+PS+SS+TF-MoM6, 12; GR+EM+NS+SS+TF-ThA11, **212**; NS+AS+BI+SP-WeM6, 136; SP+AS+EM+GR+MI+NS+SS-FrM11, 258
- Guler, M.O.: SE-ThP11, 240
- Gunawan, A.A.: EN+PS+TF-MoM4, 9; EN+PS+TF-MoM9, 10
- Gundersen, M.: EN+AS+PS-TuA9, **84**
- Gundlach, D.J.: GR+EM+MS+NS+SP-FrM7, 251
- Gunduz, I.E.: TF-ThA3, 230
- Gunlycke, D.: GR+EM+NS+SP+TF-MoA8, **37**
- Guo, D.: GR+AS+EM+NS+SS-WeA8, 159
- Guo, H.X.: HI-ThA6, **213**
- Guo, J.-H.: IS+AS+SP-FrM5, **252**
- Guo, L.: AS-ThP15, **232**
- Guo, X.: EM-ThP3, **234**
- Gupta, M.: TF+PS-ThM3, **200**; TF-ThP24, 244
- Gupta, R.: PS-MoM3, **20**
- Gupta, S.: BI+AS+IS+NL-MoM11, 7; EM-MoA6, 33; TF+MI-WeM3, 145; TF+MI-WeM5, 145
- Gusak, V.: EN+AS+NS+SS-MoA11, 35
- Gutierrez, A.P.: EN+SE+SS+TF-WeM3, **131**
- Gutttag, M.: AS-ThP4, 231
- Guvenc, H.O.: BI+NL+NS+SS-ThM11, 178
- Guziewicz, M.: AP-TuP2, **100**
- **H** —
- Ha, J.: IS-ThP1, 238; SP+AS+EM+GR+MI+NS+SS-FrM3, **257**
- Ha, T.: VT-TuP4, **121**; VT-TuP5, 121
- Haack, L.P.: SE+PS-WeA3, **164**
- Haass, M.: PS1-TuA7, 91
- Habas, S.: TC+EM+EN+TF-WeA7, 170
- Habenicht, B.: SS+AS+NS-MoM10, 23; SS+NS-WeM12, 143
- Habermeier, H.U.: NS+EM+EN-TuM4, 64
- Hacker, C.A.: TF+AS+BI+EM+SE+SS-WeA5, 171
- Haensch, W.: MS+AS+EM+NS+PS+TF-MoA3, **41**
- Haga, H.: PS2-TuA8, 94
- Haga, T.: PS-TuP24, **112**
- Hagarman, J.: BI+AS+BA+NS+SS-ThA12, 205
- Hahn, J.: EM-ThA6, 207
- Haider, A.: TF+AS+NS+SE-WeA3, 173
- Hakanoglu, C.: SS-MoA3, 47
- Halbur, J.C.: TF-TuM10, 72
- Hall, S.: EM+NS+TF-FrM6, 249
- Hallin, E.: SA+AS+MI+SS-WeM5, 139
- Halls, M.D.: MG-ThA1, **215**; SS-FrM6, 259
- Hamaguchi, S.: PS+TF-MoA10, 45; PS2-TuM5, 68; PS-ThA3, 218; PS-TuP30, 113; PS-WeM9, 138
- Hammad, M.: EW-TuA6, 85
- Hammond, J.S.: AS+BI+EM+NL+NS+SS-ThA9, 202; AS+BI-MoM5, 3; AS-ThP13, 232; AS-ThP9, 232; BI+AI+AS+BA+IA+NL+NS+SP-WeA1, **153**
- Han, C.: HI-ThA12, 214
- Han, J.: EM+AS+NS+SS-WeA1, **156**
- Han, M.: GR-ThP8, 237
- Han, S.M.: EM-MoA8, 33; SS-TuP15, **117**
- Han, S.W.: TR-TuP8, 121
- Han, W.: BI+AS+BA+NS+SS-ThA11, 204
- Hanke, M.: BI+AS+IS+NL-MoM3, 6
- Hanley, L.: AS+BI+IS-WeM12, **125**; AS-MoA3, 29; SE+EN-FrM5, 256
- Hanna, S.: SP+AS+BI+EM+MI+NS+SE+SS-ThA8, 223
- Hannappel, T.: SP+AS+EM+GR+MI+NS+SS-FrM8, 258
- Hannon, J.: GR+AS+NS+SP+SS-TuA1, 85; GR+EM+NS+PS+SS+TF-MoM3, 11; MS+AS+BA+BI+PS+TF-TuM11, 63
- Hanselmann, H.: VT-MoA6, 52
- Hansen, R.S.: TF+PS-ThM6, 200
- Hao, H.F.: HI-ThA3, 212
- Haramus, V.M.: IS+AS+SP-FrM3, 251
- Haran, B.: MS+AS+EL+EM+PS+TF-TuA9, 89
- Hardesty-Dyck, N.: NS+BI+EM-WeA7, 162
- Harker, M.: TF+VT-WeM11, 147
- Harmer, M.P.: IS+EN+SP+SS-ThA2, 214
- Harniman, R.: SP+AS+BI+EM+MI+NS+SE+SS-ThA8, 223
- Harrell, W.R.: SS-TuP28, 118
- Harris, J.: BI+AS+BA+NS+SS-ThA11, 204
- Harris, S.: MS+AS+EM+EN+NS+TF-MoM10, **16**
- Harrison, I.A.: SS2-ThA1, 226; SS2-ThA11, **227**; SS2-ThA3, 226
- Harrison, J.A.: TR+AS+NS+SS-MoA3, 51; TR+AS-MoM10, **26**; TR+AS-MoM5, 25
- Harrison, R.: TC+EM+TF-WeM1, 143
- Harriss, J.E.: SS-TuP28, 118
- Harsha, K.A.: GR-ThP4, 236
- Hart, C.: PS+AS+BI+SE-MoM11, 19
- Hartley, P.: BI+AS+BA+NS+SS-ThA2, 203
- Hartnett, J.F.: VT-TuM3, **75**
- Hartung, W.H.: HI-ThA9, 213
- Hatta, A.: NS-TuP9, 108
- Hauet, T.: MI+EM-TuM1, 61
- Hauffman, T.: SS+AS+NS+SP-WeA1, 166; TF+EM+NS+SS-FrM11, **262**
- Havela, L.: AC+AS+EN-TuA7, **77**
- Havercroft, N.: AS+BI-MoM6, 4
- Hawker, M.: PS+AS+BI+SE-MoM10, **19**
- Hawley, C.J.: NS+AS+EM-MoA11, **43**
- Hawthorn, D.: IA+BA-TuA12, 86
- Hayama, R.: BI+AS+BA+NL-TuM10, 56
- Hayashi, H.: PS2-TuA11, 94; PS-MoM4, 20
- Hayashida, M.: HI-ThM9, 185
- Hayes, A.V.: PS-TuP12, 110
- Hayman, C.: TF+EM+NS+SS-FrM3, 260
- Hazeghi, A.: PS1-TuM6, 66
- He, G.: SP+AS+EM+GR+MI+NS+SS-FrM1, 257
- He, H.: PS2-TuM9, 68
- He, H.Y.: SS+EN-ThM11, 196
- He, K.: MN+NS-TuM6, 63
- He, T.: MN+NS-MoA8, 40
- He, X.: GR+EM+NS+SS+TF-ThA10, 212
- He, Y.: VT-WeM12, 148
- Head, A.: EM+TF-MoM6, 8
- Heath, G.R.: BI+AI+AS+BA+IA+NL+NS+SP-WeA10, **154**; BI-TuP10, 102
- Hedjran, F.: BI-WeM9, 127
- Heiman, D.: NS+AS+EM-MoA1, 41
- Heiniger, L.P.: EN+AS+NS+SS-MoA11, 35
- Heinz, T.F.: GR+EM+NS+SS+TF-ThA8, **211**; TF-ThP19, 244
- Heissl, M.: SE+PS-ThM12, 193
- Heissler, S.: SS-FrM9, 260
- Heller, G.: BI+AS+BA+NL-TuM4, **56**
- Hemminger, J.C.: IA+AI+BI+IS+NL+SS-MoA10, 38; SS+AS-WeM11, 141; SS+EN-ThM9, 196
- Hemmingson, S.L.: AS+BI+EM+NL+NS+SS-ThA6, 202; SS-TuA8, **96**
- Henderson, C.: MS+AS+EL+EM+PS+TF-TuA3, **88**; NS+BI+EM-WeA11, 162
- Henderson, K.W.: TF+AS+BI+EM+SE+SS-WeA10, 172
- Henderson, M.A.: SS+EN-ThM1, 195
- Henderson, S.: AS+BI+EM+NL+NS+SS-ThA1, 202
- Hendricks, J.H.: VT-MoM3, **27**; VT-MoM4, 27
- Henegar, A.: TF+AS+EM+NS+SS-ThM12, **199**
- Henk, J.: MI-MoM8, 14
- Hennessy, J.: EM+NS+SS+TF-FrM11, **248**
- Heremans, F.J.: MI+EM-TuM3, 61
- Herman, G.S.: TC+EM+TF-WeM3, **144**
- Hermann, P.: SA-TuP4, 114
- Hermansson, K.: SS+EN-ThM6, 195
- Hernandez Maldonado, D.: AP+AS+SS-TuA12, 79
- Hernández, S.: GR+AS+BI+PS+SS-ThA6, **210**
- Hernandez, S.C.: EM+AS+EN+TF-ThM5, 180
- Hernández-Salderón, I.: SS+AS+NS-MoM8, **22**
- Hernández-Hernández, A.: NS-TuP3, 106; NS-TuP4, **107**; TF-ThP1, 241; TF-ThP13, 243
- Hernández-Hernández, L.A.: NS-TuP3, 106; NS-TuP4, 107; TF-ThP1, **241**; TF-ThP13, 243
- Herrera, V.: BI-WeM9, 127
- Herrera-Gomez, A.: AS-TuM4, **54**
- Hersam, M.C.: GR+EM+NS+PS+SS+TF-MoM6, 12; GR+EM+NS+SS+TF-ThA11, 212; NS+AS+BI+SP-WeM6, 136; SS+AS+NS+SP-WeA2, 166
- Herz, A.: SE+NS+TF-ThA10, 221
- Herzinger, C.M.: EL+AS+EM+SS+TF-WeA1, 155
- Heske, C.: EN+PS+TF-MoM1, **9**
- Heslop, S.: SS-TuP3, 115
- Hess, W.P.: NS-TuP12, 108
- Hetzl, C.: VT-WeM11, 148
- Hewitt, A.S.: SS-TuP18, 117
- Heyde, M.: TR+AS+NS+SS-MoA11, 52
- Heyne, M.H.: PS-MoA9, **46**
- Hiebert, W.K.: MN+NS-MoA3, 40; MN+NS-MoA4, 40
- Higaki, Y.: TR+SE-TuM2, **73**
- High, E.: SS2-ThA10, 227
- Highsmith, A.: TF+MI-WeM5, 145
- Hight Walker, A.R.: GR+EM+MS+NS+SP-FrM7, 251
- Higo, A.: PS-ThA8, 219
- Hilbert, J.: AS-ThP21, 233
- Hill, E.: BI+AI+AS+BA+IA+NL+NS+SP-WeA2, 153
- Hill, S.B.: VT+EN+TF-TuA7, **98**
- Hilpert, K.: IS+AS+SP-FrM3, 251
- Hilton, J.: SP+AS+EM+GR+MI+NS+SS-FrM7, 257
- Hinckley, A.: EM-ThP6, **235**
- Hinderhofer, A.: SS1-ThA2, 224
- Hines, M.A.: SS+EM-WeA10, 169; SS+EN-ThM2, 195; SS-MoA7, 48
- Hinkle, C.L.: EM-MoA3, 32; EM-WeA9, **158**; GR+EM+NS+SS+TF-ThA1, 211

- Hinterdorfer, P.:
SP+AS+BI+EM+MI+NS+SE+SS-ThA1, **222**
- Hirako, T.: SE-ThP1, 239
- Hiramatsu, T.: NS-TuP1, 106; NS-TuP6, 107; NS-TuP7, 107; NS-TuP8, 107; TF-ThP28, 245
- Hiramoto, M.: PS-TuP33, 114
- Hirose, T.: TF-ThP27, 245
- Hirshy, H.: NS+BI+EM-WeA9, 162
- Hite, J.K.: EM+NS+SS+TF-FrM6, 247
- Hitt, T.: EM+MI+NS+SS+TF-TuA10, 82
- Hjort, M.: EM+TF-MoM6, 8; MI-MoM11, 14
- Hla, S.-W.: SP+AS+BI+MI+NS+SS-ThM3, 194; SP+AS+BI+MI+NS+SS-ThM6, 194; SP+AS+EM+GR+MI+NS+SS-FrM5, **257**
- Hlaing, M.M.: BI+AI+BA+IS-MoA11, **32**
- Hlawacek, G.: HI-ThP4, **238**
- Ho, A.D.: BI+AS+IS+NL-MoM3, 6
- Ho, W.: SP+AS+BI+MI+NS+SS-ThM1, **194**; SP+AS+BI+MI+NS+SS-ThM4, 194; SS+AS+NS+SP-WeA3, 166; SS+EN-ThM11, 196
- Hobara, R.: SS+EN-ThM10, 196
- Hochberg, M.: MN+NS-MoA1, 40
- Hockenbery, D.: BI+AI+AS+BA+IA+NL+NS+SP-WeA7, 153
- Hoefer, U.: GR-WeM2, 133
- Hoffman, J.: MI+EM+MG-MoA10, 39
- Hofmann, T.: EL+AS+EM+SS+TF-WeA1, 155; EL+AS+EM+SS+TF-WeA2, 155; EL+AS+EN+PS+SS+TF-ThM9, **179**; GR+EM+MS+NS+SP-FrM7, 251
- Hogan, C.J.: PS+AS+NS+SS-ThM5, **189**
- Hohle, C.: PS2-TuM1, 67
- Hoinkis, M.: PS-MoA6, 45
- Holcomb, M.B.: SA+AS+MG+SS-TuA10, **95**
- Hollingsworth, N.: MG-ThA3, 216
- Holloway, P.: EM-TuA7, **83**
- Holmes, R.J.: AS-ThP13, 232
- Holohan, A.M.: PS1-TuA1, 91
- Holsclaw, B.S.: SS-ThM11, 198; SS-ThM4, 197
- Honda, H.: TR-TuP2, 120
- Honda, M.: PS2-TuM2, **67**
- Hone, J.C.: GR+AS+EM+MI+MN-TuM5, **60**
- Hong, B.: AS-ThP18, 233; EN-TuP3, 103; EN-TuP4, 103
- Hong, J.: SE+PS-WeA9, 165
- Hong, J.W.: TF+VT-WeM12, 147; TR-TuP8, 121
- Hönicke, P.: SA-TuP4, **114**
- Honkanen, S.: NS+BI+EM-MoM6, 17
- Hono, K.: AP+AS+EM+MI+TF-WeM4, 123
- Hoogenboom, B.W.: SP+AS+BI+MI+NS+SS-ThM11, **195**
- Hook, A.L.: BI+AS+IS+NL-MoM8, 7; BI-WeM11, **127**
- Hook, D.J.: BI-TuP14, 102
- Hopkins, M.B.: PS1-TuA3, **91**
- Hori, M.: PS1-TuA10, 92; PS2-TuA11, 94; PS-ThA6, 218; PS-TuP11, 110; PS-WeM2, 137
- Horiba, K.: GR+EM+NS+PS+SS+TF-MoM4, 11
- Horiguchi, N.: EM+PS-TuM10, 58
- Horsfall, A.B.: GR+EM+MS+NS+SP-FrM4, 250
- Hoshiya, R.: NS-TuP1, 106
- Hosseinpour, P.M.: NS+AS+EM-MoA1, **41**; NS+AS+EM-MoA2, 42
- Hou, J.: NS+EM+EN-TuM3, **64**
- Hou, T.H.: EM+PS-TuM11, **58**
- Houard, J.: AP+AS+SS-TuA10, 79; AP+AS+SS-TuA12, 79
- Houska, J.: TF+AS+EM+NS+SS-ThM9, 199
- Houssiau, L.: AS+BI-MoM10, **4**; PS+AS+NS+SS-ThM9, 189
- Howe, B.: TF+EM+NS+SS-FrM8, 261
- Howe, J.: MI-MoM10, 14
- Howell, R.S.: EM-ThP17, 236
- Hoye, R.L.Z.: TF-TuA9, 97
- Hseuh, H.-C.: VT-WeM11, **148**
- Hsiaoh, C.-N.: MN-TuP1, 104; MN-TuP2, 105; MN-TuP3, 105; NS-TuP15, 109; PS-TuP26, 112; TF-ThP17, 244; VT-TuP1, 121
- Hsieh, C.C.: PS-TuP16, 111
- Hsieh, C.H.: PS-TuP16, 111
- Hsieh, F.C.: MS-TuP2, 106; VT-TuP2, **121**
- Hsieh, J.H.: PS+TF-MoA2, **43**; TR-TuP3, 120; TR-TuP5, 120
- Hsu, C.C.: AS-ThP7, 231; PS+AS+BI+SE-MoM4, 18; PS-TuP8, 110; SE+PS-WeA12, 165; SS-TuP8, 116; TF-ThP23, 244
- Hsu, C.M.: SS-TuP8, **116**
- Hsu, C.W.: EM+PS-TuM11, 58
- Hsu, W.: MN-TuP2, 105
- Hsueh, W.J.: TF-ThP2, 241
- Hu, E.: IS+EN+SP+SS-ThA3, 214
- Hu, J.: NS+AS+EN+SS-TuA2, 89
- Hu, Q.: NS+AS+BI+SP-WeM5, 136
- Hu, S.: SS+EN-ThM6, 195
- Huang, C.Y.: MS-TuP2, 106
- Huang, J.: GR+AS+NS+SS-ThM3, 183
- Huang, J.F.: PS-MoA11, 47
- Huang, K.: TR+AS+NS+SS-MoA6, 51
- Huang, L.W.: GR+AS+NS+SS-ThM12, **184**
- Huang, M.J.: TF-ThP2, 241
- Hubert, J.: PS+AS+BI+SE-MoM5, **18**
- Hubin, A.: TF+EM+NS+SS-FrM11, 262
- Huerta, L.: SS-TuP4, **115**
- Hug, H.-J.: AS+BI-MoM6, 4
- Hughes, T.F.: MG-ThA1, 215
- Hultman, L.: SE+NS+TF-ThA1, 220; SE+NS+TF-ThA7, 221; TF+EM+NS+SS-FrM6, 261; TF+EM+NS+SS-FrM8, 261; TF+PS-ThM11, 201; TR+SE-TuM4, 73
- Hummel, H.: AS-ThP12, 232
- Hunter, C.A.: TR+AS+NS+SS-MoA8, 51
- Hussain, Z.: IS+AS+SS-ThM9, 187
- Hutton, S.J.: AS+BI-MoM4, **3**; AS-MoA6, 29; AS-WeA3, 151
- Hvam, J.: TF+EM+NS+SS-FrM2, 260
- Hwang, H.: MI+EM+MG-MoA8, **39**
- Hwang, H.S.: EM+MI+NS+SS+TF-TuA7, **82**
- Hwang, J.H.: SS-TuP21, **118**
- Hwang, S.: IS+EN+SP+SS-ThA3, 214
- Hwang, S.W.: SP+AS+EM+GR+MI+NS+SS-FrM9, 258
- Hwang, W.: EM-ThA2, 206
- Hwang, W.S.: EM+TF-MoM8, 9
- Hwang, Y.J.: IS+AS+SP-FrM7, 252
- Hyvonen, J.: EM-TuA7, 83
- I —
- Ianno, N.J.: TF-ThP25, **245**
- Ibrahim, M.: EW-WeM8, **132**
- Ichida, D.: EN+AS+NS+SS-MoA3, 34; EN-TuP2, **103**
- Ide, T.: GR+EM+NS+PS+SS+TF-MoM4, 11
- Idriss, H.: AC+AS+EN-TuA8, **77**
- Igarashi, K.: GR+AS+BI+PS+SS-ThA4, 209
- Iida, S.: AS+BI-MoM5, **3**; AS-ThP9, 232
- Iijima, T.: GR+AS+BI+PS+SS-ThA8, 210; HI-ThM9, 185
- Ilavsky, J.: SA-TuP1, 114
- Ilk, N.: SP+AS+BI+EM+MI+NS+SE+SS-ThA1, 222
- Ilton, E.S.: AC+AS+SS-TuM3, 53
- Im, M.-Y.: MI+AS+NS+SP-TuA11, 87
- Im, O.: BI+AS+BA+NS+SS-ThA11, 204
- Imada, H.: SS+AS+NS+SP-WeA4, 166; SS1-ThA1, 224
- Imai, M.: SS+AS+NS+SP-WeA4, **166**
- Imamura, T.: PS-MoM4, **20**
- Imashuku, S.: SA+AS+MI+SS-WeM12, 140
- Inui, N.: AS-MoA11, 30
- Iovine, R.: TR+SE-TuM6, 74
- Iriye, Y.: PS-ThA10, 219
- Irving, D.L.: TR-TuP4, 120
- Isarraraz, M.: TF-ThP19, 244; TF-ThP20, 244
- Ishibashi, K.: PS-ThM9, 191
- Ishii, K.: TC-TuP4, 119
- Ishikawa, K.: PS1-TuA10, 92; PS2-TuA11, 94; PS-ThA6, 218; PS-TuP11, 110; PS-WeM2, **137**
- Ishizaki, I.: AS-ThP9, 232; BI+AI+AS+BA+IA+NL+NS+SP-WeA1, 153
- Iski, E.: GR+EM+NS+PS+SS+TF-MoM6, 12; NS+AS+BI+SP-WeM6, 136
- Ismach, A.: GR-WeM3, 133
- Isobe, M.: PS-ThA3, 218; PS-TuP30, 113
- Israelachvili, J.N.: IS+AS+SP-FrM4, 252; IS+EN+SP+SS-ThA6, 215
- Itagaki, N.: EN+AS+NS+SS-MoA3, 34; EN-TuP2, 103; PS+TF-MoA11, 45
- Ito, K.: MS+AS+EL+EM+PS+TF-TuA9, 89
- Ito, M.: PS1-TuA10, 92
- Ito, T.: PS2-TuM5, 68; PS-TuP30, 113
- Itou, A.: PS-MoA8, 46; PS-MoM2, 20
- Iwao, T.: PS-ThM9, 191
- Iwasaki, T.: PS-ThA10, 219; PS-ThM12, 192
- J —
- Jacob, A.: PS2-TuM9, 68
- Jacob, D.: TF+VT-WeM9, 147
- Jacobs, B.: PS-MoM6, 21
- Jacobs, T.D.B.: TR+AS-MoM10, 26; TR+AS-MoM5, **25**
- Jaehnig, M.: GR+AS+EM+NS+SS-WeA9, 160
- Jahnes, C.: MS+AS+BA+BI+PS+TF-TuM3, 63
- Jaing, C.-C.: TF-ThP5, 242
- Jakes, J.: EM-ThP3, 234
- Jakob, P.: GR-WeM2, 133
- James, T.E.: AS+BI+EM+NL+NS+SS-ThA6, **202**; SS-TuA8, 96
- Jandhyala, S.: GR+AS+BI+PS+SS-ThA7, 210
- Jang, H.: EM-ThP4, 235
- Jang, H.-J.: TF+AS+BI+EM+SE+SS-WeA5, 171
- Jang, J.S.: TF-TuM5, 71
- Jang, L.: MS+AS+EL+EM+PS+TF-TuA9, 89
- Jang, W.: IS-ThP2, 238
- Janotti, A.: EM2-ThA3, **205**
- Jansson, U.: MI+EM+MG-MoA1, 38
- Jariwala, B.N.: GR+AS+BI+PS+SS-ThA1, 209
- Javed, M.A.: BI+AI+BA+IS-MoA1, 31
- Javey, A.: EM-MoA10, **34**; EN-TuM9, 59
- Jayanthinarasimham, A.: NS-TuP17, 109
- Jaye, C.: EM+AS+EN+TF-ThM5, 180; SA+AS+MI+SS-WeM3, 139
- Jenkins, C.: SA+AS+MG+SS-TuA10, 95
- Jensen, B.D.: MN+AS+SS-MoM4, 15; TF+PS-ThM2, 200; TF+PS-ThM9, 200
- Jensen, D.S.: TF+EM+NS+SS-FrM4, 261
- Jeon, I.: SP+AS+EM+GR+MI+NS+SS-FrM9, 258
- Jeon, J.H.: PS-TuP22, 112
- Jernigan, G.G.: GR+EM+NS+PS+SS+TF-MoM3, 11
- Jeyachandran, Y.L.: TF+AS+BI+EM+SE+SS-WeA8, 172
- Jezewski, C.J.: EM+AS+PS+TF-ThM9, 182
- Jhang, J.-H.: SS+AS-TuM11, 70
- Ji, R.: AS-ThP16, 233
- Ji, X.: TR-TuP4, **120**
- Jia, J.: MI-MoM2, **13**
- Jiang, C.: SS+AS+NS+SP-WeA3, 166
- Jiang, F.: NS+BI+EM-WeA4, **161**
- Jiang, N.: SS+AS+NS+SP-WeA2, **166**
- Jiang, Z.: EM+MI+NS+SS+TF-TuA11, 83
- Jiao, C.Q.: AS+BI+EM+NL+NS+SS-ThM12, 176
- Jimenez, J.M.: VT-WeM10, 148
- Jimenez, O.: TR-TuP6, 121
- Jing, D.: SS+EN-ThM2, 195; SS-MoA7, **48**
- Jing, L.: GR+EM+NS+SP+TF-MoA1, 36; IS-ThP2, 238
- Job, N.: PS+AS+NS+SS-ThM9, 189
- Joester, D.: AP+AS+EM+MI+TF-WeM10, 124
- Johal, M.S.: BI+AI+AS+BA+IA+NL+NS+SP-WeA11, 154; BI+AS+BA+NL-TuM4, 56; BI-TuP16, 102
- Johansson, B.: AC+MI+SA+TF-MoA1, **28**
- Johansson, L.M.: MI-MoM11, 14
- Johansson-Jøesaar, M.P.: SE+NS+TF-ThA3, 220
- Johnson, B.: BI-TuP10, 102
- Johnson, D.: MS+AS+EM+EN+NS+TF-MoM8, 16

- Johnson, E.V.: PS+TF-MoA1, **43**
 Johnson, L.E.: BI+AI+AS+BA+IA+NL+NS+SP-WeA11, 154
 Johnson, M.: EN+PS+TF-MoM10, **11**
 Johnson, M.D.: AS-TuM10, 55
 Joiner, C.A.: GR+EM+MS+NS+SP-FrM3, 250
 Joly, A.: NS-TuP12, 108
 Jones, B.A.: MG-ThA10, **216**
 Jones, E.B.: EM-ThP17, 236
 Jonker, B.T.: MI+EM-TuM5, **61**
 Joo, Y.H.: TC+EM+EN+TF-WeA4, 170
 Joseph, E.A.: MS+AS+BA+BI+PS+TF-TuM3, 63; PS-MoA6, 45; PS-MoA8, 46; PS-MoM2, 20; PS-WeM1, 137
 Joshi, P.: TC+EM+TF-WeM12, **144**
 Jouan, P.Y.: TF+EM+NS+SS-ThA8, 229
 Joubert, O.: PS1-TuA7, 91; PS-ThM2, 190; SE+PS-ThM6, 193
 Jourlin, Y.: NS+BI+EM-WeA9, 162
 Joyce, J.J.: AC+AS+SS-TuM10, **53**
 Juhel, M.: EM+PS-TuM2, 57
 Jung, D.: GR-ThP8, **237**
 Jung, E.S.: TF+VT-WeM12, 147
 Jung, H.: TF-TuM1, **71**
 Jung, J.: EM+PS-WeM4, 128; SS+AS+NS+SP-WeA11, **167**; SS1-ThA1, 224; SS-MoA1, 47
 Jung, K.: AS-MoA4, 29
 Jung, R.: MS+AS+EL+EM+PS+TF-TuA9, 89
 Jung, S.: EM-ThP12, 236
 Jung, S.B.: SS-TuP9, 116
 Junkermeier, C.: GR+AS+BI+PS+SS-ThA6, 210
 Jupille, J.: AS+BI+EM+NL+NS+SS-ThA4, **202**
 Jur, J.S.: TF+AS+SE+SS-MoA10, 50; TF-TuM10, **72**
 Jurczak, M.: EM+PS-TuM5, 57
 Jurczyk, B.: TF+PS-ThM10, 200; TF-ThP18, 244
 Jussot, J.: PS2-TuM3, 68
- **K** —
- Kaganovich, I.D.: PS-TuP19, 111; PS-TuP20, 111
 Kahng, S.-J.: SP+AS+EM+GR+MI+NS+SS-FrM9, 258
 Kaindl, G.: AC+MI+SA+TF-MoM5, **2**
 Kaiser, D.: SS-TuP15, 117
 Kaiser, U.: GR+EM+NS+PS+SS+TF-MoM8, 12
 Kakaroglou, A.: SE+PS-WeA7, 164
 Kalanyan, B.: TF-TuM11, **72**
 Käll, M.: BI+NL+NS+SS-ThM6, 177
 Kalpyris, I.: SA+AS+MG+SS-TuA9, 95
 Kaltenbrunner, M.: NS+EM+EN-TuM9, 64
 Kalutarage, L.C.: TF+AS+SE+SS-MoA1, 49
 Kamat, P.: EN-TuM1, **58**
 Kamataki, K.: EN+AS+NS+SS-MoA3, 34; EN-TuP2, 103; PS+TF-MoA11, 45
 Kaminski, M.: GR+AS+BI+PS+SS-ThA3, 209
 Kaminski, W.: SS1-ThA9, 225
 Kamon, M.: PS-MoA7, 46
 Kamra, T.: NS+EM+EN-TuM12, **65**
 Kanakasabapathy, S.: MS+AS+EL+EM+PS+TF-TuA9, 89; PS2-TuA8, 94; PS2-TuM11, **68**
 Kanan, M.: EN+AS+PS-TuA1, **84**
 Kanarik, K.J.: PS-WeA11, 163
 Kandel, S.A.: TF+AS+BI+EM+SE+SS-WeA10, 172
 Kang, H.: MS+AS+EL+EM+PS+TF-TuA9, 89
 Kang, H.-K.: TF+VT-WeM12, 147
 Kang, S.: PS+AS+NS+SS-ThM5, 189
 Kang, S.Y.: TF+PS-ThM12, 201
 Kanjolia, R.K.: TF+EM+NS+SS-ThA10, 229
 Kanyal, S.: EL+AS+EM+SS+TF-WeA8, 155; TF+EM+NS+SS-FrM4, **261**
 Kao, C.-L.: PS-MoM5, 20
 Kao, J.S.: MS-TuP2, 106; VT-TuP2, 121
 Kao, P.K.: PS-TuP8, **110**
 Kapadia, R.: EN-TuM9, **59**
 Kappera, R.: MG+AS+EM+NS+SA+SE+SP+SS+TF-FrM1, 253
 Kappes, B.B.: EN+SE+SS+TF-WeM4, **131**
 Karabacak, T.: TF+AS+NS+SE-WeA3, 173
- Karadge, M.: AS+BI-MoM8, 4
 Karahashi, K.: PS+TF-MoA10, 45; PS2-TuM5, 68; PS-TuP30, 113; PS-WeM9, **138**
 Karakalos, S.: SS-ThM2, **196**
 Karakas, E.: PS1-TuA9, 92
 Karbasian, G.: EM-ThA10, **208**
 Karim, I.: EM-ThA6, 207
 Karkare, S.: VT+AS+SS+TF-WeA7, 174
 Karpowicz, T.: EM+AS+PS+TF-ThM6, 182
 Kasahara, A.: TR-TuP2, **120**
 Kasai, H.: MG-ThA2, **216**; SS-TuP6, 115
 Kasemo, B.H.: BI+AS+BA+NL-TuM1, **55**; EN+AS+NS+SS-MoA11, **35**
 Kash, K.: EM2-ThA11, **206**
 Kasi, H.: MI+EM-TuM9, 61; PS-WeM11, 138
 Kaspar, T.C.: SS+AS-TuM10, **70**; SS+AS-TuM6, 70; SS-FrM4, 259
 Katayama, T.: SS2-ThA4, 226
 Kathrein, M.: SE+PS-ThM12, 193
 Kato, H.: NS-TuP1, 106; NS-TuP6, 107; NS-TuP7, 107; NS-TuP8, 107; TF-ThP28, 245
 Katz, K.: PS1-TuM6, 66
 Kaufman-Osborn, T.: EM+TF-MoM11, 9; EM-MoA9, **34**; SS-FrM7, 259
 Kawai, J.: SA+AS+MI+SS-WeM12, **140**
 Kawai, M.: SS+AS+NS+SP-WeA11, 167; SS+AS+NS+SP-WeA4, 166; SS1-ThA10, 225; SS2-ThA8, **227**; SS-MoA1, 47
 Kawai, Y.: GR+EM+NS+PS+SS+TF-MoM4, 11
 Kawakami, R.: GR+AS+EM+NS+SS-WeA11, 160; TF-ThP19, 244
 Kawamura, M.: TF-ThP27, **245**
 Kawarai, K.: SS-TuP10, 116
 Kawasaki, H.: BI+AI+AS+BA+IA+NL+NS+SP-WeA1, 153
 Kawasaki, J.K.: MI-MoM11, **14**
 Kay, B.D.: SS-MoA6, 47
 Kaya, S.: IS+AS+SS-ThM3, 186; SS2-ThA4, 226
 Kayser, S.: AS+BI-MoM6, 4; AS-ThP12, 232
 Kazer, S.M.: BA+AI+AS+BI+IS+NL-MoM1, 5
 Keating, P.L.: TR+AS-MoM10, 26; TR+AS-MoM5, 25
 Keblinski, P.: NS+EM+EN-TuM11, 65
 Keckes, J.: SE+NS+TF-ThA7, 221
 Keenan, M.R.: AP+AS+SS-TuA1, **78**
 Keisuke, S.: PS2-TuM12, 69
 Keith, J.: AC+AS+EN-TuA10, 78
 Kelber, J.: MI+EM-TuM9, **61**; PS-WeM11, 138
 Kelkar, S.S.: PS+AS+NS+SS-ThM11, **189**
 Kellogg, G.L.: SS+AS-TuM1, 69
 Kelly, B.J.: VT-MoM8, 27
 Kelly, J.: TF+VT-WeM9, 147
 Kelly, T.F.: AP+AS+EM+MI+TF-WeM1, 123
 Kennedy, R.J.: EM2-ThA10, 206
 Kenney, J.: PS-ThM5, 191
 Kennicutt, A.: SS-TuP35, **119**
 Kent, T.: EM+PS-TuM9, 57; SS+EM-WeA8, **168**
 Kerdsonpanya, S.: TF+EM+NS+SS-ThA3, 228
 Kerr, A.J.: EM+TF-MoM11, 9; EM-MoA9, 34; SS-FrM7, **259**
 Kersell, H.: SP+AS+BI+MI+NS+SS-ThM6, **194**
 Kesapragada, S.: EM-ThA3, 207
 Kessels, W.M.M.: EM+MI+NS+SS+TF-TuA9, 82; EN+AS+NS+SS-MoA9, 35; EN+SE+SS+TF-WeM1, **131**; TF+AS+SE+SS-MoA3, 49; TF+EN-MoM10, 25; TF+EN-MoM6, 24; TF+VT-WeM6, 147; TF-TuM12, 72
 Keszler, D.A.: TC+EM+TF-WeM5, **144**; TF+EM+NS+SS-ThA1, 228
 Ketner, M.: SS-ThM9, 197
 Keuning, W.: TF+VT-WeM6, 147
 Keville, B.J.: PS1-TuA1, **91**
 Khader, S.: NL+AS+BI-ThA7, 217
 Khosla, N.: AS+BI+EM+NL+NS+SS-ThM9, 176
 Khrabrov, A.: PS-TuP19, **111**; PS-TuP20, 111
 Kibsgaard, J.: NS+AS+BI+SP-WeM9, **136**
 Kiefer, B.: AS-TuM6, 54
 Kievit, O.: SE+PS-WeA10, 165
 Kikuchi, Y.: PS-ThA9, **219**
- Kilduff, J.: SS-TuP35, 119
 Killeen, K.: MS+AS+BA+BI+PS+TF-TuM1, 63
 Killelea, D.R.: SS-TuP3, **115**
 Killough, S.: TC+EM+TF-WeM12, 144
 Kim, A.: TC+EM+EN+TF-WeA1, 169
 Kim, B.: EM-ThP4, **235**
 Kim, C.G.: TF-ThP38, 246
 Kim, C.H.: EM-ThP7, **235**
 Kim, C.I.: TC+EM+EN+TF-WeA4, 170
 Kim, C.S.: TF-TuM5, 71
 Kim, C.-S.: SS-FrM8, 260
 Kim, D.: GR-WeM10, 134
 Kim, D.H.: SP+AS+BI+NS-ThP3, 241
 Kim, H.: EM1-WeM12, 130; EM-ThP12, **236**; EM-ThP5, 235; TF+VT-WeM3, 146; TF-TuM1, 71
 Kim, H.D.: TC-TuP2, 119
 Kim, H.-G.: TF+VT-WeM12, 147
 Kim, H.J.: EM+PS-WeM4, 128; EM-ThP7, 235; TC+EM+TF-WeM2, 143; TC+EM+TF-WeM4, 144
 Kim, H.S.: TC+EM+EN+TF-WeA4, **170**
 Kim, H.W.: SP+AS+EM+GR+MI+NS+SS-FrM9, 258
 Kim, I.-S.: TF+VT-WeM12, **147**
 Kim, J.: EM+PS-WeM9, 129; EM+TF-MoM3, **8**; GR+AS+BI+PS+SS-ThA7, 210; GR+EM+NS+SS+TF-ThA1, 211; GR-ThP9, 237; HI-ThA12, 214
 Kim, J.H.: NS-TuP2, **106**; TR+AS+NS+SS-MoA10, **52**
 Kim, J.-H.: SS+AS+NS+SP-WeA11, 167
 Kim, J.S.: SP+AS+EM+GR+MI+NS+SS-FrM9, 258; SS-TuP21, 118
 Kim, K.: EM-WeA7, 158
 Kim, K.-B.: IS+EN+SP+SS-ThA3, 214
 Kim, K.H.: TC-TuP2, **119**
 Kim, K.J.: TF-TuM5, 71
 Kim, K.H.: TF-ThP27, 245
 Kim, M.D.: NS-TuP13, **109**; TC-TuP2, 119
 Kim, M.J.: GR+EM+NS+SS+TF-ThA1, 211; TF+VT-WeM12, 147
 Kim, M.W.: TF+VT-WeM12, 147
 Kim, P.: NS+EM+EN-TuM1, 64
 Kim, P.K.: NS+BI+EM-MoM3, 16
 Kim, S.: NS-TuP16, 109; PS-TuP17, **111**; PS-TuP23, 112; SS+EM-WeA10, 169; SS-ThM10, 197
 Kim, S.H.: EM-ThA11, 208; GR-ThP5, **236**
 Kim, S.J.: EM+PS-WeM4, 128; TC-TuP2, 119
 Kim, S.W.: EM-ThA11, 208; TC-TuP2, 119
 Kim, T.: PS2-TuA7, 93; PS-MoM10, **21**; TF+AS+SE+SS-MoA4, 49; TF+EM+NS+SS-ThA6, 228
 Kim, T.G.: SS-TuP14, 117; TC-TuP2, 119
 Kim, T.H.: EM-ThA11, 208
 Kim, W.: GR+AS+NS+SP+SS-TuA10, 86; GR-ThP9, **237**
 Kim, Y.: AS-ThP18, 233; GR+AS+EM+MI+MN-TuM11, 60; GR+AS+NS+SP+SS-TuA10, 86; GR+EM+NS+PS+SS+TF-MoM5, 12; SS+AS+NS+SP-WeA11, 167; SS+AS+NS+SP-WeA4, 166; SS+AS+NS+SP-WeA9, 167; SS1-ThA1, 224; SS2-ThA8, 227; SS-MoA1, **47**; SS-TuP19, 117
- Kimmel, G.A.: SS+EN-ThM5, 195
 Kim-Ngan, N.-T.H.: AC+AS+EN-TuA7, 77
 Kimura, A.: MI-MoM5, **13**
 Kimura, K.: NS+AS+BI+SP-WeM3, **135**
 Kindlund, H.: TF+EM+NS+SS-FrM6, **261**; TF+EM+NS+SS-FrM8, 261
 King, A.J.: BI+AI+AS+BA+IA+NL+NS+SP-WeA12, 154; IS+AS+SP-FrM11, **253**
 King, M.R.: EM-ThP17, **236**
 King, S.T.: EM-ThP13, **236**
 King, S.W.: EM+MI+NS+SS+TF-TuA2, 82; EM-ThA1, 206; GR+AS+EM+NS+SS-WeA9, 160; NS+AS+BI+SP-WeM5, 136; PS-MoA10, 46; TF+VT-WeM9, **147**

- Kingshott, P.: BI+AS+IS+NL-MoM1, 6; BI-TuP4, 101; BI-TuP6, 101
- Kinlen, P.: MG+EN+MS-WeA9, 161
- Kinoshita, T.: GR+EM+NS+PS+SS+TF-MoM4, 11
- Kinsler, M.: TC+EM+TF-WeM1, **143**
- Kintaka, H.: PS1-TuM5, 66
- Kiraly, B.T.: GR+EM+NS+PS+SS+TF-MoM6, **12**; GR+EM+NS+SS+TF-ThA11, 212; NS+AS+BI+SP-WeM6, 136
- Kirchhofer, R.: AP+AS+EM+MI+TF-WeM11, 124
- Kish, E.R.: EM+AS+EN+TF-ThM1, 180
- Kiskinova, M.: IS+AS+SS-ThM5, 186; NL+AS+BI+SA-FrM4, 255
- Kitajima, T.: GR+AS+BI+PS+SS-ThA2, **209**; PS1-TuM12, 67; PS-TuP24, 112
- Kjoller, K.: NS+AS+BI+SP-WeM4, 136
- Klee, V.: TF-ThP20, 244
- Kleebe, H.J.: NS+AS+EM-MoA4, 42
- Kleinschmidt, P.: SP+AS+EM+GR+MI+NS+SS-FrM8, 258
- Klem, E.J.D.: EM+NS+TF-FrM6, 249
- Kleyn, A.W.: SS2-ThA12, **227**
- Klimczak, A.: TF+AS+EM+NS+SS-ThM9, 199
- Klingsporn, J.: SS+AS+NS+SP-WeA2, 166
- Klinterberg, M.: MG-ThA8, **216**
- Klobas, J.: NS+AS+EN+SS-TuA3, 90
- Klopf, J.M.: TF+AS+EM+NS+SS-ThM6, 198
- Knauf, J.: TF+AS+BI+EM+SE+SS-WeA11, **172**
- Knez, M.: TF+AS+SE+SS-MoA11, 50
- Knoll, A.J.: PS-WeM3, **137**; PS-WeM5, 138
- Knoops, H.C.M.: TF-TuM12, 72
- Knowles, J.: AC+AS+EN-TuA11, 78
- Knudsen, J.: EM+TF-MoM6, 8
- Knutsson, J.: EM+TF-MoM6, 8
- Ko, A.: MS+AS+EL+EM+PS+TF-TuA4, 89; MS+AS+EL+EM+PS+TF-TuA9, 89; PS2-TuA8, 94; PS-MoA1, 45
- Ko, D.-H.: EM-ThP4, 235
- Ko, E.: EM-ThA6, 207
- Ko, J.: GR+AS+NS+SP+SS-TuA10, 86
- Ko, K.: TF-TuM1, 71
- Ko, W.: SP+AS+EM+GR+MI+NS+SS-FrM9, **258**
- Kobayashi, K.: MI+AS+NS+SP-TuA7, 87; NS+AS+BI+SP-WeM3, 135; PS2-TuM2, 67
- Kobayashi, M.: TR+SE-TuM2, 73
- Kobayashi, S.: TF-ThP12, **243**
- Kobe, H.: TF-ThP28, **245**
- Kodambaka, S.: GR-WeM12, **134**
- Kodera, N.: SP+AS+BI+EM+MI+NS+SE+SS-ThA1, 222
- Koebler, J.: SP+AS+EM+GR+MI+NS+SS-FrM7, 257
- Koegler, P.: BI-TuP6, 101
- Koehl, W.F.: MI+EM-TuM3, 61
- Koel, B.: NS+AS+EN+SS-TuA2, **89**
- Koelsch, P.: IA+BA-TuA11, **86**
- Koepke, M.: PS-WeM5, 138
- Koga, K.: EN+AS+NS+SS-MoA3, 34; EN-TuP2, 103; PS+TF-MoA11, 45
- Kohout, J.: SE+NS+TF-ThA6, 221
- Kohse-Höinghaus, K.: HI-ThA7, 213; HI-ThP2, 238
- Koirala, P.: EL+AS+EN+PS+SS+TF-ThM4, **178**
- Koji, H.: NS-TuP9, 108
- Kolbeck, J.: PS1-TuM11, 67
- Kolen'ko, Y.V.: NL+AS+BI-ThA6, 217
- Kolmakov, A.: GR+AS+NS+SS-ThM2, 183; IS+AS+SS-ThM5, **186**; NL+AS+BI+SA-FrM4, 255; NS-TuP11, 108
- Kolmychek, I.: MI+EM-TuM10, 62
- Kometani, R.: PS-ThA6, 218; PS-TuP11, 110
- Kondo, H.: PS1-TuA10, 92; PS2-TuA11, 94; PS-ThA6, 218; PS-TuP11, 110; PS-WeM2, 137
- Kondo, K.: TC-TuP4, 119
- Kondo, T.: GR+AS+EM+NS+SS-WeA8, **159**; SS2-ThA2, 226; SS-TuP10, 116
- Kong, J.: GR+AS+EM+NS+SS-WeA9, 160
- Kong, L.: MI+EM-TuM9, 61
- Kongkanand, A.: TF+EN-MoM11, 25
- Kongu, A.: TF-ThP10, **242**
- Konstantinidis, S.: NS+AS+EM-MoA4, 42
- Koo, J.-Y.: SS+EM-WeA2, 168
- Koo, S.: EM-ThP4, 235
- Koop, Z.C.: EM-ThP13, 236
- Kopecky, A.: EN+AS+NS+SS-MoA10, 35
- Koppens, F.: GR+AS+EM+MI+MN-TuM3, 60
- Korte, S.: SP+AS+EM+GR+MI+NS+SS-FrM8, 258
- Kosel, T.: EM+TF-MoM8, 9
- Koster, N.B.: HI-ThM12, **186**; SE+PS-WeA10, 165
- Kostov, K.L.: GR-WeM11, 134
- Koswatta, S.: EM+TF-MoM8, 9
- Kotliar, G.: AC+MI+SA+TF-MoA3, **28**
- Kotru, S.: TF-ThP10, 242
- Kotsugi, M.: GR+EM+NS+PS+SS+TF-MoM4, 11
- Kotula, P.G.: TF-ThA2, 229
- Kozicki, M.N.: EM+PS-WeM5, **128**
- Kozimor, S.: AC+AS+EN-TuA10, 78
- Kraft, M.L.: BI+AI+AS+BA+IA+NL+NS+SP-WeA3, **153**
- Krajewski, J.: AS-WeA12, 153
- Krashennikov, A.V.: HI-ThM5, **185**
- Kraut, R.: BI+NL+NS+SS-ThM3, 177
- Kravchenko, I.: MI-MoM10, 14
- Krawiec, M.: TF+AS+BI+EM+SE+SS-WeA7, 172
- Kreil, K.: EN+SE+SS+TF-WeM9, 132
- Krim, J.: MI-TuP4, 104; TR+AS+NS+SS-MoA4, 51; TR+AS-MoM6, 26
- Krishnan, M.: MS+AS+BA+BI+PS+TF-TuM3, 63
- Krishtab, M.: PS-ThA4, 218
- Krist, B.J.: EM-ThA7, 207
- Kristiansen, K.: IS+AS+SP-FrM4, **252**; IS+EN+SP+SS-ThA6, 215
- Kroemker, B.: SA+AS+MI+SS-WeM4, 139
- Kruchinin, V.N.: TF-ThP9, 242
- Krueger, B.: TC+EM+EN+TF-WeA11, **170**
- Krueger, J.S.: EM-ThP13, 236
- Krueger, P.: MI-MoM1, 13
- Kruk, S.: MN+AS+SS-MoM6, 15
- Kruse, N.: AP+AS+MI+NS+SS-WeA11, 151; AP+AS+MI+NS+SS-WeA9, **151**
- Krylov, S.: MN+AS+SS-MoM3, **14**; MN+AS+SS-MoM6, 15
- Kryutyanskiy, V.: MI+EM-TuM10, 62
- Kubo, A.: BI+AI+AS+BA+IA+NL+NS+SP-WeA1, 153
- Kubota, J.: SE+EN-FrM6, 256
- Kubota, T.: PS-ThA10, 219; PS-ThM12, **192**
- Kuckgok, B.: EM+NS+SS+TF-FrM7, 247
- Kuhlenbeck, H.: SS+AS-TuM12, 71
- Kuhn, M.: GR+AS+EM+NS+SS-WeA9, 160
- Kühne, P.: EL+AS+EM+SS+TF-WeA1, **155**
- Kuittinen, M.: NS+BI+EM-MoM6, 17
- Kujofsa, T.: EM+AS+NS+SS-WeA4, **157**
- Kuk, Y.: IS-ThP1, 238
- Kumar, A.: PS+AS+NS+SS-ThM5, 189
- Kumar, G.: NS+BI+EM-WeA7, 162
- Kumar, K.: EM-ThA2, 206; MS+AS+EL+EM+PS+TF-TuA9, 89; PS1-TuM5, 66; PS2-TuA8, 94; PS2-TuM12, 69; PS-MoA1, **45**; PS-MoM11, 21
- Kummel, A.C.: BI-TuP3, 100; BI-WeM9, 127; EM+PS-TuM1, 57; EM+PS-TuM9, 57; EM+TF-MoM1, 7; EM+TF-MoM11, **9**; EM-MoA9, 34; MN+AS+SS-MoM10, 15; SS+EM-WeA8, 168; SS-FrM7, 259
- Kungas, R.: IS+EN+SP+SS-ThA1, 214
- Kunkel, D.: TF+AS+BI+EM+SE+SS-WeA9, 172
- Kunze, A.: BI+AS+BA+NL-TuM6, 56
- Kunze, C.: SE+NS+TF-ThA4, **220**
- Kuo, J.-M.: EM+TF-MoM8, 9
- Kuo, P.J.: PS-TuP8, 110
- Kuo, Y.: EM+PS-WeM11, **129**
- Kurasch, S.: GR+EM+NS+PS+SS+TF-MoM8, 12
- Kurtz, R.L.: SS+NS-WeM12, 143; SS+NS-WeM9, 142
- Kuruganti, P.: TC+EM+TF-WeM12, 144
- Kushner, M.J.: PS+AS+BI+SE-MoM3, 18; PS1-TuM2, 65; PS1-TuM4, 66; PS-ThM3, 191; PS-WeA7, **163**
- Kushto, G.P.: SS-FrM8, 260
- Kusuda, Y.: PS-TuP33, 114
- Kvashnina, K.O.: AC+MI+SA+TF-MoM9, 2
- Kwak, H.S.: MG-ThA1, 215
- Kwak, J.: IS+AS+SP-FrM9, 252
- Kwok, S.J.J.: BA+AI+AS+BI+IS+NL-MoM1, 5
- Kwolek, E.: SS+AS+NS-MoM11, 23
- Kwon, H.: SP+AS+EM+GR+MI+NS+SS-FrM9, 258
- Kwon, S.: GR+AS+NS+SP+SS-TuA10, **86**; SS-TuP21, 118
- Kyureghian, H.: TF-ThP25, 245
- L —**
- La Spina, R.: AS+BI+EM+NL+NS+SS-ThM10, 176
- LaBella, V.P.: NS-TuP17, 109; SP+AS+EM+GR+MI+NS+SS-FrM10, 258; TF+EM+NS+SS-ThA12, 229
- Labuda, A.: EW-WeL5, 149; SP+AS+BI+MI+NS+SS-ThM10, **195**
- Lacovig, P.: GR-WeM11, 134
- Laderman, S.: MS+AS+BA+BI+PS+TF-TuM5, **63**
- Ladroue, J.: PS-TuP1, 109
- Lafleur, T.: PS+TF-MoA1, 43
- Lagadee, M.: NS+BI+EM-MoM9, 17
- Lagally, M.G.: GR+EM+NS+SP+TF-MoA2, 36
- Lagarkov, A.N.: TF+MI-WeM4, 145
- Laha, P.: PS+AS+BI+SE-MoM5, 18
- Laino, S.: TR+SE-TuM4, 73
- Lallo, J.: GR+EM+MS+NS+SP-FrM8, 251; SS-FrM1, **258**
- Lamb, R.: SE-ThP9, 240; TF+AS+BI+EM+SE+SS-WeA12, 173
- Lambeets, S.: AP+AS+MI+NS+SS-WeA11, 151
- Lambrecht, W.R.: EM2-ThA6, **205**
- Lament, K.: SS1-ThA9, 225
- Lampenscherf, S.: MG+EN+MS-WeA3, 160
- Lancaster, J.L.: TF+EN-MoM9, 24
- Lanceros-Méndez, S.: NL+AS+BI-ThA6, 217
- Lander, G.: AC+MI+SA+TF-MoM1, **2**
- Lang, B.N.: TF+EN-MoM9, 24
- Lang, C.: TF-ThP34, 245
- Lang, X.: BA+AI+AS+BI+IS+NL-MoM6, **5**; IS+AS+SP-FrM7, 252
- Langer, R.: BI+AS+IS+NL-MoM10, 7; BI+AS+IS+NL-MoM8, 7; BI-WeM1, 126; BI-WeM11, 127
- Langhammer, C.: EN+AS+NS+SS-MoA11, 35
- Lany, S.: MG+EM+MI+MS-WeM5, **134**; MG+EM+MI+MS-WeM6, 134
- Lanza, G.: VT-WeM10, **148**
- Larabell, C.A.: NL+AS+BI+SA-FrM1, **255**
- Larciprete, R.: GR-WeM11, 134
- Larentis, S.: EM-WeA7, 158
- Larriba-Andaluz, C.: PS+AS+NS+SS-ThM5, 189
- Larson, D.: AP+AS+EM+MI+TF-WeM10, 124
- Larson, D.J.: AP+AS+EM+MI+TF-WeM1, **123**
- LaRue, J.L.: SS2-ThA4, **226**
- Laskoski, M.: EM+AS+EN+TF-ThM5, 180
- Laszcz, A.: AP-TuP2, 100
- Latkowski, J.: EW-WeM7, 132
- Latour, R.A.: BI+AS+BA+NS+SS-ThA4, **203**; BI+AS+BA+NS+SS-ThA8, 204
- Lau, C.N.: GR+EM+NS+SP+TF-MoA1, 36; IS-ThP2, 238
- Lauderbach, L.: SA-TuP1, 114
- Lauhon, L.J.: AP+AS+EM+MI+TF-WeM2, **123**
- Laukkanen, J.: NS+BI+EM-WeA9, **162**
- Lauwaet, K.: SS1-ThA3, 224
- Lavoie, C.: EL+AS+EM+SS+TF-WeA11, 156
- Lawrence, D.: AP+AS+EM+MI+TF-WeM10, 124
- Lawson, R.: MS+AS+EL+EM+PS+TF-TuA3, 88; NS+BI+EM-WeA11, 162
- Lawton, T.J.: SS-ThM4, **197**
- Lazzari, R.: AS+BI+EM+NL+NS+SS-ThA4, 202

- Lazzarino, F.: PS-ThA4, **218**
Lazzaroni, R.: PS+AS+BI+SE-MoM5, 18
le Brizoual, L.: TF+EM+NS+SS-ThA8, **229**
Le Lay, G.: GR+EM+NS+SS+TF-ThA2, **211**
Le Mogne, T.: TR+SE-TuM6, 74
Le Tarte, L.: AS-WeA4, 152
Le, D.: SS+NS-WeM5, **142**
Lea, A.S.: SP+AS+BI+NS-ThP2, **241**
LeClair, M.J.: AS-WeA10, 152
Lediou, J.: AS+BI-TuA9, 81
Lee, C.-T.: TF-ThP17, **244**; TF-ThP5, 242
Lee, G.S.: GR-ThP8, 237
Lee, H.N.: MI+EM+MG-MoA3, **39**
Lee, J.: AS-ThP7, 231; MN+NS-MoA8, 40;
MN+NS-TuM6, **63**; PS2-TuM9, 68; SS-TuP21,
118; TF+EM+NS+SS-ThA12, 229; TF-TuM1,
71
Lee, J.H.: TF+VT-WeM12, 147
Lee, J.I.: NS-TuP2, 106
Lee, J.L.: TF+VT-WeM12, 147
Lee, J.-P.: TF-TuM5, 71
Lee, J.R.I.: NL+AS+BI+SA-FrM5, 255; SS+NS-
WeM11, 143
Lee, K.: EM-WeA7, 158
Lee, K.H.: EM-ThA11, **208**
Lee, K.S.: EM-ThA11, 208
Lee, M.J.: EM-ThP17, 236
Lee, S.B.: TF+EN-MoM3, 23
Lee, S.H.: SS-TuP14, 117; TF+VT-WeM12, 147;
TF-ThP6, **242**
Lee, S.K.: SS-TuP14, 117; TF-ThP6, 242
Lee, S.M.: SS-TuP9, **116**
Lee, S.-N.: EM-ThP12, 236
Lee, S.S.: EM-ThA11, 208; TF-ThP38, 246
Lee, T.Y.: TF-ThP6, 242
Lee, V.: AS+BI+EM+NL+NS+SS-ThA1, 202
Lee, W.: TF-TuM5, 71
Lee, Y.J.: GR+EM+NS+SP+TF-MoA1, **36**; PS-
TuP22, 112
Leeser, K.: EM-ThA6, 207
Lefauchaux, P.: PS2-TuA4, 93; PS-TuP1, 109
Lefebvre, W.: AP+AS+SS-TuA12, 79
Lefever, J.A.: TR+AS-MoM5, 25
Lefevre, B.: PS-MoM3, 20
Lefevre, S.: PS2-TuA8, 94
Legedza, S.: GR+AS+EM+MI+MN-TuM2, 60
Leggett, G.J.: BP+AS-SuA5, **1**; TR+AS+NS+SS-
MoA8, **51**
Lehto, J.: PS-MoA7, 46
Lei, H.: SS+AS+NS-MoM11, 23
Leick, N.: TF+AS+SE+SS-MoA3, 49
Leighton, C.: EN+PS+TF-MoM10, 11
Lemay, J.-C.: SS-ThM12, 198
Lemire, H.M.: TC+EM+EN+TF-WeA10, 170
Lenahan, P.M.: EM-ThA1, 206; PS-MoA10, 46
Leng, S.: VT-WeM11, 148
Lenser, C.: EM+PS-WeM1, **128**
Lent, C.S.: TF+AS+BI+EM+SE+SS-WeA10, 172
Leou, K.C.: PS-TuP16, 111
Leroux, C.: EM+PS-TuM2, 57
LeRoy, B.J.: GR+AS+NS+SP+SS-TuA3, **85**
Leseq, M.: TF+EM+NS+SS-ThA8, 229
Lesker III, K.J.: VT-TuM5, **75**
Lesker IV, K.J.: VT-TuM5, 75
Létard, J.F.: SS-TuP34, 119
Levasseur, O.: SE+PS-ThM11, 193
Levin, I.: SA+AS+MG+SS-TuA11, **95**
Levitov, L.S.: GR+AS+EM+NS+SS-WeA11, 160
Lewis, E.A.: SS-TuA12, **96**
Lewis, J.S.: EM+NS+TF-FrM6, **249**
Lewis, L.H.: NS+AS+EM-MoA1, 41;
NS+AS+EM-MoA2, 42
Lewis, N.: SS+EM-WeA3, **168**
Li, A.P.: SP+AS+EM+GR+MI+NS+SS-FrM1, 257
Li, C.H.: MI+EM-TuM5, 61
Li, C.-P.: TF+PS-ThM5, 200
Li, H.: PS+TF-MoA10, **45**; PS2-TuM5, 68
Li, H.C.: SE+PS-WeA12, 165
Li, J.: EM-WeA10, 158
Li, J.J.: EN+PS+TF-MoM5, **10**
Li, L.: BI+AS+BA+NS+SS-ThA11, **204**;
GR+AS+EM+MI+MN-TuM12, **61**;
GR+AS+EM+NS+SS-WeA2, 159; IS+AS+SP-
FrM1, 251; MN-TuP5, **105**
Li, R.: EM+TF-MoM8, 9
Li, S.-L.: GR+AS+BI+PS+SS-ThA8, 210
Li, S.W.: SP+AS+BI+MI+NS+SS-ThM4, **194**;
SS+EN-ThM11, 196
Li, T.: AP+AS+MI+NS+SS-WeA7, **150**
Li, W.: EL+AS+EM+SS+TF-WeA2, 155;
GR+EM+MS+NS+SP-FrM7, **251**; PS1-TuM6,
66; PS-TuP23, **112**
Li, Y.: EL-ThP3, 234; HI-ThA9, 213;
PS+AS+BI+SE-MoM1, 18; SS+NS-WeM1,
141; VT+AS+SS+TF-WeA7, 174; VT-
WeM12, **148**
Li, Y.Y.: GR+AS+EM+NS+SS-WeA2, 159
Li, Z.: SP+AS+BI+EM+MI+NS+SE+SS-ThA4,
223; SS-MoA6, 47; TF+EM+NS+SS-FrM2,
260; VT+AS+SS+TF-WeA10, **174**
Liang, C.-K.: AS+BI+EM+NL+NS+SS-ThM3,
175
Liang, J.: EM+MI+NS+SS+TF-TuA11, 83
Liang, W.C.: PS+AS+BI+SE-MoM4, 18
Liang, X.: GR+EM+MS+NS+SP-FrM7, 251
Liang, Y.: GR+EM+MS+NS+SP-FrM7, 251
Liang, Z.: SS+AS+NS+SP-WeA9, **167**
Lieberman, A.: BI-TuP3, **100**
Licitra, C.: PS-MoM5, 20
Liddiard, S.: TF+VT-WeM11, 147
Lie, F.L.: MS+AS+EL+EM+PS+TF-TuA9, **89**;
PS2-TuA8, 94
Lie, Y.H.: TR-TuP5, **120**
Lie, Y.L.: PS+TF-MoA2, 43
Lieb, S.: HI-ThP2, **238**
Lieberman, M.A.: PS-WeA3, **163**
Liedberg, B.: BI+NL+NS+SS-ThM3, 177
Lien, S.E.: PS-TuP16, 111
Lien, S.T.: SE+PS-WeA12, 165; SS-TuP8, 116
Lietz, A.M.: PS-TuP12, **110**
Lii, T.: PS-WeM3, 137
Lilley, C.M.: SP+AS+EM+GR+MI+NS+SS-
FrM11, 258
Lim, H.: GR+EM+NS+PS+SS+TF-MoM5, **12**
Limdulpaiboon, R.: TF-ThP34, 245
Lin, C.C.: PS1-TuA11, 92; PS-TuP14, 110
Lin, C.-C.: EM+PS-WeM11, 129
Lin, C.P.: VT-TuP1, 121
Lin, C.-T.: NS-TuP15, **109**
Lin, H.B.: PS-TuP16, **111**
Lin, H.C.: EM+TF-MoM2, 8; EM1-WeM9, **130**
Lin, L.: EM+AS+EN+TF-ThM10, 181
Lin, P.H.: MS-TuP2, **106**; VT-TuP2, 121
Lin, P.A.: IS+AS+SP-FrM8, 252
Lin, Q.: EM+AS+PS+TF-ThM1, 181;
MS+AS+BA+BI+PS+TF-TuM3, 63
Lin, R.B.: AS-ThP7, 231
Lin, S.C.: PS+TF-MoA2, 43
Lin, S.W.: TF-ThP17, 244
Lin, T.H.: TF-ThP23, **244**
Lin, X.: SS-MoA6, 47
Lin, Y.H.: MN-TuP1, 104; MN-TuP2, **105**; MN-
TuP3, 105
Lin, Y.S.: TF+AS+EM+NS+SS-ThM11, 199
Lin, Y.W.: VT-TuP1, **121**
Lince, J.R.: AS+BI+EM+NL+NS+SS-ThA9, **202**
Lind, H.: SE+NS+TF-ThA3, 220
Lindahl, A.: BI+AS+BA+NL-TuM6, 56
Linford, M.R.: EL+AS+EM+SS+TF-WeA7, 155;
EL+AS+EM+SS+TF-WeA8, **155**;
TF+EM+NS+SS-FrM4, 261; TF+EM+NS+SS-
FrM5, 261
Ling, Z.: PS-TuP23, 112
Linhart, W.M.: EM2-ThA10, 206
Lionti, K.: EM+AS+PS+TF-ThM3, 182
Lipp, M.J.: AC+MI+SA+TF-MoM10, **3**
Li, B.: BI+AI+AS+BA+IA+NL+NS+SP-WeA2,
153
Liu, C.: MS+AS+EL+EM+PS+TF-TuA4, 89;
TF+EN-MoM3, **23**
Liu, D.R.: MI-TuP1, **104**
Liu, F.: SS+NS-WeM9, 142
Liu, G.: GR+EM+NS+PS+SS+TF-MoM1, 11
Liu, H.: EM+AS+PS+TF-ThM6, 182
Liu, J.: AP+AS+MI+NS+SS-WeA12, **151**; AP-
TuP1, 100; NS+AS+EM-MoA1, 41;
NS+AS+EM-MoA2, **42**; SS-TuP34, 119
Liu, J.X.: SE-ThP3, 239
Liu, L.: PS1-TuM3, 65; PS1-TuM4, 66; SS+NS-
WeM12, **143**; SS+NS-WeM9, 142
Liu, M.: TF+VT-WeM9, 147
Liu, M.-C.: TF-ThP5, 242
Liu, Q.: EM+TF-MoM8, 9
Liu, X.: AP+AS+SS-TuA11, 79; VT+AS+SS+TF-
WeA7, 174
Liu, X.Z.: TR+AS-MoM11, 26
Liu, Y.: GR+AS+EM+MI+MN-TuM12, 61;
SA+AS+MI+SS-WeM12, 140; SS+EN-ThM9,
196; TR+AS+NS+SS-MoA6, 51
Liu, Z.: IS+AS+SS-ThM9, **187**; SS+EN-ThM9,
196; TR+AS-MoM6, **267**
Lizzit, S.: GR-WeM11, 134
Lloyd, K.G.: AS-ThP8, **232**
Lo, M.: NS+AS+BI+SP-WeM4, 136;
NS+AS+BI+SP-WeM5, **136**
Lobo-Checa, J.: AS-TuM11, 55
Lock, E.H.: EM+AS+EN+TF-ThM5, **180**;
GR+AS+BI+PS+SS-ThA6, 210; PS-ThA11,
220
Loehle, S.: TR+SE-TuM6, 74
Lofaro, M.: MS+AS+BA+BI+PS+TF-TuM3, 63
Logue, M.D.: PS1-TuM4, **66**
Longo, R.: SS-EM-WeA11, 169
Longo, V.: EM+MI+NS+SS+TF-TuA9, **82**
López, G.P.: BI+AI+BA+IS-MoA6, **32**;
BI+AS+BA+NS+SS-ThA11, 204
Lopez, T.: PS+AS+NS+SS-ThM4, **188**
López-López, M.: TF-ThP13, 243
Lopez-Lopez, S.: PS-TuP21, 112
Loquet, Y.: PS-MoA3, 45
Lorch, C.: SS1-ThA2, 224
Lorenz, C.D.: BI+AS+BA+NS+SS-ThA4, 203
Lorenzo-Andrade, J.A.: SS+AS+NS-MoM8, 22
Losby, J.E.: MN+NS-MoA4, 40
Losego, M.D.: SS+NS-WeM10, 142
Loth, S.: SP+AS+BI+EM+MI+NS+SE+SS-ThA6,
223
Louie, S.G.: GR+AS+EM+NS+SS-WeA11, 160;
GR+EM+NS+SP+TF-MoA10, **37**
Lozano, K.: MS+AS+EL+EM+PS+TF-TuA11, 89
Lu, F.: NS+AS+BI+SP-WeM4, 136
Lu, J.: SE+NS+TF-ThA7, 221; TF+EM+NS+SS-
FrM6, 261
Lu, J.W.: TF+AS+EM+NS+SS-ThM5, 198
Lu, L.: AS-ThP16, 233
Lu, N.: EM+NS+SS+TF-FrM7, 247;
GR+EM+NS+SS+TF-ThA1, 211
Lu, W.: GR-WeM10, **134**; NS+AS+EN+SS-TuA1,
89
Lu, Y.: EM+TF-MoM8, 9; PS-TuP11, 110;
SS+EM-WeA11, 169
Lubomirsky, D.: PS-ThA12, 220
Lucatorro, T.B.: VT+EN+TF-TuA7, 98
Lucovsky, G.: EM+PS-WeM9, 129; PS+TF-
MoA3, **44**
Ludovice, P.: MS+AS+EL+EM+PS+TF-TuA3, 88
Lueders, M.: AC+MI+SA+TF-MoA8, 29
Luh, D.: TF-ThP30, **245**
Lukaszew, R.A.: MI+EM-TuM10, 62;
TF+AS+EM+NS+SS-ThM6, 198;
VT+AS+SS+TF-WeA10, 174
Lukens, W.: AC+AS+EN-TuA10, 78
Lukes, J.R.: AS-ThP21, 233
Luna, J.A.L.: EM-ThP1, 234; EM-ThP9, **235**; SS-
TuP22, 118
Lund, J.M.: TF+PS-ThM2, 200; TF+PS-ThM9,
200

- Lunt, B.: EL+AS+EM+SS+TF-WeA8, 155;
TF+EM+NS+SS-FrM5, 261
- Luo, L.: IS+AS+SP-FrM1, 251
- Luo, S.: NS+AS+EM-MoA2, 42
- Luo, X.: PS+AS+BI+SE-MoM3, 18
- Lusth, J.C.: MN-TuP6, 105
- Lützenkirchen-Hecht, D.: SA+AS+MI+SS-WeM11, **140**
- Lydecker, L.K.: TF+AS+BI+EM+SE+SS-WeA5, 171
- Lyding, J.W.: NS+AS+BI+SP-WeM11, **137**
- Lyeo, H.-K.: SS-TuP21, 118
- Lyubnitsky, I.: SS+EN-ThM1, **195**; SS-MoA8, 48
- Lyubovitsky, J.G.: BA+AI+AS+BI+IS+NL-MoM6, 5; IS+AS+SP-FrM7, **252**
- **M** —
- Ma, L.: SS+AS-TuM9, 70
- Ma, Q.: GR-WeM10, 134; TF-ThP19, **244**
- Ma, R.: TF+VT-WeM2, 146
- Ma, X.M.: NL+AS+BI+SA-FrM4, **255**
- Maas, D.J.: HI-ThM12, 186
- Maboudian, R.: MN+AS+SS-MoM8, **15**
- Maccallini, E.: VT-WeM3, 148
- Macco, B.: GR+AS+BI+PS+SS-ThA1, 209
- Maciazek, D.: TF+AS+BI+EM+SE+SS-WeA7, 172
- MacIntyre, S.: NS+BI+EM-WeA3, 161
- Mack, P.: AS+BI-MoM3, 3; AS-ThP1, 231; AS-WeA11, 152; EW-TuL4, 76
- Mackus, A.J.M.: TF+EN-MoM6, 24; TF-TuM12, **72**
- MacManus-Driscoll, J.L.: TF-TuA9, 97
- Madaan, N.: EL+AS+EM+SS+TF-WeA7, **155**;
EL+AS+EM+SS+TF-WeA8, 155
- Madan, A.: TF-TuM10, 72
- Madaras, E.: TF+AS+EM+NS+SS-ThM6, 198
- Madaras, S.: TF+AS+EM+NS+SS-ThM6, 198
- Madden, B.: NL+AS+BI-ThA7, 217
- Madeleine, T.: AS-ThP8, 232
- Madisetti, S.: EM+TF-MoM11, 9; SS-FrM7, 259
- Madix, R.J.: NS+AS+EN+SS-TuA3, 90;
NS+AS+EN+SS-TuA4, 90
- Magaud, L.: PS-WeM6, 138
- Magbitang, T.: EM+AS+PS+TF-ThM3, 182
- Magnone, K.: TF-ThP19, 244
- Magnus, F.: PS+TF-MoA9, 44
- Mahadik, N.A.: EM+NS+SS+TF-FrM6, 247
- Mahan, G.: SE+EN-FrM1, **255**
- Mahmoudi, M.: HI-ThA3, 212
- Majeski, M.W.: SE+EN-FrM5, **256**
- Majidi, H.: EN+AS+NS+SS-MoA4, 35
- Makinen, A.J.: SS-FrM8, **260**
- Makino, H.: TC+EM+EN+TF-WeA12, **171**
- Maklakov, S.A.: TF+MI-WeM4, 145; TF-ThP11, **243**
- Maklakov, S.S.: TF+MI-WeM4, **145**; TF-ThP11, 243
- Mallek, J.L.: TF+EM+NS+SS-ThA2, 228
- Malloy, K.: EM-ThP10, 235
- Manamdar, S.: HI-ThA9, 213
- Mancheno-Posso, P.: EM1-WeM4, **130**
- Mandlik, P.: TF+VT-WeM2, 146
- Mandrus, D.G.: MI-MoM10, 14; MI-MoM9, 14
- Mangolini, F.: AS-ThP21, **233**
- Mangolini, L.: PS+AS+NS+SS-ThM4, 188
- Manini, P.: VT-WeM3, 148
- Manjare, M.T.:
MG+AS+EM+NS+SA+SE+SP+SS+TF-FrM5, **254**
- Mann, H.S.: TF+EN-MoM9, 24
- Mann, J.: GR-WeM10, 134; TF-ThP19, 244; TF-ThP20, **244**
- Mannequin, C.: PS-MoM5, 20
- Mannix, A.J.: GR+EM+NS+PS+SS+TF-MoM6, 12; GR+EM+NS+SS+TF-ThA11, 212;
NS+AS+BI+SP-WeM6, **136**
- Manno, M.: EN+PS+TF-MoM10, 11
- Mantovani, G.: BI+AS+IS+NL-MoM2, 6
- Mao, B.: IS+AS+SS-ThM9, 187
- Mao, F.: MI+EM+MG-MoA1, **38**
- Marchione, D.: SS+AS-WeM12, 141
- Marcus, M.A.: SA+AS+MG+SS-TuA10, 95
- Marcus, P.: SS+AS+NS-MoM9, 23
- Marder, M.: MG+EN+MS-WeA11, **161**
- Mares, P.: SE+NS+TF-ThA6, 221
- Margarella, A.M.: IA+AI+BI+IS+NL+SS-MoA10, 38; SS+AS-WeM11, 141
- Margot, J.: PS-MoM8, **21**
- Maria, J.-P.: TF-ThA6, **230**
- Marin, A.T.: TF-TuA9, 97
- Marki, J.: VT-MoM9, 27
- Marks, L.: TR+AS-MoM3, **25**
- Markus, T.Z.: SS-ThM9, 197
- Marsh, J.R.: AS-ThP8, 232
- Marshall, M.: BI+AI+AS+BA+IA+NL+NS+SP-WeA2, 153
- Martin, D.: MN+AS+SS-MoM10, 15
- Martin, F.: GR+AS+EM+MI+MN-TuM1, 59
- Martin, F.: SS1-ThA3, 224
- Martin, H.: TF+EM+NS+SS-FrM3, 260
- Martin, I.T.: TC+EM+EN+TF-WeA10, **170**;
TF+EM+NS+SS-FrM3, 260
- Martin, J.M.: TR+SE-TuM6, 74
- Martin, N.: AS-MoA1, 29; GR+AS+EM+MI+MN-TuM1, 59
- Martin, N.: SS1-ThA3, 224
- Martin, R.L.: AC+AS+EN-TuA10, 78
- Martinez, E.: SA+AS+MG+SS-TuA3, 94
- Martinez, G.: SE-ThP7, **239**
- Martínez, J.: EM-ThP9, 235
- Martinez, L.: MS+AS+BA+BI+PS+TF-TuM1, 63
- Martini, A.: TR+AS-MoM11, 26
- Martins, P.M.: NL+AS+BI-ThA6, 217
- Martirez, J.M.: SS+AS-TuM5, 69
- Martz, T.: MN+AS+SS-MoM10, 15
- Marusak, K.E.: BI-TuP9, **101**
- Maskova, S.: AC+AS+EN-TuA7, 77
- Mason, Jr., J.S.: EM-ThP17, 236
- Masuko, T.: SE-ThP10, **240**
- Matei, D.: GR+EM+NS+PS+SS+TF-MoM8, 12
- Matej, Z.: AC+AS+EN-TuA7, 77
- Matsubayashi, A.: NS-TuP17, 109;
TF+EM+NS+SS-ThA12, **229**
- Matsuda, A.: PS-MoM1, **19**
- Matsuda, I.: SS+EN-ThM10, 196
- Matsui, K.: TF-ThP28, 245
- Matsukuma, M.: PS2-TuM5, 68
- Matsumoto, H.: PS2-TuA8, 94; PS-MoM2, 20
- Matsumuro, A.M.: TF-ThP22, **244**
- Matsuo, J.: AS-MoA10, **30**
- Matsushima, K.: PS+TF-MoA11, **45**
- Matta, C.: TR+SE-TuM6, 74
- Matteau, G.J.: TF-ThA8, **230**
- Matthews, A.: SE+PS-ThM1, **192**
- Matthews, D.J.: TF+EM+NS+SS-ThA1, 228
- Mattrey, R.F.: BI-TuP3, 100
- Mattsson, A.: SS+EN-ThM6, 195
- Matveev, K.A.: SE+EN-FrM4, 256
- Maurice, V.: SS+AS+NS-MoM9, 23
- Mavrakakis, K.: PS1-TuM6, **66**; PS-TuP23, 112
- Mays, E.: TF+VT-WeM9, 147
- Mazumder, B.: AP+AS+SS-TuA11, **79**
- Mazur, P.: SS1-ThA9, 225
- Mazzuco, S.: IS+AS+SP-FrM10, 253
- McAllister, K.: GR+EM+NS+SP+TF-MoA6, **36**
- McArthur, S.M.: BI+AI+BA+IS-MoA1, 31;
BI+AI+BA+IS-MoA11, 32; BI-TuP4, 101; BI-TuP5, 101; BI-TuP6, 101
- McBreen, P.H.: SS-ThM12, 198
- McCarty, K.F.: GR-WeM12, 134
- McClimont, J.: NS+AS+EN+SS-TuA10, 90
- McCormick, D.: NL+AS+BI-ThA7, 217
- McCoustra, M.R.S.: SS+AS-WeM12, **141**
- McCrate, J.M.: SS-FrM5, **259**
- McDonald, I.: NS+AS+EM-MoA1, 41
- McDonald, J.P.: TF-ThA1, 229
- McDonnell, S.: GR+AS+BI+PS+SS-ThA7, 210;
GR+EM+NS+SS+TF-ThA1, **211**
- McGuire, G.E.: EM-TuA3, **83**
- McIntyre, P.C.: EM1-WeM2, **129**; EM-MoA4, 33
- McKay, K.: AS+BI+IS-WeM5, 125
- McKenna, D.: TF+PS-ThM6, 200
- McKinley, J.L.: TF-ThP19, 244
- McLaughlin, S.R.: EM-ThP17, 236
- McNamara, J.D.: EM+NS+SS+TF-FrM3, **247**
- McPeak, S.: TF-ThP10, 242
- McVittie, J.: PS1-TuM6, 66
- Medina-Ramos, J.: EN+AS+PS-TuA3, 84
- Meeks, K.: TF-ThA4, **230**
- Mehl, M.J.: EM+NS+SS+TF-FrM6, 247
- Mehta, R.J.: EM+NS+TF-FrM3, 248;
NS+EM+EN-TuM11, 65
- Mei, A.R.B.: TF+EM+NS+SS-FrM8, **261**
- Meier, G.: MI+AS+NS+SP-TuA9, **87**
- Meier, M.: AS+BI-TuA9, **81**
- Meirer, F.: SA+AS+MI+SS-WeM9, **140**
- Meléndez-Lira, M.: NS-TuP3, **106**; NS-TuP4, 107;
TF-ThP1, 241; TF-ThP13, 243
- Melendez-Lira, M.A.: NS-TuP5, **107**
- Melton, A.G.: EM+NS+SS+TF-FrM10, 248;
EM+NS+SS+TF-FrM5, **247**; EM+NS+SS+TF-FrM7, 247
- Melzer, J.I.: AS+BI-MoM8, 4
- Membreno, D.: TF+EN-MoM4, 24
- Mende, P.: GR-WeM3, **133**
- Mendez Martin, F.: SE+NS+TF-ThA7, 221
- Mendez, N.: BI-WeM9, **127**
- Mendoza-Sánchez, B.: GR-ThP6, 237
- Meneses, M.: EM-ThP9, 235
- Meng, L.: SE+PS-ThM3, 192; SE-ThP2, **239**
- Menon, L.: NS+AS+EM-MoA1, 41
- Menzel, D.: GR-WeM11, **134**
- Mercer-Smith, A.R.: BI-TuP16, **102**
- Merche, D.: PS+AS+NS+SS-ThM9, **189**
- Merte, L.R.:
MG+AS+EM+NS+SA+SE+SP+SS+TF-FrM2, 253
- Mertz, C.: GR+AS+BI+PS+SS-ThA3, 209
- Meseck, G.R.: SE+NS+TF-ThA12, **222**
- Metz, A.: MS+AS+EL+EM+PS+TF-TuA9, 89;
PS-MoA1, 45
- Metzler, D.: PS-WeM1, **137**; PS-WeM3, 137
- Meyerbröcker, N.: BI+NL+NS+SS-ThM5, **177**
- Meyyappan, M.: NS+EM+EN-TuM5, **64**
- Mezzenga, R.: BI+AS+BA+NS+SS-ThA2, 203
- Mhatre, B.S.: SS-ThM11, 198; SS-ThM3, 197; SS-ThM4, 197
- Miao, F.: IS-ThP2, 238
- Michalak, D.J.: EM+AS+PS+TF-ThM5, **182**
- Michallon, P.: PS+TF-MoA8, 44
- Mignot, S.: MS+AS+EL+EM+PS+TF-TuA4, 89;
PS2-TuM9, 68
- Mignot, Y.: PS-MoA3, 45
- Mihut, D.M.: MS+AS+EL+EM+PS+TF-TuA11, **89**
- Mikkelsen, A.: EM+TF-MoM6, 8; MI-MoM11, 14
- Milasinovic, S.: AS-MoA3, 29
- Miles, M.: SP+AS+BI+EM+MI+NS+SE+SS-ThA8, **223**
- Miller, D.J.: IS+AS+SS-ThM3, 186
- Miller, M.: AP+AS+EM+MI+TF-WeM10, 124
- Miller, R.: TF+EM+NS+SS-FrM10, 262
- Mills, G.: HI-ThA8, 213
- Milosavljevic, V.: SE+PS-WeA4, **164**
- Milson, G.A.: SP+AS+BI+EM+MI+NS+SE+SS-ThA3, **222**
- Mily, E.J.: TF-ThA6, 230
- Mims, C.: IS+AS+SP-FrM9, 252
- Min, W.: AS-MoA4, 29
- Minami, T.: TC-TuP5, 119
- Minar, J.: MI+AS+NS+SP-TuA7, 87
- Minasian, S.: AC+AS+EN-TuA10, **78**
- Minaye Hashemi, F.: TF-TuM6, **72**
- Minegishi, T.: SE+EN-FrM6, **256**
- Minelli, C.: AS+BI+EM+NL+NS+SS-ThM5, **175**
- Minfray, C.: TR+SE-TuM6, **74**
- Minn, M.: TR+SE-TuM2, 73

- Minne, S.C.: SP+AS+BI+MI+NS+SS-ThM9, 194
 Miranda, R.: GR+AS+EM+MI+MN-TuM1, 59
 Mirando, R.: SS1-ThA3, 224
 Mirhosseini, H.: MI-MoM8, 14
 Mirkin, C.A.: SP+AS+BI+EM+MI+NS+SE+SS-ThA12, 223
 Mishra, S.: EM-ThA2, 206
 Mishra, U.K.: AP+AS+SS-TuA11, 79
 Mistry, H.: AS+BI+EM+NL+NS+SS-ThA3, 202
 Mitchell, K.N.: EL-ThP3, 234
 Mitterer, C.: SE+NS+TF-ThA7, 221; SE+PS-ThM12, 193
 Miura, R.: TR+SE-TuM6, 74
 Miura, T.: TR-TuP1, 120
 Miyake, K.: PS-TuP30, 113
 Miyamoto, A.: TR+SE-TuM6, 74
 Miyamoto, J.: TR-TuP9, 121
 Miyata, T.: TC-TuP5, 119
 Miyayama, T.: AS+BI-MoM5, 3; AS-ThP9, 232
 Miyazoe, H.: PS-MoA6, 45; PS-MoM2, 20
 Miyoshi, J.: TF-ThP4, 241
 Mizotani, K.: PS-ThA3, 218
 Mkhoyan, K.A.: EN+PS+TF-MoM4, 9
 Mochiji, K.: AS-MoA11, 30
 Mochiki, H.: PS2-TuM2, 67
 Mochizuki, S.: PS-ThA10, 219
 Moewes, A.: IA+BA-TuA12, 86
 Moffitt, C.: AS-WeA3, 151; GR-ThP6, 237
 Møgelhøj, A.: SS2-ThA4, 226
 Mohanti, N.: MS+AS+EL+EM+PS+TF-TuA4, 89
 Mohanty, N.: EM-ThA2, 206
 Mok, H.S.: GR-WeM12, 134
 Mol, J.A.: SS+AS+NS+SP-WeA1, 166
 Molina-Luna, L.: NS+AS+EM-MoA4, 42
 Molkenboer, F.T.: HI-ThM12, 186; SE+PS-WeA10, 165
 Molle, A.: EM-MoA1, 32
 Möllers, R.: AS+BI-MoM6, 4
 Molnar, M.: MS+AS+EM+EN+NS+TF-MoM3, 16
 Momose, T.: EM-ThA8, 207
 Monahan, D.: PS-TuP21, 112; PS-TuP32, 114
 Monazami, E.: GR-WeM4, 133
 Monfil, K.: EM-ThP1, 234; EM-ThP9, 235; SS-TuP22, 118
 Monfil-Leyva, K.: EN-TuP8, 103
 Monig, H.: SS+AS+NS+SP-WeA7, 166
 Monnier, J.R.: SS-TuP16, 117
 Montgomery, A.: TF+MI-WeM3, 145; TF+MI-WeM5, 145
 Montgomery, N.: AC+AS+EN-TuA11, 78
 Moon, B.-H.: PS-TuP23, 112
 Moon, C.-Y.: SS+EM-WeA2, 168
 Moon, D.: AS-MoA4, 29
 Moon, J.: TC+EM+EN+TF-WeA1, 169
 Moon, Y.: MS+AS+EL+EM+PS+TF-TuA9, 89
 Moon, Y.K.: BI-TuP15, 102
 Moon, Y.S.: TF-ThP6, 242
 Moore, T.: VT+AS+SS+TF-WeA7, 174
 Morabito, J.: BI-WeM3, 126
 Morales, A.: EM-ThP1, 234; EM-ThP9, 235; SS-TuP22, 118
 Morales, E.H.: SS+AS-TuM5, 69
 Mordi, G.: GR+AS+BI+PS+SS-ThA7, 210
 Morent, R.: AS+BI-MoM2, 3
 Moretti, J.E.: SS+AS-WeM3, 140
 Morgen, P.: TF+EM+NS+SS-FrM2, 260
 Mori, T.: SE-ThP10, 240; SE-ThP5, 239
 Morikawa, Y.: PS-TuP31, 113
 Moritani, K.: AS-MoA11, 30
 Moriya, T.: PS1-TuM9, 66
 Morkowchuck, L.: SS-TuP35, 119
 Moroz, P.: PS-ThM11, 191
 Morra, M.M.: AS+BI-MoM8, 4
 Morris, B.G.: MS+AS+EL+EM+PS+TF-TuA4, 89; PS-MoA3, 45
 Morrish, F.: BI+AI+AS+BA+IA+NL+NS+SP-WeA7, 153
 Morrison, J.: EM+AS+EN+TF-ThM10, 181
 Morvay, D.M.: EM-ThA2, 206; PS-MoA1, 45
 Moshar, A.: EW-WeL5, 149
 Mostovoy, M.: MI+AS+NS+SP-TuA12, 88
 Mota-Pineda, E.: NS-TuP5, 107
 Motoyama, S.: PS-TuP33, 114
 Moulder, J.F.: AS+BI+EM+NL+NS+SS-ThA9, 202; AS+BI-MoM2, 3; AS-ThP13, 232; AS-TuM10, 55; EW-TuL2, 76
 Mountapbeme Kouotou, P.: HI-ThA7, 213
 Mowbray, D.: SS1-ThA8, 225
 Mowll, T.R.: GR-WeM1, 132
 Mráz, S.: SE+NS+TF-ThA8, 221
 Mu, R.: SS-MoA6, 47
 Mudiysenselage, K.: IS+AS+SS-ThM6, 186
 Mueller, A.: VT+EN+TF-TuA3, 98
 Mugarza, A.: AS-TuM11, 55
 Mugumaoderha Cubaka, M.: EN-TuP1, 103
 Muhl, S.: PS-TuP34, 114
 Mühlbacher, M.: SE+NS+TF-ThA7, 221
 Muir, B.: BI+AS+BA+NS+SS-ThA2, 203
 Mukherjee, P.: NL+AS+BI-ThA7, 217
 Mukherjee, S.: NS+BI+EM-WeA7, 162
 Müllen, K.: GR+EM+NS+PS+SS+TF-MoM8, 12
 Müller, O.: SA+AS+MI+SS-WeM11, 140
 Müller, U.F.: SS+AS-WeM3, 140
 Mullins, D.R.: SS-FrM3, 259; SS-MoA10, 48; SS-MoA11, 48
 Mullis, F.: VT-MoA6, 52
 Mulvaney, S.P.: BI+NL+NS+SS-ThM12, 178; BI-WeM3, 126; EM+AS+EN+TF-ThM5, 180
 Mundle, R.M.: TF-TuM2, 71
 Muñoz Zurita, A.L.: EN-TuP8, 103
 Muñoz-Rojas, D.: TF-TuA9, 97
 Munusamy, P.: AS+BI+EM+NL+NS+SS-ThM11, 176
 Muraki, Y.: PS+TF-MoA10, 45; PS2-TuM5, 68
 Muramoto, S.: AS+BI+IS-WeM6, 125
 Muratore, C.: SE+PS-ThM5, 192
 Murayama, T.: PS-TuP31, 113
 Murphy, P.: BI+AS+BA+NS+SS-ThA12, 205
 Murphy, R.D.: TF-ThA1, 229
 Murphy, S.: SP+AS+BI+MI+NS+SS-ThM5, 194
 Murzina, T.: MI+EM-TuM10, 62
 Muscat, A.J.: EM1-WeM4, 130; EM-ThP6, 235; NS+BI+EM-WeA4, 161
 Müser, M.H.: TR+AS+NS+SS-MoA1, 50
 Musgrave, C.B.: TF+EN-MoM5, 24
 Music, D.: SE+NS+TF-ThA4, 220; SE+NS+TF-ThA8, 221
 Musselman, K.P.: TF-TuA9, 97
 Mutch, M.: EM-ThA1, 206; PS-MoA10, 46
 Myers, A.M.: EM+AS+PS+TF-ThM9, 182
 Myers-Ward, R.L.: EL+AS+EM+SS+TF-WeA1, 155; EL+AS+EM+SS+TF-WeA2, 155; GR+EM+MS+NS+SP-FrM4, 250; GR+EM+NS+PS+SS+TF-MoM3, 11
 Myhro, K.: GR+EM+NS+SP+TF-MoA1, 36; IS-ThP2, 238
 — N —
 Naaman, R.: SS-ThM9, 197
 Naboko, A.S.: TF-ThP11, 243
 Nadeau, L.J.: BI+AI+BA+IS-MoA3, 31
 Nagabhirava, B.: PS-MoA3, 45
 Nagahata, K.: PS-TuP30, 113
 Nagamoto, K.: TC-TuP4, 119
 Nagamura, N.: GR+EM+NS+PS+SS+TF-MoM4, 11
 Nagao, K.: BI+AI+AS+BA+IA+NL+NS+SP-WeA1, 153
 Nagareddy, V.K.: GR+EM+MS+NS+SP-FrM4, 250
 Naghibi, S.: TF-ThP20, 244
 Nahif, F.: SE+NS+TF-ThA8, 221
 Nahm, R.K.: EM+AS+EN+TF-ThM1, 180
 Nainani, A.: EM-MoA6, 33
 Nakagawa, S.: AS-MoA10, 30
 Nakaharai, S.: GR+AS+BI+PS+SS-ThA8, 210; HI-ThM9, 185
 Nakajima, T.: SS-TuP11, 116
 Nakakubo, Y.: PS-MoM1, 19
 Nakamura, J.: GR+AS+EM+NS+SS-WeA8, 159; GR-ThP12, 237; SS2-ThA2, 226; SS-TuP10, 116
 Nakamura, M.: PS-MoA8, 46; PS-MoM2, 20
 Nakano, T.: GR+AS+BI+PS+SS-ThA2, 209; PS1-TuM12, 67; PS-TuP24, 112
 Nakatsuka, O.: SA-TuP4, 114
 Nakazaki, N.: PS-ThM1, 190
 Nam: MS+AS+BA+BI+PS+TF-TuM3, 63
 Nam, K.-W.: IS+EN+SP+SS-ThA3, 214
 Nam, S.: PS-MoA3, 45
 Nam, S.-H.: AS-ThP18, 233
 Nanayakkara, J.K.S.: EM+NS+SS+TF-FrM10, 248; EM+NS+SS+TF-FrM9, 248
 nanayakkara, S.: NS+BI+EM-MoM9, 17
 Nandasiri, M.I.: AP+AS+MI+NS+SS-WeA1, 150; HI-ThA9, 213; NS-TuP12, 108
 Narayanan, B.: GR+AS+BI+PS+SS-ThA1, 209
 Narayanan, S.: TC+EM+EN+TF-WeA3, 170
 Nash, A.: NS+BI+EM-MoM5, 17
 Nasybuiln, E.: AS-ThP3, 231
 Nath, A.: GR+EM+MS+NS+SP-FrM4, 250
 Natzeck, C.: SS-FrM9, 260
 Naudé, N.: SE+PS-ThM11, 193
 Navin, J.K.: SS2-ThA1, 226
 N'Diaye, A.: IS+EN+SP+SS-ThA7, 215
 Ne'eman, I.: PS-MoA6, 45
 Nealey, P.F.: MS+AS+EM+NS+PS+TF-MoA6, 41
 Neeway, J.J.: AP+AS+EM+MI+TF-WeM9, 123
 Nefedov, A.: SS-FrM9, 260
 Nelin, C.J.: AC+AS+SS-TuM3, 53; SS+AS-TuM12, 71
 Nelson, C.M.: EL-ThP2, 234
 Nelson, S.F.: TF-TuA3, 97
 Nelson-Cheeseman, B.: MI+EM+MG-MoA10, 39
 Nemani, S.: PS-MoM5, 20
 Nemanich, R.J.: EM-WeA3, 158
 Nemashtalo, A.: SS-FrM10, 260
 Nemoz, M.: TF+EM+NS+SS-ThA8, 229
 Nepal, N.: EM+NS+SS+TF-FrM4, 247; EM+NS+SS+TF-FrM6, 247
 Nesterov-Mueller, A.: BI+NL+NS+SS-ThM11, 178
 Netz, R.: IA+AI+BI+IS+NL+SS-MoA8, 38
 Netzer, F.P.: SS+AS-TuM9, 70
 Ng, P.K.: SP+AS+EM+GR+MI+NS+SS-FrM11, 258
 Ng, T.: TC+EM+TF-WeM9, 144
 Nguyen, A.: TF-ThP20, 244
 Nguyen, N.: TC+EM+EN+TF-WeA11, 170
 Nguyen, N.V.: EL+AS+EM+SS+TF-WeA2, 155; GR+EM+MS+NS+SP-FrM7, 251
 Nichols, M.: EM+AS+PS+TF-ThM1, 181; EM+AS+PS+TF-ThM12, 183; EM-ThP3, 234; PS1-TuM6, 66; PS-TuP13, 110; PS-TuP23, 112
 Nie, S.: GR-WeM12, 134
 Niehuis, E.: AS+BI-MoM6, 4
 Nikogeorgos, N.: TR+AS+NS+SS-MoA8, 51
 Nikzad, S.: EM+NS+SS+TF-FrM11, 248
 Nilebäck, E.: BI+AS+BA+NL-TuM6, 56
 Nilsson, A.: IS+AS+SS-ThM3, 186; SS+AS-WeM9, 141; SS2-ThA4, 226
 Nishi, Y.: EM+AS+PS+TF-ThM1, 181; EM+AS+PS+TF-ThM12, 183; EM-ThP3, 234; PS1-TuM6, 66; PS-TuP13, 110; PS-TuP17, 111; PS-TuP23, 112
 Nishimiya, T.: PS-TuP33, 114
 Nishimura, N.: SE+EN-FrM6, 256
 Nisol, B.: SE+PS-WeA7, 164
 Nittler, L.: EN-TuP1, 103
 Noborisaka, M.: SE-ThP1, 239; SE-ThP10, 240
 Nocera, D.: EN+AS+PS-TuA7, 84
 Nogami, J.: NS+BI+EM-WeA2, 161
 Noirfalise, X.: SE+NS+TF-ThA9, 221
 Nolan, T.K.: AS-WeA10, 152
 Nold, E.: TR+SE-TuM5, 73
 Nolting, W.: NS-TuP17, 109
 Nomoto, J.: TC-TuP5, 119

- Nonnenmann, S.S.: IS+EN+SP+SS-ThA1, **214**;
NS+EM+EN-TuM3, 64
- Noonan, J.R.: VT-WeM5, **148**
- Nordell, B.: GR+AS+EM+NS+SS-WeA9, 160
- Nordlund, D.: AC+AS+EN-TuA10, 78; SS2-ThA4, 226
- Norrby, N.: SE+NS+TF-ThA3, **220**
- Norris, D.J.: EN+PS+TF-MoM9, 10
- Nørskov, J.K.: SS2-ThA4, 226
- Norton, S.E.: BI-TuP14, 102
- Notte, J.A.: HI-ThA11, 214; HI-ThM3, **185**
- Novak, J.: SS1-ThA2, 224
- Novak, M.: SS+AS+NS+SP-WeA12, 167
- Novikova, I.: TF+AS+EM+NS+SS-ThM6, 198
- Noyce, S.: MN+AS+SS-MoM4, **15**
- Ntwaeaborwa, O.M.: AS-ThP19, 233
- Nunney, T.S.: AS-ThP1, **231**; AS-ThP12, 232; AS-WeA11, 152; EW-TuL4, **76**
- Nyakiti, L.O.: EM+NS+SS+TF-FrM6, 247;
GR+EM+MS+NS+SP-FrM4, 250;
GR+EM+NS+PS+SS+TF-MoM3, 11
- Nyberg, T.: MI+EM+MG-MoA1, 38
- Nyns, L.: EM+TF-MoM2, 8
- **O** —
- Obara, Y.: TR+SE-TuM6, 74
- Öberg, H.: SS2-ThA4, 226
- O'Brien, M.: EN+PS+TF-MoM6, 10
- Ocola, L.: GR+AS+BI+PS+SS-ThA3, 209
- O'Connell, D.: PS+AS+BI+SE-MoM8, **19**
- Odén, M.: SE+NS+TF-ThA3, 220
- Odenthal, P.M.: TF-ThP19, 244
- Odom, T.W.: AS+BI-TuA12, **81**
- Oehrein, G.S.: PS+AS+BI+SE-MoM11, 19; PS-WeM1, 137; PS-WeM3, 137; PS-WeM5, 138
- Oertel, D.: VT-MoM9, 27
- Ogasawara, H.: IS+AS+SS-ThM3, **186**; SS2-ThA4, 226
- Ogawa, D.: PS-TuP27, **112**
- Ogawa, M.: SS+EN-ThM10, 196
- Ogawa, S.: GR+AS+BI+PS+SS-ThA8, 210; HI-ThM9, **185**
- Oglecka, K.: BI+NL+NS+SS-ThM3, 177
- Oh, J.: SS-TuP19, **117**
- Oh, J.S.: GR-ThP5, 236
- Oh, S.G.: PS-TuP22, 112
- O'Hara, A.: EM+NS+TF-FrM10, 250
- Ohashi, Y.: BI+AI+AS+BA+IA+NL+NS+SP-WeA1, 153
- Ohiwa, T.: PS2-TuA11, 94
- Ohkouchi, T.: GR+EM+NS+PS+SS+TF-MoM4, 11
- Ohkubo, T.: AP+AS+EM+MI+TF-WeM4, **123**
- Ohlhausen, J.A.: AS-WeA9, **152**
- Ohta, T.: GR+EM+NS+SP+TF-MoA3, **36**; PS1-TuA10, 92
- Ohtsuka, S.: PS-ThA10, 219
- Ohuchi, F.S.: EM+PS-WeM3, 128;
EN+SE+SS+TF-WeM5, 131;
TC+EM+EN+TF-WeA11, 170
- Oida, S.: GR+AS+NS+SP+SS-TuA1, **85**;
GR+EM+NS+PS+SS+TF-MoM3, 11
- Okada, T.: GR+AS+BI+PS+SS-ThA4, **209**
- Okamoto, N.: PS-ThA8, 219
- Oktyabrsky, S.: EM+TF-MoM11, 9; SS-FrM7, 259
- Okyay, A.K.: SE-ThP11, 240
- Olafsson, S.: PS+TF-MoA9, 44
- Oldham, C.J.: TF-ThP15, 243; TF-TuM11, 72
- Oleynik, I.I.: GR+EM+NS+PS+SS+TF-MoM9, 12
- Olmstead, M.A.: EM+PS-WeM3, 128;
EN+SE+SS+TF-WeM5, 131;
TC+EM+EN+TF-WeA11, 170
- Olson, D.A.: VT-MoM3, 27
- Olson, J.: SS+AS+NS+SP-WeA12, **167**
- Olszta, M.J.: AP+AS+SS-TuA9, 79
- Oliveira, S.: NS-TuP10, **108**
- Omura, M.: PS-MoM4, 20
- Ondeck, N.: AS+BI+EM+NL+NS+SS-ThM9, 176
- Ono, K.: PS-MoM1, 19; PS-ThA10, 219; PS-ThM1, 190; PS-ThM12, 192
- Opila, R.: AS-WeA12, 153; EM+AS+PS+TF-ThM2, 181
- Opsomer, K.: EM+PS-TuM10, 58
- Oraon, N.: MN-TuP6, **105**
- Orlando, T.M.: AS+BI+IS-WeM4, 124; SS+AS-WeM6, 141
- Orlov, A.O.: EM-ThA10, 208
- Oroc, M.: EM+NS+SS+TF-FrM7, 247
- Orr, J.T.: AS-WeA10, 152
- Ortega, J.E.: AS-TuM11, **55**; SS1-ThA8, 225
- Osgood, R.M.: SP+AS+BI+EM+MI+NS+SE+SS-ThA4, 223
- O'Shaughnessy, T.J.: BI-WeM3, 126
- Osher, S.: SP+AS+BI+EM+MI+NS+SE+SS-ThA12, 223
- Oshima, M.: GR+EM+NS+PS+SS+TF-MoM4, 11
- Osinsky, A.: TF+EM+NS+SS-FrM10, 262
- Osipov, A.V.: TF+MI-WeM4, 145
- Ossowski, J.W.: SS+AS+NS+SP-WeA10, **167**;
TF+AS+BI+EM+SE+SS-WeA7, 172
- Österlund, L.: SS+EN-ThM6, **195**
- Öström, H.: SS2-ThA4, 226
- O'Sullivan, D.: PS1-TuA3, 91
- Otero, R.: SS1-ThA3, 224
- Otto, J.: GR+AS+EM+NS+SS-WeA9, 160
- Ou, V.: TF+AS+EM+NS+SS-ThM11, **199**
- Ouyang, H.: PS+AS+NS+SS-ThM5, 189
- Overbury, S.H.: SS-MoA11, 48
- Overzet, L.J.: PS-TuP27, 112
- Owen, A.: TF+MI-WeM5, **145**
- Oyama, K.: PS2-TuM2, 67
- Ozawa, K.: SS+EN-ThM10, 196
- Ozawa, N.: SS-TuP5, **115**
- Ozcan, A.: EL+AS+EM+SS+TF-WeA11, 156
- Ozdemir, O.K.: SS-TuP12, 117
- Ozgit-Akgun, C.: SE-ThP11, **240**;
TF+AS+NS+SE-WeA3, 173
- Ozimek, P.: TF+AS+EM+NS+SS-ThM9, 199
- Ozkan, A.: PS-TuP29, **113**; SE+PS-ThM9, 193
- Ozkanat, O.: SS+AS+NS+SP-WeA1, 166
- Ozturk, M.: MI-TuP2, 104
- Ozturk, O.: MI-TuP2, **104**; SS-TuP12, 117
- **P** —
- Pacholski, M.: SS-TuP24, **118**
- Padama, A.A.: MG-ThA2, 216; SS-TuP6, **115**
- Padbury, R.P.: TF+AS+SE+SS-MoA10, **50**
- Padgett, M.J.: SP+AS+BI+EM+MI+NS+SE+SS-ThA8, 223
- Padmore, H.A.: AS-WeA1, **151**; VT+AS+SS+TF-WeA11, **174**
- Paek, J.: TF+EN-MoM1, 23
- Page, S.C.: AS+BI-MoM4, 3
- Palamarcic, T.: SS-TuP34, 119
- Pallem, V.: EM+AS+PS+TF-ThM2, 181; PS-MoM3, 20
- Palmer, R.E.: SP+AS+BI+MI+NS+SS-ThM5, 194;
SS+EN-ThM12, **196**; TF+AS+NS+SE-WeA11, 174
- Palmstrom, C.J.: EM+AS+NS+SS-WeA9, **157**;
MI-MoM11, 14
- Palmstrøm, C.J.: EM+AS+NS+SS-WeA11, 157
- Palumbo, F.: EM+TF-MoM2, 8
- Pan, L.: MI-TuP4, 104
- Pandey, R.: BA+AI+AS+BI+IS+NL-MoM10, 5
- Pant, S.: SS-FrM10, 260
- Pantazis, S.: VT-MoA3, **52**
- Pantoya, M.L.: TF-ThA4, 230
- Pantuso, D.: EM+AS+PS+TF-ThM5, 182
- Pap, A.: PS-MoA7, 46
- Papa Rao, S.: MS+AS+BA+BI+PS+TF-TuM3, **63**
- Papuso, C.: TF+MI-WeM1, 144
- Paquale, F.: MI+EM-TuM9, 61
- Paquette, M.: GR+AS+EM+NS+SS-WeA9, **160**
- Parakhonkiy, G.: SE+NS+TF-ThA3, 220
- Pargon, E.: PS2-TuM3, **68**
- Parikh, A.N.: BI+NL+NS+SS-ThM3, **177**
- Parise, R.J.: TF+EN-MoM9, 24
- Park, B.-G.: GR-ThP9, 237
- Park, B.K.: TF-ThP38, 246
- Park, C.D.: VT-TuP4, 121; VT-TuP5, **121**
- Park, C.-Y.: GR+AS+EM+MI+MN-TuM11, **60**
- Park, D.K.: NS-TuP16, **109**
- Park, E.H.: SS-ThM10, **197**
- Park, H.H.: EM+TF-MoM1, 7
- Park, I.-Y.: HI-ThA12, **214**
- Park, J.: NS-TuP16, 109; PS-MoM6, 21; PS-TuP11, 110; SP+AS+EM+GR+MI+NS+SS-FrM1, **257**; SP+AS+EM+GR+MI+NS+SS-FrM9, 258; SS-TuP21, 118; TF+EN-MoM1, 23; TF+VT-WeM12, 147; TF-TuM1, 71
- Park, J.W.: SP+AS+BI+NS-ThP3, 241
- Park, J.Y.: GR+AS+NS+SP+SS-TuA10, 86; SS-TuP21, 118; TR+AS+NS+SS-MoA10, 52; TR-TuP8, 121
- Park, K.T.: SS-FrM4, 259
- Park, S.: MN+AS+SS-MoM10, **15**; PS-ThA12, 220
- Park, S.-J.: TF-TuM5, **71**
- Park, S.W.: EM+TF-MoM1, 7
- Park, T.-H.: NS+BI+EM-MoM9, 17
- Park, Y.: GR-ThP9, 237
- Park, Y.D.: NS+BI+EM-MoM3, 16
- Parker, D.: EM+NS+TF-FrM3, 248
- Parkinson, B.: PS2-TuM12, 69; PS-MoM11, **21**
- Parlak, Z.: GR+AS+EM+NS+SS-WeA1, 159
- Parriaux, O.: NS+BI+EM-WeA9, 162
- Parsons, G.N.: SS+NS-WeM10, 142;
TF+AS+SE+SS-MoA6, **49**; TF-ThP15, 243;
TF-TuM11, 72
- Pascon, A.M.: GR-ThP7, **237**
- Pasquarelli, R.: TC+EM+EN+TF-WeA7, 170
- Pasupathy, A.: GR+AS+EM+NS+SS-WeA3, **159**
- Patchett, E.: EM+AS+EN+TF-ThM10, 181
- Pateau, A.: PS2-TuA3, **93**
- Patel, A.K.: BI+AS+IS+NL-MoM10, 7; BI-WeM1, 126
- Patel, S.: EM+AS+NS+SS-WeA11, **157**
- Pathiyamattom, P.J.: EN-TuP8, 103
- Patterson, M.: SS+NS-WeM12, 143
- Patz, R.: PS-MoA7, **46**
- Paul, B.: TF+EM+NS+SS-ThA3, 228
- Paul, D.F.: AS+BI+EM+NL+NS+SS-ThA9, 202;
AS-ThP6, **231**; AS-TuM10, 55; AS-WeA4, 152
- Paul, J.: PS2-TuM1, 67
- Paul, J.-F.: SE+NS+TF-ThA9, 221
- Payne, S.: BI-TuP9, 101
- Payton, O.: SP+AS+BI+EM+MI+NS+SE+SS-ThA8, 223
- Peak, D.: IA+BA-TuA12, 86
- Peck, J.: TF+PS-ThM10, **200**; TF-ThP18, 244
- Peden, C.: IS+AS+SP-FrM9, 252
- Pedersen, K.: SS+AS+NS-MoM6, **22**;
TF+EM+NS+SS-FrM2, 260
- Peethala, B.: PS-MoA3, 45
- Pegalajar-Jurado, A.: BI-WeM12, **127**;
PS+AS+BI+SE-MoM10, 19
- Pei, D.: EM+AS+PS+TF-ThM12, 183; PS-TuP13, **110**
- Pei, L.: TF+VT-WeM11, 147
- Peixoto, T.: SS+EM-WeA9, **168**
- Pelissier, B.: PS+TF-MoA8, 44
- Peña Martin, P.: EN+PS+TF-MoM8, **10**
- Pender, J.: PS-MoM5, 20
- Peng, H.: MG+EM+MI+MS-WeM5, 134
- Peng, W.: SS+EM-WeA10, **169**
- Perea, D.E.: AP+AS+MI+NS+SS-WeA1, 150;
AP+AS+MI+NS+SS-WeA12, 151;
AP+AS+MI+NS+SS-WeA2, 150; AP-TuP1, **100**; HI-ThA9, 213
- Perez, R.: SS+AS+NS+SP-WeA7, 166
- Perkins, J.: MG+EM+MI+MS-WeM6, 134
- Perng, Y.: TF+EN-MoM4, 24
- Pernicka, J.C.: VT+EN+TF-TuA1, **98**
- Perrine, K.A.: IA+AI+BI+IS+NL+SS-MoA10, **38**;
SS+AS-WeM11, 141
- Perrotta, A.: TF+VT-WeM6, **147**
- Persing, H.M.: PS1-TuA11, 92; PS-TuP14, 110
- Persson, M.: BI+AS+BA+NL-TuM5, 56

- Petek, H.: NS+BI+EM-MoM10, **17**
Peter, M.: SS+NS-WeM2, 142
Peters, A.: MS+AS+EL+EM+PS+TF-TuA3, 88
Peters, K.: AS-ThP12, 232
Peterson, D.: SE+PS-WeA9, 165
Peterson, E.: SS2-ThA10, 227
Peterson, K.A.: TC+EM+EN+TF-WeA10, 170
Petit, L.: AC+MI+SA+TF-MoA8, **29**
Petrik, N.G.: SS+EN-ThM5, **195**
Petrou, A.: EM2-ThA10, 206
Petrov, I.G.: SE+NS+TF-ThA1, **220**;
TF+EM+NS+SS-FrM6, 261; TF+EM+NS+SS-FrM8, 261; TF+PS-ThM11, 201
Petrovykh, D.Y.: NL+AS+BI-ThA6, **217**
Pettersson, L.G.M.: SS2-ThA4, 226
Pham, C.: TF+MI-WeM9, **145**
Pham, H.: EM+PS-WeM3, 128
Phillips, C.: IA+BA-TuA12, 86
Phillips, D.J.: SP+AS+BI+EM+MI+NS+SE+SS-ThA8, 223
Phillips, M.C.: SP+AS+BI+NS-ThP2, 241
Piallat, F.: PS+TF-MoA8, 44
Pianetta, P.: SA+AS+MG+SS-TuA1, **94**
Piao, H.: AS-ThP5, 231; AS-WeA4, **152**
Piatkowski, L.: IA+AI+BI+IS+NL+SS-MoA3, 37
Piazza, G.: MN-TuP4, 105
Picco, L.M.: SP+AS+BI+EM+MI+NS+SE+SS-ThA8, 223
Picher, M.: IS+AS+SP-FrM10, **253**; IS+AS+SP-FrM8, 252
Pickard, D.: HI-ThA3, **212**
Picone, A.: SS+AS-TuM9, 70
Pierce, C.C.: AS+BI-MoM8, 4
Pierre-Louis, O.: GR+AS+NS+SS-ThM3, 183
Pimpinelli, A.: SS+AS+NS-MoM3, 22
Pingle, H.: BI-TuP6, **101**
Piper, L.F.J.: EM2-ThA10, 206
Pireaux, J.-J.: EN-TuP1, 103; PS+AS+NS+SS-ThM9, 189
Pirim, C.: SS+AS-WeM6, 141
Pirlo, R.K.: BI+AI+BA+IS-MoA3, 31
Platt, H.: TC+EM+EN+TF-WeA7, 170
Pluchery, O.: TF+AS+BI+EM+SE+SS-WeA3, 171
Plucinski, L.: MI+AS+NS+SP-TuA7, 87
Plummer, E.W.: SS+NS-WeM9, 142
Podraza, N.: EL+AS+EM+SS+TF-WeA8, 155
Poelsema, B.: HI-ThP4, 238
Points, M.S.: EM-WeA7, 158
Pokholok, K.V.: TF+MI-WeM4, 145
Polak, M.: SS+NS-WeM6, 142
Poleunis, C.: PS+AS+BI+SE-MoM5, 18
Politi, A.: MI+EM-TuM3, 61
Pollard, A.J.: AS+BI-MoM9, 4
Pollentier, I.: MS+AS+EM+NS+PS+TF-MoA6, 41
Pomorski, T.A.: PS-MoA10, **46**
Poodt, P.: TF-TuA1, **97**; TF-TuA10, 97
Pookpanratana, S.: TF+AS+BI+EM+SE+SS-WeA5, **171**
Porcellii, T.: VT-WeM3, 148
Porter, A.: AS+BI+EM+NL+NS+SS-ThM11, 176
Porter, L.M.: TC+EM+EN+TF-WeA3, 170
Portoles, J.: AS+BI-MoM1, 3; AS-MoA9, 30
Posadas, A.: EM+NS+TF-FrM7, **249**
Pöschl, U.: BA+AI+AS+BI+IS+NL-MoM10, 5
Posseme, N.: PS-MoM5, **20**
Post, S.: MS+AS+BA+BI+PS+TF-TuM1, 63
Postawa, Z.: TF+AS+BI+EM+SE+SS-WeA7, 172
Potapenko, D.V.:
SP+AS+BI+EM+MI+NS+SE+SS-ThA4, **223**
Poulain, C.: SS+AS+NS-MoM9, 23
Pourtois, G.: EM+PS-TuM5, 57
Povey, I.M.: EM+TF-MoM10, 9
Powell, C.J.: AS-TuM3, **54**
Pozzi, E.: SS+AS+NS+SP-WeA2, 166
Pradhan, A.K.: NS+BI+EM-WeA10, **162**; TF-TuM2, 71
Prasad, D.K.: EW-WeL3, **149**
Prater, C.: NS+AS+BI+SP-WeM4, 136;
NS+AS+BI+SP-WeM5, 136
Preciado, E.: TF-ThP20, 244
Pregent, J.: PS-TuP28, **113**
Preiner, J.: SP+AS+BI+EM+MI+NS+SE+SS-ThA1, 222
Preuss, M.: AC+AS+EN-TuA11, 78
Price, R.: AS-ThP9, **232**
Prieto, A.: MS+AS+EM+EN+NS+TF-MoM8, **16**
Principe, E.: SA+AS+MI+SS-WeM3, 139
Prochazka, P.: GR+AS+NS+SP+SS-TuA9, 85
Profili, J.: PS+AS+NS+SS-ThM10, **189**
Prokes, S.M.: PS-ThA7, 219
Proksch, R.: EW-WeL5, 149;
SP+AS+BI+MI+NS+SS-ThM10, 195
Proksova, S.: SE+NS+TF-ThA6, 221
Prosa, T.J.: AP+AS+EM+MI+TF-WeM1, 123
Prost, W.: SP+AS+EM+GR+MI+NS+SS-FrM8, 258
Prosvirin, I.P.: TF-ThP9, 242
Provo, J.L.: VT+EN+TF-TuA10, **99**
Prusa, S.: GR+AS+NS+SP+SS-TuA9, 85
Prusnick, T.: BI+AI+AS+BA+IA+NL+NS+SP-WeA12, 154
Pujari, S.P.: TR+SE-TuM3, **73**
Punya, A.: EM2-ThA6, 205
Pushkarev, V.: SS-ThM4, 197
Putnik, M.: EN+SE+SS+TF-WeM6, 131
Pyzyna, A.: PS-MoA6, 45
— **Q** —
Qadri, S.B.: EM+NS+SS+TF-FrM6, 247
Qafoku, O.: AP+AS+MI+NS+SS-WeA12, 151
Qalandar, K.R.: MN-TuP4, **105**
Qi, M.: EM+TF-MoM8, 9
Qian, L.: EM-TuA7, 83
Qin, W.: NS+EM+EN-TuM3, 64
Qin, X.: EM+TF-MoM5, **8**; TF+EM+NS+SS-FrM7, 261
Qiu, H.: EM-ThA6, 207
Quan, J.: SS2-ThA2, **226**
Quardokus, R.C.: TF+AS+BI+EM+SE+SS-WeA10, 172
Quayle, P.: EM2-ThA11, 206
Quiñones-Galván, J.G.: NS-TuP3, 106; NS-TuP4, 107; TF-ThP1, 241; TF-ThP13, 243
— **R** —
Rabe, K.M.: MG+MI+NS-ThM5, **187**
Rack, P.D.: HI-ThM11, 186
Rademann, K.: TR+AS+NS+SS-MoA11, 52
Radovanov, S.B.: PS1-TuA11, 92; PS-TuP14, 110
Radunskaya, A.: BI+AS+BA+NL-TuM4, 56
Rafaelsen, J.: SS+AS+NS-MoM6, 22
Rafati, A.: AS+BI+EM+NL+NS+SS-ThM6, 175
Ragazzon, D.: SS-MoA9, 48
Raghavan, N.: EM+PS-TuM5, 57
Ragnarsson, L.-A.: EM+PS-TuM10, 58
Rago, P.B.: EM+AS+NS+SS-WeA3, **156**
Rahman, T.S.: MG+MI+NS-ThM10, **188**; SS+NS-WeM5, 142
Rai, V.R.: TF-ThP16, 243
Raja, L.: PS-ThM9, 191
Rajan, K.: AP+AS+MI+NS+SS-WeA4, 150
Rajput, S.: GR+AS+EM+NS+SS-WeA2, **159**
Rakowska, P.D.: BI+AS+BA+NS+SS-ThA3, **203**
Raley, A.: MS+AS+EL+EM+PS+TF-TuA4, 89;
PS2-TuM12, **69**; PS-MoM11, 21
Raman, P.: SE+PS-ThM3, **192**; SE-ThP2, 239
Raman, S.: BI+AS+BA+NS+SS-ThA9, 204
Raman, S.N.: AS-ThP13, 232
Ramana, C.V.: EN+SE+SS+TF-WeM3, 131; SE-ThP7, 239; TF+AS+EM+NS+SS-ThM10, 199;
TF-ThP10, 242; TF-ThP8, 242; TF-ThP9, **242**
Ramanath, G.: EM+NS+TF-FrM3, **248**;
NS+EM+EN-TuM11, 65; SE+EN-FrM3, 256
Ramon, C.E.: AS+BI-TuA1, 80
Ramprasad, R.P.: EM+NS+TF-FrM3, 248
Rangan, S.: EN+AS+NS+SS-MoA10, **35**; EN-TuP7, 103; IS+EN+SP+SS-ThA9, 215
Ranjan, A.: MS+AS+EL+EM+PS+TF-TuA9, 89;
PS1-TuM5, 66; PS2-TuM12, 69; PS-MoA1, 45; PS-MoM11, 21
Rao, M.: MN-TuP6, 105
Rao, M.V.: GR+EM+MS+NS+SP-FrM4, 250
Rao, Y.: BA+AI+AS+BI+IS+NL-MoM1, 5
Rappe, A.M.: SS+AS-TuM5, 69
Raschke, M.B.: SP+AS+BI+EM+MI+NS+SE+SS-ThA10, **223**; SP+AS+BI+NS-ThP2, 241
Rastogi, V.: MS+AS+EL+EM+PS+TF-TuA4, 89
Ratcliff, C.: EM+AS+NS+SS-WeA7, 157
Rauf, S.: PS-ThM5, **191**
Rawal, T.B.: SS+NS-WeM5, 142
Raymond, M.: EL+AS+EM+SS+TF-WeA11, 156
Razavi Hesabi, Z.: GR+EM+MS+NS+SP-FrM3, **250**; NS+AS+EN+SS-TuA11, **90**
Real, M.: EL+AS+EM+SS+TF-WeA2, 155
Rebholz, C.: SE-ThP8, 240; TF-ThA3, **230**
Record, B.A.: GR-ThP4, 236
Reddemann, L.: TF+AS+BI+EM+SE+SS-WeA11, 172
Reed, A.N.: SE+PS-ThM5, 192
Reed, J.: NS+AS+EN+SS-TuA12, 90
Reed, S.M.: BI+NL+NS+SS-ThM2, **177**
Rees, J.A.: VT-TuP8, 122
Rees, N.V.: SS+EN-ThM12, 196
Reeves, R.V.: TF-ThA2, 229
Regan, W.: GR+AS+EM+NS+SS-WeA11, 160
Regier, T.Z.: IA+BA-TuA12, **86**
Reid, T.: BI-WeM9, 127
Reihs, K.: TF+AS+BI+EM+SE+SS-WeA11, 172
Reilly, M.: TF+PS-ThM10, 200; TF-ThP18, 244
Reinecke, T.: GR+AS+BI+PS+SS-ThA6, 210
Reinhard, D.: AP+AS+EM+MI+TF-WeM10, 124
Reinicker, A.: SS-ThM11, **198**
Reininger, R.: SA+AS+MI+SS-WeM5, 139
Reinke, P.: GR-WeM4, 133; NS+AS+EN+SS-TuA10, **90**
Reiss, G.: HI-ThP3, 238
Relaño, M.R.: SS1-ThA3, 224
Ren, Y.: SS-TuA7, 96
Renaud, G.: AS+BI+EM+NL+NS+SS-ThA4, 202
Renault, O.J.: SA+AS+MG+SS-TuA3, **94**
Renaux, F.: SE+NS+TF-ThA9, 221
Reniers, F.A.B.: PS+AS+BI+SE-MoM5, 18;
PS+AS+NS+SS-ThM9, 189; PS-TuP29, 113;
SE+PS-ThM9, 193; SE+PS-WeA1, **164**;
SE+PS-WeA7, 164
Reshchikov, M.A.: EM+NS+SS+TF-FrM3, 247
Resta, A.: GR+EM+NS+SS+TF-ThA2, 211
Restrepo, J.S.: PS-TuP34, **114**
Reuter, M.S.+AS+BA+BI+PS+TF-TuM3, 63
Reutt-Robey, J.: SS1-ThA6, **225**
Reviakine, I.: BI+AS+IS+NL-MoM11, **7**
Reynaud, S.: NS+BI+EM-WeA9, 162
Reynolds, M.M.: BI-WeM12, 127
Reynolds, N.P.: BI+AS+BA+NS+SS-ThA2, **203**
Rezek, J.: TF+AS+EM+NS+SS-ThM9, 199
Rhallabi, A.: PS2-TuA3, 93
Rhu, H.: TF-TuM5, 71
Rice, A.: MI-MoM11, 14
Richter, C.A.: GR+EM+MS+NS+SP-FrM7, 251;
TF+AS+BI+EM+SE+SS-WeA5, 171
Ricker, J.E.: VT-MoM3, 27; VT-MoM4, 27
Riedel, S.: PS2-TuM1, 67
Riedo, E.: GR+AS+BI+PS+SS-ThA10, **210**
Rieth, L.W.: TF+VT-WeM5, 146
Rigutti, L.: AP+AS+SS-TuA10, 79; AP+AS+SS-TuA12, **79**
Rinaldi, M.: MN-TuP4, 105
Rincon Delgadillo, P.A.:
MS+AS+EM+NS+PS+TF-MoA6, 41
Ringeisen, B.R.: BI-WeM3, 126
Ringel, S.A.: EM+AS+NS+SS-WeA7, **157**
Ringer, S.P.: AP+AS+SS-TuA3, **78**
Riso, J.: VT+AS+SS+TF-WeA10, 174
Risse, T.: GR+AS+NS+SS-ThM4, **184**
Ritchey, D.: MS+AS+BA+BI+PS+TF-TuM1, 63
Ritter, C.: TR+AS+NS+SS-MoA11, 52

- Rivera, L.: SS-TuP4, 115
 Robbie, K.: TF+AS+NS+SE-WeA4, 173
 Roberts, A.J.: AS-MoA6, 29; AS-WeA3, 151; GR-ThP6, 237
 Robertson, J.: EM+MI+NS+SS+TF-TuA1, 81
 Robinson, D.E.: BI-WeM6, 126
 Robinson, E.: EM+NS+TF-FrM6, 249
 Robinson, J.A.: GR+EM+MS+NS+SP-FrM1, 250
 Robinson, J.T.: BI+NL+NS+SS-ThM12, 178; EM+AS+EN+TF-ThM5, 180; GR+AS+BI+PS+SS-ThA6, 210; MI+EM-TuM5, 61
 Robinson, M.: BI+AI+AS+BA+IA+NL+NS+SP-WeA7, 153
 Robinson, Z.: GR+EM+MS+NS+SP-FrM4, 250; GR+EM+NS+PS+SS+TF-MoM3, 11; GR-WeM1, 132
 Rockett, A.: EM-TuA1, 83; EN+PS+TF-MoM8, 10; TF+EM+NS+SS-FrM8, 261
 Rodgers, J.R.: MG-ThA6, 216
 Rodrigo, L.: SS+AS+NS+SP-WeA7, 166
 Rodríguez Fernández, J.: SS1-ThA3, 224
 Rodríguez, C.A.: EL-ThP3, 234
 Rodríguez, E.: TR-TuP6, 121
 Rodríguez, J.: IS+AS+SS-ThM6, 186
 Rodríguez, L.N.J.: TF+AS+SE+SS-MoA9, 50
 Rodríguez-Reyes, J.C.: NS+AS+EN+SS-TuA4, 90
 Rogero, C.: SS1-ThA8, 225
 Rojas Delgado, R.: GR+EM+NS+SP+TF-MoA2, 36
 Roldan Cuenya, B.: AS+BI+EM+NL+NS+SS-ThA3, 202; MG+AS+EM+NS+SA+SE+SP+SS+TF-FrM2, 253; SS-TuP29, 118
 Roldan, A.: MG-ThA3, 216
 Romero, M.: SS-TuP4, 115
 Rondinelli, J.M.: MG+MI+NS-ThM9, 187; MI+EM+MG-MoA10, 39
 Roozeboom, F.: EM+MI+NS+SS+TF-TuA9, 82
 Roqueta, F.: PS2-TuA3, 93
 Ros Bengoechea, O.: PS2-TuM3, 68
 Ros, O.: PS2-TuM6, 68
 Rosa, L.G.: SS-TuP34, 119
 Rosa, P.: SS-TuP34, 119
 Rose, V.: SP+AS+BI+MI+NS+SS-ThM6, 194
 Rosenhahn, A.: BI+AI+BA+IS-MoA2, 31; BI+AS+IS+NL-MoM3, 6; BI-TuP7, 101; IS+AS+SP-FrM3, 251
 Rosenthal, J.: EN+AS+PS-TuA3, 84
 Roshan, R.: GR-ThP4, 236
 Ross, P.: IS+AS+SS-ThM9, 187
 Rossi, A.: AS-TuM1, 53; AS-TuM12, 55
 Rossi, F.: AS+BI+EM+NL+NS+SS-ThM10, 176
 Rossi, G.: AS-TuM12, 55
 Rossnagel, S.M.: MS+AS+BA+BI+PS+TF-TuM3, 63
 Rossner, W.: MG+EN+MS-WeA3, 160
 Rotenberg, E.: MI+AS+NS+SP-TuA7, 87
 Roth, J.: BI-TuP10, 102
 Rothwell, S.: GR+EM+NS+PS+SS+TF-MoM1, 11
 Rott, K.: HI-ThP3, 238
 Rousseau, R.: SS-MoA6, 47
 Roussey, M.: NS+BI+EM-MoM6, 17
 Rout, M.P.: BI+AS+BA+NL-TuM10, 56
 Rowe, J.E.: GR+AS+EM+NS+SS-WeA10, 160
 Rowley, J.: TF+VT-WeM11, 147
 Roy, T.: GR+EM+MS+NS+SP-FrM3, 250
 Rozanov, K.N.: TF+MI-WeM4, 145
 Rubin, D.: HI-ThA9, 213
 Rubinovich, L.: SS+NS-WeM6, 142
 Rubio, A.: SS1-ThA8, 225
 Rubio, E.J.: EN+SE+SS+TF-WeM3, 131; TF-ThP8, 242
 Rubio-Zuazo, J.: EM+NS+TF-FrM9, 249; SA+AS+MG+SS-TuA4, 95
 Rubloff, G.W.: TF+EN-MoM3, 23
 Rudolf, P.: GR-WeM4, 133
 Rudolph, M.: PS2-TuM1, 67
 Rueff, J.P.: SA+AS+MG+SS-TuA9, 95
 Rumbach, P.: PS+AS+BI+SE-MoM1, 18; PS+AS+BI+SE-MoM6, 18
 Rumyantsev, S.: GR+EM+NS+SP+TF-MoA7, 36
 Ruoff, R.S.: GR+EM+NS+PS+SS+TF-MoM10, 12; GR-WeM3, 133
 Ruppalt, L.: PS-ThA7, 219
 Russell, Jr., J.N.: BI+AI+BA+IS-MoA3, 31
 Rutgers, M.: SP+AS+BI+MI+NS+SS-ThM10, 195
 Rutt, H.N.: HI-ThA8, 213
 Ruzic, D.N.: PS+TF-MoA6, 44; PS-TuP12, 110; SE+PS-ThM3, 192; SE+PS-WeA9, 165; SE-ThP2, 239; TF+PS-ThM10, 200; TF-ThP18, 244
 Ryan, J.V.: AP+AS+EM+MI+TF-WeM9, 123
 Ryan, K.E.: TR+AS+NS+SS-MoA3, 51; TR+AS-MoM10, 26; TR+AS-MoM5, 25
 Rysz, J.: SS+AS+NS+SP-WeA10, 167; TF+AS+BI+EM+SE+SS-WeA7, 172
 Ryzhikov, I.A.: TF+MI-WeM4, 145; TF-ThP11, 243
 — S —
 Sadeghi, N.: PS1-TuA7, 91
 Sadowski, J.T.: GR+AS+EM+NS+SS-WeA10, 160
 Saito, N.: PS+AS+NS+SS-ThM6, 189
 Saito, Y.: SS-TuP10, 116; TF-ThP21, 244
 Sakai, I.: PS2-TuA11, 94; PS-MoM4, 20
 Sakamoto, K.: MI-MoM1, 13
 Sakamoto, N.: TF-ThP21, 244
 Sakamoto, R.: TF-ThP28, 245
 Sakuishi, T.: PS-TuP31, 113
 Sakurai, M.: GR+AS+EM+NS+SS-WeA8, 159; SS2-ThA2, 226; SS-TuP10, 116
 Sakurai, N.: PS2-TuA11, 94
 Salmeron, M.B.: GR+AS+EM+NS+SS-WeA7, 159
 Salter, T.L.: AS+BI+IS-WeM5, 125
 Samaraweera, R.L.: EM+NS+SS+TF-FrM9, 248
 Samet, D.: TF+VT-WeM3, 146
 Samukawa, S.: GR+AS+BI+PS+SS-ThA4, 209; PS-ThA10, 219; PS-ThA8, 219; PS-ThA9, 219; PS-ThM12, 192
 Sanborn, J.: BI+NL+NS+SS-ThM3, 177
 Sanchez Casalongue, H.: IS+AS+SS-ThM3, 186
 Sanchez, L.: TF-ThP9, 242
 Sandell, A.: SS-MoA9, 48
 Sandi, G.: GR+AS+BI+PS+SS-ThA3, 209
 Sandin, A.A.: GR+AS+EM+NS+SS-WeA10, 160
 Sangiovanni, D.G.: TF+EM+NS+SS-FrM8, 261; TF+PS-ThM11, 201
 Sankaran, K.: EM+PS-TuM5, 57
 Sankaran, R.M.: PS+AS+BI+SE-MoM6, 18; PS+AS+NS+SS-ThM12, 190; PS+AS+NS+SS-ThM5, 189; PS-TuP18, 111; TF+EM+NS+SS-FrM3, 260
 Sano, N.: AS+BI-MoM1, 3; AS-MoA9, 30
 Santana-Rodríguez, G.: TF-ThP13, 243
 Sapper, E.: MG+EN+MS-WeA9, 161
 Saraf, I.: PS2-TuA8, 94
 Saraswat, K.C.: EM-MoA6, 33
 Sardashti, K.: EM+PS-TuM1, 57
 Sartory, B.: SE+NS+TF-ThA7, 221
 Sasaki, M.: TR-TuP2, 120
 Sathiyarayanan, R.: SS+AS+NS-MoM3, 22
 Sato, M.: PS-ThM12, 192
 Sato, R.: SS1-ThA10, 225
 Sato, S.: GR+AS+BI+PS+SS-ThA8, 210; HI-ThM9, 185
 Sauer, V.T.K.: MN+NS-MoA3, 40; MN+NS-MoA4, 40
 Saykally, R.J.: IA+BA-TuA1, 86
 Sazinsky, M.: BI+AS+BA+NL-TuM4, 56
 Scace, G.: VT-MoM3, 27
 Scammon, K.: SA+AS+MI+SS-WeM3, 139
 Scanlon, D.O.: EM2-ThA1, 205; EM2-ThA10, 206
 Scarel, G.S.: TF+EN-MoM9, 24
 Schaaf, P.: SE+NS+TF-ThA10, 221
 Schabel, W.: AS-ThP12, 232
 Schadler, L.: NS+EM+EN-TuM11, 65
 Schaefer, A.: SS+AS-TuM11, 70; SS-MoA9, 48
 Schaff, W.: VT+AS+SS+TF-WeA7, 174
 Schalken, J.R.G.: SE+PS-WeA8, 165
 Schall, J.D.: TR+AS+NS+SS-MoA3, 51; TR+AS-MoM10, 26
 Schamberger, F.S.: TF+EM+NS+SS-FrM9, 262
 Scharfer, P.: AS-ThP12, 232
 Schauermann, S.: SS+NS-WeM2, 142
 Scheidemann, A.: AS+BI-MoM6, 4
 Schenk, M.: HI-ThP2, 238
 Schildt, S.: NS+AS+EM-MoA4, 42
 Schiller, F.M.: AS-TuM11, 55
 Schilling, M.: SE+PS-ThM3, 192
 Schirmeisen, A.: TR+SE-TuM12, 74
 Schirwitz, C.: BI+NL+NS+SS-ThM11, 178
 Schlotter, W.F.: SS2-ThA4, 226
 Schmdit, A.B.: MI-MoM1, 13
 Schmeisser, D.: EM+PS-TuM10, 58
 Schmid, M.: NS+AS+EN+SS-TuA3, 90
 Schmidt, A.B.: MI-MoM8, 14
 Schmidt, D.: EL+AS+EM+SS+TF-WeA12, 156
 Schmidt, S.: TR+SE-TuM4, 73
 Schmidt-Mende, L.: EN+SE+SS+TF-WeM6, 131
 Schmitz, S.: PS2-TuM9, 68
 Schnadt, J.: EM+TF-MoM6, 8
 Schneider, C.M.: MI+AS+NS+SP-TuA7, 87
 Schneider, J.: TR+SE-TuM5, 73
 Schneider, J.M.: SE+NS+TF-ThA4, 220; SE+NS+TF-ThA8, 221
 Schoenfeld, W.V.: TF+EM+NS+SS-FrM10, 262
 Schofield, N.: VT-WeM1, 147
 Scholz, S.G.: NS+BI+EM-WeA9, 162
 Schram, T.: EM+PS-TuM10, 58
 Schreiber, D.: MN+AS+SS-MoM3, 14
 Schreiber, D.K.: AP+AS+EM+MI+TF-WeM9, 123; AP+AS+SS-TuA9, 79; AP-TuP1, 100
 Schreiber, F.: EM+AS+EN+TF-ThM3, 180; SS1-ThA2, 224
 Schroeder, J.: SE+PS-ThM12, 193
 Schroeder, M.: TF+EN-MoM3, 23
 Schroeder, T.: SS+AS-TuM11, 70
 Schroers, J.: NS+BI+EM-WeA7, 162; TR+AS+NS+SS-MoA11, 52
 Schubert, E.: EL+AS+EM+SS+TF-WeA12, 156
 Schubert, M.: EL+AS+EM+SS+TF-WeA1, 155; EL+AS+EM+SS+TF-WeA12, 156; EL+AS+EM+SS+TF-WeA2, 155
 Schultz, B.D.: EM+AS+NS+SS-WeA11, 157; MI-MoM11, 14
 Schultz, B.J.: AS+BI+EM+NL+NS+SS-ThA1, 202
 Schumann, F.O.: MI+AS+NS+SP-TuA1, 87
 Schwab, Y.: TF+EN-MoM9, 24
 Schwartz, D.E.: TC+EM+TF-WeM9, 144
 Schwartz, J.J.: SP+AS+BI+EM+MI+NS+SE+SS-ThA12, 223
 Schwarz, U.D.: SS+AS+NS+SP-WeA7, 166; TR+AS+NS+SS-MoA11, 52; TR+SE-TuM12, 74
 Schweidenback, L.: EM2-ThA10, 206
 Schweikert, E.A.: AS+BI+EM+NL+NS+SS-ThM3, 175
 Schwendemann, T.C.: SS+AS+NS+SP-WeA7, 166
 Scobol, P.: SA+AS+MI+SS-WeM3, 139
 Scullin, P.: PS1-TuA3, 91
 Seabaugh, A.: EM+TF-MoM8, 9
 Seaward, K.: MS+AS+BA+BI+PS+TF-TuM1, 63
 Seebauer, E.G.: SS+EM-WeA12, 169
 Seeger, S.: NS-TuP10, 108; SE+NS+TF-ThA12, 222
 Seet, H.L.: AS-ThP16, 233
 Segovia, J.: MN-TuP4, 105
 Seidler, G.: AC+AS+EN-TuA10, 78
 Seifert, H.J.: TR+SE-TuM5, 73
 Seki, T.: AS-MoA10, 30
 Sekine, M.: PS1-TuA10, 92; PS2-TuA11, 94; PS-ThA6, 218; PS-TuP11, 110; PS-WeM2, 137
 Sekitani, T.: NS+EM+EN-TuM9, 64
 Sekiya, K.: NS-TuP9, 108
 Sekol, R.C.: NS+BI+EM-WeA7, 162
 Selino Jr., A.: PS2-TuA8, 94
 Selino, A.: PS-MoA1, 45

- Sellberg, J.A.: SS2-ThA4, 226
 Sellers, J.R.V.: SS-TuA8, 96
 Semenikhin, N.: NS+AS+EN+SS-TuA11, 90
 Semetey, V.: BI+AS+BA+NS+SS-ThA10, 204
 Semidey-Flecha, L.: SS+AS+NS-MoM10, 23
 Seminario, J.: GR+AS+BI+PS+SS-ThA3, 209
 Sen, Y.: PS-ThA12, 220
 Senanayake, S.: IS+AS+SS-ThM6, 186
 Senevirathna, M.K.I.: EM+NS+SS+TF-FrM10, 248; EM+NS+SS+TF-FrM9, 248
 Sengupta, A.: EM+AS+PS+TF-ThM5, 182
 Senkbeil, T.M.: IS+AS+SP-FrM3, 251
 Sentman, C.: EN+PS+TF-MoM6, 10
 Seo, H.: EN+AS+NS+SS-MoA3, 34; EN-TuP2, 103; PS+TF-MoA11, 45
 Seo, J.H.: PS-TuP22, 112
 Seo, S.: MS+AS+EL+EM+PS+TF-TuA9, 89
 Seo, Y.: EN-TuP3, 103; EN-TuP4, 103
 Seog, J.: PS+AS+BI+SE-MoM11, 19
 Seong, D.J.: NS-TuP2, 106
 Sepehri-Amin, H.: AP+AS+EM+MI+TF-WeM4, 123
 Sequeira, D.: NL+AS+BI-ThA6, 217
 Serry, M.: MN+AS+SS-MoM11, 15
 Seshachalam, V.: EM+AS+PS+TF-ThM6, 182
 Seshadri, I.: NS+EM+EN-TuM11, 65; SE+EN-FrM3, 256
 Setsuhara, Y.: PS-WeM2, 137
 Seymour, D.L.: VT-TuP8, 122
 Sezen, H.: SS-FrM9, 260
 Sgura, I.: IS+AS+SS-ThM5, 186
 Shabani, J.: MI-MoM11, 14
 Shacham-Diamand, Y.: MN+AS+SS-MoM6, 15
 Shaffer, S.: EW-TuM7, 59
 Shah, K.: EM-ThA3, 207
 Shahar, R.: BI+AI+AS+BA+IA+NL+NS+SP-WeA9, 154
 Shahedipour-Sandvik, F.: EM+NS+SS+TF-FrM11, 248
 Shamberger, P.J.: SE+PS-ThM5, 192
 Shan, J.: MN+NS-TuM6, 63
 Shao, D.: SS+AS+NS-MoM11, 23
 Shao, M.: TC+EM+TF-WeM12, 144
 Sharaf, A.: MN+AS+SS-MoM11, 15
 Shard, A.G.: AS+BI+EM+NL+NS+SS-ThM5, 175
 Sharma, A.: TF+VT-WeM3, 146
 Sharma, K.: EN+AS+NS+SS-MoA9, 35
 Sharma, R.: IS+AS+SP-FrM10, 253; IS+AS+SP-FrM8, 252
 Shashikala, H.B.M.: GR+EM+NS+SP+TF-MoA6, 36
 Shaw, L.A.: MN-TuP4, 105; MN-TuP5, 105
 Shaw, S.: NL+AS+BI-ThA3, 217
 Shaw, T.: NS+AS+EN+SS-TuA12, 90
 Shayestehaminzadeh, S.: PS+TF-MoA9, 44
 Shears Ashby, V.:
 MG+AS+EM+NS+SA+SE+SP+SS+TF-FrM9, 254
 Sheehan, P.E.: BI+NL+NS+SS-ThM12, 178;
 EM+AS+EN+TF-ThM5, 180;
 GR+AS+BI+PS+SS-ThA6, 210
 Shen, Y.R.: BP+AS-SuA7, 1;
 IA+AI+BI+IS+NL+SS-MoA1, 37
 Shenderova, O.A.: EM-TuA3, 83; TR+AS-MoM6, 26
 Sherpa, S.D.: GR+EM+NS+SP+TF-MoA6, 36
 Sherry, A.: AC+AS+EN-TuA11, 78
 Shetty, R.: NS+AS+BI+SP-WeM5, 136
 Shi, J.: GR+EM+NS+SS+TF-ThA10, 212
 Shi, Z.: EM+AS+EN+TF-ThM6, 181
 Shiao, M.H.: MN-TuP1, 104; NS-TuP15, 109; PS-TuP26, 112; TF-ThP2, 241
 Shiao, M.-H.: MN-TuP2, 105
 Shiao, M.-H.: MN-TuP3, 105
 Shibuya, R.S.: SS-TuP10, 116
 Shimada, k.: NS-TuP8, 107; TF-ThP28, 245
 Shimizu, H.: EM-ThA8, 207
 Shimizu, R.: PS+TF-MoA11, 45
 Shimizu, T.K.: SS+AS+NS+SP-WeA4, 166; SS1-ThA1, 224
 Shimizu, Y.: AP+AS+EM+MI+TF-WeM10, 124
 Shimogaki, Y.: EM-ThA8, 207; TF-TuM3, 71
 Shin, B.G.: GR+EM+NS+SS+TF-ThA12, 212
 Shin, H.: PS1-TuM4, 66
 Shin, H.-C.: GR+EM+NS+SS+TF-ThA12, 212
 Shin, H.-J.: SS-MoA1, 47
 Shin, N.: NS+AS+EM-MoA8, 43; SS+AS+NS-MoM2, 22
 Shin, Y.H.: NS-TuP2, 106
 Shinde, D.: AP+AS+SS-TuA10, 79; AP+AS+SS-TuA12, 79
 Shinohara, T.: GR+EM+NS+PS+SS+TF-MoM4, 11
 Shirakura, A.: SE-ThP1, 239; SE-ThP10, 240
 Shiratani, M.: EN+AS+NS+SS-MoA3, 34; EN-TuP2, 103; PS+TF-MoA11, 45
 Shirato, N.: SP+AS+BI+MI+NS+SS-ThM6, 194
 Shklovsky, J.: MN+AS+SS-MoM6, 15
 Shoheit, J.L.: EM+AS+PS+TF-ThM1, 181;
 EM+AS+PS+TF-ThM12, 183; EM-ThP3, 234;
 PS1-TuM6, 66; PS-TuP13, 110; PS-TuP17, 111; PS-TuP23, 112
 Sholl, D.: SS+AS+NS-MoM10, 23
 Shong, B.: SS+EM-WeA1, 167
 Shuh, D.: AC+AS+EN-TuA10, 78
 Shukla, N.: AS+BI+EM+NL+NS+SS-ThM9, 176
 Shumaker-Parry, J.: TF+AS+BI+EM+SE+SS-WeA1, 171
 Shur, M.: GR+EM+NS+SP+TF-MoA7, 36
 Shutthanandan, V.: AP+AS+MI+NS+SS-WeA1, 150; HI-ThA9, 213; MI+EM+MG-MoA2, 38
 Shyam, R.: SS-TuP28, 118
 Shytov, A.V.: GR+AS+EM+NS+SS-WeA11, 160
 Sigle, W.: NS+EM+EN-TuM4, 64
 Sigrist, M.: SA+AS+MI+SS-WeM5, 139
 Sijbrandij, S.: HI-ThA11, 214
 Sikano, T.: GR+AS+EM+NS+SS-WeA8, 159
 Sikorski, E.M.: PS-MoA8, 46; PS-MoM2, 20
 Silvernail, J.: TF+VT-WeM2, 146
 Simoes, F.A.: BI+AS+IS+NL-MoM2, 6
 Simon, Q.: TF+EM+NS+SS-ThA8, 229
 Simpson, S.: SP+AS+BI+EM+MI+NS+SE+SS-ThA8, 223; TF+AS+BI+EM+SE+SS-WeA9, 172
 Sina, M.: IS+EN+SP+SS-ThA9, 215
 Singer, K.D.: TC+EM+EN+TF-WeA10, 170
 Singh, B.: EW-WeL6, 149
 Singh, D.J.: EM+NS+TF-FrM3, 248
 Singh, K.: EM+AS+PS+TF-ThM9, 182
 Singh, N.: EW-WeL2, 149
 Sinha, D.: TF+EM+NS+SS-ThA12, 229
 Sinha, H.: PS-TuP13, 110
 Sinitskii, A.: GR+AS+NS+SS-ThM9, 184
 Sinno, T.R.: SS-TuP15, 117
 Sinnott, S.B.: MG+MI+NS-ThM3, 187
 Sioncke, S.: SA+AS+MG+SS-TuA9, 95
 Sirse, N.: PS1-TuA2, 91
 Sirtica, M.: AS-MoA4, 29
 Sisco, E.: AS+BI+IS-WeM6, 125
 Sivaram, S.: SS+AS+NS-MoM2, 22
 Siviero, F.: VT-WeM3, 148
 Skomski, D.: SS1-ThA4, 224
 Slade, A.: SP+AS+BI+MI+NS+SS-ThM9, 194
 Slysz, W.: AP-TuP2, 100
 Smekal, W.: AS-TuM3, 54
 Smentkowski, V.: AP+AS+SS-TuA1, 78; AS-ThP5, 231
 Smets, M.: TF-TuA10, 97
 Smirnov, D.: GR+EM+NS+SP+TF-MoA1, 36
 Smit, S.: EN+AS+NS+SS-MoA9, 35
 Smith: MS+AS+BA+BI+PS+TF-TuM3, 63
 Smith, D.A.: HI-ThM11, 186
 Smith, G.D.W.: AP+AS+MI+NS+SS-WeA7, 150
 Smith, J.G.W.: BI-WeM1, 126
 Smith, J.L.: AC+MI+SA+TF-MoM3, 2
 Smith, N.: AS-MoA1, 29
 Smith, R.: EM+NS+TF-FrM10, 250
 Smith, S.W.: TF+EM+NS+SS-ThA1, 228
 Smolenski, K.: VT+AS+SS+TF-WeA7, 174
 Snead, L.L.: AC+AS+EN-TuA1, 77
 Snider, G.L.: EM-ThA10, 208
 Snyders, R.: NS+AS+EM-MoA4, 42; SE+NS+TF-ThA9, 221
 Soares, E.A.: AS+BI+EM+NL+NS+SS-ThA4, 202
 Sobolewski, M.A.: PS-ThM4, 191
 Soffa, W.A.: MI+EM+MG-MoA11, 39
 Sokaras, D.: AC+AS+EN-TuA10, 78
 Soloway, P.: BI+AS+BA+NS+SS-ThA12, 205
 Solzbacher, F.: TF+VT-WeM5, 146
 Someya, T.: NS+EM+EN-TuM9, 64
 Somorjai, G.A.: BA+AI+AS+BI+IS+NL-MoM8, 5
 Somssich, P.F.: VT+EN+TF-TuA11, 99
 Son, W.H.: SS-TuP14, 117; TF-ThP6, 242
 Song, A.: SS+EN-ThM2, 195; SS-MoA7, 48
 Song, H.: TC+EM+EN+TF-WeA12, 171
 Song, S.-H.: PS-ThM3, 191
 Song, Y.: GR+AS+EM+NS+SS-WeA9, 160
 Sood, S.: MS+AS+EL+EM+PS+TF-TuA10, 89
 Sorci, M.: BI+AS+BA+NL-TuM10, 56
 Sosa, J.: EM-ThP9, 235
 Sosolik, C.E.: SS-TuP28, 118
 Soukup, R.J.: TF-ThP25, 245
 Sousa, C.: NL+AS+BI-ThA6, 217
 Spampinato, V.: AS+BI+EM+NL+NS+SS-ThM10, 176
 Spangler, L.: EN+AS+NS+SS-MoA4, 35
 Spanier, J.E.: NS+AS+EM-MoA11, 43
 Speck, J.S.: AP+AS+SS-TuA11, 79
 Springer, H.K.: SA-TuP1, 114
 Sprunger, P.T.: SS+NS-WeM12, 143; SS+NS-WeM9, 142
 Sridhar, M.R.: GR-ThP4, 236
 Sridhar, S.: PS1-TuM3, 65; PS1-TuM4, 66
 Srinadhu, E.: SS-TuP28, 118
 Srinivasan, K.: TF+MI-WeM1, 144
 Sriraman, K.: SS+AS+NS+SP-WeA12, 167
 Sriraman, S.: PS-WeA11, 163
 Srivathanakul, S.: EM+AS+PS+TF-ThM6, 182
 Stacchiola, D.: IS+AS+SS-ThM6, 186
 Stach, E.: IS+AS+SP-FrM1, 251; IS+EN+SP+SS-ThA3, 214
 Stadler, V.: BI+NL+NS+SS-ThM11, 178
 Staemmler, V.: SS+AS-TuM12, 71
 Stafford, L.: PS+AS+NS+SS-ThM10, 189; PS-TuP28, 113; SE+PS-ThM11, 193
 Stafford, N.: PS-MoM3, 20
 Stampe, P.A.: EM2-ThA10, 206
 Stamps, B.W.: BI+AI+BA+IS-MoA3, 31
 Staples, G.: MS+AS+BA+BI+PS+TF-TuM1, 63
 Starke, U.: SA+AS+MI+SS-WeM1, 139
 Starostin, S.A.: TF+VT-WeM1, 146
 Stayton, P.: BI+AS+BA+NS+SS-ThA6, 204
 Stecher, J.: NS+BI+EM-MoM9, 17
 Stegmann, B.: TR+AS+NS+SS-MoA11, 52
 Steidl, M.: SP+AS+EM+GR+MI+NS+SS-FrM8, 258
 Steiner, M.A.: MI+EM+MG-MoA11, 39
 Steingart, D.A.: TC+EM+TF-WeM9, 144
 Stemmer, S.: EM1-WeM11, 130
 Stenberg, P.: NS+BI+EM-MoM6, 17
 Stern, L.A.: TF+AS+NS+SE-WeA10, 173
 Sterrer, M.: SS+AS-TuM12, 71
 Stevanovic, V.: MG+EM+MI+MS-WeM5, 134;
 MG+EM+MI+MS-WeM6, 134
 Stevens, A.A.E.: SE+PS-WeA8, 165
 Stevens, K.M.: MI-TuP4, 104; TR+AS+NS+SS-MoA4, 51
 Stevenson, B.S.: BI+AI+BA+IS-MoA3, 31
 Stevenson, K.J.: SS+AS-TuM1, 69
 Stickle, W.F.: AS-TuM10, 55
 Stillahn, J.: EM-ThA2, 206; PS-MoA1, 45
 Stine, R.: BI+NL+NS+SS-ThM12, 178; BI-WeM3, 126; GR+AS+BI+PS+SS-ThA6, 210
 Stock, M.: PS-MoA7, 46
 Stock, T.: NS+BI+EM-WeA2, 161

- Stoddart, P.R.: BI+AI+BA+IS-MoA1, 31;
BI+AI+BA+IS-MoA11, 32
- Stokes, E.B.: EM+NS+SS+TF-FrM5, 247
- Stolovsky: MS+AS+BA+BI+PS+TF-TuM3, 63
- Stolte, W.: IS+AS+SS-ThM9, 187
- Stolwijk, S.D.: MI-MoM1, 13
- Stone, J.A.: VT-MoM3, 27
- Stones, I.: VT-WeM1, 147
- Stötzler, J.: SA+AS+MI+SS-WeM11, 140
- Stout, P.: EM-ThA9, **208**
- Stoyanov, P.: TR+SE-TuM5, **73**
- Straccia, A.M.: SE+PS-WeA3, 164
- Stradi, D.: GR+AS+EM+MI+MN-TuM1, 59
- Stradins, P.: PS+AS+NS+SS-ThM3, 188
- strasser, P.: SS-TuP29, 118
- Strelcov, E.: NS-TuP11, 108
- Strohmeier, B.: AS+BI-TuA4, **80**; EW-TuL4, 76
- Stroschio, J.A.: IS-ThP1, 238;
SP+AS+EM+GR+MI+NS+SS-FrM3, 257
- Strouse, G.F.: VT-MoM3, 27
- Strzhemchny, Y.M.: SS-FrM10, **260**
- Stubbers, R.: TF+PS-ThM10, 200; TF-ThP18, 244
- Stüber, M.: TR+SE-TuM5, 73
- Stuckert, E.: NS+AS+EM-MoA10, **43**
- Sturm, J.C.: TF+VT-WeM2, 146
- Sturve, J.: BI+AS+BA+NL-TuM5, 56
- Styan, K.E.: BI+AS+BA+NS+SS-ThA2, 203
- Su, C.-Y.: TF-ThP5, 242
- Su, H.: TF+MI-WeM3, 145; TF+MI-WeM5, 145
- Su, J.: PS-TuP26, 112
- Suarez Segovia, C.: EM+PS-TuM2, **57**
- Suemitsu, M.: GR+EM+NS+PS+SS+TF-MoM4, 11
- Sugii, T.: NS-TuP7, 107
- Suh, H.: SP+AS+EM+GR+MI+NS+SS-FrM9, 258
- Sumant, A.V.: GR+AS+BI+PS+SS-ThA3, 209;
TR+SE-TuM11, 74
- Sun, D.: GR-WeM10, 134; TF-ThP19, 244
- Sun, H.: TF+EM+NS+SS-FrM7, **261**
- Sun, Z.: EM+AS+PS+TF-ThM6, **182**
- Sundaram, G.M.: MS+AS+EM+EN+NS+TF-MoM5, **16**
- Sundblom, A.: BI+AS+BA+NL-TuM5, 56
- Sung, Y.M.: PS-TuP23, 112
- Surla, V.: PS-MoM3, 20
- Surman, D.: AS-WeA3, 151
- Surnev, S.: SS+AS-TuM9, 70
- Sushko, P.V.: SS+AS-TuM6, 70
- Sutara, F.: SS+AS+NS-MoM8, 22
- Sutens, B.: TF+AS+SE+SS-MoA9, 50
- Sutherland, D.S.: BI-TuP2, 100
- Sutter, P.W.: GR-WeM5, **133**
- Suu, K.: PS-TuP31, 113
- Suvarna, P.: EM+NS+SS+TF-FrM11, 248
- Suzer, S.: AS-TuM9, **55**
- Suzuki, H.: TR-TuP2, 120
- Suzuki, T.: GR+AS+EM+NS+SS-WeA8, 159; PS-MoA8, 46; PS-MoM2, 20; SE-ThP1, 239; SE-ThP10, 240; SE-ThP5, 239
- Suzuki, Y.: EM-ThA8, **207**
- Svane, A.: AC+MI+SA+TF-MoA8, 29
- Svedendhal, M.: BI+NL+NS+SS-ThM6, 177
- Svedhem, S.: BI+AS+BA+NL-TuM5, **56**;
BI+AS+BA+NL-TuM6, 56
- Svrcek, V.: PS+AS+NS+SS-ThM1, **188**
- Swann, S.: EW-WeL2, **149**
- Swart, H.: AS-ThP19, 233
- Sweet III, W.J.: TF-TuM11, 72
- Sweet, W.J.: TF-ThP15, **243**
- Swinney, T.C.: VT-MoM8, 27
- Sydorenko, D.: PS-TuP20, **111**
- Sykes, E.C.H.: NS+AS+EN+SS-TuA9, **90**; SS-ThM4, 197; SS-TuA12, 96
- Symonds, J.M.: AS+BI+IS-WeM4, **124**
- Synowicki, R.A.: EL+AS+EN+PS+SS+TF-ThM11, **179**
- Szkal, C.: AS+BI+EM+NL+NS+SS-ThM4, **175**;
AS+BI+IS-WeM6, 125
- Szulfarska, I.: TR+AS+NS+SS-MoA6, **51**
- Szotek, D.: AC+MI+SA+TF-MoA8, 29
- Szulczewski, G.J.: EN+SE+SS+TF-WeM9, **132**
- T —**
- Tague, T.: EW-TuM8, 59
- Tahara, K.: SS+AS+NS+SP-WeA11, 167
- Tahara, S.: PS-ThA4, 218
- Taheri, T.: SS+AS+NS+SP-WeA1, 166
- Taing, J.: SS+EN-ThM9, 196
- Tait, S.L.: SS1-ThA4, **224**
- Tak, Y.J.: EM+PS-WeM4, 128; TC+EM+TF-WeM2, 143; TC+EM+TF-WeM4, **144**
- Takagi, N.: SS2-ThA8, 227
- Takahara, A.: TR+SE-TuM2, 73
- Takahashi, R.: TF-ThP21, **244**
- Takamizawa, H.: AP+AS+EM+MI+TF-WeM10, 124
- Takano, I.: SS-TuP11, 116; SS-TuP20, 118
- Takao, Y.: PS-MoM1, 19; PS-ThM1, 190
- Takarai, Y.: NS-TuP7, 107
- Takats, Z.: AS+BI+IS-WeM2, 124
- Takeda, K.: PS1-TuA10, 92; PS2-TuA11, 94; PS-ThA6, 218; PS-TuP11, 110; PS-WeM2, 137
- Takekuma, S.: SS-TuP5, 115
- Takemura, S.: NS-TuP1, 106; NS-TuP6, **107**; NS-TuP7, 107; NS-TuP8, **107**; TF-ThP28, 245
- Takeshita, Y.: MN+AS+SS-MoM10, 15
- Takeuchi, N.: SP+AS+BI+MI+NS+SS-ThM3, 194
- Takeuchi, R.: NS-TuP8, 107
- Takeuchi, T.: PS2-TuA11, 94; PS-WeM2, 137
- Tallarek, E.: AS-ThP12, 232
- Tallarida, M.: EM+PS-TuM10, 58
- Tamanaha, C.R.: BI+NL+NS+SS-ThM12, 178;
GR+AS+BI+PS+SS-ThA6, 210
- Tamura, M.: TF-ThP35, **246**
- Tamura, Y.: PS-ThA8, 219
- Tan, R.: SS-TuP20, **118**
- Tan, X.: EL+AS+EN+PS+SS+TF-ThM4, 178
- Tang, J.: SP+AS+BI+EM+MI+NS+SE+SS-ThA1, 222
- Tang, L.: SP+AS+BI+MI+NS+SS-ThM5, 194
- Tang, S.W.: MI-MoM10, **14**; MI-MoM9, 14
- Tang, Y.H.: MN-TuP1, 104; MN-TuP2, 105; MN-TuP3, **105**
- Tarafdar, R.: EM-ThA6, 207
- Tasnádi, F.: SE+NS+TF-ThA3, 220
- Tassa, C.: NL+AS+BI-ThA3, 217
- Tatsumi, T.: PS-MoM1, 19; PS-TuP30, 113
- Taubert, I.: BI+AS+IS+NL-MoM3, 6
- Taubman, M.S.: SP+AS+BI+NS-ThP2, 241
- Taylor, A.D.: NS+BI+EM-WeA7, **162**
- Taylor, D.M.: EM+AS+EN+TF-ThM10, 181
- Tazzoli, A.: MN-TuP4, 105
- Tchernycheva, M.: AP+AS+SS-TuA12, 79
- Tedesco, J.L.: EL+AS+EM+SS+TF-WeA1, 155
- Teh, K.: TC+EM+TF-WeM1, 143
- Tekinay, A.B.: SE-ThP11, 240
- Temmerman, W.M.: AC+MI+SA+TF-MoA8, 29
- Tempas, C.: SS1-ThA4, 224
- Temple, D.S.: EM+NS+TF-FrM6, 249
- Tenent, R.C.: TF+PS-ThM5, 200
- Teng, D.: SS+AS+NS-MoM10, **23**
- Tengco, J.M.M.: SS-TuP16, 117
- Tennyson, J.C.: PS-TuP21, 112; PS-TuP32, 114
- ter Veen, R.: GR+AS+NS+SP+SS-TuA9, 85
- Terfort, A.: SS+AS+NS+SP-WeA10, 167; SS1-ThA11, **225**; TF+AS+BI+EM+SE+SS-WeA7, 172; TF+AS+BI+EM+SE+SS-WeA8, 172
- Terrani, K.A.: AC+AS+EN-TuA1, 77
- Terry, W.D.: TF+AS+NS+SE-WeA11, 174
- Terry, H.A.: PS+AS+BI+SE-MoM5, 18; SE+PS-WeA7, 164; SS+AS+NS+SP-WeA1, **166**;
TF+EM+NS+SS-FrM11, 262
- Terstoff, J.: SS+AS+NS-MoM4, **22**
- Tesch, P.: AS-MoA1, 29
- Tessier, P.-Y.: NS+AS+EM-MoA4, 42
- Thejjoisworo, B.: PS-MoM6, **21**
- Theilacker, W.: AS+BI-TuA3, **80**
- Therien, M.: NS+BI+EM-MoM9, 17
- Thersleff, T.: MI+EM+MG-MoA1, 38
- Thevuthasan, S.A.: AP+AS+MI+NS+SS-WeA1, **150**; AP+AS+MI+NS+SS-WeA2, 150; AP-TuP1, 100; HI-ThA9, 213; NS-TuP12, 108;
TC+EM+TF-WeM3, 144
- Thiel, P.A.: AS+BI-TuA10, **81**; SS+AS+NS-MoM11, 23
- Thimsen, E.: EN+PS+TF-MoM10, 11
- Thippesamy, V.: GR-ThP4, 236
- Thissen, A.: IS+AS+SS-ThM11, 187;
SP+AS+EM+GR+MI+NS+SS-FrM2, **257**
- Thissen, N.F.W.: TF-ThP16, 243
- Thissen, P.: SS+EM-WeA11, 169
- Thomas, C.: PS-ThA8, **219**
- Thomas, J.C.: SP+AS+BI+EM+MI+NS+SE+SS-ThA12, **223**
- Thoms, B.: EM+NS+SS+TF-FrM4, 247
- Thorpe, R.: EN-TuP7, 103; IS+EN+SP+SS-ThA9, **215**
- Thrun, X.: PS2-TuM1, 67
- Thundat, T.G.: MN+AS+SS-MoM1, **14**
- Thyparambil, A.A.: BI+AS+BA+NS+SS-ThA8, **204**
- Tian, H.: BI+AS+BA+NS+SS-ThA12, 205
- Tian, Z.-Y.: HI-ThA7, 213
- Tillocher, T.: PS2-TuA4, **93**; PS-TuP1, 109
- Timilsina, R.T.: HI-ThM11, **186**
- Timm, R.: EM+TF-MoM6, **8**; MI-MoM11, 14
- Titov, A.: EM-TuA7, 83
- Tkach, I.: AC+AS+EN-TuA7, 77
- To, B.N.: PS-MoA6, 45
- Tobe, Y.: SS+AS+NS+SP-WeA11, 167
- Tobin, J.G.: AC+MI+SA+TF-MoM9, **2**
- Todorovic, M.: SS+AS+NS+SP-WeA7, 166
- Tomoya, T.: NS-TuP6, 107
- Tompkins, B.D.: TF+PS-ThM1, **199**
- Tonchev, S.: NS+BI+EM-WeA9, 162
- Topolancik, J.: BI+AS+BA+NS+SS-ThA12, 205
- Torres, F.: SS-TuP34, 119
- Torres, J.M.: EM+AS+PS+TF-ThM9, **182**
- Tosa, M.: TR-TuP2, 120
- Tosun, B.S.: EN+PS+TF-MoM4, 9
- Toyoda, S.: GR+EM+NS+PS+SS+TF-MoM4, 11
- Tran, D.: GR+EM+NS+SP+TF-MoA1, 36
- Tran, G.: SP+AS+BI+EM+MI+NS+SE+SS-ThA12, 223
- Tran, I.C.: NL+AS+BI+SA-FrM5, 255; SA-TuP1, 114
- Tran, T.: TF-ThP19, 244
- Travis, J.: TF+AS+SE+SS-MoA8, 50
- Treacy, C.: TC+EM+EN+TF-WeA3, 170
- Trenary, M.: SS+AS+NS+SP-WeA9, 167; SS-TuA7, 96
- Trogler, W.C.: BI-TuP3, 100; BI-WeM9, 127
- Trolier-McKinstry, S.: MN+NS-TuM3, **62**
- Tromp, R.M.: GR+AS+NS+SP+SS-TuA1, 85; SS-TuA9, **96**
- Tryggvason, T.K.: PS+TF-MoA9, 44
- Tsai, A.P.: AS+BI-TuA11, **81**
- Tsai, H.-Z.: GR+AS+EM+NS+SS-WeA11, 160
- Tsai, M.Y.: PS+AS+BI+SE-MoM4, 18
- Tsang, S.C.E.: AP+AS+MI+NS+SS-WeA7, 150
- Tse, J.: IA+BA-TuA12, 86
- Tshabalala, M.A.: AS-ThP19, **233**
- Tsoi, S.: GR+AS+BI+PS+SS-ThA6, 210
- Tsuiji, O.: PS-TuP33, 114
- Tsujino, J.: PS1-TuM12, **67**
- Tsukagoshi, K.: GR+AS+BI+PS+SS-ThA8, 210
- Tsutsumi, T.: PS1-TuA10, **92**
- Tu, C.: AS-ThP4, 231
- Tu, Q.: GR+AS+EM+NS+SS-WeA1, **159**
- Turchanin, A.: GR+EM+NS+PS+SS+TF-MoM8, **12**
- Turkot, R.: EM+AS+PS+TF-ThM9, 182
- Turner, K.L.: MN-TuP4, 105; MN-TuP5, 105
- Turner, K.T.: TR+AS-MoM10, 26; TR+AS-MoM5, 25
- Turner, M.M.: PS1-TuA1, 91
- Turner, S.: MS+AS+BA+BI+PS+TF-TuM9, **63**
- Turro, N.T.: BA+AI+AS+BI+IS+NL-MoM1, 5

- Tutt, L.W.: TF-TuA3, 97
Tutuc, E.: EM-WeA7, **158**
Tyagi, P.: GR-WeM1, 132
Tyler, B.J.: AS+BI-MoM9, **4**
Tyliczszak, T.: AC+AS+EN-TuA10, 78
Tymchenko, N.: BI+AS+BA+NL-TuM6, 56
Tyrode, E.C.: IA+AI+BI+IS+NL+SS-MoA7, **37**
Tysoe, W.T.: SS-ThM5, **197**
- **U** —
Uchida, G.: EN+AS+NS+SS-MoA3, **34**; EN-TuP2, 103; PS+TF-MoA11, 45
Uddin, M.: EM+NS+SS+TF-FrM5, 247
Ueda, H.: TF+PS-ThM12, 201
Ueda, S.: MI+AS+NS+SP-TuA7, 87
Uehara, S.: PS-TuP33, 114
Uhl, F.: SS+AS-TuM12, 71
Ulfig, R.: AP+AS+EM+MI+TF-WeM10, 124
Ulrich, S.: TR+SE-TuM5, 73
Umeki, T.: GR-ThP12, **237**
Únal, B.: AS+BI-TuA10, 81
Upadhyay, R.: PS-ThM9, 191
Ushikubo, T.: AP+AS+EM+MI+TF-WeM10, 124
Utz, A.L.: SS2-ThA10, **227**
- **V** —
Vahdat, V.: TR+AS-MoM10, 26
Vail, M.: TF+EM+NS+SS-FrM4, 261
Vaish, A.: BI+AS+BA+NS+SS-ThA1, 203
Vaithiyalingam, S.: TF+EM+NS+SS-FrM5, 261
Valencia, D.: SS-TuP3, 115
Vallee, C.: PS+TF-MoA8, **44**
Valley, J.: AP+AS+EM+MI+TF-WeM10, 124
Vallier, L.: PS-MoM5, 20
Valtiner, M.: BI+AS+BA+NS+SS-ThA9, **204**;
IA+AI+BI+IS+NL+SS-MoA11, 38;
IS+AS+SP-FrM4, 252; IS+EN+SP+SS-ThA6, **215**
Van Benthem, M.H.: AS-WeA9, 152
van Buuren, T.W.: NL+AS+BI+SA-FrM5, **255**;
SA-TuP1, 114
van de Sanden, M.C.M.: EN+AS+NS+SS-MoA9, 35; EN+AS+PS-TuA11, **84**;
GR+AS+BI+PS+SS-ThA1, 209; PS1-TuA12, 92; TF+VT-WeM1, 146; TF+VT-WeM6, 147
Van de Walle, C.G.: MI+EM+MG-MoA6, **39**
van den Bruele, F.: TF-TuA10, 97
Van Duyn, R.P.: SS+AS+NS+SP-WeA2, 166
van Dyk, B.: PS-MoA7, 46
Van Elshocht, S.: EM+PS-TuM10, 58; EM+TF-MoM2, 8; TF+AS+SE+SS-MoA9, 50
van Gastel, R.: HI-ThP4, 238
van Hest, M.F.A.M.: TC+EM+EN+TF-WeA7, **170**
Van Look, L.: MS+AS+EM+NS+PS+TF-MoA6, 41
Van Spyk, M.H.C.: IA+AI+BI+IS+NL+SS-MoA10, 38; SS+AS-WeM11, **141**
van Swaaij, R.A.C.M.M.: EN+AS+NS+SS-MoA9, 35
van 't Erve, O.M.J.: MI+EM-TuM5, 61
Van Tassell, B.J.: TC+EM+TF-WeM9, 144
van Veldhoven, E.: HI-ThM12, 186
Van Veldhoven, J.: SE+PS-WeA10, 165
van Zijll, M.S.: NS+BI+EM-WeA3, 161
Vandencastele, N.: PS+AS+BI+SE-MoM5, 18; SE+PS-WeA7, **164**
Vanderah, D.: BI+AS+BA+NS+SS-ThA1, 203
Vandervorst, W.: SA+AS+MG+SS-TuA9, 95
Vanfleet, R.R.: MN+AS+SS-MoM4, 15; MN+AS+SS-MoM5, 15; TF+PS-ThM2, **200**;
TF+PS-ThM6, 200; TF+PS-ThM9, 200; TF+VT-WeM11, 147
Vanleuven, D.: TF+VT-WeM9, 147
Varga, T.: AP+AS+MI+NS+SS-WeA1, 150; NS-TuP12, 108
Vargas, M.: TF+AS+EM+NS+SS-ThM10, **199**
Vasen, T.: EM+TF-MoM8, 9
Vázquez, D.: EM-ThP1, 234; SS-TuP22, 118
Vazquez-de-Parga, A.L.: GR+AS+EM+MI+MN-TuM1, **59**
- Veal, T.D.: EM2-ThA10, 206; EM2-ThA8, **205**
Vecchione, T.: VT+AS+SS+TF-WeA11, 174
Veenendaal, M.: SS+EN-ThM9, 196
Vega Lozada, E.: SS-TuP34, 119
Vega, A.: EM+TF-MoM10, 9; SS+EM-WeA11, **169**
Velasco Jr, J.: GR+EM+NS+SP+TF-MoA1, 36
Veligura, V.: HI-ThP4, 238
Vella, A.: AP+AS+SS-TuA10, 79; AP+AS+SS-TuA12, 79
Velsko, S.P.: AS+BI-TuA1, 80
Venkataraman, S.: PS-ThA12, 220
Venneguès, P.: TF+EM+NS+SS-ThA8, 229
Ventrice, Jr., C.A.: GR-WeM1, **132**
Ventzek, P.: PS-ThM9, **191**; PS-TuP19, 111; PS-TuP20, 111; TF+PS-ThM12, 201
Vera, D.: BI-TuP3, 100
Veres, J.: TC+EM+TF-WeM9, 144
Verheijen, M.A.: EM+MI+NS+SS+TF-TuA9, 82; TF+EN-MoM10, 25
Verhoeven, P.: SE+PS-WeA8, 165
Verkhoturov, S.V.: AS+BI+EM+NL+NS+SS-ThM3, 175
Versloot, T.W.: SE+PS-WeA10, 165
Versluis, R.: VT+EN+TF-TuA9, **98**
Viale, L.: VT-WeM3, 148
Vieker, H.: GR+EM+NS+PS+SS+TF-MoM8, 12; HI-ThA7, **213**; HI-ThP2, 238; HI-ThP3, 238
Vijayalakshmi, S.: GR-ThP4, **236**
Vilayurganapathy, S.: NS-TuP12, 108
Visart de Bocarmé, T.: AP+AS+MI+NS+SS-WeA11, 151
Vispute, R.D.: EW-TuL6, **76**
Viswanathan, V.: HI-ThA3, 212
Visweswaran, B.: TF+VT-WeM2, **146**
Viveros, R.: BI-TuP3, 100
Viville, P.: PS+AS+BI+SE-MoM5, 18
Vlcek, J.: SE+NS+TF-ThA6, 221
Voevodin, A.A.: SE+EN-FrM4, **256**; SE+PS-ThM5, **192**
Vogel, E.M.: EM1-WeM5, **130**; EM-WeA9, 158; GR+EM+MS+NS+SP-FrM3, 250; NS+AS+EN+SS-TuA11, 90
Vohs, J.M.: IS+EN+SP+SS-ThA1, 214
Voigtlaender, B.: SP+AS+EM+GR+MI+NS+SS-FrM8, **258**
Volksen, W.: EM+AS+PS+TF-ThM3, 182
Voronin, S.: MS+AS+EL+EM+PS+TF-TuA9, 89; PS1-TuM5, **66**
Vummaneni, K.: TR+AS+NS+SS-MoA3, 51
Vurpillot, F.: AP+AS+SS-TuA10, 79; AP+AS+SS-TuA12, 79
- **W** —
Wade, S.A.: BI+AI+BA+IS-MoA1, **31**
Wagner, B.P.: EM-ThP17, 236
Wagner, F.T.: TF+EN-MoM11, 25
Wagner, G.: AC+AS+EN-TuA10, 78
Wagner, H.D.: BI+AI+AS+BA+IA+NL+NS+SP-WeA9, 154
Wagner, J.: BI+NL+NS+SS-ThM11, 178
Wagner, M.: SS+AS-TuM9, 70
Wagner, S.: TF+VT-WeM2, 146
Wakayama, Y.: SS1-ThA8, 225
Walker, A.V.: EM+AS+EN+TF-ThM6, **181**
Walker, M.: BI+AS+BA+NS+SS-ThA1, **203**
Wall, M.: EW-WeM8, 132
Wallace, D.: EN+SE+SS+TF-WeM9, 132
Wallace, R.M.: EM+TF-MoM10, 9; EM+TF-MoM5, 8; GR+AS+BI+PS+SS-ThA7, 210; GR+EM+NS+SS+TF-ThA1, 211
Walle, L.E.: SS-MoA9, 48
Wallin, C.: BI+AS+BA+NS+SS-ThA12, 205
Wallin, M.: BI+AS+BA+NL-TuM5, 56
Wallin, P.: BI+AS+BA+NL-TuM6, 56
Walsh, J.W.: AS+BI+IS-WeM5, 125
Walters, D.: SP+AS+BI+MI+NS+SS-ThM10, 195
Walters, D.R.: VT-WeM5, 148
Walton, J.: AS+BI-MoM4, 3
- Walton, S.G.: EM+AS+EN+TF-ThM5, 180; GR+AS+BI+PS+SS-ThA6, 210; PS-ThA1, **218**; PS-ThA11, 220
Waluyo, I.: SS-TuA7, **96**
Wan, W.: VT+AS+SS+TF-WeA11, 174
Wang: MS+AS+BA+BI+PS+TF-TuM3, 63
Wang, B.: EM+NS+SS+TF-FrM7, 247
Wang, C.: TF+AS+BI+EM+SE+SS-WeA12, **173**
Wang, C.C.: TF-ThP23, 234
Wang, C.S.: GR-WeM10, 144; NS+AS+EN+SS-TuA1, **89**; TF-ThP19, 244
Wang, C.W.: AS+BI+EM+NL+NS+SS-ThM11, 176; NS+AS+EM-MoA3, **42**
Wang, C.Z.: SS+AS+NS-MoM11, 23
Wang, D.: SE+NS+TF-ThA10, 221
Wang, F.: GR+AS+NS+SP+SS-TuA7, **85**;
GR+EM+NS+PS+SS+TF-MoM1, 11
Wang, G.T.: EN-TuM11, **59**
Wang, H.: EL+AS+EM+SS+TF-WeA8, 155; HI-ThP2, 238; SP+AS+BI+NS-ThP1, 240; TF+EM+NS+SS-FrM5, **261**
Wang, I.T.: EM+PS-TuM11, 58
Wang, J.: EM+AS+EN+TF-ThM2, 180; SS-TuP18, **117**
Wang, J.-C.: PS+AS+BI+SE-MoM3, **18**
Wang, K.: TR+AS+NS+SS-MoA10, 52
Wang, L.: EM-ThA2, 206; PS-MoA1, 45; TF+AS+EM+NS+SS-ThM6, **198**;
VT+AS+SS+TF-WeA10, 174; VT-MoA7, **52**
Wang, M.: EM-ThA2, 206
Wang, P.: AS-ThP4, **231**
Wang, P.Y.: BI+AS+IS+NL-MoM1, **6**; BI-TuP6, 101
Wang, S.: EW-TuM8, **59**; PS1-TuA11, 92; PS-TuP14, **110**
Wang, W.: EM+MI+NS+SS+TF-TuA10, **82**;
TF+EM+NS+SS-ThA1, 228
Wang, X.: MI+AS+NS+SP-TuA12, 88
Wang, Y.: GR+AS+EM+NS+SS-WeA11, 160; HI-ThA3, 212; MI+EM-TuM9, 61; NS+AS+BI+SP-WeM2, 135; SP+AS+BI+NS-ThP1, **240**; SS+AS-TuM6, 70
Wang, Y.-C.: AS+BI+EM+NL+NS+SS-ThM6, 175
Wang, Z.: MN+NS-MoA8, **40**; MN+NS-TuM6, 63; NS+AS+BI+SP-WeM2, 135
Wang, Z.T.: SS+EN-ThM1, 195; SS-MoA8, **48**
Wang, Z.W.: SS+EN-ThM12, 196
Wang, Z.Y.: GR+EM+NS+SS+TF-ThA10, 212
Ward, T.Z.: TF+AS+EM+NS+SS-ThM1, **198**
Waschke, S.: SE+NS+TF-ThA4, 220
Waser, R.: EM+PS-WeM1, 128
Wasio, N.A.: TF+AS+BI+EM+SE+SS-WeA10, **172**
Watanabe, J.: TF-ThP34, 245
Watanabe, K.: SS1-ThA10, 225
Watanabe, N.: PS-ThA10, **219**
Watanabe, Y.: NS-TuP6, 107; NS-TuP7, 107; NS-TuP8, 107
Wayment-Steele, H.K.: BI+AI+AS+BA+IA+NL+NS+SP-WeA11, **154**
Weaver, J.F.: SS+AS-TuM11, 70; SS-MoA3, **47**
Weber, J.W.: GR+AS+BI+PS+SS-ThA1, 209
Weber, M.: TF+EN-MoM10, **25**
Weber, N.J.: GR+EM+NS+PS+SS+TF-MoM8, 12; SA+AS+MI+SS-WeM4, 139
Weber, O.: EM+PS-TuM2, 57
Weber, P.K.: AS+BI-TuA1, **80**
Weeks, S.L.: GR+AS+BI+PS+SS-ThA1, **209**
Wege, S.: PS2-TuM1, **67**
Wei, M.: TF+EM+NS+SS-FrM10, **262**
Wei, Y.: BI+AS+BA+NS+SS-ThA8, 204
Weickert, J.: EN+SE+SS+TF-WeM6, 131
Weidner, T.: BA+AI+AS+BI+IS+NL-MoM10, **5**;
BA+AI+AS+BI+IS+NL-MoM5, 5
Weiland, C.: AS-WeA12, 153; SA+AS+MI+SS-WeM3, **139**
Weiner, S.: BI+AI+AS+BA+IA+NL+NS+SP-WeA9, 154

- Weinert, M.: GR+AS+EM+MI+MN-TuM12, 61; GR+AS+EM+NS+SS-WeA2, 159
- Weiss, P.S.: SP+AS+BI+EM+MI+NS+SE+SS-ThA12, 223
- Weissleder, R.: NL+AS+BI-ThA3, 217
- Weitz, D.A.: BI+AS+IS+NL-MoM5, 6
- Welzel, S.: EN+AS+PS-TuA11, 84; PS1-TuA12, 92
- Wendt, A.E.: PS1-TuA11, 92; PS-TuP14, 110
- Wendt, S.: SS+AS-TuM3, 69
- Weng, C.J.: MI-TuP1, 104
- Weng, T.-C.: AC+AS+EN-TuA10, 78
- Werner, U.: HI-ThP3, 238
- Werner, W.S.M.: AS-TuM3, 54
- Wernersson, L.-E.: EM+TF-MoM6, 8
- Wheeler, V.D.: GR+EM+MS+NS+SP-FrM4, 250; GR+EM+NS+PS+SS+TF-MoM3, 11
- Whitchurch, C.B.: BI+AI+BA+IS-MoA9, 32; BI-TuP6, 101
- Whitcomb, R.: EN-TuP7, 103
- Whiting, G.L.: TC+EM+TF-WeM9, 144
- Whitten, D.G.: BI-WeM2, 126
- Whitten, J.: SS-FrM2, 258
- Whittle, J.D.: BI-WeM6, 126
- Wiame, F.: SS+AS+NS-MoM9, 23
- Wichmann, A.: SS+NS-WeM11, 143
- Widom, M.: GR-WeM3, 133
- Wijewarnasuriya, P.S.: EM+NS+TF-FrM6, 249
- Wilde, K.N.: BI-WeM2, 126
- Wilkens, H.: SS+AS-TuM11, 70
- Willem Weber, J.: EN+AS+NS+SS-MoA9, 35
- Willett-Gies, T.: EL+AS+EN+PS+SS+TF-ThM12, 179; EL-ThP2, 234; EL-ThP3, 234
- Willey, T.M.: NL+AS+BI+SA-FrM5, 255; SA-TuP1, 114; SS+NS-WeM11, 143
- Williams, A.: EM+AS+EN+TF-ThM10, 181
- Williams, A.I.: PS-TuP21, 112
- Williams, D.: EM+NS+TF-FrM10, 250
- Williams, G.P.: TF+AS+EM+NS+SS-ThM6, 198
- Williams, M.D.: GR+EM+NS+SP+TF-MoA6, 36; NS+AS+EN+SS-TuA12, 90
- Williams, P.: BI+AS+IS+NL-MoM8, 7; BI-WeM11, 127
- Williams, P.S.: TF+AS+SE+SS-MoA6, 49
- Wilson, C.J.: PS-MoA9, 46
- Wilson, T.: EN+SE+SS+TF-WeM3, 131
- Windl, W.E.: MG+EN+MS-WeA7, 161
- Winkler, D.A.: BI+AS+IS+NL-MoM8, 7; NL+AS+BI-ThA3, 217
- Winkler, K.: SA+AS+MI+SS-WeM4, 139
- Winroth, G.: TF+AS+SE+SS-MoA9, 50
- Winter, B.: IA+AI+BI+IS+NL+SS-MoA10, 38; SS+AS-WeM11, 141
- Winter, C.H.: TF+AS+SE+SS-MoA1, 49
- Winterstein, J.: IS+AS+SP-FrM8, 252
- Wirtz, T.: HI-ThA11, 214
- Wiseman, M.E.: BI+AS+BA+NL-TuM11, 56
- Wislon, K.: VT-WeM11, 148
- Wissing, S.N.P.: MI-MoM8, 14
- Wistey, M.: EM+TF-MoM8, 9
- Wittstock, A.: SS+NS-WeM11, 143
- Woicik, J.C.: SA+AS+MG+SS-TuA7, 95
- Wolcott, C.A.: SS-MoA2, 47
- Wold, K.A.: BI-WeM12, 127
- Wolden, C.A.: EN+PS+TF-MoM5, 10; EN+PS+TF-MoM6, 10; PS+AS+NS+SS-ThM11, 189; TF+PS-ThM5, 200
- Wolf, M.: SS2-ThA4, 226; SS2-ThA6, 226
- Wolf, S.A.: TF+AS+EM+NS+SS-ThM5, 198
- Woll, A.R.: EM+AS+EN+TF-ThM1, 180
- Wöll, C.: SS-FrM9, 260
- Woll, K.: TF-ThA3, 230
- Womack, F.: SS+NS-WeM12, 143
- Won, J.H.: EM-ThA11, 208
- Won, Y.: TC+EM+EN+TF-WeA1, 169
- Wong, D.: GR+AS+EM+NS+SS-WeA11, 160
- Wong, H.-S.P.: EM+MI+NS+SS+TF-TuA11, 83; MS+AS+EL+EM+PS+TF-TuA1, 88
- Woo, J.C.: TC+EM+EN+TF-WeA4, 170
- Woo, J.C.S.: EM-WeA10, 158
- Wood, T.: TF+PS-ThM2, 200
- Woodall, J.: EM-TuA9, 84
- Wouters, D.J.: EM+PS-TuM5, 57
- Wright, A.E.: AS+BI-MoM3, 3; AS-ThP1, 231; AS-WeA11, 152; EW-TuL4, 76
- Wright, N.G.: GR+EM+MS+NS+SP-FrM4, 250
- Wu, A.: SE-ThP9, 240; TF+AS+BI+EM+SE+SS-WeA12, 173
- Wu, F.: AP+AS+SS-TuA11, 79
- Wu, H.M.: TF+AS+NS+SE-WeA10, 173
- Wu, J.: TR+AS+NS+SS-MoA10, 52
- Wu, M.-F.: PS-ThM5, 191
- Wu, P.-J.: TF-ThP17, 244
- Wu, R.Q.: NS+AS+EN+SS-TuA2, 89; SS+AS+NS+SP-WeA3, 166; SS+EN-ThM11, 196
- Wu, W.: MI+AS+NS+SP-TuA12, 88
- Wu, Y.: EM+MI+NS+SS+TF-TuA11, 83
- Wu, Y.L.: SE+PS-WeA9, 165
- Wu, Z.: BI-TuP3, 100
- Wuchter, P.: BI+AS+MI+NL-MoM3, 6
- Wuest, M.: VT-MoA6, 52
- Wüest, M.: VT-MoM9, 27
- Wurch, M.: TF-ThP19, 244; TF-ThP20, 244
- Wurth, W.: SS2-ThA4, 226
- Wygladacz, K.A.: BI-TuP14, 102
- Wyrick, J.: GR-WeM10, 134
- X —
- Xia, D.Y.: TF+AS+NS+SE-WeA10, 173
- Xia, Y.: SS-FrM4, 259
- Xiao, D.: GR+EM+NS+SS+TF-ThA3, 211
- Xiao, K.: TC+EM+TF-WeM12, 144
- Xie, K.: SS-TuA11, 96; SS-TuP16, 117
- Xie, X.: TF+VT-WeM5, 146
- Xing, H.: EM+TF-MoM8, 9; EM-ThA10, 208; GR+EM+NS+SP+TF-MoA2, 36
- Xiong, Z.: PS+AS+BI+SE-MoM3, 18
- Xu, C.: SS+AS+NS+SP-WeA3, 166
- Xu, H.: VT-WeM11, 148
- Xu, K.: GR+EM+MS+NS+SP-FrM7, 251
- Xu, Q.: EN+SE+SS+TF-WeM4, 131
- Xu, W.: AS-ThP3, 231
- Xu, Y.: SS+AS+NS-MoM10, 23; SS+NS-WeM12, 143; SS-MoA11, 48
- Xue, J.: EM-TuA7, 83
- Y —
- Yaegashi, H.: PS2-TuM2, 67
- Yakimova, R.: EL+AS+EM+SS+TF-WeA2, 155
- Yakshinskiy, B.V.: VT+EN+TF-TuA7, 98
- Yamada, H.: NS+AS+BI+SP-WeM3, 135
- Yamada, T.: SE+EN-FrM6, 256; SS1-ThA10, 225
- Yamaguchi, K.: TF-ThP19, 244; TF-ThP20, 244
- Yamakawa, K.: SS-TuP5, 115; SS-TuP7, 115
- Yamamoto, H.: PS-MoM4, 20
- Yamamoto, M.: GR+AS+NS+SS-ThM3, 183
- Yamamoto, S.: SS+EN-ThM10, 196
- Yamamoto, Sh.: SS+EN-ThM10, 196
- Yamamoto, T.: TC+EM+EN+TF-WeA12, 171
- yamamura, T.: EM-ThA2, 206
- Yamanaka, T.: TC-TuP5, 119
- Yamashita, D.: PS+TF-MoA11, 45
- Yamashita, I.: PS-ThA8, 219
- Yamato, M.: PS2-TuM2, 67
- Yan, C.: PS-MoA6, 45
- Yan, C.Y.: IA+BA-TuA9, 86
- Yan, H.: SS-TuA11, 96; SS-TuP12, 117
- Yan, Y.: SE+NS+TF-ThA10, 221
- Yang, B.: EM-MoA6, 33; MG+AS+EM+NS+SA+SE+SP+SS+TF-FrM5, 254
- Yang, C.C.: MN-TuP1, 104; MN-TuP2, 105
- Yang, D.: EM+AS+PS+TF-ThM2, 181
- Yang, G.E.: GR+AS+NS+SP+SS-TuA10, 86
- Yang, G.-E.: GR-ThP9, 237
- Yang, H.: SS+AS+NS+SP-WeA9, 167
- Yang, J.: BI+AS+IS+NL-MoM8, 7; EM+AS+EN+TF-ThM6, 181; EM-WeA3, 158; IS+AS+SP-FrM1, 251
- Yang, K.: MI+EM-TuM10, 62; VT+AS+SS+TF-WeA10, 174
- Yang, L.: BI+AI+AS+BA+IA+NL+NS+SP-WeA2, 153
- Yang, P.: AC+AS+EN-TuA10, 78
- Yang, Q.: PS+AS+BI+SE-MoM11, 19; PS2-TuA8, 94; SS+NS-WeM10, 142
- Yang, R.: PS+AS+NS+SS-ThM12, 190
- Yang, X.: NS+AS+EN+SS-TuA2, 89
- Yang, X.-Q.: IS+EN+SP+SS-ThA3, 214
- Yang, Y.: EM-TuA7, 83; EN+SE+SS+TF-WeM5, 131; IS+AS+SP-FrM9, 252
- Yang, Y.C.: SE-ThP3, 239; SE-ThP4, 239
- Yang, Y.J.: PS+AS+BI+SE-MoM4, 18; SE+PS-WeA12, 165; SS-TuP8, 116; TF-ThP23, 244
- Yao, Y.: TF+AS+SE+SS-MoA4, 49
- Yarmoff, J.A.: GR+EM+NS+SS+TF-ThA10, 212; SS+AS+NS-MoM1, 21
- Yates, B.: SA+AS+MI+SS-WeM5, 139
- Yazdani, A.: MI-MoM3, 13
- Ye, D.: NS+BI+EM-MoM5, 17; TF+AS+NS+SE-WeA9, 173
- Ye, L.: NS+EM+EN-TuM12, 65; TF+AS+SE+SS-MoA7, 50
- Ye, P.D.: GR+EM+MS+NS+SP-FrM5, 250; GR+EM+MS+NS+SP-FrM7, 251
- Ye, Z.: TR+AS-MoM11, 26
- Yeates, S.: EM+AS+EN+TF-ThM10, 181
- Yee, S.: EW-WeL3, 149
- Yeh, Y.-C.: NS-TuP15, 109; TF-ThP17, 244
- Yen, L.B.: AS+BI+EM+NL+NS+SS-ThM11, 176
- Yeom, G.Y.: GR-ThP5, 236
- Yi, H.: MS+AS+EL+EM+PS+TF-TuA1, 88
- Yi, J.Y.: MI-MoM10, 14; MI-MoM9, 14
- Yin, F.: TF+AS+NS+SE-WeA11, 174
- Yin, H.: MS+AS+BA+BI+PS+TF-TuM1, 63
- Yin, J.: TF+EN-MoM11, 25; TF-TuM9, 72
- Yin, Y.: MS+AS+EL+EM+PS+TF-TuA4, 89; MS+AS+EL+EM+PS+TF-TuA9, 89
- Yngman, S.: EM+TF-MoM6, 8
- Yokoyama, N.: GR+AS+BI+PS+SS-ThA8, 210
- Yoo, H.J.: EM-ThA7, 207
- Yoon, D.H.: EM+PS-WeM4, 128; TC+EM+TF-WeM2, 143; TC+EM+TF-WeM4, 144
- Yoon, S.H.: TC+EM+TF-WeM2, 143; TC+EM+TF-WeM4, 144
- Yoon, Y.: SS-MoA6, 47
- Yoshida, T.: EM-ThA2, 206
- Yoshikawa, J.: PS-ThM9, 191; TF+PS-ThM12, 201
- You, B.Y.: TF-TuM5, 71
- You, K.H.: NS-TuP2, 106
- You, L.: BI-TuP9, 101
- You, S.J.: NS-TuP2, 106
- Young, L.E.: BI-WeM1, 126
- Young, M.J.: TF+EN-MoM5, 24
- Young, R.M.: EM-ThP17, 236
- Younkin, T.R.: MS+AS+EM+NS+PS+TF-MoA6, 41
- Yousaf, M.N.: BI+AS+IS+NL-MoM9, 7
- Yousuf, A.: EN+SE+SS+TF-WeM9, 132
- Yu, A.X.: SP+AS+BI+MI+NS+SS-ThM4, 194; SS+EN-ThM11, 196
- Yu, C.S.: MN-TuP1, 104
- Yu, H.: AS-MoA4, 29; SE+PS-ThM3, 192; SE-ThP2, 239; TF-TuM5, 71
- Yu, K.: AS-MoA4, 29; TF+EM+NS+SS-FrM3, 260
- Yu, L.: MG+EM+MI+MS-WeM3, 134
- Yu, S.: EM+MI+NS+SS+TF-TuA11, 83
- Yu, X.: IS+EN+SP+SS-ThA3, 214
- Yu, X.Y.: BI+AI+AS+BA+IA+NL+NS+SP-WeA2, 153
- Yu, Z.: EN-TuM9, 59; IS+EN+SP+SS-ThA2, 214
- Yuan, Z.: EM-MoA6, 33
- Yuk, Y.J.: TR-TuP8, 121

- Yukawa, R.: SS+EN-ThM10, 196
 Yulaev, A.: GR+AS+NS+SS-ThM2, **183**;
 IS+AS+SS-ThM5, 186
 Yun, W.S.: NS-TuP16, 109
 Yun, Y.: SS-ThM3, 197
 Yusuf, A.S.: HI-ThA3, 212
 — **Z** —
 Zacharias, H.: SS-ThM9, 197
 Zaera, F.: AS-ThP15, 232; SS+NS-WeM1, 141;
 SS-ThM2, 196; TF+AS+SE+SS-MoA4, 49;
 TF+EM+NS+SS-FrM7, 261
 Zaharia, T.: SS2-ThA12, 227
 Zaima, S.: SA-TuP4, 114
 Zakutayev, A.: MG+EM+MI+MS-WeM6, **134**
 Zandbergen, H.W.: HI-ThM12, 186
 Zandvliet, H.J.W.: HI-ThP4, 238
 Zardetto, V.: TF+EN-MoM6, 24
 Zauscher, S.: BI-TuP9, 101; GR+AS+EM+NS+SS-
 WeA1, 159
 Zeller, D.: EM+PS-WeM9, **129**; PS+TF-MoA3, 44
 Zeman, P.: SE+NS+TF-ThA6, **221**
 Zeng, Y.: SS-ThM12, 198
 Zettl, A.: GR+AS+EM+NS+SS-WeA11, 160
 Zhang, D.: IS-ThP1, **238**
 Zhang, F.: GR+EM+NS+SP+TF-MoA1, 36; SS-
 MoA3, 47
 Zhang, H.: HI-ThM10, 185; IS-ThP2, 238;
 MI+EM+MG-MoA2, 38; PS-TuP23, 112
 Zhang, J.: AS-ThP3, 231; NS+EM+EN-TuM4, 64;
 NS-TuP11, **108**
 Zhang, L.: AS-ThP8, 232; EM+PS-TuM5, 57; EM-
 MoA4, **33**; PS-MoA9, 46; TF+AS+SE+SS-
 MoA11, 50
 Zhang, Q.: EM+TF-MoM8, 9
 Zhang, X.: EN+PS+TF-MoM10, 11; SS+NS-
 WeM10, 142; SS-TuP34, **119**
 Zhang, Y.: PS+TF-MoA3, 44; PS1-TuA1, 91; PS1-
 TuM2, **65**; PS-WeM2, 137
 Zhang, Y.N.: SS+AS+NS+SP-WeA3, 166;
 SS+EN-ThM11, 196
 Zhang, Z.: IA+AI+BI+IS+NL+SS-MoA3, 37;
 SS+NS-WeM9, **142**; SS-FrM4, **259**; SS-MoA6,
 47
 Zhao, B.: EM+PS-WeM3, **128**
 Zhao, J.: SS+NS-WeM10, **142**
 Zhao, W.: MS+AS+EL+EM+PS+TF-TuA11, 89;
 SP+AS+EM+GR+MI+NS+SS-FrM8, 258
 Zhao, Y.: EN+SE+SS+TF-WeM4, 131
 Zhao, Y.P.:
 MG+AS+EM+NS+SA+SE+SP+SS+TF-FrM5,
 254
 Zhao, Z.: IS-ThP2, 238
 Zharnikov, M.: BI+NL+NS+SS-ThM5, 177; SS1-
 ThA11, 225; TF+AS+BI+EM+SE+SS-WeA8,
172
 Zhdanov, V.: EN+AS+NS+SS-MoA11, 35
 Zheng, H.: EM+AS+PS+TF-ThM12, **183**
 Zheng, R.Y.: AS-ThP16, **233**
 Zheng, X.: EM+PS-WeM3, 128
 Zheng, Y.: EM-TuA7, 83
 Zheng, Z.S.: EM-ThP2, **234**
 Zhou, C.: NS+AS+EM-MoA6, **42**
 Zhou, D.: NS+EM+EN-TuM4, 64
 Zhou, G.: EM+TF-MoM8, 9; IS+AS+SP-FrM1,
251
 Zhou, H.: MI+EM+MG-MoA10, 39
 Zhou, J.: SA+AS+MG+SS-TuA10, 95; SE+PS-
 WeA9, 165
 Zhou, W.: GR+EM+NS+SS+TF-ThA10, 212
 Zhou, Y.: HI-ThM10, **185**
 Zhou, Z.: SS+NS-WeM12, 143
 Zhu, H.: EM+TF-MoM8, 9
 Zhu, K.: SS-FrM4, 259
 Zhu, W.: PS1-TuM3, **65**; PS1-TuM4, 66; TF-
 ThP34, 245
 Zhu, W.-D.: NS+AS+EM-MoA3, 42
 Zhu, X.Y.: EN+AS+NS+SS-MoA1, **34**
 Zhu, Y.: GR-WeM10, 134; TF-ThP19, 244
 Zhu, Z.: BI+AI+AS+BA+IA+NL+NS+SP-WeA2,
 153; NS+AS+BI+SP-WeM2, **135**
 Ziggrosser, D.: VT-WeM11, 148
 Zimmermann, M.: NL+AS+BI-ThA7, 217
 Zingarelli, S.: BI+AI+BA+IS-MoA3, 31
 Zink, B.R.: EM-ThP13, 236
 Zinkle, S.J.: AC+AS+EN-TuA1, **77**
 Zoll, S.: EM+PS-TuM2, 57
 Zollner, C.J.: EL+AS+EN+PS+SS+TF-ThM12,
 179
 Zöllner, M.H.: SS+AS-TuM11, 70
 Zollner, S.: EL+AS+EM+SS+TF-WeA11, 156;
 EL+AS+EN+PS+SS+TF-ThM12, 179; EL-
 ThP2, 234; EL-ThP3, **234**
 Zonooz, P.S.: TF+PS-ThM10, 200; TF-ThP18, **244**
 Zorman, C.A.: PS+AS+NS+SS-ThM12, 190
 Zorn, G.: AS+BI-MoM8, **4**
 Zuber, S.: SS1-ThA9, 225
 Zufelt, K.: TF+PS-ThM2, 200
 Zuilhof, H.: AS+BI+IS-WeM11, **125**; TR+SE-
 TuM3, 73
 Zurek, E.: TF+AS+BI+EM+SE+SS-WeA9, 172
 Zwang, T.: BI+AS+BA+NL-TuM4, 56
 Zwicknagl, G.: AC+MI+SA+TF-MoA6, **28**